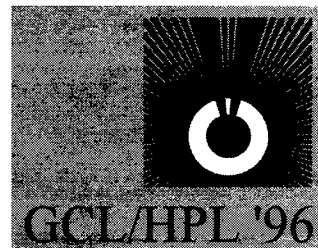


XI International Symposium on Gas Flow and Chemical Lasers *and* High-Power Laser Conference



Denis R. Hall
Conference Chair

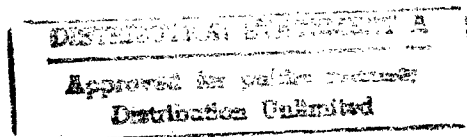
Howard J. Baker
Program Chair and Proceedings Editor

25-30 August 1996
Heriot-Watt University, Edinburgh, UK

Organised by:
Department of Physics, Heriot-Watt University

Sponsored by:
Engineering and Physical Sciences Research Council
European Office of Aerospace Research and Development (EOARD)
The International Science Foundation (ISF)
Lothian and Edinburgh Enterprise Ltd (LEEL)
Scottish Enterprise
Heriot-Watt University
City of Edinburgh Council
Institute of Physics, Quantum Electronics Group
Institution of Electronic Engineers
The Royal Society

Supported by:
Lumonics (UK) Ltd. ■ Melles Griot Ltd ■ Exitech Ltd ■ SPIE



Volume 3092

19970624 030

REPORT DOCUMENTATION PAGE

Form Approved OMB No. 0704-0188

Public reporting burden for this collection of information is estimated to average 1 hour per response, including the time for reviewing instructions, searching existing data sources, gathering and maintaining the data needed, and completing and reviewing the collection of information. Send comments regarding this burden estimate or any other aspect of this collection of information, including suggestions for reducing this burden to Washington Headquarters Services, Directorate for Information Operations and Reports, 1215 Jefferson Davis Highway, Suite 1204, Arlington, VA 22202-4302, and to the Office of Management and Budget, Paperwork Reduction Project (0704-0188), Washington, DC 20503.

1. AGENCY USE ONLY (Leave blank)		2. REPORT DATE 4 June 1997		3. REPORT TYPE AND DATES COVERED Conference Proceedings	
4. TITLE AND SUBTITLE XI International Symposium on Gas Flow and Chemical Lasers and High-Power Laser Conference				5. FUNDING NUMBERS F6170896W0143	
6. AUTHOR(S) Conference Committee					
7. PERFORMING ORGANIZATION NAME(S) AND ADDRESS(ES) Heriot-Watt University Riccarton Edinburgh EH14 4AS United Kingdom				8. PERFORMING ORGANIZATION REPORT NUMBER N/A	
9. SPONSORING/MONITORING AGENCY NAME(S) AND ADDRESS(ES) EOARD PSC 802 BOX 14 FPO 09499-0200				10. SPONSORING/MONITORING AGENCY REPORT NUMBER CSP 96-1029	
11. SUPPLEMENTARY NOTES					
11a. DISTRIBUTION/AVAILABILITY STATEMENT Approved for public release; distribution is unlimited.				12b. DISTRIBUTION CODE A	
13. ABSTRACT (Maximum 200 words) The Final Proceedings for XI International Symposium on Gas Flow and Chemical Lasers and High Power Laser, 25 August 1996 - 30 August 1996 The Topics covered include: Gas lasers, including CO2, CO, metal vapor, and xenon lasers; Iodine and chemical lasers; High average power lasers; excimer, VUV, XUV lasers; new high power laser media; laser source modeling; gas flow in lasers, including fluid dynamics, aero-optics.					
14. SUBJECT TERMS				15. NUMBER OF PAGES 788	
				16. PRICE CODE N/A	
17. SECURITY CLASSIFICATION OF REPORT UNCLASSIFIED	18. SECURITY CLASSIFICATION OF THIS PAGE UNCLASSIFIED	19. SECURITY CLASSIFICATION OF ABSTRACT UNCLASSIFIED	20. LIMITATION OF ABSTRACT UL		

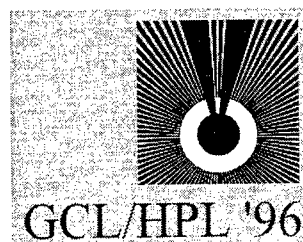
NSN 7540-01-280-5500

Standard Form 298 (Rev. 2-89)
Prescribed by ANSI Std. Z39-18
298-102

19970624 030

PROCEEDINGS

XI International Symposium on Gas Flow and Chemical Lasers *and* High-Power Laser Conference



Denis R. Hall
Conference Chair

Howard J. Baker
Program Chair and Proceedings Editor

25-30 August 1996
Heriot-Watt University, Edinburgh, UK

Organised by:
Department of Physics, Heriot-Watt University

Sponsored by:
Engineering and Physical Sciences Research Council
European Office of Aerospace Research and Development (EOARD)
The International Science Foundation (ISF)
Lothian and Edinburgh Enterprise Ltd (LEEL)
Scottish Enterprise
Heriot-Watt University
City of Edinburgh Council
Institute of Physics, Quantum Electronics Group
Institution of Electronic Engineers
The Royal Society

Supported by:
Lumonics (UK) Ltd. ■ Melles Griot Ltd ■ Exitech Ltd ■ SPIE

Published by
SPIE—The International Society for Optical Engineering



Volume 3092

SPIE is an international technical society dedicated to advancing engineering and scientific applications of optical, photonic, imaging, electronic, and optoelectronic technologies.



The papers appearing in this book comprise the proceedings of the meeting mentioned on the cover and title page. They reflect the authors' opinions and are published as presented and without change, in the interests of timely dissemination. Their inclusion in this publication does not necessarily constitute endorsement by the editors or by SPIE.

Please use the following format to cite material from this book:

Author(s), "Title of paper," in *XI International Symposium on Gas Flow and Chemical Lasers and High-Power Laser Conference*, Howard J. Baker, Editor, Proc. SPIE 3092, page numbers (1997).

ISSN 0277-786X
ISBN 0-8194-2507-9

Published by
SPIE—The International Society for Optical Engineering
P.O. Box 10, Bellingham, Washington 98227-0010 USA
Telephone 360/676-3290 (Pacific Time) • Fax 360/647-1445

Copyright ©1997, The Society of Photo-Optical Instrumentation Engineers.

Copying of material in this book for internal or personal use, or for the internal or personal use of specific clients, beyond the fair use provisions granted by the U.S. Copyright Law is authorized by SPIE subject to payment of copying fees. The Transactional Reporting Service base fee for this volume is \$10.00 per article (or portion thereof), which should be paid directly to the Copyright Clearance Center (CCC), 222 Rosewood Drive, Danvers, MA 01923. Payment may also be made electronically through CCC Online at <http://www.directory.net/copyright/>. Other copying for republication, resale, advertising or promotion, or any form of systematic or multiple reproduction of any material in this book is prohibited except with permission in writing from the publisher. The CCC fee code is 0277-786X/97/\$10.00.

Printed in the United States of America.

CONTENTS

Conference Committees	xv
Introduction	xvii
1. KEYNOTE ADDRESSES	
Applications of lasers with high beam quality in the electronics industry G.J.Notenboom <i>Philips Centre for Manufacturing Technology, The Netherlands</i>	2
High-brightness solid state lasers with phase-conjugating mirror and high average power H J Eichler, A Haase, B.Liu, O.Mahl <i>Technical University of Berlin, Germany</i>	9
2. SOLID STATE LASERS I	
High-average-power diode-pumped solid state lasers (Invited Paper) (Abstract Only) C.Bibeau, R.Beach, E.Honea, C.Marshall, S.Sutton, M.Emanuel, J.Skidmore, S. Payne <i>Lawrence Livermore National Laboratory, USA</i>	16
Design and industrial applications of high-power laser diodes P. Loosen, J.Biesenbach, K.Du, C.R.Haas, R.Propawe, H.-G.Treusch <i>Fraunhofer-Institut für Lasertechnik, Aachen, Germany</i>	17
Photorefractive phase-conjugator coupled-cavity diode laser for high-spectral-brightness operation A.Shiratori, M.Obara <i>Keio University, Japan</i>	21
Planar waveguide Nd:YAG laser face pumped by laser diode bars D.Pelaez-Millas, A.Faulstich, H.J.Baker, D.R.Hall <i>Heriot-Watt University, UK</i>	25
Diode-pumped 1-kHz high-power Nd:YAG laser with excellent beam quality, H.P.Godfried, H.L.Offerhaus <i>Nederlands Centrum voor Laser Research B.V., Enschede, The Netherlands</i>	29
High-energy diode-pumped slab amplifier M.J.Campbell, S.E.Jardine <i>Pilkington Optronics Ltd., Glasgow, UK</i>	33
3. SOLID STATE LASERS II	
High-average-power YAG lasers and applications (Invited Paper) H.Kanazawa, A.Nishimi, M.Uehara <i>Ishikawajima-Harima Heavy Industries Co, Ltd. K. Maeda, Y.Wakasa Ishikawajima System Technology Co. Ltd., Japan</i>	38
Stable resonators with variable reflectivity mirrors for multi-kW Nd:YAG lasers G.Bostanjoglo, Th.Beck <i>Laser- und Medizin-Technologie, Berlin R.Dommaschk INPRO, Berlin</i> H.Weber <i>Technischen Univ. Berlin, Germany</i>	44
High-energy Nd:Cr:GSGG lasers based on phase and polarisation conjugated multiple-pass amplifiers S.Jackel, I.Moshe, A.Kaufman, R.Lavi, R.Lallouz <i>Soreq NRC, Yavne, Israel</i>	48
High-average-power Nd:YAG laser with Cr ⁴⁺ :YAG passive Q-switch T Dascalu <i>Institute of Atomic Physics, Bucharest, Hungary H.Weber TU Berlin G.Phillips Laser und Medizin Technologie, Berlin, Germany</i>	52
Scaling Cr:LiSAF to high average power A.Mandl, D.E.Klimek, A.Zavriyev <i>Textron Systems Division, Wilmington, USA</i>	56
4. METAL VAPOUR AND NEAR-IR LASERS	
Average-power scaling of copper hybrid lasers (Invited Paper) L.Little, C.E.Little <i>St. Andrews University, UK</i>	62
Performance enhancement of elemental copper vapour lasers by bromine and hydrogenated bromine additives R.J.Carman, M.J.Withford, D.J.W.Brown, J.A.Piper <i>Macquarie University, Sydney, Australia</i>	68
CuBr vapor laser with a central electrode N.K.Vuchkov, N.V.Sabotinov, K.A.Temelkov <i>Bulgarian Academy of Sciences, Sofia, Bulgaria</i>	72

Experimental and theoretical investigation of a coaxial-pumped photolytic atomic bromine laser B.D.Rafferty, B.T.Anderson, J.Glassman, H.C.Miller, A.I.Lampson, G.D.Hager <i>USAF Phillips Laboratory, Kirtland Air Force Base, USA</i>	76
High pulse repetition rate helium-xenon laser D.A.Orchard, R.C.Hollins <i>DRA, Malvern, Worcs. UK</i>	82

5. DIFFUSION-COOLED CO₂ LASERS

High-power coaxial CO₂ waveguide laser R.Nowack, H.Bochum, Th.Hall, K.Wessel <i>DLR Inst. fur Tech. Phys., Stuttgart</i> B.Grubert <i>Bremen Inst. fur Ang. Strahltech., Bremen, Germany</i>	88
1-kW slab CO₂ laser excited by a self-excited rf generator S.Kobayashi, K.Terai, T.Tamangawa <i>Toshiba Corp., Kawasaki, Japan</i>	92
Experimental study of a DC-excited slab CO₂ laser discharge C.Leys, C.van Egmond, E.Desoppere <i>University of Ghent, Belgium</i>	96
Two-dimensional waveguide CO₂ laser arrays and beam reformatting R.Abram, P.Blair, F.Villarreal, A.D.Colley, H.J.Baker, M.R.Taghizadeh, D.R.Hall <i>Heriot-Watt University, UK</i>	100
Self-activated forced convective cooling in a pulsed slab CO₂ laser Y.Sintov, A.Gabay, S.Yatsiv <i>Racah Inst. Of Phys., Jerusalem, Israel</i>	104
High-power high-modulation bandwidth CO₂ laser D.Wheatley <i>James Howden & Co. Ltd., Dundee, UK</i>	109
Pulsed CO₂ laser with 15-kW average power at 100-Hz rep-rate M.Jung, W.Mayerhofer, G.Renz, E.Zeyfang <i>DLR Institut für Technische Physik, Stuttgart, Germany</i>	114

6. BEAM DELIVERY, BEAM SHAPING, AND NONLINEAR OPTICS

Hollow Fibre Beam Delivery Systems (Invited Paper) M.Miyagi, Y.Matsuura <i>Tohoku University, Japan</i>	120
Beam shaping for laser materials processing with nonrotationally symmetric optical elements T.Henning, M.Scholl, U.Habich <i>Fraunhofer-Inst. für Lasertechnik, Aachen</i> L.Unnebrink, R.Lebert, G.Herziger <i>Lehrstuhl für Lasertechnik, Aachen, Germany</i>	126
Energy enhancer for mask-based laser materials processing J.Bastue, F.O.Olsen <i>Tech. Univ. of Denmark, Lyngby, Denmark</i>	130
Physical and technical factors determining beam quality of high-power fast-transverse-flow CO₂ lasers M.G.Galushkin, V.S.Golubev, A.V.Korotchko, A.M.Zabelin <i>Scientific Research Center for Technological Lasers, Shatura, Russia</i>	134
Generation of continuously tuneable 16-μm radiation by four-wave mixing in a parahydrogen Raman cell L.R.Botha, C.J.Liebenberg <i>Atomic Energy Corp. of South Africa, Pretoria, South Africa</i>	138
Parametric study of intracavity degenerate four-wave mixing and phase conjugation of CO₂ and CO laser radiation in their inverted medium L.Afanas'ev, A.Ionin, Yu.Klimachev, A.Kotkov, L.Seleznev, D.Sinitsyn <i>P.N. Lebedev Phys. Inst., RAS, Moscow, Russia</i>	142

7. EXCIMER LASERS

High-efficiency excimer lasers (Invited Paper) V.F.Tarasenko <i>High Current Electronics Institute, Tomsk, Russia</i>	148
Prospects for high-average-power electron-beam-pumped KrF lasers for inertial confinement fusion and industrial applications M.J.Shaw <i>Rutherford Appleton Laboratory, UK</i>	154
60J XeCl laser for single-shot excimer laser annealing B.Godard, P.Laborde, C.Dutems, S.Prochasson, D.Zahorski, M.Stehlé <i>SOPRA, Bois-Colombes</i> J.Bonnet, D.Pigache <i>ONERA, Palaiseau, France</i>	161

- Stability of a 1-kW excimer laser with long optical pulses** J.C.M.Timmermans, T.Hofmann 165
Nederlands Centrum voor Laser Research, Enschede F.A.van Goor, W.J.Wittevan University of Twente, The Netherlands
- XeCl-excimer laser-MOPA chain for shock hardening** G.Hintz, R.Tkotz, C. Keusch, 169
M.Negendanck, J.Staudigel, J.Christiansen, D.H.H.Hoffmann *Bayerisches Laser-zentrum, Erlangen, K.Eisner, A.Lang, K.Schutte, H.W.Bergmann ATZ-EVUS, Vilseck, Germany*

8. FAST-FLOW AND PULSED CO₂ LASERS

- Fast Axial flow 25-kW CO₂ laser with unstable resonator for industrial applications** U.Habich, 174
U.-K.Jarosch, H.Maly, R.Meyer, P.Loosen, N.Wolf *Fraunhofer-Institut für Lasertechnik, Aachen*
T.Beck, C.Hertzler, R.Wollermann-Windgasse *Trumpf Laser-Forschungs- und Entwicklungsgesellschaft, Germany*
- Excitation frequency effects in a fast-axial-flow laser with a narrow gap slab RF discharge** 178
J.G.Betterton, H.J.Baker *Heriot-Watt University, UK*
- Investigation of beam quality and gain behaviour in a large aperture e-beam-controlled CO₂ laser** 182
W.Riede, W.Mayerhofer, Th.Hall, S.Walther *Inst. für Tech. Phys., Stuttgart, Germany*
- Continuous-wave carbon dioxide laser system producing output power up to 135 kW** 186
M.L.Lander, K.J.Maxwell *Anteon Corporation J.P.Reilly Northeast Science and Technology, Massachusetts R.J.Hull Wright Laboratory, Wright-Patterson AFB, USA*
- Optimisation of power deposition in rf-excited CO₂ lasers by adding gas additives to the laser gas mixtures** 190
C.Schmitz, W.Pfeiffer, A.Giesen, H.Hügel *Inst. für Strahlwerkzeuge, Stuttgart, Germany*

POSTER SESSION I

Carbon dioxide lasers:

- Working properties of compact rf-excited CO₂ slab lasers** A.Lapucci, F.Rossetti, S.Mascalchi 196
Istituto Nazionale di Ottica, Firenze, Italy
- Model of a glow discharge in a turbulent flow** G.Vlad, O.Boiron, G.Le Palec, P.Bournot 200
Institut de Mécanique de Marseille, France
- Laser marker built on multichannel or slab CO₂ lasers** E.F.Plinski, J.S.Witkowski, 206
K.M.Abramski *Technical University of Wroclaw, Poland*
- High-power microwave-excited CO₂ laser oscillator** D.Choo, Y.Takenaka, S.Yamane 210
Matsushita Industrial Equipment Co. Ltd., Osaka N.Furuya, M.Kato, Matsushita Res. Inst. Tokyo Inc., Kawasaki, Japan
- Parametric investigation of the small signal gain in a large aperture e-beam-controlled CO₂ laser** 215
W.Reide, W.Mayerhofer, Th.Hall, S.Walter, G.Renz *DLR, Stuttgart, Germany*
- Preionizing a large volume transversely excited subatmospheric-pulsed CO₂ laser for enhanced materials processing** 219
I.A.Watson, D.W.McDonald, B.Scott, C.Chatwin *University of Glasgow, UK*
- Enhanced CO₂ laser frequency doubling efficiency in AgGaSe₂** P.D.Mason, E.K.Gorton 223
DRA Malvern, UK
- Optimised homogeneity and stability of gas discharges in fast-flow CO₂ laser systems operating at the choking limit** 227
W.Pfeiffer, C.Schmitz, A.Giesen, H.Hügel *Inst. für Strahlwerkzeuge, Stuttgart, Germany*
- Temporal and spatial properties of a chopper disc Q-switched high-power CO₂ laser with an unstable resonator** 231
M.Jung, G.Renz, K.Wessel, W.Schock *DLR, Stuttgart, Germany*
- CO₂ laser excited by microwave discharge using stripline** 235
T.Tokoro, N.Matsuoka, M.Yasuda, T.Uchiyama *Keio University, Japan*

Modulation and pulse generation of a transverse flow high-power CO₂ laser by a Fabry-Perot modulator G.Michel, K.Schindler, G.Staupendahl, C.Ziener <i>Friedrich-Schiller University, Jena, Germany</i>	239
Investigation of rf-excited CO₂ slab laser discharges by measuring N₂ emission bands with high-spatial resolution U.Berkermann, A.Liffers, R.Hannemann, G.Jakob, C.Lücking, J.Mentel, G.Schiffner <i>Ruhr-Universität, Bochum, Germany</i>	243
Measurement of the impedance of rf-excited CO₂ slab lasers and discharge chambers C.Lücking, K.Fakler, U.Berkermann, J.Mentel, G.Schiffner <i>Ruhr-Universität, Bochum, Germany</i>	247
Compact four-wave mixing MOPA system with rotational symmetry W.Riede, Th.Hall <i>DLR Stuttgart, Germany</i>	250
Optical nonuniformities of active medium of high-power fast-axial-flow industrial CO₂ lasers M.G.Galushkin, V.S.Golubev, Yu.N.Zavalov, V.Ye.Zavalova, V.Ya.Panchenko <i>NICTL-RAN Laser Research Center, Shatura, Russia</i>	252
Planar waveguide 50-W cw CO₂ laser excited by a transverse radio frequency discharge with broad stripe matching network V.G.Leont'ev, V.A.Stepanov, E.F.Shishkanov <i>Pedagogical University, Ryazan</i> M.Z.Novgorodov, V.N.Ochkin <i>Lebedev Inst. Moscow, Russia</i>	256
Repetitively pulsed slab waveguide rf-excited CO₂ laser A.I.Dutov, A.A.Kuleshov, N.A.Novoselov, M.S.Yur'ev <i>Vavilov Optical Institute, St. Petersburg, Russia</i>	260
Diagnostics of active medium of an electric discharge CO₂ module by the laser spectrograph method. A.A.Adamenkov, V.V.Buzoverya, Yu.N.Bulkin, Yu.V.Kolobyanin, E.A.Kudryashov <i>Russian Federal Nuclear Center, Sarov, Russia</i>	265
Solid state lasers:	
Growth and characterisation of Nd:YAG epitaxial planar waveguides by pulsed laser deposition M.Ezaki, M.Obara, K.Adachi <i>Keio University</i> H.Kumagai, K.Toyoda <i>Inst. of Physical & Chemical Research (RIKEN), Japan</i>	269
Passive Q-switching of high-power solar-pumped Nd:YAG laser I.Pe'er, N.Naftali, D.Abramovic, A.Yogev <i>Weizmann Inst. of Sci., Rehovoth</i> M.Lando, Y.Shimony <i>Rotem Industries, Beer-Sheva, Israel</i>	273
Copper lasers:	
Precision materials processing in microelectronics with a 10-W copper-bromide laser J.Mizeraczyk, A.Otta, M.Mohamed-Seghir, J.Wasilewski <i>Inst. of Fluid Flow Machinery, Gdansk</i> A.Jurewicz, W.Janke <i>Tech. Univ. of Gdansk, Poland</i> C.E.Little <i>University of St. Andrews, UK</i> N.Sabotinov <i>Inst. of Solid State Physics, Sofia, Bulgaria</i> E.S.Livingstone <i>EEV, UK</i> I.Kostadinov, <i>Pulssvet Co., Sofia, Bulgaria</i>	277
Copper vapour laser MOPA chain for highly efficient and precise material removal K.Schutte, E.K.W.Gan, J.Koch, A.Lang <i>ATZ-EVUS, Vilseck</i> M.Hartmann, R.Mayerhofer, T.Sluneco, H.W.Bergmann <i>Univ. Erlangen-Nurnberg, Germany</i>	281
Dynamics of the metal seeding process in copper hybrid lasers L.Little, C.E.Little, <i>University of St. Andrews, UK</i>	285
Xenon lasers:	
High-energy IR lasers operating on XeI transitions V.F.Tarasenko, A.V.Fedenev, B.M.Koval'chuk <i>High Current Electronics Institute, Tomsk, Russia</i>	289
Carbon monoxide lasers:	
Network-based simulation of CO laser M.Iyoda <i>Chiba Inst. of Technology, Narashino</i> M.Taniwaki, S.Sato <i>IRI Laser Lab., Kashiwa, Japan</i>	293

Atmospheric absorption effects in beam delivery for industrial CO lasers Q.Cao, H.J.Baker, D.R.Hall <i>Heriot-Watt University, UK</i>	297
Multiquantum VV-exchange modelling of the pulsed Q-switched frequency selected CO laser A.A.Ionin, Yu.M.Klimachev, V.Sinitsyn <i>P.N. Lebedev Phys. Inst., Moscow</i> A.K.Kurnosov, I.V.Kochetov <i>Troitsk Inst. of Innovation & Fusion Res.</i> Yu.B.Konev <i>Inst. of High Temperatures, Moscow, Russia</i>	301
Short pulse (~1- to 10-μsec) e-beam-controlled discharge CO laser with selected wavelengths A.A.Ionin, L.Afanas'ev, Yu.Klimachev, A.Kotkov, L.Selesnev, D.Sinitsyn <i>Lebedev Institute, Moscow, Russia</i> H.Kobsa <i>Du Pont Science & Engineering, Wilmington, USA</i>	305
Numerical investigation of energy characteristics of the first overtone generation of a high-power supersonic e-beam-sustained CO laser B.M.Dymshits <i>LOK Co., St. Petersburg</i> B.S.Alexandrov, V.A.Belavin, J.P.Koretskiy <i>Russian Scientific Centre "Applied Chemistry" St. Petersburg, Russia</i>	309
Gas dynamic lasers:	
Heat treatment of large-scale rolling machine rolls by high-power gas dynamic laser at Cherepovetz Metallurgy Works A.A.Betev, V.T.Karpukhin, Yu.B.Konev, B.M.Kozlov, <i>Inst. of High Temperatures, Moscow</i> L.I.Danilov, Yu.V.Lipukhin <i>Cherepovetz Metallurgy Works, Russia</i>	313
Laser resonators, beam delivery, and nonlinear optics:	
New methods to obtain higher power from the laser with the unstable resonator K.Nanri, T.Fujioka <i>Tokai University, Japan</i>	317
Effects of beam launching on mode coupling in hollow infrared waveguides for high-quality beam delivery S.Somkuarnpanit, D.Su, J.D.C.Jones, H.J.Baker, D.R.Hall <i>Heriot-Watt University, UK</i>	321
Modelling of one-dimensional cavities for large-area gain media B.Wasilewski, K.M.Abramski, <i>Technical Univ. of Wroclaw, Poland</i> A.D.Colley, H.J.Baker, D.R.Hall <i>Heriot-Watt University, UK</i>	325
Calculation of coupling losses for coaxial waveguide modes B.Grubert, W.Jüptner <i>Bremen Inst. für Angew. Strahl., Bremen</i> R.Nowack <i>DLR, Stuttgart, Germany</i>	329
Transient four-wave mixing of pulsed CO₂ laser radiation in semiconductors M.G.Galushkin, K.V.Mitin <i>Scientific Res. Centre for Technological Lasers, Shatura</i> A.A.Ionin, A.A.Kotkov <i>P.N. Lebedev Inst., Moscow, Russia</i>	333
High-frequency temporal structure of laser and phase-conjugated signals at intracavity degenerate four-wave mixing of CO₂ and CO laser radiation inside their inverted medium C.Beairisto, R.Penny, S.Squires <i>White Sands Missile Range, USA</i> A.A.Ionin, A.Kotkov, L.Seleznev <i>P.N.Lebedev Inst., Moscow, Russia</i> R.Walter <i>W.J. Schafer Associates, USA</i>	337
SBS properties of high-pressure xenon A.M.Dudov, S.A.Buyko, Y.V.Dolgoplov, V.A.Eroshenko, G.G. Kochemasov, S.M.Kulikov, V.N.Novikov, A.F.Shkapa, S.A.Sukharev, L.I.Zyko <i>Russian Federal Nuclear Center, Sarov, Russia</i> A.M.Scott <i>DRA Malvern, UK</i>	341
Approximation of super-Gaussian beams by generalized flattened Gaussian beams S.-A.Amarande <i>Institute of Atomic Physics, Bucharest, Romania</i>	345
Regenerative amplification of laser-injector signal with given wavefront and problem of multislabs phasing O.B.Danilov, V.V.Lyubimov, N.N.Rozanov <i>Vavilov State Optical Institute, St. Petersburg, Russia</i>	349
Dynamic behaviour of two CO₂ lasers phase-locked through diffraction coupling W.Weingartner, K.Schröder, D.Schuöcker <i>Dept. of High Power Beam Technol., TU Vienna, Austria</i>	353

Excimer lasers and applications:

Comparison of beam quality parameters of two high-peak-power excimer laser beams	357
S.Bollanti, P.Di Lazzaro, F.Flora, G.Giordano, T.Letardi, G.Schina <i>ENEA, Frascati</i> D.Murra <i>ENEA, Policoro</i> C.Petrucci, O.Uteza <i>ENEA guest</i> C.E.Zheng, <i>EL.EN, Firenze, Italy</i>	
Improvement in the performance of a high-average-power XeCl laser	362
B.Lacour, H.Brunet, C.Gagnol, B.Vincent <i>CILAS, Marcoussis</i> H.Besaucèle <i>SOPRA, Bois-Colombes, France</i>	
Basic characteristic and application of KrF laser pumped by electric discharge	366
K.Kasuya, H.Sunami, C.Wu, E.Hotta <i>Tokyo Inst. of Technol., Kanagawa</i> , Y.Kawakita, S.Kato <i>Nissin Electric Co. Ltd., Kyoto, Japan</i>	
X-ray preionized discharge pumped KrF laser	370
J.Bonnet, D.Pigache <i>ONERA, Chatillon, France</i> M.Makarov <i>HCEI, Tomsk, Russia</i> B.Godard, M.Stehle <i>SOPRA, Bois Colombes, France</i>	
X-ray preionized molecular fluorine laser with a large discharge cross section	374
H.M.J.Bastiaens, P.J.M.Peters, W.J.Witteman <i>University of Twente, The Netherlands</i>	
Efficient VUV light sources from rare gas excimers and their applications	378
W.Sasaki, S.Kubodera, J.Kawanaka <i>University of Miyazaki, Japan</i>	
Influence of electrode roughness on the discharge quality of a high-PRF long-pulse XeCl laser	382
I.Tassy, Ph.Delaporte, B.Fontaine, B.Forestier, M.Sentis, O.Uteza <i>CNRS, Marseille, France</i>	
Kr₂⁺Cs: a new class of triatomic excimer molecules	386
Ph.Delaporte, M.Voitik, Ch.Tarras, M.Sentis, O.Uteza, B.Fontaine, B.Forestier <i>CNRS, Marseille, France</i>	
State and prospects of the XeF(C-A) optically pumped laser	390
S.V.Mitko, V.N.Ochkin <i>Lebedev Physics Institute, Moscow, Russia</i> F.A.van Goor, W.J.Witteman <i>Univ.of Twente, The Netherlands</i>	
Etching of organic optical materials by photo-material processing using an excimer lamp	394
A.Yokotani, N.Takezoe, K.Kurosawa, W.Sasaki <i>Miyazaki University</i> T.Igarashi, H.Matsuno <i>R&D Centre, Ushio Inc.</i> K.Yoshida <i>Osaka Inst. of Technology</i> T.Sasaki <i>Osaka Univ. Japan</i>	
Studies on condensation phenomena and refraction index distributions in excimer laser-induced plasma/vapour plumes	398
G.Callies, H.Schittenhelm, P.Berger, H.Hügel <i>Institute for Strahlwerkzeuge, Stuttgart, Germany</i> G.P.Pinho <i>Univ. Waterloo, Canada</i>	
Electron beams generated from a ferroelectric cathode induced by excimer lasers	402
J.Handereka <i>Univ. of Silesia, Poland</i> V.Nassisi <i>Univ. of Lecce, Italy</i> H.Riege <i>CERN, Geneva, Switzerland</i>	
Time-of-flight characterisation of pulsed laser ablation plume from NbTe₄ target	406
F.Grangéon, M.Autric <i>I.R.P.H.E Marseille</i> H.Sassoli, W.Marine <i>CNRS Marseille, France</i>	

9. LASER MICROMACHINING I

Laser ablation: processes and applications (Invited Paper)	412
P.E.Dyer <i>Hull University, UK</i>	
Q-switched CO₂ laser ablation of organic polymers	418
T.Sakai, N.Hamada, K.Minamida, R.Yoshihara <i>Nippon Steel Corporation, Kanagawa, Japan</i>	
Irradiation of fabrics of nylon and poly(ethylene terephthalate) with short frequency-selected pulses from CO₂, CO, and excimer lasers	422
A.A.Ionin <i>P.N.Lebedev Inst., Moscow</i> K.Kleine, H.Kobsa <i>DuPont, Inc., Wilmington, USA</i>	
Micro-machining with copper lasers	426
M.Knowles, A.Bell, G.Foster-Turner, G.Rutterford, J.Chudzicki, A.Kearsley <i>Oxford Lasers Ltd., UK</i>	
Excimer laser beam shaping and material processing using diffractive optics	431
S.W.Williams, P.J.Marsden, N.C.Roberts, J.Sidhu, M.Venables <i>BaE Sowerby Research Centre, Bristol, UK</i>	

10. CARBON MONOXIDE AND GAS DYNAMIC LASERS

Room temperature operating pulse rf-discharge-excited CO laser	436
M.Uehara, H.Kanazawa, <i>High Energy Technol. Dept., Ishikawajima-Harima Heavy Industries Co. Ltd., Tokyo, Japan</i>	
3-kW industrial CO laser operating at room temperature	440
W.G.McNaught (<i>formally Laser Ecosse Ltd</i>) G.Wlodarczyk <i>TWI, Cambridge, UK</i>	

Electro-gas-dynamic CO lasers with combustion products: a new scientific direction to the creation of the industrial high-power lasers I.Ya.Baranov <i>Baltic State Tech. Univ., St. Petersburg, Russia</i>	444
Multimegawatt supersonic e-beam sustained cw CO lasers: estimations of their energy characteristics and operating regimes B.M.Dymshits <i>LOK Co., St. Petersburg</i> B.S.Alexandrov <i>Russian Scientific Centre "Applied Chemistry", St. Petersburg, Russia</i>	448
Study on CO₂ gas dynamic laser driven by methane-air combustion Y.Itaya, Y.Kawamura, N.Kobayashi, C.Takami, M.Hasatani <i>Nagoya University, Japan</i>	452
Combustion-driven CO₂ gas dynamic lasers: the story may be continued A.S.Boreisho, A.G.Trofimovich <i>Baltic State Tech. Univ., St. Petersburg, Russia</i>	456

11. LASER MICROMACHINING II

High-resolution microlithography applications of deep-UV excimer lasers (Invited Paper) F.K.Tittel, J.R.Cavallaro <i>Rice Univ. USA</i> M.Erdelyi, G.Szabo, Zs.Bor <i>JATE University, Hungary</i> M.C.Smayling <i>Texas Instruments, USA</i>	462
Performance of 1-kHz KrF excimer laser for DUV lithography P.Das, R.G.Morton, I.Fomenkov, W.Partlo, R.Sandstrom, C.Maley, R.Cybulski <i>Cymer Inc., California, USA</i>	467
High-resolution microlithography using a 193-nm excimer laser source N.H.Rizvi, D.Ashworth, M.C.Gower <i>Exitech Ltd., Oxford, UK</i>	471
Deposition of diamondlike carbon films using XeCl excimer laser M-K.Wei, R.Queitsch, A.Lang, K.Schutte, H.W.Bergmann <i>ATZ-EVUS, Vilseck, Germany</i>	477
Picosecond imaging of laser-induced ablation processes and production of microstructures by picosecond laser pulses J.Jandeleit, P.Rußbüldt, G.Urbasch, D.Hoffmann, E.W.Kreutz <i>RWTH Aachen</i> H.G.Treusch <i>Fraunhofer Inst. für Lasertechnik, Aachen, Germany</i>	481
Recent developments of industrial excimer laser technology U.Stamm, R.Pätzel, I.Bragin, J.Kleinschmidt, F.Voß, D.Basting <i>Lambda Physik GmbH, Göttingen, Germany</i>	485

12. HF/DF LASERS

Improved DF performance of a repetitively pulsed HF/DF laser using a deuterated compound (Invited Paper) H.Brunet, M.Mabru, Ch.Vannier <i>CILAS, Marcoussis, France</i>	494
Closed cycle high-repetition-rate pulsed HF laser M.R.Harris, A.V.Morris, E.K.Gorton <i>DRA, Wors., UK</i>	498
Line-selected performance of a cw HF laser S.J.Gordon, L.H.Sentman, D.S.Jenkins <i>University of Illinois, USA.</i>	502
Correlations between laser performance and discharge dynamic in a photo-triggered HF laser S.Pasquiers, L.Richeboeuf, F.Doussiet, M.Legentil, C.Postel, V.Puech <i>Laboratoire de Physique des Gaz et des Plasmas, C.N.R.S, Orsay, France</i>	506
Pulsed periodical chemical laser based on chain reaction of fluorine and hydrogen with pulse energy near 5 kJ and repetition rate near 1 Hz S.D.Velikanov, G.A.Kirillov, M.V.Sinitzin, V.D.Urlin, V.V.Shchurov <i>Russian Federal Nuclear Center, Sarov, Russia</i>	510

13. LASER WELDING

Laser welding of aluminium (Invited Paper) H.E.Hügel, M.Beck, J.Rapp, F.Dausinger <i>Institut für Strahlwerkzeuge, Stuttgart, Germany</i>	516
Spectroscopic investigations of CO and CO₂ laser-induced aluminum welding plasmas M.Schellhorn and A.Eichhorn <i>Deutsch-Französisches Forschungsinstitut ISL, Saint Louis, France</i>	522
Process stabilising potential of shielding gas mixtures in laser welding with CO₂ lasers M.Kern, M.Beck, P.Berger, H.Hügel <i>Institut für Strahlwerkzeuge, Stuttgart, Germany</i>	526

Effects of different shielding gas compositions on the process of cw CO₂ laser welding in the hyperbaric range R.Ducharme, P.Kapadia <i>University of Essex, UK</i> C.Lampa, A.Ivarson, J.Powell, C.Magnusson <i>Lulea Univ. of Tech., Sweden</i>	530
Full penetration detection in Nd:YAG laser welding by analysis of oscillatory optical signals: application to overlap weld-seam tracking D.P.Hand, F.M.Haran, J.D.C.Jones <i>Heriot Watt University</i> C.Peters <i>Lumonics Ltd, Rugby, UK</i>	534
Remote optical power and focus monitoring in pulsed Nd:YAG laser welding C.-J.Jam, S.H.Baik, M.S.Kim, C.M.Chung <i>Korea Atomic Energy Res. Inst., Taejon, Korea</i>	538

POSTER SESSION II

Chemical Oxygen-Iodine Lasers (COIL):

Extraction efficiency of a 5-cm gain-length supersonic chemical oxygen-iodine laser C.A.Helms, T.L.Rittenhouse, S.P.Phipps, K.A.Truesdell, G.D.Hager <i>USAF Phillips Laboratory, USA</i>	544
Slit nozzle jet O₂(¹Δ) generator Y.Hoshino, S.Takahashi, T.Sekiguchi, T.Uchiyama <i>Keio Univ., Japan</i>	549
Investigations on the efficiency of a rotating-disk-type oxygen generator K.Grünwald, J.Handke, L.v.Entress-Fürsteneck <i>DLR., Hardthausen</i> W.L.Bohn, W.O.Schall <i>DLR, Stuttgart, Germany</i>	553
Pulsed iodine photolytic laser system PERUN B.Králiková, J.Skála, J.Krásá, L.Láska, K.Masek, K.Rohlén, P.Straka <i>Inst. Of Phys., Acad. Sci. of the Czech Republic, Prague</i>	557
Intracavity second harmonic generation of chemical oxygen iodine laser with a Brewster cut LBO crystal T.Shimizu, T.Tezuka, K.Chen, K.Hashimoto, T.Uchiyama <i>Keio University, Japan</i>	561
Optimisation of jet singlet oxygen generator for chemical oxygen-iodine laser O.Spalek, J.Kodymová <i>Academy of Sci. of the Czech Republic, Prague</i> M.V.Zagidullin, V.K.Nikolaev <i>Lebedev Institute, Samara, Russia</i>	565
1D kinetic model of COIL applied to experimental data J.Beránek, K.Rohlén, J.Kodymová, O.Spalek <i>Inst. of Phys., Acad. Sci. of the Czech Republic, Prague</i>	569
Mixing/reacting zone structure and small signal gain coefficient of a supersonic flow chemical oxygen-iodine laser W.Masuda, M.Hishida, N.Azami <i>Nagaoka Univ. of Tech.</i> H.Fujii, T.Atsuta <i>Kawasaki HI Ltd, Japan</i>	573
Liquid breakup studies for jet-type singlet oxygen generators W.O. Schall, I.Plock <i>DLR, Stuttgart, Germany</i>	577
Oxygen-iodine laser capacity at the elevated pressure A.A.Adamenkov, B.A.Vyskubenko, N.N.Gerasimenko, Yu.N.Deryugin, D.K.Zelensky, S.P.Ilyin, I.M. Krukovsky, E.A.Kudryashov <i>Russian Federal Nuclear Center, Sarov, Russia</i>	581

HF/DF Lasers:

HF laser initiated by an intense electron beam M.Gastaud, J.Bouesc, M.Autric <i>CNRS - IRPHE Marseille, France</i>	585
Experiments on optically pumped HF and DF transitions by a Cr⁴⁺:Forsterite laser P.Prigent, G.Girard, A.Lavenant, H.Brunet, P.Lemaignan <i>CILAS, Marcoussis, France</i>	589
Performance and spectral characteristics of sliding-discharge excited UV-IR laser P.A.Atanasov, Z.Y.Peshev, G.I.Furlinski, K.A.Grozdanov <i>Institute of Electronics, Sofia, Bulgaria</i>	594
Computer modelling of the pulsed DF-HBr optical resonance transfer laser (ORTL) M.A.Azarov, V.A.Ishakov, V.I.Mashendzhinov, V.E.Revich, A.P.Vorobjev <i>Russian Scientific Centre "Applied Chemistry" St. Petersburg, Russia</i>	598

Chemical laser emitting simultaneously from excited HF and DF molecules S.D.Velikanov, A.S.Elutin, A.F.Zapol'sky, D.V.Konkin, S.M.Kulikov, V.N.Novikov, M.V.Sinitzin, S.A.Sukharev <i>Russian Federal Nuclear Center, Sarov, Russia</i>	602
Ways and conditions for achieving extreme energy characteristics of pulsed chemical DF and HF lasers M.A.Azarov, B.S.Alexandrov, V.A.Drozдов, G.A.Troshchinenko <i>Russian Scientific Centre "Applied Chemistry", St. Petersburg, Russia</i>	606
Laser Interactions and Laser Processing:	
Influence of aerosols on gas-breakdowns induced by high-power-pulsed infrared laser radiation P.Bourgeois, M.Althaus, M.Hugenschmidt <i>French-German Research Institute, France.</i>	610
Investigation into the absorptivity change in metals with increased laser power K.Blidegn, F.Olsen <i>Tech. Univ. of Denmark, Lyngby, Denmark</i>	615
Model-based process planning and control: laser beam welding with CALAS M.Dahmen, B.Fürst, S.Kaierle, E.W.Kreutz, R.Propawe <i>Lehrstuhl für Lasertechnik, Aachen, Germany</i> G.Turichin <i>Tech. Univ. of St. Petersburg, Russia</i>	619
Propagation and shielding effects of surface plasmas on coated and uncoated materials due to pulsed CO₂ laser radiation R.Schmitt, M.Hugenschmidt <i>German-French Res. Inst., Saint-Louis, France</i>	623
Optimisation of the laser cutting process B.Dragsted, F.Olsen <i>Tech. Univ. of Denmark, Lyngby, Denmark</i>	627
Control of the surface plasma during pulsed laser cutting U.Bielesch, M.Napp, J.H.Schäfer, J.Uhlenbusch <i>University of Düsseldorf, Germany</i>	631
Some applications of the powerful CO₂ lasers F.K.Kosyrev, A.G.Krasjukov, V.G.Naumov, A.V.Rodin <i>Troitsk Institute for Innovation and Fusion Research, Russia</i>	635
Studies of high-average-power pulsed-CO₂-laser-radiation-material interaction phenomena M.Hugenschmidt, R. Schmitt <i>German-French Res. Inst., Saint-Louis, France</i>	639
TEA CO₂ laser ablation deposition and subsequent heat treatment of Fe and Zr thin film systems J.P.Hayes, H.V.Snelling, D.Sands, A.G.Jenner, R.D.Greenough <i>University of Hull, UK</i>	643
Optical diagnostics of laser-induced compression wave in composite material C.Prat, M.Autric <i>Institut de Recherche sur les Phenomenes Hors d'Equilibre, Marseille, France</i> K.Maeno, H.Asanuma, H.Du <i>Chiba University, Japan</i>	647
Numerical simulation of viscous shock layer with carbon ablation: preparatory research works for future reentry experiment with high-power laser and target M.Funatsu, K.Kasuya <i>Tokyo Inst. Of Technol., Kanagawa, H.Shirai Gunma University, Japan</i>	651
Novel optical techniques for remote water column temperature measurement B.Cresswell, E.Hodgson, C.Wakefield <i>University of Salford, UK</i>	655
Time dependent resistance and inductance of the laser discharge in a pulsed gas laser through waveforms of the voltage and current P.Persephonis, A.Ioannou, J.Parthenios <i>Dept. of Physics, Univ. of Patras, Greece</i>	659
Electrical behaviour of laser-damaged silicon photodiodes J.-P.Moeglin, B.Gautier, R.Joecklé <i>Inst. Franco-Allemand de Recherches, France</i>	663
Many-sided electron beam pumping of high-power lasers V.V.Ryzhov, I.Yu.Turchanovsky <i>High Current Electronics Institute, Tomsk, Russia</i>	667
Solitonic approach to the wave of reflection and conduction mechanism E.Kudriavtsev, Lebedev Institute, Moscow M.Autric <i>Institut de Recherche sur les Phenomenes Hors d'Equilibre, Marseille, France</i>	671

14. CHEMICAL OXYGEN-IODINE LASERS I

- COIL performance modeling and recent advances in diagnostic measurements** (Invited Paper) 676
K.A.Truesdell, C.A.Helms, S.Frerking, G.D.Hager *USAF Phillips Lab.* P.N.Plummer, R.J.Copland
Logicon RDA, Albuquerque, USA
- Analysis of lasing in COILs with wide aperture of the mirrors in the resonator** 682
B.D.Barmashenko, S.Rosenwaks *Ben-Gurion University, Israel*
- New type of rotating disk singlet oxygen generator** W.O.Schall, F.Duschek *DLR, Stuttgart, Germany* 686
- Experimental study of a small scale COIL using a jet type generator of singlet oxygen** 690
S.Rosenwaks, I.Blavvas, B.D.Barmashenko, D.Furman *Ben-Gurion University, Israel*
M.V.Zagidullin *P.N. Lebedev Inst, Samara, Russia*
- Improved rf plasma jet generation of singlet delta oxygen** J.Schmiedberger *Academy of Sciences, Czech Republic* 694
S.Takahashi *Energy Conversion Div. Tsukuba, Japan* H.Fujii
Kawasaki HI Ltd., Japan

15. CHEMICAL OXYGEN-IODINE LASERS II

- Industrial chemical oxygen-iodine laser** (Invited Paper) H.Fujii, T.Atsuta *Kawasaki Heavy Industries Ltd., Japan* 700
- Supersonic COIL operation at DLR, Germany** L.v.Entress-Fürsteneck, J.Handke, K.Grünwald *DLR, Lampoldhausen* W.L.Bohn, W.O.Schall *DLR, Stuttgart, Germany* 706
- Mode locking of a cw supersonic chemical oxygen-iodine laser** S.P.Phipps, C.A.Helms, R.J.Copland, W.Rudolph, K.A.Truesdell, G.D.Hager *USAF Phillips Laboratory, USA* 710
- Forward-backward-mode-coupled unstable resonator** K.Sunako, T.Kakinuma, O.Sato, T.Fujioka *Tokai University, Japan* 715
- Materials processing with a chemical oxygen-iodine laser: ceramic cladding for stainless steel substrate** A.Kar *CREOL, Florida* J.A.Rothenflue, W.P.Latham *USAF Phillips Laboratory, USA* 719
- Prospects for an industrial chemical oxygen-iodine laser** J.Vetrovec *Rocketdyne Div., Rockwell Int. Corp., California, USA* 723

16. LASER APPLICATIONS

- ORION: clearing near-Earth space debris in two years using a 30-kW repetitively pulsed laser** 728
C.R.Phipps *Photonic Associates, Santa Fe* J.P.Reilly *Northeast Science and Technology, Massachusetts, USA*
- High-gain double-pass pulsed dye amplifiers for laser guide stars** D.Kapitan, H.Booth, G.J.Murray, G.P.Hogan, C.E.Webb *Oxford University, UK.* 732
- YAG laser system with combined beams from three oscillators and its application to materials processing** H.Miura, S.Fujinaga, T.Narikiyo, A.Ohmori *The Advanced Materials Processing Inst. Kinki* K.Okino, S.Watanabe *NEC Corp., Japan.* 736
- Rust and paint stripping from power transmission towers with a pulsed Nd:YAG laser** 740
S.Ashidate *Tokyo Electric Power Company* M.Obara *Keio University, Japan.*
- Surface alloying of magnesium base alloys with high-power CO₂ laser** R.Galun, A.Weisheit, B.L.Mordike *Technische Universität Clausthal, Germany* 744
- 2-kW cw Nd:YAG laser surface hardening** G.Duffet, P.Kirat, H.Andrzejewski *Univ. de Bourgogne* A.B.Vannes *IFOS-Ecole Centrale de Lyon, France.* 748
- Laser generating metallic components** M.A.McLean, G.J.Shannon, W.M.Steen *University of Liverpool, UK.* 753

17. LASER CUTTING

Experimental study of cutting thick aluminum and steel with a chemical oxygen-iodine laser using an N₂ or O₂ gas assist (Invited Paper) D.L.Carroll <i>University of Illinois</i> J.A.Rothenflue <i>USAF Phillips Laboratory, USA</i>	758
Comparative studies of metal cutting with high-power lasers J.Xie, A.Kar <i>CREOL, Florida</i> J.A.Rothenflue, W.P.Latham <i>USAF Phillips Lab., USA</i>	764
Laser system technology for an improved workpiece tracking in 3D CO₂ laser beam cutting N.Neubauer, P.Hoffmann <i>Bayerisches Laserzentrum, Erlangen</i> M. Geiger <i>Lehrstuhl für Fertigungstechnologie, Erlangen, Germany,</i>	768
CW CO₂ laser cutting of plastics P.A.Atanasov <i>Institute of Electronics, Sofia</i> M.G.Baeva <i>Technical University of Varna, Bulgaria</i>	772
Semiquantitative approach to the effect of anodised layer thickness on laser cutting of aluminium alloy A.P.Hoult, M.Y.Shan, B.Bryden, I.R.Pashby <i>University of Warwick, UK</i>	776
High-power iodine laser application for remote D and D cutting, J.Vetrovec, R.N. Hindy, G.Subbaraman, L.Spiegel <i>Rocketdyne Div., Rockwell Int. Corp., California, USA</i>	780
Author Index	784

INTERNATIONAL ADVISORY COMMITTEE OF THE GCL SYMPOSIUM

P. Atanasov	<i>Bulgaria</i>	E. Kudriavtsev	<i>Russia</i>
M. Autric	<i>France</i>	T. Letardi	<i>Italy</i>
V. Y. Baranov	<i>Russia</i>	K. Maeno	<i>Japan</i>
N. G. Basov	<i>Russia</i>	R. Meinzer	<i>USA</i>
W. L. Bohn	<i>Germany</i>	A. N. Oraevsky	<i>Russia</i>
H. Brunet	<i>France</i>	D. Pigache	<i>France</i>
J. P. Caressa	<i>France</i>	J. P. Reilly	<i>USA</i>
C. Créput	<i>France</i>	J. Rom	<i>Israel</i>
J. D. Daugherty	<i>USA</i>	S. Rosenwaks	<i>Israel</i>
B. Forestier	<i>France</i>	D. Schuöcker	<i>Austria</i>
C. Fotakis	<i>Greece</i>	L. H. Sentman	<i>USA</i>
T. Fujioka	<i>Japan</i>	I. J. Spalding	<i>UK</i>
D. R. Hall	<i>UK</i>	T. Stamatakis	<i>UK</i>
H. Hügel	<i>Germany</i>	F. K. Tittel	<i>USA</i>
G. Inglesakis	<i>France</i>	W. S. Watt	<i>USA</i>
R. Jalin	<i>France</i>	W. J. Witteman	<i>The Netherlands</i>
K. Kasuya	<i>Japan</i>	H. X. Yan	<i>China</i>
P. G. Kryukov	<i>Russia</i>	C. Zhang	<i>China</i>

LOCAL ORGANISING COMMITTEE FOR GCL/HPL'96

Conference Chair: D. R. Hall

H. J. Baker	<i>Programme Chair</i>
M. R. Taghizadeh	<i>Treasurer</i>
A. D. Colley, F. Villarreal	<i>IS Managers</i>
J. Smith	<i>Social Events Organiser</i>
K. Defty, J. McClelland,	<i>Secretaries</i>
A. A. Cameron, J. Bethel, I. M. Alexander	<i>Administrative Assistance</i>
D. Pelaez-Millas, S. Haughey, R. J. Morley	<i>and Logistics</i>

Department of Physics, Heriot-Watt University, Edinburgh EH14 4AS, United Kingdom

PROGRAMME COMMITTEE FOR GCL/HPL'96

Programme Chair and Proceedings Editor: H J Baker *Heriot-Watt University UK*

W. L. Bohn	<i>DLR, Germany</i>	S. Rosenwaks	<i>Ben Gurion Univ. Israel</i>
D. R. Hall	<i>Heriot-Watt University, UK</i>	H. N. Rutt	<i>Southampton University, UK</i>
H. E. Hügel	<i>IFSW, Stuttgart, Germany</i>	M. J. Shaw	<i>Rutherford Lab. UK</i>
C. L. Ireland	<i>Lumonics Ltd. UK</i>	D. Schuöcker	<i>TU Vienna, Austria</i>
C. E. Little	<i>St Andrews University UK</i>	T. Stamatakis	<i>AEA Technology UK</i>
P. Loosen	<i>Fraunhofer ILT Germany</i>	K. A. Truesdell	<i>Phillips Laboratory, USA</i>
M. Obara	<i>Keio University, Japan</i>	D. V. Willetts	<i>DRA, Malvern, UK</i>
J. P. Reilly	<i>NST, USA</i>	W. J. Witteman	<i>Twente University, The Netherlands</i>

INTRODUCTION

The GCL/HPL'96 conference was held on the Campus of Heriot-Watt University, in Edinburgh, UK, in the period 25-30 August 1996 and was organised by the Physics Department of the University. The meeting combined the Eleventh Gas Flow and Chemical Laser Symposium with a more general conference emphasising all high average power lasers, following the decision by the GCL International Scientific Advisory Committee to extend the scope of the GCL Symposia to include solid state lasers. Consequently, the traditional Symposium abbreviation of GCL has been modified to GCL/HPL, reflecting the developing interest of the community in all types of high average power lasers. The meeting has aimed to continue in the very successful tradition of previous biennial GCL Symposia held over the past twenty years, whilst welcoming new colleagues from the widened range of interest.

The GCL/HPL '96 Symposium has focused on new developments in fundamental and applied research in high power lasers, high power beam characteristics and manipulation techniques, and laser/material interaction processes. It continues to represent a major international forum for these subject areas. The continuing high level of activity in laser research, combined with the attractions of Edinburgh and Scotland as a conference venue, has produced a full and high quality conference programme, with approximately 65% more papers included in these proceedings than for the previous Tenth GCL Symposium held in 1994. The Programme Committee had great difficulty in accommodating the large number of good quality contributed papers within the schedule, and resorted to the use of parallel presentations for a short section of the conference. Nevertheless, the conference maintained its reputation for ensuring close and friendly contact between all delegates, with the help of the substantial social programme.

As conference organisers, we would like to thank the delegates for attending the conference and submitting the excellent papers contained in these proceedings. In particular, we thank our colleagues from the Department of Physics who formed the Local Organising Committee and from the James Watt Conference Centre, for ensuring the smooth running and success of the conference. Our thanks go to the members of the Programme Committee, who gave up their time for reviewing the contributed papers, and who maintained the high scientific standard of this conference. Finally we thank the sponsors of the conference listed on the front cover of these proceedings for their financial help in ensuring the success of the conference.

Denis R Hall
Conference Chair

Howard J Baker
Programme Chair

1. Keynote Addresses

Application of lasers with high beam quality in the electronics industry.

Gerard Notenboom

Philips Centre for Manufacturing Technology

P. O. Box 218 , 5600 MD Eindhoven, The Netherlands

ABSTRACT

Laser micro processing has grown to a mature technology at many places in the electronics industry. When high beam quality lasers are combined with dedicated imaging and diffractive optics, excellent solutions can be offered to expand the field of applications. Standardisation of laser specifications is necessary.

Keywords: laser material processing, laser micro machining, laser labelling, laser decoration, micro laser welding, laser adjustment, standardisation of laser specifications.

1. INTRODUCTION

Philips Centre for Manufacturing Technology was involved in Laser Material Processing almost from the invention of the CO₂- and Nd YAG-lasers in the early sixties. One of the reasons, the electronic industry was one of the first users of this technology is due to the availability, at that time, of only low power systems. These systems are still most frequently used in this kind of industry, compared to the high power lasers to-day needed in e. g. the automotive industry.

The first reason to ask for a better beam quality was related to the application of Nd YAG lasers for micro spot welding, still the most important application in the electronics industry.

Generally, in production there was a need for smaller spot sizes, combined with, for practical reasons, a large working distance and depth of focus. The design of the laser resonators, at that time, only enabled

a very restricted power range where the system could meet that requirements.

The introduction of beam handling systems using optical fibres and beam splitters to serve more workstations with only one, higher powered, laser head was an extra reason to ask for improved beam quality. 300 W lasers were rather flood lights and couldn't be coupled in into the fibres, when using their total power range. This problem was solved by redesign of the laser resonators

Beam splitters used in these beam handling systems are diffractive ones

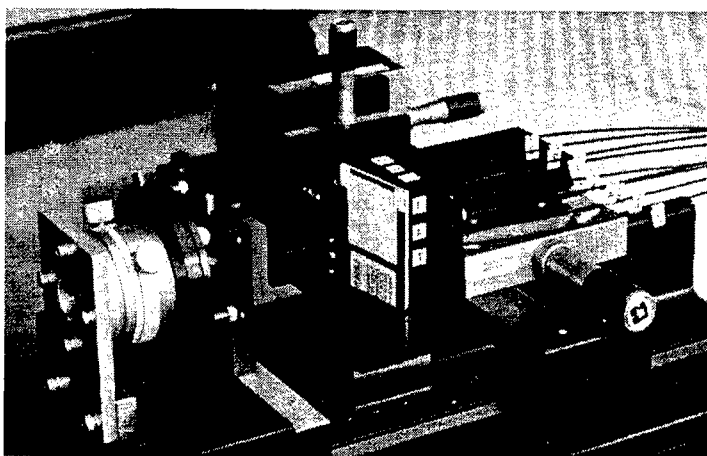


fig 1: Nine times beam splitter for a Nd YAG laser using diffractive optics

thanks to the insensibility of this type of splitters to differences in polarisation, depending on the laser power settings.

An example of a nine times beam splitter is shown in **fig.1**. The convenience of the beam splitting and flexibility of the beam handling with the optical fibres is however paid by an overall efficiency of only 60 %.

Different demands on beam quality and beam handling will be mentioned in this paper related to various applications of the technology.

2. LASER MICRO WELDING

Laser spot welding is a mature technology in the electronics industry. All manufacturers of TV tubes use this technology for the assembly of the electron guns as shown in **fig. 2**. More than one hundred tiny laser welds, applying pulsed Nd YAG lasers and fibre optics beam delivery systems, are used to

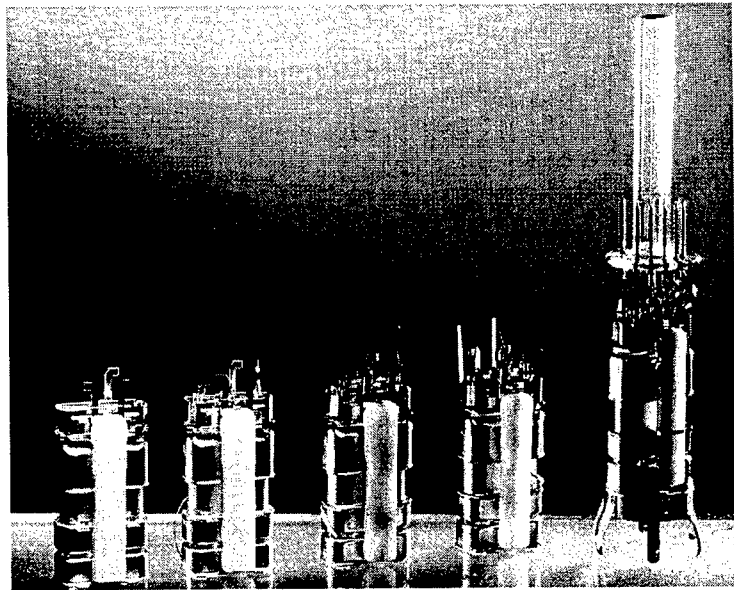


fig 2: Laser spot welding used to assemble the electron gun of a TV tube

sub-assemble the cathodes, the electron optic grids and lenses and finally assemble the gun. This product is a typical example of how laser technology generally is introduced in industry.

It started with just replacing the existing joining technology, resistance welding, for quality reasons .

The weld quality improved although the parts were still designed for the old technology. In the next generations of this product, the design of the various parts was better fit to laser joining and so the accuracy of the assembly improved too. It can be stated that the quality of modern TV picture tubes could not be realised without laser spot welding. The weld reject number improved from 0.1 % for resistance

welding to only 20 ppm for laser welding.

Thin metal strips are often used to connect

the various parts of an assembly. When fixed with only one spot weld , the strength on torsion load is rather low. The solution is to fasten them with two welds made at the same time by putting a beam splitter element in the out-coupling optics of the fibre between the collimating- and focusing-lens.

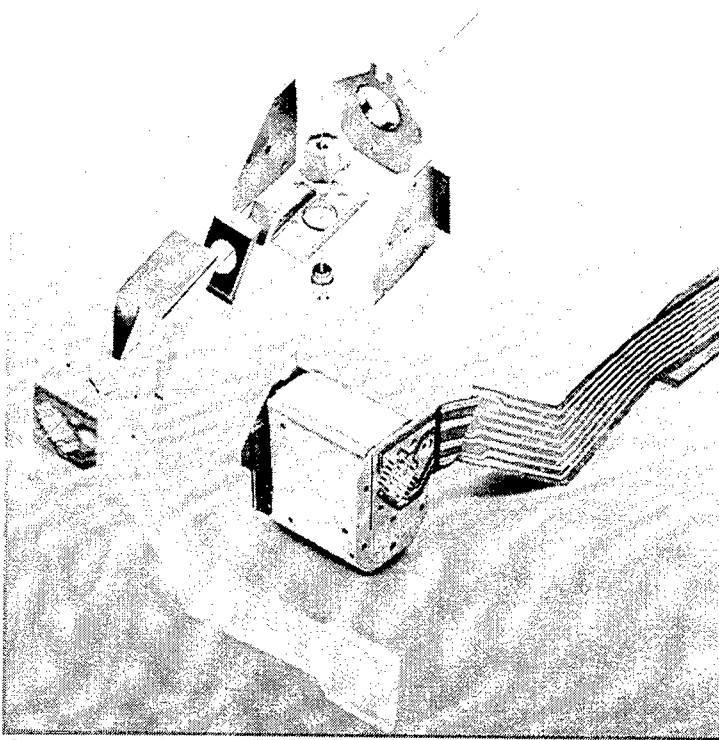


fig 3: Assembly of the light path of a CD player, laser welding is replacing resistance welding and micro gluing

For new designed products, laser spot welding has replaced not only the resistance welding technology but also micro gluing, since sensitivity for humidity of this technology can cause change in positioning accuracy during life time. An example is shown in **fig 3**. The light path of a CD player is assembled using accurate positioning, with rather expensive tools, and micro laser welding. The typical positioning time needed is about 10 sec, after fixation by laser and removal of the positioning tools, taking another 0.6 sec the remaining final accuracy is about 3 μm . When even higher accuracy is wanted another new technology is developed.

3. LASER ADJUSTMENT

Thermo-mechanical stresses induced by local irradiation of laser energy allow a contact-free accurate manipulation in (sub-)micron dimensions for thin sheet metal parts.

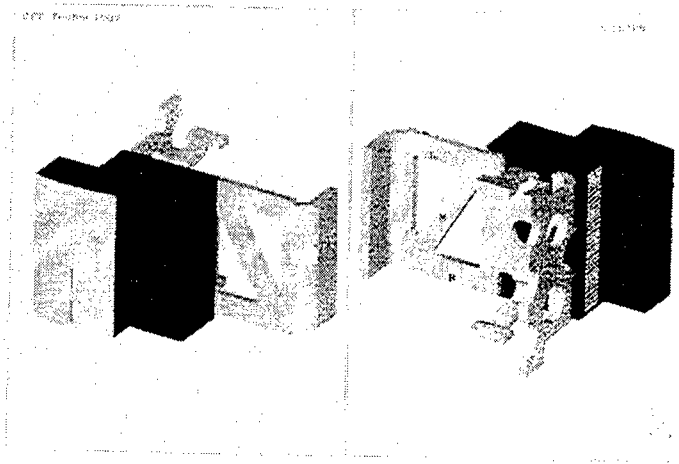


fig 4: Laser micro adjustment, to accurate position the carrier for the audio head of a DCC player.

Several thermo-mechanical mechanisms are known to obtain both bending and shortening of a part of the product. This part of the product acts as an actuator. In **fig.4** is shown how this technology is used to accurate position the carrier for the audio head of a DCC player. The special construction of the metal carrier allows an accurate adjustment of two important degrees of freedom of the chip : the track-height and the azimuth of thin film heads. The carrier fulfils the function of an actuator for fine adjustment of the audio chip. If the parts L, R, and M are irradiated by short

intense laser pulses, the lengths of these parts change, the parts become shorter by a few microns.

Laser heating at M results in a head movement downwards with a few microns (track-height), heating at L rotates the head clockwise with a few milli-radians (azimuth) and heating at R rotates the head counter clockwise with a few milli-radians (azimuth)

With this technology, having an actuator on board, being a part of the product, only "rough" positioning of the parts using simple tools, typically will only take 1 sec. Fixation (laser welding) and removal of the tools will take again 0.6 sec. Laser manipulation, using a closed loop system and computer vision, finally results in an accuracy of only 0.3 μm , taking 0.5 - 1 sec.. Compared to the above mentioned assembling procedure, the processing time is reduced with almost 80 % and the final accuracy achieved is ten times better.

With respect to the laser system used it is clear that beam handling, using optical fibres and or a controllable galvo mirror system is a prerequisite for an industrial application.

4. LASER LABELLING AND DECORATION

Laser marking is another mature technology in the electronics industry. The advantages, of course, always deal with the flexibility of the technology, to put unique information on every product in a flow line mass production, to characterise sub-assemblies, to be able to trace production equipment and date for quality inspection. Another reason to mark parts is an environmental one. By coding parts with information about the material composition, it is possible, when recycling products at the end of their life time, automatically to read out that information.

When marking plastic parts, typically two type of processes occur. On light coloured surfaces, local carbonisation, gives rise to a dark contrast, while on dark surfaces, a foaming effect results in a white contrast.

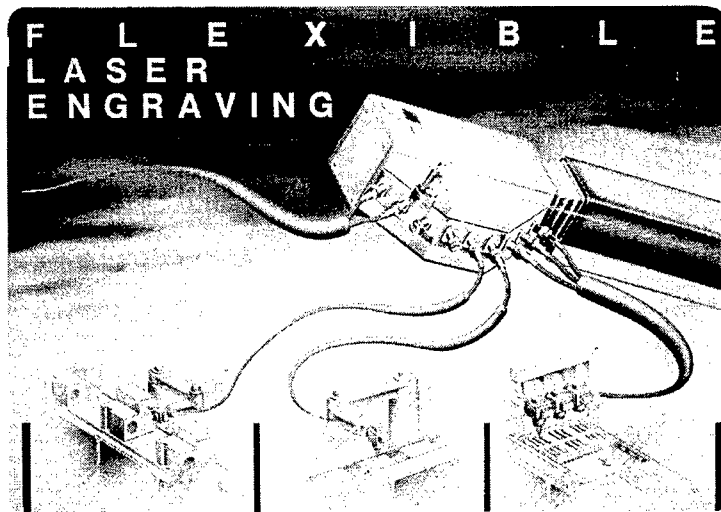


fig 5: Laser marking system to serve several work stations with one laser head.

Lasers commonly used for this application are, Nd YAG, CO₂ and Excimer, while the two technologies used are, mask imaging and direct writing via software controlled X-Y galvo mirrors.

When the latest solution is combined with fibre optics and an optical multiplexing system, it is possible to serve more production lines with only one laser, as shown in an artists impression in **fig 5**. In this technology there is a need for lasers with a shorter pulse length and an improved beam quality compared with the conventional used, lamp pumped, Q switched Nd

YAG lasers, to minimise the surface damage and to enhance the resolution of the graphics. On the short term diode pumped Nd YAG lasers will replace the lamp pumped ones. An even better solution will be the availability of the Vanadate laser that combines good beam quality and a shorter pulse length with a

higher pulse frequency. When at the same time faster galvo mirror systems become available, the total processing time of laser marking can shorten, what certainly will lead to more application of the technology.

The activities mentioned up till now are mainly dealing with putting information on part or product. Changing colours in polymer surfaces is called laser decoration and is caused by the bleaching of pigments in a multi-pigmented, coloured surface. Bleaching of the pigments is depending on the laser wavelength used. In a Brite Euram programme plastic materials are pigmented enabling to write blue, green and red in a grey coloured surface, applying wavelengths of respectively 450, 550 and 650 nm. To that aim an OPO laser was used, offering the possibility of multi-wavelength tuning. Still work have to be done to enhance the contrast of the colours. The laser used was a typical laboratory system, and needs to be developed to an industrial one. Another problem to be solved is the vulnerability of the multi-wavelength applied optics. Apart from these hardware problems, a dedicated software development is necessary to design the algorithms to fill in the graphics, most economically. The laser decoration technology competes with pad- and inkjet- printing, having the advantage of being more flexible than pad printing, better reliable than inkjet printing and more environmental friendly than both conventional technologies.

5. LASER MICRO MACHINING OF METALS

In the electronics industry there is a need for contact less micro machining of parts in a miniaturising world. The smaller the parts, quite often, the higher the accuracy in the dimensions and so the lesser the deformation, due to the forces of the tools used to remove material, accepted. Laser micro machining possibly can offer a solution for this problem. Up till now, not many industrial applications are known, used in mass manufacturing. For tool making, at that time, the company Maho was the first to introduce a CO₂ laser system for a technology they called laser caving. Material is removed by locally irradiating a metal part in an oxygen environment, resulting in the formation of oxidised chips.

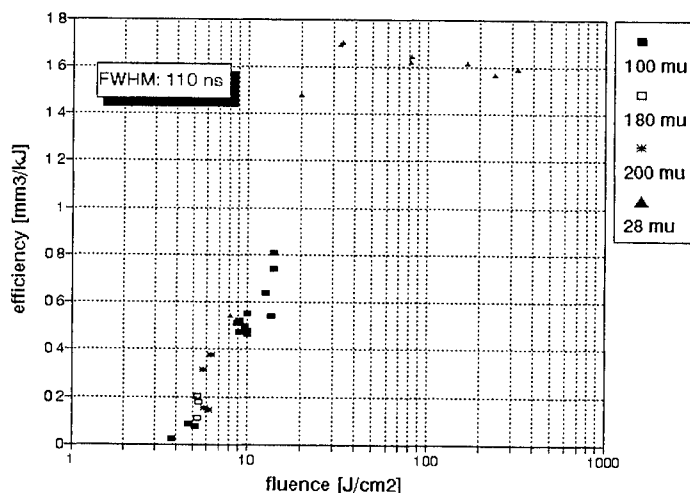


fig 6: Ablation efficiency of micro machining on stainless steel, using a Q switched Nd YAG laser.

Although the removal rate of this technology is rather high, the resulting surface quality is not good enough for most of the applications in the electronics industry. On various places there are developments to use pulsed Nd YAG lasers, with a typical pulse length between 0.1 and 2 ms, for laser micro milling. Mostly in a set up aimed for rapid prototyping. A surface roughness can be achieved of just a few microns, but with the disadvantage of a very slow milling speed, because this can only be realised by mainly evaporation of the metal surface. In the electronics industry, small and tiny metal parts

such as springs and holes and slots in grids for a TV gun have to be accurately shaped. These parts have in common, a very small heat capacity and a very small amount of material to be removed, typically 0.1 mm^3 .

For these applications, a pulse length of only 0.1 ms is already too long because, as a result of the energy density required to ablate the metal, the heat losses will result in undesired melting and therefore deformation of the rims to be shaped. It has been demonstrated that Q-switched Nd YAG lasers with a pulse length of 100 to 200 ns are better suited. In **fig 6** is shown the ablation efficiency in mm^3/KJ against the fluency in J/cm^2 for four different spot sizes and on stainless steel material. It turned out that this relation is the same for both pulsed and Q-switched Nd YAG lasers. The dependency of the spot size can be explained from smaller heat losses with decreasing spot dimensions, while saturation occurs, when plume absorption starts.

The heat affected zone in the, in this way shaped, part is very small. Depth control during processing is a must to achieve a depth accuracy better than one micron.

One possible way is to use the so called PLIM method. Between the start of the laser pulse and the start of the plume there is some time delay, called the Plume Initiation time. The length of this period depends, among others, on the energy density in the laser spot. When material is ablated with the laser focus just above the surface, the remaining surface has got some depth compared to the initial situation. The next pulse will have a slightly larger spot size which results in a lower energy density and a longer plume initiation time, which can be measured. This method can be used, by a control of the final lens position, to keep the surface in focus and by measuring the displacement, offers a control of the laser machined depth.

It must be clear that an excellent pulse to pulse stability of the machining laser is a prerequisite, although generally not the best property of a standard Q-switched Nd YAG laser. Diode pumped lasers will be better suited to that aim offering at the same time a better beam quality. Another possibly even better solution will perhaps be the development of a laser system using a phase conjugated mirror. Frequency doubling of this type of solid state lasers or employing lasers which normally already have a shorter wave length like Copper Vapour lasers, will increase the "sharpness of the machining tool". Finally the quality of the laser machining system is, apart from the quality of the laser itself, as good as the optical system chosen.

The definition of good, better, best, talking about laser parameters wanted, will be the last topic of this paper.

6. STANDARDISATION OF LASER SPECIFICATIONS

In industry, quite often, a laser system intended for material processing, is ordered from a manufacturer based upon experiments carried out by an own laser department, an laser institute or at the application laboratory of the manufacturer. At the acceptance of the system, the laser manufacturer, or a system house involved, has to prove that the laser system is able to carry out the laser process aimed for within the tolerances asked for. The customer more or less ask from the manufacturer a process guarantee. From experience is known that, in production, sooner or later and due to various reasons, the part geometry and or composition of the material will slightly change. The result can be, failure of the laser process and who will be blamed for?

From a customer point of view, one will be able to select not only the best but also the most economical laser system and therefore like to have offers from more than one manufacturer. When the

process is still confidential it is not necessary to share this information with manufacturers that finally not will deliver the laser system, when it is possible to translate, process parameters in laser parameters.

Metrology of Laser Beam Parameters :	
Laser Power:	
o time average	calorimeter (for example Prometec Lasermeter)
o time resolved	pyrodetector time constant 10 μ s with beam splitter or at back mirror (for example Weidmueller FLPM)
Beam Diameter:	
o raw beam	beam scanner (for example Prometec UFF100)
o focused beam	ref. optic and beam scanner (for example Zeiss parabola optic f300 and Prometec UFF100)
o divergence and	Rayleigh length are calculated from measured beam diameters along beam propagation
Polarisation:	
o time averaged	polarisation analyser and power meter

fig 7: Metrology of a CO₂ laser system

It is therefore recommended to specify the laser parameters needed in a process window that will tolerate an acceptable production process, rather than the process itself. In the ideal situation the laser manufacturer is able to supply all relevant parameters and measuring equipment can be installed on the production machine to have an on line control of all of them. The problem is that the influencing parameters not always directly can be measured and if, it is often a very time consuming procedure.

Only for CO₂ lasers, most of them can be measured since equipment is in the market now, see **fig 7**.

The resulting problems still are: The recently released ISO standards and draft standards on measuring principles are not commonly known and accepted, equipment is not available for all types of lasers and equipment available is not fast and accurate enough. An acceptance test

for a new laser system must only last three hours, rather than three days. Finally and related to the demand for Total Quality Management in high tech production centres, calibration of the measuring equipment has to be done from official qualified calibration laboratories, not yet available.

7.CONCLUSION

In the electronics industry, laser material processing is a mature technology for many applications. However in a miniaturising world, there is a strong demand for lasers with an excellent : beam quality, stability and reliability, to be solved by an improved design and new pumping sources. New laser types are developed but not yet industrial available. Industrial laser systems have to be offered with all relevant specifications measured with standardised measuring principles accepted by all manufacturers. The equipment enabling this must be fast enough, to be used in on line process control.

High brightness solid state lasers with phase-conjugating mirror and high average power

H.J. Eichler, A. Haase, B. Liu and O. Mehl

Technical University of Berlin, Optical Institute
Straße des 17. Juni 135, 10623 Berlin, Germany

ABSTRACT

The beam quality of conventional flash lamp pumped laser rod systems is improved by using phase conjugating mirrors based on stimulated Brillouin scattering (SBS). Pulsed multi amplifier set-ups with SBS were investigated. Nd:YALO as active medium was used to avoid stress birefringence. In case of serial arrangements an optimised optical system between the individual rods is used to achieve high efficiency independent of thermal lensing. With a two amplifier system an average output power of 1 Watt up to 210 Watt in a near diffraction limited beam was realised. In case of parallel arrangements phase coupling of the individual beams was achieved using a common SBS-cell after the first amplifier pass. Instead of a Brillouin-cell a fibre phase-conjugator can be used to reduce the power threshold down to 6 kW. An average output power of 35 Watt from a pulsed MOPA-system with such a phase-conjugator could be obtained. As applications high power second harmonic generation and applications in materials processing were realised.

Keywords: Phase conjugation, stimulated Brillouin scattering, high power solid-state laser, MOPA-system, high beam quality, Nd:YALO, fibre phase-conjugator, high average power SHG

1. INTRODUCTION

Laser applications in industry and science often require good beam quality at high average output power. The brightness of the beam, an important value for applications, depends linearly on the output power but increases quadratically with the beam quality.

In conventional solid-state MOPA-systems (master oscillator power amplifier) the oscillator beam with high beam quality cannot be amplified without degradation due to thermal lensing and stress birefringence.¹ Such problems can be reduced using diode-pumping or slab laser crystals, but for average output powers up to several 100 W the costs are still too high. A less expensive possibility to improve the beam quality of conventional laser systems is to utilise self pumped phase conjugation by stimulated Brillouin scattering in liquids, gases or solids. Most SBS-systems are using Nd:YAG as active medium because high quality crystals are readily available. Due to the thermally induced stress birefringence the Nd:YAG MOPA-schemes with SBS-mirror become complex.^{2,3} To avoid such problems we developed MOPA-systems based on Nd:YALO-rods.^{4,5} YALO shows no stress birefringence, but it has the same efficiency like Nd:YAG so that simpler laser systems are possible.

2. MOPA SET-UPS WITH SBS-MIRROR

In order to achieve average output powers of several 100 Watt, different arrangements of amplifiers were realised. Fig. 1 shows the principal set-ups. The beam from the master oscillator is coupled into the amplifier by a polarizer, is then phase conjugated and passes back. Beam distortions due to phase distortions are compensated independent of the amplifier pump power. Therefore the amplified beam shows nearly the same beam quality as the oscillator beam.

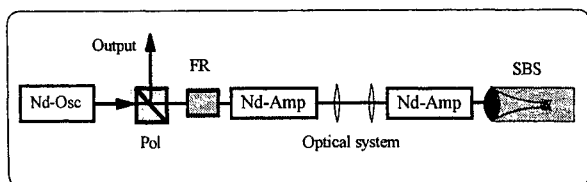


Fig. 1a. Serial amplifier arrangement with SBS-mirror.

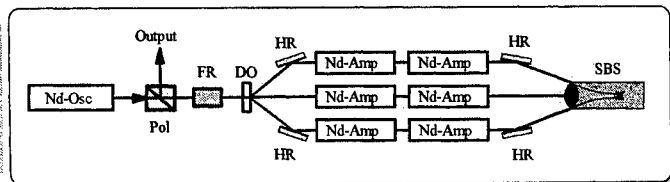


Fig. 1b. Parallel arrangement with common SBS-cell.

A serial arrangement of amplifiers has the advantage of high efficiency, but some design problems have to be considered

2.1. Serial coupling of amplifiers

Due to the variation of the beam diameter behind the first amplifier rod, the extraction efficiency of the following amplifiers decreases with thermal lensing. There is also the risk to damage optical components inside the amplifier chain. To vary the average pump power, defocused telescopes can be inserted between the amplifier rods (see Fig. 2), n is the refractive index, L is the amplifier length and Γ is the propagation constant of the quadratic index distribution in the rods.

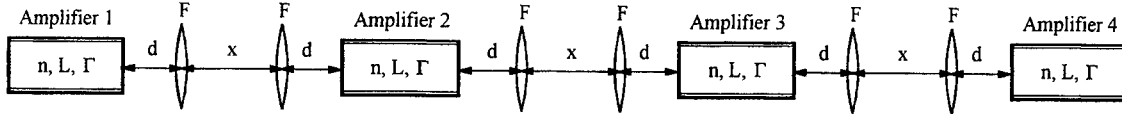


Fig. 2. Parameters of the optical system for a four amplifier system.

The optimised optical system can be calculated as follows⁶, where d can be chosen in a free way:

$$F = \frac{(1 - \cos(\Gamma_0 L))}{n\Gamma_0 \sin(\Gamma_0 L)} + d \quad (1)$$

$$x = 2F - F^2 n \sin(\Gamma_0 L) \Gamma_0 \quad (2)$$

To achieve the largest possible range for the propagation constant, Γ at the maximum pumping power is set as the limit Γ_{\uparrow} . Then Γ_0 is determined by equation (3), where N is the number of amplifier rods, w_0 the beam radius at the entrance of the first rod and w_{\uparrow} the maximum possible beam radius inside each rod. The lower limit Γ_{\downarrow} for the propagation constant is then determined by equation (4), where w_{\downarrow} is the lowest possible beam diameter at the entrance of each rod.

$$\Gamma_0 = \frac{\sqrt{2}}{L} \sqrt{1 + \frac{(2-N)}{(1-N) \cos(\Gamma_{\uparrow} L)} + \tan(\Gamma_{\uparrow} L) \Gamma_{\uparrow} L - \frac{w_{\uparrow}}{w_0 (N-1) \cos(\Gamma_{\uparrow} L)}} \quad (3)$$

$$\Gamma_{\downarrow} = \sqrt{\frac{N-2 - (N-1) \cos(\Gamma_0 L) + \frac{w_{\downarrow}}{w_0}}{(N-1)L^2 \left[\frac{\sin(\Gamma_0 L)}{\Gamma_0 L} - \frac{1}{2} \cos(\Gamma_0 L) \right]}} \quad (4)$$

Fig. 3 shows the calculated beam propagation for a system of four amplifiers including the phase conjugating SBS-cell. The average pump power varies from 1.5 kW up to 10 kW for each amplifier rod.

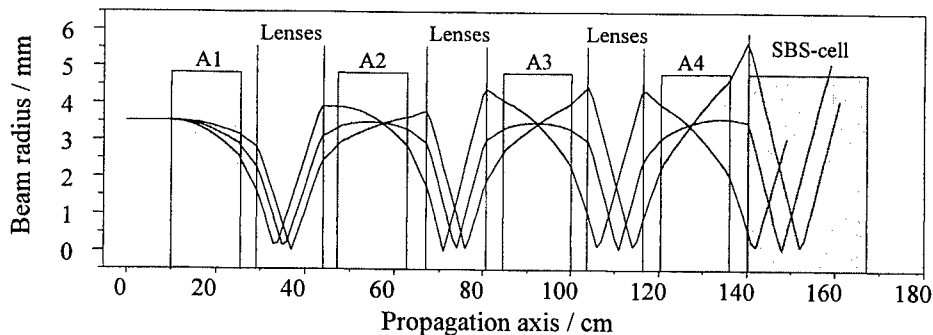


Fig. 3. Calculated beam propagation for different propagation constants Γ in a four amplifier system with SBS.

2.2. Astigmatism of thermal lensing

At high average pump power amplifier crystals show two focal lines due to the aberrations of thermal lensing. In case of Nd:YAG stress birefringence leads to a difference in the focal lengths for radial and azimuthal polarised light. In case of Nd:YALO the anisotropic crystal properties lead to an astigmatism of the amplified beam. The focal lengths differ about 7 % for an average pump power of 8 kW. This astigmatic beam propagation does not affect strongly the extraction efficiency of the amplifier rods (see Fig. 4a), but inside the SBS-cell the intensity distribution shows two flat intensity peaks resulting in low SBS-reflectivity.

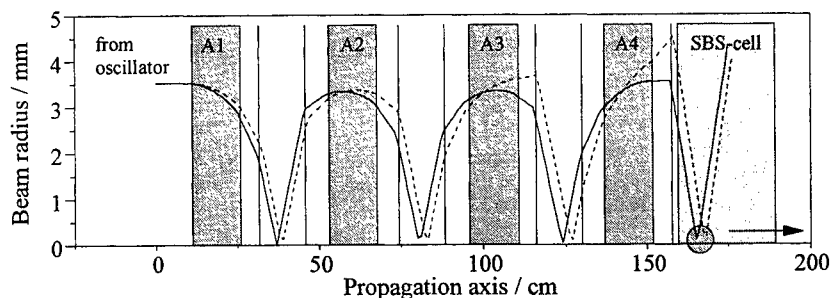


Fig. 4a. Calculated astigmatic beam radius envelope through a system of four amplifiers (A1 to A4).

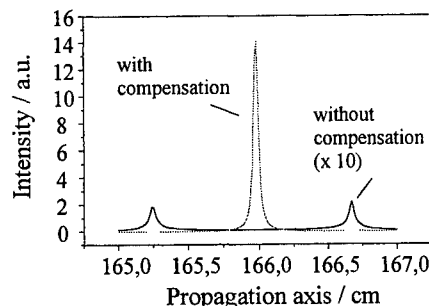


Fig. 4b. Intensity distribution inside the SBS-cell with and without compensation.

To compensate the astigmatism one half of the amplifier rods can be rotated by 90°. Due to the anisotropic gain of Nd:YALO an additional half wave plate has to be inserted to rotate the polarisation direction by 90°, too.

2.3. Performance of a serial dual amplifier system

The amplifier crystals are Nd:YALO rods with a dimension of 9.5 mm x 152 mm. The total average pump power for both amplifiers is 18 kW with a flash duration of about 130 μ s and 100 Hz repetition rate. Diffuse reflecting pump chambers were used in combination with cerium doped flow tubes to protect the YALO crystals against colour centre formation. The SBS-cell consists of a glass tube filled with carbon disulphide (CS_2).

The average output power of the system is tuneable from 1 Watt up to 211 Watt in a near diffraction limited beam (see Fig. 5a). To increase the average output power the master oscillator was also driven in a TEM_{00} - TEM_{01} mixed mode. The beam diameter is constant within a maximum deviation of 12 %.

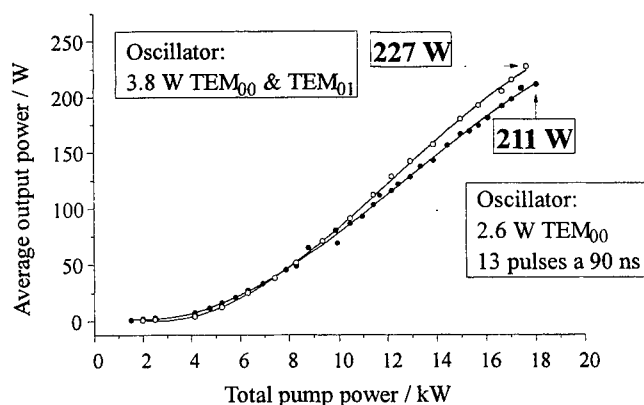


Fig. 5a. Measured average output power of a two amplifier system with SBS-mirror.

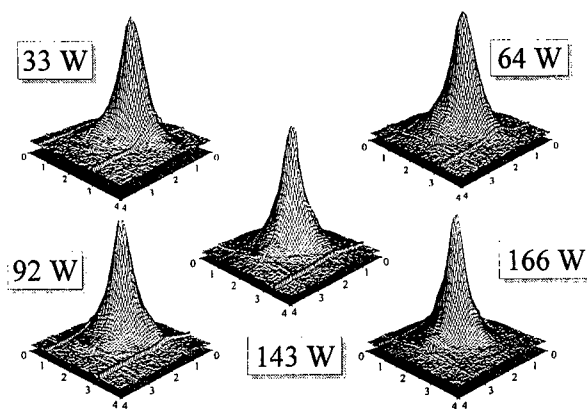


Fig. 5b. Beam profiles measured in a distance of 2.5 m.

2.4. Parallel arrangement of amplifiers with SBS-cell

The number of amplifiers and therefore the average output power, delivered from a serial arrangement, is limited. Parallel arrangements of amplifiers in conjunction with phase coupling by an SBS-cell are expected to achieve higher output powers up to the kW-range with high beam quality. In case of individual SBS-mirrors for each amplified beam, the phases between the beams fluctuate from shot to shot after reflection due to the non determined phase of the scattering sound wave. Therefore beam combination becomes difficult. However, using only one SBS-cell the beams build a common SBS-mirror and their reflected phases are coupled.

A set-up with two amplifier rods was realised delivering a preliminary average output power up to 50 Watt. To demonstrate the phase coupling the two amplified beams delivered from each amplifier rod after the second pass were interfered enclosing a small angle. Fig. 6 shows the interference pattern averaged over 70 shots using separate SBS-cells and a common SBS-cell. In case of separate SBS-cells the phase between the beams fluctuate from shot to shot resulting in a time dependent shift of the interference pattern. Therefore the interference contrast is reduced. A common SBS-mirror results in a stable interference pattern indicating phase coupling of the two beams.

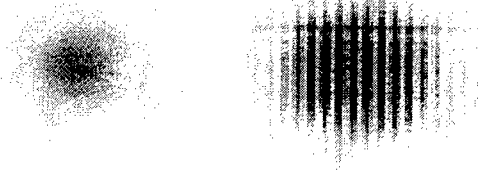


Fig. 6. Measured time average interference pattern of the individual beams after the second amplifier pass with individual SBS-cells (left picture) and a common SBS-cell (right picture).

3. MOPA-SYSTEM WITH FIBRE PHASE-CONJUGATOR

For cw-pumped MOPA-systems with high repetition rate above 10 kHz the SBS-threshold has to be decreased down to about 1 kW. For this purpose, we investigated quartz fibres exhibiting a great interaction length.⁷ With a multi mode fibre the threshold power for SBS has been reduced already down to 6 kW. Due to light guiding by the fibre the threshold power and therefore the energy reflectivity becomes nearly independent of the beam quality (see Tab. 1), whereas the reflectivity of a Brillouin-cell with focusing geometry decreases with lower beam quality.

Setup	Energy reflectivity [%]	Threshold power [kW]	Fidelity [%]
200 μm Fiber and $M^2=1.0$	50	17	90
200 μm Fiber and $M^2=10$	34	24	80
CS_2 and $M^2=1.0$	70	13	70
CS_2 and $M^2=10$	5	77	70

Tab. 1. Comparison of Energy reflectivity, threshold power and fidelity for the fibre phase-conjugator and a Brillouin-cell filled with carbon disulphide.

The fibres were tested as phase conjugating elements in a pulsed MOPA-system with 2 kHz average repetition rate (Fig. 7). Due to thermal lensing of the amplifier, the beam diameter and the astigmatism after the first amplifier pass depends on the average pump power. Therefore an optical system between the amplifier rod and the fibre entrance was developed to couple all the amplified beam energy into the fibre core, independent of the amplifier pump power. An average output power

up to 35 W could be obtained after the double pass. Thus, the fibre phase-conjugator seems to be an interesting alternative to toxic liquids such as CS_2 or gases under high pressure.

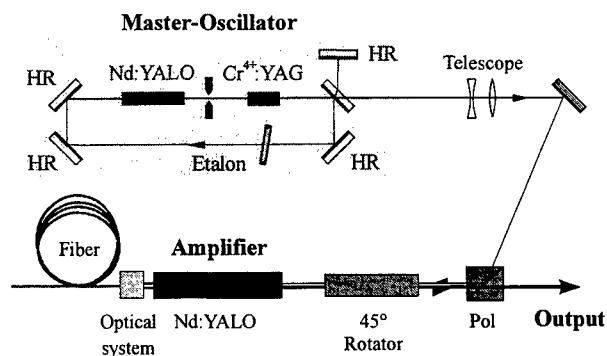


Fig. 7a. Pulsed MOPA-system with fibre phase-conjugator.

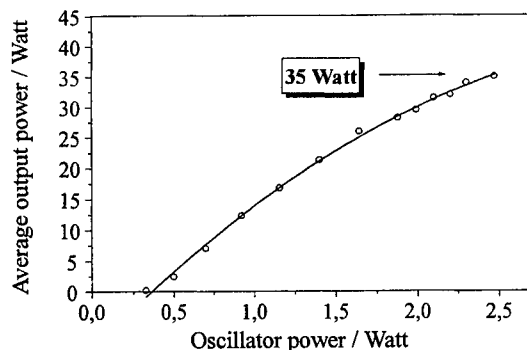


Fig. 7b. Measured average output power.

4. APPLICATIONS

4.1. Frequency doubling

High average power solid-state lasers for the visible range are of great importance for industrial applications. In the field of materials applications high cutting speed with low thickness of sections are required. Therefore kHz pulse repetition rates with average output powers of several ten Watt in conjunction with high beam quality are required. Solid-state lasers with phase conjugation are the best choice for SHG due to the high beam quality at high average output power.

High average power SHG requires a special analysis of the set-up. Due to the absorption of non-linear crystals in the visible the non-linear crystal has to be stabilised thermally. Each average output power results in a different temperature distribution inside the crystal. KTP was used due to its high non-linear coefficient and large temperature acceptance. The dimensions of the crystal were 5x5 mm aperture and 12 mm length. Type II phase-matching was used at a wavelength of 1080 nm. The maximum peak intensity was 15 MWcm^{-2} and the beam diameter was 1.75 mm. Fig. 8 shows the measured average output power of the second harmonic vs. the average input power of the fundamental wave. Due to a damage threshold of about some 100 MWcm^{-2} conversion efficiencies above 50% can be expected.

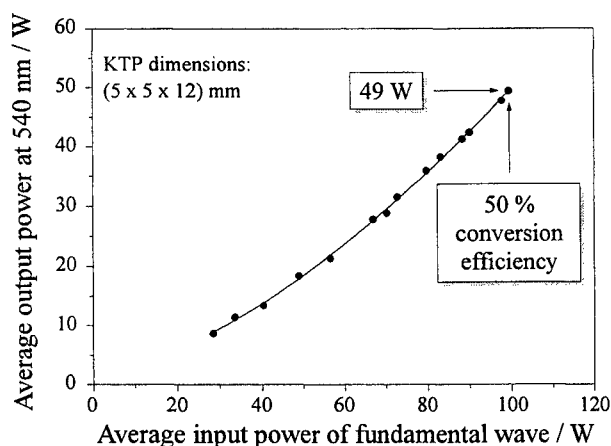


Fig. 8. Measured average output power at 540 nm vs. the used input power at 1080 nm

Due to the constant input beam diameter in front of the non-linear crystal the visible output beam shows no changes of the beam diameter (Fig. 9).

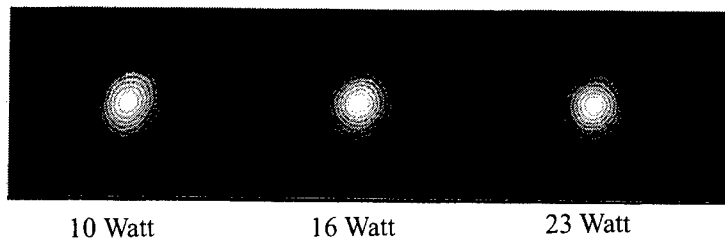


Fig. 9. Measured beam profiles at 540 nm for different average power.

4.2. Materials processing

Fast drilling and cutting in the micrometer range with high precision and aspect ratio has been demonstrated with the described laser system. For a given material thickness diffraction limited beams produce the smallest possible bores with low variations of the beam diameter along the material. To demonstrate the beam quality small holes were realised with one laser shot. Fig. 10a shows an example of a bore exit in aluminium. Fig. 10b shows a cutting kerf with a width of $28\text{ }\mu\text{m}$ in a ceramic with 1.1 mm thickness corresponding to an aspect ratio of 1:39.

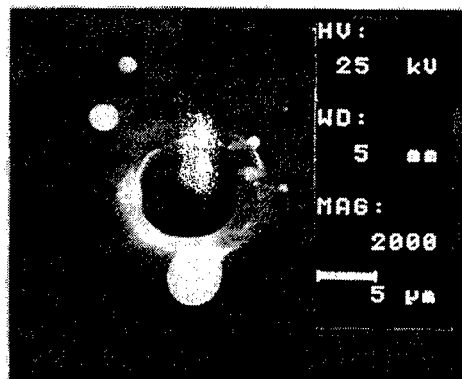


Fig. 10a. Bore in aluminium (thickness $100\text{ }\mu\text{m}$, diameter $6\text{ }\mu\text{m}$).

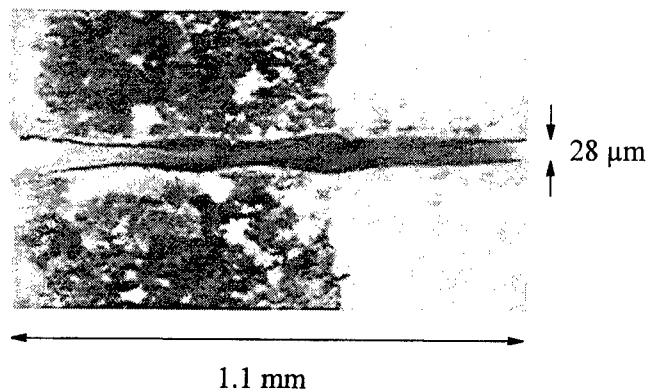


Fig. 10b. Cutting kerf in ceramics.

5. ACKNOWLEDGEMENTS

Financial support from the Bundesministerium für Bildung, Wissenschaft, Forschung und Technologie (BMBF) and the Verein Deutscher Ingenieure (VDI) is gratefully acknowledged.

6. REFERENCES

1. Q. Lü, H. Weber, Opt. Comm. **118**, 457-461 (1994).
2. N.G. Basov, V.F. Efimkov, I.G. Zubarev, A.V. Kotov, S.I. Mikhailov, M.G. Smirnov, JETP Lett. **28**, 197 (1978).
3. I.D. Carr, D.C. Hanna, Appl. Phys. B **36**, 83-92 (1985).
4. H.J. Eichler, A. Haase and R. Menzel (1995), „100-Watt Average Output Power 1.2 Diffraction Limited Beam from Pulsed Neodymium Single-Rod Amplifier with SBS Phase Conjugation“, IEEE J. Quantum Electron. **31**, 1265-1269.
5. H.J. Eichler, A. Haase, R. Menzel, „High Beam Quality by SBS Phase Conjugation of a Single Rod Nd-Amplifier up to 140 Watts Average Output Power“, Optical and Quantum Electronics **28**, 261-265 (1996).
6. H.J. Eichler, A. Haase, O. Mehl, „Serial amplifier arrangement with optical system for compensation of strong thermal lens variation“, German patent pending (1996).
7. H.J. Eichler, B. Liu, J. Kunde, A. Haase, „Fiber phase conjugators with high fidelity and reflectivity, and low power threshold“, German patent pending (1996).

2. Solid State Lasers I

High Average Power Diode-Pumped Solid-State Lasers

Camille Bibeau, Ray Beach, Eric Honea, Chris Marshall, Steve Sutton, Mark Emanuel, Jay Skidmore, and Steve Payne

Lawrence Livermore National Laboratory,
PO Box 808, L-441, Livermore, CA 94550, USA
Tel: (510) 422-7798, Fax: (510) 423-6195, Email: bibeaul@llnl.gov

The combination of our unique capabilities at LLNL in diode development, crystal growth, and system designs have allowed us to pursue a variety of research areas of interest to the commercial, medical, and defense industries. We have developed a flexible diode pumping technology which utilizes low cost silicon microchannel coolers to enable high average power diode operation and a shaped cylindrical microlens technology which allows the radiance conditioning of large two-dimensional laser diode arrays. The flexibility that this diode technology has brought to pump power generation in both average power and radiance have broadly expanded the number of ion-host combinations that can be efficiently excited and used in diode pumped solid state lasers.

Many potential applications in the area of materials processing motivate the development of efficient, compact cw 1 μm lasers systems with operational lifetimes capable of exceeding thousands of hours. Yb-doped laser hosts offer spectroscopic and laser properties that make them promising candidates for high average power 1 μm laser systems. In particular, Yb:YAG has a long storage lifetime of 951 μsec and a very low quantum defect resulting in less heat generation during lasing than comparable Nd based systems. Using a scaleable diode end-pumping technology developed at LLNL we have built and demonstrated a Yb:YAG system capable of delivering over 155 W of cw power and up to 100 W of Q-switched power at multi-kHz repetition rates.

We have also developed a Tm:YAG laser and demonstrated up to 115 W cw at 2.01 μm . There are many practical medical and defense applications for the 2 μm light produced by this system as a result of it being strongly absorbed by water and also because it is an 'eye-safe' wavelength. To allow average power scaling of the Tm:YAG laser, we wing-pump the Tm³⁺ off of the main absorption feature. This technique is highly effective at creating sufficient population inversions to overcome ground state reabsorption while at the same time allowing the pump to penetrate deeply enough into the rod that the resulting thermal load becomes manageable. Improvements and performance data from both the Yb:YAG and Tm:YAG systems will be further discussed in the presentation.

In addition to the systems above we have also been working towards developing a laser system using Yb-doped Sr₅(PO₄)₃F or Yb:S-FAP which is capable of scaling to 1 kilojoule of energy at a 10 Hz repetition rate. Several small scale demonstrations with Yb:S-FAP have been made to measure laser performance and gas face-cooling concepts. This gain medium was chosen since it is well suited for low to medium average power applications that are sensitive to overall system efficiencies. Performance data and future plans for an advanced experimental facility will be further discussed in the presentation.

This work was performed under the auspices of the US Department of Energy by Lawrence Livermore National Laboratory under contract W-7405-Eng-48.

Design and industrial applications of high-power diode-lasers

P. Loosen, J. Biesenbach, K. Du, C.R. Haas, R. Poprawe, G. Treusch
Fraunhofer-Institut für Lasertechnik (ILT), Steinbachstr. 15, D-52074 Aachen, Germany
Tel. ++49 241 8906-162, Fax. -121

Abstract

Developments concerning high-power diode lasers, optical systems for beam shaping and superposition and complete systems for direct materials processing will be discussed, along with examples of their industrial applications.

Keywords: high-power diode lasers, industrial applications, micro-optics, stacking, microchannel heat-sinks

1. Introduction

In the past few years, lasers have become a standard tool in applications such as the cutting and welding of metals. In the laboratory, numerous additional applications, e.g. surface processing, soldering or brazing, have been investigated and it has been proven that the laser generates technically excellent processing results. Often, however, it cannot be introduced onto the production line due to a lack of economic efficiency, resulting from the generally large size and high price of conventional CO₂ or solid-state lasers. This situation may change in the near future through the use of high-power diode-laser (HPDL) systems for direct materials processing, at least, that is for those applications requiring a process intensity or beam quality resp. achievable by diode lasers, as is discussed below. In these laser systems, the diodes are not utilized in the conventional way to pump a laser crystal, but are arranged, for example, in stacks, in order to increase the total output power to the desired level. The total beam is guided directly to the workpiece. Advantages of such laser beam sources are their high compactness and their production costs, which are already in the region of those of conventional lasers, and expected to decrease considerably in the near future (Fig. 1).

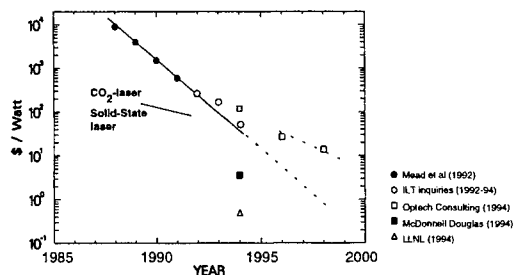


Fig. 1: Diode-laser price: development and future projection

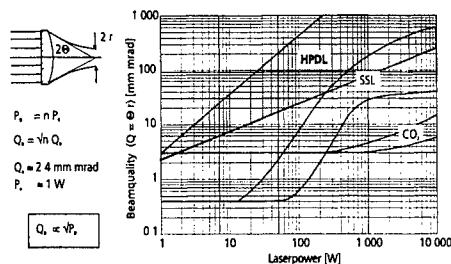


Fig. 2: Beam quality of incoherently combined diode-lasers in comparison to conventional industrial lasers

The diode laser systems discussed in this paper are based on the principle of incoherent superposition of either several diode laser bars or geometrically rearranged emitters of one single bar. For both cases, the beam parameter product (the "quality" Q) of the resulting beam is, typically, not independent of the laser power, as is the case for idealized conventional lasers, but is directly proportional to the square root of the output power. This is shown in a slightly simplified way in Fig. 2, where a number n, of individual diode laser emitters with a Q of 2.5 mm-mrad at 1 W diode laser power are combined. Such an emitter can be generated by the geometrical rearrangement of a single emitter on a diode laser bar (an emitter with a typical Q of 0.5 mm-mrad in the fast axis and 10 in the slow axis) e.g. by means of the technique described in chapter 3. As is shown in Fig. 2, in comparison to conventional CO₂ and Nd-YAG lasers, diode lasers are, in principle, able to achieve a beam quality in the high-power range, and thus a process intensity, in the range of present solid-state lasers. This is valid for the best case (lower line) without any loss of power or beam quality when combining the individual beams. Present systems, however, are far away from this limit and a lot of work, currently being undertaken, aims towards increasing the performance of these diode laser systems, this is further discussed in chapter 2. The range of industrial applications for present systems is, nevertheless, far reaching, as will be illustrated by two examples in section 3.

2. Components for diode laser systems

Two main R&D topics which aim towards broadening the application range for diode lasers are the increase of the output power of one diode bar, to yield higher process intensity and lower production costs, and the increase of the optical quality of the components for beam processing, especially the fast-axis collimation lens.

A key factor for increasing output power is to build efficient heat-sinks, with low thermal impedance, in order to dissipate the waste heat of the diode laser bar at a low temperature level. We have developed microchannel structures, first introduced by LLNL for heat-sinking with diode lasers /1/, our concept being based, however, on copper instead of silicon. Copper has been chosen due to its excellent thermal and electrical conductivity and ease of machining. The heat-sinks are built up by several layers of copper sheet, produced by laser-cutting, and are bonded together by a diffusion-welding process /2/. With such heat-sinks and a Siemens G5 semiconductor bar (diode footprint 0.6 mm x 10 mm), a maximum output power of 116 W has been achieved (Fig. 3). The characteristic thermal impedances of the heat sinks is in the range of 0.4 - 0.5 K/Watt waste heat, with which the diodes can be safely operated at 30 - 40 W laser power, with a temperature rise in the junction of about 20-30 K.

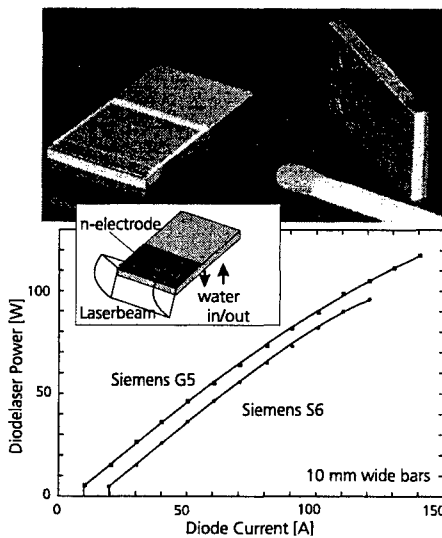


Fig. 3: (left) Design and performance of diode-lasers, mounted on Cu-microchannel heat-sinks

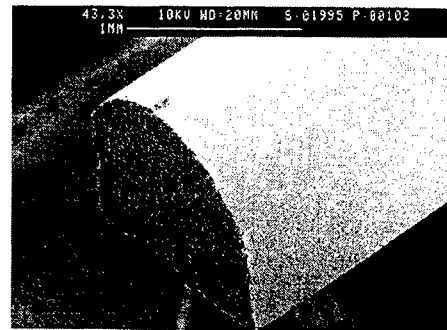


Fig. 4: (right) High-quality aspherical lens, made from high-index glass (Schott LAFN 21) by an ultra-precision grinding process. The total transmission of the AR-coated lens is above 90%, the beam quality in the fast direction behind the lens is $M^2 < 4$ for a diode laser with a NA of 0.8

As discussed in section 1 the potential of direct HPDL applications broadens, the higher the intensity is raised at the workpiece. In comparison to the pumping of solid-state laser crystals, the demands on beam-shaping and beam-combining devices are much higher if the laser diode radiation is to be applied directly to the workpiece. The beam from a diode laser is strongly divergent in the direction perpendicular to of the diode junction plane, with a NA up to 0.8, and all current techniques for beam combination start with collimating the beam in that direction as a first step. One of the key issues in the development of HDPL-modules for direct applications is, therefore, to optimize micro-optical elements for fast-axis collimation and to minimize losses in beam quality and beam power.

Although manufacturing techniques have been examined, some of which have led to commercial products /3,4/, it seems that the specific requirements for fast-axis collimation at high power levels, and with the beam characteristics required here, are not fully met by the micro-optics available. Our work takes advantage of the capabilities of present ultra-precision machining technologies. A glass-lens, as shown in Fig. 4, made from high-index glass is fabricated with an ultra-precision grinding technique on a Rank-Pneumo ASG 2500 /7/. Using the technology of the ductile grinding of glass, very high shape accuracy and extremely low surface roughness can be obtained. A ray-tracing program was used for the calculation and optimization of the aspheric lens surfaces. The lenses, which are now available at small lot-sizes have a total power throughput over 90% and achieve a normalized beam parameter product behind the lens of $M^2 < 4$ for the best lenses, applied to a diode laser with a fast-axis NA of 0.8.

3. Diode-laser modules and industrial applications

In the following, two different methods will be discussed for shaping the emission of the diode laser in order to apply it directly for materials processing: the beam transformation of a single diode laser bar and the stacking of a number diode laser bars.

The beam transformation of a single diode laser bar is suited to low-power applications. Symmetrical beams are generated, with some tens of watts, which can then be coupled into fibers and scaled to a higher power by way of fiber bundling. Different techniques for the transformation of the line-shaped beam, which has strong beam quality differences in the fast- and slow-axis, have been proposed, e.g./5,6/. We are employing a technique which utilizes two step-shaped mirrors to geometrically rearrange the individual emitters of a bar in such a way, that the beam size as well as the beam quality in the two orthogonal directions are matched. Fig. 5 shows a diode laser module, based on this technology. Our standard modules of this kind produce about 30 W laser power out of a fiber with a core diameter 0.6 mm and a NA of 0.2. Modules are under development to produce the same output power from a 0.3 mm fiber of the same NA. In Fig. 6, a module, such as that shown in Fig. 5, is combined with a beam scanner and a computer control system and integrated into a commercial machine for the soldering of SMD-parts and for the welding of plastics..

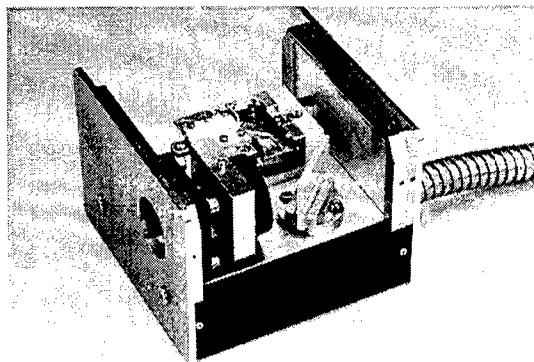


Fig. 5: Diode laser with beam transformation by two "step-mirrors", with this transformation technique more than 30 W out of a 0.6 mm fiber (NA 0.2) has been achieved

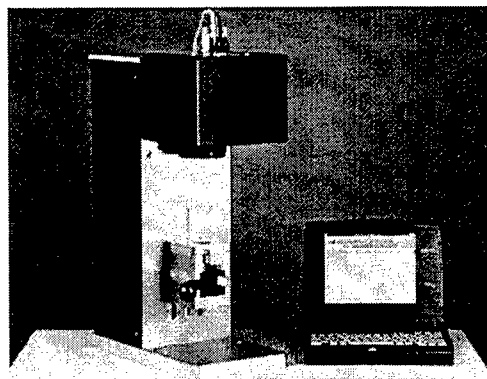
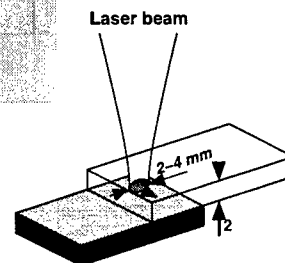
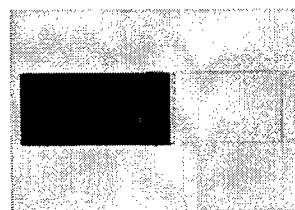
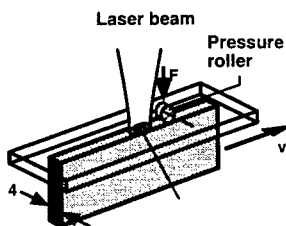
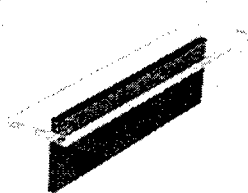


Fig. 6: Machine for laser welding of plastics, soldering etc.. A diode-laser module as shown in fig. 5 is combined with a scanner and a computer control system

Fig. 7 compares the welding of LURAN parts in T-joint- and overlap geometry. In this specific case, a transmissive and an absorptive component have been combined so that the laser power is absorbed directly at the joining interface. In order that the cross-section of the join be large, the beam diameter at the workpiece was chosen in the range of 2 - 4 mm. In comparison to the standard manufacturing technique, ultra-sonic welding, the strength of the join was found to be over 50% higher. Applications of this welding process include use in the production of plastic parts for the automotive industry and the production of casing boxes and housings in the electronic industry.

Fig. 7: Application of the machine shown in fig. 6 for the welding of plastics (LURAN)



In order to increase the total laser-power to a level relevant for high-power applications, a stacking technology has been developed as an alternative to bundling the fibers of the diode laser modules, with the advantage of lower costs. As illustrated in fig. 8, the diode lasers, with a total height of 1.7, mm have been supplied with collimating lenses and are stacked together. After the collimation of the slow axis divergence with a cylinder-lens, the total emission pattern is focused down with an ordinary photographic lens. With the polarization coupling of two stacks, each incorporating 20 diode lasers, the maximum values achieved for output power and the intensity at the focal spot (F#2) were 1 kW and $2 \cdot 10^4$ W/cm² resp. . Depending on the specific application, the beam is either focused directly onto the workpiece or onto an array of fibers, located at the focal position of the lens.

Such stacks can, for example, be applied in surface treatment, laser-assisted machining, brazing [7] and soldering of larger components, for instance electric components in the automotive industry (Fig. 9).

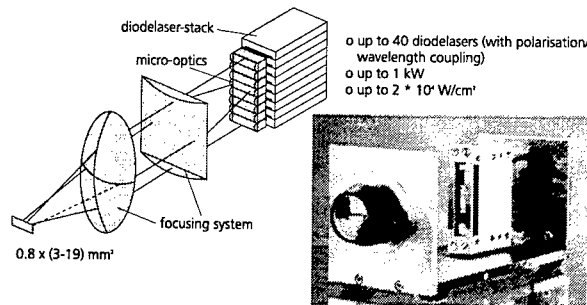


Fig. 8: Principle and laboratory set-up of a diode-laser stack for materials processing

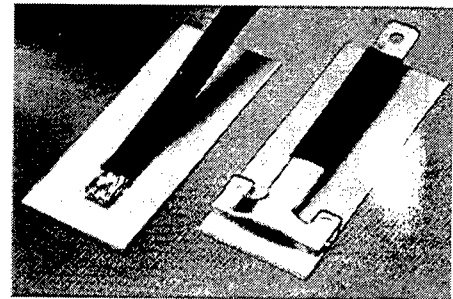


Fig. 9: Application of a stack as shown in fig. 8: soldering of electric components ($P = 150 - 300 \text{ W}$)

4. Conclusion

Diode laser bars, mounted on copper-microchannel coolers, as discussed above, yield a maximum output power of approx. 120 W. The diode lasers can be operated safely and reliably at a power-level of approximately 30 W. With ultra-precision machined micro-optics for fast-axis collimation a collimated beam with $M^2 < 4$ beam quality, at a power throughput above 90 %, has presently been achieved in the best scenario. Diode laser modules have been built, based on a beam transformation technique with step-shaped mirrors, to be applied to a number of low-power industrial applications, such as the soldering of SMD-parts, plastics welding or the pumping of solid-state lasers. Through the use of stacking techniques, the total output-power has been raised, so far, up to 1 kW, in the near future multi-kW stacks will be built up and tested for direct materials-processing applications. By further increase in the quality of the packaging technology, narrowing the quality spread of the collimation lenses, and the employment of new beam transformation and combination schemes, the beam quality at the kW level should, in the near future, be increased by a factor of about 10.

The authors believe that stacks and diode modules, either applied directly to the workpiece, or via a fiber-bundles, will have numerous applications and thus a large industrial market. As discussed above, the technical advantages of direct diode laser applications can already be tested and proven, the true economical success and market volume, however, being subject to the future increase in diode lifetime and reliability, and the reduction of price per watt diode power. If the prices indeed decrease, as predicted in many scenarios, some tens of megawatt total diode power may be needed for direct diode laser applications.

5. Acknowledgments

The main part of this work has been supported by the BMFT under contracts no. 13N6501 and 13N6385, which is gratefully acknowledged.

6. References

1. D.F. Welch: Advances in high power semiconductor diode lasers and their applications, Technical Digest to the Conference on Lasers and electro-Optics Europe, Amsterdam, IEE Catalog No. 94TH0614-8 (1994)
2. V. Krause et. al.: Microchannel coolers for high power laser diodes in copper technology, SPIE OE/LASE, Los Angeles 1993, Proc. B, Int. Soc. Opt. Eng. USA, Vol. 2148, pp. 351-358, 1994
3. J.M. Snyder et. al.: Fast diffraction limited cylindrical microlenses, Appl. Opt. Vol. 30(19), p. 2743, (1991)
4. LIMO Corp. in "Laser Focus World", June 1996, p. 157
5. W.A. Clarkson, B. Nielsen, C. Hanna: Diode laser bar beam shaping technique, CLEO 1994, Anaheim/USA, Technical Digest CFH6
6. European patent application EP 0484 279, Fisba Optik Corp., Switzerland
7. P. Loosen et.al., High-power diode lasers and their direct industrial applications, SPIE Proc. Series Vol. 2382, pp. 78-88, 1995

Photorefractive phase-conjugator coupled-cavity diode laser for high spectral-brightness operation

Akira Shiratori and Minoru Obara

Department of Electrical Engineering, Faculty of Science and Technology, Keio University
3-14-1 Hiyoshi Kohoku-ku Yokohama 223 Japan

ABSTRACT

Narrow spectral width oscillation of an AlGaInP index-guided diode laser (638 nm) has been achieved with an external stimulated photorefractive backscattering phase-conjugator. The emission spectral width was narrowed down to 5.3 GHz (7.2 pm) due to the very narrow spectral bandwidth of the 2k gratings formed by the stimulated photorefractive backscattering process in a photorefractive barium titanate crystal. The spectral brightness increased ~50 times as high as a free-running diode laser. We have also suppressed the self-scanning of the laser frequency, and successfully achieved wavelength-stable oscillation in the phase-conjugator coupled-cavity diode laser.

keywords : phase conjugation, photorefractive effect, AlGaInP diode laser, external cavity diode laser

2.INTRODUCTION

External cavity operation of a diode laser has been used to improve its spectral properties, leading to a high spectral-brightness operation as well as a single longitudinal mode operation, spectral line-narrowing, and frequency stabilization^{1,2}. However, the laser system is quite sensitive to the variations in external cavity length, therefore, a precise temperature control and an anti-vibration system are required. Moreover, the alignment of the external mirror is extremely difficult because of the small active region of the diode laser. An attractive candidate for the stable and robust external cavity system is a phase-conjugator coupled-cavity, where an external phase-conjugate mirror is employed instead. Since the reflected phase-conjugate wave traces exactly back to the small active region of the diode laser, no alignment is necessary for the external phase-conjugate mirror, leading to the mechanically stable laser system. In many media which can generate the phase-conjugate wave, the photorefractive crystals have been the simplest, the most useful, and the most efficient phase-conjugate mirror since Feinberg developed a self-pumped (cat) phase conjugator³.

With a photorefractive barium titanate (BaTiO₃) self-pumped phase conjugator, phase-conjugator coupled-cavity operation of diode lasers⁴ and a diode laser array⁵ have been experimentally demonstrated. In their experiments, the full-width at half-maximum (FWHM) of the emission spectral width was narrowed to ~ 1nm, however, they oscillated with multiple longitudinal modes. This is owing to the spectral bandwidth of the transmission gratings formed in the cat conjugator, which is expected to ~ 1nm. In order to obtain the narrowest spectral bandwidth in the phase conjugator, the interference of two counterpropagating beams is required, which induces refractive index gratings with the shortest grating

period (2k grating). The phase conjugation, induced by the 2k gratings, is known as stimulated photorefractive backscattering (SPBS)⁶. Thus, the use of the SPBS conjugator as an external phase conjugator can be expected to improve the spectral properties of the diode laser much better than the cat conjugator. In this paper, we have demonstrated the narrow spectral width operation of an AlGaInP index guided diode laser coupled to a SPBS conjugator.

3. EXPERIMENT

3.1 Mechanism of phase conjugation

There have been reported three mechanisms of self-pumped phase conjugation in a single photorefractive crystal without the use of any external mirror; four-wave mixing from internal reflections (cat conjugation)³, SPBS⁶, and their hybrid process⁷. It is known that the mechanism of phase conjugation in the photorefractive crystal depends on the dopant density as well as the incident beam parameters such as power, diameter, and wavelength⁸. The BaTiO₃ crystal used is doped with cobalt (100 ppm in melt), leading to the high photorefractive response for longer wavelength and increase of backscattered light which starts the SPBS process. In preliminary experiment with a He-Ne laser we have obtained the phase-conjugate wave by means of SPBS process, not four-wave mixing process. We confirmed the SPBS process, by observing the optical path in the crystal. The phase-conjugate reflectivity reached ~ 80%.

3.2 Phase-conjugator coupled-cavity diode laser

The experimental setup is shown in Fig. 1. The laser source is a cw index guided MQW AlGaInP diode laser, emitting in the visible spectral region ($\lambda = 638$ nm @20°C). The reflectivities of the front and rear facet of the diode laser are 2% and 30%, respectively. This diode laser oscillates with several longitudinal modes and the FWHM of the total emission spectral width is 260 GHz (0.36 nm) at an injection current of 80 mA, corresponding to the output laser power of 10 mW from the low reflectivity facet. The laser beam is loosely focused by the collimating lens, and it is incident on the photorefractive BaTiO₃ crystal (4.2×4.4×5.1 mm³), which terminates the 50 cm long external cavity. The precise geometry of the photorefractive crystal and the laser beam is shown in the inset of Fig. 1. The laser output is coupled out with a beam splitter (R = 17%), and the laser wavelength and spectral width is monitored by spectrum analyzer and monitor etalon (FSR:100GHz), respectively.

Figure 2 shows the temporal evolution of laser wavelength and spectral width of the phase-conjugator

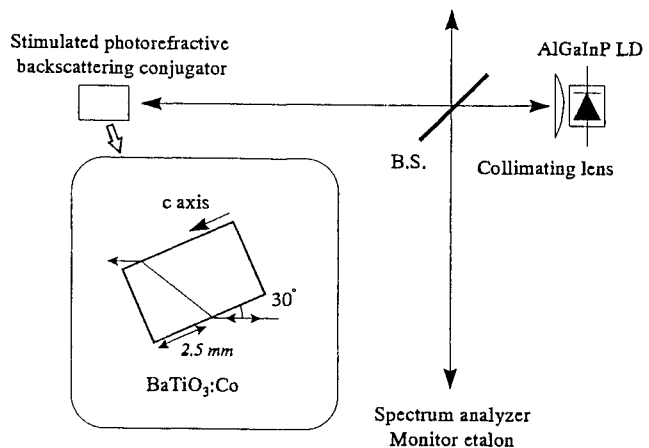


Fig. 1 Experimental setup of a photorefractive phase-conjugator coupled-cavity diode laser. Precise geometry of the stimulated photorefractive backscattering conjugator is shown in the inset. B.S.: Beam splitter (R=17%)

coupled-cavity diode laser. The spectral properties were affected by the phase-conjugate wave, a few tens of seconds from the switch-on at $t = 0$ s. Until $t = 95$ s, the phase-conjugate reflectivity R_{PCM} was quite low ($< 1.8 \times 10^{-3}\%$), and which was lower than the detection limit of our detector. Here, one longitudinal mode was enhanced by the phase-conjugate feedback, however, other longitudinal modes were not suppressed completely. At $t = 100$ s, R_{PCM} dramatically increased up to 50%, and the laser spectral width was narrowed below resolution limit of the spectrum analyzer. We measured the spectral width of ~ 5.3 GHz (7.2 pm) with the monitor etalon. The laser output increased 1.3 times as high as the free-running diode laser. All of the laser output power, phase-conjugate reflectivity and laser wavelength were observed stable in this case.

Under the stable operational conditions, the total internal reflection using a crystal corner³ was not observed in the crystal, which does not mean the mechanism is the four-wave mixing process. From this fact, we conclude the mechanism of phase conjugation is SPBS process. The calculated spectral bandwidth of the 2k gratings formed by the SPBS process is ~ 9.4 GHz (12.8 pm)⁹, where wavelength $\lambda = 638$ nm, refraction index $n = 2.5$, and index modulation $n_1 = 5 \times 10^{-5}$. This value would explain the experimental spectral width of 5.3 GHz, and the theoretical and experimental results show the much narrower spectral-width operation by means of the 2k gratings than the transmission gratings^{4,5}.

3.3 Wavelength stability

Under the phase-conjugator coupled-cavity operation using a self-pumped phase conjugator, self-scanning of the laser frequency was reported¹⁰⁻¹², which results in the frequency-unstable oscillation. This phenomenon is attributed to the frequency shift of the phase-conjugate wave^{10,11} or mode competition between the longitudinal mode of the external cavity and the photorefractive ring resonator^{12,13}, and both of which result from the four-wave mixing conjugator employed in all of these experiments. We observed no self-frequency scanning in the experiment, except for small frequency hopping before buildup of the stable phase-conjugate wave output. The wavelength-stable oscillation in our phase-conjugator coupled-cavity diode laser is due to SPBS process which induces no frequency shift⁶ and forms no photorefractive resonator in the crystal.

4. CONCLUSION

We have demonstrated the operation of the photorefractive phase-conjugator coupled-cavity diode laser

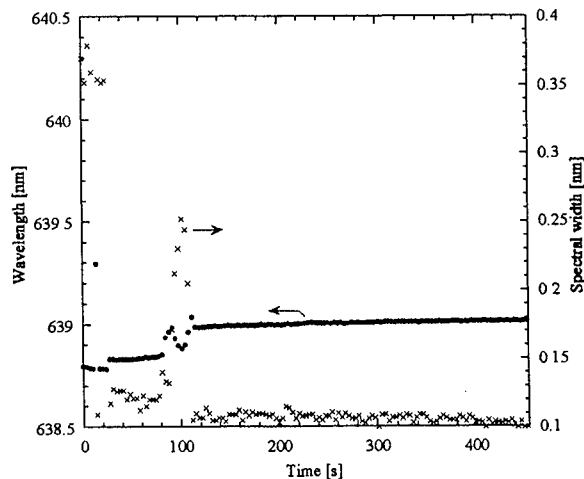


Fig. 2 Temporal evolution of the laser wavelength and the emission spectral width. The laser beam is incident on the crystal surface at $t=0$.

using SPBS process in a BaTiO₃:Co crystal. Narrow spectral-width to 5.3 GHz has been achieved by means of narrow spectral bandwidth of 2k gratings induced by SPBS process, and the spectral brightness increased ~50 times as high as the free-running diode laser. Additionally, we have also suppressed the self-frequency of the laser frequency, and successfully achieved wavelength-stable oscillation in the phase-conjugator coupled-cavity diode laser.

5. ACKNOWLEDGMENT

We thank Dr. I.Mito and Dr. K.Kobayashi of NEC for providing AlGaInP diode lasers.

6. REFERENCES

1. B.Tromborg, J.H.Osmundsen, and H.Olesen, "Stability analysis for a semiconductor laser in and external cavity," *IEEE J. Quantum Electron.* QE-20(9), 1023-1032 (1984).
2. M.W.Fleming and A.Mooradian, "Spectral characteristics of external-cavity controlled semiconductor lasers," *IEEE J. Quantum Electron.* QE-17(1), 44-59 (1981).
3. J.Feinberg, "Self-pumped, continuous-wave phase conjugator using internal reflection," *Opt. Lett.* 7(10), 486-488 (1982).
4. S.Maihot and N.McCarthy, "Influence of phase conjugate optical feedback on the emission properties of visible low-power diode lasers," *Can. J. Phys.* 71, 429-433 (1993).
5. S.MacCormack and J.Feinberg, "High-brightness output from a laser-diode array coupled to a phase-conjugating mirror," *Opt. Lett.* 18(3), 211-213 (1993).
6. T.Y.Chang and R.W.Hellwarth, "Optical phase conjugation by backscattering in barium titanate," *Opt. Lett.* 10(8), 408-410 (1985).
7. Y.Lian, H.Gao, P.Ye, Q.Guan, and J.Wang, "Self-pumped phase conjugation with a new mechanism in KTa_{1-x}Nb_xO₃:Fe crystals," *Appl. Phys. Lett.* 63(13), 1745-1747 (1993).
8. S.X.Dou, H.Gao, J.Zhang, Y.Lian, H.Wang, Y.Zhu, X.Wu, C.Yang, and P.Ye, "Studies on formation mechanisms of self-pumped phase conjugation in BaTiO₃:Ce crystals at wavelengths from 570 to 680 nm," *J. Opt. Soc. Am. B* 12(6), 1048-1055 (1995).
9. P.Yeh, *Introduction to photorefractive nonlinear optics*, p.59, Wiley, New York, 1993.
10. W.B.Whitten and J.M.Ramsey, "Self-scanning of a dye laser due to feedback from a BaTiO₃ phase-conjugate reflector," *Opt. Lett.* 9(2), 44-46 (1984).
11. J.Feinberg and G.D.Bacher, "Self-scanning of a continuous-wave dye laser having a phase-conjugating resonator cavity," *Opt. Lett.* 9(9), 420-422 (1984).
12. M.Cronin-Golomb and A.Yariv, "Self-induced frequency scanning and distributed Bragg reflection in semiconductor lasers with phase-conjugate feedback," *Opt. Lett.* 11 (7), 455-457 (1986).
13. M.D.Ewbank and P.Yeh, "Frequency shift and cavity length in photorefractive resonators," *Opt. Lett.* 10(10), 496-498 (1985).

A planar waveguide Nd:YAG laser, face pumped by laser diode bars

D. Pelaez-Millas, A. Faulstich, H. J. Baker, and D. R. Hall.

Department of Physics, Heriot-Watt University
Edinburgh, EH14 4AS, United Kingdom

Abstract

A planar YAG waveguide with a 200 μm Nd doped core, produced by a diffusion bonding process, has been face pumped by an array of qcw laser diode bars, producing 9.3 W of average output power at 8% duty cycle, with 24% conversion efficiency. The multi-pass pumping using a slotted mirror reflective pump chamber has been modelled by a matrix method, accounting for both laser diode temperature tuning effects and the pumping efficiency found in the experiment.

Keywords: planar waveguide, slab laser, diode pumped, Nd:YAG.

1. Introduction

High average power solid state lasers using bulk crystals are limited in power output by thermal conduction to the cooled surface of the crystal. For a slab shaped laser medium, improved heat removal, and hence high power output per unit volume, can be obtained by reducing the thickness and increasing the power density of pumping, until some limit is met, such as the inefficient absorption of pump light. This leads to the idea that a slab waveguide is potentially the highest power density solid state laser configuration, which can be scaled in power proportional to the area.

Previously, Nd:YAG waveguides have been epitaxially grown on YAG substrates [1], but the limited thickness of the active layer has required pumping by high beam quality diode laser light, coupled into the waveguide through an edge. In the narrow guides, waveguide loss also reduces the power conversion efficiency. In this paper, we report on a new configuration, where a much thicker active layer (200 μm) is formed by diffusion bonding of pieces of bulk YAG and Nd:YAG crystals [2]. The pump absorption in a single pass through the thin direction is now sufficient to allow face pumping with low beam quality laser diode light. Previously, we have reported a new configuration for efficient coupling of light into thin Nd:glass slabs [3], which uses a slotted mirror in a rectangular highly reflecting pump chamber to transmit pump light from closely coupled diode bars. This has now been used to pump the Nd:YAG planar waveguide laser.

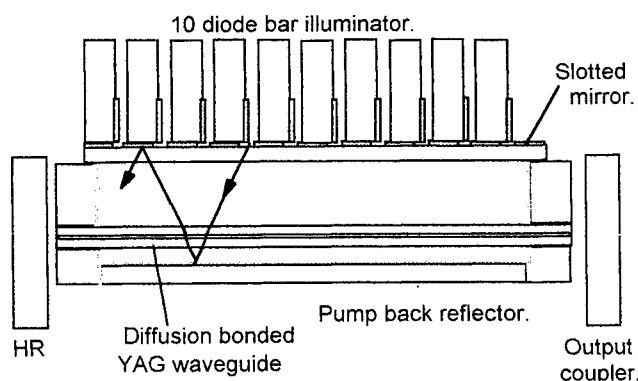


Fig.1 Side cross-section of pumping set-up

Figure 1 shows the pumping geometry. The planar waveguide has dimensions of 60 mm x 11 mm x 1 mm, with the 200 μm , 1% doped active layer sandwiched between 400 μm undoped YAG claddings. An illuminator formed by 10 quasi-CW diode laser array bars is used as the pumping device. Each diode is mounted on a water cooled copper heat sink, with an accurate spacing of 5 mm between each bar. In front of the illuminator, a slotted mirror is positioned with transmitting slots well aligned with the emitting facets of the diode bars. This is fabricated by deposition of a silver coating on a 1 mm thick quartz substrate, followed by etching of the 300 μm wide slots. The optical reflectivity of the mirror coating is 97%, whilst the geometrical reflectivity is 94%, giving an effective overall

reflectivity of 91.2% for pump light returning to the mirror from the pump chamber. In order to achieve a homogeneous pump radiation density, the planar waveguide slab is mounted 5 mm below the slotted mirror, making use of the large angular divergence of the diode bar radiation.

The pump back reflector is a 96% reflectivity gold mirror a few millimetres below the planar waveguide. Gold coated side and end walls are used to confine the pump radiation further. In this way multi-pass pumping of the thin absorbing layer is obtained. The waveguide slab is cooled with a nitrogen gas flow injected into the cavity through slots in the side walls.

2. Pumping efficiency modelling

For the 200 μm active layer thickness, the peak single pass absorption at a wavelength of 808 nm is only 14%. This means that precise tuning of the emission spectrum of the illuminator to the absorption peak of the gain medium is required to maximise pumping. Also it is essential to efficiently recirculate the light in the pumping chamber. It is thus important to have a model to calculate the fraction of the pump light absorbed in the slab waveguide, and that lost in the boundaries of the pumping chamber. This model should take into account the varying absorption of the gain medium as a function of the wavelength, the finite reflectivity from mirrors and boundaries in the pumping chamber, and the multiple reflections at each dielectric interface. The laser diode light has a limited angular spread which is maintained during multiple reflections from only plane interfaces. Light spreading laterally and longitudinally is returned by the reflecting side and end walls. The effect of localised loss such as light returning through the slots is quickly averaged out by the angular spread of the diode laser light. However, the angular spread of the diode laser radiation after refraction into YAG is not sufficiently great to require detailed modelling, and can be represented as propagating through the absorbing layer with slightly reduced absorption coefficient. It is thus possible to use a one dimensional model, assuming uniform lateral and longitudinal power density in the pump chamber. Figure 2 shows the circulation of light within the pump chamber in this one dimensional approximation.

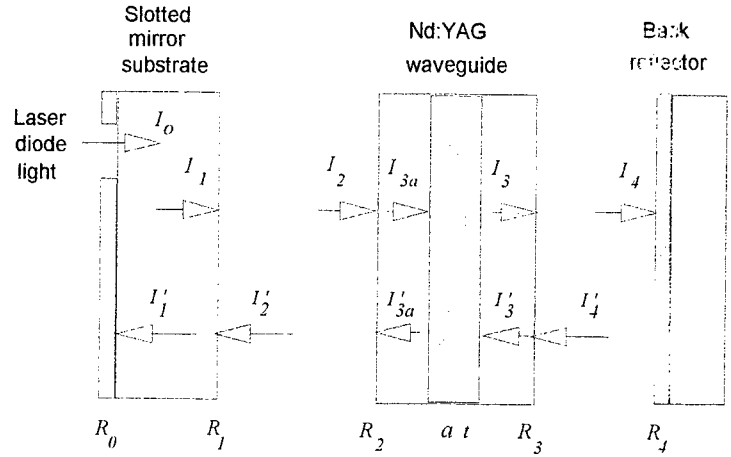


Fig. 2 Circulation of pump light in pump chamber

To fully account for multiple reflections, we have used a modification of the matrix method used for multi-layer coatings design. Each interface is represented by an intensity transmission matrix, but propagation phase shifts are not used, representing the incoherence of the light from the many independent laser diodes. For a reflecting interface, the forward and reverse intensities, represented by a column vector, are transformed by the equation:

$$\begin{bmatrix} I_n \\ I'_n \end{bmatrix} = \begin{bmatrix} 1 & -R_n \\ \frac{1-R_n}{R_n} & \frac{1-2R_n}{1-R_n} \end{bmatrix} \times \begin{bmatrix} I_{n+1} \\ I'_{n+1} \end{bmatrix} \quad (1)$$

An absorbing layer of thickness t has the following function in matrix notation:

$$\begin{bmatrix} I_n \\ I'_n \end{bmatrix} = \begin{bmatrix} \exp(\alpha t) & 0 \\ 0 & \exp(-\alpha t) \end{bmatrix} \times \begin{bmatrix} I_{n+1} \\ I'_{n+1} \end{bmatrix} \quad (2)$$

Such relations are useful in that the sequence of reflections in the cavity can be described by the cascaded multiplication of matrices. Following the notation defined by Fig. 2, the total pump power per unit area passing through the slotted mirror, I_0 , required to produce unit intensity incident on the back mirror ($I_4 = 1$) is given by the following two equations:

$$I_1 = I_0 + R_0 I'_1 \quad (3)$$

$$\begin{bmatrix} I_1 \\ I'_1 \end{bmatrix} = \begin{bmatrix} 1 & -R_1 \\ \frac{1-R_1}{R_1} & \frac{1-2R_1}{1-R_1} \end{bmatrix} \cdot \begin{bmatrix} 1 & -R_2 \\ \frac{1-R_2}{R_2} & \frac{1-2R_2}{1-R_2} \end{bmatrix} \cdot \begin{bmatrix} \exp(\alpha t) & 0 \\ 0 & \exp(-\alpha t) \end{bmatrix} \cdot \begin{bmatrix} 1 & -R_3 \\ \frac{1-R_3}{R_3} & \frac{1-2R_3}{1-R_3} \end{bmatrix} \times \begin{bmatrix} 1 \\ R_4 \end{bmatrix} \quad (4)$$

Equations (3) and (4) give the incident power which is required to produce unit intensity at the back reflector. The power incident on the Nd doped layer for unit back reflector intensity is then calculated by:

$$\begin{bmatrix} I_3 \\ I_3' \end{bmatrix} = \begin{bmatrix} \frac{1}{1-R_3} & \frac{-R_3}{1-R_3} \\ \frac{R_3}{1-R_3} & \frac{1-2R_3}{1-R_3} \end{bmatrix} \times \begin{bmatrix} 1 \\ R_4 \end{bmatrix} \quad (5)$$

The power absorbed in the active layer for light travelling in both directions is given by:

$$P_a = I_3 (\exp(\alpha t) - 1) + I_3' (1 - \exp(-\alpha t)) \quad (6)$$

$$\text{The pumping efficiency is then given by:} \quad \eta(\alpha) = P_a / I_0 \quad (7)$$

The matrix formulation of the problem is easily handled by Mathcad™ software, to give the pumping efficiency as a function of the absorption coefficient α , and thus indirectly as a function of wavelength. For the conditions of the experiment, $R_0 = 91.2\%$, $R_1 = 4\%$, $R_2 = R_3 = 8\%$ and $R_4 = 96\%$. The absorption coefficient of 1.1% doped Nd:YAG as a function of wavelength between 795 nm and 815 nm is then used to calculate the pumping efficiency shown in Fig. 3. A peak value of 68% is attained at 808 nm.

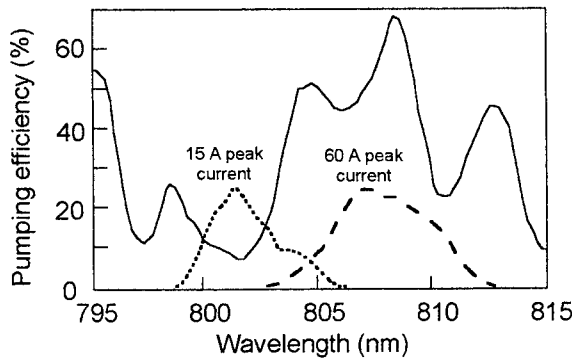


Fig. 3 Calculated pumping efficiency dependence on wavelength. For comparison, the diode laser spectra at 15 A and 60 A peak current are shown, operating at 8% duty cycle

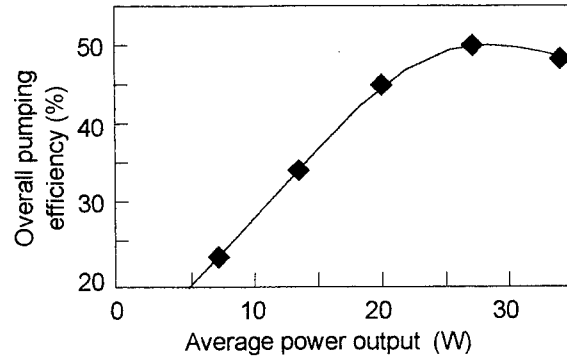


Fig. 4 Overall pumping efficiency, allowing for the diode laser spectral width and temperature tuning, calculated for varying duty cycle and hence average output power.

Fig. 3 shows measured spectra for the 10 McDonnell-Douglas 4501 laser diodes used in the experiments. These diodes individually have a spectral width of 2 to 3 nm (FWHM) and temperature tune at a rate of ~ 0.3 nm/K. The thermal impedance of each water cooled heat sink is in the range 3 to 7 K/W, producing tuning of the centre wavelength of the light at a mean rate of 1.5 ± 0.3 nm/W, and also an increase in spectral width for the array of ten bars. This effect is shown in Fig. 3 for an increase in peak current from 15 A to 60 A at a fixed 8% duty cycle, and 20°C cooling water. It can be seen from Fig. 3 that the diode laser spectrum is broader than the structure in the pumping efficiency curve and it is necessary to integrate over the pump laser spectrum $S(\lambda)$ to get the overall effect:

$$\text{Pumping efficiency} = \frac{\int S(\lambda) \cdot \eta(\lambda) \cdot d\lambda}{\int S(\lambda) \cdot d\lambda}$$

The variation of overall pumping efficiency with the average power generated by the diode lasers is shown in Fig. 4, with the duty cycle of operation varied to produce this curve. With the present diode/cooler thermal characteristics, the illuminator typically tunes to the optimum emission wavelength at 8% pulse duty cycle, 50 A injection peak current, and a coolant temperature of 20°C, providing a peak power of 400W, and an average power of 32 W. At this point the pumping efficiency is 50%. Maximum efficiency operation at lower average power can be obtained by increasing the water coolant temperature, whilst for higher peak current, the water temperature has been reduced to the dew point limit, giving > 40 W of pump power near the optimum pump efficiency point.

In the future, it will be possible to improve the pumping efficiency to ~80% by using dielectric coated mirrors and AR coatings on the YAG pumping faces, together with somewhat narrower slots. However, as will be shown, the present efficiency is sufficient to attain strong laser output from the planar waveguide.

3. Laser operation

The laser is operated with plane mirrors spaced approximately 1 mm from the AR coated facets of the YAG waveguide, forming a dual case 1 waveguide resonator. The waveguide is multi-mode with a 200 μm core, supporting tens of guided modes. However, laser action is found to be in only the first two or three transverse waveguide modes, because of mode dependent coupling loss between the guide ends and the mirrors. Single transverse mode operation at reduced power is obtained by spacing one mirror away from the waveguide facet. In the lateral direction, there is currently no mode control, and the output is highly multimode.

In agreement with the pump modelling, the laser efficiency is found to maximise at pump powers where the combined diode laser spectrum is centred at 808 nm. Figure 5 shows the optimisation of the output power from the laser by variation of the output coupling, when pumped at 8% duty cycle and with 40 W average power emitted by the 10 diode bars in 600 μs pulses. The optimum output coupling is 25% from which an average output power of 9.3 W is obtained at an optical-optical efficiency of approximately 24%. The measured slope efficiency is 25% when the diode coolant temperature is varied to hold the emission at 808 nm, and consequently the threshold pump power is very low. From Fig. 5 the intra-cavity loss is estimated at 2.5% per round trip, whilst the peak gain per round trip is 570 % , giving a peak small signal gain of 17 m^{-1} . As the pumping efficiency with the present reflecting cavity is only ~50%, the efficiency of converting *absorbed light* is ~50%, which is a high value for a Nd:YAG laser using side pumping.

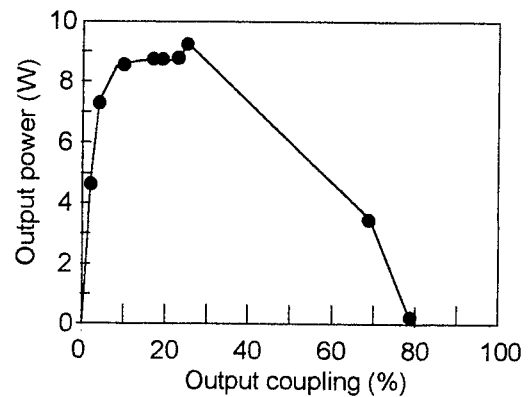


Fig. 5 Output power from YAG planar waveguide laser with 38W of pump power coupled through slotted mirror.

4. Conclusions

The preliminary results reported here show that high gain and reasonable conversion efficiency can be obtained using a planar waveguide laser fabricated by diffusion bonding. The low threshold observed in the present results shows that in the future, true cw operation of the laser configuration should be possible, leading to waveguide devices with powers beyond 100W. Such a development will require the installation of water cooling, and improvements in the reflectivity of the pump chamber components, in addition to cw rated diode bars. The pumping efficiency analysis presented here will be of value in improving overall conversion efficiency of such devices.

The use of waveguiding is expected to avoid the effects of thermal lensing at higher powers, as the step index guiding is sufficiently strong to keep control of the mode size. The one-dimensional thermal distortions in the planar geometry should also reduce the depolarising effects of stress birefringence found in cylindrical diode pumped lasers. Future efforts must concentrate on single transverse mode selection techniques and the use of a one dimensional resonator in the lateral direction to provide a high beam quality, high power source.

5. Acknowledgements

Support from the Engineering and Physical Science Research Council and EU "Human Capital and Mobility" are gratefully acknowledged

6. References

1. D C Hanna, A C Large, D P Shepherd, A C Tropper, I Chartier, B Ferrand, D Pelenc, "A side pumped Nd-YAG epitaxial waveguide laser" *Optics Comm.* **91**, 229-35 (1995)
2. The diffusion bonded waveguide was manufactured by Onyx Optics, Dublin, California, USA
3. A Faulstich, H J Baker, D R Hall, "Face pumping of thin solid state slab with laser diodes" *Optics Lett.* **21**, 594 -6 (1996)

Diode pumped 1kHz high power Nd:YAG laser with excellent beam quality

H.P. Godfried and H.L. Offerhaus

Nederlands Centrum voor Laser Research B.V.
P.O. Box 2662,
NL-7500 CR Enschede,
the Netherlands

ABSTRACT

The design and operation of a one kilohertz diode pumped all solid-state Nd:YAG master oscillator power amplifier system with a phase conjugate mirror is presented. The setup allows high power scaling without reduction in beam quality.

Keywords: solid-state lasers, Nd:YAG, diode pumping, phase conjugation, stimulated Brillouin scattering, pulse amplification, Q-switching, beam quality

1. INTRODUCTION

In recent years high power diode pumped all solid state lasers have emerged as viable sources of high brightness radiation. Both cw and high repetition rate pulsed sources are increasingly becoming available due to the increased availability and decreasing costs of the pump diodes. Diode pumping combines many technological advantages over lamp pumping such as reduced heat load in the laser crystals, resulting in better beam quality, smaller size requirements allowing a more compact design, higher efficiency, longer lifetimes resulting in less maintenance and downtime, and better stability, resulting in less output noise and fluctuation. At NCLR a high repetition rate all solid-state tunable laser system is under development for use in spectroscopy and advanced materials processing. This system is of the master oscillator power amplifier (MOPA) type and consists of a Q-switched single mode ring zigzag slab Nd:YAG master oscillator and a 4-pass Nd:YAG zigzag slab power amplifier. In order to preserve the excellent beam quality of the oscillator, stimulated Brillouin scattering phase conjugate reflection is employed after the second pass through the amplifier. The design and operation of this system is described in this paper. In the next sections each of the components in our system and overall system performance will be discussed in detail.

2. OSCILLATOR

Previously we reported on a standing wave oscillator with either a brick shaped or a Brewster angled Nd:YAG slab.¹ The oscillator crystal was pumped with a 5-bar quasi-CW diode array from Spectra Diode Labs. The duration of the pump pulse was $200\mu\text{s}$ at maximum current. The $2 \times 2 \times 20\text{mm}^3$ Nd:YAG-slab was mounted in the vertical plane between two copper blocks for cooling. The slab dimensions were chosen for optimal side pumping and mode volume control, with Brewster-angle faces for low-loss transmission without coatings. The linear cooling geometry caused thermally induced astigmatism which could be partially compensated for with

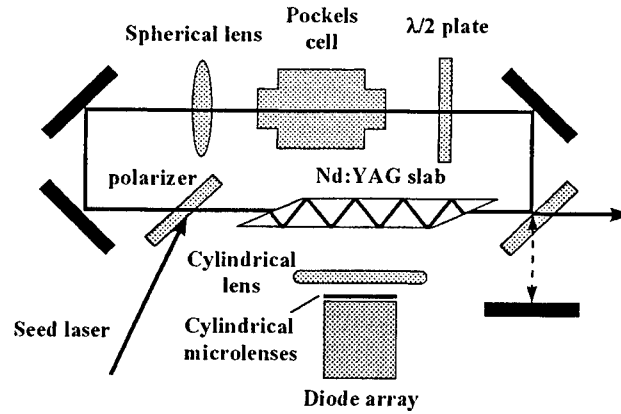


Figure 1: Schematic of the oscillator

cylindrical intracavity optics. However non-cylindrical aberrations and depolarization eventually limited the output of this oscillator and the maximum repetition rate in Q-switched mode. An improved oscillator involving a zigzag slab to compensate for thermal lensing and depolarization was therefore designed similar to the cw oscillator of Shine *et al.*² A 16-bounce, 1.8 by 1.7mm cross section, 1% Nd:YAG Brewster angle crystal was used with a total pumped length of 28mm. The non-TIR faces were clamped between gold-coated specularly reflecting glass plates to avoid coolant flow along these surfaces. Teflon coatings were used to insulate the total internal reflection (TIR) faces from coolant water turbulence and shield the O-rings from radiation. In Q-switched mode small diffractive light losses which spilled over the edges of the slab were a problem in that they would burn the O-rings due to the high intensity. This would result in an absorbing layer of carbonized rubber on the teflon coating which if left unattended would eventually damage the slab surfaces. A gold leaf coating has been applied to alleviate this problem. In the previous standing wave cavity design single longitudinal mode (SLM) operation was achieved by seeding with a commercial cw single mode Nd:YAG laser and a home built locking scheme. Due to the polarizing Brewster end faces twister mode operation in that cavity was impossible and spatial hole burning reduced the SLM output energy to approx. 85% of the unseeded value. Therefore it was decided to operate the current oscillator in a ring cavity mode. This reduces round trip gain with respect to output coupling but improves extraction efficiency. Output coupling was optimized following Degnan,³ with some slight modifications to account for the zigzag slab amplifying medium and the ring cavity geometry. Unidirectional lasing in the ring was achieved with an external mirror which during the buildup phase of the pulse would reflect the output in one direction back into the cavity, thereby favoring the opposite direction. Although seeding could also impose unidirectional lasing, the improved stability of the output in long pulse mode and the ease of alignment made this the preferred setup for unidirectionality. The cavity length was approx. 48cm and in order to obtain a stable cavity a $f = 1.5m$ lens was added. Single transverse operation was monitored with a beam profiler and self-referencing interferometer.⁴

3. AMPLIFIER

The amplifier was a commercial odd-bounce zigzag slab amplifier with a rectangular cross section of $6 \times 3mm^2$. The slab was pumped over approx. 60mm by an 80-bar diode array with a max. 15% duty cycle. Output from the oscillator was fed through a square aperture which was relay imaged into the amplifier. In the second pass the beam was spatially separated from the first pass and again relay imaged into the amplifier to avoid diffraction

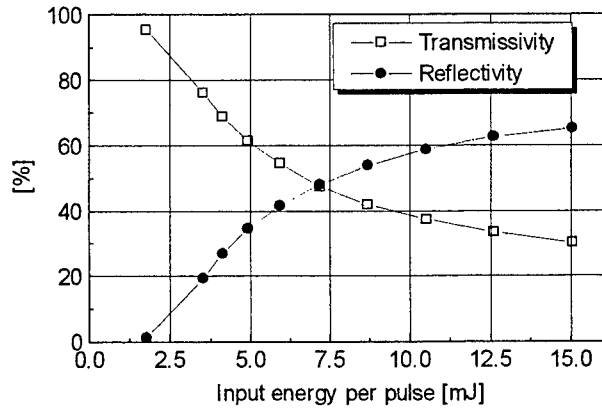


Figure 2: Brillouin reflectivity and transmissivity

losses and possible hot spots in the beam profile. After two passes through the amplifier the beam intensity profile was severely distorted even without pumping. In view of the high pulse energies in 4-pass amplification phase conjugation was essential to correct for these aberrations and thereby avoid amplifier damage. A Faraday isolator separated the overlapping input and output beams from the amplifier. Subsequently the radiation could be used in non-linear optical wavelength conversion schemes.

4. PHASE CONJUGATION

Filtered HPLC-grade Freon-113 was used in the SBS phase conjugator. A MOPA type double cell setup was used to lower the threshold and enhance reflectivity. The incoming square cross section $3 \times 3 \text{ mm}^2$ beam was focused with $f = 200 \text{ mm}$ and $f = 50 \text{ mm}$ lenses into the quartz cells. In Fig.2 the Brillouin reflectivity is shown at a pulse repetition rate of 400pps for 25ns pulses. Due to the poor beam profile the intensity at the focus is difficult to predict but repeatable phase conjugation with high fidelity could be routinely obtained. Measurements of the beam profile and phase front before and after amplification showed excellent phase front restoration. Even for a double moded input (due to damage on the oscillator slab) the phase conjugation faithfully reproduced the input mode structure.

5. SYSTEM PERFORMANCE

Previously the Brewster angled and brick slab oscillators were limited to operation up to 400Hz.⁵ The current zigzag slab oscillator allowed operation up to 1kHz with pulse energies up to 3.5mJ. This relatively low pulse energy was due on the one hand to higher losses in the zigzag slab and on the other hand to a smaller stored energy. For a doubled pumping load the pulse energies increased to 7.5mJ but residual thermal lensing and deformation of the slab limited the operation to 400Hz. Higher pumping load caused degraded output quality and damage to the LiNbO₃ Q-switch. Measurements of the amplifier gain showed a cw small signal gain of approx. 3 at maximum diode current. However the pulsed gain was significantly lower due to saturation and possibly transient effects, as shown in Fig.3. At low repetition rate the amplifier pump pulse duration could be extended resulting in an increased gain. At high repetition rate the maximum duty cycle of the amplifier limited

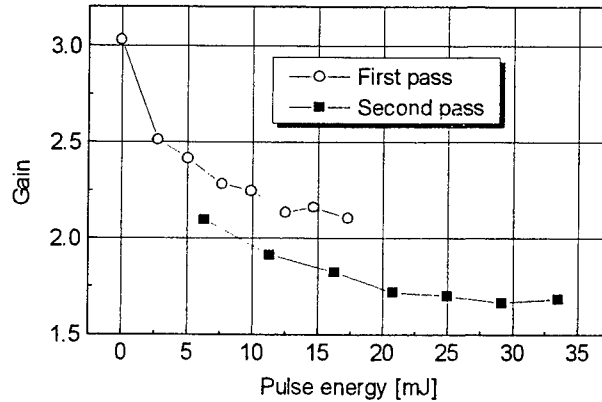


Figure 3: Amplifier gain at 10pps as a function of input energy.

the gain. Due to the non-linear dependence of the SBS reflectivity on the input pulse energy, most efficient 4-pass amplification occurred at 400pps resulting in an output of over 20W. At higher repetition rates the decreased oscillator pulse energy in combination with the limited pump pulse duration in the amplifier limited the efficiency and ultimately the output power. For example at 800pps the average output power had increased to just over 25 Watt. Higher pumping power in the amplifier will further increase the efficiency and result in good SBS reflection at higher repetition rate. Current work is also aiming at improving the thermal management in the oscillator slab which will enable higher oscillator energies and better SBS reflection.

6. REFERENCES

- [1] H.P. Godfried, E.A.J.M. Bente, and H.L. Offerhaus, "Single transverse mode, diode pumped Nd:YAG Q-switched oscillator," *OSA Proceedings on Advanced Solid State Lasers*, B.H.T. Chai and S.A. Payne, Eds., Vol. 24, pp. 420-422, Optical Society of America, Washington, DC, 1995.
- [2] R.J. Shine, A.J. Alfrey, R.L. Byer, "40W TEM₀₀ diode laser pumped Nd:YAG miniature slab laser," *Opt. Lett.*, **20**, 459-461, (1995).
- [3] J.J. Degnan, "Theory of the optimally coupled Q-switched Laser," *IEEE Journal of Quantum Electron.*, **QE-25**, 214-220, (1989).
- [4] C.B. Edwards, P. Lee, and M. Tatarakis, "Single shot wave front measurements of sub-ps laser pulses," *SPIE Proceedings on Beam Control, Diagnostics, Standards, and Propagation*, W. Lindsay, A. Giesen, D.H. Leslie, and H. Weichel, Eds., Vol. 2375, pp. 254-260, SPIE, Bellingham, WA, 1995.
- [5] H.L. Offerhaus, H.P. Godfried, and W.J. Witteman, "All solid state diode pumped Nd:YAG MOPA with stimulated Brillouin phase conjugate mirror," *Opt. Comm.*, **128**, 61-65 (1996).

High Energy Diode Pumped Slab Amplifier

M J Campbell & S E Jardine

Pilkington Optronics Ltd,
1 Linthouse Road, Glasgow, G51 4BZ, Scotland.

ABSTRACT

Design and performance details of a High Energy Diode Pumped Slab Amplifier (HEDPSA) system are given. The output from a 200 millijoule commercial gaussian coupled Nd:YAG laser is amplified to 1 Joule per pulse with good beam quality at a repetition rate of 20 Hz. The system comprises two zigzag geometry Nd:YAG slab amplifier stages pumped by 2D semiconductor laser diode arrays. Details of the amplifier optical design are given, highlighting the techniques used for compensation of thermal distortions in the laser slabs. Thermal lensing results show good agreement with thermal and optical models of the system. Good agreement is also shown with theoretical models of amplifier performance.

Keywords: Diode pumped; Nd:YAG slab amplifier

1. INTRODUCTION

Pilkington Optronics Glasgow (POG) has been assessing, under contract to the Defence Research Agency (DRA), the design options and performance limits for a diode-pumped Nd:YAG zigzag slab amplifier system producing 1 Joule per pulse at a repetition rate of 20 Hz. The system has been designed as a laboratory demonstrator and has employed commercial grade optics and mounts throughout with the exception of the zigzag slab pumphead assemblies, which were developed in-house. The design of the pumphead is such that, with relatively little effort, it can be substantially reduced in size and absorbed into the body of a suitably designed laser frame. The number of optics and mount can also be reduced for an engineered version of this system, with the necessary adjustments greatly simplified.

One of the major goals of this work was to assess the achievable beam quality of such a system avoiding the use of spatial filtering or phase conjugation techniques which are extremely sensitive to mechanical and thermal instabilities and do not lend themselves readily to the production of engineered or militarised systems.

2. AMPLIFIER DESIGN

The output from a commercial, flashlamp-pumped scientific Nd:YAG laser was amplified in a two-stage zigzag slab amplifier to produce 1 Joule per shot at 20 Hz in a 20 ns pulse. The oscillator is a gaussian mirror-coupled unstable resonator which is pumped at a fixed 20 Hz in order to match the rod thermal lens to the cavity. Lower repetition rate Q-switching can be achieved by reducing the frequency at which the Q-switch is fired according to $\frac{20}{N}$ Hz, where N is a whole number from 1 to 20. The diode pumped amplifier system however, can operate at any repetition rate from 1 to 30 Hz without active compensation for induced thermal lensing. The complete optical layout is shown in Figure 1.

Key features of the amplifier design are the off-axis orientation of the 11-bounce Nd:YAG slabs and the use of a 45° tilted porro prism to provide astigmatism compensation. Two slab amplifier stages were used in order to minimise the heat load per stage and to avoid high pumping levels in the slabs, avoiding significant ASE losses. The porro knife edge is oriented at 45° to the slab x and y axes. This provides beam mixing such that when the system is double passed, the beam x and y axes are interchanged and all parts of the beam experience the same degree of wavefront distortion. This technique compensates for astigmatism and produces an output beam which has a very small amount of spherical lensing only and which can be easily corrected by spherical optics in the output leg. The porro also flips the linear polarisation from p-plane in the first pass to s-plane in the second pass, which is then coupled into the output leg by the output coupling polariser. Each slab tip is angled at 36°, with each slab orientated at 18° to the circulating beam so that the end face coatings can provide low loss for both s and p polarisations. This permits (by way of increased efficiency) the pumping, and hence the heatload in each slab, to be

minimised which in turn reduces the resultant thermal distortions. Thus, the resultant spherical lens is also very small. The simulated corner cube, composed of an amici prism and a right angle prism, was necessary due to the relatively large separation of the two amplifier legs; a single piece used here would carry a higher risk of self-focusing damage and would be relatively expensive. In a future engineered system, the two stages could be much closer together and a more traditional, solid corner cube could be used.

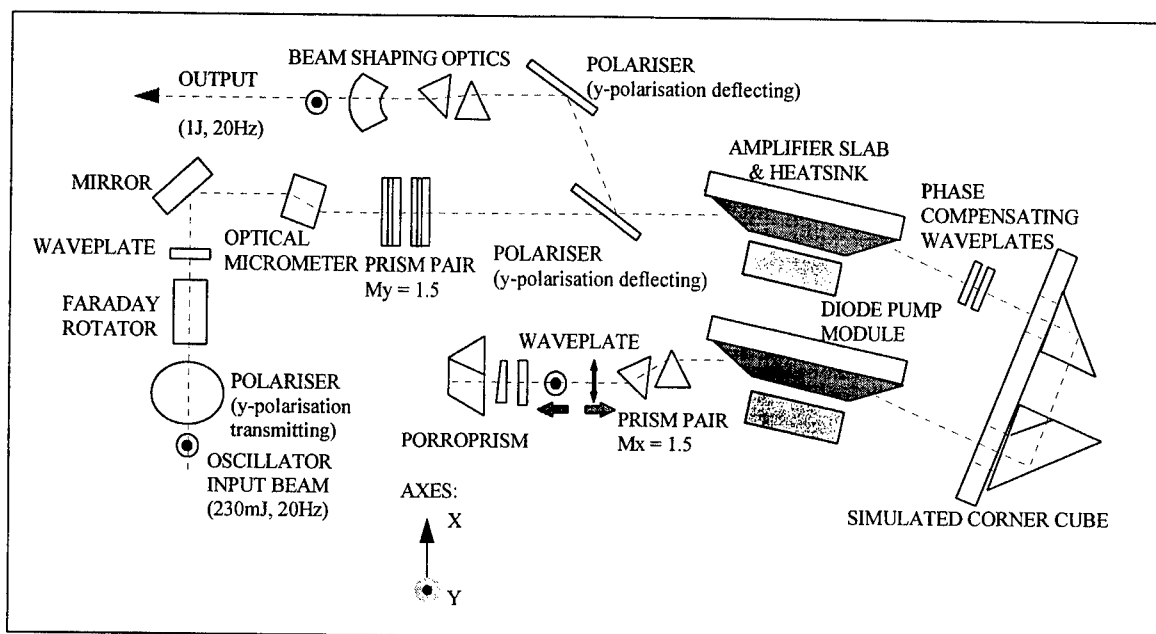


Figure 1 Schematic of Slab Amplifier Optical Layout

Each slab is pumped by a 2D array of quasi-cw diode laser bars comprising 4 modules of 50 stacked bars (200 bars total per column). These were fabricated to order by McDonnell Douglas Aerospace, St. Louis, Mo. and include integral heatsinks and water cooled mounts. Each diode column forms an emitting area 6cm long by 1cm wide which is close coupled to the slab pump surface. At 55A drive current, each column produces close to 10kW of peak power with the emission wavelength centred on $806 \pm 2\text{nm}$. Figure 2 shows the two slab pumpheads with their respective diode arrays in close proximity.

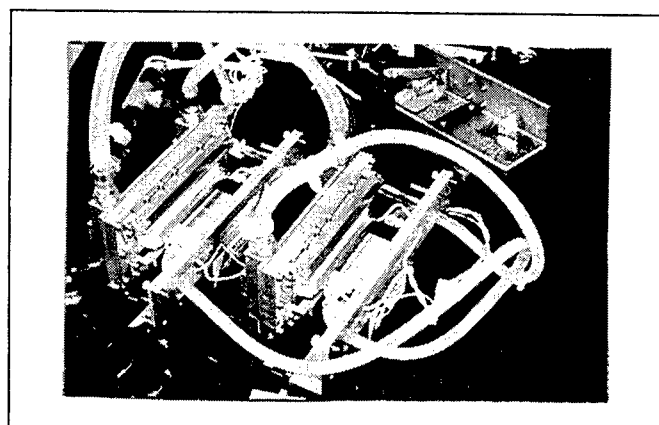


Figure 2 Photograph of Slab Pumpheads and Diode Columns

The slab heatsinks and the diode columns are cooled in series using a closed loop arrangement with a recirculating chiller maintaining a coolant temperature of 23°C . The coolant consists of a 25% solution of ethylene glycol in water to provide freeze protection to -12°C . A corrosion inhibitor is also included in the solution since there are dissimilar metals in the slab pumpheads and diode pump column heatsinks. Approximately 150W total waste heat is removed from the system at a flowrate of 2 litres per minute.

3. RESULTS

In order to achieve good beam quality preservation throughout the amplifier system, it is vitally important that the slabs be bonded to their heatsinks in a stress-free manner. This is achieved at POG by a proprietary process which results in very low stress-induced wavefront distortion (Strehl ratios typically greater than 0.8 are routinely achieved) and little or no stress-induced depolarisation across the slab width, as indicated in Figure 3. Early test results also show little change in the depolarisation levels over wide temperature ranges (-20°C to +50°C).

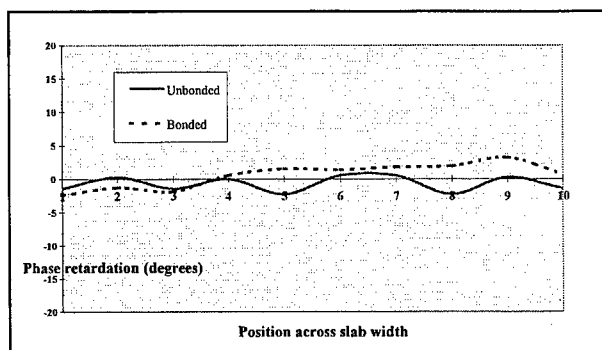


Figure 3 Slab Depolarisation After Bonding

Finite element models of the slabs were constructed to model the thermal effects on distortion of an ideal wavefront propagating through a pumped slab. A full 3-dimensional absorption map is matched to the Finite Element mesh, and with simulated water cooling at the base of the slab heatsink, a thermal solution for the model was generated using ANSYS, a Finite Element Analysis tool. The optical behaviour of the pumped slabs was assessed by calculating the deviation of different ray paths through the slabs. Beam deviations occur due to path length variations caused by local refractive index changes, thickness variations and reflections at distorted slab surfaces. These individual components were calculated and added to produce a composite deviation for both s and p polarisations in the zx and zy planes. From this, an effective beam divergence was evaluated, which was minimised by the application of a suitable spherical lens to the raw data, giving an indication of the active power in the slabs. These calculations indicated pump induced lenses of around 0.068 dioptries for the double passed system with astigmatism compensation. Measurements of the pump induced lensing in a single slab have confirmed weakly formed thermal lenses, and identical measurements using a plane mirror indicated astigmatism, as expected, which was not present using the 45° porro prism. The system, double passed with a 45° porro prism, exhibited an active lens of 0.063 dioptries when pumped at 20Hz at a diode current of 45A, equivalent to an absorbed heat load of 7.3W per slab.

Small signal gain measurements show gain clamping above diode currents of 45A. This could be due to ASE but is more likely to be the result of a parasitic oscillation since the roll-off observed is quite abrupt. Figure 4 shows gain measurements at three positions across the slab width, indicating good gain uniformity, and the predicted gain from a computer analytical model. During the course of system optimisation, it was determined that pumping around the 50A drive level was sufficient to ensure 1J output from the system (Figure 5), so the gain clamping observed did not significantly impact the system performance or efficiency.

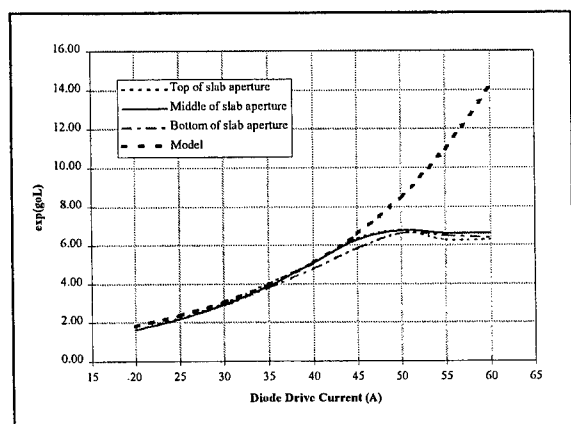


Figure 4 Single Pass Small Signal Gain in Single Slab

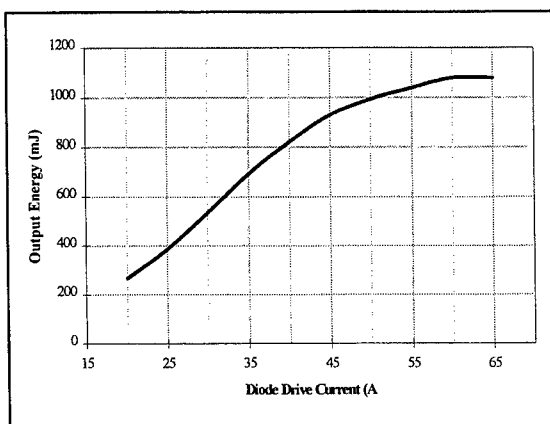


Figure 5 Full System Output Energy vs Diode Drive Current

At a system output of 1J, the total diode pump optical power was 62W, indicating an optical to optical amplifier (extraction) efficiency of 27%. With a diode electrical to optical efficiency of 40%, diode driver efficiency of $\geq 80\%$ and high voltage power supply efficiency of 88%, this indicates a total amplifier electrical to optical efficiency of 6.8% (excluding cooling).

Beam quality preservation was observed to be excellent for the double passed system. The input beam from the commercial oscillator was analysed just after passing through the output coupling polariser on entry into the amplifier chain. The divergence-diameter product was measured to be 2.5 mm.mrad for 90% contained energy using a Big Sky Beamcode™ 6.0 beam profiling system. At 1J output and 20Hz repetition rate, the output beam was measured to be 3.1 mm.mrad. This was only 1.24 times worse than the input beam, within the target specification of 30% beam quality degradation. Figure 6 shows the far field beam profiles of the input and output beams. Shot to shot jitter was measured to be less than $10\mu\text{rad}$.

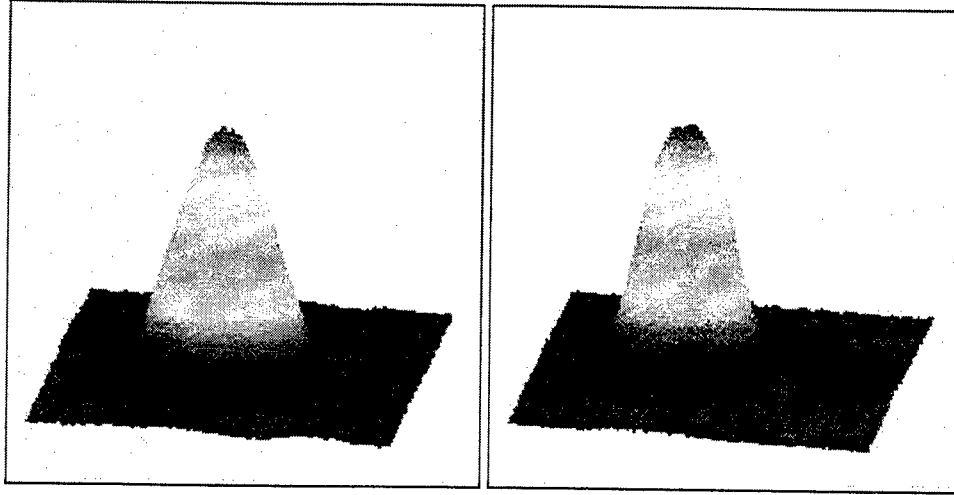


Figure 6 Far Field Spatial Profiles of Input Beam (left) and Amplified Output Beam (right)

4. CONCLUSIONS

We have demonstrated operation of a 1J, 20Hz diode-pumped Nd:YAG zigzag slab amplifier system. Beam quality preservation was shown to be excellent and within the 30% degradation limit set by the customer specification. The astigmatism compensation technique described was used successfully to produce an output beam with a very small amount of active spherical power and with low jitter. The slab pumphead geometry is such that it can be incorporated into a ruggedised design with relatively little effort. Future upgrades to this system can include a diode-pumped oscillator which will allow operation at any repetition rate up to 30Hz or above, depending on the type of cooling used.

5. ACKNOWLEDGEMENT

This work was performed under the auspices of the UK Defence Research Agency, Malvern by Pilkington Optronics (Glasgow) under contract number MAL1b/2077.

3. Solid State Lasers II

Invited Paper

High average power YAG lasers and applications

Hiroataka Kanazawa, Akihiro Nishimi, Minoru Uehara, Keinosuke Maeda,* and Yutaka Wakasa *

High Energy Technology Department, , Mechatronics Development Center,
Ishikawajima-Harima Heavy Industries Co., Ltd.
1-15, Toyosu 3-chome, Koto-ku, Tokyo 135, JAPAN
* Ishikawajima System Technology Co., Ltd.
1-15, Toyosu 3-chome, Koto-ku, Tokyo 135, JAPAN

ABSTRACT

A novel multi-rod cw Nd:YAG laser with 4kW output power through a optical fiber has been developed. We adopted an unique YAG rod arrangement which minimizing a distance between adjacent rods. By using such a resonator, the laser output power of 4.8kW was extracted from the laser resonator at an oscillation efficiency of 3.9%. The fiber power transmission with a fused silica fiber of 1.0mm diameter is possible for the delivered laser power of 4.4kW with transmission efficiency of about 92%, which is as same as a theoretical reflection loss at end surfaces. Welding experiments using the developed 4kW YAG laser with a fiber-connected multi-joint robots showed excellent performance of 10mm penetration for stainless steel welding and of more than 4mm penetration for aluminum alloys.

Keywords:YAG laser, laser resonator, fiber delivery, optical fiber, welding, stainless steel, aluminum alloy

1.INTRODUCTION

Recently, high average power Nd:YAG lasers more than 2kW have been developed and already used as industrial tools. Such high power YAG lasers can be used for deep penetration welding, high speed welding, thick plate cutting, high speed cutting, surface treatment and so on, which have been performed by CO₂ lasers. Compared to CO₂ lasers, YAG lasers have following advantages as an industrial laser;

- * shorter wavelength, results in higher absorption for metals,
- * transmission of laser power through flexible optical fibers,
- * normal, cheap fused silica optics can be used,
- * high peak pulse oscillation is possible,
- * compactness of laser head.

The most popular method to increase output laser power of YAG laser is to arrange multiple rods pumped by arc lamps in serial within the laser resonator^{1,2}. Other type of YAG lasers, such as a slab type³⁻⁶ and a LD-pumped⁵⁻⁷, have also been developed, but their output power is still lower and they are not sophisticated as an industrial laser up to now. Another approach such as combining several laser beams^{8,9} have also been investigated, which increase the laser power at a work piece. But these systems inevitably be more complicated and larger, which are not suitable for practical use.

In order to develop industrial high power continuous wave (cw) YAG lasers, we chose YAG rod as a laser medium and Kr arc lamp as a method of laser pumping. We have adopted unique rod arrangement suitable for maximizing the laser output power and developed YAG lasers of 2,3,4kW, respectively. In this paper, we describe features and characteristics of the developed 4kW YAG laser and results of application experiments using the 4kW YAG laser system.

2.LASER SYSTEM

2.1 Design and construction

In case of the multi-rod, arc-lamp-pumped cw YAG lasers, two methods are possible to increase output laser power. One is to increase the power per rod, another is to increase the number of rods. We chose the latter method, because the cost of long rod (200-250mm) was much more expensive. Design concept of our YAG laser is to maximize the output laser power while keeping the beam quality necessary for coupling into an optical fiber. In order to accomplish the above purpose, we minimize distance between adjacent YAG rods by inventing a structure of lamp house¹⁰. Fig.1 shows comparative schematic drawings of our laser construction and conventional one. In case of the developed laser, one of the pumping unit composed by one YAG rod and two arc lamps is rotated axially with respect to the neighboring units and the protruded lamps are overlapped with the neighboring rod. By utilizing such a modular arrangement, the rod spacing between adjacent two rods can be shortened, thus resulting in lower coupling losses between the adjacent rods and also in easy alignment of optical axis of YAG rods.

Fig.2 shows a developed 4kW YAG laser oscillator, which uses 8 rods of 153mm length and 16 arc lamps. The size of it is 2400mm in width, 900mm in depth and 1700mm in height, which must be very compact.

One of the important parameter of multi-rod YAG laser is a curvature of YAG rod. Fig.3 shows the relationship between the rod curvature and the beam divergence angle (full angle) at the maximum output in case of one rod test equipment. The divergence angle decreased monotonously with decreasing the rod curvature. This result was well agree with theoretical one calculated using a ray matrix method¹¹. In this case the maximum output laser power also decreased slightly, but the beam intensity calculated by these two parameters increased with decreasing the curvature.

It was also confirmed experimentally that these results with one rod system well agreed with those with any multi-rod systems. We chose the rod curvature of -1m concave for the 4kW system, because it is small enough to launch into 1.0mm fiber.

2.2 Performance of 4kW YAG laser

Fig.4 shows the change of the laser power and the beam divergence angle against the input lamp power with 4kW system. A maximum laser power of 4.8% was obtained at an oscillation efficiency of 3.9% and the slope efficiency of about 6%. It is also possible to operate at pulse oscillation mode by using a lamp current modulation, which enables to enhance the peak laser power to about double of the averaged laser power.

Fig.5 shows the result of fiber delivery test with 4kW YAG laser, where the type of silica fiber is step index (SI), a core diameter is 1.0mm, a numerical aperture (NA) is 0.20, and a length is 10m. The transmission efficiency was 92-93% which almost as same as a theoretical reflection loss at the fiber end surfaces. Even at the fiber delivery experiments with a 100m fiber, the transmission loss increased only about 5%.

3.APPLICATIONS OF YAG LASERS

3.1 Experimental setup

One of the advantages of fiber beam delivery is use of multi-joint robot for a material processing system with YAG laser, because the multi-joint robot is suitable for 3-dimensional processing and it is much cheaper than a gantry type system used for CO₂ laser. Fig.6 shows a schematic of YAG laser processing system, where the 4kW YAG laser is connected with a 6-axis multi-joint robot by the optical fiber.

A focusing unit which uses 4 fused silica lenses to converge the laser beam was installed at a wrist of the robot,. A shielding gas was supplied coaxially with the laser beam from the center of the focusing unit nozzle. The minimum spot diameter obtained by this focusing unit is about 1.0mm.

In order to investigate basic welding properties of 4kW YAG laser, bead-on-plate welding tests were performed

using test pieces of stainless steel and aluminum alloys. In case of aluminum alloy welding, the focusing unit was inclined slightly in order to avoid damage of an exit end of optical fiber caused by a reflection of laser beam from the surface of aluminum alloy test pieces.

3.2 Welding performance of 4kW YAG laser in stainless steel

10mm thickness test pieces of stainless steel type 304 were used for the bead-on-plate welding test.

The effect of the laser power on the penetration depth and the bead width is represented in Fig.7, where the welding speed is 17mm/s and the oscillation mode is cw. The penetration depth increased with the laser power. But at the point around 1.6kW, the penetration depth increased extremely. It must be the threshold point for the change from the heat conduction type welding to the keyhole type welding, corresponding to the laser beam intensity at the test piece of $2.0 \times 10^5 \text{ W/cm}^2$. This value with YAG laser is much lower than that with CO₂ laser of 10^6 W/cm^2 [12], which is explained by the difference of absorption coefficient of laser beam. As for the change of the bead width in Fig.7, it also increased extremely at 1.6kW, but the increasing rate above the threshold is lower than that of the depth. So that it can be found that the aspect ratio of the weld bead increases with increasing the laser power.

Fig.8 shows the effect of the welding speed and the shielding gas sort on the penetration depth and the bead width, where the oscillation mode is cw. The penetration depth increased with decreasing the welding speed. There was no saturation phenomenon of penetration depth caused by plasma absorption as observed in CO₂ laser welding at slow welding speed [13]. To study the effect of the sorts of shielding gas, He, Ar and N₂ were used respectively. It can be said from Fig.8 that the effect of the shielding gas sort is negligible for the case of stainless steel welding.

The effect of pulse mode oscillation on the welding characteristics was represented in Fig.9 comparing with cw oscillation, where the averaged laser power is 2kW. The waveform of pulse oscillation is rectangular, the frequency is 100Hz, the duty is 50%, so that the peak power is 4kW. The penetration depth was found to increase by changing the oscillation mode from cw to pulse by 1.5-2 times. On the other hand the bead width with pulse oscillation was much smaller than that with cw oscillation. So it can be said that it is possible to control the weld cross section by changing the pulse waveform.

3.3 Welding performance of 4kW YAG laser in aluminum alloys

Generally with 2kW class cw YAG lasers, the pulse oscillation which enables to enhance the peak laser power is used for aluminum alloy welding, because the beam intensity is insufficient to keyhole welding. But it is possible to obtain deep penetration more than 3mm with cw oscillation mode by using the developed 4kW YAG laser. Fig.10 shows the effect of the welding speed on the penetration depth with cw oscillation mode of 4.2kW, where the thickness of test piece is 6mm, material of test pieces are A5052 and A5083 respectively.

In case of cw welding shown in Fig.10, the aspect ratio of the weld bead is low (less than 1) because of the effect of heat conduction. As same as the case of stainless steel welding shown in Fig.9, it is possible to increase penetration depth, resulting in the aspect ratio, by using the pulse oscillation. Fig.11 shows the cross section of welds with pulse oscillation, where the averaged laser power is 3.8kW and the peak laser power is 6.5kW. Full penetration is observed in Fig.11 for 6mm of A1100, 4mm of A6N01 and 4mm for A5052. But the evaporation of impurity metals involved in aluminum alloys causes a formation of underfill defect at the surface of test piece, when the pulse oscillation is used. As for the stability of welding and the appearance of bead surface, cw oscillation is better than pulse oscillation.

3.4 Practical applications of 4kW YAG laser

We have also studied practical applications of high power YAG lasers. Example of applications are listed below;

- * high speed butt welding of sheet metal: 0.7mm+1.4mm at 100mm/s
- * high speed lap welding of sheet metal: 0.8mm+0.8mm at 58mm/s
- * thick plate butt welding of stainless steel with filler wire: 7.6mm+7.6mm (acceptable gap is 0.8mm)

- * underwater welding of stainless steel at water depth of 30m
- * high speed, large area laser cladding of steel

4.CONCLUSIONS

The novel multi-rod, arc-lamp-pumped 4kW cw YAG laser was developed and the laser performance and the welding properties were studied experimentally. From these experiments the following results could be obtained.

- 1) A maximum laser power of 4.8kW was attained at an oscillation efficiency of 3.9%.
- 2) A laser power of 4.4kW could be delivered stably with a transmission efficiency of 92% through the silica fiber of 1.0mm diameter.
- 3) A maximum penetration of 10mm was obtained for stainless steel welding with 4kW YAG laser.
- 4) A deep penetration welding more than 3mm could be performed with cw oscillation of 4kW YAG laser for aluminum alloys.
- 5) A full penetration welding more than 4mm could be performed with pulse oscillation of 4kW YAG laser for aluminum alloys.

Appearance of 4kW YAG lasers extends an application field of high power cw YAG lasers. Such high power YAG lasers will be used not only in place of low cost welders, such as arc welder and spot welder, but also in place of CO₂ lasers in the near future.

5.REFERENCES

- 1.D.M.Filgas,"Advances in High Power CW YAG Lasers and Fiberoptic Beam Delivery," *Proc. ICALEO '92*, pp.63-69, 1992.
- 2.D.M.Filgas,"A 3 Kilowatt CW Nd:YAG Laser with Fiberoptic Multiplexing," *Proc. ICALEO '93*, pp.323-327, 1993.
- 3.N.Hodgson, S.Dong and Q.Lu,"Performance of 2.3-kW Nd-YAG-slab laser system," *Opt. Lett.*, **18**(20),1727-1729, 1993.
- 4.M.Seguchi and K.Kuba,"1.4-kW nd:YAG slab laser with a diffusive closed-coupled pump cavity," *Opt. Lett.*, **20**(3), 300-302, 1995.
- 5.B.Comaskey, G.Albrecht, R.Beach, S.Sutton and S.Mitchell,"1000-W diode-pumped folded zigzag slab laser," *CLEO'93 Digest*, CW15, Vol.11, p.276, 1993.
- 6.H.Injeyan et al., "diode array-pumped kilowatt laser development," *CLEO'94 Digest*, CThC1, Vol.12, p.281, 1994.
- 7.R.Burnham, G.Witt, D.DiBiase, K.Le and W.Koechner,"Diode-pumped solid-state lasers with kilowatt average power," *SPIE Vol.2206*, pp.489-498, 1994.
- 8.H.-G.Treusch, E.Onkels, H.Adamietz, V.Krause and P.Loosen,"Modular 3kW-solid-state-laser with fiber optic beam delivery," *SPIE Vol.2206*, pp.408-415, 1994.
- 9.I.Norris, C.Peters and P.Wileman,"Welding with a 3kW Nd:YAG Laser," *Proc. ICALEO '92*, pp.53-62, 1992.
- 10.US Patent No.5,289,490. European Patent No.0531199.
- 11.A.E.Siegman, *Lasers*, University Science Press, 1986.
- 12.M.Beck, F.Dausinger and H.Hugel,"Study of Energy Coupling at Deep Plasma Welding," *Laser und Optoelektronik*, **21**, pp.80-84, 1989.
- 13.I.Miyamoto, H.Maruo and Y.Arata,"Beam absorption mechanism in laser welding," *SPIE Vol.668*, pp.11-18, 1986.

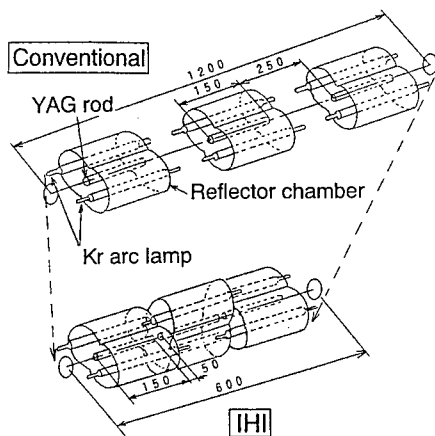


Fig.1 Schematic drawings of YAG laser construction

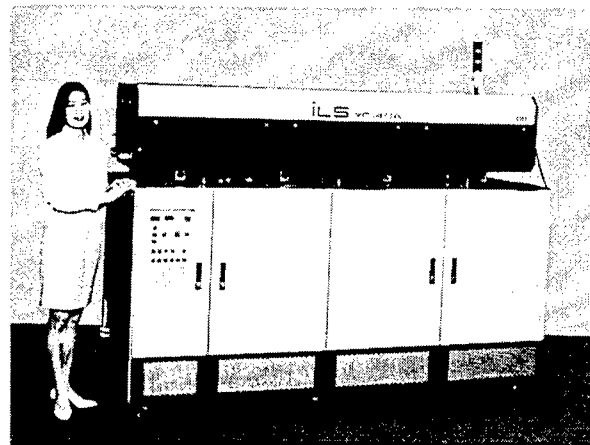


Fig.2 4kW YAG laser

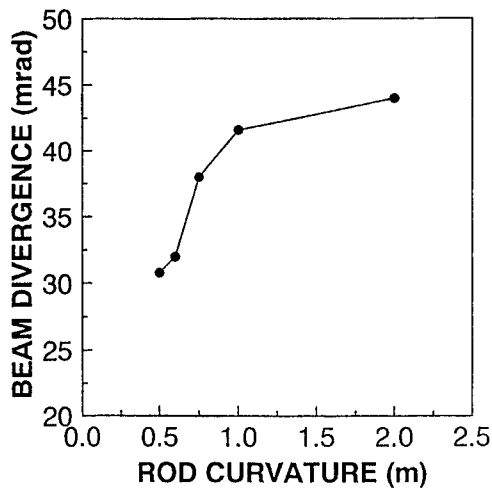


Fig.3 Relationship between rod curvature and beam divergence angle with one rod test equipment

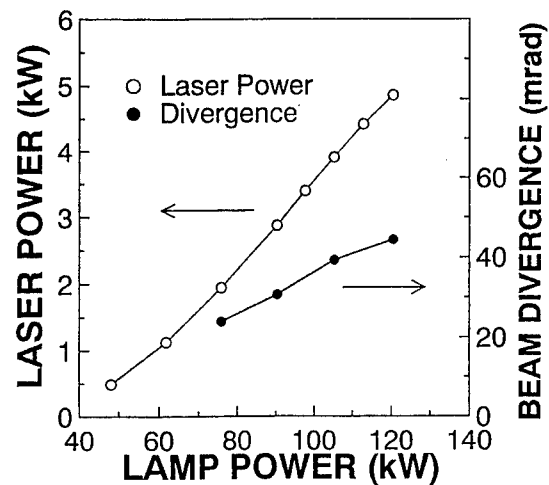


Fig.4 Change of laser power and beam divergence angle against input lamp power

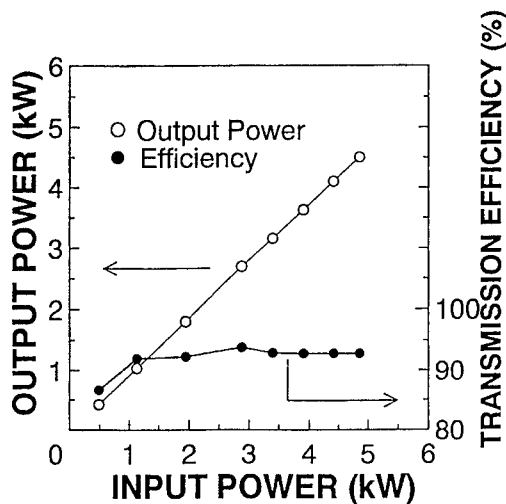


Fig.5 Change of delivered laser power and transmission efficiency against fiber input laser power

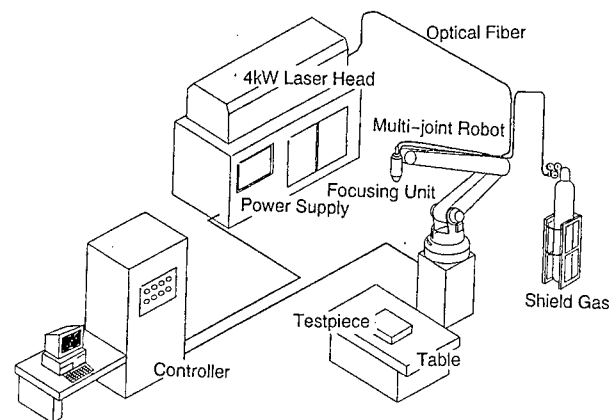


Fig.6 Schematic of laser processing system

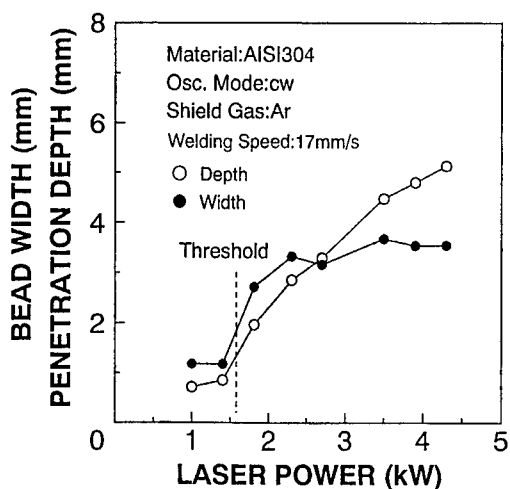


Fig.7 Effect of laser power on penetration depth and bead width for stainless steel type 304

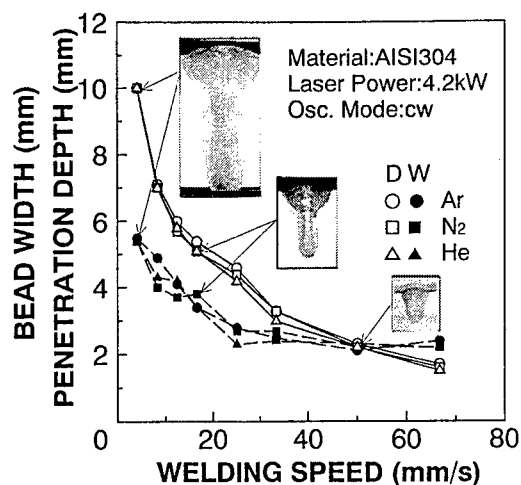


Fig.8 Effect of welding speed and sort of shielding gas on penetration depth and bead width for stainless steel type 304

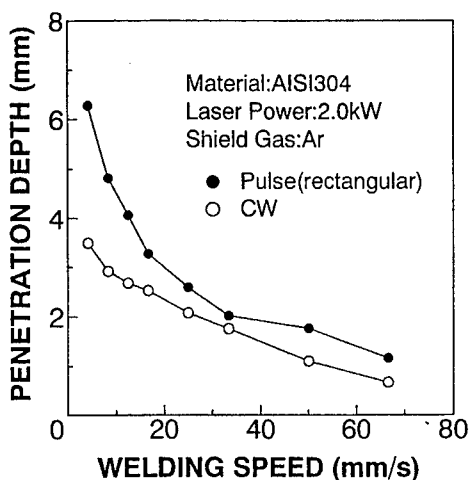


Fig.9 Effect of oscillation mode on penetration depth for stainless steel type 304

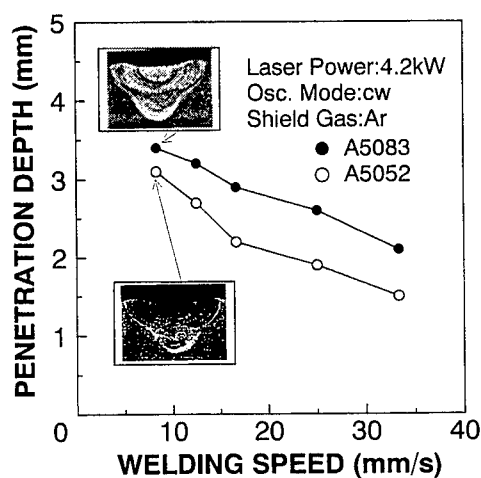
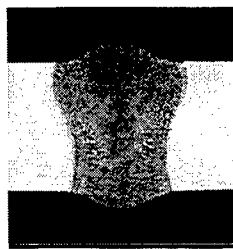


Fig.10 Effect of welding speed on penetration depth with cw oscillation for A5052 and A5083



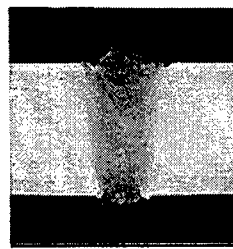
A1100

Laser power: 3.8kW
Welding speed: 8.3mm/s
Thickness: 6mm



A6N01

Laser power: 3.8kW
Welding speed: 13mm/s
Thickness: 4mm



A5083

Laser power: 3.8kW
Welding speed: 20mm/s
Thickness: 4mm

Fig.11 Cross section of welds with pulse oscillation for aluminum alloys

Stable resonators with variable reflectivity mirrors for multi-kW Nd:YAG lasers

G. Bostanjoglo, R. Dommaschk*, Th. Beck, H. Weber**

Laser- und Medizin-Technologie Berlin gGmbH, Rudower Chaussee 6,
Building 19/2, D-12489 Berlin, Germany
Tel.: 0049 30 6705-400, Fax.: -500

* INPRO Innovationsges. für fortgeschrittene Produktionssysteme in der Fahrzeugindustrie, Hallerstr. 1, D-10587 Berlin

** Optisches Institut der Technischen Universität Berlin, Str. des 17. Juni 135, D-10623 Berlin

ABSTRACT

A new method for obtaining high-power laser beams with drastically improved beam quality for fibre coupling is presented. The central idea is to use variable reflectivity mirrors (VRM) as outcoupling mirrors for high-power solid-state lasers with stable resonators, operated near the maximum power. The reflectivity profile of the VRM, properly chosen, acts singular to a mode aperture. Without any further modifications of the laser, the beam parameter products were substantially reduced: The maximum values at intermediate pumping power were reduced to the beam parameter product occurring at the highest input power. The laser power, however, was not reduced within the principal working interval.

Different Nd:YAG laser systems with 350 W, 1.9 kW, and 3kW maximum output power were equipped with VRM. The 1.9 kW system was coupled without any loss of power into a 400 μm fibre instead of the 600 μm fibre normally used. The influence of the VRM spot size on laser power and beam parameter product (BPP) was investigated. Furthermore, was shown, that better beam quality is achieved by adding further laser cavities inside the resonator instead of using them as external amplifiers.

Keywords: High-power laser, stable resonator, variable reflectivity mirror, Gaussian mirror, beam quality, fibre coupling coupling

1. INTRODUCTION

High power Nd:YAG lasers have become reliable, commercially available products for materials processing. Compared with CO₂-laser radiation, the 1.06 μm wavelength is better coupled into the material, and the handling is flexible due to fibre delivery. Standard fibre core diameter in the kW class is 600 μm . With outcoupling optics, the endface of the fibre is imaged onto the workpiece. The laser beam parameters after a fibre, thus the focusing properties, are dependant on the fibre core diameter and the fibre entrance angle, also roughly being the fibre exit angle¹. To increase the laser power density, respectively the workpiece positioning tolerances, better beam quality and therefore smaller fibre core diameters are necessary.

2. STABLE RESONATORS AND VRM

VRM^{2,3,4} for stable resonators in the 5 W- power range substituted mode apertures to suppress higher order modes⁵. For higher powers around 400 W, VRM utilisation for beam quality improvement was characterized by a laser power loss of at least 50%⁶. For efficient operation, the laser has to be operated near the stability limit. The beam parameter products (BPP) of solid state lasers with stable resonators depend on the pumping power via the thermally induced refractive power of the laser rod. The trace is parabola-shaped, with the lowest values occurring at the edges of the stable region. After a maximum, the near field diameter w decreases monotonously with rising pumping power, whereas the far field divergence angle θ becomes larger (measurements: see fig. 4).

The resulting beam parameter product $w\theta$ of resonators of sufficient lengths therefore exhibit a distinct maximum. This maximum beam parameter product is related to the stable operating regime of a resonator by

$$\frac{(w\theta)_{\max}}{r^2} = c \frac{\Delta D}{4} \quad (1)$$

r rod radius

ΔD interval of refractive power of the thermal lens, for which the resonator is stable

c constant: $c=1$ if confocal point of the stability diagram is hit; otherwise $c=2$

The coupling optics as well as the fibre diameter have to be chosen to ensure safe coupling for this maximum value of the beam parameter product. The main operating regime of high power lasers is usually near the maximum power, having

much better beam quality than at intermediate input power levels. By fibre transmission, however, it is generally made equal to the maximum value of the beam parameter product.

The use of variable reflectivity mirrors, also known as gradient reflectivity or (super-) Gaussian mirrors, limits the maximum of the BPP to a chosen value by restricting the near field on the outcoupling mirror to the size of its reflecting area⁷. At low pumping powers, the laser power is reduced due to missing backcoupling of radiation into the resonator. At higher input powers, the thermal lens of the rod contracts the beam size on the mirrors. Therefore, the whole beam diameter is coupled back and no reduction of laser output power occurs. For optimum operation, the diameter of the VRM has to be chosen to fully support the beam at the desired pumping power, i.e. the diameter of the reflecting area of the VRM should roughly be equal to the beam diameter on a homogeneous outcoupling mirror at maximum input power.

3. SINGLE ROD LASER EXPERIMENTS

First experiments for experimental verification of this behaviour were performed using a single-rod, flashlamp-pumped Nd:YAG laser⁸ (Lumonics MS700, rod size \varnothing 9.6mm, length 160mm). With a flat-flat resonator of 1.2 m length, this system has a maximum laser output power of 360 W at 12 kW input power. The homogeneous outcoupling mirror was exchanged for VRMs with the same centre reflectivity. Their radial supergaussian reflectivity profiles are characterised by

$$R(r) = R_0 e^{-2(r/w)^n} \quad (2)$$

w : $1/e^2$ radius of the reflecting area; R_0 : centre reflectivity; r : radial coordinate; n : super-Gaussian exponent.

Profiles with different diameters ($w=1.45\ldots 2.5$ mm) but with an identical centre reflectivity ($R_0=46\%$) and supergaussian exponent ($n=12$) were used. With the smallest VRM, the maximum beam parameter product was reduced from 16 to 10 mm*mrad. The maximum output power remained unchanged (360 W). The results are shown in fig. 1.

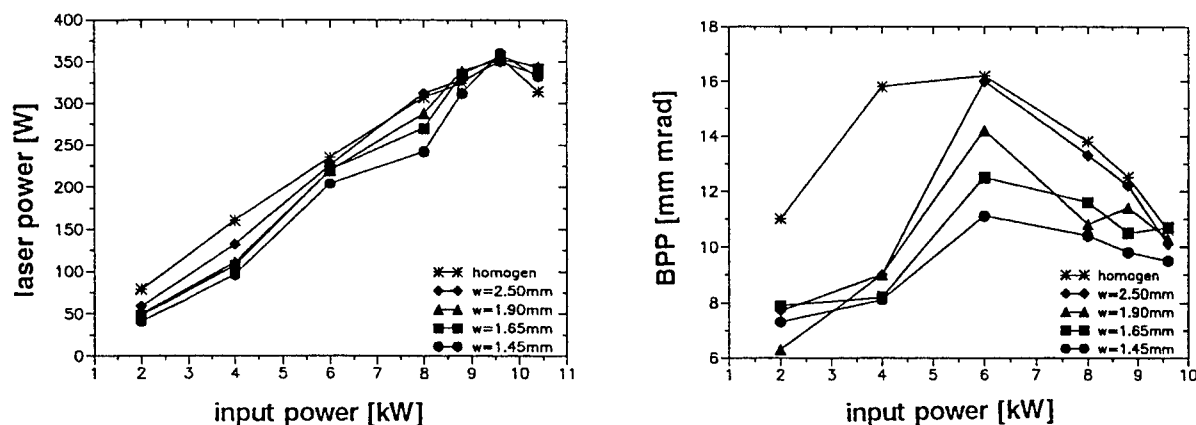


Fig. 1: Measured output power (left) and beam quality (right) of symmetric 1.2m flat-flat resonators with one \varnothing 9.6 mm, 160mm long Nd:YAG laser rod⁸ (Lumonics MS700). Outcoupling mirrors were a homogeneous standard mirror ($R=46\%$) and a set of gradient reflectivity mirrors with $R_0=46\%$, $n=12$, but different widths w of the supergaussian reflectivity profile: homogeneous (not profiled), 2.50 mm, 1.90 mm, 1.65mm, 1.45 mm.

The beam parameter product was determined by measuring the near field radius and the far field divergence angle with a CCD camera connected to a digital image processing system. All values of beam radii, angles, and parameter products refer to a power content of 86.5%.

4. MULTI-ROD CW-LASER EXPERIMENTS

4.1: Four rods

The measurements were repeated with a four-cavity multirod laser with plane resonator mirrors. The rods were equally spaced, so that the thermal lenses acted like a symmetric lens duct. The resonator length was 2.88 m, being equivalent with a resonator module length of 0.72 m. The laser rods (\varnothing 8 mm, length 200mm) had a refractive power of 0.4dpt/kW each, and were cw-pumped with discharge-lamps up to 16 kW each (commercial HAAS cavities and power-supplies). The optimum reflectivity of the homogeneous outcoupling mirror was found to be 25% for the 4-rod resonator. The maximum laser power was 1.9 kW, and the maximum BPP was 22.0 mm*mrad.

With a VRM, characterized by $R_0=25\%$, $w=1.4\text{mm}$ and $n=9.5$, also 1.9 kW were obtained, whereas the maximal beam parameter product decreased to $17.5\text{ mm}\cdot\text{mrad}$. The laser beam was coupled into a $400\mu\text{m}$ core diameter quartz fibre with cleaved endfaces. The coupling optics was a telescope consisting of a spherical $f=750\text{ mm}$ lens and a aberration-corrected $f=44\text{ mm}$ lens. The cladding/core ratio of the used fiber is 1.2. Behind the fibre, the transmitted power measured was 1.9 kW, meaning that no coupling losses occurred.

4.2: Six rods

To obtain laser powers of 3 kW, two identical cavities were added as amplifiers. They were positioned outside the resonator at the same equal distances as the rods inside the resonator. The measured maximum output power was 3.0 kW, the largest BPP $26.8\text{ mm}\cdot\text{mrad}$. This is a severe degradation of beam quality compared with the above four-rod laser. It is caused by gain saturation, which results in stronger amplification of the slopes of the laser beam.

Therefore, the set-up was transformed into a six-cavity resonator, now being 4.32 m long. The module length was not changed. The optimum reflectivity of the homogeneous outcoupling mirror was found to be 15% for the 6-rod resonator. The homogeneous outcoupling mirror was substituted by a VRM similar to the one used with four rods, the centre reflectivity being $R_0=15\%$. This yielded 3.0 kW maximum laser power. At all pumping powers, the BPP was less than $21.0\text{ mm}\cdot\text{mrad}$ (see fig. 3). Further improvements can be obtained by using smaller VRM spot radii and longer resonators.

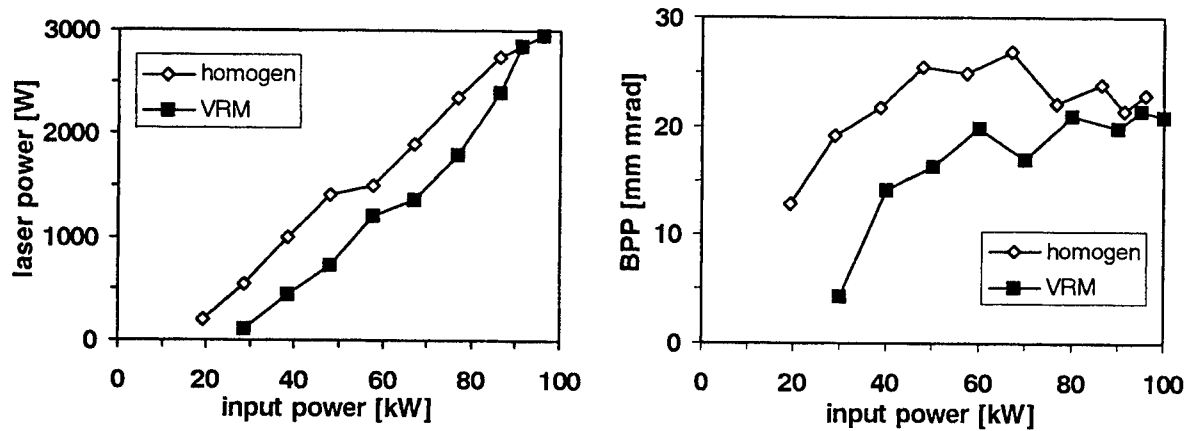


Fig. 3: Measured laser output power (left) and beam parameter product (right) of the the six-rod 3kW Nd:YAG laser. The laser power at the maximum input power is not reduced by substituting the homogeneous outcoupler by a VRM. The beam parameter product is reduced if the VRM is used instead of the standard outcoupler. This is caused by the reduced near field radius.

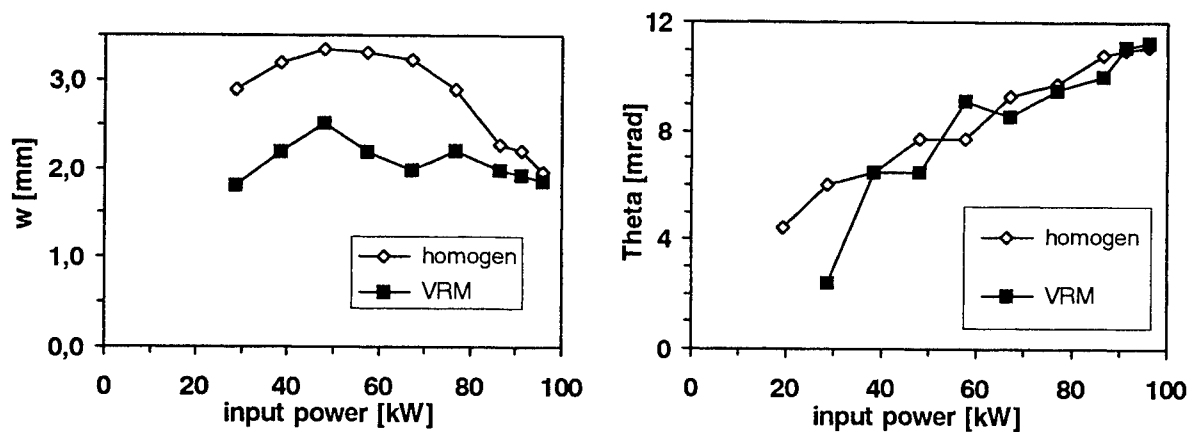


Fig. 4: Measured input power dependance of the near field radius w (left) and far field divergence angle θ (right) of the six-rod 3kW Nd:YAG laser described above. It can clearly be seen, that the use of VRM reduces the near field radius on the outcoupling mirror. A VRM with a smaller reflecting area will lead to further near field reduction for pumping powers between 30-35 kW. The divergence angle is hardly effected, except for low pumping powers.

5. SUMMARY AND OUTLOOK

The transverse containment of the near field distribution by using VRM as outcoupling elements has proven to increase the beam quality of different Nd:YAG power lasers: The maximum beam parameter product of a 350 W, 1.2 m flat-flat resonator was reduced from 16 to 10 mm*mrad, that of a 1.9 kW and 3.0 kW multi rod laser (resonator module length 0.72 m) from 22.0 to 17.5 mm*mrad and from 26.8 to 20.9 mm*mrad, respectively. The maximum output powers were not reduced by this modification.

All VRM used in the experiments were fabricated on a Balzers BAK 640 box coater of the LMTB gGmbH⁴. Partially, a newly developed method gaining ultra-high damage thresholds was used.

These results open new perspectives for 6 to 7 kW Nd:YAG lasers by building oscillator-amplifier-setups on a modular basis⁹. One possible solution consists of two identical six-rod-laser systems. The first system is left unchanged except for the outcoupling mirror, which is replaced by a VRM. The laser beam is coupled into a 400 μ m fiber. The resonator of the second laser system is removed. The endface of the 400 μ m fiber is imaged with a 1:1 telescopic imaging optics onto the former position of the high-reflectance resonator mirror. After passing the six amplifier stages, the beam is coupled into the 600 μ m fiber commercially attached to the laser system.

6. REFERENCES

1. N. Reng, Th. Beck, „Transmission properties of all-silica fibres for high-power Nd:YAG lasers“, *Opt. Laser Technol.* **25**(2) (1993), 117-124
2. P. Lavigne, N. McCarthy, J. G. Demers, „Design and characterization of complementary Gaussian reflectivity mirrors“, *Appl. Opt.* **24** (1985), 2581-2586
3. G. Duplain, P. G. Verly, J. A. Dobrowolski, A. Waldorf, S. Buissiere, „Graded-reflectance mirrors for beam quality control in laser resonators“, *Appl. Opt.* **22** (1993), 1145
4. G. Bostanjoglo, A. Bernhardt, „Variable reflectivity mirrors for Nd:YAG- and Er-YAG-lasers at 1.06 and 2.94 μ m“, *Proc. SPIE* Vol. **2253**, „Optical Interference Coatings“ Editor F. Abèles (1994), 791-801
5. J. Kasinski, P. Bournes, R. Burnham, „High-Power Single-Mode Diode-Pumped Graded-Reflectivity-Mirror/Stable Oscillator“, *Technical Digest Series* Vol. 2, „Advanced Solid-State Lasers / Compact Blue-Green Lasers“, Optical Society of America (1993), 11-13
6. X. Wenjan, L. Zhengjia, Z. Changhong, Y. Huashan, Q. Junlin, „Continuous wave high power solid state lasers with VRM output coupler“, *Proc. SPIE* Vol. **2379**, „Solid State Lasers and Nonlinear Crystals“, Editors G. Quarles, L. Esterowitz, L. Cheng (1995), 317-324
7. G. Bostanjoglo, „Laseranordnung mit verbesserter Strahlqualität bei stark veränderlichen resonatorinternen Brechkräften unter Beibehaltung der Ausgangsleistung“, German patent application No. 1 95 43 596.6 (1995)
8. G. Bostanjoglo, H. Weber, „1.06 and 1.44 μ m Nd:YAG Lasers with Apodized reflectors“, *Proc. SPIE* Vol. **2788**, „High Power Lasers: Gas and Solid State Lasers“ (1996)
9. Th. Beck, „Oszillator-Lichtleiter-Verstärkeranordnung für Laserstrahlen“, German patent application No.1 96 06 555.0 (1996)

High energy Nd:Cr:GSGG lasers based on phase and polarization conjugated multiple-pass amplifiers

S. Jackel, I. Moshe, A. Kaufman, R. Lavi, and R. Lallouz
Nonlinear Optics Group - Soreq NRC, 81800 Yavne, Israel

Abstract

Lasers based on Nd:Cr:GSGG low-energy oscillator / multiple-pass amplifiers produced 1.7 J pulses in a $M^2 \approx 2$ divergence beam at 2.4 % electrical efficiency. Thermal lensing and birefringence correction were major factors.

I. Introduction

High energy, high efficiency laser development is advancing. Electrical efficiency of high energy, diode pumped YAG lasers can reach 5%. Flashlamp pumped YAG has an efficiency of 1 to 2 % in Q-switched power oscillators. Higher efficiencies and higher energies may be achieved using other flashlamp pumped media. Thus Cr^{3+} in Nd:Cr:GSGG (gadolinium scandium gallium garnet) crystals absorbs over broad bands at 450 and 640 nm, and transfers energy to Nd via nonradiative and radiative transitions.⁽¹⁾ A twofold improvement in electrical efficiency results. GSGG has a lower cross-section than YAG, resulting in twice the energy storage capacity.⁽²⁾ GSGG costs three times as much as YAG. Its thermal characteristics are inferior, resulting in significant aberrations at power levels 20% that of YAG.⁽³⁾ Thermal limitations manifest themselves as beam distortions and reduced output energy. In this work, phase conjugate mirrors (PCMs) and Faraday rotators (FRs) were used to correct phase distortions and birefringence in a quadruple-passed GSGG rod amplifier.

II. Experimental Setup

The high brightness laser consisted of a TEM OO multiple longitudinal mode (MLM) oscillator followed by a telescope and then the PCMPA (figure 1). The GSGG oscillator was of the reentrant type and contained a 3 m radius back mirror separated from the 40% reflectivity output coupler and 100% reentrant mirror by a 1.5 m cavity.⁽⁴⁾ Tilted etalons consisting of a 0.2 cm thick 20% reflectivity etalon and a 0.02 cm thick uncoated etalon were used to obtain multi-peaked spectra with bandwidths (measured with a Burleigh Wavemeter) of 40 and 10 GHz (FWHM) without and with etalons. (PCM fidelity was better with the narrower bandwidth). Durations varied with PFN energy, but were kept at 50 to 70 ns.

The beam into the PCMPA was circular, of Gaussian intensity profile without diffraction rings, and had a 0.5 cm beam diameter. The undersized input beam, with 0.5 fill factor, is typical of high gain, heavily saturated systems where unsaturated edge gain converts a Gaussian input into a flat-top output with only modest diffraction modulation.⁽⁵⁾

The PCMPA consisted of a laser head surrounded by optics required for beam path control and aberration correction. The Kigre FDM 104 head housed a 1 by 10 cm rod and two close coupled flashlamps (xenon fill, bore = 0.5 cm, arc length = 8.4 cm, $K_0 = 22.7$) in a diffuse reflector. The diffuser substantially reduced, but did not totally eliminate, pump inhomogeneities. The power supply, from Kigre, provided 150 μs pulses at energies up to 91 J for average power to 2 KW.

The GSGG amplifier rod was from Litton-Airtron. Rod faces were 6° parallel and AR coated. The barrel surface was initially fine ground, but was reworked to have 0.03 cm deep circular grooves to test whether whispering mode parasitic oscillations limited gain at the highest pump energies. The Nd and Cr concentrations were 1.65 and 2.47 at. % respectively.

All optics used to control the beam were dielectric coated. AR coatings were important not only to minimize losses, but also to limit parasitic oscillations and stray damage producing beams. Because double pass gain could reach 730, reflections from AR coated surfaces had to be less than 0.14 % to prevent parasitic oscillations with the 100 % reflectivity dielectric double pass mirror. This is lower than specified AR reflectivities, so all surfaces were tilted. Stray beams (≥ 10 mJ) were a hazard if they originated from or impacted on concave beam focusing surfaces. Damage occurred during testing.

Faraday rotators (FR) were from Electro-Optics Technology (TGG crystals in permanent magnet housings). The damage issue was critical because once initiated, a black compound formed and rapidly increased in size.

Oscillator pulse width was fixed by damage threshold. Beam overlap in the heavily saturated amplifier resulted in light electric fields that were largest in the second polarizer, where three passes overlapped. This is one reason that 50-70 ns pulses were. Extra protection (1.4X) to some optics was provided by inserting the $1/4\lambda$ plate after polarizer 2.

One reflection from a single phase conjugate mirror was used. This arrangement was based on past experience that showed beam quality degradation (filaments) as the number of single or multiple cell reflections increased. The present arrangement produced no hot spots, but stressed the PCM in that it had to correct for two passes of phase distortion. The PCM consisted of a stainless steel cell containing 70 atm of CH_4 . The rear of the cell contained a conical, diffuse scattering beam dump that eliminated parasitic oscillation inducing retroreflections. The cell was sealed with a 1 cm thick AR/AR coated window. The focusing lens was a R=50 cm planoconvex AR/AR coated lens. The lens could be tilted to add

astigmatism, and thus counter some of the astigmatism incurred during the first two passes. This resulted in better ray mixing within the focal region and in better high average power PCM fidelity. Uncorrected astigmatism in nonstigmatic focus PCMs has been reported.⁽⁶⁾ Methane was selected because its reflection characteristics were the least sensitive to input bandwidth of all materials tested by us. The long focal length lens insured that high energy (1 J) breakdown did not occur. CH₄ is a slow SBS material with a characteristic response time of 40 ns (Another reason to use 50-70 ns pulses).

A divergence compensating telescope was placed between FR2 and the 0° dielectric mirror. This telescope was added when it was found that strong thermal lensing caused the beam to focus onto the PCM input window resulting in damage. The telescope was set to produce a collimated double pass beam (It did nothing to compensate for astigmatism.). A secondary damage route that the telescope was to eliminate, was the residual beam that did not undergo birefringence correction after four passes and was reflected from the PCM for another two passes. This beam, too, could, focus down and cause damage. Beam collimation, to the extent possible, minimized this threat. The primary job of the telescope was damage prevention. It was the task of the PCM to correct phase distortions. Use of the telescope aided to a limited extent in birefringence correction since rays must exactly retrace to be fully effective.

III. Stored Energy

Single pass small signal gain was measured to determine stored energy available for amplification. Stored energy E_{stored} can be calculated using the relation $E_{\text{stored}} \approx h\nu A [\ln(G_{ss})]/\sigma = 0.49 [\ln(G_{ss})]$,⁽⁷⁾ where h is Planck's constant, ν is the laser frequency, A is the beam area, G_{ss} is the small signal gain, and σ is the stimulated emission cross-section between the specific lasing sublevels. We take $\sigma = 3 \times 10^{-19} \text{ cm}^2$, assume uniform gain cross section, and a beam that fills the rod aperture. Note that E_{stored} represents stored energy available for pulsed lasing, i.e., without change in the R1 - R2 sublevel energy distribution. The total energy stored in the $^4F_{3/2}$ level is approximately 2.4 times as great as the calculated value.

Measurements were performed by placing an Ophir 30A-P-CAL calorimeter after the first pass. A first series defined the oscillator input range over which small signal gain could be measured (< 0.5 mJ). Use of the equation for E_{stored} together with G_{ss} data as a function of PFN energy, yielded energy storage efficiency (figure 2). Efficiency peaks at 2.5% and drops to 1.8% at the highest pump energies. The efficiency drop could be due to saturation in the Cr to Nd transfer efficiency, or due to increased losses by amplified spontaneous emission or parasitic oscillations.

In order to check for whispering mode parasitic oscillation, the gain was compared to earlier data obtained before the rod was grooved. Results were identical, so parasitic oscillations appear to be an unlikely cause of efficiency decrease.

In concluding this section, the stored to electrical pump energy efficiency of GSGG and YAG are compared. In previous work, YAG PCMPAs were developed and completely characterized. From this work, $G_{ss}(\text{YAG}) = 33$ at a PFN energy of 88 J. For a stimulated emission cross-section of $\sigma = 6 \times 10^{-19} \text{ cm}^2$, the calculated stored energy efficiency is 0.0098. Thus, GSGG is measured to be 1.9 times more efficient than YAG in converting electrical into stored laser energy.

IV. Birefringence Correction

A primary consideration in developing this PCMPA was to conjugate out static and dynamic birefringence. The second Faraday rotator (FR2) performed this task.⁽¹⁵⁾ Alternative schemes exist such as a "Sagnac" interferometer."

To see how a polarization conjugator (POC) [FR or Sagnac] works, a simple model can be considered: A polarizer in front of the amplifier defines x,y axes. After one amplifier pass, the polarization is elliptical and the relative phase difference between components along the ellipsoid axes (x', y') is given by $\Delta\phi$, where $\Delta\phi$ itself may be a function of x', y'. The beam passes through the POC and again through the amplifier. We want to calculate the E_x , E_y double pass components. The end result is: $E_x(\text{double pass})=0$ and $E_y(\text{double pass})=(-)E_0 e^{i\Delta\phi}$. Output double pass polarization is linear, so there is no birefringence. The difference between the input and output is a 90° polarization rotation and addition of a $e^{i\Delta\phi}$ phase factor. Since $\Delta\phi$ varies from point to point, the beam will suffer from a birefringence induced lensing.

The POC requires exact ray retracing to fully compensate for birefringence. Thermal lensing does, however, occur whenever there is spatially dependent birefringence. A PCM used by the FR will correct for temperature dependent refractive index and rod length induced ray deflections, but not $e^{i\Delta\phi}$ POC lensing. A divergence compensating telescope by the FR can correct for focusing (but not aberrations). Its use should yield better birefringence correction than a plane mirror.

The GSGG laser was run as a double pass amplifier with 5 mJ laser input. Light rejected by Pols 2 and 1 were the compensated and uncompensated components. Figure 3 shows the results. Use of a POC reduced by at least one order of magnitude, the double-pass static birefringence. The POC with the PCM gave the best dynamic results, followed by the POC with a flat mirror. The largest birefringence occurred when no measures were taken to correct for phase and birefringence distortions. Taking 10% loss as an upper limit (because of secondary beams with different divergence and direction), then maximum permissible pump powers are 300 and 200 W when a PCM and a plane mirror are used.

V. Quadruple-pass Amplifier

The quadruple-pass amplifier was tested with the divergence compensating telescope. Output energy is shown in figure 4. Laser input of 40 mJ was sufficient to drive the amplifier into saturation. A maximum of 1.74 J was obtained at a PFN energy of 80 J (efficiency = 2.1%). The peak efficiency was 2.4% , where 1.62 J was obtained at a PFN energy of 67 J.

The dependence of output energy on average pump power is shown in figure 5. For a given PFN energy, each point represents a PRF incremented by one. Output energy was nearly independent of PRF. Note, however, that the energy included that of the primary (80 to 90%) and secondary beams. The measurements were terminated at pump powers of 250 W, because laser induced breakdown was heard to emanate from FR1 or the GSGG face closest to FR1. Considering the energies involved, it seems probable that the source is quadruple passed nonbirefringence compensated light. Steps are being taken to eliminate this breakdown so that PRF can be increased.

Far field measurements were performed to determine divergence (figure 6). The measurements were performed with a 200 cm focal length lens, a Cohu CCD camera, and a Spirocon beam analyzer. Divergence gradually increased with average pump power and per pulse PFN energy. The laser can be characterized as twice diffraction limited.

VI. References

1. W. Krupke, M. Shinn, J. Marion, J. Caird, S. Stokowski, "Spectroscopic, optical, and thermomechanical properties of neodymium- and chromium-doped gadolinium scandium gallium garnet," J. Opt. Soc. Am. B **3**, 102-113 (1986)
2. J. Caird, M. Shinn, T. Kirchoff, L. Smith, and R. Wilder, "Measurements of losses and lasing efficiency in GSGG:Cr:Nd and YAG:Nd laser rods," Appl. Optics **25**, 4294-4305 (1986)
3. E. Zharikov, V. Kitaeva, V. Osiko, I. Rustamov, and N. Sobolov, "Elastic, photoelastic, and thermophysical properties of gadolinium scandium gallium garnet," Sov. Phys. Solid-State **26**, 922-923 (1984)
4. S. Jackel, A. Kaufman, and R. Lallouz, "High-repetition-rate oscillators based on athermal glass rods and on birefringence correction techniques," Opt. Eng. **33**, 3008-3017 (1994)
5. A. Ashmead, "Watch out for diffraction effects on laser-beam profiles," Laser Focus World **27**, 83-92 (1991)
6. J. Bellum, T. Crow, and E. Camp, "Experimental investigation of phase conjugation in stimulated Brillouin scattering of beams with mild cylindrical aberrations," Opt. Lett. **13**, 36-38 (1988)
7. W. Koechner, "Solid-State Laser Engineering Vol. 3, Springer-Verlag, New York, 146 (1992)
8. I. Carr and D. Hanna, "Performance of a Nd:YAG oscillator/amplifier with phase-conjugation via stimulated Brillouin scattering," Appl Phys. B **36**, 83-92 (1982); N. Andreyev, A. Matveyev, A. Kocherov, O. Palashov, G. Pasmanik, and E. Khazanov, "Phase conjugation to upgrade efficiency of solid-state laser energy conversion to narrow-band TEM00 mode pulses," IEEE J. of Quantum Electron. **30**, 305-313 (1994)

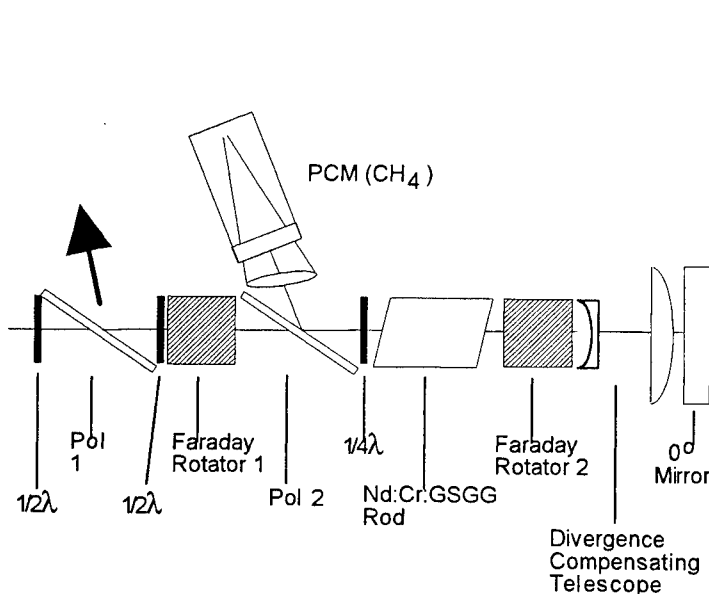


Figure 1-Quadruple pass PCMPA

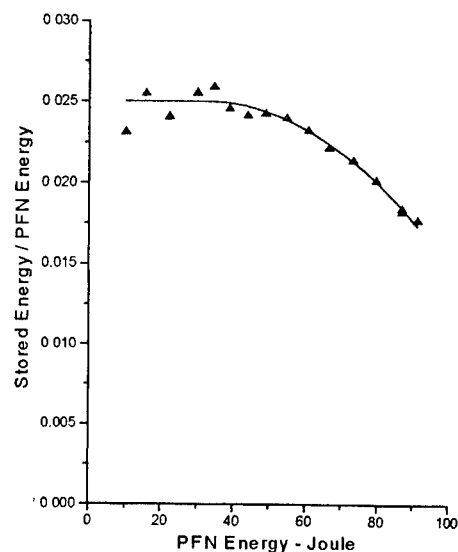


Figure 2 - Energy Storage Efficiency of the Flashlamp Pumped GSGG Amp.

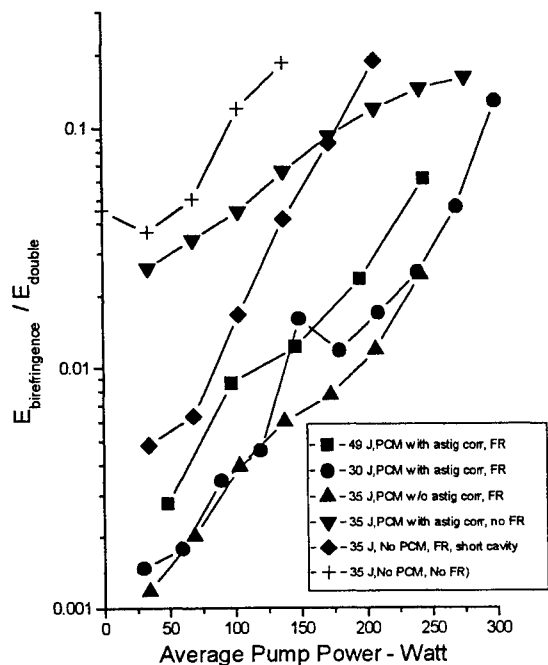


Figure 3 - Birefringence compensation

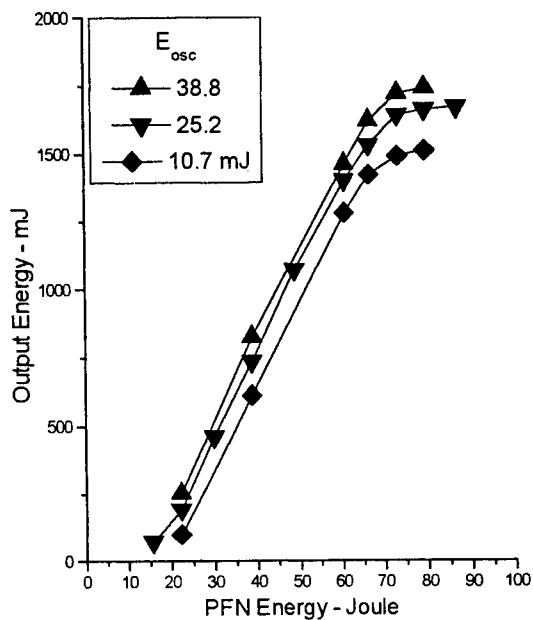


Figure 4 - Output energy of the quadruple-pass PCMPA

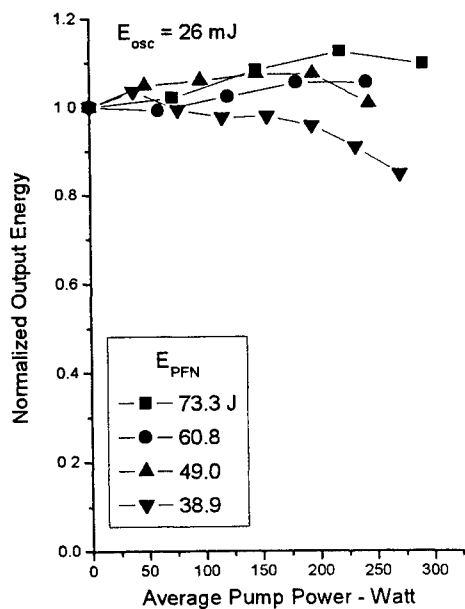


Figure 5 - Pump power dependence of the quadruple-pass amplifier output energy

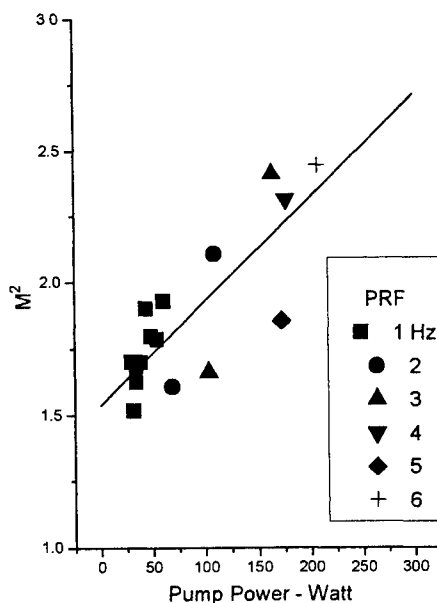


Figure 6 - Beam divergence of quadruple-pass PCMPA

High average power Nd:YAG laser with Cr⁴⁺:YAG passive Q-switch

Traian Dascalu

Institute of Atomic Physics, str. Fizicienilor 1,
sector 5, Bucharest, 76900, Romania

Horst Weber

Optisches Institut der Technischen Universität Berlin, strasse des 17 Juni 135,
D-10623 Berlin, Germany

Gerd Philipps

Laser- und Medizin Technologie, strasse des 17 Juni 135,
D-10623 Berlin, Germany

ABSTRACT

Passive Q-switching of high power CW pumped Nd:YAG laser by using phototropic Cr⁴⁺ ion centers in YAG was investigated in detail. Over 180 W average output was obtained at 15 kW input power with two cavities. The Q-switch efficiency is about 70 %. The beam parameter product is 7.5 mm mrad and longitudinal mode selection was observed.

Keywords: Nd:YAG laser, Cr⁴⁺:YAG, passive Q-switch

1. INTRODUCTION

Q-switched CW pumped solid state lasers with high average output power are required for research and applications. Pulses with high repetition rate (kHz range), high average and high peak power are very attractive for various applications as frequency doubling and material processing. Passive Q-switching of CW pumped Nd:YAG laser is possible by using LiF:F₂⁻ colour centers crystals but only at low average output power. New potential saturable absorbers are crystals with impurity centers characterised by a long time stability, a high optical strength, high thermal conductivity, and good chemical stability^{1,2}. Cr⁴⁺:YAG crystals were used in our experiments as passive Q-switch in Nd:YAG lasers. Three different crystals with small signal transmission from 83% to 90% and saturation transmission of 98% were investigated.

2. THERMAL EFFECTS IN CR⁴⁺:YAG PASSIVE Q-SWITCH

The Cr⁴⁺:YAG crystal's spectroscopic data, ³A₂ - ³E(³T₂) and ³B₂ (³T₂) - ³E(³T₁) transitions' cross section and the ³B₂ level lifetime were used in the laser rate equations. The four level model explains the behaviours of Cr⁴⁺:YAG crystal as passive Q-switch³. Because of low quantum efficiency of ³B₂ - ³B₁ transition detailed investigations on thermal effects in Cr⁴⁺:YAG were made. The using of the Cr⁴⁺:YAG crystal as passive Q-switch is limited by heat deposition in the Cr⁴⁺:YAG crystal. Heat deposition in the Cr⁴⁺:YAG crystal has two important effects: mechanical stress and the temperature increasing. The increasing temperature of the crystal decreases the lifetime of the level ³B₂ and that leads to efficiency decreasing; this process is supposed to be responsible for the

decreasing in laser energy pulse when the crystal is working without a cooling system. Heat deposition measurements in Cr^{4+} :YAG crystal are performed by using the set-up shown in Fig. 1. Fig. 2 shows the movement of the fringe pattern for 1mm respective 1.5mm crystal length. On channel 2 the time of AOM working is represented, and repetition rate was 10 kHz at 3.9 kW laser input power. The changes in optical path are given by the following equation:

$$\Delta(nl) = l\Delta T\left(\frac{dn}{dT} + \alpha_T(n-1)\right) = N\lambda$$

where: n and l is refractive index and length of the Cr^{4+} :YAG crystal, T temperature, N is the number of fringes measured by photodiode. The data are presented in table 1

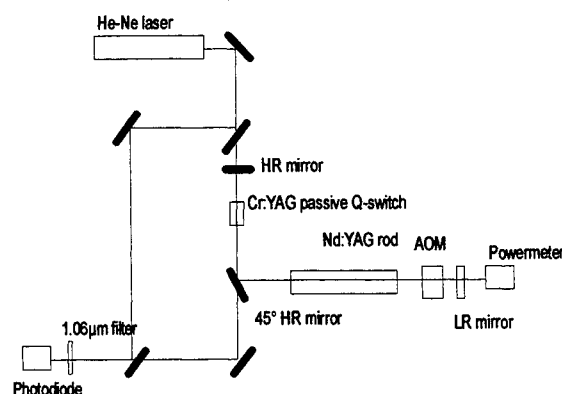


Fig. 2. Cr^{4+} :YAG heat deposition measurement set up
Mach-Zender interferometer

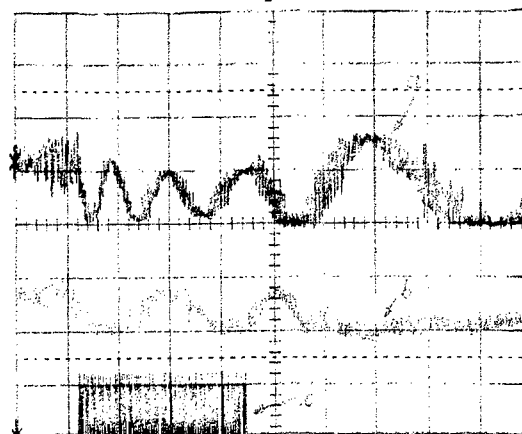


Fig.2. Fringe pattern displacement due to heat deposition in Cr^{4+} :YAG passive Q-switch (a)- 1 mm crystal length; (b)- 1.5 mm crystal length; (c)- time working of Nd:YAG laser (time base 1 s /div)

TABLE 1 Power heat deposition measurements for Cr^{4+} :YAG crystal.

Crystal length [mm]	dT/fringe [°K]	fringe/second	Power heat deposition [W]
1	49.23	0.8	2.9
1.2	41	0.9	3.3
1.5	32.8	1.5	4.9

In order to decrease the temperature gradient in the Cr^{4+} :YAG crystal, a cooling system was used which uses pure water for cooling the end faces of the Cr^{4+} :YAG crystal. By using this cooling system no temperature gradient was detected by interference method.

3.EXPERIMENTAL RESULTS

In our measurements three crystals of Cr^{4+} :YAG were used. The crystals were cut from the same Cr^{4+} :YAG crystal and small signal absorption coefficient was calculated from small signal transmission and length data measurements. Small signal transmission were between 83% and 90.5%. Saturation transmission was measured to be 98%-98.5%. The Nd:YAG rod with 4 mm diameter and 100 mm length was pumped by one lamp in diffuse pumping cavity. The flat-flat symmetric resonator with 0.5 m length was used.

The laser output power and laser pulse energy were measured by a RK5720 Power Radiometer, and RJ7100 Energymeter respective. Pulse duration was measured by a PBX-65

photodiode with 2 ns risetime and a LeCroy 9450 oscilloscope. The measurements on beam quality were made by using a CCD camera system.

By using this system up to 40 W average output laser power, passive Q-switched, was obtained. The laser pulses repetition rate increases from 1.5 to 12 kHz by increasing the input power. Pulse width was 150 nsec, and it has 40% variations from the average value that remains relatively constant when pumping power increasing. The far field intensity distribution for passive Q-switch and beam parameter product, at two different input power, is shown in Fig.3 and Fig.4. An increasing in the number of transversal modes by pumping power increasing is observed. The beam parameter product changes from 5.42 mm mrad corresponding to the 3.7 kW input power to 6.3 mm mrad corresponding to the 5.1 kW input power.

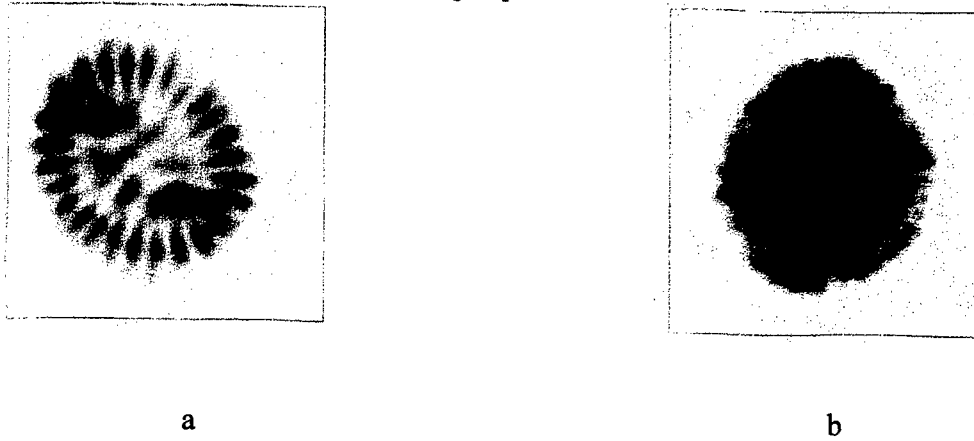


Fig.3. Far field intensity distribution; (a)- $P_{input}=3.7$ kW; (b)- $P_{input}=5.1$ kW

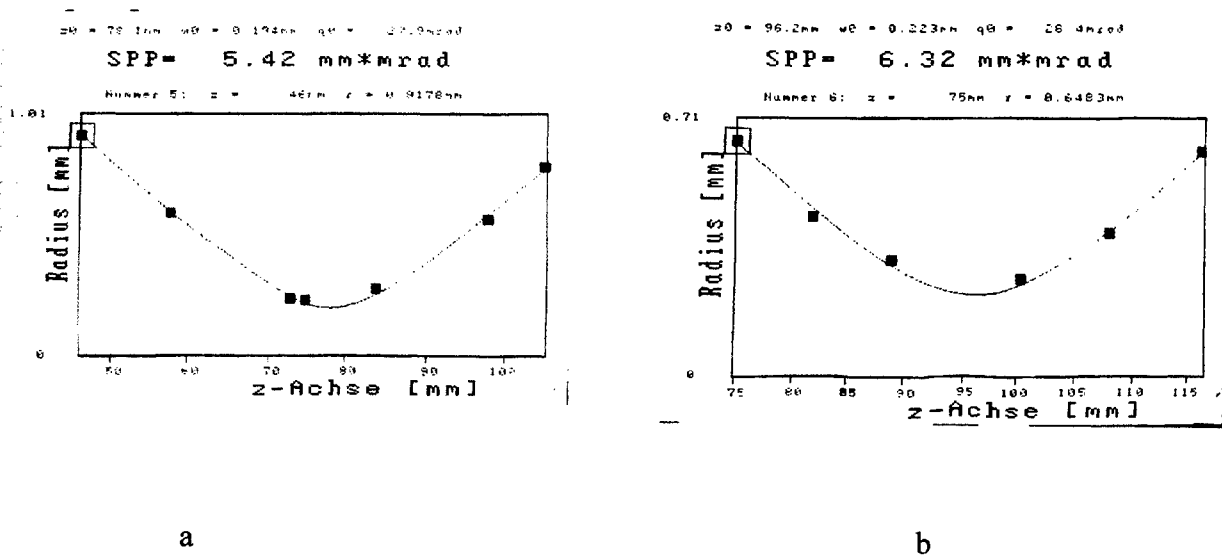


Fig.4. Beam parameter product; (a)- $P_{input}=3.7$ kW; (b)- $P_{input}=5.1$ kW

In order to increase the average output power, investigations were made on two cavities passive Qswitch laser. Over 180 W average output power was obtained at 15.3 kW input power. If losses inserted by cooling system are subtracted the Q-switch efficiency is found to be 70-72%. Figure 5 shows average output power versus pumping power for two cavities laser. The Cr^{4+} : crystal actions as a mode selector in laser resonator, especially at low input power as Fig.6 shows.

4.CONCLUSION

In this work the experimental results obtained on the Cr^{4+} :YAG crystal used as passive Q-switch in Nd:YAG lasers are described.

The average laser output power over 180 W was obtained in two rod CW Nd:YAG laser passive Q-switched by Cr^{4+} :YAG. This value is the highest reported up to now for passive Q-switched CW pumped Nd:YAG laser's oscillator. The output power can be scaled to the kW range by using long Cr^{4+} :YAG crystal with low density of phototropic Cr^{4+} ions that is more suitable for cooling. By using the Cr^{4+} :YAG crystal as passive Qswitch an improving in the laser beam quality was demonstrated.

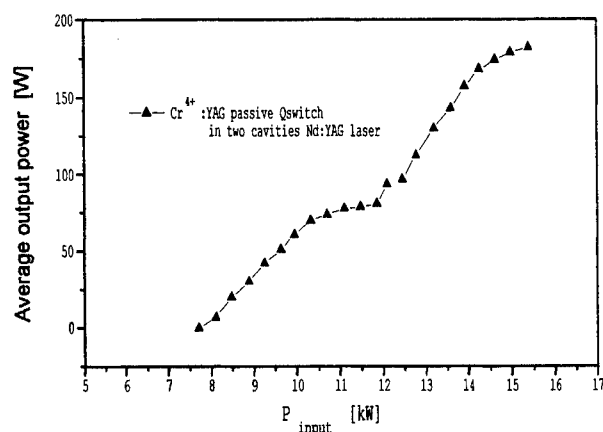


Fig.5. Average output power in two rod Nd:YAG laser with passive Q-switch Cr^{4+} :YAG

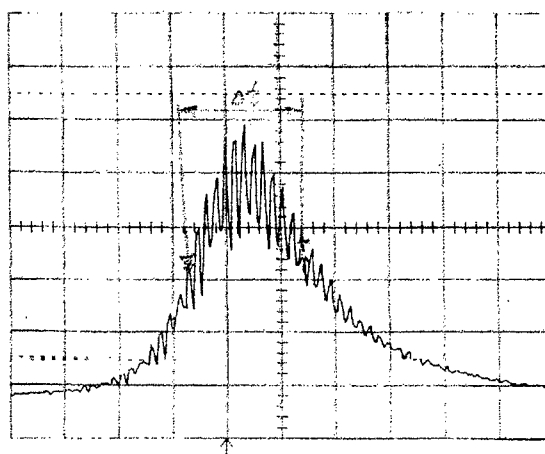


Fig.6. Laser pulse length in two rod Nd:YAG laser with passive Q-switch Cr^{4+} :YAG; $\Delta t = 430$ ns;

5.ACKNOWLEDGEMENT

This research was supported by KONFERENZ DER DEUTSCHEN AKADEMIEN DER WISSENSCHAFTEN - VOLKSWAGEN STIFTUNG and OPTICHES INSTITUT-TECHNICHEN UNIVERSITAT-BERLIN

6. REFERENCES

1. L.I.Krutova, A.V.Lukin, V.A. Sandulenko, E.A.Sidorova and V.M.Solntsev, "Phototropic centers in chromium-doped garnets," *Opt.Spectrosc.*, **63**(5), 693
2. W.Jia, H.Liu, Y.Wang, U.Homerich, H.Eilers, K.R.Hoffman and W.M.Yen, "Origin of the NIR emission in chromium doped forsterite, $\text{Y}_3\text{Al}_5\text{O}_{12}$ and Y_2SiO_5 ," *J. Luminescence*, **60**,158-161(1994)
3. K.Spariosu, W.Chen,R.Stultz, and M.Birnbaum and A.V.Shestakov, "Dual Q-switching and laser action at 1.06 and 1.44 μm in Nd:YAG-Cr:YAG oscillator at 300 K," *Optics Lett.*, **18**(10),814-816,(1993)

Scaling Cr:LiSAF to high average power

A. Mandl, D. E. Klimek, and A. Zavriyev
Textron Systems Division
Wilmington, MA 01887
(508) 657-6725
e mail: amandl@tsd.textron.com

1. ABSTRACT

We report on the status of an experimental activity to scale Cr:LiSAF to high average power using a unique zig-zag optical cavity design.

KEYWORDS: Cr:LiSAF, slab laser, zig-zag laser.

2. INTRODUCTION

Over the past several years, we have been developing zig-zag optical cavities for a variety of lasers. This development has been successful in the performance of high power dye lasers using this new design. In brief, we have demonstrated single mode, 7 J per pulse, 10 Hz, near diffraction limited operation of a laser pumped liquid dye laser.^{1,2} When compared to the operation of a comparable power dye laser which used a more conventional optical cavity, we achieved an improvement in beam quality of about an order of magnitude and a comparable improvement in RMS jitter performance. We have also demonstrated that this laser can be operated virtually chirp free.³ More recently, we have applied some of the design approaches used for the liquid dye laser to the design of a solid state plastic dye laser. The resulting laser pumped plastic dye laser operated near the diffraction limit with a beam quality about an order of magnitude improvement over plastic dye lasers which use more conventional optical cavities.^{4,5} This plastic host device also achieved record energy output for a plastic dye of about 1 J.

3. EXPERIMENT

We are now in the process of applying this approach to the operation of more standard solid state materials. In particular, we report in this paper some initial experiments that were performed lasing Cr:LiSAF, an interesting new crystal which lases over a broad wavelength range about 250 nm wide centered at about 850 nm. Cr:LiSAF has a 67 μ s storage time and so can be efficiently laser diode or flashlamp pumped. A flashlamp pumped dye laser was used as the pump source for this study. Some of the key features of this design have been confirmed. However, because of a fabrication error, the crystal that was tested operated below optimum.

The key to scaling lasers to high average power while maintaining good optical quality is the thermal control of the lasing medium. As with many solid state crystals, Cr:LiSAF has poor thermal properties. Our approach is to use thin, 1.5 mm, slabs of the crystals immersed in a flowing index matched fluid which acts as a thermal reservoir. A schematic diagram illustrating the design approach is shown in Figure 1. A simple stable optical cavity is pictured. The cell is made of fused quartz with a 4 mm wide flow channel that is 20 mm high and 165 mm long. Two 1.5 mm X 110 mm slabs are positioned in Dimethylacetamide (DMA) which has an index of refraction, $n = 1.43$, a good match to quartz ($n = 1.46$) and Cr:LiSAF ($n = 1.40$). Laser flux is coupled into and out of the cavity through quartz prisms. Single sided optical pumping is used.

The dye laser pump source operated at 590 nm with Rhodamine-590 dye and is capable of single pulse energies up to 12 J with an $\sim 3 \mu$ s pulse length. The pump laser output is passed through an optical

scrambler which produces a spatially uniform vertical intensity profile with a 9 mm X 90 mm optical footprint at the zig-zag cell.

A stable optical cavity was set up without Q-switch control. The laser output (shown in Figure 2) occurred during the excitation pulse and consisted of a pair of pulses of comparable energy separated by over 1 μ s. The first pulse was the more intense of the two with a pulsewidth of about 125 ns. Initial laser measurements demonstrated total energy output \sim 1 J at an intrinsic photon efficiency of > 20 percent.

There were several significant losses associated with the 5.5 percent doped Cr:LiSAF crystals used in these tests. This material was manufactured by Lightning Optical several years ago with a reported intrinsic scattering loss of 3% / cm. Recent improvements in Cr:LiSAF processing by the vendor have improved intrinsic scattering losses by about an order of magnitude and newer crystals should produce improved laser performance.

A more serious gain loss occurred due to a manufacturing error. The crystal was fabricated with the c-axis perpendicular to the face of the crystal, i.e., in the laser pump direction as shown in Figure 1, whereas a vertical c-axis had been specified. For the c-axis orientation shown in Figure 1, the effective gain cross-section is reduced since there is only gain for the component of the E vector parallel to the c-axis in our zig-zag geometry, i.e., the E vector is approximately 45° to the c-axis. When a new crystal is installed with a vertical c-axis, laser performance should improve substantially.

A computer model of the Cr:LiSAF laser was also developed and used to compare with the measurements. Although agreement is only qualitative, we calculate the double pulse features but the energy in each pulse and the timing of the second pulse are not quantitatively modeled.

4. REFERENCES

1. A. Mandl, D.E. Klimek, H.P Chou, L. Litzenberger and Y. Wang, "Single mode operation of a long pulse flashlamp pumped dye laser," *IEEE Journal of Quantum Electronics*, **Vol. 31**, pp. 346 - 351 (1994).
2. A. Mandl and D.E. Klimek, "Multipulse operation of a high average power, good beam quality zig-zag dye laser," *IEEE Journal of Quantum Electronics*, **Vol. 32**, pp. 378 - 382 (1996)
3. A. Mandl, A. Zavriyev and D.E. Klimek, "Chirp control of a single mode, good beam quality, zig-zag dye laser," Submitted to *IEEE Journal of Quantum Electronics* (1996).
4. A. Mandl, A. Zavriyev and D.E. Klimek, "Energy scaling and beam quality improvement of a zig-zag solid state plastic dye laser," *OE/Lase'96, SPIE, Solid State Lasers V*, Vol. 2698 (1996).
5. A. Mandl, A. Zavriyev and D.E. Klimek, "Energy scaling and beam quality studies of a zig-zag solid state plastic dye laser," to be published in *IEEE Journal of Quantum Electronics* (October 1996).

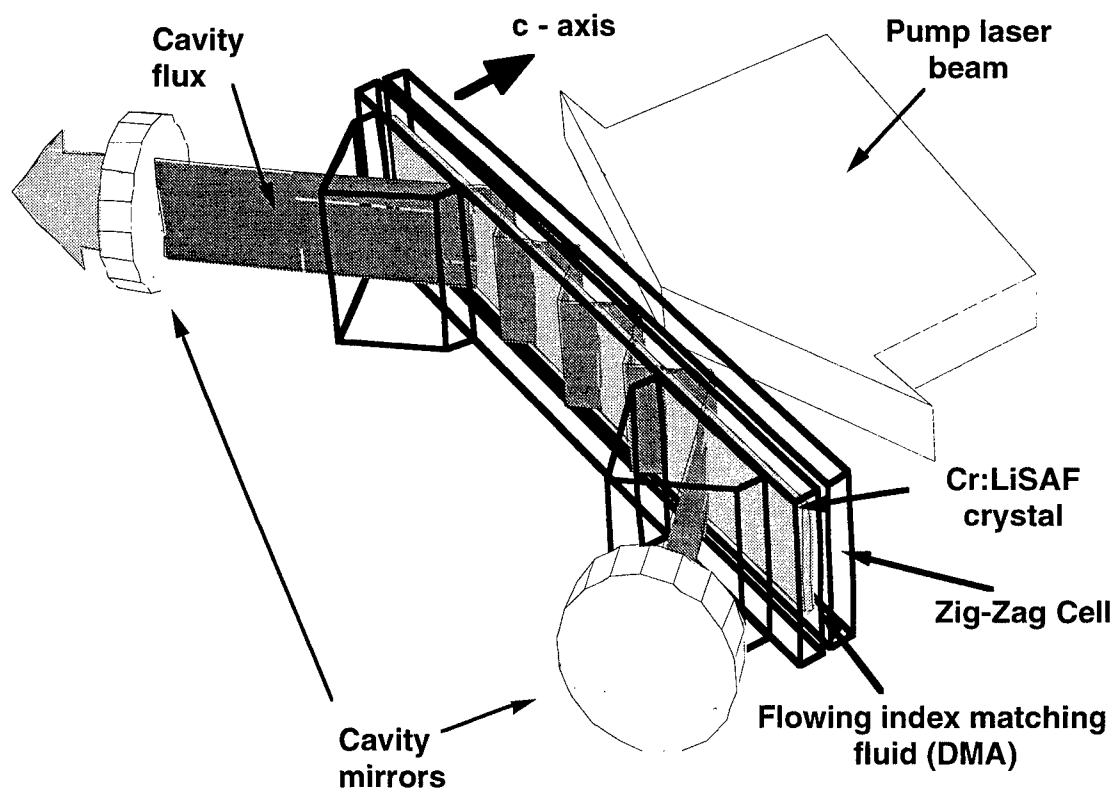


Figure 1. Three dimensional perspective drawing of the zig-zag laser showing key features.

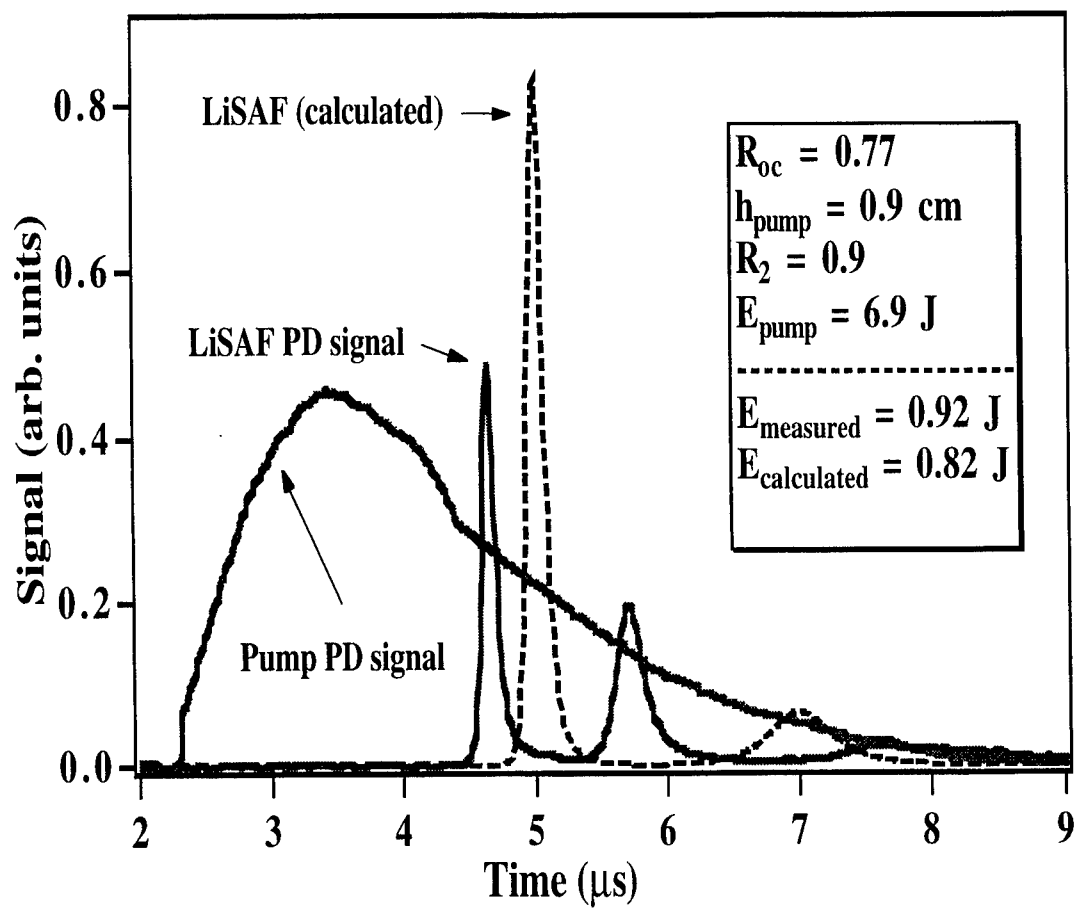


Figure 2. Cr:LiSAF laser measurements compared to model calculations.

4. Metal Vapour and Near-IR Lasers

Average power scaling of copper hybrid lasers

L Little and C E Little

University of St Andrews, School of Physics and Astronomy
North Haugh, St Andrews, Fife KY16 9SS, Scotland

ABSTRACT

Copper lasers are the highest efficiency high average power visible lasers (510.6 and 578.2 nm). The most efficient of them all is the copper hybrid laser, which has been demonstrated to produce 200 W average power with 1.9% efficiency. The prospects for increasing the average output power from single or double tube devices into the kilowatt regime are discussed. With practically no plasma skin effect, a long gain duration (~100 ns), and rapid plasma relaxation between pulses, copper lasers with hydrogen halide additives (hybrid lasers) hold promise for scaling in tube bore, active length and PRF to kilowatt average output powers with efficiencies of ~2%, and ~600 W at 3.5% efficiency.

Keywords: copper lasers, hybrid lasers, high power, kilowatt power, visible, efficient, power scaling

INTRODUCTION

Copper hybrid lasers have produced average output powers of up to 201 W at efficiencies (based on stored energy) of just under 2% at the wavelengths 510.6 nm and 578.2 nm. At the 120 W average power level, the efficiency reaches 3.2% [1]. Their characteristics differ markedly from those of elemental copper vapour lasers (CVLs). The copper hybrid (hydrogen bromide in discharge) laser is essentially a CVL which includes typically 5-10% by volume hydrogen halide with the noble-gas buffer. The most successful buffer-gas/hydrogen-halide combination to date has been Ne/HBr. In most studies of hybrid lasers, the HBr has been added to laser tubes operating at wall temperatures of 600-800°C. Recently, HBr and other hydrogen halide donors have been added to a CVL operating at the more usual 1500-1600°C wall temperature, with improvements in output characteristics which approach the high performance of low-temperature (LT) hybrid lasers [2].

In the LT hybrid laser, the copper metal in the tube is in solid form, and copper bromide vapour is formed *in situ* by reaction of bromine and the copper metal. Free copper atoms are then liberated by dissociation of the CuBr molecules and their polymers by electron impact in the multi-kilohertz PRF discharge. This is the classic copper hybrid laser, in which a flowing Ne-HBr buffer gas is used, and where the copper density in the discharge volume is determined by copper bromide formation and destruction processes; the copper bromide density is quickly and easily controlled and optimized by adjusting the HBr inlet pressure.

In the high-temperature (HT) hybrid laser, the copper atoms are supplied to the discharge by vaporization of copper liquid in the tube. The copper density is by and large a function of the tube temperature, *i.e.* of input power.

As we shall see, hybrid lasers are volume scalable devices, making it possible for a double-tube MOPA or ILD system to deliver 1 kW of usable average output power.

HIGHEST POWERS ACHIEVED FROM COPPER LASERS TO DATE

The largest average output powers and energies are generated by CVLs operated in MOPA configurations. In 1991, Warner [3] reported 1.4 kW high-quality average power from a MOPA chain with a 25 W MO and 3 PAs, each of which contributed an output power of 400-450 W. He also mentioned that a specially configured PA had provided an extracted output power of 650 W at an efficiency of 1%, although no details were provided. Aoki et al. [4] described more fully an 80 mm bore, 300 cm discharge length CVL that produced 260 W as an amplifier, and 211 W as an oscillator. In 1995, Chang et al. [5] reported an increase in output power of an 80 mm bore amplifier from 255 W to 325 W by the use of Mo plates or 'septa' placed along the inside of the discharge tube to cool the gas on the discharge axis. These 'high-power' lasers were all conventional CVLs, where the copper was provided by vaporization in the active zone, and a small (0.5-1%) amount of H₂ was added to the Ne buffer gas.

Recently, Bokhan and Molodykh [6] numerically examined the scaling of metal vapour lasers in average power to the level of kilowatts per metre. Their solution was to abandon conventional longitudinal discharge excitation and apply the concept of runaway-electron beam excitation.

The purpose of the present paper is to ascertain whether or not it is possible to construct copper lasers of kilowatt-scale average output powers using current technology. Copper hybrid lasers have features that make them particularly well suited to volume scaling in order to achieve high output powers. The reasons for hybrid lasers' good performances are related to the presence of the hydrogen halides in the discharge volume.

INFLUENCE OF HYDROGEN HALIDES ON KINETICS OF COPPER LASERS

Recently, it was concluded by Isaev et al. [7] that the species HBr is the main agent responsible for the improvement in output power and efficiency in copper lasers with added HBr, and in copper bromide lasers with added hydrogen. Previously, all fingers had pointed to hydrogen as the agent. The chief mechanism by which the HBr is believed to affect the discharge kinetics is via the process of dissociative attachment:



which has a peak cross section of $2.7 \times 10^{-16} \text{ cm}^2$ for an electron energy of 0.28 eV. In the early afterglow, dissociative attachment acts to remove electrons quickly to produce bromine negative ions. A density of $\sim 10^{14} \text{ cm}^{-3}$ HBr in the tube is sufficient to remove the electrons with the characteristic time of $\sim 5 \mu\text{s}$ which is measured in a hybrid laser [8]. Fast two-body processes of ion recombination can then remove the negative ions and replenish the ground-state copper density.

Provided the prepulse electron density is small enough, when the electric field is still low and the current is low, the process of electron attachment impedes and delays the electron avalanche [7]. As the evolution of the electron energy distribution function (EEDF) tends towards higher electron energies, the rate constant for the attachment process compared to ionization falls, and avalanche proper occurs. The influence of attachment in delaying avalanche is evinced by the large *increase* in tube impedance that occurs when the field is first applied and the current remains low. The result is that the laser tube acts as its own switch with an in-built delay mechanism. When electron avalanche does begin, the applied field is usually close to maximum, and the increase in current is fast ($\sim 70 \text{ ns}$ from 10% to 90% of peak current in a 60 mm bore, 200 cm active length discharge tube).

Because of the different evolution of the EEDF during the excitation pulse in hybrid lasers compared to CVLs, the kinetics of lower and upper laser level populations differ [7]. Before avalanche, ionization is balanced by attachment, and the electron number density is kept low, which prevents early population of the lower laser levels. When the electron avalanche proper begins at the maximum of the applied field, T_e is suited to excitation of the upper laser levels. Because the value of applied voltage in a hybrid laser at onset of avalanche is considerably higher than in a conventional CVL, the T_e in the hybrid laser can provide more effective upper level pumping relative to the lower laser levels. The larger inversion that can be obtained is reflected in the fact that when hydrogen is added to a CuBr laser, or HBr is added to a CVL, the specific output pulse energy and efficiency are doubled.

Another reason for the increased efficiency of copper lasers with the presence of HBr is the improved matching of the discharge tube to the pulse modulator, which is evinced by the increase in tube wall temperature for the same PRF and charging voltage, and by the much lower negative voltage excursion that appears on the thyatron anode following the excitation pulse. Therefore, both the kinetics and the electrical characteristics of copper lasers are improved by the addition of hydrogen halides or donors of their constituent atoms.

VOLUME SCALING OF CONVENTIONAL CVLS

Conventional CVLs are limited in the amount of volume scaling they can tolerate before output characteristics begin to deteriorate. In the case of increasing tube bore, the plasma skin effect begins to affect laser performance with tube bores as low as 42 mm [9]. The skin effect manifests itself by the development at larger bores of a radially dependent longitudinal electric field which reduces from a maximum near the wall to an on-axis minimum in the discharge tube. Furthermore, the electric field exhibits a noticeable delay between onset of excitation and lasing near the wall and on the tube axis. In the CVL of 42 mm bore, in the absence of HBr, the prepulse electron density was $\sim 30\%$ of the peak electron density, and the prepulse conductivity was $4800 \Omega^{-1}\text{m}^{-1}$ [10]. The widest CVLs reported have tube bores of 80 mm. The influence of the skin effect in a CVL can be reduced, but not eliminated, by operating at higher buffer gas pressures, and by cooling the gas at the centre of the tube by the presence there of septa [11, 12].

A second factor that restricts the increase of tube bore in conventional devices is the increase in gas temperature away from the tube wall. The gas temperature controls the prepulse metastable lower laser level populations. The higher the prepulse metastable densities, the smaller the maximum inversion density, and the shorter the gain duration. The requirement for plasma and gas relaxation necessitates lower PRFs as the tube bore is increased (due to the increase in input power per unit length, as the on-axis temperature is independent of tube bore [13]).

Input pulse energy and peak current must be increased greatly as tube bore is raised, whilst maintaining 'fast' ($\leq 100 \text{ ns}$ rise-time) discharge excitation. This places great demands on the switch and modulator. Also, because the conductivity of the CVL channel is high, impedance matching is difficult even for tubes of 60 mm bore, and will be more so at larger tube bores.

With regard to length scaling, the largest length is determined by the gain duration. It is desirable to have 4 or more cavity round-trips during gain in order to reduce the time-averaged divergence. The longest CVL oscillators and amplifiers reported have discharge lengths of 300 cm [4].

ADVANTAGES OF HYDROGEN HALIDE ADDITIVES FOR VOLUME SCALING

The high discharge channel impedance afforded by the presence of HBr in a hybrid laser leads to many advantages over conventional CVLs for scaling. First, there is almost no skin effect in a hybrid laser. In a 60 mm bore hybrid laser [1], lasing at the wall and on the tube axis began within 3 ns of each other. The penetration of the longitudinal electric field into the active medium is highlighted by the fact that the output beam intensity profile of the 60 mm bore laser is close to Gaussian in form, i.e. there is a strong central maximum in laser beam intensity. The pseudo-Gaussian intensity profile is maintained throughout the pulse duration, which is important for machining applications.

We can use the data of [7] to calculate typical plasma skin depths and electric field penetration times in a 25 mm bore hybrid laser. Current and voltage data lead to a tube conductivity of $0.8 \Omega^{-1}\text{m}^{-1}$ during the application of the tube voltage. (This corresponds to a remanent electron density of 10^{10} - 10^{11} cm^{-3} , or 0.01-0.1% of the peak electron density in the same laser; cf. 30% of the peak electron density remaining in a CVL [8].) Therefore, the plasma skin depth in the hybrid laser is 350 mm (independent of tube bore assuming the same conductivity), and the penetration time for an 80 mm bore hybrid laser is 0.25 ns. These figures should be compared with 30 mm and 43 ns, respectively, for an 80 mm bore CVL [14]. Therefore, because of the efficient removal of free electrons between excitation pulses in a hybrid laser, the electric field can penetrate 100's mm depth of plasma in less than a nanosecond.

The lower wall temperature of LT hybrid lasers is an advantage in keeping gas temperature effects at bay. Even the output beam of a 60 mm bore hybrid laser displays a strong central maximum in its transverse intensity profile, indicating no deterioration in gain on the tube axis due to gas temperature effects, even at PRFs of 15-20 kHz [1]. The 2-3 times higher efficiency of hybrid lasers means 2-3 times more output power can be achieved from those devices compared to CVLs for the same input power per unit length. Specific input powers of $\sim 15 \text{ kW.m}^{-1}$ can be applied to large-bore ($\geq 80 \text{ mm}$) CVLs [15].

The improved matching of the modulator to the laser tube with HBr at high impedances, together with the faster plasma relaxation, means that these lasers can be operated with smaller capacitances at higher PRFs than their non-HBr counterparts. This also makes for more effective excitation as the current pulse risetime can be shorter, and the input excitation pulse better temporally matched to the gain period in a hybrid laser. The more effective excitation contributes to higher laser efficiency. The input pulse energy and, in general, the peak current density required are lower in hybrid lasers, making scaling of hybrid lasers in tube bore more practical from the point of view of the modulator/switch requirements.

Finally, the laser pulse duration is longer with added HBr. While a 60 mm bore CVL produces a laser pulse lasting $\sim 40 \text{ ns}$ (FWHM), a 60 mm bore hybrid laser generates a laser pulse lasting 60 ns (FWHM). The hybrid laser can therefore afford longer cavities than conventional CVLs when operated as an oscillator.

Copper lasers with hydrogen halides in the gas mixture therefore have some attractive features additional to their high specific average output powers and efficiencies. The very weak plasma skin effect allows the tube bore to be increased by 100's mm. The longer gain period means long optical cavities can be fitted without great detriment to beam quality, making scaling by length more feasible compared to CVLs, which have already been scaled to 300 cm discharge length. The rapid and volumetric nature of plasma relaxation between pulses enables high-PRF (15-20 kHz) operation of tubes with large bore sizes ($\geq 60 \text{ mm}$). The ability to operate with lower input energies and peak currents also favours scaling by tube bore in hybrid lasers as opposed to CVLs.

VOLUME SCALING BEHAVIOUR OF COPPER HYBRID LASERS

The results of experiments on hybrid lasers with a 4.5 mm [16], 12.5 mm [17], 45 mm [18] and 60 mm [1] bore are summarized in Fig. 1, where average output power per unit length is plotted versus tube bore. Included in that Fig. is also a point corresponding to a 40 mm bore HT hybrid laser [2]. It can be seen that the output power per unit length is a good linear function of tube bore. The true dependence is probably slightly steeper, as the output powers of the 45 and 60 mm bore lasers did not saturate completely with the highest charging voltages used. If we accept that the hybrid laser can be scaled up to at least 300 cm discharge length, as has been demonstrated for CVLs, then we can see that an average output power of 1 kW is predicted for a tube bore of 250 mm, well within the plasma skin depth limit. The field penetration time for such a tube would be 2-3 ns.

The dependence on tube bore of the PRF for maximum average output power is shown in Fig. 2. There are two regimes of operation: a small-bore ($\leq 25 \text{ mm}$) regime, where diffusion and volumetric processes play major roles in determining the upper limit to PRF; and a large-bore ($\geq 25 \text{ mm}$) regime, where the PRF is determined

entirely by volumetric processes, i.e. the PRF (~17 kHz) is independent of tube bore. The 250 mm bore tube is therefore expected to optimize at a PRF of 17 kHz.

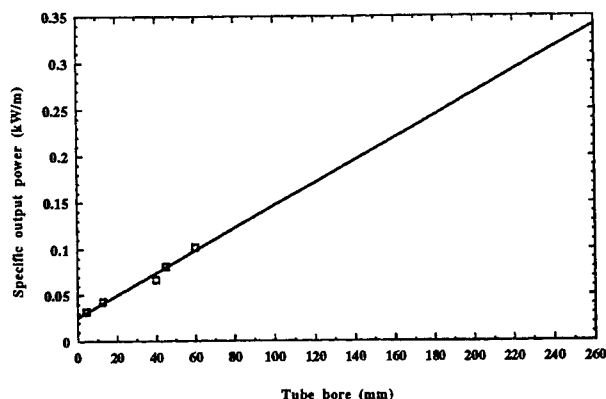


Fig. 1. Lineal average output power vs tube bore.

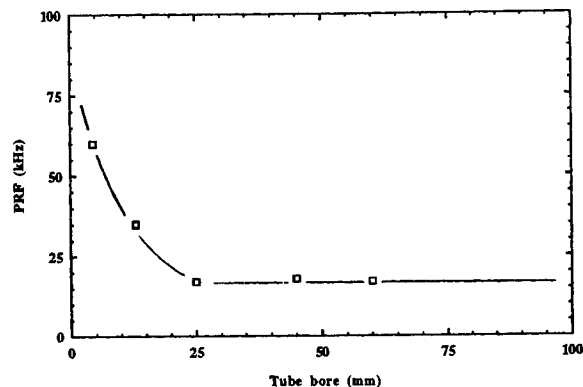


Fig. 2. PRF for maximum output power vs tube bore.

In order to determine the other operating parameters, we plot the dependence of the characteristic parameters pR and E/p , where $2R$ is the tube bore, p is the buffer gas pressure and E is the maximum applied field, assuming, as is usually found to be the case, that the charging voltage is similar to the maximum tube voltage. Fig. 3 shows these two parameters calculated as functions of tube bore. Again we can see the transition from a diffusion-dominated regime at low tube bores to one where volumetric processes dominate. In the case of a 250 mm bore tube, E/p tends to $500 \text{ V.m}^{-1}\text{.torr}^{-1}$ and pR tends to 1500 torr.mm . The value for pR sets the Ne pressure at ~12 torr, which in turn specifies the maximum applied (or charging) voltage over 300 cm as ~18 kV. Assuming the same volumetric processes control the operating efficiency in the 250 mm bore laser as in the 60 mm and 45 mm bore lasers, we find that the laser efficiency (based on stored energy) at maximum power will be ~2%. Then, the input power to the laser will be 50 kW, so that the storage capacitance C_s must be 19 nF for the given PRF and charging voltage.

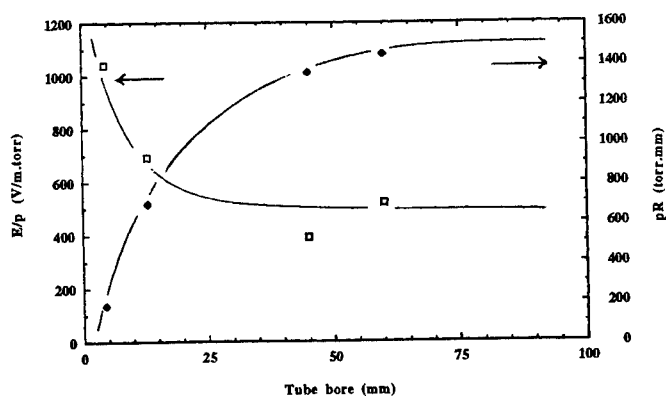


Fig. 3. E/p and pR versus tube bore.

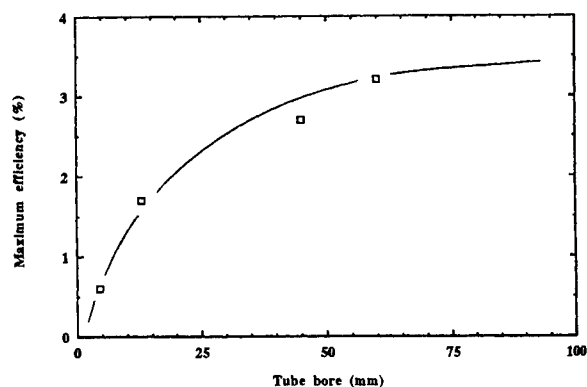


Fig. 4. Maximum efficiency versus tube bore.

We can do the following check on storage capacitance. The impedance of the 60 mm bore, 200 cm active length tube can be related through the change in bore and length to the impedance of the 250 mm bore, 300 cm long laser by the factor 0.086. As the optimum peaking capacitance C_p for the 60 mm tube was 0.95 nF, the peaking capacitor suitable for matching into the 250 mm bore laser will be ~11 nF. Based on previous studies of hybrid lasers, the optimum storage capacitance will be approximately twice the peaking capacitance, i.e. ~22 nF, which compares favourably with our independent calculation above of C_s of ~19 nF.

Finally, we need to check that the tube inductance does not prevent the current pulse rise-time from being ≤ 100 ns for efficient copper excitation. The inductance per unit length of coaxial conductors is $\frac{1}{2\pi}\mu_o \ln \frac{b}{a}$, where

b is the radius of the coaxial current return, and a is the radius of the inner conductor. Assuming the bulk of the discharge current to be carried in the central half (125 mm) of the laser tube, and a diameter for the coaxial current return of 350 mm, we find the inductance L_h of the 300 cm long discharge tube to be ~200 nH. The excitation

pulse rise-time is given by $\frac{\pi}{4}\sqrt{L_h C_p}$. Allowing for placement of peaking capacitors etc., setting L_h as 300 nH gives an excitation pulse rise-time of 45 ns, which is well suited to excitation of the atomic copper transitions.

The 50 kW input power required by the 1 kW hybrid laser can be handled by 3-5 thyratrons operating in parallel. Note that 3 thyratrons are used in parallel to drive present-day commercial 100 W CVLs. Gabay et al. [19] have operated a 120 W CVL with a single-thyratron circuit, where 10 kW power was delivered to the laser head (80 mm bore, 150 cm active length) in a circuit with magnetic assist and 3-stage magnetic pulse compression. Pulse energies of 3.6 J (1.8 J to the laser tube) were switched at 5.5 kHz in the circuit. By contrast, the 1 kW copper hybrid laser requires pulse energies of 3.1 J to be delivered to the discharge tube at 17 kHz PRF. All-solid-state modulators are used to drive CVL PAs at Lawrence Livermore National Laboratory with input powers of 30 kW and PRFs of 4-5 kHz [20]. With modifications for high PRF operation, a similar system could also be applied to the copper hybrid laser.

For 50 kW total input power, the specific input power required is 16-17 kW.m⁻¹, which is similar to that already known to be applied to CVLs (~15 kW.m⁻¹) [15]. Bearing in mind the 600-700°C lower wall temperature of LT hybrid lasers, we can see that gas heating is unlikely to be a problem, although the input power is radially more uniform in a CVL. The 15 kW.m⁻¹ CVL uses septa placed vertically along the middle of the discharge tube to cool the gas at the centre of the tube, and reduce the remanent metastable state density there. By making use of septa in a LT (~800°C) hybrid laser, we estimate that it is possible to obtain 1 kW output power from a 300 cm long discharge tube of 230 mm bore. The temperature profile in the gas should be similar to that expected in a laser with only 8-9 kW.m⁻¹ input power, as the temperature of the septa in the middle of the tube should be close to the wall temperature. The PRF would be 17 kHz, the gas pressure 13 torr, the charging voltage 19.5 kV, and the storage and peaking capacitances 15 nF and 7.5 nF, respectively. The laser would still require ~50 kW input power, of course. If the septa were made of copper, they could double as the copper reservoir in the tube. Alternatively, ceramic (BeO, alumina) septa could be used.

We therefore see that development of a kilowatt average power copper hybrid laser tube is a practical proposition. In order to ensure that the beam is of high quality (≤ 2 times the diffraction limit), and to prevent parasitic depletion of the inversion by photons which do not contribute to the output beam, it is necessary to extract the output power using the tube as either a PA or as an injection-locked oscillator (ILO). As a PA, around 25% extra output power should be available, giving 1.25 kW extractable power. For the ILO configuration, as long as the cavity is flooded with high quality light (1-2 times the diffraction limit) for at least 10-20 ns corresponding to the onset of gain in the tube, the majority of the light output should also be of high quality.

Finally, we should mention that hybrid lasers also tend to operate at maximum efficiency with around 60% of the maximum output power. The trend for maximum efficiency (based on stored energy) as tube bore is varied is shown in Fig. 4. It can be seen that the efficiency reaches a maximum of ~3.5%. We therefore expect the scaled hybrid lasers discussed here to generate ~600 W at ~3.5% efficiency, i.e. with an electrical input power of only 17 kW. Such a laser is realizable now.

CONCLUSIONS

Copper lasers with hydrogen halide additives are well suited to scaling in volume to tube bores around 350 mm and discharge lengths of at least 300 cm. The rapid and volumetric nature of relaxation of the active medium in the interpulse period enables high-PRF (15-20 kHz) operation, even at larger (≥ 60 mm) bore sizes. Evidence has been presented that the parameters E/p , pR and the PRF are effectively constant for tube bores larger than 25-

40 mm. This is a result of most the key laser kinetics being determined by volumetric processes in large bore tubes. The output power per unit length is a linear function of tube bore.

Kilowatt average output powers appear possible using only current technology. As a starting point for the development of kilowatt-class copper hybrid lasers, the recommended laser tube dimensions for 1 kW output power are 250 mm bore, 300 cm discharge length. The laser should have a buffer gas pressure of 10-15 torr, and be driven at 15-20 kHz with ~20 kV charging voltage. The storage and peaking capacitances should be 15-20 nF and ~7.5-10 nF. Between 3 and 5 thyratrons could be used with magnetic assist and multi-stage magnetic pulse compression to drive the laser with 50 kW input power. It may be necessary to cool the gas at the centre of the tube by radiation to the wall using septa.

REFERENCES

1. D. R. Jones, A. Maitland and C. E. Little, "A high-efficiency 200 W average power copper HyBrID laser," *IEEE J. Quantum Electron.* **QE-30**(10), 2385-2390 (1994).
2. M. J. Withford, D. J. W. Brown, R. J. Carman and J. A. Piper, "Kinetic enhancement in copper vapour lasers using halogen donor gas additives," *IQEC'96 Technical Digest* 238 (1996).
3. B. E. Warner, "Status of copper vapor laser technology at Lawrence Livermore National Laboratory," *CLEO'91 Technical Digest* 516-518 (1991)
4. N. Aoki, H. Kimura, C. Konagai, S. Shirayama, T. Miyazawa and T. Takahashi, "High-power copper vapor laser development," *SPIE 1412 Gas and Metal Vapor Lasers and Applications*, eds J J Kim and F K Tittel 2-11 (1991).
5. J. J. Chang, B. E. Warner, C. D. Boley and E. P. Dragon, "High-power copper vapour lasers and applications," in *Pulsed Metal Vapour Lasers - Physics and Emerging Applications in Industry, Medicine and Science*, ed. C E Little and N V Sabotinov (Kluwer Academic Publishers: Dordrecht) 101-112 (1996).
6. P. A. Bokhan and E. I. Molodykh, "Output limiting mechanisms and the prospects for metal vapour lasers with average output power above 1 kW/m," *op. cit.* 137-48 (1996).
7. A. A. Isaev, D. R. Jones, C. E. Little, G. G. Petrash, C. G. Whyte and K. I. Zemskov, "Characteristics of pulsed discharges in CuBr and HyBrID lasers," *Opt. Comm.* (submitted) (1996).
8. G. P. Hogan, C. E. Webb, C. G. Whyte and C. E. Little, "Experimental studies of CVL kinetics," in *Pulsed Metal Vapour Lasers - Physics and Emerging Applications in Industry, Medicine and Science*, ed. C. E. Little and N. V. Sabotinov (Kluwer Academic Publishers: Dordrecht) 67-72 (1996).
9. R. R. Lewis, "The operating regime of longitudinal discharge copper vapour lasers," *Opt. Quantum Electron.* **23** S493-512 (1991).
10. G. P. Hogan and C. E. Webb, "Pre-ionization and discharge breakdown in the copper vapour laser: the phantom current," *Opt. Comm.* **117** 570-9 (1995).
11. J. J. Chang, C. D. Boley, M. W. Martinez, W. A. Molander and B. E. Warner, "Beam characteristics of a large-bore copper laser with radiatively cooled plasma," *SPIE 2118 Gas, Metal Vapor and Free Electron Lasers and Applications*, eds V N Smiley and F K Tittel 2-8 (1994).
12. Y. Iseki, K. Hayashi, I. Watanabe, E. Noda and S. Suzuki, "Characteristics of a large-bore copper vapor laser with gas-cooling plates," *Jap. J. Appl. Phys.* **33** Part 2(6B) L860-2 (1994)
13. G. G. Petrash, "Diagnostics of CVL plasma," *SPIE 2619 Int. Conf. on Atomic and Molecular Pulsed Lasers, Tomsk, Russia, 27-30 March, 1995*, eds V F Tarasenko, G V Mayer and G G Petrash 68-75 (1995)
14. M. J. Kushner and B. E. Warner, "Large-bore copper-vapor lasers: kinetics and scaling issues," *J. Appl. Phys.* **54**(6) 2970-82 (1983).
15. W. A. Molander, "Measurement of ground state copper density using hook spectroscopy," *SPIE 1041 Metal Vapor, Deep Blue and Ultraviolet Lasers* 11-18 (1989).
16. N. V. Sabotinov, F. Akerboom, D. R. Jones, A. Maitland and C. E. Little, "A copper HyBrID laser with 2 W/cm³ specific average output power," *IEEE J. Quantum Electron.* **QE-31**(4) 747-53 (1995).
17. L. Little and C. E. Little, "Dynamics of the metal seeding process in copper hybrid lasers," *Proc. XI International Symposium on Gas Flow and Chemical lasers and High Power Laser Conference, Edinburgh, UK, 25-30 August 1996*, Paper PI-28 (1996).
18. D. R. Jones, A. Maitland and C. E. Little, "A copper HyBrID laser of 120 W average output power and 2.2% efficiency," *Opt. Quantum Electron.* **25** 261-9 (1993).
19. S. Gabay, P. Blau, M. Lando, I. Druckman, Z. Horvitz, Y. Yfrah, I. Hen, E. Miron and I. Smilanski, "Stabilization of high-power copper vapour laser," *Opt. Quantum Electron.* **23** S485-92 (1991).
20. E. G. Cook, D. G. Ball, D. L. Birs, J. D. Brantum, S. E. Peluso, M. D. Langford, R. D. Speer, J. R. Sullivan and P. G. Woods, "High average power magnetic modulator for copper lasers," *Proc. 8th IEEE Int. Pulsed Power Conf., San Diego, CA 17-19 Jun. 1991* (1991).

R.J. Carman, M. J. Withford, D.J.W. Brown and J.A. Piper.

Centre for Lasers and Applications, Macquarie University, Sydney, NSW 2109, Australia

Fax: 612-9850-8983, e-mail: ph_carman@hope.ocs.mq.edu.au

ABSTRACT

The results of a detailed study investigating the effects of HBr, Br donors and other halogens on the electrical and optical lasing characteristics in an elemental copper vapour laser is reported.

Keywords: copper vapour laser, buffer gas additives, HBr, hydrogen, halogens, plasma kinetics, dissociative attachment.

1. INTRODUCTION

Copper vapour lasers (CVLs) have developed into a mature, commercially viable technology with devices producing high powers (up to 100W) in the visible (511 and 578nm) at efficiencies of ~1%. Elemental CVLs rely on raising the temperature of the plasma tube to >1500°C which sets the copper densities ($\sim 10^{20} \text{ m}^{-3}$) necessary for lasing in these devices. In recent years, there has been a significant development in a variant of the copper halide laser, the copper hybrid laser (Cu:HyBrID), which can produce output powers up to 200W at wallplug efficiencies of 2%¹. These devices generate copper vapour in the laser medium at much reduced temperatures (typically ~500°C) by introducing HBr into the neon buffer gas, which primarily reacts with solid copper in the plasma tube to form CuBr which evaporates into the volume. Added HBr also has the subsidiary effect of modifying the plasma kinetics within the gain medium of these devices, resulting in significantly reduced prepulse electron densities² which in turn give rise to improved spatio-temporal gain characteristics. In particular, Cu:HyBrID lasers have a relatively long pulse duration (~80-100ns compared to <60ns for elemental CVLs) and a gaussian-like radial intensity profile which is well suited to the efficient extraction of high beam quality output when utilising high magnification unstable resonators. Naturally, it would be highly desirable if these characteristics could be reproduced in elemental CVLs.

To date, there has been no comprehensive study examining the effects of halogens and hydrogenated halides on the performance of conventional high-temperature CVLs. A study of this nature is of significant interest because the role of HBr additive on the kinetic processes within the gain region can be investigated independently from its role in copper vapour production as in the Cu:HyBrID laser. In this paper, the results of a preliminary study investigating the effects of HBr, Br donors and other halogens on the electrical V/I characteristics, the output power and spatio-temporal evolution of CVL output, are described.

2. EXPERIMENTAL DETAILS

A medium-sized CVL plasma tube (25mm bore x 1m length) was used in the present study with a standard thyatron-switched pulse charging circuit and storage/peaking capacitor values of 1.5/0.7nF. The pulse-repetition frequency (PRF) was set at 17kHz throughout (a typical value for a Cu:HyBrID laser) giving a input power of around 3.2kW. The CVL was operating with a flat/flat optical cavity comprising an AR coated high reflector (>99%) and 4% reflecting output coupler. The laser output power was measured using a calorimetric power meter (Scientech 360001), and laser pulse shapes were monitored using a fast vacuum photodiode (Hamamatsu 1193a) coupled to a storage oscilloscope (100MHz Tektronix TDS 320).

The various buffer gas mixtures used in this study were produced in a dedicated ultra-high vacuum gas handling system³ which included a mass quadrupole spectrometer (Inficon Quadrex 100). Unless otherwise stated, the buffer gas mixtures were introduced to the plasma tube at flow rates of ~3 atm.cc/min while maintaining a buffer gas pressure of 40 torr as measured at the input port (cathode end) of the plasma tube.

3. RESULTS

The variation of the total output power from the CVL for different concentrations of the various buffer gas additives (H_2 , HBr, Br_2) is shown in Fig. 1. For these operating conditions, the maximum power enhancement occurred when 2% H_2 was added to the buffer gas, increasing the output power by a factor of 2 compared with the case for pure neon. A smaller increase (25%) was obtained for a 1% admixture of HBr, a similar increase was observed when HCl was added to the buffer gas although larger partial pressures ($\sim 2\%$) were required. In contrast, the output power was observed to decrease linearly with increasing concentration of a Br_2 additive, or Cl_2 additive (not shown). The addition of either H_2 or HBr over the range of concentrations shown in Fig. 1 also resulted in small increases ($\sim 50^\circ C$) in the temperature of the plasma tube envelope.

The addition of Br_2 (up to 5%) produced no discernible effect on the observed excitation voltage and current pulses. At optimum concentrations of H_2 (2%), however, a significant increase in the peak voltage (by 30%) and decrease of the peak excitation current was observed as reported previously⁴. The same concentration of HBr (2%) perturbed the voltage/current (V/I) pulse shapes to an even greater degree with the peak voltage increasing by 50% and peak current down by 60% compared with a pure neon buffer gas. Similar changes to the V/I characteristics were observed when HCl was used as an additive, however, approximately twice the concentration ($\sim 4\%$) was required to obtain the same peak V/I values obtained for 2% HBr.

The temporal behaviour of the laser output pulses for pure neon gas, and for 2% H_2 , and 2% HBr admixtures is shown in Fig. 2 (For ease of comparison, the pulses shapes are referenced so that they share a common starting point in time). For the 2% H_2 admixture, the pulse rise-time and intensity of the first peak were very similar to that observed for pure neon. In the tail-end of the pulse, however, the intensity was greatly enhanced for the case of H_2 , thus increasing the full-width half-maximum duration of the output pulse. The addition of HBr (Fig. 2) and HCl (not shown) modified the temporal evolution of the output pulses in a different manner to H_2 . The peak intensity of the leading edge of the pulse was significantly reduced whereas the intensity of the trailing edge was much higher indicating that the peak gain had shifted to later times. Overall, the pulse duration increased dramatically from 35ns (pure neon) to 70ns (HBr). The absence of significant round-trip type modulations of the pulse intensity for the case of the HBr additive (compared with H_2) also suggests that formation of the intracavity laser radiation field by the amplification of a "seed" of spontaneous emission⁵ occurs over a much longer timescale in the case of added HBr. Finally, small concentrations of Br_2 additive reduced the peak power of all temporal components of the output pulse.

The far-field intensity profiles for the laser output are shown in Fig. 3. For a pure neon buffer gas, the intensity profile at 17kHz was highly annular, whereas it became peaked on-axis when a 2% H_2 admixture was used. The intensity profile also became peaked on axis when a 2% HBr admixture was used although it appeared to be slightly more constricted than for the 2% H_2 additive. The peaked far-field intensity profiles for the case of the HBr additive are thus very similar to those observed from a Cu:HyBrID laser¹.

The variation of laser output power with flow rate for a 1% HBr-Ne mixture is shown in Fig. 4. It was found that the output power increased dramatically as the flow rate was elevated, eventually peaking at $\sim 28W$ at a flow rate of 90 atm.cc/min. Some instability in the output power levels was observed at elevated flow rates, however, the general increase in output power by a factor of between $\times 2$ - $\times 2.5$ was reproducible. An increase of the laser output power to $\sim 20W$ was also obtained using a 2% HCl-Ne mixture using a moderately fast flow rate (60 atm.cc/min).

4. DISCUSSION

It has been shown previously⁴ that the influence of an H_2 additive on the excitation voltage and current pulses, and on the spatio-temporal evolution of the laser pulse, is consistent with a reduction of the pre-pulse electron density in the CVL. This behaviour has been attributed to an improved rate of Cu^+/e recombination due to enhanced electron cooling via elastic collisions with H and H_2 . HBr additives influence the V/I characteristics in a similar manner to H_2 additives implying these too reduce the pre-pulse electron density. However, a small concentration of HBr ($\sim 2\%$) modifies the V/I characteristics by a larger extent than an identical concentration of H_2 additive. These results cannot be wholly attributed to enhanced electron cooling by elastic collisions with the various halogen species, owing to the lower mass ratio of the collision partners compared to the case with hydrogen, nor to elastic interactions with the small concentrations of free H expected to be produced via HBr dissociation within the plasma region. Initial modelling calculations of the plasma kinetics of the CVL with halogen donor additives, based on earlier studies of laser kinetics⁶, suggest that there should be a significant reduction of the pre-pulse electron density due to the dissociative attachment (DA) process during the afterglow period:



The calculations suggest that the pre-pulse electron density will be reduced by more than an order of magnitude if the concentration of undissociated HBr molecules is around 1-2% of the buffer gas pressure for the duration of the afterglow period. Cross-sections for the DA process^{7,8} for a various halogen donor species and hydrogen are shown in Figs. 5 & 6. For HBr, reaction (1) is slightly endothermic ($*E_1 \sim 0.28\text{eV}$), but this energy deficit falls well within the range of typical electron energies in the afterglow period ($E_1 = 0.2\text{-}0.6\text{eV}$)⁶. Our observation that the effects of added HBr on CVL performance can be reproduced with larger concentrations of HCl additive is consistent with the DA process reducing the pre-pulse electron density. The peak DA cross-section for HCl is about an order of magnitude lower than for HBr (Fig.5), and the energy deficit is larger ($*E_1 \sim 0.81\text{eV}$) and less well matched to the electron energies in the plasma. Hence, larger concentrations of HCl are required to modify the V/I characteristics by a comparable amount to HBr. In addition, added Br₂ had little influence on laser performance, implying the DA process with molecular bromine is less important, consistent with a smaller cross-section for pure halogen molecules compared with hydrogen halides (eg. DA cross-sections for I₂ and HI in Fig 6.). It is also noteworthy that the dissociation energies of the pure halogens are significantly lower than those for the hydrogen halides (eg. $E_{\text{diss}} = 1.971\text{eV}$ for Br₂ compared with $E_{\text{diss}} = 3.75\text{eV}$ for HBr). Thus, the fractional dissociation of the pure halogen molecules due to electron and/or heavy body collisions is likely to be higher than for hydrogen halide molecules, thereby reducing the number of molecules available for dissociative attachment reactions.

Following the production of Br⁻ ions via reaction (1), modelling calculations suggest that there is a rapid quenching of the Br⁻ population via mutual neutralisation with positively charged copper ions:



This reaction has a rate coefficient⁹ ($\rho \sim 10^{-13} \text{ m}^3 \text{ s}^{-1}$) which is approximately three orders of magnitude larger than that for 3-body (electron-assisted) recombination which is the principal volumetric loss mechanism for copper ions in a conventional CVL⁶ with a buffer gas of pure neon. The rapid recombination of copper ions and recovery of the copper ground state population is an crucial factor in overcoming the radial cataphoresis effect⁶ to allow high repetition rate operation.

5. CONCLUSIONS

We have shown that HBr additives can significantly modify the spatio-temporal output characteristics of a conventional high-temperature CVL. In particular, we have observed significant increases in the output power ($\sim \times 2.5$), pulse duration ($\sim \times 2$) and efficiency ($\sim \times 1.5$) for high repetition rate operation (17kHz). Improvements in the pulse duration and in the spatial uniformity of the output pulse are particularly important for the efficient extraction of high beam quality output when utilising unstable resonators. The results show that the enhanced kinetic effects of HBr on CVL performance can be harnessed separate from the additional requirements for Cu vapour production required in the case for Cu:HyBrID lasers.

6. REFERENCES

1. D.R. Jones, A. Maitland and C.E. Little, "A high-efficiency 200W average power copper HyBrID laser", *IEEE J. Quant. Electron.*, **30**, 2385, (1994).
2. D.R. Jones, S.N. Halliwell and C.E. Little, "Influence of remanent electron density on the performance of copper HyBrID lasers", *Opt. Comm.*, **111**, 394, (1994).
3. M.J. Withford, D.J.W. Brown and J.A. Piper, "Investigation of the evolution of trace impurities from a newly constructed copper vapour laser", *J.Phys.D: Appl. Phys.*, **29**, 315, (1996).
4. M.J. Withford, D.J.W. Brown and J.A. Piper, "Investigation of the effects of hydrogen and deuterium on copper vapour laser performance", *Opt. Comm.*, **110**, 699, (1994).
5. R.J. Carman, "Modelling of the intracavity optical fields in a copper vapour laser", *Opt. Comm*, **119**, 415, (1995).
6. R.J. Carman, D.J.W. Brown and J.A. Piper, "A Self-consistent model for the discharge kinetics in a high-repetition rate copper-vapour laser", *IEEE J. Quant. Electron*, **30**, 1876, (1994).
7. D.C. Frost and C.A. McDowell, "Electron Capture processes in the hydrogen halides", *J.Chem.Phys.*, **29**, 503, (1958).
8. L.G.Christophorou and J.A.D.Stockdale, "Dissociative electron attachment to molecules", *J.Chem.Phys.*, **48**, 1956, (1968).
9. M.R. Flannery, "Electron-ion and ion-ion recombination processes", in *Advances in Atomic, Molecular and Optical Physics*, **32**, 117, (1994).

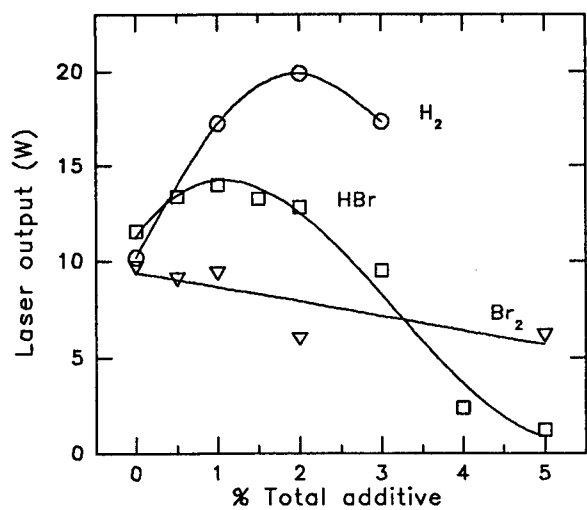


Fig.1. Laser power vs additive concentration

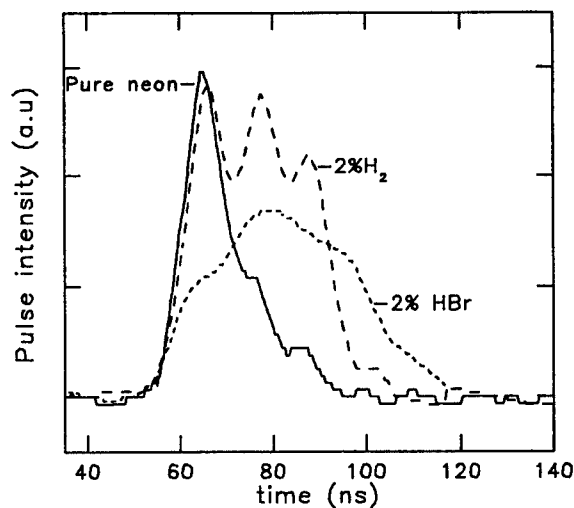


Fig.2. Laser pulse shapes for different admixtures

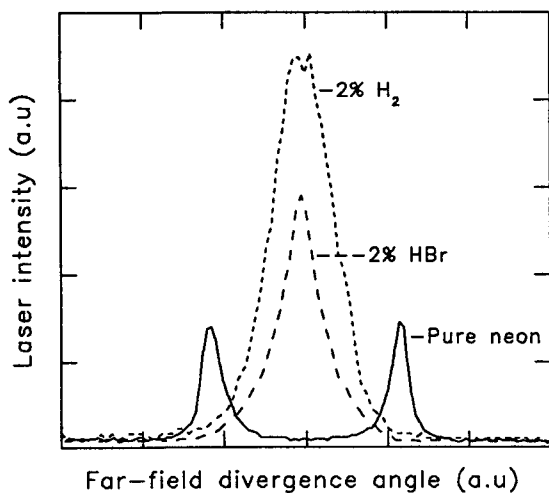


Fig.3. Far-field spatial beam profiles

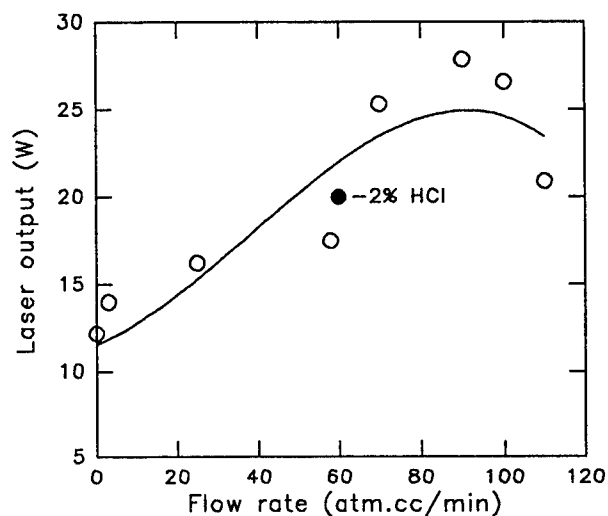


Fig.4. Laser power vs flow rate for 1% HBr

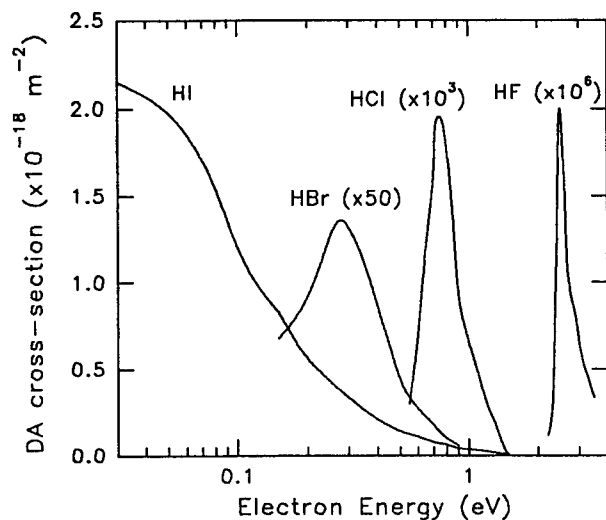


Fig.5. DA cross-sections for the hydrogen halides

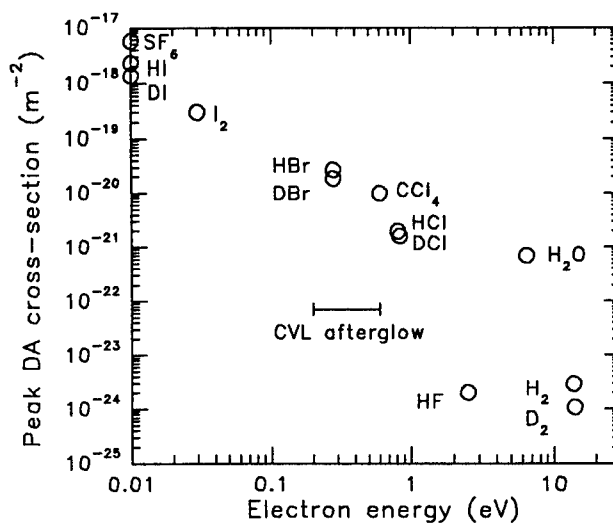


Fig.6. Peak DA cross-sections for different molecules

A CuBr vapor laser with a central electrode

Nikolay K. Vuchkov, Nikola V. Sabotinov, Krassimir A. Temelkov

Department of Metal Vapor Lasers, Institute of Solid State Physics, Bulgarian Academy of Sciences,
Tzarigradsko Chaussee 72, Sofia 1784, BULGARIA

ABSTRACT

A CuBr laser with a central electrode is reported. Up to the 2 kW input power the laser produce maximum output power of 47 W (at efficiency 2.35 %) and maximum efficiency 2.5 % (at 42 W output power). Some features of the excitation circuit and laser operation are given.

Keywords: metal vapor lasers, copper and copper halides lasers, excitation circuits.

1. INTRODUCTION

The specific average output power of the CuBr vapor laser increases with the decrease of the laser active volume. A CuBr laser¹ with an active volume of 4.77 cm³ produced a specific output power of 1.4 W/cm³. A 2 W/cm³ specific power from a copper HYBrID laser (the laser tube has the same dimensions and active volume) is reported². On the other hand, with the increase of the active volume of the laser tubes (more than 1000 cm³), although the specific power decreases, the average output power and laser efficiency increases very strongly - up to 200 W and 3 % respectively^{3,4}. Moreover, for each active volume above a certain input power in the discharge, a decrease in laser efficiency is observed.

It is supposed that increasing of the discharge tube dimensions causes a decrease in the ratio E/p , i.e. in electron temperature, and in discharge current density as well. Besides, the discharge circuitry inductance, involving the laser tube, increases too. So, the increasing of the discharge tube dimensions leads to an increase of the output power and efficiency, but this requires a higher input power in the discharge and, hence, a higher voltage between the tube electrodes. This is associated with certain difficulties.

One way to avoid these problems is to create a two-arms laser with a central electrode (CE).

In this work we report investigation of a CuBr vapor laser with a CE. The special features of the excitation circuit and operation condition of the laser are described.

2. EXPERIMENTAL APPARATUS AND RESULTS

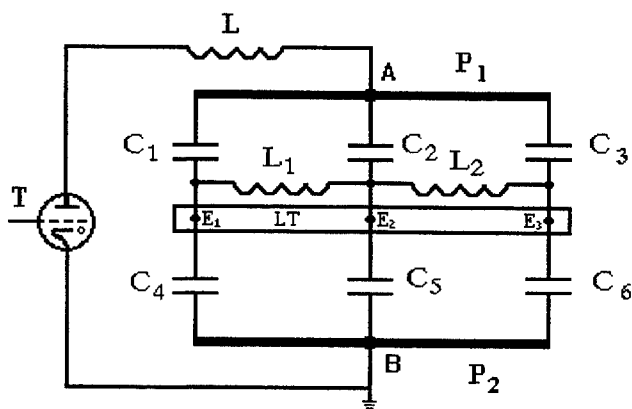


Fig. 1. Schematic diagram of the electrical circuit use the CuBr laser with CE excitation.

The discharge tube is made of 40 mm inside diameter fused silica. The distance between the two end electrodes is 114 cm, so the active length of each of the arms is 55.5 cm (the total active volume is about 1400 cm³). The CuBr powder is placed in six side reservoirs, which are heated externally. The buffer gas is a mixture of 16 torr Ne and 0.45 torr H₂. The laser cavity consists of two flat mirrors: a 99.8 % reflectivity mirror and a plane-parallel quartz output coupler.

The CuBr vapor laser with CE is IC-excited (the interacting circuits IC excitation of the CuBr laser is described in details in previous papers^{5,6}). The electrical scheme for the IC - laser excitation is shown in Fig. 1. The switch T is a thyatron TGI 1000/25. The value of the matching inductor L is determined experimentally. Two inductors L₁ and L₂ are used to level the voltage between

the three electrodes E_1 , E_2 and E_3 during the period of charging of the capacitance bank formed by six capacitors C_1+C_6 . Two metal plate P_1 and P_2 are located close to the laser tube LT.

Initially, some experiments to determine the best excitation circuit configuration were carried out. Varying the design of the plates P_1 and P_2 and the capacitors C_2 and C_5 different excitation circuits were experimented:

1. The plates P_1 and P_2 are each in one piece and are common for both laser tube arms. The capacitors C_2 and C_5 are connected to the middle of the plates P_1 and P_2 (Fig. 1).
2. The plate P_1 is divided into two equal parts, one for each laser arm. The capacitor C_2 is replaced by two equal capacitors to form two independent circuits with the common capacitor C_5 . The plate P_2 remains in one piece.
3. The plate P_1 is in one piece, while P_2 is divided into two. The capacitor C_5 is replaced by two capacitors forming two independent circuits with the common capacitor C_2 .
4. An excitation circuit with four metal plates and eight capacitors is also tested.

The best results with respect to output power, efficiency and stability of laser operation - simultaneous charging the discharge in the two arms and identical current pulses (amplitude and time behaviour) are obtained with the first excitation circuit, shown in Fig. 2 All further experiments are made using this excitation circuit.

The capacitors C_2 and C_5 which are common for the two arms of the laser tube are connected to the central electrode E_2 . The potential of E_2 electrode is lower than that of the other two electrodes E_1 and E_3 . It is well known that for this type of lasers the electrode which has a higher potential in operation condition is much warmer than the other electrode. In our case the current through the central electrode E_2 is twice the current through the other two electrodes E_1 and E_3 , so the temperature of the three electrodes is almost levelled.

Table: $C_1...C_6$ -nominal-value capacitances; C_0 -hot-value bank capacitances; P^{\max} -maximal output power; η^{\max} -maximal efficiency; $P_{H2}=0.44$; Torr ; $P_{Ne}=16$ Torr; $f=21.7$ kHz;

capacitor banks	C_1 , pF	C_2 , pF	C_3 , pF	C_4 , pF	C_5 , pF	C_6 ,pF	C_0 , pF	P^{\max} , W	η^{\max} , %
CB1	770	235	770	70	3300	70	1130	36.2	2.30
CB2	770	235	777	70	2670	70	1030	40.5	2.34
CB3	940	235	940	90	2200	90	1030	42.8	2.52
CB4	1100	235	1100	90	1650	90	1000	42.3	2.47
CB5	1100	235	1100	90	2200	90	1110	42.3	2.46

From the high number of variations for capacitors C_1+C_6 , five capacitors banks (CB), giving the best output laser characteristics, are chosen and they are investigated at different operation conditions. The following parameters for the five CB are given in the Table: C_1+C_6 - nominal-value capacitances; C_0 - hot value bank capacitance measured in the points A and B (Fig.1) at 1.7 kW input power in the discharge; P^{\max} - maximal output power and η^{\max} - maximal efficiency obtained with the corresponding CB. Two peaks are observed in the discharge current pulses form, the first being the excitation pulse. It is found that the ratio between the amplitudes of the first and the second peak is changed when changing the capacitors C_1 , C_3 and C_5 . For the five CB this ratio is changed from 5:3 for CB1 to 5:1 for CB5.

The dependence of the output power and efficiency from the pulse recurrence frequency is similar for all CB and different input power. Two peaks in the output power are observed - the first around 16.5 kHz and the second, which is much higher, at 21.7 kHz. The observed minimum at 18 kHz is due to discharge striation and instability.

The dependence of laser output power and efficiency on input power in the discharge (determined from the charging voltage of the CB) for the CB3 at 21.7 kHz is shown in Fig. 2. Unfortunately, the employed power supply limited the input power in the discharge maximum up to 2 kW. For that reason the investigations are made for input power up to 1.8 kW. The thermal insulation of the discharge tube is changed depending on the input power to maintain an equal temperature of the discharge tube wall. The capacitance value C_0 of the CB is measured for each input power and the input power is determinate from C_0 and the corresponding charging voltage. The dependence of the output power has not reached a plateau with increasing of the input power which indicated that high output power is possible to obtain at higher input

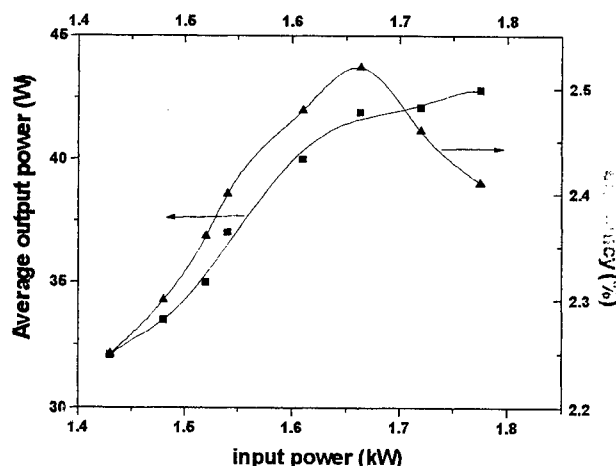


Fig.2. Laser output power and efficiency as a function of pulse recurrence frequency for CB3.

efficiency, can be noted.

1. Low inductance of the discharge circuit.

In the used excitation circuit (Fig.1) the inductance of each discharge circuit is smaller than the inductance involving the whole length of the laser tube (a discharge tube with the same active length but with two electrodes). Moreover, the discharge circuits are designed in such way, that the discharge current in the two arms flows in opposite directions and, hence, there is a positive effect on the circuit reactive resistance due to the mutual inductance. All this leads to an increase of the current rise rate. The measured duration of the current pulses rise-time at the electrodes E_1 , E_2 and E_3 is 40 ns.

2. High voltage between the electrodes in the two arms.

In the CuBr lasers with two electrodes even when IC-excitation is used, the voltage pulse amplitude between the two electrodes unsurpasses the voltage to which the storage capacitor or the CB are charged. At the CuBr lasers with CE for some combinations of capacitors forming the CB, the sum of the voltage pulse amplitudes between the electrodes in the two arms is higher than the CB charging voltage.

3. Low value of the CB of the excitation circuits in the two arms.

It is well known that with CuBr and HyBrID³ lasers there is a clear trend towards higher operating efficiencies at lower capacitance of the storage capacitor or the CB. This requires a higher voltage between the electrodes (or a high value capacitors has to be used, which leads to a decrease of the laser efficiency). At the laser with CE the circuits forming the excitation circuits of the two arms are connected in parallel (C_2 and C_5 are common) in the interpulse period (the process of the charging). This allows to use a comparatively low values of the CB for each separate arm but the common capacitance is higher, which allows a higher input power in the discharge at the optimal value of the CB.

4. High pulse recurrence frequency.

The dependence of the laser output power on the pulse recurrence frequency of the laser with CE is similar to this for a 50 cm long laser tube⁵ but the second peak is much higher. This allows, in spite of the bigger active volume to operated at high frequency which leads to a higher power input into the discharge at lower charging voltage.

5. Requirement to maintain an equal vapor density in the two laser arms.

It is very important to maintain an equal vapor density in the two laser arms. Eventual change in the metal vapor concentration in one of the arms causes discharge instability and vanishing of the oscillation in this arm.

In conclusion, a sealed-off CuBr laser with a CE is described. With this laser a maximal efficiency of 2.5% at output power of 42 W and maximal output power of 47 W at efficiency of 2.35% are obtained. The results show that there seems to be no fundamental limitation to obtain a high output power from a CuBr laser with a CE increasing both the input power and the laser tube dimensions.

Maximum efficiency of 2.5% at output power 42 W is obtained. At input power 2 kW (for a short time - a few minutes) an average output power of 47 W at efficiency of 2.35% is obtained with CB3.

3. DISCUSSION

We have demonstrated that the sealed-off CuBr laser can be operated with two arms and a CE, to yield an average output power exceeding 40 W at an efficiency of 2.5%. The obtained results show that in the investigated range of input power - up to 1.8 kW, the output power and efficiency of the CuBr laser with CE are comparable to these obtained with a copper HyBrID laser³, although the investigated laser tube has a smaller active volume.

Some peculiar features in the CuBr laser with CE which help to obtain a higher output power and

4.ACKNOWLEDGMENTS

The investigations were performed under the project CITA-CT94-0214, "New Generation Lasers for High-Precision Materials Processing" of Copernicus Programme funded by European Community.

5.REFERENCES

1. D.N. Astadjov, K.D.Dimitrov, C.E.Littel, N.V.Sabotinov, N.K.Vuchkov, "A CuBr laser with 1.4 W/cm^3 average output power", IEEE J.Quant.Electr. **30**, 1358-1360 (1994).
2. Sabotinov N.V., Kerboom A.F., Jones D.R., Maitland A., Little C.E., "A copper HyBrID laser with 2 W/cm^3 specific average output power", IEEE J.Quant.Electr. **31** 747-753 (1995).
3. Jones D.R., Sabotinov N.V., Maitland A., Little C.E., "A high-power high-efficiency Cu-Ne-HBr (1510.6, 578,2 nm) laser", Optics Commun. **94**, 289-299 (1992).
4. Jones D.R., Maitland A., Little C.E., "A high-efficiency 200 W average power copper HyBrID laser", IEEE J.Quant.Electr. **30**, 2385-2390 (1994).
5. Vuchkov N.K., Astadjov D.N., Sabotinov N.V., "A new circuit for CuBr laser excitation", Optical and Quantum Electronics **23**, S549-S553 (1991).
6. Vuchkov N.V. Astadjov D.N. Sabotinov N.V., "Influence of the excitation circuits on the CuBr laser performance", IEEE J.Quant.Electr. **30**, 750-758 (1994).

Experimental and theoretical investigation of a coaxial pumped photolytic atomic bromine laser

B. D. Rafferty, B. T. Anderson, J. Glassman, H. C. Miller, A. I. Lampson, and G. D. Hager

USAF Phillips Laboratory, LIDB
3550 Aberdeen Ave. SE
Kirtland AFB, NM
87117-5776, USA

ABSTRACT

Results of parametric studies on a high efficiency, 2.7 μm atomic bromine laser, produced by photolyzing IBr with 532 nm radiation, are presented. Concurrently, the results of a rate equation computer model show excellent agreement with experimental measurements.

1. INTRODUCTION

Iodine monobromide (IBr) exhibits strong, continuous absorption throughout the 450 nm to 550 nm range,¹ which makes pumping with a frequency doubled Nd:YAG laser (532 nm) ideal. Absorption of pump photons results primarily in excitation into the $B^3\Pi_0^+$ electronic state, which preferentially dissociates (quantum yield Φ of 68%)² to form $I + Br(^2P_{1/2})$. The dominance of the diabatic dissociation channel immediately results in a population inversion between the $Br(^2P_{1/2})$ state and the $Br(^2P_{3/2})$ ground state. Lasing may therefore be achieved at 2.714 μm via the magnetic dipole transition between the states. Examination of the hyperfine levels of the two states reveals six allowed transitions, of which the $2 \rightarrow 3$ transition is the observed lasing transition.

2. EXPERIMENTAL

Two separate types of experiments were performed: small signal gain and lineshape experiments, and laser power extraction experiments. The first type were performed to directly measure the atomic bromine gain and hyperfine transition lineshape as a function of time. This was accomplished by measuring the gain with a tunable F-center laser. The F-center laser produces 2.7 μm laser radiation tunable over a 100 GHz range; therefore, it may be tuned through, or locked onto, any of the $Br(^2P_{1/2}) \rightarrow ^2P_{3/2}$ hyperfine resonances. As shown in Figure 1. The F-center beam is combined with the 532 nm output from a frequency doubled Nd:YAG laser by means of a Pellin-Broca prism. The combined beams pass through the IBr cell and then are separated. The 2.7 μm beam passes through a filter and onto an indium arsenide (InAs) detector. The small signal gain of the 2.7 μm light was measured directly by monitoring the gain intensity while the F-center laser was locked to the $2 \rightarrow 3$ hyperfine transition frequency. This was done for a number of 532 nm pump energies varying from 5 mJ to 155 mJ.

In order to determine whether the $Br\ 2 \rightarrow 3$ hyperfine transition lineshape was varying with time, the following approach was employed. First, a time slice at a certain delay in the small signal gain profile was selected with a gated integrator. Then the F-center laser was tuned through the $2 \rightarrow 3$ hyperfine transition frequency. The FWHM of the integrated signal is therefore the transition linewidth for the selected delay in time. By repeating this at different time delays, the transition lineshape is mapped out as a function of time. In the same manner, the iodine atom absorption lineshape could be measured by monitoring the absorption of a tunable 1.3 μm diode laser sweeping through the $3 \rightarrow 4$ hyperfine transition of the atomic iodine $^2P_{1/2} \leftarrow ^2P_{3/2}$ transition.

The laser power extraction experiment is shown schematically in Figure 2. The 532 nm light passes through a lens which ensures the 532 nm beam is expanding when it reaches the IBr cell. The 532 nm light is coupled onto the cell axis by a hole-coupler, which is a 45° mirror through which a small hole has been drilled. The hole is orientated at 45° to the mirror surface and aligned along the cell axis. The Nd:YAG laser used in this experiment produces an annular mode, and the hole in the mirror is slightly smaller than the 532 nm beam inner diameter. The 532 nm beam is centered around the hole, allowing the pump energy to be coupled onto the cell axis with

minimal loss. A 2.7 μm hemispherical laser cavity is arranged around the cell and along its axis. The 2.7 μm laser mode passes unmolested through the hole-coupler. This geometry allows for the pumped volume to be completely enclosed within the cone of the 2.7 μm laser mode. Having the 532 nm beam expanding through the cell results in a higher degree of overlap between the two volumes. Zinc selenide flats of differing transmissions are used as the output couplers. The 2.7 μm laser light is detected and analyzed by an energy meter and a fast gold doped germanium detector (Ge: Au).

3. Rate Equation Model

The gain α of this laser system is modeled by the following equation

$$\alpha = \sigma_{2-3} \left(\frac{5}{8} [\text{Br}^*] - \frac{7}{16} \cdot \frac{5}{7} [\text{Br}] \right) \quad (1)$$

where the cross-section σ_{2-3} is defined as

$$\sigma_{2-3} = \lambda^2 A_{2-3} f(\nu) (8\pi)^{-1} \quad (2)$$

λ is the lasing wavelength, A_{2-3} is the probability of spontaneous emission (Einstein A coefficient), and $f(\nu)$ is the lineshape function. $[\text{Br}^*]$ and $[\text{Br}]$ are the total populations in the $^2\text{P}_{1/2}$ and $^2\text{P}_{3/2}$ states, respectively. Fast relaxation between the hyperfine levels is assumed, causing the population to be distributed statistically among the hyperfine levels, hence the 5/8 and 7/16 statistical weighting coefficients. The 5/7 coefficient is the degeneracy ratio between the lasing levels.

A value of 0.629 sec^{-1} is used for A_{2-3} which is deconvoluted from the total lifetime $(1.1 \text{ sec})^3$ for the transition. This value is also consistent with experimental measurements of the cross-section of $1.0 \pm 0.2 \times 10^{-17} \text{ cm}^2$ for a single isotope.⁴

Bromine consists of two isotopes in nearly equal abundance; the isotopic splitting for the 2 - 3 hyperfine transition is 156 MHz,⁵ nearly equal to the Doppler width of each line at 300° K. It is assumed, however, the laser operates on a single frequency, with an expanded lineshape. Therefore, a normalized two-Gaussian lineshape function is used

$$f(\nu) = \frac{\sqrt{\ln 2}}{\Delta \nu_D} \left\{ \exp \left[\frac{-4 \ln 2 (\nu - \nu_o)^2}{\Delta \nu_D^2} \right] + \exp \left[\frac{-4 \ln 2 (\nu - \nu_o + \nu_s)^2}{\Delta \nu_D^2} \right] \right\} \quad (3)$$

where $\Delta \nu_D$ is the Doppler width, and ν_s is the isotope splitting. The value of the lineshape function is evaluated at its peak value, and this is used in the gain calculation. Interestingly, above 400° K, the temperature dependence of this equation is nearly constant.

The gain equation is coupled to kinetic equations, based upon the rate constants for the seventeen chemical reactions^{6,7} between the gaseous species following photolysis. However, on the time scale of the laser pulse (within several hundred nanoseconds of photolysis), few reactions have fast enough rate constants or high enough reactant concentrations to effect the lasing system. The three exceptions are deactivation of excited bromine atoms by IBr and by iodine atoms, and removal of ground state bromine atoms by IBr. Differential equations for the time dependence of the chemical species during the photolysis and lasing processes are derived, and these equations constitute the rate equation model.

4. RESULTS AND DISCUSSION

Shown in Figure 3 are the results of the line-center small signal gain measurements plotted as a function of the absorbed pump energy. Values of the small signal gain were recorded 100 ns after the excitation pulse, after thermal relaxation has occurred. If no kinetics occur, the gain should be a linear function of the absorbed pump energy. Also shown are lines for the associated error bands for the cross-section and quantum yield. The three inner lines are associated with the $\pm 5\%$ reported error bands for Φ ;² the outermost two lines are the boundaries due to the $\pm 20\%$ error band reported for the cross-section.⁴ The curvature of the measured gain data is due to the combined kinetic effects of the three reactions discussed earlier during the 100 nanoseconds between the excitation pulse and the gain measurement. At low pump energies, removal of ground state bromine atoms by IBr dominates due to the low dissociation and high concentration of IBr. This reaction increases the observed gain by removing the lower lasing level. As the pump energy increases, IBr becomes more fully dissociated, creating higher concentration of I atoms. In this regime, deactivation of excited Br by iodine atoms becomes dominant, decreasing the observed gain.

Figure 4 shows the experimentally measured lineshapes for the 2-3 hyperfine transition in bromine (which shows gain), and the 3-4 hyperfine transition in iodine (which shows adsorption). The lineshape profiles were taken at different time delays with respect to the excitation pulse. Both the bromine and iodine lineshapes reach a temporal quasi steady state between 50 ns and 100 ns after the excitation pulse. This is interpreted as being due to the rapid thermalization of the excess kinetic energies carried by the photolysis photofragments. While it is not possible to extract a temperature from the lineshapes (due to the strong temperature variation along the cell axis), the linewidths are much broader than 300° K Doppler widths.

Shown in Figure 5 is a comparison of the rate equation model with the experimental energy extraction data. The two curves correspond to the model having values of the quantum yield of 0.68 and 0.58. Of the various adjustable parameters in the rate equation model, changes in the quantum yield exhibit the greatest effect on the results. Adjusting the value of the quantum yield allowed for a quantitative match to the experimental power extraction data while still preserving the qualitative features of the curves. As can be seen, the best fit to the experimental data is achieved by reducing Φ from its measured value of 0.68 to 0.58. Without the reduction in Φ , the experimental data is approximately 70% of the model results. The observed dip in the curves is a result of the kinetic effect of the ground state Br atom removal.

Figure 6 is the comparison of the experimentally measured mode build up times with the rate equation model results. In this case the agreement between theory and experiment gets worse as the quantum yield is reduced. However, for short mode build up times where the chemical kinetic processes are expected to have the smallest effect, reasonable agreement is still shown for Φ of 0.58. It is important to note the rate equation model has no axial dependence; absorption of pump energy and emission of laser light is assumed to be constant throughout the IBr cell. Since the temporal behavior of the output pulse is dependent upon the local emission along the cell axis, it is more sensitive to the constant absorption assumption than the output energy. Therefore to improve the agreement between the rate equation model and the experimental mode build up times would require adding an axial dependence to the rate equation model.

5. CONCLUSION

Direct gain experimental results are well within the error limits for the accepted values of the cross-section and quantum yield. Deviations from linearity of the results are understood by examination of the relevant chemical kinetic effects. The Br atom lineshape relaxes to a quasi steady state on a fast time scale, and remains essentially constant through the lasing lifetime. A rate equation model was developed which explains the experimental laser power extraction and mode build up time results. Given the caveats of this model, excellent agreement between theoretical and experimental results exists. While better agreement to the power extraction data is made with an adjustment to the quantum yield, 70% of the theoretical energy is extracted. Improvements to the mode build up time results would require implementation of an axial dependence in the rate equation model.

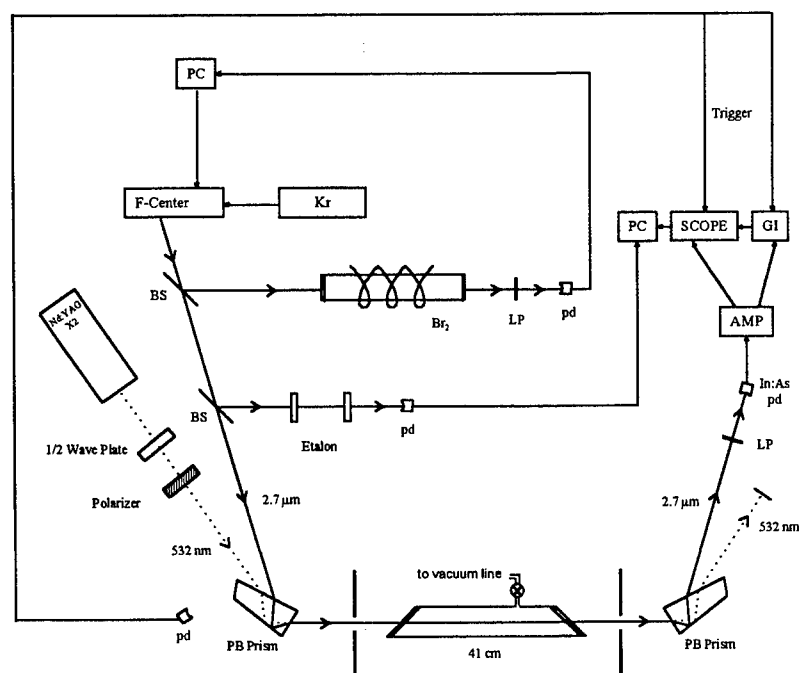


Figure 1. Experimental arrangement for small signal gain and atomic lineshape measurements.

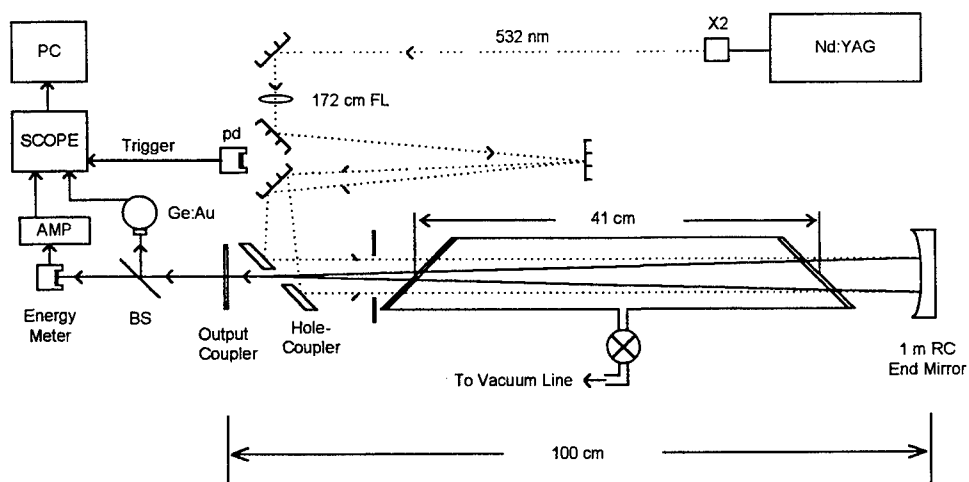


Figure 2. Experimental arrangement of the 2.7 μm atomic bromine laser. In actual experimental geometry, the 532 nm beam (dashed line) is entirely enclosed within the 2.7 μm laser mode volume (solid line) along the entire gain length of the cell.

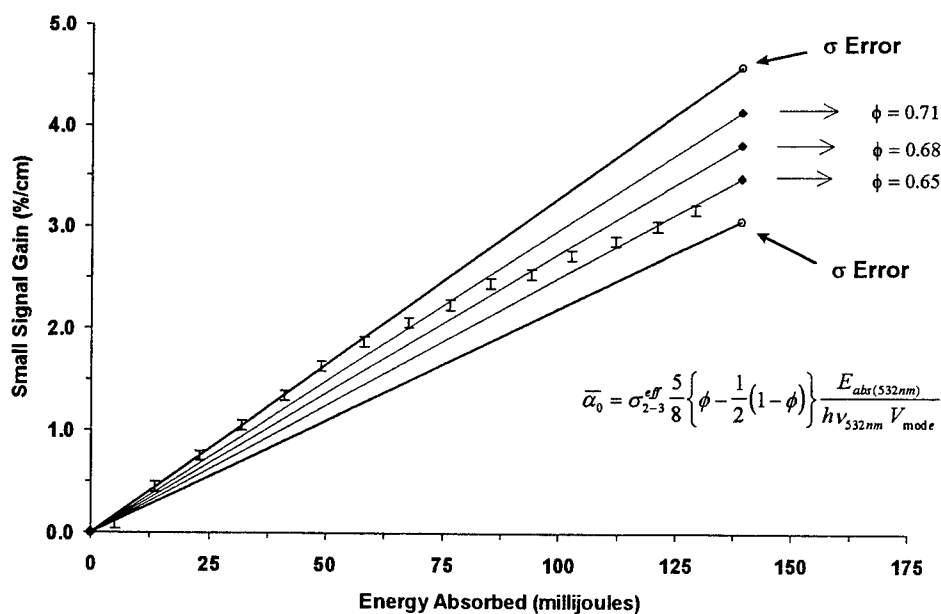


Figure 3. Experimentally measured small signal gain as a function of absorbed pump energy. Data points indicate error bands on their measurements. Solid lines indicate range of values for the reported errors in the quantum yield² ϕ and cross-section⁴ σ .

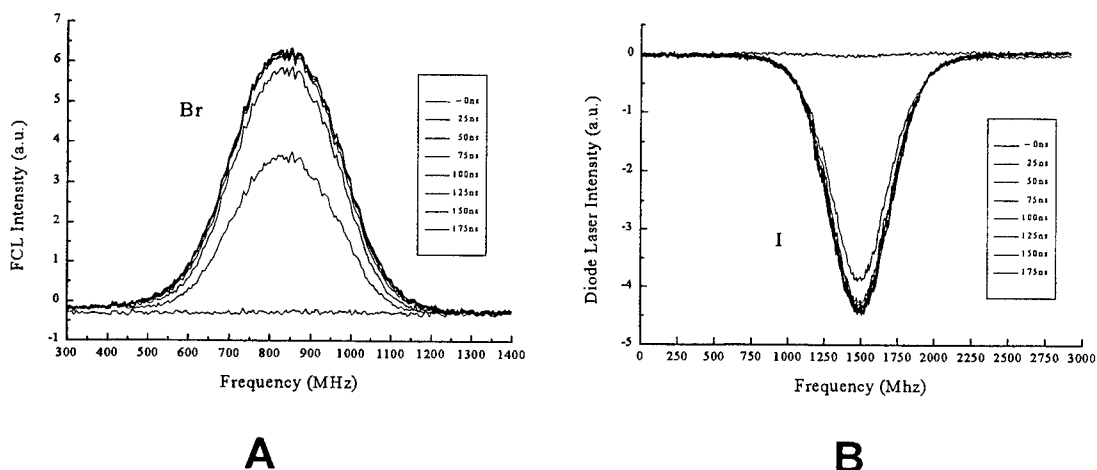


Figure 4. Experimentally measured atomic lineshapes showing time evolution of their relaxation to equilibrium.

- A. Bromine $2 \rightarrow 3$ hyperfine transition of the $^2P_{1/2} \rightarrow ^2P_{3/2}$
 B. Iodine $3 \leftarrow 4$ hyperfine transition of the $^2P_{1/2} \rightarrow ^2P_{3/2}$

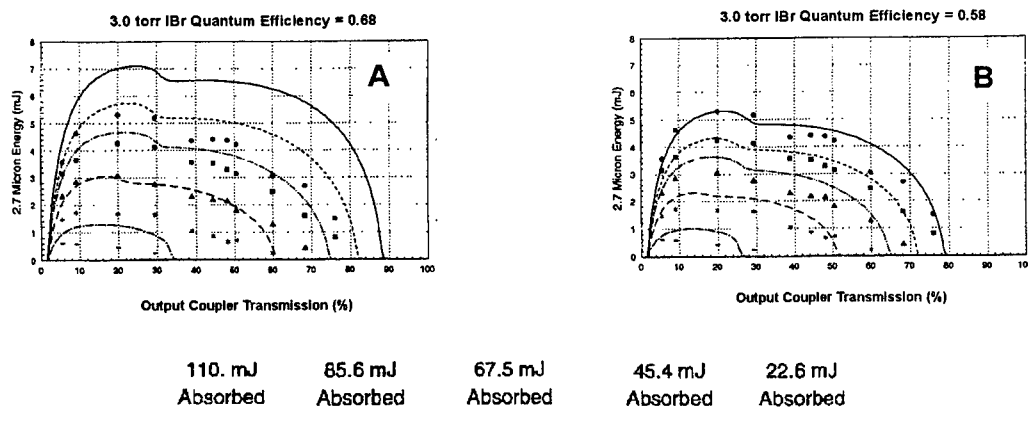


Figure 5. 2.7 μ m bromine laser output energy vs. output coupler transmission; comparison of rate equation model results to experimentally measured values. Quantum yield equal to (A). 0.68 (B). 0.58.

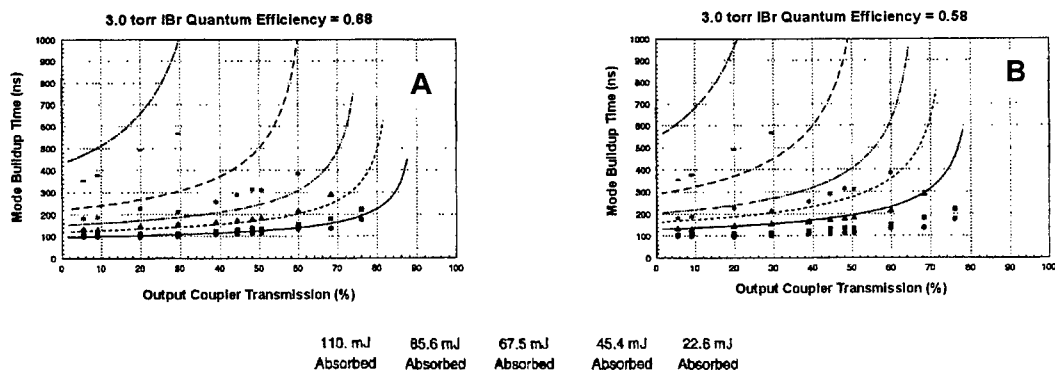


Figure 6. 2.7 μ m bromine laser mode build up time vs. output coupler transmission; comparison of rate equation model results to experimentally measured values. Quantum yield equal to (A). 0.68 (B). 0.58.

5. REFERENCES

- ¹ D. J. Seery and D. Britton, J. Phys. Chem. **68**, 2263 (1964).
- ² H. K. Haugen, E. Weitz, and S. R. Leone, J. Chem. Phys. **83**, 3402 (1985).
- ³ I. A. Boriev, E. B. Gordon, A. I. Nadkhin, and S. A. Sotnichenko, Opt. Spectrosc. (USSR) **54**, 233 (1983).
- ⁴ A. A. Efimenko, I. A. Boriev, and E. B. Gordon, Sov. J. Quantum Electron. **15**, 1127 (1985).
- ⁵ D. D. Nelson, A. Schiffman, K. R. Lykke, and D. J. Nesbit, Chem. Phys. Letters **153**, 105 (1988).
- ⁶ W. L. Harries and W. E. Meador, Space Solar Power Rev. **4**, 189 (1983).
- ⁷ R. L. Pastel, J. K. McIver, H. C. Miller, and G. D. Hager, J. Chem. Phys. **100**, 3624 (1994).

A high pulse repetition rate helium-xenon laser

D A Orchard and R C Hollins

Defence Research Agency, St Andrews Road,
Great Malvern, Worcestershire WR14 3PS, UNITED KINGDOM

ABSTRACT

A high pulse repetition rate helium-xenon laser is described. The laser produces output at four principal wavelengths and can be tuned to several others. The primary laser excitation mechanism is identified as recombination pumping in the afterglow. The importance of rapid quenching of the discharge current is demonstrated and an excitation circuit to achieve this is described.

Keywords: xenon laser, pulsed laser, infrared laser, recombination

1. INTRODUCTION

Atomic xenon is an attractive candidate for a mid-infrared laser source due to its large number of lasing transitions and its inert chemistry. In addition, several of the strongest laser wavelengths such as $2.03\mu\text{m}$ and $3.51\mu\text{m}$ are well matched to atmospheric transmission windows. CW xenon lasers driven by a longitudinal dc discharge are generally quite bulky and inefficient. However, other excitation schemes can be fairly compact with efficiencies of up to several per cent.

There has been an ongoing programme of xenon laser research at DRA for several years and a variety of different types of laser has been built and investigated. These range from large, pulsed, e-beam systems to compact, rf-excited cw waveguide xenon lasers. This paper describes a longitudinal discharge-excited pulsed xenon laser capable of operation at pulse repetition frequencies (prf) ranging from a few hundred hertz to tens of kilohertz.

2. LASER CONSTRUCTION

Single-shot xenon lasers are frequently of the TEA laser type similar to excimer lasers. Pulse energies of a few tens of millijoules are easily obtainable from such a device. However, in order to operate at high prf's a flow loop is required to clear the gas in the discharge between pulses. Otherwise, the residual non-uniformities in the gas from a discharge pulse can result in the formation of arcs in subsequent pulses. This is detrimental to the laser performance. Ever increasing gas flow speeds are required as the prf increases and thus the maximum prf from a TEA laser is limited to typically a few hundred hertz.

An alternative approach developed at DRA is to employ a longitudinal discharge. Since the cross-section of the discharge is small, non-uniformities can be more easily tolerated and the relaxation time of the gas improves. This enables prf's of tens of kilohertz to be achieved with little or no gas flow.

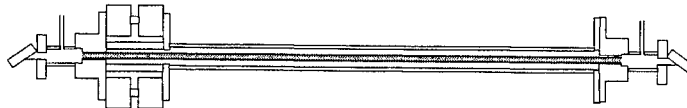


Fig. 1.

A section of the laser is shown in figure 1. The laser discharge tube is a narrow-bore (6mm i.d.) fused silica tube with a 700mm discharge length. The tube is surrounded by a tubular metal earth return with a short insulating section near the cathode. Water flowed through the volume between the jacket and the tube acts as both a coolant and a dielectric medium. A pair of discharge capacitors is mounted on the insulated section in a low inductance geometry to maximise the speed of the

discharge circuit. The laser medium is a mixture of helium and xenon at a pressure of a few hundred torr. The typical gas mixture has a He:Xe ratio of 250:1. A slow flow of gas was maintained through the laser to sweep out any impurities.

The excitation circuit of the laser is shown in figure 2. In operation, the discharge capacitors are resonantly charged through an inductor and diode to twice the power supply voltage. A thyatron switch connected through a saturable inductor across one of the capacitors is then fired. This inverts the voltage across that capacitor and hence delivers a voltage of up to four times the power supply voltage across the discharge. Gas breakdown normally occurs before this voltage is reached and the capacitors discharge through the laser. The prf of the laser is limited only by the resonant frequency of the charging circuit to around 25kHz.

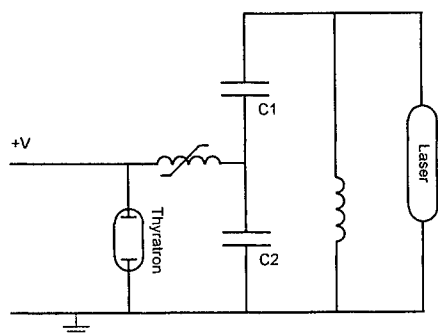


Fig. 2. Basic excitation circuit

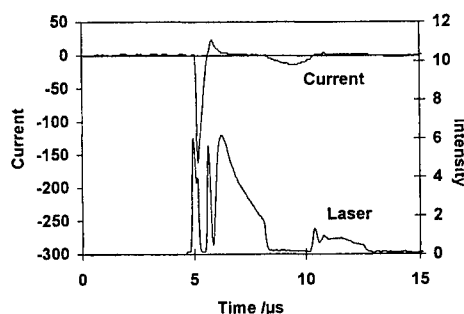


Fig. 3. Time-resolved laser pulse

The time resolved output from the laser is shown in figure 3. A somewhat surprising feature is the appearance of laser output slightly before the start of the anode current. This effect arises from the initial breakdown of the laser gas. At the start of the pulse, the electric field is concentrated along a short section of the discharge near the cathode due to the shielding effect of the coaxial earth return. When this section breaks down the gas conducts and the field penetrates into the shielded region. A 'breakdown wave' then propagates along the tube. Since the current probe is situated near the anode, no current is registered until the entire discharge length has broken down. The laser output during this time arises from the displacement current as energy is transferred to the capacitor formed between the discharge and the earth return. The presence of the water substantially increases the capacitance of this section and can give rise to propagation delays of up to several microseconds when the applied voltage is close to the breakdown voltage of the tube. Another benefit from the arrangement is that, since the breakdown of the gas occurs sequentially, the voltage applied to the tube need only be sufficient to maintain the existing discharge plus that required to break down a short additional length of plasma. Thus, the length of the tube can be scaled without significantly increasing the applied voltage.

The other major feature of the laser pulse is the strong output during the afterglow. This is indicative of recombination pumping of the laser levels. It is apparent that the presence of any residual discharge current during this time is highly detrimental to laser performance. This could be due either to direct electron excitation of the lower laser level or to an increase in the electron temperature which would reduce the recombination rate. Even very small residual currents can quench the laser completely.

3. IMPROVED EXCITATION CIRCUIT

In view of the quenching of the laser output by residual oscillations in the discharge circuitry, a more elaborate scheme was required to remove any residual energy remaining after the initial discharge pulse. This was achieved by the incorporation of a pair of fast high-voltage diodes as shown in figure 4. Diode D1 blocks the reverse current when the oscillations begin. Diode D2 provides an alternative path for the reverse current. A pair of resistors was also included to provide critical damping of the oscillations so that the energy was dissipated before the next oscillation. In order for the circuit to work efficiently, both diodes must withstand large reverse voltages and high forward currents. They should also switch on and off quickly to minimise hysteresis losses. The diodes used for this work were constructed from a network of small fast semiconductor diodes in a series-parallel arrangement. Each individual diode was rated to withstand 1kV reverse voltage and 3A dc forward current. The number of diodes in each of D1 and D2 was chosen as appropriate.

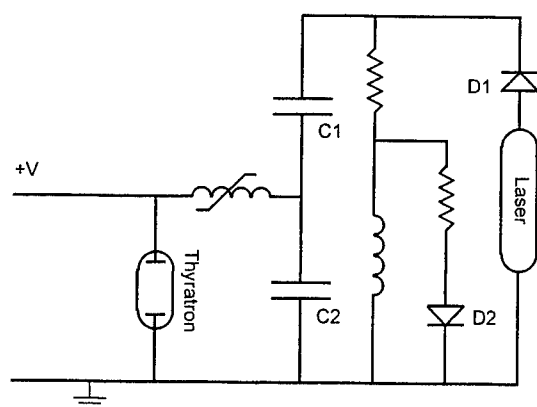


Fig. 4. Improved excitation circuit

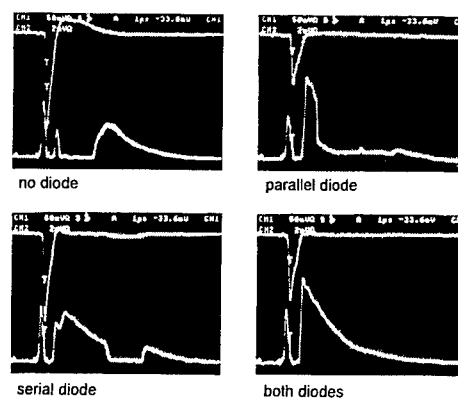


Fig. 5. Effects of pulse-shaping diodes

The effects of incorporating various combinations of diodes are shown in figure 5. The current oscillations in the absence of any diodes are clearly visible in the first frame and laser output after the discharge pulse appears initially only as a short spike as the current passes through zero. The parallel diode D2 reduces the reverse current by acting as a shunt across the discharge. This produces an increase in the amplitude of the initial spike and allows weak laser output in the early afterglow. The series diode D1 effectively blocks the reverse current but the output is quenched by subsequent oscillations. The combination of both diodes effectively removes any oscillations and the result is a substantial increase in pulse energy. An estimate of the improvement can be made by comparing the area under the curve on each graph. The overall increase is around a factor of two in both power and efficiency.

4. LASER PERFORMANCE

The laser can be operated at any prf in the range 20Hz to 20kHz. The upper limit is set by the charging circuitry. Operation at higher frequencies is possible but the performance is reduced due to a reduction in the charging voltage. At low frequencies the inter-pulse period is too long for any significant excitation to remain in the gas immediately prior to the following pulse and this can lead to some discharge instability. This can be mitigated somewhat by increasing the storage capacitance, and hence the energy deposited in each pulse, but stable operation is difficult at prf's below about 700Hz. At prf's below ~2.5kHz the output energy per pulse increases slightly with increasing prf due to the improved pre-ionisation. At higher prf's, the output energy per pulse falls but the average power increases. At prf's above ~8kHz, the output power falls slowly. The frequency for maximum output power depends on the storage capacitance. The values quoted here are dependent on the exact operating conditions but a typical set of performance data is shown in figure 6.

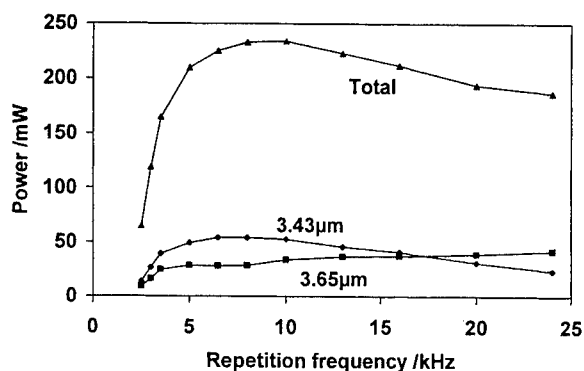


Fig. 6. Frequency dependence of output power

The output is divided among four principal wavelengths; 2.03 μm , 2.65 μm , 3.43 μm and 3.65 μm . The 2.03 μm is the strongest line and is the only wavelength present in the initial 'pre-discharge' spike. The other lines appear primarily in the afterglow. When the total laser output power is 250mW, the ratio 2.03:2.65:3.43:3.65 is typically 12:3:5:5. The exact ratio is dependent on both the operating conditions and also on the laser cavity. The lower curves in figure 6 show the frequency dependence of the two longer wavelengths. The output power at 3.43 μm closely follows the total whereas the output power at 3.65 μm continues to increase even at 24kHz. There is also some evidence of competition for gain between the two wavelengths. When different laser mirrors are used the relative intensities of the two wavelengths change although the total power in the two lines remains roughly constant. The two transitions operate from different energy levels and hence there must be some coupling between them. This has important consequences for single line operation.

Some initial work has also been carried out using a grating in place of the high-reflectivity mirror. This has resulted in the production of several additional laser lines, notably a transition at 3.16 μm which, to the author's knowledge, has not been previously reported as a laser line. Other wavelengths which have been obtained include 3.05 μm , 3.51 μm , 3.89 μm and 3.99 μm . Some of these require somewhat different operating conditions and the characterisation and optimisation of these transitions has not yet been completed.

5. SUMMARY

A xenon laser capable of operating at pulse repetition rates in the multi-kilohertz range has been described. The average output power of the laser is 250mW at 6kHz. The primary excitation mechanism is via recombination pumping in the afterglow of the discharge pulse. The sensitivity of the laser to weak currents in the afterglow has been demonstrated and an excitation scheme has been devised to remove any such currents. Four primary wavelengths have been observed using a standard untuned laser cavity. Additional wavelengths can be obtained from a grating-tuned cavity. The occurrence of laser output at 3.16 μm from the $7p[5/2]_2 - 7s[3/2]_2$ transition in neutral xenon is reported for the first time.

5. Diffusion-Cooled CO₂ Lasers

High power coaxial CO₂ waveguide laser

R. Nowack, H. Bochum, Th. Hall, K. Wessel

DLR, Institute of Technical Physics
Pfaffenwaldring 38-40, D-70503 Stuttgart, Germany

B. Grubert

BIAS, Bremen Institute of Applied Beam Technology
Klagenfurter-Straße 2, D-28359 Bremen, Germany

ABSTRACT

A coaxial CO₂ waveguide laser with rf excitation at 96.5 MHz and an output power exceeding 1.3 kW is described. This laser uses a new concept of electrode segmentation for discharge homogenization in addition to a new kind of optical resonator for the coaxial geometry called the toothed mirror resonator.

Keywords: CO₂ laser, diffusion cooled, slab laser, planar waveguide laser, coaxial waveguide laser, rf excitation, discharge homogenization, electrode segmentation, annular resonator.

1. INTRODUCTION

Diffusion cooled large area CO₂ waveguide lasers offer some striking advantages in comparison to fast flow systems for the design of high power industrial lasers. Expensive blowers and gas handling systems are no longer needed and the lasers have a strong potential for sealed off operation to minimize gas consumption. With planar laser systems and stable-unstable waveguide hybrid resonator area specific output powers of more than 2 W/cm² with excellent beam quality at a total output power exceeding 1 kW could be achieved^{1,2,3,4}. The concept is well suited for the design of very compact and low cost laser systems of high performance with laser powers of several kilowatts. In former times a planar laser system with an active area of 10 x 60 cm² and an electrode gap of 1.5 mm was investigated at the DLR. With rf excitation at 96.5 MHz an output power of 1350 W at an efficiency of 12 % could be coupled out with gold plated copper electrodes. With a beam shaping telescope a beam quality of $M^2=1.2$ was achieved. This laser system was transferred to industry and a commercial laser system with a laser power of 2.5 kW is available now (Fig.1). For laser output powers exceeding 5 kW the coaxial CO₂ waveguide laser is a promising candidate because it offers enhanced mechanical and optical stability for the large electrode surfaces needed. Investigations concerning a 1.3 kW coaxial laser system are reported. The coaxial geometry as well from the electrical as from the optical point of view is more sophisticated than the planar geometry. A new concept of electrode segmentation to achieve homogeneous coaxial waveguide discharges at 100 MHz is presented. The coaxial waveguide resonator still represents an unresolved problem. A new kind of optical resonator, the toothed mirror resonator, makes the laser acting like an annular phased array.

2. LARGE AREA COAXIAL RF WAVEGUIDE DISCHARGE

The main problem of large area small gap rf laser discharges operated at about 100 MHz in order to minimize the thickness of the boundary layers which do not contribute to laser excitation is discharge homogeneity. Spatial modulations of the electrical field strength and hence of laser excitation are induced without special precautions because the electrode dimensions are of the same order of magnitude as the wavelength of the rf field. Standard compensation methods like shunting the discharge gap by inductances along the electrodes as in the case of the planar waveguide laser are not applicable in coaxial systems without interfering with the optical radiation field. From the electrical point of view the coaxial waveguide with metallic walls and discharge represents a dissipative open ended rf transmission line. The effect of voltage modulation on laser excitation is neglectable (<10%) if the length of the transmission line is in the order of $\lambda/10$ of the rf

field. A new concept of electrode segmentation called the concept of "virtual" electrode for homogeneous excitation in elongated coaxial devices is shown in Fig2. One of the electrodes - in this case the outer electrode - is divided into segments of length $\lambda/10$. Adjacent segments are connected symmetrically to the rf. The inner electrode acts as a "virtual" electrode and connects two neighbouring discharges in series each of them being quite homogeneous. The optical radiation field is not disturbed by electrical connections. The voltage between the outer electrode segments is twice as high as the voltage between each segment and the inner electrode. To keep waveguide losses small arising from the segmentation and to prevent parasitic discharges the gap between the segments has to be very small following the Paschen law or bridged by ceramic material.

3. OPTICAL RESONATORS FOR COAXIAL WAVEGUIDE LASERS

Coaxial laser systems require specially adapted optical resonators for good beam quality because case I waveguide Fabry Perot resonators operate in high azimuthal mode order, the width of the waveguide gap forcing fundamental mode in radial direction⁶. Resonators with internal axicon are difficult to realize especially with waveguide lasers because of the coupling losses between the mirrors and the waveguide. Two promising resonator concepts are the helical mirror resonator⁷ and the toothed mirror resonator (Fig.3) working with all metal resonator optics as needed for the large diameters of high power lasers. To achieve good beam quality both resonators need an additional beam shaping optic.

The helical mirror resonator with quadratic or linear mirror slope in principle is identical with the stable-unstable waveguide hybrid resonator well known from the planar waveguide laser but in circular geometry. Because of the large circumference of the annular waveguide aperture this kind of resonator has a very large outcoupling aperture and does not seem well suited for high power systems. Moreover the resonator mirrors are very hard to manufacture.

The toothed mirror resonator is a kind of array of many coupled individual resonators. Both resonator mirrors are plane. At the outcoupling mirror outcoupling holes alternate with fully reflecting mirror segments which provide diffraction coupling between the individual resonators. Parameters of this kind of resonator are the number of periods of mirror segments and the ratio of width of the reflecting segments to that of the outcoupling apertures.

4. PERFORMANCE OF THE COAXIAL WAVEGUIDE LASER SYSTEM

The concept of the coaxial waveguide laser system was realised with a 53 cm long waveguide device having an annular discharge diameter of 57 x 1.5 mm. The experimental setup of this laser is schematically shown in Fig.4. The laser was operated with unsegmented and segmented outer electrode. To study laser performance and to compare it to that of the planar CO₂ waveguide laser investigations first were carried out with a case I Fabry Perot resonator. Results of the experiment are summarized in Tab.1. With unsegmented outer electrode and single ended rf input maximum laser power achieved was 600 W at an efficiency of 6.7 %. This laser power could be more than doubled by deviding the outer electrode into two parts of 26.5 cm length and connecting them symmetrically to the rf following the principle of "virtual" electrode. Maximum laser power coupled out was 1340 W and maximum efficiency 10.4 %. With an maximum area specific laser power of 1.34 W/cm² the laser did not reach the typical 2 W/cm² of planar systems. Saturation of laser power occurs already at a pressure of 115 mbar and an area specific electrical power density of about 15 W/cm². Computation of discharge homogeneity following transmission line theory shows that electrode segments with a length of 26.5 cm are still too long. Under the influence of laser plasma the wavelength of the rf field shortens from 3 m free space to about 1.5 m on the electrode structure. Increasing the number of electrode segments from two to four the coaxial waveguide laser system is expected to show same performance as planar systems.

Concerning the toothed mirror resonator experiments with 30 and 60 element mirrors were carried out until now. Fig.5 shows an outcoupling mirror made from antireflection and gold coated ZnSe and a spark eroded and diamond turned copper mirror. The 30 element mirrors did not show phase coupling around the circumference of the waveguide aperture. Typical near and far field burn patterns of a 60 element mirror resonator are shown in Fig.6. The near field shows a zero of intensity in the middle of each outcoupling hole, the far field a symmetrical ring pattern with a pronounced intensity zero at the centre as expected for the case of phase coupling around the annular aperture of the resonator. Comparing the far field angles of the burn pattern with those computed for a symmetric and antisymmetric annular phased array following Fresnel Kirchhoff diffraction theory (Fig. 7) shows that the laser acts as an antisymmetric phased array consistent with theory of the toothed mirror resonator⁸. Maximum laser output power until now is 780 W and maximum efficiency 6.4 %. These data are only 60 % of those achieved with case I Fabry Perot resonator (Tab.1). The reason for this is the insufficient utilisation

of the gain medium in the axis of the outcoupling apertures. Power density of the radiation field on these axes is only 440 W/cm² in comparison to 2.5 kW/cm² of saturation intensity. An improvement is expected from an increase of the number of mirror segments.

5. CONCLUSIONS

Diffusion cooled coaxial CO₂ waveguide lasers are promising candidates for industrial laser systems with output powers of 10 kW and more. In laboratory a 1.3 kW laser with an efficiency of 10.4 % has been demonstrated. The proof of operation of a new concept of electrode segmentation and a new kind of optical resonator for the annular waveguide laser geometry with all metal resonator optics has been given.

6. ACKNOWLEDGEMENT

This research was supported by the german federal ministry of education, science, research and technology (BMBF).

7. REFERENCES

1. R. Nowack, H. Opower, U. Schaefer, K. Wessel, Th. Hall (DLR) - H. Krüger, H. Weber (Siemens), "High Power CO₂ Waveguide Laser of the 1 kW Category," *Proceedings ECO 3, Den Haag 1990, SPIE Vol. 1276*, p. 18, (1990).
2. "Slab-waveguide CO₂ laser output power exceeds 1 kW," *Laser Focus World*, p. 9, Nov. 1990.
3. R. Nowack, H. Opower, K. Wessel (DLR) - H. Krüger, W. Haas, N. Wenzel (Siemens), "Diffusion-cooled Compact CO₂ High Power Laser," *Laser und Optoelektronik* **23**, 68 (1991).
4. A. D. Colley, H. J. Baker, D. R. Hall, "Planar waveguide, 1 kW cw, carbon dioxide laser excited by a single transverse rf discharge," *Appl. Phys. Lett.* **61**, 136 (1992).
5. photograph by Rofin Sinar Laser GmbH, Hamburg, Germany
6. H. Bochum, R. Nowack, W. Schock, "Koaxiale CO₂-Wellenleiterlaser," *Proc. of the 12th International Congress Laser '95, Munich 1995*, 358 (1995).
7. D. Ehrlichmann, U. Habich, H.-D. Plum, P. Loosen, G. Herziger, "Azimuthally Unstable Resonators for High-Power CO₂ Lasers with Annular Gain Medium," *IEEE J. of Quant. Electr.* **30**, 1441 (1994).
8. B. Grubert, W. Jüptner (BIAS) - R. Nowack (DLR), "Calculation of coupling losses for coaxial waveguide modes," *these Proceedings, GCL/HPL 96, Edinburgh Sept. 1996*.

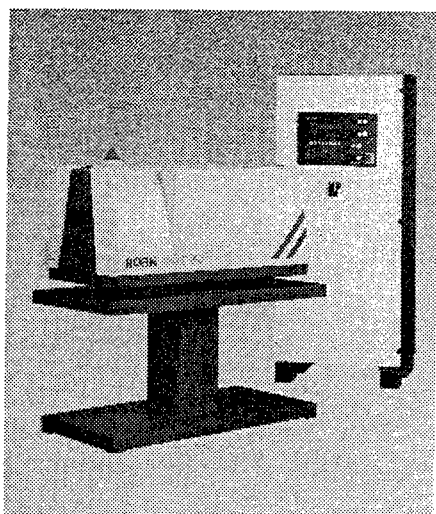


Figure 1: Commercial 2.5 kW CO₂ slab laser⁵

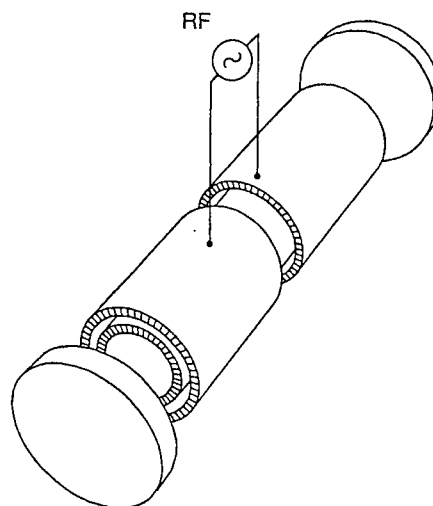


Figure 2: Electrode segmentation with "virtual electrode"

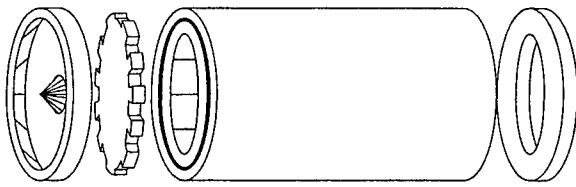


Figure 3: Toothed mirror resonator

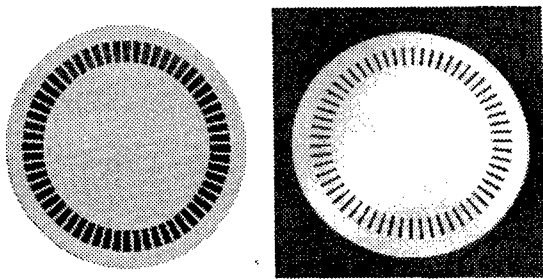


Figure 5: ZnSe and copper outcoupling mirror

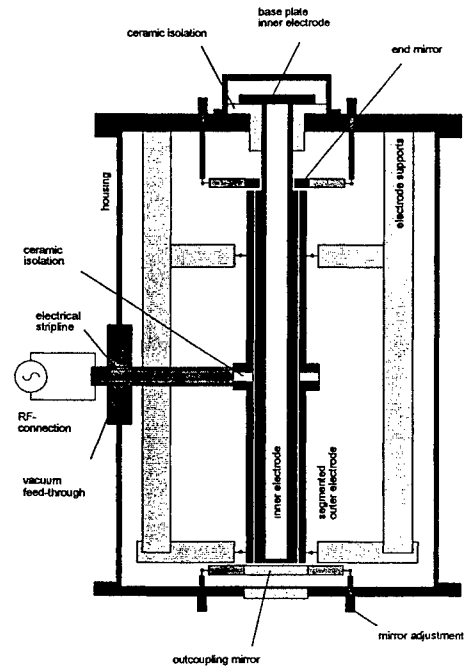


Figure 4: Scheme of the experimental setup

Parameters :		Experimental condition:	Results:	
electrode area:	$\varnothing 6 \times 53 = 1000 \text{ cm}^2$	Dual case I resonator:	outcoupling:	$T = 10\%$
discharge gap:	1.5 mm	- single ended rf input:	$P_L = 600 \text{ W}$	$\eta = 6.7\%$
gas mixture:	$\text{He:N}_2:\text{CO}_2 = 3:1:1 + 5\% \text{ Xe}$	- segmented electrode:	$P_L = 1340 \text{ W}$	$\eta = 8.4\%$
pressure:	100...160 mbar		$P_L = 1200 \text{ W}$	$\eta > 10\%$
rf power:	8...16 kW (96.5 MHz)	-saturation coaxial laser:	$p = 115 \text{ mbar}$	$p_{ei} = 15 \text{ W/cm}^2$
		-saturation planar laser:	$p = 160 \text{ mbar}$	$p_{ei} = 20 \text{ W/cm}^2$
		Toothed mirror resonator:	60 elements	$T_{\text{Geo}} = 50\%$
		-segmented electrode:	$P_L = 780 \text{ W}$	$\eta = 4.9\%$
			$P_L = 640 \text{ W}$	$\eta = 6.4\%$

Table 1: Performance of the coaxial laser system

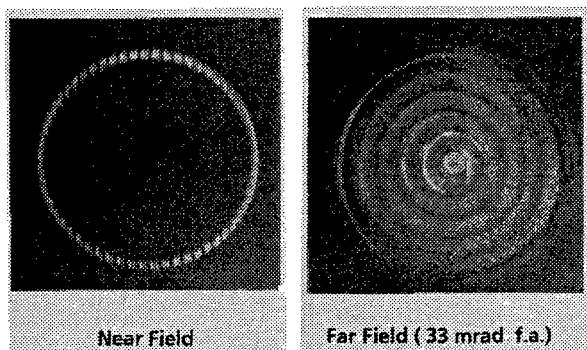


Figure 6: Plexiglas burn pattern of a 60 element mirror

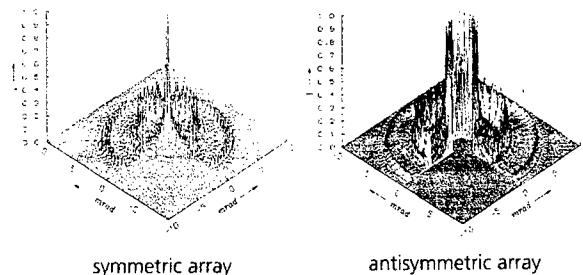


Figure 7: Far field of a 60 element annular phased array

1 kW slab CO₂ laser excited by a self-excited RF generator

S. Kobayashi, T. Murata, K. Terai, and T. Tamagawa

Heavy Apparatus Engineering Laboratory, Toshiba Corporation
2-1 Ukishima-cho, Kawasaki-ku, Kawasaki 210, Japan

Abstract

A 100MHz RF discharge excited slab CO₂ laser with the near diffraction limited output power of 1.07kW and the efficiency of 12.6% was studied. The size, including the laser head and the RF generator, is 1/4 of the fast axial flow laser. The self-excited RF generator with a cavity resonator made the laser simple and compact. To determine the RF excitation frequency, the discharge characteristics were studied at both frequencies of 40MHz and 100MHz.

Keywords: CO₂ lasers, slab lasers, diffusion cooled, self-excited RF generator

1. Introduction

A low cost, compact laser is required for various such as material processing or construction. Recently, a super slab CO₂ laser has been paid attention as one candidate.¹⁻⁴ Since the slab CO₂ laser is excited by RF discharge, it is important to understand the discharge physics. The RF generator strongly depends on their discharge characteristics.

Some researches to establish scaling laws for the slab CO₂ lasers has been done^{4,5}, especially by measuring the voltage and current characteristics of alpha RF discharge. We studied the frequency dependence of laser excitation characteristics by carrying out laser oscillation experiments at both frequencies of 40MHz and 100MHz. Based on the experimental results and technical aspect, a self-excited RF generator for a 1kW slab laser was fabricated.

In this paper, we present the experimental results at each frequency and the characteristics of the laser. We also show the possibility for applying the slab CO₂ laser to the new fields.

2. Discharge Physics and Technical Aspects

A schematic diagram of the slab laser is shown in Fig. 1. The water cooled planer parallel electrodes are made of aluminum alloy and their dimensions are 100×600mm. The laser gas is set to a pressure of 10.6kPa and the mixing ratio is He:N₂:CO₂:Xe=34:7:7.4. The electrodes are connected each other by several coils to cancel the imaginary part of the impedance in the longitudinal direction by the parallel resonance method. Thus, the nonuniformity of discharge is reduced to less than 10%.

To find the optimum laser excitation, the discharge observation and the laser oscillation experiments were carried out with varying RF frequencies and electrodes separation. The discharge views for each frequency f obtained using CCD

camera are shown in Fig. 2. The sheath thickness $ds=(ds_1+ds_2)/2$ are 0.16 ± 0.02 mm at 100MHz and 0.37 ± 0.02 mm at 40MHz which are proportional to $1/f$. The laser output power was measured at RF frequencies of 40MHz and 100MHz, electrode separations is the range from 1.0mm to 6.5mm. The resonator used is a waveguide-stable configuration; it consists of a flat ZnSe mirror with a reflectance of 80% as an output coupler and a copper mirror with a curvature of 3.0m concave for vertical direction and 6.25m concave for horizontal direction. The measurement results are shown in Fig. 3, in which the result obtained at a frequency of 125MHz⁴ is also shown. A dotted line shows the $1/d$ scaling law in which the specific output power depends on only the gas temperature. The higher specific power was obtained with a 100MHz RF discharge rather than that of 40MHz. In the case of 40MHz, even if the electrodes separation reduced to less than 4.0mm, the specific power didn't increase according to the $1/d$ scaling law but greatly deviated and decreased. The similar tendency was also observed in the region of the electrode separation less than 1.5mm at a frequency of 100MHz. Our results well agreed with the tendency at a frequency of 125MHz. We considered that the deviation of specific power from $1/d$ scaling law with small electrode separations are caused by ion loss in the sheath region of alpha RF discharge; the ion loss increases as the frequency f decreases because the sheath thickness $ds (\propto 1/f)$ is getting bigger and hence sheath voltage is getting higher as being to proportional to $1/f^2$, when the current density is constant.

According to the above results and previous work⁵, optimum frequency to make the slab laser is ~ 100 MHz to 300MHz. When we also consider technical aspect, ~ 100 MHz is desirable, as the RF generator is compact and cheap.

3. The Slab Laser

1kW slab CO₂ laser was studied; a self-excited RF generator with a vacuum tube and cavity resonator was used in order to reduce the cost. The circuit diagram is shown in Fig. 4. The RF generator is directly connected to the matching circuit and can feed a maximum power of 10kW to the laser head.

The oscillation circuit consists of the short stub as inductance L_c , the air gap capacitor as capacitance C_c and discharge load. As for a self-excited RF generator, especially in case of discharge load, great care should be paid to impedance matching and the Q value. In this laser, RF frequency depends on the discharge load. The matching circuit changes the RF frequency to maintain the matching condition. Moreover, the frequency band width of the RF depends on the Q value of the circuit. This laser can operate at a frequency of 100 ± 2 MHz of an appropriate the Q value of 80. A conversion power ratio (RF/DC) of 63% was achieved in this RF generator.

The laser resonator used is the same as shown in Fig. 1 and the gas mixture is He:N₂:CO₂:Xe=34:7:7:4 at a pressure of 10.6kPa. The laser output power of 1.07kW was obtained with laser power to RF power efficiency of 12.6%. The beam quality is the near diffraction limited mode ($M^2_w \sim 2.0$ in the waveguide direction and $M^2_u \sim 2.3$ in the unstable direction). The size of this laser, including laser head and RF generator, is $1000\text{mm}^L \times 700\text{mm}^D \times 700\text{mm}^H$ which is 1/4 of that of a fast axial flow laser. The laser can be regarded as one small component of the machine system.

We are planing to apply this laser to new fields. 300W laser using an all solid state RF generator (DC to RF conversion ratio of 75%) was successfully installed in a robot arm as a mechanical part.

4. Conclusions

1kW slab CO₂ laser excited by 100MHz RF discharge was studied, based on the results of studies on discharge physics. The size of this laser including laser head and RF generator is reduced to 1/4 of that of a fast axial flow laser. Slab geometry and a self-excited RF generator make this laser simple and inexpensive. Output power of 1.07kW was obtained with an efficiency of 12.6% and the near diffraction limited mode ($M^2_w \sim 2.0, M^2_v \sim 2.3$). The laser would be applied the new fields.

5. References

1. K.Terai, T.Murata and T.Tamagawa, "Characteristics of RF excited CO₂ lasers", The Review of laser engineering, 21(4), 475(1993).
2. D.He and D.R.Hall, "Frequency dependence in RF excited waveguide CO₂ lasers", IEEE J. Quantum Electron, QE-22, 749(1986).
3. R. Nowack, H. Opower and K. Wessel, "Diffusion - Cooled Compact CO₂ High Power Lasers", Laser and Optoelectronik 23(3), pp68-81(1991).
4. K.M.Abramski, H.J.Baker, A.D.Colley, D. R. Hall, C.J.Shackleton, P.Vitruk, "Compact Diffusion - Cooled Array and slab Carbon Dioxide Lasers at 1 kWatt level", Proceeding of LAMP92(Nagaoka),pp73-77(1992).
5. P. P. Vitruk, H. J. Baker and D.R.Hall, "Similarity and Scaling Diffusion-Cooled RF Excited Carbon Dioxide Lasers", IEEE J. Quantum Electron, vol.QE-30,pp1623-1634(1994).

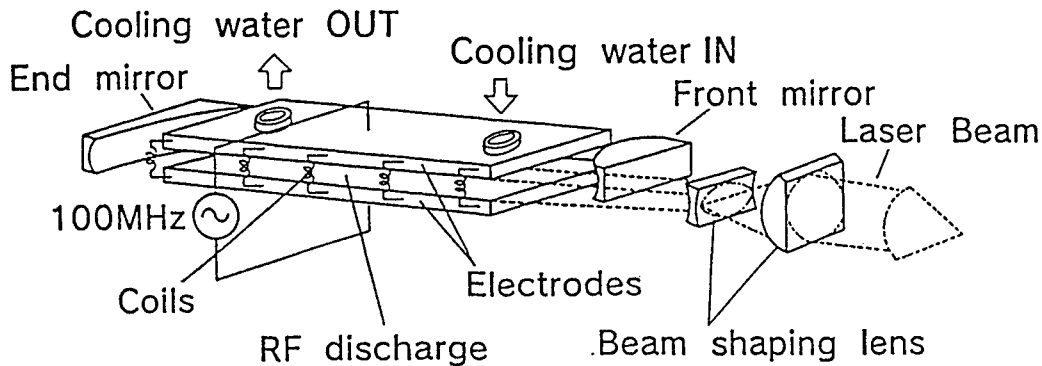


Figure 1 Configuration of the slab laser

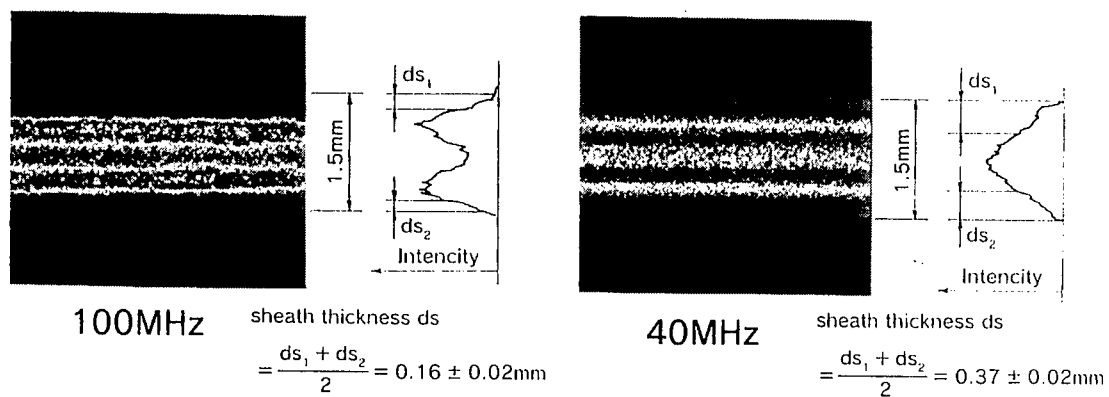


Figure 2 Photograph of the discharge emission.

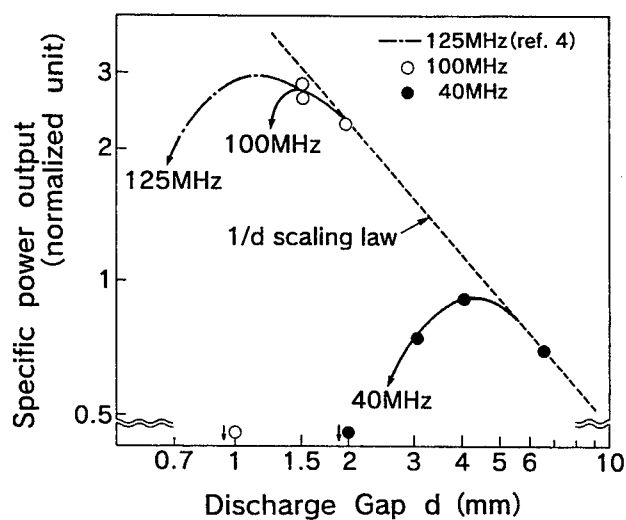


Figure 3 Specific power output versus electrode gap d .

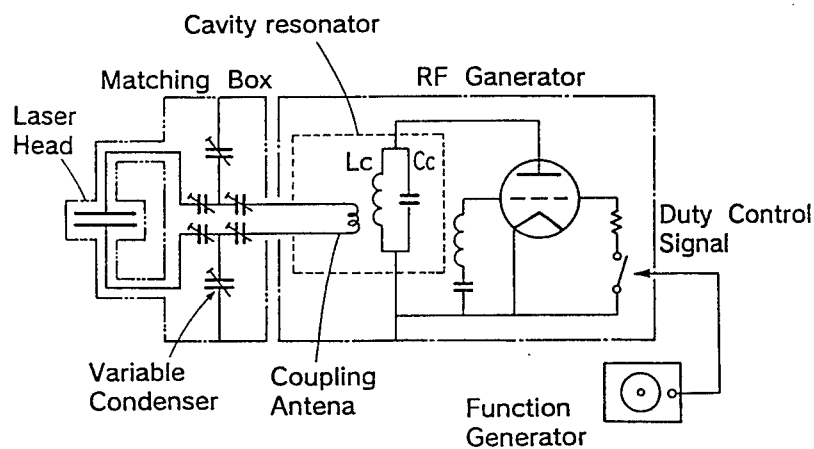


Figure 4 A configuration of the self-excited circuit and cavity resonator of the developed 1kW slab CO_2 laser.

Experimental study of a DC-excited slab CO₂ laser discharge

C Leys, C van Egmond, E Desoppere

University of Ghent, Department of Applied Physics
Rozier 44, B-9000 Ghent, Belgium

ABSTRACT

The suitability of a slab-shaped DC-excited discharge as active medium of a compact high power CO₂ laser is investigated. Measurements of several plasma and laser parameters indicate the effectiveness of the adopted discharge stabilization technique.

Keywords: gas discharge, CO₂ laser, magnetic discharge stabilization, vibrational kinetics, emission spectroscopy

1. INTRODUCTION

Whereas in conventional CO₂ laser geometries the diffusion-cooling approach limits the output power to about 100 W per meter of discharge length, slab lasers combine compactness with high power¹. A further reduction of cost may be obtained by changing the transverse RF excitation scheme for a multi-pin configuration fed by a DC power supply. Since at high power loadings a DC-excited discharge is subject to contraction, the plasma has to be homogenized in some way to make it fill the major part of the slab-shaped chamber. Macken obtained homogeneous discharge operation in a slab by imposing a transverse magnetic field and contouring the electric field². In the laser reported here the plasma is effectively stabilized by the combined action of a Lorentz drift and a flow-induced gradient in the plasma conductivity. In Section 2 the essential features of the discharge stabilization mechanism are explained.

A number of diagnostics have been implemented on the discharge module to investigate the properties of the active medium. Langmuir probe measurements yield the reduced electrical field strength. The excitation efficiency of the upper laser level is probed with an emission spectroscopy technique: the population of the vibrational N₂ levels is determined by measuring the relative intensities of the vibrational bands of the N₂ second positive system (C³π_u - B³π_g). A CO₂ probe laser is used to measure the small signal gain. The various measurements are covered in Section 3.

2. DISCHARGE STABILIZATION

The discharge volume of the experimental slab laser module measures 168×140×10 mm³. A row of eight individually ballasted pin electrodes is placed along either long side of the slab. The spacing between neighbouring anodes or cathodes is 24 mm. The adopted discharge stabilization scheme is similar to that of a "Macken discharge" in the sense that a transverse magnetic field is applied which induces a Lorentz force on the charged particles². However, no "launcher" electrode is present, i.e. the anode-cathode distance is constant along the slab. The magnetic field is generated by ferrite magnets mounted on magnetic yokes enveloping the discharge chamber. To limit the decomposition of the laser mixture the gas is flown through the discharge chamber. In the reported experiments the slow gas flow is, unless stated otherwise, in the opposite direction to the Lorentz drift of the charged particles. To allow for visual observation of the discharge a pyrex plate closes the discharge chamber on one side. On the other side a water-cooled enamel-coated stainless steel plate provides for the (asymmetric) diffusive cooling of the discharge slab.

Depending on the strength of the magnetic field and the gas pressure, three different discharge burning modes are observed. At a pressure of a few tens of Torr and zero magnetic field a single stationary filament with a diameter of a few millimeter stretches from one particular anode pin to the nearest cathode. Under the influence of a magnetic field this filament is bent in the $E \times B$ direction and eventually jumps to the next electrode pair, upon which a new current channel is launched in the gap between the first electrodes. The resulting discharge pattern is that of thin filaments being swept through the slab in the direction of the magnetic drift. The velocity of the moving filament increases with increasing magnetic field strength until the latter reaches a critical value B_c at which the cyclic motion of current channels stops and the entire slab volume appears to be filled with a uniform glow discharge. Only in the homogeneous glow regime, which is established at supercritical magnetic fields, the discharge can be qualified as a laser active medium (see Section 3).

As collisions with neutrals tend to randomize the Lorentz drift motion of the charged particles the critical magnetic field strength increases with increasing gas pressure (Fig. 1). Furthermore, it is observed that the gas flow is instrumental,

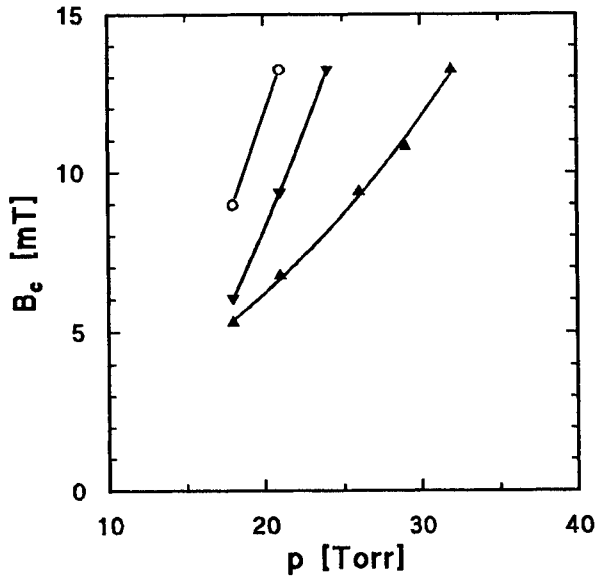


Fig.1. Critical magnetic field vs pressure: no gas flow (O) – gas flow in the same (▼) and opposite (▲) direction of the magnetic drift.

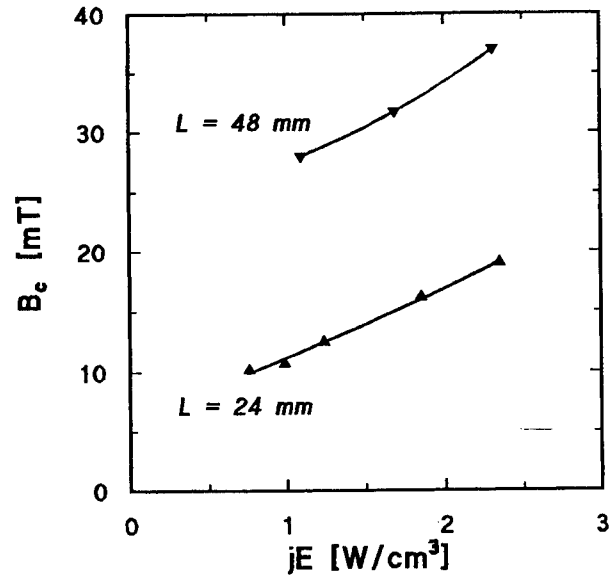


Fig.2. Critical magnetic field vs input power density for two different distances L between neighbouring anodes; $p = 25$ Torr.

yet not essential, in stabilizing the discharge. At a given gas pressure the critical magnetic field is lowest if the flow is directed opposite to the Lorentz drift. This can be attributed to the fact that, as the time constant for CO_2 dissociation is of the same order of magnitude as the gas residence time, the plasma-chemical composition of the gas may vary along the flow (in fact, at high electrical power loadings a gradual change of the colour of the discharge is perceived). Moreover, since the self-sustaining reduced field decreases with increasing CO_2 dissociation degree³ the plasma conductivity increases in the direction of the flow. It follows that if the flow is directed opposite to the Lorentz drift, discharges will predominantly initiate in the downstream region which therefore plays the same role as the launcher electrode pair in Macken's discharge configuration. In general, the critical magnetic field will be relatively low when the discharge geometry allows for a reproducible cyclic motion of filaments in the subcritical discharge regime.

In crossed electrical and magnetic fields the Lorentz force induces an ambipolar drift of the charged particles in the $E \times B$ direction. The Lorentz drift velocity is given by

$$v_L = \frac{(\mu_e + \mu_i)\mu_e\mu_i EB}{\mu_e(1 + \mu_i^2 B^2) + \mu_i(1 + \mu_e^2 B^2)} \approx \mu_e\mu_i EB$$

where $\mu_{e,i}$ are the zero-field electron and ion mobilities. At pressures of a few tens of Torr and magnetic fields of the order of 10 mT the Lorentz drift velocity lies in the range 5-30 m/s. Although these magnetic drift velocities are markedly lower than typical neutral gas velocities in fast-flow lasers, it is believed that magnetic and convective stabilization techniques bear on the same mechanism, i.e. the transport of plasma perturbations out of the discharge region in a time which is shorter than the characteristic growth time τ_g for thermal instabilities. In fact, the data in Fig.2 suggest that the transition to the homogeneous glow regime occurs when the transit time $\tau_t = L/v_L$ (L : distance between neighbouring anodes) for the drifting filament between subsequent electrode pairs is smaller than τ_g . This surmise is further backed up by the observation that B_c remains constant when the number of subsequent electrodes is reduced, i.e. B_c does not depend on the total length of the discharge slab in the $E \times B$ direction. The (qualitative) stability criterion, $\tau_t < \tau_g$, is exactly the same as in fast-flowing discharges where τ_t stands for the gas residence time in the discharge region. The positive slope of the curves in Fig.2 is due to the fact that the instability growth time decreases with increasing power density⁴. Note that the smaller length scale in the case of magnetic stabilization (the distance between neighbouring electrodes rather than the total length of the discharge) compensates for the smaller transport velocities when compared to convective stabilization.

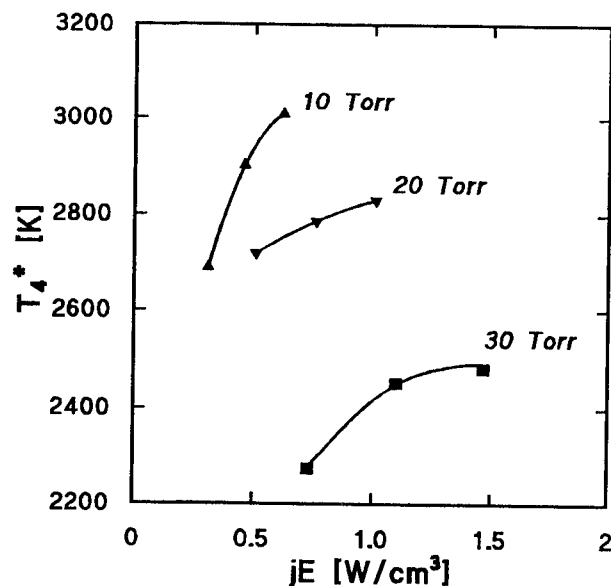


Fig.3. Vibrational temperature of the $C^3\pi_u$ -state of N_2 vs input power density at different gas pressures.

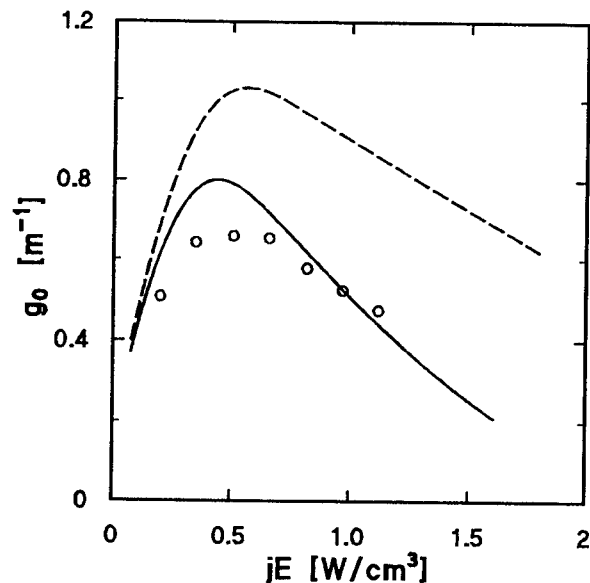


Fig.4. Small signal gain: experimental (O) – three temperature model calculation with pyrex plate (full curve) and with cooling plate (dashed); $p = 20$ Torr.

The resulting transit times being of the same order, it is possible, with regard to stability, to operate DC slab discharges at the same power loading levels as in fast-flow lasers.

3. ACTIVE MEDIUM PROPERTIES

As mentioned above, at supercritical magnetic fields the aspect of the discharge is that of a uniform glow. Its suitability as amplifying medium is to be demonstrated by a more quantitative assessment of the discharge properties. Probe measurements of the self-sustaining reduced electrical field strength in a 6:24:70 $CO_2/N_2/He$ mixture yield E/N values from 2.4×10^{-20} Vm^2 down to 1.9×10^{-20} Vm^2 in the pressure range 10-40 Torr. The computation of the corresponding electron energy distribution functions⁵ shows that under these conditions 85-90 % of the input electrical power goes to the excitation of the CO_2 asymmetric stretch mode and the N_2 ($v = 1-8$) vibrational levels (the theoretical vibrational excitation efficiency reaches a maximum of 91 % at $E/N = 1.86 \times 10^{-20}$ Vm^2).

The vibrational kinetics of the slab discharge are studied experimentally by means of an emission spectroscopy technique: from the measurement of the relative intensities of the vibrational bands of the nitrogen second positive system ($C^3\pi_u - B^3\pi_g$) the non-equilibrium vibrational temperature T_4^* of the $C^3\pi_u$ -state is derived⁶. The data in Fig.3 reveal the decrease of the relative densities of vibrationally excited N_2 molecules with pressure due to the collisional relaxation of the CO_2 (00^0_1) level. Assuming that the $C^3\pi_u$ -levels are populated by direct electron impact, the vibrational temperatures T_4^0 of the N_2 electronic ground state can be calculated using Franck-Condon factors⁶. The latter are found to be about 1000 K lower than the corresponding T_4^* values. It follows that in the homogeneous glow regime 7-16 % of the ground state N_2 molecules is vibrationally excited ($v \geq 1$) and contribute to the population of the upper laser level. Ground state vibrational temperatures in fast-axial-flow lasers are typically higher⁷. However, it should be noted that the use of an uncooled pyrex plate (for diagnostic purposes) limited the range of accessible power loadings. In fact, the data at 30 Torr suggest a thermal saturation effect.

The small signal gain, as derived from the amplification of a probe laser beam, is shown in Fig.4. At a pressure of 20 Torr the recorded values range between 0.45 m^{-1} and 0.65 m^{-1} . The measured gain values are in fair agreement with the results of a vibrational kinetics calculation based on a three temperature model⁸ (full curve). The relatively steep decrease in gain at higher power loadings should again be attributed to the asymmetrical cooling of the gas. The three temperature model calculations indeed show that substantially higher values of the gain are to be expected if proper cooling is applied (dashed). In sum, the reported measurements indicate the effectiveness of a magnetic stabilization scheme in producing a slab-shaped active medium for a DC-excited CO_2 laser.

4. ACKNOWLEDGMENTS

The authors acknowledge the financial support of the Flemish Institute for the Promotion of Scientific-Technological Research in Industry (IWT) under contract IWT 93-211 and of the COPERNICUS Programme of the European Commission under contract CIPA-CT94-0183. The help of T.Bostoen, P.Nollet and D.De Roest in carrying out the spectroscopic experiments is highly appreciated. Finally, the authors are indebted to the expertise of Ing.K.Meseure of the Belgian Research Centre for the Applications of Steel (OCAS) in fabricating the enamel coatings.

5. REFERENCES

1. A.D.Colley, H.J.Baker, D.R.Hall, "Planar waveguide, 1 kW cw, carbon dioxide laser excited by a single transverse rf discharge", *Appl.Phys.Lett.* **61**(2), 136-138 (1992).
2. J.Macken, "DC Slab CO₂ Lasers", *Proceedings of LAMP '92*, pp. 67-72, June 1992.
3. C.Leys, C.van Egmond, E.Desoppere, "Ionization equilibrium in flowing CO₂ laser mixtures", submitted to *J.Phys.D: Appl.Phys.*, 1996.
4. W.L.Nighan, W.J.Wiegand, "Causes of arcing in cw CO₂ convection laser discharges", *Appl.Phys.Lett.* **25**(11), 633-636 (1974).
5. W.L.Morgan, B.M.Penetrante, "ELENDF: a time-dependent Boltzmann solver for partially ionized gases", *Comp.Phys.Commun.* **58**, 127-152 (1990).
6. M.Z.Novgorodov, V.N.Ochkin, N.N.Sobolev, "Vibrational temperatures in a CO₂ laser", *Sov.Phys.-Tech.Phys.* **15**(6), 977-982 (1970).
7. M.Spiridonov, C.Leys, D.Toebaert, S.Sazhin, E.Desoppere, P.Wild, S.M.P.McKenna-Lawlor, "Investigation of the active medium of a direct-current-excited fast-axial-flow CO₂ laser using a tunable diode laser", *J.Phys.D: Appl.Phys.* **27**, 962-969 (1994).
8. S.Sazhin, P.Wild, C.Leys, D.Toebaert, "The three temperature model for the fast-axial-flow CO₂ laser", *J.Phys.D: Appl.Phys.* **26**, 1872-1883 (1993).

Two-dimensional waveguide CO₂ laser arrays and beam reformatting

R Abram, P Blair, F Villarreal, A D Colley, H J Baker, M R Taghizadeh, D R Hall

Department of Physics, Heriot Watt University, Riccarton
Edinburgh EH14 4AS, Scotland, UK

ABSTRACT

A high power, two-dimensional, 16x4 element waveguide array CO₂ laser is presented and properties such as beam quality and spatial power distribution are assessed, together with beam reformatting techniques to produce compact beams.

1. INTRODUCTION

The square bore waveguide, excited by a transverse radio frequency discharge, is recognised as having the highest specific output power per unit volume of all the diffusion cooled CO₂ lasers [1]. However, a limitation of the square bore waveguide laser is in length scalability. Devices longer than 0.4 m suffer from power distribution difficulties due to transmission line effects when using RF excitation. In addition, the high optical flux in such devices may damage or thermally deform the resonator mirrors.

A natural progression from the square bore waveguide laser has been to develop the slab geometry laser by increasing the width of the bore to enlarge the active gain region [2] whilst keeping the electrode spacing small to maintain efficient gas cooling. The area scaled slab waveguide in combination with a hybrid waveguide-unstable resonator has allowed much greater powers to be extracted from RF excited diffusion cooled lasers. The slab laser is still limited in length by RF standing waves and non-uniform discharge loading, which results in a non-isotropic gain media and an associated loss in efficiency. To date the maximum power attained by a single discharge in a slab is in the region of 2.5 kW.

However, by employing homogeneous power deposition among multiple discharge regions in a parallel array [3 - 6], diffusion cooled lasers can be volume scaled to achieve powers far in excess of those at present. Such a technology will be a viable alternative to the fast flow laser currently employed by industry for many material processing applications. In this paper we emphasise the development of a 2 dimensional array of square bore waveguide lasers. This will provide a volume scaled laser structure incorporating the excellent power densities currently achieved by an individual square bore waveguide.

2. TWO DIMENSIONAL ARRAYS OF SQUARE BORE WAVEGUIDE LASERS

The simplest form of array consists of a set of independent laser oscillators, where the output from each laser is un-correlated with that of its neighbours, each operating at a different frequency and/ or random phase. It is this type of *incoherent* array that is presented in this paper.

The array concept as applied to the CO₂ laser was first demonstrated by Kozlov *et al* [3] who reported an output power of 3 kW from a 2-D array of 78 longitudinally DC excited discharges of circular cross-section. More recently a 2-D array of square bore waveguide lasers with RF excitation was developed by Abramski *et al*. [4] It achieved 750 W output using a 3 level structure, each containing 13 waveguide elements of 375 mm in length. The levels were connected electrically in series and therefore required high striking and running voltages. The volume scalability of this method was found to be limited by the increasing problem of electrical breakdown to the mirrors and the running of unwanted discharges outside the gain regions. Also the increased thermal load reduced the specific laser output from 70 W/m for a 1 level structure containing 13 elements, to 51 W/m for a 3 level structure.

3. MULTI - KILOWATT 2-DIMENSIONAL ARRAY

To achieve higher powers a new array structure has been developed shown schematically in Fig. 1. Each of the discharge regions is electrically driven in parallel to avoid the high operating voltages and the resulting external discharge problems associated series operation, as noted above. Parallel connection also simplifies the design of coolant manifolds, allowing for higher fluid flow rates and hence more efficient cooling. The 2-D array incorporates 64 square bore waveguides of active length 590 mm in a 4 by 16 matrix, with each waveguide element producing a high quality EH₁₁ beam with an M² value of around 1.15. Each channel has a 2.25 x 2.25 mm cross section. Micro-channel type structures are incorporated within each electrode to greatly enhance the heat transfer from the electrode surfaces to the cooling water. This should prevent some

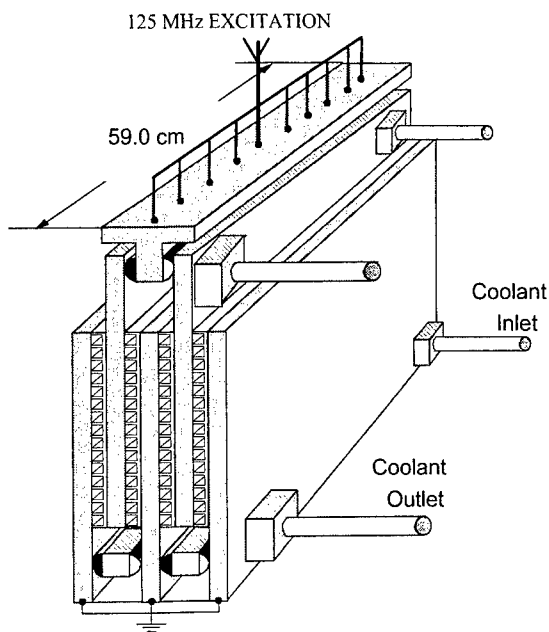


Figure 1 Simplified Schematic of Multi-Kilowatt Array

the voltage uniformity has been made for the two level array. In the future with the the array set up to run with four levels, improved longitudinal and transverse uniformity will be established, and significant increases in power and efficiency are expected from this improvement.

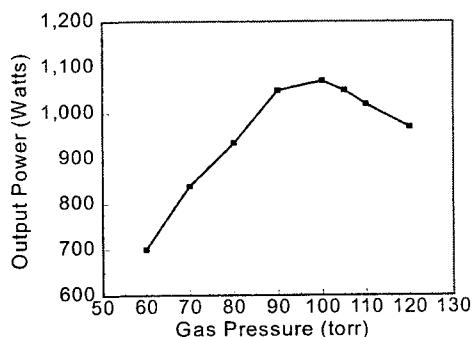


Fig. 2 Max. Output Power vs Gas Pressure

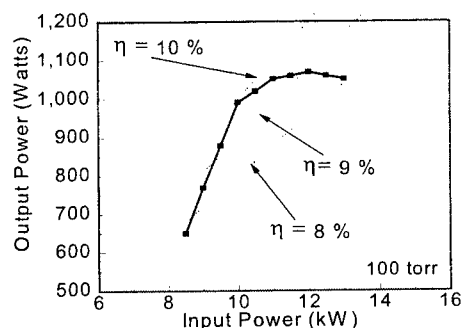


Fig. 3 Laser Output vs Input Power @ 100 torr

3. BEAM PROPAGATION CHARACTERISTICS

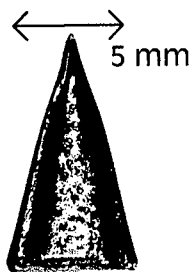


Fig. 4 Far-field

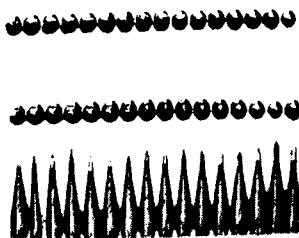


Fig. 5 Near-Field at Re-Image

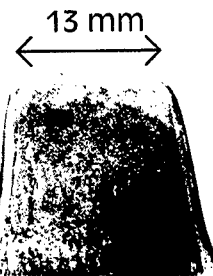


Fig. 6 "Flat Top" beam

of the thermal derating that occurred with the previous laser with multiple levels in the structure [4]. The plane resonator mirrors, in a dual Case I configuration shared by all the channels, are water cooled to reduce thermal distortion. The entire system is enclosed in a vacuum enclosure of dimensions 200 mm by 200 mm by 1000 mm. The RF generator operates at 125 MHz.

The results for the preliminary tests on the 2-D array are shown in Figs. 2 and 3 for the operation of just two levels (32 active elements). Fig. 2 shows the maximum laser output power versus gas pressure (gas mix 3 He:1 N₂:1 CO₂ +5% Xe) indicating an optimum pressure of 100 torr. Figure 3 shows that the maximum power attained at 100 torr is currently 1.07 kW at an efficiency of 9%. This corresponds to a specific power of 55 W/m of waveguide, considerably below the value of 70 W/m expected when derating by thermal loading and heat transfer effects in the laser electrodes are avoided.

However, the waveguides are 590 mm in active length, significantly longer than the 375 mm used previously [4] for which the 70 W/m value was established. The increased effective length of the transmission line formed by the laser structure requires greater measures to control voltage uniformity. Up to the present, no systematic optimisation of

The output from the 2 x 16 array was focused using a nominally 1m radius mirror, and burn patterns using perspex were made at points of key interest. The far-field pattern shown in Fig. 4 occurs at a distance 540 mm from the mirror where all the beams cross, and it is a single spot with no side lobes or irregular structure. Figure 5 shows the near-field in the form of a re-image at a distance 1040 mm from the focusing mirror.

Fig. 6 shows a flat top hat profile which occurs between the far field and the re-image at a distance of 730 mm. This beam shape with its sharp cut-offs and uniform power profile is due to the lack of coherence effects, as each waveguide laser is operating independently. There are many materials processing applications where such a high power density, highly homogeneous beam is desirable. Conventional coherent laser sources usually require some form of beam homogeniser or scanning system to remove the unwanted structure present in the beam to produce a similar spatial power distribution.

4. BEAM REFORMATTING

The ability to reformat or manipulate the spatial distribution of power within the composite array beam is possible because each of the waveguides is an independent laser source of high beam quality. With the present packing density, the beams do not begin to overlap until ~ 0.3 m from the output mirror, allowing optical components to be placed close to the laser to redirect individual beams. Beam reformatting will allow several different tasks to be performed on the laser outputs, such as increasing the packing density of the array beam by reducing the "dead space" between each of the beams, or repositioning beams to form novel 2-D shapes. An example of the latter will be a close packed hexagon formed by transforming the beams from a rectangular array. This type of composite beam will produce a uniform top hat beam with an approximately circular boundary at the appropriate distance from a lens.

The ability to close pack the array beams outside the laser allows greater freedom when designing the 2-D array. The fill factor across each level is 80% in the present design, but between levels it is much less due to the necessary electrode thickness required to allow water cooling. Consequently, the "raw" beam quality factor is very low in the stacking direction [4], but this is no longer a serious concern if the array packing density can be modified outside the laser.

For initial demonstration of two reformatting techniques, a linear 7 element array has been used as the laser source.

a) Two mirror beam shaping

The first method uses two rectangular mirrors set parallel to each other, but with both a vertical and horizontal offset. The two mirrors are then tilted as a pair to specific angles in the x and y plane relative to the array beam. The mirror pair is then positioned as in Fig. 7 to allow the first 3 beams of the array directly through, whilst the next 3 beams are doubly reflected and emerge alongside the first three. The seventh beam makes two passes through the mirror pair and thus is shifted by twice the amount in the x and y planes. This method was first demonstrated by Clarkson *et al.* [7] for a linear laser diode array as a method of decreasing the M^2 of one plane by increasing it in the other. The method is much easier to implement with the CO₂ array, due to the good beam quality and hence large Rayleigh range within which to carry out the reformatting.

Fig. 8 shows the results of the reformatting and the trade of M_x^2 for M_y^2 . The reduction in peak intensities of the reformatted beam is not due to mirror losses, but is a result of beam divergence due to the increased propagation paths of the shifted beams. In the future, the mirror separation should be decreased and the angles of incidence of the mirror pair increased, to minimise the path length differences between the different beams exiting the reformatting optics.

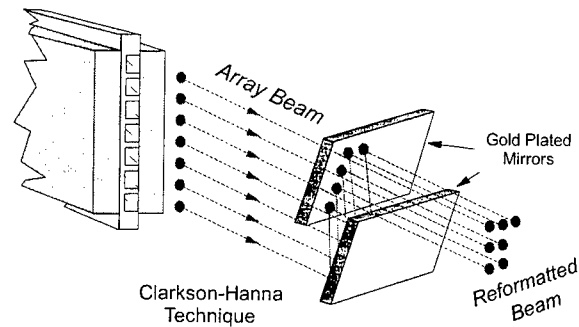


Fig. 7 Two mirror beam reformatter

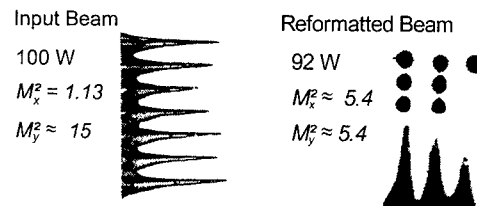


Fig. 8 Reformatted 7 element beam

b) Diffractive optic beam reformatting

The technique is shown in Fig. 9, and uses a matched pair of diffractive optic elements (DOEs) fabricated using standard VLSI methods. In an initial demonstration, the linear array is converted into a non-close packed hexagonal structure. The first array of DOEs redirects the individual beams to form the new pattern at a desired plane, where the second DOE is placed to restore the beams to parallelism. The initial DOEs are gold coated fused silica substrates and use a four level binary amplitude surface relief. The resulting spatial distribution at the second DOE position is shown in Fig. 10, and it can be seen that some of the power is not being fully redirected due to the limited diffraction efficiency of the four level structure. The present experiment demonstrates some of the design and optical alignment issues of the technique. Future improvements will use 16 level DOEs with a theoretical efficiency of 98% with silicon substrates for better power handling, and will aim for higher packing density.

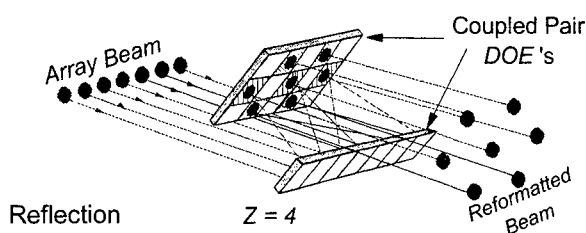


Fig.9 Coupled pair of DOE arrays

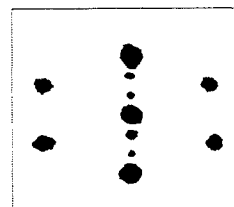


Fig. 10 Spatial distribution of power in reformatted beam

5. CONCLUSION

A new constructional architecture for densely packed CO₂ waveguide arrays has been introduced to allow volume scaling of the total power output of sealed-off, diffusion cooled lasers into the multi-kilowatt regime. Such lasers will be of value where there is a requirement for custom shaped beam profiles on a workpiece, such as surface treatment, cladding, etc. The beam reformatting techniques discussed here give a high level of flexibility in the arrangement of the multiple beams, for example by increasing the packing density of the beams to improve the average beam brightness, converting linear and rectangular arrays to a circular cross section, or generating process specific beam shapes.

6. REFERENCES

1. W. J. Witteman, M. Llieva, B.L. Llyukhin V. N. Kolesnikov, V. N. Ochkin, Yu. B. Udalov, "Waveguide CO₂ laser with a power per unit length of about 1W/cm." *Sov. J. Quantum Electron.* **22**, 879-80 (1992)
2. K. M. Abramski, A. D. Colley, H. J. Baker, D. R. Hall, "Power scaling of large area transverse radio frequency discharge CO₂ lasers." *Appl. Phys. Lett.* **54**, 1833 (1989).
3. G. I. Kozlov, V. A. Kuznetsov, V. A. Masyukov, "High power multi-beam CO₂ laser." *Sov. Tech. Phys. Lett.* **4**, 53-54 (1978)
4. K. M. Abramski, A. D. Colley, H. J. Baker, and D. R. Hall, "High power two -dimensional waveguide CO₂ laser arrays." *IEEE. J. Quantum Electronics*, **32**, 340-48 (1996).
5. A. Lapucci, G. Cangioli, "Triple slab radio-frequency discharged CO₂ laser." *Appl. Phys. Lett.* **62**, 7-9 (1993)
6. J. D. Strohschein, W. D. Bilida, H. J. J. Seguin, C. E. Capjack, "Enhancing discharge uniformity in a multi-kilowatt radio frequency excited CO₂ slab array" *Appl. Phys. Lett.* **68**, 1043-45 (1996)
7. W. A. Clarkson, D. C. Hanna, "Two-mirror beam-shaping technique for high power diode bars." *Optics Lett.* **21**, 375-377 (1996)

Self activated, forced convective cooling in pulsed slab CO₂ laser

Y. Sintov, A. Gabay and S. Yatsiv
Racah Institute of Physics, The Hebrew University
Jerusalem 91904, Israel

ABSTRACT

A marked improvement is observed in the performance of pulsed microwave excited slab CO₂ laser when the gas is permitted to expand following a discharge pulse. The gas pressure changes following each discharge pulse indicate a heating followed by expansion and contraction stages. a sequence of over ten reciprocating cycles is observed after each pulse.

Two modes of operation (Open vs. Closed) were investigated. The gas motion in and out of the discharge space in the open structure, leads to a faster overall cooling than for fully confined gas.

Pressure changes driving the reciprocating motion of the activated gas are monitored.

Maximum average output power of 20W with 10% efficiency and about 1KW peak power were obtained from the open structure at gas pressure of 210mmHg. The absence of the expansion cooling mechanism in the closed structure caused about 40% reduction in the output power and efficiency.

The results of the present research suggest a new architecture for pulsed lasers that provides a gas cooling markedly faster than the conductive cooling of a stagnant gas in the same geometry.

Keywords: CO₂ laser, convective cooling, slab laser, microwave excitation, elevated pressure, pulsed operation

1. INTRODUCTION

In this paper we present a new method for cooling the activated gas of a pulsed slab CO₂ laser operating at elevated pressure.

Following the discharge pulse, the gas is free to expand out of the discharge space and subsequently contract back, mixed with cold gas swept from the outside.

The effect of this cooling was discovered in a pulsed microwave excited laser, where the discharge volume is limited to a small fraction of the cavity space.

The original design is based on the strip-line (slab) concept^{1,2,3}. In This configuration a narrow gas layer permits a high conductive heat flux to the confining metal walls. The results of the present research indicate that, for pulsed operation, the enhanced convective heat flow can practically replace conduction as a prime channel for heat disposal.

At the beginning of the 90's Nishimae et al⁴ and Marz et al⁵ extended the stripline technique to microwave excited CO₂ lasers. The reduced stability of the microwave excited plasma was countered by the introduction of a dielectric ballast strip in series with the plasma column. This, combined with a high repetition rate microwave pulses (10KHz-40KHz), enabled a quasi-CW laser operation at low pressures.

The original motivation of the present research was to extend the application of cooling across a thin gas layer, to a pulse mode operation at elevated pressures without gas flow. A rapid heat disposal across a thin gas sheath yields considerable peak and average laser powers.

Evidence for the contribution of an additional cooling channel due to motion of the gas driven by the discharge pulse, was noted when gas from the active region was permitted to expand out of the discharge space and return to its original position after cooling. Improved performance of the laser in an open structure is observed.

2. EXPERIMENTAL SET-UP

Figure 1(a) illustrates the system design. Four Hitachi 2M130 oven magnetrons feed separately the laser head through an impedance matching network consisting of a directional coupler, matching screws and a quarter wave transformer. The laser head is used both as a microwave resonator and a laser cavity. The cross section of the laser head is shown in fig. 1(b). Microwave radiation is introduced, through a Quartz coupling window, into the laser head, constructed from a double ridge waveguide with 3.5mm Quartz slab attached to the lower ridge. the guided wavelength ($\lambda_g=17.3\text{cm}$) of the ridge waveguide and its length (34.5cm) support a TE_{104} resonance mode only.

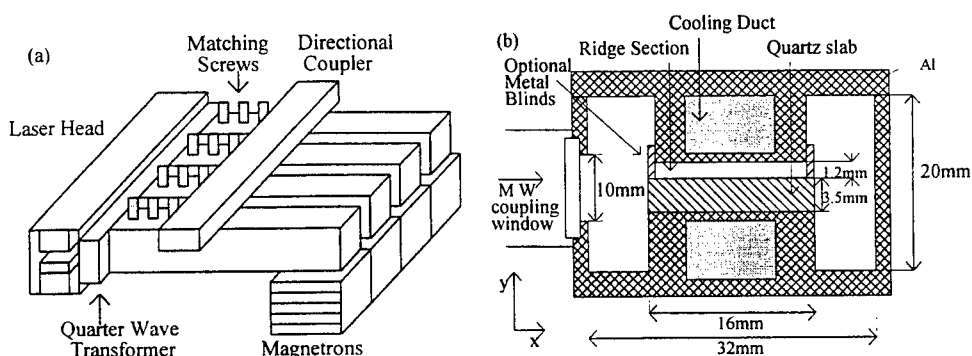


Fig. 1: (a) Experimental set up. (b) Cross section of the laser head

The discharge strikes only in the ridge section where the microwave electric field is largest. The plasma height is 1.2mm long. Standard laser gas mixture ($\text{CO}_2:\text{N}_2:\text{He} \equiv 1:1:8$) at a pressure of 210mmHg occupies the entire resonator space.

The laser resonator is a spherical total reflector with 5m radius of curvature and a 90% reflection plane output coupler, posted at both ends of the laser head. It generates a Hybrid laser mode with a waveguide properties in the y axis and Hermit-Gauss mode in the x axis.

Metal blinds can be posted on both sides of the ridge slab, Confining the gas and preventing its expansion.

Each of the four 2M130 magnetrons can deliver 10KW microwave power in 10 μsec long pulses and 2KHz repetition rate. Overall peak microwave power introduced into the plasma can reach 30KW.

Average power dissipation in the plasma was measured calorimetrically by two thermometers posted at the cooling water inlet and outlet. water flow capacity was $4.3 \frac{\text{liter}}{\text{min}}$. Average laser power was monitored by Ophir Power Meter. Pressure changes were monitored by a Kistler Piezotron pressure transducer (211B5) located at the middle of the discharge cross section.

The gas temperature outside the ridge space was monitored by a chromel alumel thermocouple placed at the center of one side lobe of the cavity.

3. RESULTS

Each of the four magnetrons feed the discharge section facing its coupling window.

At 210mmHg (optimal for laser operation), The pulse duration is constrained by stability considerations to 10 μ sec. Longer pulses result in the appearance of filaments between the upper ridge plate and the quartz slab. At gas pressure lower than 180mmHg, spurious discharges appear at the coupling windows, accompanied by a reduction in the laser performance.

Considering the cross section of a ridge waveguide (fig.1(b)), Two modes of operation were applied:

- An open structure permitting the gas, heated by a discharge pulse, to expand out of the ridge space and return following its cooling.
- A closed structure, confining the gas to the ridge space by metal blinds electrically insulated from the bottom electrode.

Average laser power and efficiency are plotted as a function of the pulse rep rate in figure 2. The microwave pulse duration and peak power are 10 μ sec and 16KWatt, respectively. It is to be noted that the laser average power and efficiency remain equal in both structures up to about 600Hz. The average laser power (fig. 2(a)) reaches a maximum at 1.55KHz in the open and at 1.05KHz in the closed structure, indicating a lower cooling rate between discharge pulses at the closed structure. An average power increase of up to 60% is measured in the open compared to the closed structure.

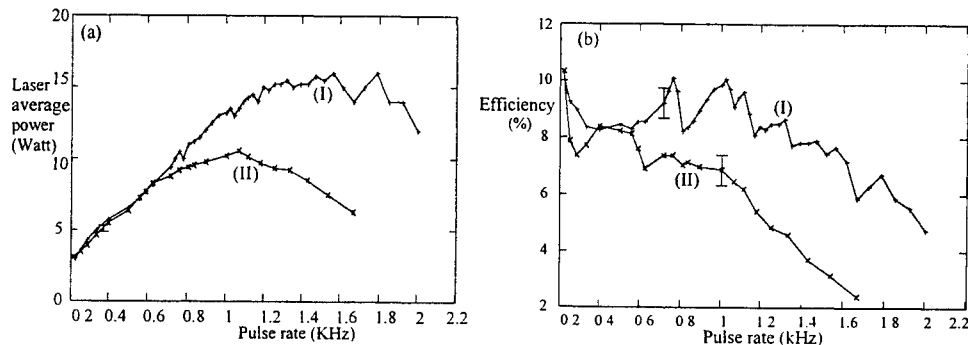


Fig. 2: laser Average power and efficiency dependence on pulse repetition rate.
(I) open structure. (II) closed structure.

Maximum efficiency of Over 10% (fig. 2(b)) was reached in the open structure for 1KHz rep rate and declined at higher rates. In the closed structure, maximum efficiency of 8% was reached around 500Hz.

Fig. 3 illustrates gas pressure oscillations in the open configuration following a discharge pulse. Over ten pressure cycles follow each pulse, indicating a reciprocating gas motion, in and out of the ridge space, in the open geometry. The frequency of these free pressure oscillations is about ten times higher than a characteristic pulse rep-rate.

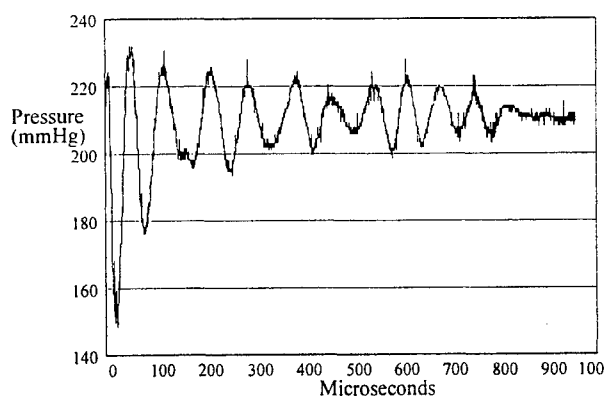


Fig. 3: Pressure oscillations induced by a single discharge pulse.

Fig. 4 shows the temperature of the gas, outside the ridge space as a function of the average power deposited in the discharge. For 250W (optimal for laser operation) a temperature of 20° above ambient was recorded.

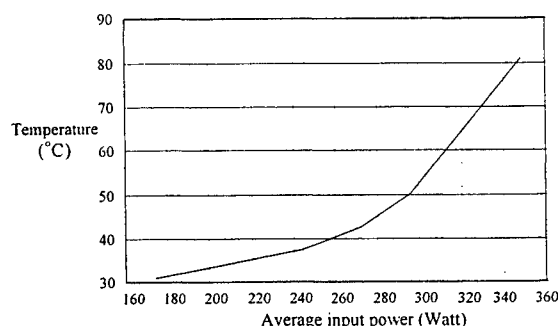


Fig. 4: Gas temperature at the middle of a ridge side lobe, for different input powers.

4. DISCUSSION

The foremost result of the present investigation is the enhanced average laser power, at the higher pulse repetition rate, in the open structure (Figs 2(a) and 2(b)). We associate this with the improved gas cooling due to its motion in and out of the discharge ridge space.

At low rep-rates the time between consecutive pulses is long enough to permit the gas temperature, heated by the discharge, to fall back to its level before excitation, by diffusive cooling alone. At such pulse rates there is therefore no observable difference between open and closed geometries (Fig. 1(a) and 1(b)).

For a given discharge pulse energy, the average input power is proportional to the pulse rate. For a train of pulses in a steady state, the gas, heated by a discharge pulse, must cool down to its initial temperature, during the interval between pulses. As the pulse repetition rate increases, the time between consecutive pulses becomes shorter and the steady state gas temperature at the beginning of each pulse rises above the ambient. The energy of each single laser pulse goes down. It follows that as the pulse rate increases, the average laser power is affected by two opposing trends: A decline of the single pulse energy due to the temperature rise and a power increase due to the higher rep-rates.

For an optimal laser average power, a trade-off must therefore be found between these opposite trends. In the present research the results of this trade off were determined empirically.

Optimal average pulse-train power improves with the efficiency of gas cooling between pulses. In an ideal situation, where the gas can be cooled to the temperature of the cooling water for any rep-rate frequency, the average power could increase toward the peak power level.

In the practical situation of the present research, optimal average laser power was higher in the open than the closed geometry, indicating a faster cooling.

Extra cooling in an open structure is due to a combination of the forced convective cooling and a diffusive cooling of the gas in the ridge space. The effectiveness of the convective cooling improves upon lowering the temperature of the gas in the side lobes. In our setup this takes place by conduction to the metal walls and thence to the water in the single cooling duct.

Still higher rep-rate frequencies and laser average powers can be obtained in an open structure in a system designed for a better cooling of the gas outside the ridge space. We predict progressively higher laser average powers with improvement of gas cooling in the cavity side lobes (fig. 1(b)).

5. SUMMARY

Self activated forced cooling provides an additional channel for cooling a laser gas mixture in pulsed mode operation. The "burden" of cooling is shared between conduction to the confining walls in the ridge space and forced convection to the cavity side lobes. It is as if we effectively increase the gas contact area with the water cooled walls and the entire cavity becomes part of a heat converter. Since the excitation by microwaves is not unique, the same cooling "philosophy" could be applied also for RF excitation or for a repetitive discharge of a capacitor.

For a system designed well for utilizing this self activated forced cooling the advantage of cooling in a thin sheath strip-line gas layer becomes less important.

At high rep-rates, a clear advantage is gained in an open versus closed structure, provided by a better cooling due to the gas motion.

The cooling mode described in the present research is a basis for a new compact breed of pulsed lasers with interesting capabilities for material processing and medicine.

6. REFERENCES

1. S. Yatsiv 1987 *Gas Flow And Chemical Lasers* (Berlin : Springer) 252-257.
2. K. M. Abramski, A. D. Colley, H. J. Baker and D. R. Hall, "Power scaling of large area transverse radio frequency discharge CO₂ laser", *Appl. Phys. Lett.* **54**, 1833 (1989).
3. R. Nowak, H. Opower , U. Schafer, K. Wessel, Th. Hall, "High power CO₂ waveguide laser in the 1KW category", in *CO₂ lasers and applications II* (SPIE Vol. **1276**, The Hague (1990)).
4. J. Nishima and K. Yoshizawa, "Development of CO₂ laser excited by 2.45GHz microwave discharge", *SPIE* **1225** 340-8 (1990).
5. M. Marz and W. Oestreicher, "Microwave excitation of a diffusion cooled CO₂ laser", *J. Phys. D: Appl. Phys.* **27** 470-474 (1994).

A High Power, High Modulation Bandwidth CO₂ Laser

David Wheatley

James Howden & Co Ltd, Howden Laser Division

Kings Cross Road, Dundee, DD2 3EL, UK

ABSTRACT

A 1kW laser capable of full depth modulation in excess of 200kHz has been developed to satisfy a significant need within the printing plate engraving industry. The Howden Laser LE1500-OA design is based upon a 1.5 kW diffusion cooled CO₂ laser converted into an oscillator-acousto-optic-modulator-amplifier configuration. A novel method is used to limit unwanted noise emissions from the high gain amplifier at the 'zero' setting.

The design is being used successfully within systems manufactured by ZED Instruments Ltd to engrave flexographic printing plates at several production sites involved in packaging and label printing.

Keywords: Carbon dioxide laser, fast modulation, super-radiance control, flexography, printing.

1. INTRODUCTION

In a recent article, it was suggested that¹

'... the challenge for laser gravure and flexography cylinder etching is to increase the modulation bandwidth of very-high-power lasers significantly above 30kHz.'

This statement highlights a significant gap in laser technology. The problem is associated with the use of the pumping mechanism itself to control laser output. In lasers capable of high power cw output, the pumping mechanism generally involves a long time constant which limits the ability of the laser output to respond to rapid changes of the input.

For high power CO₂ lasers modulated through their DC or RF discharges, this time constant is of the order of 0.1ms, limiting the full-depth response to a few kilohertz. The bandwidth can perhaps be stretched to 10kHz by gas adjustments, usually at the expense of power. Further modest gains can be made in practice if the process can tolerate movements away from full-depth modulation. Nevertheless, for bandwidths 'significantly above 30kHz', a different approach is required.

The need for a wide bandwidth laser source came to the fore when ZED Instruments Ltd sought to improve the speed of its well-established range of laser engravers. ZED were seeking a two- to three-fold increase in processing capability and judged that a specification of 200kHz would open up considerable possibilities for fast processing at high resolution. Switching speed, so long a limiting factor in the many processes not requiring great engraving depth, would essentially cease to be a consideration. Howden Laser Division (formerly Laser Ecosse Ltd) recognized that such a device would fill a significant gap in laser technology and offer opportunities in a range of applications such as perforating, scribing, non-metal and even metal processing. Accordingly, a development programme for a 200kHz device was agreed between ZED and Howden Laser, with a specification of 1kW cw output power.

2. CHOICE OF TECHNOLOGY

Devices such as electro-optic modulators (EOMs) and acousto-optic modulators (AOMs) provide the means for switching CO₂ laser beams quickly. However, they are typically limited to handling a few tens of watts of laser power. Although AOMs are now being developed for handling a few hundred watts of laser power, these are expensive, relatively untried devices made from a material (germanium) susceptible to catastrophic failure. Taking into account its likely efficiency, an AOM would need

to handle over 1.5kW to provide a modulated 1kW output. As such, it was clear that the direct approach did not represent a viable engineering solution to the problem of controlling a 1kW output beam.

In order to make use of standard switching devices, it was decided to use an oscillator-modulator-amplifier configuration. The modulator would operate within its power capability and its output would be amplified to the 1kW level. While the EOM route offered some theoretical advantages, experience suggested that these devices involved problems in performance repeatability and in sourcing. On the other hand, AOMs were a relatively standard technology offering repeatable performance and fairly wide availability. It was therefore decided to adopt an oscillator-AOM-amplifier configuration.

Previous work on an oscillator-amplifier design had indicated that a slow flow device could provide good amplification of low power beams as a result of its necessarily long gain length. A fast axial flow device, on the other hand, usually has relatively little gain length since its strength lies in its high saturation intensity. As a rough guide, therefore, a fast axial flow amplifier is efficient at amplifying high power beams (say 1kW and above) while a slow flow amplifier is more efficient at lower power levels. The need to amplify a beam from tens of watts up to 1kW therefore pointed to a slow flow design of amplifier as being the most efficient choice.

3. DESIGN OF THE DEVICE

The Howden MF1500 laser is a slow flow device producing in excess of 1.5kW of CO₂ laser power. It consists of 12 'legs' of discharges in V-fold configuration providing 24m of gain length. It was decided to use this laser as the basis of an oscillator-amplifier system, using 1 leg for the oscillator and the remaining 11 legs for the amplifier.

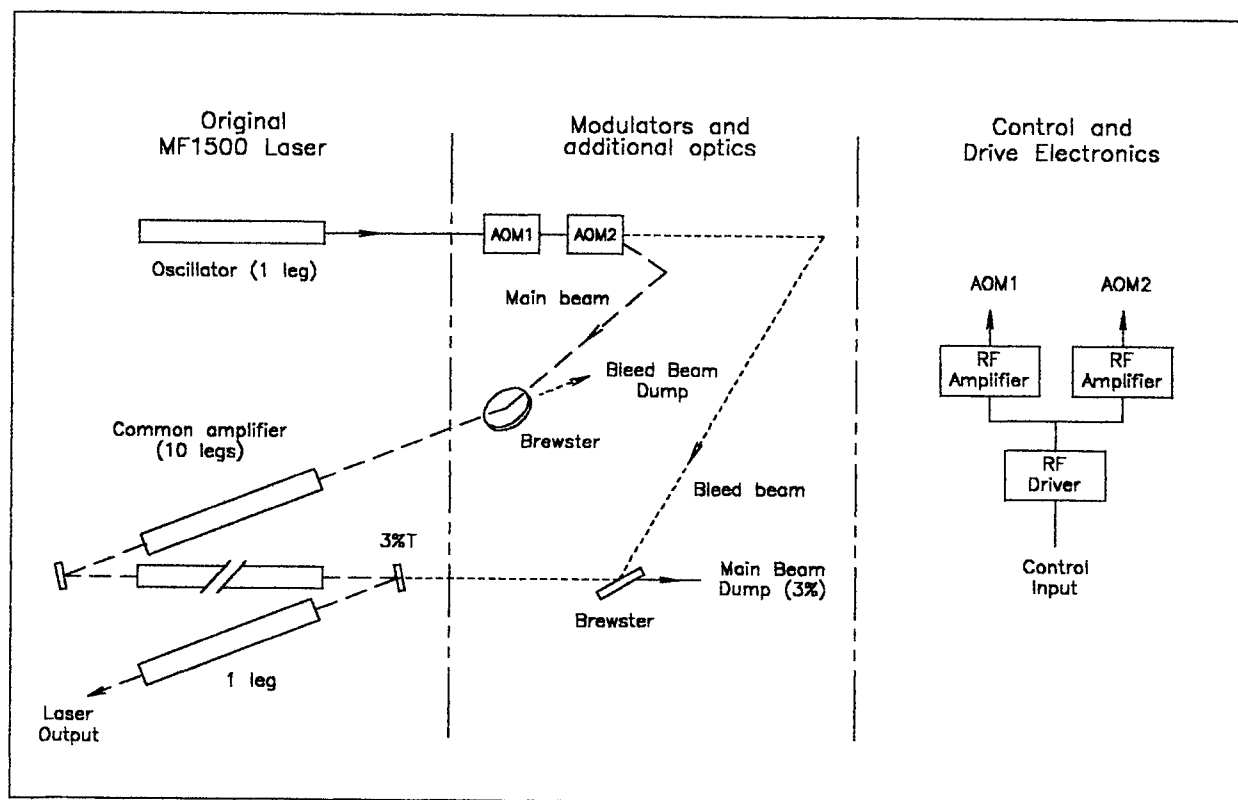


Figure 1. Schematic of the LE1500-OA Laser

It is characteristic of AOMs that they impose on the beam a frequency shift equal to the RF drive frequency (here 40MHz). Given a free spectral range of around 50MHz for the oscillator, and pressure broadening of around 100MHz in the amplifier, this would have a noticeable effect upon the beam amplification. By using 2 AOMs driven from the same RF source and arranged for zero net frequency shift, this effect can be removed.

One serious problem with a very high gain amplifier is its super-radiant output in the absence of any input. Measurements indicate that the present amplifier is capable of generating around 200W of super-radiant output from each end of the amplifier – a problem for the process at one end and the AOMs at the other. One method of overcoming this is to give the amplifier something else to amplify when the main input is zero or very low. In this design, a second beam is introduced into the amplifier with linear polarization orthogonal to that of the main beam.² This second beam bleeds off power from the amplifier when the main input is itself too low. The 'main' and 'bleed' beams are separated at each end of the amplifier by Brewster windows.

A schematic of the system is shown in figure 1. A single leg oscillator generates a linearly polarized beam which is attenuated and then directed into the pair of AOMs. The AOMs are driven by RF power which allows each AOM to deflect between 0% and over 70% of the beam into the first order in a continuously variable fashion. The deflected beam emerging from the 2 AOMs is used as the main beam input which is directed into the 11 leg amplifier to provide the laser output. The undeflected beam emerging from the 2 AOMs is used as the bleed beam input, which is made to enter the amplifier with its polarization orthogonal to that of the main beam. In order to avoid contamination of the output beam by bleed beam power, the bleed beam is fed backwards down the amplifier. For reasons of convenience in the physical layout, the bleed beam is only fed down ten of the amplifier legs.

Because of the very high small signal gain of the amplifier, it was found that a relatively small bleed beam input signal would suffice to produce an output considered large enough to suppress super-radiance. Accordingly, the bleed beam is introduced into the amplifier via a 3% transmissive window. When the main beam input is low or zero, this input generates a high output. When the main beam input is high, the main / bleed output ratio is roughly equal to the input ratio. The small consequent loss to the main output power is minimized by the action of the AOMs which reduce the bleed beam input as they increase the main beam input in correct synchronization. The result is that the amplifier always generates at least 500–600W of laser power, suppressing any tendency towards super-radiance. The amplifier is effectively operated as a 'flip-flop' or 'see-saw', generating wanted power from one end and/or unwanted power from the other. A calculated graph of the powers is shown in figure 2.

The two beams are separated at each end of the amplifier by enhanced Brewster windows. At the main beam input position, the main beam input reflects from the Brewster as s-polarization while the amplified bleed beam is transmitted to a dump as p-polarization. At the bleed beam input position, the bleed beam input reflects from the Brewster as s-polarization while around 30W of the amplified main beam, which is inevitably leaked by the 3% transmissive window, is transmitted to a dump as p-polarization.

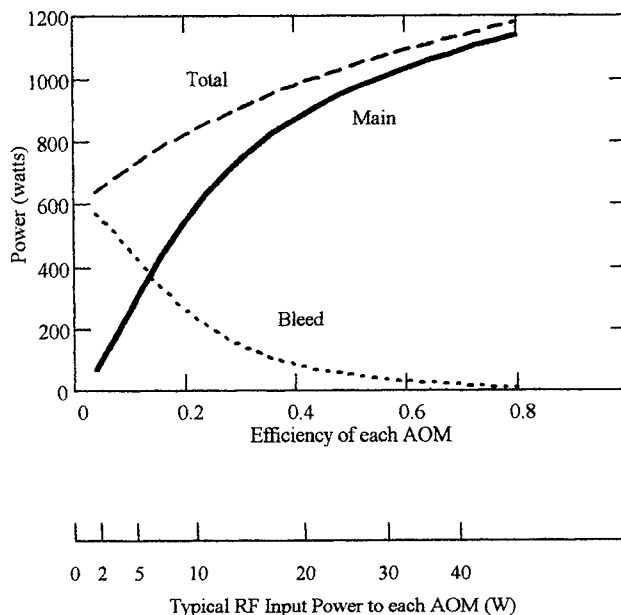


Figure 2. Calculated Behaviour of the Main and Bleed Output Powers as the AOM Deflection Efficiency is Varied

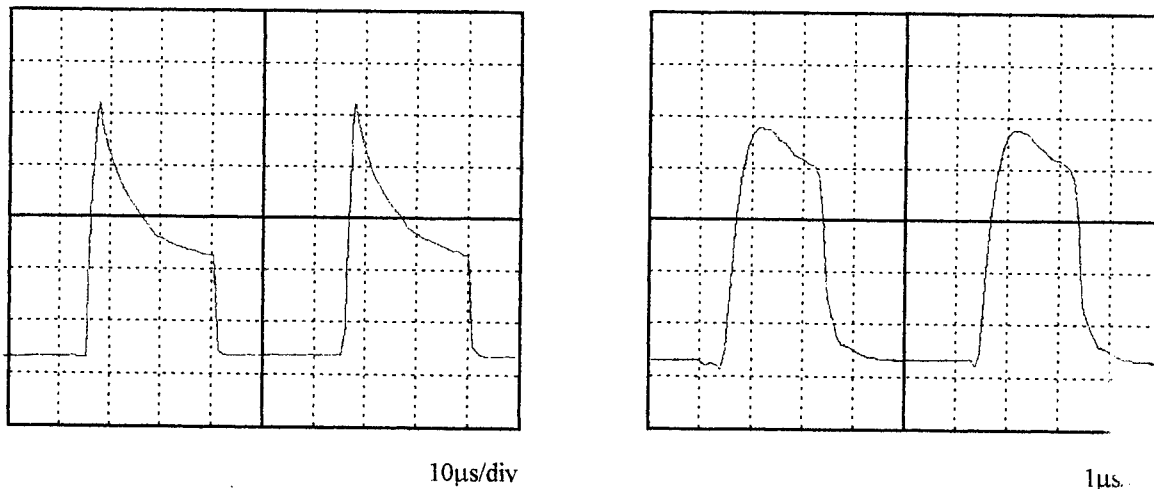


Figure 3. Power Output Traces from the LE1500-OA Laser
Power measured on a cadmium-mercury-telluride detector (vertical scales differ)
Laser operating with 50% duty cycle control input at 20kHz (left trace) and 200kHz (right trace)

4. LASER PERFORMANCE

Trials with a basic oscillator-amplifier configuration indicate that the device is capable of generating in excess of 1400W cw compared with a typical 12-leg oscillator output of 1750W. With the AOMs fitted, the oscillator output is attenuated to around 35W to protect the AOMs, which are specified for 100W operation. The main beam input is then less than 20W taking into account the efficiency of, and losses in, the AOMs. The cw output of the oscillator-AOM-amplifier configuration is around 1100W maximum.

When 'zero' power is selected, some power has been found to emerge from the laser through backscattering of the bleed beam from internal surfaces. However, the polarization of this unwanted output is that of the bleed beam and can therefore be attenuated to the desired level. The LE1500-OA 'zero' output is specified to be below 2W and would typically be below 1W. The cw power level can be varied continuously between the zero and maximum levels by varying the control signal level to the RF driver. Figure 2 includes typical values for the RF input power as the AOM efficiency and laser output vary.

Figure 3 illustrates the laser output obtained when the RF driver is fed with a square wave (ie 50% duty cycle) control input at 200kHz. The trace represents the output of a cadmium-mercury-telluride detector sensing a fraction of the laser output. The switch-on and switch-off both occur within 1 microsecond, easily achieving full depth modulation at the 200kHz frequency. Experience indicates that full depth modulation extends to around 500kHz, with significant modulation being

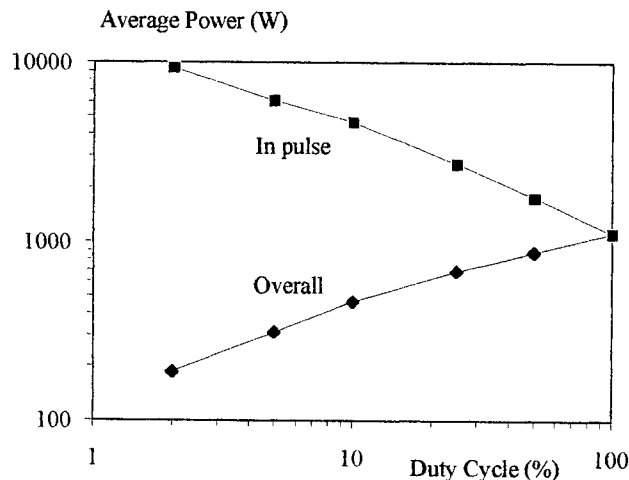


Figure 4. Measured Power Enhancement in 1μs Pulses

achievable above 1MHz. Also evident is a slight shortening of the 'on' time, which is caused by small differences in the time the acoustic signal reaches the beam in the 2 AOMs and by the 'AND' nature of their operation.

Figure 3 also shows a square wave trace at 20kHz which emphasizes the enhancement obtained at the leading edge of the pulse. Measurements of average power at different pulse settings confirm a significant pulse enhancement for low 'on' times. Figure 4 illustrates the average power emitted by the laser for different duty cycles with a constant 'on' time of 1 μ s. From these figures are derived values for the average power within each pulse. (Experiments at a constant frequency of 20kHz produced an almost identical graph which has therefore been omitted for clarity.) At the lowest duty cycle of 2% (1 μ s pulse every 50 μ s) the average output power is nearly 200W with pulses averaging nearly 10kW. At 10% duty cycle, pulses averaging 4.5kW are available at an average power of 450W. For applications where pulse enhancement is not unacceptable at an 'on' transition, it has been found that the effect can be much reduced by using a ramped rather than sharp control signal. This technique has been used successfully in the flexography application.

5. FLEXOGRAPHY APPLICATION

Flexographic printing is based upon the principle of the rubber stamp. A polymeric surface is engraved such that the non-printing surface is removed while the remaining raised surface becomes the printing surface. The polymer in question forms the surface of a metal roller typically 200 to 400mm in diameter and 1 to 2m long. The polymer may be in the form of a seamless sleeve or surface coating, or a plate wrapped around the surface.

In laser engraving of flexographic rollers, a nozzle focuses the beam onto the surface of the polymer. By spinning the roller at the same time as tracking the nozzle slowly along the roller axis, both at constant speed, the nozzle describes a helical path over the whole surface of the polymer. The polymer material is removed directly by the high power beam to a depth depending upon the power and the rotation speed. The image is formed by switching the laser off (printing surface) or on (non-printing surface), with an element of ramping being imposed at each transition in order to provide a shoulder or buttress to strengthen the print surface. The controllability of the laser power at this stage allows the system to produce precise shoulder profiles in a manner not available in chemical-etching systems.

For a 40 μ m axial movement of the nozzle per revolution (ie less than the beam focus diameter), a target production speed of 1m²/hour implies a surface rotation speed of around 7m/s. Assuming that a similar circumferential resolution is required, the laser switching speed required is $7\text{m/s} \div 40\mu\text{m} = 175\text{kHz}$. Note that this resolution easily exceeds the 200 μ m dot pitch encountered in a good, 120 dots per inch half-tone (grey-scale) image. The LE1500-OA has achieved these speeds in a production environment. Although higher speeds have been found to be within the laser's modulation capabilities, the process can then become power limited.

6. FUTURE WORK

The LE1500-OA laser has now proved itself over nearly two years at several production sites engaged in packaging and label printing. Consideration is being given to a higher power version for increased depth and/or production speed. In addition, a test programme is being developed to assess the capabilities of the technology for non-printing applications. While the design has obvious advantages for perforating applications, the significant power enhancement available may prove beneficial for scribing and both metal and non-metal processing³.

7. REFERENCES

- 1 Gibbs R, 'Printing benefits from new technologies', *Laser Focus World*, pp 77-82, Nov 1995.
- 2 British Patent Application no. 9408439.9 'High Power Laser Amplifier'.
- 3 Michaelis A, Schäfer J-H, Uhlenbusch J, Viöl W, 'Cutting and welding of aluminum with a high repetition rate pulsed CO₂ laser', *CO₂ Lasers and Applications II*, SPIE Vol 1276, pp 231-241, 1990.

Pulsed CO₂-laser with 15 kW average power at 100 Hz rep-rate

G. Renz, M. Jung *, W. Mayerhofer, and E. Zeyfang

DLR, Institut für Technische Physik, Pfaffenwaldring 38-40, D-70569 Stuttgart, Germany

ABSTRACT

An electron-beam controlled, pulsed CO₂-laser with an average output power of more than 15 kW will be presented. Laser operation has been achieved for pulse energies up to 180 J at repetition rates of 100 Hz, pulse durations variable between 3 and 10 μ s, and bursts of 1000 shots with an unprecedented reliability.

Keywords: high-average power pulsed CO₂-laser, electron beam controlled laser

1. INTRODUCTION

Pulsed high-pressure CO₂-laser development has been conducted now for over three decades, resulting in the availability of a laser system with high output power and high output energy per pulse¹. The application of the pulsed high-pressure concept to CO₂-laser gases has been performed by different excitation techniques during the stages of laser development. Beginning with the earlier method of discharge current limitation through arrays of pins and resistors, the development continued toward the UV-preionized discharge and the electron-beam controlled discharge. The most successful method of producing a plasma having the properties of being uniform, large in volume, and stable, is done by the use of an electron-beam controlled discharge. There, the electron beam is switched on and off, and controls the ionization of the gas. The separate discharge electric field can be chosen for an optimized pumping process and can be delayed with respect to the electron beam. Recently, attention in CO₂-laser development has shifted toward a laser system with a high degree of reliability at higher repetition rates and, consequently, at higher average output power, as well as longer bursts of operation. With the advent of economical and reliable solid state components in the inverter circuits of the constant current power supply system, a high reliability as well as a significant weight and volume reduction of the overall pulsed power system has been achieved. This paper will present the design and the experimental verification of a repetitively pulsed high power CO₂-laser based on the principles of an electron beam preionized configuration. Preionization refers here to the presence of charged particles in the laser medium prior to the initiation of the main discharge. With an average output power of more than 15 kW, a variable pulse duration between 3 and 10 μ s at a laser gas pressure of approximately 0.75 atm, a pulse repetition rate of up to 100 Hz and pulse trains of 1000 shots, the laser system operates with an unprecedented reliability.

2. POWER CONDITIONING OF THE LASER SYSTEM

The electrical design of the laser system divides the pulsed power parts of the e-beam and the main discharge CO₂-laser into three major sub-systems: the power supplies, the modulators (Pulse Forming Networks: PFNs), and the load. The efficiency of the CO₂-laser is commonly known to be approximately 10 %. A laser pulse energy of typically

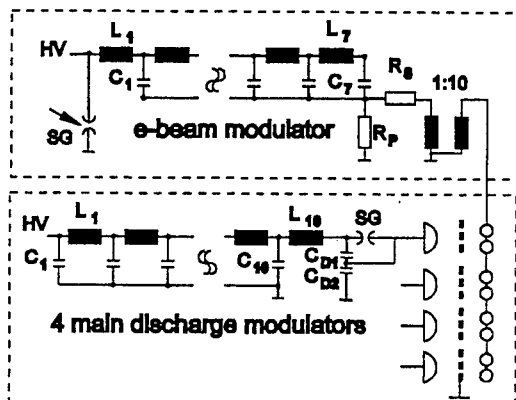


Figure 1. Electrical circuits of the laser system.

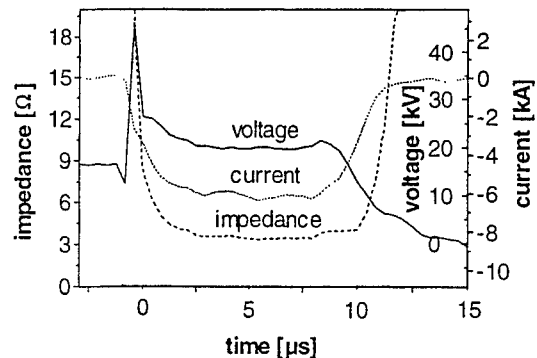


Figure 2. Temporal behavior of main discharge.

* present address: AMS, Fraunhoferstr. 22, 82152 Martinsried/München

150 J and a repetition rate of 100 Hz requires a minimal electrical stored energy in the PFNs of 1.5 kJ per pulse and a charging rate of 150 kJ/s. The power supply of the main discharge is divided into 20 parallel units (constant current modules, Maxwell Laboratories) each having 11 kJ/s at a loading voltage of 50 kV. At a repetition rate of 100 Hz (10 ms), the interpulse period for the charging process can take up to 8 ms. The remaining 2 ms are required for the charge control and the recovery of the spark gaps². The power supplies feed 4 modulators (PFNs) with an impedance of 3 Ω (10 elements: $L = 6 \mu\text{H}$, $C = .04 \mu\text{F}$, 10 μs duration; $L = 3 \mu\text{H}$, $C = 10 \times .04 \mu\text{F}$, 5 μs duration; cf. Fig. 1), and a stored energy of 500 J per pulse and per PFN³. As an electrical switch, a self-triggered air spark gap (Beverly III and Associates) with a super-sonic gas flow is used for each individual PFN⁴. At a loading voltage of 45 kV, a current of 6 kA ($di/dt = 2 \text{ kA}/\mu\text{s}$), is supplied from the PFNs to the CO_2 -laser gas load. The temporal structure of a main discharge pulse with a pulse duration of 10 μs is shown in Fig. 2. By the use of a capacitive voltage divider (cf. Fig. 1), an internal synchronization technique was applied to the main discharge (see Section 4). The main discharge is delayed with respect to the penetrated electrons from the e-beam accelerator by 1 to 2 μs , and therefore they preionize the laser gas with high energy electrons of 200 keV. During the time of discharge, the impedance of the main discharge decreases to 3 Ω . The maximum gas loading reaches 150 J/l atm. The average field strength between the main discharge electrodes is 2 kV/cm and the current density is 3 A/cm². This leads to an input power density of 6 kW/cm³. Assuming a drift velocity of $3 \cdot 10^6 \text{ cm/s}$, the electron number density calculates to $5 \cdot 10^{12} \text{ 1/cm}^3$.

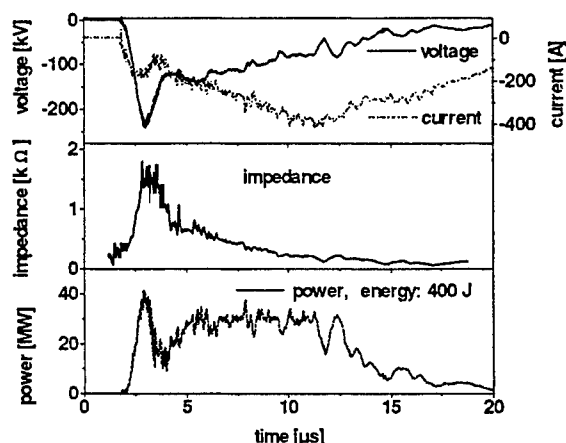


Figure 3. Temporal behavior of cold-cathode electron beam accelerator.

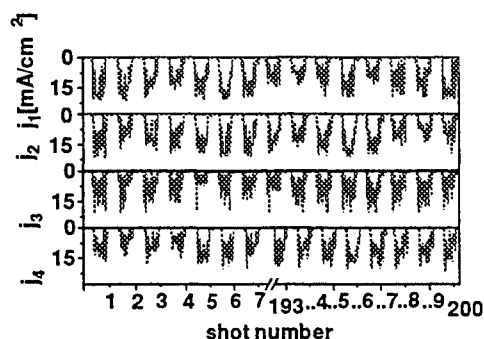


Figure 4. Electron current density of e-beam accelerator measured at the 4 segmented main discharge electrodes at a laser gas pressure of $\frac{3}{4}$ atm.

The power supply system for the e-beam accelerator is divided into 10 parallel units, each having 10 kJ/s. These power supply units feed 2 PFNs with an impedance of 2.4 Ω (7 elements: $L = 3 \mu\text{H}$, $C = .15 \mu\text{F}$, 10 μs duration) at a stored energy of 1 kJ per pulse (cf. Fig. 1). The electrical switch of the e-beam is a triggered spark gap with a super-sonic air flow. The voltage of max. 30 kV and the current of 7.5 kA is then transformed with a pulse transformer (ratio 1:10, Stangeness) up to 250 kV in the peak. Figure 3 shows the temporal behavior of the voltage, current, and impedance at the secondary side of the cold-cathode e-beam accelerator. The temporal behavior of the impedance is determined by the impedance of the e-beam PFNs, the parallel resistor $R_p = 100 \Omega$, the series resistor $R_s = 0.6 \Omega$ (low inductance resistor), and the e-beam load (cf. Fig. 1). The secondary impedance rises in the first 2 μs to 1.5 k Ω due to the cable impedance of approximately 200 pF (AA 7583) between the transformer and the e-beam load; then the impedance falls off to nearly 0.3 k Ω , which is determined by the series resistor R_s , until the closure time ends the electron extraction from the graphite plasma. In Fig. 4, the electron beam current density, measured with Rogowski-coils at the 4 segmented main discharge electrodes, is shown. The laser gas pressure was set to 0.75 atm. The electron current density of the e-beam accelerator at the main discharge electrodes is reduced to 10 mA/cm² due to scattering effects of the electrons at the gas molecules. The electron number density at the entrance of the laser chamber is calculated to $5 \cdot 9 \cdot 10^{10} \text{ 1/cm}^3$. This initial electron number density is in the same order of magnitude as compared to UV-preionized TEA- CO_2 -lasers^{5, 6, 7}. There, preionization is an indispensable mean for self-sustained discharges at high pressure. This

leads to the conclusion that the parameters of the e-beam accelerator are well suited for the preionization of the laser gas, as well as for maintaining an entire stable discharge pulse.

3. THE LASER SYSTEM

The complete 15 kW laser system is shown in Fig. 5. The laser beam is extracted on the left hand side of the picture by a scraper of an unstable resonator ($R_1 = -11.6$ m, $R_2 = 18$ m, $L = 3.18$ m). The effective main discharge volume is 24 liters ($10 \times 12 \times 200$ cm³).

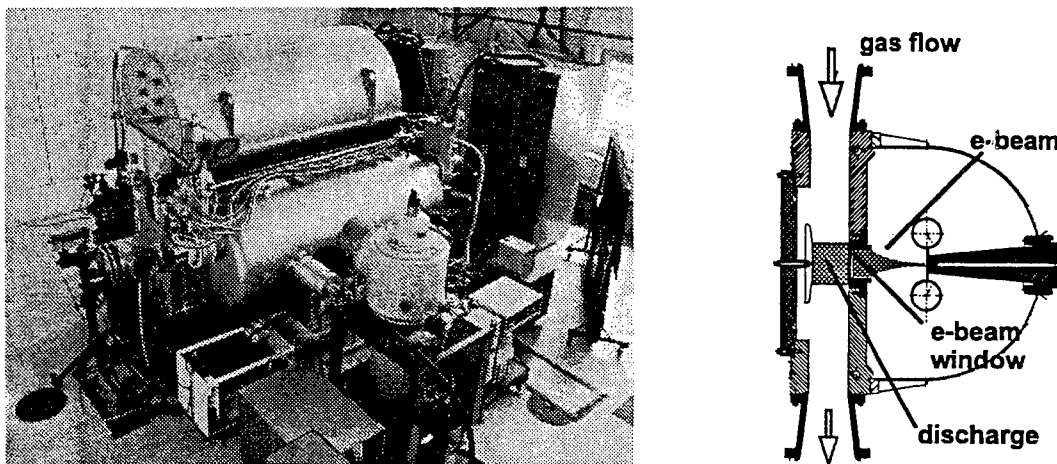


Figure 5. Electron-beam controlled CO₂-laser system (left), cross-sectional view of laser (right).

The power supply units (100 kJ/s for the electron beam accelerator, 220 kJ/s for the main discharge) are located on the far right side of the system. The 4 modulators (PFNs) of the main discharge cannot be seen in this picture because they are hidden by the laser gas circulating chamber. The front part of the laser system shows the electron beam accelerator with the vacuum system (1 diffusion pump in the middle of the electron beam chamber, 2 cryogenic pumps on the sides). The 2 modulators (PFNs) are located underneath the vacuum chamber of the electron beam accelerator. The presented laser system has been tested at full specifications in sequences of 1000 pulses at 100 Hz and intermissions of 10 minutes. This time interval is used to reduce the pressure in the electron beam accelerator chamber to less than $1 \cdot 10^{-6}$ mbar. During operation of the e-beam accelerator, the pressure rises to a constant level of approximately $5 \cdot 10^{-5}$ mbar. The right hand side of Fig. 5 shows a cross-sectional view of the laser cavity with the in- and outlets of the gas flow and the electron beam accelerator chamber. The extracted electrons from the graphite plasma of the cold cathode beam accelerator are guided to the anode window (Hibatchi structure) by the use of electrostatic forces from the corona ring structure. The distance between the graphite cathode and the electron beam window is 15 cm. The transparency of the window grid is approximately 75 %. For voltages higher than 100 kV, almost all electrons pass the 25 μ m Kapton foil without substantial energy loss. The overall shot number of the laser system has so far reached $1 \cdot 10^5$ pulses with a very good reproducibility from shot to shot. The temporal structure of 3 laser pulses at a laser gas pressure of 0.75 atm for different PFN inductances is shown in Fig. 6 (left) as well as 7 pulses of a burst of 1000 shots for a pulse duration of 10 μ s at a repetition rate of 100 Hz (right). The power loading of the main discharge is 150 J/l atm and the specific output energy gives 10 J/l atm. The temporal behavior of the laser pulse follows the temporal behavior of the voltage at the main discharge electrode (cf. Fig. 2). The tail of the laser pulse is in a steady state, nonself-sustained regime ($E/N \cong 1 \cdot 10^{-16}$ Vcm²)⁸. The peak of the laser pulse results from the transient behavior of the laser light and laser medium interaction and is delayed by a few hundred nanoseconds with respect to the onset of the main discharge.

4. INTERNAL SYNCHRONIZATION OF MULTIPLE MODULATORS

In the charging sequence, the 4 modulators of the main discharge are loaded to a maximum of 50 kV. At an operating pressure of 0.75 atm in the laser chamber and an interelectrode separation of 12 cm, the self-breakdown voltage between the electrodes is approximately 20 kV. When using a voltage divider (cf. Fig. 1, $C_{D1} = C_{D2} = 2$ nF), the voltage between the main discharge electrodes is kept below the self-breakdown limit until the electrons from the electron

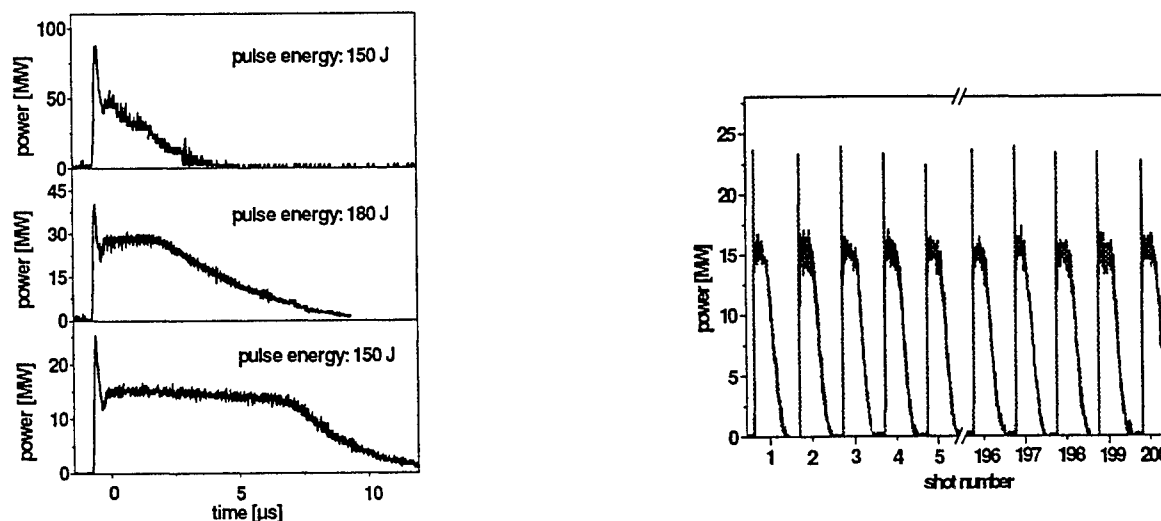


Figure 6. Temporal behavior of laser pulses (left), burst of laser pulses at 100 Hz (right).

beam accelerator are drifting into the laser cavity. The impedance of the laser gas is then reduced and the full loading voltage appears across the spark gap electrodes and initiates the breakdown in the switch. The only trigger signal used in the system is the trigger pulse for the ignition of the electron beam accelerator switch. This internal synchronization scheme is very cost effective and very reliable in operation.

5. SUMMARY

The successful development of a high-pressure, pulsed CO₂-laser with an average output power of more than 15 kW has been accomplished. The laser system operates at a repetition rate of up to 100 Hz, pulse energies of up to 180 J, and variable pulse length between 3 and 10 μs. The overall system has been tested for bursts of 1000 shots, and a total shot number of $1 \cdot 10^5$ has so far been achieved without any major misfunctions of the system. One main key element of the system is the reliable operation of the cold cathode electron beam accelerator with a voltage of up to 250 kV. The laser pulses show an unprecedented reproducibility from shot to shot at full specifications of the system.

6. REFERENCES

- [1] W.L. Bohn, 'High gas laser research in Germany', in: Gas lasers -Recent developments and future prospects, *NATO ASI Series, 3. High Technology- Vol. 10*, Kluwer Academic Publisher, 1996.
- [2] E. Strickland, F. Cathell, K. Harris, D. Bilak, and J. Jichetti, 'High regulation, capacitor charging power supplies', Maxwell Lab. Inc., San Diego, Ca., presented at the 1995 SPIE Conference in San Jose, Ca., USA.
- [3] M. Jung, W. Mayerhofer, G. Renz, and E. Zeyfang, 'High power CO₂-laser at 100 Hz rep-rate', *Power Modulator Symposium*, Boca Raton, FL, USA, 1996.
- [4] R.E. Beverly III and R.N. Campbell, 'Transverse-flow 50-kV trigatron switch for 100-pps burst-mode operation', *Review of Scientific Instruments*, Vol. 67, p. 1593, 1996.
- [5] R.K. Garnsworthy, L. Mathias, and C. Carmichael, 'Atmospheric-pressure pulsed CO₂-laser utilizing preionization by high-energy electrons', *Appl. Phys. Lett.*, Vol. 19, No. 12, p. 506, 1971.
- [6] O. Wood, II, 'High pressure pulsed molecular lasers', *Proc. of the IEEE*, Vol. 62, No. 3, p. 355, 1974.
- [7] S. Suzuki, Y. Ishibashi, M. Obara, and T. Fujioka, 'Dependence of laser output on initial photoelectron density density in TEA CO₂ laser', *Appl. Phys. Lett.* 36(1), p. 26, 1980.
- [8] W. L. Nighan and W.J. Wiegand, 'Influence of negative-ion processes on steady-state properties and striations in molecular gas discharges', *Phys. Rev. A*, Vol. 10, No. 3, p. 922, 1974.

6. Beam Delivery, Beam Shaping, and Nonlinear Optics

Hollow Fiber Beam Delivery Systems

Yuji Matsuura and Mitsunobu Miyagi
Department of Electrical Communications
Tohoku University, Sendai, 980-77, Japan

ABSTRACT

For delivery of high-power IR laser light, hollow-core fibers have advantages of ruggedness, environmental stability, and high-power threshold over the IR solid-core fibers, such as fluoride glasses, metal halides, and chalcogenides fibers. In this paper, we focus on the hollow-fiber beam delivery system for high power mid-IR lasers with more than 1-kW CW power or 1000 mJ pulse energy and review the current status of hollow fibers by showing the system designs and the tested results.

Keywords: infrared fibers, hollow waveguides, infrared lasers

1. INTRODUCTION

Hollow fibers are a leading candidate for use as a delivery system of mid-infrared lasers because of the advantages of high power thresholds, ruggedness, and no end reflection.¹ Specially for the high-power lasers with CW-power of more than 1 kW or pulsed-energy more than 1000 mJ, hollow fibers show the best performances as a flexible delivery system since solid-core fibers specially designed for mid-IR light usually have lower power capability due to the end reflection and the absorption slightly remained in the core region.

Recently, high-power lasers represented by CO₂ lasers have become very popular in laser-machining, printing, and welding applications. Simultaneously, some groups have developed and tested beam delivery systems for the high powered lasers using hollow fibers. In this paper, we review the current status of hollow fibers by showing the system designs and the tested results.

2. TYPES OF HOLLOW FIBERS

Hollow-core fibers for high-power laser delivery are categorized into two groups by the structures. First one is a dielectric-coated metal fiber and the second one is a fiber utilizing attenuated total reflectance.

2.1 Dielectric-coated, metal, hollow fibers

Though the metal-tubing fibers have the high attenuation specially for TM and hybrid modes, an inner dielectric coating which is properly designed reduces the attenuation loss drastically. The basic concept of this type of fiber was proposed in Ref. [2] and the structure is shown in Fig. 1. The fiber is consisted of a metal tube or a metal film deposited on the inside of a supporting tube, and a single or multiple dielectric film which is transparent at the desired wavelengths. The optimum thickness of the single dielectric film is²

$$d_{opt} = \frac{\lambda}{2\pi\sqrt{n_1^2 - 1}} \tan^{-1} \left[\frac{n_1}{(n_1^2 - 1)^{1/4}} \right] \quad (1)$$

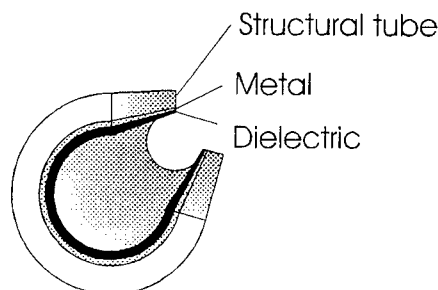


Fig. 1: Structure of dielectric-coated metal hollow fiber

where λ is wavelength and n_1 is refractive index of the dielectric. The power-attenuation constant 2α of the lowest order, HE_{11} mode is theoretically expressed as

$$2\alpha = 2\left(\frac{u_0}{\pi}\right)^2 \cdot \frac{\lambda^2}{(2T)^3} \cdot \frac{n}{n^2 + \kappa^2} \cdot \left[1 + \frac{n_1^2}{\sqrt{n_1^2 - 1}}\right]^2 \quad (2)$$

where $n-j\kappa$ is a complex refractive index of the metal layer. $2T$ is the bore diameter, and u_0 is a mode-dependent parameter which equals 2.4048 for the HE_{11} mode.

Various materials have been employed as the metal and dielectric layer and some fabrication methods have been proposed. The research group, fabrication methods, and metal and dielectric materials used in the fibers are summarized as follows.

- 1) A metallic fiber based on a nickel supporting tube which is formed by the electroplating technique was developed at Tohoku University.³ A silver film is employed as the metal layer because of the lower $n/(n^2 + \kappa^2)$ value in Eq. (2) than nickel in the mid-IR region. As the dielectric material, Ge,⁴ ZnSe,⁵ and ZnS⁶ were employed and ZnS is the most preferable due to the lower refractive index, high chemical stability, and no toxicity.
- 2) Plastic hollow fibers fabricated by using a wet chemistry technique was developed at Tel Aviv University.^{7,8} A silver film is firstly deposited on the inside of the plastic tubing and then an AgI layer is formed by flowing iodine inside.
- 3) A group at Rutgers University modified the Croitoru's technique and adopted silica capillary tubing as the supporting tube.⁹ Because of the surface smoothness and uniform circularity of the glass supporting tube, the fiber shows very low-loss and excellent performances in the output beam quality.¹⁰
- 4) Laakman *et al.* developed a fabrication technique employing a metal strip coated with Ag and PbF₂.¹¹ The strip is rolled and inserted into the stainless-steel supporting tube.
- 5) Morrow *et al.* employed an extruded silver tube as the supporting material. They first etch the bore to make it smooth and then, an AgBr is deposited by flowing Br₂ down the bore.¹²
- 6) A group at Tohoku University deposited a polyimide¹³ or a fluorocarbon-polymer¹⁴ film on the inside of silica capillary tubing on which a Ag film is coated inside in advance by the wet chemistry method. The polymer films are deposited by using a liquid-flowing deposition technique.

2.2 Attenuated total reflectance fibers

This type of hollow fibers utilizes the anomalous dispersion of metal oxides. As shown in Fig. 2, complex refractive indices $n-j\kappa$ of metal oxides show resonance dispersion in the mid-IR wavelengths. In the region where $n < 1$ and $\kappa \ll 1$, the fiber shows behavior that is similar to the solid-core fibers whose clad index is lower than the core index. From the viewpoint of geometrical optics, the $n < 1$ clad-index causes high reflectance that is close to total reflectance at the inside surface of the fiber and, thus, it leads to the low attenuation. Some groups have studied the properties of oxide glasses as tubing material of the attenuated total reflectance fibers.

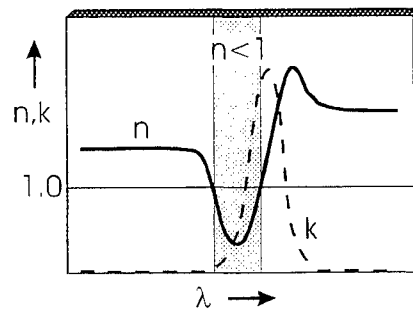


Fig. 2: Complex indices of metal oxides

- 1)Hidaka *et al.* firstly proposed the concept and investigated the characteristics of $\text{GeO}_2\text{-ZnO-K}_2\text{O}$ glasses for CO_2 laser light transmission.¹⁵
- 2)Worrell's group studied the optical properties of oxide glasses for using as a CO_2 waveguide lasers.¹⁶
- 3)Because Al_2O_3 has the $n < 1$ region at around $10\text{ }\mu\text{m}$ wavelength, low attenuation is expected at the CO_2 laser wavelength. Sapphire-crystal hollow fibers for CO_2 laser light was investigated at Rutgers University.^{17,18} Sapphire hollow fibers have very high heat resistivity and, therefore, it is appropriate material for transmission of high-power laser light.

3. HIGH-POWER LASER DELIVERY SYSTEMS USING HOLLOW FIBERS

3.1 CO_2 laser delivery systems

A. Ge-Ag system

A laser delivery system for a kW-class CO_2 lasers by using the metal hollow fiber coated with Ag and Ge films was developed at Hitachi Cable.^{19,20} The fiber is fabricated by the following method:

- 1)Ge and Ag films are sputtered onto a leachable Al tubing.
- 2)a Ni structural layer is formed on the films by electroplating, and
- 3)the Al tubing is removed by flowing alkaline solution inside.

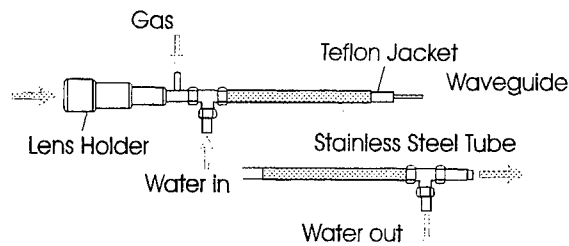


Fig. 3: Protective jacket for Ge-Ag hollow waveguide

Though the fiber itself is rugged and has high heat resistivity, for high-power lasers of kW-class, it is better to use a jacket to protect the fiber from mechanical shock and temperature increase. Figure 3 shows the protective cooling jacket of the hollow fiber for high-power delivery system that is designed for applications of laser material processing.¹⁹ The fiber has a $0.45\text{-}\mu\text{m}$ thick Ge and $0.1\text{ }\mu\text{m}$ -thick Ag films and the bore diameter is 1.7 mm . The total length of the delivery system is 2 m . The fiber is cooled by water from outside and Ar gas from inside.

Figure 4 shows the transmission of straight and bent fibers. The loss for 3 kW -input power is as low as 0.33 dB/m and, as shown in Fig. 5, the fiber bent with 70-cm displacement of the output end is still low as 1.5 dB .²⁰

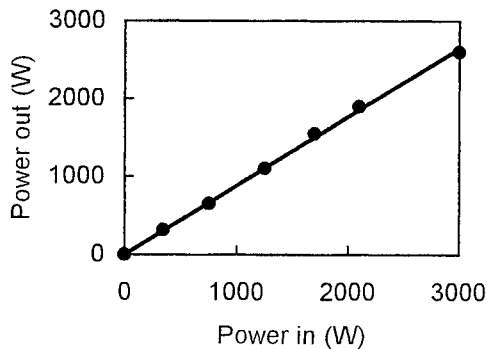


Fig. 4: Transmission of Ge-Ag hollow fiber

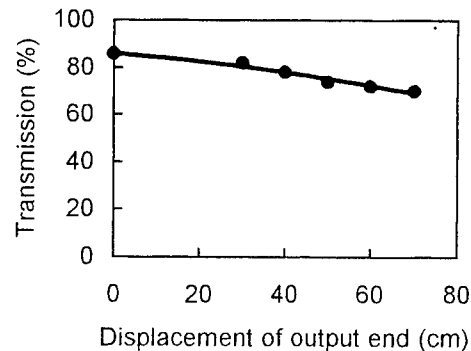


Fig. 5: Bend losses

B. AgI-Ag system

Harrington *et al.* tested their AgI-Ag hollow fiber that is formed on glass-capillary tubing for high-power. CO₂ laser light.²¹

Figure 6 is a schematic of the fiber cooling jacket used in the high-power test. The water jacket is 1/4-in. polyethylene tubing and cooling water of 18 °C is forced over the fiber. The fiber is 1.5-m long and the bore diameter is 700 μm.

Figure 7 shows the transmission of the AgI-Ag glass hollow fiber. The maximum output power from the straight fiber is 1010 W that is limited only by the laser power source and the attenuation is 0.46 dB/m. The fiber bent in a 15-cm-radius 360° loop is also as low as 0.89 dB/m.

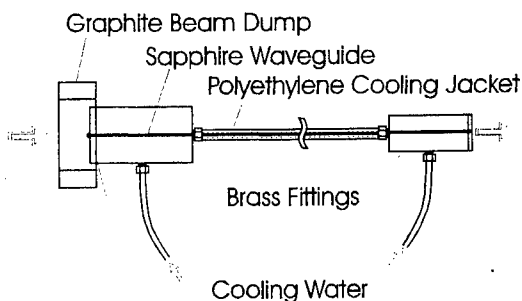


Fig. 6: Cooling jacket for AgI-Ag fiber

C. Sapphire hollow fiber

The transmission properties of the sapphire hollow fiber for the high-power lasers were investigated by Harrington *et al.* using the same cooling jacket as in Fig. 3.²¹ Figure 8 is the measured transmission of the sapphire hollow fiber. The length and bore size are 1.2 m and 1070 μm, respectively. The maximum output power of 1900 W was obtained for the 2500 W input. The attenuation is 0.99 dB/m that is affected by the poor quality of the input beam-profile.

Though the sapphire crystal fiber is somewhat stiff, it can be bent in relatively large radii. The transmission of the bent sapphire fibers is 85% of the straight fiber for 40 cm-deflection of output end.

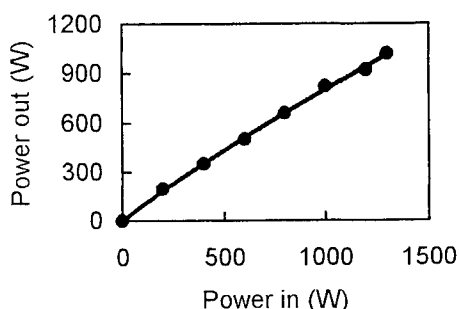


Fig. 7: Transmission of AgI-Ag fiber

3.2 Er:YAG laser delivery systems

A. ZnS-Ag system

The ZnS-Ag coated metal fiber fabricated by sputtering and electroplating technique was tested by Miyagi *et al.*²² They employed an acid-soluble glass as a leachable mandrel to get the inner-surface smoothness. High pulse energy of 1.6 J at 5 pps was used in the test, however, a water cooling jacket is not necessary because the low average power of 8 W that has almost no heating effect on the fibers.

Figure 9 is the input-output energy of the 800-μm bore, 116-cm long fibers. The straight fiber shows the loss of around 0.75 dB that is independent of the input energy. The loss of the fiber bent 180° at a 30-cm radius is 1.8 dB.

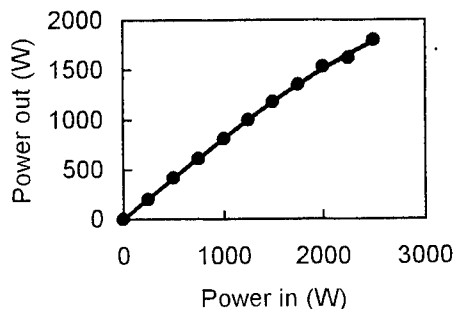


Fig. 8: Transmission of sapphire hollow fiber

B. Polyimide-Ag system

Figure 10 shows the transmission of the polyimide and Ag-coated fiber with the bore size of 700 μm and the length of 2.3 m.^{23,24} The straight fiber show the loss of 0.75 dB at 1100 mJ input energy without any damage on the fiber. The bend loss is 1.2 dB in a 15 cm-radius, 180° bent.

3.3 Other lasers

The dielectric-coated hollow fibers transmits any wavelengths in the mid-IR region when the dielectric is properly chosen and the thickness is designed for the wavelength. There have been some experimental reports on 5- μm -wavelength CO laser,²⁵ and 6.45- μm free-electron-laser delivery.^{26,27}

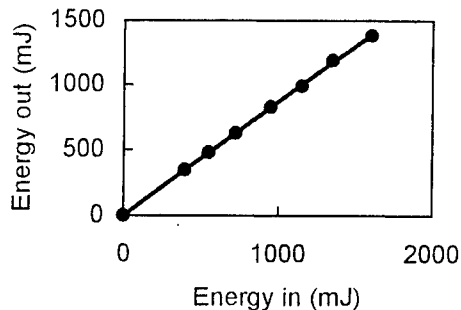


Fig. 9: Transmission of ZnS-Ag fiber for Er:YAG laser

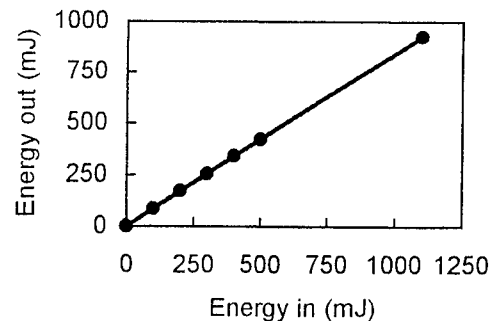


Fig. 10: Transmission of Polyimide-coated fiber for Er:YAG laser

4. CONCLUSION

Many types of hollow fibers have been developed for high-power laser delivery and they all have merits and demerits. The dielectric-coated fibers using a metal structural tube have very low transmission loss and high mechanical strength, however, the fabrication process is complicated and costly. The glass-based, dielectric-coated fibers have high flexibility and the liquid-phase deposition methods used in the fabrication are simple and appropriate for mass production. However, the glass tubing is somewhat brittle in destructive environment. Though the sapphire hollow fiber stands extremely high temperature, it is stiff and the fabrication tends to be costly.

It has been proved and established that the hollow fibers are the excellent media for the delivery of high power IR-lasers because of the ruggedness, flexibility, and low losses. It is now necessary to choose the best type of hollow fibers for each practical uses.

REFERENCES

1. J. A. Harrington, Ed., *Selected Papers on Infrared Fiber Optics*, Milestone Series Vol. MS-9, SPIE, Bellingham, WA, 1990.
2. M. Miyagi and S. Kawakami, "Design theory of dielectric-coated circular metallic waveguides for infrared transmission," *IEEE J. Lightwave Technol.*, vol. LT-2, pp. 116-126, 1984.
3. M. Miyagi, A. Hongo, Y. Aizawa, and S. Kawakami, "Fabrication of germanium-coated nickes hollow waveguides for infrared transmission," *Appl. Phys. Lett.*, vol. 43, pp. 430-432, 1983.
4. A. Hongo, K. Morosawa, T. Shiota, Y. Matsuura, and M. Miyagi, "Transmission characteristics of germanium thin-film-coated metallic hollow waveguides for high-powered CO₂ laser light," *IEEE J. Quantum Electron.*, vol. 26, pp. 1510-1515, 1990.
5. Y. Matsuura, M. Miyagi, and A. Hongo, "Loss reduction of dielectric-coated metallic hollow waveguides for CO₂ laser light transmission," *Opt. Laser Technol.*, vol. 22, pp. 141-145, 1990.

6. Y. Matsuura and M. Miyagi, "Low-loss metallic hollow waveguides coated with durable and nontoxic ZnS," *Appl. Phys. Lett.*, vol. 61, pp. 1622-1623, 1992.
7. N. Croitoru, J. Dror, E. Goldenberg, D. Mendlovic, and S. Ruschin, "Use of metallic and dielectric films for hollow fibers," *Fiber and Integrated Opt.*, vol. 6, pp. 347-361, 1987.
8. N. Croitoru, J. Dror, and I. Gannot, "Characterization of hollow fibers for the transmission of infrared transmission," *Appl. Opt.*, vol. 29, pp. 1805-1809, 1990.
9. T. Abel, J. Hirsch, and J. A. Harrington, "Hollow glass waveguides for broadband infrared transmission," *Opt. Lett.*, vol. 19, pp. 1034-1036, 1994.
10. Y. Matsuura, T. Abel, and J. A. Harrington, "Optical properties of small-bore hollow glass waveguides," *Appl. Opt.*, vol. 34, pp. 6842-6847, 1995.
11. K. D. Laakman and M. Levy, "Hollow lightpipe and lightpipe tip using a low refractive index inner layer," U. S. A. Patent no. 5,005,944, 1991.
12. P. Bhardwaj, O. J. Gregory, C. Morrow, G. Gu, and K. Burbank, "Performance of a dielectric-coated monolithic hollow metallic waveguide," *Materials Lett.*, vol. 16, pp. 150-156, 1993.
13. Y. Kato, M. Osawa, M. Miyagi, S. Abe, M. Aizawa, and S. Onodera, "Loss characteristics of polyimide-coated silver hollow glass waveguides for the infrared," *Electron. Lett.*, vol. 31, pp. 31-32, 1995.
14. M. Osawa, Y. Kato, T. Watanabe, M. Miyagi, S. Abe, M. Aizawa, S. Onodera, "Fabrication of fluorocarbon polymer-coated silver hollow waveguides for the infrared by the liquid-phase coating method," *Opt. Laser Technol.*, vol. 27, pp. 393-396, 1995.
15. T. Hidaka, J. Kumada, J. Shimada, and T. Morikawa, "GeO₂-ZnO-K₂O glass as the cladding material of 940-cm⁻¹ CO₂ laser light transmitting hollow-core waveguide," *J. Appl. Phys.*, vol. 53, pp. 5484-5490, 1982.
16. C. A. Worrell, "Transmission properties of some hollow glass waveguides at 10.6 μ m wavelength," *Electron. Lett.*, vol. 25, pp. 570-571, 1989.
17. J. A. Harrington and C. C. Gregory, "Hollow sapphire fibers for the delivery of CO₂ laser energy," *Opt. Lett.*, vol. 15, pp. 541-543, 1990.
18. C. C. Gregory and J. A. Harrington, "Attenuation, modal, polarization properties of n<1, hollow dielectric waveguides," *Appl. Opt.*, vol. 32, pp. 5302-5309, 1993.
19. A. Hongo, K. Morosawa, T. Shiota, K. Suzuki, S. Iwasaki, and M. Miyagi, "Transmission of 1 kW-class CO₂ laser light through circular hollow waveguides for material processing," *Appl. Phys. Lett.*, vol. 58, pp. 1582-1584, 1991.
20. A. Hongo, K. Morosawa, K. Matsumoto, T. Shiota, and T. Hashimoto, "Transmission of kilowatt-class CO₂ laser light through dielectric-coated metallic hollow waveguides for material processing," *Appl. Opt.*, vol. 31, pp. 5114-5120, 1992.
21. R. K. Nubling and J. A. Harrington, "Hollow-waveguide delivery systems for high-power, industrial CO₂ lasers," *Appl. Opt.*, vol. 34, pp. 372-380, 1996.
22. T. Watanabe, M. Miyagi, S. Schrunder, T. Ertl, G. Muller, L. Beerstecher, "Transmission of 1.6 J Er:YAG laser light by ZnS-coated silver hollow waveguides," *Opt. Laser Technol.*, vol. 27, pp. 389-391, 1995.
23. A. Hongo, M. Miyagi, Y. Kato, M. Suzumura, S. Kubota, Y. Wang, and T. Shimomura, "Fabrication of dielectric-coated silver hollow glass waveguides for the infrared by liquid-flow coating method," *Proc. SPIE*, vol. 2677, pp. 55-63, 1996.
24. L. W. Beerstecher, and M. Miyagi, private communications.
25. Y. Matsuura and M. Miyagi, "Er:YAG, CO, and CO₂ laser delivery by ZnS-coated Ag hollow waveguides," *Appl. Opt.*, vol. 32, pp. 6598-6601, 1993.
26. I. Gannot, R. W. Waynant, J. Dror, A. Inberg, N. I. Croitoru, "Experiments in transmission of free electron laser radiation by flexible waveguides," *Proc. SPIE*, vol. 2677, pp. 99-102, 1996.
27. Y. Matsuura, K. Matsuura and J. A. Harrington, "Power delivery of free electron laser light by hollow glass waveguides," *Appl. Opt.*, 1996, in press.

Beam shaping for laser materials processing with non-rotationally symmetric optical elements

Thomas Henning¹, Marcus Scholl¹, Lars Unnebrink²,
Uwe Habich¹, Rainer Lebert², Gerd Herziger³

¹Fraunhofer-Institut für Lasertechnik, Steinbachstr. 15
D-52074 Aachen, Fed.-Rep. Germany

²Lehrstuhl für Lasertechnik, RWTH Aachen, Steinbachstr. 15,
D-52074 Aachen, Fed.-Rep. Germany

³Deutsche Forschungsanstalt für Luft- und Raumfahrt, Linder Höhe,
D-51147 Köln, Fed.-Rep. Germany

ABSTRACT

This paper gives an overview of recent developments made in using non-rotationally symmetric optical elements (NOEs) for the beam shaping of high power laser radiation at the Lehrstuhl für Lasertechnik and the Fraunhofer-Institut für Lasertechnik. Several applications of NOEs in the IR- and UV-wavelength regions demonstrate the innovative potential of NOEs for laser materials processing.

1. INTRODUCTION

Many applications of materials processing with laser radiation require the workpiece to be illuminated by an intensity distribution which is adapted to the specific process. The intensity profiles produced by commercial high power lasers differ considerably from the profiles best suited to several applications. Thus, the beam delivery system together with optical elements for beam shaping are key components of a laser machine.

A new type of optical element, which can transform the output beam of a high power laser to the desired process-adapted beam profile, is the so called non-rotationally symmetric optical element.¹ NOEs are diamond turned mirrors with an almost arbitrary surface shape so that complex phase transformations can be realised. In the following, fundamental design concepts, experimental investigations and applications of NOEs are presented.

2. BEAM TRANSFORMATION

The principle of beam transformation is the multiplication of a given coherent electromagnetic field by a specific phase function so that, in an image plane, the desired intensity distribution is observed.² Usually beam transformation is realised by diffractive optical elements because the power redistribution from the transformation plane into the image plane requires optical elements having non-rotationally symmetric transfer functions.

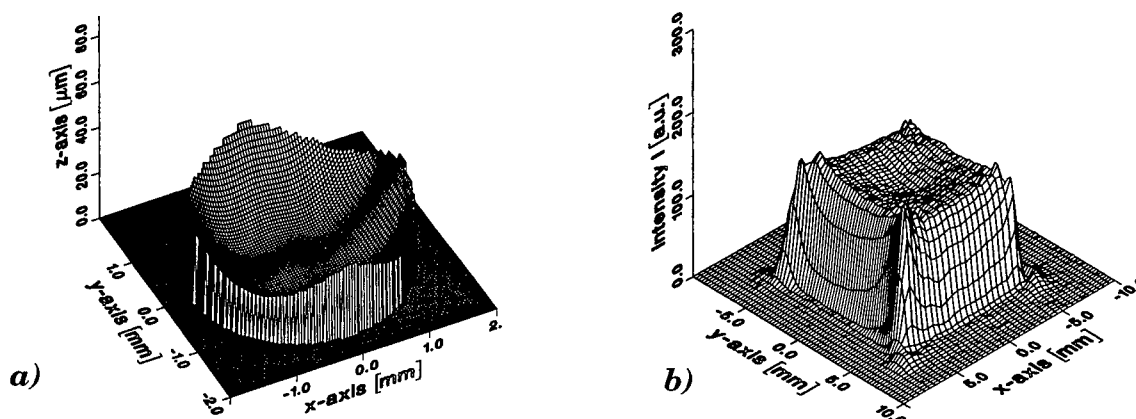


Figure 1. Gaussian to square beam transformation with NOE mirror. (a) Surface function of the mirror, (b) measured intensity profile in focal plane of the mirror (CO_2 laser, TEM_{00} mode, laser power $P_L = 40$ W)

The main disadvantages of using diffractive optical elements in the high power regime are the damage to the surface structure, due to absorption effects and the low efficiency caused by diffraction losses. These problems can be overcome through the use of NOEs. NOEs have the same high radiation resistance than other diamond turned metallic mirrors and the optical energy transfer efficiency between the transformation and image planes is given by the reflectivity of the substrate material.

The most commonly encountered problem with beam transformation is the conversion of a Gaussian laser beam to a square-shaped beam with uniform intensity. Several authors have described the phase function for this transformation.² Using a NOE mirror, the conversion of a 40 W fundamental mode laser beam is performed successfully, with an efficiency of 98 %, cf. figure 1.

3. BEAM INTEGRATION

Beam integration with multifaceted integrating mirrors is the most common concept used in creating homogeneous beam profiles of rectangular geometry. The principle of beam integration is to separate the incident beam into a large number of beamlets and to superpose these beamlets in the focal plane. In a simple geometric optical understanding, the averaging which results from the superposition homogenizes the intensity distribution.

The main disadvantages of conventional multifaceted integrating mirrors are their complex and, therefore expensive manufacture and the limited possibilities for varying the surface shape of the facets in order to generating process-adapted beam profiles.

Monolithic multifaceted integrating mirrors, with almost arbitrary facet surface shape, can be realised using NOE-technology. However, while in the short wavelength region of excimer laser radiation and by application of Nd:YAG laser radiation the beam integration works well, the high degree of spatial coherence of CO₂ laser radiation produces well-known intensity distributions, characterised by interference and diffraction structures, cf. figure 2. The interference is caused by the coherent superposition of the beamlets and the diffraction is caused by the apertures of the facets involved.³

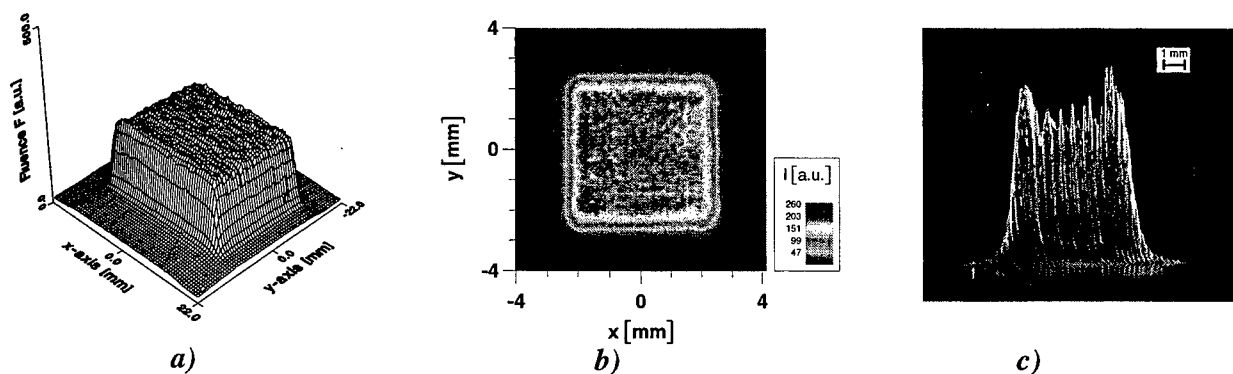


Figure 2. Measurements of beam profiles in the focal plane of NOE multifaceted integrating mirrors at different wavelengths. (a) KrF excimer laser ($\lambda = 248$ nm), (b) Nd:YAG laser ($\lambda = 1.06$ μ m), (c) CO₂ laser ($\lambda = 10.6$ μ m), burn-in in PMMA

4. REDUCTION OF COHERENCE

In many applications, e.g. transformation hardening, the peaks of the integrated intensity distribution of figure 2. c) cause a decline in the surface quality obtained by the laser processing. Theoretical and experimental investigations of the imaging process of a multifaceted integrating mirror show, that a well-aimed reduction of the spatial coherence of the laser radiation can suppress the contrast of the diffraction structure, therefore optimising the homogeneity of the integrated beam profile.³

For a given integrating mirror, the optimal coherence parameters are determined through statistical optics. With the help of a random process, described by these coherence parameters, a statistical rough surface for a NOE phase modulating mirror can be computed. By inserting the NOE phase modulating mirror directly in front of the integrating mirror, and by rotating

it around the axis normal to the surface, statistical phase fluctuations are transferred to the incident laser radiation. This results in a reduction of the spatial coherence, cf. figure 3. a). The experimental results depicted in figure 3. b) confirm that the reduction of the spatial coherence, by the NOE phase modulating mirror, considerably improves the homogeneity of the integrated beam profile. By applying the phase modulating mirror to surface hardening, undesired surface meltings, caused by the diffraction peaks, can be completely avoided.

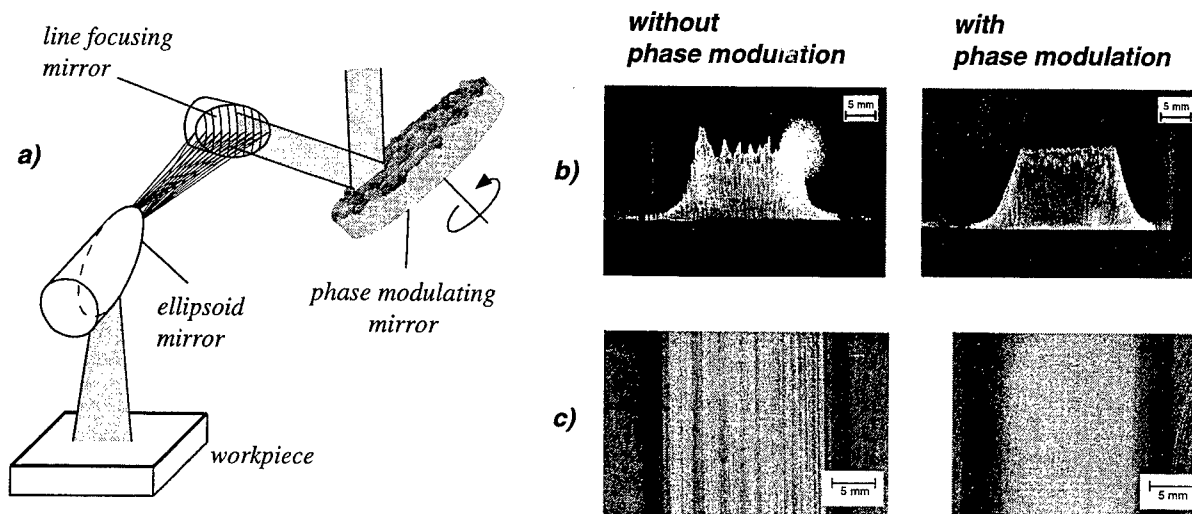


Figure 3. Reduction of the spatial coherence of CO_2 laser radiation by a NOE phase modulating mirror and application to surface hardening. (a) Optical set-up, (b) burn-in in PMMA in plane of workpiece and (c) topview of hardening tracks (material: 40CrMnMo7, laser power $P_L = 1.8 \text{ kW}$, velocity $v_s = 360 \text{ mm/min}$). The dark lines in the left picture indicate surface melting.

5. Beam integration with beamlet shaping

Particularly in UV laser radiation processing, optical components are needed for complex optical transformations to create process-adapted beam profiles. Due to the large losses at the mask, mask imaging processes show low processing efficiencies. Here an appropriate beam shaping should be used to concentrate the optical energy on the apertures of the mask, which results in an improvement of the processing efficiency.

NOE integrating mirrors with arbitrary shaped facet surface profiles offer an appropriate tool for approaching the task of mask-adapted beam shaping. It can be shown that a given beam profile can be obtained, in the focal plane of an integrating mirror, through a suitable choice of individual facet surface function.⁴ This concept of beam integration with beamlet shaping combines the advantages of beam transformation and beam integration. Beam transformation offers the possibility of generating a process-adapted beam profile. Beam integration ensures that the generated beam profile is then independent of the intensity distribution of the incident laser beam.

The concept of beam integration with beamlet shaping is examined for ablation with KrF excimer laser radiation. The task is to ablate acicular shaped geometries in $80 \mu\text{m}$ polyimide foil by means of mask projection techniques. In an experiment, we determined the efficiency of the beam shaping obtained with the optical set-up depicted in figure 4. a). The efficiency is defined by the pulse energy in plane II divided by the pulse energy in plane I. For conventional beam shaping, with an imaging integrator device, an efficiency of 8 % was measured. In the plane of the workpiece an energy density of 963 mJ/cm^2 was measured and 400 pulses were required to generate the desired geometry in the foil. Concentrating the laser energy on the aperture of the mask, through the use of a NOE integrating mirror with non-plane facets⁴, the efficiency can be improved to 34%, cf. figure 4. b). Thus, in the plane of the workpiece, the same energy density can be achieved with only 25% of the input pulse energy in plane I.

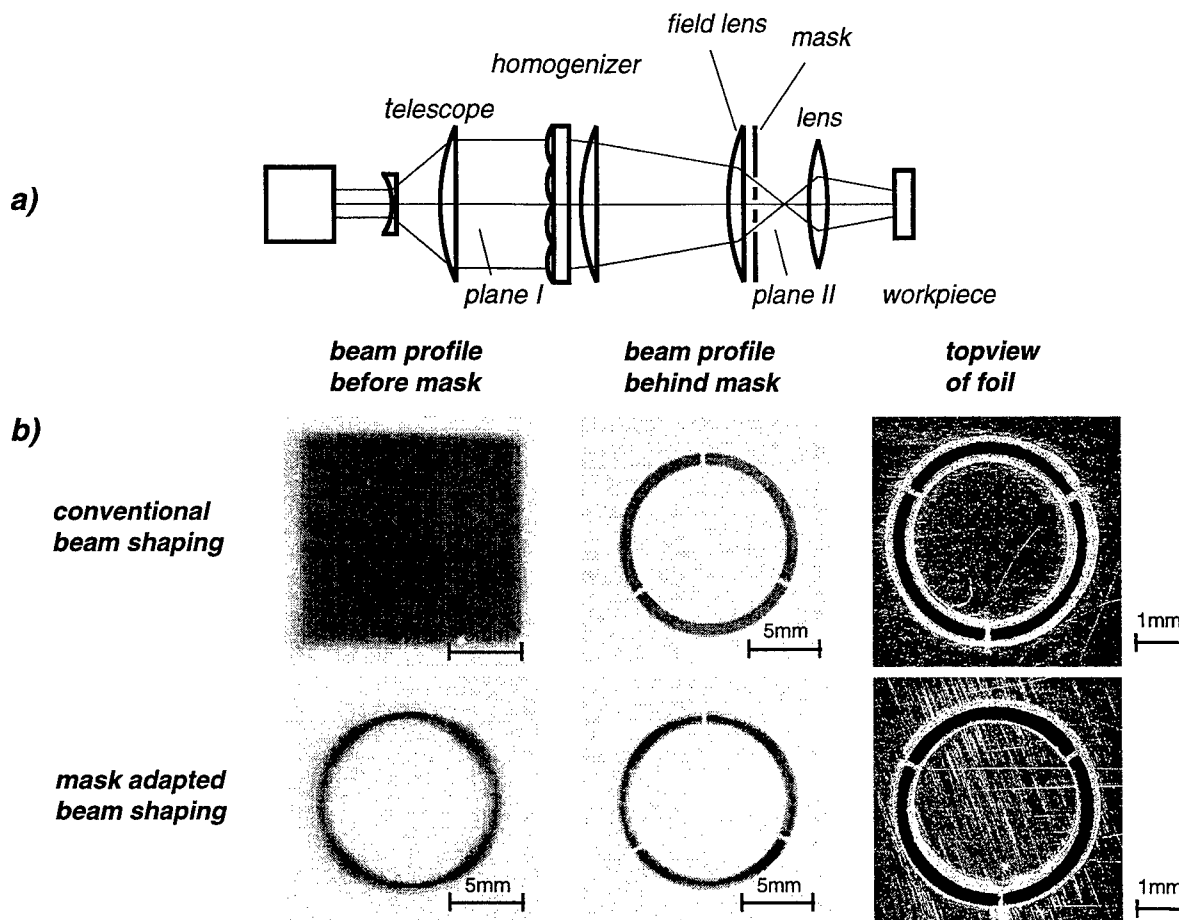


Figure 4. Ablation of polyimide foil with UV laser radiation ($\lambda = 248 \text{ nm}$). (a) Optical set-up for microstructuring by means of mask projection techniques and (b) experimental results. With mask-adapted beam shaping, the required pulse energy for the same processing result can be reduced to 25%.

6. CONCLUSIONS

In this paper the performance of non-rotationally symmetric optical elements (NOEs) for the beam shaping of high power laser radiation is investigated. NOEs are diamond turned mirrors with an arbitrary shaped surface profile.

With a NOE mirror, the conversion of a 40 W fundamental mode CO_2 laser beam into a square beam is performed successfully with an efficiency of 98%. Beam integration at CO_2 , Nd:YAG and Excimer wavelength can be realised through the use of NOE mirrors. Interference and diffraction structures, caused by the integrating process of CO_2 laser radiation, are suppressed by a rotating NOE phase modulation mirror. This mirror controls the degree of transversal coherence. It enables the hardening of workpieces without any local surface melting. An advanced concept of beam shaping is used to concentrate the optical energy on the apertures of a mask. In microstructuring, by means of mask imaging techniques, the processing efficiency can be considerably improved by this new concept. The experimental results demonstrate the potential of NOEs for innovating laser materials processing. The quality of the processing can be improved and the costs reduced through the use of NOEs for beam shaping.

7. REFERENCES

1. M. Weck, H. Özmeral et al, Proc. of 10. Annual Meeting of the ASPE, Oct. 13-20 1995, Austin
2. C.C. Aleksoff, K.K. Ellis, B.D. Neagle, SPIE Proc. Series **883**, Holographic Optics: Design and Applications, 220 (1989)
3. T. Henning, M. Scholl, in: Laser Beam Characterization, H. Weber et al, editors, 117, Berlin (1994)
4. T. Henning, L. Unnebrink, M. Scholl, SPIE Proc. Series **2703**, Laser as Tools for Manufacturing, 62 (1996)

Energy enhancer for mask based laser materials processing

Jens Bastue and Flemming O. Olsen

Department of Manufacturing Engineering, Thermal Processing of Materials
Technical University of Denmark, Building 425.I, 2800 Lyngby, Denmark

ABSTRACT

A device capable of drastically improving the energy efficiency of present mask based laser materials processing systems is presented¹. Good accordance between experiments and simulations for a TEA-CO₂ laser system designed for laser marking has been demonstrated. The energy efficiency may be improved with a factor of 2 - 4 for typical mask transmittances between 10 - 40%.

Keywords: TEA-CO₂ lasers, materials processing, mask based laser materials processing, laser marking

1. INTRODUCTION

The basic idea behind conventional mask based laser materials processing systems (MBLMPS) is to direct laser light onto a mask with the desired information (e.g. text), and subsequently image the light transmitted through the mask onto the workpiece. Our energy enhancer uses special designed mirror components to "catch" the light reflected at the mask, and redirect it back towards the mask, thus reusing otherwise wasted energy, and consequently a higher energy efficiency is obtained (in the following denoted energy enhancement). A sketch of the energy enhancer set-up is given below in [Figure 1](#)

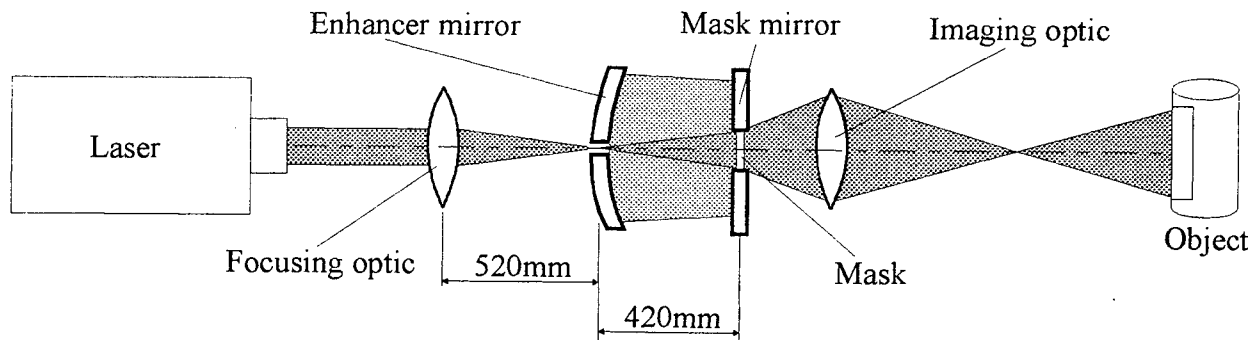


Figure 1 Sketch of the energy enhancer set-up.

Figure 1 shows that the energy enhancer basically consists of 5 components:

1. A simple 2 inch diameter plano convex lens used to focus the light through the small hole in the enhancer mirror.
2. A specially designed enhancer mirror (100 x 100 mm, height x width) used to redirect the light reflected at the mask or mask mirror back towards the mask.
3. A plane mask mirror (100 x 100 mm, height x width), with a hole in the middle, where the mask is placed.
4. A mask with the desired information etched through it. The information area on the mask is 26 x 16 mm (height x width).
5. A simple 3 inch diameter plano convex lens used to image the mask pattern onto the workpiece.

In this paper we will give a review of the applications, where MBLMPS are utilised. How such applications may benefit from the energy enhancer will be described. Additionally, we will present obtained experimental and simulated results determining the achievable energy enhancement as a function of mask transmittance, and the reflectivities of the 3 mirror components (enhancer mirror, mask mirror and mask).

2. APPLICATIONS OF MASK BASED LASER MATERIALS PROCESSING SYSTEMS

Laser marking is the dominant application for MBLMPS with CO₂ laser. All kinds of materials can be marked, including anodised aluminium, painted metals, glass, ceramics, integrated circuits and many plastics and paper products². Laser marking has several advantages compared to e.g. ink-jet systems: permanent and more clean and legible marks, lower environmental impact, better reliability, longer time between scheduled maintenance, lower consumable costs, and consequently higher return of investment^{2,3,4}. Laser marking may be performed without masks, using instead galvanometric mirrors to direct the focused beam of a high rep rate laser - CO₂ or YAG - onto the workpiece, and thus creating marks consisting of small dots. Such systems have a higher degree of flexibility than the mask based systems, but are likewise slower and more expensive.

A vast number of applications exist for MBLMPS with excimer laser. The major advantages of excimer lasers are of course the short wavelength, which allows a very high spatial resolution, and the short pulse time, which leads to a small thermal interaction between light and material. A fast growing market is microdrilling of such diverse objects as medical plastic catheters (a few microns diameter holes), and polyimide and ceramic ink-jet nozzles (typically 50 microns diameter holes)⁵. Micromachining with excimer laser in glass and ceramics is advantageous due to the absence of microcracking and fractures. Micromachining diamond with excimer laser avoids the graphitization, which results in the HAZ, when CO₂ or YAG lasers are utilised. Wire stripping (removal of insulation) is popular because the method is very precise, and leaves the bare wire undamaged⁵. Marking with excimer lasers is likewise advantageous, as it allows indelible marks without any material removal, because certain plastics change colour when exposed to the excimer light. This phenomenon is particularly important when marking plastic cables for the aircraft industry or when marking micro/semiconductor electronics.

3. ADVANTAGES OBTAINED USING THE ENERGY ENHANCER

Different types of TEA-CO₂ lasers are available for marking purposes. Generally, one has to choose between high rep rate or high pulse energy. In some industrial installations the speed of the production line is actually limited by the speed (i.e. the rep rate) of the marking system. Use of the energy enhancer will, of course, allow the use of a laser with a lower pulse energy and thus higher rep rate.

Another encouraging perspective for systems with a higher energy efficiency is to exchange the high pulse energy, expensive, large and water cooled lasers with their smaller, less expensive and air cooled cousins, which may deliver enough energy, if combined with an energy enhancer.

Of course, the most obvious advantage of the energy enhancer is that it becomes possible to produce larger marks, which may contain more information e.g. multiple lines of text.

In general, most of the excimer applications are characterised by the fact that multiple shots are needed to perform the desired work. Implementation of the energy enhancer will decrease the number of necessary shots, and consequently increase the process speed and decrease the cost of operation. MBLMPS for excimer lasers are often equipped with a beam homogeniser to ensure a uniform light intensity distribution across the mask (and workpiece). Such a device is superfluous, if an energy enhancer is utilised, as the energy enhancer is designed to produce a uniform light distribution across the mask. However - as the case is for most beam homogenisation systems - the energy enhancer introduces a larger divergence of the beam after the mask, and this makes the imaging more complicated. This is especially the case for applications, where high image demagnification ratios are needed.

4. SIMULATED AND EXPERIMENTAL RESULTS

Perhaps the most important parameter, when considering the efficiency of the energy enhancer, is the mask transmittance. This parameter is defined as the percentage of the total mask area containing information (i.e. the percentage of open areas ("holes") in the mask). Figure 2.a illustrates how the energy enhancement depends on the mask transmittance. The energy enhancement is defined as the ratio between the amount of laser pulse energy, which is transmitted through the mask with and without the enhancer mirror. It is assumed for both of the simulation series, that all of the mirror components (enhancer mirror, mask mirror and mask) have the same reflectivity R.

Figure 2.a shows, that the energy efficiency may be improved with a factor of 2 - 4 for typical mask transmittances between 10 - 40%.

Note that the experimental results are positioned between the two simulation series, which have reflectivities between 98% and 100%. We measured a reflectivity of 98.5% for the Al 99.5 used to manufacture the enhancer mirror and mask mirror, and it is reasonable to assume, that the BeCu masks have the same reflectivity as pure Cu (98%⁵). Consequently good accordance between experiments and simulations is found from Figure 2.a. Figure 2.a likewise illustrates, that little is gained by trying to improve the reflectivity of the mirror components, unless the mask transmittance is small (below 20 %).

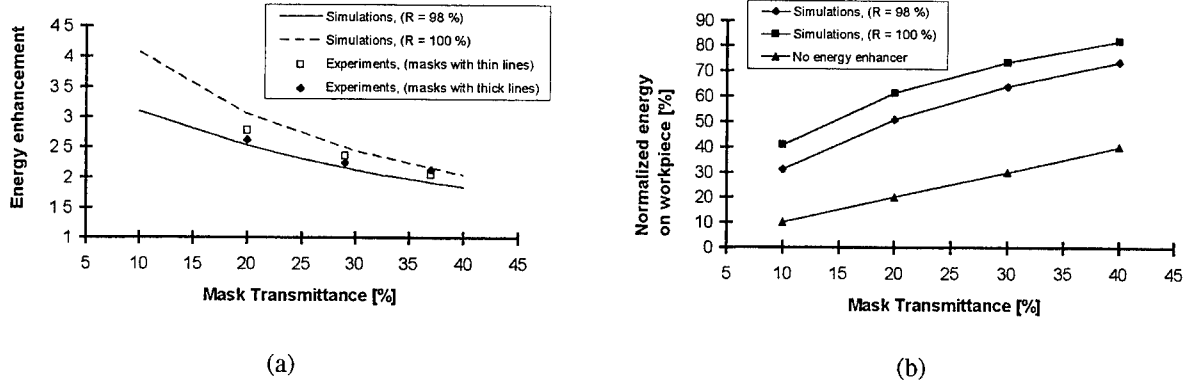


Figure 2. a) Energy enhancement as a function of mask transmittance, simulated and experimental results.
b) Normalised energy on workpiece as a function of mask transmittance, simulated results

Please note that even though the energy enhancement is inversely proportional to the mask transmittance, this does not imply that the mask transmittance should be minimised. On the contrary - the amount of energy received at the workpiece will, of course, always be proportional to the mask transmittance.

Figure 2.b illustrates how the energy on the workpiece is proportional to the mask transmittance. This energy is normalised with respect to the total pulse energy subtracted by the “waste energy”. The “waste energy” (this energy is lost in conventional MBLMPS) is the part of the beam, which initially hits outside the mask. Introducing the enhancer means that this “waste energy” will contribute to the energy enhancement, and consequently that the fitting of the size and shape between the beam and mask is much less critical.

The standard mask material in industry today is stainless steel, as it is cheap, strong and has a good stability of shape. However, the reflectivity is not as good as for BeCu. The dependence of the energy enhancement upon the mask material reflectivity R_{mask} is shown in Figure 3. In the simulations it is assumed that the reflectivity of the enhancer mirror and mask mirror is 98%.

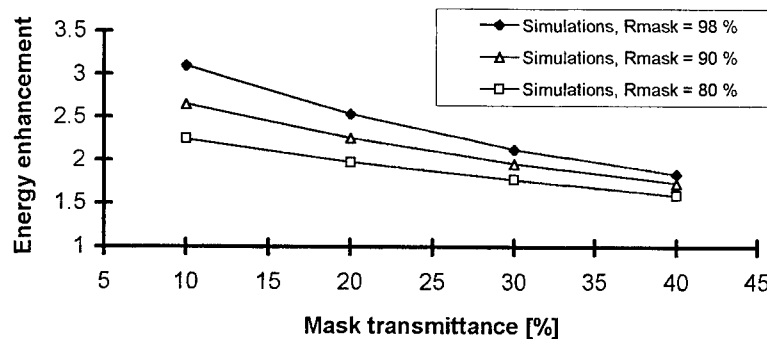


Figure 3 Energy enhancement as a function of mask transmittance for various mask reflectivities (R_{mask}), simulated results.

Once again the general rule is applicable that the lower the mask transmittance the more critical is the choice of materials (reflectivities). Stainless steel has a reflectivity around 90%. Consequently it follows from Figure 3, that for mask transmittances higher than 20% the difference in the energy enhancement is less than 10% for the two mask materials.

5. IMAGE QUALITY

The set-up used, is designed for use as laser marking. Thus a mark is considered as good quality, if it is clear and readable. Earlier versions of the energy enhancer suffered from a non uniform illumination of the mask, typically resulting in marks with low contrast near the edges (due to lack of light intensity), and sometimes smearing in the centre part (because of too high a light intensity). Figure 4 demonstrates how such problems have now been eliminated.

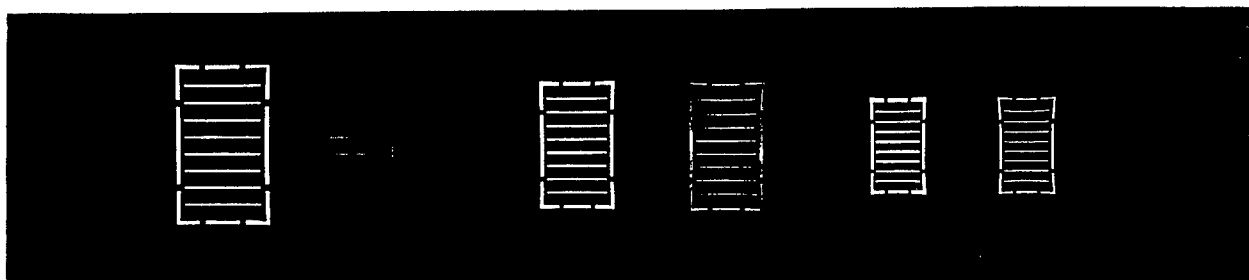


Figure 4 Marks obtained with and without the enhancer, for 3 different image magnifications: $M = 0.82, 0.66$ and 0.50 . The left mark of each pair is produced with the enhancer and the right mark without it.

Since the marks in Figure 4 are clear and readable, they demonstrate that one simple imaging lens is sufficient to obtain the image quality necessary for laser marking. Using the enhancer results in a larger beam divergence after the mask. In general, this fact decreases the image quality (since the numerical aperture is increased), but for laser marking purposes not in a ruining way.

The beam divergence may be a problem for applications where large demagnifications and thus small image aberrations are needed, e.g. hole drilling and micromachining. This, however, remains to be investigated in depth.

6. CONCLUSIONS

We have presented a device called an energy enhancer, which is capable of improving the energy efficiency of typical MBLMPS with a factor of 2 - 4 for typical mask transmittances between 10 - 40%. We have developed a simulation model and demonstrated good accordance with experimental results. Several applications of MBLMPS, where the energy enhancer may be very beneficial, have been described and analysed.

7. ACKNOWLEDGEMENTS

The authors wish to thank Prof. Dr. Leo H. J. F. Beckmann for his considerable contribution to the development of the simulation model.

8. REFERENCES

1. F. Olsen, "Optical system for lasermarking", US patent 5,011,253, April 30. 1991.
2. Jenifer Bunis, "Sealed CO₂ lasers update industrial processing", Laser Focus World, pp. 49-51, June 1995.
3. Lasertechnics, "Lasers leave a lasting mark", Industrial Laser Review, pp. 7-8, May 1994.
4. Bob Klumpp, "Dot matrix technology", Industrial Laser Review, pp. 6-7, December 1995.
5. K. Pippert and G. Zaal, "Excimer lasers carve out industrial market niches", Industrial Laser Review, pp. 13-16, April 1995.

The physical and technical factors, determining beam quality of high -power industrial fast transverse flow CO₂ lasers.

M.G. Galushkin, V.S. Golubev, A.V. Korotchenko, A.M. Zabelin.
Laser Research Center NICTL, Shatura 140700, Russia

ABSTRACT

The results of the investigation of the beam quality in the high - power industrial CO₂ laser generating in the 10 kW range are presented. As a result of these investigation, a scheme of the modified stable - unstable resonator is proposed, that uses only reflective mirrors. In this scheme, the plane of the unstable telescopic resonator is transverse to the flow in the discharge chamber. In the plane parallel to the electrodes this scheme represents a single - mode stable resonator. High efficiency of this resonator and high beam quality have been pointed out.

The acuteness of the problem of laser beam quality is closely connected to beam power level. It is especially difficult to get the single-mode beam of fast-transverse flow industrial lasers in the range above 1.5 kW. In these lasers it is difficult to attain the complete coupling of the optical system with the gas discharge chamber (GDC) because in this case the interelectrode distance considerably exceeds the cross size of the lowest mode of the stable resonator.

However with high beam powers the wavefront aberrations increase, both the linear and non-linear ones. The general approach to the problem of high beam quality and stability consists in localisation of the reasons for wavefront aberrations, then all the necessary steps to eliminate them are undertaken, and finally the high space selection resonator schematic properly coupled with the GDC, should be chosen.

The steps of elimination of the wavefront aberrations consist in compensation of large-scale aberrations by a system of automatic self-adjustments. As for small-scale aberrations due to gas flow turbulence, it was found that they are negligible in comparison to large-scale aberrations for beam powers up to 10 kW.

Thermal deformations of the semi-transparent coupling mirror have a decisive role in the deterioration of single -mode beam generation. This is the reason for the power restriction of gaussian beams generation in stable resonators.

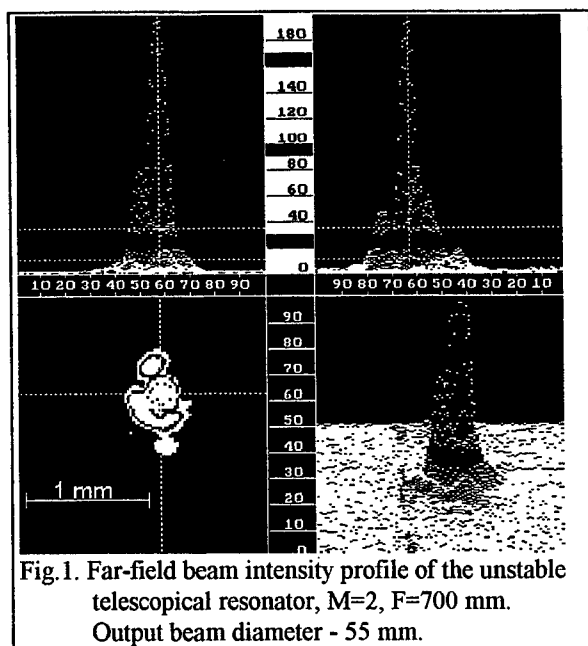
The beam power range of 5 kW and above can be afforded by fast -transverse flow lasers with a DC-GDC containing the segmented cathodes. As a rule, these lasers are provided with telescopic unstable resonators [1,2]. Thus, the industrial TL5M CO₂ laser developed at the NICTL uses the discharge chamber with segmented electrodes and 60...70 mm discharge gap. The active gas mixture N₂: He: CO₂ in the ratio 10 : 10 : 1 is flowing through the discharge chamber under 5,5 kPa total pressure. The electric power input into discharge reaches 50 kW [3].

As the resonator, a telescopic 5-pass unstable resonator with M=2 magnification factor is used. The output beam has the form of a ring with 55 mm outer diameter.

The measurement of this laser focused beam profile showed (Fig.1) that along with the narrow kern, there exists rather energy-intensive environment (pedestal) that contains more than a half of the total beam power. The total divergence therewith approached 1 mrad.

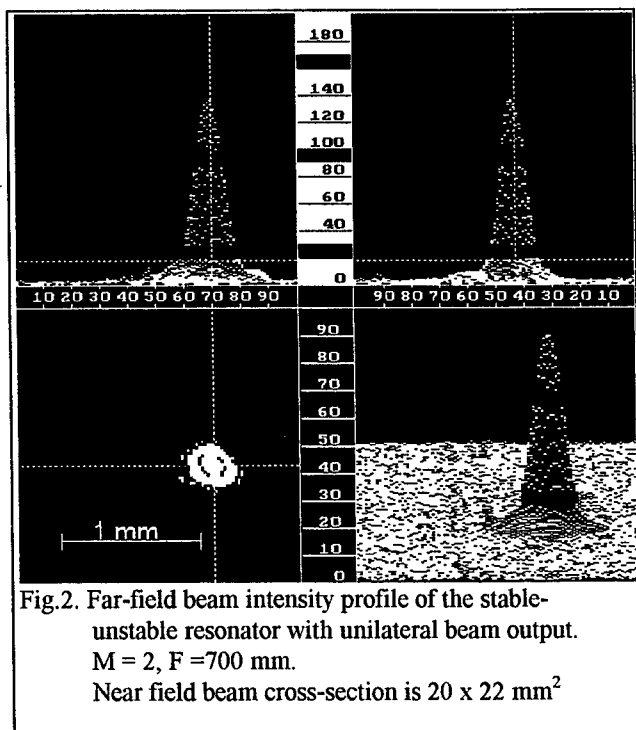
This is the reason why we have proposed and used a special scheme of the optical resonator [4]. It has the properties of an unstable telescopic resonator only in the plane perpendicular to the electrode walls, and it is stable in the plane parallel to these walls (Fig.3, 7), as opposed to the known schematic of the stable - unstable resonator wherein the plane of the unstable resonator is parallel to the electrodes, and the plane of the stable resonator is perpendicular to the gas flow and electrodes [5].

The resonator includes two end mirrors, one of them is spherical and another is cylindrical. The generatrix of the cylindrical mirror is parallel to the electrode walls. This resonator allowed to increase the far-field beam intensity



resonator with $1.5 < M < 2$ magnification. The output power of the laser employing the modified stable-unstable resonator was achieved to be 7 kW, i.e. no marked decrease in efficiency was practically observed.

In the near-field region the beam intensity had the gaussian profile in the plane parallel to the electrodes and the rectangular one in the plane perpendicular to it. With growth of output power increase of the size of a beam in a plane of the stable resonator up to 20 mm and increase of curvature of wavefront only in



by a factor of 2-3 in comparison to an ordinary telescopic resonator. One of the very important advantages of the "stable-unstable" resonator is a good space coupling of the resonator and GDC volumes. The geometry of the optical folding of this resonator takes into consideration the optimal utilisation of gas discharge zones, being not included into the volume of the laser optical field. This became possible due to the flow of the excited gas.

The two schemes of the modified stable unstable resonator have been used.

One of them is the design with the unilateral beam output in the plane of the unstable resonator (Fig.3). In this case, only the lowest gaussian mode of the stable resonator was selected by the output mirror that served as a diaphragm. The principal mode size in our case was approximately 12 mm by $1/e^2$ level.

The unstable resonator axis was located close by one of the electrode, the resonator caustic accounted for 50 mm, and the output beam size was 20 mm. As the practical applications require the compact beam, so we have to use the

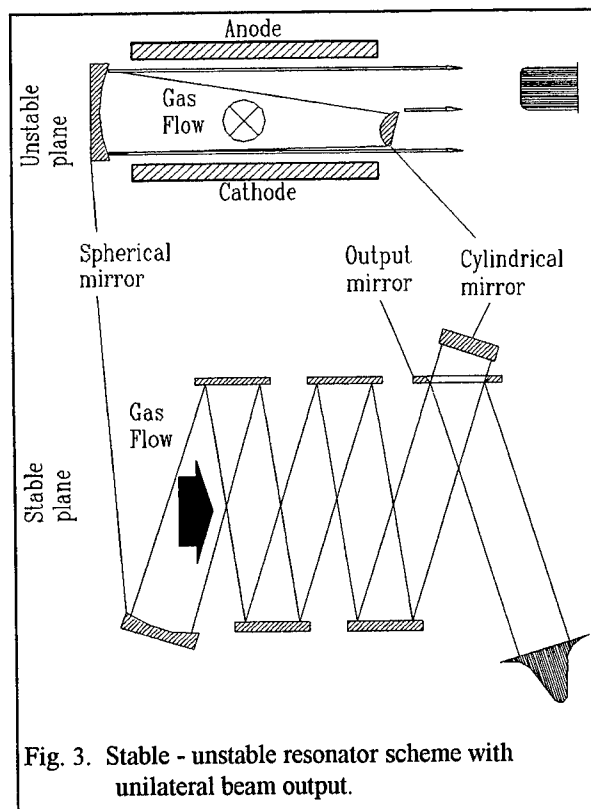
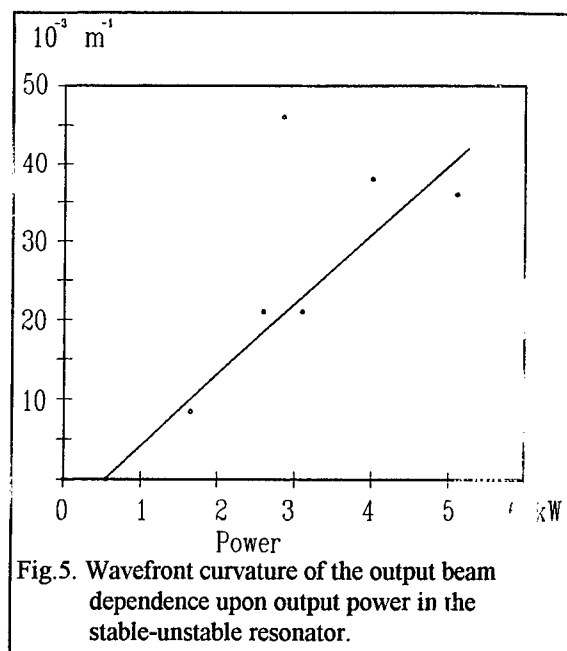
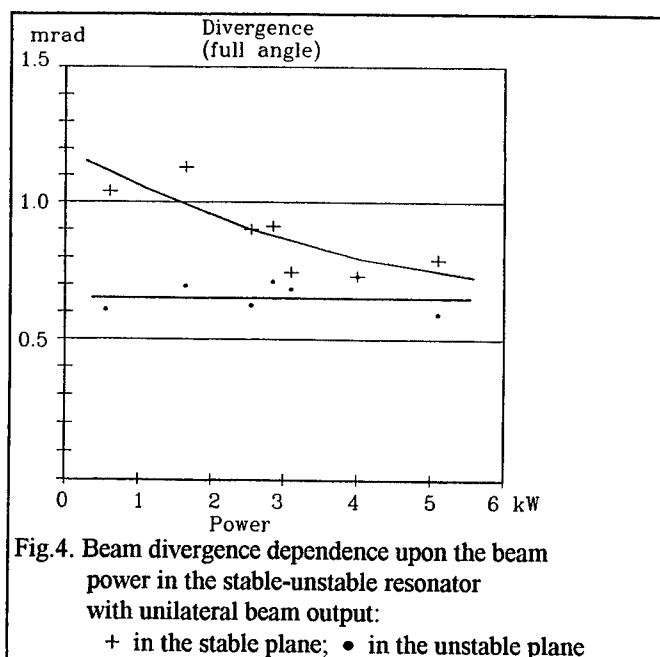


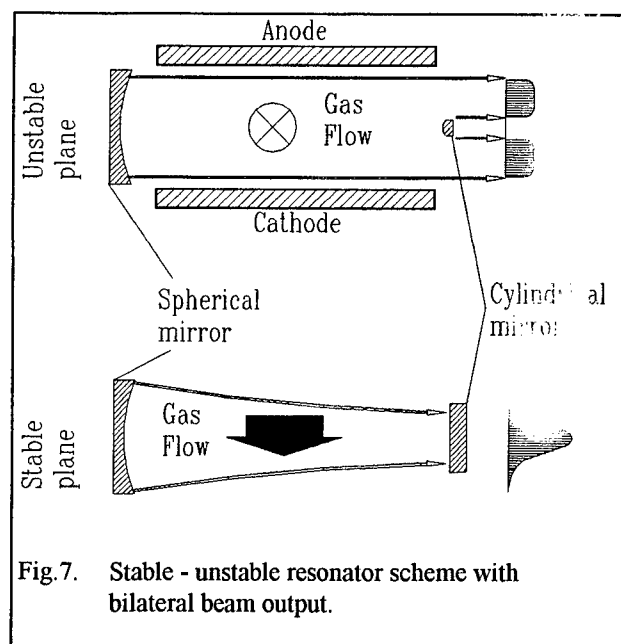
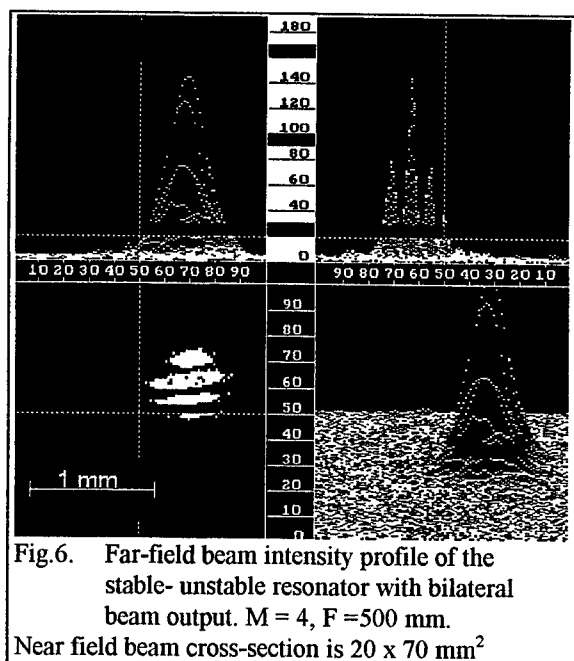
Fig. 3. Stable - unstable resonator scheme with unilateral beam output.



a plane of the unstable resonator was observed [Fig. 5 .].

This effect is caused by thermal deformation of mirrors of the resonator. The beam intensity profile in the lens focus was very much like the gaussian (the difference was less then 10 % , Fig.2). The divergence by $1/e^2$ level from the intensity maximum was only 0.65 mrad (Fig.4).

Another design under study was the modified stable-unstable resonator with the bilateral output (Fig.7). This scheme is of interest when very large magnification ($M=4...10...$) is used. As the resonator transparency in our case is described by the factor $t = 1-1/M$, but not by $t_0=1-1/M^2$, as in the usual unstable resonator, the efficiency of the stable-unstable resonator with $M = 16$ can be expected the same as in the usual unstable resonator where $M=4$.



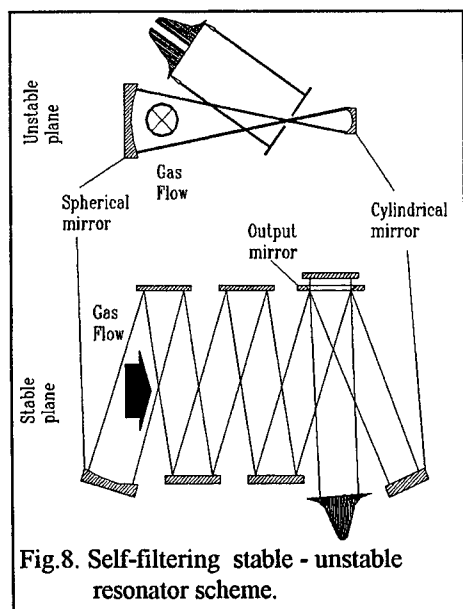


Fig.8. Self-filtering stable - unstable resonator scheme.

This permits to obtain the output beam of rectangular section, and in the far field the profile close to gaussian is achieved in both the planes. The obtained beam is then transformed to the circular section by the use of two cylindrical mirrors. The advantage of the schematic with the bilateral output is the substantially lower intensity of the beam falling to the resonator mirrors, as well as to the output window, thus resulting in smaller aberrations of optical components.

The further improvement of the beam quality is possible when changing to the scheme of the self-filtering stable-unstable resonator (Fig.8).

In conclusion we would like to underline, that, at our opinion, the transverse flow high beam quality industrial CO₂-laser with beam power range 1.5 ÷ 5 kW, there should be used the modified "stable-unstable" resonator with unilateral beam output scheme. In this case of 5 ÷ 10 kW beam power, there should be used the same resonator but with bilateral beam output scheme and subsequent beam compactisation.

REFERENCES

1. V.S.Golubev, "Recent investigation of gas discharge and beam quality problems of fast-flow CO₂ -lasers", *Proc. SPIE*, **2502**, pp.111-119 (1994).
2. M.G.Galushkin, V.S.Golubev, A.M.Zabelin, "Optical systems of high-power industrial CO₂ lasers, *Izvestiya AN, Ser. Fiz.*, **57**, pp. 63-68 (1993).
3. G.A.Abilsiitov, A.I.Bondarenko, V.S.Golubev, V.V.Vassiltsov et al. , "Industrial lasers of the Research Center on Technological Lasers", *Kvantovaya Elektronika*, Vol. 17, pp. 672-677.
4. A.M.Zabelin, A.V.Korotchenko and V.V.Samarkin, "A study of laser beam quality in industrial CO₂-5 kW laser with the stable-unstable resonator", *Proc. of V-th Intern. Conf. ILLA '95, Shatura*, 1995.
5. A.Borghese, R. Canevari, V. Donati and L. Garifo, " Unstable-stable resonators with toroidal mirrors", *Applied Optics*, **20**(20), pp.3547-3552 (1981).

Generation of continuously tunable 16 micron radiation by four-wave mixing in a parahydrogen Raman cell

L R Botha and C J Liebenberg
Atomic Energy Corporation of South Africa
P O Box 582, Pelindaba, South Africa

ABSTRACT

Continuously tunable output in the mid-infrared was generated via four-wave mixing in a parahydrogen Raman cell. Continuously and line tunable CO₂ master oscillator power amplifier chains produced the 10 micron input for the Raman cell.

Keywords: CO₂ laser, four-wave mixing, stimulated Raman scattering.

1 INTRODUCTION

Four-wave mixing, based on stimulated Raman scattering (SRS), allows for the efficient generation of tunable output in the mid-infrared. Four-wave mixing involving two different input beams and based on SRS was first achieved by Giordmaine and Kaiser in calcite.¹ Harris and Byer² proposed utilizing four-wave mixing to achieve a tunable IR source. Sorokin et al³ generated line tunable radiation in the mid-infrared using four-wave mixing between the pulses of a Ruby laser and a CO₂ laser. Line tunable output was achieved by tuning the frequency of the CO₂ laser. Gilbert et al⁴ and Giorgi et al.⁵ used four wave mixing between two CO₂ lasers to produce line tunable output in the mid-infrared region. In this report the generation of continuously tunable output in the mid-infrared region utilizing four-wave mixing between continuously and line tunable CO₂ laser pulses is reported. A similar system was reported by Tashiro and Nemoto.⁶

2 THEORETICAL BACKGROUND

Let E_{LP} and E_{LS} be the complex electric fields associated with the line tunable pump and Stokes frequencies and E_{CP} and E_{CS} that associated with the continuous pump and Stokes wavelengths. Using the slowly varying amplitude approximation the coupled mode equations can be written as⁷

$$\begin{aligned}\frac{\partial E_{LP}}{\partial z} &= -\frac{\omega_{LP}}{2cn_{LP}}\chi_R \left(|E_{LS}|^2 E_{LP} + E_{CP}E_{CS}^*E_{LS}e^{i\Delta kz} \right) \\ \frac{\partial E_{LS}}{\partial z} &= +\frac{\omega_{LS}}{2cn_{LS}}\chi_R \left(|E_{LP}|^2 E_{LS} + E_{CP}^*E_{CS}E_{LP}e^{-i\Delta kz} \right) \\ \frac{\partial E_{CP}}{\partial z} &= -\frac{\omega_{CP}}{2cn_{CP}}\chi_R \left(|E_{CS}|^2 E_{CP} + E_{LP}E_{LS}^*E_{CS}e^{i\Delta kz} \right) \\ \frac{\partial E_{CS}}{\partial z} &= +\frac{\omega_{CS}}{2cn_{CS}}\chi_R \left(|E_{CP}|^2 E_{CS} + E_{LP}^*E_{LS}E_{CP}e^{-i\Delta kz} \right)\end{aligned}$$

Here the ω 's are the radial frequencies of the respective electric fields, the χ 's the Raman non-linear

susceptibilities and the n 's the refractive indices of the respective fields. In the above four equations the first term in brackets is the stimulated Raman scattering term and the second term in brackets is the four wave mixing term. If the equation for the continuous Stokes E_{CS} is investigated, it can be seen that the four-wave mixing term is proportional to the product of the fields of the line tunable laser E_{LP} , the Stokes generated by the line tunable laser E_{LS} as well as the continuous tunable laser field E_{CP} . The four-wave mixing part for the generation of continuously tunable Stokes output can be written as

$$E_{CS} = E_{LP}^* E_{LS} E_{CP} e^{-i\Delta k z}$$

Thus if the line tunable system (E_{LP}) is powerful enough to generate a Stokes output beam (E_{LS}), via stimulated Raman scattering and a continuously tunable pump beam is present then the continuous tunable Stokes pulse (E_{CS}) will also be generated via the four-wave mixing process. Therefore, continuously tunable 10 micron pulses, which are individually below the Raman threshold, could be converted to Stokes pulses with this method. Requirements for this is that the line and continuously tunable pump pulses overlap in space and time, the line tunable system must be over the Raman threshold and, furthermore, the phase mismatch Δk must be small. The phase matching condition can be written as (co-linear propagation):

$$\Delta k = 2\pi \left(\frac{n_{LS}}{\lambda_{LS}} - \frac{n_{LP}}{\lambda_{LP}} \right) + 2\pi \left(\frac{n_{CP}}{\lambda_{CP}} - \frac{n_{CS}}{\lambda_{CS}} \right)$$

If it is assumed that the difference in refractive index for the different pump beams is small then Δk will be small.

3 EXPERIMENTAL CONFIGURATION AND RESULTS

3.1 Generation of the pump laser pulses

Line tunable 10 micron pulses were produced by one atmosphere transversely excited CO_2 lasers. Single longitudinal mode operation was obtained by injection seeding of these lasers with a frequency stabilized CW CO_2 laser. A chain of amplifiers increased the output of the oscillator to more than 2 J. The long optical path length that the beams have to travel, through the amplifiers as well as the multi-pass Heriot cell used for Raman conversion, necessitated a high beam quality. This was ensured by an intra-cavity variable aperture. The measured M^2 of the oscillator was less than 1.3.

Continuous tunability was obtained by utilizing the pressure broadening of CO_2 . This continuously tunable MOPA chain consisted of an oscillator with a three mirror resonator with the grating in near grazing incidence and an amplifier that was double passed. Because the electrode spacing was too small to enable the use of a geometric double pass scheme a polarization flip double pass was used. The grazing incidence grating prevented gain pulling and it ensured a narrow bandwidth. A partial reflector was installed to increase the effective reflectivity of the grating and an intra-cavity variable aperture was installed to ensure close to TEM_{00} operation. A low pressure CW CO_2 laser with wavelength stabilization provided a reference wavelength by combining its output with the zero order of the grazing incidence grating. This ensured that the wavelength of the laser could be monitored continuously without disturbing its output. Bandwidth measurements were done with a Ge wedged etalon in combination with a pyroelectric array detector. Beam quality measurements were carried out by a modified scanning slit method.

Gain pulling to the different CO₂ lines were observed. However, because the wavelength was continuously measured, the tuning linearity was not important for this application. The bandwidth measurements were done with the grating of the oscillator tuned to a position between the normal CO₂ R-lines. The measured bandwidth of the laser was less than 1.1GHz. The mode spacing of this laser was 90MHz, thus between 8 and 11 modes were lasing simultaneously.

The lifetime of the CO₂ in the continuously tunable laser was increased by a catalyst. In tests of the long term operation of the laser with the catalyst, at a laser pulse repetition rate of 20 Hz, the energy dropped to 80% of its starting value within 20 minutes and it was kept constant at this value for a period of 180 minutes, thus approximately 2.2×10^5 pulses, at which stage the test was terminated. The M² value of the continuously tunable oscillator was better than 1.3.

3.2 Four-wave mixing

The experimental four-wave mixing configuration is shown in figure 1. The output of the continuously and line tunable lasers were combined on a grating and were then circularly polarized to increase the Raman gain and to prevent the generation of anti-Stokes radiation. The combined pulses pumped a multiple pass Heriot type cell. A master timer system synchronized the pulses in time. The Heriot cell was filled with parahydrogen and cooled by liquid Nitrogen to a temperature of 77 K. A grating situated after the Raman cell separated the four output beams. The energy of each was measured by a pyro-electric energy meter and time evolution was measured with a photon drag detector. The halfwidth of both the Stokes pulses, as measured by the photon drag detector, was approximately 40 ns. The conversion efficiency for the line tunable system was better than 20 % and that of the continuously tunable system better than 2.5%. Better conversion efficiency for the continuously tunable system can be expected if the temporal overlap between the continuously tunable pulses and the line tunable pulses were better. The half width of the continuously tunable system was approximately three times that of the line tunable system. An advantage of these long pulses is that the influence of the relative time jitter between the laser pulses is smaller than would be expected if the continuously tunable pulses were shorter. A typical 16 micron output pulse, as measured with a photon drag detector, is shown in figure 2.

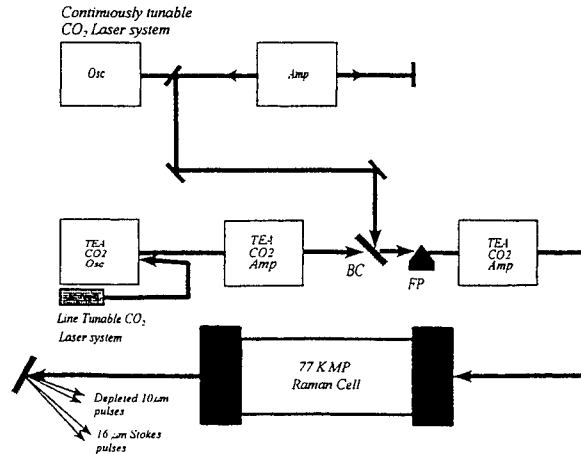


Figure 1: Four-wave mixing experimental configuration

4 CONCLUSION

Continuously tunable mid-infrared laser pulses were generated via four-wave mixing and stimulated Raman scattering. The output of two 10 micron CO₂ laser chains pumped a parahydrogen filled multi-

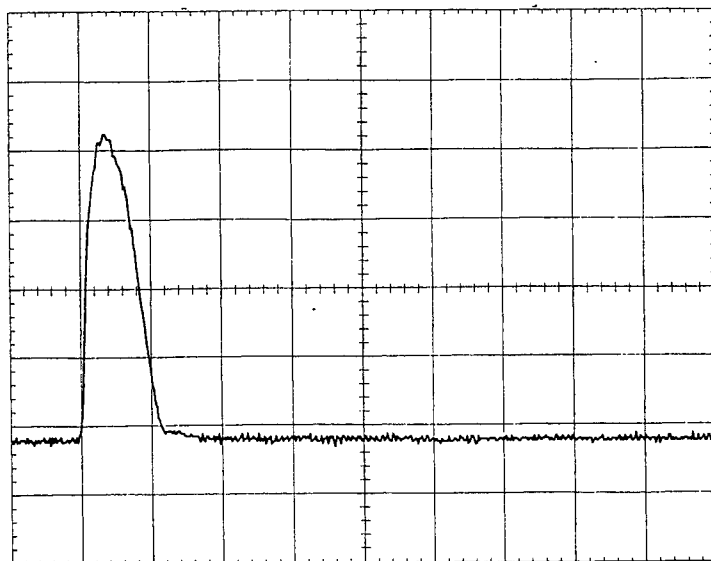


Figure 2: Typical output Stokes pulse as measured with a photon drag detector. Left is the line tunable and right is the continuously tunable pulse. The timescale was 50 ns/div and the amplitude scale 10 mV/div.

pass Heriot type Raman cell. Continuous tunable 10 micron pulse were produced by utilizing pressure broadening in a CO₂ laser. The system produced line as well as continuously tunable mid-infrared output pulses. Long term operation of the system was obtained with a closed loop gas flow system and a catalyst.

5 REFERENCES

- [1] J. A. Giordmaine and W. Kaiser, "Light scattering by coherently driven lattice vibrations," Phys. Rev., vol. 155, pp. 676-688, Apr. 1966.
- [2] S. E. Harris and R. L. Byer, "Tunable optical sources," Stanford University Microwave Laboratory, Stanford, CA, Report 1918, Dec 1970.
- [3] P.P. Sorokin, M. M. T. Loy and J R Lankard, "A 16- μ m radiation source utilizing four-wave mixing in cooled parahydrogen gas," IEEE J. Quantum Electron. QE-13(10), pp 871-875 (1977)
- [4] M. Gilbert, J. M. Weulersse, P. Isnard and G. Salvétat, "Multiphoton dissociation of UF₆ at $\lambda = 16\mu$ m in supersonic jets," Congress of the society of photo-optical instrumentation engineers (SPIE), Quebec, Canada, Jun 1986.
- [5] M. Giorgi et. al., "Total Stokes or antistokes conversion from four-wave mixing process in para-H₂," ENEA report RT/TIB/85/10.
- [6] H.Tashiro and K. Nemoto, "Present state of development of the technology for Uranium enrichment using a laser method," T.IEE Japan, Vol 114-A, No. 3, 1994.
- [7] W. R. Trutna, Ph.D dissertation, Stanford Univ, (1979)

Parametric study of intracavity degenerate four-wave mixing and phase conjugation of CO₂ and CO lasers radiation in their inverted medium

L. Afanas'ev, A. Ionin, Yu. Klimachev, A. Kotkov, L. Seleznev, D. Sinitsyn
P.N. Lebedev Physics Institute of Russian Academy of Sciences 53 Leninsky pr., 117924, Moscow, Russia

ABSTRACT

An influence of different parameters such as gas pressure, specific input energy, laser mixture content, intensity ratio for probe and co-propagating pumping wave, coherency and geometry etc. upon characteristics of phase conjugation (PC) signal and PC reflectivity (PCR) at intracavity degenerate four-wave mixing (DFWM) of long pulse CO₂ and CO lasers radiation in their inverted medium has been studied.

Key words: CO₂ laser, CO laser, e-beam controlled discharge, phase conjugation, four-wave mixing, active medium.

1. INTRODUCTION

The DFWM technique seems to be more suitable for PC of high power (HP) CO₂ and CO lasers radiation. However, the usage of semiconductors and liquids as PC mirrors for HP CO₂ (CO) lasers can be strongly restricted on account of heating and feasibility of destroying a nonlinear medium itself. The active medium of gas lasers, which can be removed from an interaction region very rapidly, might appear to be the best PC mirror for HP pulsed and repetitively pulsed CO₂ (CO) lasers (in particular for e-beam controlled discharge (EBCD) lasers, operating in long pulse mode: ~10-50 μ s for CO₂ and ~100-1000 μ s for CO laser).

For the first time PC signal at DFWM inside active medium was experimentally observed in ¹ for short laser pulse ($\tau_{out} < 0.2 \mu$ s) and was connected with resonance (amplitude) mechanism of creating diffraction grating of saturated gain in inverted medium. A backscattered signal observed in ^{2,3} with very high reflectivity of ~30-50% and PC signal with PCR of 0.2% ⁴ for long pulse CO₂ laser were connected only with a thermal mechanism of creation of phase diffraction grating of refractive index. We demonstrated in ^{5,6} that the two mechanisms can be responsible for PC process in active medium of CO₂ laser, PCR being 2% for CO₂ laser and 0.2% for CO laser. The objective of the paper is to understand the influence of different laser parameters on PCR and on the contribution of each PC mechanism in active medium of CO₂ and CO laser.

2. EXPERIMENTAL LASER INSTALLATION

The experiments were carried out on EBCD CO₂ (CO) laser with active length of 120cm. CO laser operated at gas temperature of 100K. Gas density varied between 0.1 and 0.8 Amagat. The laser resonator length varied between 3.0 and 18.0 m. The laser beam waist on the output coupler was 10-15 mm. The diffraction grating was used in case of frequency selected resonator. CO₂ laser operated on P(20) line of 10.6 μ m band. The wavelength of CO laser can be selected within wide spectral range of 4.9-6.6 μ m. The probe beam E₃ was directed to the active medium under the interaction angle of 10-40 mrad (Fig.1). Backscattered signal E₄ was detected by photodetectors with response time of 0.5 μ s and calorimeters.

3. EXPERIMENTAL RESULTS

Existence theorem. Because of a discrepancy between experimental results for reflectivity obtained in ²⁻⁵ we paid a great attention to evidence of PC signal observed. The time history of backscattered signal differed from probe one does not seem to be any evidence of PC signal, for there is a good condition for parasitic oscillation (with quite different temporal profile) in channel of the wave E₃ due to small interaction angle and a feasibility of injection of laser radiation from channel of wave E₁. The restoration of an optical image in near field and an angular divergency in far field ⁵ is a reliable evidence of PC process, though is fairly complicated on account of application of expensive IR vidicon camera. Thus we also carried out the polarization test, which proved, at least, the existence of diffraction grating in active medium. The plane of polarization for the probe signal was rotated at 90° with respect to the pumping wave (Fig.1). There was practically no useful backscattered signal (S/N~1). In case of the same polarization for probe and intracavity waves a signal/noise ratio was S/N=100.

Parametric study for CO₂ laser. There is a lot of laser parameters which affect the PC process by influencing upon small signal gain (SSG), saturation intensity etc. These parameters have strong effect on temporal behaviour of PC and PCR signals, that reflects the relative contribution of resonance and thermal mechanisms. It can be seen, for instance, from Fig.2 a relative small contribution of amplitude mechanism characterized ⁵ by projection at the front (upper trace) and approximately equal contribution for both mechanisms (bottom trace) entirely separated from each other.

The dependence of PCR (on energy) on specific input energy (SIE) for various gas pressures is presented in Fig.3. The experimental data strongly differ from theoretical ones ⁷ being extremely less. One can see from Fig.4 that SIE rise leads to a decrease of rear of PCR pulse, i.e. to a decrease of relative role of the thermal mechanism ^{6,7}.

An alteration of Q factor of laser resonator results in changing time delay of laser pulse itself, and also its length, profile and intensity. The relative contribution of the amplitude mechanism increases due to the effect of lasing switching on at higher SSG. The maximal PCR shifts towards the pulse tail (Fig.5) with a decrease of Q factor, PCR (on energy) being 1.2-1.5 times higher as compared to that obtained for high Q factor.

Gas pressure rise leads to an increase of PCR (Fig.6), but not so rapidly as it follows from the theory ⁷ which predicts approximately square PCR rise with gas pressure. The temporal profiles for PC and PCR pulses (Fig.7) demonstrate that there is PCR rise in the rear of the pulse that indicates the accumulation of thermal grating with a decrease of laser intensity. By comparing front and rear of PC and PCR signals, one can conclude, that thermal mechanism prevails over the amplitude one for higher pressures.

An increase of partial pressure for nitrogen leads also to PCR rise (Fig.3). The reason seems to be a decrease of relaxation rate for vibrational energy and a decrease of heat liberation power in active medium. The maximal PCR reached 1.5% for laser mixture $\text{CO}_2\text{:N}_2\text{:He}=1\text{:}2\text{:}4$ ($p=0.4\text{atm}$) and 2.8% for $1\text{:}5\text{:}3$ ($p=0.28\text{atm}$). The usage of the mixture with high nitrogen content leads to separation in time of two mechanisms of nonlinearity (Fig.2)

The PCR increases rapidly when decreasing an interaction angle (Fig.6) on account of geometrical rise of interaction length. The best results on PCR were obtained at $\theta=10\text{mrad}$. When using smaller angle of 5mrad a strong background radiation with intensity comparable with PC signal was observed. Apart from interaction angle the different geometrical parameter or optical delay between probe and co-propagating wave affects the PCR. While increasing it up to a half of resonator length PCR decreases 1.2-1.5 times. If increasing it up to resonator length, PCR was one fifth-one tenth as much as that obtained for zero delay.

Some laser parameters such as a degree of linear polarization, spectral range (9.6 or $10.6\mu\text{m}$) do not influence upon characteristics of PC process. We studied also in far field with IR vidicon camera an influence of I_1/I_3 ratio on PCR and optical quality of PC process, the latter being defined as a ratio of angular divergencies for probe and PC signal $\theta_{\text{probe}}/\theta_{\text{PC}}$. One can see from Fig.8 that in the whole range of the ratio I_1/I_3 the peak PCR (defined in the maximum of IR distribution in far field) lies within the interval 0.6-1.2% and reaches its maximal value at $I_1/I_3 \sim 15$. The optical quality is changed from 0.8 to 1.3 and has its minimum at the same ratio being altogether an inversion of the dependence for PCR.

Parametric study for CO laser. For the first time we studied PC process at DFWM for frequency selected CO laser. Data for EBCD CO laser operating within spectral region with spectral width of 15cm^{-1} and central lines of $P_{10-9}(14)$ ($\lambda=5.39\mu\text{m}$) and $P_{8-7}(14)$ ($\lambda=5.25\mu\text{m}$) are presented in Fig.9. The SIE does not seem to affect the PCR for CO laser strongly, as in case of CO_2 laser (Fig.9 and Fig.3). The dependencies of PCR on gas density (Fig.9) has different behaviour for different spectral lines. For instance, gas density rise leads to gradual increase of PCR up to 0.8% (PCR on intensity) at $N=0.5\text{Amagat}$ for $P_{10-9}(14)$ line. For other line $P_{8-7}(14)$ the dependence had different behaviour reaching its maximum at $N=0.2\text{Amagat}$ and decreasing when increasing gas density. The typical temporal behaviour for probe, PC and PCR pulses (SIE=300J/l Amagat, $\lambda=5.39\mu\text{m}$) is presented in Fig.10. One can see that maximal peak value of PCR (on intensity) is at front of laser pulse. The maximal value is approximately twice as much as that of averaged value of PCR (on energy). PCR decreases nearly proportional to the intensity of the probe wave falling down towards the end of the laser pulse. That behaviour is quite different from that of CO_2 laser and can be connected with noninertial PC mechanism, i.e. resonance one. A contribution of the thermal mechanism seems to be very low for CO laser, that is in agreement with theory ⁸.

4. DISCUSSION

Parametric study of PC process demonstrated that experimental data for PCR of CO_2 laser were of the order of magnitude less than theoretical ones. Temporal characteristics demonstrated that two principal mechanisms (amplitude and phase ones) which are responsible for PC process have a comparable contribution to PC reflectivity, that also contradicts the theory having predicted the phase mechanism is to be prevailed one over the amplitude mechanism, in particular at higher pressures. An analysis of temporal behaviour of PC and PCR signals suggests that there are some reasons which prevent the thermal mechanism from operating strongly. These reasons manifest themselves when increasing laser intensity and could be connected with laser induced medium perturbation, which on the one hand, creates regular phase grating due to DFWM applied, and on the other hand, destroys the same grating via optical disturbances of active medium. In case of CO laser the thermal mechanism has a weak influence upon the PC process, the amplitude one being prevailed over it.

5. CONCLUSIONS

The influence of laser parameters upon characteristics of PC and PCR signals at DFWM of long pulse CO_2 and CO laser radiation has been studied experimentally, the PCR (on energy) being up to ~3% for CO_2 laser and 0.5% for CO laser. The relative role of resonance and thermal mechanism of PC process has been studied for both lasers. A comparison of experimental and theoretical data demonstrates a disagreement between them. A theory should be developed taking into

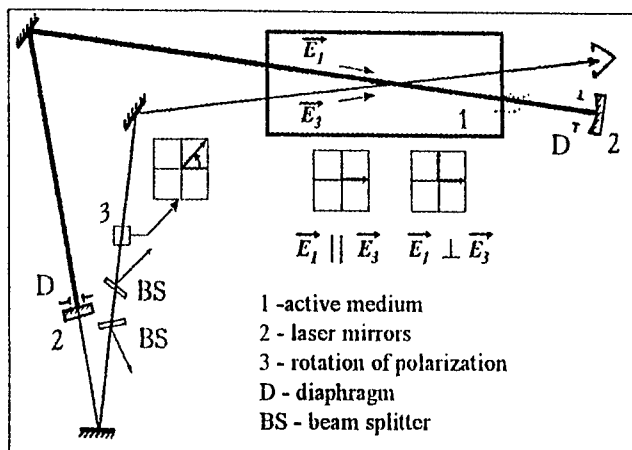


Fig.1. Optical scheme for DFWM experiments and polarization test.

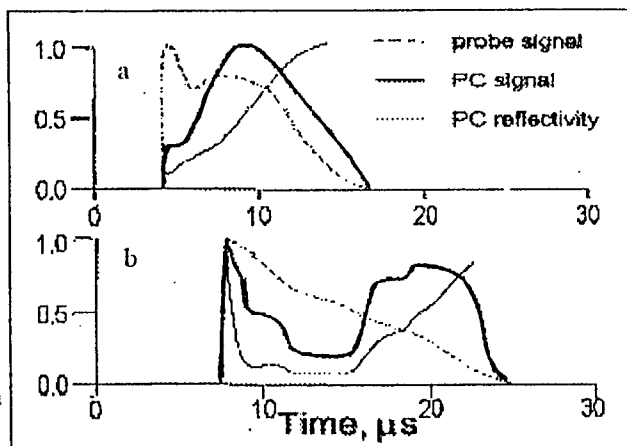


Fig.2. Probe, PC & PCR signals: $p=0.28$ atm, $\text{CO}_2:\text{N}_2:\text{He}=1:2:4$, SIE ~120 J/l atm (a) and 1:5:3, SIE ~280 J/l atm (b).

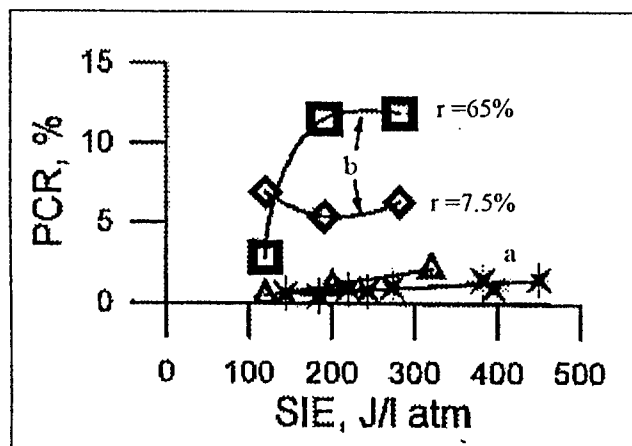


Fig.3. The dependence of PCR (on energy) upon SIE: $p=0.28$ atm. Experiment (a) $\text{CO}_2:\text{N}_2:\text{He}=1:2:4$ (X), 1:5:3 (Δ), $r=46\%$.

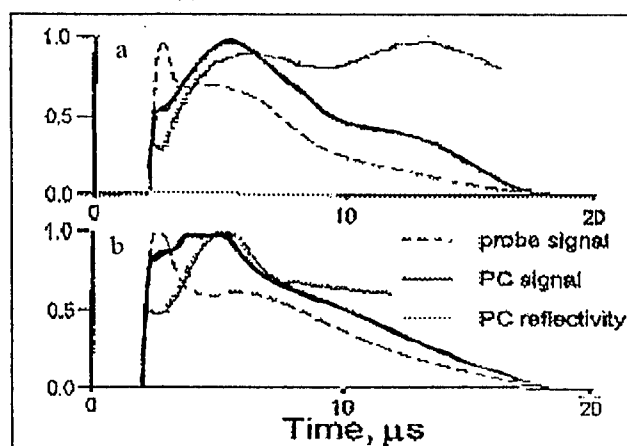
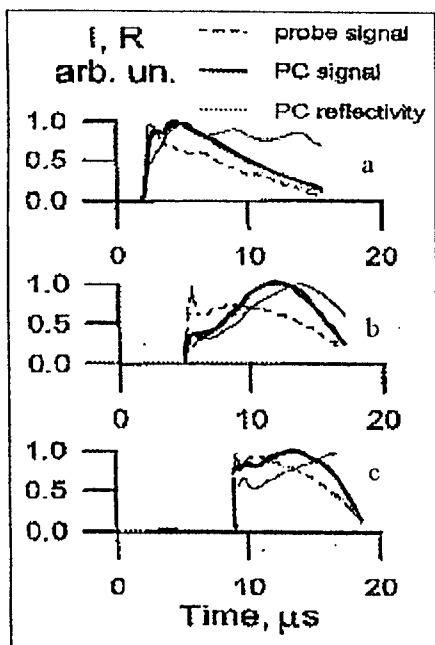


Fig.4. Probe, PC & PCR signals: $p=0.28$ atm, $\text{CO}_2:\text{N}_2:\text{He}=1:2:4$, SIE ~190 J/l atm (a); 280 J/l atm (b).



Theory (b) 1:2:4.

Fig.5. Probe, PC & PCR signals for different output couplers with $r=65\%$ (a); $r=45\%$ (b); $r=7.5\%$ (c)

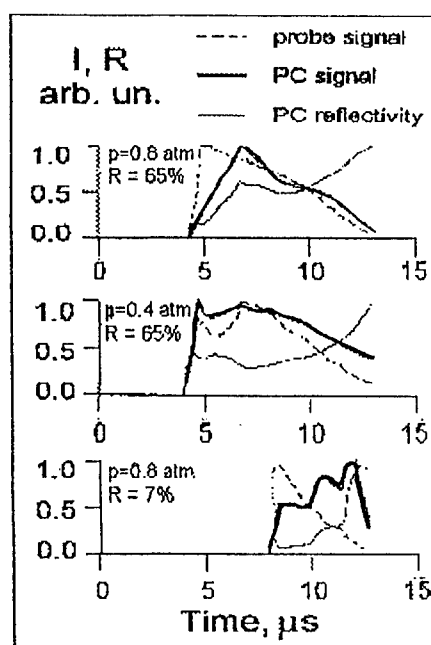


Fig.7. Probe, PC & PCR signals for different gas pressures $\text{CO}_2:\text{N}_2:\text{He}=1:2:4$, SIE ~250 J/l atm.

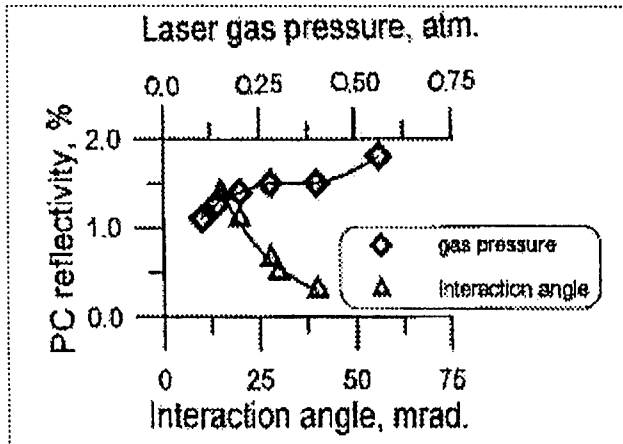


Fig.6. The dependence of PCR (on energy) on gas pressure and interaction angle $\text{CO}_2:\text{N}_2:\text{He}=1:2:4$.

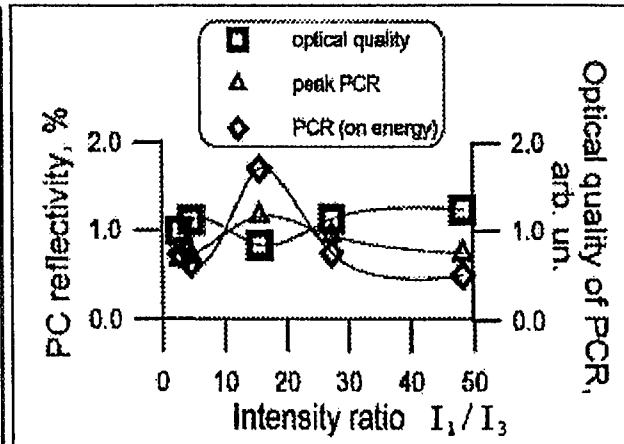


Fig.8. PCR and optical quality of PCR vs I_1/I_3 ratio.

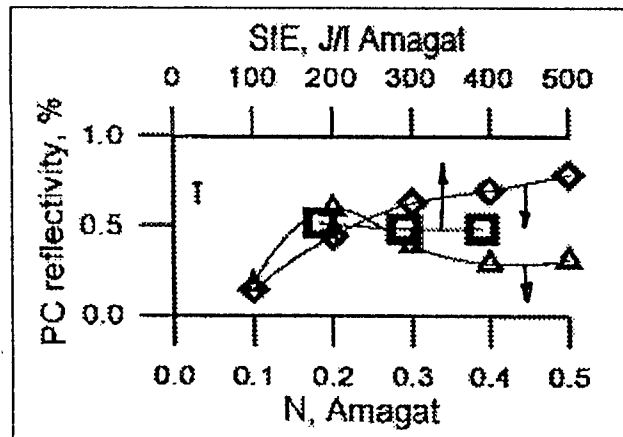


Fig.9. PCR (on energy) vs SIE and gas density for CO laser.
(\diamond \square - $\lambda=5.39 \mu\text{m}$; Δ - $\lambda=5.25 \mu\text{m}$).

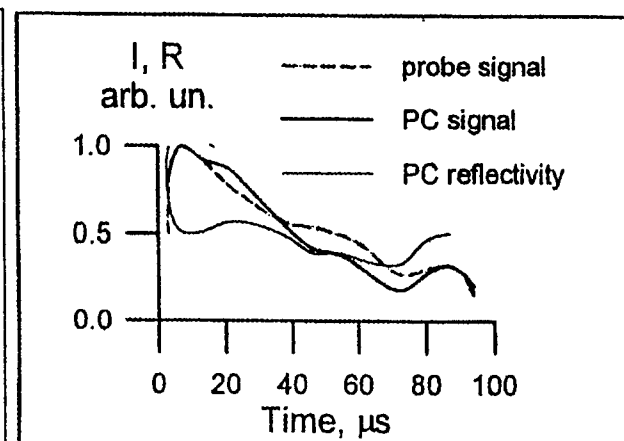


Fig.10. Probe, PC & PCR signals for CO laser
 $\text{CO}:\text{N}_2:\text{He}=1:4:5$, $N=0.3 \text{ Amagat}$.

account laser induced medium perturbation, which seems to create not only phase diffraction grating at DFWM, but also destroy it via optical disturbances. For the better understanding the phenomena the experiments should be carried out on smaller temporal scale with nanosecond resolution.

6. ACKNOWLEDGMENTS

The research work has been done in accordance with contract SPC-95-4043 of EOARD.

7. REFERENCES

1. E.E.Bergman, I.L.Bigio, B.J.Feldman and R.A.Fisher, *Optics Lett.*, **3**, 82 (1978).
2. M.G.Galushkin, S.A. Dimakov et al, *Izvestija AN USSR, ser.Phys.*, **54**, 1042 (1990).
3. A.A.Ageichik, S.A. Dimakov et al, *Proc. SPIE*, **1840**, 166 (1991).
4. E.K.Gorton and A.M.Richmond *Opt. Comm.*, **86**, 341 (1991).
5. L.A.Afanas'ev, A.A.Ionin, A.A.Kotkov et al, *Quantum Electronics*, **24**, 513 (1994).
6. L.A.Afanas'ev, M.G.Galushkin, A.A.Ionin et al, *Izvestija RAN, ser.Phys.*, **60**, 41 (1996) (in Russian).
7. L.A.Afanas'ev, M.G.Galushkin, A.A.Ionin, A.A.Kotkov, K.V.Mitin et al, "Degenerate four-wave mixing and phase conjugation of molecular mid-IR lasers radiation in their inverted medium", Report of Lebedev Physics Inst. on contract SPC-95-4043 with EOARD, Moscow, 1996.
8. A.V.Berdyshev, A.K.Kurnosov, A.P.Napartovich, *Kvant. Electron*, **20**, 529 (1993) (in Russian).

7. Excimer Lasers

High Efficiency Excimer Lasers

Victor Tarasenko

High Current Electronics Institute
Siberian Department of Russian Academy of Sciences,
4, Akademicheskoy Ave., Tomsk 634055, Russia

ABSTRACT

The results of high efficient excimer (exciplex) lasers investigations are presented. Processes of exciplex molecules formation are described as well as the data on the highest radiation parameters of the noble-gas-halides lasers are given. Conditions of high efficiencies production of the noble-gas-halides excimer (exciplex) lasers are analyzed.

Keywords: excimer (exciplex) lasers, high efficiency, electron-beam pumping, discharge pumping.

1. INTRODUCTION

It has been more than 20 years since the development of the excimer (exciplex) lasers operating on transitions RX^* molecules. Work is now underway toward the creation of new lasers and laser systems based on exciplex lasers. The term "exciplex" (from English "excited complex") is usually in photochemistry denotes chemical compositions (complexes), stable in the excited state but dissociate easily upon going to the ground state [1]. An excimer, however, is an exciplex consisting of identical atoms or atomic groups (e.g., dimer, trimer, etc.). Lasers based on photodissociative transitions of the exciplex molecules are naturally called as exciplex ones [2, 3]. Usually, exciplex molecules contain noble gas atoms and halides. Being in the ground state, these gases as a rule do not produce chemical joints (but XeF_2) due to their electron shell is full. The inert gas excited atom R^* with its chemical properties is relative to alkaline metals: it captures one electron with a weak energy dependence. That is why, for the most of exciplex lasers, there is one atom of inert gas in the working molecule.

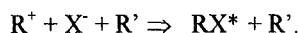
Generation on noble-gas-halides was produced for the first time in 1975 by different pumping methods [4-9]. At present, the most effective are the inert-gas-halides lasers: KrF^* ($\lambda = 250$ nm), XeF^* ($\lambda = 350$ nm), $XeCl^*$ ($\lambda = 308$ nm), ArF^* ($\lambda = 193$ nm) [6,9-23]. Note, that traditionally lasers on exciplex molecules are called not exciplex but excimer. Table 1 lists the data on the first generation on different exciplex molecules, and also there are references on the papers where it was announced about the effective generation possibility on the known molecule.

A particular interest to exciplex lasers is based first of all on the energy density of the radiation obtained (up to 40 J/dm³) with considerable (9-12 %) efficiency [17] of their active media. The inversion scheme and e-beam pumping methods provide the use of big (~ 1 m³) active medium volumes [18-21]. Besides, the range of the exciplex lasers operating transitions covers the area from visible to VUV, which is of great interest for many technical applications. The important merit of the exciplex lasers is their effective operation by different pumping methods: e-beam, electrodischarge and e-beam-controlled discharge. Moreover, to produce generation one pumping system may be used with various mixtures and different molecules. Very often, the same methods are used as for CO_2 -lasers: a self-sustained TEA-discharge and its modifications with preionization, UV and X-ray radiation, low-current electron beam. Presently, the inert-gas-halide exciplex lasers are known as very powerful sources of stimulated radiation in the UV region. Generation was obtained at many transitions (see Table 2).

2. FORMATION OF EXCIPLEX MOLECULES

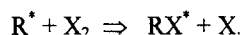
The exciplex lasers have essential advantages over inert-gas-dimers lasers, mainly for peculiar structure of their electronic terms, and due to this, comparatively large cross-sections of photodissociation. The attachment of the excited atom R^* with halogen atom X is very strong. The excited electron is localized on halogen atom filling in its shell, and the complex R^+X^- , characterized by ionic bond, is formed. This complex is tied together by Coulombic forces which are considerably great (energy of the bond is ~ 5 eV at the distance 0.3 nm between nuclei). Due to high energy of dissociation of the excited electronic term, photon "possesses" less energy than inert-gas dimers, correspondingly, the operating radiation wavelength of RX -lasers is excessive.

Electron relaxation on atomic and molecular excited levels in the dense complex component plasma has more complicated character than it is in the inert gas plasma. Used for mathematical description of the RX-lasers active medium kinetics are models taking into account hundreds of chemical reactions [24, 25]. A crucially new channel of the RX-plasma relaxation in comparison with R-plasma appears due to negative ions X^- availability. For the most of mixtures population of the working state proceeds through triple collisions of positive and negative ions



By its variation from pure inert gases not every atom and molecule ionization act leads to exciplex RX^* population, the basic part of the relaxation flow goes "bypassing". Choosing the optimal mixture through the working state RX^* it is possible to pass through up to 20-30 % of this flow.

Besides, through ion-ion recombination, in the row of lasers an essential contribution to working molecule forming gives harpoon reaction .



With chemical composition complication of medium usually exceeds the role of light absorption by intermediate products of chemical reactions - not only dimers R_2 , but trimer-exciplexes $R'RX^*$, and also negative ions X^- . Non-controlled dopants may influence on the absorption essentially. Particularly, they are the most hazardous for the lasers with a high quantum energy: $ArCl^+$, ArF^+ , $KrBr^+$.

All well-known noble-gas halides exciplex lasers are able to operate either in conditions of non-equilibrium recombination (e-beam pumping, generation in subsequent illumination), or ionization (self-sustained discharge pumping). Nevertheless, it is more effective the generation by non-equilibrium recombination [26]. For e.g., the generation efficiency of exciplex lasers pumped by self-sustained discharge not exceed 5 % [22, 20], and pumped by e-beam it is more than 10% [17] via energy input into the working gas.

3. EXCIPLEX LASERS AND ITS CHARACTERISTICS

Presently, many different techniques for pumping of exciplex lasers are known, for which electron and ion beams, self-sustained discharge, optical pumping, e-beam-controlled discharge, nuclear energy, microwave discharge are used. Most abundant of them are self-sustained discharge and electron beam. In order to obtain maximal radiation efficiency in the single pulse it is necessary to provide the following conditions: uniform pumping of the whole active volume; optimal powers and wavelengths of pumping, of the pumping pulse that differ for different molecules essentially, optimal composition and pressure of the working mixture; optimal resonator for the given active medium length; not big cross sections of the laser active volume because of amplified spontaneous radiation losses to the wall sides.

Besides, while operating in the regime of repetitive pulses or in pulse-periodical regime it is necessary to conserve the initial mixture and prevent reaching of the dopants from the wall sides of the laser chamber and electrodes, and also in pauses between pulses to use mixture circulation and its cooling. Fig.1 and Fig.2 give a design of lasers pumped by electron beam [27,28], and a schematic of a laser pumped by a self-sustained discharge [22], with which rather high energy parameters of radiation were obtained. To pump cylindrical laser chambers, electron accelerators producing radially convergent electron beams were used. The first accelerator consisted of a high-power low-inductance vacuum-insulated Marx generator and a vacuum diode. The vacuum insulation and the minimized inductance of the discharge circuit made it possible to attain high output power of the accelerator without using an intermediate energy store and substantially reduce its overall dimensions. The Marx generator has nine stages, rated at an operating voltage up to 100 kV. Measurements have shown that the vacuum diode of this electron accelerator is capable of producing electron beams of electron energy up to ~ 600 keV and beam current ~ 70 kA with a total current pulse duration of ~ 1 ms, the beam power pulse FWHM duration being ~ 300 ns. The active space of the laser chamber was ~100 cm long and 20 cm in diameter. The second accelerator had 12 Marx generators. The active space of the laser chamber was ~ 200 cm long and 60 cm diameter. Experiments on studying the laser radiation on $XeCl^*$ molecules and KrF^* molecules were carried out on the first accelerator, and on $XeCl^*$ molecules were carried out on the second accelerator. When pumping by electron beam, the last was admitted into the cylinder laser chamber from all the sides from 12 cathodes that provided the uniform pumping and radiation energy up to 2 kJ [20] with the efficiency with respect to input energy ~ 5 %.

On pumping by a self-sustained discharge a special profile of electrodes was used (that provided uniform pumping at the discharge space section), the volume discharge was formed from one generator, and the basic energy input was produced by the other one in the impedant regime. Owing to this, generation efficiency on the molecules XeCl^* reached $> 4\%$ with respect to stored energy, and laser energy reached $> 4\text{ J}$ [22].

In our works [20,29] designs and outcomes of tests on versatile pulsed FOTON, LIDA-D and LIDA-M model lasers pumped by a self-sustained discharge are presented. The FOTON lasers have a simple and readily manufacturable design capable of delivering high-power outputs in different spectral regions. FOTON model laser action was obtained on molecular transitions in F_2 ($\lambda = 157\text{ nm}$), ArF^* (193 nm), KrCl^* (222 nm), KrF^* (249 nm), XeCl^* (308 nm), N_2 (337 and 1040 nm), N_2^+ (428 nm), XeF^* (350 nm) and CO_2 (10.6 μm) and from atomic transitions in F (635.4, 641, 713, 740 and 755 nm). The harnessing of the "electric wind" improved PRR up to $\sim 50\text{ Hz}$. The LIDA-D lasers are also easy to produce, admit variation of the pulse duration and provide $\sim 1\text{ J}$ energies at $\lambda = 308\text{ nm}$. It should be pointed out that a similar laser in $\text{SF}_6\text{-H}_2$ generated an output energy of $\sim 1.2\text{ J}$ at several wavelengths around $2.8\text{ }\mu\text{m}$. The LIDA-M lasers furnish high lasing efficiency ($\sim 3\%$) at $\lambda = 308\text{ nm}$ with a pulse duration of about 300 ns and an output energy of about 0.4 J. Fig.3 presents the dependence of radiation efficiency of electrodischarge KrCl-laser via pumping power. It is seen that at $\sim 5\text{ MW/cm}^3$ the efficiency reaches 2.6% [29].

4. CONCLUSION

Due to small size of this publication it is not possible to cover in detail all the aspects of kinetic processes that take place in halide - inert gas mixtures, designs of the concrete exciplex lasers, means and technical decisions to provide the highest parameters. Here we present tables with the best characteristics of exciplex lasers pumped by a self-sustained discharge and by electron beam taken from [17,18,20,22,23,30] (Table 3). In more detail, the characteristics and designs of exciplex lasers are presented in books [20,31,32,33,34].

5. ACKNOWLEDGMENTS

The author would like to thank E.N.Abdullin, A.S.Gorbachev, A.M.Efremov, A.V.Fedenev, B.M.Koval'chuk, V.V.Kremnev, S.V.Loginov, M.I.Lomaev, V.F.Losev, A.N.Panchenko, V.S.Tolkachev, V.S.Skakun, E.A.Sosnin, P.M.Shchanin and V.B.Zorin for creation of the accelerators, for help in the creation of the electrical discharge lasers, for help in carrying out the experiments and for useful discussions, and so S.P.Bugaev and G.A.Mesyats for support of this work.

6. REFERENCES

1. J.B. Birks, *The exciplex*, Academic Press, N.Y.-San-Francisco-London, 1975.
2. S.K. Searles, "XeBr exciplex laser" *Appl. Phys. Lett.*, Vol. 28, No 10. pp. 602-603 1976. -
3. M.S. Lakoba and S.I. Yakovlenko, "Active media of exciplex lasers (review)", *Kvant. Electron.* Vol.7, pp. 677-719, 1980.
4. S.K.Searles and G.A.Hart, "Stimulated emission at 218.8 nm from XeBr^* ", *Appl. Phys. Lett.*, Vol. 27, pp. 243-245, 1975.
5. J.J. Ewing and C.A. Brau, "Laser action on the $^2\Sigma_{1/2}^+ \rightarrow ^2\Sigma_{1/2}^+$ bands of KrF^* and XeCl^* ", *Appl. Phys. Lett.*, Vol. 27, pp. 350-352, 1975.
6. E.R. Ault, R.S. Branford, and M.L. Bhaumik, "High-power xenon fluoride laser", *Appl. Phys. Lett.*, Vol. 27, pp. 413-415, 1975.
7. C.A. Brau and J.J. Ewing, "354-nm laser action on XeF^* ", *Appl. Phys. Lett.*, Vol. 27, pp. 435-437, 1975.
8. J.A. Mangano and J.H. Jacob, "Electron beam controlled discharge pumping of KrF-laser", *Appl. Phys. Lett.*, Vol. 27, pp. 495-498, 1975.
9. G.C. Tisone, A.K. Hays, and J.M. Hoffman, "100 MW, 248.4 nm KrF laser excited by electron beam", *Opt. Commun.*, Vol. 15, pp.188-189. 1975.
10. J.M. Hoffman, A.K. Hays, and G.C. Tisone, "High-power UV noble-gas-halide lasers", *Appl. Phys. Lett.*, Vol. 28, pp. 538-539, 1976.

11. V.N. Ischenko, V.N. Lisitsin, A.M. Razhev, "Powerful light superemission of ArF, KrF, and XeF excimers in an electrical discharge", *Pisma Zh. Tekh. Fiz.*, Vol.2, pp.839-842, 1976.
12. W.R. Waynant, "A discharge-pumped ArCl superfluorescent laser at 175.0 nm", *Appl. Phys. Lett.*, Vol. 30, pp. 234-235, 1977.
13. Yu.I. Bychkov, V.F. Losev, G.A. Mesyats, and V.F. Tarasenko, "An electron-beam-pumped XeCl laser", *Pisma Zh. Tekh. Fiz.*, Vol.3, pp. 1233- 1236, 1977.
14. W.R. Waynant, "Noble Gas-Halides VUV Lasers", *Kvant. Electron.* Vol.5, pp. 1767-1770, 1978.
15. I.N. Konovalov and V.F. Tarasenko, "A XeBr laser excited by an electron beam", *Kvant. Electron.* Vol.6, pp. 400-402, 1979.
16. G. Balog, B.K. Sander, and E. Seegmiller, "The mechanism of energy decrease in the XeBr-laser", *Appl. Phys. Lett.*, Vol. 35, pp. 727-728, 1979.
17. J.K. Rice, G.C. Tisone, and E.L. Patterson, "Oscillator performance and energy extraction from a KrF laser pumped by a high-intensity relativistic electron beam", *IEEE Trans. Quant. Electron.*, Vol. QE-16, pp. 1315-1325, 1980.
18. "Inertial confinement fusion at Los Alamos. The physics and chemistry of electron beam. Pumped KrF lasers.", Compiled by D.C. Cartwright, *Los Alamos*, Vol. 2, 1989.
19. Y. Owadano, I. Okuda, Y. Matsumoto et al., "ASHURA: a 1-kJ laser", *Proc. Conf. "Lasers and Electro-Optics"*, - Anaheim, Vol. 7, pp. 2-4, 1988.
20. G.A. Mesyats, V.V. Osipov, and V.F. Tarasenko, *Pulsed Gas Lasers*, SPIE Optical Engineering Press, Bellingham, Washington USA, 1995.
21. J.A. Sullivan, "Design of a 100-kJ KrF power amplifier module", *Fusion Technology*. Vol. 11, pp. 684-704, 1987.
22. W.H. Long, M.J. Plummer, and E.A. Stapaerts, "Efficient discharge pumping of an XeCl laser using a high-voltage prepulse", *Appl. Phys. Lett.*, Vol. 43, pp. 735-737, 1983.
23. Champagne L.F., Dudas A.J., Harris W.W. "Current rise-time limitation of the large volume X-ray preionized discharge pumped XCl-laser", *J. Appl. Phys.*, Vol. 62, N 5. - P. 1576-1584, 1987.
24. F. Kannari, M. Obara, and T. Fujioka, "An advanced kinetic model of electron beam excited KrF lasers including the vibrational relaxation in KrF(B) and collisional mixing of KrF(B,C)", *J. Appl. Phys.*, Vol. 57, pp. 4309-4322, 1985.
25. A.M. Boichenko, V.I. Derzhiev, and S.I. Yakovlenko, "Kinetic models for active media of an ArF laser", *Laser Physics*, Vol. 2, pp. 210-220, 1992.
26. S.I. Yakovlenko, "Plasma Lasers", *Laser Physics*, Vol. 1, pp. 565 - 589, 1991.
27. E.N. Abdullin, S.P. Bugaev, A.M. Efremov, V.B. Zorin, B.M. Koval'chuk, V.V. Kremnev, S.V. Loginov, G.A. Mesyats, V.S. Tolkachev, P.M. Shchanin "Electron Accelerators Based on Vacuum-Insulated Marx Generators" *Priory I Tekhnika Eksperimenta*, No. 5, pp. 138-142, 1993.
28. E.N. Abdullin, S.I. Gorbachev, A.M. Efremov, B.M. Koval'chuk, S.V. Loginov, V.S. Skakun, V.F. Tarasenko, V.S. Tolkachev, A.V. Fedenev, E.A. Fomin, and P.M. Shchanin "Powerful compact laser with $\lambda = 308$ and 249 nm pumped by radially convergent electron beam", *Kvantovaya Elektronika*, Vol. 20, No. 7, pp. 787-790, 1993.
29. A.N. Panchenko, V.F. Tarasenko "Maximum Performance of Discharge-Pumped Exciplex Laser at $\lambda = 222$ nm." *IEEE J. of Quantum Electron.* Vol. 31, pp. 1231-1236, 1995.
30. M. Inoue et al. AMMTRA Overseas Technology Exchange, pp. 28-37, 1994.
31. *Excimer Lasers* (Edited by Ch.K. Rhodes), 240 p., Springer-Verlag, Berlin, 1979.
32. *Gas Lasers* (Edited by E.W. McDaniel), 550 p., Academic Press, New York, 1982.
33. V.Yu. Baranov, V.M. Borisov, Yu.Yu. Stepanov "Electric-discharge excimer noble-gas-halids lasers", 216 p., Energoatomizdat, Moscow, 1988.
34. B. Lacour "Fundamental And Current Status Of Excimer Lasers" *High Power Laser - Science and Engineering*, NATO ASI Sries, Vol. 7, pp. 619-660, 1995.

Table 1. First announcement about generation.

Molecules	λ , nm	Method of excitation in first	First announcement about generation	First announcement about efficient generation
XeF ⁺	~350	E-beam	Brau C.A., Ewing J.J. Appl.Phys.Lett., <u>27</u> , 435, 1975	Ault E.R., Bradford R.S. Bhattacharya M.L. Appl.Phys.Lett., <u>27</u> , 413, 1975
XeCl ⁺	308	E-beam	Ewing J.J., Brau C.A. Appl.Phys.Lett., <u>27</u> , 350, 1975	Bychkov Yu.I., Losev V.F., Mesayts G.A., Tarasenko V.F., Pisma v ZTF, <u>3</u> , 1233, 1977
XeBr ⁺	382	E-beam	Searles S.K., Hart G.A. Appl.Phys.Lett., <u>27</u> , 243, 1975	Konovalov I.N., Tarasenko V.F. Kvantovaya electronica, <u>6</u> , 400, 1979 Balog G., Sander B.K., Seeger E. Appl.Phys.Lett., <u>35</u> , 727, 1979
KrF ⁺	~250	Discharge controlled by E-beam, E-beam	Mangano J.A., Jacob J.H. Appl.Phys.Lett., <u>27</u> , 495, 1975 Ewing J.J., Brau C.A. Appl.Phys.Lett., <u>27</u> , 350, 1975	Tisone G.C., Hays A.K., Hoffman J.M. Opt. Commun., <u>15</u> , 188, 1975 Opt. Commun., <u>18</u> , 117, 1976 (108 J)
KrCl ⁺	222	E-beam	Murray J.R., Powell H.T. Appl.Phys.Lett., <u>29</u> , 252, 1976	Mel'chenko S.V., Panchenko A.N., Tarasenko V.F. Pisma v ZTF, <u>12</u> , V.3, P.171, 1986
ArF ⁺	1	Fast discharge	Ishchencko V.N., Lisitsin V.N., Ragev A.M. Pisma v ZTF, <u>2</u> , 839, 1976	Tisone G.S., Hays A.K., Hoffman J.M. Opt. Commun., <u>18</u> , 117, 1976 (92 J)
ArCl ⁺	175	Fast discharge	Waynant R.W., Appl.Phys.Lett., <u>30</u> , 234, 1977	—
KrBr ⁺	206.5	Fast discharge	Waynant R.W. Kvantovaya electronica, <u>5</u> , 1767, 1978	—

Table 2. Molecules on which the generation (g) was obtained and fluorescence (f) was detected. In the brackets the wavelength of radiation with maximal intensity is shown. The wavelengths known only from calculation are marked by (*).

	F	Cl	Br	I
He	88 nm*	~80 nm*	~83 nm	-
Ne	f (115 nm)	~100 nm*	~93 nm	-
Ar	g, f (199 nm)	g, f (175 nm)	~162 nm*	-
Kr	g, f (248 nm)	g, f (222 nm)	g, f (204 nm)	185 nm*
Xe	g, f (350, 490 nm)	g, f (308 nm)	g, f (282 nm)	g, f (253 nm)

Table 3. Maximal radiation energies, efficiencies and average powers of exciplex lasers radiation

Molecule	λ , nm	Method of pumping	Maximal parameter	Reference
KrF ⁺	248	E-beam	Pulsed radiation energy, 5 kJ	[18]
XeCl ⁺	308	E-beam	Pulsed radiation energy, 2 kJ	[20]
KrF ⁺	248	E-beam	Efficiency, 12 %	[17]
XeCl ⁺	308	Discharge	Pulsed radiation energy, 66 J	[23]
XeCl ⁺	308	Discharge	Average radiation power, ~2 kW	[30]
XeCl ⁺	308	Discharge	Efficiency, > 4%	[22]

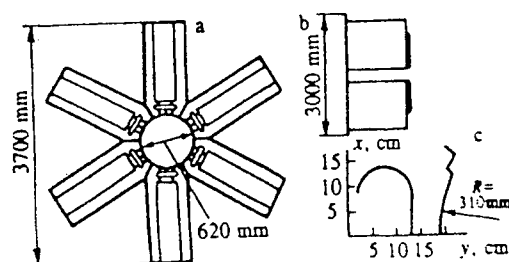


Fig. 1. Accelerators to excite a 600-liter laser : a) horizontal cross section; b) diagram of section location; c) diode section [27].

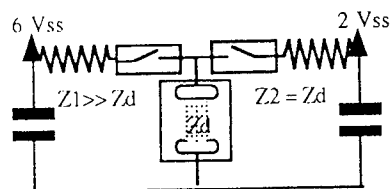


Fig. 2. Practical circuit with two generators [22].

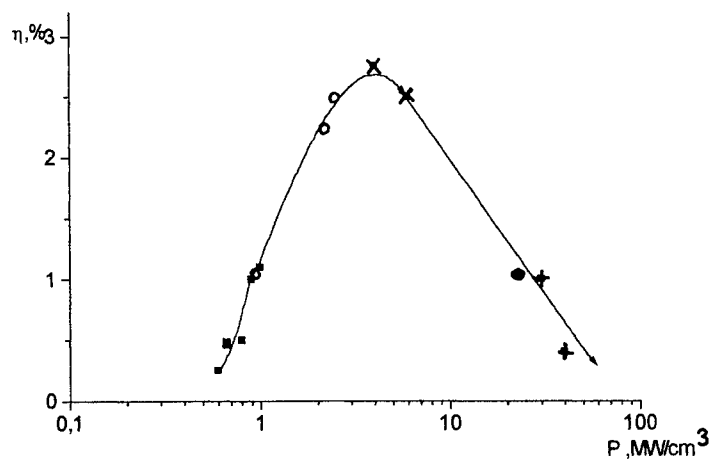


Fig. 3. Dependence of laser efficiency at $\lambda = 222$ nm based on pumping power on specific pumping power. ■-results of Hueber et al.; ●-results of Armandillo et al.; ○, ×, + - results of the present work: ○ -LIDA, $L = 60$ cm; × -FOTON, $L = 60$ cm; + -DILAN, $L = 20$ cm.

Prospects for high average power electron-beam-pumped KrF lasers for inertial confinement fusion and industrial applications

M J Shaw

Rutherford Appleton Laboratory, Chilton, Didcot, Oxon. OX11 0QX
Tel: 0123 544 5227, Fax: 0123 544 5888
e-mail: mick.shaw@rl.ac.uk

ABSTRACT

The development of high energy KrF lasers to the high average power required by inertial confinement fusion and industrial applications will be reviewed. Techniques which maintain high beam quality will be emphasised.

Keywords: inertial confinement fusion, semiconductor annealing, electron beam, excimer laser, pulsed power, adaptive optics.

1. INTRODUCTION

The KrF laser possesses all the requirements necessary for application as a driver for inertial confinement fusion (ICF). The wavelength is short, permitting good coupling to the fuel pellet; the bandwidth is large, which provides excellent beam smoothing, and the intrinsic efficiency of around 10% is enough for viable fusion power station design. Multi-kilojoule energy from a single module has been obtained, but reliable operation at multi-Hz repetition rate (which will be required for fusion power applications) has yet to be demonstrated.

Coincidentally, the majority of properties mentioned above are also required for a major industrial application, namely: large area semiconductor annealing. In this application, highly uniform beams with kilojoule energy levels are required to process areas the size of TV screens in a single shot.

To date, KrF lasers for industrial applications have been discharge pumped. It is the contention of this paper that electron-beam-pumped lasers are the obvious choice for large single pulse energy and that there is no physical reason why the repetition rate and reliability required cannot be attained.

In this paper, I will review the current status of electron-beam-pumped KrF lasers and compare them with discharge lasers. The technical challenges for the pulsed power system posed by the requirement of repetition rate will be discussed. In particular, I will highlight the work at Rutherford Appleton Laboratory (RAL) on the new KrF laser system "Titania". This laser, which has delivered more than 850 J in a single pulse, is being configured to produce intensities $> 10^{20} \text{ W cm}^{-2}$ on target. Such high intensities are of interest in the "fast ignition" route to ICF.

For operation at high repetition rate, beam quality becomes a major issue. I will describe work on two techniques used at RAL to control phase distortion, namely Raman beam clean-up and adaptive optics. Raman beam clean-up has been employed for a number of years and has the added advantage of providing power gain by combining many beams into a single beam. Adaptive optics is a new programme which at present is focused on development of deformable laser mirrors using the "bimorph" principle.

2. FUSION AND INDUSTRIAL APPLICATIONS

2.1 KrF lasers for fusion

In inertial confinement fusion, short wavelength light with an extremely high degree of uniformity is used to compress a spherical pellet of DT (deuterium/tritium) fuel to ultra-high density and temperature so that the fuel ignites. The requirement of radiation uniformity is crucial if compression to high density is to be attained against the effects of Rayleigh-Taylor instabilities which tend to destroy the spherical symmetry of the compression. In the large ICF fusion facilities currently under construction in the USA and France, megajoule-sized Nd:glass lasers are used to heat the inside of a hollow target to provide a source of uniform soft X-ray radiation, which in turn compresses the DT pellet. This "indirect" way to ICF is also proposed where ion beams act as the fusion driver. The problem with this approach for fusion power application is the inefficiency of the conversion of driver energy to X-rays.

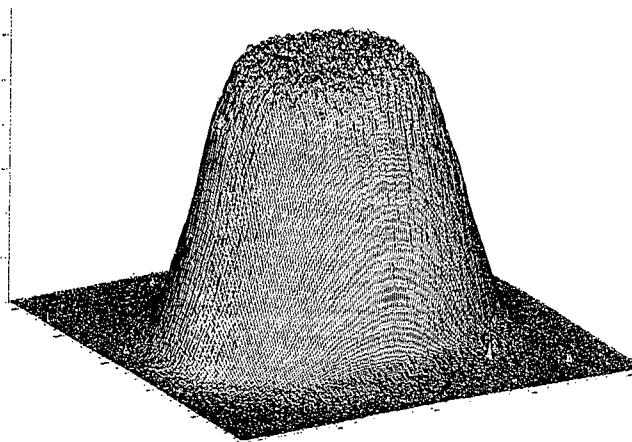


Fig. 1. Beam profile on target of a single beam from the Nike laser

A more efficient approach is to use the driver energy to compress the pellet directly. This imposes severe requirements on the illumination uniformity, but it would appear that the short wavelength and broad bandwidth of the KrF laser makes it admirably suitable in this application. The Nike KrF laser system¹ at the US Naval Research Laboratory in Washington, DC has been configured as a test bed for this "direct drive" approach to ICF. The key to achieving uniform illumination is the technique known as echelon-free induced spatial incoherence² (ISI). In this technique, a partially coherent laser beam having an angular spread $\Delta\theta \gg \lambda/D$ (i.e. many times diffraction limit) relays an image of a uniformly illuminated object to target through the amplifier chain. The beam is thus split into coherence zones of dimension $\lambda/\Delta\theta$, and provided $\Delta\theta$ also greatly exceeds the aberration limited divergence of the system, a faithful image is reproduced on target. The instantaneous image will consist of a speckle pattern formed by the interference between coherence zones, however the interference is averaged on a timescale $\Delta\nu^{-1}$, where $\Delta\nu$ is the bandwidth of the laser beam which is typically 2 THz for KrF operating broadband. Fig. 1. shows the beam profile of a single Nike beam on target with a top flat to better than 1%. The spot size is sub-millimetre and a total of 2.8 kJ is delivered to target in 56 multiplexed beams. The intensity of the overlapped beams is $10^{14} \text{ W cm}^{-2}$ with a time averaged uniformity better than 0.2%. Optical multiplexing enables efficient extraction of the long pulse amplifiers by sequential 4 ns pulses which are demultiplexed i.e. overlapped in time, on the target.

Ignition of the DT fuel in the above scheme occurs in a manner exactly analogous to that of a Diesel engine; adiabatic compression of DT gas in the centre of the pellet to temperatures high enough to start the fusion reaction. An alternative approach to ignition has recently been proposed which is analogous to a petrol engine. The DT fuel is assembled cold and the ignition is provided by a very intense short laser pulse at the point of maximum compression. This "fast ignition" scheme relaxes the compression requirements and holds the promise of improved efficiency and lower threshold energy. The short wavelength of KrF makes it the ideal candidate for the igniter laser. Short wavelength favours penetration to higher densities through the plasma blown-off during pellet compression. Petawatt power in the picosecond region with near diffraction limited beam divergence will be required for this technique to succeed.

The present generation of lasers for fusion are all single shot devices. For operation in a power station environment a repetition rate of a few Hz to a few tens of Hz will be required, depending on fusion gain and optimum power output. Cooling of the laser medium becomes important and gas lasers such as KrF will have advantages over solid state lasers where heat extraction is concerned.

2.2 Excimer lasers for semiconductor annealing

Excimer lasers are increasingly finding application in the semiconductor industry as a cost effective way of annealing silicon to its polycrystalline state after processes such as ion implantation or CVD. Laser annealing is particularly attractive for large-area electronics-on-glass applications such as flat panel displays where exposure to high temperatures is not possible³. Excimer lasers are already being installed by semiconductor manufacturers for this application. Large areas are annealed by scanning high repetition rate laser beams

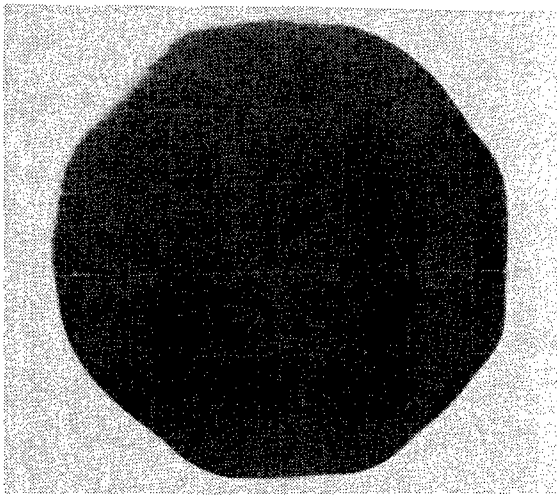


Fig. 2. Near field burn pattern, 42 cm in dia from the Titania laser beam. Average fluence: 0.6 J/cm^2

across the surface. For some applications the non-uniformity caused by this step-and-repeat process causes problems and the ability to anneal the whole display in a single shot is appealing. The fluences required to melt the silicon are typically in the range of $150 - 300 \text{ mJ/cm}^2$ and with display sizes of interest ranging from $200 \times 300 \text{ mm}$ for computer monitors to $550 \times 650 \text{ mm}$ for high definition TV screens, the required single-shot energy is in the region of $100 - 1000 \text{ J}$. Such energies are well within the state-of-the-art for electron-beam-pumped excimer lasers but represent a considerable challenge for discharge technology. The uniformity requirements are nowhere near as severe as the fusion application but some applications may require uniformity at the percent level.

For the scanning lasers used at present, repetition rates up to kHz are used with average powers of a few hundred Watts. For single shot annealing, the same average powers will be obtained at a sub-Hz repetition rate and the peak production rate is unlikely to exceed one display per second. In this area too, the industrial application has more modest requirements than that of fusion. Fig. 2 shows the large area irradiation capability of the RAL Titania KrF laser beam.

4. PULSED POWER REQUIREMENTS

4.1 Discharges vs electron beams

The discharge excited excimer laser has made enormous strides since its discovery and many difficult technical problems have been solved to bring it into the market place as a reliable industrial laser. The cost per Joule, however, is still high compared with the $\$100/\text{J}$ target for fusion power applications. To obtain the cost benefits of scale, module energies need to be in the region of kJ or even 10's of kJ. The output energy of KrF is given by $E_0 = \eta g_0 L I_s t_p a^2$ where η is the extraction efficiency, $g_0 L$ the gain length product, I_s the saturation energy, t_p the pulselength and a the aperture. Clearly, maximising energy involves increasing the aperture and the pulselength. Doing this with discharge lasers is very difficult due to discharge instabilities. In fact, of all the excimers, a scale-up of aperture and pulselength has only been obtained with XeCl, with typical energies limited to a few tens of Joules.

With electron beams, on the other hand, large apertures and long pulselengths are a natural consequence of the means of excitation. The electron energy needs to be several hundred kV to pass efficiently through the

foil separating the electron acceleration region from the laser gas. In gases around atmospheric pressure the typical electron range is several tens of cm, so large apertures are pumped efficiently. The limit to pulselength is primarily set by halogen depletion and can exceed 1 μ s at low excitation. The largest KrF laser ever operated was the Aurora laser at Los Alamos which produced 10 kJ from a 1 x 1 m aperture in a 0.5 μ s pulse.

4.2 Power switching

The main differences between the pulsed power requirements of discharges and electron beams are the voltage and impedance which are typically ten times greater in the latter case, i.e. hundreds of kV and a few ohms for e-beams versus tens of kV and fractions of ohms for discharges. This affects the choice of switch; which for discharges are frequently commercially available thyratrons or even solid-state switches whereas electron beam machines to date have used spark gap switches to deliver the power to the load.

All spark gap switches suffer from electrode erosion and have a limited lifetime between servicing of between 10^3 and 10^5 shots. Thyratrons, on the other hand, can work for 10^8 shots, and solid-state switches even more. If electron-beam-pumped excimer lasers are to make it into the industrial market place and show the way forward for fusion power applications, spark gap switches will need to be replaced by solid state switches.

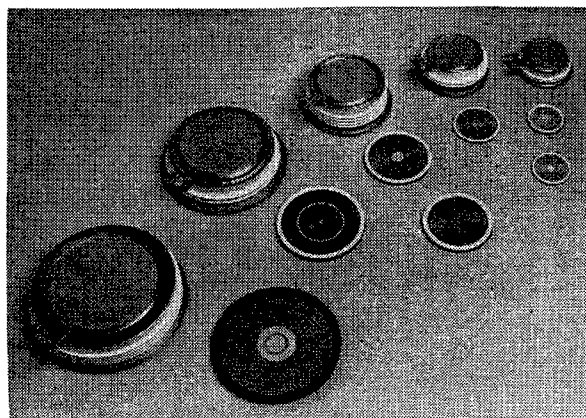


Fig.3. Range of fast turn-on GTO thyristors manufactured by Westcode Ltd. For scale, the disc second from left is 66 mm dia.

Advances in power semiconductor switches are in the direction of higher voltages and higher rates of rise of current. For example Fig. 3. shows a range of fast turn-on GTO Thyristors manufactured by Westcode Ltd. For the 66 mm device WG20045, the hold-off voltage is 4.5 kV and peak anode current is greater than 60 kA at a di/dt of more than 10 kA/ μ s. Performance limits depend on the specific application but average switched powers per device of tens of kW at tens of Hz repetition rate should be attainable. The losses are small compared with the switched energy which can amount to many kJ per device. These devices have been successfully operated in series⁴ (10x stacks to give 45 kV hold-off) and parallel operation is also possible.

Such voltages and current risetimes are still a long way from the requirements of an electron-beam-pumped laser, but the way forward has been shown by the RHEPP II machine at Sandia National Laboratories which provides an example of a prototype high repetition rate electron beam generator in using all solid-state switching. This machine produces over 300 kW of electron beam power at a repetition rate of up to 120 Hz.

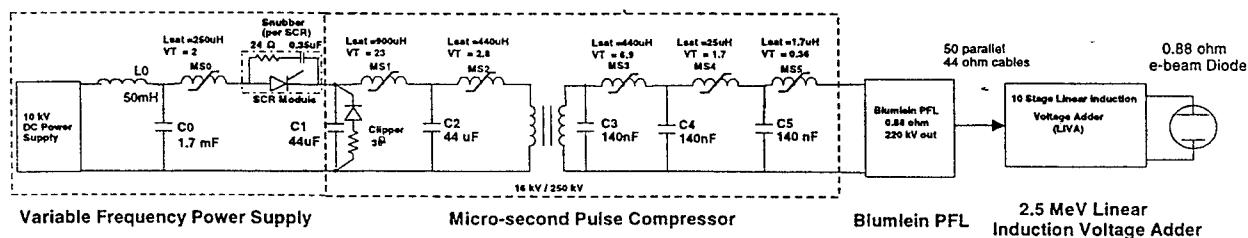


Fig. 4. Circuit diagram of the RHEPP II machine at Sandia National Laboratories

Fig. 4. shows the circuit of this system. At the front end SCR stacks provide the initial switching, after which magnetic compression stages arranged as a Melville line compress the pulse from 5 ms to 1.2 μ s. A magnetically switched Blumlein line produces a flat-topped 60 ns pulse which is stepped up from 220 kV to

2.5 MV using a linear voltage adder. The efficiency from wall-plug to electron beam is 50% and greater than 10^6 shots have been obtained.

The main factor influencing the use of magnetic switches for compressing the pulse is the volume of magnetic material required. In a Melville line, the compression takes place in a number of stages with a current gain per stage of G . The energy handled per unit core volume (E/V) is given by⁵:

$$\frac{E}{V} = \frac{4\Delta B^2}{G^2 \pi^2 \mu_0} \quad (1)$$

where ΔB is the flux swing in the core. METGLAS amorphous magnetic alloy is generally used as the core material in this application because of its large saturation flux and low losses. If the core is reverse saturated before switching, a flux swing of 3.4 Tesla is possible and with a typical stage gain of 5 eqn (1) gives a specific energy handling capability per switch of 10^5 J m^{-3} , amounting to around 13 J kg^{-1} . The present cost of METGLAS is around \$100/kg in small quantities, so with several compression stages required, the cost of magnetic material can be a significant part of the pulsed power system.

METGLAS cores are also used in the linear induction voltage adder (LIVA) stage which is an efficient way to step up the voltage at the output end of the pulsed power system to the voltages required at the electron-beam diode. The LIVA is essentially an assembly of 1:1 transformers with the primaries connected in parallel and the secondaries connected in series. As such, it is the inductive equivalent of a Marx generator, but its placement at the output end of the pulsed power system, rather than at the beginning, which is usual for Marx generators, means that the bulk of the pulse forming is done at a voltage of V_{diode}/n (where n is the number of LIVA stages) rather than $2 \times V_{\text{diode}}$ as in conventional impedance-matched pulsed power machines.

4.3 Foil lifetime

The electron beam which pumps the laser gas has to be accelerated in vacuum and then transported through a thin foil into the high pressure (typically 1 bar) laser gas. The question of survivability of the foil is crucial to the industrial application of electron beam machines. Fig. 5 shows the foiling arrangement on the RAL Titania laser module⁶. With such single-shot machines getting foil lifetime statistics is difficult. The Titania module has demonstrated 10^3 shot lifetime to date whilst its predecessor, Sprite, gave 10^4 shots before foil failure. There are however, a number of large research machines where the foil only survives a few tens of shots. Two things which seem to affect foil lifetime the most are post pulse and applied magnetic field. The plasma cathodes used in existing systems result in plasma crossing the a-k gap at some time not long after the end of the main pulse. If there is sufficient drive voltage left on the diode this (generally non-uniform) plasma will collapse to an arc and destroy the foil. Magnetic field, which in some machines is applied in the same direction as the electron trajectory to prevent beam pinching, exacerbates this effect by confining post arcs to smaller dimensions.

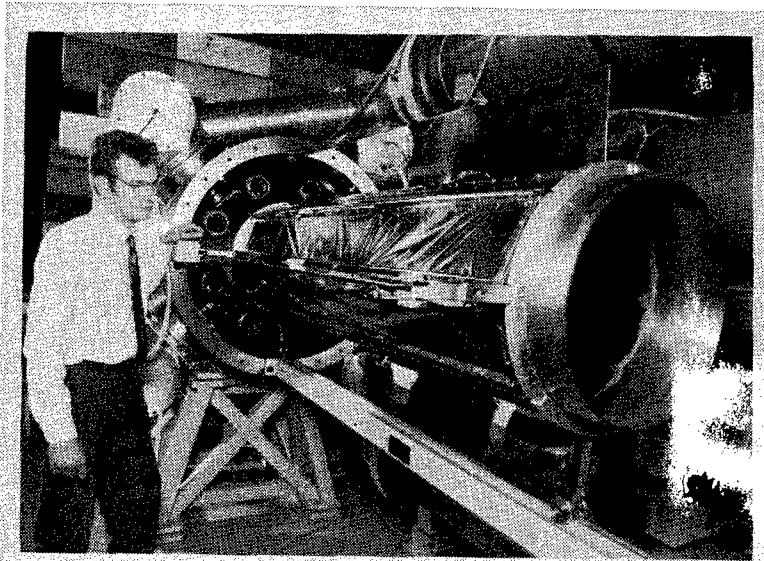


Fig. 5. Laser vessel extracted from the diode vacuum chamber on the 42 cm Titania KrF laser module at RAL. Two foils are used; a $12\mu\text{m}$ prefoil and a $35\mu\text{m}$ thick pressure foil. Both foils are made of pure rolled titanium.

Although the foil is much thicker on the RHEPP machine than on typical KrF lasers ($250\mu\text{m}$ compared to $40\mu\text{m}$) and the voltage much higher, the foil lifetime is reportedly 10^6 shots, and similar industrial radiation

sources achieve 10^7 shots. In electron-beam-pumped lasers, the energy loss in transporting the beam from the diode to the laser gas is the largest in the power train. So the question of whether long lifetime and high efficiency can be simultaneously achieved is an important one. R & D needs to be directed to this area in the future.

5. BEAM QUALITY

5.1 The need for adaptive optics

The technique of echelon-free ISI, as pioneered by The US Naval Research Laboratory, has been conspicuously successful in demonstrating that ultra uniform beams can be realised on target. This powerful

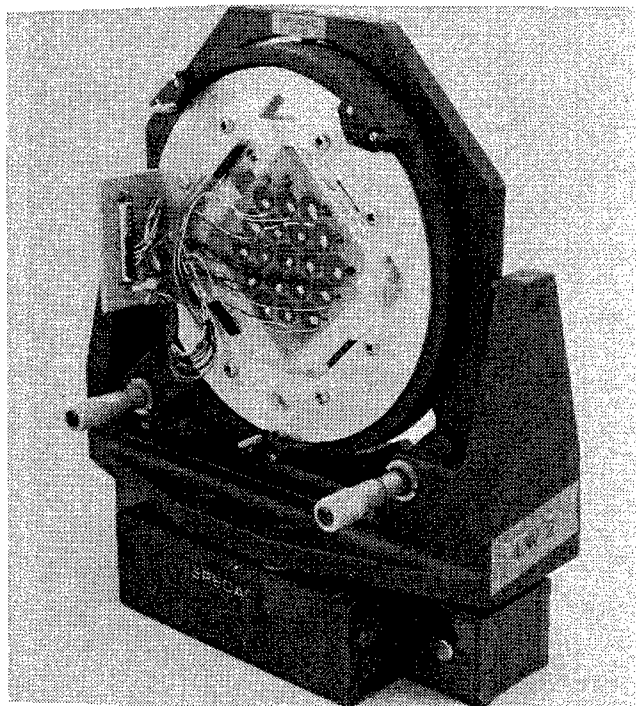


Fig.6. Multi-element bimorph mirror

technique is equally applicable to large area annealing. One of the major advantages of using ISI is the possibility of placing the amplifiers in the Fourier plane of the object and image. In this plane, all points on the image are distributed across the amplifier aperture and the effects of gain inhomogeneity can be eliminated. Phase aberrations, on the other hand, can be a problem if the condition that the propagating field angles are much larger than the aberrated divergence angle is not realised. In large aperture electron-beam-pumped KrF lasers which use high refractive index krypton/argon buffer gases phase errors under high repetition rate operation are likely to be substantial and active means of controlling them will be required.

At RAL we have initiated an R&D programme to apply adaptive optics to the Vulcan Nd:glass laser and the Titania KrF laser with a view to reducing phase errors to close to the diffraction limit. The bandwidth of aberrations on these systems is in the region DC - 3 Hz, but much higher bandwidth correction, suitable for high repetition rate operation is feasible.

As a low cost technology we are developing bimorph mirrors, which use piezoceramic plates bonded to the back of a thin mirror substrate to deflect the mirror by a process analogous to the bi-metallic strip. They are simple to construct and, by using simple screen printing techniques, can be made with an arbitrary number and shape of electrodes at the same cost. Fig. 6 shows our first prototype multi-element mirror, which has 19 circular elements printed onto a 70x70x0.2 mm thick PZT plate bonded to a 1.5 mm thick glass mirror substrate.

Our main concern about adopting this technology has been that such mirrors have in the past been almost exclusively designed with relatively few elements to compensate for low order modal aberrations. We have shown that high order control is also possible with bimorph mirrors. We have shown that the mirror can be made to mimic the behaviour of a point deflection actuated mirror where only one element is actuated. Outside the actuated region the rest of the mirror could be maintained very nearly flat by the application of suitable reverse curvature to the control elements. Experimental work on this first prototype mirror has only just begun but we have demonstrated that large deflections (many microns) can be obtained with applied voltages of less than 65 volts. This low voltage technology, which derives from the special PZT used, means that we can envision driving a rather large number of channels at relatively low cost.

5.2 Raman beam clean-up and ultra bright beams

Another beam quality enhancing technique which has been pioneered at RAL is Raman beam clean-up⁷. In this technique many pump beams (in our case at the KrF wavelength of 248 nm) pump a Raman medium (CH_4) contained in a lightguide. A single Stokes shifted beam (268 nm) extracts energy from the pump beams without being imprinted with the pump phase aberrations. Amplitude imprinting persists but this can be small where many pump beams are averaged.

The far-field patterns of the pump and Stokes output beams recorded by a UV sensitive CCD camera placed at the focus of a telephoto lens are shown in Fig. 7. The Stokes far field is characterised by a core with a FWHM of $1.7 \times$ the diffraction limit. This measure of beam divergence (which is frequently used) gives an over-estimate of the beam brightness since there is a considerable excess of energy in the wings of the far field. The peak brightness for the shot shown in Fig. 7 is $1.5 \times 10^{20} \text{ W cm}^{-2} \text{ sterad}^{-1}$ and the Strehl ratio is 0.22.

Such beams are of great interest to the ICF fast ignition scheme. Semiconductor processing with short pulses may also be of interest in some applications and this technique may well find application where energies up to 100 J are required in the pulselength region of tens to a few hundreds of ps.



Fig.7. Top: Far field of a typical pump beam to the Raman amplifier $\sim 20 \times \text{DL}$. Bottom: far field of Stokes beam $\sim 1.7 \times \text{DL}$

6. CONCLUSIONS

The challenge of developing large electron-beam-pumped excimer lasers for fusion applications is a formidable one. However it is fortunate that many of the developments required for fusion can be applied, at a significantly smaller scale, to important industrial applications.

7. ACKNOWLEDGEMENTS

The author wishes to acknowledge helpful discussions with his colleagues at RAL, in particular, Graeme Hirst, Ian Ross and Chris Hooker. He is also grateful for information supplied by Stephen Bodner and John Sethian at NRL, Larry Schneider at Sandia Laboratories, Dave Forster at AWE and Roger Youdan and Frank Wakeman at Westcode Semiconductors.

8. REFERENCES

1. S P Obenschain et al "The Nike KrF Laser Facility: performance and initial target experiments" *Physics of Plasmas* 3, 2098 (1996)
2. R H Lehmburg and J Goldhar "Use of incoherence to produce smooth and controllable irradiation profiles with KrF fusion lasers" *Fusion Tech.* 11, 532 (1987)
3. S D Brotherton et al, "Excimer laser annealed poly-Si thin film transistors", *IEEE Trans. on Electron Devices*, 40, 407 (1993)
4. E Carlier et al "Solid state switch application for the LHC extraction kicker pulse generator" paper presented at the Power Modulator Symposium (1996)
5. D L Bix et al "Experiments in magnetic switching" *Proc 3rd International Pulsed Power Conference IEEE* 1981 p 262
6. E J Divall et al "Titania - a $10^{20} \text{ W cm}^{-2}$ ultraviolet laser", *J. Mod Optics* 43, 1025 (1996)
7. M J Shaw et al "Ultrahigh-brightness laser beams with low prepulse obtained by stimulated Raman scattering" *Optics Letts.* 18, 1320 (1993)

60J XeCl laser for Single Shot Excimer Laser Annealing

Bruno Godard, Patrick Laborde, Cyril Dutems, Sylvie Prochasson, Dorian Zahorski, Marc Stehlé
SOPRA - 26, rue Pierre Joigneaux - 92270 BOIS-COLOMBES
Tel : 33-1 47 81 09 49 - Fax 33-1 42 42 29 34

Jean Bonnet, Daniel Pigache
ONERA - Fort de Palaiseau - Chemin de la Hunière et des Joncherettes - 91120 PALAISEAU
Tel : 33-1 69 93 60 60 - Fax 33-1 69 93 61 82

ABSTRACT

1 kW average power (13J x 80 Hz or 10J x 100 Hz) has been obtained in 1992¹ and up to 22J per pulse and per module has been reached in 1995² in the frame of Eureka Programm EU205 by SOPRA. This work is the prolongation of these studies and gives to the flat panel industry an unique tool in the world for Silicon annealing. Gathering three modules, we obtain 60J per pulse at 308 nm. The first module is an oscillator ; the two others work as amplifiers. We tested different kinds of cavity (stable and unstable) ; finally, we choose an unstable cavity ($M = 1.2$) with special output mirror. The pulse duration is about 200 ns FWHM but can be tuned if necessary. The flat panel industry asks a repetition rate of 0.16 Hz, so there is no need for circulation of the gas mixture. Work on synchronisation of the 3 modules will be shown.

Main applications of these lasers are shock hardening, soft X-Rays generation, surface treatment by photo-ablation and "Single Shot Excimer Laser Annealing (SSELA). For the first ones, the laser beam has to have a low divergence and for surface treatment, the beam must be very homogeneous (typically $\pm 3\%$). That is the reason why we designed an homogeniser and we solved problems of self focussing and plasma creation. The 3 modules and the process in cleanroom are driven by a control command system for an industrial use.

Keywords : excimer laser, XeCl, long pulse, MOPA, unstable cavities, high energy per pulse, Silicon annealing, homogenizer, shock hardening, photoablation, self-focussing

1. INTRODUCTION

In the frame of EUREKA Program EU205, SOPRA developed his own way : high energy per pulse instead of high pulse repetition rate. So, in 1992, SOPRA obtained more than 1 kW average power (13J x 80 Hz) for the first time with a laser made for industrial application¹.

We now decided to enter the market of Excimer Laser Annealing (ELA) and especially with a Single Shot on the screen if possible (one screen, one shot) and we called this process SSELA. For some screens, 13J is enough but there was a demand of several big customers to have 45J on the sample with a repetition rate of only 0.16 Hz, 24h a day.

This was the challenge we decided to take and up to now, we have obtained a maximum of 60J per pulse. Other applications are also aimed like surface treatment, like shock hardening or soft X-Ray generation.

For all these applications, high energy is important ; for some, divergence has to be as small as possible ; for others, there is a compromise for the divergence. For all applications, pulse duration and pulse shape are also important criteria but the best is not the same in each case.

2. DESCRIPTION OF THE SET-UP

To obtain 60J, three modules are used. The modules are almost identical for maintenance reasons.

We tried different combinations :

A) three oscillators gathered by the beam homogenizer

- B) one oscillator and two amplifiers
- a) with two mirrors between each module to have alignment easier
 - b) in line (we avoid losses on four mirrors)

Finally, we use the last one B) b).

2.1) Description of one module

Each module is an extrapolation of the VEGA laser which is described in previous works (see for instance reference²). There is no blower and no circulation loop. Only small tubes are connected to a gas purifier GP2000 (OXFORD LASERS) and a gas reservoir tank.

It is X-Ray preionized. The amplifying medium is $10 \times 7 \times 130 \text{ cm}^3$ (except for the oscillator : $9.5 \times 7 \times 130 \text{ cm}^3$). The length between mirrors or windows is 2 metres. There are eight capacitor benches associated with eight synchronized thyratrons.

The power supplies, gas filling, pressures, temperatures, energy of laser per pulse, number of pulses, pulse repetition rate etc... are controlled by a master computer (Control Command).

2.2) Three modules

The three modules are triggered with a tunable timing. All three are controlled by the same computer.

There is one optical system between the oscillator and the first amplifier. This system matches the height of the oscillator beam (9.5 cm) to the amplifier height (10 cm) ; it can also correct a little bit the convergence or the divergence of this beam. It is composed of a diverging lens followed by a converging lens.

At the output of the third module, we often put an afocal system to reduce the flux and the divergence of the beam.

2.3) Different kinds of oscillator

We study different oscillators :

- a) plano-concave (stable cavity)
- b) plano-plano
- c) unstable cavity : convex - concave

Concave is R_{max} ; the radius of curvature is R_{CC} . Convex is the output mirror. It is a meniscus with the same radius of curvature R_{CX} on both sides.

$$M = R_{\text{CC}} / R_{\text{CX}}$$

M	DIMENSION * (mm)	REFLEXION RATIO (%)
1.25	76 x 50	10
1.7	55 x 36	17
2.45	38 x 25	40

* Dimension of the central zone of convex dioptr

Not as in the usual unstable cavity, the output mirror is partially transparent (and partially reflecting) around its center and totally transparent outside this zone (anti-reflection coated). The reflection coefficient R of the center zone is related to the optimum reflexion coefficient R_{opt} in a plano-plano cavity by the relation :

$$R = R_{opt} M^2$$

The frontier between the central zone and outside can be sharp or soft. The size of the central zone is directly related to M . All the coatings are inside the cavity ; outside is anti-reflection coated. In this case, the mirrors are also the window between inside cavity and outside. We can also put windows with anti-reflection coating and an angle of about 6° ; in this case, the mirrors are in the air and are easier to be precisely tuned.

2.4) Measurement

Energy is measured by a calorimeter with Pelletier element ; this calorimeter has a cross section of $13 \times 13 \text{ cm}^2$ and is calibrated with a calorimeter Scientec at an energy level of about 10J. We print the beam either on an old thermic fax paper or on "Kodak linegraph" paper. Laser pulse is measured with a photo-diode PIN 3D connected to a multi-way oscilloscope Tektronix TDS420 or TDS520. Current is measured by a very simple set-up made by SOPRA in connection with the same oscilloscope.

3. RESULTS

3.1) Oscillator

As reported in previous works², one module gives a maximum of 22J per shot with a plano-plano ($M = 1$) cavity with an efficiency of 2 % ; the pulse duration is 200 ns Full Width Half Maximum (FWHM). We obtain the same energy value with stable and different unstable cavities ($M = 1$; $M = 1.2$; $M = 1.7$). Higher is the value of M , smaller is the divergence of the oscillator, but higher is the coherence degree. Often, we have to choose the best compromise. Convex mirror with sharp edges between outer and central zone gives diffraction fringes. The same mirror with soft edges (about 2 mm edges) decrease very much these fringes, again with the same energy. Furthermore, there are no holes in the print of the beam. This is much better to homogenize the beam after. For $M = 1.7$, we obtain a beam divergence of typically 63 μrad and 120 μrad in the 2 orthogonal directions (100 μrad and 180 μrad at the maximum energy).

3.2) A) : Oscillator + first amplifier

We confirm that the delay to obtain pulse laser or amplification from a given time t_0 changes with :

- a) the high voltage applied to the laser electrodes
- b) partial pressure of the mixture Xe, HCl, Ne
- c) distance between the laser electrodes.

It probably changes also with the quality of the preionization. We take that into account by matching the delay between oscillator and amplifier at the optimum when a), b), or c) changes. So we verify that the amplifier is well in saturated amplification regime i.e. amplifier gives about the same extra energy when the input energy varies a little. A module give about the same energy when it is amplifier or oscillator.

B) Oscillator + first amplifier + second amplifier.

When oscillator and first amplifier are correctly tuned, we take them like a big oscillator ; so we applied the same procedure as in A) to match the delay of the second amplifier. The second amplifier gives again its own contribution in saturated amplification regime, but some energy is lost between each module ; these losses are due to divergence of the beam and edges of the amplifiers and to partial reflexions on the windows and lenses.

At the output of the second amplifier, a maximum of energy of 60J has been obtained and 52J is typically obtained. The pulse duration is typically 200 ns (FWHM) ; but when changing some conditions, pulse duration can vary from 180 ns to 250 ns. With some extra set-up, we can vary the pulse duration from 35 ns to 250 FWHM ; in this case, up to now, energy is reduced. In single pass, it is reduced proportionally to the duration ; in multipass, energy is increased.

4. APPLICATIONS

Main applications for this laser is Single Shot Excimer Laser Annealing (SSELA), surface treatment, shock hardening and X-Ray generation. SSELA and surface treatment claim a very good homogeneity of beam ; shock hardening and X-Ray generation claim a high energy per cm² in a window of time of 10 to 40 ns for shock hardening and 1 to 5 ns for X-Ray generation.

Unstable cavities give about the same energy and reduce a lot divergence with 200 ns ; at 1 ns, it is more difficult. The first experiments in shock hardening are full of hope.

SOPRA makes homogenizers which give an almost flat ± 2 % energy density on a surface of 12 x 16 cm² for SSELA. We have to put it in vacuum to avoid self focussing and plasma creation.

Annealing of amorphous silicon is a process to convert amorphous silicon (a-Si) into poly crystalline silicon (poly-Si), it is a melt-crystallization process and it is necessary to increase the n and p mobility of a-Si. This application is largely described in reference³.

These three modules and process in clean room and analysis by Spectroscopic Ellipsometry are driven by a control command system for an industrial use 24 hours a day.

5. ACKNOWLEDGEMENTS

This research has been done at SOPRA with the collaboration of ONERA's team. The authors wish to thank Magali Maugé and Carine Ancellet for their fruitful participation.

6. REFERENCES

- Ref. 1 : B. Godard, P. Murer, M. Stehlé, J. Bonnet and D. Pigache, *"REALIZATION OF A 1 kW XeCl LASER"*, 9th GCL, SPIE Vol 1810, p 372, Heraklion/GREECE, Sept. 1992
- Ref. 2 : B. Godard, P. Murer, M. Stehlé, J. Bonnet, D. Pigache, *"VEL 15 - SECOND GENERATION OF SOPRA's VEL INDUSTRIAL EXCIMER LASER, ENERGY UP TO 20J"*, CLEO/Pacific Rim Conference, Japan, July 10-14, 1995
- Ref. 3 : M. Stehlé, *"EXCIMER LASERS ANNEAL FLAT PANEL DISPLAYS"*, LASER FOCUS WORLD, May 1996 issue, p 101-110

J.C.M Timmermans, Th Hofmann, F.A. van Goor* and W.J. Witteman

* University of Twente, Department of Applied Physics, P.O. box 217, 7500AE Enschede, The Netherlands

For high repetition operation of excimer-lasers care has to be taken of the changing performance of the electrical circuit, gas dynamic effects and contamination of the gas mixture to avoid deterioration of the laser performance. The parameters that influence the stability of the discharge are discussed. With the proper settings 1kW of average power can be reached.

1. INTRODUCTION

2. DISCHARGE CIRCUIT

The diagram illustrates the experimental setup for studying the electron avalanche mechanism in a gas discharge. The main components are:

- Settling chamber**: The initial section of the discharge tube.
- Contraction**: A narrow section of the tube where the discharge is initiated.
- X-ray preionizer**: A device used to preionize the gas in the contraction region.
- Diffuser**: A section of the tube that expands after the contraction.
- Heat exchanger**: A component used to manage the temperature of the gas.
- Centrifugal blower**: A device used to circulate the gas through the system.

The electrical system includes:

- Main power supply**: Provides a +10 kV potential.
- Pulse forming network**: A network of capacitors and inductors used to shape the discharge pulse.
- Pulse compressor**: A device used to compress the pulse.
- Prepulse power supply**: Provides a +50 kV potential for the preionization stage.

The discharge is build up in three phases. First the gas is pre-ionised by X-rays. Then a spiker-sustainer also called a prepulse main-pulse circuit provides a fast high voltage pulse to breakdown the gas followed by the main current pulse at matched voltage to deposit the stored energy into the discharge.

The X-rays are generated in an external source and penetrate the laser chamber through a 1mm window in the anode. The collimated X-ray beam pre-ionises the laser gas homogeneously. The width of the discharge is mainly determined by the width of the X-ray window. The profile of the electrical field, as determined by the shape of the electrodes, is less important than in case of UV pre-ionisation where the whole volume between the electrodes is pre-ionised. With a separate X-ray source there are no auxiliary electrodes that disturb the electrical field or the gas flow or contaminate the gas as they wear.

To have a stable discharge a minimum dose of X-rays is needed. During the prepulse the pre-ionisation electrons are multiplied in an avalanche process. The pre-ionisation electrons density must be high enough that the heads of the avalanches from individual pre-ionisation electrons overlap. Increasing the X-ray dose does hardly add to a more stable discharge with more output as shown in figure 2.

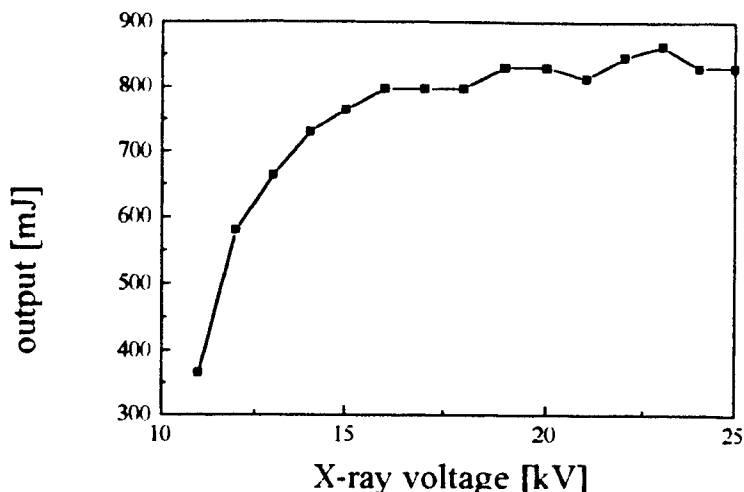


fig. 2: output as function of the X-ray gun voltage.

With a space charge limited current the dose is proportional to the $7/2^{\text{th}}$ power of the voltage.

The second step is the avalanche of the electrons by the pre-pulse or spiker. The high voltage pulse must have a short rise time to obtain a homogeneous breakdown of the laser gas. With a slow rise time the breakdown can occur at one spot and cause a voltage collapse before the breakdown on the whole discharge area occurs. To obtain a short rise time a pulse compressor is inserted in the prepulse circuit. The capacitors of the pulse compressor are charged relatively slowly to avoid a high peak current in the thyatron. When the capacitors are charged the ferrites in the pulse compressor saturate and the capacitors quickly discharge into the peaking capacitors close to the laserhead. The ferrites at the bottom of the pulse forming network (PFN) prevent this voltage pulse from disappearing into the low impedance PFN. When these ferrites saturate charge is quickly transferred from the big PFN to the small peaking capacitors, resulting in a high voltage overshoot and the breakdown of the gas. Typical waveforms of voltage current and output at this mode of operation known as the resonant overshoot mode^[1] are shown in figure 3.

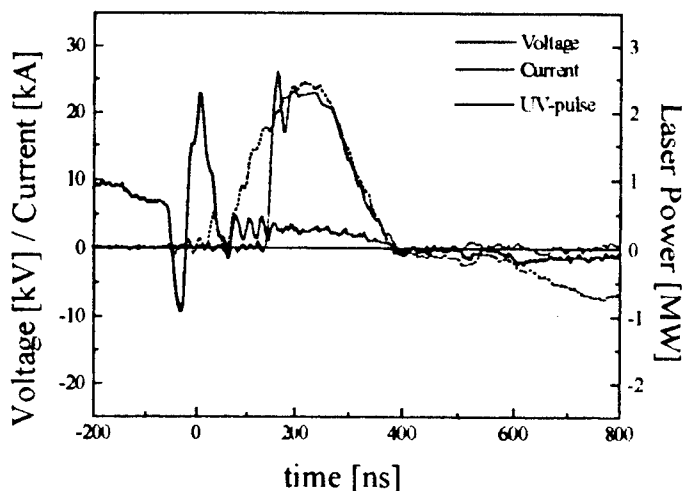


fig. 3: typical waveforms of the overshoot mode.

Finally when a good conducting plasma is formed the PFN is discharged and the XeCl-molecules are formed to give the UV-laserbeam. The PFN must be charged to twice the steady state voltage of the discharge to achieve a matched discharge with no ringing of the current. With a higher voltage the output will be higher but with a ringing current the discharge will end in an arc. At high PRF these arcs will lead to severe erosion of the electrodes and contamination of the gas.

3. DISCHARGE STABILITY

Two parameters with a strong influence on the discharge stability will be discussed. These parameters are: the HCl-concentration and the gasflow.

3.1 HCl-concentration

Due to the high attachment rate of electrons to HCl-molecules the discharge becomes unstable. If locally the initial electron density is higher than ambient the electron surplus will grow as described by the halogen depletion theory of Coutts and Webb [2]. The time before the discharge becomes unstable is inversely proportional to the square root of the HCl-concentration. To verify this relation the PFN is configured to obtain long pulses of about 500 ns. When the HCl-concentration is increased, the discharge becomes unstable and the UV-pulse terminates before the end of the current pulse. The stability time is defined as the time between the onset of the current pulse and the end of the UV-pulse. This stability time is plotted in figure 4. Below a HCl-pressure of 0.7 mbar the discharge remains stable and the stability time is just the duration of the current pulse. For higher HCl-pressures the stability time can be described with the fitted square root curve as expected.

The output first increases with the HCl-pressure because the gain becomes higher, but with higher pressures the output drops because the pulse duration gets shorter. For efficient operation the HCl-concentration must be chosen within a very limited interval.

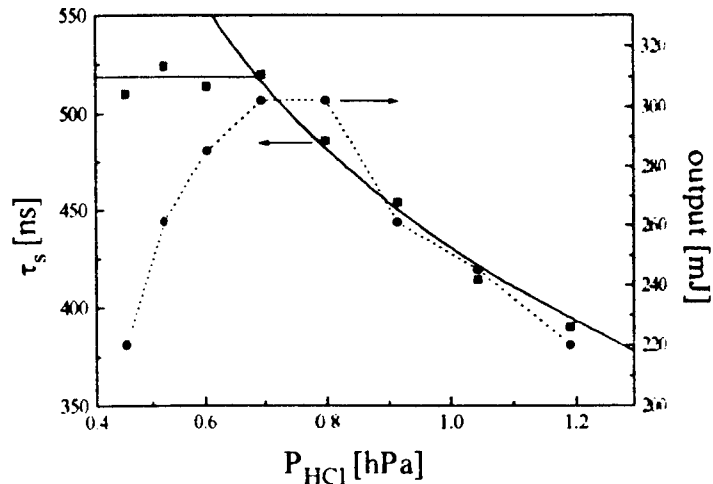


fig. 4: stability time and output as function of the HCl-pressure

The growth of instabilities can also be seen in the cathode layer. Due to the high energy deposition in this layer hot spots are formed on the cathode. From the hot spots arcs start growing into the discharge as can be seen in figure 5. These arcs form an inhomogeneous layer. The grow rate of this layer depends on the HCl-concentration as plotted in figure 6.

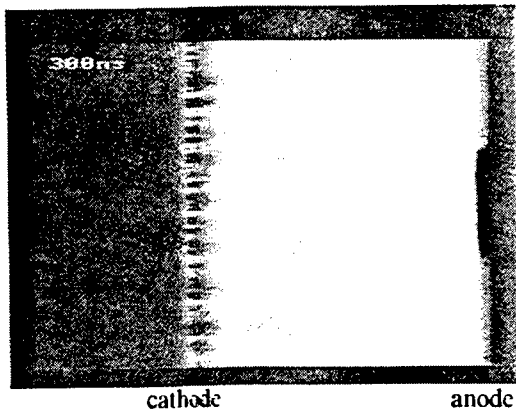


fig. 5: picture of the discharge with hot spots on the cathode.

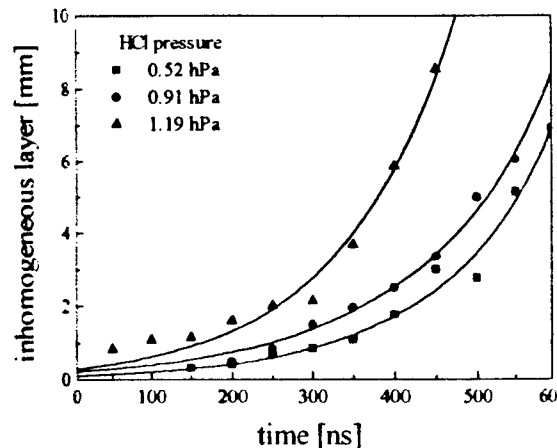


fig. 6: grow rate of the hot spot region from the cathode

3.2 Gas flow

Before the next shot can be fired the hot and turbulent used gas must be removed and fresh homogeneous gas must be provided between the electrodes. In the used gas long living ions are still present and can cause a premature and arcing breakdown of the lasergas. Therefor the used gas must be blown away to an area with a lower electrical field some distance

away from the discharge region. The clearing ratio is defined as the ratio of the distance the used gas is blown away compared to the discharge width. In figure 7 can be seen that a clearing ratio of 3 is enough for a wide range of PRF. This means that the speed of the gasflow is linear with the PRF. With an interferometer the removal of the used gas can be seen very nicely. The used gas on the left of figure 8 is turbulent and no interference can be seen. On the other hand the fresh gas gives a nice interferogram. The horizontal line in figure 8 is a shockwave. When the interferogram is filmed with a gated camera it can be seen that this shockwave originates from the cathode and bounces between the electrodes. After about 500 μ s this wave has disappeared. The shockwave is visible not only in the used gas, but also in the fresh gas. This means that the shockwave is not blown away by the gas flow. For 1 kHz operation the shockwaves cause no problems, but for a PRF higher than 2 kHz the shockwaves might form a serious limit.

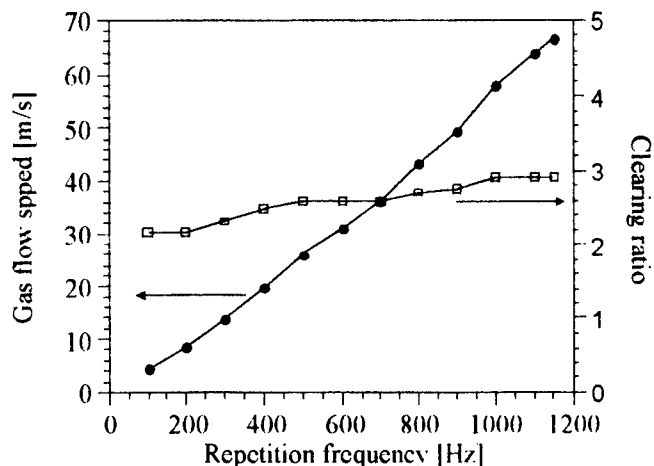


fig. 7: minimum required clearing ratio for an arcfree discharge.



fig. 8: interferogram of the discharge area 210 μ s after the discharge. Left the used turbulent gas, right fresh homogeneous gas is flowing in. A shock wave bouncing between the electrodes (on top and bottom) is clearly visible.

In the flow loop, specially near the discharge region, all plastic material should be avoided. The UV-radiation from the discharge will decompose the plastics which leads to contamination of the lasergas. For the insulation around the high voltage electrode a durable material like ceramic is necessary. With no plastic material and a gentle discharge to avoid erosion of the electrodes we have achieved 50 million shots in total with the same gas mixture without any noticeable degradation. Only HCl has to be added a few times.

4. PRESENT STATUS

It has been demonstrated that in our laser the clearing ratio and shockwaves are no limiting factors for operation at 1 kHz. With all precautions taken to obtain a matched and gentle discharge we managed to operate the laser for long times: 10 minutes at 1000 Hz and more than 1 hour at 500 Hz. These operating times are limited by technical failures of components like the power supplies, trigger circuits, the X-ray source and broken cables. With an unstable resonator the laser has been used for application experiments and demonstrated the high efficiency of long optical pulses for micro-machining. In total more than 50 million shots are taken with the same gas mixture with no degradation of the gas.

In a matched discharge the pulse energy is reduced to 600 mJ. To re-establish the targeted 1J a new bigger laserhead is designed and built. In single shot this laserhead is tested and gave 1.28 J in a matched discharge. The next step will be to install this new laserhead in the flowloop for operation at high PRF and to demonstrate 1 kW of average power.

5. REFERENCES

1. J.W. Gerritsen, A.L. Keet, G.J. Ernst, W.J. Witteman, "High-efficiency operation of a gas discharge XeCl laser using a magnetically induced resonant voltage overshoot circuit," J.Appl. Phys. 67(7), 3517-3519, (1990).
2. J.Coutts and C.E. Webb, "Stability of transverse self-sustained discharge-excited long-pulse XeCl lasers," J.Appl Phys. 59(3), 704-710, (1986).

XeCl-excimer-laser MOPA chain for Shock Hardening

G. Hintz, R. Tkotz*, C. Keusch, M. Negendanck, J. Staudigel, J. Christiansen and D.H.H. Hoffmann**;
K. Eisner***, A. Lang***, K. Schutte***, H. W. Bergmann***

Bayerisches Laserzentrum, Schallershofer Straße 108, D-91056 Erlangen, Germany

* Bayern Innovativ, Kilianstr. 142, D-90425 Nürnberg, Germany

** Physics Department I, University of Erlangen-Nürnberg, Erwin-Rommel-Str. 1, D-91058 Erlangen, Germany

***ATZ-EVUS, Rinostr. 1, 92249 Vilseck, Germany

ABSTRACT

An excimer laser in master oscillator power amplifier (MOPA) configuration ($E = 2.3 \text{ J}$, $\tau = 25 - 50 \text{ ns}$, $f = 10 \text{ Hz}$) was used for shock treatments of metallic samples. The process was studied and optimised using physical investigations concerning the pressure development. The effect of the laser treatment on the microstructure of the material could be demonstrated by micrographs of irradiated samples and could be quantified by roughness and hardness measurements as well as by residual stress analysis.

Keywords: shock hardening, XeCl laser, pressure measurement

1. INTRODUCTION

For strengthening of metals, depending on their chemical composition different methods are applied. Conventional techniques (with exception of cold forming) all include thermal processing steps, which principally cause deformation of the component and thus a mechanical after treatment is necessary. Using cold forming techniques (e.g. shot peening) a treatment of finished components is not possible due to the deterioration of the surface quality.

That is the point of departure for laser shock treatment. This method, which was developed in the seventies in the U.S.A.¹, was realised in the past using high energy, short pulsed solid state lasers². The laser pulse was used to generate high temperature, high pressure plasma at the surface of the irradiated sample. Due to the high pressure (in the GPa range) a shock wave starts propagating into the sample. A modification of irradiating directly the materials surface is the confined ablation configuration, which means that the surface is coated with two different layers. The first one is opaque to the laser light (e.g. black paint), the second one has got a high transmissivity for the incident laser radiation (e.g. distilled water or quartz glass). The benefits of such a confined ablation consists of a significant increase of pressure due to the trapping of the plasma by the transparent layer. Furthermore, the easily vaporised absorptive coating protects the samples surface, thus no crater formation occurs.

Compared to the solid state lasers used in previous investigations (repetition rates $\ll 1 \text{ Hz}$), the application of gas lasers for shock treatments would reveal the step to more adequate processing times for future industrial use. The presented work is an approach to demonstrate the potentials of gas lasers for shock treatments of metals.

2. THE EXCIMER LASER SYSTEM

For this special application a commercial laser which has all desired properties is not available. Either lasers with high pulse energy which have a high beam divergence and an undesired pulse shape or lasers which keep the requests regarding beam divergence and pulse length, but have too low pulse energy can be bought from the shelf³. Thus, a laser system called MOPA system (master-oscillator-power-amplifier) had to be built. An oscillator module creates a laser pulse with desired attributes regarding pulse length and pulse shape. This pulse will be increased in energy by using further laser modules.

In order to accomplish an easy implementation in industrial production processes, the conception has been realised by using only commercial products. An EMG 150 ES from Lambda Physik was used as oscillator, and in the final version of the MOPA chain two XP2020 from Rofin Sinar as amplifiers.

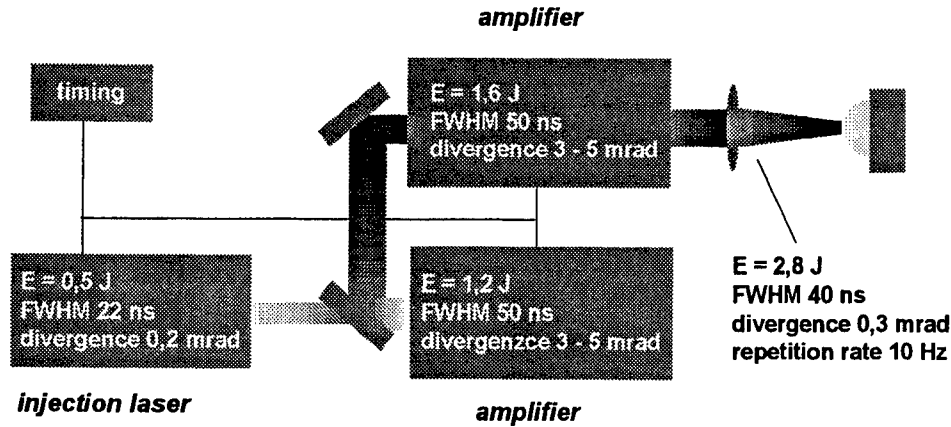


Fig. 1. Scheme of the experimental set-up.

The scheme of the optical set-up of the MOPA system is shown in figure 1. The EMG 150 was used with its original optics - an unstable resonator, the XP 2020 was fitted with a Cassegrain's telescope. The synchronisation was realised by using an electronic four channel delay generator from EG&G Model 9650. It is also possible to install a dynamical regulation system with an accuracy of nanoseconds to improve pulse to pulse stability. Such a system is normally used within the XP2020 laser.

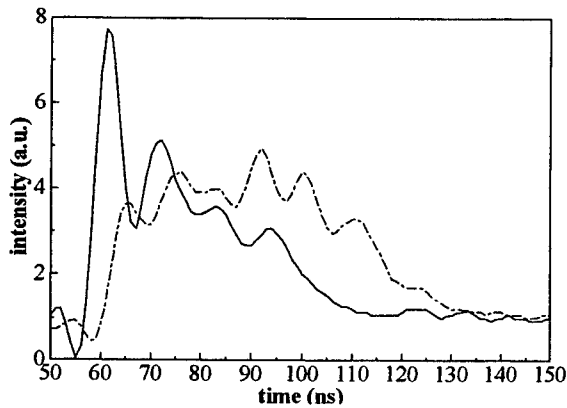


Fig. 2. Pulse shape of the MOPA system (two stage system - dashed lines long pulse mode).

The beam divergence of the system was determined by copper burnings. For this the laser beam was attenuated and focused on a polished copper target. The copper burnings were analysed under a microscope. The bounds of the laser spot interaction zone were found to be very defined, so that an energy deposit of more than 80 % can be estimated. The beam divergence was calculated to be 600 μrad in the first version, in the three stage version a final divergence of 300 μrad was obtained.

The most important advantage of this construction is the possibility to vary the pulse shape of the laser pulse. While all single stage systems have a slow rise of intensity by reason of starting oscillations, systems based on oscillator amplifier construction offer a much faster rising. Figure 2 shows two possible pulse shapes. One has a FWHM of 30 ns and a very short pulse risetime of approximately 4 ns. The other one has a pulse duration of 50 ns FWHM and a long pulse rise of 10 ns.

3. PRESSURE MEASUREMENTS

In literature an evident correlation between materials modification and achieved maximum pressures has been reported⁴. In order to measure the maximum pressures and the temporal development of the laser induced pressure pulses we have carried out measurements by means of piezoelectric gauges (PVDF - Sensor, Type M - 25 - 01 - PL). In figure 3 a) a scheme of the experimental set-up is given.

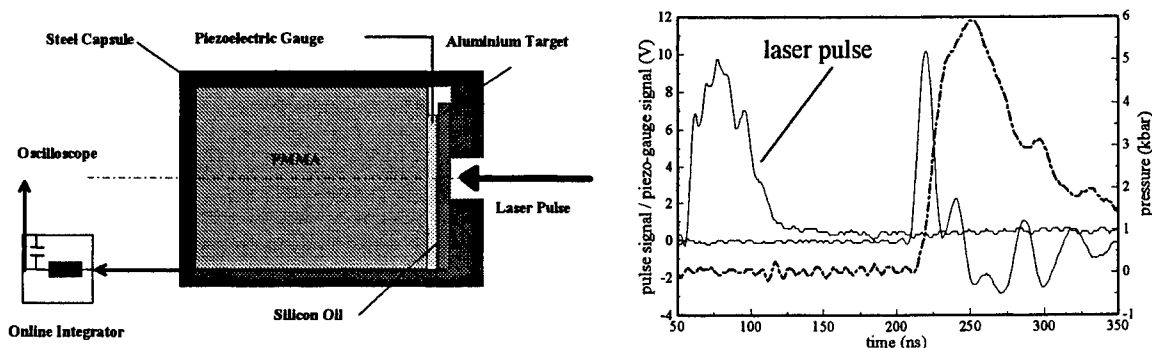


Fig. 3. a) Scheme of the arrangement for the pressure measurement. b) Typical piezo probe signal with the calculated pressure pulse (dashed lines). Parameters: 35 ns MOPA (version 1) pulse, spot diameter 1.2 mm, water confinement.

The signals of the piezoelectric gauge were calibrated with respect to the acoustic impedances⁵ of the different layers in the experimental set-up. A low inductive, passive integrating system, consisting of a 50 Ω resistance and 8 parallel grounded capacitors of 3.3 nF each, was used at the input of the oscilloscope. In order to calibrate the passive integrator the pressure signal was compared with a numerically integrated piezo probe signal. Both, pulse shape and maximum amplitude were identical within an error of 2 %. This method allowed us a very fast analysis of the experimental data.

In figure 3 b) a typical piezo probe signal and the numerically calculated pressure pulse is shown. It is necessary to realise, that the pressure is measured underneath an aluminium target of 1.0 mm thickness. In order to evaluate a realistic value for the peak pressure which is, under normal condition applied on a workpiece, the measurement of the attenuation with respect to thickness of the target was carried out. This results enabled us to give an estimation for the applied pressure pulse on the target surface.

	MOPA (two stage)	MOPA (three stage)
laser pulse energy	1.1 Joule	2.3 Joule
spot diameter	1.2 mm	2.0 mm
pulse length	25 - 30 ns	45 ns
confinement	water	water
max. measured pressure	6 kbar	10 kbar
attenuation factor	1.9	1.9
calculated max. pressure on target surface	11 kbar	19 kbar

Table 1. Main parameters for pressure measurement experiments using the MOPA systems.

4. LASER SHOCK TREATMENT OF METALS

The effect of laser shock treatment on the material (titanium, stainless steel 1.4301) was studied after irradiating samples in direct and confined ablation (black paint, distilled water) configuration. The power density in the studies was 8 GW/cm² realised by the two stage laser system (laser spot diameter 0.8 mm). Working with this relatively small laser spots, an one dimensional propagation of the generated shock wave is only expected for the first 0.4 mm. In deeper zones below the surface three dimensional effects can not be neglected anymore. Due to the attenuation of the shock wave the peak pressure decreases below the yield strength of the treated material, which marks the threshold for plastic deformation. In order to increase the plastically affected depth the number of laser impacts were accumulated in the experiments.

After scanning a polished and recrystallized titanium sample (8 GW/cm^2 , 8 pulses) with several overlapped laser pulses (overlap rate 40 %) a structural modification of the surface occurred (Fig. 4 a). The grains react to the pressure with the titanium typical twinning. The depth of the shock affected zone depends on the number of pulses and could be increased from $350 \mu\text{m}$ (8 pulses), over $450 \mu\text{m}$ (16 pulses) up to $550 \mu\text{m}$ (32 pulses). The increase of the plastically affected depth with the number of laser pulses shows a non linear behaviour. This could be an indication that the shock wave propagation has already reached a three dimensional condition. Thus, a further increase of the affected zone can not be realised effectively by accumulating further laser impacts.

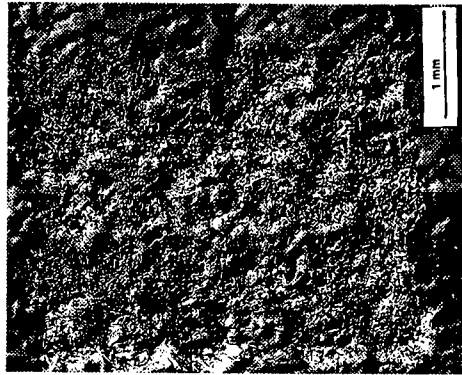
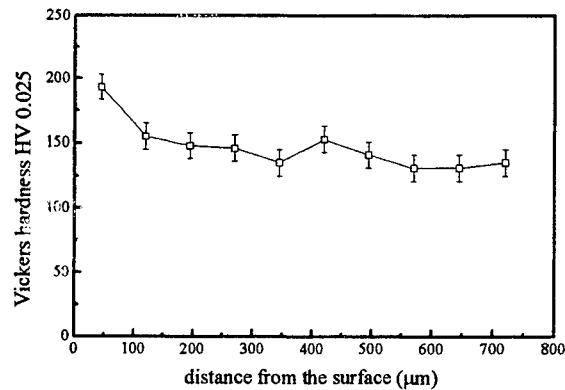


Fig. 4 a) Microstructural modification.



b) Hardness profile perpendicular to the surface.

Vickers microhardness measurements have been performed for an irradiation with 16 pulses in confined ablation (8 GW/cm^2). The hardness measurements were tested at the surface and perpendicular to the surface. At the surface of the treated sample an average hardness of $181 \text{ HV } 0.025$ was measured compared to $140 \text{ HV } 0.025$ of an untreated surface. The in depth hardness profile is depicted in Fig. 4 b). For the investigated titanium sample shock treatment only creates an hardness increase of maximum 30 % in the first $50 \mu\text{m}$ below the surface.

Residual stresses were analysed after a laser shock treatment (8 GW/cm^2 , 8 pulses) of stainless steel samples in direct and confined ablation method. In case of direct ablation method a laser treatment induces tensile residual stresses of $+210 \text{ MPa}$ at the surface due to the thermal effects of the laser irradiation. After $10 \mu\text{m}$ electrolytic polishing the tensile stresses are inverted to compressive stresses of -180 MPa . When using the confined ablation configuration, laser shock application acts as a pure mechanical treatment on the sample and a thermal effect can be excluded. The shock treatment results in compressive stresses at the surface of the specimen of -350 MPa .

5. CONCLUSION

An excimer laser in MOPA configuration seems to be an interesting system for laser shock processes which were mainly reserved in the past for Q-switched Nd : YAG prototype lasers with poor repetition rates. Using excimer lasers with the advantage of higher processing speeds could help to introduce laser shock treatments to future industrial applications.

6. REFERENCES

1. N. C. Anderholm: "Laser-generated Stress Waves", Appl. Phys. Lett., Vol. 16, No. 3, February 1970
2. R. Fabro et. al.: "Physical study of laser-produced plasma in confined geometry", J. Appl. Phys., Vol. 68, No. 2, July 1990
3. "Marktübersicht über Excimer-Laser", Physikalische Blätter 46, Nr. 3, 1990
4. T. Z. Blazynski: "Materials at high strain rates", page 18, Elsevier applied Science Publishers ltd, Essex, 1987
5. M. Hugenschmidt: "Experimental studies of High Average Power Pulsed CO_2 -Laser-Induced Thermomechanical Processes", *Spie*, Vol. 1276, CO_2 Lasers and Applications II, 1990

8. Fast-Flow and Pulsed CO₂ Lasers

Fast axial flow 25 kW CO₂-laser with unstable resonator for industrial applications

Uwe Habich, Uwe-Klaus Jarosch, Heiko Maly, Rudolf Meyer, Peter Loosen, Norbert Wolf; (1)
Thilo Beck, Christoph Hertzler, Reinhard Wollermann-Windgasse; (2)

(1) Fraunhofer-Institut f. Lasertechnik ILT

(2) Trumpf Laser-Forschungs- und Entwicklungsgesellschaft TLE

Steinbachstr. 15, 52074 Aachen, Germany

ABSTRACT

A high-power industrial CO₂ laser with fast axial gas-flow was set up with eight radio-frequency-excited discharge tubes and four turbo-blowers. With an unstable resonator the maximum output power is 25 kW. The gas flow and the electrodes for the rf-excitation were shaped carefully to achieve homogeneous gas discharges and thus an active medium that introduces only minor aberrations into the beam of the unstable resonator. The beam propagation behaviour near focus was studied for a diagnostic optics with long focal length and for processing optics with shorter focal lengths, respectively. Various welding applications in mild steel and stainless steel were carried out.

Keywords: industrial CO₂ laser, fast axial gas flow, rf-excitation, unstable resonator, aerodynamic window, materials processing, welding

1. SET-UP OF THE LASER DEVICE

A picture of the laser device is shown in Fig. 1. The laser is of the fast axial flow type¹. The cylindrical silica discharge tubes are excited by a transverse radio-frequency (rf) discharge. The tubes and the blowers are arranged in four flow-modules containing one blower and two discharge tubes, each. The length of the discharge tubes is 800 mm, the tube diameter is 46 mm and the length of the helical electrodes is 600 mm. Each blower has a volume rate of 3500 m³/h at an input gas pressure of 120 hPa and a pressure ratio of 1.6. The gas mixture is 80.2 % He, 16.3 % N₂, 3.5 % CO₂. The flow-modules are mounted in parallel in a square cross-section on a central stainless steel tube, which also carries the resonator end mirrors and folding mirrors (Fig. 2). This arrangement results in a compact overall design of the laser device. The discharges are excited by two rf-generators with a maximum output of 100 kW, each. The excitation frequency is 27 MHz. A positive branch unstable resonator with three U-type foldings and an aerodynamic window are used for power extraction. The optical arrangement of the aerodynamic window has two flat folding mirrors and two parabolic mirrors for focusing and recollimating the laser beam. The window itself is of the free vortex type².

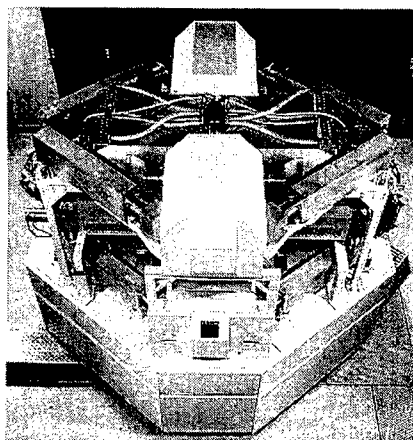


Fig. 1: Photograph of the laser device

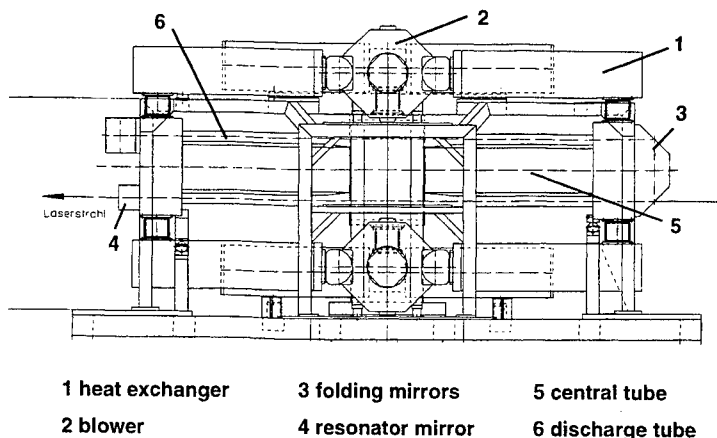


Fig. 2: Sketch of the laser device (side view)

2. LASER OUTPUT CHARACTERISTICS

The output beam of an unstable resonator is influenced more severely by fluctuations in the active medium than the beams of stable resonators³. Therefore, in preliminary experiments, the discharge and gas flow were optimised, with respect to the input power per discharge tube and the optical homogeneity, by choosing appropriate shapes for the inlets and outlets of the tubes and the rf-electrodes^{4,5}. These experiments were carried out at one flow module only, without laser activity. The maximum input power depends on the mass flow rate of the laser gas. Enhancing the mass flow rate is achieved by minimising the pressure drop in the gas flow circuit. The highest pressure loss occurs in the outlet of the discharge tubes, which also performs the remixing of the separate flows. Thus, optimising the flow contour of the outlet is essential for enhancing the input power per discharge tube. Additionally, proper shaping of the inlet geometries of the discharge tubes is important for the homogenisation of the gas discharge, regarding the power density distribution as well as the optical properties of the active medium. The degree and scale of the turbulence of the flow and the resulting fluctuations in the refractive index of the medium depend on the shape of the inlet geometries. The optimisation of the gas flow resulted in a maximum input rf-power of 30 kW per discharge tube and a minimised variance of the optical path difference within the tube diameter of 0.3 μm per flow module, measured at 632 nm.

When operated with the unstable resonator, the maximum input rf-power is 160 kW, resulting in a maximum output power of 25 kW. Long term fluctuations of the output power, measured with a calorimeter within an interval of four hours, were less than 2 %. The resonator length is 11.8 m, the curvatures of the convex and concave resonator mirrors are -25 m and 32 m, respectively. The bore diameter of the scraper mirror is 16 mm. With an outer aperture diameter of 46 mm the magnification of the unstable resonator is $M = 2.9$. The beam propagation behaviour was measured near the focus of a focusing optics with two spherical mirrors with a focal length of 1.25 m, which was specially designed for beam diagnostic purposes. Fig. 3 shows a power density distribution near the waist of the focused beam. The beam diameter was determined at different positions along the propagation (z-)axis. At each z-position an averaged power density distribution was recorded with a scanning pin-hole device. The beam diameter was calculated by evaluating the second moments of the power density distribution. The numerical integration was truncated at the borders of the measurement windows, respectively. The beam propagation factor is determined by fitting a hyperbola to this beam diameters. Measured at a distance of one meter to the laser device, the beam propagation factor is $K = 0.33$ ($M^2 = 3$). Fig. 4 shows a power density distribution measured at a handling unit in a distance of 10 m. The laser beam was focused by parabolic mirror, which was used for materials processing applications, in this case. The beam propagation factor was diminished to $K = 0.23$ by a slight misalignment of the focusing mirror.

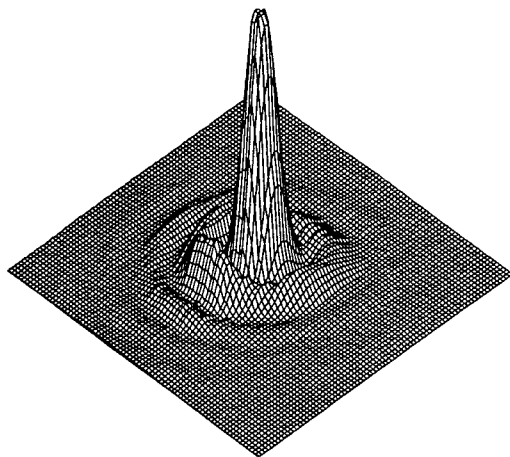


Fig. 3: Power density distribution at focus, 23 kW, window size 3 mm \times 3 mm, $f = 1250$ mm

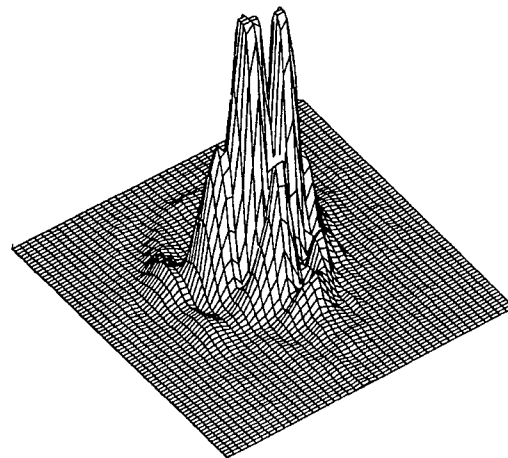


Fig. 4: Power density distribution with slightly misaligned parabolic mirror, $f = 682$ mm, 19 kW, distance to laser 10 m, 2 mm \times 2 mm

3. WELDING APPLICATIONS

Beams of unstable resonators are well suited for welding applications⁶. Care has to be taken to avoid degradation of the beam by the beam guiding system and the focusing optics. The phase front of the output beam of unstable resonators generally is very smooth, compared to the phase front of higher order beams of stable resonators. Small aberrations, induced by the beam guiding device or the focusing optics, will have a much stronger effect on the peak power density in focus for beams of unstable resonators than for multimode beams of stable resonators⁷. The astigmatism (ratio between distance of focal points and Rayleigh length) caused by the misalignment of a parabolic mirror, corresponding to the power density distribution shown in Fig. 4, is 30 %. The central lobe of the power density distribution is changed into a double lobe. Fig. 5 compares the sensitiveness of beams from stable and unstable resonators to the astigmatism caused by a misalignment of a focusing mirror. The curves are the results of calculations with a diffraction algorithm and show the dependence of the peak power density at the focal point and of the beam propagation factor on the degree of astigmatism in terms of the peak-to-valley optical path difference (PV-OPD). For beams of unstable resonators the maximum power density can already be reduced drastically, even when there is no measurable degradation of the beam propagation factor.

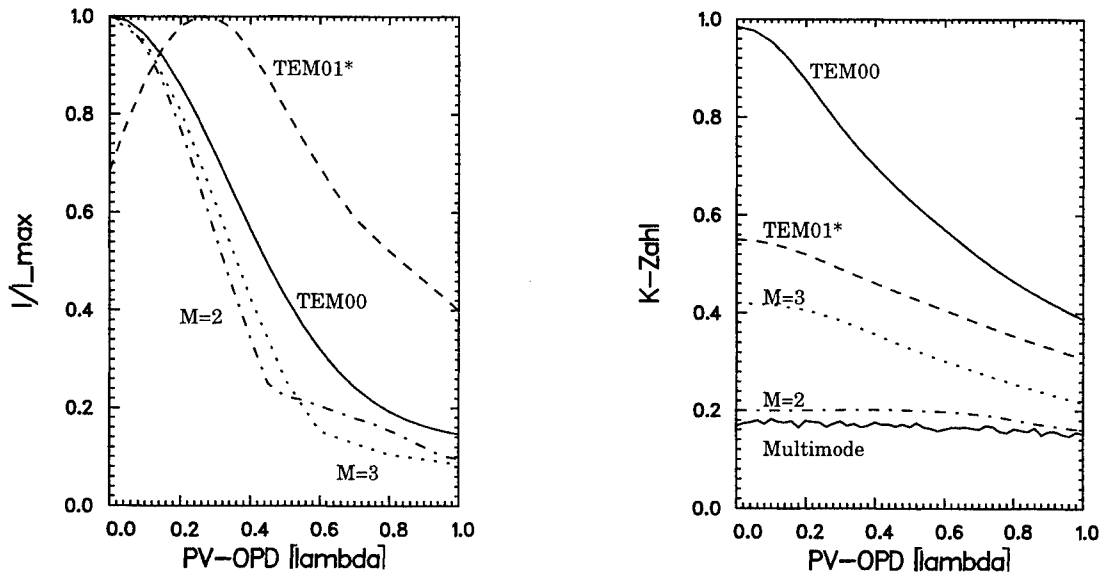


Fig. 5: Calculated peak power density (left) and beam propagation factor (right) as a function of the peak-to-valley optical path difference (PV-OPD) caused by the astigmatism of a misaligned parabolic mirror for different laser beams of stable and unstable resonators⁷

Welding applications were carried out in mild steel and stainless steel. The weld penetration was superior to other high power laser devices, which were available for comparison. Particularly, at higher welding velocities, the high beam quality enables deep weld penetration and very narrow welds. With a laser power of 19 kW at the workpiece 20 mm plates of mild steel were welded with a welding velocity of 1.1 m/min (Fig. 6). At a velocity of 5 m/min the weld penetration was more than 11 mm. The properties of the weld seam, for example the width, can be adjusted by varying the welding parameters. High quality welds, regarding to the visual appearance of the welding seams, were performed in high strength steel (S355N) and stainless steel (X 5 CrNi 1810) for plates with a thickness ranging from 8 mm to 20 mm. The welding experiments were carried out in horizontal position (PC). The linearly polarised beam was focused by a parabolic mirror (25 °) with a focal length $f = 715$ mm. Helium with a flow rate of 30 l/min was used for plasma suppression and for general shielding of the top of the weld. Argon (10 l/min) was used for root shielding for the welding of the stainless steel.

Cross sectional views of bead-on-plate weldings in 10 mm plates of are illustrated in Fig. 7. Despite of the similar welding conditions, the cross sections of the welding seams are different due to the different heat conduction coefficients of the materials. Particularly for the stainless steel, the width of the weldings is very narrow and comparable to a width achieved with electron beam welding.

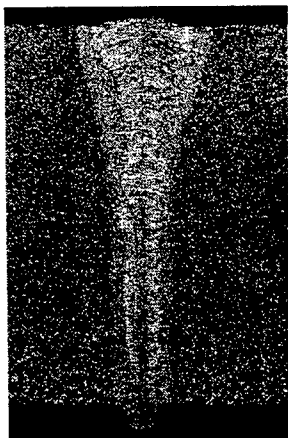


Fig. 6: Cross section of bead-on-plate welding seam in 20 mm high strength steel S355N, laser power 19 kW, 1.1 m/min

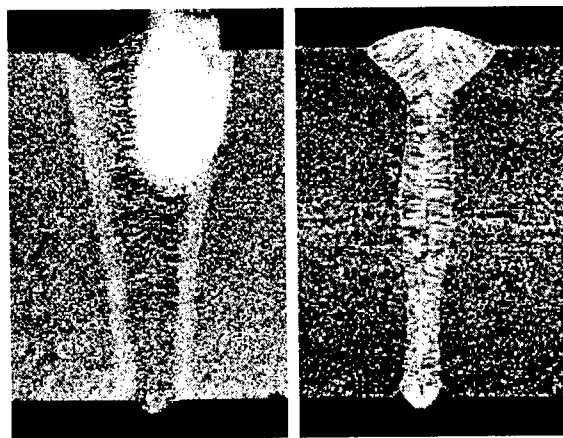


Fig. 7: Cross sections of bead-on-plate welding seams in 10 mm plates; laser power 12 kW
left: high strength steel S355N, 1.4 m/min;
right: stainless steel X 5 CrNi 1810, 1.5 m/min

4. CONCLUSIONS

A fast axial flow CO₂-laser with rf-excitation delivers 25 kW laser power in a beam with high focusability, utilising a positive branch unstable resonator and an aerodynamic window. Care has to be taken to avoid degradation of the beam by the beam guiding device and the focusing optic, since beams from unstable resonators are more sensitive to aberrations than multimode beams from stable resonators. The high focusability enables comparably deep weld penetration and very narrow weldings at high welding velocities.

5. ACKNOWLEDGEMENTS

This work is supported by the Minister für Wirtschaft, Mittelstand und Technologie des Landes Nordrhein-Westfalen, Germany.

6. REFERENCES

1. U. Habich, P. Loosen, C. Hertzler, R. Wollermann-Windgasse; "Industrial 30 kW CO₂ laser with fast axial gas flow and rf-excitation"; *SPIE vol. 2702*, pp. 374 - 384, 1996
2. W. Krepulat, P. Berger, H. Hügel.; "Investigation of a low-pressure free-vortex aerodynamic window for industrial lasers"; *SPIE vol. 2502*; pp. 559-564, 1994
3. K. Du, P. Loosen; "Influences of statistical phase distortions of active medium on laser performance"; *Optics Communications*, vol. 95, pp. 64-70, 1993
4. K. Du, J. Niehoff, C. Steven, P. Loosen; "Measurement of statistical phase distortions of active medium"; *SPIE vol. 2502*, pp. 571-576, 1994
5. J. Niehoff, U. Jarosch, P. Loosen; "Optimisation of power incoupling and statistical phase distortions by flow shaping of fast axial flow CO₂ lasers"; *SPIE vol. 2502*, pp. 536-541, 1994
6. J. Franek, K. Du, S. Pflüger, R. Imhoff, P. Loosen; "Comparison of welding results with stable and unstable resonators"; *SPIE vol. 1397*, pp. 791ff.; 1991
7. D. Ehrlichmann; "Focusing mirrors and telescopes in laser technology", *Internal report, Fraunhofer-Institut f. Lasertechnik*, 1995 (in German)

Excitation frequency effect in a fast axial flow laser with a narrow gap slab RF discharge

G Betterton and H J Baker

Physics Department, Heriot-Watt University, Riccarton, Edinburgh EH14 4AS, U.K.

ABSTRACT

A rectangular cross-section flow tube has been used in the fast axial gas flow configuration to investigate the excitation of the CO₂ laser with narrow electrode gap RF discharges. Stable discharges at a power density of 80 W.cm⁻³ have been obtained, and the influence of excitation frequency in the range 27 to 125 MHz investigated. No localised thermal instability has been detected, and discharge shrinkage at high frequency is the main frequency dependent effect found. A beam power of 132 W.cm⁻² per discharge section has been obtained. Current density measurements have confirmed that conditions similar to planar waveguide, diffusion cooled CO₂ lasers are attained.

Keywords: CO₂ laser, fast axial gas flow, rf excitation, slab shaped laser medium.

1. INTRODUCTION

Recently, the development of high average power CO₂ lasers has been following two distinct paths. For very high powers (>10 kW), fast axial flow designs are using large diameter, circular cross section discharges and RF excitation to achieve stable discharges at both high power density and flow velocity. Care over both the fluid dynamics and discharge electrode shaping has allowed 25 kW to be produced from 8 discharge sections in series, with good beam quality [1,2]. Whilst improvements in the size of gas pumps and in heat exchanger design have been made recently, such lasers remain of large physical volume. For powers in the 1 to 10 kW region, efforts are being placed more on diffusion cooled lasers, where RF excitation combined with one-dimensional waveguiding allows very compact multi-kilowatt lasers to be constructed [3,4], which can operate in a self-excited-off mode and which require no pumps or heat exchangers. Table 1 compares the key properties of the two laser approaches.

	RF, fast axial flow	Planar waveguide, diffusion cooled
Discharge cross-section	≤46 mm diameter	~1.7 mm x ≤200 mm
Electrical power density	~20 W.cm ⁻³	60 to 70 W.cm ⁻³
Operating pressure	~85 torr	100 torr
Generator frequency	13 or 27 MHz	80 to 125 MHz
Mass flow per kilowatt output	18 kg/hour	None
Max. output per discharge section	3 kW	2.5 kW
Resonator	2-d unstable, annular beam	1-d unstable

Table 1. Comparison of fast-flow and diffusion cooled laser properties

In this paper, we investigate a laser configuration which is intermediate between the two approaches outlined above, and which aims to combine the better aspects of each. Fast axial gas flow in a high aspect ratio *rectangular* flow tube is used. This means that the beam power may be increased in proportion to the width, with a 1-d unstable resonator similar to that of the planar waveguide diffusion cooled laser. With current flow across the narrow direction of the flow tube, both higher pressure and higher power density discharges are possible without the thermal instabilities found in the large cross section flow lasers. Thus it may be possible to increase the pressure to obtain an increased mass flow per unit area of beam, to counter the limitation of gas velocity to less than the sound speed in the axial flow configuration. A single discharge section laser is reported here which is used to provide preliminary data on this concept.

2. LASER CONSTRUCTION

Figure 1 shows the essential features of the laser. The rectangular, fused silica flow tube has internal dimensions 300 mm x 50 mm x 5 mm and 3 mm wall thickness and has integral input and output tapered sections. The discharge within the tube is 200 mm long, created by external plane electrodes. The gas flow loop has a Roots pump, fitted with an electronic speed control, giving 1000 m³/hour free displacement at 50 Hz electrical frequency. A "Torbar" averaging pitot gauge is used for flow

velocity measurements, and pressures and gas temperatures around the loop are recorded. Current density is monitored at four points in the discharge by probes built into the lower electrode. A stable resonator with 8% output coupling is used in these preliminary studies, giving fundamental transverse mode and multiple lateral mode operation. The gas mixture is 70% He:20% N₂:10% CO₂ for all the results reported here.

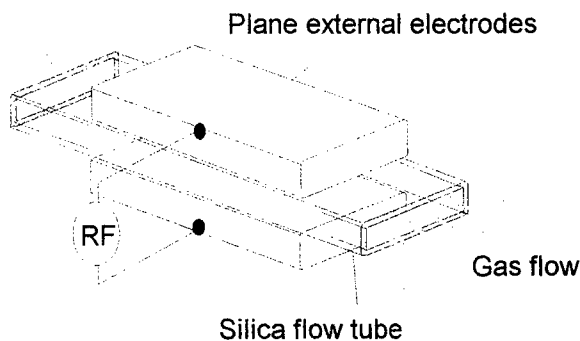


Fig. 1(a) Laser discharge region

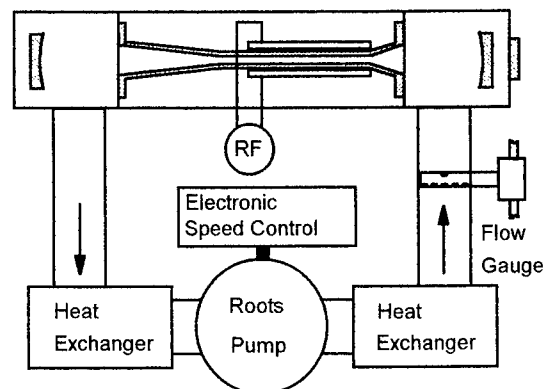


Fig. 1(b) Gas flow loop

3. GAS FLOW MEASUREMENTS

The pressure drop across the narrow gap flow section has been measured as a function of gas flow, pressure and discharge power. With mean pressures within the loop less than 100 torr, a fundamental limit to gas flow is reached where the mean exit gas velocity approaches the sound speed as shown in figure 2(a). This choking limit is described in detail by Pfeiffer *et al.* [2] for a large diameter, circular cross section laser. Increasing pump rotor speed serves mainly to increase pressure drop as this limit is reached. For higher pressures, a second more technical limit is found, shown in Fig. 2(b). The maximum rotor speed becomes limited by the electric motor current capability, and the choking limit is not attainable at maximum pump power. However, the maximum mass flow does continue to increase progressively as higher fill pressures are used, up to 300 torr. Fig. 2(b) shows also the increased pressure drop caused by the introduction of RF power into the flow.

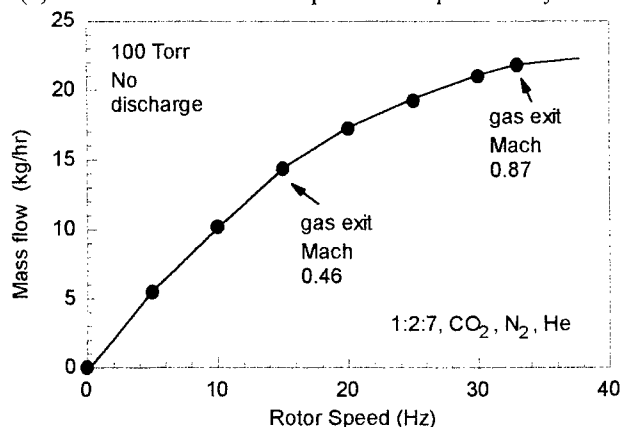


Fig. 2(a) Mass flow with varying pump rotor speed, showing limit as exit gas velocity approaches Mach 1.0

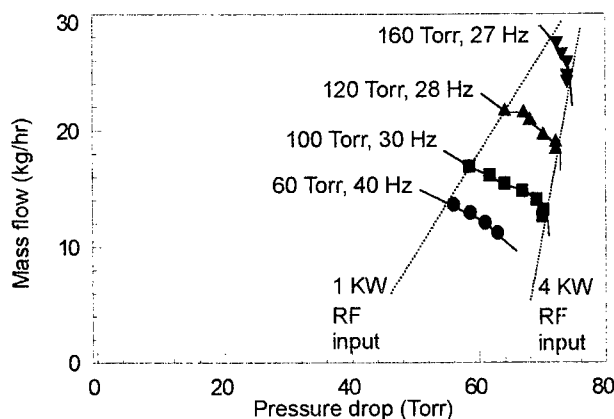


Fig. 2(b) Mass flow variation with pressure drop across the discharge section

3. EXCITATION FREQUENCY EFFECTS

An important issue in the operation of RF excited CO₂ lasers is the choice of frequency. Generators have lower cost at lower frequency, but in the case of fast flow lasers using silica dielectric tubes, low frequencies (<13.6 MHz) result in very high external electrode voltages when a high current density is required. For diffusion cooled lasers with metallic electrodes, the discharge current density is controlled only by the series capacitance of ion sheaths. For ~2 mm gap waveguide devices, the ion sheaths have the correct series ballast property only at ~100 MHz, where unwanted power loss in the sheaths is small, and sheath voltages are low enough to avoid the α to γ sheath breakdown instability [5]. The fast flow slab is required to operate at

the high current density characteristic of waveguide slab lasers, but with about three times the plasma column length. In this case, there is increased possibility of thermal filamentation since the plasma voltage may now be comparable with the sheath voltage drop. However, there is also a total thickness of 6 mm of silica and ~1 mm of air in series with the discharge which acts to control the current density for large scale length instability, and which dominates the effects due to ion sheaths. Furthermore, it is not clear that the alpha type of ion sheath properties can survive in the high velocity gradients next to the wall of the narrow gap fast flow laser.

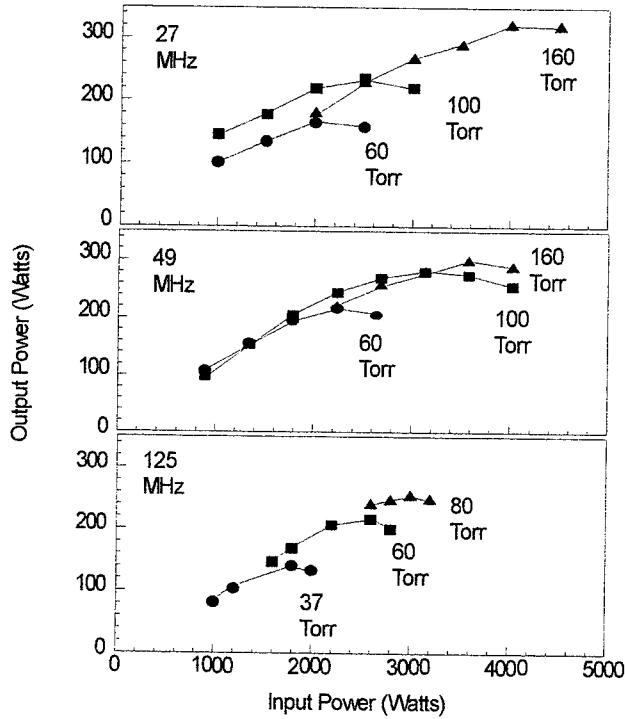


Fig. 3 Laser output at maximum gas flow for three excitation frequencies

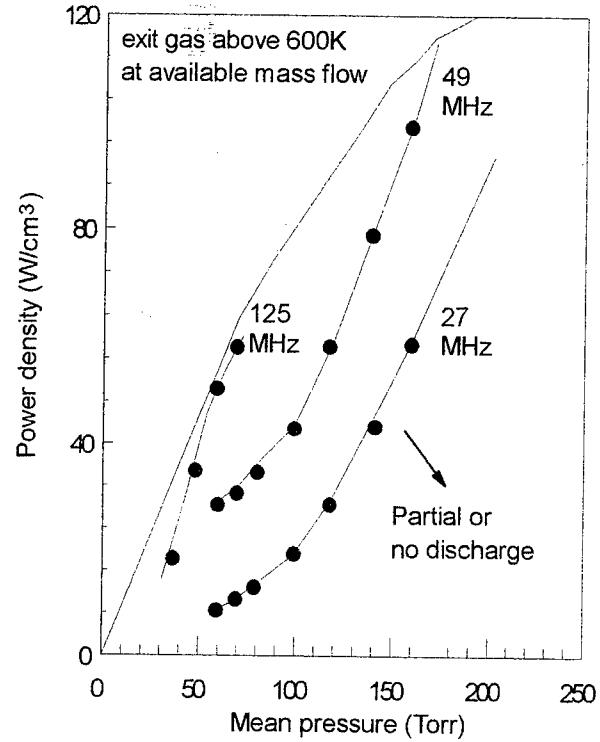


Fig. 4 Minimum power density for a stable uniform discharge

In view of these frequency dependent issues, the laser and electrical properties of the discharge section have been studied at three fixed frequencies, 27 MHz, 49 MHz and 125 MHz, to compare both discharge stability and laser efficiency. Fig. 3 shows a comparison of laser power measurements, taken at the maximum flow rate achievable for each of the pressures noted. For all three frequencies, the slope efficiency is approximately 10 % and the turnover in the power corresponds to the gas temperature at the output of the discharge reaching ~600 K. However, the range of pressures and power inputs that can be used changes with frequency. For 125 MHz, there is difficulty in obtaining uniform, fully lit discharges and the data is restricted to low pressures, with low mass flow in the choking limit. For 27 MHz, fully lit discharges with good visual uniformity could be obtained at up to 300 torr with 5.8 kW input: however in this case the gas exit temperature is too high for efficient laser operation. No evidence of discontinuous changes in current density corresponding to an α to γ transition or visual evidence of small scale filamentation is found at all three frequencies.

Fig. 4 shows the operating envelope of the slab discharge in terms of pressure and discharge power density. The upper power density limit is indicated by the shaded area where the exit temperature exceeds 600 K with the maximum available gas flow. The experimental data points form a second boundary, below which the discharge shrinks or will not ignite. The increase in the minimum power density for stable discharges with operating frequency is the most significant frequency dependent effect found in these experiments. It may represent the reducing effectiveness of the dielectric ballast at the highest frequency, where the voltage drop on the dielectric is similar in magnitude to the internal plasma voltage.

4. CURRENT DENSITY AND PLASMA VOLTAGE MEASUREMENTS

The current density in the discharge, J , has been monitored at four points along the flow direction using the arrangement in Fig. 5(a). The sensing area is 8 mm in diameter, and the current collected by each probe is measured by an RF voltmeter as the

voltage across a 50 Ω load. The internal plasma voltage V_p is calculated from the current density and the electrical power density. Typical V_p -J data for 49 MHz are plotted in Fig. 5(b). Under conditions where the discharge uniformly fills the discharge, the combinations of J and V_p are the nearly the same for all three frequencies.

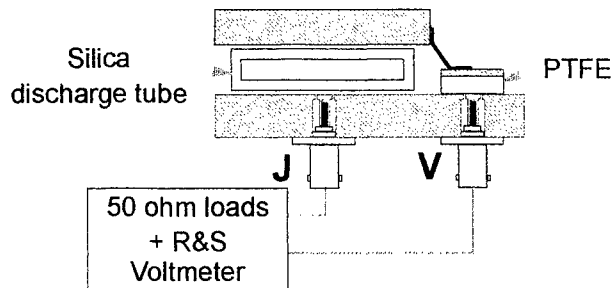


Fig. 5(a) Current density monitoring.

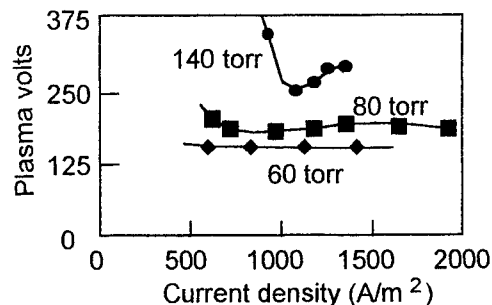


Fig. 5(b) Electrical characteristics of plasma at 49 MHz

At the minimum power density point where the discharge shrinks, the plasma voltage rises rapidly, as for the 140 torr data in Fig. 5(b). The mean value of reduced field E/p is 6 V/cm/torr at 50 torr fill pressure, reducing smoothly to 3 V/cm/torr at 160 torr, similar to the values encountered in narrow gap diffusion cooled lasers. The current density values are only slightly less than those measured by similar methods for a 1.75 mm gap discharge [6], whilst the plasma voltages is ~ 3 times larger. Near 140 torr, the power density at maximum laser output is 80 W.cm⁻³. No significant fluctuations are seen in the current to the 8 mm diameter area of the probe nearest the gas exit, indicating that thermal filamentation is not a problem under the conditions investigated so far.

5. DISCUSSION

The experimental slab discharge section has shown that the high current and power density characteristics of narrower diffusion cooled lasers can be attained in fast flow lasers, but with much lower radio frequency. A specific output power of 33 kW.m⁻² has been achieved, compared to the typical values of 15-20 kW.m⁻² for diffusion cooled slab lasers. Currently the output power per discharge section *per unit area of beam* is 132 W.cm⁻², compared to a value of 195 W.cm⁻² achieved with large circular cross section tubes [1]. The low efficiency of the present laser is currently under investigation. By varying the output coupling, and performing a Rigrod analysis, it has been seen that the gain of the test section is adequately high, but there is flow velocity dependent cavity loss sufficient to reduce the efficiency. The high gas density, coupled with the highly turbulent flow may be producing significant scattering of radiation from the closely confined fundamental mode in the narrow section. In future, it may be necessary to increase the narrow dimension to reduce these losses. However, it is expected that the advantage of discharge stability at high power density will be maintained, and it will be easier to design resonators for multi-section discharge devices

6. ACKNOWLEDGEMENTS

The provision of a studentship to JGB by the Engineering and Physical Sciences Research Council, and valuable technical discussions with P P Vitruk are gratefully acknowledged.

7. REFERENCES

1. U Habich, U -K Jarosch, H Maly, R Meyer, P Loosen, N Wolf, T Beck, C Hertzler, R Wollermann-Windgasse. "Fast axial flow 25 kW CO₂ laser with unstable resonator for industrial applications" Proc. GCL/HPL'96, Edinburgh 1996, pub. by SPIE
2. W Pfeiffer, C Schmitz, A Giesen, H Hügel "Optimized homogeneity and stability of gas discharges in fast flow CO₂ lasers operating at the choking limit" Proc. GCL/HPL'96, Edinburgh 1996, pub. by SPIE.
3. A D Colley, H J Baker, D R Hall "Planar waveguide, 1 kW cw carbon dioxide laser excited by a single transverse discharge" Appl. Phys. Lett. **61**, 136-8 (1992)
4. Rofin Sinar GmbH, Hamburg, DC series of CO₂ lasers
5. P P Vitruk, H J Baker, D R Hall "Similarity and scaling in diffusion cooled RF excited carbon dioxide lasers" IEEE J. Quantum Electron. **30**, 1623-34, (1994)
6. H J Baker "Direct measurement of the electrical impedance of narrow gap radio-frequency gas discharges in the 100 MHz region" Measurement Science and Technology, *in press*

Investigation of beam quality and gain behaviour in a large aperture e-beam controlled CO₂ laser

W.Riede, W.Mayerhofer, Th.Hall, S.Walther

Institut fuer Technische Physik, DLR Stuttgart
Pfaffenwaldring 38 - 40, 70 569 Stuttgart, Germany

ABSTRACT

An investigation of the parameters influencing the small-signal gain and the beam quality of the laser emission from a stable TEM₀₀ cavity within a large aperture e-beam controlled CO₂ laser discharge unit was performed. An almost linear dependency of the small-signal gain as a function of the energy loading was monitored. Small-signal gains of up to 2.4 %/cm in the centre of the discharge region were found for an energy loading of up to 140 J/(l bar) at a wavelength of 10.59 μ m. The beam quality evaluation was done by M² parameter measurements according to the ISO standard. The fluence distribution was recorded with a beam analyzing system of 100 μ m spatial resolution. No increase of the M² parameter was found within the limits of measurement accuracy for a stable resonator configuration when the energy loading almost doubled from 61.7 J/(l bar) to 112.5 J/(l bar).

Keywords: pulsed CO₂ lasers, beam quality measurements, small-signal gain measurements.

1. INTRODUCTION

Beam quality, pulse energy and small-signal gain are of great importance in the layout of a master oscillator power amplifier (MOPA) system¹. Ideally, such a system should produce high energy densities to saturate the inverted medium whereas phase distortions produced during amplification can be cancelled when phase conjugation techniques are used. In a compact MOPA geometry, the available gain volume incorporates the power amplifier and the master oscillator cell. Low M² parameter values together with high pulse energies, extracted from the master oscillator, are a prerequisite in the assessment of beam quality deterioration. In achieving this goal, we investigated in a first experimental step the laser emission from stable (TEM₀₀) and unstable cavities which were set up within the aperture of an e-beam controlled CO₂ laser discharge unit. For comparison, different types of output couplers with constant reflectivity and a variable reflectivity mirror (VRM) were used. Furthermore, small-signal gain measurements were performed by using a low power single-frequency line-tunable CO₂ laser. These results are only briefly discussed in this paper. A more detailed discussion of the small-signal gain measurements and the technical details of the discharge unit can be found in Ref[2] in this volume.

2. EXPERIMENTAL

The experimental setup for beam quality evaluation and the different resonator configurations are depicted in Fig.1 and Fig. 2, respectively. In Fig. 1, the resonator is set up by a high reflecting (HR) mirror 1 and an output coupler 5. The optical axis of the resonator is placed in the centre of the discharge volume 2 which has a cross-section of 10 * 10 cm². The discharge volume is sealed by a 4" HR mirror 1 and by a 2" AR/AR coated ZnSe window 3. A circular aperture 4 is used to support TEM₀₀ emission. Its diameter is adjusted to 14.5 mm, which corresponds to a Fresnel number of $F = 1.88$. To prevent lasing between the (metallic) blades of the aperture 4 and the HR mirror 1, we covered its inner surface (facing the discharge) with a water containing cream. The emitted CO₂ laser pulses had a typical gain-switch shape with a leading spike of 100 - 200 ns duration and an overall duration of 10 μ s. Outside the cavity, the radiation is focused with a ZnSe lens 6 of 3 m focal length. After passage of the lens 6, the radiation is directed on a pyroelectric array 12 with four HR mirrors 9 and two ZnSe wedges 11. Two HR mirrors 9 on a movable bench are setting up an optical delay line 10. By using this delay line,

the fluence distribution can be monitored with the pyroelectric array at different locations (length variation 4 m) before and after the beam waist. The pyroelectric array (Spiricon Pyrocam 1) consists of 128×128 pixels with $100 \mu\text{m}$ pixel spacing. The pyroelectric array is placed in an all-metal box 13 to prevent electrical interference. Fast-response detectors 8 (pyroelectric or photon drag type) are used to record the temporal distribution in the near- and far-field. The beam-splitter 7 ($R = 1\%$) is placed directly behind the lens 6.

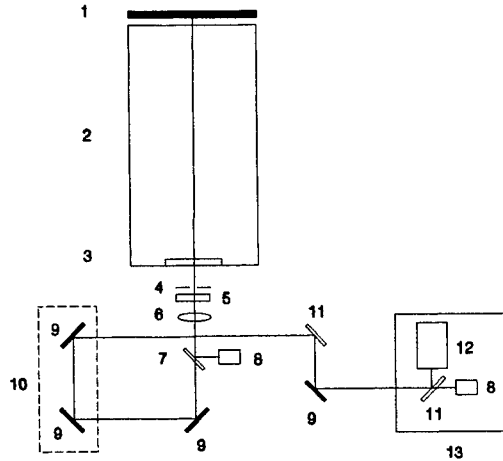


Fig. 1 Experimental set-up for beam quality evaluation.

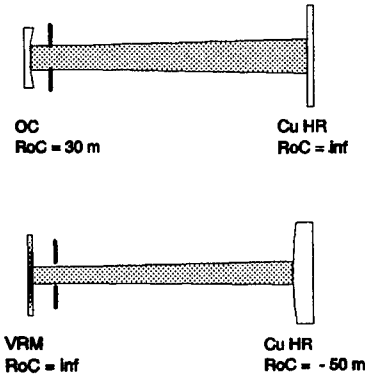


Fig. 2 Resonator configurations (TEM_{00} cavity (above) and cavity with VRM mirror (below)).

Two types of output couplers were used, resulting in two resonator configurations, having the same length of $L = 2.64 \text{ m}$; firstly, an output coupler with constant reflectivity ($R = 58.4\%$) and a radius of curvature (RoC) of 30 m for TEM_{00} cavity configuration (Fig. 2, above) and secondly, an output coupler with radially varying reflectivity (VRM) with $\text{RoC} = \infty$ for unstable resonator configuration (Fig. 2, below). The VRM was coated by BIFO GmbH, Berlin, Germany. It was designed as a supergaussian mirror with a radially varying reflectivity dependence $R(r) = R_0 \exp[-(r/w)^n]$, with $R_0 = 61\%$, $w = 4.9 \text{ mm}$ and $n = 5$ (Fig. 3). Energy densities of up to 4 J/cm^2 were applied to the VRM.

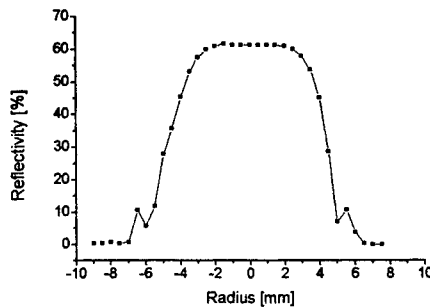


Fig. 3 Measured radial reflection dependence of the VRM.

3. EVALUATION PROCEDURE OF BEAM PARAMETERS

The beam profiles, which were recorded with the pyroelectric array, have been further processed on the PC to calculate the center-of-mass position and the beam width of each fluence distribution. Several fluence distributions were recorded in each plane. A discrimination of the beam parameters in horizontal direction (parallel to the discharge) and in vertical direction (orthogonal to the discharge) was found to be useful. The calculation of the M^2 parameters was done

according to the ISO standard 11 146, where it is proposed to infer the beam widths $d_{\sigma x}(z)$, $d_{\sigma y}(z)$ from a calculation of the second moment of the fluence distribution $F(x,y,z)$. Here, x,y,z define the horizontal, vertical and optical axis, respectively. The horizontal beam width is given by

$$d_{\sigma x}(z) = 4 \sigma_x(z) \quad ; \quad \sigma_x^2(z) = \frac{\iint (x-x_0)^2 F(x,y,z) dx dy}{\iint F(x,y,z) dx dy}$$

and the center-of-mass position (x_0, y_0) is defined by

$$x_0 = \frac{\iint x F(x,y,z) dx dy}{\iint F(x,y,z) dx dy}$$

Similar expressions hold for σ_y^2 , $d_{\sigma y}$ and y_0 . Crucial for the calculation of the beam widths is the precise nulling of the background amplitude level. A hyperbolic fit through the measured points in the curves $d_{\sigma x}(z)$, $d_{\sigma y}(z)$ allows the determination of the parameters M_x^2 and M_y^2 .

The pointing stability was evaluated according to the ISO standard 11 670. It is calculated from fluence distributions taken in the focal plane of a lens and is defined to be twice the standard deviation obtained from the calculation of the center-of-mass position.

4. RESULTS AND DISCUSSION

4.1 M^2 parameter and pointing stability

The results of the M^2 parameter measurements are summarized in Tab. 1. Low M^2 parameters were recorded in case of the TEM₀₀ cavity, where an increase in the loading from 61.7 J/(l bar) to 112.5 J/(l bar) showed little effect on the M^2 parameter values. In case of the unstable VRM cavity a small increase in the M^2 parameter was found. Additionally, higher values were monitored in horizontal direction than in vertical direction.

	TEM ₀₀ cavity		unstable VRM cavity	
Loading [J/(l bar)]	61.7	112.5	61.7	112.5
M_x^2	1.34	1.39	1.55	1.7
M_y^2	1.34	1.31	1.19	1.33

Tab. 1 M^2 parameter values for different resonator configurations and energy loadings.
(x: horizontal direction, y: vertical direction)

An investigation of the pointing stability (TEM₀₀ cavity) showed, that the angular fluctuations were more pronounced in vertical direction (300 μ rad) than in horizontal direction (50 μ rad). This finding can be explained by the discharge instability orthogonal to the direction of the electric field.

4.2 Pulse energy and small-signal gain

A linear increase in pulse energy for TEM₀₀ cavity and unstable VRM cavity, up to 1.9 J and 1.3 J, respectively, was recorded for 140 J/(l bar) loading. The energy extractable from the unstable VRM cavity can be increased by selecting a higher central reflectivity R_0 , but the higher risk of optical damage in the coating is then to be taken into account.

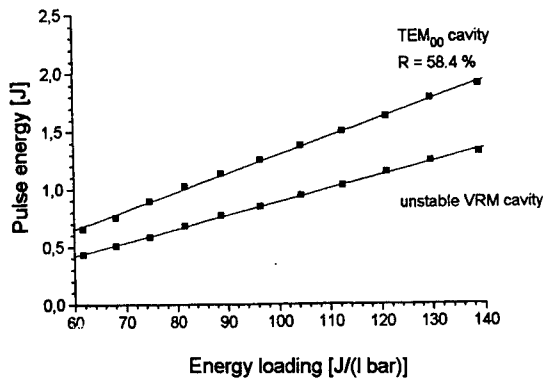


Fig. 4 Pulse energy dependence as a function of the energy loading.

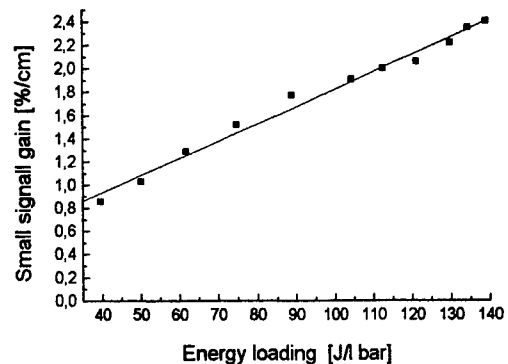


Fig. 5 Small-signal gain as a function of the energy loading at a wavelength of $\lambda = 10.59 \mu\text{m}$ of the probe laser measured along the centerline of the discharge region.

The small-signal gain also increased linearly with the loading (Fig. 5). As the laser gas, a mixture of 1 : 2 : 7 (CO_2 : N_2 :He) at overall pressure of 500 mbar was used. The set-up and further experimental details can be found in Ref. [2].

5. CONCLUSION

In conclusion, the results of the measurements of beam quality, extractable pulse energy and small-signal gain in a cavity that is imbedded into a large aperture discharge unit were promising for the layout of a MOPA system. Scalability of the pulse energy of the master oscillator came along with only a small decrease of the beam quality when stable a TEM₀₀ cavity was set up in the centre of the discharge volume. M^2 parameter values of 1.3 - 1.4 were found for a pulse energy of 2 J.

6. LITERATURE

- 1 W. Riede, Th. Hall, H.Klingenberg, "Numerical simulation of a high-power four-wave mixing MOPA system", SPIE Vol 2502, pp. 554 - 558, 1994.
- 2 W. Riede, W. Mayerhofer, Th. Hall, S. Walther, "Parametric investigation of the small-signal gain in a large aperture e-beam controlled CO_2 laser", GCL/HPL 1996, this volume.

Continuous-wave carbon dioxide laser system producing output power up to 135 Kilowatts

Michael L. Lander, Keith J. Maxwell
Anteon Corporation
P.O. Box 33647
Wright-Patterson AFB, Ohio 45433 USA

James P. Reilly
Northeast Science and Technology
117 North Shore Blvd.
East Sandwich, Massachusetts, 02538 USA

Robert J. Hull
Wright Laboratory, Materials Directorate
WL/MLPJ, 3005 P St., Suite 1
Wright-Patterson AFB, Ohio 45433 USA

ABSTRACT

The operational characteristics of a 135kW continuous wave carbon dioxide laser system are described. A brief description of the fast-flowing electrical discharge coaxial laser system is presented followed by a detailed discussion of the operational and output characteristics of the device. Diagnostics systems configured to measure electrical discharge voltage and current, mass flow, laser cavity pressure, laser output power, output spatial intensity distribution and output temporal stability are described. The data collected with these systems are summarized with subsequent analyses presented and compared with theory. The 135kW carbon dioxide laser is located at the Laser Hardened Materials Evaluation Laboratory (LHMEL) at Wright-Patterson Air Force Base, Ohio, USA. The device was developed and is currently operated for the purpose of characterizing the thermal response of materials.

Keywords: Carbon Dioxide Laser, High Power Laser, Electric Discharge Coaxial Laser (EDCL), Gas Lasers, Fast-Flow Axial Laser, Laser Power Measurement

1. 135 kW FAST-AXIAL FLOW LASER

The LHMEL 135kW carbon dioxide laser system was developed to characterize the response of materials subjected to extreme thermal conditions.¹ The device was designed to meet specific operational parameters required for materials testing, namely, output beam power level to 100kW while maintaining optimum spatial uniformity and temporal stability. The device, first operated in August 1989, demonstrated volume scaling principles for electric discharge coaxial lasers (EDCL).² Shown schematically in Figure 1, this fast-axial flow system operates in open-loop configuration for durations of up to 80 seconds at a maximum power of 135kW. A careful balance between the performance limiting factors of flow velocity (M), electric field (E), electron number density (n_e), pressure (P), number of excited molecules (N) and power deposition into the gas resulting in temperature change (ΔT) governs the operation of the EDCL. For optimized operation, an energy balance condition must be established where the product of electron number density and the time required for a molecule to traverse the discharge flow length is constant.

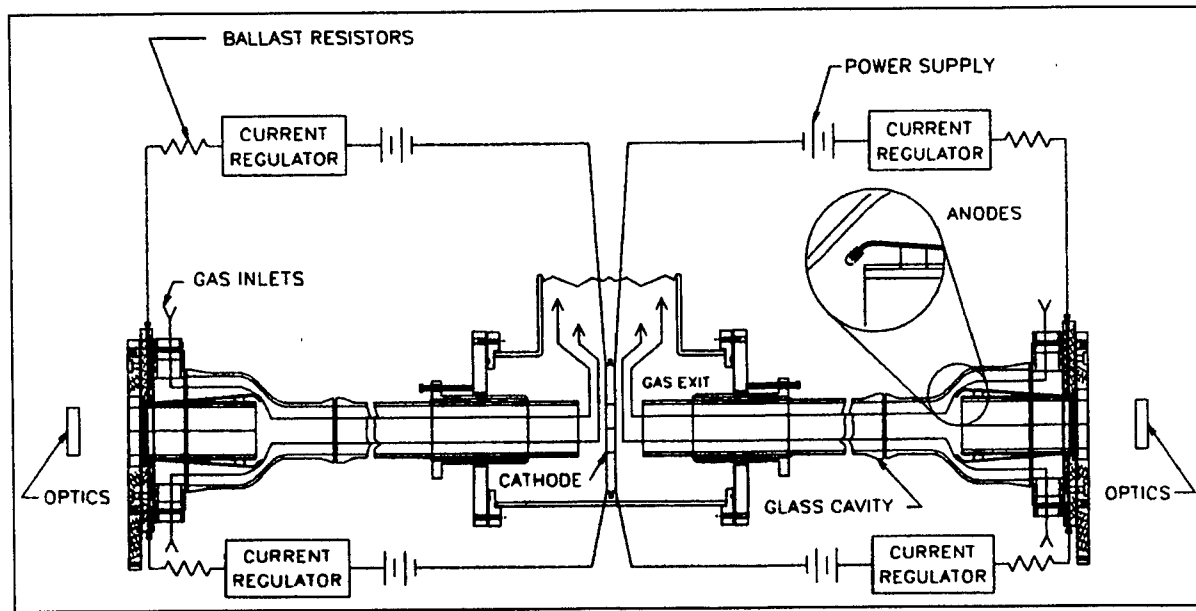


Figure 1. LHMEL electric discharge coaxial laser geometry.

The electrical power deposition (P) and gas flow heating rate relationship can be defined as:

$$P = I * V = \dot{m} C_p \Delta T \quad (1)$$

where I is current, V is voltage, \dot{m} is mass flow, C_p is the gas heat capacity and ΔT is the change in gas temperature. Incorporating electric field properties into a low pressure flowing discharge through a cylindrical volume and accounting for Rayleigh Line Physics limiting the mean gas velocity, the following relationship for power input into the gas medium can be established:

$$P = \left(e \frac{n_e}{n_H} V_D n_H A_F \right) * V^* \quad (2)$$

where e is electron charge, n_H is the molecular number density, V_D is the electron drift velocity, A_F is the flow cross sectional area and V^* represents the applied voltage. For stable discharge conditions V^* is limited to a narrow range of values (ΔV) dependent upon the molecular number density over flow length. For the device's operating pressure ranging from 30 to 70 torr, discharge conditions are stable for E/n_H values corresponding to 3.0 to 4.5 kV/Amagat-cm.

$$V^* = \left(\frac{E}{n_H} \right) * n_H * G \quad (G = \text{anode-to-cathode gap}) \quad (3)$$

With applied voltage and molecular number density fixed over a narrow range of values by E/n_H , the only parameters of Equation 2 able to be increased in scale while maintaining stable discharge conditions are those relating to cross sectional area.

Considering the above analysis, the diameter of the discharge volume was increased substantially. In addition, electrode configuration and geometry was optimized for localized flow conditions while current monitoring and conditioning systems were improved. Finally, the discharge length was increased proportional to gas pressure and flow conditions maintaining an E/n_H within the range

previously specified. The end result was an increase in output power by a factor of ten over all previous EDCL's while improving discharge stability and uniformity.

The device employs a stable optical resonator capturing approximately 107 Fresnel zones, given by:

$$F = \frac{\left(\frac{d}{2}\right)^2}{(L \cdot \lambda_0)} \quad (4)$$

where d , the clear aperture = 20cm, L , the cavity length = 880cm, and, λ_0 corresponds to the primary laser transition at 10.6 μ m. The resulting multimode beam completely fills the clear aperture of the device and is spatially uniform to within 17%.

2. LASER OUTPUT POWER MEASUREMENT

Power meters and total capture calorimeters are used to measure the output power of LHMEI lasers. The power meters are calibrated on a daily basis to the calorimeters described below. Power meters are used because they provide a faster response and can be incorporated into the beam path with a beamsplitter allowing power to be measured during a laser test. Figure 2 shows a typical measurement made during laser operation. In this case the desired power level was 100kW at the target plane for an irradiation duration of 7 seconds. The maximum power delivered to a target to date is 127kW. The data shows that the laser achieves the desired power level within 5 seconds. The laser can operate at full power for a maximum duration of 80 seconds before heating in the device necessitates shut-down.

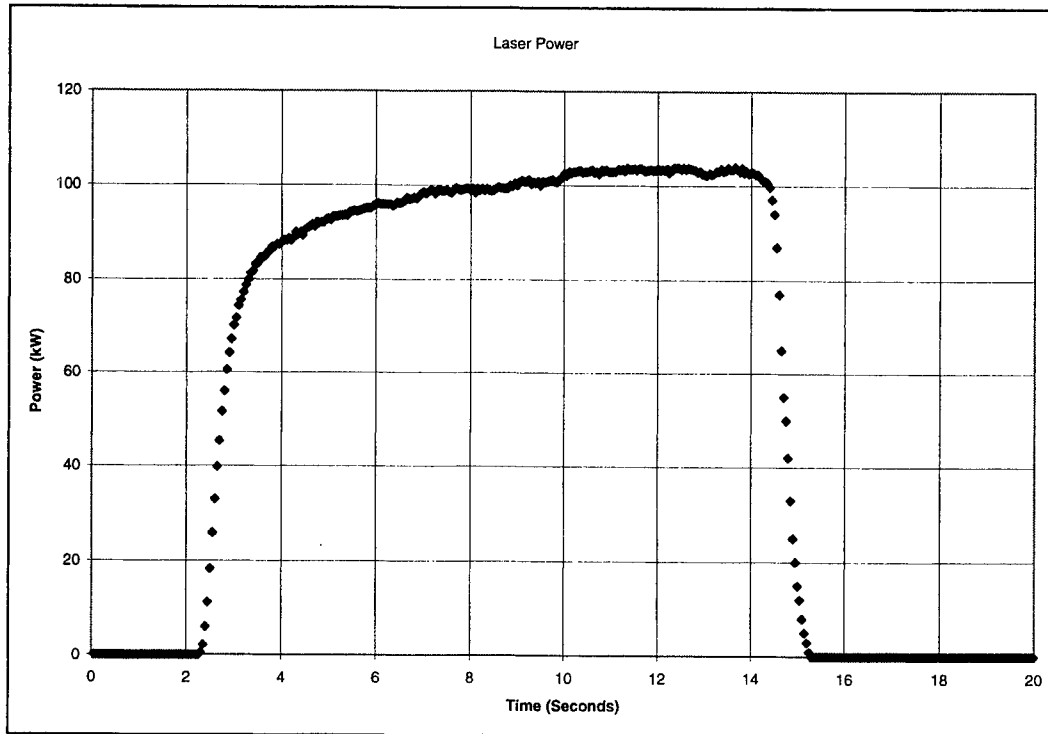


Figure 2. Measurement of the output laser power demonstrates temporal stability to within $\pm 5\%$ after the laser reaches the desired power level, in this case 100kW.

Longer run durations can be achieved at lower power operational levels.

A total capture calorimeter consisting of a cast aluminum sphere with an external copper wire winding is used to measure total output energy over a specific run duration. The laser beam is directed into the sphere. The thermal energy transferred from the laser beam into the sphere and copper winding induces a resistance change that is calibrated in J/ohm. The output responses of the LHMEEL total capture calorimeters are calibrated annually to the U.S. primary reference standard for high power laser calorimetry.³ These calorimeters have been used to verify output laser power up to 135kW.

3. SPATIAL INTENSITY PROFILE MEASUREMENT

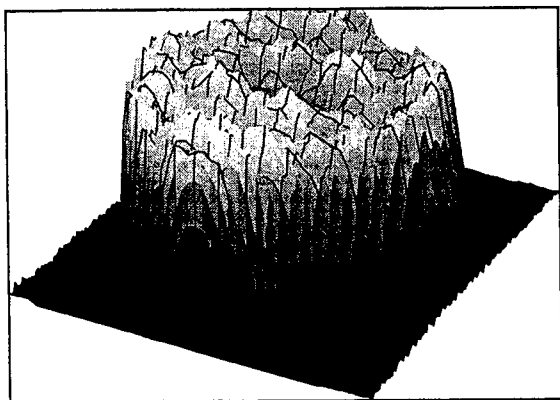


Figure 3. The spatial intensity distribution of the 135kW laser beam is uniform to within $\pm 17\%$.

The spatial intensity profile of the LHMEEL laser beam is measured using a pyroelectric vidicon (PEV) camera sensitive to optical radiation in the 8 to 12 μ m wavelength region. A beamsplitter is used to direct a reduced power portion of the main laser beam to an optical system re-imaging the beam onto the 1.8cm diameter tri-glyceride-sulfide detector array. Calcium fluoride absorbing plates and germanium filters are incorporated into this optical system to provide additional protection for the detector as well as wavelength selectivity. Figure 3 shows a surface plot representing the output laser beam as measured by the PEV camera. The data produced by this measurement method has been verified by alternate methods using scanned thermocouple arrays and materials burns.

4. SUMMARY

Operation of a fast-flow carbon dioxide EDCL system at power levels up to 135kW has been achieved for durations up to 80 seconds. The device validates volume scaling projections for formation of and power extraction from the gain medium formed in a fast-flow EDCL system. The device has exhibited exceptional performance throughout eight years of operational service. The stable multimode resonator produces output beam characteristics ideal for materials testing and characterization. The laser is located at the Laser Hardened Materials Evaluation Laboratory, which is part of the Wright Laboratory Materials Directorate, Wright-Patterson Air Force Base, Ohio, USA.

¹ K. Maxwell, M. Lander, D. Daniels, M. Wolf, D. Seibert, C. Oblinger, J. Bagford, "The Laser Hardened Materials Evaluation Laboratory (LHMEEL)," Report submitted to Wright Laboratory Materials Directorate, Report # WL-TR-93-4119, (1993).

² J. P. Reilly, M. L. Lander, K. Maxwell, R. Hull, "Design construction and operation of a 65kW carbon dioxide electric discharge coaxial laser device," Madrid, Spain. SPIE 8th international symposium on gas flow and chemical lasers, No. 1397-108B, 339-354 (1990).

³ M. L. Lander, J. O. Bagford, D. B. Seibert II and R. J. Hull, "High power calibration of commercial power meters using and NIST-traceable secondary standard," *Journal of Laser Applications*, 8, 103-107 (1996).

Optimization of power deposition in rf-excited CO₂ - lasers
by adding gas additives to the laser gas mixtures

C. Schmitz, W. Pfeiffer, A. Giesen, H. Hügel

Institut für Strahlwerkzeuge (IFSW), Universität Stuttgart, Pfaffenwaldring 43, D-70569 Stuttgart

ABSTRACT

The properties of the laser active medium were investigated using a drift chamber, and the effect of gas additives on the laser power is evaluated. The transport coefficient drift velocity is measured in CO₂ - laser gas mixtures. The dependence of the drift velocity on the applied electric field is very similar for the different gas compositions in the positive column of the discharge, and a semi-empirical formula is given. The influence of gas additives is investigated a) selective energy reduction due to elastic impacts with Ar, b) striking voltage reduction by adding C₄H₁₀ to the laser gas.

Keywords: CO₂ - laser gas, gas additives, drift velocity, gas amplification, drift chamber, Penning ionization

1. MOTIVATION

The development of a high efficiency CO₂ - laser requires a detailed investigation of fundamental gaseous electronics. The self sustained discharge of such a laser is a balance between high electron density (high values for E/n) and optimal mean electron energy (1...2.5 eV, E/n should be low for effective excitation). The electron density and energy is a result of the basic processes: vibrational and electronic excitation, ionization and electron attachment, whereby the probability of these processes is expressed as the relevant cross section weighted by the fractional concentration of the gas composition. An integral measure of the effects involved is the electron drift velocity. This velocity is a result of both the acceleration due to the electric field and the loss of energy occurring between two electron impacts. The variation of the electron drift velocity v_D , with the fraction of gas components is an easy method to investigate gas additives, especially their influence on the mean electron energy and also on the excitation efficiency. It can be shown rigorously [1] to be

$$v_D = \frac{2}{3} \cdot \frac{eE}{m_e} \cdot \left\langle \frac{l_e(v)}{v} \right\rangle + \frac{1}{3} \cdot \frac{eE}{m_e} \cdot \left\langle \frac{d}{dv} l_e(v) \right\rangle, \quad (1)$$

where e is the charge of the electron, m_e the mass, v the random velocity of the electron and E denotes the electric field. The mean free pass $l_e(\epsilon) = 1/(n_g \cdot \sigma_m(\epsilon))$ is a function of the neutral gas density n_g and of the electron energy $\epsilon = m_e/2 \cdot v^2$ due to the energy dependence of the momentum-transfer cross - section $\sigma_m(\epsilon)$. The brackets indicate that averaging has to be done on the distribution function $f(\epsilon)$. For a rough estimation we can present very simple arguments based on energy conservation [1]:

$$e \cdot E \cdot v_D = \frac{\Lambda(\epsilon) \cdot \epsilon}{\tau} = \Lambda(\epsilon) \cdot \epsilon \cdot \sqrt{\frac{2 \cdot \epsilon}{m_e}}, \quad (2)$$

where $\Lambda(\epsilon)$ is the mean fractional energy loss between two collisions in the time τ . Assuming a power law for the dependence of Λ and l_e on ϵ : $\Lambda(\epsilon) = \Lambda_0 \cdot \epsilon^m$, $l_e(\epsilon) = l_0 \cdot \epsilon^{-n}$ and using eqs. (1) and (2) leads to:

$$v_D \sim E^{\frac{m+1}{m+2n+2}} \quad \text{and} \quad \epsilon \sim E^{\frac{2}{m+2n+2}}. \quad (3)$$

2. MEASUREMENT OF THE ELECTRON DRIFT VELOCITY WITH A DRIFT CHAMBER

The drift chamber (Fig. 1) in its simplest form consists of a very thin sense wire ($D_j = 20 \mu\text{m}$) and a potential tube ($D_a = 20 \text{ mm}$) which is connected to a negative bias voltage. The sense wire is connected to a resistor and a pre - amplifier, and the whole system is mounted in a cavity (indicated by dotted line in Fig. 1) in order to separate the gas mixture from the environment and to adjust the gas pressure in the range which is typical for cw CO₂ - lasers

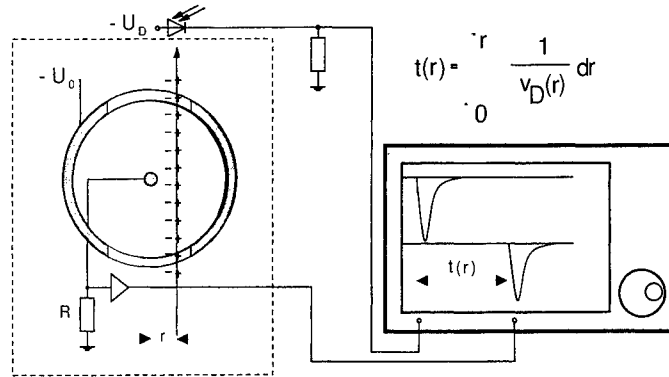


Fig. 1: Measurement of electron drift velocity with a drift chamber.

Electrons which are produced in a primary process, drift a distance r from the sense wire, then drift to the anode under the influence of the applied electric field. In the region around this wire secondary processes take place if the electrons gain sufficient energy between collisions to ionize the neutral gas. These newly released electrons are able to ionize the neutral gas again if the electric field is high enough, and so this process repeats itself. It is possible to gain from one electron $10^4 - 10^6$ electrons which are now detectable with the help of a pre-amplifier. This avalanche effect is called *gas amplification* and is a well known technique in high energy physics [2], [3]. The primary ionization is done using a Nd:YLF laser whereby the frequency of the light has been quadrupled ($\lambda = 264 \text{ nm}$) and the energy of the photons is $E_\gamma = 4.6 \text{ eV}$. This energy is high enough to ionize, by a two photon process, the impurities (like hydrocarbon) which are normally present in the laser gas [4], [5]. A pin-photodiode is used to obtain the start signal for the drift time measurement (see Fig. 1), and the stop signal is provided by the drift chamber. With a variation of the distance r , and the measurement of the drift time t , one gets the relation $t(r)$ (see Fig. 2). The drift velocity is given by the inverse of the derivative of $t(r)$ and therefore

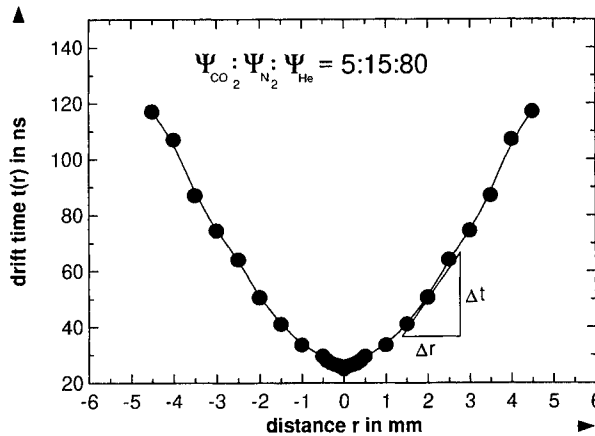


Fig. 2: Drift time relation for a typical CO_2 -laser gas mixture and pressure.

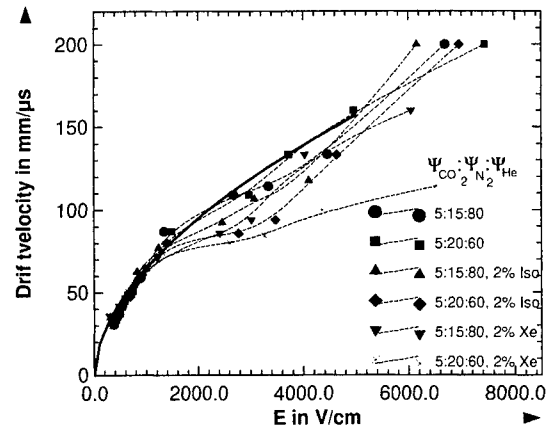


Fig. 3: Drift velocity as a function of the electric field; $p = 150 \text{ hPa}$. Two typically gas compositions with two additives are shown.

$v_D(r) = \left(\frac{d}{dr} t(r) \right)^{-1}$. With the knowledge that $E(r) \Rightarrow r(E) \Rightarrow v_D(E)$, one gets the drift velocity as a function of the applied electric field. Fig. 3 shows that for typical laser gas mixtures and the usual values for the electric field ($E(r) = (0 \dots 2000) \text{ V/cm}$, [6]), the drift velocity is very similar for the shown gas compositions. In this range the curves can be fitted using eq. 3 (solid line in Fig. 3). This leads to:

$$v_D(E) = 1,45 \frac{\text{mm}}{\mu\text{s}} \cdot \left(\frac{E}{\text{V/cm}} \right)^{0.55} . \quad (4)$$

The exponent indicates that these gas compositions are dominated by He (with respect to the drift velocity at electric field values smaller than 2000 V/cm). This is due to the cross-section of He being independent of the electron energy for $\varepsilon < 10$ eV. This means $m = 0$, $n = 0$, with eq. (3) $\Rightarrow v_D \sim E^{1/2}$. For electric fields higher than 2000 V/cm inelastic collisions will be dominant.

3. INVESTIGATION OF GAS ADDITIVES

Using gas additives provides two possibilities to increase laser efficiency. First: adding a gas with a momentum-transfer cross - section having a minimum at the excitation energy of the vibrational states. An increasing cross - section for higher electron energy leads to a selective energy reduction of fast electrons by electron impact. The noble gases Ar, Xe, Kr exhibit these characteristics with a Ramsauer minimum for electron energy around $\varepsilon = 0,3\text{eV}$ [2]. The influence of the concentration of Ar on the drift velocity is shown in Fig. 4. and exhibits a relatively strong variation of the drift velocity with the concentration of argon. This is due to the reduction of the fast electrons which, in combination with the relatively big cross - section for inelastic impacts, leads to a shift in the mean electron energy. The influence on laser power is shown in Fig. 5. It confirms the interpretation stated above. The addition of 2% Ar to the gas mixture improves the laser power by 6%, which agrees with [7].

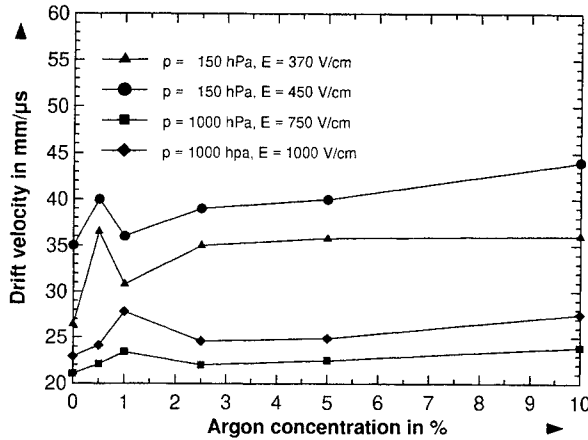


Fig. 4: The Ar influence on the drift velocity.

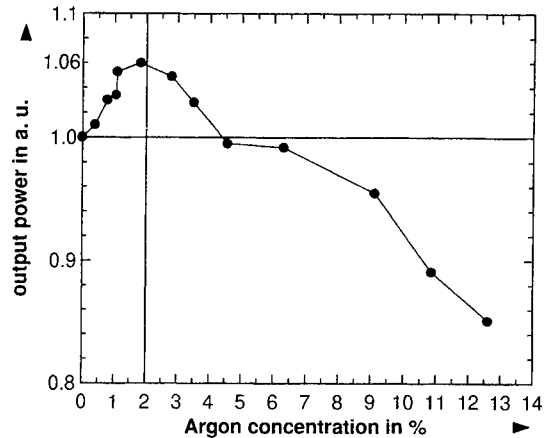


Fig. 5: The Ar influence on the laser output power.

Second: using a gas additive (molecules), with low ionization energy raises the electron density due to the lower effective ionization potential and by exploitation of the electronic states of the gas by Penning ionization. The drift chamber can be used to investigate this effect. The gas amplification of the drift chamber as a function of the bias voltage U_0 , can be calculated and is dependent on the gas mixture and the pressure. The output signal of the drift chamber is proportional to the electron density and it can be shown [8]:

$$U_C = A \cdot \frac{p}{k \cdot T} \cdot P^2 \cdot \exp \left(2 \cdot \sqrt{\frac{p \cdot r_i}{k \cdot T \cdot \ln(r_a/r_i)}} \cdot \alpha \cdot \sqrt{U_0} \cdot \left(\sqrt{\frac{U_0}{U_S}} - 1 \right) \right) . \quad (5)$$

Here A is a proportionality constant; p the pressure; P the power of the Nd:YLF laser; T the Temperature; r_i, r_a the radius of the sense wire and the potential tube respectively, and k the Boltzman constant. U_S is the threshold voltage where the gas amplification starts and it is strongly correlated with the striking voltage of the glow discharge of such a gas mixture; α depends on the gas, including the cross sections and the ionization potential. The gas amplification is shown in Fig. 6, whereby two typical gas compositions are investigated. The ratio $\psi_{\text{CO}_2} : \psi_{\text{N}_2}$ is 1:3, (80% He) for mixture 1 and 1:4, (70% He) for mixture 2. Gas 1 exhibits a lower threshold voltage due to the lower effective ionization potential and

the higher amount of He. The effect of penning ionization of C_4H_{10} is shown in Fig. 7, and one can see the reduction of U_S . The addition of 2% C_4H_{10} results in a threshold reduction of $\approx 10\%$. This has two advantages. First, the exploitation of the electronic states of N_2 and CO_2 due to the Penning ionization leads to an increase in efficiency of electron production. Second, the electric field in a discharge is reduced, which leads to a lower E/n where the vibrational excitation is more efficient. Experiments with a glow discharge showed that these findings are adaptable to a laser system. We reduced the necessary striking power for a typical CO_2 - laser discharge from $P_{in, min} = 1850$ W to $P_{in, min} = 1000$ W by changing the $\psi_{CO_2} : \psi_{N_2}$ ratio from 1:4 to 1:3.

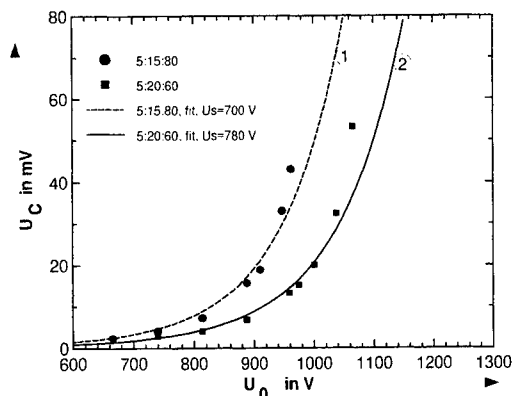


Fig. 6: Chamber output signal height for different gas compositions: 5:15:80 and 5:20:60.

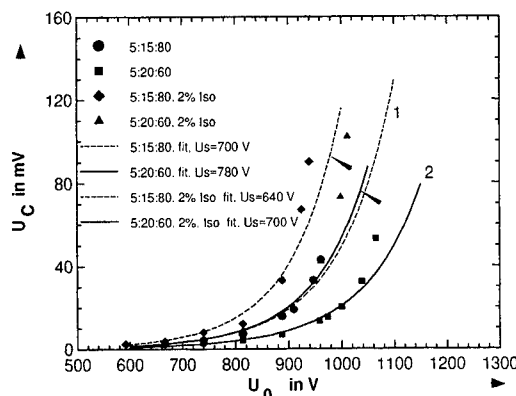


Fig. 7: Shift of threshold voltage due to the addition of isobutane C_4H_{10} .

4. CONCLUSION

It is shown that by using a drift chamber a detailed view of the gas electronics is possible. An improvement of laser power following the addition of a particular amount of argon to the laser gas is observed. The reduction of the striking voltage by Penning ionization due to the addition of isobutane is shown.

ACKNOWLEDGEMENTS

This work was supported by the German Federal Ministry of Education, Science, Research and Technology BMBF (contract number: 13 N 6574).

REFERENCES

- [1] V. Palladino and B. Sadoulet, „Application of the classical theory of electrons in gases to multiwire proportional and drift chambers“, *Lawrence Berkeley Laboratory Report LBL-3013* (1974)
- [2] K. Kleinknecht, *Detektoren für Teilchenstrahlung*. Stuttgart: Teubner, 1992.
- [3] H. Staub, *Experimental in Nuclear Physics* (Ed. E. Segre), J. Wiley Verl. New York (1953), Vol. I, p.1
- [4] H.J. Hilke, „On a Formation and Application of Laser induced Ionisation Track in Gases“, *NIM* 174 (1980) 145
- [5] J. Bourette and B. Sadoulet, „Ionisation of Multiwire Proportional Chamber Gas by Double Photon Absorption“, *NIM* 173 (1980) 463.
- [6] K. Breining, *Auslegung und Vermessung von Gasentladungsstrecken für CO_2 - Hochleistungslaser*. Universität Stuttgart, Teubner, Dissertation, 1996 (Forschungsberichte des IFSW, B. G. Teubner Stuttgart)
- [7] T. Chatterjee, S.K. Sehgal and U.K. Chatterjee, „An inexpensive method of efficiency improvement in fast axial flow, high-power cw CO_2 lasers by addition of argon“, *Optics and Laser Technology*. Vol. 23 No. 2 (1991)
- [8] M.E. Rose and S.A. Korff, „An Investigation of the Properties of Proportional Counters“, *Physical Review*, 59, 850 (1941)

Poster Session I

Working properties of compact rf-excited CO₂ slab lasers

Antonio Lapucci, Francesco Rossetti and Silvano Mascalchi

Istituto Nazionale di Ottica, Largo Enrico Fermi 6, 50125 Arcetri - FIRENZE - I T A L Y

ABSTRACT

We have characterised three compact CO₂ laser modules in terms of pulsed and CW power, beam quality and temporal stability. The three modules differ in the electrodes dimensions, and have been equipped with resonators based on two different hybrid stable-unstable schemes. Advantages and drawbacks are shown.

Keywords: Lasers (CO₂), diffusion-cooled lasers, rf-discharge lasers, slab lasers, slab laser resonators.

1. THE THREE EXPERIMENTAL MODULES

We have constructed and tested three experimental devices based on two closely spaced flat aluminium electrodes determining a wide slab of gain medium, as indicated in Ref.1. The electrodes have been cooled by means of water flowing in channels drilled in them or sealed over them and they have been kept separated 2 mm apart by means of ceramic holders. This kind of structure determines gain regions disadvantageously characterised by one narrow transverse dimension and a much larger second one. The natural solution to this problem is obtained coupling such a gain region with a hybrid resonator, unstable in the large Fresnel Number transverse direction and stable in the small Fresnel Number direction². A resonator of this kind can be realised with a spherical concave mirror and a cylindrical convex one, as already proposed in 1979 for rare gas halide slab lasers³. In this way the cavity determines a one-sided confocal positive-branch unstable resonator in the wide transverse direction and a near-CASE I guided resonator in the narrow direction.

A second possible design⁴ employs a negative-branch unstable scheme in the large Fresnel Number direction. Such a solution enables in our case the use of two concave spherical mirrors determining on the narrow transverse direction a guided resonator with the guide to mirror distances settled in such a way as to phase-match the fundamental EH guided mode. The two resonators we have been studying are schematically shown in Fig.1 and will be named in the following the *positive branch resonator* and the *negative branch resonator*.

The three lasers have been powered by means of two standard VHF-FM broadcast transmitters capable of delivering a radio signal in the band 80-100 Mhz with power up to 6 or 15 kW, respectively. They have been operated in CW- or pulsed-mode by switching the RF signal. Lasers n.1 and 3 have been operated with a single RF feed while for laser n.2 we have adopted a double feed scheme. Static gas fills of 1:1:3 or 1:1:5 CO₂, N₂, He, with or without the addition of Xe have been examined.

2. POWER EXTRACTION AND PULSE SHAPE

The dimensions of the three modules and the power extraction performances with Xe-free 1:1:3 gas mixture are compared in Table I.

Laser pulses have very fast rise and fall times resulting in an almost square-wave shape with the peak power lasting over 200-300 μ s, depending on the RF power density. After this interval the extracted power drops down to the CW value. Switch on delay times of the order of 20 μ s allow Pulse Repetition Rates up to 20 kHz¹.

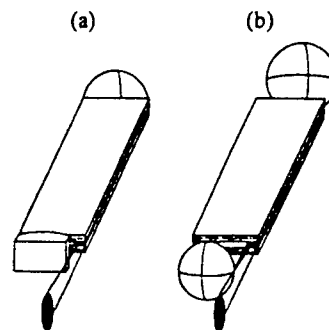


Fig. 1. Schematic view of the two hybrid resonators investigated: (a) positive-branch resonator, (b) negative-branch resonator.

Typical pulse shapes are reported in Fig.2 and the power extracted from laser n.1 is plotted in Fig.3 versus the pulse duration for different duty cycles.

Table I

	Electrodes Dimensions l x w x h (mm)	CW power (W)	Peak Pulse Power (W)	Max. Duty for P.P.P.	Efficiency CW @ P _{max}	Max Efficiency	Resonator Branch
module 1	320 x 60 x 2	100	480	10 %	9 %	22 %	+ / -
module 2	700 x 80 x 2	420	780	25 %	10 %	16 %	-
module 3	700 x 110 x 2	750	1550	20 %	10 %	21 %	+

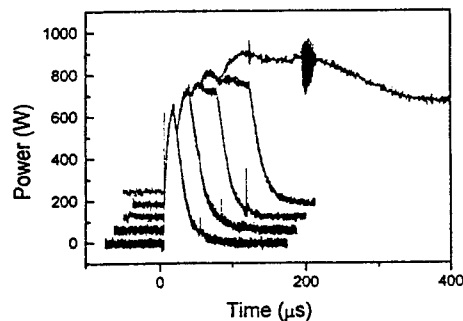
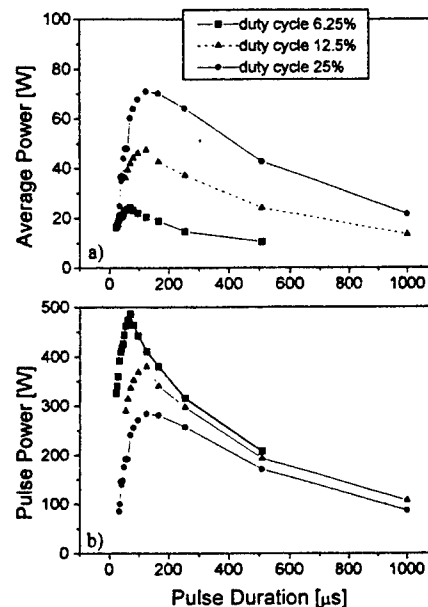


Fig.2. 30 to 500 μ s long pulses from the laser module n.2

Fig.3. Average (a) and Pulse power (b) versus Pulse Duration measured from laser module n.1, for different duty cycles



The maximum duty cycle that can be adopted without losing power during the pulse duration reveals the crucial role played by an efficient cooling. Indeed laser modules n.2 and 3 have drilled channels while laser n.1 has sealed ones. The reduced maximum efficiency of module n.2 is instead due to the partially equalised RF multiple feed circuit.

3. BEAM SHAPE AND QUALITY

All the adopted resonators define rectangular output apertures determining asymmetric emerging beams with an elliptic shape and a strongly astigmatic wavefront. The beam profiles have been characterised scanning them on a fast photovoltaic HgCdTe detector by means of a galvanometric movable mirror. The beam is quasi-gaussian on the guided transverse direction and squarish, uniphased on the other direction with ripples related to the Equivalent Fresnel Number and to the alignment conditions². As a consequence the Far-field beam profile in the unstable transverse direction consists of a diffraction limited main lobe with several low power side lobes. Cavity misalignments affect only the number and importance of these side lobes.

We have concentrated our study to the properties of this transverse profile. Near-field and Far-field patterns are plotted in Figs. 4 and 5, respectively in comparison with those obtained by means of numerical simulations of field propagation inside the cavity².

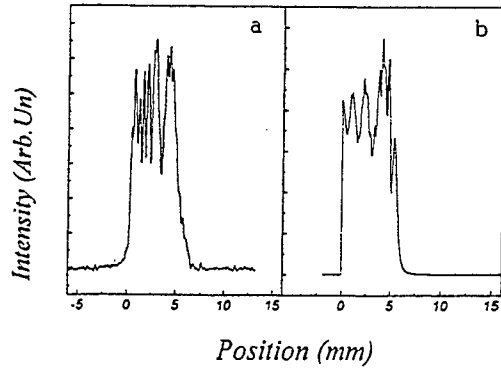
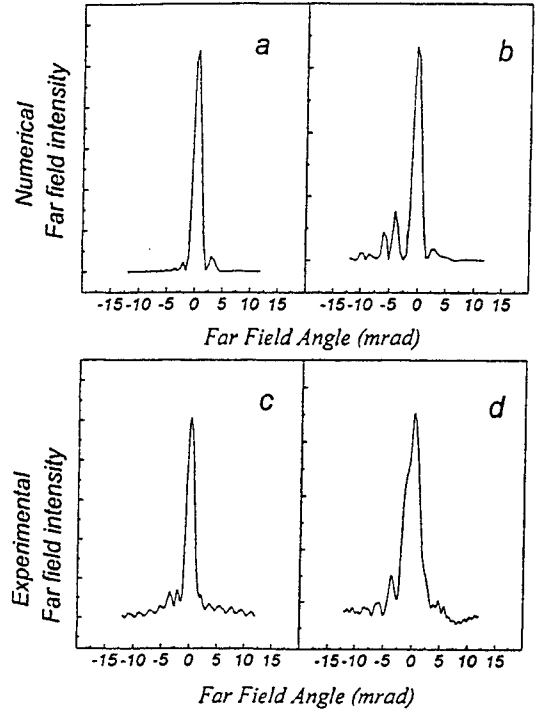


Fig.4. Near-field unstable-direction profile for the beam emerging from laser n.1 with the negative branch resonator. (a) experimental, (b) numerical.

Fig.5. Positive branch resonator Far-fields, numerical and experimental. (a) and (c) : best alignment. (b) and (d) with 100 μ rad misalignment.



The quality of these beams has been analysed on the two principal planes by means of a Coherent Mode-Master MM-6. It is summarised in Table II in terms of the quality factor M^2 . This characterisation is in fact a little arbitrary having the far field patterns several low-power side lobes propagating at large angles.

In this way the second moment of the Far-field distribution is strongly affected by the adopted integration angle². In the table we report the M^2 measured collecting on a 20 mrad angle and the result is in agreement with numerical estimations.

A better information can be gained from Encircled energy plots as those reported in Fig.6. One can easily see that the unstable-resonator direction beam both in the case of positive- and negative- branch resonators keeps being close to the gaussian beam with the same variance and better then the gaussian with the same aperture up to an 80% energy level. In other words one can focus with such a beam an amount of energy between 87 and 90% in a circle in which the ideal gaussian beam with the same aperture focuses 99% of its energy. The positive-branch resonator shows a little difference in the encircled energy function for different alignment conditions whereas the negative-branch resonator almost does not.

Table II

	Module 1 Negative Branch	Module 1 Positive Branch
θ_x	3.1 mrad	2.8 mrad
θ_y	9.5 mrad	9.5 mrad
M^2_x	1.35 ± 0.1	1.25 ± 0.1
M^2_y	1.1 ± 0.1	1.1 ± 0.1

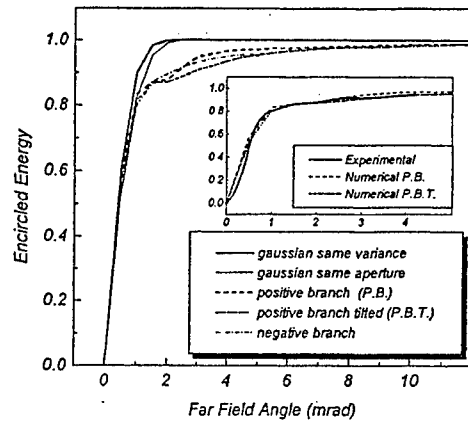


Fig.6. Encircled energy vs. Far-field angle.

4. STABILITY

As already stated the beam quality in the unstable transverse direction is not much affected by cavity misalignments. The power sensitivity to misalignments is instead deeply different for the two resonators. The positive-branch resonator shows a sizeable power drop for misalignments as small as $100\text{ }\mu\text{rad}$ whereas the negative branch maintains the maximum power extraction also for misalignments of the order of 5 mrad^2 . This fact is related to the different magnitude of mirror curvatures for the two resonators. Naturally the negative-branch resonator shows a larger criticality to cavity collimation. A two millimeters error in the cavity set-up length can cause a dramatic reduction in the extracted power.

Finally we have tested the long term power stability. This tests show that the negative branch resonator can be affected by power fluctuations due to emission line jumps. This is shown in Fig.7 for laser n.2 in situations when the electrodes and mirrors were not thermally stable. This effect is to be related to the wave-length dependent guide-to-mirror coupling coefficient in the case of short radius spherical mirrors⁵.

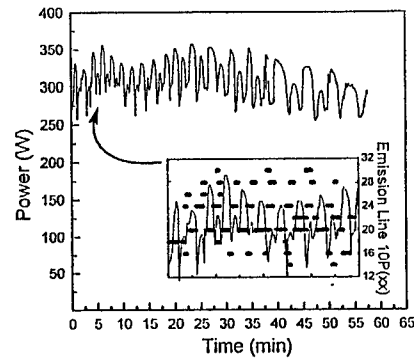


Fig.7. Power fluctuations and emission line jumps in laser n.2 with electrodes not correctly cooled and mounted.

5. CONCLUSIONS

In conclusion we have made several tests on three prototypes of compact, medium power, slab type CO_2 laser sources, investigating the behaviour of two different hybrid stable-unstable resonators, both numerically and experimentally. Simulations and experiments show a higher sensitivity of the positive-branch resonator to alignment variations. On the other hand the negative-branch resonator reveals a higher sensitivity to the cavity focusing. The beam emitted from both the resonators carries around 90% of the energy in a main diffraction limited lobe, the remaining part of the energy being scattered in low power side lobes. This beam property results to be only slightly affected by cavity misalignments particularly in the case of the negative-branch resonator. An acceptable power stability can be obtained provided that attention is paid to thermal effects in the design of cavity and electrodes.

6. REFERENCES

1. A.Lapucci, S.Mascalchi, F.Rossetti, "Pulse behaviour of a compact R.F. discharge CO_2 slab laser", *Optics and Laser Technology* **28** (3), 187-191, (1996).
2. A.Lapucci, A.Labate, F.Rossetti, S.Mascalchi, "Hybrid stable-unstable resonators for diffusion cooled CO_2 slab lasers", *Applied Optics* **35** (18), 3185-3192, (1996).
3. O.L. Bourn, P.E. Dyer, "A Novel Stable-Unstable Resonator for Beam Control of Rare-Gas Halides Lasers", *Opt. Commun.* **31**, 193-196, (1979).
4. A.E. Siegman, "Stable-Unstable resonator design for a wide tuning-range free-electron laser", *IEEE J. Quantum Electron.* **QE-28**, 1243-1247, (1992).
5. F.Rossetti, S.Mascalchi, A.Lapucci, "Experimental measurement of the mirror to guide coupling coefficient for CO_2 waveguide lasers", *to be published*.

Model of a glow discharge in a turbulent flow

G. Vlad, O. Boiron, G. Le Palec, P. Bournot

Institut de Mécanique de Marseille, UNIMECA, 60 rue Joliot Curie,
Technopôle de Chateau Gombert, 13453 Marseille Cedex 13, FRANCE

ABSTRACT

In this paper, a model of the temperature field in a laser cavity, is proposed. This model includes the calculation of the electron concentration in a turbulent flow. First, a 1D study is validated with experimental data of Leys et al. Second, the model is applied to a 2D argon flow. This study shows that the knowledge of the temperature field allows to characterize the correlation between the plasma oscillations and turbulence fluctuations of the neutral gas.

1. INTRODUCTION

In the last years, the use of fast axial flow lasers yielded to take into consideration the study of glow discharges in a permanent gas flow. In these lasers (EDL), ionization is due to a high voltage electric discharge and vibrational excitation occurs from electronic collisions between both the gas molecules and free electrons produced by the electric discharge.

In a previous study¹, we have presented some results about the velocities and temperature fields in a laser cavity consisted in a 55 mm diameter cylindrical tube. The laser mixture (CO₂-N₂-He) was introduced by means of a nozzle which axis was the same as the axis of the tube. The electric discharge was created by electrodes located at the entrance and exit section of the tube. As a first approach, the power injected has been considered constant throughout the tube, which means that a constant current density was assumed. In fact, this one is subjected to high variations in the radial direction (that is from the axis to the wall of the tube), which can explain the discrepancies observed between theoretical previsions and experimental results.

In order to predict a correct temperature field, the knowledge of the current density is necessary: this one is very close to the electronic density so that we propose a model of the electron concentration in a turbulent flow. We assume that the gas flow acts on the electron distribution and the Shwartz² model is used in order to model the changes of the diffusion coefficients due to turbulence.

2. GOVERNING EQUATIONS

A. Model 1D:

The charge neutrality is assumed. We consider only direct ionization. The influence of turbulence is taken into account through the ambipolar diffusion phenomena. We suppose that the electric current do not present axial variations. As electrons and ions have equal radial velocity in order to maintain charge neutrality, just one equation is needed for the conservation of charge particles:

$$\frac{1}{r} \frac{d}{dr} \left(r D_a^* \frac{dn_e}{dr} \right) + k_i N n_e = 0 \quad (1)$$

where D_a^* is the ambipolar diffusion coefficient and n_e is the electronic density. Similar to the diffusion phenomena of a species into a gas, we write :

$$D_a^* = D_{aL} + D_{aT} \quad \text{where} \quad D_a^* = D_a \left[1 + \left(\frac{Sc}{Sc_t} \right)_i \frac{\mu_t}{\mu} \right] \quad (2)$$

where μ_l and μ_t are the dynamic viscosity and the turbulent viscosity respectively. Da_L and Da_T are the "laminar" diffusion coefficient and the "turbulent" diffusion coefficient respectively. In this study we suppose $Sc=Sc_t$.

B. Model 2D

In the case of a two-dimensional flow, the influence of neutral gas flow on the charge particles distribution and the electron drift were taken into account. The conservation equation of the electronic density is then :

$$\frac{\partial}{\partial z}(n_e w) + \frac{1}{r} \frac{\partial}{\partial r}(r n_e v) = \frac{1}{r} \frac{\partial}{\partial r} \left(r D_a \frac{\partial n_e}{\partial r} \right) + k_i N n_e + \mu_e E_z \frac{\partial n_e}{\partial z} \quad (3)$$

where w and v are the axial velocity and the radial velocity respectively. N (m^{-3}) is the neutral gas density. In this equation the laminar diffusion coefficient and the electron drift velocity are constant :

$$D_{aL} = 0,037 \text{ m}^2/\text{s}; \quad v_d = \mu_e |E_z| = 4,6 \cdot 10^3 \text{ m/s} \quad (4).$$

On the positive column of a glow discharge domain the electric current is constant. The current conservation equation is :

$$I(z) = 2 \pi e \mu_e |E_z| \int_0^R n_e r dr = I_0 = \text{constant} \quad (5).$$

3. NUMERICAL MODEL

The electron density conservation equation and the momentum equations are solved separately. We suppose the neutral gas flow frozen. When the thermal effect of the discharge on the gas flow is under study, we suppose the charged particles distribution fixed. The density is not constant, however, apart from a small region near the entrance of the tube, the density variations do not exceed 10% and the derivative of N is negligible. Then, in order to simplify the equations we consider the neutral gas density constant. In order to verify the current conservation equation, the ionization rate (k_i) is calculated numerically. In this study the diffusion coefficient and the electron drift velocity do not depend on the electron density variations. In the vicinity of the wall, recombination between electrons and ions imply a zero electron density at the wall. The electron flux who disappear at the wall through recombination phenomena is :

$$-D_{aL} \left(\frac{\partial n_e}{\partial r} \right)_{r=R} \quad (6).$$

We suppose that turbulent diffusion do not concern the wall vicinity. The choice of the near wall grid cell size will influence electron loss and ionization rate. If the near wall grid cell is larger than the laminar boundary layer high, the electron loss and the ionization rate are under estimated.

4. BOUNDARY CONDITIONS

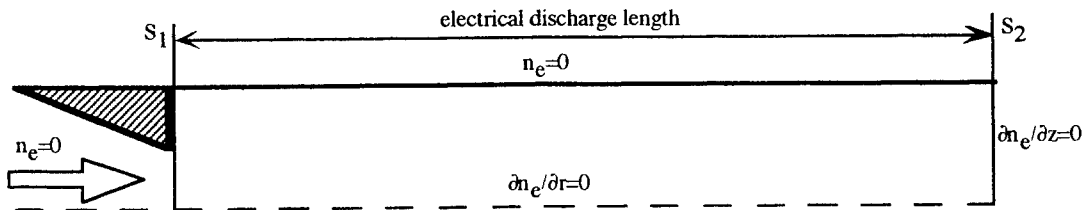


figure 1. boundary conditions.

The boundary conditions are represented in the figure 1. We suppose that the gas passing through the S1 surface do not convey electrons. The recombination phenomena is important at the wall. Then, we consider a zero electron density at the wall. On the axis tube, the axisymmetrical conditions impose zero derivatives.

5. RESULTS

A. Model 1D

We consider the flow and the electric discharge steady. First we calculate the turbulent density for a flow through a pipe at several Reynolds numbers. The ambipolar diffusion coefficient (fig.2) is calculated using equation 2. Then, equation 1 is solved in order to obtain the electron density (fig.3). Increasing the Reynolds numbers tends to flatten the electron density profiles. The growth in the ionization rate in a turbulent flow (fig.4) is necessary in order to balance the increased loss of charged particles to the walls which is caused by increased turbulent diffusivity.

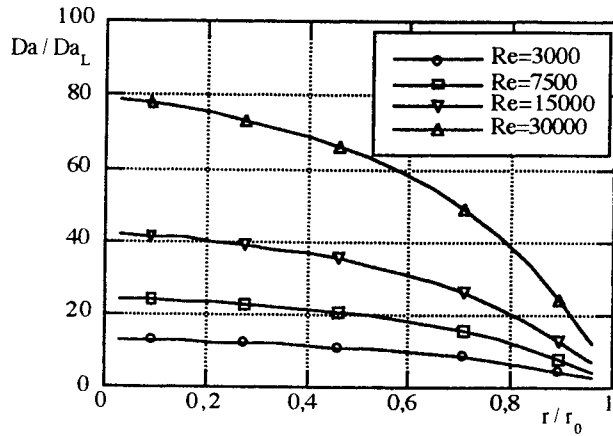


fig.2. Ambipolar diffusion coefficient in a turbulent flow

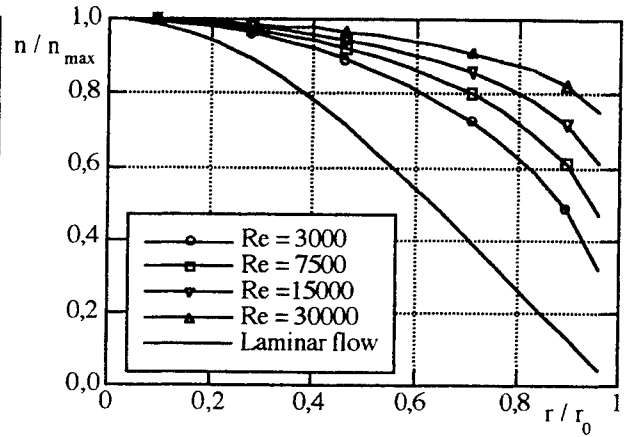


fig.3. Electron density profiles in a turbulent flow.

The increase in the ionization rate for high Reynolds numbers is in agreement with experimental observations^{3,4}. However, the values are below the predicted values of Shawrtz & Lavie². Indeed, the grid size at the wall was chosen for the low Reynolds numbers. The increase in the Reynolds number leads to a thin boundary layer and the model underestimates the electron loss. It seems then only an accurate estimation of the electron loss can lead to correct predictions.

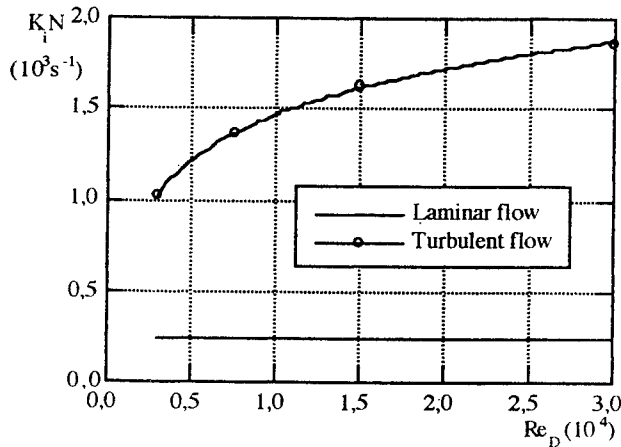


fig.4. Ionization rate vs Reynolds number

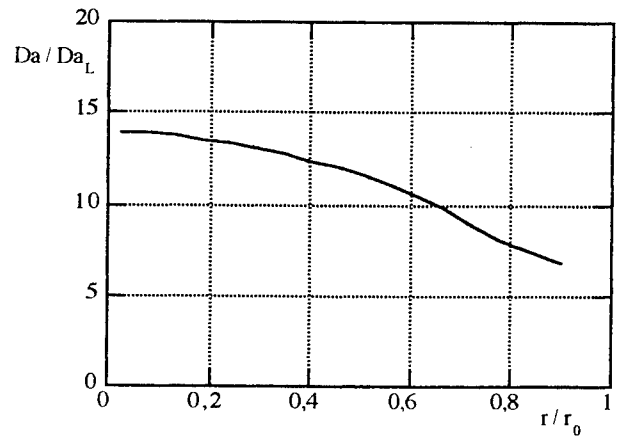


fig.5. Ambipolar diffusion coefficient profile at Re=5000

In order to validate our model we use the experimental results of Leys & al.⁵. They measure electron concentration in a discharge tube of a CO₂ laser. The gas flow was turbulent and the Reynolds number is Re=5000. The ambipolar diffusion coefficient (fig.5) is calculated with equation 2 where the eddy viscosity for turbulent flow through a

pipe was estimated numerically. The first grid cell near the wall is $0,2r_0$ high. Comparison between numerical results and experimental data⁵ show good agreement, as seen from figure 6.

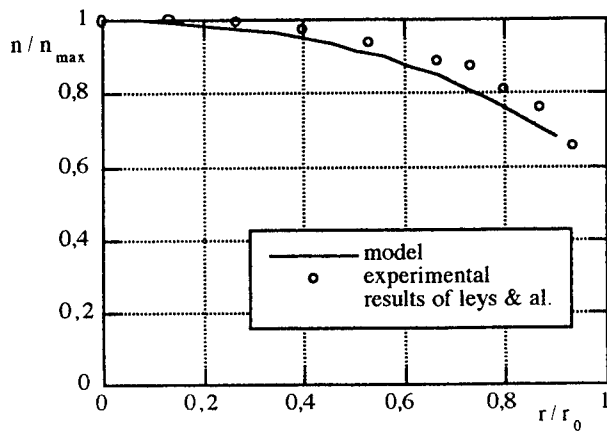


fig.6. Electron density profile.

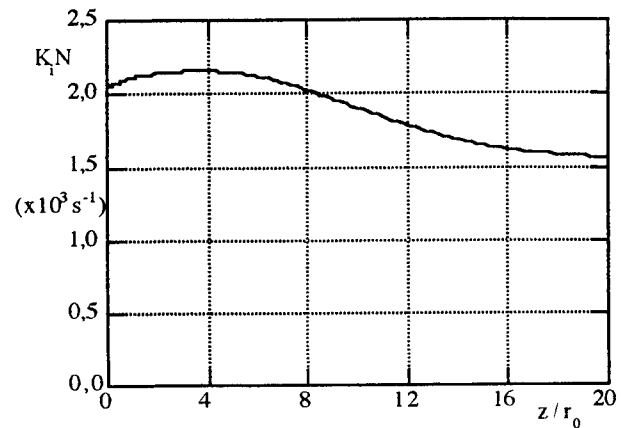


fig.7. Axial variation of the ionization rate.

B. Model 2D

We will show now the influence of the flow on the electron density. First we suppose that the electron drift do not interact with neutral gas and the discharge has no thermal effect on the flow. The conservation equation 3 of the electron density and the momentum equations (of the neutral gas) are solved separately. The flow under study is a 2D axis-symmetric recirculating turbulent Argon flow at $Re=4000$. The model used to calculate momentum equations and eddy viscosity was presented in a previous paper¹. The condition $I_0=\text{constant}$ allows to calculate the ionization rate (fig. 7). We calculate the ambipolar diffusion coefficient (fig. 8,9) with equation 2. Then we solve the electron density conservation equation. We see that the recirculating zone acts on the electron density profile (fig.10,11). Indeed, in this zone the turbulence intensity and the ambipolar diffusion coefficient are important. The high turbulence intensity tends to flatten the electron density profile.

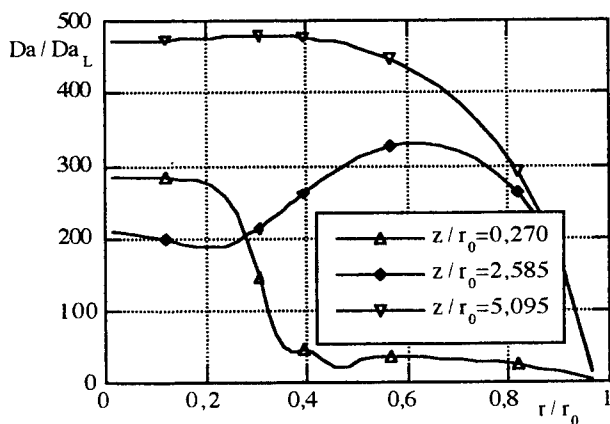


fig.8. Ambipolar diffusion coefficient profiles.

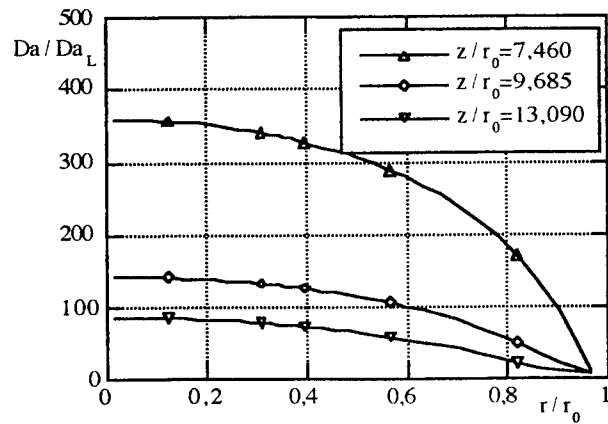


fig.9. Ambipolar diffusion coefficient profiles.

In the vicinity of the reattachment point radial velocity get high values. However, the effects on the electron distribution due to mass transfer are negligible compared to the effects due to turbulent diffusion. Downstream, the effect

of the recirculating zone disappears and the electron density profile is similar to the electron distribution obtained with the 1D model.

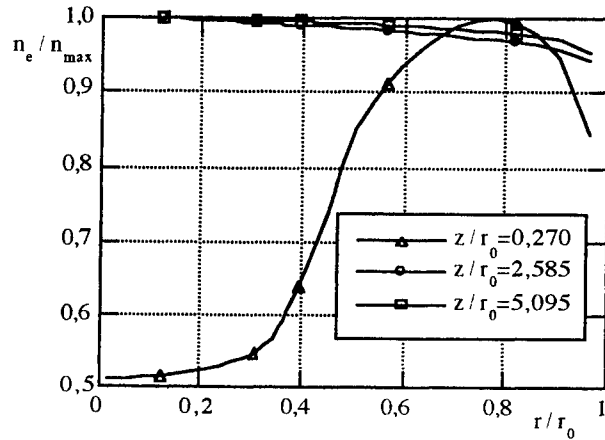


fig.10. Electron density profiles.

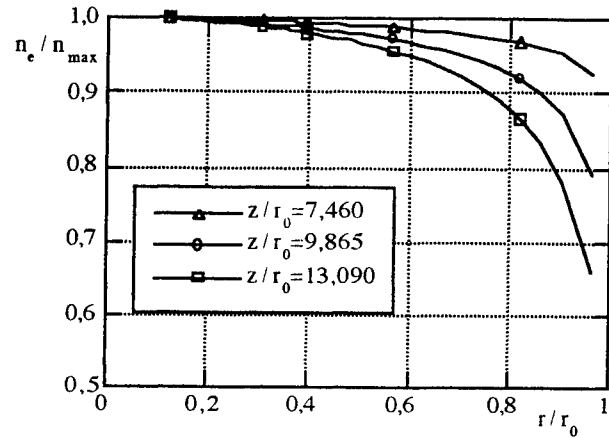


fig.11. Electron density profiles.

The correlation between the turbulent motion of the ions and that of the neutral gas depends on physical and geometrical characteristic of the flow 4,6. We want to now if the ions and the neutral gas motion are correlated. We dispose of experimental measures⁷ of temperature in to the discharge tube at $z/r_0=10,6$ and $15,4$. First we determinate the electron distribution (fig. 12,13) with and without turbulent ambipolar diffusion. If the ions and the neutral gas motion are not correlated then the electric current is constricted in a region near the tube axis. If they are correlated, the axial current density value drops 50% approximately. Second, we suppose the electron distribution fixed and the momentum and energy equations are solved. Comparison between measured and calculated enthalpy (fig. 14,15) shows that a better predicted temperature profiles are obtained if only laminar is taken into account. It seems that in the case under study correlation do not take place.

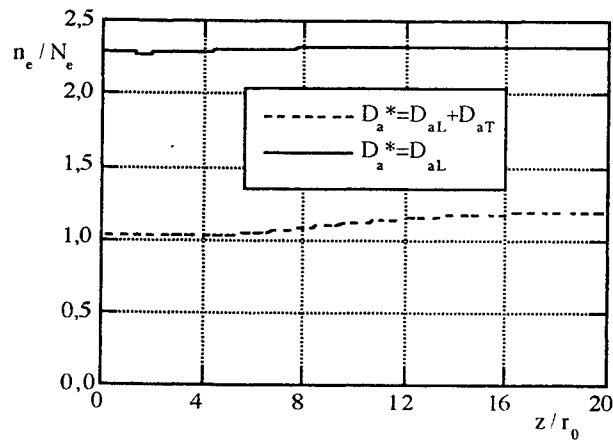


fig.12. Axial variation of electron density.

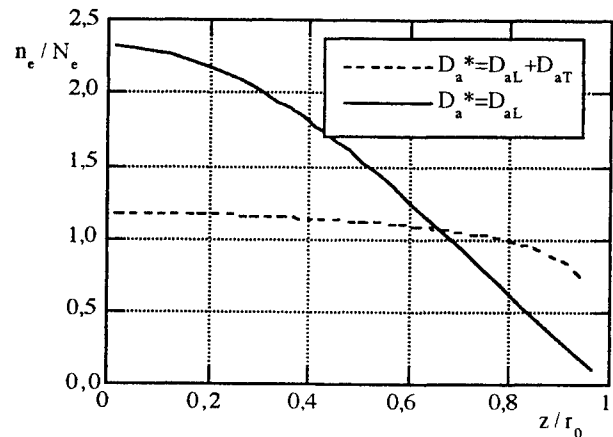


fig.13. Electron density profile at $z/r_0=15,4$ ($N_e \approx 4,8 \times 10^{10} \text{ cm}^{-3}$)
Effect of turbulent ambipolar diffusion coefficient.

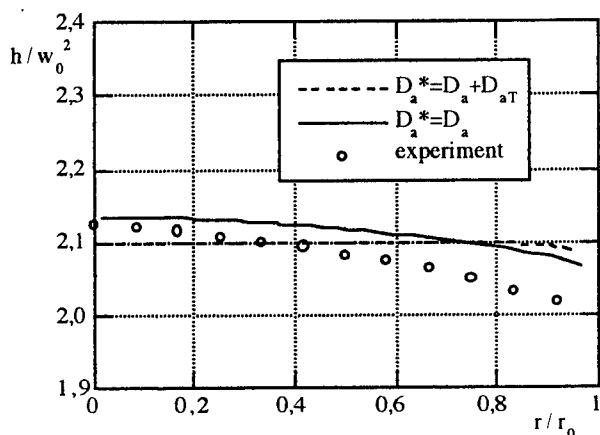


fig.14. Static enthalpy profile at $z/r_0=10,6$ ($w_0=275\text{m/s}$).

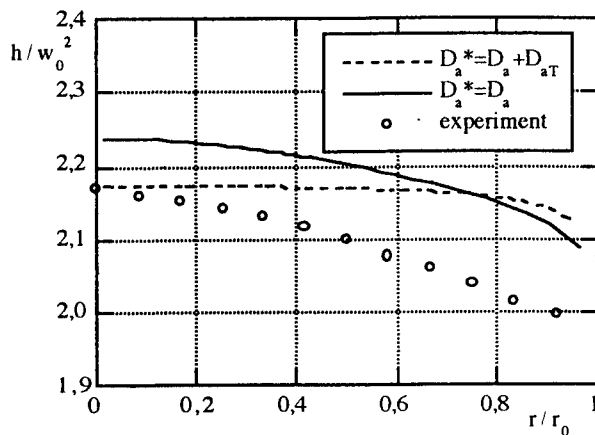


fig.15. Static enthalpy profile at $z/r_0=15,4$ ($w_0=275\text{m/s}$).

6. CONCLUSIONS

In this paper we propose a model of a glow discharge in a turbulent flow. The electron density is calculated using a conservation equation. First, the study of a 1D steady, axisymmetric, turbulent and compressible flow with a stable electric discharge shows the effects of the turbulence on the electron density. This model is validated with experimental data of Leys et al³. In this particular case of a CO₂ laser cavity, theoretical results are in good agreement with the reported measures. Second, the model was applied to a 2D argon flow for which experimental temperature radial profiles in two sections of the discharge tube were available. The temperature distribution is calculated by assuming that the heating of the gas does not act on the current density which, in turn, highly influences the temperature distribution throughout the tube. This study shows that the knowledge of the temperature field allows to characterize the correlation between the plasma oscillations and turbulence fluctuations of the neutral gas.

7. REFERENCES

1. Vlad, Boiron, Le Palec, Bournot, "Numerical Simulation of the compressible turbulent flow in a CO₂ laser cavity", Int. J. Heat Mass Transfer, vol. 38, n° 14, pp 2623-2633, 1995.
2. J. Shwartz, Y. Lavie, "Effects of turbulence on a weakly ionized plasma column", AIAA Journal, Vol. 13, No. 5, pp. 647-652, 1975.
3. V. L. Granatstein, "Structure of Wind-Driven Turbulence as Resolved by Continuum Ion Probes", The Physics of Fluids, Vol. 10, pp.1236-1244, June 1967.
4. G. A. Garosi, G. Bekefi, M. Schultz, "Responce of a Weakly Ionised Plasmе to Turbulent Gas Flow", The Physics of Fluids, Vol. 13, No.11, pp.2795-2809, November 1970.
5. C. Leys, D. Toebaert, E. Desoppere, "Spatially resolved measurment of the electrical power density and gas velocity in a fast axial flow CO₂ laser", Proc. 21st Int. Conf. on Phenomena in Ionized Gases (Bochum, Germany), Vol. 2, pp. 98-99, 1993.
6. V. L. Granatstein, A. M. Levine, M. Subramanian, "Laser probing of a weakly ionised turbulent gas: Comparison of neutral and plasma fluctuations", Phys. Fluids, Vol. 14, No. 12, pp. 2581-2587, 1971.
7. R. Michel, "Etude thermique du tube à décharge d'un laser CO₂ à flux axial rapide de 10kW de puissance", report, Univ. Aix-Marseille I, 1994.

Laser marker built on multichannel or slab CO₂ lasers

E.F.Plinski, J.S.Witkowski, K.M.Abramski

Institute of Telecommunication and Acoustics
The Technical University of Wrocław

ABSTRACT

We present the marking technique based on computer-controlled electromechanical diaphragm array and focusing system, which allows codes to be laser-written on dot-array sequences basis.

Key words: multiwaveguide CO₂ laser, CO₂ slab laser, Talbot selection, laser marker.

INTRODUCTION

One of the applications of the technological lasers is marking [1]. Usually a laser beam is directed using an optical system on a target making a fast trace. For a proper shape of the trace, laser beam is deflected in two planes using computer controlled mirrors. Advantages of these type of the markers is marking any shapes - characters or drawings. Disadvantages are slow speed of the marking and relatively high price of the optical deflected systems.

CONSTRUCTION

We built two laser sources for multidot marking. In the first version it was a multiwaveguide RF excited CO₂

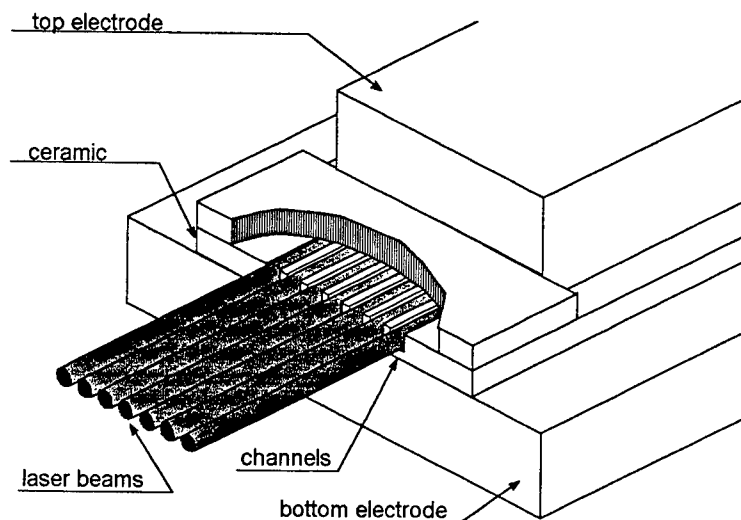


Fig. 1. Construction of the multiwaveguide laser

laser. The construction of the multiwaveguide laser was based on the known "sandwich" type (see Fig. 1). Top and bottoms electrodes was cooled with tap water. We cut off 7 channels in alumina ceramic with dimensions of 2.3 x 2.3 mm. A silicon total reflecting and 92% reflecting ZnSe mirrors we used as an optical resonator of 400 mm in length. CO₂:N₂:He + Xe = 1:1:3 + 5% gas mixture at 100 Torr of pressure was used. The laser was supplied with a 125 MHz generator. At 1000 W of input we achieved 100 W of output distributed into 7 channels. Each laser channel operated in singular waveguide EH₁₁ mode [2]. The best distance for multidots marking is beyond the focus, in the reimage area.

The alternative construction for multidot operation was the Talbot selected RF excited CO₂ slab laser. The construction of the slab laser was similar to above one. Instead of the multiwaveguide channel we used a slab, cut off in the

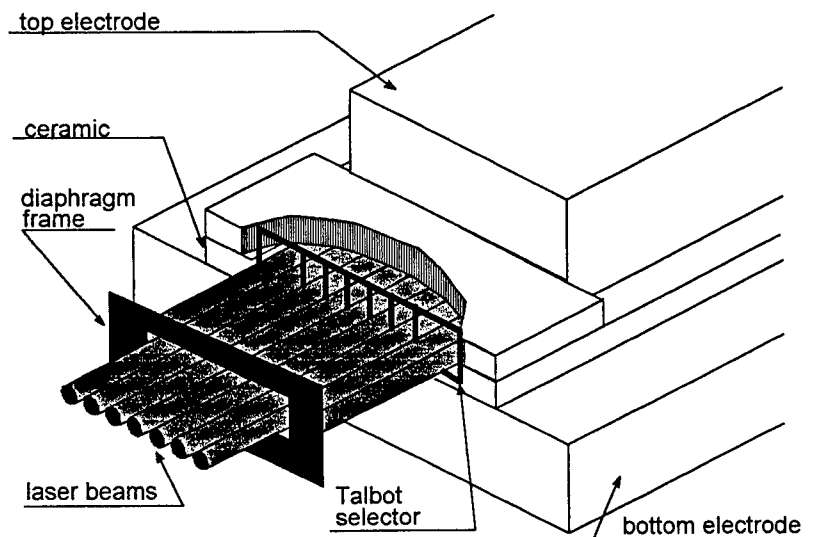


Fig. 2. Slab laser with Talbot selection EH_{9,1} mode and seven diaphragmed dots required for marking

CONSTRUCTION

We built two laser sources for multidot marking. In the first version it was a multiwaveguide RF excited CO₂ laser. The construction of the multiwaveguide laser was based on the well known "sandwich" structure (see Fig.1). Top and bottoms electrodes were cooled with tap water. The laser structure consists of seven channels cut off in alumina ceramic with dimensions of 2.3 x 2.3 mm. A total reflecting mirror and 92% reflecting ZnSe mirror formed an optical resonator of 400 mm in length. CO₂:N₂:He + Xe = 1:1:3 + 5% gas mixture at 100 Torr of pressure was used. The laser was supplied with a 125 MHz generator. At 1000 W of input we achieved 100 W of output distributed into 7 channels. Each laser channel operated in singular waveguide EH_{1,1} mode^{2,3}. We used short focal lens ($f = 10\text{cm}$) for the reimage of laser output. The reimage plane behind the focus point is also the best area for multidot marking process.

The alternative construction for multidot operation was the Talbot selected RF excited CO₂ slab laser⁴. The construction of the slab laser was similar to above one. Instead of the multiwaveguide configuration we used a slab structure with Talbot selected grids. The slab dimensions were 18.63 mm width (9x2.07) and 1.7 mm high. We placed the grids of gold wires 50 μm in diameter in front of each end of the slab channel (see Fig. 2) forming Talbot conditions for mode selection. The distance between the wires was 2.07 mm. The total output power of the laser was 75 W.

In the proposed marker, the laser beams were switched by a electromechanical diaphragm array, printing the characters on a moved target as is shown in Fig.3.

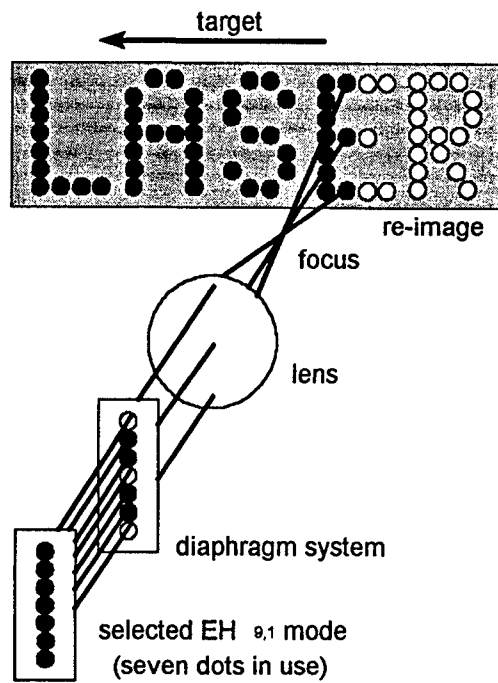


Fig. 3. Principle of the multidot laser marking

EXAMPLES

The Fig. 4 shows the examples of marked patterns using above laser marker.

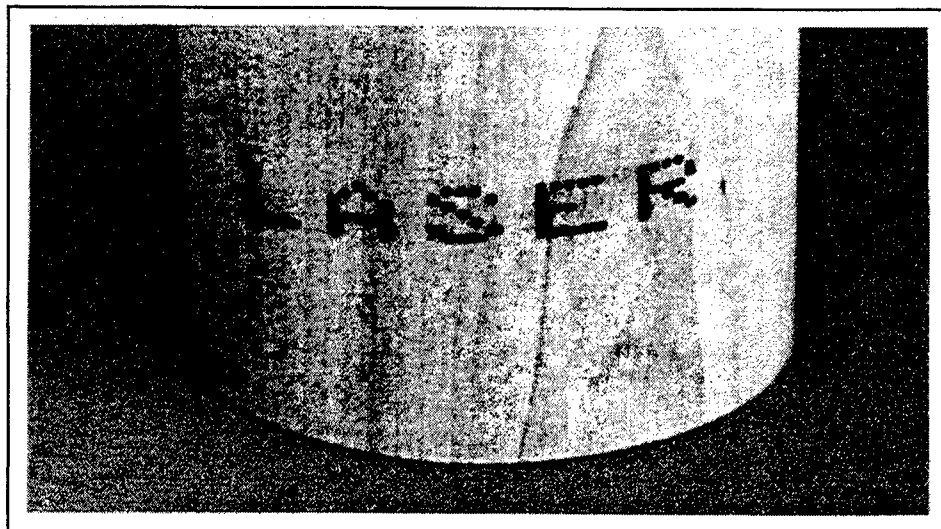


Fig. 4a. Marked pattern on a piece of wooden cylinder

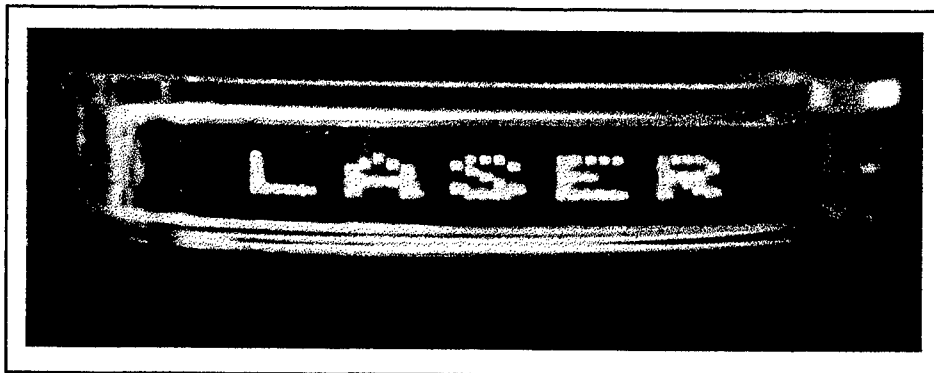


Fig. 4b. Marked pattern on a plastic box

CONCLUSIONS

The proposed method of marking can be quicker and cheaper than used optical deflecting systems. The main advantage is the simplicity of the optical system (lack of galvano scanners). The dimension of the characters can be easily set using an optical system with chosen magnification. Disadvantage of the method is inability of drawing of continuous lines: the obtained picture consists a mosaic of dots.

Speed of the device in the first non-optimized experiments was 4 characters per second. We work on improving the marking speed. The efficiency of device could be also improved by pulsing the laser output. Synchronisation of the laser pulsing with external electromechanical switching system would increase the energy per pulse per dot.

The proposed method of marking can be applied in production processes where manufactured objects are moving, in their nature, perpendicularly to the observer.

REFERENCES

- [1] R.G.Driggers, K.Barnard, E.E.Burroughs, R.G.Deep, O.Williams: Review of infrared scene projector technology - 1993; *Optical Engineering* 33, 2408-2417, (1994).
- [2] K.M.Abramski, E.F.Plinski, J.S.Witkowski, R.Nowicki: Multiwaveguide CO₂ laser with diffractive coupled channels; *CLEO/EUROPE'94 Conference, Amsterdam*, CTuK43, 117, (1994).
- [3] K.M.Abramski, A.D.Colley, H.J. Baker, D.R.Hall, High power two-dimnsional waveguide CO₂ laser array, *IEEE Journal of Quantum Electronics*, 32, 340, (1996)
- [4] K.M.Abramski, H.J.Baker, A.D.Colley, D.R.Hall, Single-mode selection using coherent imaging within a slab waveguide CO₂ laser, *Applied Physics Letters*, 60, 2469, (1992)

High Power Microwave Excited CO₂ Laser Oscillator

D.Choo Y.Takenaka S.Yamane

Matsushita Industrial Equipment CO.,LTD.
3-1-1 Inazu-cho Toyonaka Osaka, JAPAN 561
and

N.Furuya M.Kato

Matsushita Research Institute Tokyo, Inc.
3-10-1 Higashimita Tama-ku Kawasaki, JAPAN 214

1. ABSTRACT

Microwave discharge has been proposed for high power laser oscillator. However, there are few practical high power (over 1kW) microwave excited CO₂ laser oscillator since it is difficult to establish a homogeneous discharge region across and along a laser tube for coaxial fast gas flow laser.

This paper proposes a practical high power microwave excited CO₂ laser oscillator by

- 1) employing orthogonal crossing electric field for radial homogeneity of the discharge
- 2) dividing the axial discharge region of the laser tube into several discharge sections for stable discharge
- 3) selecting the optimized gas flow to maximize the laser output laser power.

Applying these technologies, the experimental apparatus achieved 270W laser output at 1.4 kW input microwave power per the waveguide. The equipment is also able to scale up by connecting tubes, which consist of five waveguides per tube, and confirmed 1.8 kW for the same volumetric gas flow rate and the structure of a conventional 1.8 kW DC laser.

The proposed methods may provide a practical high power microwave excited CO₂ laser oscillator that exceeds the conventional DC discharge one.

2. INTRODUCTION

It has been expected that microwave discharge is suitable for high power and high frequency pulse laser oscillator because of high input power density, less gas contamination, less degradation of optics, low supply voltage, low cost of power source and quick response of a magnetron compare with DC or RF discharge. However, there are few practical high power microwave excited CO₂ laser oscillator since it is difficult to obtain a homogeneous discharge region across and along a laser tube.^{1,2,3,4} Although much study and research has been done to date, more practical laser oscillators need to be proposed to widely use for many applications.

This paper presented a practical high power microwave excited CO₂ laser oscillator. At the same time, the basic performance of the proposed waveguide and of the multichanneled waveguides are also discussed.

3. UNIDIRECTIONAL ELECTRIC FIELD (UDEF) WAVEGUIDE

Figure 1(a) shows the structure of discharge unit of the experiment setup, which consists of a laser tube and a waveguide. The waveguide, so called unidirectional electric field (UDEF) waveguide, consists of a magnetron (based on Panasonic type 2M244), which is widely used for a microwave oven, and stub tuners. The laser gas flows inside the tube coaxial with the optical axis and is excited by the microwave.

The microwave, which is emitted from the magnetron, propagates with TE₀₁ mode in the waveguide and forms standing wave between stub tuners and the end wall of the waveguide. A laser tube (21mm I.D.) is located at the center of antinode of the standing wave. The electric field applies perpendicular to upside wall of the waveguide and switches its direction from upside to bottom wall, vice versa.

To modify the distribution of the electric field intensity in the waveguide, a ridge is widely applied. The shape of a ridge determines to be optimized the electric field distribution the shape of the distribution and is optimized. Figure 1(b) shows the image of the discharge distribution, taken by CCD camera, across the tube. It shows the discharge image is related to the electric field and the discharge area covers only 40% of the cross section of the tube.

4. ORTHOGONAL CROSSING ELECTRIC FIELD (OCEF) WAVEGUIDE

4.1 Performance of OCEF waveguide in radial direction

Like other waveguides used for microwave excited lasers, UDEF gives lean discharge area because of its fixed electric field direction. The small discharge area causes local gas temperature rise, generation of undesired arcs, and leads the saturation of output laser power. To randomize the electrical field and broaden the discharge area, the orthogonal crossing electric field (OCEF) is developed.⁵ OCEF achieved an unfixed electric field by synthesizing two electric field vectors which have slightly distinct frequencies respectively. Figure 2(a) shows the typical OCEF waveguide, which is composed by right-angled waveguides, two magnetrons and two sets of stub tuners. Two waveguides intersect each other at the center of a laser tube.

Two magnetrons emit microwave simultaneously, whose frequencies are different from each other. The microwaves form two orthogonal electric fields at the center of the tube. The fields' vectors are synthesized to one rotational vector. The locus of the rotational vector depends on the difference of the frequencies of magnetrons.

Figure 2(b) shows the image of discharge distribution across the tube and it shows the homogeneous discharge distribution and the discharge area covers 70% in the radial direction of the tube.

4.2 Performance of OCEF waveguide in longitudinal direction

Since the intensity of the electric field must be zero at the wall of the waveguide and at the nodes, it is difficult to achieve homogeneous discharge distribution along the tube axis. Figure 3 shows the visible light intensity distribution of discharge area along the tube axis taken by optical fiber and avalanche photo diode as a function of the position from the center of the waveguide. The gas flows from -to + direction.

It shows the peak of the visible light intensity distribution moves to downstream and it depends on input microwave power. This leads the practical discharge region is much smaller than the width of the waveguide. Therefore, the waveguide can provide very compact discharge volume and this leads high output laser power density compare to the conventional DC discharge. On the other hand, the visible light intensity distribution for longitudinal direction become unstable, which jumps to upstream from downstream in the waveguide cyclically, under the high input microwave power. It implies the limitation of the input microwave power in the waveguide.

Figure 4 shows the local small signal gain coefficient as a function of distance from the wall of the waveguide. The coefficient decreases along the distance. It shows the existence of the gain at the downstream of the waveguide and the decay of the gain. This decay must be considered to extract output laser power.⁶

Figure 5 shows output laser power vs. input microwave power for OCEF and UDEF waveguides. OCEF waveguide achieved 270 W output laser power for 1.4 kW input microwave power.

4.3 Performance of OCEF waveguides

To obtain high output laser power laser oscillator, the number of OCEF waveguide (i.e. the number of channel) and the distance between the OCEF waveguide must be optimized. The optimization is based on the simulation. The characteristics of the microwave excited laser oscillator depend on the length of laser tube strongly as well as operating conditions. Figure 6 displays a typical result of the calculation under the four OCEF waveguides set along the tube (length is 680mm). It shows the ratio of the number of excited N_2 to the number of N_2 as a function of position of waveguide where set origin at gas inlet of the tube. From the figure, four steep peaks that caused by each waveguide can be observed. According to the simulation, five OCEF waveguides gives maximum power for experiment oscillator (tube length = 636mm).

The laser gas flow is also optimized for five OCEF waveguides. Figure 7 shows the output laser power vs. input microwave power for different gas flow, in gas velocity distribution. The uncontrolled gas flow is assumed turbulent at inlet, laminar at laser gas outlet of the tube. On the other hand, the controlled gas flow is the rotational flow accompany with straight flow at inside of the flow.

4.4 Apply OCEF waveguides to DC laser oscillator

To compare the maximum output laser power of microwave excited CO_2 laser oscillator to a conventional DC excited laser oscillator, apply OCEF waveguides to 1.8 kW DC laser under same volumetric gas flow rate and the structure. The oscillator consists of four laser tubes and has five OCEF waveguides for the tube. It marked 1.8 kW as DC marks (Figure 8).

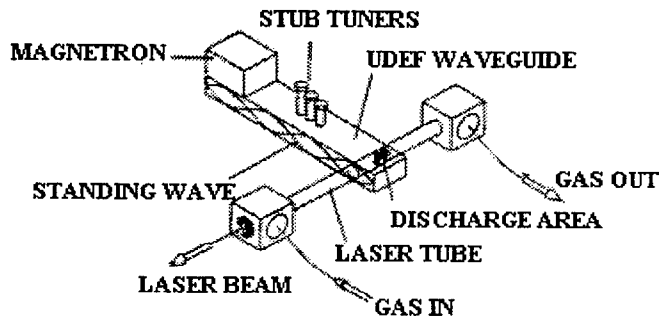
5. CONCLUSION

A practical high power microwave excited CO₂ laser oscillator has been developed. It marks 1.8 kW output laser power for the same volumetric gas flow rate and structure of a conventional DC discharge one. It is realized by

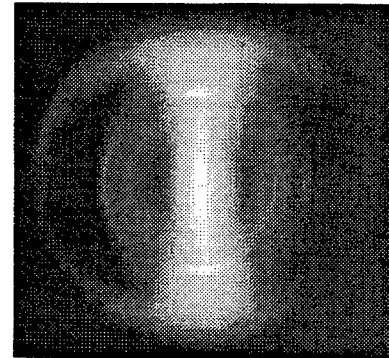
- 1) employing orthogonal crossing electric field for radial homogeneity of the discharge
- 2) dividing the axial discharge region of the laser tube into several discharge sections for stable discharge
- 3) selecting the optimized gas flow to maximize the laser output laser power.

6. REFERENCES

1. P.Hoffmann, H.Hügel, W.Schall, and W. Schock, "Cw carbon monoxide laser with microwave excitation in the supersonic flow," *Appl.Phys.Lett.* 37(B), pp.673-674, 15 October 1980
2. B.Freisinger, J.H.Schafer, J.Uhlenbusch, and Z.B.Zhang, "Microwave excited CO₂-lasers," *SPIE Vol. 1132 H.P.Laser & Laser Machining Tech.*, pp22-28, 1989
3. R.Wester, G.Herziger, and H.Schulke, "High frequency excitation of coo lasers," *CO₂ Vol.801 H.P.Lasers*, pp14-22, 1987
4. P.Hoffmann, "Discharge behavior of a RF excited high power CO₂ laser at different excitation frequencies," *SPIE Vol.650 H.P.Lasers & their Ind. Appls*, pp23-28, 1990
5. M.Kato, K.saito, H.Yajima, K.Sato, M.Kimura, and N.Furuya, "Microwave-discharge-excited CO₂ laser using orthogonally crossing electric fields," to be published in proceeding of CLEO/QELS'96
6. K.Grunewald, A.Giesen, and H.Hügel, "Theoretical investigation on CO₂ laser design," *SPIE Vol. 1810 G.C.L.*, pp.99-102, 1992

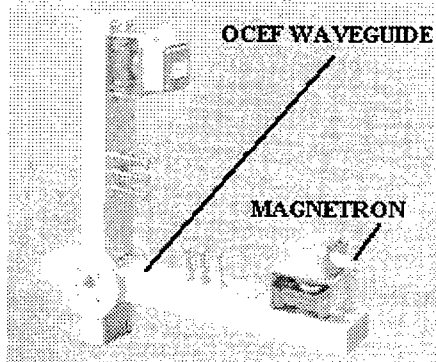


(a)

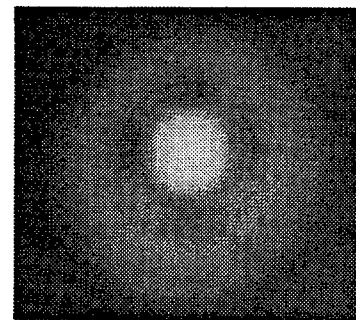


(b)

Figure 1 Experiment setup with UDEF waveguide (a) and discharge image across tube (b)



(a)



(b)

Figure 2 Scheme of a typical OCEF waveguide (a) and discharge image across tube (b)

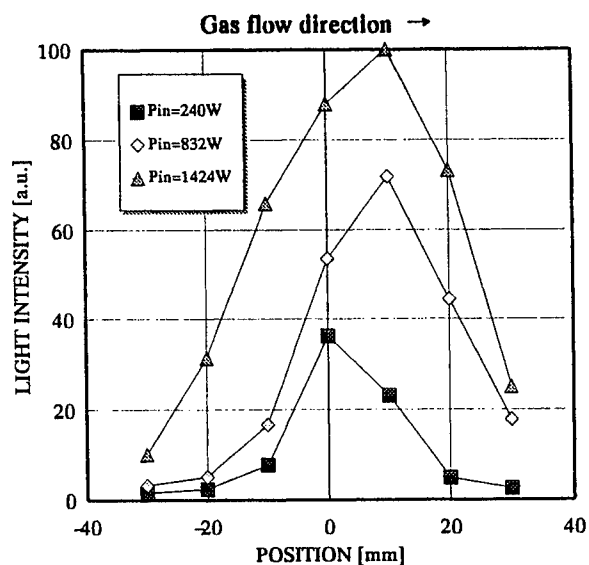


Figure 3 Light intensity distribution along tube axis

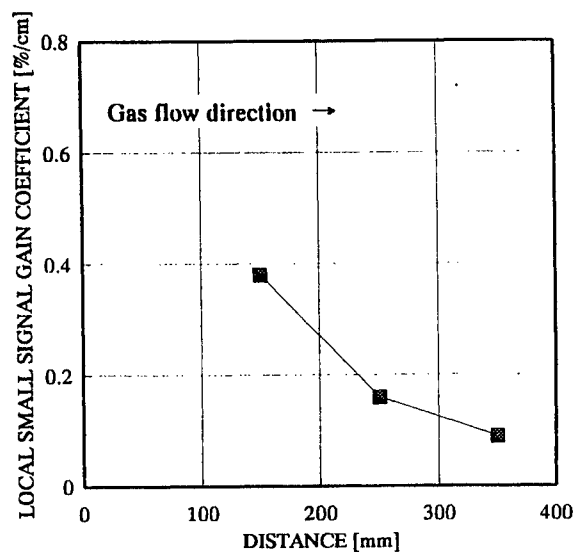


Figure 4 Local small signal gain coefficient along tube axis

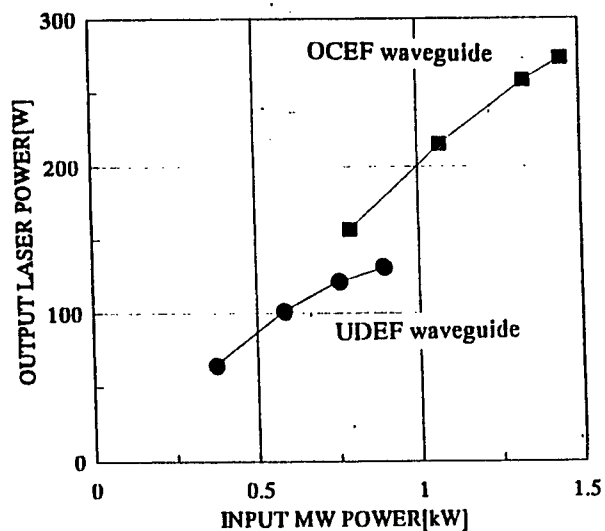


Figure 5 Output laser power of OCEF and UDEF

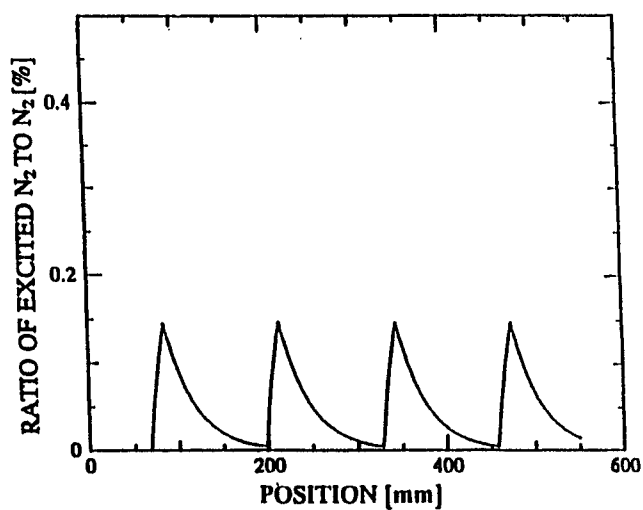


Figure 6 A typical result of simulation of the number of excited N_2 to N_2

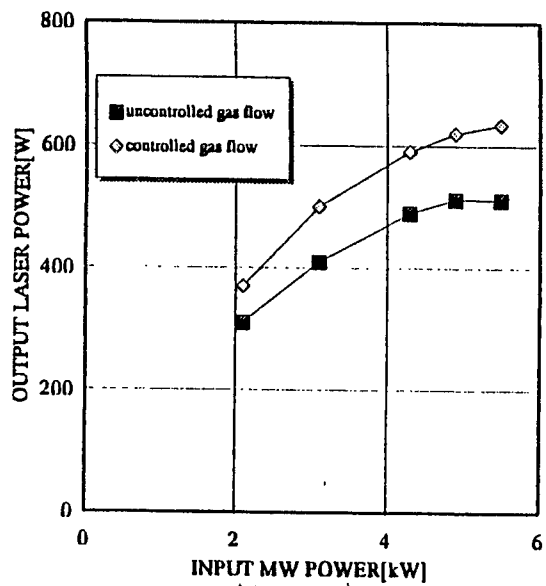


Figure 7 Output laser power for controlled and uncontrolled gas flow

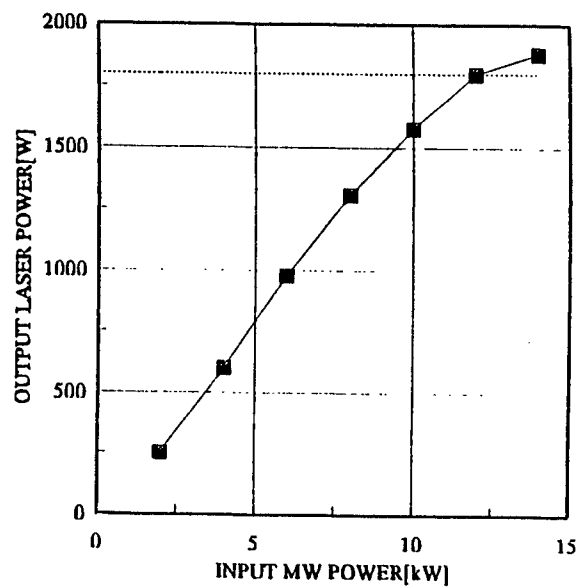


Figure 8 Output laser power vs. input microwave power

Parametric investigation of the small-signal gain in a large aperture e-beam controlled CO₂ laser

W.Riede, W.Mayerhofer, Th.Hall, S.Walther and G.Renz

Institut fuer Technische Physik, DLR Stuttgart
Pfaffenwaldring 38 - 40, 70 569 Stuttgart, Germany

ABSTRACT

In an e-beam controlled CO₂ laser unit the spatial, temporal and spectral properties of the small-signal gain were investigated in a single pass geometry. A smooth spatial distribution was found with peak values of 2.9 %/cm near the cathode at 112.5 J/(l bar). No reduction in the gain value was monitored up to repetition rates of 60 Hz when circulating the laser gas with a gas flow velocity of 100 m/s. A HeNe laser probe beam, being collinear to the CO₂ laser beam, was used to monitor shock waves or mechanical vibrations by measuring its deflection. This investigation showed, that the small-signal gain measurements were not interfered by any disturbances.

Keywords: e-beam controlled CO₂ laser, small-signal gain measurements.

1. INTRODUCTION

The precise knowledge of the small-signal gain distribution at different energy loadings is important for the layout of a phase conjugate MOPA scheme. Phase conjugation by 4WM will be applied in such a system for the cancelation of phase aberrations as it is a standard technique in the 10 μ m wavelength range.

2. EXPERIMENTAL

The small-signal gain measurements were performed within the discharge volume of a repetitively pulsed e-beam controlled CO₂ laser. The unit is completely sealed with an active volume of 12 litres and a gain length of 1.2 m. In an unstable resonator configuration, the laser is capable of emitting laser pulses with energies of up to 120 J at repetition rates of up to 60 Hz. The e-beam source has been designed to produce electron pulses of more than 150 keV energy and current densities of about 100 mA/cm². The e-beam pulse duration is typically 10 μ s. A gas mixture with a partial pressure ratio of CO₂ : N₂ : He = 1:2:7 is used, having an overall pressure of 500 mbar. Additional information on the technical details can be found in Ref [1].

A sketch of the experimental layout is shown in Fig. 1. A wavelength-tunable 6 W cw CO₂ laser 1 is used as the probe laser. Its wavelength and power are measured with spectrum analyser 2 and thermopile detector 3. A HeNe laser beam 6 is adjusted collinearly to the probe laser beam with mirrors 7 and beamsplitter 8 (1 % reflectivity at 10.6 μ m). With two HR mirrors 7, the radiation is directed to a collimation lens 9 (focal length 2 m) and a x/y translation stage 10, which allows a horizontal/vertical scan of the discharge volume. The probe beam radiation is amplified when the discharge is fired. The discharge volume is sealed by two KCl windows 11. The 1/e² diameter of the CO₂ probe laser beam near the exit window 11 was measured to be 10 mm. After a single pass through the discharge volume 12, the radiation is directed through two apertures 13 and a shutter unit 14. The shutter unit which is synchronized to the discharge unit, opens for a period of 10 ms. During this period, the e-beam and the main discharge are activated. This prevents thermal damage of the CO₂ laser detector 20. Photodiode 17 following the HeNe filter 16 is used to measure the deflection of the HeNe laser beam. A ZnSe lens 19 with a focal length of $f = 25,4$ mm collects the CO₂ laser radiation onto the active area of the photo-electromagnetic detector 20.

Fig. 2 depicts the cross-section of the discharge volume with the e-beam window on the left and the cathode on the

right with a separation of 10 cm. The arrows indicate the location of linear scans of the probe beam through the discharge volume (cf Fig. 3). The circle corresponds to the contour of the KCl window.

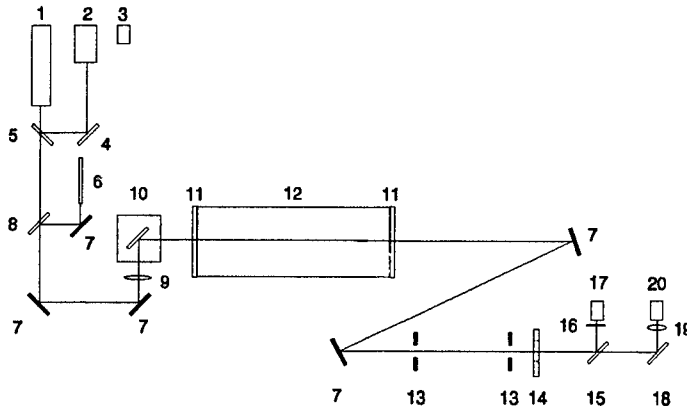


Fig. 1 Experimental setup for small-signal gain measurement.

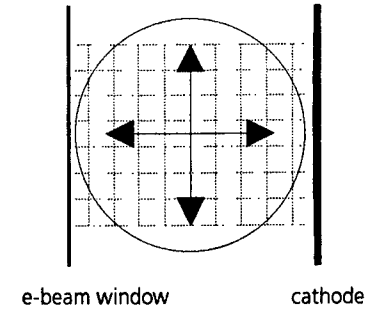


Fig. 2 Cross-section of discharge volume (downstream view). The arrows indicate linear scans of the probe laser in the gain volume.

3. RESULTS AND DISCUSSION

3.1 Temporal measurements

All the small-signal gain values are calculated from the peak values of the temporal dependence of the laser light amplitude (Fig. 3). The delay of the peak of the amplified probe laser beam compared to the peak of the discharge current pulse is approximately $6.5 \mu\text{s}$, independent of the energy loading. The amplified probe laser duration at FWHM decreases from $31.8 \mu\text{s}$ at 61.7 J/(l bar) to $24 \mu\text{s}$ at 121 J/(l bar) .

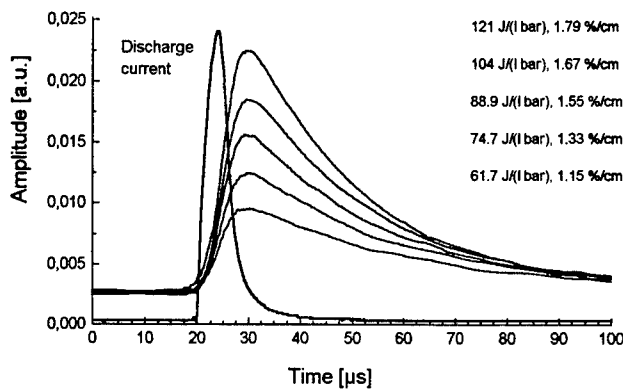


Fig. 3 Temporal dependence of the CO_2 laser light amplitude ($\lambda = 10.59 \mu\text{m}$) after firing the discharge at different energy loadings measured along the centerline of the discharge region.

To check for the interference from shock waves and mechanical vibrations on the small-signal gain measurement the deflection of a collinear HeNe laser beam was recorded simultaneously with the CO_2 laser beam (Fig. 4). The lower trace in Fig. 4 shows a slight increase in amplitude due to the opening of the shutter, followed by the amplified pulse. The upper trace corresponds to the HeNe reference beam, which is unaffected during the gain process. A distinct decrease in amplitude approximately $100 \mu\text{s}$ after the peak of the lower trace is probably due to shock waves triggered by the discharge.

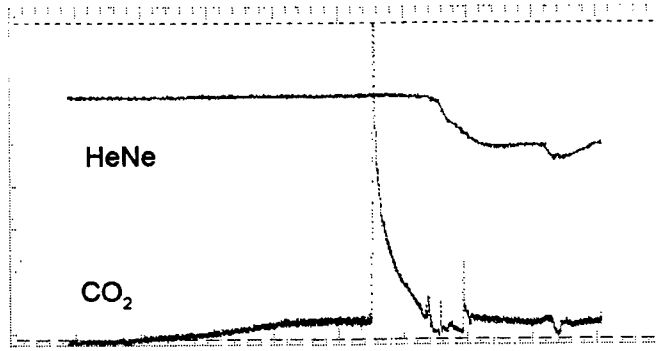


Fig. 4 Simultaneous recording of HeNe and CO₂ laser amplitudes (horizontal scale: 100 μs/DIV). The HeNe laser beam served as a reference to monitor mechanical vibrations and shock waves. The active gain length in this measurement was 2.4 m.

3.2 Spatial measurements

The spatial measurements were done in horizontal and vertical direction at energy loadings of 61.7 J/(l bar) and 112.5 J/(l bar) (Fig. 5). Smooth distributions were found with the highest small-signal gain values of 2.9 %/cm at 112 J/(l bar) 1 cm apart from the cathode. In the vertical direction, a symmetrical distribution was found with a maximum in the centre of the discharge region. This can be explained from discharge geometry. The electric field is highest near the cathode, which results into higher small-signal gain values in this region.

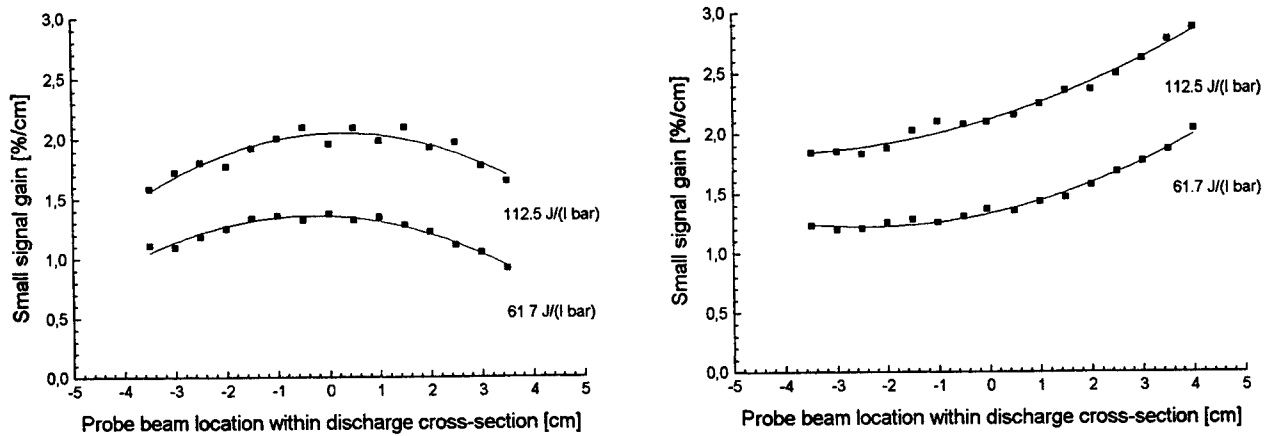


Fig. 5 Measurement of the small-signal gain distribution by vertical (left figure) and horizontal (right figure) line scans at two different energy loadings at a probe laser wavelength of $\lambda = 10.59 \mu\text{m}$.

3.3 Spectral measurements

The spectral dependence in the 10 μm P branch is shown in Fig. 6. The maximum value at the 10 P(16) laser line at 61.7 J/(l bar) is shifted to longer wavelengths (10 P (16) - 10 P(20)) when the energy loading was increased to 112.5 J/(l bar), resulting into higher thermal loading of the laser gas.

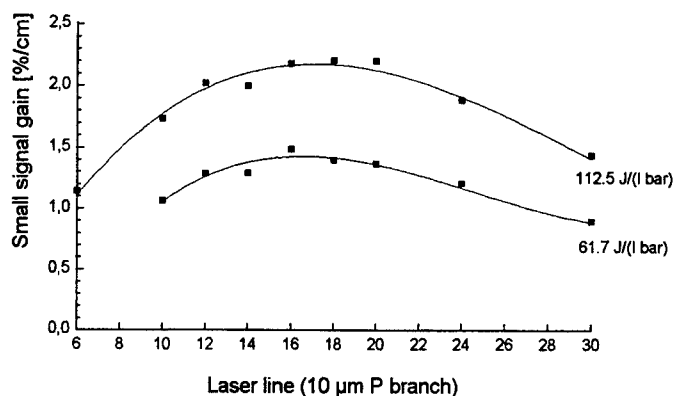


Fig. 6 Spectral dependence of the small-signal gain in the 10 μm P branch in the centre of the discharge region.

3.4 Repetition rate measurements

The necessity of gas circulation can be inferred directly from the left part of Fig. 7, where the result from repetitive pulse experiments with and without gas flow is depicted. Without gas circulation the small-signal gain drops within several pulses to 60 % of its initial value. In case of flowing gas, the small-signal gain stays constant at higher repetition rate (60 Hz) and energy loading (112.5 J/(l bar) (Fig. 7, right part).

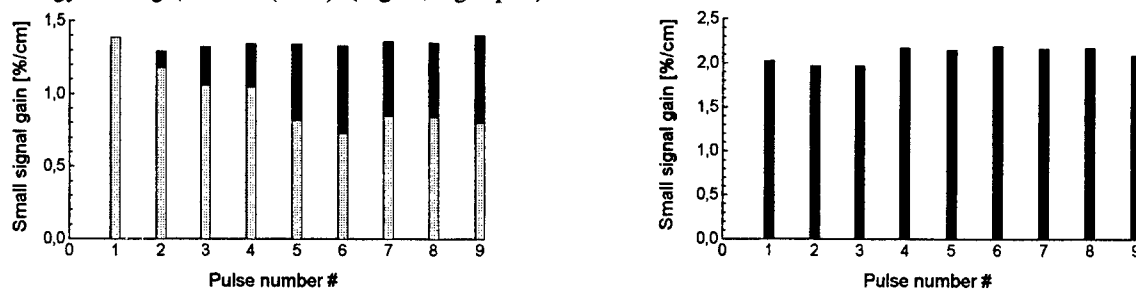


Fig. 7 Small-signal gain under repetitively pulsed conditions. The figure on the left was monitored with a repetition rate of 50 Hz at 61.7 J/(l bar) with flowing laser gas at 100 m/s (black columns), and no laser gas circulation (light gray columns). The figure on the right depicts the result of a 60 Hz repetition rate measurement at 112.5 J/(l bar).

4. SUMMARY

In summary, precise and reproducible measurements of the small-signal gain distribution in an e-beam controlled CO_2 laser discharge unit were performed. In addition, the spectral, temporal and repetitive pulse behaviour was monitored.

5. LITERATURE

- 1 M.-U. Beth, Th. Hall, W. Mayerhofer, "Optimization of discharge parameters of an e-beam sustained repetitively pulsed CO_2 laser", GCL 1990, SPIE Vol 1397, pp. 577 - 580.
- 2 W. Riede, W. Mayerhofer, Th. Hall, S. Walther, "Investigation of beam quality and gain behaviour in a large aperture e-beam controlled CO_2 laser", GCL/HPL 96, this volume.

Preionizing a large volume, transversely excited, sub-atmospheric, pulsed CO₂ laser for enhanced materials processing

Ian A. Watson, Donny W. McDonald, Brian F. Scott, Chris R. Chatwin

Laser and Optical Systems Engineering Centre,

Department of Mechanical Engineering, University of Glasgow, Glasgow, G12 8QQ.

Tel: +44 (0)141 330 5258/4972 Fax: +44 (0)141 330 4358 E-mail: i.watson@mech.gla.ac.uk

ABSTRACT

Two methods of exciting a trigger wire double discharge electrode system are investigated for the generation of high repetition frequency pulsed discharges in a sub-atmospheric, transversely excited CO₂ laser. Specifically, a 10 μ s Pulse Forming Network excited, 2 litre, transverse discharge was initiated by a corona discharge generated from trigger wires placed above a planar cathode. The discharge was pumped at pulse repetition frequencies up to 10 kHz and input pulse energies of 10 J. Two electrical systems for exciting the auxiliary preionizing discharge are considered viz. direct capacitive coupling from the anode voltage and separate high voltage pulse excitation. The laser itself was designed to improve materials processing capabilities of CO₂ lasers. This followed from a detailed theoretical analysis of the laser-material interaction process and it was concluded that pulse repetition frequencies of about 5 - 10 kHz were needed with optical pulse lengths of 6-8 μ s and plateau powers of between 20 - 150 kW. A stable single pass resonator was installed and used to assess the performance of both discharge initiation circuits by measuring the laser output pulse energy with a photon drag monitor. For the separately excited preionizer, the delay time between the preionizing pulse and the main discharge pulse was optimised by maximising the laser output pulse energy as a function of the delay time. The discharge was modelled using SPICE to investigate the effects of the preionizing electron density on the discharge voltage and current.

Keywords: Preionization, preionizer, CO₂ laser, materials processing

1. INTRODUCTION

Generation of stable, glow discharges suitable for pumping pulsed, laser discharges rely on efficient preionization of the gas and high, uniform gas velocities to clear dissociation products from the discharge region and minimise temperature/density inhomogeneities. The preionization mechanism was identified in CO₂ lasers as being due to ionisation of impurities (in He gas bottles) by VUV radiation^{1,2} generated by corona discharges. Palmer³ developed a simple model of the preionization mechanism and concluded that an initial preionizing electron density, n_0 , greater than $\sim 10^4 \text{ cm}^{-3}$ was required to ensure discharge uniformity. Through theoretical and experimental work Levatter and Lin⁴ reduced Palmer's predicted value of n_0 by a factor of ~ 600 and showed that the preionizing voltage pulse must have a fast rise time (of the order of 10^{-8} s at atmospheric pressures) to prevent an electron-free region developing close to the cathode which enhances the probability of discharge instabilities developing. Further efforts to extend the operating regime of gas discharges and maximise the laser output efficiency led to examination of the effects of seeding the gas mixture with low concentrations of low ionisation potential gases⁵, optimisation of the laser pumping circuit configuration^{6,7}, and investigations into the effects of gas velocity on the discharge stability⁸ and the laser output⁹. An industrial prototype laser has been developed, reported in detail elsewhere^{10,11}, with a simple, robust design satisfying the design requirements to achieve enhanced material processing capabilities^{12,13}, i.e. laser output pulse lengths from 6-8 μ s with workpiece plateau pulse powers of approximately 10-150 kW and maximum pulse repetition frequencies up to 10 kHz.

Figure 1 shows a schematic of the pumping circuit and laser head geometry. The discharge volume was approximately 2.0 litres, with a discharge gap of 4 cm and electrode width of 6.0 cm; the maximum pumping pulse energy was 10 J, delivered over a pulse length of up to 10 μ s. Two Roots blowers were used to convectively clear the gas from the discharge region at a velocity of about 50 ms^{-1} . The maximum laser operating pressure was approximately 200 mbar. The specific discharge energy densities were low and, because of the lower pressure and the subsequently lower absorption of the preionizing VUV radiation, the preionization requirements were less stringent than for TEA lasers. A set of trigger wires, comprising 105 brass rods clad in Pyrex and placed 2 mm above the cathode, were fabricated and used to generate an auxiliary corona discharge for preionizing the anode/cathode gap. To compare the effectiveness of the trigger wires as a preionization source, two methods were used to initiate the preionization: the coupling capacitive technique, and a separately excited preionizer. A circuit model of the gas discharge was developed using SPICE; this was used to investigate the effect of the preionizing electron density on the formative time lag, and the discharge current and voltage.

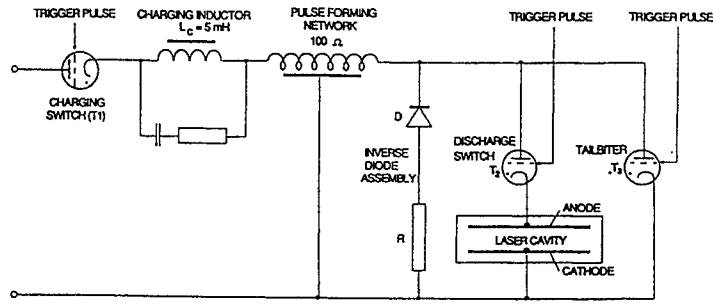


Figure 1 Pumping circuit configuration

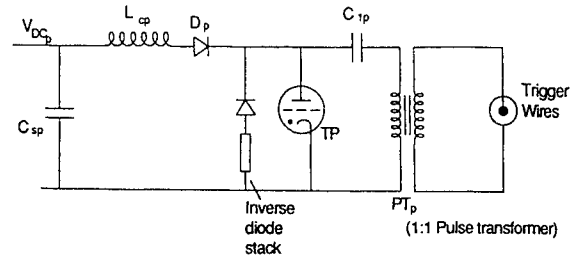


Figure 2 High voltage preionizer circuit

2. PREIONIZATION SYSTEMS

2.1 Coupling capacitance

A fraction of the main discharge energy was coupled into the preionization via capacitor C_c . The voltage drop across the trigger wires was dependent on the value of C_c and the stray trigger wire capacitance (C_s), which in the present case was measured at approximately 0.36 nF and was dependent on the trigger wire design i.e. the dielectric constant of the medium surrounding the trigger wires, their diameter and number. No significant difference was found in the discharge stability provided that $C_c > 1$ nF. However, if $C_c < 1$ nF, the discharge collapsed into arcs; this was probably because the preionization energy was too low. It was found that the voltage drop across the trigger wires was dominated by the value of C_s . For the results reported herein, a value of $C_c = 10$ nF was used and inductance L_a (36 μ H), was positioned on the anode of the discharge thyatron to limit the rate of growth of the discharge current and increase the thyatron's lifetime. The stray, circuit inductance L_s was insignificant compared to L_a , and therefore the value of L_a limited the maximum dV/dt .

2.2 Preionizer design

Figure 2 shows a schematic of the preionizing circuit, coupled to the trigger wires via a 1:1 pulse transformer (PT_p). The high voltage transformer used to supply the preionizer was independent of the main discharge power supply and rated at 30 kVA with a maximum voltage of 10 kV. The preionizer smoothing capacitance ($C_{sp} = 0.5$ μ F) was resonantly charged via inductor L_{cp} within 80 μ s; this allowed operation of the preionizer up to 10 kHz with a 10 μ s recovery period for the preionizer thyatron (TP) and 10 μ s pumping pulse widths. The inverse diode stack dissipated any negative residual on C_{Ip} between pulses and the charging diode D_p prevented current reversal through L_{cp} . The pulse transformer was used to provide electrical isolation between the trigger wires, the thyatron and C_{Ip} . Moreover, it enabled the cathode of thyatron TP to be grounded and the trigger wire polarity easily reversed. This latter feature was seen as beneficial as Marchetti¹⁴ reported obtaining significant differences in the preionizing electron density by reversing the preionizing source polarity.

3. EXPERIMENTAL RESULTS

The trigger wire voltage, their current characteristics and laser output pulse energy were observed and compared for single shot and continuous pulse mode for both excitation schemes.

3.1 Testing into trigger wires : single shot and burst mode

The voltage and current waveforms from a single pulse, or the first pulse of a pulse train, showed rapidly varying transients that lasted for about 50 ns; these were found to be, over the range of values used, independent of the gas pressure and gas composition. Subsequent pulses, when the laser was operating in the continuous pulsed mode, had smoother and temporally broader waveform characteristics with current pulse widths of approximately 450 ns and no rapidly changing transients. Figure 3 shows the voltage and current traces for the second pulse of a pulse train. Because there was no voltage doubling of capacitor C_{Ip} for the first pulse, and with $V_{dc} = 10$ kV, the energy stored on C_{Ip} for the first and subsequent pulses was 0.25 J and 1 J respectively. Consequently, the preionizing current for the first pulse was lower by a factor of 2 than it was for subsequent pulses. However, these rapid transient breakdown characteristics were similarly observed when capacitive coupling preionization was employed. Interestingly, for each preionization initiation scheme, the waveforms became more stable as the laser frequency was increased. Above 1 kHz the shot to shot variation in the pulse shape was less than 1 %. Clearly, the trigger wires, once breakdown had been initiated, were much easier to breakdown on subsequent pulses. No detailed investigation was performed, but this was believed to be due to the presence of long lived metastable states contributing to the preionization of the discharge after the first pulse and smoothing out of irregularities in the preionizing electron density. A sharp increase in current was observed prior to the main displacement current. Typically, these current

pulse widths (FWHM) were in the ratio of about 1:6, the peaks were approximately 1:1.75, and dl_{TW}/dt was about $2.7 \times 10^9 \text{ As}^{-1}$. Figure 4 shows, for a 1:1:4 gas mixture at 156 mbar, the trigger wire voltage and current characteristics with the coupling capacitor connected. However, the current and voltages with this excitation scheme were not found to differ significantly for the range of gas mixtures and pressures investigated. The peak trigger wire current achieved with the preionizer was larger, by about a factor of 4, than that obtained with the coupling capacitor connected.

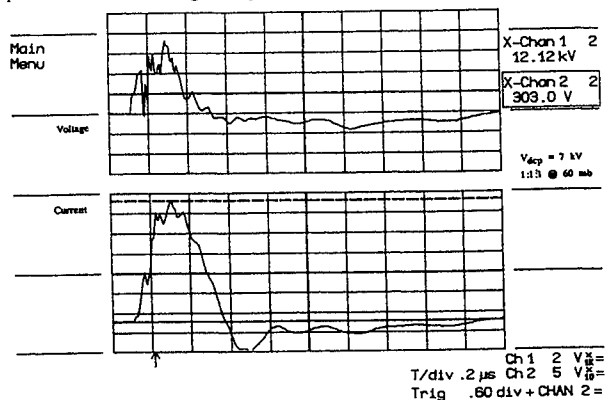


Figure 3 Trigger wire voltage and current : preionizer

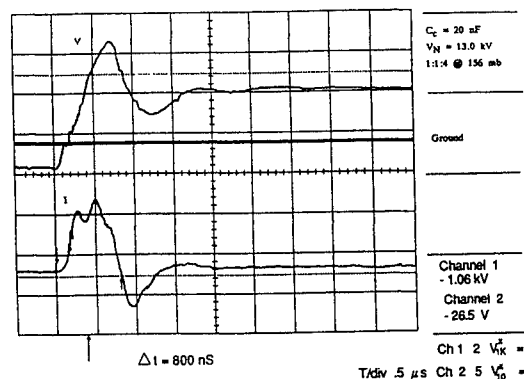


Figure 4 Trigger wire voltage and current: capacitive

3.2 Laser output results

Because the laser output is dependent on the initial preionization electron density¹⁵ the performance of the two preionization methods can be compared by measuring the relative laser pulse energy for the two excitation schemes. With the preionizer connected, the laser output was measured as a function of the delay time between the preionizing pulse and the main pumping pulse to find the optimum delay. For both discharge initiating schemes, no effort was made to maximise the laser output energy as only the relative performance of the two systems was compared. Consequently, to simplify resonator alignment only a single pass resonator was used, which utilised approximately 10 % of the discharge volume. A 1:1:0 gas mixture was used at a total pressure of 40 mbar, with a network voltage of 12 kV. The single pass resonator had a rear mirror radius of curvature, $R_c = 10 \text{ m}$, and a plane output window reflectivity, $r_f = 75 \%$. The delay between the preionizing pulse and pumping pulse, τ_I , was adjusted from approximately 100 ns to 500 ns. Ten values of the laser output pulse energy were measured at each value of τ_I and the mean value of the laser output pulse energy and the standard error of the mean were calculated. For long or short time delays where: $535 \text{ ns} < \tau_I < 120 \text{ ns}$, the discharge became striate and filamentary. Moreover, the laser output power dropped, the pulse shape became distorted, high order ripples appeared on the pulse plateau, and the output delay between the start of the pumping pulse and the laser output increased. For delays 20-30 ns beyond these limits the discharge arced. The preionizer was disconnected and a 10 nF coupling capacitor connected between the trigger wires and the discharge anode, the laser output was measured with the same gas fill that was used for the previous experiment. Following this, the preionizer was reconnected and the laser output measured again to ensure repeatability. Figure 5 shows the variation of the laser output pulse energy, E_o , as a function of τ_I , with the preionizer and with the coupling capacitor connected: the latter was drawn as a straight line for comparison of the two preionization techniques. The optimum value of τ_I was about 200 ns and the output was comparable in both cases at this value, with an overlap in the error bars. The maximum pulse repetition frequency (PRF) for the coupling capacitive scheme was about 1.4 kHz, whereas with the separate excitation circuit the maximum frequency was 1.7 kHz; this represents an increase of 20 % for the separate excitation circuit.

4. EFFECT OF PREIONIZING ELECTRON DENSITY

The discharge was modelled using SPICE¹⁶, to assess the effects of the pumping circuit components, gas composition and pressure, and preionization electron density. In the present case, the effects of the preionizing electron density (n_0) on the formative time lag of the discharge were examined. Figures 6 shows the calculated discharge current from the SPICE simulation for values of n_0 of: 10^7 , 10^8 and 10^9 cm^{-3} . The formative time lag, peak discharge current and voltage, and the rate of change of the discharge voltage and current were inversely proportional to n_0 .

5. CONCLUSIONS

Provided that the relative firing time between the preionizing and main pumping pulse was optimised at about 200 ns the pulse energies for both excitation schemes were comparable. The maximum PRF was achieved with the separately excited preionizer, and was approximately 20% greater. Large, irregular transients were observed for the first pulse with both

excitation schemes, however, for subsequent pulses the waveforms were much more stable. This effect may be due to the presence of long lived dissociation products perturbing the initial preionization conditions for subsequent pulses. A discharge model was developed using SPICE to assess the effects of pumping circuit components and preionizing electron density on the transient development of the discharge voltage and current. The formative time lag, peak discharge current, and the rate of change of the discharge voltage and current were inversely proportional to n_0 .

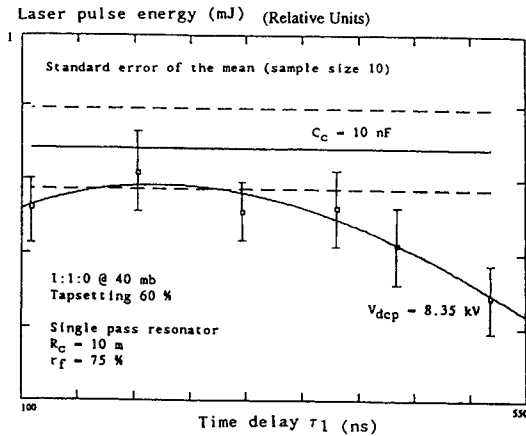


Figure 5 Laser output for both excitation schemes

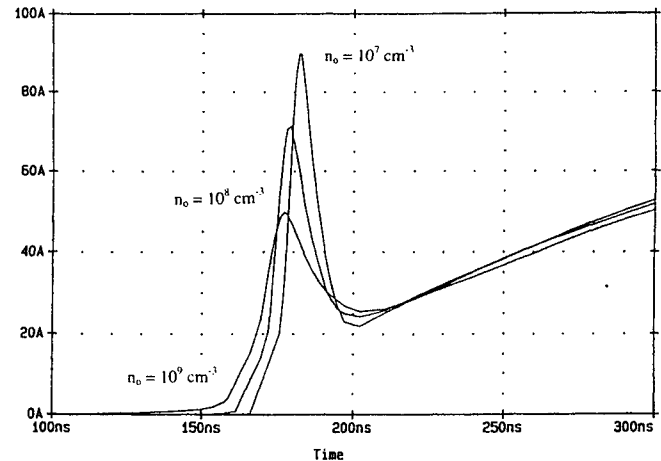


Figure 6 Modelled discharge current

REFERENCES

1. D. Mcken, H. Seguin, J. Tulip, "Photoionization parameters in the CO₂ laser gas," *IEEE J.QE.*, QE. **12** (8), 470-482 (1976).
2. H. Seguin, D. Mcken, J. Tulip, "Photoabsorption cross-sections in a seeded CO₂ laser mixture," *Appl. Optics*, **16**(1), 77-82 (1977).
3. A. Palmer, "A physical model on the initiation of atmospheric-pressure glow discharges," *App. Phys. Letts* **25**(3), 138-140 (1974).
4. J. Levatter, S. Lin, "Necessary conditions for the homogeneous formation of pulsed avalanche discharge at high pressures," *J. Appl. Phys.*, **51**(1), 210-218 (1980).
5. E. Morikawa, "Effects of low ionisation gas additive with uv photo-preionization on CO₂ TEA laser operation," *J.Appl. Phys.* **48**(3), 1229-1239 (1977).
6. J. Crindland, S. Howells, "The dependence of transversely excited atmospheric CO₂ laser performance on circuit configuration," *J. Appl. Phys.*, **53**(6), 4016-4019 (1982).
7. A. Bushnell, M. Gundersen, T. Burkes, "Effect of a small capacitor in parallel with a pulsed CO₂ TEA laser," *IEEE J. QE.*, QE. **12** (7), 447 (1976).
8. G. Dzakowic, S. Wutzke, "High pulse rate glow-discharge stabilization by gas flow," *J. App. Phys.*, **44**(11), 5061-5063 (1974).
9. C. Byabagambi, "Surface heating in metals irradiated by fast I.R. laser pulses," Ph.D Thesis. Department of Mechanical Engineering, University of Glasgow, UK. (1987).
10. C. Chatwin, D. McDonald, B. Scott, "Design of a High PRF CO₂ laser for Processing High Damage Threshold Materials," selected papers on Laser Design, *SPIE Milestone Series*, MS **29**, pp 425-433, Editor H.Weichel (1991).
11. I. Watson, C. Chatwin, "Segmented ballasted electrodes for a large volume, sub-atmospheric, transversely excited pulsed laser," *J. Phys. D: Appl. Phys.* **28**, 258-268 (1995).
12. B. Bakewell, "Performance of pulsed laser systems in relation to machining mechanisms," Ph.D Thesis. Department of Mechanical Engineering, University of Birmingham, UK. (1973).
13. J. Kharha, "Optimisation of the output characteristics of a pulsed CO₂ laser for processing materials," Ph.D. Thesis. Department of Mechanical Engineering, University of Birmingham, U.K. (1979).
14. R. Marchetti, E. Penco, "Optimisation of corona discharge photopreionization for CO₂ lasers," *J.Appl.Phys.* **54**(10), 5672-5675 (1983).
15. S. Suzuki, Y. Ishibashi, et al. "Dependence of laser output on initial photoelectron density in TEA CO₂ lasers," *App. Phys. Letts*. **36**(1), 26-28 (1980).
16. Donny McDonald, Ian Watson. "Simulation of pulsed laser discharges using SPICE," *Proceedings of the Tenth International Conference on Gas Discharges and their Applications*, Editor W.Terry Williams (1992).

Enhanced CO₂ Laser Frequency Doubling Efficiency in AgGaSe₂

P D Mason and E K Gorton

DRA Malvern, St Andrews Road, Great Malvern, Worcs, WR14 3PS, UK

ABSTRACT

Single-shot performance of tandem and folded frequency doubling schemes has been investigated in AgGaSe₂. These give rise to enhancements of up to a factor of approximately 3 in conversion efficiency. Experimental results are compared to theoretical predictions.

Keywords: silver gallium selenide, second harmonic generation, tandem frequency doubling, carbon dioxide laser.

1. PRINCIPLE OBJECTIVE

Frequency doubling at carbon dioxide (CO₂) laser wavelengths provides a useful source of coherent mid-infrared radiation in the 4.6μm to 5.4μm waveband. This paper reports preliminary investigations into possible techniques to enhance obtainable second harmonic conversion efficiency from commercially available single crystal specimens of negative uniaxial AgGaSe₂, which have good optical quality but short effective length.

2. ENHANCEMENT TECHNIQUES

Two simple techniques for enhancing frequency doubling conversion efficiency from AgGaSe₂ specimens have been employed. These are tandem frequency doubling^[1] and folded frequency doubling^[2] techniques. The former of these methods involves a sequential arrangement of non-linear specimens. Two anti-reflection (AR) coated AgGaSe₂ (SGSe) samples have been used for tandem measurements, labelled SGSeA and SGSeB. The four possible tandem sample geometries, 1 to 4, relative to the incident pump beam are indicated in figure 1a. In the latter folded method both generated harmonic and unconverted pump signal are returned through a single non-linear sample for additional passes. Two folded beam geometries have been investigated both of which utilise a single AgGaSe₂ sample, SGSeB. The first of these uses a plane gold coated mirror to return both pump and harmonic beams through the sample for an additional pass. Double-pass conversion is then measured by reflection off a calibrated beamsplitter. This geometry is subsequently referred to as the plane geometry. The second geometry introduces a spatial offset in both return beams by reflection from a roof mirror. This geometry is subsequently referred to as the roof geometry and double-pass conversion is measured by reflection off a plane gold coated mirror. Both plane and roof folded geometries are indicated in figure 1b.

3. AgGaSe₂ SAMPLE SPECIFICATION

Physical and optical properties of both AgGaSe₂ samples SGSeA and SGSeB used during this investigation are summarised in the following table.

Sample	l_{crystal} (mm)	l_{eff}^* (mm)	θ_{cut} (deg)	α_{ω}^{**} (m ⁻¹)	$\alpha_{2\omega}^{**}$ (m ⁻¹)	d_{36}^{***} (pm/V)	AR 9.4μm ^{****}		AR 4.7μm ^{****}	
							$R_{9.55}$ (%)	$R_{4.78}$ (%)	$R_{9.55}$ (%)	$R_{4.78}$ (%)
SGSeA	25.0	25.0	48.02	2.5	1.2	22 ± 4	0	~10.4	~2.6	0
SGSeB	25.0	23.9	48.02	2.5	1.0	23 ± 5	0	~10.5	~2.2	0

* Effective interaction length derived from Type(I) external angle tuning curves.

** Absorption coefficient values α_{ω} measured @ 9.55μm and $\alpha_{2\omega}$ measured @ 4.775μm.

*** Second-order non-linear optical coefficient evaluated by comparison of experimental single-shot conversion efficiency values with theoretical conversion predictions.

**** Reflection coefficient values for each AR coated face have been estimated from infrared transmission spectra.

During tandem geometry assessment crystal-to-crystal separation was restricted to 60mm. The first AgGaSe₂ sample SGSeB was orientated at the Type(I) external phase match angle. An external angle tuning curve for the second crystal SGSeA was then measured. Finally, optimum external energy conversion efficiency measurements were obtained at the peak angle of the second crystal tuning curve, for varying incident pump intensity values. A similar procedure was employed for plane mirror folded geometry assessment except that optimisation of second pass conversion was achieved after measuring a plane mirror angle tuning curve. Tuning curve and external energy efficiency measurement was then repeated at various mirror-to-crystal separations between 3 and 100mm. External energy efficiency measurement during roof mirror folded geometry assessment was obtained after optimisation of roof mirror alignment at a fixed mirror-to-crystal distance of 50mm.

5. EXTERNAL ANGLE TUNING CURVES

Measured external angle tuning curves obtained during tandem and folded geometry assessment are shown in figure 3. Theoretical angle tuning curves have also been derived taking into account a phase shift $\Delta\phi$ between the second harmonic signal generated in the first crystal (or first pass) and that generated in the second^[1]. For tandem geometry 2 and 4, $d_{\text{eff}}(A)=+d_{\text{eff}}(B)$ and $\Delta\phi=0$ solid curve, whereas, for geometry 1 and 3, $d_{\text{eff}}(A)=-d_{\text{eff}}(B)$ and $\Delta\phi=\pi$ thin-dashed curve. The theoretical plane mirror angle tuning curve has been generated using an estimated value of $\Delta\phi=-\pi/2$, thick-dashed curve.

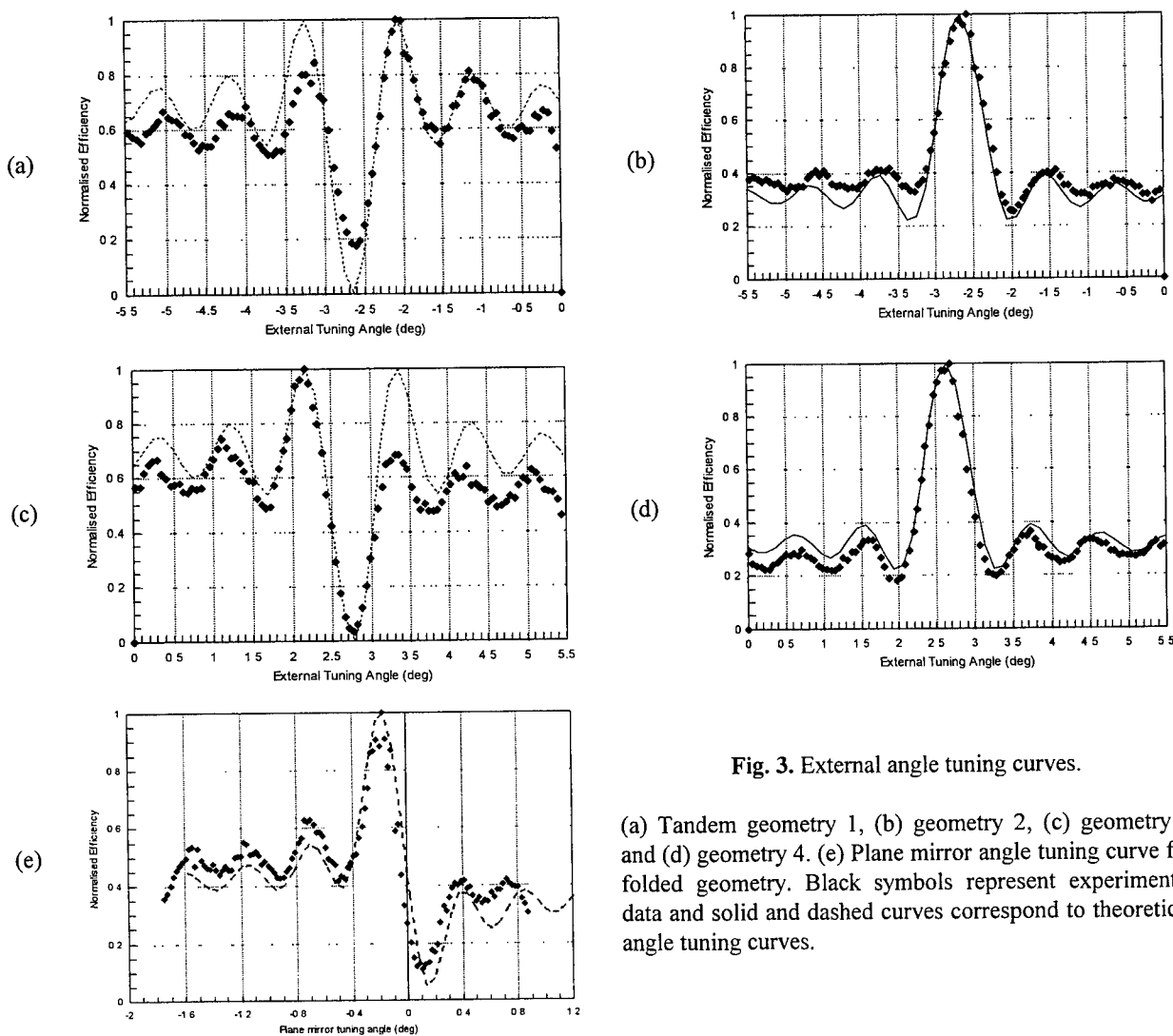


Fig. 3. External angle tuning curves.

(a) Tandem geometry 1, (b) geometry 2, (c) geometry 3 and (d) geometry 4. (e) Plane mirror angle tuning curve for folded geometry. Black symbols represent experimental data and solid and dashed curves correspond to theoretical angle tuning curves.

6. EXTERNAL ENERGY EFFICIENCY RESULTS

Optimum external energy conversion efficiency variation with incident pump intensity for both tandem and folded beam geometries is shown in figure 4. Also included are measured single-pass energy efficiency values through SGSeB. Theoretical energy conversion predictions have been obtained using a numerical solution to the coupled wave equations for plane waves. This model incorporates pump depletion and absorption at both pump and harmonic wavelengths. Energy conversion efficiency values are derived from peak efficiency predictions taking into account fixed pump temporal (T) and spatial (S) pulse characteristics. Assuming a triangular temporal profile and TEM₀₀ Gaussian spatial profile, T and S have values of 0.66 and 0.5, respectively. Beam walkoff is not included in the numerical model. Appropriate crystal parameters for each sample are tabulated earlier in section 3. A predicted single-pass energy conversion curve has been obtained assuming negligible dephasing within SGSeB under phase match conditions. The predicted second-crystal (or second-pass) conversion curve has been calculated assuming AR coating face geometry 4 or 1, figure 1. Optimum second crystal (or double-pass) alignment is assumed with $\Delta\phi=0$.

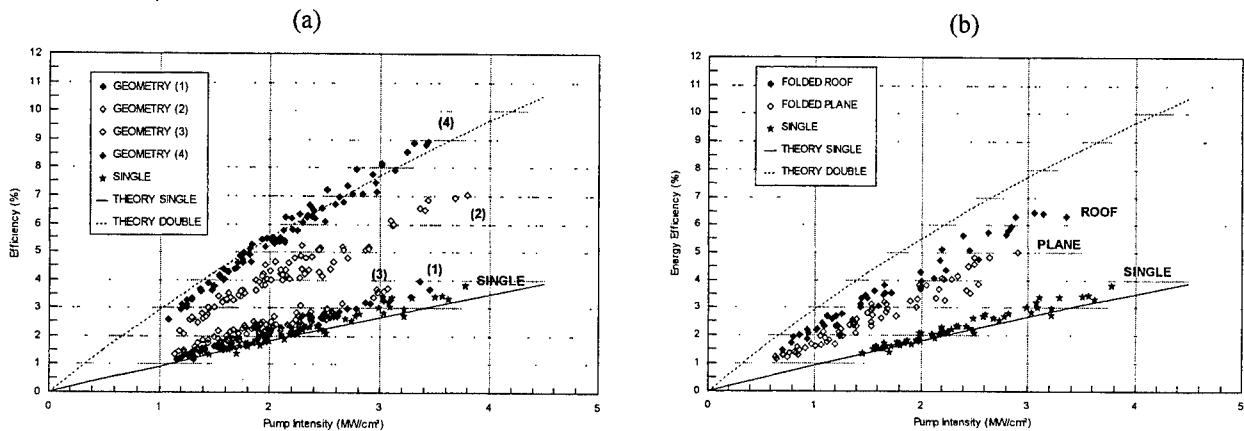


Fig. 4. External energy conversion efficiency results for (a) tandem and (b) folded beam geometries. Experimental data points are indicated by symbols. Predicted single-pass and double-pass energy conversion is represented by solid and dashed curves, respectively.

7. SUMMARY

Maximum second harmonic energy conversion efficiency enhancement was measured for tandem geometry 4. This gave rise to a measured external energy efficiency of 8.9% at a pump intensity of 3.4 MW/cm². This corresponds to a factor of ~2.8 increase on measured single-pass energy conversion. This value is in good agreement with the calculated theoretical improvement of 2.83 measured at the same pump intensity level. By virtue of relative optic axis alignment, tandem geometries 3 and 4 provide beam walkoff compensation^[2]. Folded geometry assessment yielded a maximum energy conversion efficiency enhancement factor of 2.2 for the roof geometry. This corresponded to an energy efficiency of 6.3% at 3.0 MW/cm². Optimum plane mirror energy efficiency was limited to 5.3% at an equivalent pump intensity. This represents an energy efficiency enhancement of 1.8. Measured energy conversion for the plane mirror geometry was independent of mirror-to-crystal separation. The precise reason for the apparent performance difference between roof and plane mirror geometries is unclear at this stage. Asymmetry in second-crystal and plane mirror tuning curves may be accounted for by an additional dispersive phase-shift introduced by AR coatings. This has yet to be characterised fully.

8. REFERENCES

- [1] D Eimerl, *IEEE J. of Quantum Electronics*, **QE-23**, No.8, pp1361-1371, December 1987.
- [2] S Tanaka et al, *CLEO'95 poster paper*, CTuI22, 1995.

Optimized homogeneity and stability of gas discharges in
fast flow CO₂-laser systems operating at the choking limit

W. Pfeiffer, C. Schmitz, A. Giesen, H. Hügel

Institut für Strahlwerkzeuge (IFSW), Universität Stuttgart, Pfaffenwaldring 43, D-70569 Stuttgart

ABSTRACT

The design of compact and efficient laser sources having high beam-quality and high beam-power is an objective of gas laser research. Therefore, it is necessary to realize highest input power densities while producing only minimized distortion of the optical quality of the laseractive fluid. A non-concentric helical configuration of electrodes in combination with a particular swirl flow allowing for homogeneous deposition of 28 kW of electrical power in a single tube element and operating at the choking limit, while producing only 350 nm of maximum phase distortion, is shown in theory and experiment.

Keywords: non-concentric helical electrodes, swirl flow, choking, temperature boundary layer, phase distortion.

1. LIMITATION DUE TO CHOKING

According to the law of conservation of energy, an increase in input power has to be accompanied by an increase in mass flow rate if a maximum gas temperature should not be exceeded. The well-known one-dimensional modelling of the distribution of the gas parameters (temperature, density, pressure and velocity) in the direction of the flow yields that in a discharge tube of constant cross section the physical limitation of the power input is reached when sonic velocity is approached at the end of the discharge tube and the flow chokes.

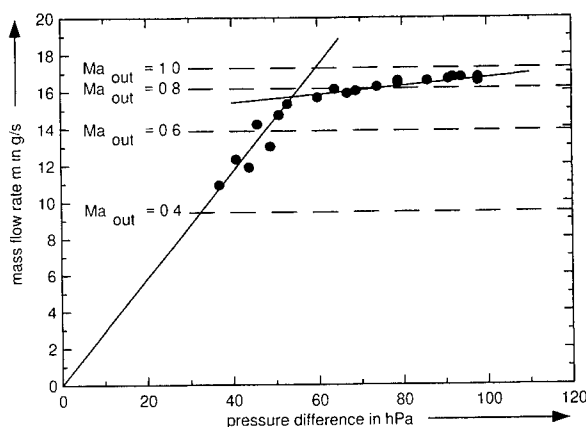


Fig. 1: Measured mass flow rate and calculated maximum Mach number at the tube outlet versus driving pressure difference of the pumping system; input power 20 kW.

For an experimental investigation of such conditions a homogenous discharge has to be realized. In the experiments an input power of 20 kW and gas pressure of 145 hPa in the entrance region of the tube were kept constant. The gas mixture was He:N₂:CO₂ = 80:15:5 and the inner tube diameter 46 mm. The mass flow rate, measured by a pitot-static tube, was raised by increasing the pumping power, i.e. the driving pressure difference, see Fig. 1. The discharge at these conditions cannot be maintained below 11 g/s because of the onset of temperature-induced discharge instabilities. If the pressure difference is increased, mass flow increases approximately linearly. When about 16 g/s are reached the increase in mass flow rate lessens significantly. The one-dimensional modelling yields that for these parameters the Mach number at the tube outlet approaches Ma = 0.8.

If, however, the typical velocity profile for turbulent tube flow is taken into account, one can see that the average velocity (which is considered in the one-dimensional modelling) equals 80% of the peak velocity. Hence, the peak velocity equals sonic velocity and the state of choking is already reached in the center axis of the tube. When the mass flow rate is further raised, the choked flow area centered on the flow axis is enlarged as well, increasingly blocking the flow. This leads to an increase in flow resistance.

In view of these facts, one-dimensional modelling has to be modified in order to account for the two-dimensional nature of the tube flow. Choking already starts at conditions corresponding to a one-dimensional value of Ma = 0.8, and thus

operation of stable discharges in partially choked flows appears to be possible. However, in order to realize a compact yet efficient laser system, the maximum (one-dimensional) Mach number 0.8 should not be exceeded.

2. OPTICAL QUALITY AND DISCHARGE STABILITY

Highest optical quality and discharge stability can be expected when the gas density varies only along the flow direction z . Therefore, radially distorting effects have to be reduced or compensated. Such effects might be due to non-uniform discharges and temperature effects in the boundary layer. Even in the case of a homogeneous discharge (which can be realized with a sophisticated electrode geometry) the latter effect has to be considered since kinetic energy of a high-speed flow is dissipated within the boundary layer. The temperature profile is coupled with the velocity profile [1] by

$$T(r, z) = T(0, z) + \sqrt[3]{Pr} \cdot \frac{v^2(0, z) - v^2(r, z)}{2c_p} \quad (1)$$

where $\sqrt[3]{Pr}$ is the recovery factor for turbulent flows. Radial heat transfer can be disregarded when a discharge stabilizing air gap [2] is used between the rf-electrodes and the quartz tube. The velocity profile in the short tube changes from a rather flat profile in the entrance region to an almost completely developed turbulent velocity distribution. In [3] the development of velocity profiles in entrance regions of tubes at Reynolds-numbers 10000–50000 was experimentally investigated. Within the operating range of typical fast flow laser discharge tubes, the profiles can be fitted using

$$v(r, z) = v_{max} \cdot \left(1 - \frac{r}{R}\right)^{n(z)}, \quad \text{with} \quad n(z) = 6 + 24 \cdot \exp\left(-\frac{z}{10R}\right). \quad (2)$$

R is the tube radius and v_{max} is the peak velocity in the center axis of the tube. It can be shown, that the thickness of the viscous sublayer in the immediate neighbourhood of the tube wall is approximately 90 μm . Therefore, the sublayer is disregarded.

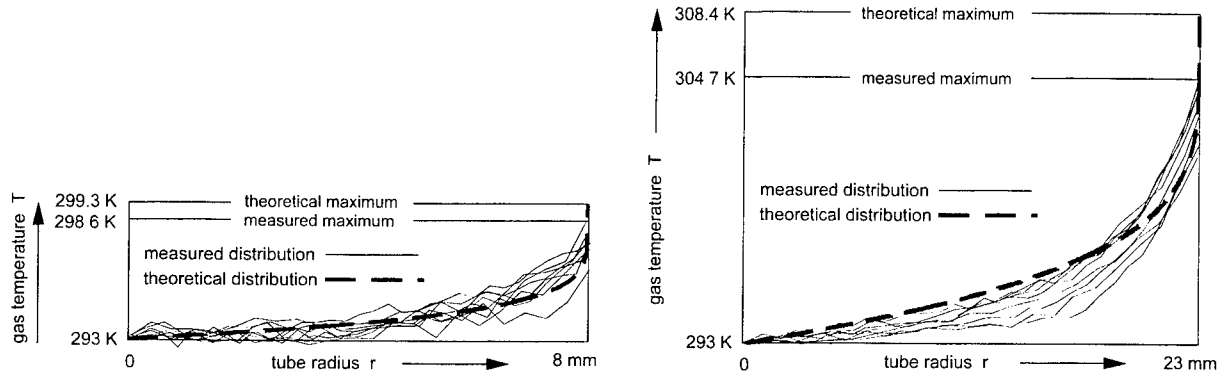


Fig. 2: Temperature boundary layer in unexcited tube flows. Comparison of interferometric measurements and adiabatic modelling for two different tube dimensions and mass flow rates. Left side: $\dot{m} = 1.8 \text{ g/s}$, $v_{max} = 120 \text{ m/s}$, $R = 8 \text{ mm}$; right side: $\dot{m} = 25 \text{ g/s}$, $v_{max} = 270 \text{ m/s}$, $R = 23 \text{ mm}$

In order to demonstrate the boundary layer effect, theoretical modelling of the flow as well as interferometric measurements were performed yielding radial density and temperature profiles, respectively. To find the averaged (along the tube length) temperature profile $T(r)$, eq.1 has to be integrated along the flow direction. The interferometrically measured and calculated temperature profiles, displayed in Fig. 2, correspond well. One can see that noticeable temperature profiles due to energy dissipation are already present at relatively slow, unexcited gas flows. When a gas discharge is applied, this boundary layer effect is even more significant as the velocity increases, see eq. 1.

Using linear electrodes for an rf-discharge, the effect of the temperature boundary layer can be compensated only partially with the design of the electrode shape. As displayed in Fig.3a (bottom), the interferometrically measured phase distortion shows an almost undisturbed temperature layer in the y-direction but a complete compensation in the x-direction. In the corresponding model (Fig.3a, top), the distribution of the input power in a tube cross section was fitted using the relation

$\exp(-(x/R)^2)$. In addition to the one-dimensional modelling of the flow parameters and the temperature profile the turbulence-determined thermal diffusivity was taken into account. It was interferometrically measured that the diffusivity was raised by a factor of 130 due to turbulence.

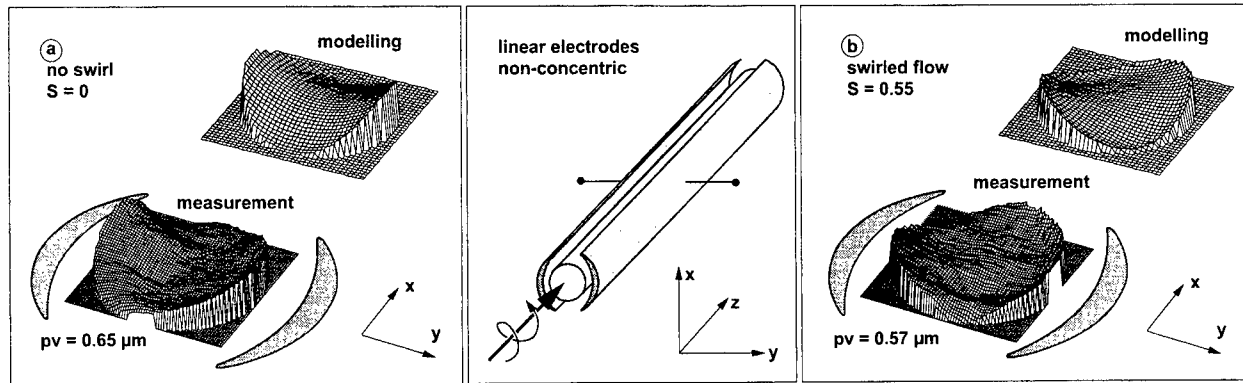


Fig. 3: Measured and calculated phase distortions produced by an rf-discharge using linear electrodes of an optimized shape; input power 20 kW; mass flow rate 16 g/s; $Ma = 0.8$; two different swirl flows: (a) no swirl flow and (b) $S = 0.55$. The phase distortion is denoted by the interferometrically measured peak-valley value: pv .

A swirled tube flow can be used to reduce the phase distortion. If the swirl number is defined at the tube entrance by $S = (w_{max}/v)$, where w_{max} is the maximum tangential velocity, it has to be considered that S should be below 0.7 in order to maintain the characteristics of a forced vortex flow. Otherwise, a free vortex is established, which negatively affects the gas discharge. The measured phase distortion (Fig.3b, bottom) shows a twisting angle of 35° and less distortion. The modelling includes the characteristics of an exponentially decaying swirl flow [4] and was calculated using $S = 0.55$.

If a helical electrode system [5] is used and a matched counter-oriented swirl flow is applied, the compensation of the temperature boundary layer is improved further and the phase distortion shows a good circular symmetry with the least amount of distortion (see also Fig.5).

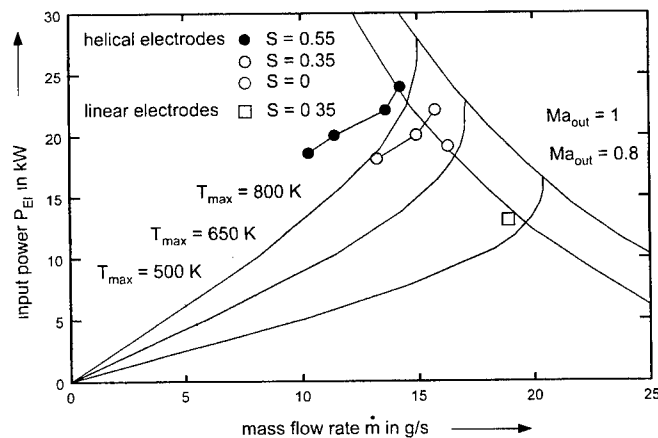


Fig. 4: Measurement of the discharge stability; helical and linear electrodes; different swirl states; Calculated maximum gas temperature and Mach number.

Homogeneous power deposition corresponds not only to optical quality of the fluid but is also a prerequisite for a high degree of discharge stability as displayed in Fig.4. The symbols stand for a particular degree of filamentation: one slight filament per one ms time range. Since this inhomogeneity is not detectable with the naked eye, it has been measured with a high shutter speed camera. It is evident that helical electrodes are superior to linear electrodes and counter-oriented swirl flow is of further advantage since input power increases while mass flow rate decreases. A stable discharge reaching the requested low filamentation level using linear electrodes without swirled flow was not possible. The maximum degree of discharge stability was realized in an experiment with a helical electrode system and a swirl number $S = 0.55$. An input power of 24 kW at a mass flow rate of 13.5 g/s, hence, a specific energy density of 1780 J/g in a gas flow approaching $Ma = 0.8$ was established. The maximum gas temperature approached 800 K.

A high level of optical quality and discharge stability can be even further exploited by raising the gas pressure. With that either the maximum temperature can be lowered or the input power can be raised. With a gas pressure of 162 hPa at the tube entrance it was possible to establish a stable discharge at 28 kW input power in a swirled tube flow at 15.5 g/s. The measured and modelled optical quality is displayed in Fig.5. The used non-concentric helical electrodes have been designed to actively compensate the effect of the temperature boundary layer. As a result, the produced phase distortion is less when the discharge is turned on (Fig.5.b) than when the gas flow is unexcited (Fig.5.a) at the same mass flow rate.

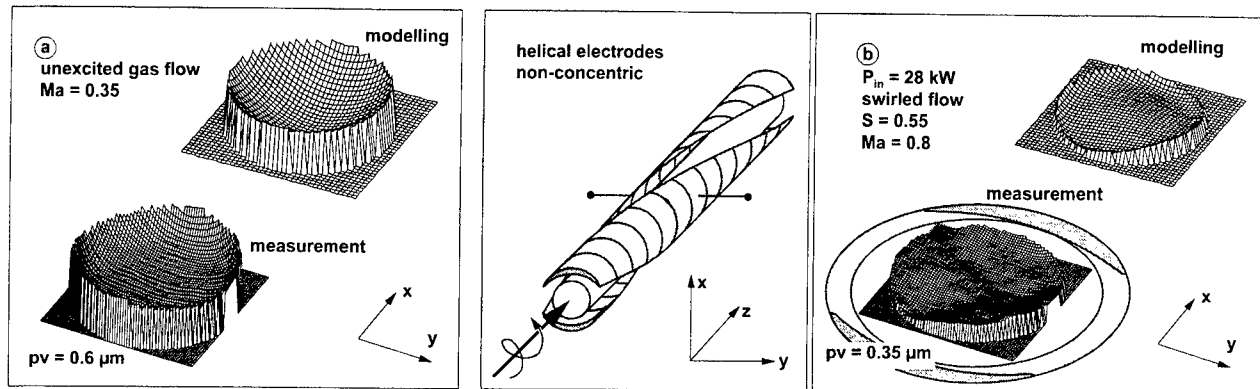


Fig. 5: Measured and calculated phase distortions produced by an unexcited gas flow (a) and a 28 kW rf-discharge using helical electrodes of an optimized shape (b), both with the entrance gas pressure 162 hPa, mass flow rate 15.5 g/s and swirl number 0.55. The phase distortion is denoted by the interferometrically measured peak-valley value: pv .

3. CONCLUSION

It has been shown by modelling and measurements that the goals of realizing compact and efficient laser systems can be achieved at flow conditions yielding an exit Mach number of 0.8. Furthermore, it was demonstrated, that the build-up of a temperature boundary layer is the main distorting effect for the optical quality of the flow in the discharge tube. Consequently, a particular combination of non-concentric helical electrodes and counter-oriented swirl flow was applied allowing for a homogeneous power deposition and therefore high optical quality and discharge stability. This was achieved because of the active compensation of the temperature boundary layer due to the specific electrode shape. At an input power of 28 kW to a single discharge tube element the flow approached choking conditions.

4. ACKNOWLEDGEMENTS

This work was supported by the German Federal Ministry of Education, Science, Research and Technology BMBF (contract number: 13 N 6627).

5. REFERENCES

- 1 Eckert, E., R., G.; Drake, R., M.: *Analysis of heat and mass transfer*, McGraw-Hill Book Company, 1972.
- 2 Paul, R.: *Optimierung der HF-Anregung für schnell längsgeströmte CO₂ laser*. Teubner, Dissertation, 1994 (Forschungsberichte des IFSW, B. G. Teubner Stuttgart).
- 3 Schiller, L.; Kirsten, H.: „Die Entwicklung der Geschwindigkeitsverteilung bei der turbulenten Rohrströmung“ *Deutsche Zeitschrift für technische Physik* 10, 1929.
- 4 Ward-Smith, A., J.: *Internal fluid flow*, Clarendon press, Oxford, 1980.
- 5 Pfeiffer, W.; Bea, M.; Herdtle, A.; Giesen, A.; Hügel, H.: „Minimized phase distortion in industrial high-power CO₂ lasers.“ *IEEE Proceedings of SPIE Vol 2502, p.583. 10th Int. Symp. on GCL, Friedrichshafen, 1994.*

Temporal and spatial properties of a chopper disc Q-switched high power CO₂-laser with an unstable resonator

M. Jung *, G. Renz, K. Wessel, and W. Schock

DLR, Institut für Technische Physik, Pfaffenwaldring 38-40, D-70569 Stuttgart

ABSTRACT

A numerical model will be presented to describe the influence of the diffraction on the temporal and spatial properties of a Q-switched CO₂-laser. The model includes the interaction of the spatial distribution of the laser field with the spatial distribution of the gain medium, the diffraction of the laser field due to edge effects of the rotating chopper disc, as well as the unstable resonator configuration. A RF-excited 5kW CO₂-laser has been used to produce a Q-switched peak power of 600kW at a pulse duration of 200ns and an average output power up to 1.3kW. Comparison of the numerical results with the experimental data will be shown.

1. INTRODUCTION

Continuous wave CO₂-lasers with an output power of up to 5kW are commercially available for materials processing, like for instance cutting and welding of metals. With the production of more powerful laser pulses at high repetition rates and inherently higher average output powers, applications of Q-switched laser systems appear possible like for instance surface treatment, isotope separation, etc.^{1,2} The Q-switched CO₂-laser with a rotating chopper disc is one of the favorite candidates³. In fig. 1 the schematical drawing of the RF-excited CO₂-laser with a transverse gas flow is shown.

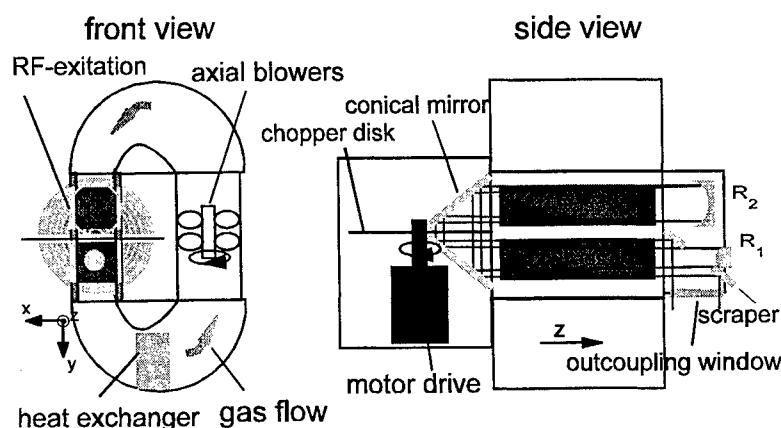


Figure 1. Q-switched CO₂-laser.

The RF-modulator (50kW, 27MHz) applies a discharge power density of 25Wcm^{-3} (cw-mode, 5kW laser power) and 100Wcm^{-3} (super pulse-mode, 20kW laser power)⁴. The gas cooling system is placed on the bottom part of the gas circulation system. In the side view of fig.1 the double pass of the unstable resonator is shown. The aperture of the used pass for the Q-switched laser is $2.8 \times 2.8\text{ cm}^2$. The laser beam is extracted with a scraper at the outcoupling window. The two optical passes are connected with a 90° conical mirror which acts as a telescope for the laser beam. The chopper disc is placed in the plane of the line focus of the conical mirror. It has a diameter of 26cm and a thickness of 150 μm . The number of slits is 18. The single slit has a length of 4cm and a width of 500 μm . At a rotation frequency of 400Hz of the chopper disc, the angular velocity at the outer part of the disc is 326ms^{-1} . The line focus extends from the outer slit edge (326ms^{-1}) to the inner slit edge (220ms^{-1}). At a rotation frequency of 400Hz, this leads to an interpulse frequency of 2.4kHz (pump pulse time in cw-mode: 400 μs). In order to suppress an early laser pulse development due to the high reflectivity of the polished chopper disc, the disc is positioned in an angle of 20° to the optical axis. The laser gas composition is CO₂:N₂:He = 5:15:80 at a pressure of 10kPa. At a frequency of 2.4kHz a max. power of 600kW with an energy per pulse of 180mJ was measured. This gives an average output power of 1.3kW.

* present address: AMS, Fraunhoferstr. 22, 82152 Martinsried/München

2. NUMERICAL SIMULATION

In order to calculate the field distribution of the electromagnetic wave in the resonator configuration, the Kirchhoff-Fresnel integral equation has to be solved. The integration is done with a summation over a 2-dim array. For the calculation of one round trip in the resonator, the following modules have to be treated in a sequential order: concave mirror, laser medium in 1st pass, chopper disc, laser medium in 2nd pass, convex mirror, laser medium in 2nd pass, chopper disc, laser medium in 1st pass, concave mirror (see fig. 2).

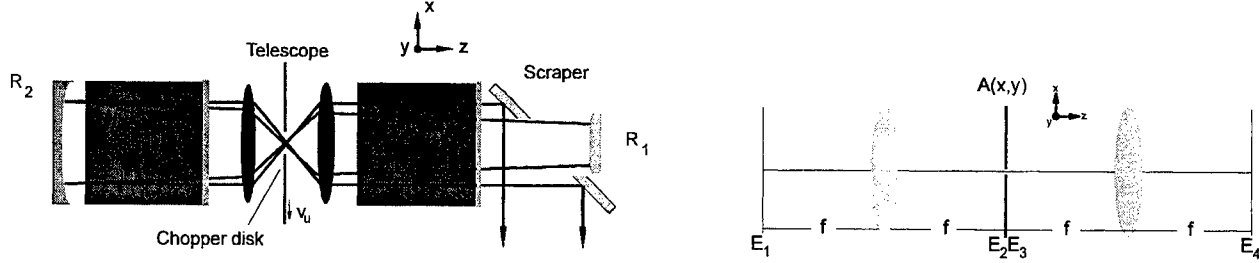


Figure 2. Unfolded resonator configuration (left) and telescope model (right).

The pass between the mirror and the chopper disc is calculated with the diffraction formula. The small signal gain of the laser medium is determined in an experimental measurement and is included in the simulation. The conical mirror and the chopper disc is treated in the framework of a spherical lens telescope and a 1-dim slit. Therefore, only the influence of the diffraction at the edge of the slit is calculated. The telescope is described with the help of the 2-dim, complex Fourier optics. The transformation from the mirror plane E₁ into the focus E₂ and to E₄ is given by:

$$E_2(x_2, y_2) = \frac{j}{\lambda \cdot f} \mathcal{F} [E_1(x_1, y_1)] \quad E_4(x_3, y_3) = \frac{j}{\lambda \cdot f} \mathcal{F} [\underbrace{E_2(x_2, y_2) \cdot A(x, y)}_{E_3(x_3, y_3)}]$$

with the aperture function $A(x, y) = \text{rect}(x - x_0(t))/s$ and s being the slit width. In the y -direction the disc is treated as being infinite. The Fourier transformation of the given product is equivalent to the convolution:

$$\mathcal{F} [E_2(x_2, y_2) \cdot A(x, y)] = \underbrace{\mathcal{F} [E_2(x_2, y_2)]}_{\mathcal{F} [E_1(x_1, y_1)] \Rightarrow E_1(-x_1, -y_1)} * \mathcal{F} [A(x, y)]$$

The simulation starts at the concave mirror R₂ with a Gauss distribution of the laser field intensity at the spontaneous emission level and a constant phase distribution (see fig. 3).

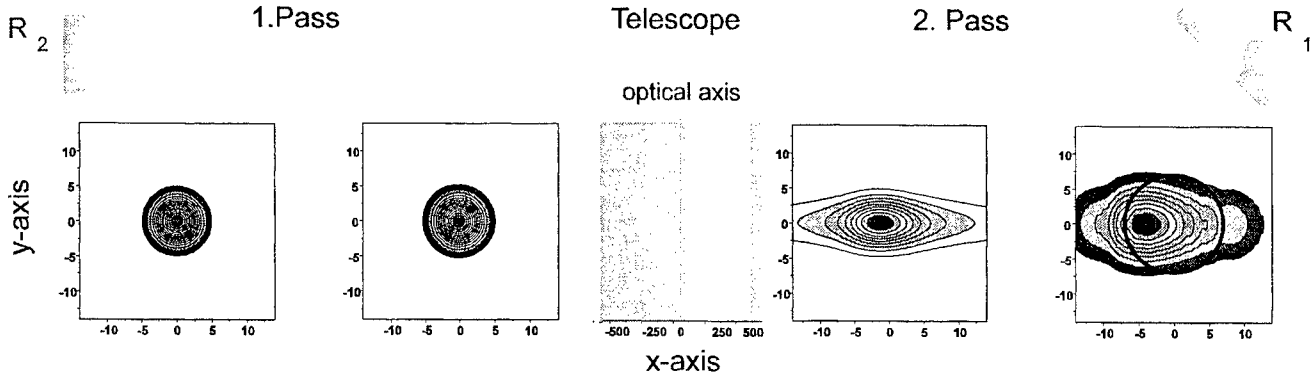


Figure 3. Temporal development of the transverse field distribution.

After the first pass through the laser medium, the field distribution has not changed its shape, but the phase distribution shows a curvature. In the focus of the telescope the part of the field between 25μm and 525μm can pass. After the exit of the telescope, the field distribution is stretched in the x -direction due to diffraction effects at the chopper disc.

After passing the 2. pass of the laser medium, the field distribution is distorted and only the field in the circled area is reflected at the mirror R_1 . The reflected field and phase distribution is shown in fig. 4 on the right hand side.

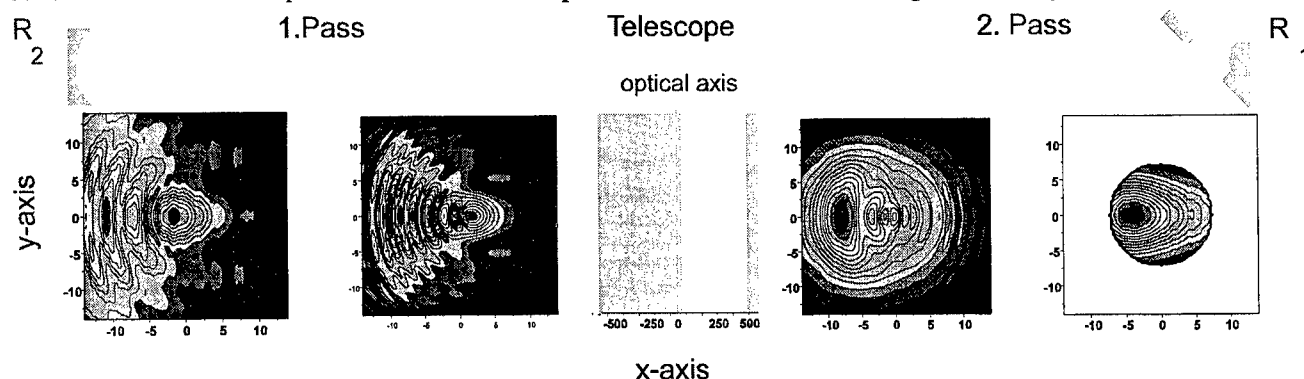


Figure 4. Temporal development of the transverse field distribution.

After the transfer through the laser medium in the 2. pass, the field is expanded into the y-direction. The slit of the chopper disc has now moved to the position $20.8\mu\text{m}$ with an opening to $520.8\mu\text{m}$. The subsequent transformation through the telescope develops a strong diffraction effect in the x-direction with phase disturbances on the side of the edge of the slit. After the next pass through the laser medium, more than half of the diffraction maximas are moved outside of the resonator. In fig. 5 the development of the transverse mode distribution, considered in the plane of the outcoupling mirror R_1 , is shown.

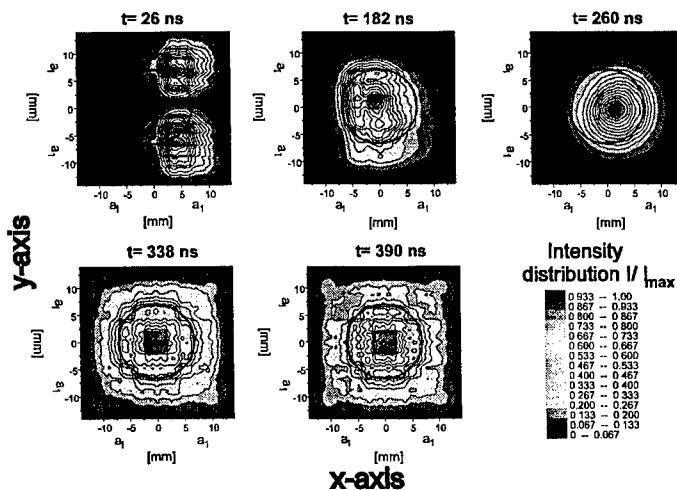


Figure 5. Field distribution at the outcoupling mirror.

Four resonator round trips after exceeding the laser threshold at time $t=26\text{ns}$, two intensity maximas have developed. Six further resonator round trips later ($t=182\text{ns}$), there is only one intensity maximum left. This intensity distribution shows after three more round trips a radial symmetry ($t=260\text{ns}$) which is close to a transverse ground mode. Due to the reduction of the small signal gain on the optical axis in the following round trips, the intensity moves outwards and leads to higher outcoupling losses. In fig. 6 the results of the numerical calculation of the temporal behavior of the laser power, the outcoupling loss, and the diffraction loss is shown.

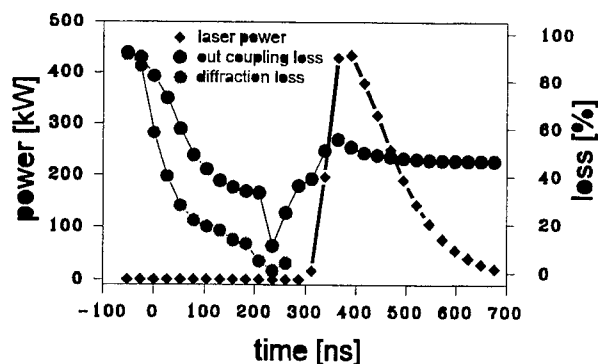


Figure 6. Simulation of temporal behavior of the laser action.

The angular velocity of the chopper disc is 320ms^{-1} and the used small signal gain is 0.7m^{-1} . Due to the high outcoupling- and diffraction losses of the laser field, the start-up of the laser amplification begins after the edge of the chopper disc slit has passed the optical axis at $t=0$. In fig. 7 the far field distribution is displayed. The experimental picture shows a rotational symmetry effect due to the rotation of the chopper disc.

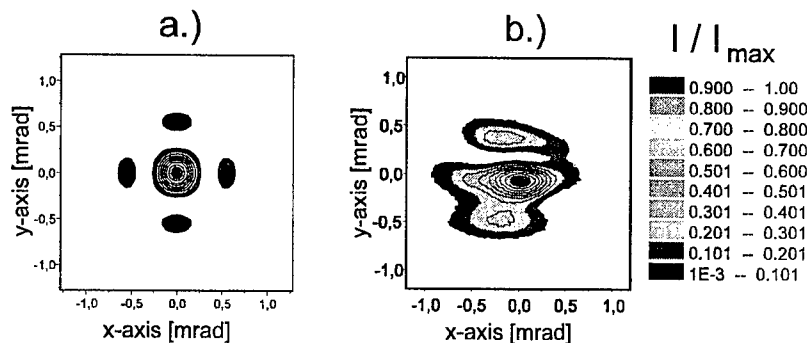


Figure 7. Far field : a) simulation, b) experiment.

3. SUMMARY

By using Fourier optics, the transient behavior of a Q-switched CO_2 -laser has been simulated. At the unstable resonator configuration, diffraction effects at the chopper disc have to be taken into account. An experimental verification of a laser system with a peak output power of 600kW, a pulse energy of 180mJ, and a pulse duration of 200ns at a repetition rate of 2.4kHz has been achieved.

4. REFERENCES

1. Schäfer, J., Uhlenbusch, J., Viöl, W., "Laserschneiden von Aluminium mit einem gepulsten CO_2 -Lasersystem hoher Pulsfolgefrequenz", *Int. Magazin für Industrie, Forschung und Praxis*, 5, 501 (1989).
2. D'Ambrosio, C., Fuß, W., Schmid, W. Kompa, K., "High power cw discharge multikilohertz repetition rate Q-switched CO_2 -laser", *6th International Symposium on Gas Flow and Chemical Lasers*, vol. 15, 284 (1985).
3. Fuß, W., Loosen, P., Märten, O., Schmid, W.E., "Scaling of high-repetition rate Q-switched CO_2 -lasers for industrial applications", *Gas Flow and Chemical Lasers*, vol. 1810, 79. SPIE (1992).
4. Schock, W., Hall, Th., Wildermuth, E., Wessel, K., Gehringer, E., Schnee, P., Hadinger, F., "Compact transverse flow CO_2 -laser with RF-excitation", *Gas Flow and Chemical Lasers*, vol.1031, 76 SPIE (1988).

CO_2 laser excited by microwave discharge using stripline

Tomokazu TOKORO, Naoya MATSUOKA, Masayuki YASUDA, Taro UCHIYAMA
Department of Electrical Engineering, Faculty of Science and Technology, Keio University,
3-14-1, Hiyoshi, Kouhokuku, Yokohama, Japan

ABSTRACT

Recently CO_2 laser excited by microwave discharge has been studied to achieve higher efficiency and lower cost laser system[1][2][3]. In this study a stripline was used to guide microwave with TEM mode. This mode has almost homogeneous intensity distribution of electric field and almost homogeneous discharge could be obtained.

keywords: CO_2 laser, microwave discharge, stripline, TEM mode

1 INTRODUCTION

Conventionally DC discharge has been used as excitation of CO_2 laser. The disadvantage of this method is that laser gas is degraded for the presence of metallic electrode in the gas. And RF discharge has been increasingly used for the absence of electrode, but RF power generators are relatively expensive. So microwave discharge excited CO_2 lasers have been studied recently. In this case, usually TE or TM mode with rectangular waveguide has been used. But it is difficult to generate a homogeneous discharge over a wide volume, because the electromagnetic distribution of TE or TM mode is sine curve. So we suggest TEM mode using stripline. Because the electromagnetic distribution of TEM mode is almost homogeneous against the width of stripline. It is considered that homogeneous discharge could be obtained and gain volume will spread.

2 MICROWAVE PROPAGATION LINE

Microwave propagation line used in this study is shown in Fig.1.

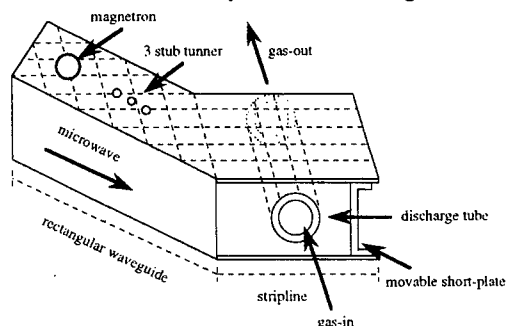


Fig.1 Stripline type microwave propagation line.

Electric field of TE_{10} mode in a rectangular waveguide can be written in the following form:

$$\begin{aligned} E_y &= E_{10} \sin(\pi x/a) \exp(-i\beta z) \\ &= E_{10} \{ \exp(i\pi x/a) - \exp(-i\pi x/a) \} \exp(-i\beta z)/2i \end{aligned} \quad (1)$$

where x is the coordinate axis of height, y is that of width, z is that of propagation direction, a is the width of rectangular waveguide and β is propagation constant in it respectively. Using the relationship of wave number vector (Fig.2), it follows that $\pi/a = k \sin \theta$, $\beta = k \cos \theta$.

So E_y can be reduced to:

$$E_y = (-i/2) E_{10} \{ \exp(-ikr') - \exp(-ikr) \} \quad (2)$$

where $x = r \sin \theta$, $z = r \cos \theta$, $-x = r' \sin \theta$, and $z = r' \cos \theta$. Equation (3) shows that TE_{10} mode is the synthesis of two plane waves which advance at an angle of $\pm \theta$ from z -axis. So microwave generated by magnetron is propagated through the rectangular waveguide with TE_{10} mode, and then can be transformed into TEM mode in the stripline connected with the rectangular waveguide diagonally. [4] The width of stripline becomes $2a \cos \theta$. The part of connection is shown in Fig.3.

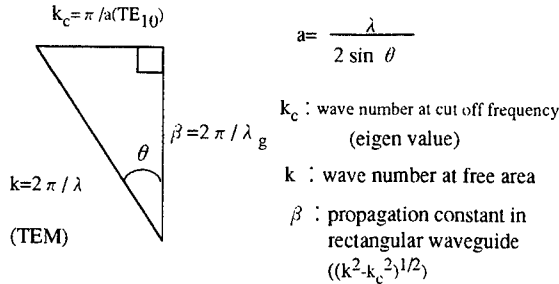


Fig.2 The triangle relationship of wave number vector.

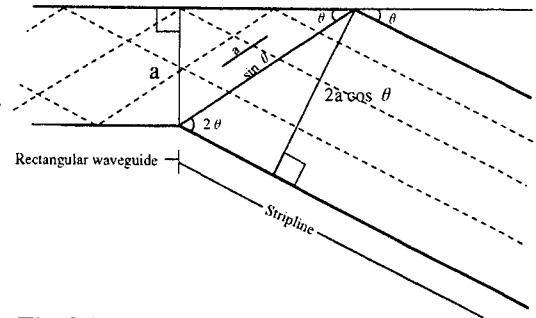


Fig.3 Transformation of rectangular waveguide into stripline.

3 EXPERIMENTAL SET-UP

The basic structure in this study is shown in Fig.4.

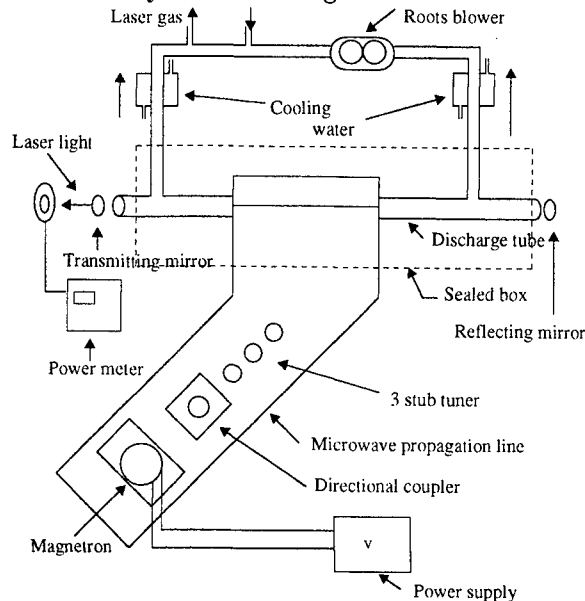


Fig.4 Experimental Set-up

We used a magnetron on the market for microwave oven. The magnetron works with a pulse repetition frequency of 50 kHz. A directional coupler is set between the magnetron and a discharge tube, we can match impedance by three stub tuner. The magnetron generates 2.45 GHz frequency($\lambda = 12.3\text{cm}$). The discharge tube consists of a standard quartz pipe(25mm-bore. 1.5mm-thickness.). Laser gas mixture used is $\text{He} : \text{N}_2 : \text{CO}_2 = 81 : 15.6 : 3.4$. The gas is circulated by a root blower, the flow rate is 200m/s. A spherical mirror(99.5% reflectivity) is used as total reflection mirror, a plane mirror(95% reflectivity) is used as partial transmission mirror. The length of resonator is 0.735m.

4 RESULTS AND DISCUSSION

Table I shows the laser output power dependent on the angle connected stripline and rectangular waveguide. So we thought that the connected angle of 45° was the best, all the following measurements were taken at the

connected angle θ	width of stripline	maximum laser output power	maximum efficiency
70°	44mm	34.0W (pressure 20Torr)	6.7% (pressure 15Torr)
40°	143mm	44.0W (pressure 10Torr)	8.0% (pressure 10Torr)
45°	123mm	46.0W (pressure 20Torr)	10.9% (pressure 20Torr)

Table 1: Laser output as a function of connected angle

angle of 45° (the width of stripline is 123mm). Fig.5 shows the laser output power as a function of the input microwave power with 123mm-width stripline.

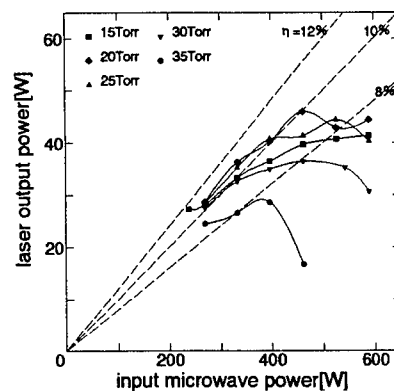


Fig.5 Laser output power as a function of input microwave power with 123mm-width stripline.

At low gas pressure discharge existed all over cross section of discharge tube. But discharge became narrow discharge shape like letter of I against the cross section exceeding 25torr. (Fig.6)

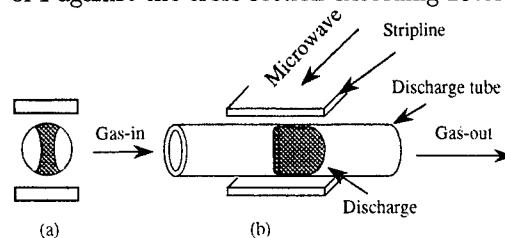


Fig.6 Sketch of discharge

(a) view from optical axis.

(b) view from microwave propagation direction.

We thought, discharge occurred in the center of the tube, and the voltage of the edges fell down, so the voltage down made it difficult to generate discharge all over the cross section. Then we set ceramic electrodes to generate homogeneous discharge against the cross section at higher gas pressure. Ceramic electrodes are mounted between the stripline. This set-up is shown in Fig.7. These electrodes are designed as microwave dielectric resonators[6]. The electrodes are made of $(Mg_{0.5}Ca_{0.5})TiO_3$. The diameter is 8.6mm, the height is 4.3mm and the specific dielectricity is 26.8. We could get homogeneous discharge all over the cross section at 25torr. But the length of discharge didn't change. Fig.8 shows laser output power as a function of the input microwave power with ceramic electrodes. We find that the efficiency are improved at 2% and it is difficult to saturate laser output power using ceramic electrodes.

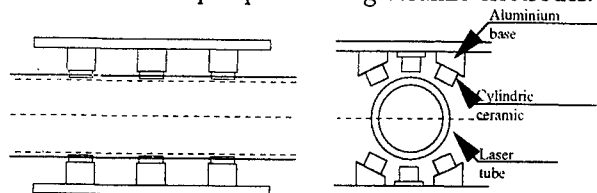


Fig.7 Arrangement of ceramic electrode.

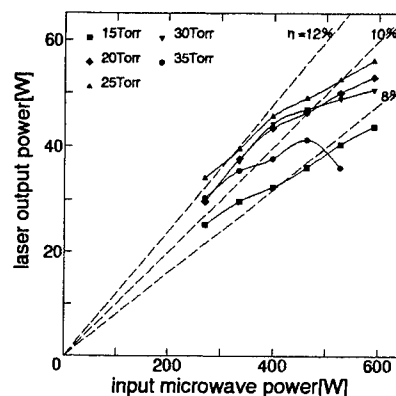


Fig.8 Laser output power as a function of input microwave power with ceramic electrodes

5 CONCLUSION

The steady discharge was got all over the cross section perpendicular to optical axis with 123mm-width stripline connected rectangular waveguide at an angle of 45° using ceramic electrodes, the length of discharge was 4cm. Maximum laser output power is 56W(9.5% efficiency). Maximum efficiency is 12.6%(output 34.2W) at 25Torr.

6 REFERENCES

1. M.Danno et al: The Review of LASER ENGINEERING, 22 (1993) 203.
2. B.Freisinger et al: Proc.SPIE 1397 (1990) 129.
3. J.Nishimae, K.Yoshizawa: Proc.SPIE 1225 (1990) 340.
4. G.Kuraishi: Microwave circuit (Tokyo electric Univ, 1983) p.78.
5. A.Yariv: Quantum Electronics. New York: Wilkey, 1975 p.179
6. The ceramic society of Japan : Cerami Engineering Handbook (Gihoudou, 1989) p.1895

Modulation and pulse generation of a transverse flow high power CO₂ laser by a Fabry-Perot modulator

G. Michel, K. Schindler, G. Staupendahl and C. Ziener

Friedrich-Schiller-University Jena, Technical Institute
Löbdergraben 32, 07743 Jena, Germany

ABSTRACT

A new resonator design for a transverse flow high power CO₂ laser based on a fast tuneable Fabry-Perot modulator was developed. It allows a very effective modulation and pulse generation.

1. INTRODUCTION

Many applications of CO₂ lasers require pulsed radiation or a well defined fast modulation of the laser light. For high power transverse flow CO₂ lasers it is complicated to modulate their radiation in the desired manner.

This paper reports on a new possibility for modulation and pulse generation of this laser type by a new optical method.

2. PRINCIPLE OF OPERATION

The modified resonator design of the used 5 kW transverse flow CO₂ laser shows fig. 1.

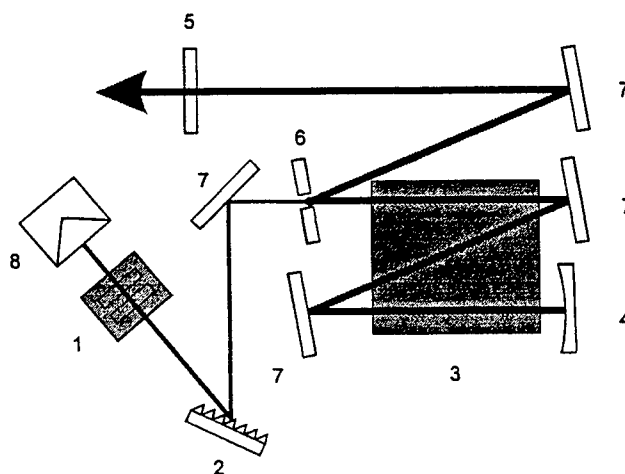


Fig. 1: Resonator design of the transverse flow 5 kW CO₂ laser

1 - Fabry - Perot Modulator

2 - grating

3 - active medium

4 - end mirror

5 - ZnSe window

6 - output coupler

7 - folding mirrors

8 - power meter

In difference to the normal resonator configuration one end mirror is replaced by a Fabry-Perot modulator 1 and a grating 2. By this arrangement it is possible to modulate the high output power of the laser by modulating a relatively small part of the radiation.

Grating 2 guarantees the laser operation on the desired wavelength necessary for the correct function of the modulator.

The well known working principle of the used modulator illustrates fig. 2.

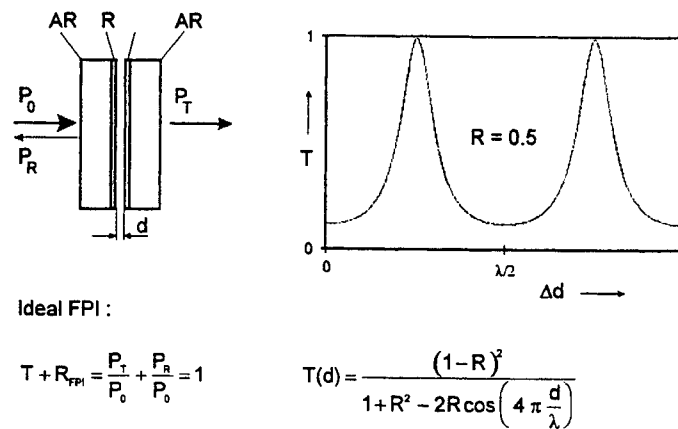


Fig. 2: Working principle of the Fabry - Perot modulator

The fast tuning of the distance d of the interferometer plates is realized by piezoelectric translators up to frequencies of 11 kHz. By this the reflectivity R_{FPI} could be changed between $R_{min} = 0$ and $R_{max} = 0.89$.

The interval $\langle R_{min}, R_{max} \rangle$ includes the threshold reflectivity R_{thr} . This means that by a simple tuning of the modulator an effective modulation and pulse generation of the laser is possible.

3. EXPERIMENTAL RESULTS

The effect of the modulator tuning on the laser output is illustrated by the following experimental results.

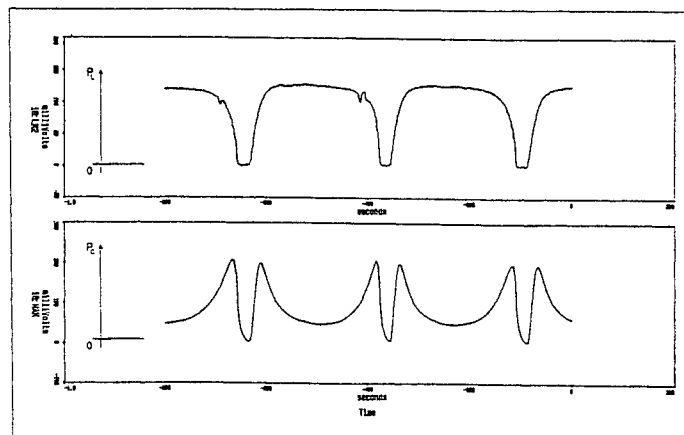


Fig. 3: Illustration of slow modulator tuning (see text)

In fig. 3 the output power P_L of the laser (upper curve) and the power P_C monitored by the power meter 8 (lower curve) is shown in dependence on d slowly varied with time. It is to be seen that such a tuning of the modulator allows a modulation of the laser output power over the full range $0 \leq P_L \leq P_{L,max}$, i.e. any value of P_L can be selected.

A fast modulator tuning over a sufficient wide range of R leads to pulse generation. Typical pulses are shown in fig. 4. In maximum peak powers of 10 kW could be reached.

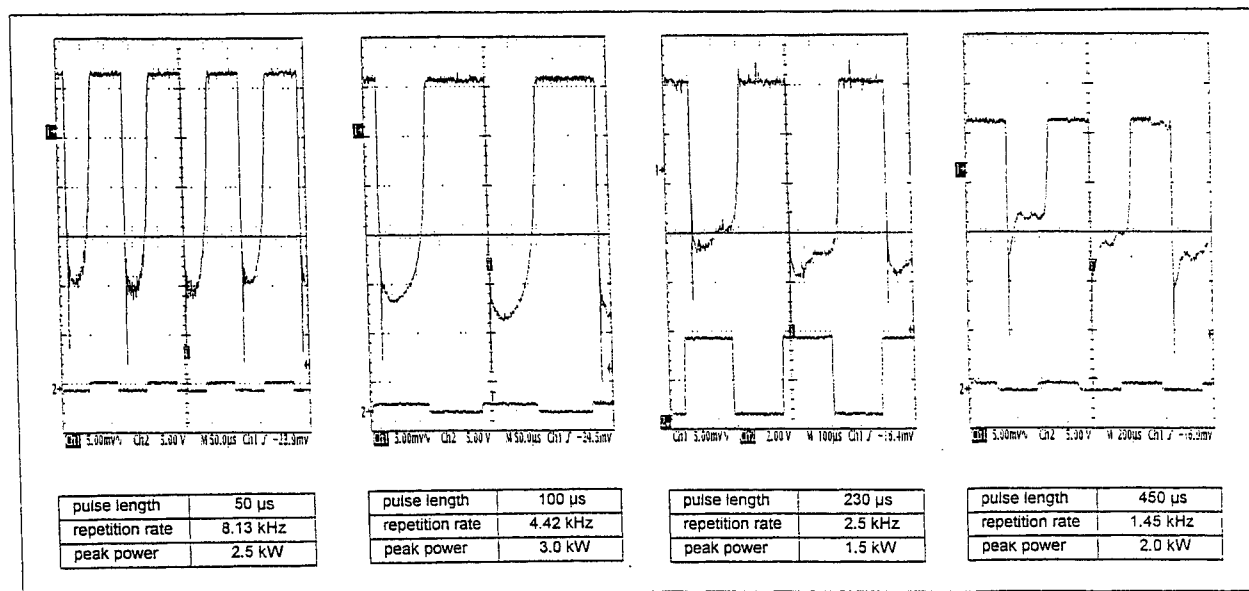


Fig. 4: Illustration of fast modulator tuning - generation of pulses

4. GENERATION OF NANOCRYSTALLINE ZIRCONIA - POWDERS WITH PULSED RADIATION

To demonstrate the potential of this method pulses with variable durations were used to produce nanocrystalline zirconia powders by evaporation of ZrO_2 with the radiation of the described transverse flow CO_2 laser.

The diameter of the particles and their density distributions (shown in fig. 5) can be controlled by the pulse length. This dependence is given in fig. 6.

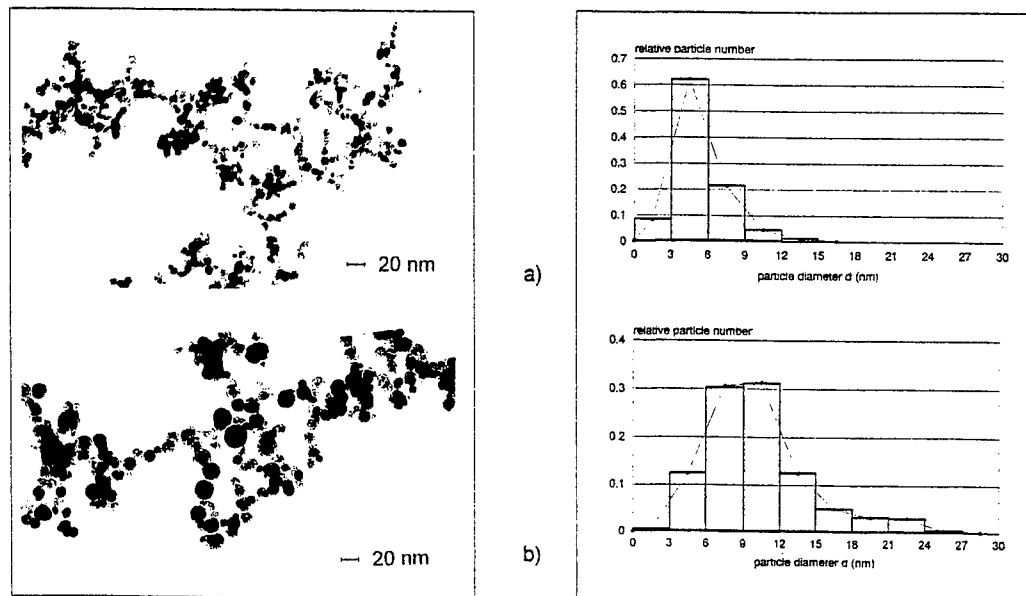


Fig. 5: REM photographs of nanosized zirconia powders and their density distributions for 50 μ s pulses (a) and 450 μ s pulses (b)

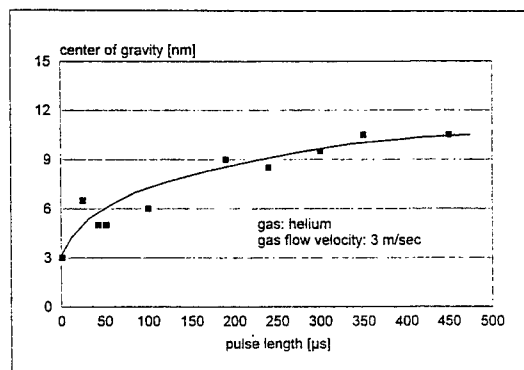


Fig. 6: Center of gravity of the density distribution in dependence on pulse length for nanocrystalline zirconia powders

5. ACKNOWLEDGMENT

Parts of this work were supported by the Deutsche Forschungsgemeinschaft, FRG.

6. REFERENCES

1. G. Staupendahl, „Universeller Modulator für CO₂-Laserstrahlung und seine Einsatzmöglichkeiten“, *Laser und Optoelektronik*, **23** (3), 126-133 (1991).
2. K. Schindler and G. Staupendahl, „Ein neuartiger CO₂-Impulslaser für die Materialbearbeitung“, *Jahrbuch LASER*, 3. Edition, Vulkan-Verlag, 9-14 (1993).
3. W. Triebel, G. Michel, and P. Linke, „Generation of high peak-power kHz repetition-rate laser pulses in a cw discharge transverse flow CO₂ laser by a Q-switching technique“, *J.Phys. D: Appl. Phys.*, **25**, 1293-1297 (1992)

INVESTIGATION OF RF EXCITED CO₂ SLAB LASER DISCHARGES BY MEASURING N₂ EMISSION BANDS WITH HIGH SPATIAL RESOLUTION

U. Berkermann, A. Liffers, R. Hannemann, G. Jakob, C. Lücking, J. Mentel, G. Schiffner

Ruhr-University Bochum
Department of Electrotechnical Engineering, Division AEE0
Universitätsstraße 150, D-44780 Bochum, Germany

ABSTRACT

Spectroscopic measurements of N₂ molecular bands emitted by the discharge of a sealed off test chamber and a 2 kW CO₂ slab laser deliver detailed rotational temperature and intensity profiles in the gap between the electrodes as a function of different discharge parameters. The results give basic information on the behaviour of the discharge and the main plasma parameters for further investigations.

Keywords: Spectroscopic measurements, N₂ molecular bands, sealed off CO₂ laser, intensity profiles, rotational temperature profiles, discharge parameters

2. INTRODUCTION

A well known problem associated with the CO₂ laser is the partial dissociation of CO₂ in an electrical gas discharge environment. To understand the basic principles of this lifetime limiting effect and to regulate it for an optimized operating lifetime in a sealed off system, it is necessary to have a good knowledge of the main discharge parameters, discharge behaviour and plasma chemistry as a function of special electrode surface layers and gas composition. In this work, we report our spectroscopic observations of N₂ molecular emission UV bands and HeI lines emitted by discharges in a test chamber with up to 300 W, 80 MHz rf input power and a CO₂ slab laser with up to 2 kW output power. These measurements are incorporated in our plasma physical investigations for an optimized efficiency of the sealed off transverse rf excited CO₂ slab lasers.

3. MEASUREMENTS

The $v' \rightarrow v''$ transition $0 \rightarrow 0$ of the second positive system of N₂ ($C^3\Pi_u - B^3\Pi_g$, bandhead at 337.13 nm) is observed for several gas pressures, gas composition and input power variations. The optics, consisting of quartz lenses and a diaphragm in a telecentric arrangement, limit the aperture so, that only light emitted within a small fixed spatial angle along a line parallel to the slab walls is selected. Thus the spectra are imaged with high optical depth and low perspective distortion onto a slit of an 1 m monochromator and are recorded with a photomultiplier, connected to a digital analyser system. The spectral resolution was estimated to be 0.01 nm. To achieve a good spatial resolution, the aperture is nearly closed and the spectra are recorded at up to 40 equidistant measuring points across the gap width by moving the last lens with a micrometer screw in a direction orthogonal to the monochromator.

For the test chamber, the observations are made from the small front side through the whole gap. The dimensions of the watercooled copper electrodes are 10 cm by 1 cm. The gap has a width of 2 mm.

For the 2 kW slab laser, measurements are performed side on at two positions along the slab, one in the centre and one at the edge of the electrode configuration.

4. DETERMINATION OF THE ROTATIONAL GAS TEMPERATURE FROM THE EMISSION BANDS OF N₂

The population of the upper rotational levels results primarily by collisions of the heavy particles. The contribution of electron impact on the other hand is negligible because of the different masses. So, with the assumption that the population structure of the rotational levels is preserved under excitation of the molecule by electron impact, the rotational temperature T_{Rot} of an emission band is the same as the gas temperature T_{gas} .

The population of the rotational levels with the quantum number J and the term energy $F(J)$ of one vibrational transition corresponds to a Boltzman distribution

$$dn/n \sim (2J+1) \exp (-F(J)hc/kT_{\text{Rot}}) \quad (1)$$

and can be determined by measuring the intensity distribution. By comparing the intensity distribution of the measured rotational lines with a calculated spectrum of the same transition, it is possible to determine the rotational temperature of the gas.

The reliability of this comparison increases with growing rotational numbers J , therefore it is an advantage to take a vibrational band with a high intensity and no disturbance by other bands to get clear intensities from the higher J levels. For the calculation of the spectra it is necessary to have a good knowledge of the molecular constants and line strength factors. Therefore the well known 2nd positive system of N_2 is chosen. It is a ${}^3\Pi - {}^3\Pi$ transition and so the spin splitting has to be taken into consideration for the simulation of the spectrum.

5. ROTATIONAL TEMPERATURE PROFILES

With the above mentioned procedure, we simulate the measured spectra numerically with a computer program of Behringer¹. By critical comparison of the calculated spectrum with the measured one, temperature profiles across the discharge gaps are determined. The absolute uncertainty of the results is estimated to be 50 K and the relative error between the measuring points is estimated to be 10 K.

For the 2 kW slab laser, temperatures are determined for the centre and edge position of the electrode region. In the centre region, the temperature is 340 K in the middle of the slab and 325 K nearby the watercooled electrodes, having a constant temperature of 293 K. At the edge of the electrodes we determined 370 K in the middle of the slab and 290 K nearby the electrodes.

For the small test chamber, temperatures at the centre of the slab are between 340 K to 540 K and near the watercooled electrodes between 300 K to 370 K. These measurements are carried out for different gas pressures, gas compositions and rf power inputs.

6. INTENSITY PROFILES

For varied gas pressures, gas compositions and rf power inputs we observe different shapes of the intensity profiles across the gap, measured at the 337.13 nm bandhead of N_2 in gas mixture discharges and for the pure He discharges at the 388.86 line of HeI. An explanation for this effect may be the inhomogeneity of the electron energy distribution across the gap. Nearby the electrodes, the energy may be too high for a strong excitation of N_2 , whereas it seems to be more appropriate for the excitation of He.

7. RESULTS

Fig. 1 shows the resulting temperature profiles for the slab laser, measured in laser operation with an output power of 1 kW for the centre and edge region of the electrodes. Fig. 2 to Fig. 4 show the resulting temperature profiles in turn in dependence on different discharge parameters for the small test chamber. In these figures the position of the electrodes is estimated at the end of the fitted curves. Fig. 5 to Fig. 8 show the resulting intensity profiles, measured in the small test chamber in dependence on different discharge parameters. Here the position of the electrodes is estimated to correspond to the lens positions $1.05 \cdot 10^4$ and $1.22 \cdot 10^4$ μm (see description above).

8. ACKNOWLEDGMENTS

Our plasma physical investigations for an optimized efficiency of the sealed off transverse rf excited CO_2 slab lasers are supported by the German Ministry for Education and Science (BMBF) under the projekt number 13N6571.

9. REFERENCES

1. K. Behringer, "Diagnostics and Modelling of ECRH Microwave discharges", *Plasma Phys. Contr. Fusion* Vol. 33, pp. 997 - 1028, 1991.

Fig. 1: Gas temperature profile, slab CO₂ laser, in operation at 1 kW output power, p = 155 mbar, special gas mixture

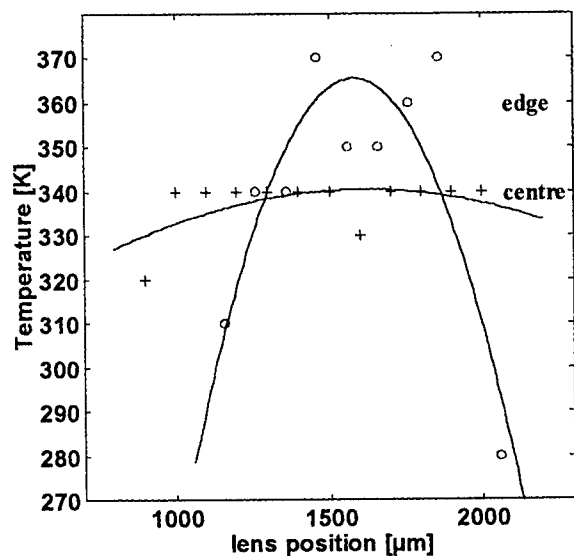


Fig. 3: Gas temperature profile, small test chamber, variation of rf input power, p = 100 mbar, CO₂ : N₂ : He (1 : 1 : 3)

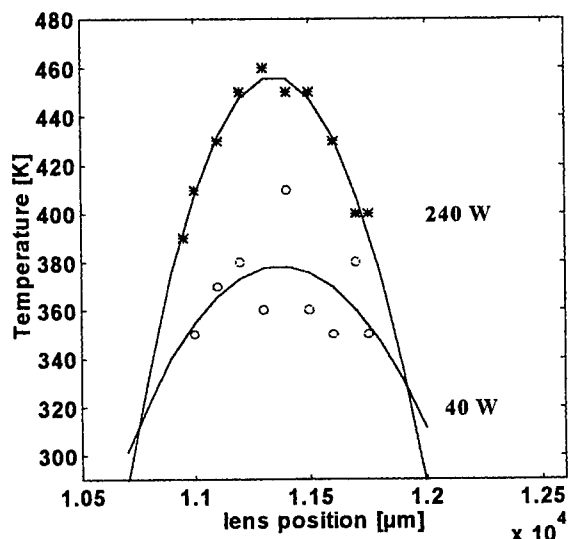


Fig. 2: Gas temperature profile, small test chamber, variation of pressure, rf input power 240 W

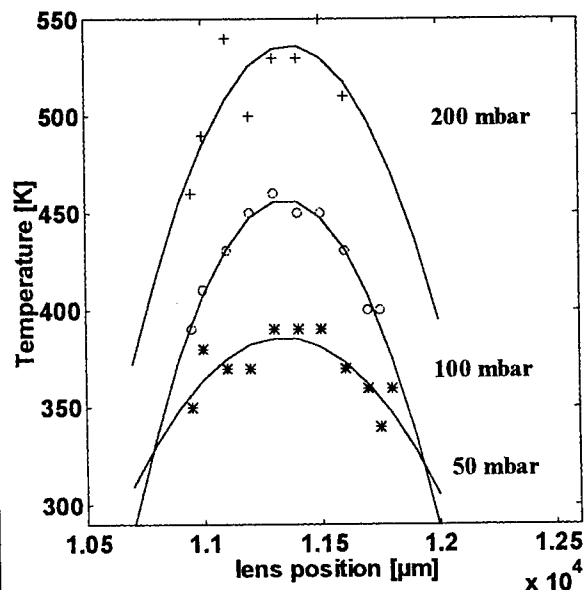


Fig. 4: Gas temperature profile, small test chamber, variation of pressure, rf input power 240 W, CO₂ : N₂ : He (1 : 1 : 3)

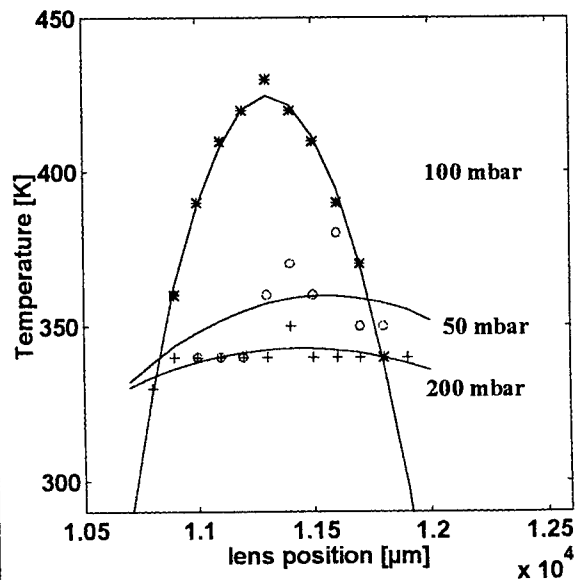


Fig. 5: Intensity profile, small test chamber, variation of rf input power, $p = 100$ mbar, $\text{CO}_2 : \text{N}_2 : \text{He} (1 : 1 : 3)$

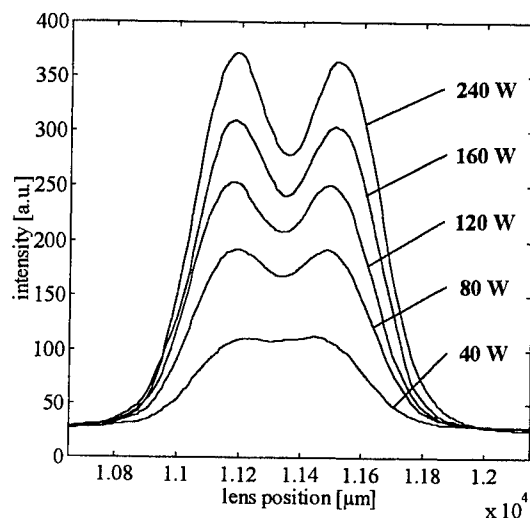


Fig. 7: Intensity profile, small test chamber, pure Helium, $p = 60$ mbar, rf input power 40 W, wavelength = 388.86 nm

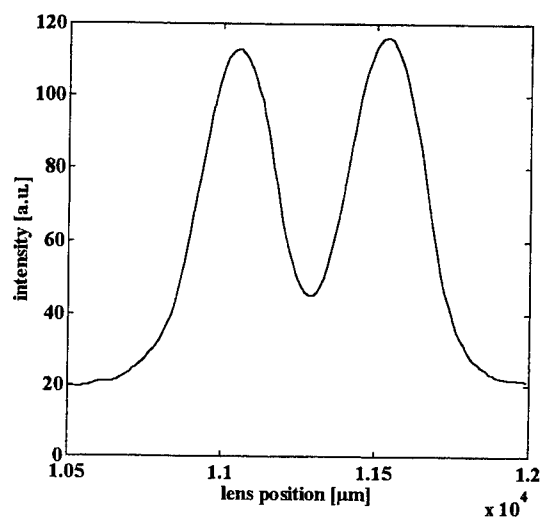


Fig. 6: Intensity profile, small test chamber, variation of rf input power, $p = 100$ mbar, $\text{CO}_2 : \text{N}_2 : \text{He} (1 : 1 : 10)$

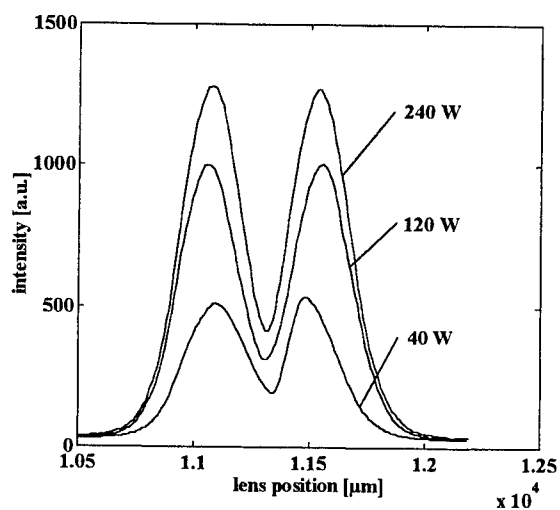
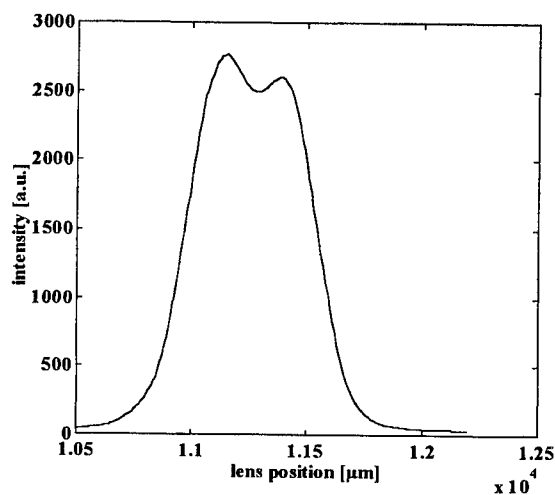


Fig. 8: Intensity profile, small test chamber, pure N_2 , $p = 20$ mbar, rf input power 40 W, wavelength = 337.13 nm



Measurement of the impedance of rf excited CO₂ slab lasers and discharge chambers

C. Lücking, K. Fakler, U. Berkermann, J. Mentel, G. Schiffner

Ruhr-University Bochum
Department of Electrotechnical Engineering
Division AEEO
Universitätsstraße 150, D-44780 Bochum, Germany

ABSTRACT

Two independent methods are applied to measure the impedances of an rf excited CO₂ slab laser and of a discharge test chamber. The rf feedthroughs are chosen as reference ports for the measurements. One method using an adjusted matching network and a network analyser is compared with another method measuring two signals representing current and voltage with a digital oscilloscope and processing them using a computer.

Keywords: rf excited CO₂ slab lasers, impedance of a discharge, matching network for gas discharges, measurement of discharge impedance

1. INTRODUCTION

Matching design requires knowledge of the discharge impedance and its dependence on the input rf power, gas pressure and operation modes. Hence measurements of the discharge impedance are important to achieve a model for the slab laser and to calculate the plasma impedance.

2. MEASURING WITH A NETWORK ANALISER (INDIRECT METHOD)

The laser is connected with a matching network to minimize the reflected power to the generator, Fig 1. Between the rf generator and the matching network a bi-directional coupler is connected to control the reflected power. This matching network is built up with adjustable components and with low electrical losses.

The matching network is removed from the system when the matching procedure has been completed. At the input port of the network a resistance of 50 Ω is connected and at the output port the impedance Z_{meas} is measured using a network analyser. The impedance $Z_{discharge}$ at the rf feedthrough is the conjugate complex impedance of the matching network at the output port:

$$Z_{discharge} = Z_{meas}^* \quad (1)$$

3. MEASURING WITH A DIGITAL OSCILLOSCOPE (DIRECT METHOD)

The arrangement is the same as for the network analyser method, but two special probes are inserted in the matching network, Fig 2. With these probes two signals representing current and voltage are recorded using a two channel digital oscilloscope. For calibration three calibration standards (shortcut, open, 50 Ω) are connected in succession, instead of the discharge, to get two probe signals for each element. With these signals a matrix of the system is calculated by the computer. After this calibration process the discharge is connected and the two signals are recorded. These two signals are calculated with the matrix of the system to give the impedance of the discharge.¹

4. CONCLUSIONS

With both methods measurements of the impedances of the discharge chamber were made at the rf feedthrough as reference port. The comparison shows that the resistive components of the discharge impedances have comparable absolute values and that the reactive components show similar dependences on input power, Fig. 3, Fig. 4, Fig. 5, Fig. 6. The measurements on the CO₂ slab laser show dependences of resistive and reactive components on input power, Fig. 7, Fig. 8.

5. FUTURE WORK

For the direct method a new calibration procedure is used to achieve a better precision. Then measurements for higher input powers and pulsed mode are performed.

Both methods are used to get knowledge about the plasma impedance.

6. ACKNOWLEDGMENTS

This research was supported by the German Ministry for Education and Science (BMBF) during the project Plasma physical investigations on rf excited CO₂ slab lasers (13N6571).

7. REFERENCES

1. B. Schiek, "Meßsysteme der Hochfrequenztechnik", Hüthig Verlag, Heidelberg, 1984

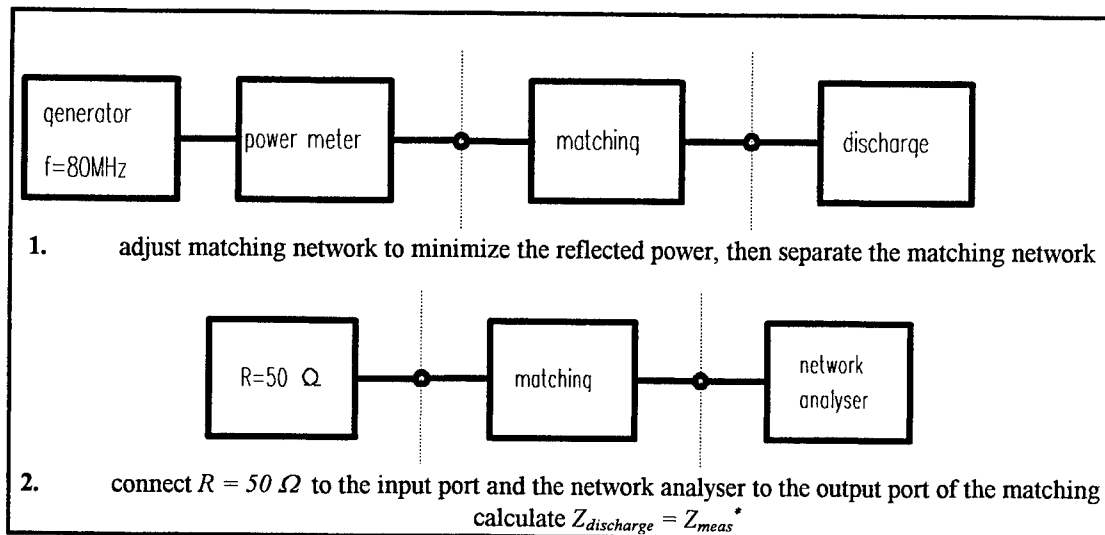


Fig 1: impedance measurement by indirect method

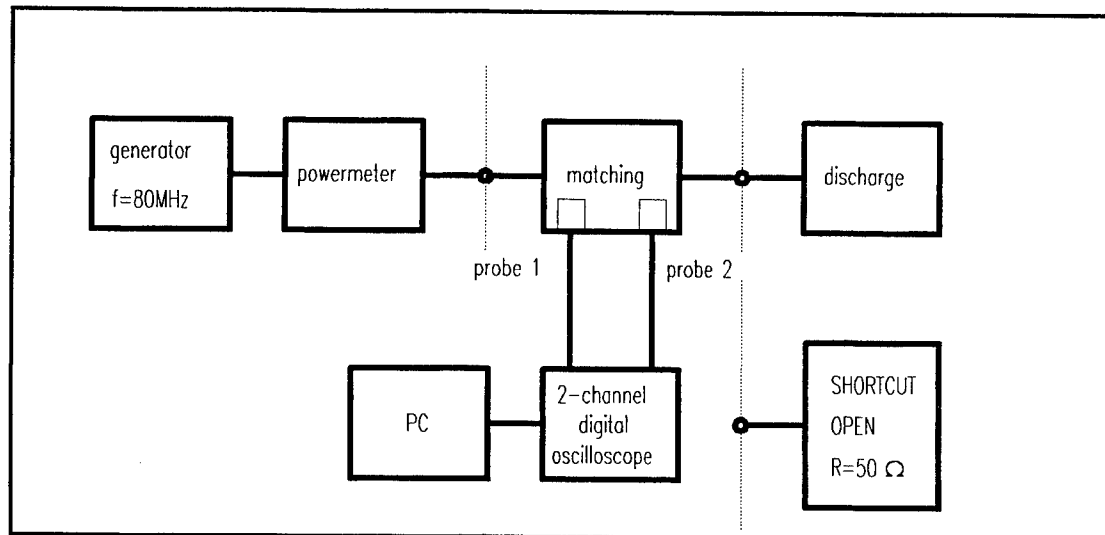


Fig 2: impedance measurement by direct method

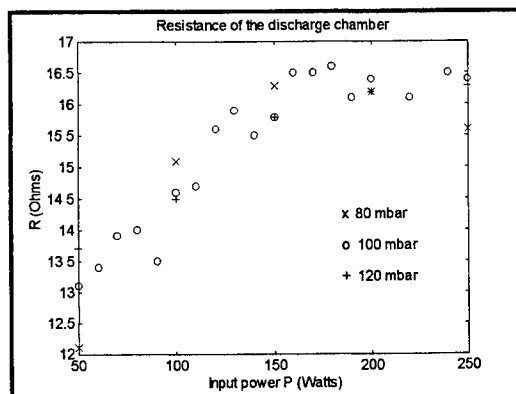


Fig. 3

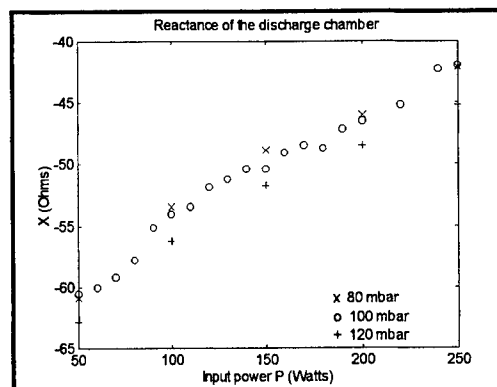


Fig. 4

Fig.3 and Fig.4: impedance of the discharge chamber using indirect method

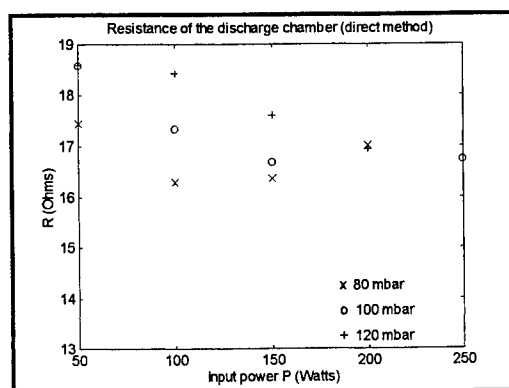


Fig. 5

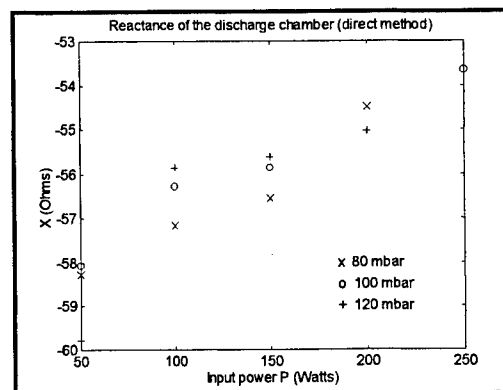


Fig. 6

Fig. 5 and Fig.6: impedance of the discharge chamber using direct method

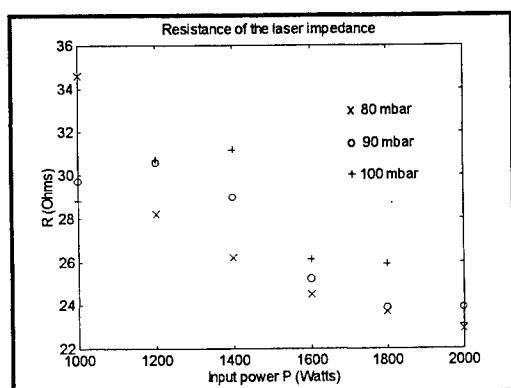


Fig. 7

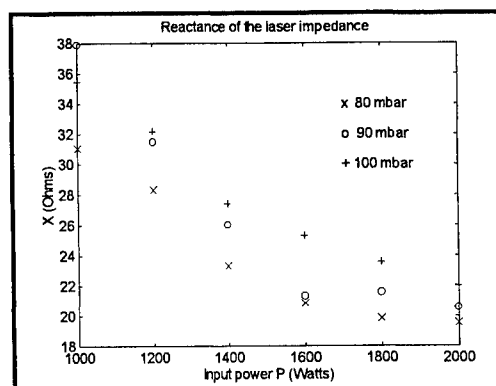


Fig. 8

Fig.7 and Fig. 8: impedance of the slab laser using indirect method

A compact four-wave mixing MOPA system with rotational symmetry

W.Riede, Th.Hall

Institut fuer Technische Physik, DLR Stuttgart
Pfaffenwaldring 38 - 40, 70 569 Stuttgart, Germany

ABSTRACT

A new concept for a master oscillator power amplifier (MOPA) system that is based on phase conjugation by four-wave mixing is presented. The system has a rigorous rotational symmetry with respect to amplification and phase conjugation allowing for a compact design. Numerical resonator calculations on the basis of the Fresnel-Kirchhoff technique were used to support the layout.

1. INTRODUCTION

Phase distortions like shock waves and lens effects in the laser medium, and convection effects are a concomitant of gas lasers with high pulse energy and/or high average power. These effects are usually of a dynamical nature, appearing on short timescales down to the microsecond range. Phase conjugate mirrors based e.g. on four-wave mixing [1] can cancel these aberrations due to their high temporal and spatial bandwidth. The proposed system is applicable especially to pulsed molecular gas lasers with high gain operating in the middle infrared.

2. SYSTEM DESCRIPTION

The system is depicted in Fig. 1. It consists of a master oscillator, set up by the resonator mirrors 7 and 11, having a high and low transmission, respectively. The master oscillator is operating in a fundamental spatial mode (TEM_{00} cavity) with a high degree of spatial coherence. A polarizing element 10 is placed into the cavity to ensure a polarized output. The discharge volume is sealed with two AR coated windows 8. The pump beam, coupled out via mirror 7, is passing the polarizing beam splitter 6 and focusing lens 5. The focusing lens 5 has a hole in the center, allowing for a diffraction free propagation of the pump beam to the 4WM cell 3. The cell windows 2,4 are AR coated at the laser wavelength. Additionally, window 2 has a $\lambda/4$ coating, which will rotate the polarization of the pump beam by 90° after retroreflection from HR mirror 1. This mirror is providing the counterpropagating pump beam. The curvature of its surface should coincide with the curvature of the wave-front of the pump beam. The backcoupling of radiation into the master oscillator is prevented by the polarizing beam splitter 6. The signal beam, coupled out via mirror 11, is transmitted through a polarizing beam splitter 12 and aimed at a waxicon 13. This waxicon reflects the signal radiation back into the (amplifying) discharge volume in the form of a ring, which is concentric to the optical axis of the system. The signal radiation is amplified in the discharge volume 9 and slightly focused into the 4WM cell 3 with lens 5. The phase conjugate signal beam is orthogonally polarized with respect to the signal beam [2]. It retraverses the path of the signal beam, i.e. it is amplified, reflected off the waxicon 13 and coupled out at the beam splitter 12.

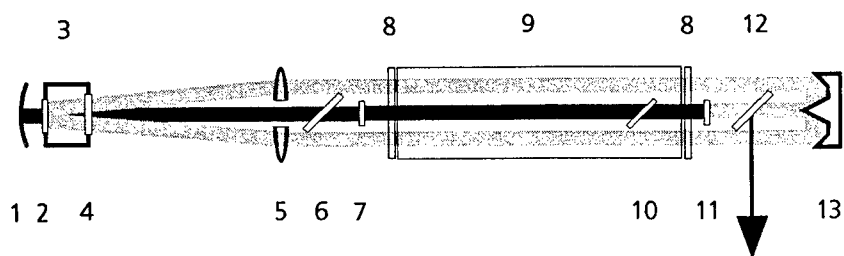


Fig.1 Setup of the MOPA system.

3. DISCUSSION

Preliminary results of Fresnel-Kirchhoff calculations are used to support the layout of the MOPA system. Fig. 2 shows the intensity distribution of the intracavity master oscillator radiation, the amplified phase-conjugate signal and the signal beam in the plane defined by the optical element 8 (Fig. 1). A phase conjugate power reflectivity of 50 %, and a small signal gain of 1.5 %/cm with a gain length of 1.2 m were assumed for the calculation of the phase conjugate signal beam.

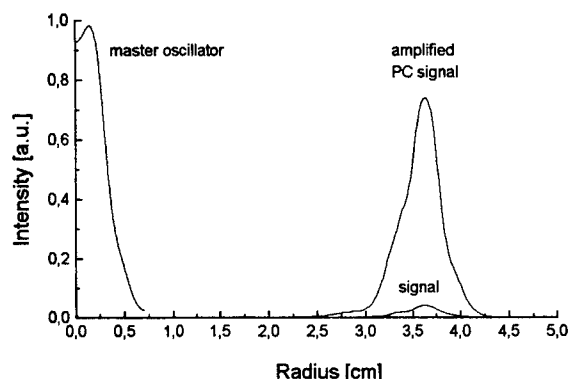


Fig. 2 Intensity distribution of fundamental mode of master oscillator, signal beam and phase conjugate signal beam.

The resonator data used in the numerical calculation are identical to resonator data of Ref. [3], where an experimental characterization of such a master oscillator was made. The power loss of the signal beam during propagation through the optical elements can be kept at a low level which is essential for high-quality phase conjugation. The diffractive losses which accumulated during propagation of the signal beam without gain were calculated to be on the order of 1 %.

4. LITERATURE

- 1 M. Gower, D. Proch, " Optical Phase Conjugation", Springer-Verlag, Berlin, 1994.
- 2 A. Brignon, J.-P. Huignard, "Transient analysis of degenerate four-wave mixing with orthogonally polarized pump beams in a saturable Nd:YAG amplifier", IEEE J. Quantum Electron. 30, 2203 (1994).
- 3 W. Riede, W. Mayerhofer, Th. Hall, S. Walther, "Investigation of beam quality and gain behaviour in a large aperture e-beam controlled CO₂ laser", GCL/HPL 1996, this volume.

Optical nonuniformities of active medium of high-power fast-axial-flow industrial CO₂ lasers.

M.G.Galushkin, V.S.Golubev, Yu.N.Zavalov, V.Ye.Zavalova, V.Ya.Panchenko

NICTL RAN - Laser Research Center
Shatura 140700, RUSSIA

ABSTRACT

It was shown theoretically and by experiment that a thermal defocusing gaseous lens formed in industrial fast-axial-flow CO₂ lasers may affect the diffraction losses of the generator and the beam parameters.

Keywords: CO₂ laser, fast-axial flow, nonlinear optical nonuniformities

1. THE GOAL OF THE INVESTIGATIONS

Optical nonuniformities of the active medium are affect the laser beam spatial characteristics, this problem is given much attention.^{1,2} The paper performs the theoretical analysis of laser medium optical quality and shows its interrelation with main parameters of a high-power fast-axial flow (FAF) CO₂ lasers. The primary emphasis of consideration of wave front aberrations in the active medium is placed on variations in refraction index $\Delta n(r)$, averaged over the longitudinal co-ordinate (Z axis). The emergence of refraction index radial nonuniformity in FAF lasers is related to the radial inconstancy of gas flow velocity. In this case, the regular large-scale optical lens emerges owing to radial symmetry of heat release and gas flow velocity.

2. GOVERNING EQUATIONS

To calculate the radial optical nonuniformities, it is required to determine variation along the tube radius of the temperature T , described by heat-balance equation:

$$c_p \rho \left[u \frac{\partial T}{\partial z} - \chi \frac{1}{r} \frac{\partial}{\partial r} \left(r \frac{\partial T}{\partial r} \right) \right] = Q_0(r) + Q_1(r), \quad (1)$$

here c_p , ρ are specific heat capacity and density of the gas, u is gas flow velocity, χ is thermal diffusivity, z is the co-ordinate along the flow, $0 \leq z \leq l_t$, where l_t is the distance from the beginning of discharge region to the tube end (discharge length $l_d < l_t$), $Q_0(r)$ is the function describing heat release in the discharge ($0 \leq z \leq l_d$). For function Q_0 and Q_1 we have the expressions:

$$Q_0 = \beta_1 j E; \quad Q_1 = \delta_1 N \left[h\nu_2 (e_2 - e_{2T}) / \tau_1 + \kappa_b (\Theta_3 - 2\Theta_2) e_3 / \tau_2 \right], \quad (2)$$

where β_1 is the discharge energy portion going into direct heating of gas, k_b is the Boltzmann constant, e_j , Θ_j are the average amount of vibrational quantum and characteristic temperature of j -mode: $j=2$, CO₂(010), $j=3$, CO₂(001), $h\nu_2$ is the energy of vibrational quantum CO₂(010), $W=jE$ is the energy input into the discharge, W/cm^3 , δ_j are molecular portions of mixture components CO₂, N₂ and He.

Functions e_j are described by the linearized equations of kinetics³:

$$u \frac{\partial e_3}{\partial z} - D \frac{1}{r} \frac{\partial}{\partial r} \left(r \frac{\partial e_3}{\partial r} \right) = \frac{\eta_{34}}{\Delta E_3} \frac{W(r)}{\delta_1 N} - \frac{e_3}{\tau_2} - \frac{\alpha J}{\delta_1 N h \nu_0}, \quad (3)$$

$$u \frac{\partial e_2}{\partial z} - D \frac{1}{r} \frac{\partial}{\partial r} \left(r \frac{\partial e_2}{\partial r} \right) = \frac{\eta_{12} W(r)}{2 \Delta E_2 \delta_1} + \frac{3}{\tau_2} e_3 - \frac{1}{\tau_1} (e_2 - \bar{e}_2) + \frac{2 \alpha J}{N h \nu_0 \delta_1}, \quad (4)$$

where D is the coefficient of diffusion of vibration-excited molecules, η_{12} , η_{34} are the portions of power going into excitation of vibrational modes of N_2 , $CO_2(100+010)$, $\Delta E_2=2k_b\Theta_2$, $\Delta E_3=k_b\Theta_3$, $Nk_{32}=1/\tau_2$, $Nk_{20}=1/\tau_1$, k_{32} , k_{20} are kinetic constancy of vibrational energy interchange between modes 1 and 2 and velocity of VT- relaxation of combined mode vibrational energy, N is gas particles density, $h\nu_0$ is quantum energy of laser radiation, α is gain index, J is radiation intensity, and:

$$W(r)=\begin{cases} jE, z \in [0, l_d] \\ 0, z \in [l_d, l_t] \end{cases}, \quad \alpha = 5.8 \cdot 10^{-18} \frac{\exp(-223/T)}{T} \frac{2H(b,0)}{\Delta\nu_d} (e_2 - e_1) \frac{N\delta_1}{Q}, \quad (5)$$

$e_j = r_j / (\exp(\Theta_j/N_j) - 1)$, $H(b,0)$ is the Voigt function for the line centrum; $\Delta\nu_d$ is Doppler line width, Q is the statistic sum of CO_2 molecule vibrational modes. The relations $\rho u = \rho_0 u_0$, $D\rho = \text{const}$ are also fulfilled.

For calculation of the gaseous lens power near the resonator axis we use the decomposition of functions $Q(r) \cong Q_0 + 0.5Q''r^2$, $J \cong J_0 - J_0 r^2/w^2$, (w is the beam radius whereon the field amplitude is reduced by the factor of e),

$$\bar{e}_3 \cong \bar{e}_3(0) + \bar{e}_3'' \frac{r^2}{2}, \text{ where } Q'' = \frac{\partial^2 Q}{\partial r^2} \Big|_{r=0}, \quad \bar{e}_3'' = \frac{\partial^2 \bar{e}_3}{\partial r^2} \Big|_{r=0} \dots \text{ Let consider the values of } \bar{e}_3, \bar{Q}_1, \text{ and } \bar{T} \text{ functions}$$

being averaged by the gas discharge tube length. Allowing for the high velocity of $CO_2(010)$ mode relaxation $e_3 < e_1$, $e_1 \cong e^2$. After substitution into (1-5) let find the coefficients in view of the boundary conditions $e_3(0)=0$, $e_3(l_t) \cong 0$:

$$\bar{e}_3(0) = \frac{b}{a}, \quad \bar{e}_3'' = \frac{v_2'}{D} \frac{b}{a} - \frac{\eta_{34} W_0}{\delta_1 N \Delta E_3 D} \frac{l_d}{l_t}, \text{ where} \quad (6)$$

$$b = \frac{\eta_{34}}{\delta_1 N \Delta E_3} \frac{l_d}{l_t} \left(W_0 \frac{v_2'}{D} + W'' \right), \quad a = \frac{(v_2')^2}{D} - \frac{2}{w^2 \tau_2} \frac{J_0}{J_s}, \quad v_2' = \frac{1}{\tau_2} \left(1 + \frac{J_0}{J_s} \right), \quad (7)$$

J_0 is the summary intensity of two on coming waves in the stable resonator (assumed to constant along Z). The equation for temperature \bar{T} being averaged by the tube length follows from (1)

$$c_p \rho \left[u(T_k - T_0)/l_t - \frac{\chi}{r} \frac{\partial}{\partial r} \left(r \frac{\partial \bar{T}}{\partial r} \right) \right] = Q_0(r) \frac{l_d}{l_t} + \bar{Q}_1(r), \quad (8)$$

where $T_k(r)$ is the temperature in the output plane of gas-discharge tube ($z=l_t$). For determination of $T_k(r)$ function, allowing for rather monotonous growth of $T(z,r)$ along z . Thus, the following dependences were obtained

$$\bar{T}'' = \frac{l_t}{2c_p \rho u} \left(Q_0'' \frac{l_d}{l_t} + \bar{Q}_1'' \right), \quad \bar{T}(0) = \frac{1}{2c_p \rho u} \left[Q_0(0) l_d + \bar{Q}_1(0) l_t \right] + T_0 + \frac{l_t}{u} \chi \bar{T}'', \text{ where} \quad (9)$$

$$\bar{Q}_1(0) = \delta_1 N \left(\frac{\eta_{12} W_0}{2\delta_1 N} + h\nu_a \frac{\bar{e}_3(0)}{\tau_2} + \frac{2v_2}{v_0} \bar{e}_3(0) \sigma J_0 \right); \quad \bar{Q}_1''(0) = \delta_1 N \left(\frac{\eta_{12} W''}{2\delta_1 N} + h\nu_a \frac{\bar{e}_3''}{\tau_2} + 2h\nu_2 \frac{\bar{e}_3''}{\tau_2} \frac{J_0}{J_s} - \frac{2v_2}{v_0} \bar{e}_3(0) \frac{2}{w^2} \sigma J_0 \right).$$

The spatial nonuniformity of temperature causes a variation in the refraction index in conformity with the well known formula: $\Delta n(r) \cong K_G \Delta \rho(r) \cong -K_G \rho \frac{\Delta T(r)}{T}$, where K_G is Gladstone-Dale coefficient, $\Delta T = T''r^2$, $T = \bar{T}(0)$. With expression (6-7,9) the optical power of thermal gaseous lens⁴ is found:

$$\frac{1}{f} \cong 2n_2 l_t, \text{ where } n_2 = K_G \rho \frac{T''}{T} \quad (10).$$

3. RESULTS

As follows from the obtained solutions, the optical power of thermal lens is determined by radiation intensity due to thermal self-action in the active medium of CO₂ laser. The results of the investigations represented on the Fig.1-3. In calculations, the parameters of the fast-axial-flow TLA-600 CO₂ laser were used; the laser has 8 gas-discharge tubes located sequentially along the beam path in the 4-pass resonator of 5.25 m length; the dimensions of tubes are given in [7]. The thermal defocusing lens in the active medium of the cw fast-axial-flow CO₂ laser is produced near the optical axis mainly caused by radial nonuniformity of self - sustained dc discharge in gas-discharge tubes of limited cross-section; for the typical parameters of industrial FAF lasers, the focus of this lens can be about 50 m per 1 m of the amplifying medium. Thermal lens is nonlinear in itself owing to heat release dependence on radiation intensity in the amplifying medium. The degree of this nonlinearity is governed by the amplifying medium saturation and by gaussian beam cross-section.

In the stable resonator the defocusing lenses bring about broadening of the gaussian beam and variation in the output beam wave front curvature. The additional wave front curvature produced in this way can be corrected by the external focusing device. The emergence of the scattering lens inside the resonator with the fixed Fresnel leads to the increase of the volume occupied by the radiation mode and to the respective growth of diffraction losses for this mode. Calculating these losses it has been assumed that an optically thin defocusing thermal gaseous lens is located at the centre of each gas-discharge tube; the optical power of this lens is determined by formula (10). The method described in [5] was used to calculate the equivalent parameters of the stable resonator having the specified sequence of lenses and the typical radius of gaussian beam. Then the diffraction losses were found from the curves given in [6].

Fig.4 illustrates the results of calculation of diffraction losses as a function on energy input into the discharge for TEM₀₀ mode (the case is considered when both the output and end mirrors have the radius of inner surface curvature 30 m, and the radius of diaphragm is 8.5 mm).

The results of measurements⁷ are also presented in Fig.4. It was assumed that the part of total radiation losses occurred at 6 internal mirrors and amounted for nearly 9%. In these experiments the substitution of the flat mirror for the one having the surface curvature radius 16 m permitted to improve the electro-optical efficiency from 14% to 18%. This result is explained by the influence of the thermal scattering gaseous lens upon the diffraction losses, that is supported by the calculations above.

4. ACKNOWLEDGMENTS

The authors express their thanks for the Russian Foundation of Basic Research (grant N96-02-17784) for the partial support of this research.

5. REFERENCES

1. M.Moissl, R. Paul, K. Breining et al. *SPIE*, **1397**, 395, 1990.
2. M.G.Galushkin, V.S.Golubev, V.V.Dembovetsky, Yu.N.Zavalov, V.Ye.Zavalova *Quant. Electronics*, **26**(8), 1993.
3. M.G.Galushkin, V.S.Golubev, V.V.Dembovetsky, Yu.N.Zavalov, V.Ye.Zavalova *Quant. Electronics*, **26**(6), 1993.
4. W.J.Witteman. *The CO₂ Laser* (Berlin: Springer,1988).
5. Ernst G.J., Witteman W.J. *IEEE J. of Quant. Electr.*, **QE-9**, 911 (1973).
6. Li T., *Bell System Tech. J.*, **44**, 917, (1965).
7. V.V.Dembovetsky, Yu.N. Zavalov In: *R.Kossowsky et.al.-(eds.), Proc. of NATO ASI "High Power Lasers- Science and Engineering"*, **3/7**, 603-618 (Kluwer Academic Publ., 1996).

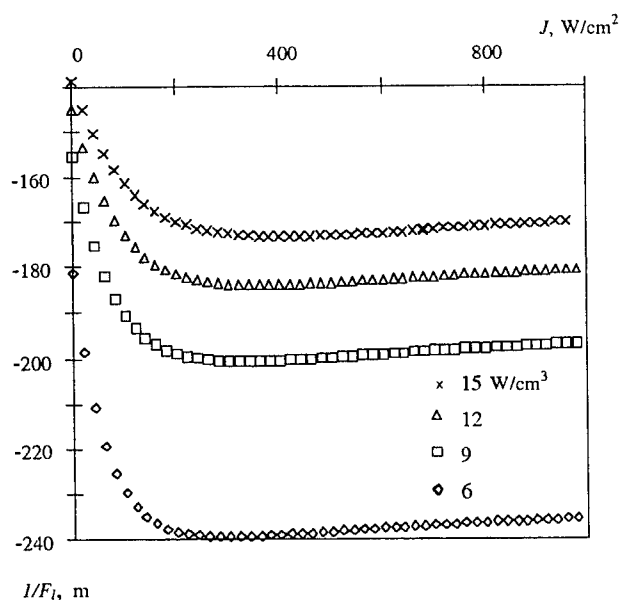


Fig.1. Calculated dependence of thermal lens focus on intensity inside the resonator with $(w/R)^2=0.5$ (specific energy input is varied).

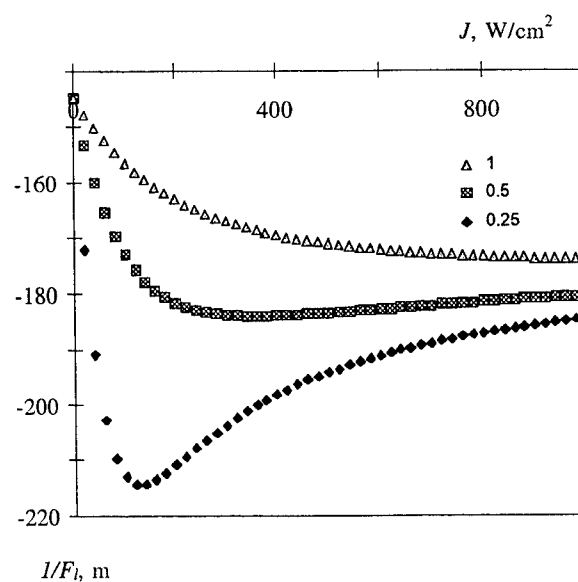


Fig.2. Calculated dependences of thermal lens focus on beam intensity with energy input 12 W/cm³ (beam parameter $(w/R)^2$ is varied).

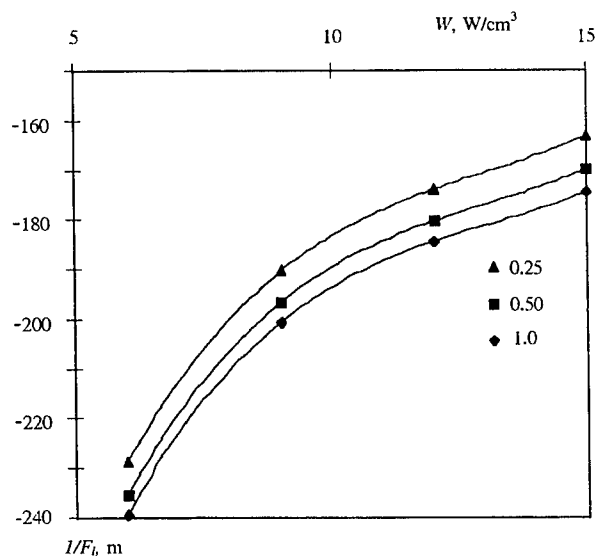


Fig.3. Calculated dependence of thermal lens focus on specific energy input in the discharge for different values of beam parameter $(w/R)^2$.

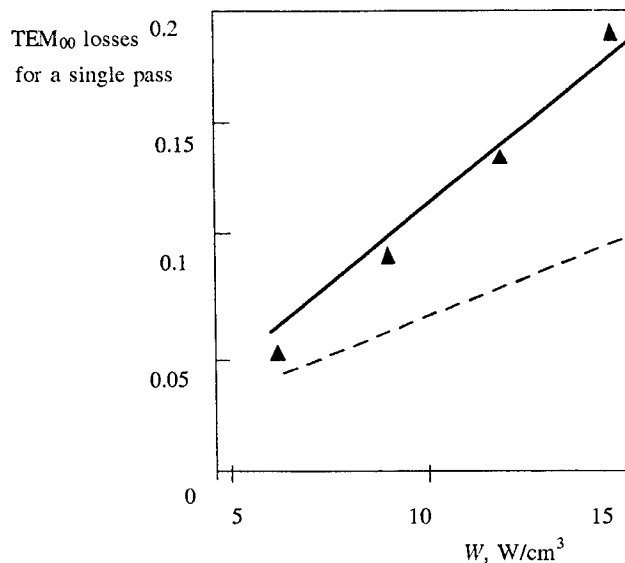


Fig.4. Dependence of diffraction losses TEM₀₀ mode on specific input. For the case when the radius of the output mirror $R_1=30$ m and the radius of the flat mirror $R_2=30$ m: the calculated results are shown by the solid line; the symbols are for the experimental results. The results of calculations for $R_1=30$ m and $R_2=16$ m are presented by the dashed line.

Planar waveguide, 50 W cw, CO₂ laser excited by a transverse
radio frequency discharge with broad stripe matching network

V. G. Leont'ev, V. A. Stepanov, E. F. Shishkanov
Department of Physics, Pedagogical University, 46 Svoboda St., 390000 Ryazan Russia

M. Z. Novgorodov, V. N. Ochkin
Lebedev Physical Institute, Russian Academy of Sciences, 53 Leninsky pr., 117924 Moscow Russia

ABSTRACT

A transverse radio frequency discharge excited, CO₂ slab laser has been operated cw with a hybrid waveguide and unstable resonator to produce an output power of 54 W from the active volume of 280 x 40 x 2.5 mm³. An impedance matching network consists of coaxial cable lines and has not discrete L, C reactive elements.

Keywords: CO₂ slab laser, transverse radio frequency discharge, hybrid waveguide and unstable resonator, impedance matching network, output power.

1. INTRODUCTION

The efficient extraction of high power outputs from carbon dioxide sealed-off compact lasers has been realised by exploiting the area-scaling concept in slab waveguide geometries with transverse radio frequency discharge excited¹. Such type of discharge structure together with an unstable-waveguide resonator with a radiation spreaded in a free space as well as in a waveguide with the radiation output beyond the bounds of one of the mirrors permits to obtain high laser power at a fundamental hybrid mode which is a combination of the lowest mode of the planar waveguide and the lowest mode of the small-bore unstable resonator.

For constructional simplicity and to obtain effective generation from slab laser, it is clearly desirable that large area of discharge be achieved with a single pair of directly water cooled, metallic electrode², what leads requirement to uniformly input rf power to discharge electrode structure. In this paper we indicate description of a rf power transfer system capable of delivering of 600 W uniformly to single piece metal electrodes of 50 W cw CO₂ slab laser via a single 50 Ω cable feed, in a manner which provides electric discharge conditions which optimize laser excitation efficiency.

2. LASER CONSTRUCTION

Waveguide is provided by the two planar electrodes with drilled water cooling channels, giving an active area of 40 x 280 mm². The electrodes are separated by 2.5 mm and provide in the transverse dimension single order mode operation which approximates closely to a gaussian profile in the far field. In the lateral dimension a positive branch confocal unstable resonator have been employed. The cavity uses two copper mirrors separated by 310 mm, with 5.0 m concave and 4.38 m convex radius of curvature, respectively, and the convex mirror is offset to produce a 5 mm coupling port.

The cavity is adjustable by means of mechanical mirror adjusters, and also by piezoelectric actuator (for concave mirror).

Laser has a sealed-off metal-ceramic construction in which a cylindrical housing made of Al-oxide ceramics is a base of optical resonator and a gas medium bore simultaneously. All the metal-metal and ceramic-metal joints are soldered or welded. The laser output is taken through an GaAs window in the vacuum envelope. The whole laser vessel is backfilled to the desired gas pressure with a 3:1:1 mixture of He, N₂, and CO₂, to which is added 5 % xenon. The laser includes stabilisers of the gas composition³, which ensures efficient conversion of CO back to CO₂, so that the concentration of CO₂ remains constant during prolonged operation of the laser.

A rf generator, capable of a maximum power of 600 W at a frequency of 81.36 MHz, is connected to the laser head by a single 50 Ω coaxial cable via an impedance matching network, a schematic of which is shown in Fig. 1. This matching network consists of 50 Ω coaxial cable lines and has not discrete L and C reactive elements. The rf input energy is delivered through the end parts of the electrodes, the homogeneity of the rf voltage distribution along the channel is improved by connecting inductance coil to electrode middle, parallel to the discharge gap. This coil reduces the difference between the potential drop between the electrodes at the middle of the discharge channel and the voltage at the points where the energy is delivered.

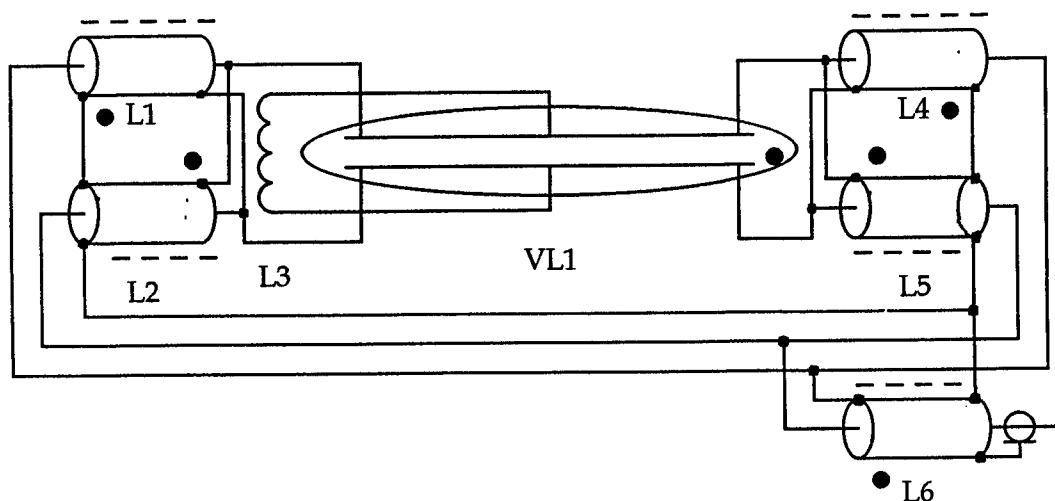


Fig. 1. Electrical circuit supplying rf power to the laser head

3. LASER CHARACTERISTICS

In order to evaluate energy features of laser in various gas pressures the radiation power versus applied rf power characteristics are researched. Shown in Fig. 2 are these dependencies. In order to measure rf power applied to a discharge bore a thermal calorimetric technique has been used. When researching the laser characteristics an autotransformer impedance matching network was used which it is possible to get a minimum of a reflected wave in a system "rf generator - laser head" at any meaning of rf applied power and with each of the gas filling. The results of researching show that impedance of discharge structure consists 12.5 Ω for applied rf power 600 W and gas pressure

which is shown in Fig. 1. As this matching network has broad stripe of signal passing and the quality factor (Q-factor) of the parallel resonance is reduced to a low value, perhaps not far from unity⁴, the work of this laser on different frequencies of excitation of discharge is possible. In order to evaluate the frequency dependencies of matching network for different impedance are researched. Shown in Figs. 3(a) and 3(b) are these dependencies. One can see there are some impedance meanings when the standing wave coefficient of matching network is less than 1.5.

The matching network has executed for work on the frequency of $f = 81.36$ MHz for easy laser construction. However it is possible that $50\ \Omega$ cable lines can be located on ferrite rings⁵ when the broad stripe of signal passing will increase (for low meanings of the frequency f).

It is note that discharge structure capacitance neutralization is unnecessary. Capacitance between electrodes $C < 100$ pF because there are not ceramic plates-calibres in the discharge structure (for example, these plates are in^{2, 4}) and the electrode separation is constant as the electrodes are hardly fixed on external ceramic cylinder. In this case displacement current is very smaller than general current across the laser.

Moreover the matching network schematic and the laser head construction provide a symmetrical rf discharge. Unfortunately in practice almost all systems^{2,4} are asymmetrical. When one electrode of our device was earthing then electromagnetic interferences were observed in electronic devices in the vicinity of the laser head which is a severe problem in the case of an unsymmetric schematic. The interferences were observed on harmonics of the frequency $f = 81.36$ MHz, what confirm non-linear discharge current for unsymmetric system⁶. These effects were absent when both electrodes were equal to earthed metal chamber.

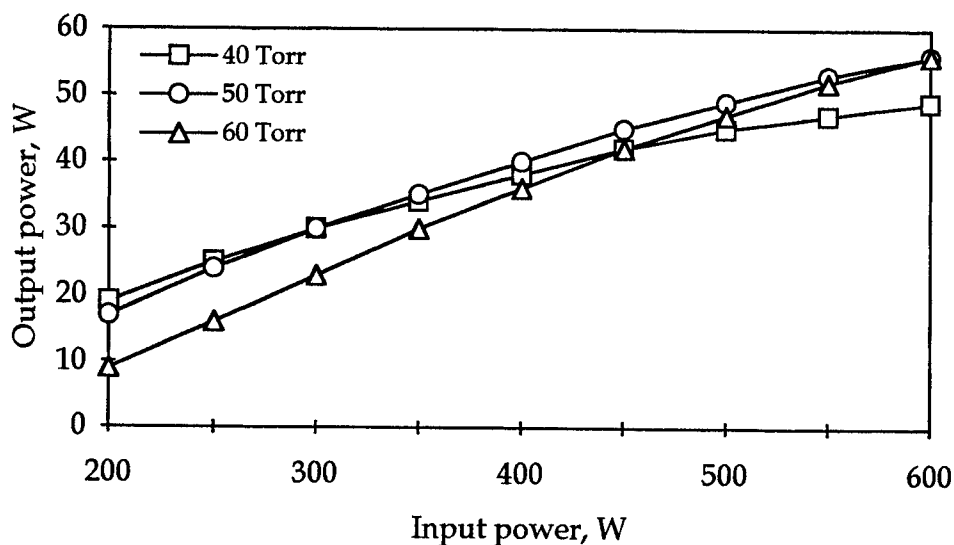


Fig. 2. Output power as a function of input power

4. CONCLUSION

There has been shown that a 50 W slab waveguide CO₂ laser may be operated with a single, continuous rf discharge from a single rf feed cable. The beam quality produced by the unstable

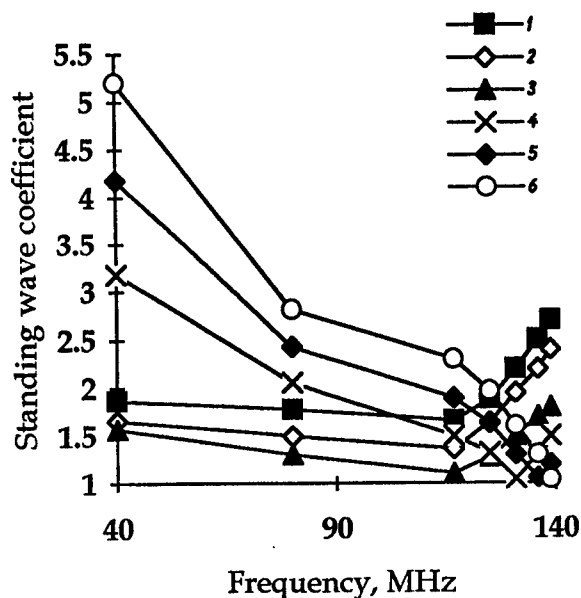


Fig. 3 (a). Measured standing wave coefficient of matching

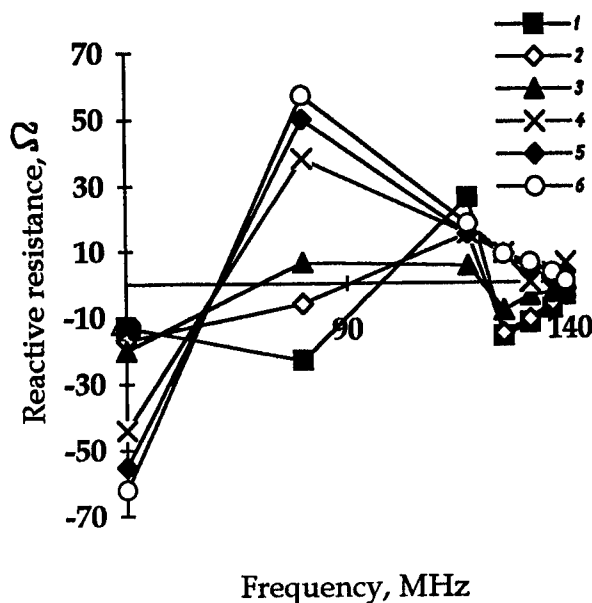


Fig. 3 (a). Measured reactive resistance of matching network

1 - $R_{\text{active}}=20 \Omega$, L_3 - no; 2 - $R_{\text{active}}=16.6 \Omega$, L_3 - no; 3 - $R_{\text{active}}=12.5 \Omega$, L_3 - no;
4 - $R_{\text{active}}=12.5 \Omega$, $L_3=70 \text{ nH}$; 5 - $R_{\text{active}}=12.5 \Omega$, $L_3=50 \text{ nH}$; 6 - $R_{\text{active}}=12.5 \Omega$, $L_3=30 \text{ nH}$

resonator is good and analogous with results in⁵. The maximum power output in Fig. 3 is limited by the generator size; operation at slightly higher power and pressure may be possible better.

5. REFERENCES

1. V.G.Leont'ev, E.F.Shishkanov. Outlook on an unstable-waveguide cavity usage in gas lasers. SPIE, v. 2773, pp. 16 - 22 (1996).
2. A.D.Colley, H.J.Baker, and D.R.Hall. Planar waveguide, 1 kW cw, carbon dioxide laser excited by a single transverse rf discharge. Appl. Phys. Lett., 61 (2), pp. 136 - 138 (1992).
3. V.V.Avdon'kin, V.G.Leont'ev, A.Y.Payurov, E.F.Shishkanov. Sealed-off CO₂ laser with a transverse discharge. Patent of Russia, N 2012112 C1 5H01S 3/036. Bulletin of inventions N 8 (30.04.94).
4. A.D.Colley, F.Villarreal, A.A.Cameron, P.P.Vitruk, H.J.Baker, D.R.Hall. High power cw molecular gas lasers using narrow gap slab waveguides. Proceedings of the NATO Advanced Research Workshop ARW 950443 on Gas Lasers - Recent Developments and Future Prospects, Moscow, Russia, July 2 - 5, 1995, pp. 89 - 103, Klumer Academic Publishers. The Netherlands (1996).
5. A.A.Kuznetsov, V.V.Kun, V.G.Leont'ev, M.Z.Novgorodov, V.N.Ochkin, E.F.Shishkanov. CO₂ - waveguide lasers with slab geometry. J. of Russian Lasers Research, v. 17, N 1, pp. 1 - 14 (1996).
6. Y.P.Raizer, M.N.Shneider, N.A.Yatsenko. Radio-frequency capacitive discharges: Physics. Experimental technique. Applications. 320 pages, Moscow (1995).

Pulsed - repetitively slab waveguide RF - excited CO₂ laser

A. I. Dutov, A. A. Kuleshov, N. A. Novoselov, M. S. Yur'ev

Institute for Laser Physics, Vavilov Optical Institute,
St.-Petersburg, 199034, Russia

ABSTRACT

Research and development of pulsed-repetitively slab RF-excited CO₂ laser is presented. The experiments were carried out for two modes operation: meander mode (duty factor $\delta = 50\%$) and pulse repetition mode at $\delta = 12.5\%$. The range of $240 \div 4000$ Hz of pulse repetition frequency was used. Pulse power about 400 W for meander mode and up to 700 W for the second mode have been obtained. Input power, radiation pulse shape and output beam divergence were measured.

Keywords: slab CO₂ laser, RF-pumping, pulsed-repetitively modes operation.

1. INTRODUCTION

There is a current interest in pulsed - repetitively CO₂ lasers for material processing, medical and laser radar applications. In the field of material processing the pulse modes operation with small and moderate energy level gives new possibilities for glass cutting and drilling because of an insignificant heating of object ("cold ablation" process). In previous studies of pulses in such regime it was utilized UV - preionized, recirculating transversely excited atmospheric-pressure (TEA) lasers¹. The use of UV-preionized devices leads to a rather small lifetime due to the fast degradation of laser mixture.

An alternative approach to operation in this mode utilizes of pulsed-repetitively RF - pumping slab waveguide lasers. There is diffuse and stable discharge in such lasers without use of any preionizator. RF exciting allow to use a slab configuration of a gap, when spacing between extended electrodes is only $1 \div 3$ mm. It causes effective heat removal from the pumped volume of active medium by the heat conduction and diffusion of gas mixture to the cooled electrodes. For pulsed-repetition mode the gain is much more than for CW one². Besides, the slab lasers are much more compact than UV - preionized devices.

2. EXPERIMENTAL SETUP

We performed our investigations with a slab waveguide CO₂ laser of planar configuration with sealed-off nonflowing operation. The discharge channel was formed by two aluminum alloy electrodes (60×580 mm), finished with optical quality, and separated by 2 mm discharge gap. No any coating on electrode surfaces was used. The RF driver consisted of an oscillator-amplifier arrangement. This allowed to easily modulate RF-discharge pumping by signals from an external oscillator. The system operated at the frequency $F = 81.36$ MHz in two modes: meander or repetitive-rate with duty factor $\delta = 12.5\%$. For both modes pulse - repetition frequency (PRF) was in the range $250 \div 4000$ Hz. Pulse duration was varied from 2 ms to $125\mu\text{s}$ for meander mode operation while from $500\mu\text{s}$ to $30\mu\text{s}$ for second one. The RF-power was coupled into the discharge structure via a matching network that included a parallel-resonant distributed-inductance arrangement. Measurement of the power put into the discharge plasma was done by means of the calorimetric method. The error of the measurement did not exceed 10%.

The study was carried out in $\text{CO}_2\text{:N}_2\text{:He:Xe} = 1:1:6:0.4$ gas mixture at $40 \div 150$ torr. We performed our experiments mainly with confocal unstable resonator formed by two concave spherical mirrors (the negative branch of instability)³. Magnification of resonator was equal $M=1.17$. This type of resonator has a weak sensibility to misalignments.

3. LASER POWER AND EFFICIENCY

3.1. MEANDER (M) MODE OPERATION

For M mode the studies were carried out for gas pressure $p = 50 \div 90$ torr and average input power $P = 600 \div 1700$ W. Pulse input power is twice as average one. The dependence of lasing energy on pulse duration is shown in Fig. 1. Input power and pressure were constant. One can see from Fig. 1 the pulse energies $E = 40 \div 340$ mJ for $f = 500 \div 4000$ Hz were obtained. Maximal pulse energy $E = 740$ mJ was obtained for $f = 250$ Hz. One can see that the dependence of E on pulse duration τ_p is nearly linearly. Such dependence of pulse energy on gas pressure is also obtained. (See Fig. 2). Fig. 3 presents pulse energy versus input RF power. The average power of laser radiation reaches in these experiments more than 200 W and efficiency is varied from 8% up to 13.5%.

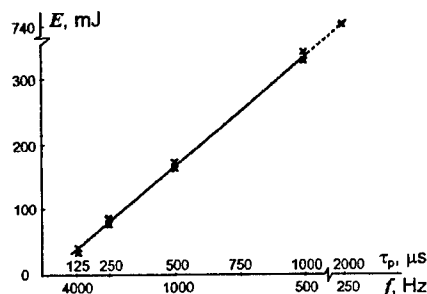


Fig. 1. Dependence of pulse lasing energy on pulse duration for M mode operation.
 $p = 80 \div 90$ torr.
Pulse power $P \approx 2.2$ kW.

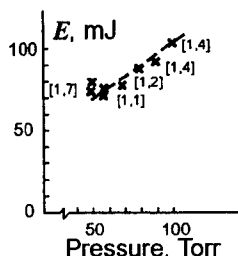


Fig. 2. Dependence of pulse lasing energy on gas pressure for M mode.
 $f = 2000$ Hz. $\tau_p = 250$ μs .
The values in brackets are average pumping powers in kW.

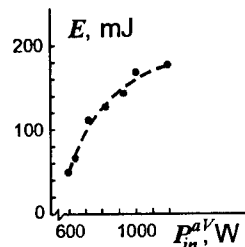


Fig. 3. Dependence of pulse lasing energy on average input power for M mode.
 $f = 1000$ Hz. $\tau_p = 500$ μs .
 $p = 81$ torr.

3.2. PULSE - REPETITIVELY (PR) MODE OPERATION ($\delta = 12.5\%$).

We studied this mode operation of slab CO_2 laser at the gas pressure $p = 40 \div 150$ torr and at the input power $P = 2 \div 5.6$ kW. The volume of active medium was 70 cm^3 , and, consequently, the specific input power was in the range $30 \div 80 \text{ W/cm}^3$. Fig. 4 and Fig 5 present the output lasing energy versus gas pressure for the whole range of pulse duration and PRF. One can see that lasing energy varied from 3 up to 300 mJ, and dependence of E on gas pressure is nearly linearly in the studied range of pulse durations and PRF's. Only for $\tau_p = 30$ μs ($f = 4000$ Hz) the saturation in the dependence of E on pressure was obtained.

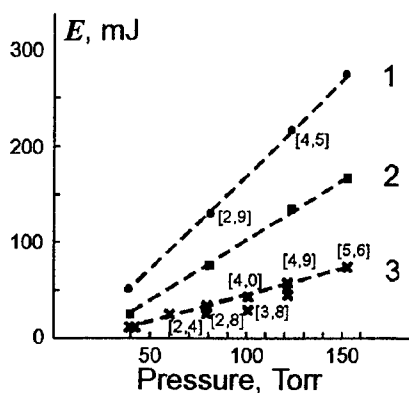


Fig. 4. Dependence of pulse lasing energy on gas pressure for PR mode.

1 - $f = 250$ Hz. $\tau_p = 500$ μ s.

2 - $f = 500$ Hz. $\tau_p = 250$ μ s.

3 - $f = 1000$ Hz. $\tau_p = 120$ μ s.

The values in brackets are average pumping powers in kW

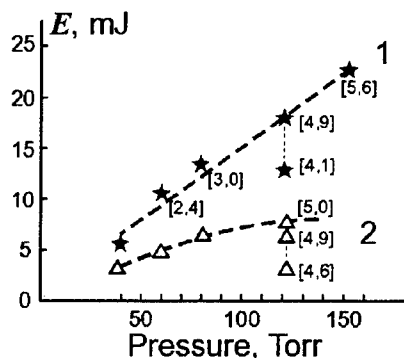


Fig. 5. Dependence of pulse lasing energy on gas pressure for PR mode.

1 - $f = 2000$ Hz. $\tau_p = 60$ μ s.

2 - $f = 4000$ Hz. $\tau_p = 30$ μ s.

The values in brackets are average pumping powers in kW.

4. SHAPE OF LASER PULSES

In these experiments the lasing pulse shape was registered by germanium - based photodetector doped with mercury with time resolution better, then 10^{-7} s. The pumping envelope shape was recorded by means of a loop network placed in RF cable.

The radiation pulses have nearly triangular shape. The pulse rise time was approximately equal to pumping pulse duration τ_p in our range of the gas pressure (40 ÷ 150 torr) and the input power. Intensity maximum is achieved during 5 ÷ 10 μ s after pumping pulse switching-off. The pulse fall time was approximately equal τ_p besides the case of the small pressure and the short pumping pulse duration ($p = 40$ torr, $\tau_p = 30$ μ s). This result is closed to Ref. 4 data obtained for $\text{CO}_2\text{:N}_2\text{:He} = 1\text{:}1\text{:}5$ mixture. For this case pulse fall time was much greater then τ_p . There are not any quasistationary plateau and powerful leader spike in the studied cases. These facts distinguish our case both the TEA lasers and results of Ref. 5 , where in the slab CO_2 laser at the great input power (600 ÷ 700 W/cm^2 , $p = 114$ torr) pulse shape was like TEA lasers one.

Leader spike duration was about 0.5 μ s, peak energy was very small. It is interesting to note that the leader amplitudes for $p = 40 \div 60$ torr were significantly smaller than basic pulse ones (see Fig. 6). If the gas pressure increases ($p = 120 \div 150$ torr) the peak amplitude also increases proportional to pressure and input power. Only if $\tau_p \approx 30$ μ s then the peak amplitude becomes more then basic pulse one.

A small power of the peak can be explained to a moderate level of input power in our experiments. A small part of CO_2 molecules in the mixture is another possible reason. Indeed, we operated with gas mixture initial composition $\text{CO}_2\text{:N}_2\text{:He:Xe} = 1\text{:}1\text{:}6\text{:}0.4$ where CO_2 molecules part is only 12%. It is known dissociation level of CO_2 molecules in RF discharge of the cw CO_2 slab laser reaches up to 70 ÷ 80 %⁶. Therefore, it can suppose that the part of CO_2 molecules in our experiments was still less then initial one.

The obtained results show that it can receive rather smooth lasing pulses with insignificant leader spike by varying gas pressure, mixture composition and using moderate level of RF pumping.

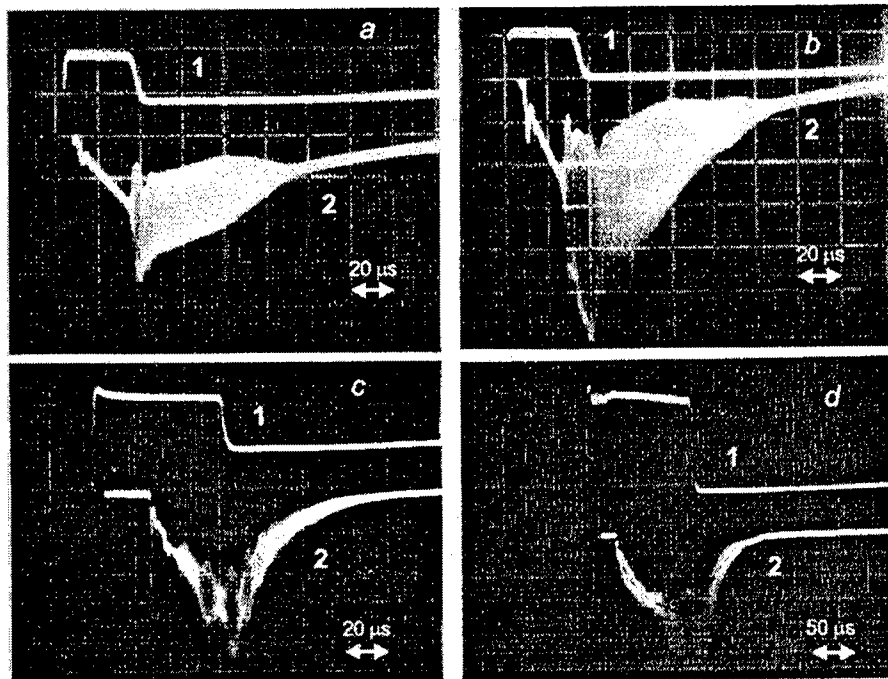


Fig. 6 Oscillograms,

1 - pumping pulse. 2 - lasing pulse.

a) - pulse pumping power - 2 kW. $p = 40$ torr. $f = 4000$ Hz. $\tau_p = 30$ μ s.

b) - pulse pumping power - 2.5 kW. $p = 60$ torr. $f = 4000$ Hz. $\tau_p = 30$ μ s.

c) - pulse pumping power - 4.1 kW. $p = 123$ torr. $f = 2000$ Hz. $\tau_p = 60$ μ s.

d) - pulse pumping power - 5.6 kW. $p = 150$ torr. $f = 1000$ Hz. $\tau_p = 125$ μ s.

5. DIVERGENCE OF LASER RADIATION

For measuring angular divergence we used a two-shoulder scheme². In this scheme the part of radiation power transmitted through the calibrated diaphragm located in the focal plane of the objective was registered. Fig. 7 presents results of measurements for confocal unstable resonator with magnification $M=1.17$. It is seen that divergence of radiation at 0.8 of the total power is about 2 mrad in the horizontal direction and 11 mrad along the vertical direction. The divergence values proved to be close to the diffraction limit⁷. Fig. 7 shows also the total divergence of laser radiation after correction of the vertical component performed by means of a cylindrical lens. The total beam divergence was 2.5 mrad at 0.8 of the total power has been obtained. The beam intensity distribution was found to be near Gaussian one. The divergence of radiation in M mode is practically equal the divergence in PR mode.

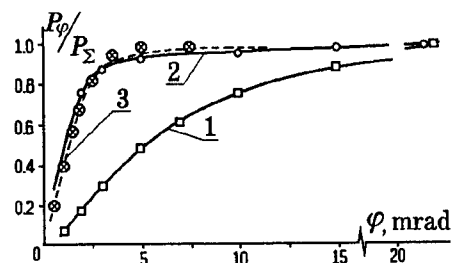


Fig. 7. Angular distribution of radiation power for two coordinates. Radiation power is 200W. Gas pressure 80 torr. 1 - vertical divergence; 2 - horizontal divergence; 3 - total divergence after beam shaping cylindrical lens.

6. CONCLUSIONS

The studies of the two pulse modes operation of slab CO₂ laser with small and moderate pumping power and gas pressure in the range of 40 ÷ 150 torr were carried out. It was shown that it can receive rather smooth lasing pulses with insignificant leader spike by varying gas pressure, mixture composition and using moderate level of RF pumping. These results can be useful for some applications, for example at the fragile materials processing.

7. ACKNOWLEDGMENTS

The authors are grateful to the Bilor Co. LTD (St.-Petersburg, Russia) for financial support of this work.

8. REFERENCES

1. R.T.Brown, "CO₂ TEA lasers", in: *Handbook of Molecular Lasers*. P.K.Cheo, Ed. NY: Dekker, pp. 93 - 164, 1987.
2. A.I.Dutov, A.A.Kuleshov, V.N.Sokolov, "Slab waveguide RF-excited CO₂ laser for material processing", *Proc. SPIE*, Vol. 2713, pp. 51 - 57 (1995).
3. J.Nishimae, K.Yoshizawa, "Development of CO₂ laser excited by 2.45 GHz microwave discharge", *Proc. SPIE*, Vol. 1225, High-Power Lasers, pp. 340-348, (1990).
4. A.D.Colley, F.Villareal, A.A.Cameron, P.P.Vitruk, H.J.Baker, D.R.Hall, "High Power CW Molecular Lasers Using Narrow Gap Slab Waveguides", in: *Gas Lasers - Recent Developments and Future Prospects*, W.J.Witteman and V.N.Ochkin, Eds. 1996. Kluwer Academic Publishers.
5. R.T.Brown, L.A.Newman, M.W.Murray, and R.A.Hart, "Large - Volume Pulsed RF-Excited Waveguide CO₂ Lasers", *IEEE Journ. of Quant. Electronics*, Vol. 28 (2), pp. 404 - 407, (1992).
6. W. Haas, T.Kishimoto, "Investigation of the gas composition in sealed-off RF-excited CO₂ lasers", *Proc. SPIE*, Vol. 1276, pp. 49-56 (1990).
7. A.I. Dutov, I. Yu. Evstratov, V.N. Ivanova, A.A. Kuleshov, S.A. Motovilov, N.A. Novoselov, V.E. Semenov, V.N. Sokolov, M.S. Yur'ev. "Experimental investigation and numerical simulation of slab waveguide CO₂ laser with rf pumping". *Quantum Electronics*. Vol. 26 (6), pp. 484 - 488 (1996).

DIAGNOSTICS OF THE ACTIVE MEDIUM OF AN ELECTRIC-DISCHARGE CO₂ MODULE BY THE "LASER SPECTROGRAPH" METHOD

A A Adamenkov, V V Buzoverya, Yu N Bulkin, Yu V Kolobyatin, E A Kudryashov

Russian Federal Nuclear Centre (VNIIEF), 607190, Sarov, Nizhni Novgorod Region, Russia
Fax: (831) 30 54565; Phone: (831) 30 56646, e-mail: bulkin_2566@rfnc.nnov.su

ABSTRACT

The gains were measured for the lines in the traditional band 00^01-10^00 , 00^01-02^00 , in the second band of the 00^02-10^01 sequence, and in the hot band 01^11-11^10 emitted by the active medium of an electric-discharge CO₂ module. The experimental results were used in a generalised theoretical model to find the translational and vibrational temperatures, and the concentration of the active molecules. The Fermi resonance between the 10^00 and 02^00 did not ensure a Boltzmann distribution of their populations under the conditions in the electric-discharge module. The degree of dissociation of the CO₂ molecules in the discharge did not exceed 22% when the maximum input power density was near 6 W/cm³.

Keywords: line, band, gain, sequence, medium, electric-discharge, dissociation, translational, vibrational, temperature, population, concentration

Information on the parameters of the active media is essential for the optimisation of the operational characteristics of molecular lasers. In the case of CO₂ lasers these parameters are the translational and vibrational temperatures T , T_1 , T_2 , T_3 [1], and the concentration n of the active molecules. The vibrational temperatures in the active medium of an electric-discharge CO₂ laser have been determined experimentally on a number of occasions (see, for example, Refs [2-5]). However, the vibrational temperature T_1 of the lower active level has not been found (and we have shown [6] that this may lead to a large error in determination of the concentration n), and the remaining temperatures have been calculated on the basis of an approximate model. It has been shown theoretically in Ref [7-8], that the parameters of an inverted medium can be determined unambiguously without any simplifying assumptions if the gains have been measured for the lines in four bands: the traditional bands 00^01-10^00 and 00^01-02^00 , the second sequence band 00^02-10^01 , and the hot band 01^11-11^10 . In Ref. [9] the literature data on the gain measurements for the lines in traditional bands 00^01-10^00 and 00^01-02^00 of continuous operating and pulsed CO₂ lasers have been analysed. On the basis of this analysis it was shown, that under any experimental conditions, performed in the above papers, no vibrational equilibrium has occurred between symmetric (ν_1) and bending (ν_2) modes. In Ref. [6], describing the diagnostics of the active medium of the waveguide CO₂ laser, it was confirmed the absence of an equilibrium between the symmetric and bending modes; the experiments show that the difference between vibrational temperatures T_1 and T_2 achieved the value of 150 K and increased with the increase of the discharge current. In Ref. [10], describing the diagnostics of the active medium of the homogeneous gasdynamic CO₂ laser, it was shown, that the Fermi resonance between the 10^00 and 02^00 levels does not ensure a Boltzmann distribution of their populations, and consequently the vibrational temperature for a symmetry mode $T_1 > T_2$ and the difference between the values of temperatures reach up to 0.5 T_2 , when the stagnation pressure is decreased. Dissociation of the CO₂ molecules was not detected in the active medium of homogeneous gasdynamic laser.

Our aim was to determine the translational and vibrational temperatures, and the concentration of the active molecules in an electric-discharge CO₂ module from the experimentally determined gains using the theoretical scheme, put forward in Ref. [7-8]. This electric-discharge CO₂ module is distinguished from the waveguide CO₂ laser, investigated formerly in Ref. [6], mainly by the essentially smaller specific input power. An important aspect of this work was the versatility demonstration of the "laser spectrograph" method, which had been evaluated by us previously in Ref. [6,10] at the waveguide and gasdynamic CO₂ laser active media diagnostics.

An electric-discharge CO₂ module (an active cell), manufactured from molybdenum glass, consists of discharge tube (\varnothing 15 mm, $L \approx 140$ cm), jacket cooling system and reserve balloon. The output windows, sealed in the metallic end face sections, were manufactured from the gallium arsenate. A cylindrical electrode placed into one of the end face section served as an anode. The separate glass bulb, placed at the other end face section, contained a cathode. Discharge gap was about 118 cm. A dc discharge was excited by a high-voltage power supply unit taken from an industrial ILGN-704 laser.

Cooling was made by the circulating flux of the 40% ethillemum alcohol. In the stable operational regime of the active cell, the temperature of the cooled liquid was supported near $T_{cool} \approx 265K$ by means of heat interchanger. An active cell was filled with working mixture of $14 CO_2 + 20 N_2 + 70 He + 6 Xe$ composition of dry gases. The gas pressure in the tube was 10 Torr.

Table 1 lists the values of the discharge current I , of the voltage U , of the electrical power P delivered to the discharge, and of the pump power per unit volume S . The schematic diagram of the apparatus used in measurements of the gains of the different lines in the active medium of the CO_2 laser is shown in Fig.1. The apparatus was similar to that described earlier [6] except that in the present paper an automatic CO_2 laser, developed by ourselves, tunable through the lines of five bands was used as a probe CO_2 laser.

Table 1. Parameters of the electric discharge in the electric-discharge CO_2 module

I (mA)	U (kV)	P (W)	S (W/cm ³)
9	10.5	94.5	1.82
16	9.5	152	2.92
24	8.5	204	3.92
32	8.0	256	4.92

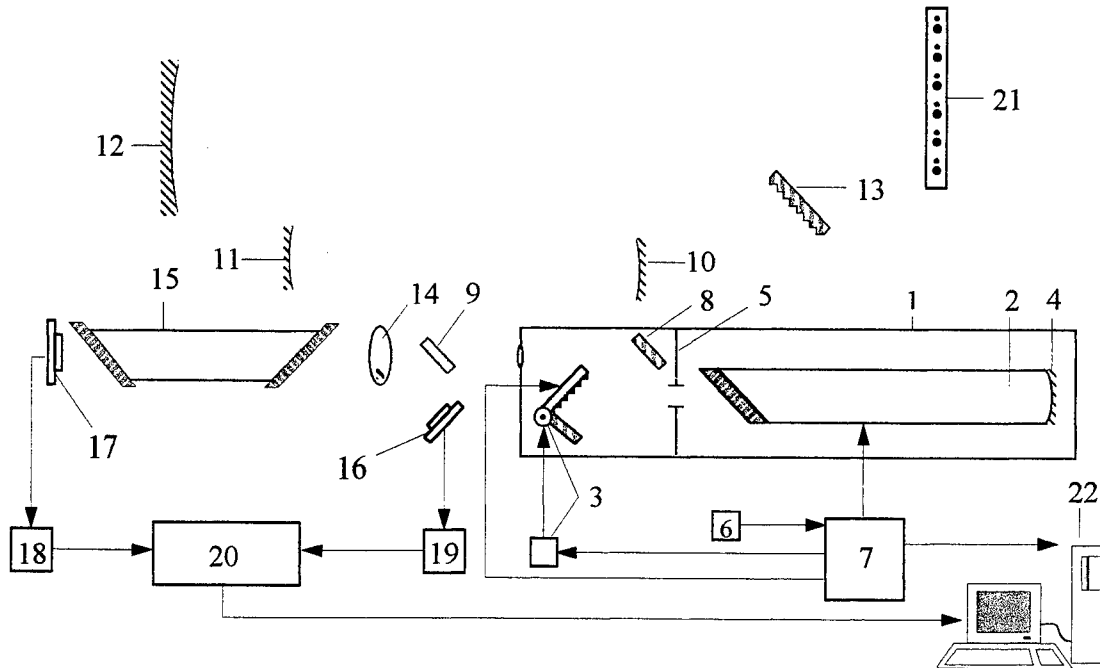


Fig.1. Schematic diagram of the apparatus used in measurements of the different lines gains in four bands

(00^01-10^00 , 00^01-02^00 , 00^02-10^01 , 01^11-11^10) in the active medium of the electric-discharge CO_2 module:

1 - automatic tunable CO_2 laser; 2 - active cell; 3 - assembly for the corner reflector positioning with diffraction grating and piezocorrector; 4 - nontransmitting mirror with $R=3$ m; 5 - diaphragm; 6 - pyroreceiver (MG-30); 7 - power supply, blocks for the automatic trimming system and step motor control system; 8 - turning mirror; 9 - NaCl deviating plate covered by dielectric material; 10, 11, 12 - spherical mirrors; 13 - diffraction reflective grating; 14 - chopper; 15 - electric-discharge CO_2 module; 16, 17 - pyroreceivers; 18, 19 - amplifiers; 20 - analog-to-digit converter; 21 - thermoscreen; 22 - personal computer.

The gains of the active medium were measured for the following five lines: P(18) in the 00^01-10^00 band, P(40) (00^01-10^00), P(18) (00^01-02^00), P(33) (00^02-10^01), and P(19) (01^11-11^10). These specific lines were selected on the basis of the following criteria. All of them should not be too close to the adjacent lines. For this reason we selected P(18) and not P(20) line from the 00^01-10^00 band, since the P(20) line was located close to the P(23) line in the hot band 01^11-11^10 ($\Delta\lambda \approx 0.01$ cm⁻¹). The fairly distant P(40) line in the 00^01-10^00 band was selected to reduce the error in determination of the

translational temperature T . The P(18) (00^01-02^00) line was chosen to simplify the calculations (its rotational number was $J = 18$, which was the same as for the 00^01-10^00 band). The P(19) line in the 01^11-11^10 band and the P(33) line in the 00^02-10^01 band were selected because they were sufficiently powerful and well-resolved. The measurements were carried out at the centre of the gain profile of each line in the active medium of the electric-discharge module. The probe radiation power was always sufficiently low to avoid the saturation effect. Let's mark, that the gain integrated over the cross section was determined during the probe. Ten measurements of gain were made for each of the five lines and this was done at four different values of the discharge current ($I = 9, 16, 24$, and 32 mA). Then the standard method [11] of the experimental data processing was used to find the average value of the gain and the error. The experimental values of the gain k , obtained at different values of the discharge current, are listed in Table 2 for five lines.

Table 2. Experimentally determined gain.

Discharge current (mA)	Line gain, $k(m^{-1})$				
	P(18) 00^01-10^00	P(40) 00^01-10^00	P(33) 00^02-10^01	P(19) 01^11-11^10	P(18) 00^01-02^00
9	0.898	0.357	0.187	0.102	0.766
16	0.751	0.340	0.229	0.119	0.681
24	0.634	0.319	0.245	0.123	0.513
32	0.507	0.297	0.226	0.102	0.465

The temperature model of Ref.[1,7-8] was used to write a system of four equations with four unknowns T , χ_1 , χ_2 , and χ_3 . The system can then be solved quite readily by a numerical method. This numerical solution can be obtained by taking the probabilities of the spontaneous radiation $A(J)$ and the collisional width of the laser transition from Ref.[8] and the rotational constants B_{m,l_s} from Ref.[12], and substituting the experimental gains from Table 1 in place of k_i . The translational and vibrational temperatures obtained in this way can then be substitute, for example, in the expression for the gain of the P(18) (00^01-10^00) line, which yields the concentration of the CO_2 molecules. Table 3 lists the calculated values of the temperatures T , T_1 , T_2 , and T_3 and the concentrations n of the CO_2 molecules in the active medium of the electric-discharge module.

For clarity, the results obtained are plotted in Fig.2 in the form of the dependencies of the translational and vibrational temperatures on the discharge current. We can see that an increase in the discharge current (and, consequently, in the specific input energy) results in saturation of the temperature T_3 (as against Ref.[6]). Obviously, this can be explained by the relatively low specific input power ($1.8...5$ W/cm³), which is typical of electric-discharge CO_2 lasers operating at a low pressure of the working mixture. The other temperatures T , T_1 , and T_2 increase linearly. The linear increase of the difference between T_2 and T , occurred when the discharge current is increased can be attributed to the interaction between the vibrational energy of the mode ν_2 and kinetic energy, determined by equation:

$$dE_2(T_2)/dt = -[E_2(T_2) - E_2(T)]/T_2$$

For the relatively low T the velocity of the mode ν_2 cooling is proportional to T_2-T , and because of the flux of energy to the mode ν_2 is proportional to the discharge current, the difference T_2-T is proportional to the discharge current, too [13].

Another important result is that the difference between the vibrational temperatures T_1 and T_2 is fairly large and that this difference increases, when the discharge current is increased, i.e. in the electric-discharge CO_2 module the Fermi resonance between the 10^00 and 02^00 levels does not ensure an equilibrium between T_1 and T_2 .

Table 3. Calculated temperatures and concentrations of active molecules in the medium of the electric-discharge CO_2 module.

I(mA)	T(K)	T_1 (K)	T_2 (K)	T_3 (K)	n(%)
9	389	513	452	1664	11.4
16	419	646	531	1963	10.6
24	448	718	596	2192	10.1
32	500	740	633	2284	9.9

Fig.3 demonstrates the dependence of the CO_2 molecules concentration on the discharge current. It was interesting fact, that the degree of dissociation of the CO_2 molecules occurred insignificant under the conditions of our experiment

and did not exceed 25% even for the maximum discharge current. Small dissociation degree molecules can likely to be explained by such fact that electric-discharge CO₂ module switched on only for the time of measurement, which was a few minutes for each line, and before every measurement a mixture had been renovated.

The majority of the reported determinations of the concentration of the CO₂ molecules were made by either chromatographic or mass-spectroscopic methods (see, for example, Ref.[14]). In both cases a sample was taken from the exit of the gas-circulation system. The 'laser spectrograph' method described above made it possible to determine the concentration to the CO₂ molecules directly in the charge. Therefore, we were able to carry out, for the first time, a full diagnostic analysis of an electric discharge CO₂ laser and to find the main parameters of the active medium (T, T_1, T_2, T_3, n) in the operating regime, which could then be used to predict the energy characteristics of lasers of this type more precisely.

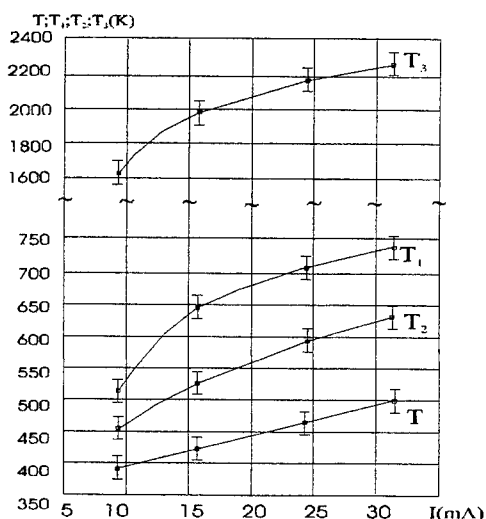


Fig. 2. Dependences of the translational (T) and vibrational (T_1, T_2, T_3) temperatures on the discharge current.

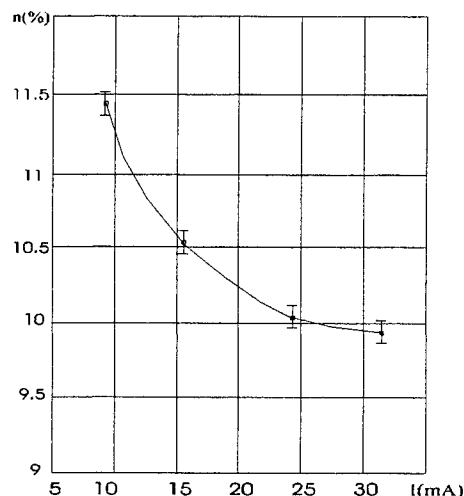


Fig.3. Dependences of the concentration n of the CO₂ molecules on the discharge current.

REFERENCES

1. Gordiets B F, Osipov A I, Shelepin L A *Kineticheskie Protssessy v Gazakh i Molekularnye Lazery* (Kinetic Processes in Gases and Molecular Lasers) (Moscow: Nauka, 1980)
2. Bertel' I M, Petukhov V D, Solodukhin A S, et al., in *Neravnovesnye Prozessy v Gasovoi Dinamike* (Nonequilibrium Processes in Gas Dynamics) (Minsk: Institute of Heat and Mass Transfer, Academy of Sciences of the Belorussian SSR, 1983) pp 86-120
3. Siemsen R.J., Reid J., Dang G. *IEEE J. Quantum Electron.*, QE-16 668 (1980).
4. Brimacombe R.K., Reid J. *IEEE J. Quantum Electron.*, QE-19 1674 (1983).
5. Reid J., Chewchun J., Garside B.K. *Appl. Phys.*, 17, 348 (1978).
6. Adamenkov A A, Buzoverya V V, Bulkin Yu N, et al., *Kvantovaya Elektron. (Moscow)* 22 29 (1995) [*Quantum Electron.* 25 23 (1995)]
7. Artamonov A V, Gontar' V G, Surgutenko *Kvantovaya Elektron. (Moscow)* 10 1088 (1983)
8. Nevdakh V V *Kvantovaya Elektron. (Moscow)* 12 2437 (1985) [*Sov.J. Quantum Electron.* 15 1610 (1985)]
9. Nevdakh V V *Kvantovaya Elektron. (Moscow)* 12 1324 (1985)
10. Adamenkov A A, Bulkin Yu N, Kolobyanin Yu V et al., *Kvantovaya Elektron. (Moscow)* 22 117 (1995)
11. Taylor J R *Error Analysis: The Study of Uncertainties in Physical Measurements* (Mill, CA: University Science Books, 1982)
12. Rothman L.S. *Appl. Optics*, 25, 1795 (1986)
13. Witteman W J. CO₂-laser (The CO₂ Laser) (Moscow: Mir 1990)
14. Zhang X.S., Baker H.R., Hall D.R. *J.Phys.D.*, 26, 359 (1993).

Growth and characterization of Nd:YAG epitaxial planar waveguides by pulsed laser deposition

Mizunori Ezaki*, Hiroshi Kumagai, Kyoichi Adachi*, Koichi Toyoda, Minoru Obara*

RIKEN, the *Institute of Physical and Chemical Research*
2-1 Hirosawa, Wako, Saitama, 351-01, Japan
TEL: +81-48-462-1111 ex.4523, FAX :+81-48-462-4682
e-mail: ezaki@riken.go.jp

*Department of Electrical Engineering,
Faculty of Science and Technology, Keio University
3-14-1 Hiyoshi, Kohoku-ku, Yokohama 223, Japan

ABSTRACT

Epitaxial rare-earth (Re: Nd, Yb) doped yttrium aluminum garnet ($\text{Re}_x\text{Y}_{3-x}\text{Al}_5\text{O}_{12}$ or Re:YAG) films have been grown on various substrates by pulsed laser deposition for the purpose of fabricating diode-pumped waveguide lasers. The films were characterized by Rutherford backscattering, x-ray diffraction, and photo-luminescence measurements. These Nd:YAG films on (100) silicon substrate having a large lattice mismatch show oriented stoichiometric growth. On the other hand, the films of rare-earth doped YAG on garnet substrates show the epitaxial growth with the smooth surfaces. Their characterization of rare-earth doped YAG thin films on various substrates was comparable to that of the Nd:YAG bulk laser crystal.

Keywords: waveguide lasers, pulsed laser deposition, Nd:YAG, Yb:YAG, rare-earth doped laser crystal, waveguide structure, solid-state lasers, micro-chip lasers

1. INTRODUCTION

The solid-state laser crystal with waveguide structure has several advantages over bulk one due to the optical confinement which leads to the low-threshold and efficient oscillation. A common solid-state laser material consists of an optically transparent host such as glass, YAG ($\text{Y}_3\text{Al}_5\text{O}_{12}$) sapphire (Al_2O_3), etc., doped with a small amounts of rare-earth oxides. Among various solid-state laser media, rare-earth-doped yttrium aluminum garnet (such as Nd:YAG, Yb:YAG) waveguide has strong potential for application to diode-pumped waveguide lasers¹⁻³ and is desirable for integrated optoelectronics applications such as Q-switched microchip lasers which can be realized by monolithically combining their waveguide lasers with other optical components (e.g. Cr:YAG thin film) on the same substrate^{4,5}. Thus, the possibility of fabricating rare-earth doped YAG thin films with waveguide structure on various substrates will widen their applications in the fields of integrated optics.

The Nd:YAG and Yb:YAG waveguides on various substrates were prepared by pulsed laser ablation of Nd_2O_3 - Y_2O_3 - Al_2O_3 and Yb_2O_3 - Y_2O_3 - Al_2O_3 sintered mixtures, respectively; the guiding structure was made either by depositing a layer of rare-earth doped YAG on undoped-YAG substrate which have a lower refractive index, or by successive deposition of two layers with respective refractive indices of n_2 - n_1 ($n_1 < n_2$) on Si, GGG substrates⁶. The latter process allows the difference in refractive index to be controlled by modifying the rare-earth ion (Nd^{3+} and Yb^{3+}) content of YAG layer; thus single-mode guides can be obtained. Since silicon is the most developed material for electronics, the use of it as a substrate may lead to the realization of combining Si electronic devices with the optical waveguide on the same Si substrate. However, Si substrate have the different crystal structure (cubic, diamond) with a relatively small lattice constant of 5.43072\AA as compared with that of YAG (misfit factor (m.f.) = $100 \times |a_{\text{YAG}} - a_{\text{sub}}| / a_{\text{sub}} = 54.8\%$), while the GGG ($\text{Gd}_3\text{Ga}_5\text{O}_{12}$) and SGGG (Zr- and Sc-doped $\text{Gd}_3\text{Ga}_5\text{O}_{12}$, *Crismatec Company*) substrates have the same garnet structure as the Nd:YAG films (cubic, $Ia3d$). These lattice constants of GGG and SGGG are 12.376\AA (m.f. = 4.02%) and 12.492\AA (m.f. = 3.06%), respectively which are slightly larger than of YAG, 12.0089\AA ⁸. In this letter, we report the preparation of high-quality rare-earth doped YAG thin films on various substrates by PLD, and then the evaluation of the structure, crystallinity and optical property of the deposited films.

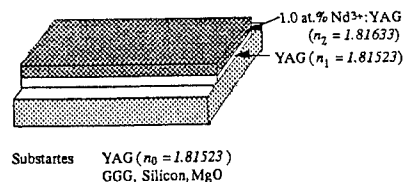


Fig.1. Rare-earth doped YAG planar waveguide.

2. EXPERIMENTAL

A high-purity(99.99%), high-density sintered pellet prepared by mixing appropriate amounts of Y_2O_3 , Al_2O_3 and Nd_2O_3 or Yb_2O_3 was used as a target for the deposition process. The KrF excimer laser beam (wavelength : 248 nm, repetition rate : 10 Hz, pulse-width : 30 ns, fluence : $1.0\text{--}5.3 \text{ J/cm}^2$) was focused with a lens onto the target rotating at about 30 rounds per minute in a stainless-steel vacuum chamber as shown in Fig. 2. Single-crystal (100)-oriented Si, (111)-oriented GGG, and YAG wafers were used as substrates which was loaded in the vacuum chamber and fixed on the black quartz that was put on the quartz rod, through which infrared rays were introduced, and then the substrate was heated up to substrate temperature (T_{sub}) of $100\text{--}970^\circ\text{C}$. The stage temperature was determined by a thermocouple embedded in the stage just below the substrate surface. Prior to the insertion into the chamber, the silicon wafers were ultrasonically cleaned with acetone and then dipped in 4.7 % HF to remove the native oxide. All rare-earth-doped yttrium aluminum oxide films were formed in vacuum at a pressure of $3.0\text{--}5.0 \times 10^{-7}$ Torr. The composition, crystalline quality and orientation of the films were investigated by Rutherford backscattering spectrometry (RBS), x-ray photo-electron spectroscopy (XPS) and x-ray diffraction (XRD). The surface topography of the films was determined by atomic force microscopy (AFM). The optical properties of rare-earth doped YAG thin films were investigated by photoluminescence measurements.

3. RESULTS & DISCUSSION

3.1. Composition of the film by PLD

Rutherford backscattering (RBS) experiments were carried out on the films to determine the composition. Figure 2 shows RBS spectrum from the film deposited at 500°C by using 20 at.% Yb doped stoichiometric target, along with the simulated spectrum for a film thickness of 89 nm and a composition of $\text{Yb}_x : \text{Y}_{3-x}\text{Al}_5\text{O}_{12}$ ($x=0.60$, Yb: 20.0 at.%). The good fit between the experimental spectrum and the simulated spectrum (dotted line) indicates that the composition of the film is the same as that of Yb:YAG gamet crystal. The composition of Nd doped YAG films on (100) oriented Si and (111)-oriented YAG substrates was also determined from the RBS and XPS analyses to be $\text{Nd}_x : \text{Y}_{3-x}\text{Al}_5\text{O}_{12}$ ($x=0.011\text{--}0.25$, Nd: 0.37-8.3 at.%)⁶.

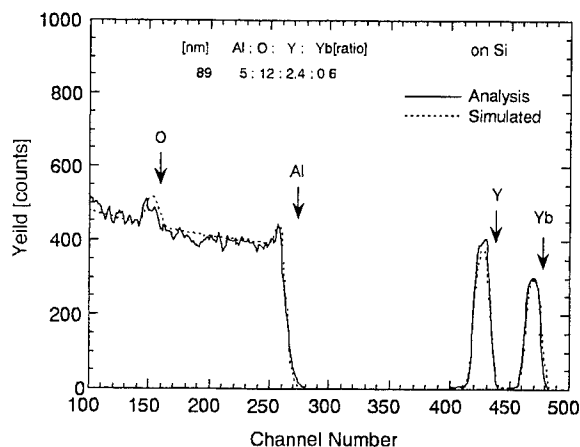


Fig. 2. Rutherford backscattering spectrum of Yb:YAG film grown on (100) Si substrate at 500°C . The line is the experimental result and the dotted line represents the fit obtained assuming the compositions described in the figure.

3.2. The film structure and crystallinity

The film structure and crystallinity were characterized by x-ray diffraction technique ($\text{Cu } K\alpha$ radiation). Figure 3 shows the XRD diffraction pattern of a typical Nd-doped yttrium aluminum oxide film deposited at $T_{\text{sub}} = 700^\circ\text{C}$. The XRD patterns have a sharp peak at 33.54° which corresponds to the (420) reflection of the YAG phase at 33.32° . Textured Nd:YAG crystalline thin films have been grown on Si single-crystal substrate by the pulsed laser deposition technique for the first time, despite the large lattice mismatch of 54.8 % to YAG⁶. From XRD analysis, it indicates that the films grown at $T_{\text{sub}} < 500^\circ\text{C}$ have amorphous structure and the films grown at $500^\circ\text{C} < T_{\text{sub}} < 700^\circ\text{C}$ have poly-crystalline structure.

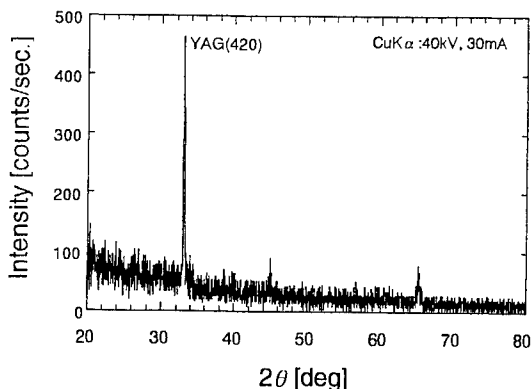


Fig. 3. X-ray diffraction pattern of Nd-doped YAG thin films grown on Si(100) at 700°C .

Figure 4 shows a cross-sectional SEM photograph of a typical bilayer of Yb:YAG (Yb: 20.0 at.%) and undoped YAG grown on (111) GGG substrate under the conditions mentioned above with laser fluence 4.5 J/cm^2 , T_{sub} at 500°C and post-annealed with T_{sub} at 980°C . The thickness of Yb:YAG and undoped-YAG layers were $9.3 \mu\text{m}$ and $3.6 \mu\text{m}$, respectively.

In this photograph there were some droplets which will increase the waveguide loss. However, under the appropriate experimental conditions (lower laser fluence, target-substrate distance), the films with very smooth surface could be obtained. Then the films on SGGG and YAG substrates have smooth surfaces with the standard deviation of surface roughness of 1.31 nm and 0.56 nm , respectively⁶.

Figure 5 shows a x-ray diffraction pattern of a typical Yb:YAG (Yb: 20.0 at.%) and undoped YAG bilayer grown on (111) GGG substrate as shown in Fig.4. In addition to a strong (444) peak of GGG substrate, there is a peak at 51.96° (d spacing of 1.7584\AA) which corresponds to the (444) reflections from Yb:YAG and non-doped YAG bilayer. Epitaxial films of Nd:YAG and undoped YAG were also grown on (111)-oriented GGG and SGGG substrates.

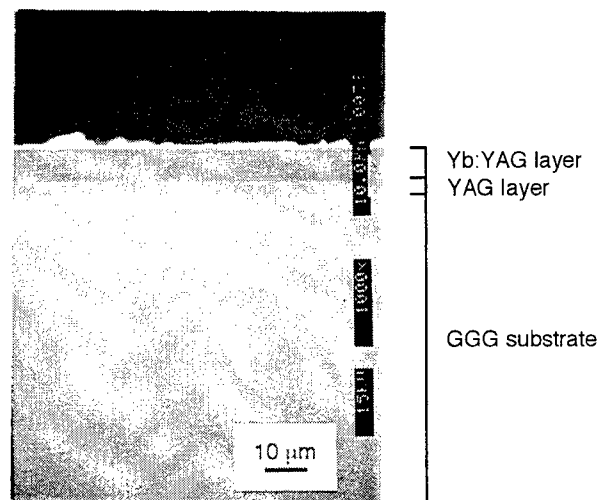


Fig. 4. Cross-sectional SEM image of bilayer of Yb:YAG and undoped-YAG grown on GGG(111) substrate.

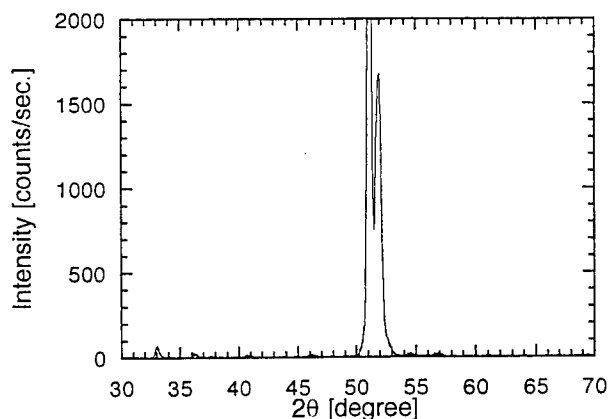


Fig.5. X-ray diffraction pattern of bilayer of Yb:YAG (Yb: 20.0 at.%) and undoped YAG grown on (111) GGG substrate.

3.3. Optical properties of the film by PLD

The refractive index of the film was measured by a variable-angle spectroscopic ellipsometer (VASE) made by J.A. Woollam Company. Then the optical constants were determined by numerically fitting the VASE data and the index of refraction n for Nd:YAG/YAG bilayer on GGG were given as⁹

$$n(\lambda) = 1.7845 \pm 0.0139 + (0.10155 \pm 0.00989) / \lambda^2 + (0.10155 \pm 0.00989) / \lambda^4$$

$$n(1.064 \mu\text{m}) = 1.824 \pm 0.024$$

This index agrees well with one of YAG and Nd1.0 at.% doped YAG ($n(1.064 \mu\text{m}) = 1.81523$ and 1.81633 , respectively). However, the small difference between Nd:YAG and YAG layers couldn't be detected in this case by using the VASE.

The optical properties of Nd:YAG thin films on Si(100) and YAG(111) substrates were also investigated by photoluminescence (PL) measurements. Photoluminescence spectra of Nd:YAG films were excited with 808 nm radiation from Ti:Sapphire laser. The $^4F_{3/2} \rightarrow ^4I_{11/2}$ transitions of Nd^{3+} ions in YAG in the region of $1.06 \mu\text{m}$ were observed clearly for the films

grown on Si(100) at T_{sub} greater than 600°C. On the other hand, the transitions of Nd^{3+} ions for the film grown at T_{sub} lower than 500°C exhibits a broad peak because the films were amorphous. Epitaxial films of Nd:YAG were grown on (111)-oriented YAG, GGG, SGGG substrates. Figure 6 shows the PL spectrum of 2.1 μm -thick epitaxial Nd:YAG film on YAG substrate grown at $T_{\text{sub}} = 910^\circ\text{C}$. $^4F_{3/2} \rightarrow ^4I_{9/2}$ and $^4F_{3/2} \rightarrow ^4I_{11/2}$ transitions of Nd^{3+} ions in YAG in the region of 0.9 μm and 1.06 μm were observed clearly. The PL spectrum was the same as that of the Nd:YAG bulk crystal.

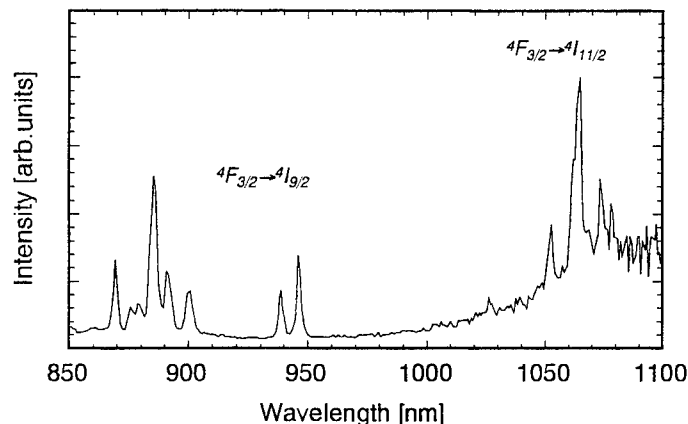


Fig. 6. Photoluminescence spectrum of Nd:YAG epitaxial planar waveguide grown on (111) undoped YAG substrate.

4. SUMMARY

In summary, epitaxial films of rare-earth doped YAG were prepared on (111) garnet substrates by Pulsed Laser Deposition (PLD). The films of Nd:YAG on Si show oriented stoichiometric growth despite the large lattice mismatch of 54.8 % with YAG. The x-ray diffraction and photoluminescence spectra indicate that the film is a Nd doped YAG crystal comparable to bulk laser one. These results suggest that PLD can be an alternative growth scheme that offers the potential to produce optical thin films with quality rivaling that of LPE- and MOCVD-grown films.

5. ACKNOWLEDGMENT

The authors would like to acknowledge assistance from Professor H. Takai, T. Hiwatari and M. Jyumonji of Tokyo Denki University for the RBS and X-ray diffraction measurements. The authors also wish to acknowledge Mr. Michio Suzuki of J.A. Wollam Company for ellipsometry measurements.

One of the authors, M. Ezaki gratefully acknowledges the research support by The Foundation "Hattori-Hokokai". This work was also partially sponsored by the Research Fellowships of the Japan Society for the Promotion of Science. M. Ezaki acknowledges the Research Fellowships of the Japan Society for the Promotion of Science for Young Scientists.

REFERENCES

- 1) I. Chartier, B. Ferrand, D. Pelenc, S.J. Field, D.C. Hanna, A.C. Large, D.P. Shepherd and A.C. Tropper: *Opt. Lett.* **17**, 810 (1992).
- 2) D.C. Hanna, A.C. Large, D.P. Shepherd, A.C. Tropper, I. Chartier, B. Ferrand and D. Pelenc: *Appl. Phys. Lett.* **63**, 7 (1993).
- 3) I. Chartier, Ch. Wyon, D. Pelenc, B. Ferrand, S.J. Field, D.P. Shepherd and D.C. Hanna, *Mater. Res. Soc. Symp. Proc.* **329**, 179 (1994).
- 4) J.J. Zayhowski and C. Dill III, *Opt. Lett.* **19**, 1427 (1994).
- 5) S. Zhou, K.K. Lee, Y.C. Chen and S. Li, *Opt. Lett.* **18**, 511 (1993).
- 6) M. Ezaki, H. Kumagai, K. Toyoda, and M. Obara, *Jpn. J. Appl. Phys.* **34**, 6838 (1995).
- 7) X-ray powder diffraction data card: JCPDS #13-0493.
- 8) X-ray powder diffraction data card: JCPDS #33-40.
- 9) H. Kumagai, M. Matsumoto, K. Toyoda, M. Obara, M. Suzuki, *Thin Solid Films*, **263**, 47 (1995).

Passive Q-switching of high power solar-pumped Nd:YAG laser

Idit Pe'er, Nir Naftali, Dov Abramovic, Yoram Noter, Amnon Yogev
Weizmann Institute of Science, Rehovot 76100, Israel

Mordechai Lando, Yehoshua Shimony
Rotem Industries, P.O.B. 9046, Beer-Sheva 84190, Israel

ABSTRACT

High power lasers operating at high repetition rates at the kilohertz regime are attractive for a variety of applications. Such high repetition rates can be achieved by Q-switching a CW laser using either an acousto-optic, an electro-optic or a passive Q-switch. Since passive Q-switching needs no external electric circuit, it may be valuable for solar pumped lasers to be used at space. In recent years, Cr^{4+} :YAG has been extensively used for passive Q-switching of flashlamp pumped Nd:YAG lasers. For high average power lasers, the excellent thermal characteristics of Cr^{4+} :YAG give it an edge over other saturable absorbers. In the present paper we report on the first passive Q-switching of solar pumped high power Nd:YAG laser. This solar pumped Nd:YAG laser, which employed 3 and 4 mm diameter Nd:YAG rods, emitted up to 50 watts in the CW mode. The laser rod was side-pumped by solar irradiation using a three stage concentrating system. The Cr^{4+} :YAG device rear surface was coated by high reflection dielectric coating, serving as cavity rear mirror, while the output mirror had a reflectivity of 90%. An average output power of 9 watts was obtained from the passive Q-switched solar pumped laser at 15-40 kHz, twice previous results for a passive Q-switched Nd:YAG laser, results which had been obtained under continuous flashlamp pumping.

Keywords: Cr:YAG, Nd:YAG, saturable absorber, Q-switch, concentration, solar laser, repetition rate, thermal

1. INTRODUCTION

In the last decade, solar pumped lasers attracted much attention as candidates for wireless power transmission in space^{1,2}, for free space optical communication and for photochemistry³. The resulted research of solar pumped solid state lasers succeeded in achieving efficiencies of several percents^{4,5}, CW output power in the hundreds watts regime⁶, and tunable lasing. Solar pumped lasers have been operated in a variety of configurations; stand alone oscillator, a cluster of rods in common resonator⁵, and a master oscillator power amplifier(MOPA)⁷. For various applications, it may be needed to shape the temporal and spectral characteristics of the solar pumped laser beams, by turning the laser into a high repetition rate mode of operation, and shifting the laser output frequency via non-linear interactions. High repetition rates are achieved by switching the Q-factor of the laser resonator by either of the conventional techniques. Passive Q-switching a laser potentially offers the advantages of low cost, reliability and simplicity in fabrication and operation compared to acousto-optic or electro-optic active techniques. This is of special importance for space based applications, in which one would like to minimize electrical power usage.

In the past, Cr^{4+} :YAG have been used as a passive Q-switch for pulsed Nd:YAG lasers, and recently it was also introduced by Shimony *et al*⁸ as passive Q-switch for continuously flashlamp pumped solid state laser. This was made possible due to the excellent thermal characteristics of the YAG host material. Shimony *et al*⁸ have obtained up to 4 watts of average power at rates of 2-29 kHz, and 80-300 ns pulsewidths, without active cooling of the Cr^{4+} :YAG crystal.

In the present paper we report on the first operation of a passive Q-switched solar pumped Nd:YAG laser. An average power of 9 watt at 36% switching efficiency was obtained, using water cooled Cr^{4+} :YAG saturable absorber. The three stage solar concentrator, which was employed for pumping the laser, the resonator and the experimental results are discussed in the next sections.

2. EXPERIMENTAL

Solar radiation has a relatively low power density, of less than 1000 W/m^2 . To overcome the lasing threshold, the pump power density must be increased by a combination of imaging and non-imaging optics⁴. The present study was performed at the Solar Tower at Weizmann Institute^{6,7}, and the solar radiation was concentrated before pumping the Nd:YAG laser by a three stage solar concentrator. The first concentrating stage was composed of 3-10 Fresnel parabolic heliostats, each having an area of 56 m^2 . The concentrated light then enters a reflective 3-D compound parabolic concentrator (CPC), and finally a reflective 2-D CPC.

The laser oscillator, including the 2-D CPC, is depicted in Fig. 1. Over 90% of the solar radiation entered at the rectangular 2-D CPC entrance, irradiates the laser rod, located along the 2-D CPC axis. The laser rod is placed within a quartz jacket which allows a flow of organic liquid of high refractive index to cool the laser rod. The organic liquid in turn is cooled down by liquid nitrogen in a separate heat exchanger. The 7.7mm diameter 1.48mm thick Cr^{4+} :YAG disk, shown in Fig. 2, served as both passive Q-switch and rear mirror. For this sake, it was coated on both sides; the front surface was anti-reflection coated to prevent parasitic lasing, and the water cooled back surface had high reflection coating for $1.06\mu\text{m}$. With doping level at 0.25% ionic weight, the measured non-saturable transmission of the Cr^{4+} :YAG was found to be 72%, while the plane output mirror had 90% reflectance. The power emitted was monitored with an Ophir power meter, while small portion of the beam was deflected towards a pin-photodiode, connected to a Le-Croy oscilloscope. The solar pumping power was measured calorimetrically by the difference of the laser rod coolant at entrance and exit of the cooling jacket.

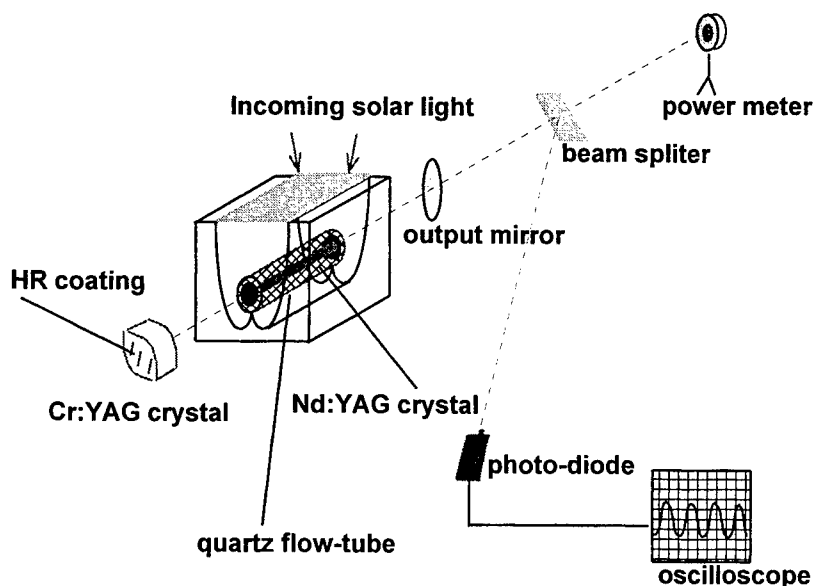


Fig. 1. The passive Q-switch experimental system

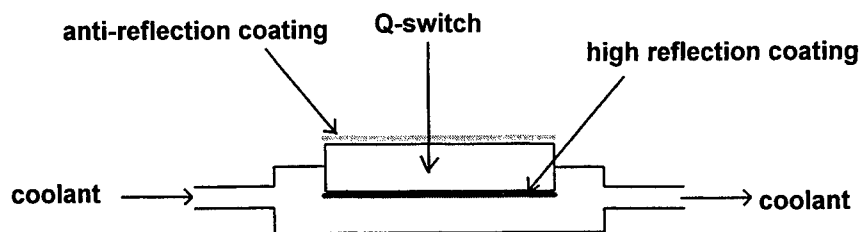


Fig.2 The passive Q-switch device, which served also as rear mirror

3. RESULTS

Initial experiments have been conducted with a 4 mm laser rod, emitting 50 watt CW power, and resulted in 5 watt Q-switched power in 180 ns pulses and repetition rate of 11.9 to 13.6 kHz. Later experiments, to be described here with more details, have been done with 3 mm laser rod, emitting 25 watts in CW mode. When the water cooled passive Q-switch was introduced into the laser resonator, replacing the high reflecting rear mirror, the output power was reduced to 9 watts, indicating a switching efficiency of 36%. The laser output power is presented in Fig.3 as function of the solar pumping power. These results represent a slope efficiency of 1.4%, and a total efficiency of 0.7%.

Taken at average output power of 4 watts, a typical train of pulses manifested average repetition rate of 24kHz. One of the pulses is depicted in Fig.4, with unequal rise and fall time, and pulsewidth of 500 nsec. Elevating the pump power increased the repetition rate from 15kHz near threshold to 40kHz at the maximum average power, and decreased the pulse width, as found by Shimony *et al*⁸. Full description of the temporal behavior will appear elsewhere¹⁰.

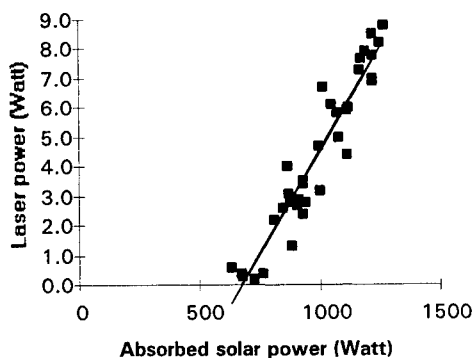


Fig. 3 Average laser power vs absorbed solar power

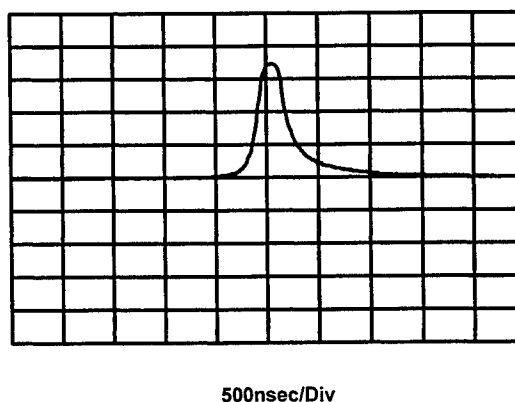


Fig. 4 A single laser pulse

4. CONCLUSIONS

The measured non-saturable transmission of the Cr^{4+} :YAG was 72%, corresponding to quite high saturated absorption, which have not been measured. Despite the resulting large thermal loads on the Cr^{4+} :YAG crystal, we have achieved up to 9 watt of average pulsed power without any breakdown of the Q-switch. Nevertheless, the high saturated absorption affected the switching efficiency, keeping it well below the 55% switching efficiency measured by Shimony *et al*⁸ for a Q-switch with Fresnel losses. Shimony *et al*⁸ predicted up to 87% switching efficiency for a Q-switch without Fresnel losses. Similarly, with appropriate doping level and wafer thickness, we expect to get 85-95% switching efficiencies with future models. Moreover, we estimate the thermal load on the Q-switch to be up to 18 watts, due to laser beam absorption and thus expect a water cooled Q-switch with decreased saturable absorption to withstand laser power in the hundred watt regime.

An important feature of Cr^{4+} :YAG Q-switch is having the same host as the laser rod. Following that, Aubert⁹ described a microchip laser with one part doped with Nd^{4+} ions, operating as the active laser material, while the other portion doped with Cr^{4+} ions, serving as a Q-switch. A similar design might be also applicable for solar pumped laser with a YAG rod of several mm diameter.

To conclude, solar pumping elevates Q-switching of solid state lasers to power levels not obtained till now with other pumping schemes. It thus demonstrated the potential of solar pumped lasers as platforms for development of high power solid state laser component, and as candidates to various terrestrial and space applications.

5. ACKNOWLEDGMENTS

We would like to thank Dr. Vladimir Krupkin for preliminary experiments with uncooled Q-switch. We also thank the Israeli Ministry of Trade and Industry for partial funding through the MAGNET program, Consolar consortium for concentrated solar energy.

6. REFERENCES

1. U. Brauch, J. Muckenschnabel, H. Opower, W. Wittner, "Solar Pumped Solid State Lasers for Space to Space Power Transmission", Space Power, 10, 285-294, 1991.
2. M. Duchet, L. Cabaret, A. Laurens, J. C de Miscalut, "Space Power Supply Networks Using Laser Beams", Space Power, 11, 241-250, 1992.
3. R. B. Hall, "Lasers in industrial chemical synthesis", Laser Focus, September 1982, 57-62.
4. D. Jenkins, M. Lando, J. O'Gallagher, R. Winston, A. Lewandowski, C. Bingham, R. Pitts, "A solar-pumped Nd:YAG laser with a record efficiency of 4.7 watt/m² of primary mirror area", Bulletin of IPS, 42, 101, 1996.
5. G. A. Thompson, V. Krupkin, A. Yogev, M. Oron, "Solar Pumped Nd:Cr:GSGG parallel array laser", Optical Engineering 31, 2644-2646, 1992.
6. G. Thomson, V. Krupkin, M. Oron, A. Yogev, "High power solar pumped solid state lasers" in CLEO, (OSA), 11, 590-592, 1993.
7. I. Pe'er, "High power solar pumped amplifier for free space optical communication", submitted to Weizmann Institute of Science as a M. Sc. thesis. 1996.
8. Y. Shimony, Z. Burshtein, A. Ben-Amar Baranga, Y. Kalisky, M. Strauss, "Repetitive Q-switching of a CW Nd:YAG laser using Cr^{4+} :YAG saturable absorber", IEEE J-QE, 32, 305-310, 1996.
9. J.J. Aubert, "Q-Switched microchip lasers bring new application to light", Laser Focus World, June 1995, s11-13.
10. Y. Noter, N. Naftali, I. Pe'er, A. Yogev, M. Lando, Y. Shimony, "Performance of a Q-switched solar pumped high power Nd:YAG laser", submitted for presentation in the 10th Meeting on Optical Engineering in Israel, to be held in Jerusalem, March 1996.

Precision materials processing in microelectronics
with a 10 W copper bromide laser

J.Mizeraczyk,¹⁾ A.Otta,¹⁾ M.Mohamed-Seghir,¹⁾ J.Wasilewski,¹⁾ A. Jurewicz,²⁾ W. Janke,²⁾ C.E.Little,³⁾ N.Sabotinov,⁴⁾
E.S.Livingstone,⁵⁾ I.Kostadinov,⁶⁾

¹⁾ Institute of Fluid Flow Machinery, Polish Academy of Sciences, 80-952 Gdańsk, Fiszera 14, Poland

²⁾ Technical University of Gdańsk, 80-952 Gdańsk, Narutowicza 11/12, Poland

³⁾ School of Physics and Astronomy, University of St Andrews, North Haugh, St Andrews, Fife KY16 9SS, United Kingdom

⁴⁾ Institute of Solid State Physics, 1784 Sofia, Tzarigradsko Chaussee 72, Bulgaria

⁵⁾ EEV Limited, 106 Waterhouse Lane, Chelmsford, Essex CM1 2QU, England

⁶⁾ Pulssvet Co., Sofia 1231, Nadezhda-4, bl. 463-A, ap. 50, Bulgaria

ABSTRACT

In this contribution experimental results in high-precision processing of various reflecting metals employed in microelectronics carried out with a 10 W copper bromide laser are presented.

Keywords: laser CuBr, high precision laser machining

1. INTRODUCTION

In the last few years lasers based on the green (510.6 nm) and yellow (578.2 nm) transitions in neutral copper have matured into the most efficient direct generators of visible coherent radiation available at high output powers.¹ Today the *conventional copper vapour lasers* producing 100 W average output power at 5 kHz pulse recurrence frequency and about 1% efficiency are at the laser market. However, due to their high operating temperatures (1500-1600 degrees C), conventional copper vapour lasers are of complex construction, require flowing gas system, and have long warm-up time (90-120 minutes). The *copper bromide (CuBr) laser*² is another type of copper laser, which does not exhibit the disadvantages associated with conventional devices. CuBr lasers have been demonstrated to have high-efficiency (2-3%) and high specific output powers (0,1-1 Wcm⁻³). There is no other type of laser which can deliver such high average powers in the visible range with high efficiency and high beam quality.

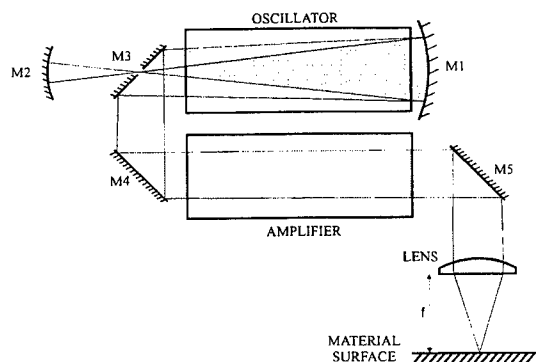


Fig. 1. CuBr laser system for the material processing.

At present introducing the copper vapor lasers to industry is in its initial stage³⁻⁵, although the properties of the beam of copper vapour laser, such as the coupling of the laser radiation to the material surfaces and ability to form smaller spot sizes, are suitable for the materials processing. Among hundreds of possible applications of copper lasers, the microprocessing of materials and surface diagnostics in electronics is of high interest.

In this contribution experimental results in high-precision processing (cutting) of various reflecting metals employed in microelectronics carried out with a 10 W copper bromide laser are presented. Laser cutting of the computer controlled patterns in stainless-steel (thickness of 50 μm), brass (thickness of 150 μm) and copper (thickness of 70 μm) was made and the cut quality was assessed.

2. EXPERIMENTAL SET-UP

The experimental set-up consists of a 10 W CuBr laser, computer controlled XY tables (resolution $4\mu\text{m}$, speed range $0.1 - 8 \text{ mm}\cdot\text{s}^{-1}$), optical system for transmitting and focusing the laser beam, microscope for direct observation of the laser machining process, TV system for observation of the laser machining process, microscope (magnification 500) for inspection of the samples after the machining. Also a scanning electron microscope (SEM) is available for this purpose.

The CuBr laser consists of an oscillator formed by a discharge tube placed in an unstable confocal negative-branch resonator, and an amplifier (Fig. 1). The negative-branch confocal resonator is formed by mirrors M_1 ($R_1 = 2400 \text{ mm}$) and M_2 ($R_2 = 80, 40, \text{ and } 22 \text{ mm}$). The respective magnification are 30, 60 and 110. The oscillator and amplifier discharge tubes with an active length of 70 cm have bores of a diameter of 20 mm. A low-divergence laser beam generated with the oscillator is injected via mirrors M_3 and M_4 into the amplifier, and after amplification is transmitted with a mirror M_5 and lens towards the surface of working piece. After the amplification the laser output power amounts to 8-10 W. The laser beam diameter is about 14 mm. The divergence of the laser beam is 0.24, 0.15 and 0.12 mrad when the mirror M_2 of a curvature of $R_2 = 80, 40$ and 22 mm is used, respectively. The beam pulse duration is about 40 ns at a recurrence frequency of about 18 kHz.

Positioning of the mirror M_5 and lens is controlled with micro screws. A mechanical shutter of a time gate range of $10^{-3} - 1 \text{ s}$ is used to switch the beam onto the workpiece. Using an achromatic lens of an F-number of 2.5 (a diffraction limited spot size is about $3.5 \mu\text{m}$) the beam quality was about 3 times the diffraction limit.

3. CuBr LASER CUTTING

Among hundreds of possible applications of CuBr laser, the micromachining of materials in microelectronics is of high interest. This experiment was aimed at assessing the CuBr laser application to the production of metal masks (stencils) for the surface mount technology in microelectronics. For this purpose the laser cutting was made in a stainless-steel foil having other cuts produced by etching technology. The quality of both cuts, made by the laser and etching, was compared. For comparison, also the CuBr laser cutting were performed in copper and brass foils. It is recognized that the laser drilling and cutting in copper and brass foils is more difficult than in steel because of their high reflectivity.

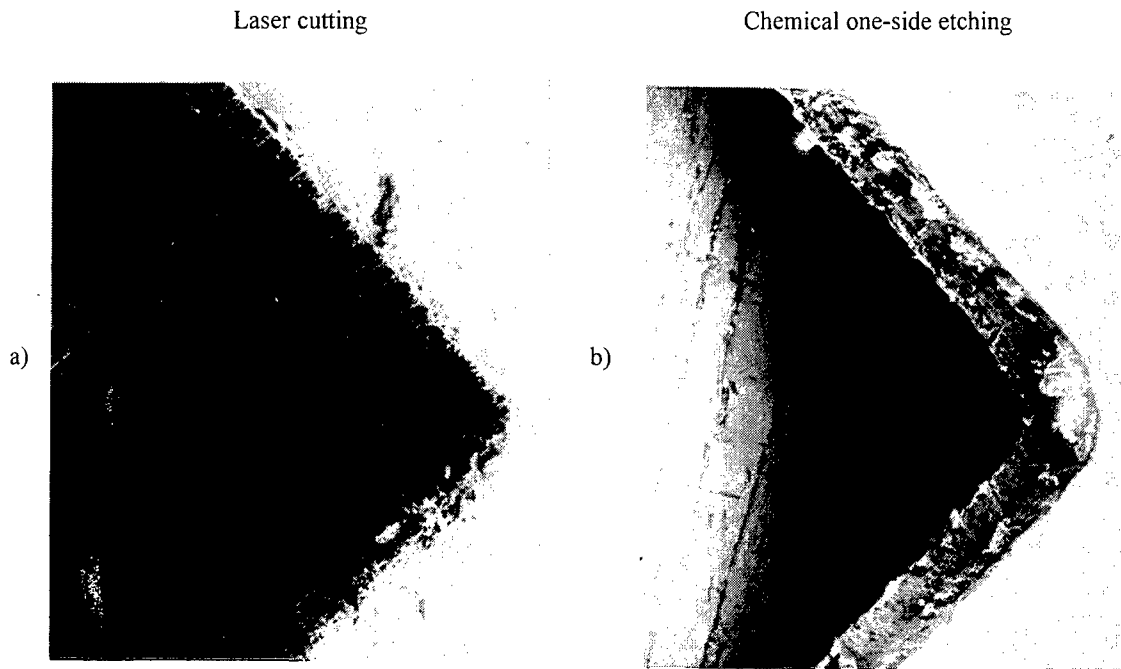


Fig. 2. Comparison of the CuBr laser cut and chemical one-side etching in a $50\mu\text{m}$ thick stainless steel foil: a) Laser cut at a speed of $0.3 \text{ mm}\cdot\text{s}^{-1}$ (laser entrance side), b) Chemical one-side etching (etching side). Laser power: 2W. Achromatic 35mm-focus lens. Enlargement of the SEM photographs 150.

During the cutting process, the CuBr laser power was set at 2 W (the peak laser power density was about $5\text{--}10\text{ GW}\cdot\text{cm}^{-2}$ at the focus). The cutting speed was varied from 0.3 to $1\text{ mm}\cdot\text{s}^{-1}$. It enabled obtaining widths of the cut kerf in the range of $10\div 50\text{ }\mu\text{m}$ on the bottom side depending on the material and its thickness.

3.1 Cutting in a $50\text{ }\mu\text{m}$ thick stainless-steel foil

In Fig. 2 the cuts produced by CuBr laser and chemical one-side etching in a $50\text{ }\mu\text{m}$ thick stainless-steel foil used for the production of metal masks in microelectronics are compared. The comparison shows that:

- the laser cutting produces more square corners than the chemical etching which produces usually rounded corners,
- in the laser cut the so-called striations⁶ were found, while in the cut produced by the one-side etching the bottom of the edge is less etched than the top (the etched-off edge is tapered, becoming narrower towards the edge bottom),
- the laser cut is not free from a heat affected zone (HAZ) and dross. The HAZ in the cuts made with a lower cut speed (e.g., $0.3\text{ mm}\cdot\text{s}^{-1}$) is more pronounced than that made with a higher speed (e.g. $1\text{ mm}\cdot\text{s}^{-1}$).

3.2 Cutting in a $150\text{ }\mu\text{m}$ thick brass foil

Examples of the CuBr laser cut in a $150\text{ }\mu\text{m}$ thick brass foil are presented in Fig. 3. It is seen that:

- the corners produced in the brass foil by the laser cutting are square and not rounded as with chemical etching and most other thermal cutting techniques,
- the cut edges are relatively smooth and clean,
- dross is almost avoided,
- there is a narrow HAZ,
- striations at the topside of the edges occurs but not along the whole depth of the edges.

3.3 Cutting in a $70\text{ }\mu\text{m}$ thick copper foil

Fig. 4 presents examples of the laser cut in a $70\text{ }\mu\text{m}$ copper foil. The main characteristics of the cut are as follows:

- the corners made in the copper foil are square,
- cut edge exhibits striations on the whole its depth,
- the narrow HAZ is more distinct than in the case of brass foil,
- dross is found in the HAZ.

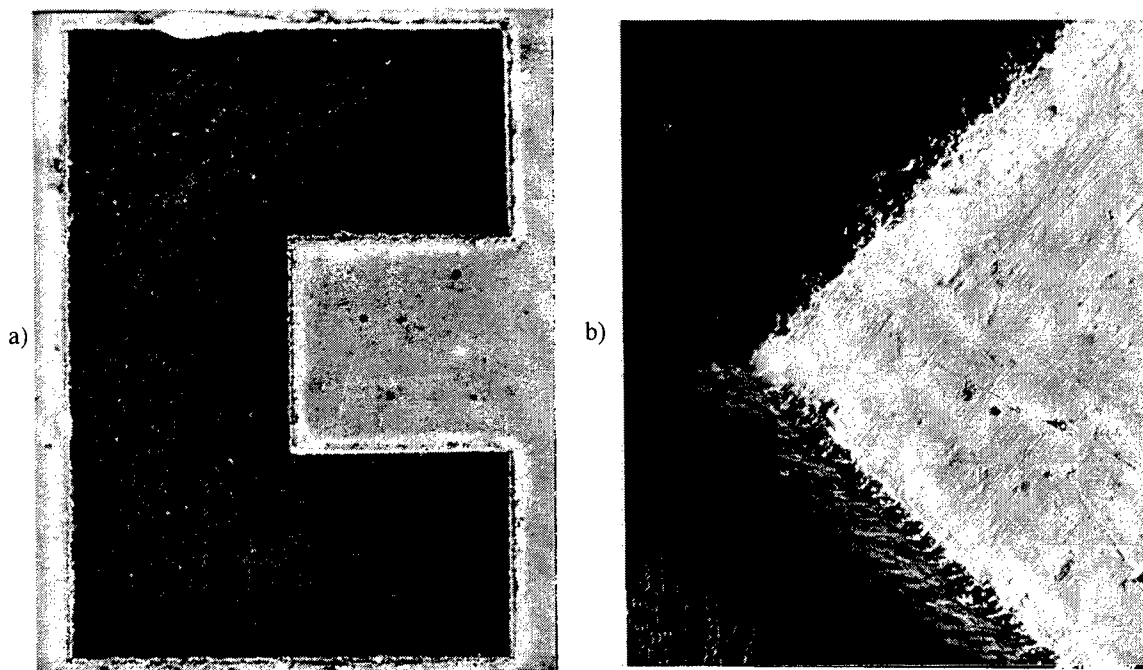


Fig. 3. SEM photographs of the CuBr laser cut of a pattern in a $150\text{ }\mu\text{m}$ thick brass foil: a) Laser entrance side, SEM enlargement 35; b) Laser entrance side, SEM enlargement 150. Laser power: 2W. Achromatic 35mm-focus lens. Cut speed: $1\text{ mm}\cdot\text{s}^{-1}$.

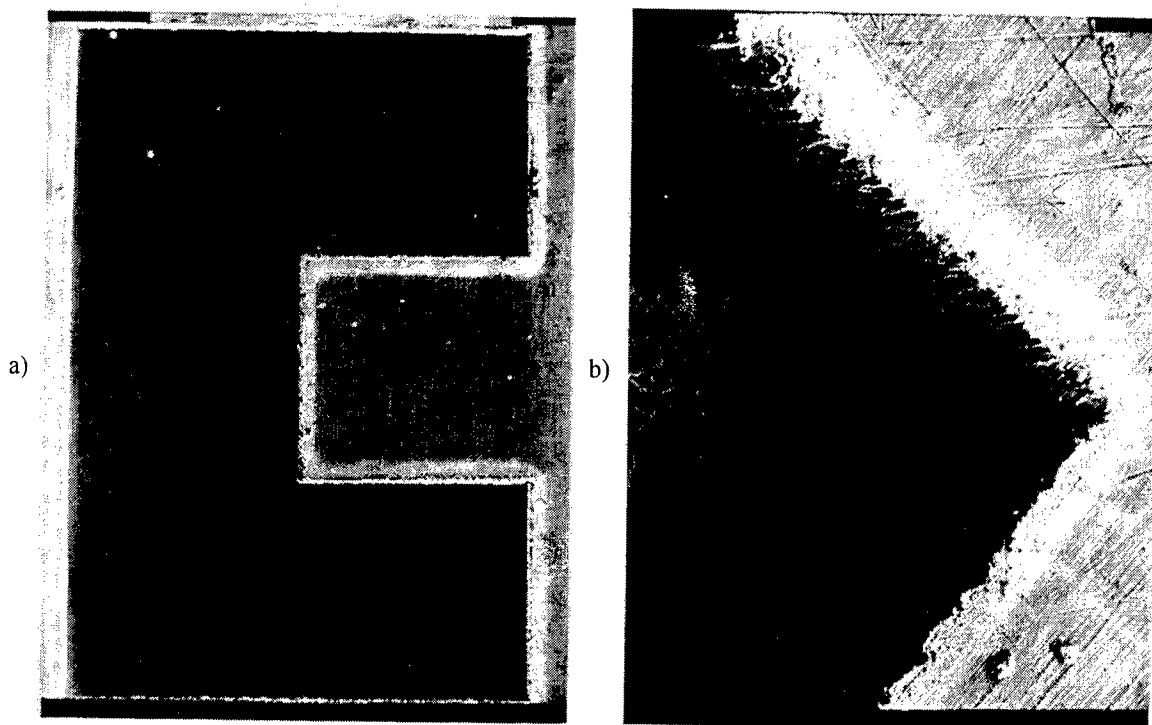


Fig. 4. SEM photographs of the CuBr laser cut of a pattern in a 70µm thick copper foil: a) Laser entrance side, SEM enlargement 35, b) Laser entrance side, SEM enlargement 150. Laser power: 2W. Achromatic 35mm-focus lens. Cut speed: 1mm·s⁻¹.

4. CONCLUSIONS

The cutting carried out with a relatively low power (2 W) CuBr laser in several materials: stainless steel, brass and copper foils indicated the potential for the use of a CuBr laser in the material processing. The advantages of using the CuBr laser are:

- the CuBr laser cutting produces more square corners than chemical etching or other thermal cutting techniques,
- the laser cuts do not show significant taper,
- the cuts edges are relatively smooth and clean, in particular in the case of brass,
- in the case of brass, dross is almost avoided and the HAZ is relatively narrow.

The above results showed that the CuBr laser is able to process reflecting foils, particularly brass, with a quality which is of commercial interest, and that at the present CuBr laser technology state the CuBr laser can be competitive to the conventional copper vapour laser in some applications where a laser power of 5-20W is sufficient. Among possible applications of the CuBr laser having an output power of 5-20 W, the micromachining of materials in microelectronics is of high interest. For example, the metal masks (stencils) for the surface mount technology produced by us using the CuBr laser showed better roughness of the inner walls of the cut-off apertures than those produced by etching technology. This means that the CuBr laser technology may be competitive in the stencil production through offering environmentally friendly processing of precise print masks.

5. ACKNOWLEDGMENT

This work was supported by the European Commission under Copernicus Programme CIPA-CT-94-0214.

6. REFERENCES

1. *Pulsed Metal Vapour Lasers*, Ed.: C.E.Little and N.V.Sabotinov, Kluwer Academic Press, 1996
2. N.V.Sabotinov, "Copper bromide lasers," *ibid.*, pp.113-124
3. H.W.Bergmann, C.Körner, M.Hartmann, R.Mayerhofer, "Precision machining with copper vapour lasers," *ibid.*, pp. 317-330
4. B.E.Warner, C.D.Boley, J.J.Chang, E.P.Dragon, M.A.Havstad, M.Martinez, W.McLean II, "Industrial application of high-power copper vapor lasers," *ibid.*, pp. 331-346
5. A.J.Kearsley, M.Knowles, R.Foster-Turner, "Copper laser machining of ceramics," *ibid.*, pp.353-358
6. W.M.Steen, *Laser Material Processing*, Springer Verlag, 1996, p. 80-81

A Copper Vapour Laser MOPA-Chain for Highly Efficient and Precise Material Removal

Karsten Schutte, Eric K.W. Gan, Jürgen Koch, Adolf Lang

Martin Hartmann[#], Roland Mayerhofer[#], Tomas Slunecko[#], Hans Wilhelm Bergmann[#]

Applikations- und Technikzentrum ATZ-EVUS, Rinostraße 1, D-92249 Vilseck

[#]Universität Erlangen-Nürnberg, Lehrstuhl WTM, Martensstraße 5, D-91058 Erlangen

1. ABSTRACT

Copper Vapour Lasers in a MOPA-chain (MOPA, Master-Oscillator-Power-Amplifier) configuration with low divergence can be used for the high precision machining of metals and ceramics. The fundamental interaction phenomena, ablation process and possible industrial applications are presented. The following paper relates the results and experiences in the operation of a Copper Vapour Laser MOPA Chain, consisting of an oscillator and up to three amplifiers, with the triggering points for these lasers exactly variable through a Master-Timing-System. In principle, a low-divergent laser beam is generated (511 and 578nm wavelengths) via an off-axis unstable resonator scheme, with precise synchronization of the Amplifiers producing average powers of over 140W. Due to the excellent beam focusability, peak power densities of some 10^{10} W/cm² are achievable in a 50ns pulse duration, which provides almost material-independent precision machining at high velocities. Beginning from the principles of beam-target reciproproation, the removing and cutting of metallic as well as non-metallic materials with copper vapour lasers will be described. Additionally, the potential of copper vapour lasers for industrial applications is illustrated through precision machining examples.

Keywords: copper vapour laser, materials processing, precision machining, cutting, drilling, master-oscillator-amplifier

2. THE COPPER VAPOUR LASER MOPA CONFIGURATION

In materials processing, the most commonly preferred type of metal vapour laser is the copper vapour, which emits at 511nm (green) and 578nm (yellow) wavelengths, and provides an average output power in the range of 20W to 200W for a single tube. With typical pulse durations of 20ns to 80ns, CVL's can be operated in a broad range of mean repetition rates between 2kHz and 32kHz.

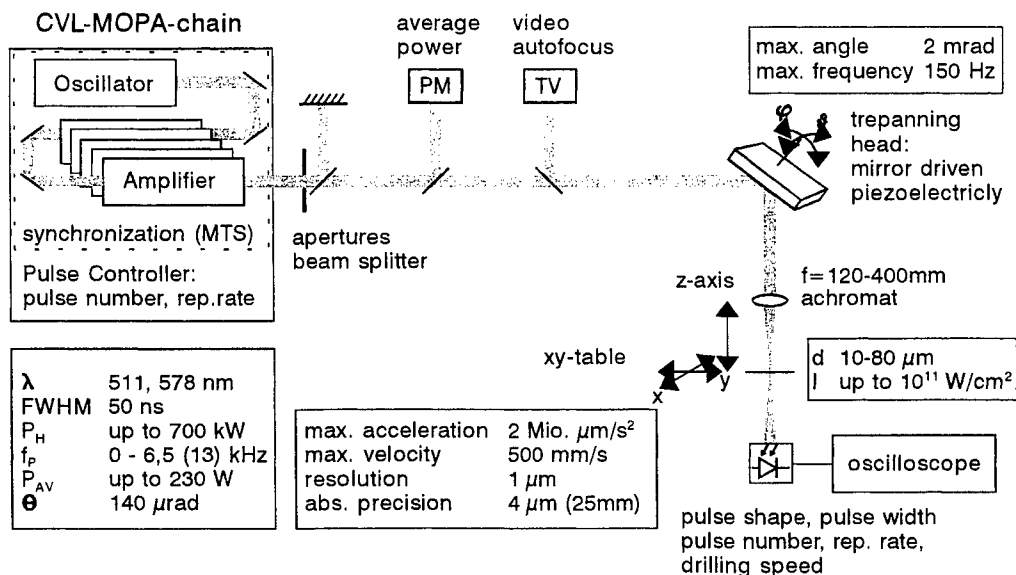


Fig. 1: Experimental setup of the Copper Vapour Laser MOPA-Chain

Near-diffraction-limited laser radiation can be initiated using a single oscillator, or by an oscillator-amplifier configuration. In the case of precision micromachining, high average powers as well as low divergence are desired. A single oscillator tube will exhibit different beam properties depending on the resonator configuration employed. A maximum efficiency (typically 1%) can be obtained with a plane-plane resonator arrangement, but then the beam divergencies are often too high for applications in precision materials processing. Resonator concepts to generate considerably lower divergent beams (such as the unstable off-axis resonator, SFUR, etc.) have been developed over the last decade. However, there are limitations in that high output power as well

as laser efficiencies (0.2-0.8%) are quite poor. A solution to this problem is to generate these low-divergent laser pulses in an oscillator with small output powers (1-5W), but of superior beam quality, and to amplify these pulses in one or more higher-powered laser tubes. The total efficiency of this design will be comparable to that of the plane-plane resonator as the power consumption of the oscillator is low compared to that of the amplifiers.

The experiments and results for this paper were obtained with a setup of one Oscillator, with an unstable off-axis resonator, and up to three Amplifiers. The maximum average power of the system is about 140W at a repetition rate of 6.5kHz. By using suitable apertures and a beam expansion unit, a low-divergent, 2-times-diffraction-limited laser radiation with 3W average power is generated. The beam is then amplified in the following stages (Figure 1) without any degradation to the overall beam quality. Due to the short gain period (80-100ns) of the excited copper species, the exact synchronization of these CVLs is essential. The Master-Timing-System (MTS) provides the synchronous triggering of the individual laser tubes and compensates for any internal timing drifts as well. The MTS is also able to synchronize as many lasers as desired, with the ability of being able to even combine the use of different laser types in a single chain.

The copper vapour laser has a predictable chronological sequence, which is characterized by transmission, amplification, absorption and again transmission. This unique property, which is not available from any other laser type, can be specially used for materials processing. By varying the timing pattern of the oscillator-amplifier arrangement, the output power, divergency, as well as, the pulse shape is modifiable from one pulse to the other ¹. This specific amplification curve of the copper vapour has led to the realization of a delay-free shutter for the existing CVL MOPA Chain. For this task, the synchronization module of the last Amplifier has a newly-developed electronic circuit, which provides the probability of shifting the triggering point between two pulses from the states of amplification to absorption, and vice versa. Therefore, the modulation of the repetition rate and single pulse processing is possible without any changes to the laser pulse properties ².

3. DRILLING OF MATERIALS

3.1 Fundamentals

The fundamental investigations have shown that the maximum drilling depth obtained by a single CVL pulse of 50ns FWHM in metals is indirectly proportional to the binding energy or the shear modulus of the irradiated material. For example, 100 μm deep drill holes are achievable in aluminium with intensities above 10^{10} W/cm^2 in a single pulse. Theoretical considerations yield to a model of the materials removal process, which is characterized by the temporal sequence of heating, non-stationary drilling and stationary drilling with a constant drilling speed ³. The experimental proof of this removal behaviour has been attained by measuring the time necessary to drill through aluminium foils of thicknesses between 0.8 and 75 microns with a single pulse. Figure 2 shows the drilling times measured for different foils at a pulse power of 120 kW and the drilling speeds calculated from this. At 10 ns after the initiation of the laser pulse, stationary drilling with 1500 m/s takes place. A comparison of drilling speeds with single laser pulses of different pulse powers shows clearly that there is no increase in the speed of the stationary drilling above 40 kW (Fig. 3). This saturation, however, is not due to the shielding effects of the laser induced air plasma, as can be seen by measurements under vacuum conditions, but has to be considered as the highest possible drilling speed. This, however, is limited to the speed of sound in the material drilled, which is strongly dependent on the state of the material (solid, liquid or

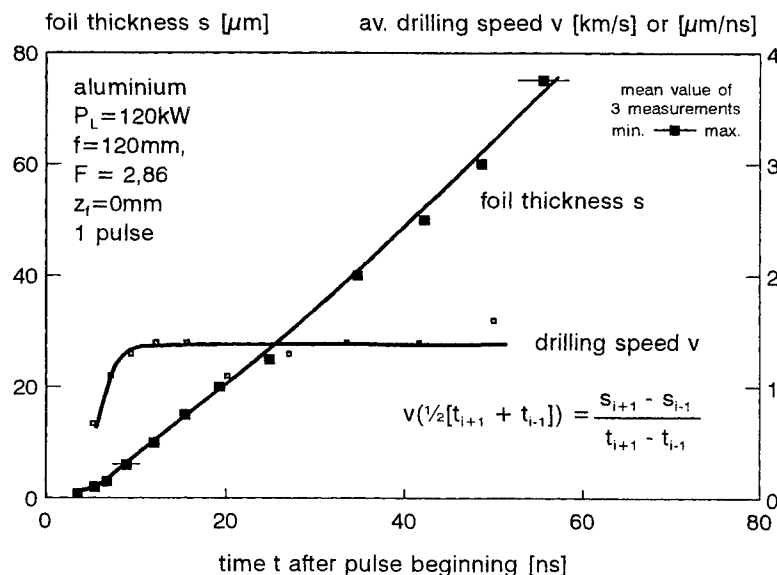


Fig. 2: Influence of the pulse power on the stationary drilling speed in aluminium

gaseous) at the drill hole bottom during the irradiation. The drilling depth achievable by a single CVL pulse is not only due to the above mentioned physical properties of the various metals, but is also dependent on specific properties in the same material. To clarify this, we have investigated the influence of the sample temperature, the orientation of the irradiated grains, as well as, the influence of the microstructure in differently heat-treated steel.

3.2 Influence of the power density

The drilling process can be sub-divided into two elementary processes; the thermal phase (heating, melting, evaporation) and the removal / discharge phase (ejection of the material from the drill hole bottom). For a single pulse, the removal is the determining factor. A problem, however, emerges when machining deep drill holes using the percussion method. In this case, a certain amount of material ablated at the bottom is unable to leave the drill hole and, therefore, recondenses onto the walls. For single pulse processing of copper, Figure 3 demonstrates the influence of the power density on the removal rate. The power density is calculated from the pulse full-width-half-maximum (50ns), pulse power and an experimentally measured focal diameter of 30 μ m. The shape of the curve, also observed with other short pulsed lasers⁴, is represented by low removal rates at low intensities (less than 10^9 W/cm²), a strong increase at medium power densities (10^9 up to 10^{10} W/cm²) and the beginning of saturation at intensities above 10^{10} W/cm². This saturation is not due to the onset of a plasma shielding effect, but is more likely the result of the maximum possible speed of the ejected metal vapour outside the drill hole. The maximum removal for a single laser pulse on copper with a power density of 4×10^{10} W/cm² is about 55 μ m. A top view into the drill hole illustrates the pulse removal process, which leads to a flake-shaped formation of the walls.

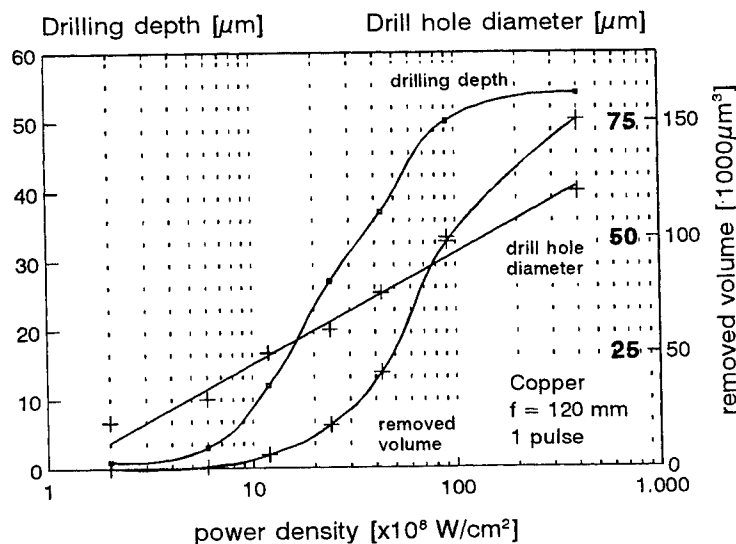


Fig. 3: Influence of the power density on single pulse drilling

3.3 Influence of the material

3.3.1 Metals

Besides the influence of focusing conditions, the maximum processing speeds which are attainable for the CVL drilling of metals also depend on the actual physical properties of the irradiated materials themselves. A single pulse with a pulse power of 129kW in aluminium produces a crater of 80 μ m depth. A comparison of all the materials experimentally investigated here demonstrates that metals with a body-centered cubic (bcc) structure will generally show a lower removal rate than face-centered cubic (fcc) or hexagonal metals.

3.3.2 Ceramics

In contrast to metals, irradiating ceramics with CVL pulses will result in a completely different removal behaviour, as the high removal rates in a single pulse due to the physical and reological properties are not achievable. Increasing the numbers of pulses will also lead to an almost linear increase in the drilling depth, with a materials dependency showing higher removal rates for Al₂O₃ and SiC than for Si₃N₄. Compared to metallic materials (e.g. copper 250 μ m thick: 47mm/s with 54kW pulse power), a distinctly lower drilling speed is observed (Al₂O₃ 250 μ m thick: 5mm/s with 55kW pulse power).

3.2.3 Glass

The suitability of the copper vapour laser for the damage-free drilling of glass has been reported earlier ⁵. The critical condition that determines the possibility and also the quality of a laser drill hole in transparent materials is the power density of the laser pulses. Due to the high transparency of glass for visible light, a specific threshold has to be exceeded for each type of glass to achieve an optical breakdown, which precedes the drilling process. Experimental investigations have shown that the intensity threshold for pure quartz glass is about $2 \times 10^9 \text{ W/cm}^2$. With increasing concentration of network transformers, metallic impurities and combined water molecules, this threshold will decrease. To establish a non-linear absorption of the laser light, it is necessary to generate defects (e.g. colour centres) within the first laser pulses. However, the working range of the power density has an upper limit; any additional increases in the lasing pulse intensity after a certain period will simply inhibit the drilling process due to thermal damage at the beam entrance side. Using optimized parameters, aspect ratios of up to 250:1 are achievable.

4. CUTTING OF MATERIALS

Materials sublimation cutting with CVLs can be interpreted as drilling with a relative motion either of the laser beam or the working piece. Therefore, principle results obtained from experimental investigations of drilling, i.e. concerning the focusing conditions, the materials dependency or the influence of the repetition rate, can be transferred to laser beam cutting experiments. The quality of the cut, however, will depend on the preciseness of the beam handling system and also on the effect of the laser parameters. The main criterion for the cutting quality of precision micromachining lies within the cut width, size of material damage (thermal, mechanical and chemical), parallelity, as well as, the roughness of the cut kerf. Processing techniques can be differentiated into cuts with only a single forward motion and those with a repetitive cut of the same contour. Generally, the latter method will provide higher cutting speeds as well as an increase in the cut kerf roughness ⁴. Due to its diminutive focal diameter, the copper vapour laser is an excellent tool for precision micro-cutting.

5. POSSIBLE INDUSTRIAL APPLICATIONS

The copper vapour laser is, due to its excellent focusability and high initial absorptivity in almost all materials, a very suitable tool for a variety of processing tasks in engineering and technology. Applications such as in illumination sources (laser light profiling, stroboscope) and also in medical areas (removing or cutting of human tissue or skin) have been well-established. An expansion to machining tasks in materials processing will unlock, however, a much larger market potential for this laser type in an oscillator-amplifier arrangement, with possible areas of application being differentiated into drilling, cutting, removing, as well as, combinations of laser-supported and conventional techniques. For materials processing of the drilling variety, the fabrication of nozzles can be one of the major applications which has up to now not been adequately solved using other laser processing techniques. In the manufacturing of these drill holes of μm -region diameters, the paradoxon increasing both the processing speed and the precision can be solved combining excellent beam quality and high average power of the CVL.

As for applications in materials cutting, the fields of electronics and fine mechanics offer great promise. As typical examples of the former, the cutting of prototypes of lead frames and semiconductor chips has to be noted. Employment of CVL processing in the field of classical fine mechanics can be implemented in the cutting of wires or in the manufacture of precision components.

Processing methods for the superficial removal of material can be divided into plane machining (paint stripping, removal of hard coating on working tools) and surface modification techniques. Even in the latter case, the high pulse repetition rate of the CVL will lead to high processing speeds. Due to the fact that the processing speed diminishes with increasing sheet thickness, a combination of laser-supported and conventional techniques may be necessary for some applications to achieve economical production costs. So, for example, laser beam perforating or scratching of working pieces may be followed by a fracture technique. This method, however, is limited to brittle metals (e.g. body-centered cubic metals) or ceramic materials.

6. ACKNOWLEDGEMENTS

The fundamental work, described in this paper, was financially supported by the German Ministry of Education, Research and Technology (BMBF) within the national LASER 2000 programme, and the application oriented work was sponsored by the Bavarian Research Foundation (BFS) within the framework of the Bavarian laser association FORLAS.

7. REFERENCES

1. H.W. Bergmann and M. Hartmann, "Drilling of Metals with Copper Vapour Lasers", in Mazumder J., Mukherjee K., Mordike B.L.: *Laser Materials Processing IV*, The Minerals, Metals and Materials Society (1994)
2. H.W. Bergmann, R. Mayerhofer, T. Sluneko, M. Hartmann and E. Gan, "Improved Drilling and Cutting with Copper Vapor Lasers", in *Proceedings of the Conference on Lasers and Electro-Optics Europe CLEO '94*, Amsterdam (1994), p. 295
3. R. Kupfer, "Laser drilling using copper vapour lasers", PhD Thesis University of Erlangen-Nürnberg (1992)
4. K. Schutte, "Process diagnostics and application oriented investigations of excimer laser materials processing", PhD Thesis University of Erlangen-Nürnberg (1993)
5. R. Pini, R. Salimbeni, M. Vannini and G., "Copper Vapor Laser High Aspect Ratio Drilling Process on Transparent Materials", *Proceedings of the International Conference Laser '92*, Houston (1992)

Dynamics of the metal seeding process in copper hybrid lasers

L Little and C E Little

*University of St Andrews, School of Physics and Astronomy
North Haugh, St Andrews, Fife KY16 9SS, Scotland*

ABSTRACT

A small-bore (12.5 mm) hybrid laser delivers its highest average output power for a gas flow rate of around 1 litre.atm.hr⁻¹ and an HBr pressure of 2-4 torr in 34 torr Ne. It is estimated that the atomic bromine pressure at the wall is ~2 mtorr. The number density of copper in atomic and molecular forms averaged throughout the tube is 4×10^{16} cm⁻³. Significant numbers of Cu_xBr_x polymers and CuH must exist in the laser discharge to lock up the large pool of copper atoms in the discharge. The copper hybrid laser produced an average output power of 12.8 W, corresponding to a specific average output power of 348 mW.cm⁻³, at a PRF of 35 kHz.

Keywords: copper lasers, hybrid lasers, metal seeding, high power, visible, efficient

INTRODUCTION

The copper hybrid (hydrogen bromide in discharge) laser is the highest efficiency, high-power visible laser source to be demonstrated [1]. It lases on the well known 510.6 and 578.2 nm pulsed transitions of atomic copper. A large-bore (6 cm) copper hybrid laser has produced an average output power of 201 W at an efficiency (based on stored energy) of just under 2%, and 120 W at an efficiency of 3.2% [2]. It is believed that HBr is the species responsible for the higher (by 2-3 times) efficiencies and larger (by a factor of 2) specific average output powers of hybrid lasers compared to conventional copper vapour lasers (CVLs) [3].

As well as improving the kinetics of laser generation, HBr additive in a copper hybrid laser controls the density of free copper atoms in the discharge. A slow flow of Ne-HBr buffer gas is passed through the laser tube, along the discharge channel of which are placed copper metal pieces. The laser tube wall is self-heated to 600-800°C by the multi-kilohertz PRF discharge. The halogen donor molecules are dissociated in the pulsed discharge, and the products react with the copper surfaces to produce gaseous CuBr. The CuBr molecules polymerize [4] to Cu₃Br₃ and Cu₄Br₄ and diffuse into the discharge. In the body of the pulsed discharge, the copper bromide molecules are dissociated by electron collision and hydrogen reduction to yield the free copper atoms.

The purpose of this present paper is to present preliminary results of a study of the metal seeding mechanism in a copper hybrid laser. The discussion does not apply to high-temperature CVLs to which HBr has been added.

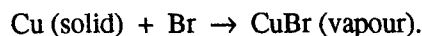
EXPERIMENTAL DETAILS

The copper hybrid laser studied was identical to that described in [5]. Briefly, the active zone was confined within a 12.5 mm bore, 30 cm long alumina ceramic discharge tube. The alumina tube was sleeved within a fused silica tube, which was sealed to metal end-flanges by Viton O rings. The electrodes were cylinders of molybdenum or stainless steel, and were push-fitted into the endflanges so as to project up to each end of the alumina tube. The tube was draped with a light insulation so that the outside (quartz) wall temperature was 550-650°C. A plane-parallel resonator was used. Ne buffer gas and HBr additive were mixed via needle valves before entering the laser tube at the anode end. The gases were exhausted downstream of the cathode via a halogen filter and a rotary vacuum pump. A standard peaking circuit with resonant charging was used to excite the laser, with storage and peaking capacitances of 0.66 nF/0.33 nF (measured at working temperature). The optimum gas pressure was 38-90 torr (2-4 torr HBr) for a gas flow rate of 0.8 litre.atm.hr⁻¹. An output power of 12.8 W was obtained at 35 kHz PRF, and the charging voltage was 11 kV; this output power corresponds to a record specific average output power of 348 mW.cm⁻³ for copper lasers of ≥12.5 mm bore.

CURRENT UNDERSTANDING OF THE METAL SEEDING PROCESS

The processes that control the copper bromide vapour density are similar to those exploited in the well-known 'hot-filament' process of metal purification [6]. In the copper hybrid laser, the 'plasma' process is cyclical in the same way as the hot filament process is. The only difference between the two processes is that dissociation of the halide does not take place at the surface of a filament, but in the non-localized plasma of the gas discharge.

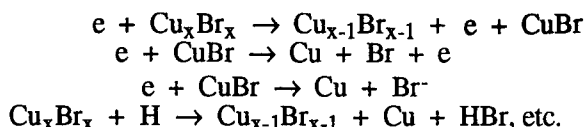
The reaction to remove copper from the pieces proceeds by the action and/or mediation of an active species from the discharge, most probably atomic bromine, *e.g.*



In the reaction of solid copper with HCl vapour, Cu_3Cl_3 trimers are present above the metal surface in a greater number than CuCl molecules [7]. The bromide is also known to exist mainly as polymers [6], and such polymers have been found in a hybrid laser [4]. Therefore, polymerization of CuBr must occur above the copper pieces:



Copper bromide molecules will diffuse towards the centre of the tube. In the discharge, gas-phase depolymerization and copper atom liberation occurs by electron impact and hydrogen reduction:



The halide molecules lost by dissociation are replaced by molecules diffusing from the wall, which deliver further copper atoms to the discharge. The density of copper atoms in the discharge is elevated above what would have been available, had the copper only been sourced as solid halide, as the numbers of halogen atoms, which transport copper atoms into the discharge, are larger (by an order of magnitude) in a hybrid laser. (There is 2-4 torr added HBr in a hybrid laser compared with ~0.3 torr CuBr vapour in a conventional halide laser [8].) Therefore, the specific output pulse energy can also be higher in a hybrid laser than in a halide laser.

Free copper atoms are also reduced in number between excitation pulses of the discharge channel by reassociation with bromine to the monomer and polymeric forms of copper bromide, and by diffusion to the wall of the tube. The copper bromide molecules can be removed from the gaseous phase on the copper surface (or any hot surface) by thermal dissociation



and by hydrogen reduction



RESULTS AND DISCUSSION

The laser tube was loaded with copper in various configurations. In the first, 12 copper pieces 5 mm x 10 mm x 0.25 mm were placed in pairs at intervals of 5 cm along the floor of the 30 cm long alumina discharge tube. In the other configurations, the copper metal was placed in the alumina tube at the upstream end, immediately adjacent to the anode. The isolated copper sources took the form of cylinders of 0.25 mm thick copper sheet, which were close fits within the alumina tube. Cylindrical copper sources of 1 mm, 2 mm, 5 mm, 10 mm and 20 mm length were used. For each of the copper source configurations, the average output power of the laser was measured as a function of buffer-gas flow rate. The buffer gas pressure was maintained at 38 torr during the experiments.

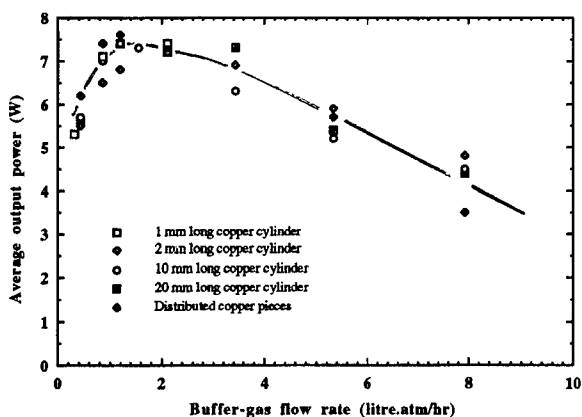


Fig. 1. Output power versus buffer-gas flow rate.

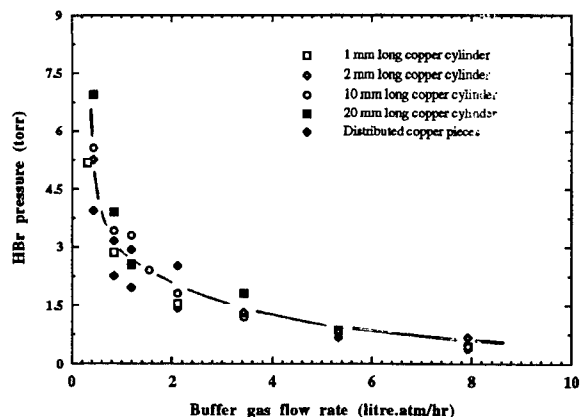


Fig. 2. Optimum HBr pressure versus buffer-gas flow rate.

In Fig. 1 it can be seen that the dependence of average output power on gas flow rate can be fitted with a single curve. This means that there is no difference in the performance of a laser which has copper pieces evenly distributed along the discharge channel, and one where the copper is placed on the upstream side of the discharge. Furthermore, a ring of copper just 1 mm thick is sufficient to supply the discharge with copper bromide. For the 12.5 mm bore, 30 cm long discharge tube, an output power of 7-8 W was obtained for a flow rate of ~ 1 litre.atm.hr⁻¹. The corresponding HBr partial pressures for maximum output power at each flow rate are plotted in Fig. 2. At low flow rates, the required HBr pressure is ~ 5 torr (corresponding to 14% of the gas mixture), and the output power is low. At 1 litre.atm.hr⁻¹ flow rate, only 3 torr HBr is necessary for maximum output power. At higher flow rates, the output power falls again, as does the HBr pressure for maximum output power at each flow rate. The maximum HBr pressure at the high flow rates was marked by the onset of discharge instabilities. At 8 litre.atm.hr⁻¹, only ~ 0.5 torr HBr could be tolerated, and the output power reached only 4-5 W.

The behaviour in Figs 1 and 2 can be explained as follows. At flow rates above 3 litre.atm.hr⁻¹, the gas temperature can fall and copper bromide vapour can condense in the active volume, leading to discharge instabilities and non-uniformities, lower output power and the tendency to tolerate less HBr. At the highest flow rates, it is likely that turbulence was induced in the tube, leading to the largest spread in output powers. At the optimum flow rate of 1 litre.atm.hr⁻¹, the volume of the active volume is replaced every 9 seconds. At the lowest flow rates, the output power falls, probably because of loss of CuBr by diffusion against the gas flow into the tube, with a subsequent loss of CuBr by condensation upstream of the anode. The formation of deposits of copper bromide near the anode was noted for the lowest flow rates.

We checked how sensitive the laser parameters were to the tube wall temperature. The laser tube was wrapped with heavy thermal insulation, switched on, and set to 10 kV charging voltage and 35 kHz PRF, with a gas flow rate of ~ 1 litre.atm.hr⁻¹. When the outside wall temperature reached 440°C, 3 torr HBr was added. Lasing began immediately, and reached a maximum of 11 W at 500°C, where the power remained (± 0.5 W) up to the temperature of 850°C some 15-20 min. later. We conclude that the copper bromide equilibrium pressure above the copper surfaces and the laser generation processes are independent of outside tube temperature in the range 500-850°C (inside temperature is 100° higher). Thus, the flow rate dependence of output power is related to changes in copper entrainment (low flows) and gas temperature (high flows), rather than tube temperature.

It was found that the copper source need only be placed at the upstream end of the discharge tube for proper laser operation. The 12 pieces of copper were weighed before and after operating the laser for a period of 185 min. The buffer gas flow rate was 0.85 litre.atm.hr⁻¹, the HBr pressure was 3 torr (set for maximum output power), the charging voltage was 10 kV and the PRF was 20 kHz. The weights of the 6 pairs of copper pieces are given in Fig. 3 as functions of position in the laser tube, before and after the 185 min. period. It is seen that the first pair of copper pieces was entirely consumed in the seeding reactions. Some of the consumed copper was deposited near the cathode. The balance of the copper was lost as copper bromide in the laser end-flanges.

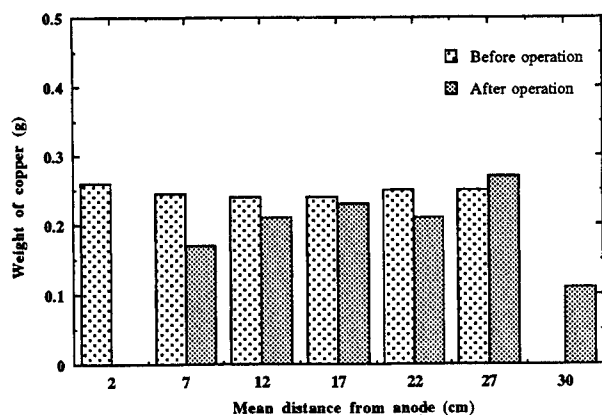


Fig. 3. Distribution of copper in laser tube, before and after 185 min. operation.

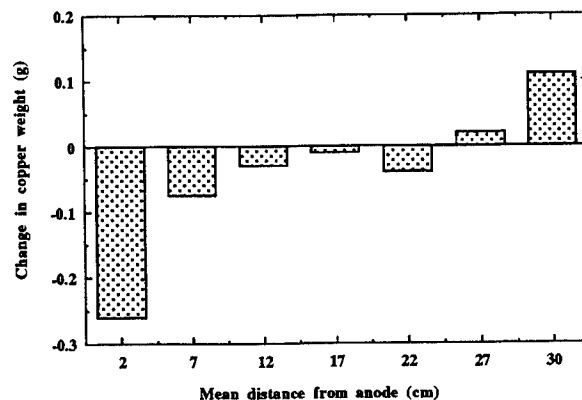


Fig. 4. Changes in copper distribution under the same conditions as in Fig. 3.

To further quantify the rate of reaction of copper with HBr and its dissociation products, we determined how much copper was spent in the laser tube, when it was fitted with a 10 mm long cylindrical copper source near the anode. A weight of 0.21 g copper was consumed in 132 min. when the flow rate was 0.85 litre.atm.hr⁻¹, the total gas pressure was 38 torr, and the HBr partial pressure was 4 torr. We find that the rate of removal of copper atoms

was $6.2 \times 10^{16} \text{ cm}^{-2}\text{s}^{-1}$. Assuming every third collision of a Br atom leads to a CuBr molecule, we calculate that the number density of atomic bromine must be $2 \times 10^{13} \text{ cm}^{-3}$, or just 2 mtorr.

Because of diffusion losses of copper in the form of copper bromide into the anode region, where deposition occurred, we were not able to obtain an accurate value for copper density in the laser tube. If we assume that half the copper generated by reaction at the copper piece is immediately lost from the tube due to diffusion against the slow gas flow, we can calculate that the number density of copper (in atomic/molecular form) averaged radially is $4 \times 10^{16} \text{ cm}^{-3}$. Such a large number of copper atoms can only exist if a significant amount of the copper is locked up as Cu_xBr_x polymers in the discharge with x being weighted between 3 and 4, as suggested by the results of [9]. This supports the view that the CuBr monomers polymerize very quickly above the copper pieces.

Knowing that HBr was added to the tube at a partial pressure of 4 torr, we can place an upper limit on the radially averaged number density of Cu_xBr_x polymers of $6 \times 10^{15} \text{ cm}^{-3}$ which, for $x = 3.5$, can only account for around half the copper atoms in the tube. We hold that the balance of copper atoms are present as free atoms and in CuH molecules, which are relatively stable (dissociation energy of 2.73 eV [10]).

The axial density of Cu atoms in a 25 mm bore hybrid laser was measured as $9.4 \times 10^{14} \text{ cm}^{-3}$ [11]. As the ratio of specific average output pulse energies between the 12.5 mm and 25 mm bore lasers is ~ 2 [1], we assume that the average number density of Cu atoms in the 12.5 mm bore laser is ~ 2 times higher than in the 25 mm bore laser. We can therefore expect copper in atomic form at an average density of the order of $4 \times 10^{15} \text{ cm}^{-3}$.

We shall estimate the number densities of $\text{Cu}_{3.5}\text{Br}_{3.5}$ polymers, CuH, Cu and HBr in the tube. We know that $2.1 \times 10^{16} \text{ cm}^{-3}$ of HBr was added to the tube, and assume that the average Cu density is $4 \times 10^{15} \text{ cm}^{-3}$. Then, assuming also that the densities of Br, H and Br_2 can be neglected (the first two are highly reactive and the last is unstable), and that the HBr density is equal to the H_2 density, we find from equations of atom conservation that the following number densities (radial averages) are consistent with the data: $1.3 \times 10^{15} \text{ cm}^{-3}$ (HBr), $1.3 \times 10^{15} \text{ cm}^{-3}$ (H_2), $4 \times 10^{15} \text{ cm}^{-3}$ (Cu), $5.6 \times 10^{15} \text{ cm}^{-3}$ ($\text{Cu}_{3.5}\text{Br}_{3.5}$) and $1.7 \times 10^{16} \text{ cm}^{-3}$ (CuH). It is evident that there must be significant number densities of both $\text{Cu}_{3.5}\text{Br}_{3.5}$ and CuH in the discharge of our copper hybrid laser.

CONCLUSIONS

The highest average output powers in a 12.5 mm bore hybrid laser are obtained for a gas flow rate of around 1 litre.atm.hr⁻¹ and an HBr pressure of 3-4 torr in 34 torr Ne. It is estimated that the Br pressure needed near the wall to account for the observed copper metal removal rate is ~ 2 mtorr; the number density of copper in atomic and molecular forms averaged throughout the tube is $4 \times 10^{16} \text{ cm}^{-3}$. Significant numbers of Cu_xBr_x polymers and CuH must exist in the laser discharge to account for the large pool of copper atoms that exists in the active zone.

REFERENCES

1. L. Little and C. E. Little, "Average power scaling of copper hybrid lasers," *Proc. XI International Symposium on Gas Flow and Chemical lasers and High Power Laser Conference, Edinburgh, UK, 25-30 August 1996*, invited paper (1996).
2. D. R. Jones, A. Maitland and C. E. Little, "A high-efficiency 200 W average power copper HyBrID laser," *IEEE J. Quantum Electron.* **QE-30**(10), 2385-2390 (1994).
3. A. A. Isaev, D. R. Jones, C. E. Little, G. G. Petrash, C. G. Whyte and K. I. Zemskov, "Characteristics of pulsed discharges in CuBr and HyBrID lasers," *Opt. Comm.* (submitted) (1996).
4. P. Coutance, G. Sitja and J. P. Pique, "Copper bromide polymers concentration in a Cu/HBr laser," *IQEC'96 Technical Digest* 239 (1996).
5. E. S. Livingstone, D. R. Jones, A. Maitland and C. E. Little, "Characteristics of a copper bromide laser with flowing Ne-HBr buffer gas," *Opt. Quantum Electron.* **24** 73-82 (1992).
6. R. F. Rolsten, *Iodide Metals and Metal Iodides* (New York: John Wiley and Sons) (1961).
7. L. Brewer and N. L. Lofgren, "The thermodynamics of gaseous cuprous chloride, monomer and trimer," *J. Am. Chem. Soc.* **72** 3038-45 (1950).
8. D. N. Astadjov, N. K. Vuchkov and N. V. Sabotinov, "Parametric study of the CuBr laser with hydrogen additives," *IEEE J. Quantum Electron.* **QE-24**(9) 1927-35 (1988).
9. M. Guido, G. Balducci, G. Gigli and M. Spoliti, "Mass spectrometric study of the vaporization of cuprous chloride and the dissociation energy of Cu_3Cl_3 , Cu_4Cl_4 , and Cu_5Cl_5 ," *J. Chem. Phys.* **55**(9) 4566-4572 (1971).
10. K. P. Huber and G. Herzberg, *Molecular Spectra and Molecular Structure. IV. Constants of Diatomic Molecules* (Van Nostrand Reinhold Co.: New York) (1979).
11. G. P. Hogan, C. E. Webb, C. G. Whyte and C. E. Little, "Experimental studies of CVL kinetics," in *Pulsed Metal Vapour Lasers - Physics and Emerging Applications in Industry, Medicine and Science*, ed. C. E. Little and N. V. Sabotinov (Kluwer Academic Publishers: Dordrecht) 67-72 (1996).

High energy IR lasers operating on XeI transitions

V. F. Tarasenko, A.V. Fedenev, B.M. Koval'chuk

High Current Electronics Institute, SB of Russian Academy of Sciences,
634055, Akademicheskii Ave. 4, Tomsk, Russia

ABSTRACT

An experimental investigation was made of the parameters of lasing as a result of atomic transitions in xenon observed when Ar-Xe and He-Ar-Xe mixtures were excited by an electron beam in a laser chamber with an active volume of ~ 600 liters. Electron beam from six double acceleration diodes were injected axially symmetric into this chamber. This ensured a more efficient utilization of the pump energy and a uniform distribution of the laser radiation energy over a transverse exit aperture in the maximum specific input energies. An output radiation energy of the order of 100 J was generated with an efficiency of about 2% at $\lambda = 1.73 \mu\text{m}$ and of the order of 50 J with an efficiency of about 1% at $\lambda = 2.03 \mu\text{m}$. An analysis was made of the experimental results and of criteria for the optimization of the pump parameters in order to improve the output characteristics of a wide-aperture laser operating on the basis of atomic transitions in xenon.

Keywords: xenon laser, atomic transitions, electron beam, high energy, high efficiency.

1. INTRODUCTION

The main advantages of a high-pressure gas laser emitting as a result of atomic transitions excited by an electron beam are a relatively narrow emission line and the feasibility of increasing the output laser radiation energy by increasing the active volume (scaling up). The requirements in respect of the quality of the output radiation beam lead to specific criteria for selecting the way of injecting an exciting beam so as to ensure a uniform distribution of the current density, the optimal pump pulse duration, and an increase in the energy of the accelerated particles.

A laser based on atomic transitions in xenon is currently one of the most promising sources in near-IR radiation. The very first experiments in which electron beams were used to pump gaseous mixtures of xenon with buffer gas (argon) at pressures of 1-3 bar yielded record output parameters: a specific output energy up to 3 J liter^{-1} and an efficiency of 2%-3%¹⁻⁶. However, when an Ar-Xe mixture in a wide-aperture laser with an active volume of 270 litres was pumped by an electron beam from one side, the lasing efficiency was found to be just 0.5%⁷. A report was published in 1990⁸ that a laser radiation energy of 650 J was obtained by pumping an Ar-Xe mixture in a region of $0.5\text{m} \times 0.65\text{m} \times 3\text{m}$ dimensions⁸. The excitation was provided by wide-aperture electron beams injected from opposite sides of the laser chamber. The output radiation energy was maximized at the expense of uniformity of the input energy over a transverse section of the laser chamber (so that the ratio of the whole volume of this chamber to that excited efficiency was approximately 2:1), which was the reason for relatively low lasing efficiency⁸ (0.57% - 0.85%). It was also reported⁸ that preliminary mixing of the gas mixture increased considerably the output radiation energy. The duration of the pulses generated by pumping such a large volume was twice the duration of the electron beam pulses. This was explained⁸ by energy accumulation in excited states of xenon dimers, followed by the emission of VUV radiation ($\lambda = 172 \text{ nm}$) and photoionization of Xe_2^+ .

We carried out an experimental investigation of lasing as a result of atomic transitions in xenon when Ar-Xe mixtures were excited by an electron beam in a laser chamber with an active volume about 600 litres. Efficient utilization of the pump energy and a uniform distribution of the output radiation over a transverse exit aperture were ensured, in contrast to the solution^{7,8}, by employing apparatus⁹ in which electron beams from six double acceleration diodes were injected axisymmetrically into laser chamber.

2. APPARATUS

We used the pump configuration described in detail⁹. The electron acceleration facility consisted of 12 modules supplied from 12 voltage generators located in a shared evacuated enclosure. The output voltage of these generators was 0.6 MV, the current was 60-80 kA, the duration of the leading edge of the voltage pulses was 0.1 - 0.2 μs , and the pulse duration at half-amplitude was 0.5 - 0.7 μs . A cylindrical laser chamber, 3 m long and 0.6 m in diameter (active volume 600 litres), included a plane-plane cavity formed by an aluminum-coated mirror and a quartz plate. The pump and output radiation parameters were

determined by methods¹⁰. The energy deposited in the gas by an electron beam was recorded by the pressure pump method. The total output radiation energy and its distribution over the exit aperture were measured by an automated system based on TPI-2M.1 calorimetric sensors. The working area of one calorimeter was 36 cm². The measuring panel, consisting of 31 calorimeters forming a single block, was used. An electric signal from each calorimeter passed through a multiplier (with standard CAMAC interface), reached the input of a digital voltmeter, and then passed (in the digitized form) to a DVK-3 computer where it was processed and stored. The time characteristics of the laser radiation were recorded with an FSG-22 germanium photoresistor and an S8-14 oscilloscope.

3. EXPERIMENTAL RESULTS AND DISCUSSION.

The accelerator ensemble made it possible to vary the pump energy by altered the number of the voltage pulse generators which were switched on. This made it possible to select the optimal, in respect of the efficiency, excitation regime. The pressure dependencies of the output energy obtained from a mixture of the Ar:Xe = 100:1 composition demonstrated (Fig. 1) that, when all 12 accelerators were used, the laser efficiency was considerably less than that achieved by just two electron beams. More efficient utilization of the electron beam energy and more effective excitation of the whole gas-filled chamber, and also a high uniformity of the output energy density over the laser beam cross section, were ensured by the use of acceleration modules located on opposite sides of the laser chamber and at different relative levels. The maximum output energy at wavelength 1.73 μm obtained from the Ar:Xe - 100:1 mixture at 1.5 bar was 100 J, corresponding to an efficiency of ~ 2% relative to the energy deposited in the active media.

In this case, an increase in the energy deposited in the gas by increasing the number of operating acceleration modules resulted in a near-exponential fall of the output energy (Fig. 2). The use of all 12 voltage pulse generators reduced the output energy to 10 J, which could be explained by an increase in the rate of electron-impact mixing of the active levels of the xenon atom when the electron concentration in the plasma increased^{6,11}. At high specific pump powers (near axis of 1 kW/cm³) the addition of a lighter buffer gas (helium) increased the output energy of the Xe laser and/or the lasing efficiency, and it also altered the emission spectrum¹²⁻¹⁴. In these experiments it was found that dilution of the Ar-Xe mixture by one third with helium (curve 2 in Fig. 2) reduced the output energy at $\lambda = 2.03 \mu\text{m}$, which initially was 50 J for two accelerators, in the same way as at $\lambda = 1.73 \mu\text{m}$ for the Ar-Xe mixture.

Pumping by a 0.03-2.5 millisecond electron beam. Laser oscillation on Xe-atom transitions with $\lambda = 1.73, 2.03, 2.63, 2.65, 3.37 \mu\text{m}$ (with 90% power at 1.73 μm) was obtained and studied under excitation by e-beam accelerators with plasma cathodes and planar or radially converging electron beam¹⁵. The optimum pressure in an Ar:Xe = 100:1 mixture at a current density on the order of 0.04 A/cm² and at pulse duration of 0.1 ms was about 1 atm. A specific output energy of 1 J liter⁻¹, at an efficiency 2% in terms of energy deposited by electron beam, and a total energy of 6 J were achieved in this case. At a beam current density of about 10 mA/cm² and duration of excitation of 2.5 ms the pulse length of laser oscillation threshold of 0.12 mA/cm² was achieved by using of radially convergent e-beam for lasing at 2.03 μm in Ar:Xe = 100:1 (p= 1 atm) gas mixture.

The laser oscillation at the same five Xe-atom transitions were also investigated by using of 5 ns and 40 ns pulse duration e-beams with average electron energy of 150 keV and current densities of 1 kA/cm² and 80 A/cm² respectively. The most intense lines (1.73, 2.03 and 2.65 nm) have a common upper operation level. It was shown that due to the strong competition between these transitions it is passable by variation of cavity Q, gas mixture and pressure, additions of molecular gases (see ref. 14) and pumping power to achieve a primarily lasing at each of these wavelength.

The results of our experiments thus enabled us to draw a number of conclusions and recommendations on the design and construction of an efficient wide-aperture IR laser based on transitions in the Xe atom and characterized by a high uniformity of the distribution of the output radiation energy over the laser beam cross section.

It is obvious that a uniform transverse distribution of the output radiation energy over a large (diameter in excess of 10 cm) aperture of the laser beam is best achieved by coaxial configurations of the electron accelerator and the laser chamber. Several modules of this type (differing in respect of the electron-accelerator cathodes) have recently become available and they are relatively simple, compact, and reliable^{9,10,15}.

Another problem is selection of the optimal, for a given laser chamber geometry, electron beam parameters (electron energy and current density) because of the possibility of over-excitation of a gas mixture in a Xe laser and exceeding the critical plasma-electron density at which electron-impact mixing of the active levels becomes significant. The available suites of application programs for numerical simulation of an Xe laser^{6,7,11} and current methods for calculating the distribution of the energy deposited by an electron beam¹⁶ make it possible to carry out this task with a sufficient degree of precision. Fig. 3 gives

the experimental dependencies of the Xe laser efficiency on the specific pump power plotted on the basis of the results obtained in the present and previous^{2,3,5,7,8,13} investigations at various pressures in the gas mixture. These dependencies are based on the results of experiments in which electron-beam pulses of microsecond duration were used and the laser chambers had an active volume in excess of 10 litres. The pump power densities were taken from the original papers or were estimated on the basis of the data given in¹⁷. At pump power densities exceeding 10 kW/cm^2 , the lasing efficiency fell with increase in the input energy and the rate of fall was greater at lower pressures in the mixture.

Another possibility of effective attainment of high output energies is a reduction in the pump power by increase of the pulse generation. For example¹⁵, if the duration of the pump current pulses amounts to tens and hundreds of microseconds and if the current density is reduced correspondingly, the efficiency can be up to 2% in the range of pump power densities $20 - 120 \text{ W/cm}^2$.

4. REFERENCES

1. Losev V.F., Tarasenko V.F. *Kvantovaya Electron. (Moscow)* **7** 663 (1980) [*Sov. J. Quantum. Electron.* **10** 381 (1980)].
2. Basov N.G., Danilychev V.A., Ustinovskii N.N., Kholin I.V., Chugunov A.Yu. *Pis'ma Zh. Tech. Fiz.* **8** 590 (1982).
3. Bychkov Yu.I., Losev V.F., Tarasenko V.F., Tel'minov E.N. *Pis'ma Zh. Tech. Fiz.* **8** 837 (1982).
4. Baranov V.Yu., Isakov I.M., Leonov A.G., Malyuta D.D., Novobrantsev I.V., Smakovskii Yu.B., Strel'tsov A.P. *Pis'ma Zh. Tech. Fiz.* **9** 1124 (1983) [*Sov. Tech. Phys. Lett.* **9** 483 (1983)].
5. Baranov V.V., Danilychev V.A., Dudin A.Yu., Zayarnui D.A., Ustinovskii N.N., Kholin I.V., Chugunov A.Yu. *Pis'ma Zh. Tech. Fiz.* **11** 173 (1985) [*Sov. Tech. Phys. Lett.* **11** 70 (1985)].
6. Sereda O.V., Tarasenko V.F., Fedenev A.V., Yakovlenko S.I. *Kvantovaya Electron. (Moscow)* **20** 535 (1993).
7. Bunkin F.V., Datskevich N.P., Derzhiev V.I., Karlov N.V., Kuz'min G.P., Mesyats G.A., Skakun V.S., Tarasenko V.F., Yakovlenko S.I. *Kvantovaya Electron. (Moscow)* **13** 878 (1986) [*Sov. J. Quantum. Electron.* **16** 576 (1986)].
8. Litzenberger L.N., Trainor D.W., McGeoch M.V. *IEEE J. Quantum. Electron.* **26** 1668 (1990).
9. Abdulin E.N., Bugaev S.P., Efremov A.M., Zorin V.B., Koval'chuk B.M., Kremnev V.V., Loginov S.V., Mesyats G.A., Tolkachev V.S., Shchanin P.M. *Prib. Tech. Eksp.* (5) 138 (1993).
10. Abdulin E.N., Gorbachev S.I., Efremov A.M., Koval'chuk B.M., Loginov S.V., Skakun V.S., Tarasenko V.F., Tolkachev V.S., Fedenev A.V., Fomin E.A., Shchanin P.M. *Kvantovaya Electron. (Moscow)* **20** 652 (1993).
11. Ohwa M., Kushner M.J. *IEEE J. Quantum Electron.* **26** 1639 (1990).
12. Derzhiev V.I., Zhidkov A.G., Sereda O.V., Skakun V.S., Tarasenko V.F., Fedenev A.V., Yakovlenko S.I. *Kvantovaya Electron. (Moscow)* **17** 985 (1990) [*Sov. J. Quantum Electron.* **20** 902 (1990)].
13. Suda A., Wexler B.L., Riley K.J., Feldman B.J. *IEEE J. Quantum Electron.* **26** 1304 (1990).
14. Skakun V.S., Tarasenko V.F., Fedenev A.V. *Opt. Spektrosk.* **71** 669 (1991) [*Opt. Spectrosc. (USSR)* **71** 387 (1991)].
15. Bugaev A.S., Koval' N.N., Ryzhov V.V., Tarasenko V.F., Turchanovskii I.Yu., Fedenev A.V., Shchanin P.M. *Kvantovaya Electron. (Moscow)* **17** 17 (1990) [*Sov. J. Quantum. Electron.* **20** 11 (1990)].
16. Bugaev A.S., Koval' N.N., Lomaev M.I., Mel'chenko S.V., Ryzhov V.V., Tarasenko V.F., Turchanovskii I.Yu., Fedenev A.V., Shchanin P.M. *Laser Part. Beams* **12** 663 (1994).
17. *Plazmennye Lasery Vidimogo i Blizhnego UF Diapazonov* (Plasma Lasers of Visible and Near-UV Ranges) *Tr. Inst. Obshch. Fiz. Akad. Nauk* **21** (1980) [whole volume].

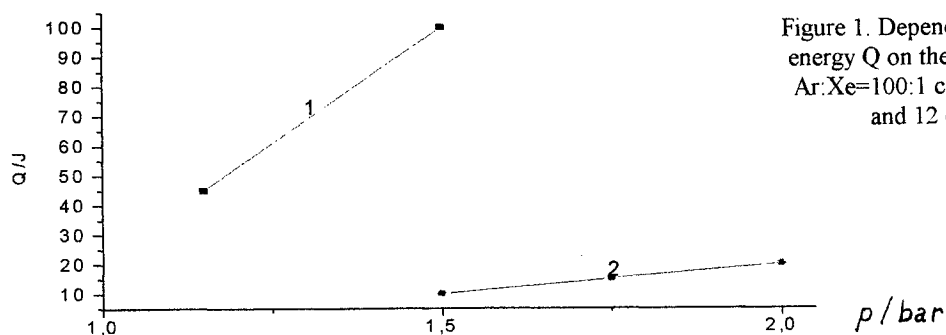


Figure 1. Dependences of the output radiation energy Q on the pressure in a mixture of the Ar:Xe=100:1 composition pumped by 2 (1) and 12 (2) voltage pulse generators.

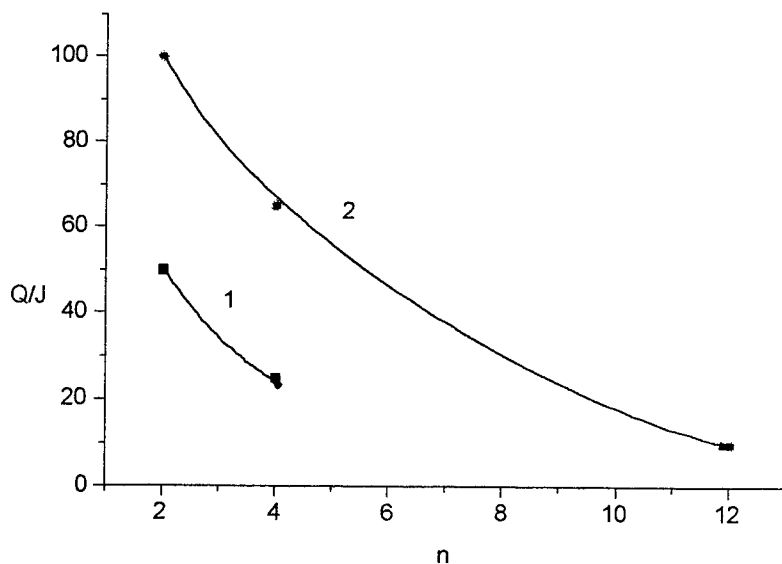


Figure 2. Output energy Q obtained from He:Ar:Xe = 0.4:1.1:0.01, $p=1.5$ bar (1), and from Ar:Xe = 100:1, $p=1.5$ bar (2) mixtures, plotted as a function of the number n of the acceleration modules used for excitation.

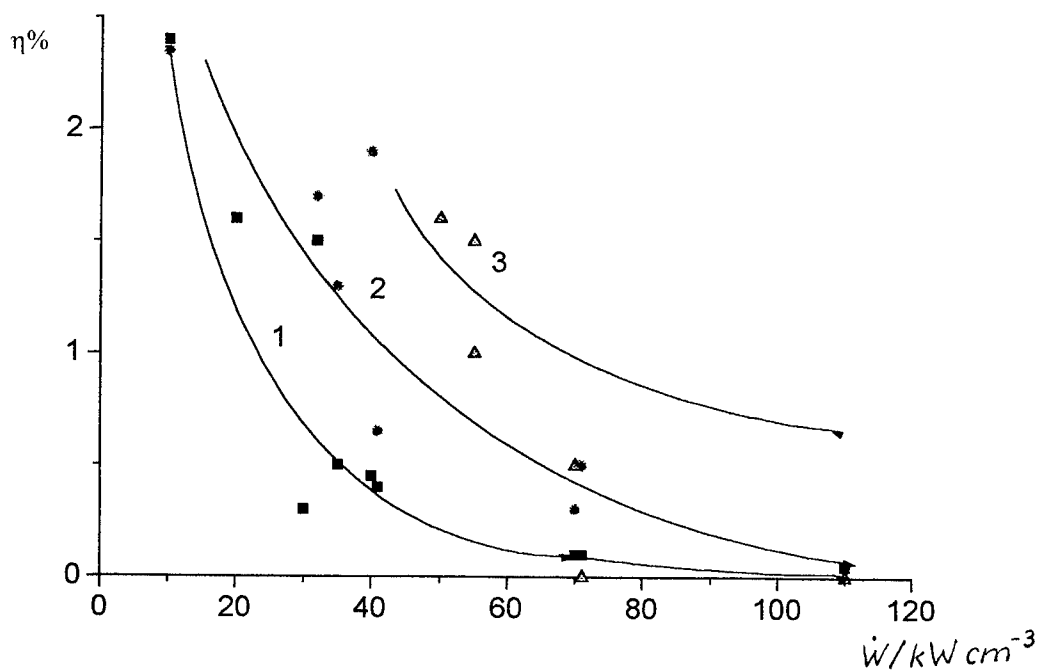


Figure 3. Dependences of the efficiency of the investigated Xe laser ($\lambda = 1.73\ \mu\text{m}$, Ar-Xe mixture) on the pump power density delivered to mixtures at pressures $p = 1.5$ bar (1), 2.0 bar (2), and 2.5 bar (3), plotted on the basis of the results obtained in the present study and those previously reported^{2,3,5,7,8,13}.

Network-based simulation of CO laser

Mitsubiro Iyoda, Manabu Taniwaki* and Shunichi Sato**

Chiba Institute of Technology, Department of Computer Science, 2-17-1 Tsudanuma, Narashino 275, Japan

Telephone: +81 474 78 0530, Telefax: +81 474 78 0549

E-mail : iyoda@iyo.cs.it-chiba.ac.jp

* ** Institute of Research and Innovation, Laser Laboratory, 1201 Takada, Kashiwa 277, Japan

Telephone: +81 471 44 8811, Telefax: +81 471 44 8939

*E-mail : taniwaki@po.ijnet.or.jp

**E-mail : syuniti@po.ijnet.or.jp

ABSTRACT

The simulation code for the analysis of CO laser has been adapted for the recent computer network environment. The workstations, personal computers (PCs), and Macintoshes (MACs) are linked to the network where the simulation is carried out by the fast back-end machine and the input/output interfaces are built in the front-end PCs and MACs. The typical example can be displayed in the Web homepage.

Keywords: simulation, network, computer, PC, Macintosh, workstation, WWW

1. INTRODUCTION

Although CO lasers were operated below 200K in the beginning of development, they are now operated at room temperature. It is very important to analyze and predict the performance of CO laser, as the multi-KW laser setup for the industrial applications is huge and complex. The authors developed several simulation codes¹⁻⁷ describing all the detailed processes, such as electron impact in discharge, V-V energy transfer, spontaneous and stimulated photon emission. The large codes were carried out by the world-fastest supercomputer. However, it is now possible^{6,8} to run them by workstations and even by PCs and MACs in spite of the relatively long calculation time. As the processing speed increases year by year, the time problem will be less serious. In consideration of the recent progress in the computer networks, the authors have developed another simulation code suitable for the network environment.

2. NETWORKS

Before the development project of CO laser simulation code started, it had not been strange that the computer users had to operate at the computer centers to input, execute, and output the processing. The operating system (OS) was the time sharing system (TSS) for the multi-user processing. The monitor terminals were connected to the on-line ports of the host computer. In order to cope with the remote operation, the computer connection was extended via telephone lines by converting the digital information into analog signal with modems. The connection was 1:N (host computer : remote user sites) as shown in Fig.1. Although the speed of data transfer was as low as 300 bits per second (bps) at the beginning, it is now in the much faster range of 9.6 - 28.8K bps. Instead of the spacial terminals, PCs and MACs with the communication software are used as the intelligent terminals. The log records are stored in the local disks. This conventional type of connection is also popular for personal communication, such as Compuserve and AOL.

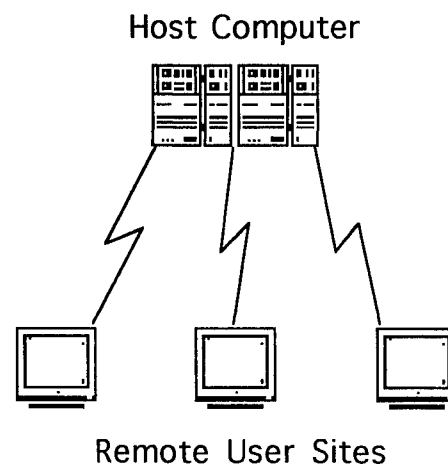


Fig. 1. Conventional remote connection.

The progress in technology was observed in the local area network (LAN). At the early stage of development, there existed several networks, such as OmniNet for PCs, LocalTalk for MACs, Ethernet for workstations. The services were mainly file sharing and printer sharing for PCs and MACs. The workstations were designed to process the TCP/IP (Transmission Control Protocol / Internet Protocol) network communication. Due to the development of inexpensive Ethernet devices, the number of PCs and MACs for TCP/IP communication increases.

As shown in Fig.2., the internet is constructed by connecting LANs by router devices and exchanging the TCP/IP packets. The LAN users can seamlessly access from their own sites to the internet. Although the flexibility of internet is much higher, main applications were e-mail and ftp (file transfer) for a long time. Recently, World Wide Web (WWW) have spread around the world. The Web homepages are described in HTML (hyper text markup language) easily. A number of homepages are published and browsed by the internet users.

In addition to the internet, companies and universities pay attention to "intranet" where the same applications as those of internet are used for the internal information processing. However, most of scientific calculations are operated by the conventional login access. The authors propose the new type of simulation based on intranet, where the mathematical calculation is processed by the server and the input/output operations are performed in the homepage.

3. DATA PROCESSING

It is possible to send the data to Web server and request the processing. The typical examples are the databases to search homepage addresses and shopping products. The mechanism called CGI (common gate interface) transfers the data and launches the background processing. In the authors' project, the simulation is processed instead of database. The followings are the flow of data processing.

- [1] A user requests the simulation homepage from the browser by pointing the page address.
- [2] The requested Web server returns the hypertext to the user site.
- [3] The homepage with the data input fields is displayed in the browser.
- [4] The user inputs the simulation parameters in the field and submits them.
- [5] The server receives the data and launches the simulation process.
- [6] The simulation is executed and the results is returned to the server.
- [7] The Web server transfers the simulation results to the user site.
- [8] The page of simulation results is displayed in the browser.

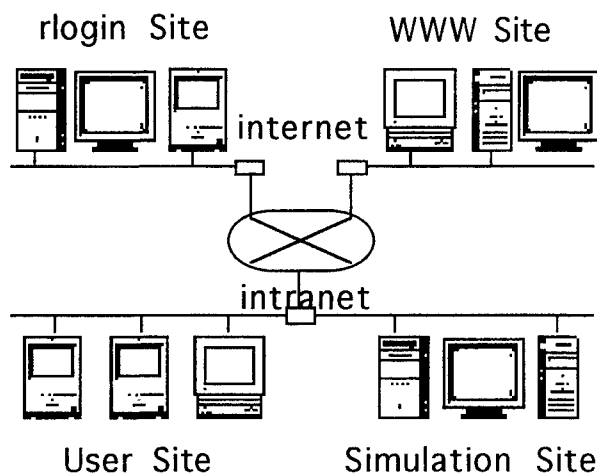


Fig. 2. Connection of internet and intranet.

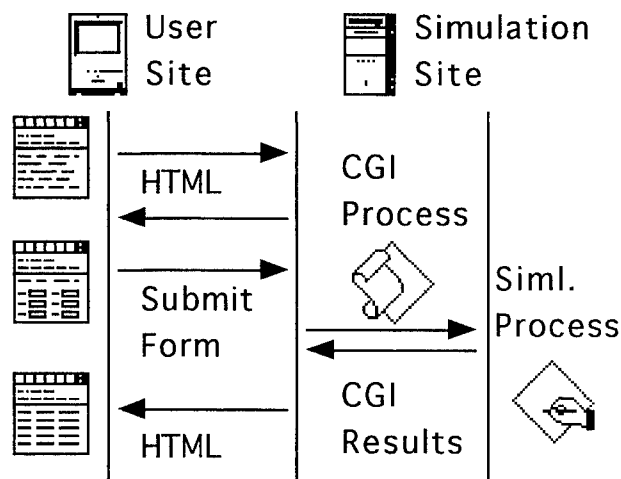


Fig. 3. Data flow between user and simulation sites.

In order to perform the simulation, the set of submission page, CGI script, and simulation code should be described to correctly transfer the input parameters and output results. For example, the input field data are packed as "CO=7&He=76&Temp=273" when they are transferred from the browser to the server. The first step of CGI is to unpack the data by removing the delimiters "&" and "=". On the other hand, the text data from the server to the browser should be described in HTML format. The CR (carriage return) code of plain text results in no line increment in the browser.

4. RESULTS AND DISCUSSION

In this paper an example of the discharge module is explained. The basic Boltzmann's equation is described as Eq.(1). The electron energy distribution function, $f(u)$, is obtained by solving the equation. The 3rd and 4th terms represent the energy loss from $(u+u_j)$ to u and from u to $(u-u_j)$, respectively. The 6th and 5th terms represent the reverse processes. The previous code for the super computer is converted for the server processing.

$$\begin{aligned} & \frac{E}{3N} \frac{d}{du} \left(\frac{u}{Q_1(u)} \frac{df(u)}{du} \right) + \frac{2m_e}{M} \frac{d}{du} \left\{ u^2 Q_2(u) \left(f(u) + \frac{k_B T}{e} \frac{df(u)}{du} \right) \right\} \\ & + \sum_j (u + u_j) f(u + u_j) Q_j(u + u_j) - u f(u) Q_j(u) \\ & + \sum_j (u - u_j) f(u - u_j) Q_j(u - u_j) - u f(u) Q_j(u) = 0 \end{aligned} \quad (1)$$

The example of the simulation homepage is designed as Fig.4. The advantage of HTML is the simple description to arrange the page format. The input fields and buttons are easily described, such as `<input name="CO">` and `<input type="submit" value="Send">`. If the same user interface is described in the conventional programming language, the list must be much more complex. The user sets the parameters in the input fields. Any values in the fields can be rewritten before the submission. The "Reset" button is prepared to clear all the fields and reset the submission. After the input is finished, the data processing is submitted by the simple click of "Send" button. When the submission fails, the error message page is displayed.

At the server site, the parameters are unpacked and the simulation process is launched. The authors selected a MAC, instead of workstation, as the Web simulation server to examine the possibility of simple and compact host. The operation of Mac Web server is very easy. The CGI process is described in AppleScript which can launch not only the simulation but also the popular applications, such as FileMaker and Excel. On the other hand, the performance and the style of Web browser are almost independent on a variety of computers.

After the simulation process is finished, the page with termination message is returned as shown in Fig.5. The input parameters and the time stamp of the acceptance are displayed. The link pointer to the main results is located in the text "Results Here." By clicking the pointer, the user can browse the page of the simulation results as shown in Fig.6. Although this example is simple, the display can be decorated by adding the HTML tags to the text at the server site.

The screenshot shows a Netscape browser window with the title "Netscape: CGI11 Sample Page". The address bar shows "http://202.17.17.88/GCL11b.html". The main content area has a large "Mac Lab" title. Below it, there are several input fields: "CO Ratio" with value 7, "He Ratio" with value 76, "Gas Temp" with value 273, "N2 Ratio" with value 17, "O2 Ratio" with value 0.3, and "E/N Field" with value 1.73e-16. There are "Send" and "Reset" buttons. Below these, there is a section labeled "Which CPU?" with a radio button and the text "CPU 1".

Fig.4. Submission of input form.

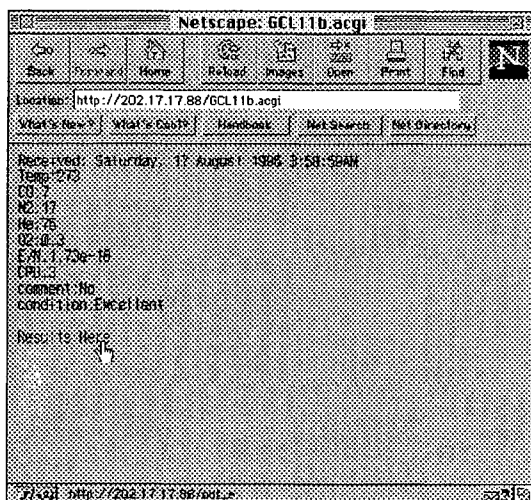


Fig. 5. Message of termination.

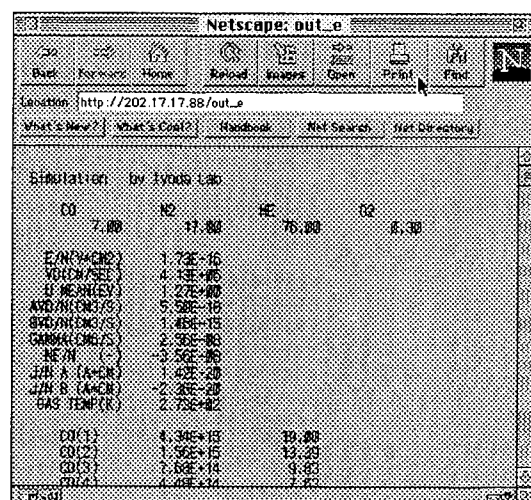


Fig. 6. Simulation results.

5. SUMMARY

The possibility of network-based simulation has been examined. Instead of the conventional rlogin access, the Web server-browser system is one of the attractive approach to the simulation. The parameters are transferred from the browser to the server where the simulation is processed. The results are returned from the server to the browser. The construction of the server is not so difficult. No special training is required for the user as the operation of Web browser is very easy and popular. The recent progress in Web is so fast and great that the functions are continuously enhanced. The animation of the simulation will be realized by the new mechanism, such as Java and Shochwave.

6. REFERENCES

1. M.Iyoda, M.Hori, S.Sato, T.Fujioka, "Theoretical studies on subsonic flow transverse discharge CO laser," *5th International Symposium on Gas Flow and Chemical Lasers*, Oxford, 20-24 August, 1984.
2. M.Iyoda, K.Terunuma, S.Sato, and T.Fujioka, "Parametric analysis of a cw CO EDL by computer simulation," *6th International Symposium on Gas Flow and Chemical Lasers*, Jerusalem, 8-12 September, 1986.
3. M.Iyoda, S.Sato, H.Saito, T.Fujioka, T.Murota, and M.Akiyama, "Computer simulation for the efficient operation of a cw CO electric discharge laser," *7th International Symposium on Gas Flow and Chemical Lasers*, Vienna, 22-26 August, 1988.
4. M.Iyoda, S.Sato, T.Murota, and M.Akiyama, "Two-dimensional computer modeling of discharge-excited CO gas flow," *8th International Symposium on Gas Flow and Chemical Lasers*, Madrid, 10-14 September, 1990.
5. M.Iyoda, T.Murota, M.Akiyama, and S.Sato, "1D and 2D computer models of industrial CO laser," *Modeling and Simulation of Laser Systems II, SPIE International Conference on High Power Lasers*, Los Angeles, 20-25 January, 1991.
6. M.Iyoda, Y.Yamaguchi, H.Okaya, M.Akiyama, M.Taniwaki, and S.Sato, "PC-based beam mode analysis of CO laser," *9th International Symposium on Gas Flow and Chemical Lasers*, Crete, 21-25 September 1992.
7. M.Iyoda, H.Okaya, M.Akiyama, M.Taniwaki, and S.Sato, "FFT analysis of CO laser beam mode based on PC and workstation," *10th International Symposium on Gas Flow and Chemical Lasers*, Friedrichshafen, 5-9 September, 1994.
8. M.S.Taylor, "High level, PC-based Laser System Modeling," *Modeling and Simulation of Laser Systems II, SPIE International Conference on High Power Lasers*, Los Angeles, 20-25 January, 1991.

Atmospheric absorption effects in beam delivery for industrial CO lasers

Q. Cao, H. J. Baker, D. R. Hall

Department of Physics, Heriot-Watt University
Edinburgh EH14 4AS, United Kingdom

Abstract

Spectrally resolved atmospheric absorption has been investigated to determine the problems of long path beam delivery of high power industrial CO laser light for material processing. A dry gas purged beam path is found to be essential if the natural CO laser spectrum is used. However, an unpurged beam delivery system may be satisfactory over typical distances when the spectrum is modified to avoid coincidence with strong water lines by the use of an intra-cavity absorption section.

Key words : CO laser, water vapour IR absorption, beam delivery system.

1. Introduction

The $5\mu\text{m}$ high power carbon monoxide laser has advantages over the well-developed $10\mu\text{m}$ carbon dioxide laser in the field of materials processing. The shorter wavelength offer produces smaller focused spot size, brighter beams, narrower kerfs and higher absorption that may give rise to faster processing rates. Previous investigations have shown that CO lasers have better performance than CO_2 lasers in cutting, hardening, welding, crystal growing and other surface treatments of metals or ceramics [1]. Recently efforts have been made to develop room temperature CO laser technology at multi-kilowatts level.[2,3]

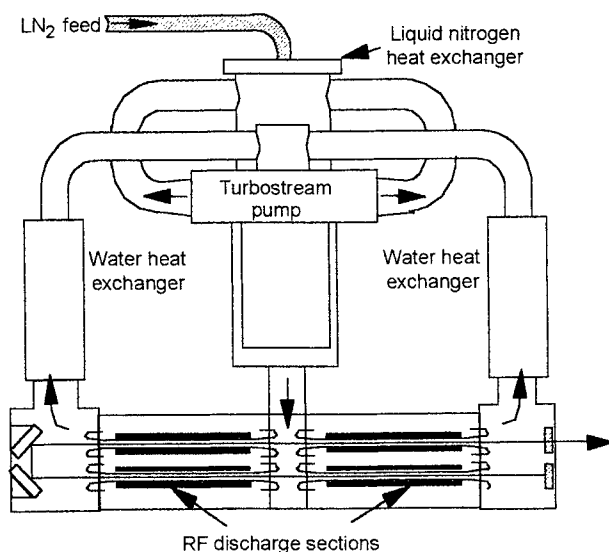


Fig.1 1kW fast flow CO laser

CO lasers must operate with a multi-line spectrum spreading over 5 to 6 μm range to extract power efficiently from the ladder of CO vibrational levels excited by the gas discharge. The ν_2 fundamental absorption band of water vapour centred at 6.2 μm spreads into the $5\mu\text{m}$ region in the form of discrete absorption lines and a much weaker continuum [4]. Water vapour absorption of CO laser light in the beam delivery path is thus highly line specific, giving rise to variable power loss and beam distortion due to thermal blooming. Schellhorn *et al.* [5] have reported that a relative humidity of only 25% leads to a decrease of the near field intensity by 50%. We have also observed significant beam distortion in profile measurements and power attenuation by simply moving the power meter progressively away from the laser.

In this paper we describe a set-up to quantify atmospheric absorption in the propagation of high power carbon monoxide laser beams and to assess implications for beam delivery in high power industrial laser material processing by monitoring the spectral variations. The laser used here, as illustrated in Fig.1, is a cryogenically cooled, RF-excited, compact table-top design with a U-shaped stable laser resonator capable of a

maximum power output 1.08kw at 28% efficiency [6]. The laser has been operated in two configurations: in the first, the resonator is wholly inside the gas envelope while in the second, one mirror is outside the gas envelope giving a 20 cm intracavity air path.

2. Set-up and experiments

As shown in Fig.2, the set-up provides a total enclosed length of 2.4 m between the laser output window and the pyroelectric detector, using a system of tubes and boxes that can be gas purged. The Bentham monochromator was set at minimum

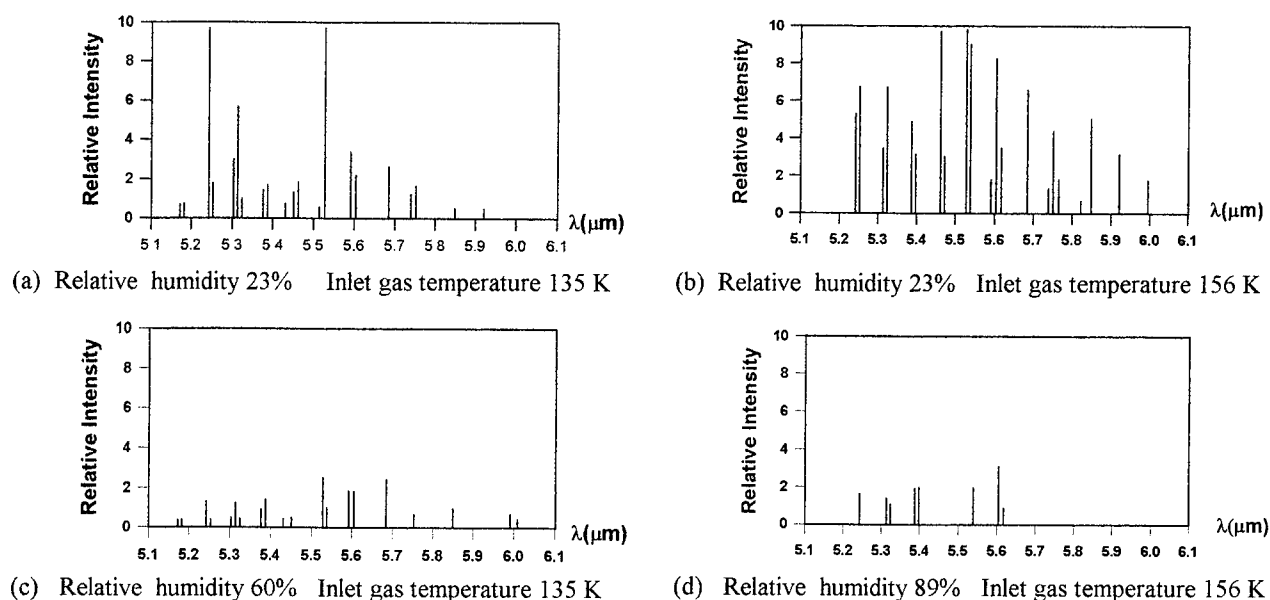


Fig.4 Dependence of laser spectrum on gas inlet temperature and beam path water vapour absorption

With resonator mirrors inside the gas envelope as shown in Fig.1, the intensity of the major laser lines is shown in Fig. 5 as laboratory air at 23% humidity is displaced by nitrogen with a measured exit humidity of 16%. The additional 7% humidity causes intensity decreases of 8% to 35% depending on the line. Long term purging of the beam path with dry nitrogen to attain less than 1% humidity will be necessary to reduce atmospheric absorption to acceptable levels under these spectral conditions.

An investigation has been made of the modification of the laser spectrum to remove lines which are strongly absorbed by water vapour, by the introduction of a section containing water vapour into the laser cavity as in Fig. 6. The double pass through 20 cm of air at 23% humidity and 23°C is estimated to provide up to 20% in cavity loss for CO lines which overlap water absorption lines, based on the data in Fig.5. This loss is expected to be sufficient to cause the particular rotational lines which are strongly absorbed to drop out of the laser line spectrum. The experimental results are encouraging in that we do obtain different dominant spectral lines, and as can be seen from Fig.7,

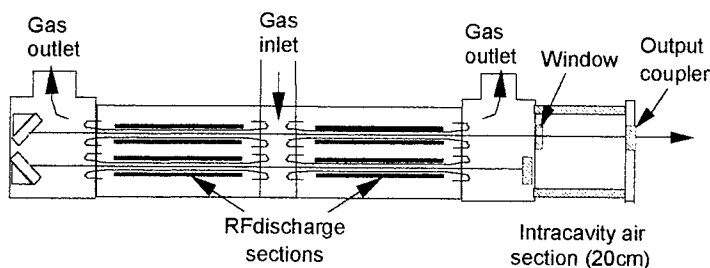


Fig.6 Intracavity air path set-up

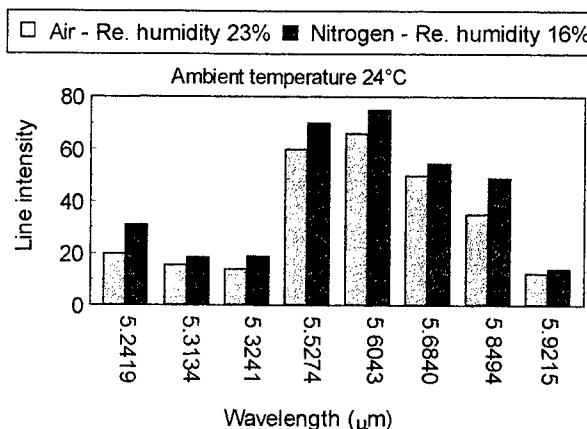


Fig.5 Absorption of specific lines with increasing humidity. (Resonator mirrors are inside gas envelope)

many lines show no measurable intensity difference with an increase of humidity of 7% in the test path. However, some lines still show a small degree of absorption with the humidity change. This may be expected in that there will inevitably be high gain lines in the CO laser spectrum which only partially overlap discrete water absorption lines. The in-cavity absorption loss in these cases will be much less than the 30% output coupling, and they may continue to lase efficiently without switching to an alternative rotational line.

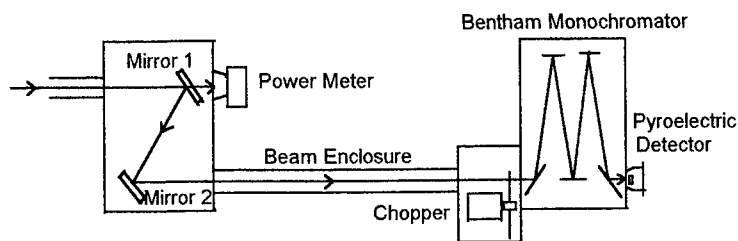


Fig.2 Experimental set-up

The CO laser is typical of diatomic molecules with the infrared vibrational-rotational transitions occurring within the $X^1\Sigma^+$ ground electronic state. The CO molecules are vibrationally excited by electronic impact in the discharge and transferred to higher V states by collisions, resulting in the so-called partial inversion with respect to the lower V states for specific combinations of rotational levels. Between a particular pair of vibrational levels, there is considerable variation in the rotational transitions that can contribute to the laser spectrum, due to changes in operating conditions such as gas temperature, the location of axial mode frequencies, etc. The preferred J values are those corresponding to the highest population difference, controlled by the Boltzman distribution function and local gas temperature, resulting in strong temperature-dependence of the spectrum. Analysis of the typical spectral output of the fast flow laser gives the V, J transitions shown in Fig. 3. The figure shows the expected cascading transitions down the vibrational ladder. There are two groupings of observed $V-J$ transitions, which are believed to arise from the large temperature change along the resonator axis. At the low temperature inlet region the Boltzmann distribution has a maximum at low J and anharmonic pumping favours low V values. Near the gas outlets the gas temperature is ~ 150 K higher, and the peak in the rotational distribution moves towards $J \sim 20$, whilst the population inversion occurs only for higher V . The laser spectrum adjusts to make use of contributions to the gain from both these regions. The effect of gas temperature on the detailed laser spectrum is shown in Fig. 4 (a) and (b). The spectrum shifts from longer wavelength to shorter wavelength as the inlet gas temperature is reduced. At lower temperature, the inversion between lower vibrational bands and the anharmonic structure of the vibrational manifold favours emission at shorter wavelength.

entrance and exit slit widths to give 0.5nm resolution, fully resolving the CO laser line spectrum. Two AR/AR ZnSe mirrors were used to pick off a few watts as a sample from the typically 800 W laser beam, with the rest going to a power meter with which the laser output is monitored. The set-up was designed to sample the whole beam to reduce speckle pattern fluctuations.

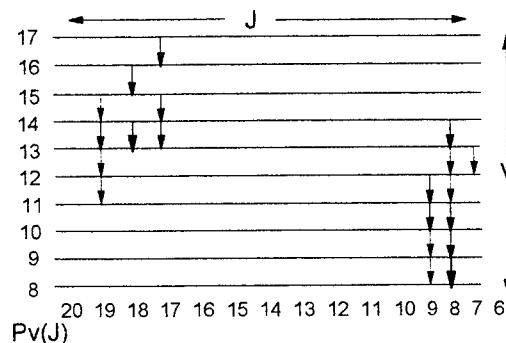


Fig.3 Main transitions in laser spectrum at 156 K inlet temperature and no in-cavity water absorption

When water vapour is artificially added to the beam path, by the circulation of high humidity air from a water bath, significant power loss can be observed in a spectrally resolved form, as shown in Fig. 4(c) and (d). Total power losses up to more than 60 per cent and 85 per cent respectively occurred in the cases of water concentration in the path corresponds to 60% and 89% relative humidity at 23°C. The strongest absorption is in the longer wavelength region where lines with wavelength over 5.65 μm were absorbed to such an extent that they could hardly be observed. This observation is in agreement with published results of field measurements of atmospheric transmittance, where the transmission is effectively zero between 5.6 μm and 7.0 μm at sea level over a 0.3 km path.

In compiling the spectra in Fig. 4, it was found that there was considerable difficulty in keeping the laser spectrum unchanged over a time sufficient to complete a spectral scan using the monochromator motor drive. The detailed spectrum varies on the time scale of thirty seconds or so, due to competition of rotational transitions linking specific vibrational states. This is believed to be caused by cavity length drift and gas inlet temperature fluctuations generated by boiling in the LN_2 heat exchanger. It is thus not possible to calculate reliable atmospheric absorption coefficients for specific laser lines from two spectra taken at different times. To avoid this problem, we have carried out individual line investigations by alternately switching the nitrogen gas purge on and off in the enclosed beam path, while continuously monitoring the laser power at a fixed wavelength selected by the monochromator. This method allows us to differentiate between laser power changes caused by the spectral fluctuations and that caused by the introduction of water vapour, and base absorption coefficient changes on time averages.

3. Conclusions

It has been shown experimentally that the variability of the CO laser spectrum combined with atmospheric water absorption of the radiation in a lab or workshop environment can cause serious power losses and unpredictable power delivery to a workpiece, over path lengths used in typical beam delivery systems. In addition, heating of the air and subsequent convection may produce blooming-induced beam quality degradation. The cryogenically cooled CO laser has an intrinsically very low water vapour pressure within the cavity, and hence many of the lines emitted may be strongly absorbed, with up to 50% total power loss being possible over several metres of open air. Using the natural laser spectrum, very low water vapour pressures are needed in an enclosed beam path, strongly purge with dry nitrogen. There may also be a need for an initial bake out of the enclosure to release adsorbed water

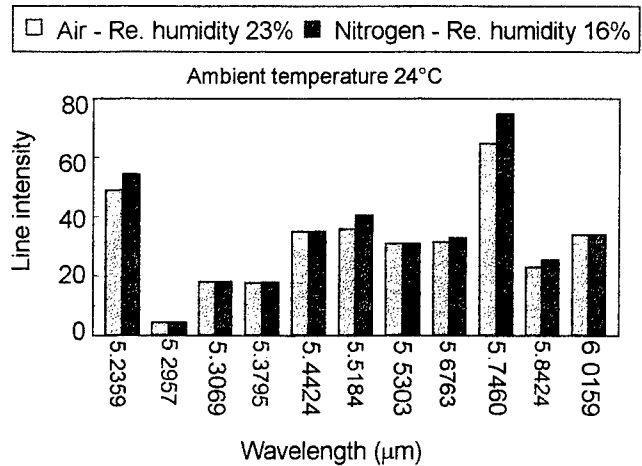


Fig.7 Absorption of modified spectral lines

With moderate amounts of water vapour in the in-cavity absorption region, the laser adjusts the rotational lines used to saturate the gain to avoid the strongest water vapour lines, without significant loss of power output. This is possible because of the rapid rotational thermalisation at the pressures used in the laser, and also because of the relatively close longitudinal mode spacing of the long laser cavity. However, there remain lines in the spectrum which do show some water vapour absorption over the 2.4 m test path, for example the 5.746 μm line in Fig 7. With the much reduced overall power loss using the open section within the cavity, it may be possible to use a relatively short beam delivery path without resorting to dry gas purging.

4. Acknowledgement

Support for this work from DTI under the EU113 Eureka Programme is acknowledged.

5. References

1. A.Maisenhlder "Material processing by CO lasers", Proceedings of the Laser Advanced Materials Processing Conference, LAMP'92 Nagaoka, Japan , pp43-50 (1992)
2. M Uehara, H Kanazawa "A room temperature operating pulse RF discharge excited CO Laser" Proceedings of GCL/HPL'96 Conference, Edinburgh, to be published by SPIE
3. W G McNaught, G Wlodarczyk "A 3 kW industrial CO laser operating at room temperature" Proceedings of GCL/HPL'96 Conference, Edinburgh, to be published by SPIE
4. W L. Wolfe, G J. Zissis " The infrared handbook " Environmental Research Institute of Michigan
5. M.Schellhorn, H von Blow "High power gasdynamically cooled CO-laser with unstable resonator " SPIE Proceedings . **2502**, 63-68 (1995)
6. Yu, H. J. Baker, N. A. S. Rodrigues and D. R. Hall " Compact high-efficiency carbon monoxide laser at 1 kW", Appl. Phys. Lett. **65**, 2904-6 (1994)

Multi-quantum VV-exchange modeling of the pulsed Q-switched frequency selected CO laser

A.A.Ionin*, Yu.M.Klimachev*, Yu.B.Konev**, A.K.Kurnosov***, I.V.Kochetov***, V.Sinityn*

* P.N.Lebedev Institute of Physics, Moscow 117924, Russia

** Institute of High Temperatures, Izhorskaya Str., 13/19, Moscow 127412, Russia, Ph./Fax (095)485 8066

*** Troitsk Institute of Innovation and Fusion Research, Troitsk, Moscow Region, 142092

ABSTRACT

The results are presented of computer modeling jointly with preliminary results of experimental investigations of sequentially Q-switched frequency selected CO laser. Calculations show the essential difference in pulse form and inversion restotation time between the models of single- and multi-quantum vibrational exchange kinetics.

Keywords: CO laser, multi-quantum vibrational exchange, Q-switching

1. INTRODUCTION

Vibrational exchange kinetics is of great importance in wide diversity of processes, such as high speed non-equilibrium gas dynamics, plasma chemistry, isotope separation, atmosphere physics, laser etc. There are two general groups of molecules important in applications, which differ in the physical mechanisms of vibrational exchange: homonuclear diatomics (N₂, O₂ are examples) and heteronuclear polar diatomics (CO, NO, isotopically substituted homonuclear diatomics etc.). The last group also may include an important case of vibrational modes of simple polyatomic molecules with strong IR transitions.

The vibrational exchange in the first group of molecules is relatively slow, single quantum exchange (SQE) processes predominate in the wide range of vibrational quantum numbers, Ref.1. The second group is characterized by fast vibrational exchange, rate constants of which increase rapidly with vibrational quantum numbers and become of the order of gas kinetic rate constant at relatively low levels. Numerical calculations in Ref.2 showed that multi-quantum exchange (MQE) is of the same rates as single-quantum for these molecules.

Theoretical models of vibrational kinetics are mostly consider SQE. The model is formulating in this case in very general and relatively simple terms. It was widely used in various applications of vibrational kinetics. The justification of this model lays in satisfactory agreement with measurements of population vibrational distribution functions (VDF), Ref.3. Poor physical background of simplified model of vibrational kinetics made us to develop the more complicated model, taking into account the MQE processes, Ref.4. The calculations were performed for CO molecule, which also might be considered as good model molecule, especially remembering that information is available in literature on rate constants of multiple vibrational processes in CO. Qualitatively, the results may be applicable to a rather wide group of molecular vibrational modes with strong IR transitions.

Calculations showed that MQE model explains stationary and transient VDF equally well as SQE model. But more complicated phenomena may differ considerably in two models. For example, it was shown in Ref.4, that double resonance measurements of restoration of VDF after local perturbation is the phenomena of this kind. Many other processes are also sensitive to the details of kinetics. In this paper the results are presented of comparative investigation of another process - consequent Q-switching of frequency selected CO laser. Preliminary experimental results on two consequent Q-switching of frequency selected CO laser are also presented.

2. MODEL

The system of kinetical equations for vibrational level populations of CO and N₂ molecules, including MQE in CO, is presented in details in Ref.4. The only change was that induced transitions in preselected vibrational band were included.

In calculations, it was supposed that specific characteristics and composition of active medium were the same as in experiment, Ref.5, that is mixture CO/N₂=1/9, discharge specific energy 250 J/g, discharge pulse duration 80 mcs. Total molecule density was supposed to be $N=0.05$ Amagat, temperature of active media - $T=100$ K. Q-switching began in 30 mcs after termination of discharge pulse. To model Q-switching it was supposed that resonator threshold gain decreased linearly

from the value, which was several times higher than the active media gain on the selected transition, to the preselected value, equal 1.5×10^{-3} 1/cm for the time 0.25 mcs, went on constant at this value for 0.5 mcs and increased linearly to the initial value for 0.25 mcs. Thus, the full Q-switching process duration was 1 mcs. Time delay between sequential Q-switching varied in the range 0.5-2 mcs. Preselected transition changed in the range from $\nu=9-10$ to $\nu=31-30$.

3. THE RESULTS OF CALCULATIONS

In Fig.1 and Fig.2 the results are presented of calculations of two consequent Q-switching pulses on various transitions using MQE and SQE models respectively. The measure of restoration of VDF is coincidence of two consequent pulses in form and amplitude. One can easily observe that SQE model provides practically full restoration of VDF between pulses. Restoration of VDF at high levels in MQE model is much slower, just as it was observed in Ref.4 for calculations of double-resonance experiments.

At low vibrational levels SQE rate constants are nearly the same in both models, MQE processes are of small importance. Thus, the results in both models differ unessentially (Fig.1a and Fig.2a). At high vibrational levels rate constants of quasi-resonant exchange in SQM are very large and exceed gas kinetic rate constant an order of magnitude at high vibrational levels. Restoration of populations is very fast, two consequent pulses are nearly the same (Fig.2). Long quasi-stationary phase of lasing is due to fast VV-pumping from neighbour levels. In MQE model rate constants of vibrational exchange are much less, restoration of VDF is incomplete, pulse amplitudes differ considerably (Fig.1). Pumping from neighbour levels is relatively small, quasi-stationary phase of pulses may be not observed (Fig.1,c).

4. THE RESULTS OF EXPERIMENTS

Preliminary results of measurements of two consequent Q-switched pulses at preselected vibrational transition $\nu=20-19$ were performed to observe the tendencies in variation of pulse form at various delays and high-Q duration time. Experiments were performed using sub-nanosecond IR detector and fast computerized oscilloscope. Fig.3a shows laser pulses in the cases, when high-Q duration was about 2.5 mcs, Fig.3b and Fig.3c - 1.25 mcs respectively. Pulse delay between Q-switching was about 2.5 mcs in Fig.3a, 0.62 mcs in Fig.3b and 1.25 mcs in Fig.3c. Pulse delay relative current pulse was 570 mcs in Fig.3b and 3c, 510 mcs in Fig.4a. The restoration of inversion is not complete in Fig.3b and 3c. In Fig.3a pulses are very similar in form and amplitude. Pulses in Fig.3 are strongly modulated as the result of mode beating. Pulse forms in Fig.3 are in qualitative agreement with calculations. Quantitative analysis may be a useful tool for experimental and more precise determination of rate constants of vibrational exchange, which are known till now only from calculations. Though one should keep in mind that laser action is complicated process which depends on parameters, usually badly known or even only estimated.

5. ACKNOWLEDGEMENTS

Measurements of pulse forms were performed in P.N.Lebedev Institute of Physics with participation of Drs. C.Beairisto, R.Penny and S.Squires (Directorate of Applied Technology, USA) and Dr. R.Walter (W.J.Schafer Associates, Inc., USA). We are grateful them for collaboration.

This work has been performed under financial support of Russian Foundation of Basic Research.

6. REFERENCES

1. B.F.Gordietz, A.I.Osipov, L.A.Shelepin. Kinetical processes in gases and molecular lasers. Nauka Publ., Moscow, 1980 (in Russian).
2. G.D.Billing. "Vibration-vibration and vibration-translation multi-quantum energy exchange by atom-diatom and two diatom molecule collisions". *Nonequilibrium vibration kinetics*. Ed. by M.Capitelli. Ch. 4. Springer, Berlin, 1986.
3. R.Farrenq, C.Rossetti, G.Guelashvili, W.Urban. *Chem.Phys.*, **292**, p.389, 1985.
4. Yu.B.Konev, I.V.Kochetov, A.K.Kurnosov, B.A.Mirzakarimov. "Kinetic model of multi-quantum vibrational exchange in CO". *J.Phys.D: Appl. Phys.*, **24**, N10, pp.2054-2058, 1994.
5. A.A.Ionin, H.Kobsa, Y.Klimachev, D.Sinityn. OE/LASE'96, Proc. SPIE **2702**, p.51, 1996.

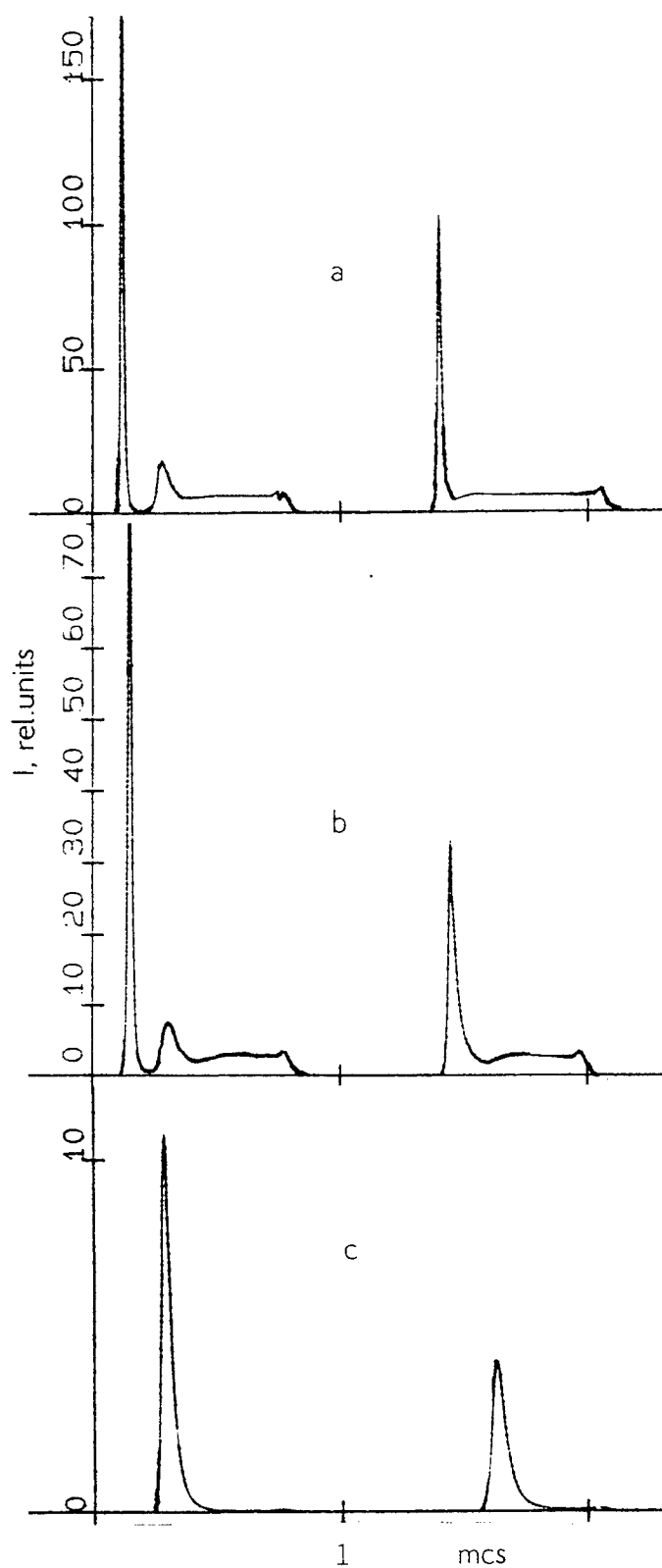


Fig.1. Pulse forms, calculated in MQE model.
a - $v=15-14$, b - $v=20-19$, c - $v=31-30$ transitions.

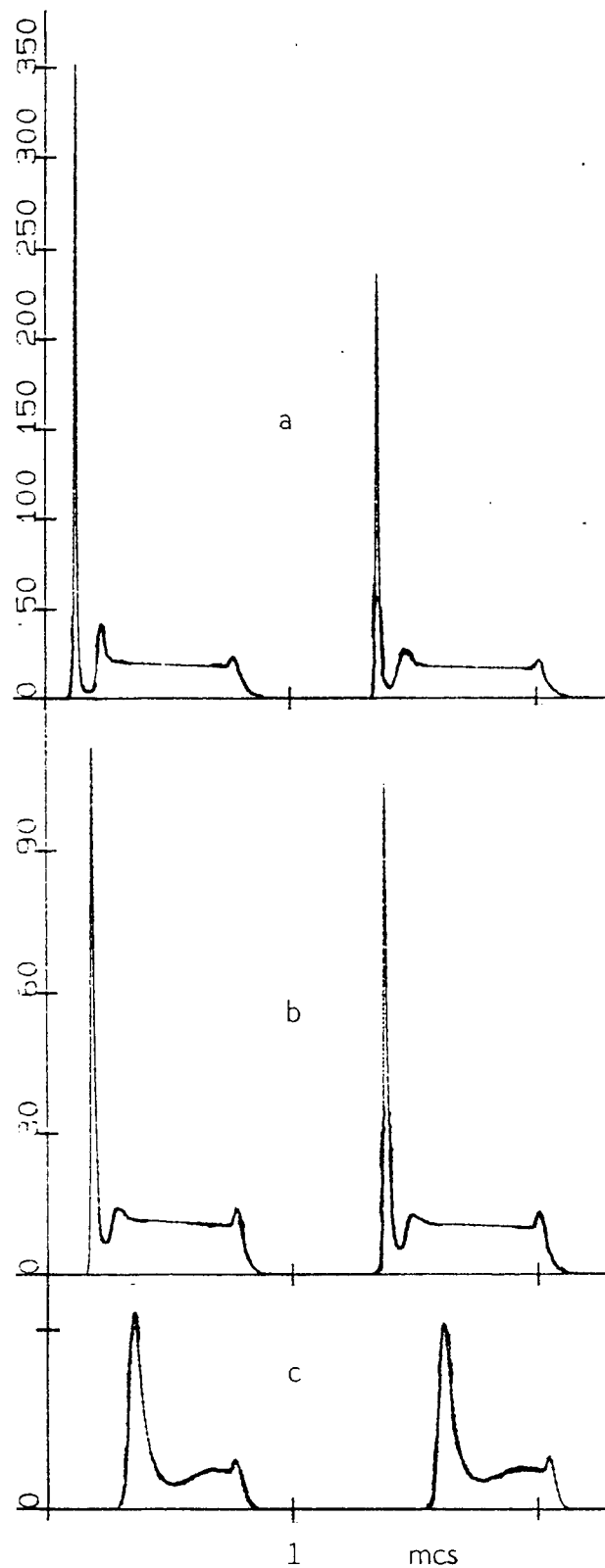


Fig.2. Pulse forms, calculated in SQE model.
a - $v=15-14$, b - $v=20-19$, c - $v=31-30$ transitions.

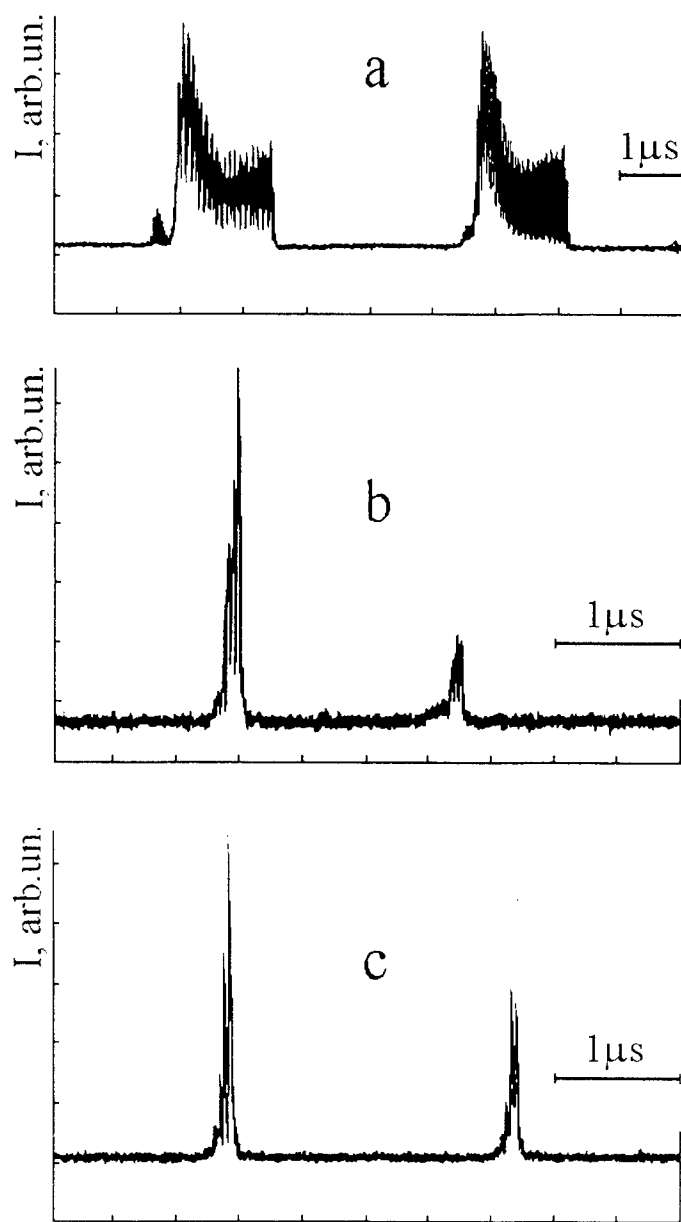


Fig.3. Pulse forms, measured on $v=20-19$ transition.

Short pulse ($\sim 1\text{-}10\mu\text{s}$) electron-beam-controlled discharge CO laser with selected wavelengths

L. Afanas'ev, A. Ionin, Yu. Klimachev, H. Kobsa⁺, A. Kotkov, L. Seleznev, D. Sinitsyn

P.N. Lebedev Physics Institute of Russian Academy of Sciences, 53 Leninsky pr., 117924 Moscow, Russia

⁺DuPont Science and Engineering, Chestnut Run Plaza, Wilmington, DE 19880-0715, USA

ABSTRACT

A frequency selected (FS) Q-switched (QS) e-beam controlled-discharge (EBCD) CO-laser has been researched and developed. The laser generates short pulses ($\tau_{0.1} \sim 1\text{-}10\mu\text{s}$) having different spectral content including single line one within $4.92\text{-}6.54\mu\text{m}$ spectral range. An influence of spectral content of CO laser radiation "locked" or "blocked" inside a laser resonator on output energy and efficiency of lasing on selected wavelengths has been studied.

Key words: CO laser, frequency selection, Q-switching, electron-beam-controlled-discharge laser.

1. INTRODUCTION

Pulsed IR laser radiation with determined pulse duration and wavelengths is necessary for some applications of CO laser. For instance, for some laser isotope separation processes, laser stimulation of chemical reactions, laser surface heat treatment of selectively absorbed materials etc., high power CO laser radiation on wavelengths within $5\text{-}6.5\mu\text{m}$ interval can be used^{1,2} with selected wavelengths and short pulse duration ($\tau_{0.1} \sim 1\text{-}10\mu\text{s}$).

The only way to produce high power FS short CO laser pulses is the using of Q-switching of laser resonator³. Because of a peculiarity of inversion population formation for multi-level CO molecule, a considerable reduction of laser efficiency and output energy takes place. Up to now there were only a few research works where some attempts had been done to obtain short ($\tau_{0.1} < 1\mu\text{s}$) CO laser pulses by Q-switching with spectral selection^{4,5}. There were no publications, which would have demonstrated FS short pulse CO laser with output energy higher than 10 mJ, at least. In this connection FS QS EBDCD CO laser has been researched and developed. A special attention has been given to lasing near the edge of the CO laser spectrum ($\lambda \sim 6\mu\text{m}$), where strong absorptive lines do exist for different molecules having carbonyl groups.

2. EXPERIMENTAL LASER INSTALLATION AND EXPERIMENTAL TECHNIQUE

The cryogenically cooled EBDCD laser installation with active volume of ~ 1 litre has been used in the experiments. The laser mixture density can be varied from 0.1 up to 0.5 Amagat, (1 Amagat corresponds to a gas density at normal conditions), the gas temperature being changed within 100 - 300K interval. Normally, we have used gas mixture at density of 0.25 Amagat. Different laser mixtures with different percentage of CO, N₂, He and Ar have been used. The electrical pumping pulse length can be varied within the interval of 10-1000 μs . Normally, the pumping pulse length of $\sim 60\mu\text{s}$ has been used. An optical scheme with spatial intracavity spectral and pulse length selection has been chosen, which has enabled us to change flexibly the CO laser wavelength, spectral width, pulse length and the number of short pulses in a train. A rotating mirror has been applied for Q-switching. The optical scheme chosen has also enabled us to study an influence of spectral content of laser radiation "locked" or "blocked" inside the laser resonator on output energy and efficiency of lasing on selected wavelength(s). The term "locked" means that the CO laser radiation on locked wavelengths exists, but it is not extracted from laser resonator through the output mirror, though taking part in cascade mechanism of lasing. The term "blocked" means that there is no lasing on given (blocked) wavelengths.

3. EXPERIMENTAL RESULTS AND DISCUSSION

The main experimental data were obtained from dependences of output energy Q_{out} on delay time τ_d between the beginning of the electrical pumping pulse and the moment of laser resonator Q-switching for different experimental conditions (Fig. 1). These data give us the important information about physical processes of energy transformation taking part inside the multi-component multi-level active medium of CO laser:

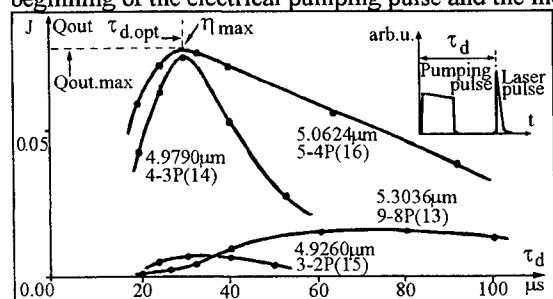


Fig. 1. Typical dependences of FS QS CO laser output Q_{out} on time delay τ_d for different selected lines ($\tau_{0.1} = 5\mu\text{s}$, $N = 0.27$ Amagat, $T = 130\text{K}$, $\text{CO:N}_2 = 1:9$).

physical processes of energy transformation taking part inside the multi-component multi-level active medium of CO laser:

a). The QS lasing began after the time delay of $15\text{-}20\mu\text{s}$ between starting of pumping pulse and the moment of Q-switching irrespective of the selected laser transition (at least for laser vibrational bands $V \rightarrow V-1 = 10 \rightarrow 9$ and lower). The fact indicates, that the formation of population inversion in our conditions of pumping began almost simultaneously. This feature was not specially investigated, but it might be explained by the process of direct CO molecules excitation by electron impacts in electron beam controlled discharge.

b). The time dependent growth of QS laser output up to its maximal value corresponds to the transformation of vibrational energy distribution function in transient conditions of vibrational-vibrational

(V-V) energy exchange, vibrational-translational (V-T) relaxation, cascade lasing (in case of using partial or total laser radiation "locking") and laser gas heating during pumping pulse. The intensities and the rates all of these processes strongly depend on the laser gas mixture content, selected laser transition line (wavelength) and other parameters (initial gas temperature, pressure, "lock" & "block" combinations etc.). Therefore the QS laser output itself and the optimal time delay $\tau_{d,opt}$ (when QS output reached its maximal value $Q_{out,max}$) depended strongly on selected wavelength chosen. And what is more, for different selected spectral lines there are respectively different sets of optimal (corresponding to the maximal laser output) parameters mentioned above.

c). Further decreasing QS CO laser output (and the rate of this decrease) at time delay $\tau_d > \tau_{d,opt}$ is mainly characterized by the processes of V-T relaxation.

If we compare the values of $\tau_{d,opt}$ for different selected laser lines, we can obtain the information about the propagation of vibrational excitation wave through the complicated multi-level structure of active gas mixture containing CO molecules.

3.1. Single line FS QS CO laser mode.

The influence of "locking" and "blocking" CO laser radiation on laser output has been studied for FS QS CO laser operated in single line mode for different laser gas mixtures and for different combinations of laser radiation "locking" and "blocking" (Fig.2). Lasing takes place within the spectral region of 4.92-6.54 μm . (Laser pulse length on the level of 10% of a peak intensity $\tau_{0.1}=5\mu\text{s}$). As one can see from Fig.2, for each selected wavelength (single line FS QS CO laser operation mode) the optimal sets of laser parameters (gas mixture content, "lock" and "block" combinations) are different (even for neighbouring vibrational bands). The general trends for this mode of FS QS CO laser operation were as follows: the highest output characteristics appeared to be at high CO percentage in laser gas mixture (up to 50%) and in conditions of intracavity "blocked" lasing on lower transitions (than selected one) plus "locking" or "blocking" (for different selected lines) of lasing on upper transitions.

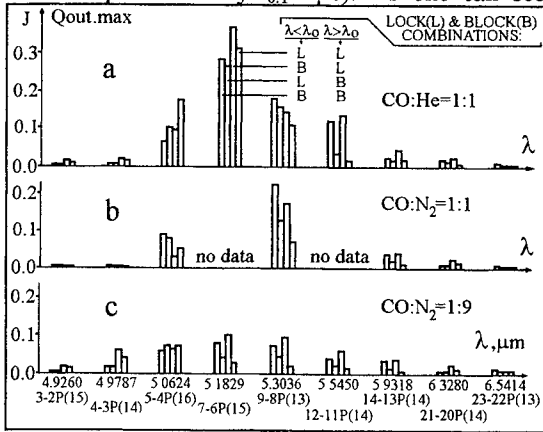


Fig.2. The influence of gas mixture content and "lock" & "block" combinations on maximal single line QS CO laser output $Q_{out,max}$. ($N=0.27\text{ Amagat}$, $T=130\text{K}$, $\tau_d=\tau_{d,opt}$, $\tau_{0.1}=5\mu\text{s}$, $Q_{in}\sim 450\text{J/l Amagat}$).

Reliably detectable QS ($\tau_{0.1}=5\mu\text{s}$) output (output energy of 2-3mJ and higher) was obtained for laser transitions from $3\rightarrow 2\text{P}(15)$ ($\lambda=4.926\mu\text{m}$) up to $23\rightarrow 22\text{P}(13)$ ($\lambda=6.541\mu\text{m}$). The values of maximal single line FS QS CO laser efficiencies and corresponding experimental conditions for three spectral lines (in the middle and near the short- and long-wave edges of working spectral range) are presented in following table:

Line	$\lambda_0 [\mu\text{m}]$	CO:N ₂ :He	$\lambda < \lambda_0$ $\lambda > \lambda_0$	$\eta_{max} [\%]$
4 \rightarrow 3P(14)	4.9787	1 : 9 : 0	Block Lock	0.09
7 \rightarrow 6P(15)	5.1829	1 : 0 : 1	Block Lock	0.56
21 \rightarrow 20P(14)	6.3280	1 : 1 : 0	Block Lock	0.03

3.2. Lasing at the long-wave edge of CO laser spectrum.

For some practical applications it is necessary to form laser radiation pulses with different spectral and temporal parameters. There are some polymeric materials and chemical substances, which have relatively wide and intensive absorption bands near $\sim 6\mu\text{m}$ and could be effectively treated by CO laser radiation containing several (3-5) neighbouring lines. In the most cases short (1-10 μs) laser pulses are needed for material processing. Also it is very important to use physical properties of population inversion formation processes taking place in active medium of CO laser (inversion life time can reach hundreds microseconds; V-V energy exchange can restore the population inversion on selected laser transition(s) after Q-switching) for increasing QS CO laser efficiency by developing the multi-pulse (train) mode of QS CO laser operation at a single pumping pulse. Finally, laser pulses of different lengths could be effectively used for treatment of materials with different absorbancy/thermal conductivity ratio. Taking into account all reasons mentioned above, detailed study of FS QS CO laser operating in 5.8-6.1 μm spectral range was carried out for different spectral widths of output laser radiation ($\Delta\nu=20\text{-}60\text{cm}^{-1}$), for different laser pulse lengths (3-9 μs) both in single pulse mode and in multi-pulse train mode (up to 8 pulses in train). Special attention was paid to obtaining maximal laser output energy characteristics. Also the influence of laser gas mixture content, temperature and density on FS QS CO laser output was investigated.

The laser gas mixture content was optimised for two wavelengths ranges ($\Delta\nu=40\text{cm}^{-1}$) separated by very short spectral interval: $\lambda_0=5.81\mu\text{m}$ (central line $15\rightarrow 14\text{P}(16)$) - Fig.3a and $\lambda_0=6.10\mu\text{m}$ (central line $18\rightarrow 17\text{P}(18)$) - Fig.3b. These data were obtained at the same laser pulse length ($\tau_{0.1}=5\mu\text{s}$), temperature ($T=125\text{K}$) and gas density ($N=0.25\text{ Amagat}$) conditions for each laser gas mixture. Maximal specific energy input $Q_{in,max}$ (limited by electrical breakdown) was higher to some extent for laser gas mixtures without He and reached the value of 500-600 J/l Amagat (Fig.3, bars 1, 3, 5, 6, 8, 9). $Q_{in,max}$ for He-containing mixtures (Fig.3, bars 2, 4, 7, 10) was on the level of 300-400 J/l Amagat.

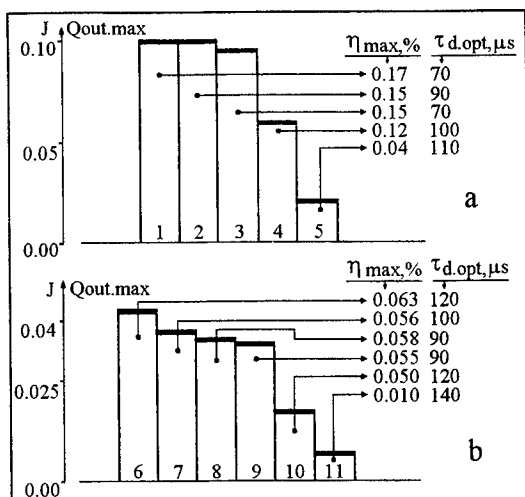


Fig.3. Maximal FS QS CO laser output $Q_{out,max}$ for different laser gas mixtures CO:N₂:He:Ar= 1:1:0:0 (1,8), 1:1:1:0 (2,7), 1:1:0:1 (3,9), 1:0:1:0 (4), 1:0:0:0 (5), 1:3:0:0 (6), 1:0:3:0 (10), 2:0:1:0 (11).

molecules amount) but intensified the V-V energy exchange and V-T relaxation processes (the decrease of the optimal time delay $\tau_{d,opt}$ corresponding to the moment of maximal population inversion and, respectively, maximal laser output on selected wavelength took place).

The FS QS CO laser characteristics are much better for lower temperature. That fact were a trivial one, but for a very weak dependency on temperature had taken place within the temperature interval of 100-150K ($\Delta v=40cm^{-1}$, $\tau_{0,1}=5\mu s$). And what is more, the maximal efficiency of FS QS CO laser operated on $\lambda_0=5.81\mu m$ at the temperature higher than 190K became lower, than one corresponding to $\lambda_0=6.10\mu m$ (optimal laser gas mixtures were used for each selected wavelengths). The role of low temperature for CO laser is well known and one can observe a deterioration of FS QS CO laser characteristics with temperature rise. However, we do not have yet a reasonable explanation for the very weak decrease of laser output within temperature interval of 100-150K.

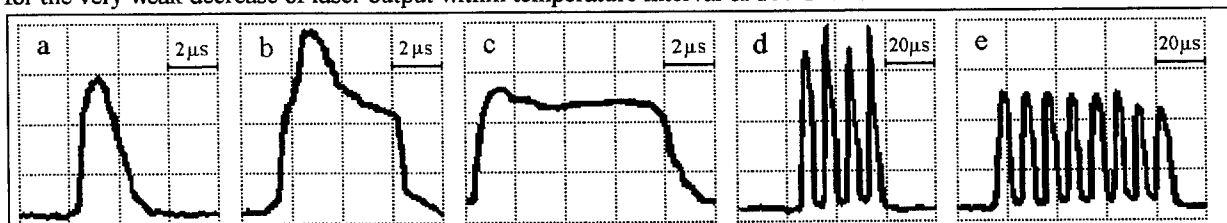


Fig.5. Typical oscillograms of FS QS CO laser pulse temporal shapes (single pulse mode - a, b, c; multi-pulse train mode - d, e) obtained with time resolution of $\sim 0.5\mu s$.

The FS QS CO laser output and efficiency are higher for longer pulse length, for instance, 1.75 times higher for 9 μs laser pulse then for 5 μs one. The longer is a short QS CO laser pulse, the higher is the output energy (Fig.5a-c), because of compensation of inversion population depleting by vibrational-vibrational pumping. For any application one should try to apply longer CO laser pulses because of higher output efficiency of the laser. (The other way is a use of multi-pulse lasing.)

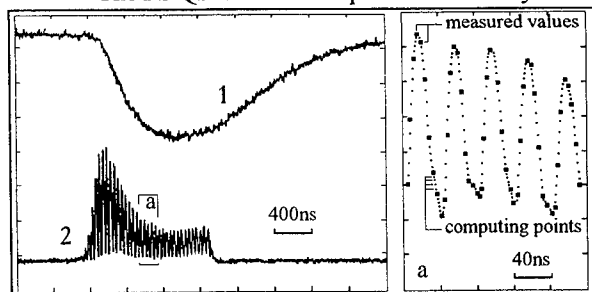


Fig.6. Typical FS QS CO laser pulse time profile measured with time resolution $\sim 0.5\mu s$ (1) and $\sim 10ns$ (2,a). [These data were obtained in our joint experiments with C.Beirsto, R.Penny, S.Squires (Directorate of Applied Technology, USA) and R.Walter (WJSA, USA) at Lebedev Institute].

The best mixtures for obtaining maximal laser efficiency η_{\max} (these values are presented in Fig.3) for these two spectral intervals, separated only by $\Delta\lambda=0.3\mu m$, appeared to be CO:N₂ with different optimal CO percentages: 50% for $\lambda_0=5.81\mu m$ ($\eta_{\max}=0.17\%$) and 25% for $\lambda_0=6.1\mu m$ ($\eta_{\max}=0.063\%$).

The maximal laser output $Q_{out,max}$ and efficiency η_{\max} are increased with the increase of gas density N (Fig.4, $\Delta v=40cm^{-1}$, $\tau_{0,1}=5\mu s$), notwithstanding the decrease of the maximal specific energy input limited by electrical breakdown. The use of higher density (Fig.4) is useful to increase the rate of vibrational-vibrational pumping of CO molecules and the number of molecules radiating per a time interval. Because of a pure technical reason we did not increase gas density higher than 0.27 Amagat, though the higher is density, the higher is laser output. There should be an optimum for density (0.5-0.7 Amagat) because of decreasing a threshold of electrical breakdown (in J/l Amagat units) for higher densities. The Fig.4 also illustrates the fact, that the increase of laser gas density not only caused the increase of QS CO laser output (due to the increase of active CO

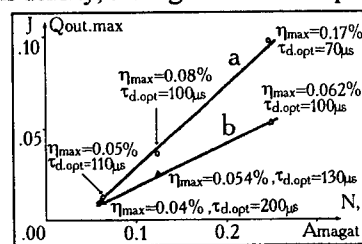


Fig.4. Dependence of FS QS CO laser maximal output $Q_{out,max}$ on gas mixture density N ($T=125K$) for $\lambda_0=5.81\mu m$ (CO:N₂=1:1) - (a) and $\lambda_0=6.10\mu m$ (CO:N₂=1:3) - (b).

It should be pointed out, that all observations of laser pulse temporal parameters $\tau_{0,1}$ and τ_d were carried out by measuring system with response time of $\sim 0.5\mu s$ (Fig.5, 6-1). Some additional study was made to investigate the laser pulse profile with nanosecond time resolution. It was shown (Fig.6), that strong

regular oscillations of laser radiation intensity took place during the lasing. The oscillations arose for all laser pulse lengths $\tau_{0,1}$ from 1 μs up to 30 μs . Typical oscillogram for $\tau_{0,1}=1.3\mu s$ (Fig.6) shows the quasi-sinusoidal temporal behaviour of laser radiation intensity with time period of 40ns (corresponding to round-trip

period of $2L_{\text{res.}}/c$) and high degree of modulation (in some cases up to 100%). It was the first case, when we observed experimentally this temporal behaviour of short pulse CO laser radiation intensity, which can be explained by the effects of a small number (2-3) of longitudinal modes beating or mode locking due to saturated absorbers (for example, atmospheric water vapours) inside the long laser resonator. These temporal experiments has the illustrative character and some additional study is needed to investigate in details the process of CO laser pulse profile formation.

The spectral width of the selected spectral interval chosen near the wavelength of $6\mu\text{m}$ did not influence strongly on laser output, having been changed from 10 cm^{-1} up to 60 cm^{-1} . The weak influence of a spectral width on the laser output takes place because of lasing on discrete vibrational-rotational lines. In the most of experiments we had only two-three spectral lines within the selected spectral interval $\Delta\nu=20\text{--}60\text{ cm}^{-1}$, because fast rotational relaxation and relatively high level of laser resonator losses ($\sim 80\%$) allowed to support lasing only on laser lines, that had maximal gain at the moment of Q-switching (one line in each vibrational band separated by spectral interval about 30 cm^{-1}).

The laser output is also strongly depends on the number M of the short pulses in a train for a single electrical pumping pulse. In these experiments the total (summarised on all laser pulses in train) laser efficiency reached the value of 0.4% for four pulses in train, and 0.62% for eight pulses ($\lambda_0=5.81\mu\text{m}$) ($\tau_{0.1}+\tau_A=F^{-1}$, F - pulse repetition rate, τ_A - the time interval between the short pulses). The multi-pulse QS lasing for a single pumping pulse, first demonstrated in ⁶ for nonselected mode, enables us to increase a total efficiency, because of giving a possibility for recovering inversion population for a time delay τ_A . Comparison of our data with those obtained in ⁶ demonstrated the strong difference between selected and nonselected modes of multi-pulse QS CO laser operation: time interval τ_A corresponding to $\sim 80\%$ -recovering of second laser pulse energy with respect to first one was about $30\text{--}40\mu\text{s}$ (the best result from ⁶ was for following conditions: $N=0.5$ Amagat, $T=100\text{K}$, gas mixture $\text{CO:N}_2=1:9$ for nonselected mode of QS CO laser operation). In our experiments we observed almost the total recovering of population inversion (and, respectively, single laser pulse energy in a train) on selected wavelength (even for lower gas density $N=0.25$ Amagat) at the value of $\tau_A=5\mu\text{s}$ (see oscillograms in Fig.5d,e). These facts could be explained by different mechanisms of population inversion recovering. In case of nonselected mode of QS CO laser operation, the multi-wavelength lasing decreases the population on all laser levels taking part in laser action, and respectively long time is needed to recover all population distribution function by V-V energy exchange. In case of FS mode of QS CO laser operation, population inversion decreased only on selected laser transition and it is recovered much faster (at about an order of magnitude) by CO molecules V-V energy exchange with neighbouring vibrational levels (with respect to selected one).

It should be pointed out, that the laser efficiency obtained in the experiments is not an upper limit, which might be reached, and the optical scheme applied in the experiments enables us to increase much more the number of pulses in train, $(\tau_{0.1})^{-1}$, $(\tau_A)^{-1}$ etc., opening an opportunity for further increase of FS QS CO laser efficiency. The fact is a very important feature, especially for practical application of FS QS CO laser.

4. CONCLUSIONS

The maximal output characteristics of FS QS CO laser for every selected wavelength(s) strongly depend on a lot of parameters: laser mixture content, gas density (pressure) and temperature, pulse length, "locking" or "blocking" laser radiation inside the laser cavity.

For FS QS CO lasing on longer wavelengths (near $6\mu\text{m}$) the best way is "blocking" lower transitions lasing and "locking" upper transitions lasing.

There have been obtained for a single pulse ($\lambda_0=5.81\mu\text{m}$, $\Delta\nu=40\text{ cm}^{-1}$, $\tau_{0.1}=5\mu\text{s}$): $Q_{\text{out,max}}=0.1\text{J}$, $\eta_{\text{max}}=0.17\%$. Maximal laser output and efficiency are increased with increase of gas density and pulse length: $Q_{\text{out,max}}=0.15\text{J}$, $\eta_{\text{max}}=0.21\%$ ($\tau_{0.1}=9\mu\text{s}$).

Output energy and efficiency do not strongly depend on gas temperature within the interval of $T=100\text{--}150\text{K}$.

For the first time, the temporal behaviour of FS QS CO laser pulse intensity was observed experimentally with nanosecond time resolution. All laser pulses appeared to be quasi-sinusoidally modulated with modulation period of 40ns and high (up to 100%) modulation degree.

Q_{out} and η_{max} are increased with the number of pulses M in a train for a single pumping pulse. $Q_{\text{out}}=0.43\text{J}$, $\eta_{\text{max}}=0.62\%$, $M=8$ ($\tau_{0.1}=5\mu\text{s}$). The efficiency obtained is not an upper limit for FS QS CO laser.

5. ACKNOWLEDGEMENTS

The research work has been initiated and supported by DuPont.

6. REFERENCES

1. T.Simijoshi, A.Shiratori, Y.Ninomiya, M.Obara, *Proc.SPIE*, **2502**, 602 (1995).
2. V.B.Laptev, E.A.Rjabov et al, *Quant.Electron.* (Moscow), **22**, 6, 633 (1995) (inRussian).
3. R.M.Osgood, E.R.Nichols et al, *Appl.Phys.Lett.*, **15**, 69 (1969)
4. A.V.Nurmikko, *Appl.Phys.Lett.*, **25**, 465 (1974)
5. A.V.Nurmikko, *J.Appl.Phys.*, **46**, 2153 (1975)
6. V.Yu.Ananiev, N.G.Basov, A.A.Ionin et al, *Quant.Electron.* (Moscow), **12**, 1666 (1985) (in Russian)

Numerical investigation of energy characteristics of the first overtone generation
of a high power supersonic e-beam sustained CO laser

B. M. Dymshits

LOK Co., 14, Dobrolubov Av., St. Petersburg, 197198, Russia

B.S.Alexandrov, V.A.Belavin, J. P. Koretskiy

Russian Scientific Centre "Applied Chemistry", 14, Dobrolubov Av., St. Petersburg, 197198, Russia

ABSTRACT

For operating conditions of the high power supersonic e-beam sustained CO laser a numerical investigation of the energy and spectral characteristics of the first overtone generation is conducted. It is shown that electro-optical efficiency of the first overtone generation can be more than 30%. The efficiency of a spectrum selection both on fundamental and first overtone transitions is evaluated. On the basis of numerical calculations the engineering evaluations for several variants of such a device are executed.

Keywords: CO-laser, supersonic, e-beam sustained, first overtone, spectrum selection efficiency, numerical study.

1. INTRODUCTION

Up to now CO₂ lasers were the only technological lasers whose power exceeded 5 kW. Economically reasonable fields of their application are determined mainly by the cost of their energy and the wavelength 10.6 μ . The CO lasers with subsonic gas flow, the wall-plug efficiency of which is close to that of CO₂ lasers, turned out to be, at the same power, appreciably more expensive and bulky than CO₂ lasers.

20 years ago the extremely high values of efficiency and specific output energy for a CW supersonic e-beam sustained CO laser (SSCO-EIL) were predicted¹. Principal advantages of such a laser are: (1) The system including a supersonic nozzle, a supersonic channel and a diffuser, is a very efficient, cheap, reliable and very compact refrigerating machine. (2) The coincidence of the resonator and the discharge zone allows keeping a low specific vibrational energy in gas mixture. This leads to a low heat flow caused by V-T relaxation. This is very important for increasing the SSCO-EIL efficiency because of lower temperatures and energy expenditures on gas pumping in a closed-cycle system. (3) The surfaces of mirrors and output window forming the walls of supersonic channel are cooled by supersonic gas flow. Such a cooling provides the possibility of using the steady-state operation with a radiative flux of tens of kilowatts per cm². (4) Argon is the largest part of the gas mixture. This provides the possibility of using for pumping of gas mixture in closed-cycle operation a turbo-compressor - high efficient, high productive and very compact device. Up to 1993 the advantages of SSCO-EIL were an alluring perspective only. In 1993 LOK Company launched an open-cycle full-scale mock-up of CW supersonic e-beam sustained CO laser and received in experiments the following results²: output power, $W_{out} = 130-200$ kW; electro-optical efficiency, $\eta_{eo} = 44-49$ %; wall-plug efficiency in an open-cycle regime exceeds 40 %; the duration of continuous operation is up to 1.0 s; e-beam current density in discharge zone, $j_b = 0.02$ mA/cm²; about 70% of output power is concentrated in two spectral lines with wavelength 5.00 and 5.06 μ .

The experiments demonstrating very effective performance of the supersonic e-beam sustained CW CO laser (SSCO-EIL) of power hundreds of kilowatts operating by fundamental transitions² and the possibility of creating the SSCO-EIL of multi-megawatt power³ instill the confidence that a technological SSCO-EIL will be created soon. The use of such a laser will lead to expansion of the field of laser technologies because of increasing output power, making laser energy cheaper and extending the range of operating wavelengths. A number of projects concerning the use of lasers in Earth-orbital space and some technologies (e.g., in production of ultrafine "laser" powders, isotope separation) require using lasers of power units, tens and hundreds of megawatts and different wavelengths. Additional extension of the wavelength range can be reached by using a version of SSCO-EIL which operates by the first overtone transitions (SSCO-EIL-over). Being a record-holder for energy effectiveness among CO and CO₂ lasers SSCO-EIL has all prerequisites for operating well in the range of 2.5-4.0 μ .

In this work, the potential ability of SSCO-EIL to generate by the first overtone transitions of CO molecule has been numerically calculated, the calculations of the efficiency of wavelength selection for the operation of SSCO-EIL by both the fundamental transitions and the first overtone have been made. On the base of the calculations, an engineering analysis for several versions of SSCO-EIL and SSCO-EIL-over has been made.

2. RESULTS

The results presented below have been obtained by solving numerically the system of kinetic equations for a large number of vibrational levels of gas components and equations of one-dimensional gas dynamics. The computational model is based

on the generally accepted theory of CO lasers and SSCO-EIL in particular. The correctness of the model has been confirmed by the fact that full-scale mock-up of SSCO-EIL has been made on the base of this model and its performance is in accordance with the model predictions². Tests conducted with the participation of scientists from USA⁴ have confirmed the energy characteristics of the mock-up and the reliability of the experimental results presented in².

The computation have been performed for two gas mixtures: CO:Ar = 0.1:0.9 and CO:N₂:Ar = 0.05:0.15:0.8 (in the experiments CO:N₂:Ar ≈ 0.06:0.09:0.85). It is adopted in our computations that the following values are the same as they were in testing the mock-up²: the molecular number density at the entrance to discharge zone $N_1/N_0 = 0.2$ (N_0 is Loschmidt number); the gas temperature at the entrance to discharge zone $T_1 = 80\text{K}$; the gas temperature at the entrance to the supersonic nozzle $T_0 = 293\text{K}$; the e-beam gun current density $j_b = 0.02 \text{ mA/cm}^2$; the ratio of electric field strength to particle concentration $E/N = 5.1 \cdot 10^{-17} \text{ V} \cdot \text{cm}^2$; the length of discharge zone along the flow $X = 0.7 \text{ m}$. It is supposed that the discharge take place in the channel of constant pressure, in which $E/N = \text{const}$. Variants with $X = 1.08 \text{ m}$ and $N_1/N_0 = 1.21$ have been considered additionally.

In calculating the optical resonator parameters we adopt that the losses are caused by absorption and scattering by the mirrors and in the gas and are attributed only to the mirrors, including the semitransparent one, i.e. the losses on each mirror per one pass of radiation between resonator mirrors are equal to a and the reflectance of reflective mirror is $R = 1 - a$. The reflectance of semitransparent mirror is calculated subject to the given value of resonator loss factor κ . Considering the overtone generation we suppose that the reflectance of each mirror at wavelengths of fundamental transitions R' is equal to 0.01. Estimations show that in this case the generation by fundamental transitions does not take place. The reflectances and losses for the mirrors used in the experiments⁵ ($R' > 0.997$, $a < 0.003$, $R' < 0.01$) are much more preferable than those adopted in our computations. In calculating the wavelength selection we assume that for the selected lines the loss factor of resonator is the same as in the case of free-running lasing and for the rest of spectral range the lasing is excluded because of high level of resonator losses.

The results of the computation of the energy and spectral characteristics of SSCO-EIL ($\Delta v = 1$) are presented in Table 1 and Fig.1,2,4. The characteristics of SSCO-EIL-over ($\Delta v = 2$) are presented in Table 2 and Fig.3, 5. The following symbols are used: E_{in} - specific input energy; B_d - dimension of discharge zone along the laser beam; h_1 - height of supersonic channel at the entrance to discharge zone; $\eta_{T_1, E_{in}}$ - efficiency of the conversion of discharge energy into radiation inside the resonator; η_{res} - efficiency of resonator; G_d - gas flow rate through the discharge zone; $\eta_{eo} = \eta_{res} \cdot \eta_{T_1, E_{in}}$ - electro-optical efficiency; $W_{out} = E_{in} \cdot \eta_{eo} \cdot G_d$ - laser output power. As a spectral range, the vibrational level numbers are shown for which the line radiation power is more than 1 % of power for all generating transitions together. The number of upper level is shown, i.e. the transitions $v \rightarrow v-1$ or $v \rightarrow v-2$ respectively take place.

Fig.1 shows the spectra of free-running lasing calculated at the values of parameters that took place in testing the mock-up (for variants 1,4 of Table 1. See also column 1 of Table 1 in³). The ratios of the total output power of selected lines to the output power of free-running lasing for variant 4 of Table 1 are presented in Fig.2. The spectra of free-running overtone lasing for variants 1.3 and 1.4 of Table 2 and the ratios of the output power of four selected lines ($v-v-1..v+3-v+1$) to the output power of free-running overtone lasing for the same variants are presented in Fig.3.

The spectra of free-running fundamental lasing for variants 3 and 6 are shown in Fig.4 (among all the variants the values of E_{in} are maximum in these variants). The spectra of free-running overtone lasing for variants 3.1, 3.2 and 6.1, 6.2 are shown in Fig.5.

3. CONCLUSIONS

An apt conjunction of the properties of operating gas mixture with the characteristics of the discharge sustained with e-beam, the understanding, more detailed than earlier, of the processes in SSCO-EIL and, as a consequence, the success in realization of such a laser which take place at present - all this opens the way to create supereffective, supercompact and superpower lasers of multi-megawatt power and different wavelengths.

For free-running lasing the electrooptical efficiency exceeds 50% for generation by fundamental transitions and 30% for generation by first overtone transitions.

The output power of selected lines can be many times more than the output power of the spectral lines corresponding the same transitions of free-running lasing. The spectrum selection extends considerably the wavelength range of generation.

All this gives a hope that economically reasonable fields of laser applications will be significantly extended.

The experimental verification of the main calculation results can be realised at the existing device.

Table 1. Energy and spectral characteristics of SSCO-EIL ($\Delta v=1$)

¹	Gas mixture	N_1/N_0	X, m	B_d , m	h_1 , cm	G_d , kg/s	a	κ , m^{-1}	η_{res}	E_{in} , J/g	$\eta_{T_1 E_{in}}$	η_{eo}	W_{out} , MW	spectral range (v)
1	CO:Ar= 0.1:0.9	0.2	0.7	0.5	5.4	4.56	0.02	0.35	0.769	104.6	0.631	0.483	0.23	5 - 12
2		1.21	0.7	0.5	5.4	27.61	0.02	0.35	0.769	232.0	0.683	0.525	3.38	6 - 15
3		1.21	1.08	2.5	9.25	231.4	0.02	0.25	0.88	332.6	0.697	0.613	48.3	7 - 16
4	CO:N ₂ :Ar= 0.05:0.15:0.8	0.2	0.7	0.5	5.4	4.58	0.02	0.35	0.769	88.1	0.575	0.453	0.18	5 - 12
5		1.21	0.7	0.5	5.4	27.69	0.02	0.35	0.769	197.7	0.676	0.52	2.85	6 - 15
6		1.21	1.08	2.5	9.25	232.0	0.02	0.25	0.88	287.3	0.697	0.614	41.0	6 - 15

Table 2. Energy and spectral characteristics of SSCO-EIL -over ($\Delta v=2$).

	Gas mixture	N_1/N_0	X, m	B_d , m	h_1 , cm	G_d , kg/s	a	κ , m^{-1}	η_{res}	E_{in} , J/g	$\eta_{T_1 E_{in}}$	η_{eo}	W_{out} , MW	spectral range (v)
1.1	CO:Ar= 0.1:0.9	0.2	0.7	0.5	5.4	4.56	0.01	0.05	0.55	103.2	0.469	0.258	0.121	8 - 21
1.2							0.02	0.05	0.17	103.2	0.469	0.079	0.037	8 - 21
1.3							0.01	0.10	0.74	102.6	0.353	0.261	0.122	9 - 25
1.4							0.02	0.10	0.53	102.6	0.353	0.187	0.087	9 - 25
2.1		1.21	0.7	0.5	5.4	27.6	0.01	0.05	0.55	223.0	0.571	0.315	1.94	10 - 27
2.2							0.02	0.05	0.17	223.0	0.571	0.097	0.60	10 - 27
2.3							0.01	0.10	0.74	216.5	0.458	0.339	2.02	13 - 35
2.4							0.02	0.10	0.53	216.5	0.458	0.243	1.45	13 - 35
3.1		1.21	1.08	2.5	9.25	231	0.01	0.10	0.90	296.4	0.382	0.344	23.54	16 - 41
3.2							0.02	0.10	0.82	296.4	0.382	0.313	21.45	16 - 41
4.1	CO:N ₂ :Ar= 0.05:0.15:0.8	0.2	0.7	0.5	5.4	4.58	0.01	0.05	0.55	87.2	0.402	0.221	0.088	8 - 22
4.2							0.02	0.05	0.17	87.2	0.402	0.068	0.027	8 - 22
4.3							0.01	0.10	0.74	86.8	0.273	0.202	0.080	10 - 25
4.4							0.02	0.10	0.53	86.8	0.273	0.145	0.057	10 - 25
5.1		1.21	0.7	0.5	5.4	27.7	0.01	0.05	0.55	191.3	0.556	0.306	1.62	10 - 27
5.2							0.02	0.05	0.17	191.3	0.556	0.095	0.501	10 - 27
5.3							0.01	0.10	0.74	186.3	0.437	0.323	1.67	14 - 35
5.4							0.02	0.10	0.53	186.3	0.437	0.231	1.195	14 - 35
6.1		1.21	1.08	2.5	9.25	232	0.01	0.10	0.90	257.2	0.355	0.319	19.06	16 - 40
6.2							0.02	0.10	0.82	257.2	0.355	0.291	17.37	16 - 40

4. ACKNOWLEDGEMENTS

The authors are grateful to GCL/HLP'96 Organizing Committee and Chairman Prof. D.R.Hall for financial support which made real their participation in Symposium.

5. REFERENCES

1. D.J.Monson, "Potential efficiencies of open- and closed-cycle CO supersonic electric-discharge lasers", *AIAA Journal*, **14** (5), 614-620 (1976).
2. B.M.Dymshits, G.V.Ivanov, A.N.Mescherskiy, I.B. Kovsh, "CW 200 kW supersonic CO laser", *Proceedings of the Int. Symposium on High Power Lasers and Laser Application V*, SPIE, Vol.2206, pp.109-120, Vienna, April 1994.
3. B.M.Dymshits, B.S.Alexandrov, "Multi-megawatt supersonic e-beam sustained CW CO lasers: an estimations of their energetic characteristics and operating regimes", *Proc. of XI Int. Symp. GCL/HPL '96* (to be published).
4. R.O.Johnson, B.M.Dymshits, G.V. Ivanov, A.N.Mescherskiy, J.P.Reilly, M.L.Lander, "Laser-material test results from Russian high power carbon monoxide laser", *Proceedings of the 27 Annual Symposium on Optical Materials for High Power Lasers*, Boulder, CO, Oct.30-Nov.1, 1995.
5. L.H.Sentman, D.L.Carrol, P.T.Theodoropoulos, J.W.Otto and S.J.Gordon, "CW HF overtone chemical laser", SPIE, Vol.2502, pp.365-374.

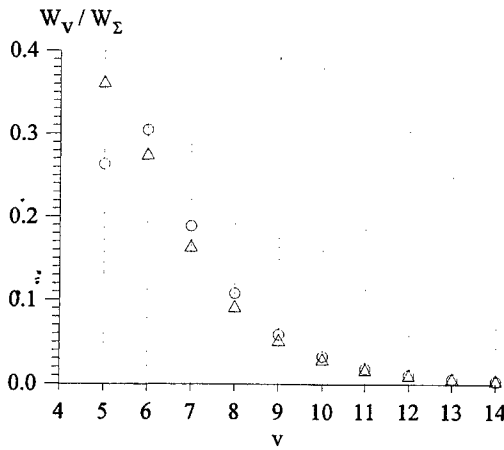


Fig. 1. The ratios of generation power W_v for transitions $v \rightarrow v-1$ to the total output power W_Σ of the free-running lasing;
○ - variant 1; △ - var. 4 (table 1).

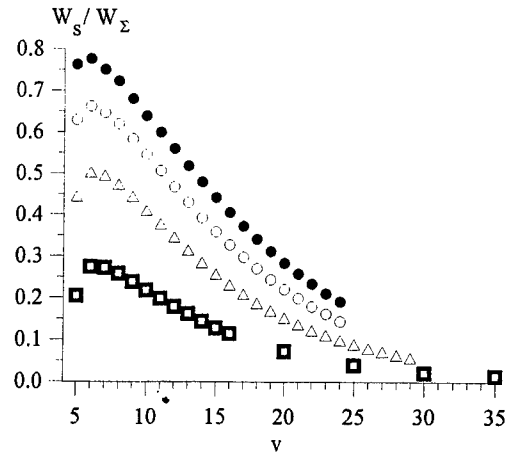


Fig. 2. The ratios of the total output power of selected lines W_s to the W_Σ ; variant 4.

- - one selected transition $v \rightarrow v-1$;
- △ - two successive transitions $v \rightarrow v-1, v+1 \rightarrow v$;
- - three transitions $v \rightarrow v-1 \dots v+2 \rightarrow v+1$;
- - four transitions $v \rightarrow v-1 \dots v+3 \rightarrow v+2$.

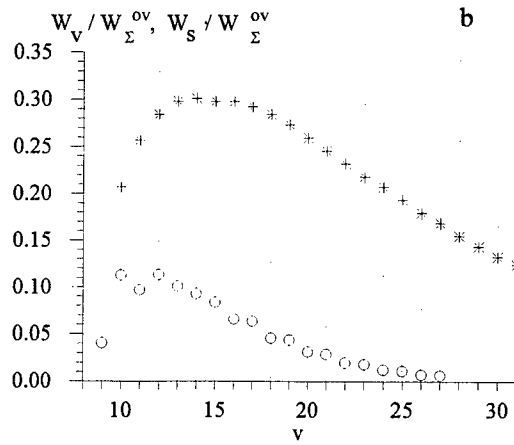
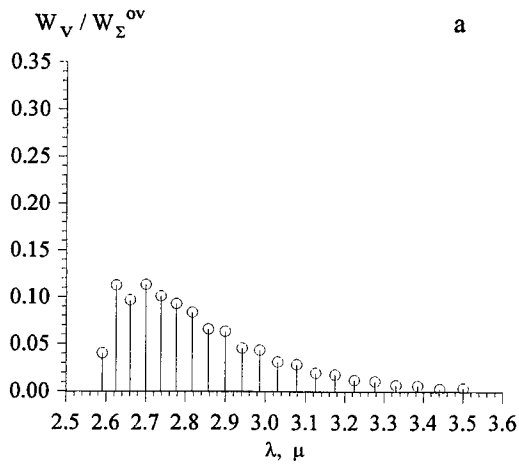


Fig. 3. ○ - (a) the spectrum of free-running overtone lasing as a function of wavelength λ , variants 1.3, 1.4 (table 2);
○ - (b) the same spectrum versus transition number $v \rightarrow v-2$;
* - (b) the ratios of the output power of four selected transitions $v \rightarrow v-2 \dots v+3 \rightarrow v+1$ to the W_Σ^{ov} for free-running overtone lasing

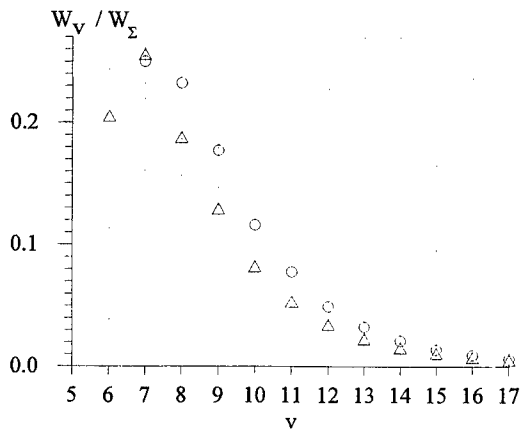


Fig. 4. The spectra of free-running fundamental lasing for variants 3 (○) and 6 (△).

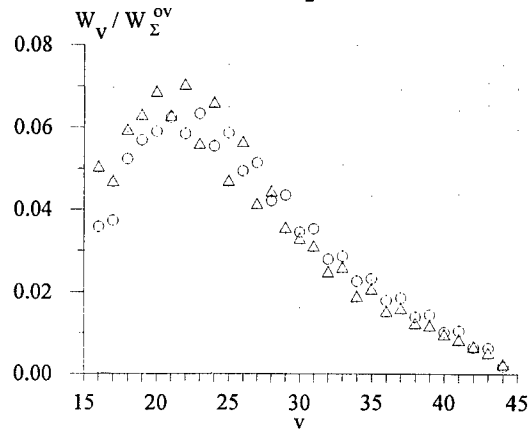


Fig. 5. The spectra of free-running overtone lasing for var. 3.3, 3.4 (○), and 6.3, 6.4 (△).

Heat treatment of large-scale rolling machine rolls by high power gas dynamic laser at Cherepovetz Metallurgy Work

A.A.Betev, V.T.Karpukhin, Yu.B.Konev, B.M.Kozlov

Institute of High Temperatures RAS, Izhorskaya Str., 13/19, Moscow 127412, Russia
Ph./Fax: (095) 485 8066

L.I.Danilov, Yu.V.Lipukhin

Cherepovetz Metallurgy Work "SeverStahl", Cherepovetz 162600, Russia

ABSTRACT

The results are presented of measurements of surface hardness and wear resistivity of rolling machine 2000 rolls which were under heat treatment by high power gas dynamic laser at Cherepovetz Metallurgy Work. Surface hardness of rolls increased from 70 HSh to 80-85 HSh. Wear resistivity also showed considerable increase as compared with untreated rolls.

Keywords: surface hardening, rolls, gas dynamic laser

1. INTRODUCTION

It was announced in Ref.1 about test runs of high power gas dynamic CO₂ laser (GDL) installed at Cherepovetz Metallurgy Work. High mass flow rate (about 10 kg/s) allowed to use GDL in developing of technologies needed for laser treatment of large scale equipment which is in use in ferrous metallurgy. GDL applications in technology is the most cost effective in heavy industry, where components of laser gas mixture may be produced as byproducts of the main production process (nitrogen may be byproduct of air separation, CO₂ may be produced by burning of stack gases). Besides, high output power of GDL and diversity of technological operations with large scale equipment make perspective of building the multi-purpose laser treatment centre on the base of GDL.

One of operations, where GDL might be of interest is surface hardening of rolls from large rolling machine. Some recently obtained results on laser heat treatment of rolls from rolling machine 2000 are presented in this paper.

2. DESCRIPTION OF GDL INSTALLATION

Laser and technological area are installed at rolling mill in the vicinity of rolling machine 2000. The overall view of GDL installation is shown in Fig.1. In the centre one can see the main parts of GDL. Two regenerative high temperature heat exchangers, which connected through high pressure switching valves with plenum chamber, follow by slot nozzle array, supersonic rectangular wind tunnel and optical resonator, supersonic and subsonic diffusers. On the foreground the rectangular aerodynamic output window, feeding by nitrogen from bended rectangular gas-guide, follow by two folding mirrors directing the laser beam to the system of light beam transportation and formation (not shown in Fig.1) and further to the work-place. Aluminium oxide ceramic spheres inside the heat exchangers accumulate the heat provided by burning the natural gas/air mixture in combustors, installed on the roof of heat exchangers. On the background additional heat exchanger, filled by metallic rolls, is seen, which utilizes remaining burner heat to provide high pressure water vapor in laser mixture. The installation also includes the special system for cooling strongly heated constructions: nozzle array and walls of wind tunnel, diffuser and heat exchangers.

The wind tunnel in the area of optical resonator is about 100 mm in height, 200 mm in flow direction and 1000 mm in transverse flow direction. One passage unstable resonator with $M=1.5$ magnification coefficient is used. Reflecting area of copper mirrors is cooled by flowing water.

More than 200 runs were performed for two-year period of exploitation. Mean run duration was about 150 s.

3. LASER TREATMENT OF ROLLING MACHINE ROLLS

Rolls from rolling machine 2000 are about 800 mm in diameter and 2000 mm in width. Working area is about 1000 mm in width. Roll surface is formed by cast iron trade mark LPXNd-70.

The process of roll restoration began from usual operations - turning, roll body profiling and polishing. After these operations completed roll surface etched by 4% solution of HNO₃ in alcohol and washed by distilled water. Afterwards, special absorbing paint on the base of graphite was deposited on the roll surface in the layer 20-30 mcm thick.

Rolls under irradiation were installed in special support and rotated with controllable speed to adjust surface beam velocity in the range up to 70 mm/s. Beam spot as formed by beam formation system was near rectangular with dimensions of 10x30 mm. Surface temperature under irradiation was measured by vidicon optical pyrometer.

In the process of laser heat treatment, firstly the surface temperature sharply increased above phase transition temperature, then it maintained in the range above this temperature, but under melting point, for several tenth of second and fastly decreased after termination of irradiation due to termoconductivity into depth of metal with the formation of fine grain martensite. Treatment was performed in the geometry of parallel rings in the central part of roll surface. The intervals between rings were approximately equal to beam spot width, that is about 30 mm. The width of laser treated part of surface was about 100 cm. Measurements showed the surface hardness in the zones under irradiation increased from about 70 HSh to 80-85 HSh.

The process of roll treatment is shown in Fig.2. Laser beam came out of rectangular protecting shield, reflected from two folding curved mirrors, which formed the beam spot, and struck the roll surface. Heated zone is seen as bright spot on the surface.

Pairs of rolls after irradiation were installed at rolling machine and tested for full 8 hour production cycle. After rolls were extracted surface hardness and wearing profiles were thoroughly measured. Irradiated zones preserved increased hardness in the range 75-80 HSh.

Changes in surface profile of roll pairs after irradiation were compared with those which were not irradiated. Fig.3 and 4 show the results of measurements and comparison for upper and lower rolls in pair respectively. Positive changes correspond to fattening, negative - to wearing of surface. One can not distinguish the contributions of clear wearing, deposition of additional materials and inelastic deformations in the rolling process. Nevertheless, the decrease of roll mass was more than 5 times less for irradiated roll in comparison with that which was not irradiated for rolls presented in Fig.4. For rolls compared in Fig.3 the changes of mass were in the range of uncertainty of measurements.

Analysis of measurements similar to those presented above show that rolls after laser irradiation preserved their surface hardness and profile and need not in restoration for at least two times longer than unirradiated rolls.

4. REFERENCE

1. A.Betev, L.Danilov, V.Karpukhin, Yu.Konev, Yu.Lipukhin. High power gas dynamic laser installation for laser technology at Cherepovetz metallurgy work. Gas Flow and Chemical Lasers: Tenth International Symposium, Willy L.Bohn, Helmut Hugel, Editors, Proc. SPIE 2502, pp.81-86 (1995).

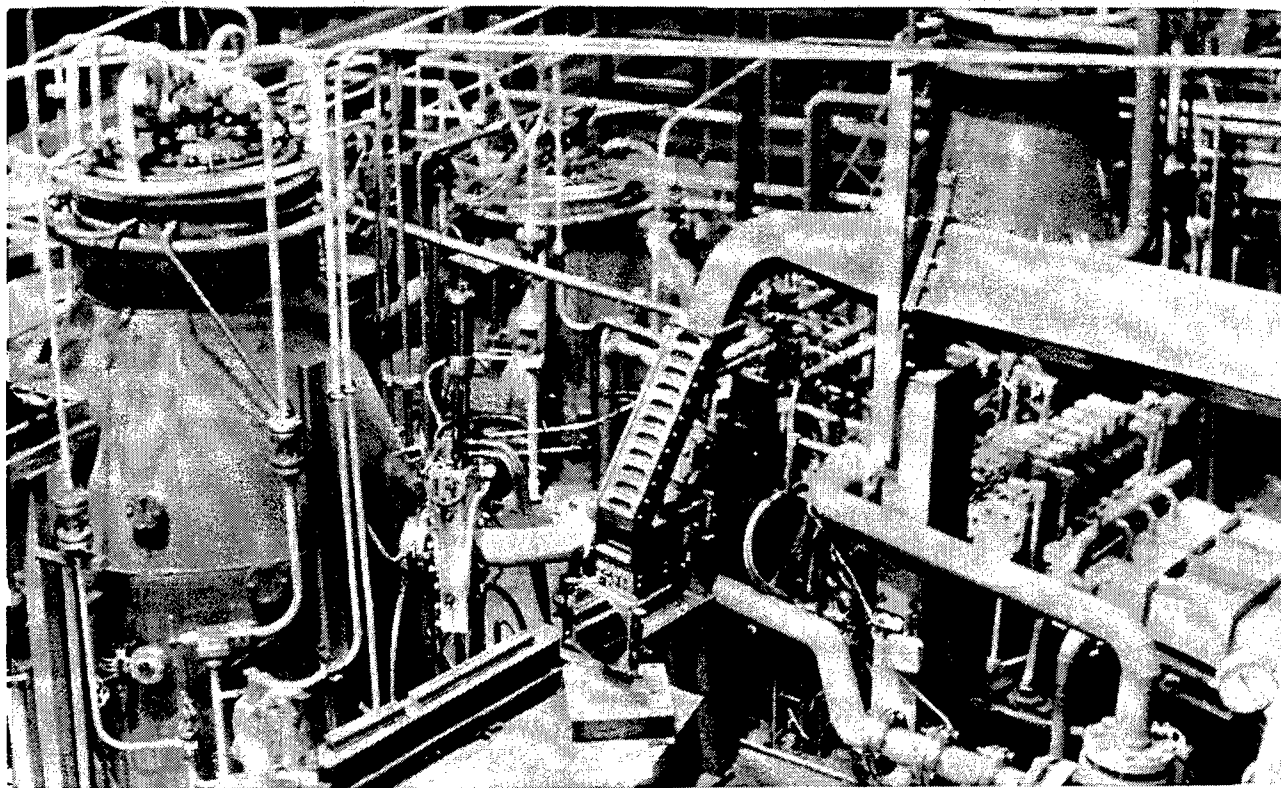


Fig. 1. General view of gas dynamic laser installation.

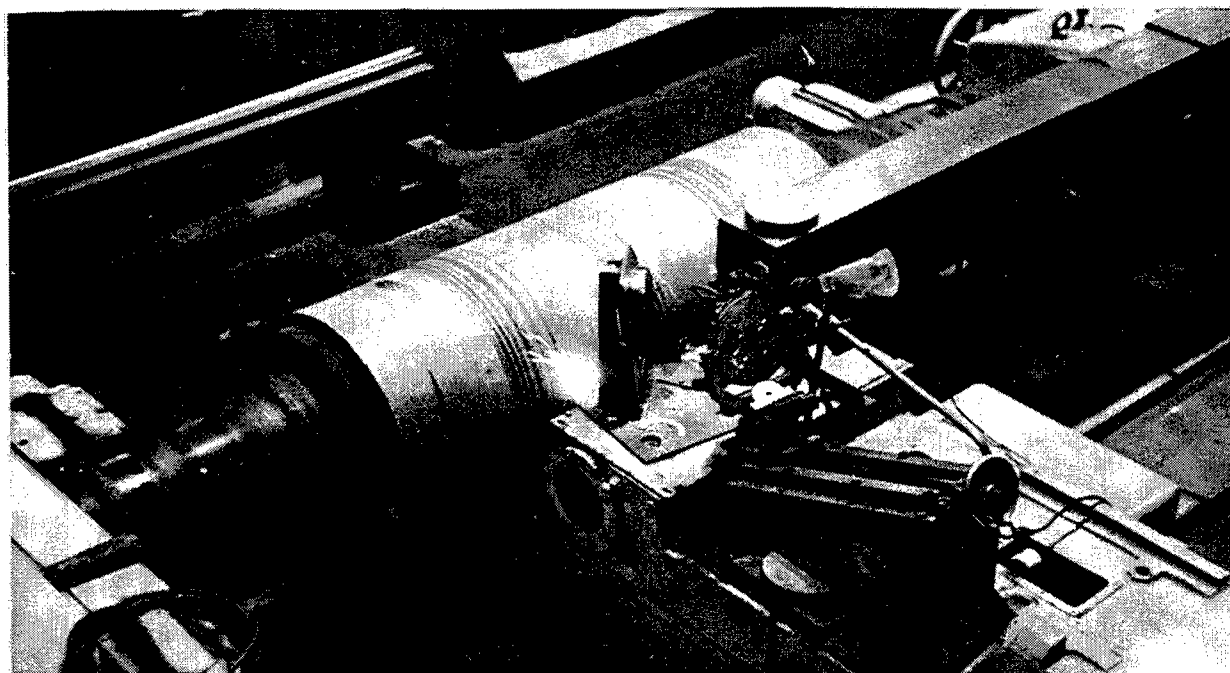


Fig. 2. The process of laser roll surface treatment.

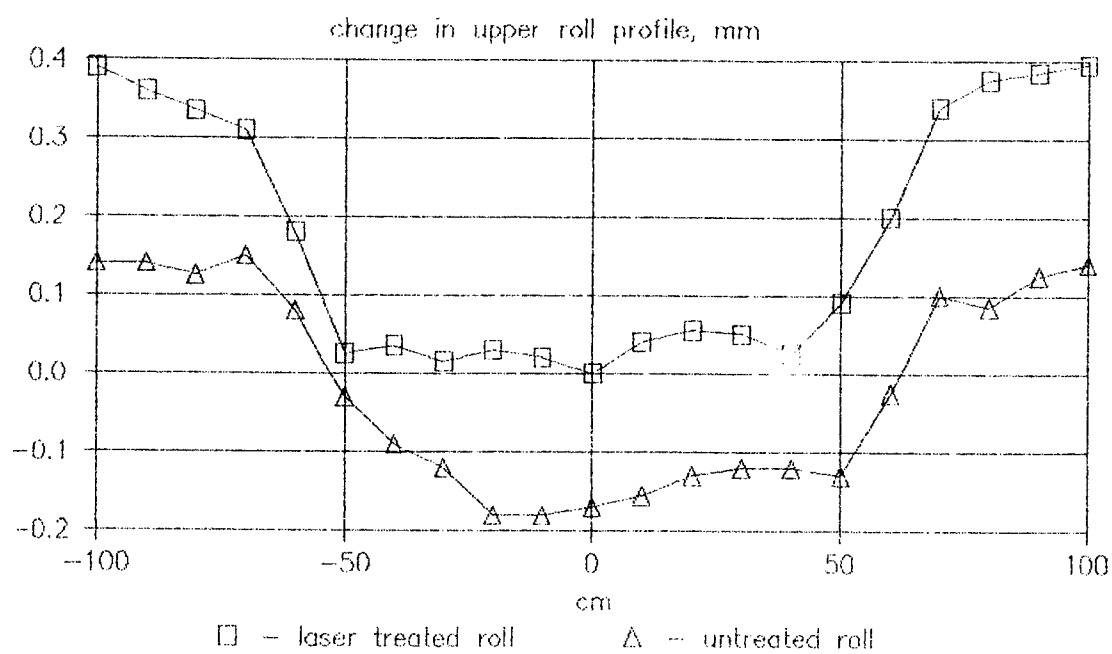


Fig. 3.

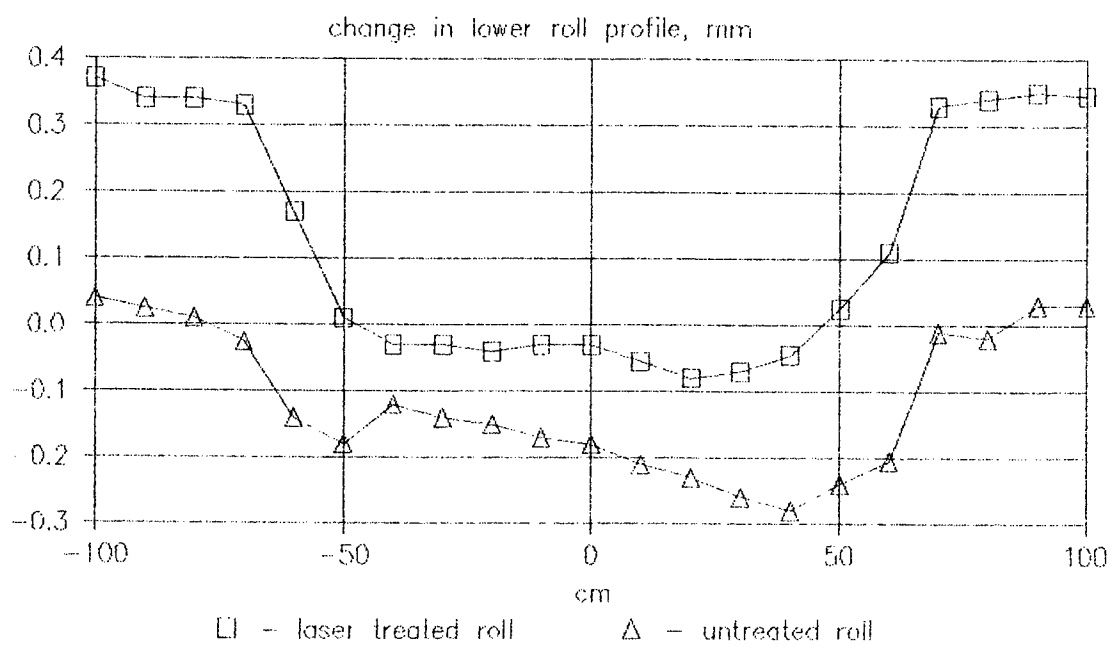


Fig. 4.

New methods to obtain higher power from the laser
with the unstable resonator

Kenzo Nanri and Tomoo Fujioka

Department of Physics, School of Science, Tokai University
1117 Kitakaname, Hiratsuka, Kanagawa 259-12, Japan

ABSTRACT

New methods to obtain higher power from the laser with the unstable resonator are proposed. Calculations are performed for expanding radius of concave or convex mirror to reduce the diffraction loss power from the concave mirror and to convert the power spread out from it into the output power. The Fresnel-Kirchhoff formula is used for the iterative computer calculation in the passive resonator and for a CO₂ laser. The calculations show that the increase of the output power can be obtained more than 20 percent with expanding concave mirror in the CO₂ laser.

Keywords: stable resonator, unstable resonator, Kirchhoff diffraction equation, low gain laser, large aperture laser, CO₂ laser

1. INTRODUCTION

Since the proposition by Siegman,¹⁾ the unstable resonator has been well known as a good resonator to obtain high power from large volume laser medium. In the unstable resonator, any photons can not be trapped in the resonator and get out from it after bounces on both mirrors. Even the photons started from the center region go to the edge of mirrors, so this resonator seems to be suitable for large cross section in order to increase the volume of the laser medium. In addition, the single mode-like output beam with coherent phase is easily gotten from the large bore laser.

The unstable resonator, however, has been hardly used for the industrial high power lasers because the output power from the laser is nearly half of that with stable resonator of multimodes. The light wave started from the center region increases with bouncing back and forth and goes to the edge of the mirrors. The laser medium in the center region does not meet with the saturated strength of the internal lasing power, though almost whole laser medium do in the laser with multimode stable resonator. The power gotten from the unstable resonator seems to be smaller than that from the multimode stable resonator and to be one of the demerit of it.

To improve the demerit of the unstable resonator, we propose new methods to increase the output power from the unstable resonator and numerically analyze them in this paper.

2. ANALYSIS

The field distribution in the unstable resonator is solved by the iterative computer calculation of the Fresnel-Kirchhoff formula²⁾ in a passive resonator and for a CO₂ laser. In this calculation, the higher order modes can not be separated, but the calculations are simple and the cost of the working time for the computer is not expensive.

In the real laser medium, the active medium exists and the higher order modes couple each other. And in any high power lasers, as the distributions of gain and refractive indexes, etc. are not uniform and fluctuating, the precise comparison between the analysis and the experiment is very difficult. So, we do not

need to persuade the precise, but complicated calculation such as fast Fourier analysis,³⁾ and the iterative computer calculations are enough for our objects.⁴⁾

Calculations are performed in a passive resonator and the CO₂ laser by changing magnification value M ($M=1.5-3.0$) and Fresnel number N ($N=10-30$). For the most of the calculations, the small signal gain and the saturation intensity are taken to be 1.0 %/cm and 1.0 kW /cm², respectively, which are reasonable value for cw CO₂ laser.

3. EFFECT OF THE EXPANSION OF THE CONCAVE MIRROR

The positive confocal unstable resonator shown in Fig.1 (a) has the merit that a single mode like beam with coherent phase can be taken out from a large bore laser medium in the uni-directional beam.

In the unstable resonator, larger M value is preferable because the wider width of the ring like output results in the better concentration of the power in the focal point. The M value is expressed by R_1/R_2 , where R_1 and R_2 are the radius of curvature of concave (Mirror 1) and convex (Mirror 2) mirrors and also expressed by a_1/a_2 as shown in Fig.1 (a). The smaller the M value is the thinner the width of the output beam becomes. The energy in the side lobe of the focused spot in the thinner annular beam is high and distribute in the large area.

In Fig. 2, extraction power ratio (a), diffraction power ratio (b), and coupling efficiency (c) are shown as function of N number for various M value in the unstable resonator with a positive branch. The extraction and the diffraction powers mean the useful and loss power. The extraction power ratio is the ratio between the power spread out from the Mirror 2 and the power stored inside of the resonator. The diffraction power ratio is the ratio between the power spread out from the Mirror 1 and the power stored inside of the resonator. The coupling efficiency means the ratio between the power spread out from the Mirror 2 and the power spread out from the both Mirror 1 and 2.

The diffraction power spread out from the Mirror 1 can not be ignored as shown in Fig.2 (b). The diffraction power loss is larger than the extraction power at $N = 1$ and $M = 1.5$. The diffraction power normally decreases with increasing Fresnel number, but still exceed 30 % of the extraction power at the Fresnel number of more than 10. So the diffraction power could be a severe obstacle which decrease the obtainable useful output power from the unstable resonator.

To reduce the diffraction power and to obtain higher output power from lasers with the unstable resonator, we propose to expand the radius of a_1 as shown in Fig.1 (b), which convert the power spread out from the concave mirror into the output power. The effect of the expanding concave mirror is shown in Fig. 3 as function of N number for various ratio of a_{1p}/a_1 , where a_{1p} is the expanding radius of concave mirror. The M value consists with the ratio between the radius of curvature of these concave and convex mirrors. So the M value is given as constant while changing the ratio of a_{1p}/a_1 . The ratio of $a_{1p}/a_1 = 1$ means the usual confocal unstable resonator, and the ratio of $a_{1p}/a_1 = 1.3$ means the concave mirror expanded outwardly about 70 % of the size.

In Fig. 3(a), the extraction power ratio increases with increasing the ratio of a_{1p}/a_1 , because of increasing area of the concave mirror. On the other hand, the diffraction power spread out from the Mirror 1 drastically decreases by the expansion of the concave mirror as shown in Fig. 3(b). Fig. 3(c) shows the total power

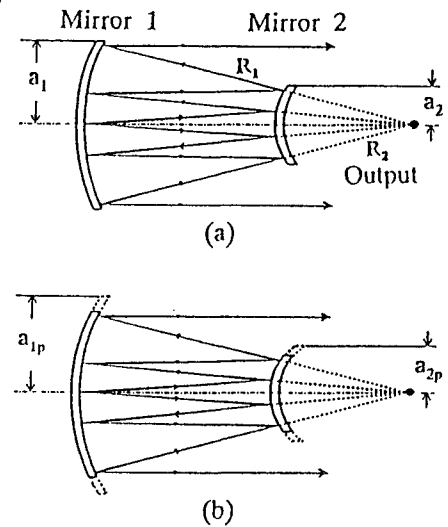


Fig.1. A positive confocal unstable resonator (a) and an expansion of the mirror(b).

ratio spread out from the both mirrors, that is the ratio of the extraction power and diffraction power against the internal power. This ratio does not change so much by the expansion of the concave mirror. That is, the most of the diffraction power at the ratio of $a_{1p}/a_1 = 1.0$ is converted to the extraction power by the expansion of the concave mirror. The effect of the expanding concave mirror is well shown by the coupling efficiency as shown in Fig. 3(d). The extraction power increases more than 10 %, sometimes 60 % for the case of lower Fresnel number.

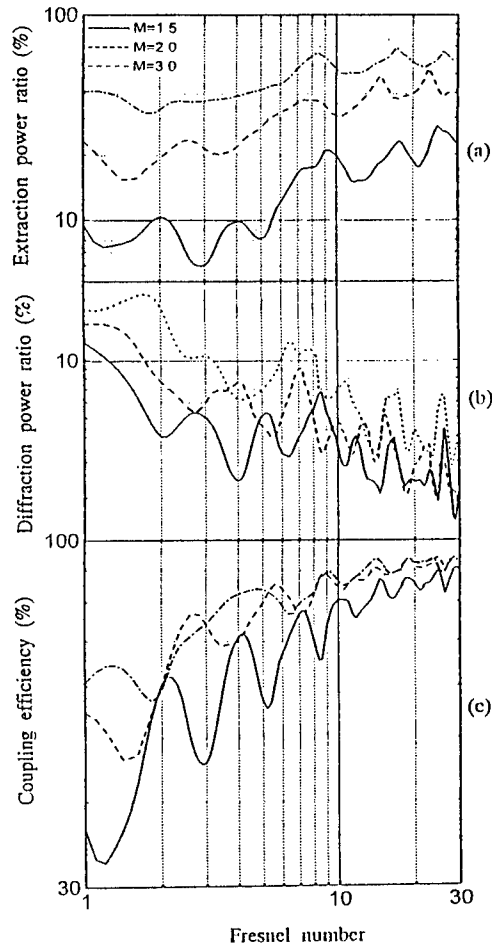


Fig.2. Extraction power ratio (a), diffraction power ratio (b), and coupling efficiency (c) versus Fresnel number for various M value in the passive resonator.

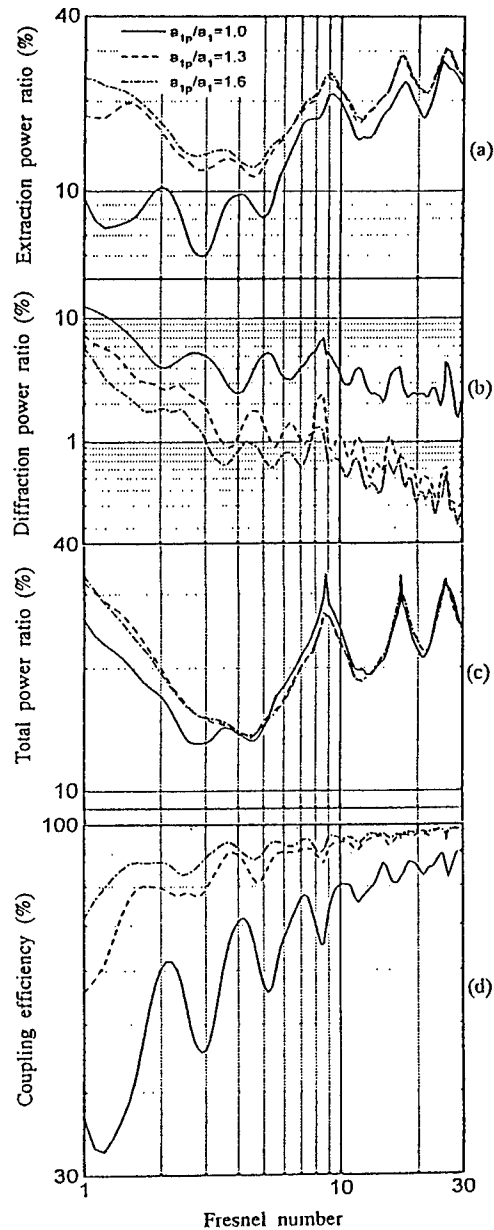


Fig.3. Extraction power ratio (a), diffraction power ratio (b), total power ratio (c), and coupling efficiency (d) versus Fresnel number for various a_{1p}/a_1 in the passive resonator.

4. FOR THE CO₂ LASER

As the effect of the expanding concave mirror becomes clear for the passive unstable resonator, the calculations are performed for the CO₂ laser. The relative internal and output powers versus a_{1p}/a_1 are shown for various M value and N number in Figs. 4 (N = 10) and 5 (M = 1.5). These powers are normalized by the power at the value of a_1 chosen by the M value. The internal power is determined by the M value and N number. Then the relative internal power almost constant without a_{1p}/a_1 . On the other hand, the relative

output power increases rapidly with increasing a_{ip}/a_1 through 1.4 and increases almost linearly.

The expanding concave mirror is effective for smaller M value and smaller N number. In the case of smaller M value, the width of the output beam is thinner and the diffraction power is larger. For smaller N number, the diffraction power is also larger. According to the calculations, more than 20 % of the output of the CO₂ laser can be expected with the expanded concave mirror.

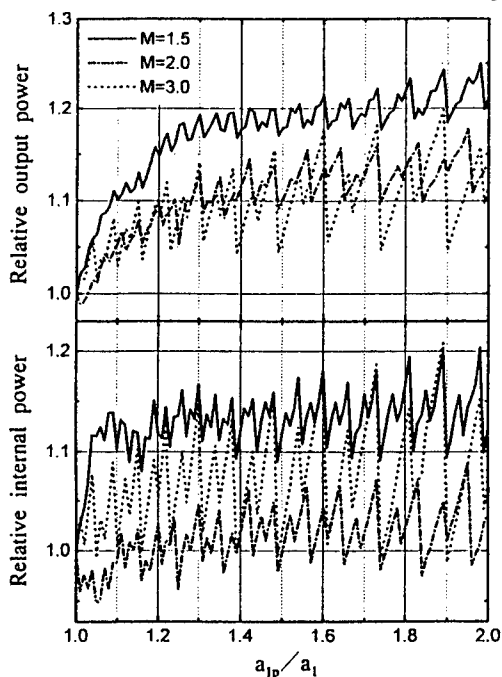


Fig.4. Relative internal power and relative output power versus a_{ip}/a_1 for various M value in the CO₂ laser ($N = 10$).

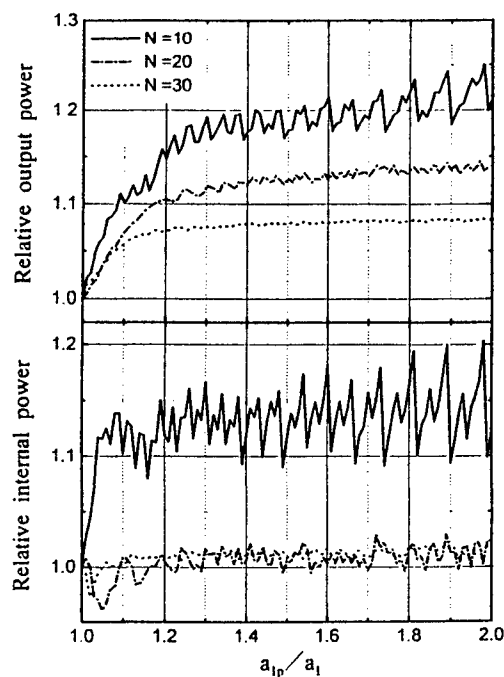


Fig.5. Relative internal power and relative output power versus a_{ip}/a_1 for various Fresnel number in the CO₂ laser ($M = 1.5$).

5. CONCLUSION

In the case of the stable resonator, the best size and the transparency of the resonator could be approximately obtained analytically for a given laser medium. But the best M, N, a_1 , a_2 etc. could not be determined analytically in the unstable resonator.

We proposed the methods to obtain higher power from the laser with the unstable resonator, the expansions of the concave mirror. The calculations showed that the increase of the output power can be obtained more than 20 percent with the expanding concave mirror in the CO₂ laser. However, the parameters for the highest output power could not decide analytically. For designing the best resonator, for any given laser medium, we must calculate the power with changing those parameters to decide the best ones.

In anyway, we believe the unstable resonator has become more useful with new design method presented here.

6. REFERENCES

1. A.E. Siegman, "Unstable Optical Resonator", *Appl. Opt.* **13**(2), 353-367 (1974)
2. A.G. Fox and T. Li, "Resonant modes in a maser interferometer" *Bell Syst. Tech. J.* **40**(3), 453-488 (1961)
3. E.A. Sziklas and A.E. Siegman, "Mode calculations in the unstable resonators with flowing saturable gain 2. Fast Fourier transform method" *Appl. Opt.* **14**(8), 1874-1889 (1975)
4. K. Nanri, K. Mabuchi, and T. Fujioka, "The Unstable Resonator with a Stable Resonator Core" *Jpn. J. Appl. Phys.* **35**(3), 1744-1750 (1996)

Effects of Beam Launching on Mode Coupling in Hollow Infrared Waveguides for High Quality Beam Delivery

S. Somkuarnpanit, D. Su, J.D.C. Jones, H.J. Baker and D.R. Hall

Department of Physics, Heriot-Watt University,
Riccarton, Edinburgh EH14 4AS,
United Kingdom

ABSTRACT

The mode coupling of hollow infrared optical fibres was investigated as a function of beam launching conditions, i.e. fibre transverse and longitudinal misalignment and tilting. Experimental results with a TEM₀₀ CO₂ laser and hollow sapphire and dielectric coated metallic waveguides are compared with geometrical optics and mode coupling theories.

Keywords: optical fibres, CO₂ beam delivery, hollow waveguide, laser beam delivery

1 INTRODUCTION

Hollow fibres have been developed for laser beam delivery for the long-wavelength radiation, especially for 10.6µm CO₂ lasers¹. They are normally large core and have a high loss compared with solid core glass fibres. Although large core size is necessary for high power transmission, the disadvantage of a large core size is the degradation of beam quality. CO₂ lasers can provide much higher power at high beam quality compared with other laser sources, but when delivered through large core waveguides the beam normally becomes multimode and low quality. Bend-induced mode coupling and launching conditions are the main factors contributing to beam degradation. Although the bend parameters can be configured to reduce the mode coupling effect², accurate launching at the input is necessary to make them effective. The effect of transverse, longitudinal and tilt misalignment on the power transmission and beam profiles are investigated. Theories of mode coupling and geometric optics are compared for predictions of power transmission.

2 THEORY

Geometrical optics and mode coupling theory have been used to evaluate the output transfer property of optical fibres^{3,4}. When the number of modes is small mode coupling theory⁵ can be used to match the input Gaussian beam to individual waveguide modes, therefore providing information for overall power transmission and beam profiles for waveguide modes. But the calculation of mode matching is time consuming, especially when a large number of modes are involved, and is therefore appropriate when only few guided modes have to be considered.

In this section the mode coupling theory is used to calculate modal excitation as well as power transmission as a function of misalignment, and the geometric optics is used to estimate power transmission only, as it is not suitable for estimate beam profiles in this case with high quality input beam.

In mode coupling theory, the power coupling efficiency into an individual waveguide LP_{*l,m*} mode can be written as⁶

$$\eta_{l,m}(\text{launch parameter}) = \frac{\left| \int_0^{2\pi} \int_0^a e(r, \theta, \text{parameter}) \cdot LP_{l,m}(r, \theta) \cdot r dr d\theta \right|^2}{\int_0^{2\pi} \int_0^a (e(r, \theta, \text{parameter}))^2 r dr d\theta \int_0^{2\pi} \int_0^a e(r) \cdot (LP_{l,m}(r, \theta))^2 r dr d\theta}$$

where the $e(r, \theta, \text{parameter})$ is the field of the input beam, r and θ are the radius azimuthal angle coordinates, a is the fibre core radius, and the *parameter* represents variables of launching alignment which could be transverse, longitudinal or tilt misalignment. This analysis could be time consuming if the number of expected modes is large. In view of this it is rather a less efficient way of predicting total transmission as a function of launching conditions. On the other hand the mode coupling theory is a simple way of investigating the proportion of power in a particular waveguide mode coupled into the

waveguide as a function of launching conditions. The normalised coupling efficiency for longitudinal, transverse and tilting misalignments were calculated for the first nine modes for different launch spot sizes.

Theory shows that a large number of modes are excited when the diameter of the input laser spot is small (0.2 of the core diameter); the nine modes included in the calculation only contain less than 90% of the beam, even when there is no misalignment. The power in the fundamental mode ($LP_{0,1}$) is low. Hence this is apparently a favourable launching condition for mode scrambling. For small transverse misalignment (<0.3 of core radius) the condition for the best output beam quality is when the spot size to core ratio matches that of the best launching condition in the accurately aligned case, i.e. 0.64 of the core size as shown in fig.1. But when the displacement is large (>0.4 of core radius) a larger launching spot size is preferable. The output beam is generally multi-peaked. Figure 2 shows that the mode structure is relatively less sensitive to the longitudinal misalignment. The change in modal power distribution is very small in the displacement range of up to millimetres irrespective of the launching spot size. Because of axial symmetry, theoretically only $LP_{0,m}$ modes exist. The spot to core ratio of 0.64 is still the best when the tilt angle is small, but for large angles of tilting a smaller spot size might be preferable for efficient power transmission.

When a large number of modes exist in a low loss fibre, geometric optics can be used to calculate power transmission, i.e. the total power launched into the fibre, the total coupling efficiency, η_{total} may be written as:

$$\eta_{total}(\text{launch parameter}) = \left| \int_0^{2\pi} \int_0^a e(r, \theta, \text{parameter})^2 r dr d\theta \right|$$

From the intrinsic nature of the two theories, geometric optics would give an optimistic result for overall power transfer, and the mode coupling theory gives a pessimistic one, depending on the number of modes included in the calculation; therefore it is expected that the actual power transmission would fall somewhere in-between.

3 EXPERIMENT

In the experiment a sealed, linearly polarised CO_2 laser with a nearly TEM_{00} beam ($M^2 < 1.10$) was used and the wavelength is stabilised at $10.6 \mu m$. Two sapphire hollow fibres with core diameters of $0.4 mm$ ($2.1 dBm^{-1}$ loss) and $1.1 mm$ ($0.3 dBm^{-1}$ loss) were used to study the effects of fibre misalignment. A $1.0 mm$ diameter core silver halide coated silver waveguide with loss of $0.2 dBm^{-1}$ was used to investigate the effects of fibre tilting. A pair of $75 mm$ focal length ZnSe lenses were used to change the beam spot size at launching. The input and output power were measured with a thermopile power meter. The far field output beam profile from the fibre was recorded with a pyro-electric thermal camera and then digitised and stored

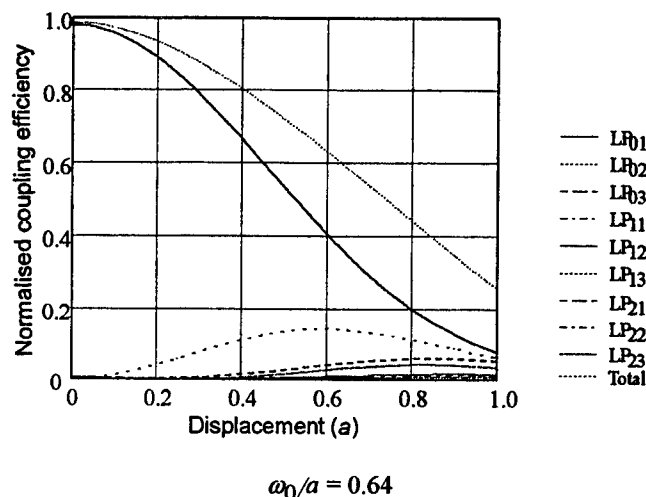


Figure 1 The coupling efficiency in the presence of transverse misalignment, where ω_0 is the beam spot radius.

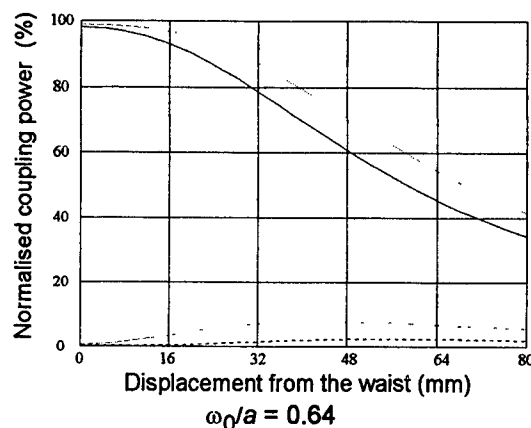


Figure 2 Coupling efficiency as a function of the longitudinal misalignment of the $1.1 mm$ core diameter fibre. The lines —, —, ···· and ···· represent the total coupled power, $LP_{0,1}$, $LP_{0,2}$ and $LP_{0,3}$, respectively.

on a PC for subsequent image analysis. During the experiments the fibres were mounted on a metal bar and remain straight. The ends of the metal bar were fixed on two translation stages and the misalignments were achieved by adjusting the stages.

4 RESULTS

The power transmission of the 0.4mm core sapphire fibre is shown in figure 3 as a function of transverse misalignment.

Similar results for the 1.1mm core sapphire fibres are shown in figures 4. The maximum output transmission is 60% for the smaller core fibre, which corresponds to the theoretical transmission value for the fundamental waveguide mode^{7,8}. Compared with the results of the large core fibre, the beam profile of the smaller core fibre is relatively less sensitive to the change of launching condition, while the power transmission falls faster with transverse misalignment than for the 1.1 mm core fibre. Two groups of theoretical curves are also shown in figure 3; they are from mode coupling and geometric optics theory. The mode coupling theory included the fundamental mode only. It is shown that the experimental results fall in-between the two theories. The mode coupling theory under-estimated the transmission and the geometric optics over-estimated.

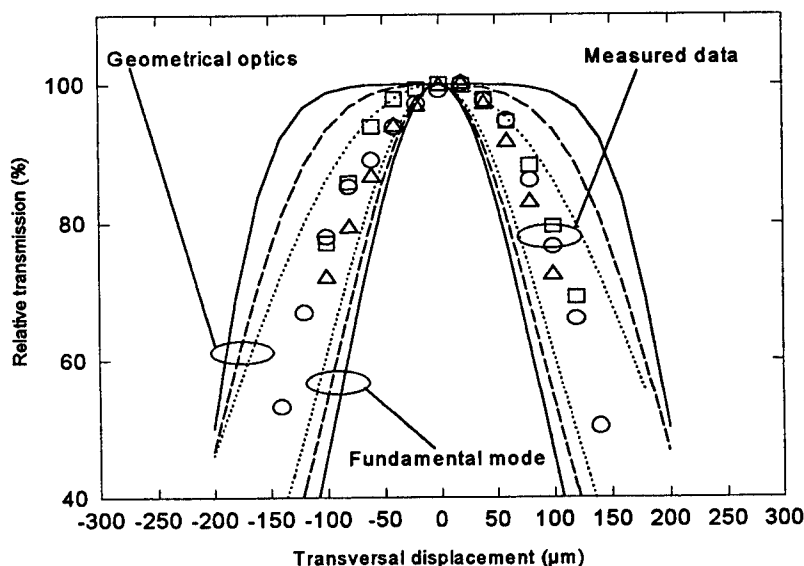


Figure 3 The power transmission of the 0.4 mm core fibre as a function of transverse misalignment. (—, ○), (---, □) and (---, Δ) represent the results for ω_0/a values of 0.40, 0.60 and 0.87 respectively.

The power transmission of the 1.1mm core sapphire fibre for the transverse misalignment agrees well with the geometrical theory as shown in the figure 4. The output profile changes more evidently with transverse misalignment than with the smaller core fibre. The multiple-peak profile can be observed for the launch beam with small spot size and this feature is not evident in the small core fibre, indicating a low modal differential loss in the large core fibre and hence more modes.

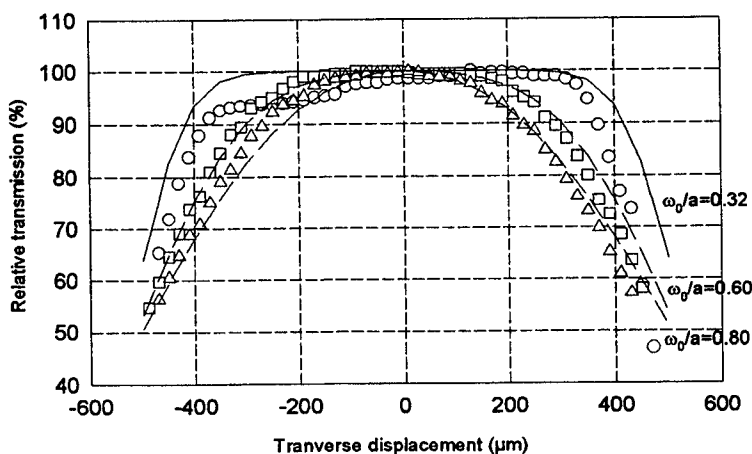


Figure 4 The power transmission of the 1.1 mm core versus fibre transverse misalignment. (—, ○), (---, □) and (---, Δ) represent the results for ω_0/a values of 0.32, 0.60 and 0.8 respectively.

In both cases, the large and small core fibres, the output transmission and profiles are less sensitive to longitudinal alignment than the transverse one and remain unchanged for a relatively long distance in the range of millimetres.

Figure 5 shows the beam profile as a function of tilting for the 1mm diameter core dielectric coated metallic waveguide. The transmission is approximately constant for tilt angles up to about 10 mrad and falls dramatically for larger angles. The beam pattern gradually changes from a single peak to a distinctive two-peak one with resemblance to the $LP_{1,1}$ mode with nearly constant transmission.

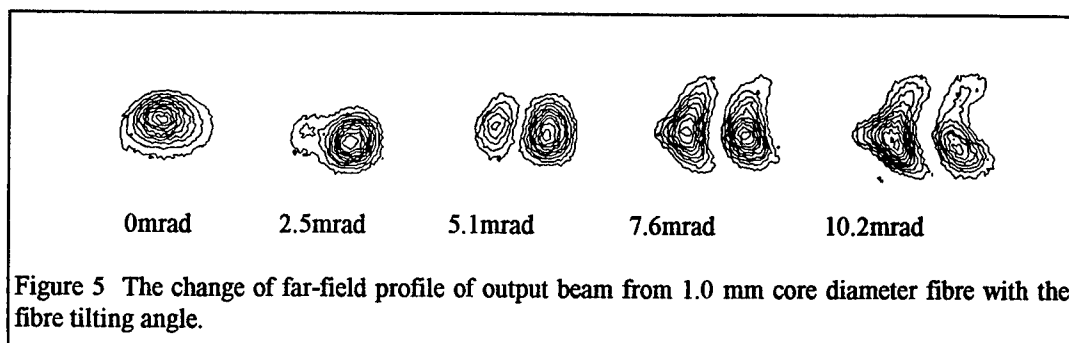


Figure 5 The change of far-field profile of output beam from 1.0 mm core diameter fibre with the fibre tilting angle.

5 DISCUSSION AND CONCLUSIONS

The intrinsic differential loss of the small core fibre is one of the factors that controls the output beam profile. Because of the high modal loss, the small core fibre seems to have a more uniform output. The influence of the launching condition on the output is reduced by the reduction of higher order modes. The draw-back is that the overall transmission is low.

In the case of large core low loss fibre, most of the modes excited can be transmitted through the fibre, therefore any change in the launching condition would produce a change in the output profile, which normally results in a beam with multiple peaks. The total power transmission is relatively less sensitive to the launching condition.

The mode coupling theory can be used to estimate the mode distribution at the input, and is useful particularly for small core fibres where few modes exist. It is also preferable in estimating the power transmitted in a small core fibre, when geometric optics theory gives an over-estimate. However, geometrical optics can be used for prediction of power transmission for large core low loss fibres, and is simple and fast in calculation.

6 ACKNOWLEDGEMENTS

This work was supported by the Design and Integrated Production Committee of the EPSRC (UK); one of us (SS) gratefully acknowledges financial support from the Government of Thailand.

7 REFERENCES

- 1 J.A. Harrington and Y. Matsuura, "Review of hollow fibre waveguide technology.", SPIE Proc., 2396 (1995).
- 2 D. Su, S. Somkuarnpanit, D.R. Hall and J.D.C. Jones, "Hollow waveguide for high quality CO₂ laser beam delivery: exploitation of bend-induced mode coupling", Opt. Comm., 114, 255-261 (1995).
- 3 D.Su, A.A.P. Boechat and J.D.C. Jones, "Beam delivery by large-core fibres: effect of launching conditions on near-field output profiles", Appl. Opt., Vol.31, No.27, 5816-5821 (1992).
- 4 J.Saijonmaa, A.B. Shama and S.J. Halme, "Selective excitation of parabolic-index optical fibres by Gaussian beams", Applied Optics, Vol.19, No.14, 2442-2452 (1980).
- 5 D. Marcuse, "Coupled mode theory of round optical fibers", The Bell Syst. J., Vol.52, No.6, 817-841 (1973).
- 6 J.J. Degnan, "Waveguide laser modes patterns in the near and far field.", Appl. Opt., 12(5), 1026-1030 (1973).
- 7 E Palik, ed., Handbook of Optical constants of solids, Academic Press, New York (1985).
- 8 E.A.J. Marcatili and R.A. Schmeltzer, "Hollow metallic and dielectric waveguide for long distance optical transmission and lasers.", Bell Syst. Tech. J. 43, 1783-1809 (1964)

Modelling of one-dimensional cavities for large-area gain media

Bartosz Wasilewski, Krzysztof M Abramski

Institute of Telecommunications and Acoustics, Technical University of Wrocław,
Wybrzeże Wyspiańskiego 27, 50-370 Wrocław, POLAND

Alan D Colley, Howard J Baker, Denis R Hall

Department of Physics, Heriot-Watt University,
Riccarton, Edinburgh EH14 4AS, UK

ABSTRACT

We present a method and results of modelling of the large-area CO₂ lasers, including gain saturation and dephasing effects. Numerical calculations are based on iterative evaluating of Fresnel-Kirchoff integral using fast convolution algorithm.

Keywords: modelling of lasers, numerical modelling, numerical simulation of lasers, laser simulation, unstable resonator, Diffractive Optical Element (DOE) resonator, Talbot resonator, laser simulation, laser resonator synthesis, Graded Phase Mirror (GPM)

1. INTRODUCTION

The need for determination of transverse mode parameters in the large-area laser media stimulates the development of modelling techniques. An effective method of simulating laser operation, with non-linear, distributed gain included into model has been developed. As a result of this procedure, a realistic estimate of laser beam profiles and their output powers have been obtained.

Slab-waveguide cavities are comparatively novel resonator designs for molecular lasers. They are characterized by an unusual aspect ratio (very long slab of large width and very small height). Since in the transverse direction the mode is always a low-order waveguide mode, it is possible to separate the orthogonal dimensions and consider only the free-space, lateral dimension in the model, which greatly reduces the computational complexity.

Computations were carried out by iterative propagation of the beam profile within the laser cavity. The modelling was aimed at including the effects of saturable gain, noise (spontaneous emission) and reflecting sidewalls on the beam profile. Matlab® computational software was used for all calculations.

Propagation of the beam profile was performed by iterative evaluating the Fresnel-Kirchoff integral for free-space using fast convolution method [1]. Nonlinear, saturable gain was included in the form of multiple thin-film model, with gain characteristics updated after each layer according to the saturation curve. Other effects like reflections from sidewalls, irregularities of the mirror surfaces, and roughness of sidewalls have also been included. As the calculations were performed on densely sampled beam profiles and the effort was put for minimizing the errors of the method, the simulation results are believed to model the experimental behavior more accurately. Both near-field and far-field patterns were obtained.

A gaussian resonator has been modelled and the free spectral range tuning for single-frequency model was demonstrated. Unstable confocal resonators, both positive and negative branch, have been modelled and were checked against the results published previously. An attempt was made to model a resonator with Talbot filtration and another one using diffractive optical element (DOE). The results agreed well with experimental data, especially for the DOE resonator. The modelling technique presented is an efficient tool for evaluation of properties of slab resonators, and can find applications in modelling and design of resonators for slab-waveguide CO₂ lasers for lidar, Inter-Satellite Links (ISLs) for Space Communications, industrial applications (cutting, welding, marking, etc.), medical applications (surgery).

2. METHOD OF MODELLING

Propagation of the beam profile was performed by calculating Fresnel-Kirchoff integral for one-dimensional propagation, in the form shown below (Eqn. 1)

$$u(x, z) = \sqrt{\frac{j}{\lambda}} \int u_0(x_0, z_0) \cdot \frac{e^{jkr(x_0, z_0)}}{\sqrt{r(x_0, z_0)}} dx_0 \quad (1)$$

where:

$u(x, z)$ - beam profile after propagation

$u_0(x_0, z_0)$ - initial beam profile (complex amplitude)

$\frac{e^{jkr(x_0, z_0)}}{\sqrt{r(x_0, z_0)}}$ - propagation kernel

The Fresnel-Kirchoff integral accurately describes propagation between apertures within and at ends of the laser medium. It can be converted to a convolution, and then evaluated with low numerical complexity using fast convolution algorithm. In order to obtain accurate numerical results, guard bands at both sides of each aperture have to be provided, and sampling requirements have to be met [2]. Correct numerical realisation of fast convolution ensures errors at the level of these of the numerical coprocessor involved [3]. The only errors that have to be accounted for are sampling (aliasing) error, and Fresnel zones error. Integral (1) is evaluated iteratively using fast convolution algorithm at several cross-sections of a laser beam within the laser cavity. Additional phenomena (gain, reflections, etc.) are included after each iteration. To improve accuracy of modelling gain saturation the gain medium is divided into sections. As the gain medium is a slab, and the beam profile in the narrower dimension is well defined EH1 waveguide mode, one-dimensional approach correctly models slab geometry, yielding information about the profile in the wider dimension. Similarly to previously published results of modelling, the simulation is single-frequency, but it has been checked that there is a possibility of creating linewidth (multi-frequency) simulation, although that requires significantly more computational effort. Both phase-sensitive and phase-insensitive simulations were carried out, giving information about the modes supported by mirror combinations, and about what happens when a laser is tuned. Free Spectral Range Tuning was demonstrated for gaussian resonator. The model allowed to correctly estimate output powers of various resonator configurations. In particular, output beam shape and power for a Diffractive Optical Element resonator was correctly predicted.

A range of physical phenomena were included into modelling. These are non-linear, saturable gain (thin-film gain model, gain medium divided into sections, gain value updated individually at each point according to the intensity of electromagnetic wave at this point [2]), spontaneous emission (modelled in the form of complex noise added to beam profile after each propagation of the beam), reflecting sidewalls (modelled by mirroring of the fragments of the beam responsible for waveguide propagation after each section of a laser), temperature gradients and other dephasing factors (simulated by multiplication of complex beam amplitude profile by the phase profile of an irregularity, done after each section of a laser), and irregularities of mirror surfaces and roughness of cavity walls (represented by random phase added to each mirror/wall phase profile).

3. RESULTS OF MODELLING

3.1. Laser with Fabry-Perot resonator. This laser has been simulated with ideally aligned mirrors, and with one of the mirrors tilted. (100 μ rad). Output beam intensity shapes for these two cases are shown below (Figure 1). It can be seen that even for small mirror tilts the beam quality is degraded and output power decreases rapidly.

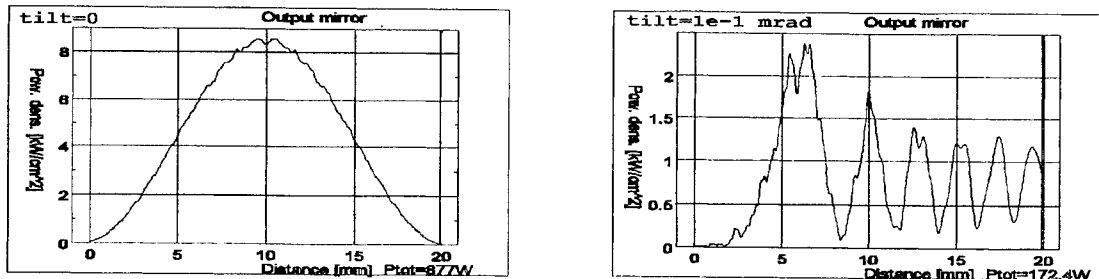


Figure 1. Output beam intensity profile for a Fabry-Perot resonator with ideally aligned and with tilted mirrors

3.2. Free Spectral Range Tuning of a laser with gaussian resonator. Example shows changes in modal structure of the beam profile when a gaussian resonator is tuned within half of the operating wavelength, are shown in Figure 2. The aperture of the gain medium was sufficient to operate in modes higher than fundamental.

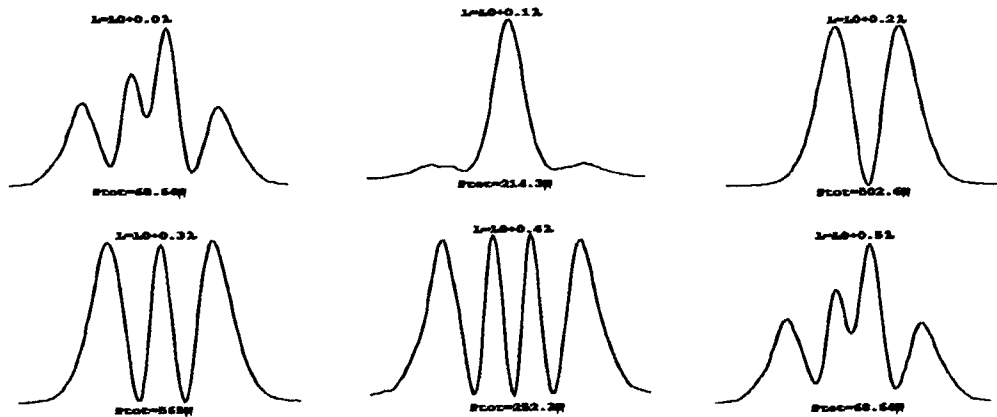


Figure 2. Free Spectral Range Tuning of a gaussian resonator.

3.3. Confocal unstable resonator - positive branch. Laser parameters: length=400mm, width=30mm, height=2mm, magnification=1.16, saturation intensity $I_{sat}=6\text{kW/cm}^2$, small-signal gain $2\alpha=0.3$. Output beam of a slab CO₂ laser with unstable, positive branch resonator is shown in Figure 4. The result agrees well with experimental data.

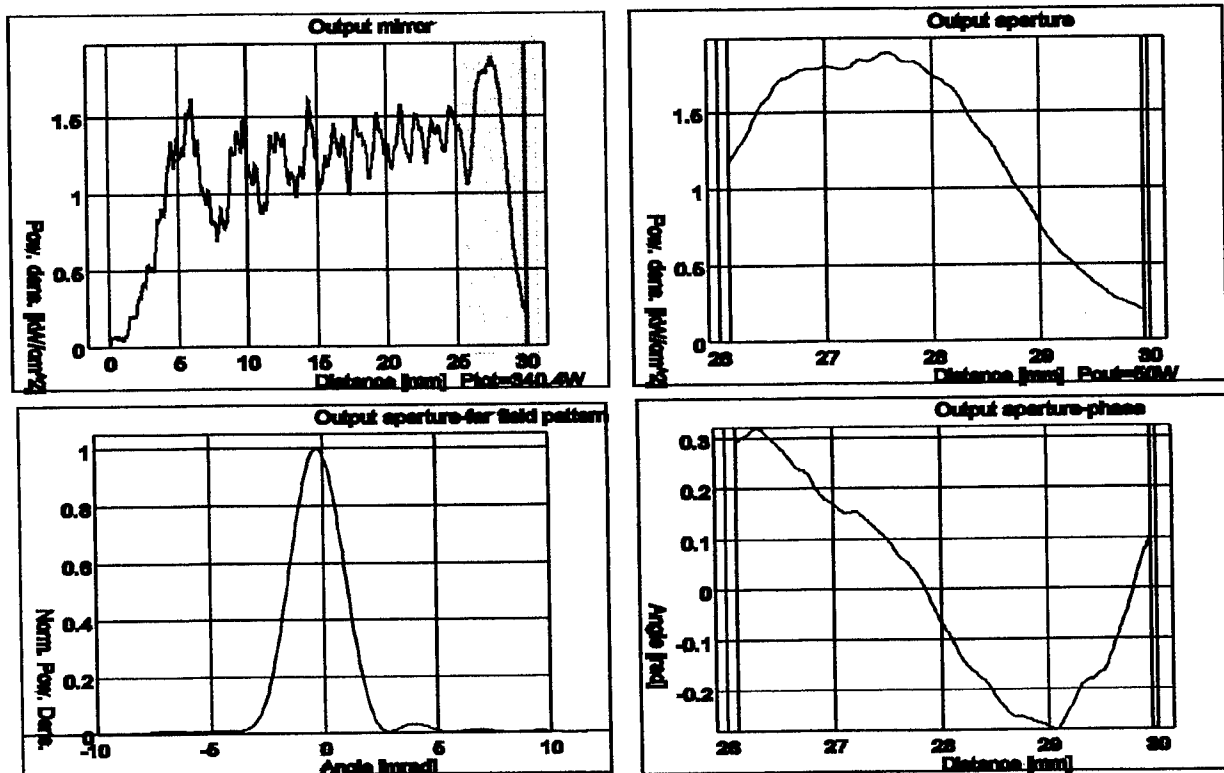
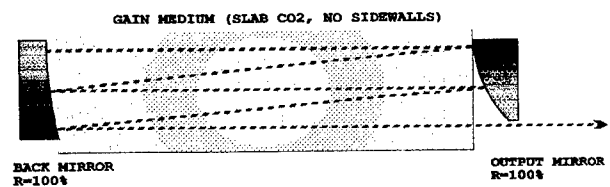


Figure 4. Output beam profiles for a laser with confocal, unstable resonator (positive branch).

3.4. Diffractive Optical Element (DOE) resonator.

The DOE used was a planar mirror with $1\mu\text{m}$ deep phase profile etched in it. The phase profile corresponds to a spherical mirror radius twice the resonator length. The results obtained by numerical simulation agree well with experiments carried out at Optoelectronics and Laser Engineering Group, Heriot-Watt University.

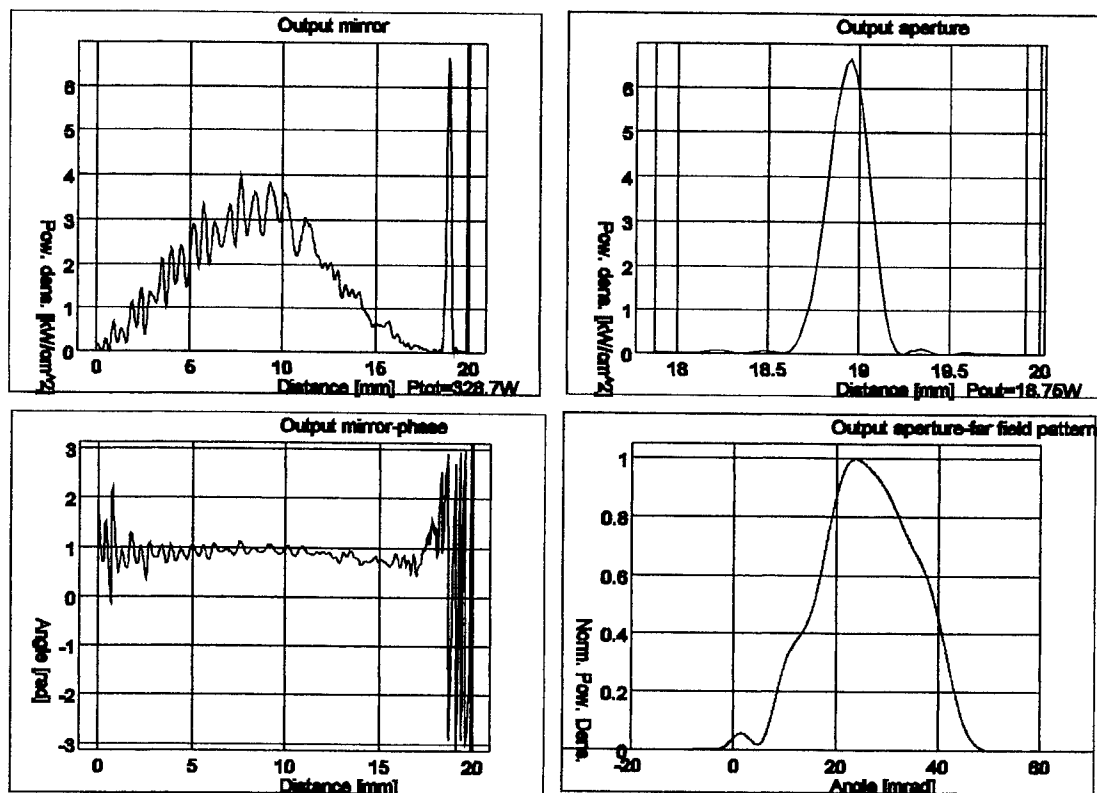
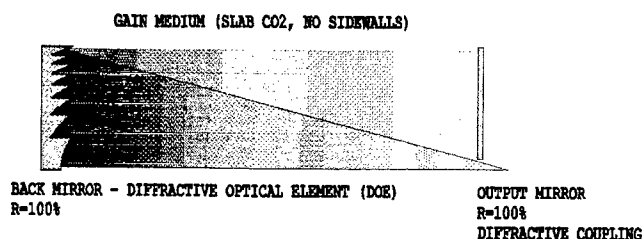


Figure 6. Output beam intensity and phase for a laser with DOE resonator.

4. CONCLUSIONS

Variety of new resonators has been modelled, and new phenomena were included into modelling. The model is believed to have improved accuracy as compared to previously published. Calculations of output power of a laser became possible. Both near-field and far-field patterns are obtainable. The model presented good agreement with experimental results. In particular, a successful simulation of a Diffractive Optical Element (DOE) resonator, is worth mentioning. The method of modelling and accuracy of the model opens the way to synthesis of laser resonators yielding output beam of arbitrary shape.

5. REFERENCES

1. A. E. Siegman, et al. "Lasers", University Science Books, 1986
2. APPLIED OPTICS, E. A. Sziklas, A. E. Siegman, "Mode calculations in unstable resonators with flowing saturable gain. 2: Fast Fourier Transform method", Applied Optics Vol 14 No 8, August 1975
3. S. Haykin, et al. "Adaptive Filter Theory", Second Edition, Prentice-Hall 1991

Calculation of Coupling Losses for Coaxial Waveguide Modes

Bernd Grubert, Werner Jüptner
Bremen Institute of Applied Beam Technology

Rolf Nowack
DLR-Institute of Technical Physics

ABSTRACT

Calculations of the waveguide mode coupling losses due to free space propagation between the waveguide endings and the resonator mirrors of a coaxial Cu-waveguide will be presented. The results show that the mode coupling losses have a strong influence on the mode selection in a coaxial waveguide laser.

1. INTRODUCTION

Calculations of the mode propagation losses of a coaxial Cu-waveguide used in a diffusion cooled CO₂-laser show, that for higher order (> 15) azimuthal modes, the mode with the lowest radial mode number is not the one with lowest propagation loss. This is in contradiction to the results of experiments on such a laser system, which were performed in cooperation with the ITP-DLR, Stuttgart (see "High Power Coaxial CO₂ Waveguide Laser"). These results show that even for higher order azimuthal modes in radial direction always the basic mode is observed.

To explain this discrepancy between theory and experiment, the coupling losses are taken into consideration. Including these losses in the round trip losses, one has to calculate the free space propagation of the field components of the waveguide modes from the waveguide endings to the resonator mirror and back to the waveguide. Figure 1 shows schematically the geometry. The resulting coupling losses follow from the calculation of the overlap integral of propagated field components with the waveguide mode components. A large amount of literature exists treating the problem of coupling losses (see e.g.¹).

Difficulties in calculating the free space propagation inside the resonator probably arise from the fact that the ratio of waveguide diameter to waveguide gap is in

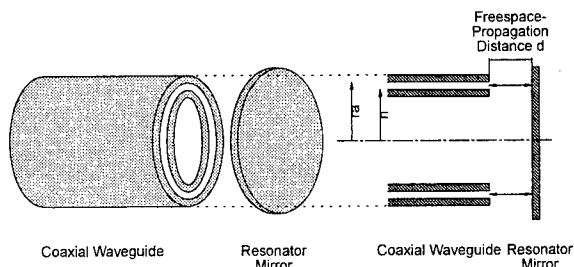


Figure 1: Schematic setup for coupling loss calculations

the order of 40 and the distance between waveguide ending and resonator mirrors is of the same order of magnitude as the gap resulting in a large Fresnel number. The premises of the Fresnel approximation normally used in this case are not strictly fulfilled and one has to be careful using this approximation.

Two methods to calculate the free space propagation of the waveguide-modes in the gap between waveguide and resonator mirrors will be discussed.

The first method is based on the decomposition of the mode fields in cylindrical wave functions, which are solutions of the wave equation in cylindrical coordinates. The advantage of this method is, that it is an exact solution of the wave equation. The disadvantage of awkwardness and slowness limits the use of this method in laser mode calculations, but for simple cases (e.g. Dual Case I configuration with plane mirrors) the results could be used as a reference to those of the second method. The second method is based on the Fresnel integral in cylindrical coordinates, which is much faster.

The two Methods will be described in the next section.

2. CALCULATION OF COUPLING LOSSES

2.1. Coupling losses

Let \vec{E}'_{wl} denote the electrical field of a waveguide mode with radial mode number w and azimuthal mode number l after free space propagation from a waveguide ending to the resonator mirror, transformation by the mirror and back propagation to the waveguide ending. Then the (self-)coupling efficiency χ_{wl} of \vec{E}'_{wl} into a waveguide mode with the same radial and azimuthal mode order can be calculated from the overlap integral for an absorbing waveguide²

$$\chi_{wl} = \frac{\iint_A \vec{E}'_{t,wl} \times \vec{H}^*_{t,wl} dA}{\iint_A \vec{E}_{t,wl} \times \vec{H}^*_{t,wl} dA} \quad (1)$$

where the index t denotes the transversal components of the fields and A is the cross sectional area of the coaxial waveguide. The coupling losses are defined as

$$\Gamma_{wl} = 1 - |\chi_{wl}|^2 \quad (2)$$

2.2. Consideration of polarization

The electrical field of a cylindrical waveguide mode possesses the same symmetry as the waveguide. Since the waveguide gap is large compared to the wavelength, the z -components of the electric and magnetic field are small compared to the other components, the field is assumed to be transversal electromagnetic (TEM). In this case the x - and y -polarized components propagate independently and the TEM-field after a propagation distance d follows from the superposition of the separately propagated cartesian components. Between the cartesian and polar coordinate field components the following relation holds:

$$\begin{aligned} E_{x,wl} &= \frac{1}{2} (u_{+,wl}(r) e^{i(l+1)\varphi} + u_{-,wl}(r) e^{i(l-1)\varphi}), \quad (3) \\ E_{y,wl} &= \frac{1}{2} (-i u_{+,wl}(r) e^{i(l+1)\varphi} + i u_{-,wl}(r) e^{i(l-1)\varphi}). \end{aligned} \quad (4)$$

where

$$u_{\pm,wl}(r) = u_{r,wl}(r) \pm i u_{\varphi,wl}(r), \quad (5)$$

[†]The complex conjugate refers only to the azimuthal part of the field, for the radial part the unconjugated version has to be used²

and $u_{r,wl}$ and $u_{\varphi,wl}$ represent the r -depending part of the r and φ respectively component of the electric field. As can be seen from the equations above, the problem of calculating the propagation x - and y -components is reduced to the propagation of expressions of the form $u_{\pm,wl} \exp(i(l \pm 1)\varphi)$.

2.3. Methods for free space propagation

In order to calculate the mode coupling losses the free space propagation of expression of the form $E(r, \varphi, 0) = u(r) \exp(i l \varphi)$ along a distance d between to parallel planes orthogonal to the propagation axis has to be calculated.

The first method bases on a representation of the source field by linear combination of elementary cylindrical wave function, which are the solutions of the wave equation within a homogeneous, isotropic domain.³

$$E'(r, \varphi, d) = \int_{-\infty}^{\infty} U(k_t) \psi_{l,k_t}(r, \varphi, d) k_t dk_t, \quad (6)$$

where

$$\psi_{l,k_t}(r, \varphi, z) = e^{i l \varphi} J_l(k_t r) \exp(i \sqrt{k_0^2 - k_t^2} z) \quad (7)$$

is the elementary cylindrical wavefunction and J_l denotes the Bessel function of first kind. The weighting factors $U(k_t)$ of the elementary wave functions follow from the Fourier-Bessel transform calculated at $z = 0$ ³

$$U(k_t) = \int_0^{\infty} u(r) J_l(k_t r) r dr \quad (8)$$

The second method is based on the Fresnel integral in cylindrical coordinates, which is applied on the radial part u only. In the configuration under investigation the argument $\frac{k_0 r' r}{d}$ is much larger than the azimuthal order l and the halfwidth $\varrho_0 = \frac{r_2 - r_1}{2}$ of the ring is much smaller than the mean radius $r_0 = \frac{r_1 + r_2}{2}$ (see fig. 1). In this case an asymptotic expansion for the Hankel function can be used.⁴

$$\begin{aligned} u(\varrho' + r_0) &= \sqrt{\frac{i k_0}{2\pi d}} (\varrho' + r_0) e^{-i k_0 d} \sum_{k=0}^{\infty} \frac{P_k}{\left(\frac{k_0 r_0^2}{d}\right)^k} \times \\ &\int_{-\varrho_0}^{\varrho_0} u(\varrho + r_0) \sqrt{\varrho + r_0} \exp(-i k_0 \frac{(\varrho^2 - \varrho')^2}{2d}) d\varrho. \end{aligned} \quad (9)$$

where P_{lk} are polynom coefficients with

$$P_{l0} = 1, \text{ and}$$

$$P_{lk} = P_{l,k-1} \frac{i}{8k} |4l^2 - (2k-1)^2| \text{ for } k > 0.$$

An analysis of the necessary sampling density leads to the result that for equally space discretisation points the condition for the minimum number N of samples is given by $N > 4 \frac{e_0^2 k_0}{2\pi d}$. In the configuration considered here the number N should be larger than 400.

The diffraction integral can also be interpreted as the convolution of the quadratic exponential term with the function $u(\varrho + r_0)\sqrt{\varrho + r_0}$. Since the Fourier transform of the exponential term can be calculated analytically (see e.g.⁵) the convolution can be performed by application of the well known convolution theorem.

$$u'(\varrho' + r_0) = e^{-ik_0 d} \sum_{k=0}^{\infty} \frac{P_{lk}}{\left(\frac{k_0 r_0^2}{d}\right)^k} \times \mathcal{F}^{-1} \left\{ \mathcal{F} \left\{ u(\varrho + r_0) \sqrt{\varrho + r_0} \right\} \Big|_s \exp \left(id \frac{(2\pi s)^2}{2k_0} \right) \right\} \Big|_{\varrho' + r_0} \quad (10)$$

Due to the inverse relation between spatial and frequency spacing the condition defines an upper limit for the number of sampling points $N < 4 \frac{e_0^2 k_0}{2\pi d}$. In this case an additional lower limit of N is following from the condition that the spacing has to be narrow enough to describe the source and destination field properly. The advantage of this method lies in the lower number of required discretisation points. For the calculation of the Fourier transform of discrete data the Fast Fourier Transform can be used.

3. NUMERICAL RESULTS

All numerical calculations were done on a personal computer using C++ as programming language. The calculation of coupling losses was performed for a coaxial waveguide made of copper with a complex refractive index⁶ $n=12 + i50$. The inner and outer radii of the waveguide were 28.5 mm and 30.0 mm respectively. The vacuum wavelength of the radiation was $\lambda=10.6 \mu\text{m}$. The waveguide modes were calculated following a method described by Ehrlichmann et.al.⁷ The resulting hybrid-modes can be divided into transverse electric-like (TE) and transverse magnetic-like (TM)-types, depending on their main polarization being azimuthal or radial.⁷ In the following only the TE-mode

will be regarded. The TM-modes can be neglected due to their higher propagation losses. The following figure 2 shows the propagation losses of the modes for a waveguide of length $L=0.53 \text{ m}$. For azimuthal mode orders l less than 15 the lowest radial mode has the lowest propagation loss. But with increasing l the modes with higher radial mode order have a lower propagation loss.

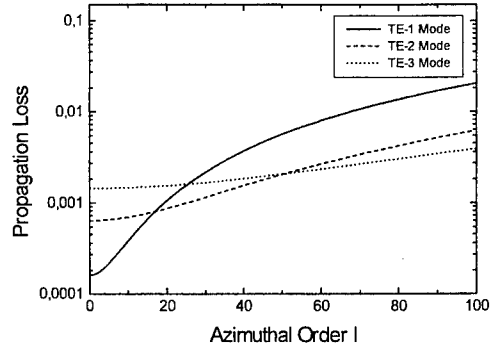


Figure 2: Propagation losses of TE-modes

Figure 3 shows the calculated coupling losses. The resonator mirror was a plane mirror and the distance between waveguide ending and mirror was 2 mm. The losses were calculated with the cylindrical wave expansion, using 128 sampling points in the spatial domain and 8192 samples in superposition integral of equation (6). The figure shows that the coupling losses are in-

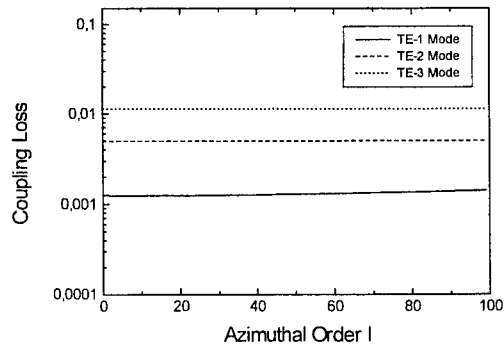


Figure 3: Coupling losses

creasing with increasing radial mode order. The dependence of the azimuthal mode order is only weak.

Figure 4 shows the combination of the propagation and coupling losses from figures 2 and 3. The azimuthal mode order up to which the lowest radial mode has the lowest losses is now expanded to $l \approx 70$ and the losses have increased by a factor of 10 compared to the pure propagation losses.

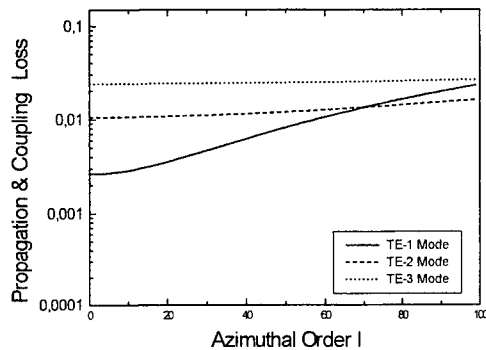


Figure 4: Propagation and coupling losses

The convolution method was also used to calculate the coupling losses. In order to compare both methods the sampling rate was again chosen as 128 points in the spatial domain. The coupling losses calculated by this method differ only slightly from those calculated by the cylindrical wave method. The figure 5 shows the relative differences of the coupling losses calculated by both methods. The values differ only by few percent and are therefore in good agreement. Due to its higher numerical effort the cylindrical wave method is about 20 times slower than the Fresnel method. This fact makes only the latter usable for resonator mode calculations.

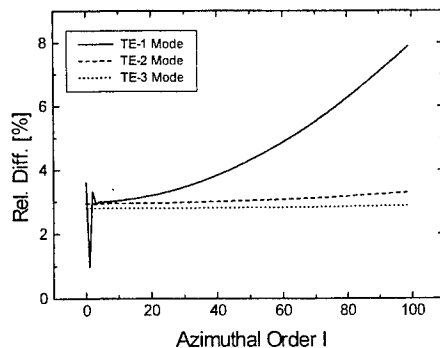


Figure 5: Difference coupling loss values

4. SUMMARY

The comparison of the results of the two methods shows, that the Fresnel method could also be used for the calculation of the coupling losses. Furthermore the calculations indicate, that the coupling losses are of the same order of magnitude as the propagation losses and favour the modes with lower radial mode number. Even for higher order azimuthal modes the lowest radial mode is the one with the lowest round trip losses.

5. ACKNOWLEDGEMENTS

This work was supported by the German Ministry for Education, Science, Research and Technology (BMBF).

6. REFERENCES

- [1] D. R. Hall and C. A. Hill. Radiofrequency-Discharge-Excited CO₂ Lasers. In P. K. Cheo, editor, *Handbook of Molecular Lasers*, Laser Handbooks, chapter 3, pages 165–258. Marcel Dekker, 1987.
- [2] A. W. Snyder and J. D. Love. *Optical Waveguide Theory*. Chapman and Hall Ltd., 1983.
- [3] J. A. Stratton. *Electromagnetic Theory*. McGraw-Hill Book Company, Inc., 1941.
- [4] V. L. Gamiz. Propagation of thin annular scalar field distributions. In U. R. Stone, editor, *New Methods for Optical, Quasi Optical, Acoustic, and Electromagnetic Synthesis*, pages 13–18. Proc. SPIE **294**, 1981.
- [5] A. Papoulis. *Signal Analysis*. McGraw-Hill, Inc., 1977.
- [6] B. Dold and R. Mecke. Optische Eigenschaften von Edelmetallen, Übergangsmetallen und deren Legierungen im Infrarot (1. Teil). *Optik*, 22(6):435–446, 1965.
- [7] D. Ehrlichmann, U. Habich, and H.-D. Plum. High-power CO₂ laser with coaxial waveguide and diffusion cooling. *IEEE J. Quantum Electron.*, 29(7):2211–2219, 1993.

Transient four-wave mixing of pulsed CO₂ laser radiation in semiconductors

M.G. Galushkin*, A.A. Ionin**, A.A. Kotkov**, K.V. Mitin*

*Scientific Research Center on Technological Lasers of Russian Academy of Sciences, Shatura, Moscow Region, Russia.

**P.N. Lebedev Physics Institute of Russian Academy of Sciences, Moscow, Russia.

ABSTRACT

A temporal behaviour of a phase conjugation reflectivity R at degenerate four-wave mixing (DFWM) in InSb for a pulsed CO₂ laser radiation is theoretically investigated. It is shown, that R at a transient DFWM is determined by a response time of a nonlinear medium, which depends on intensity of a radiation, and can be some times higher then a reflectivity for non-transient condition.

INTRODUCTION

A high nonlinearity, high response and small size can be regarded as advantages of semiconductors as a nonlinear component of a PC mirror. That is why a great attention was given to experimental and theoretical investigations of DFWM for a CO₂ laser radiation in semiconductors¹⁻⁵. Up to now, the theoretical investigation of DFWM of mid-IR radiation in semiconductors were applied to the description of a nontransient process experimentally observed fairly frequently. However, the phase conjugation of the short pulses of radiation ($\sim 10^{-9} - 10^{-8}$ s) can be the practically important problem. For this case the consideration of transient DFWM, that involves the final response time of nonlinearity in semiconductors, becomes very important. This problem is also significant if one uses DFWM as a diagnostic method of semiconductor parameters (a concentration of impurities, free carriers lifetime, a coefficient for two-photon absorption etc.), so far as a temporal behaviour of a PC signal at DFWM contains much more information about the medium nonlinearity than nontransient characteristics of PC.

The properties of the transient DFWM of a CO₂ laser radiation in semiconductor, nonlinearity of which is stimulated by two-photon absorption (TPA), are theoretically investigated in the paper. The calculations and theoretical analysis of a time behaviour of DFWM are carried out for indium antimonide (InSb) as an example. In this semiconductors free nonequilibrium carriers are generated owing to TPA, their concentration depending on intensity of radiation⁶⁻⁸. This research work was stimulated by the theoretical and experimental study of transient DFWM of a pulsed CO₂ laser radiation in an inverted medium⁹.

A DESCRIPTION OF THE MECHANISM OF THE NONLINEARITY

Inasmuch as the real part of dielectric constant of the semiconductor is connected with a free carrier concentration, the nonlinearity of a refractive index arises at absorption of laser radiation. The process can be represented as follows:

$$\delta J \rightarrow \delta p \rightarrow \delta(n_e) \rightarrow \delta n, \quad (1)$$

where δJ , δp , δn_e , δn are the spatial-temporal variations of radiation intensity, concentration of holes, electron concentration and refractive index. The mechanism of refractive index nonlinearity (phase nonlinearity) stimulated by generation of free carriers at TPA of radiation has a great interest for DFWM in semiconductors.

The absorption in InSb can be presented in the following form⁸:

$$\beta = \beta_0 + \frac{\beta_n J}{2} + \sigma_e n_e + \sigma_p p, \quad J = \frac{nc}{4\pi} \sum_{j=1}^4 |A_j(z)|^2 \varphi_j(t) \quad (2)$$

where β_0 is the coefficient of linear absorption, β_n is the TPA coefficient, $\sigma_{p,e}$ is the cross-section of absorption on nonequilibrium holes and electrons, p and n_e are the concentration of nonequilibrium holes and electrons, $\varphi_j(t)$ is the profile of radiation pulses. In general case functions $\varphi_j(t)$ depend on longitudinal coordinate Z . If this dependence being weak it is possible to use values of these functions averaged on interaction length.

The value of a refractive index is determined by a free carrier concentration in semiconductor. The nonequilibrium holes introduces the main contribution into n in the case of InSb, because for InSb $\sigma_e \ll \sigma_p$. Thus the expression for refractive index has the following form:

$$n = \frac{\lambda_e e^2}{2\pi c^2 n m_{ch}} p, \quad m_{ch} = 0.013 m_0 \quad (3)$$

where λ is the wavelength of radiation, e and m_0 are the charge and the mass of an electron, c is the speed of light in vacuum. The value of p can be found from kinetic equation for nonequilibrium holes:

$$\begin{aligned} \frac{d}{dt} p = & \frac{\beta_n}{2 \hbar \omega} J^2 + D \nabla^2 p - \xi(n_{e0} + n_e)(p_0 + p) + \xi n_{e0} p_0 - \\ & - \eta_p(n_{e0} + n_e)(p_0 + p)^2 - \eta_e(n_{e0} + n_e)^2(p_0 + p) + \eta_p n_{e0} p_0^2 + \eta_e n_{e0}^2 p_0, \end{aligned} \quad (4)$$

where n_{e0} , p_0 are the equilibrium concentrations of electrons and holes, D is the coefficient of ambipolar diffusion, ξ is the coefficient of radiative recombination, η_e , η_p are the coefficients of Auger recombination for electrons and holes. Further, for clarity, we shall consider the n -type semiconductor as one being used frequently in experiments. We shall not consider the influence of the trapping centers (we assume here that their concentration is negligible) on free carrier kinetics, i.e. $p = n_e$. The value of η_p in (4) can be neglected because the mobility of electrons is of some orders of magnitude higher than for mobility of holes. Then the equation (4) can be written in the following form

$$\frac{d}{dt} p = \frac{\beta_n}{2 \hbar \omega} J^2 - (\xi n_{e0} + \eta_e n_{e0}^2 - D \nabla^2) p - 2(\xi + 2 \eta_e n_{e0}) p^2 - \eta_e p^3. \quad (5)$$

Also we assume the classical scheme of DFWM to take place in our case. A probe wave E_3 interferes with the counter-propagating pumping waves E_1 and E_2 conjugated. In the result of the interference the space modulation of the radiation intensity takes place:

$$\begin{aligned} J & \approx \frac{c}{4\pi} (|E_0|^2 + 2E_0 \Delta E) \\ E_0 & = E_1 + E_2; \quad \Delta E = E_3 + E_4 \\ E_j & = \frac{1}{2} A_j \exp(i\omega t + i\vec{k}_j \vec{r}) + K. C. \quad (j=1, 2, 3, 4) \end{aligned} \quad (6)$$

where $E_4 \sim (E_3)^*$ is the PC wave, A_j is the slowly varying complex amplitudes, ω is the frequency of radiation, \vec{k}_j is the wave vector. A condition $|A_3|, |A_4| \ll |A_1|, |A_2|$ is assumed to take place for maintenance of the cubic nonlinearity in semiconductor. Then the variation of radiation intensity has the following form:

$$\delta J = 2 \frac{c}{4\pi} (E_0 \Delta E). \quad (7)$$

We shall consider, that E_0 and ΔE in (4) do not contain high-frequency temporal oscillations which nonlinear medium has no time to react upon. The spatial-temporal variation of radiation intensity induces the amplitude and phase gratings in a nonlinear medium through the mechanisms of nonlinearity described above. A PC wave E_4 is formed as a result of scattering of pumping waves on these gratings.

The interaction of electromagnetic waves at DFWM is described by nonlinear Helmholtz equation. Its solution has been found by numerical calculations used previously for nonlinear medium of CO₂ laser^{9, 10}. As a result, the phase conjugation reflectivity was calculated.

The values of relaxation times and parameters of DFWM we have taken for calculations from⁵. Thus, for the sample of n-InSb with a concentration of equilibrium electrons $n_{e0} \approx 2 \cdot 10^{16} \text{ cm}^{-3}$ ($T=300\text{K}$) let $\beta_0 = 7 \text{ cm}^{-1}$, $\beta_n = 5.5 \text{ cm} \cdot \text{MW}^{-1}$, $\xi = 5 \cdot 10^{-11} \text{ cm}^3 \cdot \text{s}^{-1}$, $\eta_e = 10^{-25} \text{ cm}^6 \cdot \text{s}^{-1}$, $\sigma_p = 9 \cdot 10^{-16} \text{ cm}^2$. In addition we shall take the angle between interacting waves $\theta_{13} \approx 1^\circ$ and the time $\tau_D \approx 3 \cdot 10^{-7} \text{ s}$. Also we assume that the second pumping wave is formed by reflection from mirror and interaction length $L_n = 0.05 \text{ cm}$.

A temporal behaviour of PC reflectivity, hole concentration p and $(\delta p_{jm}/\delta J_{jm})^2$ for rectangular pulse of radiation at various pumping wave intensities $J_1(0)$ is presented in Fig. 1. The PC reflectivity replicates precisely a temporal behaviour of $(\delta p_{jm}/\delta J_{jm})^2$ in transient part for a weak intensity of pumping waves. Maximums are observed in temporal dependence of R and $(\delta p_{jm}/\delta J_{jm})^2$ at the higher pumping intensities. Their location is shifted with $J_1(0)$ growth to the origin of temporal axis. A shortening of a transient region with a wave intensity increase is a feature of temporal behaviour of DFWM (see Fig. 2). The dependence of maximal transient PC reflectivity R_{max} and steady-state one R_{st} on intensity of the first pumping wave is

presented on Fig. 3. The behaviour of R_{st} is in good agreement with the dependence described in ⁵. A nontransient function of the PC reflectivity has a maximum close to $J_1(0) \approx 0.1 \text{ MW cm}^{-2}$. Unlike R_{st} , R_{max} continues to grow with intensity increase. Thus, the transient PC reflectivity can reach a value of unit at a certain $J_1(0)$.

THE CONDITIONS OF EXPERIMENTAL OBSERVATION OF TRANSIENT DEGENERATE FOUR WAVE MIXING IN INDIUM ANTIMONIDE

Further we shall briefly discuss main conditions for an experimental observation of transient DFWM in InSb. As mentioned above, out of cavity DFWM is more convenient for this purpose because an optical isolation between pulsed CO_2 laser and PC mirror is available. In such optical scheme an influence of a semiconductor optical element on a spatial-temporal parameters of the laser radiation is excluded. The special demand for experimental setup involves a high response time of nonlinearity of the semiconductor. In practice, the pulse of an electron beam controlled discharge (EBCD) CO_2 laser of duration up to 20 - 30 μs is strongly modulated in time and represents a sequence of short spikes of different amplitude which are the result of longitudinal modes beating¹¹. The nonlinearity of the medium with small response time reacts on each spike from the radiation pulse. Therefore the temporal synchronization of pumping and probe waves should correspond to a duration of a single spike (the shortest of them). Then each spike forms a phase grating and accordingly is scattered on it with a PC signal formation. Thus one can expect an increase of a degree of PC radiation modulation with respect to temporal modulation of pumping wave, because PC reflectivity is proportional to a square of pumping intensity. For more complete experimental investigation of PC in InSb it is very interesting to investigate DFWM of a series of regular short pulses of tCO_2 laser operating at a mode-locking regime. This regime of a EB CD CO_2 laser operation can arise, for example, with laser plasma formation near the surface of a resonator mirror¹². The EB CD CO_2 laser with plasma mirror generating pulses with duration of $\sim 10 \text{ ns}$ with period of $\sim 100 \text{ ns}$ was investigated, for example, in experiments on PC at DFWM in active medium of CO_2 laser (Fig. 4).

CONCLUSIONS

Temporal behaviour of PC reflectivity of short pulses of a CO_2 laser radiation at DFWM in indium antimonide is determined by the kinetics of free carrier concentration.

It follows from the calculations for the pulses of radiation of duration $\sim 10^{-9} - 10^{-8} \text{ s}$ that in transient region PC reflectivity can be much more higher than maximum steady-state reflectivity. The maximum value of transient PC reflectivity R_{max} rises with growth of intensity of pumping waves, a duration of transient region being shortened.

Both the intensity of radiation and lifetime and equilibrium concentration of free carriers influence strongly on value of R_{st} and R_{max} in semiconductor. This dependence can be used for diagnostics of semiconductor materials.

REFERENCES

1. R.K.Jain. "Opt. Engineering", **21**, 199 (1982).
2. N.G.Basov, V.I.Kovalev, M.A.Musaev, F.S.Faizulov. "Proc. Lebedev Physics Inst. Acad. Sci. USSR", **172**, 147. Nova Science, New York (1988).
3. A.A.An, V.I.Kovalev. "Soviet J. of Quantum Electron.", **17**, 1075 (1987).
4. V.I.Kovalev, V.A.Trofimov. "Kvantovaya elektronika", **18**, 1336 (1991) (in Russian).
5. V.I.Kovalev. "Infrared Phys.", **32**, 235 (1991).
6. A.M.Danishevskii, A.A.Patrin, C.M.Rivkin, I.D.Yaroshevskii. "Gurnal Experimentalnoy i Teoreticheskoy Fiziki", **56**, 1457 (1969) (in Russian).
7. I.P.Areshev, M.G.Gusseinaliev, A.M.Danishevskii et al. "Fizika Tvyordogo Tela", **22**, 1456 (1984) (in Russian).
8. I.P.Areshev, A.M.Danishevskii, S.F.Kochegarov, V.K.Subashiev. "Optika i Spektroskopiya", **48**, 975 (1980) (in Russian).
9. L.A.Afanas'ev, M.G.Galushkin, A.A.Ionin et al. "Izvestiya Akademii Nauk", seriya Fizicheskaya, **60**, 41 (1996) (in Russian).
10. L.A.Vasil'ev, M.G.Galushkin, A.M.Seryogin, N.V.Cheburkin. "Kvantovaya elektronika", **9**, 1228 (1982) (in Russian).
11. L.A.Afanas'ev, A.A.Ionin, E.A.Kiselev et al. "Quantum electronics", **21**, 557 (1994).
12. N.G.Basov, I.A.Beregnoy, V.A.Boyko et al. "Pisma v Gurnal Tehnicheskoy Fiziki", **1**, 1105 (1975) (in Russian).

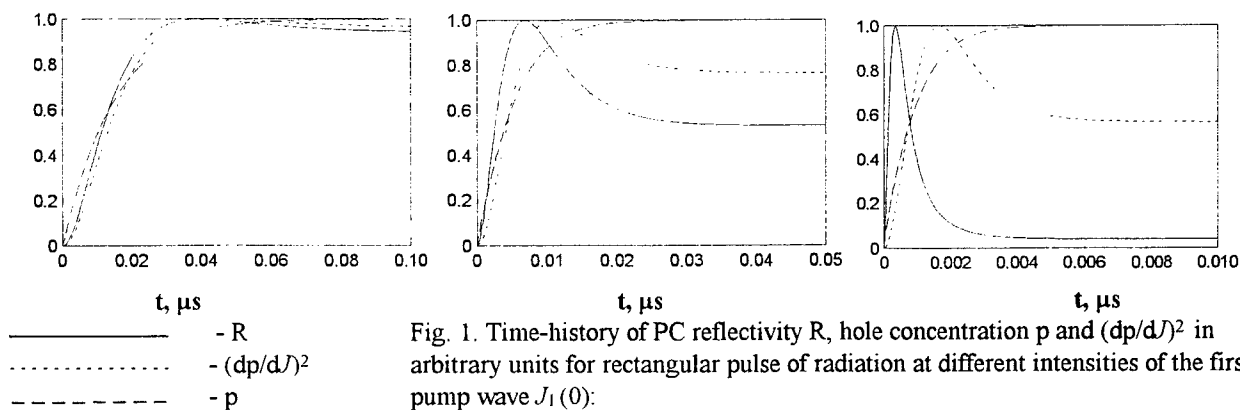


Fig. 1. Time-history of PC reflectivity R , hole concentration p and $(dp/dt)^2$ in arbitrary units for rectangular pulse of radiation at different intensities of the first pump wave $J_1(0)$: a). 0.03 MW/cm^2 , b). 0.1 MW/cm^2 , c). 0.5 MW/cm^2 .

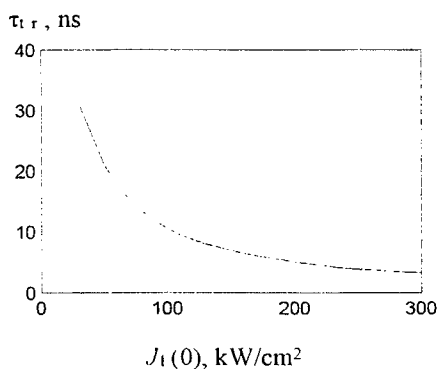


Fig. 2. Dependence of transient region duration on the first pump wave intensity.

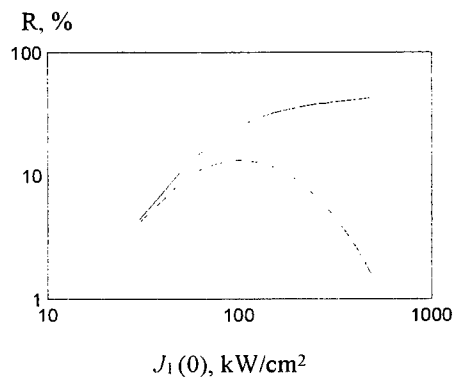


Fig. 3. PC reflectivity versus first pump wave intensity. — maximal transient PC reflectivity, steady-state PC reflectivity.

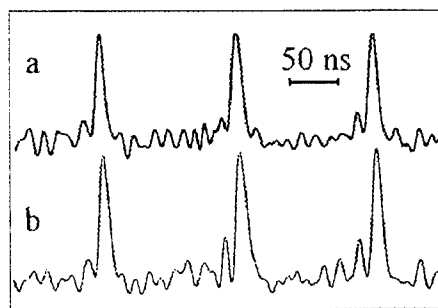


Fig. 4. Time-history of a probe (a) and PC signal (b) at DFWM of radiation of EBCD CO_2 laser with plasma mirror in inverted medium obtained by A.Ionin, A.Kotkov, L.Selesnev (P.N.Lebedev Institute, Russia), C.Beairsto, R.Penny, S.Squires (Directorate of Applied Technology, USA), R.Walter (W.J.Schafer Associates., USA) in joint experiments at Lebedev Institute.

High frequency temporal structure of laser and phase conjugated signals at intracavity degenerate four-wave mixing of CO₂ and CO laser radiation inside their inverted medium

C.Beairsto*, A.Ionin, A.Kotkov, R.Penny*, L.Seleznev, S.Squires*, R.Walter**

P.N.Lebedev Physics Institute of Russian Academy of Sciences, 53 Leninsky pr., 117924 Moscow, Russia

* Directorate of Applied Technology, White Sands Missile Range, New Mexico, USA

** W.J.Schafer Associates, Inc., Albuquerque, New Mexico, USA

ABSTRACT

The high frequency temporal structure of probe (laser) and phase conjugation (PC) signal under intracavity degenerate four-wave mixing (DFWM) of long pulse CO₂ and CO laser radiation inside their inverted medium has been studied experimentally with nanosecond resolution over the full pulse length.

Key words: CO₂ laser, CO laser, phase conjugation, four-wave mixing, temporal structure, nanosecond resolution.

1. INTRODUCTION

The intracavity DFWM of pulsed CO and CO₂ laser radiation involves an appearance of PC signal backscattered relative to a probe wave^{1,2}. The PC signal is proved to have a complicated time behaviour³ due to transient mechanisms of formation of diffraction gratings (saturated gain (or amplitude) grating and thermal (or phase) one) inside an active medium. The theory describing the PC process and the experiment itself³ dealt with relative "smooth" CO₂ laser pulses not taking into consideration the high frequency (HF) temporal structure on the round-trip period (RTP) that can arise due to longitudinal mode beating and mode locking. As a matter of fact, the real CO₂ laser pulses, even "long" ones do have such structure². The same situation seems to take place also for CO lasers, though up to now nobody attempted measurement of the structure. The objective of the paper is the experimental research of the temporal structure, including HF one on the RTP, for laser (probe) and PC signals at DFWM of long pulse CO and CO₂ lasers radiation with nanosecond resolution over the full pulse length.

2. EXPERIMENTAL SETUP AND OPTICAL SCHEME

The experiments were carried out on the e-beam controlled discharge (EBCD) CO₂ (CO) laser installation with active length of 120 cm. The pulse length for input power was 20 μ s, input energy being changed between 100 and 400 J/l Amagat. CO laser operated at gas temperature of \sim 100K. Laser mixture CO₂:N₂:He = 1:2:4 and CO:N₂:He=1:4:5 were used for CO₂ (CO) laser. Gas density amounted to 0.3 Amagat. The laser resonator length was 18 m (RTP=120 ns). The laser beam waist on the output coupler was 15 mm. The output energy was approximately about one Joule both for CO and CO₂ laser. The center of the active medium was situated at $l=7.5$ m from the output coupler (RT time is 50 ns). The diffraction grating was used in case of spectral selective resonator. The probe beam I_3 was directed to the active medium under the small angle of 10mrad to the optical axis of the laser. There was no time delay between the probe pulse I_3 and intracavity co-propagating laser pulse I_1 within the accuracy of ± 0.3 ns. In measuring pulse profile and HF structure of the probe and PC signals HgCdTe and photon drag photodetectors with nanosecond response time and oscilloscope "TEKTRONIX" TDS680B were used.

3. EXPERIMENTAL RESULTS AND DISCUSSION

Temporal behaviour of probe and PC signals for CO₂ laser. The time measurement confirms the existence of complicated structure on large temporal scale being dependent on a number of parameters such as specific input energy and power, intensity ratio for probe and co-propagating pumping wave etc. As it was emphasized in³ these parameters strongly influence upon the relative role of two principal mechanisms of nonlinearity such as amplitude and phase ones. One can see from Fig.1a bearing in mind the previous results the relative high amplitude of PC signal at the front of the pulse due to amplitude mechanism and strong PC reflectivity at the rear part due to thermal mechanism. An increase of input power pulse length (Fig.1b) leads to an increase of probe pulse length, a decrease of its average intensity and results in strong decrease of PC reflectivity on the front of pulse and rise of the PC signal on the pulse tail. When increasing specific input energy together with intensity of probe beam, the oscillation of the tail both of probe and PC signal with period of ~ 2 μ s is observed (Fig.1c) being more distinctive for the PC signal.

One can see in Fig.2 that both probe and PC pulses have a periodic structure with period of 120 ns corresponding to RTP and also have very deep, nearly 100% modulation. The first peak of the PC pulse, which can be seen in Fig.2a, follows the probe pulse nearly noninertially, its front being more sharp. A spike with maximal amplitude of the first peak of the PC pulse does not always fit to that of the probe pulse. The strong spike in PC signal correlates with weak one in probe signal very frequently on various temporal scales. Fig.2b demonstrates the time behaviour of probe and PC signal for pulses of Fig.1c at

the seventh microsecond from the beginning of the laser pulse. The PC signal has an oscillation with the same period of 500 ns like for probe signal, however with opposite phase.

The typical first peak of the laser and PC pulses is presented in Fig.3. The 100% modulation can be observed very clearly. The diagrams could explain the process of writing down and reading out the diffraction grating during first peak of the laser pulse, which, as was shown in ^{2,3} was brought about by amplitude mechanism. One can easily see from Fig.3a, that PC signal is observed of 50 ns later relatively the probe one. The reason of it that the grating begins to be written down in the active medium when a first spike goes out the laser resonator (wave I_3) comes back to the active medium and interferes there with the same spike reflected from the output coupler back to the active medium. The amplitude grating is read out by spike of intracavity wave I_2 shifted on $\tau_{shift} = 2l/c = 50$ ns relatively spikes of waves I_1 and I_3 . As a result of diffraction of the intracavity pulse I_2 on the grating we observe PC signal I_4 . Thus on the diagrams of Fig.3 we have the signal reading out the diffraction grating (upper trace) and one being read by that signal, i.e. PC signal (bottom trace). This description explains the formation of large scale grating with period of λ/θ .

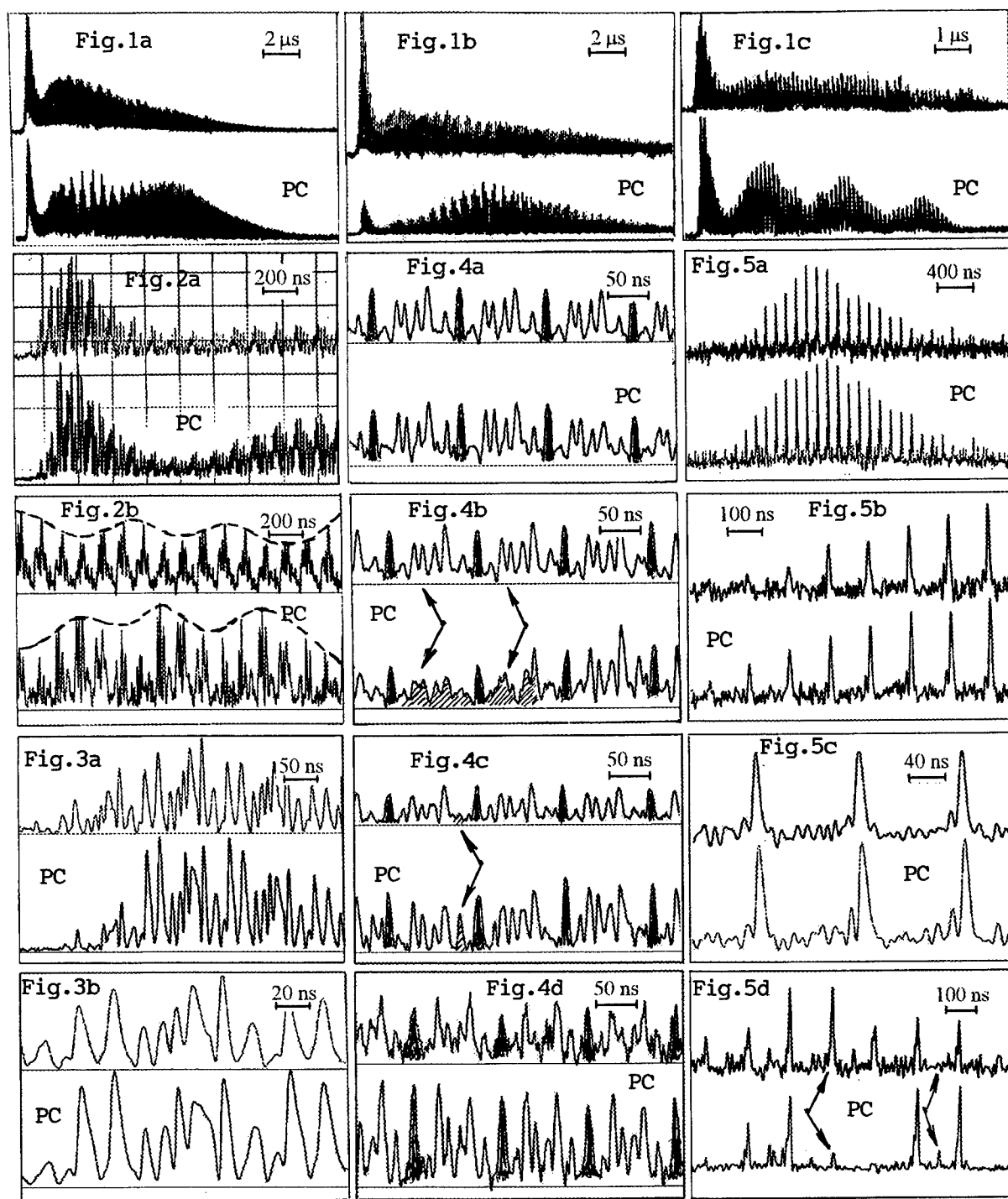
Inasmuch as the CO₂ laser pulse consists of spikes with length of ~ 10 ns determined by pressure broadening, one should take into account the fact of existing of small scale grating with spatial period of $\lambda/2$ which has never been considered for CO₂ and CO lasers, for they have believed that this grating is destroyed very quickly by heat conductivity. These two diffraction gratings can work together resulting in complicated structure of PC signal on RTP.

Of course, the process of formation of PC signal is much more complicated. The inhomogeneities can bring forth the anomalies taking place on RTP during the laser pulse. One of the laser pulse and its PC signal (Fig.1a) was analyzed with nanosecond resolution during its full length (Fig.4). Though the laser probe signal is regular one, there is some destruction of PC signal (see Fig.4b). Sometimes very weak probe signal brings forth strong PC signal (Fig.4c). In general, regular structure is kept till the end of laser pulse (Fig.4d), where thermal nonlinearity operates. It should be noted, that even for a very weak probe signal with intensity of one hundredth as much as that of the first peak of the laser pulse, we did observed yet PC signal (Fig.4d) with PC reflectivity (on intensity) approximately twice as higher as for the first peak of the laser pulse.

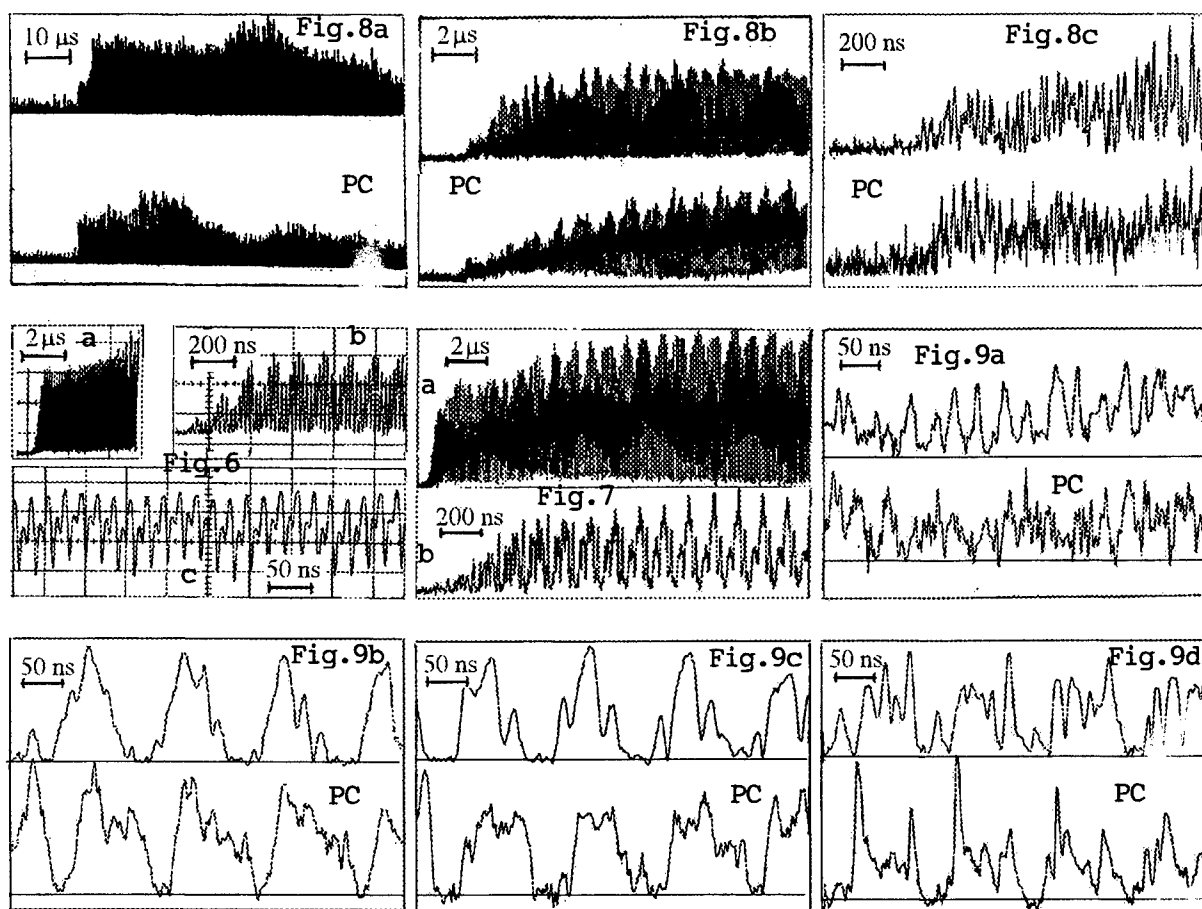
The mode locking leads to a higher intensity spike on the RTP. In our experiments the mode locking regime of operation for EBCD CO₂ laser was brought about by use of a plasma mirror ⁴. The laser pulse consists of a set of pulses, some of them being mode locked with a regular spike structure. Fig.5 illustrates one of the pulses. Here the PC signal does arise by diffraction of reading out wave on thermal grating produced by previous pulses, the last of which takes place ~ 6 μ s before the mode locked pulse presented on Fig.5. Actually, the strong PC signal on amplitude grating could not arise because there was no strong spike writing down the grating at ~ 50 ns before the reading out spike. The analysis of the results demonstrates, that the active medium should be situated near the output coupler (or near the rear mirror) to produce the same three spikes (probe one and two laser spikes for the two intracavity waves) in the same place simultaneously (in case the rear mirror, the reading out spike would be shifted at RTP with respect to writing down spikes). It should be noted, that for mode locking regime some anomalies also were observed like in case of free-running mode. See Fig.5d where one can see disappearing of some spikes from PC signal and strong PC signal for the very weak spike.

Time history of laser and PC signal at DFWM of CO laser radiation. CO laser also has periodic structure both for single line P₁₀₋₉(15) and multiline (nonselected) pulses with very deep modulation (Fig.6). The structure could arise as a result of longitudinal mode beating and/or mode locking due to a saturable absorber such as water vapour in long length laser cavity. That modulation refers to the low number of longitudinal modes taking part in lasing. The interaction of probe beam with intracavity laser radiation (Fig.7) disturbs slightly the regular structure on RTP though the strong modulation is kept during the full CO laser pulse. The PC signal differs from probe one, though also has regular structure with deep modulation both on large and small temporal scale (Fig.8). It has sharper front. In case of strong probe signal (Fig.8a) there are holes in PC signal intensity corresponding to maximums of probe signal. At the front part of PC pulse maximum (on the temporal scale of ~ 1 μ s) also does not correspond to maximum of probe pulse. Like for CO₂ laser oscillations takes place both for probe and PC signal (see Fig.2 and Fig.8b,c.). The reason for these oscillations like in the case of CO₂ laser could be acoustical disturbances taking place in the active medium of both lasers.

The HF structure for probe and PC signals of CO laser has rather more complicated behaviour than for CO₂ laser. Part of the PC and probe signal are presented in Fig.9a. The front of the laser pulse itself has a relative irregular structure being noticeably changed from one RTP to another. This behaviour strongly differs from that of CO₂ laser pulse which has strong periodic structure on its front (Fig.3). It should be noted that intensity of probe and PC signal approximately 100 times less than that of CO₂ laser, particularly for its first peak. The regular periodic structure for both signal could be much easily seen far from the beginning of the pulse (~ 10 -25 μ s), where laser intensity was much higher (Fig.9b-d). As compared to that of CO₂ laser, the structure of CO laser itself is changed slightly from one RTP to another (see Fig.9b,c and d, obtained for ~ 10 and 24 μ s, Fig.9d corresponds to the different laser pulse).



FIGURES: in all figures except Fig. 6 and Fig. 7 upper trace corresponds to probe (laser) and bottom trace to PC signals. Fig. 1. Probe and PC signals for free-running CO₂ laser $q=165$, $I_1/I_3=4$ (a); $q=220$, $I_1/I_3=11$ (b); $q=300$ J/l atm, $I_1/I_3=0.4$ (c). Fig. 2. First peak (a) and the seventh microsecond (b) of CO₂ laser and PC pulse. Fig. 3. First peak of CO₂ laser and PC pulse. Fig. 4. CO₂ laser and PC pulses for different time intervals: 1.8 μ s (a), 3.2 μ s (b), 6.2 μ s (c), 12.4 μ s (d). Fig. 5. Probe and PC signals for mode locked CO₂ laser. Fig. 6. CO laser pulse without DFWM. Fig. 7. CO laser pulse with DFWM. Fig. 8. Probe and PC signals for free-running CO laser, $q=220$ J/l Amagat, $I_1/I_3=1$, multiline (a); $I_1/I_3=3.5$, single line (b,c). Fig. 9. The signals for CO laser, $q=220$ J/l Amagat, single line, $I_1/I_3=3.5$, 640ns (a); 10.0 μ s (b); 23.5 μ s (c); $I_1/I_3=1$, 10 μ s (d).



The HF structure of PC signal for CO₂ laser at long distance (Fig. 4a-d) nearly repeats that of probe pulse. The fact, as was mentioned above, refers to prevailing role of thermal PC mechanism at large temporal scale for CO₂ laser. The situation seems to be quite different for CO laser. The HF structure of PC signal strongly differs from that of probe signal, reminding the HF structure behaviour for a first peak of CO₂ laser pulse (Fig. 2), where amplitude mechanism is responsible for the PC process. In many cases the beginning of the probe spike (Fig. 9d) has much stronger PC reflectivity than following spikes. As a matter of fact, the amplitude mechanism, as was emphasized in ⁵ should be the main one for CO laser because of a slow V-T relaxation rate of CO molecule. The combination of mutual disposition of writing down and reading out spikes leads to the complicated temporal behaviour of HF structure for CO laser on long distance like for first peak of CO₂ laser on relatively short distance.

4. CONCLUSIONS

The HF structure for PC signal of free-running and mode locked CO₂ laser, and for probe and for PC signal of free-running CO laser at DFWM in inverted medium was observed for the first time.

Together with large temporal scale behaviour the HF structure refers to two principal mechanisms of PC process (resonance and thermal ones) in CO₂ laser and resonance mechanism in CO laser. The existence of HF structure on nanosecond scale both for CO₂ and CO laser, which have never been taken into consideration both in experiment and theory makes reconsider the role of small scale diffraction grating in active medium, and also makes take into account the small temporal scale CO₂ and CO laser kinetics (for instance, hole burning in vibrational-rotational gain distribution etc.).

5. REFERENCES

1. E.E.Bergman, I.L.Bigio, B.J.Feldman and R.A.Fisher, *Optics Lett.*, **3**, 82 (1978).
2. L.A.Afanas'ev, A.A.Ionin, A.A.Kotkov et al, *Quantum Electronics*, **24**, 513 (1994).
3. L.A.Afanas'ev, M.G.Galushkin, A.A.Ionin, et al, *Izvestija RAN, ser.Phys.*, **60**, 41 (1996) (in Russian).
4. N.G.Basov, I.A.Beregnoy et al, *Technical Physics Letters*, **1**, 1105 (1975) (in Russian).
5. A.V.Berdyshev, A.K.Kurnosov, A.P.Napartovich, *Kvant. Electron*, **20**, 529 (1993) (in Russian).

SBS properties of high-pressure xenon

A.M.Dudov, S.A.Buyko, Y.V.Dolgoplov, V.A.Eroshenko, G.G.Kochemasov, S.M.Kulikov, V.N.Novikov, A.F.Shkapa,
S.A.Sukharev, L.I.Zykov

Russian Federal Nuclear Center, Mira 37, Sarov, Nizhniy Novgorod region, 607190, Russia
Phone: 7-83130-56646, fax: 7-83130-54565, e-mail: dudov_2566@spd.rfnc.nnov.su

A.M.Scott

DRA, St. Andrews Road, Malvern, Worcestershire WR14 3PS, UK

ABSTRACT

For xenon at temperature $t = 19.3^\circ\text{C}$ in a range of density $0.3\text{ g/cm}^3 \leq \rho \leq 1.0\text{ g/cm}^3$ SBS gain coefficient (g) and phonon lifetimes are measured. It is shown that at the densities higher than $\rho = 0.5\text{ g/cm}^3$ SBS gain g levels out, reaching the value $g \approx 100\text{ cm/GW}$, and the phonon lifetimes decrease down to $\tau_{ph} = 25\text{ ns}$ with approaching to a critical point of Xe.

Keywords: Stimulated Brillouin Scattering, xenon, critical point, threshold power, iodine laser.

INTRODUCTION

Phase conjugation at Stimulated Brillouin Scattering (SBS) is widely used for improvement of a laser radiation characteristics. Compressed gases, for example, Xenon are promising as an active SBS-medium for gaseous lasers because of their transparency in UV and IR spectral regions, and small Stokes frequency shift. Theoretical researches predict increase of SBS gain coefficient (g) as $g \propto \rho^2$ at increasing of gas density¹. In a pressure range below critical point ($p_{cr} = 57.6\text{ atm}$, $T_{cr} = 289.7^\circ\text{K}$) experimental results are in good agreement with this prediction. For example: $g = 1.4\text{ cm/GW}$ at $p = 10\text{ atm}$ ($\rho = 0.058\text{ g/cm}^3$)², and $g = 44\text{ cm/GW}$ at $p = 39\text{ atm}$ ($\rho = 0.30\text{ g/cm}^3$)³. However the attempt of the authors⁴ to receive high SBS gain in Xe at pressure of 220-240 atm did not give expected results. In the work⁵ with approaching to critical point ($\rho \geq 0.7\text{ g/cm}^3$) an appearance of optical inhomogenities in Xe have been registered which raised a SBS threshold. In the given work we investigate SBS excitation in Xe at density range of $0.3\text{ g/cm}^3 \leq \rho \leq 1.0\text{ g/cm}^3$ and at a conditions when influence of optical inhomogenities on SBS threshold was not essential because the cell with Xe has been well thermostated.

1. EXPERIMENTAL SETUP

Scheme of experiments of SBS threshold power (P_{th}) measurements in steady-state excitation regime is shown in Fig. 1. Single-mode iodine laser radiation was used for SBS excitation. Laser radiation parameters are:

Wavelength $\lambda = 1.315\text{ }\mu\text{m}$

Energy $E \approx 10\text{ J}$

Pulse duration $\tau_L \approx 100\text{ }\mu\text{s}$

Radiation divergence $\theta_{0.84E} \approx 10^{-4}\text{ rad}$

Laser beam diameter $D \approx 7\text{ cm}$.

Parameters of the pumping, reflected and passed through SBS cell radiation were registered by calibrated photodiodes with the time resolution 50 ns. Pumping power was measured in the far zone of positive lens by photo diodes with different apertures, it allowed to measure pumping power in different angles : $1 \cdot 10^{-3}$, $1 \cdot 10^{-4}$, $5 \cdot 10^{-5}\text{ rad}$ and to

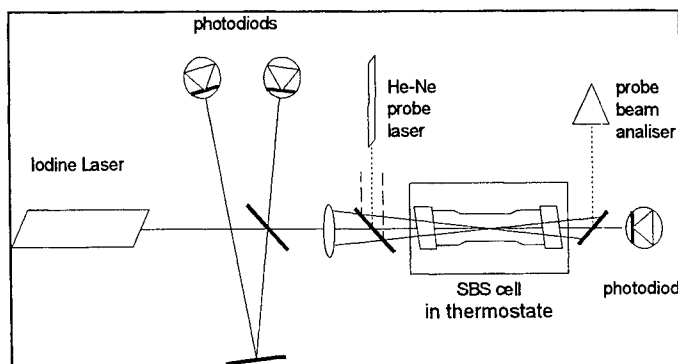


Fig. 1. Experimental setup.

control power divergence. The laser radiation was focused into SBS cell with length of 25 cm and diameter of 1.5 cm by means of lens with focal length $F = 138$ cm. The special attention was given to Xe cleanness. To exclude influence of impurities, only metal (indium) linings were used in the cell construction, and it have been filled with the use of special filters, detaining aerosol particles (efficiency of clearing from such particles with diameter more than $0,01 \mu\text{m}$ is more then 99.9999 %). Thermostat maintained the cell temperature at value of $t = 19.3 ^\circ\text{C}$, temperature drift did not exceed $0.03 ^\circ\text{C}$ per an hour. Xe pressure in the cell have been measured with relative error of 2 %, density of Xe have been determined by cell weighing.

Optical quality of SBS medium was supervised with the help of He-Ne laser which parameters were selected in such a manner that its beam simulated a pump beam in cell. The intensity distribution in focal plane inside the cell with Xe - $I_1(\varphi)$ have been compared with distribution obtained in the absence of cell - $I_2(\varphi)$. Measurements of intensity distribution were carried out in the image of focal plane with the help of diaphragm scanning in horizontal section. The He-Ne radiation power passed through the diaphragm was registered by photo diode and measured by the digital voltmeter. Comparison of both distributions ($I_1(\varphi)$ and $I_2(\varphi)$) allowed us to estimate quantitatively deformation of diffraction limited beam at passage it through SBS-cell. For all investigated points these distributions coincided with accuracy of $\approx 5 \%$, and only at $\rho = 1,02 \text{ g/cm}^3$ the intensity in a maximum fell down from $I_2^{\text{max}} = 1$ in the absence of the cell to $I_1^{\text{max}} = 0.62$ at the presence of it. This was taken into account at P_{thr} calculation.

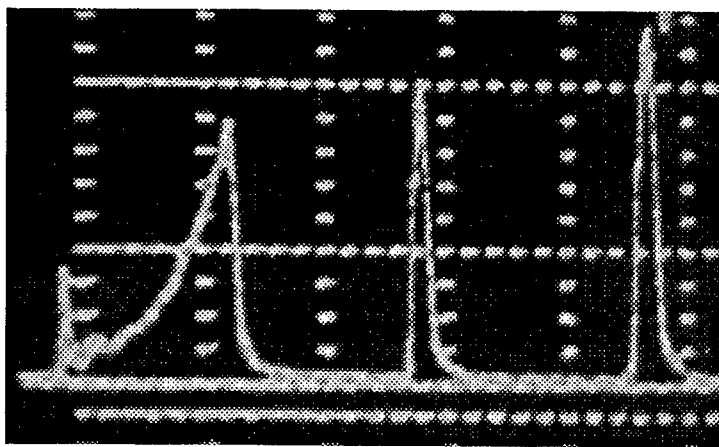


Fig. 2. Typical pumping pulse shape. Horizontal scale - $20 \mu\text{s/div}$.

Under influence of Stokes radiation, as SBS excitation occurred, the mode of iodine laser generation has changed and became pulse-periodic (see Fig. 2). Only the first pulse with duration of leading front of about $20 \mu\text{s}$ where steady-state excitation conditions are satisfied and pump energy does not exceed the critical energy of thermal defocusing W_c was used to determine the P_{thr} . The value of pumping power P_L providing SBS reflection coefficient of $R_S = 1\%$ have been taken as P_{thr} :

$$P_{\text{thr}} \langle R = 1\% \rangle = P_L \langle \theta = 5 \cdot 10^{-5} \text{ rad} \rangle \cdot \frac{I_1^{\text{max}}}{I_2^{\text{max}}}.$$

2. RESULTS AND DISCUSSION

The basic results of experiments are shown in Table 1, where averaged over several experiments P_{thr} values are shown. The standard deviation obtained in each series of experiments did not exceed 15 %. Experimentally measured values labeled by an asterisk and values, calculated using Pitser's three-parameter correlation by method of Li-Kesler ⁶, giving the best approximation to experiment, are shown for gas density.

Table 1.

p, atm	39,8	43	46	47,4	50	54	56	59,2	59,7	60,5	61	61,3	62
ρ , g/cm ³	0.30 0.30*	0.34	0.38	0.41	0.45	0.53	0.60 0.59*	0.78	0.83	0.90	0.94	0.97	1.04 1.02*
P_{thr} , kW	27	24	19	14	16	11	10	11	12	12	11	11	12

On obtained data we have determined SBS gain coefficient g_i using as a reference value $g_0 = 44 \text{ cm/GW}$ for Xe density of 0.3 g/cm^3 given in work ³:

$$g_i = \frac{P_{\text{thr}}^0}{P_{\text{thr}}^i} g_0,$$

where $P_{\text{thr}}^{0,i}$ - corresponding threshold powers.

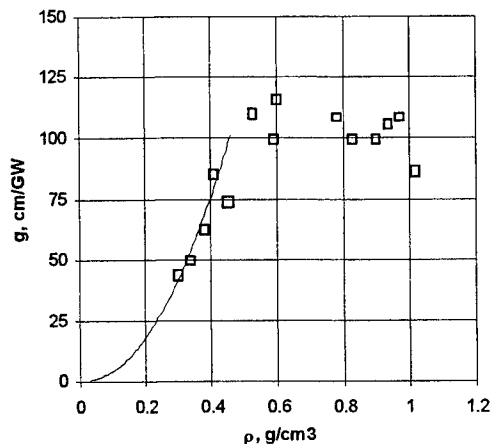


Fig. 3. SBS gain coefficient versus Xe density.
□ - experiment, — theory.

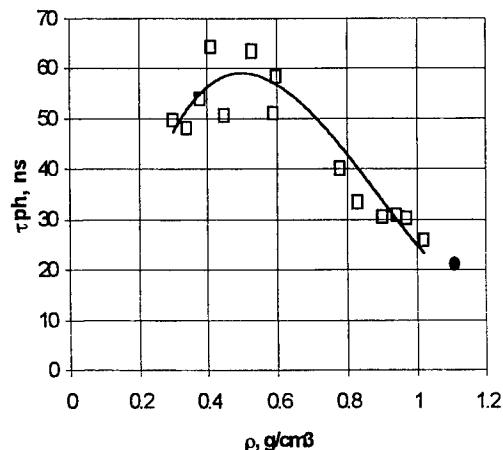


Fig. 4. Phonon lifetime versus Xe density.
□ - experiment, — - fitting curve,
• - calculation using data from work ⁸.

These results are shown in Fig. 3. The results of calculation of g for $\rho < 0.5 \text{ g/cm}^3$ using available thermodynamic parameters ⁷ are also shown in Fig. 3. We can see that beginning with $\rho = 0.5 \text{ g/cm}^3$ g does not increase, what could take place in our experiments only due to phonon lifetime decreasing. Phonon lifetime τ_{ph} have been determined using g_i values in accordance with equality :

$$\tau_{\text{ph}} = g \left(\frac{16\pi^2 n \rho \left(\frac{\partial n}{\partial \rho} \right)^2}{\lambda^2} \right)^{-1},$$

where n - refractive index, c - light velocity, v - hypersound velocity.

The results of calculation of τ_{ph} are shown in Fig. 4. Value of $\tau_{\text{ph}} = 21.2 \text{ ns}$, calculated with the use of data of hypersound absorption at $\rho = 1.11 \text{ g/cm}^3$ and $t = 19.4^\circ \text{C}$ ⁸ is also shown in Fig. 4. A good agreement between our results and that received in the work ⁸ is observed.

Finally, experience show that Xe of high cleanliness is the most promising active SBS medium for powerful lasers. Value of gW_e , serving as a figure of merit of the given substance for effective SBS of long laser pulses in Xe is almost 10 times higher than in other widely used SBS-substances ⁹.

3. ACNOWLEDGMENTS

The work was supported by DRA, UK, contract ELM/0878.

4. REFERENCES

1. M.J.Damzen, M.H.R.Hutchinson and W.A.Schroeder, "Direct measurement of the acoustic decay times of hypersonic waves generated by SBS", *IEEE J.Quant.Electron.*, vol. QE-23, no.3, 328-334 (1987).
2. G.W.Faris, L.E.Jusinski and A.P.Hickman, "High-resolution stimulated Brillouin gain spectroscopy in glasses and crystals", *J.Opt.Soc.Am.*, B, vol.10, no.4, p.587 (1993)
3. V.V.Ragulsky, *Optical phase conjugation by stimulated scattering*, Nauka, Moscow, 1990
4. V.B.Ivanov, S.B.Paperny, D.A.Snegko and V.R.Starcev, *Izvestiya Akademii Nauk SSSR seriya fizicheskaya*, vol.52, no.2, p.224, 1991
5. J.A.Betts, S.J.Pfeifer, C.G.Koop, and C.Clendening in *Technical Digest, CLEO'91*, paper CMG2
6. R.Rid, J.Prausnitz and T.Sherwood, *Properties of liquids and fluids*, Himiya, Leningrad, 1982
7. N.B.Vargaftic, *Thermophysical properties of liquids and fluids*, Nauka, Moscow, 1972
8. C.W.Garland, D.Eden, and L.Mistura, "Critical sound absorption in xenon", *Phys. Rev. Lett.*, **25**(17), 1161-1165 (1970).
9. Y.V.Dolgoplov, A.M.Dudov, V.A.Eroshenko, G.G.Kochemasov, S.M.Kulikov, V.N.Novikov, A.F.Shkapa, S.A.Sukharev, L.I.Zykov, "Lasers with phase conjugation operating in a free-running mode", *Proc. NPL '94*, Vol.2, pp.229-245, 1995.

Approximation of supergaussian beams by generalized flattened gaussian beams

S.-A. Amarande

Institute of Atomic Physics, IPTDR, Laser Department,
P.O. Box MG-36, RO-76900 Bucharest, ROMANIA

ABSTRACT

Propagation of supergaussian beams, which can be generated by graded-phase resonators, has been treated by approximating these beams with generalized flattened gaussian beams. An optimum approximation is discussed by using characterization parameters and the fitting of the amplitude profiles. Beam propagation factor M^2 and kurtosis parameter add further quantitative information which is appropriate for and confirm the approximation.

Keywords: supergaussian beams, generalized flattened gaussian beams, beam propagation factor, kurtosis parameter

1. INTRODUCTION

High power lasers need often to use optical resonators with large aperture. A suitable way for extracting efficiently a good-quality optical beam is offered by the supergaussian beam (SGB). Custom SGB's (beams with prescribed parameters) have been recently obtained by Bélanger et al.¹ by using resonators with graded-phase mirror. One can conclude that, for a material processing requiring a laser beam with specified parameters, the optical cavity can be designed accordingly.

The propagation of SGB's has been first treated numerically by Parent et al.² and then, more convenient, analytically by Palma and Bagini.³ For the analytical treatment they shown that SGB's can be approximated accurately with the generalized flattened gaussian beams (FGB's). Two types of flattened gaussian beams (FGB's) were originally introduced by Gori.⁴ Both of them are one-parameter beams: the first type has the beam width as the relevant parameter; the second type, called rescaled FGB, has steepness as the parameter (the width being approximately constant). Both of them are coherent beams and a propagation formula for the second type of FGB was also given.⁴ A third, and more general type of FGB was then introduced as generalized FGB.³ It is a two-parameter FGB having both width and steepness as parameters.

Then, the characterization of FGB's has been extended^{5,6} by using the beam propagation factor M^2 and the kurtosis parameter. These beam parameters are significant also in material processing as tool parameters as shown by Herziger et al.⁷ In this paper we recall in Section 2 the main results concerning this extension. In Section 3 we discuss a procedure which can be used to approximate SGB's by generalized FGB's, considering characterization parameters. Finally, some conclusions are presented.

2. CHARACTERIZATION PARAMETERS OF THE FLATTENED GAUSSIAN BEAMS

The field of the FGB's represented in cartesian coordinates is given by

$$U_{N,w_0}(x,z) = \sum_{n=0}^N c_n \cdot \Psi_{2n}(x,z), \quad N=0,1,\dots, \quad (1)$$

where N is the beam order,

$$c_n = A \cdot \left(\frac{\pi}{2}\right)^{1/4} \cdot \frac{2^n}{[(2 \cdot n)!]^{1/2}} \cdot \sum_{k=n}^N \frac{1}{2^{3k} \cdot k!} \cdot \frac{(2 \cdot k)!}{(k-n)!} \quad (2)$$

and the Hermite-Gauss beam of order n , say $\Psi_n(x, z)$, has the following spatial distribution

$$\Psi_n(x, z) = \left(\frac{2}{\pi \cdot w^2(z)} \right)^{1/4} \cdot (2^n \cdot n!)^{-1/2} \cdot H_n(\sqrt{2} \cdot x/w(z)) \times \exp \left[-\frac{x^2}{w^2(z)} - i \frac{k \cdot x^2}{2 \cdot R(z)} - i \cdot k \cdot z + i \cdot \left(n + \frac{1}{2} \right) \cdot \Phi(z) \right], \quad (3)$$

where as usual

$$w(z) = w_0 \sqrt{1 + \left(\frac{z}{z_R} \right)^2}, \quad R(z) = z + \frac{z_R^2}{z}, \quad \Phi(z) = \tan^{-1} \left(\frac{z}{z_R} \right) \quad \text{and} \quad z_R = \frac{\pi \cdot w_0^2}{\lambda}.$$

Drawing field distribution at $z=0$ for a few values of N we obtain the curves presented in Fig. 1a.

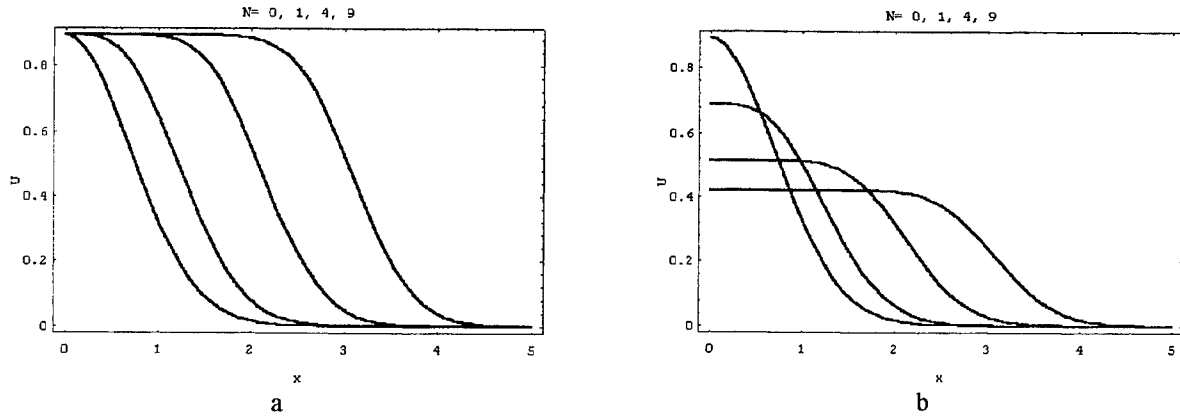


Fig. 1: a) Transverse intensity profiles of FGB with beam orders $N=0, 1, 4$ and 9 versus x ;
b) Transverse intensity profiles of normalized FGB's (with same beam orders) versus x .

As FGB's are a superposition of Hermite-Gauss beams suitably weighted, we can consider them formally as a kind of multimode beams. Then we can normalize mode coefficients, c_n , so that the total power $\sum |c_n|^2 = 1$, obtaining for the constant A the expression

$$A = \left(\frac{\pi}{2} \right)^{-1/4} \cdot \left\{ \sum_{n=0}^N \frac{2^{2n}}{(2 \cdot n)!} \cdot \left[\sum_{k=n}^N \frac{1}{2^{3k} \cdot k!} \cdot \frac{(2 \cdot k)!}{(k-n)!} \right]^2 \right\}^{-\frac{1}{2}}, \quad N=0, 1, \dots \quad (4)$$

The graphs of field distribution corresponding to these normalized FGB's are presented in Fig. 1b. We evaluated M^2 factor for every beam order N . The results appear in Fig. 2a. As expected, for $N=0$ we encounter a pure gaussian beam for which M^2 equals 1, the minimum value for this parameter.

The kurtosis parameter, K ,⁸ which describes the degree of flatness (or sharpness) of any beam intensity distribution, is defined as

$$K = \frac{\langle x^4 \rangle}{\langle x^2 \rangle^2}, \quad (5)$$

where the second and the fourth-order moment are obtained by putting $n=2$ and, respectively, $n=4$ in the equation

$$\langle x^n \rangle = \int_{-\infty}^{\infty} x^n |U(x)|^2 dx, \quad (6)$$

which defines the n -th order moment of the intensity distribution $I(x) = |U(x)|^2$. The FGB kurtosis behaviour can be explored by the analysis of the kurtosis propagation vector as shown by Martínez-Herrero et al.⁹ According to their classification :

- for a beam order $N=0$, $K(z)$ is constant (FGB belongs to type VII);

- for a beam order $N=1,2,3$, $K(z)$ has either (a) two maxima and one minimum, or (b) two minima and one maximum (FGB's belong to type III);
- for a beam order $N \geq 4$, $K(z)$ exhibits either a unique maximum or a unique minimum (FGB's belong to type VI).

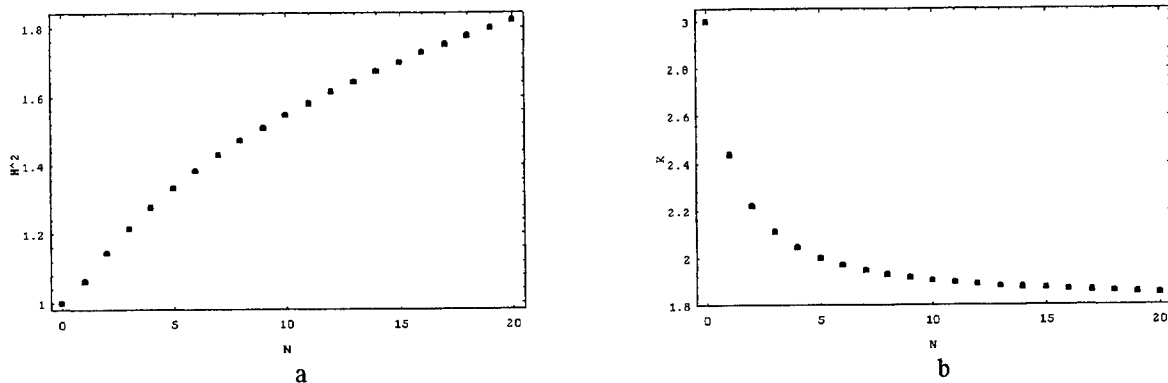


Fig. 2: a) Beam propagation factor M^2 versus beam order N ; b) Kurtosis parameter $K(z=0)$ versus beam order N .

The kurtosis parameter can be calculated at $z=0$ as a function of the beam order N . The result is presented in Fig. 2b. For $N=0$ the FGB is a pure gaussian beam and K has the maximum value equal to 3. This profile is denoted as mesokurtic. The beam profiles for which K is lower are denoted as platykurtic. After a mode order around 5 the kurtosis decreases slowly, and after a mode order approximately 10 this parameter is rather constant and equal to 1.85.

3. PROCEDURE FOR APPROXIMATION OF SUPERGAUSSIAN BEAMS BY FLATTENED GAUSSIAN BEAMS

The question is: if a SGB specified by the index of supergaussianity, PW , and by a spot size, w_i ,

$$V_a(x,0) = \exp\left[-(x/w_i)^{PW}\right], \quad (7)$$

is given, what are the beam order, N , and the steepness, $1/w_0$, of a generalized FGB's which allows an optimum approximation?

We may first to calculate the beam propagation factor M^2 of the SGB with the following equation, which can be readily obtained

$$M^2(PW) = \frac{PW \cdot \sqrt{\Gamma(3/PW) \cdot \Gamma(2 - 1/PW)}}{\Gamma(1/PW)}. \quad (8)$$

We can find then the beam order, N , of a generalized FGB which has a beam propagation factor M^2 as close as possible (because N must be an integer), by using a graph as in the Figure 2a. We apply this procedure to approximate SGB's which have been produced experimentally by Bélanger et al.¹ These beams are presented in the Table. One can see that N value

Table: Comparison between SGB's and generalized FGB's parameters.

SGB					generalized FGB				
$V_a(x,0) = \exp\left[-(x/w_i)^{PW}\right]$					$U_{N,w_0}(x,z) = \sum_{n=0}^N c_n \cdot \Psi_{2,n}(x,z), \quad N=0,1,\dots$				
PW	w_i	$M^2(PW)$	$K(PW)$	K type	N	$1/w_0$	$M^2(N)$	$K(N)$	K type
2	1	1	3	VII	0	1	1	3	VII
4	1	1.18	2.19	III	2	3.3	1.15	2.21	III
6	1	1.4	1.86	VI	7	9	1.47	1.92	VI

identified in such a way assures a good correlation between the values of kurtosis parameter. Also, the way that K changes in propagation is the same for the original and for the approximate beam. To find the steepness, $1/w_0$, we may then fit the profile of the generalized FGB to the profile of the SGB, as shown in Fig. 3. As a quantitative criterium the minimization of the rms

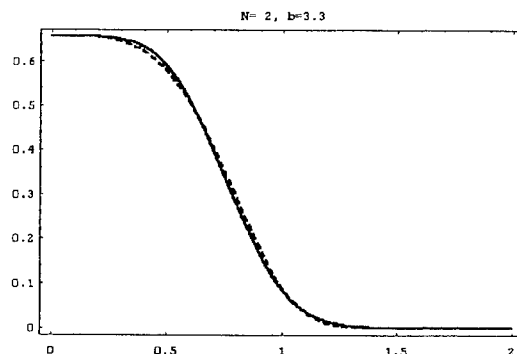


Figure 3: Intensity profile of a generalized FGB (dashed line) fitted to the intensity profile of a SGB (continuous line)

deviation between the two profiles can be used, as suggested by Palma and Bagini.³ For the approximation of SGB with $PW=4$ rms value is 0.008, and respectively for that of $PW=6$ is 0.016.

4. CONCLUSIONS

An optimum approximation of the supergaussian beams by the generalized flattened gaussian beams is discussed by using characterization parameters and the fitting of the amplitude profiles. Beam propagation factor M^2 and kurtosis parameter add further quantitative information which is appropriate for and confirm the approximation.

5. ACKNOWLEDGMENTS

This work was partially supported by Romanian Ministry of Research and Technology under contract 35/A40 MCT. The author wishes to thank Local Organizing Committee for the assistance in attending *GCL/HPL '96 Symposium*.

6. REFERENCES

1. P. -A. Bélanger, R. L. Lachance, Super-Gaussian output from a CO₂ laser by using a graded-phase mirror resonator, *Opt. Lett.*, Vol. 17, pp. 739-741, 1992.
2. A. Parent, M. Morin, P. Lavigne, "Propagation of super-Gaussian beams field distributions", *Opt. and Quantum Electron.*, Vol. 24, pp. 1071-1079, Sept. 1992.
3. C. Palma and V. Bagini, "Propagation of super-Gaussian beams", *Optics Comm.*, Vol. 111, pp. 6-10, 1994.
4. F. Gori, "Flattened gaussian beams," *Optics Comm.*, Vol. 107, pp. 335-341, 1994.
- A. E. Siegman, *Lasers*, Chap. 16, University Science, Mill Valley, Calif., 1986.
5. S. -A. Amarande, "An extended characterization of flattened gaussian beams", in *High Power Lasers - Science and Engineering NATO ASI*, R. Kossowski et al., Eds. (Kluwer Academic Publishers, Dordrecht, 1996) pp.365-372.
6. S. -A. Amarande, "Beam propagation factor and the kurtosis parameter for flattened gaussian beams", *Optics Comm.*, (in press).
7. G. Herziger, M. Scholl, P. Loosen, "Beam characterization for material processing", in *Laser Beam Characterization*, H. Weber et al, eds., (FLI, Berlin, 1994).
8. M. Sanchez, J. L. H. Neira, J. Delgado, G. Calvo, "Free propagation of high order moments of laser beam intensity", in *Eighth Intl. Symp. on Gas Flow and Chemical Lasers*, J. M Orza et al, eds., Proc. SPIE 1397, pp. 679-682, 1990.
9. R. Martínez-Herrero, G. Piquero and P. M. Mejías, "On the propagation of the kurtosis parameter of general beams", *Optics Comm.*, Vol. 115, pp. 225-232, 1995.

ABSTRACT

Slab CO₂-laser is the most compact system now¹. In ² and ³ the possibility of multislabs structure phasing had been studied on base Talbot-system and intracavity optical connection between separate slabs. In ⁴ the possibility of given wavefront injector signal regenerative amplification has been considered. Use of this method for multislabs structure phasing is interesting. But in this case it is necessary to strive a frequency conformation of laser-injector and regenerative amplifier because of necessity of conditionally steady regime realizing⁵. In ⁶ possibility of lasing upsetting by aperture in unstable resonator spherical mirror was shown. In ⁷ this aperture had been used for laser-injector signal input and frequency locking of more powerful CO₂-laser.

The goal of this paper is to consider conditions for abnormal high losses of regenerative amplifier unstable resonator main mode. In this case we can realize phasing without necessity of frequency locking into injector-regenerative system. For this conditions the optimal regime of input and propagation of radiation along regenerative amplifier is considered.

Key words: laser-injector, slab CO₂-regenerative amplifier, asymmetrical unstable resonator, mode losses.

1. ABOUT INFLUENCE OF UNSTABLE RESONATOR ASYMMETRY TO MAIN MODE LOSSES

1.1. Symmetrical unstable resonator with spherical mirrors

The equation for modes of symmetrical unstable resonator with spherical mirror is the following ⁸:

$$\Delta_{\perp} \mathbf{f} + \left[s^2 + 4(\gamma + \gamma^2) \right] \mathbf{f}(\xi, \eta) = 0, \quad (1)$$

where $\xi^2 + \eta^2 = \rho^2$, $\rho = r\sqrt{k/l}$, r - radius-vector with outset in mirror center, $k=(2\pi/\lambda)$, $\xi = x\sqrt{k/l}$, $\eta = y\sqrt{k/l}$, $\gamma=(l/2R_0)$, l - distance between mirror. R_0 is the mirror caviture radius. The energy losses of a mode are the following:

$$\Lambda = 1 - m^{-2\text{Re } v - 1}, \quad (2)$$

where $m = 1 + 2\gamma + 2\sqrt{\gamma + \gamma^2}$ is resonator multiplication.

Parameter v is the root of the equation:

$$\left. \begin{aligned} (2\pi N_{\text{equiv}})^{v-0.5} &= 2 \ln m \frac{\Gamma(\frac{n+1}{2} + \frac{v}{2} + \frac{1}{4})}{\Gamma(\frac{n+1}{2} - \frac{v}{2} - \frac{1}{4})} e^{i\varphi} \\ \varphi &= 2\pi p - 2\pi N_{\text{equiv}} + \frac{\pi}{2}(n+2); \quad N_{\text{equiv}} = \frac{N}{2} \left(m - \frac{1}{m} \right) \end{aligned} \right\} \quad (3)$$

Here $N=a^2/\lambda l$; a - mirror radius; Γ - gamma-function⁹; n and p - whole numbers; n - asimutal mode index and $n=0$ below.

If $\varphi=0$:

$$N_{\text{equiv}} = N_{0,\text{equiv}} = p + \frac{n}{4} + \frac{1}{2}. \quad (4)$$

Here v is real valued only. If there is the aperture in the center of spherical mirror, the most soundness modes are those formed by reflection from mirror brink and caustic surface on aperture border. From equation (1), the condition of caustic surface formation is following¹⁰:

$$s^2 + 4(\gamma + \gamma^2)\rho_c^2 = 0, \quad (5)$$

where $\rho_c = r_c \sqrt{k/l}$, r_c is the caustic surface radius which is equal the mirror aperture radius.

From(3), (4) and (5) it is following:

$$N_{\text{equiv}} - N_{0,\text{equiv}} = \frac{(\gamma + \gamma^2)\rho_c^2}{\pi}. \quad (6)$$

Computer simulation⁸ shows that $\text{Re } v \sim 0.5(N_{\text{equiv}} - N_{0,\text{equiv}})^2$ for main mode. That is:

$$\text{Re } v \sim 0.5 \left[\frac{(\gamma + \gamma^2) \cdot \rho_c^2}{\pi} \right]^2. \quad (7)$$

One can see (the curve (7) is presented in Fig.1.a) that mode losses, which lead to lasing upsetting, is realized for $\rho_c \sim 10$; that is the aperture diameter $\sim 15 \div 20$ mm for CO_2 -laser typical parameters.

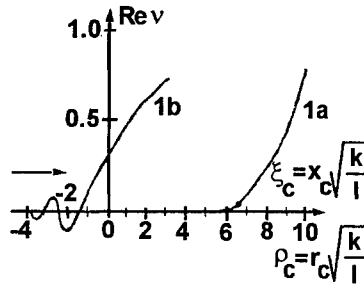


Fig.1. Dependence of $\text{Re } v$ (mode losses, see (2)) on dimension of aperture for injector beam.

- 1a - symmetrical unstable resonator with spherical mirrors;
- 2a - asymmetrical unstable resonator with cylindrical mirrors.

1.2. Asymmetrical unstable resonator with cylindrical mirrors

For case of asymmetrical unstable resonator with cylindrical mirrors the other dependence for mode losses, as a function of optical connection's aperture dimension takes place¹¹. Here we present the result which is interesting for us only.

The asymmetry is realized by consecutive cutting of resonator's mirrors along ξ_k -axis from left to right (see fig 1b). One can see that diffractive modes losses fluctuates itself around zero until the resonator takes place on both sides of cylindrical mirror center. With approach of the resonator mirror brink to its axis the monotonous raise of mode losses

start. If to pay attention that $\sqrt{k/l} \sim 10 \text{ cm}^{-1}$ and $\alpha_0 \sim (5 \div 8) \cdot 10^{-3} \text{ cm}^{-1}$ for usual slab CO_2 -laser, then the $\text{Re } v \sim 0.5 \div 0.7$, which leads to lasing upsetting, is realized for $\sim 1 \text{ mm}$ optical connection's aperture. This fact gives possibility to use a low power laser-injector. Resonator mode lasing upsetting leads to raising conditions for sequence frequencies between injector-laser and regenerative amplifier and for conditionally steady regime.

2. ABOUT PECULIARITY OF INJECTOR SIGNAL PROPAGATION ALONG REGENERATIVE SLAB CO_2 -AMPLIFIER

2.1. Energetics

We consider the problem in conditions of modes complete suppression, low mirror losses ($1-R \ll 1$) and low multiplication of asymmetrical unstable resonator ($m-1 \ll 1$). In this case we can average resonator losses and average resonator multiplication (along length of gain medium). One can write the equation for average intensity and conditions of CW radiation and stationary regime:

$$\frac{dJ}{dZ} = \frac{\alpha_0}{1+J} J - \beta J \quad (8)$$

where Z - longitudinal coordinate, α_0 - unsaturational gain, $\beta = [(1-R)/l + (m-1)/2l]$ - effective unsaturated losses. Here the intensity is presented as saturation intensity (I_s) units. That is $J = I/I_s$, $[I] = \text{W/cm}^2$.

Solution of equation (8) is following:

$$\frac{J}{J_0} \left| \frac{(\frac{\alpha_0}{\beta} - 1) - J_0}{(\frac{\alpha_0}{\beta} - 1) - J} \right|^{\alpha_0/\beta} = e^{(\alpha_0 - \beta)Z_\Sigma} \quad (9)$$

where $J_0 = J|_{Z=0}$, Z_Σ - complete gain medium length. The solution (9) has the special point. That is $J = \frac{\alpha_0}{\beta} - 1 = J_\infty$,

which is realized for $Z \rightarrow \infty$. In this case the saturated gain is equal the unsaturated losses as usual for laser generation. But the laser generation is upset. Therefore if to move away from the special point $J = J_\infty$ and if we know the number of beam passes into resonator, the synonymous connection of laser-injector signal phase and output signal phase take place. This fact gives possibility for multislab structure phasing.

2.2. Peculiarity of putting into slab CO_2 -amplifier and intra slab radiation's propagation

First of all we suppose that laser-injector radiation is agreed with main mode of slab waveguide (in closed direction). One of main condition for beam propagation by consecutive reflections from mirrors of asymmetrical unstable resonator are minimal beam covering and maximum beam packing simultaneously. It's not hard to show that it is realized for injector-beam dimension $a_0 \sim \sqrt{2\lambda l}$ and injector beam divergence $\varphi_0 \sim \sqrt{\lambda / 2l}$ (in opened direction of slab). In this case the point (on ξ -axis) for beam-injector putting into asymmetrical unstable resonator is following:

$$\xi_{in} \cong \frac{2\sqrt{\pi}}{m-1} \quad (10)$$

The condition (10) increases unstable resonator asymmetry and leads to its modes suppression in addition.

After passing of n double passes (forward and back) along asymmetrical unstable resonator between cylindrical mirrors, the beam dimension (in opened direction of slab) is following:

$$a_n \sim \sqrt{2\lambda l} \{ m^n + 0.5[m^n + m^{n-2} + K + m^{-(n-2)}] \} \quad (11)$$

2.3. The example for regenerative slab CO₂-amplifier value

Used parameters: $I_s \approx 2 \text{ kW/cm}^2$, $\alpha_0 \approx 6 \cdot 10^{-3} \text{ cm}^{-1}$, $R \sim 0.985$, $l \sim 50 \text{ cm}$, slab height $\sim 0.2 \text{ cm}$, $m \sim 1.05 \div 1.1$.

Using formula (9), (10) and (11) it's not hard to obtain output power $\sim 500 \text{ W}$. In this case specific power is about $(1 \div 2) \text{ W/cm}^2$ (relatively of slab electrode surface). The relation between input and output powers is in the region $(1 \div 100) \div (1 \div 50)$. Output beam dimension (in opened direction) is about 15 mm . These parameters are realized after ~ 7 double passes only. Because here we can control an output beam phase by change of injector-laser beam phase. These results are a base for formation of injector-regenerative laser-optical system for multislab structure phasing.

3. REFERENCES

1. R.Nowack, H.Opower, U.Schafer, K.Wessel, Th.Hall, H.Kruger and H.Weber, "High power CO₂ waveguide laser of the KW category," *Proc.SPIE*, Vol.1276, pp.18-28, 1990.
2. V.V.Lyubimov, "Intracavitve methods for increasing of beam lasers optical quality," *Izvestia of Sc.Academy* (In Russian), Vol.54, pp.2323-2327, 1990.
3. J.G.Xin, S.Q.Zhon, Z.Y.Wang, P.Wang, X.Y.Peng, and G.Z.Fang, "RF-exited slab waveguide array CO₂ laser with mutual injection phase coupling," *NATO ASI Series, 3.High Technology*, Vol.10, pp. 125-133, 1996.
4. O.B.Danilov, V.V.Lyubimov, and N.N.Rosanov "Regenerative amplification of laser-injector signal with given wave front," *Proc.SPIE*, Vol.2771, pp.243-251, 1996.
5. K.Smith, and R.M.Tomson, "Computer modeling of gas laser," Plenum Press, N.Y. and London, 1978.
6. A.V.Gorlanov, B.A.Kalinina, V.V.Lyubimov, I.B.Orlova, V.F.Petrov, "Investigation of possibility of high gain telescopical amplifiers elaboration," *Journal of Applied Spectroscopy*, Vol.17, pp.617-622, 1972.
7. V.A.Antonov, E.V.Danshikov, F.V.Lebedev, V.V.Lihansky, and A.P.Napartovich, "About measurement of phase difference between output beams of two connective CO₂-laser," *Kvantovaya Elektronika* (In Russian), Vol.17, pp.159-161, 1990.
8. G.N.Vinokurov, V.V.Lyubimov, and I.B.Orlova, "Investigation of opened unstable resonator selective properties," *Optika i Spectroscopia* (In Russian), Vol.34, pp.741-751, 1973.
9. G.Batman and A.Ardane, "Highest transcendental functions," "Nauka" Press (In Russian). Moscow, 1968.
10. L.A.Vainstain, "Opened resonators and opened waveguides," "Sov. radio" Press, Moscow (In Russian), 1966.
11. V.V.Lyubimov, N.N.Pevgenen, and V.F.Petrov, "Asymmetrical unstable resonators," *Optika i spectroscopia* (In Russian), Vol.35, pp.1132-1137, 1973.
12. J.Nishimae, and K.Yoshizawa, "Development of CO₂-laser exited by 2.45 GHz microwave discharge," *Proc.SPIE*, Vol.1225, pp.340-348, 1990.
13. Yu.A.Ananjev, "Optical resonator and problem of laser beam divergenic," Nauka press (In Russian.), Moscow, 1979.

Dynamic behaviour of two CO₂ lasers, phase-locked through diffraction coupling

W. Weingartner, K. Schröder, D. Schuöcker

Department of High Power Beam Technology
TU Vienna, Arsenal Obj. 207, 1030 Vienna, Austria

ABSTRACT

A method of phase locking two CO₂ lasers through diffraction coupling is presented, which is achieved by the parallel propagation of the two laser beams along a common so-called coupling path. This is done by folding the resonator twice by mirrors and extraction of the output radiation by a common output coupler. As this method is only utilising reflective optics (except of the output coupler), it is also practicable as a technique for phase-locking lasers with powers in the multi-kW range. Diffraction leads to an overlap of the optical fields of the two lasers, establishing a phase-locked state, if several locking conditions are fulfilled. The amount of energy, diffracted from one resonator to the second cavity which is necessary to establish phase-locking, depends highly on the length detuning between the two resonators. Phase-locked operation is detected by measuring the beat signal between the two laser beams. Since the coupling between the lasers is small, a stable phase-locked operation can only be obtained, if the length of one resonator arm is actively controlled with a PC-based electronic stabilisation loop, driving a piezoelectric translator for resonator length tuning.

1 INTRODUCTION

Advanced materials processing with lasers in industrial production processes requires not only laser sources with higher output power but also a near diffraction limited beam mode which is a difficult task especially at powers in the multi-kW range. One method to achieve good optical properties at high powers is to operate several gain cells in series by folding the resonator. This approach provides on the one hand an excellent beam quality but requires a mechanically complex layout of the resonator and the discharge sections. Furthermore all optical components are loaded by the full intra-cavity radiance which can reduce their lifetime or reliability. On the other hand the power can be increased through compact plasma dimensions, yielding a large aperture and a small length of the active medium. The large Fresnel number which characterizes this layout, however, results in a very poor beam quality when conventional resonators are used.

The parallel operation of the gain cells while maintaining the high radiation quality inherent to each individual module is a different approach to these problems which offers some advantages in opposite to the usual serial operation. Each discharge section is loaded only by a fraction of the total power, yielding a smaller discharge cross section, improved discharge stability and reduced stress for optical components. The maximum power density of a number of N lasers with amplitudes of the electric field strength $E_1 = E_2 = \dots E_N = E$ in an unlocked mode is obtained by adding the individual power densities:

$$\eta E_1^2 + \eta E_2^2 + \dots + \eta E_N^2 = N\eta E^2 \quad (1)$$

During phase-locked operation the individual electric fields superimpose yielding the total power density:

$$\eta (E_1 + E_2 + \dots + E_N)^2 = N^2 \eta E^2 \quad (2)$$

where η means the field characteristic impedance. Consequently phase-locking of N lasers increases the irradiance by a factor of N relative to that of unlocked operation.

There are several techniques for phase-locking of lasers, differing through their methods of exchanging energy between their individual resonators. The first treatment was given by M.B. Spencer¹ who was using semitransparent mirrors for the coupling of lasers. Other methods are for example the exchange of energy between the resonators through bores in the back mirrors^{2,3}, waveguide lasers with transmitting windows⁴ or not fully separating walls between their channels⁵ and four-wave mixing⁶. Common to all these techniques is their high sensitivity for misalignment or their high losses.

Other methods are the self imaging properties of periodic structures or a diffractive energy exchange between two or more beams along a common so called coupling path⁷. The latter method is the technique applied in this work.

2 EXPERIMENTAL SET-UP

Fig. 1 shows the concept of diffraction coupling and the technique utilised for resonator length control. The two DC excited 30W CO₂ lasers are built with two sealed off gain cells with Brewster windows on both ends, each cell with an external concave back mirror of a radius of curvature of 5m and a common flat output coupler. The resonator of each branch is folded twice, a common segmented mirror forming a so called 'coupling path' L_c which leads to an exchange of radiation energy due to diffraction effects. The length of the coupling path is adjustable from 5..70cm, thus altering the resonator length from 150 to 215cm, while the beam spacing d within this path can be varied from 2..10mm by moving the segmented mirror. Length tuning of one resonator arm is done by using a piezo translation stage (displacement $\Delta x > 5.6\mu\text{m}$). The movement of the mirror is measured with a Michelson interferometer with one mirror fixed on the back of the mirror on the translation stage.

Phase-locked operation is demonstrated by measuring the beat frequency with a fast HgCdZnTe-detector on which both beams are combined through a scraper mirror.

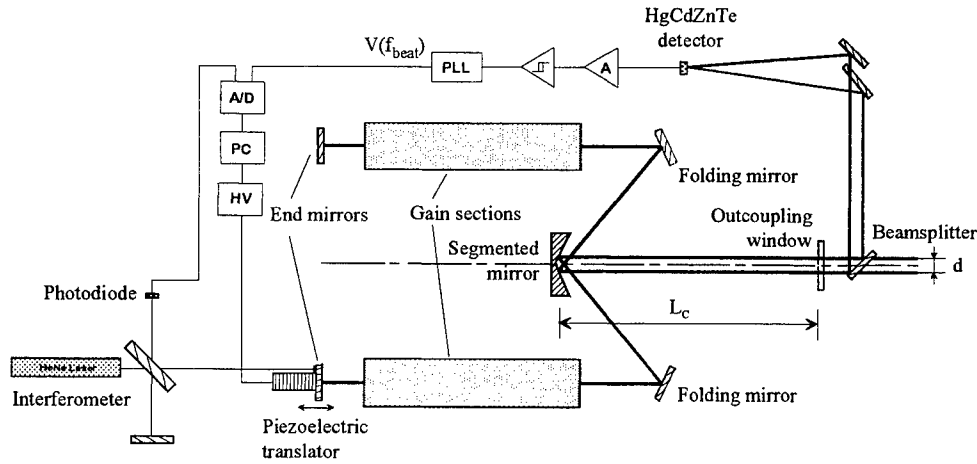


Fig. 1 Experimental set-up

3 EXPERIMENTAL RESULTS

3.1 Measurement of the coupling factor

The first issue investigated was the coupling of energy from one laser branch to the other depending on the coupling length L_c and the beam separation d . An experiment was conducted to evaluate a so called coupling factor k_c which is defined as the ratio of the irradiance, diffracted from one cavity to the other, to the inter-cavity irradiance. It is evaluated by exciting only one gain cell and measuring the power P_{IC21} diffracted from one branch to the other arm at the end mirror of the 'cold' gain cell. The intracavity power of the excited gain cell P_{IC1} is calculated from the output power P_1 at the output coupler and the reflectivity R of the output coupler.

$$k_c = \frac{P_{IC21}}{P_{IC1}} = \left(\frac{1}{R} - 1 \right) \frac{P_{IC21}}{P_1} \quad (3)$$

The coupling coefficients were measured for different distances d between the beams and for different coupling lengths L_c . Due to increasing diffracted power the coefficient is growing with increasing length of the coupling path and decreasing separation d between the beams. The graph demonstrating these dependencies is shown in Figure 2.

It has to be mentioned that coupling coefficients in the range of 1% are not practicable for the segmented mirror used in this set-up, as it is constructed with two ordinary rectangular mirrors which are forming a gap of 0.2mm where their edges are meeting. This gap causes considerable losses by scattering when the distance between the gap and the two lasers is reduced in order to get a strong overlap and thus a high coupling factor. These losses lead to a rapid degradation of output

power with decreasing separation of the beams in the coupling path. This problem can be solved by the use of altered segmented mirrors which can be parabolic or by using different coupling strategies with the segmented mirror in a prismatic form.

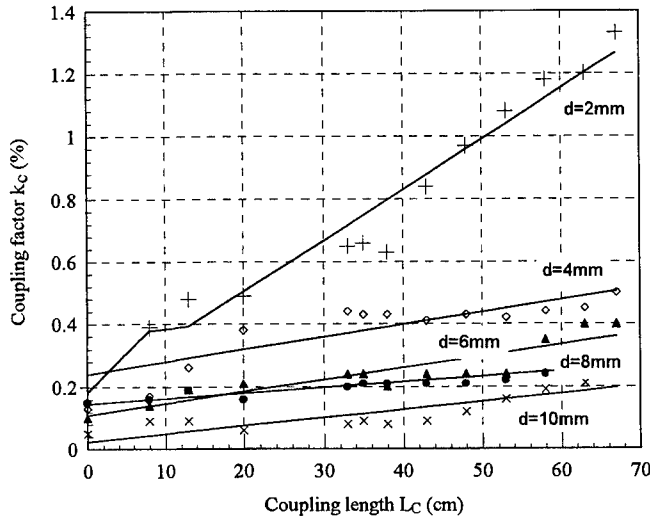


Fig. 2 Coupling factor k_C for different coupling lengths L_C in dependence of beam distance d

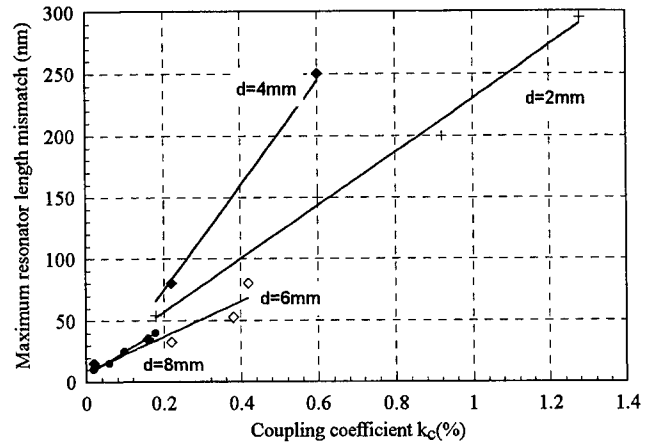


Fig. 3 Maximum resonator length mismatch for phase-locked operation for different coupling coefficients k_C

3.2 Measurement of the phase-locking range

The next experiments concentrated on the demonstration of phase-locked operation and on its dependence on the resonator length mismatch. Phase-locked operation was monitored by directing both beams onto a fast HgCdZnTe-detector and recording of the rf-component of the detector signal, giving thus the beat signal. The phase locking range of the two lasers was investigated by introducing a ramp signal on the piezo translator, thereby changing the length of one resonator and consequently the frequency of oscillation. The displacement was determined by using a Michelson interferometer.

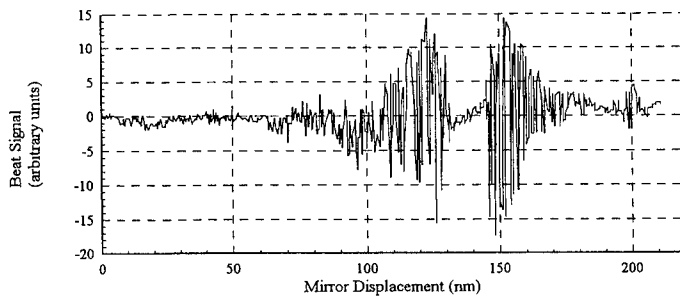


Fig. 4 Beat signal for weak coupling of $k_C=0.02\%$

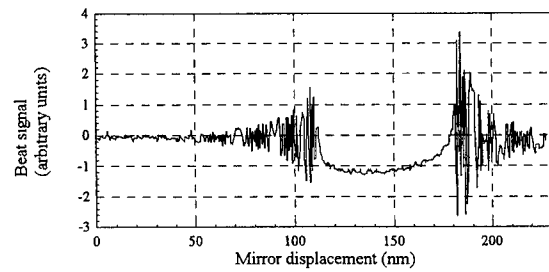


Fig. 5 Beat signal for coupling of $k_C=1\%$

The resulting beat signal under very weak coupling conditions ($k_C=0.02\%$) can be seen in Fig.4. The movement of the translator in direction of the optical axis, as measured with the interferometer, is drawn on the x-axis. As soon as the length difference between the two resonator arms is less than $\lambda/700$ the beat signal vanishes, as both lasers oscillate at the same frequency. The pull-in range of the lasers depends on the amount of exchanged energy described by the coupling factor k_C . Fig.5 gives the typical beat signal under coupling of $k_C=1\%$, the phase locking range now being $\lambda/60$.

The corresponding experimental dependencies of the locking range on the coupling factor k_C which can be changed by variation of the length of the coupling path L_C , are shown in Fig.3. The graphs for different beam separations d are indicated. The maximum coupling coefficient achieved is given as 1.3%, leading to a locking range of $\lambda/36$ which corresponds to a locking bandwidth of 5Mhz for this set-up.

3.3 Active length control

Due to resonator length mismatch resulting from mechanical vibrations and heating effects, continuous phase-locked operation can only be achieved by employing a feedback control mechanism for active length tuning to keep the two lasers within the locking range which depends on the coupling coefficient, as shown above.

Stable phase-locking is achieved by the use of an electronic stabilization loop (Figure 1), measuring the beat signal at the detector and transforming its frequency, after amplification and discretisation through a comparator, into a proportional voltage through a phase-locked-loop (PLL) which is then fed into a PC where it is taken as an indicator of locked operation. As an alternative to the PLL a frequency-to-voltage converter was used, but it showed to be too sensitive on noise in the beat signal. Any change in the beat frequency is detected by a control algorithm, deriving the direction and displacement of the mirror movement to reach phased state again. This output is then used to control the resonator length by a piezoelectric translation stage. This kind of control circuit gives a stable and easy to operate lock. Another advantage is the fact that the locking range can be found from any starting frequency of the system through appropriate software. The coupling coefficient during the experiments with the active length control was set to 0.12%, resulting in a detuning range of 24nm. Common phase locking techniques which have been constructed for laser locking at an offset frequency⁸ are not applicable in this situation, as the beat signal at the boundaries of the phase-locked regime does not yield the information in which direction the mirror has to be moved to reach phased operation again.

The control algorithm, however, is not yet capable of compensating strong mechanical disturbances which could arise in an industrial environment.

In the future, improvements of the control algorithm shall be made in order to provide phase-locking when mechanical vibrations are present. It is the aim to develop the active length control further up to a level, where an optical table is not necessary any more for stationary phase-locking.

4 CONCLUSIONS

The investigated set-up for phase-locking of two CO₂ lasers is properly operating under laboratory conditions. The dependencies of the locking range on the different coupling coefficients were identified. The thermal drift of the set-up as well as mechanical vibrations which arise despite the optical table can be compensated by a computerised control of the resonator length. Stronger mechanical disturbances can not yet be compensated by the control loop.

5 ACKNOWLEDGEMENTS

This work was supported by the Fonds zur Förderung der wissenschaftlichen Forschung (Austrian Science Foundation) under project number P 11547-ÖTE.

6 REFERENCES

- ¹ M.B. Spencer and W.E. Lamb, "Theory of two coupled lasers", Phys. Rev. A, Vol.5 (2), pp. 893-898, Feb. 1972
- ² G.E. Palma and W.J. Fader, "Coupled resonator beam combining", Proc. of the SPIE, Vol.440, pp. 153-160, Washington, 1985
- ³ V.V. Antyukhov and E.V. Dan'shchikov and I.V. Masyukov, "Stimulated emission of collective modes in two optically coupled CO₂ lasers", Sov. J. Quantum Electron., Vol.22 (3), pp. 203-209, March 1992
- ⁴ D.G. Youmans, "Phase locking of adjacent channel leaky waveguide CO₂ lasers", Appl. Phys. Lett., Vol.44 (4), pp. 365-367, 1984
- ⁵ L.A. Newman, R.A. Hart, J.T. Kennedy, A.J. Cantor and A.J. DeMaria, "High power coupled CO₂ waveguide laser array", Appl. Phys. Lett., Vol.48, (25), pp. 1701-1703, 1986
- ⁶ K.M. Abramski, H.J. Baker, A.D. Colley and D.R. Hall, "Phase-locked operation of intersecting CO₂ waveguide lasers by four-wave mixing", Opt. Commun. 90, pp.61-64, 1992
- ⁷ K. Schröder, A. Müller and D. Schuöcker, "Phase-locking of CO₂ lasers by using diffraction effects", Appl. Opt., Vol.(34), p. 8252, (1995)
- ⁸ M.J. Padgett, N. Bett and R.J. Butcher, "A simple frequency discriminator circuit for offset locking of lasers", J. Phys. E: Sci. Instrum., Vol.21, pp.554-557, (1988)

Comparison of beam quality parameters of two high peak power excimer laser beams

S. Bollanti, P. Di Lazzaro, F. Flora, G. Giordano, T. Letardi, D. Murra*, C. Petrucci**, G. Schina,
O. Uteza+, C. E. Zheng++

ENEA, Dip. Innovazione, Divisione Fisica Applicata, Centro Ricerche Frascati, P.O. Box 65, 00044 Frascati (Rome), Italy

* ENEA, Dip. Innovazione, Divisione Fisica Applicata, Centro Ricerche Trisaia, P.O. Box 1, 75025 Policoro (Matera), Italy

** ENEA guest

+ ENEA guest. Permanent address: IRPHE, UM 138, CNRS, Université Aix-Marseille II, Marseille (France)

++ EL.EN., Firenze

ABSTRACT

A comparison is made between the beam quality parameter M^2 and a new times-diffraction-limit-factor (TDL) for two high peak power XeCl lasers. The laser systems, equipped with unstable resonators, emit beams with different geometrical characteristic and optical quality. The results show that the M^2 -factor is always larger than the TDL value and this discrepancy increases if the beam is almost diffraction-limited. A novel method to obtain the far-field profile of coherent supergaussian-like beams and a simple technique to estimate the beam angular stability of a pulsed laser are also presented.

Keywords: laser beam quality, times-diffraction-limit, M^2 , excimer laser, beam propagation, beam pointing stability.

1. THE LASER BEAM QUALITY CONCEPT

Recently a large effort was done to define a standardisation procedure and a universal parameter to characterise a laser beam¹. Nowadays, the most used quality parameter is the M^2 -factor, introduced by Siegman², which represents how many times a laser beam is *far* from the TEM₀₀ gaussian and it is named *times-diffraction-limit-factor* by the relevant ISO document³. The main advantage of the M^2 -factor is that it is invariant under an ABCD transformation. Since it is based on the comparison of the beam outcoming from a generic resonator with the theoretical gaussian beam, it takes into account either the phase and the gaussian-shape deviations. On the other hand, assuming that a diffraction-limited beam is a beam having a constant-phase wavefront at its waist⁴, the TDL factor should only consider the near-field phase deviations. This is also suggested by the fact that phase distortions are much more detrimental for the diffraction pattern than a poor intensity uniformity, principally concerning the power-in-the-bucket value⁵⁻⁷. Moreover, according to the ISO. document³ the M^2 "...may not apply to highly diffractive beams...", and problems in the application of the M^2 -method for sharp-edge beams are well known⁸.

Starting from these considerations, we propose a TDL factor which is based on a comparison between the real beam and a "reference beam" having the same near-field energy density (NFED) profile of the real beam, and a constant phase wavefront. In this way, the far-field pattern of the reference beam represents the diffraction-limited profile of the real beam. This TDL factor can be used for any stable/unstable hard/soft-edged resonator beam.

To make a quantitative comparison between the reference and the real beam let us introduce the parameter $Q = k / \theta^2$, where k is the percentage of the total energy emitted within a full angle θ in the far-field zone, and θ can be chosen starting from a fixed energy content k , or at $1/e^2$ of the energy density maximum. Then, the TDL factor can be defined as:

$$TDL = \sqrt{\frac{Q^{RB}}{Q^{real}}} \quad (1)$$

where the superscripts *RB* and *real* refer to the Q parameter for the reference and the real beam, respectively. In essence, this TDL definition is proportional to the ratio between the angular spread of a phase-distorted beam and that of a constant-phase beam with the same NFED profile, taking into account the respective energy contents, so that it could be read as a sort of generalised Strehl ratio⁹.

From Eq. (1) it follows that when the far-field energy density (FFED) distribution of the reference and the real beam have a similar shape, then the TDL factor reduces to the ratio between the respective divergence angle values.

The procedure to obtain the TDL factor can be summarised as follows¹⁰:

- Measurement of the real beam NFED distribution;
- Measurement of the real beam FFED distribution obtained by focusing the beam through an optical system;
- Definition of the reference beam by the interpolation of the NFED distribution and calculation of the FFED profile of the interpolating function, supposed spatially coherent, by means of the Kirchoff integral using the parameters of the focusing system;
- Calculation of the Q parameter (at $1/e^2$ or at a fixed k) of the FFED distribution both for the reference and the real beam and use of Eq. (1)

We have measured this TDL- and the M^2 -factor for two high peak power excimer laser beams with very different optical quality, as discussed in Section 3.

2. THE EXCIMER LASER SYSTEMS

In the Excimer Lasers Laboratory in the ENEA Research Centre of Frascati, two high peak power XeCl laser systems, named Hercules and Ianus¹¹⁻¹³, have been equipped with different unstable resonators and their main features are reported in Table 1.

Features Laser systems	Near-field beam size @84% energy [cm ²]	Output energy [J]	Laser pulse FWHM [ns]	Divergence @84% energy [μ rad]	Radiance [W/(cm ² ster)]	Max repetition rate [Hz]
IANUS (GSFUR)	$\pi (0.37)^2$	0.01	75	59	$8.1 \cdot 10^{13}$	100
HERCULES (PBUR)	7.5×4.7	5	120	170×100	$6.2 \cdot 10^{13}$	10

Table 1. Main features of Ianus and Hercules laser systems (emission wavelength $\lambda = 308$ nm).

A confocal positive branch unstable resonator (confocal PBUR) with magnification 5 and hard-edge output coupler has been mounted on Hercules, a large aperture laser (electrode gap [x] x discharge width [y] x discharge length [z] = $5 \times 9 \times 100$ cm³) pumped by a X-ray triggered discharge¹⁴⁻¹⁶. The 5 J, 120 ns full-width half maximum (FWHM) output pulse was monitored by collecting the visible fluorescence generated by the radiation incident on an alumina target with a video digital system (tv camera, A/D converter, frame memory). The NFED distribution along the vertical (y) axis is plotted in fig. 1a, together with a best-fit function whose expression is described in the following Section.

In order to focus the beam, the resonator has been put out of the confocal position, to obtain an equivalent focal length of 26 m. The FFED profile has been measured by using the knife-edge method. Fig. 1b shows the experimental measurement along the y direction, together with the interpolating function which represents the FFED profile of the real beam.

The double-head, spiker-sustainer pumped Ianus laser system has been operated in a power oscillator- power amplifier (POPA) configuration¹⁷. A negative branch, generalised self-filtering unstable resonator (GSFUR)¹⁸ with absolute magnification 8 has been mounted on the smaller of the two discharge regions (cell 1: $2 \times 1.5 \times 90$ cm³), while the second active medium is used for one-pass amplification (cell 2: $3 \times 2 \times 90$ cm³). The GSFUR output beam has a circular symmetry, with a 10 mJ, 75 ns FWHM pulse. The NFED profile is reported in fig. 2a, and the knife-edge-scanned FFED distribution, obtained by focusing the beam by means of a mirror with an effective focal length of 3.16 m, is shown in fig. 2b.

The oscillator beam was injected into the second discharge region and the amplified pulse had an output energy of 90 mJ and 85 ns FWHM, maintaining the circular symmetry either in the near- and far-field. Fig. 3a shows the energy density profile in the near-field, while fig. 3b shows the corresponding far-field measurement obtained by focusing the amplified pulse by a mirror with an effective focal length of 2.75 m.

3. RESULTS AND DISCUSSION

We have applied the method reported in the ISO document³ to calculate the M^2 -factor for our laser beams whereas a simple technique has been used to interpolate the NFED distribution and to obtain the corresponding FFED profile. This technique is based on the representation of a supergaussian-like function by means of the convolution product (CP) of a gaussian with a rectangle function. The propagation of a beam in the far-field zone, obtained by the Kirchoff integral, reduces to a Fourier transform (FT) when the paraxial beam is focused. Because the FT of a CP is the product of the FT of

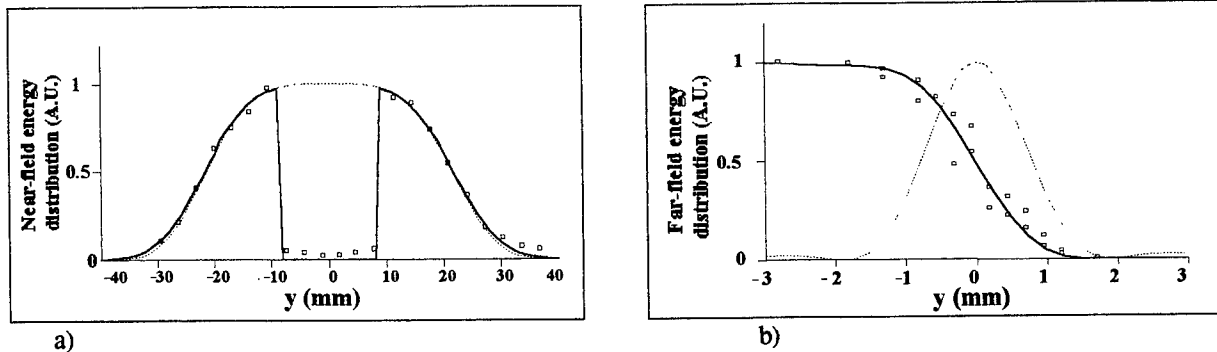


Fig. 1: a) near-field profile (at $x = 0$) of the Hercules beam along the y -axis; b) far-field integrated energy distribution of the beam measured by the knife-edge method (squares and solid line) and corresponding far-field energy density distribution (dotted line).

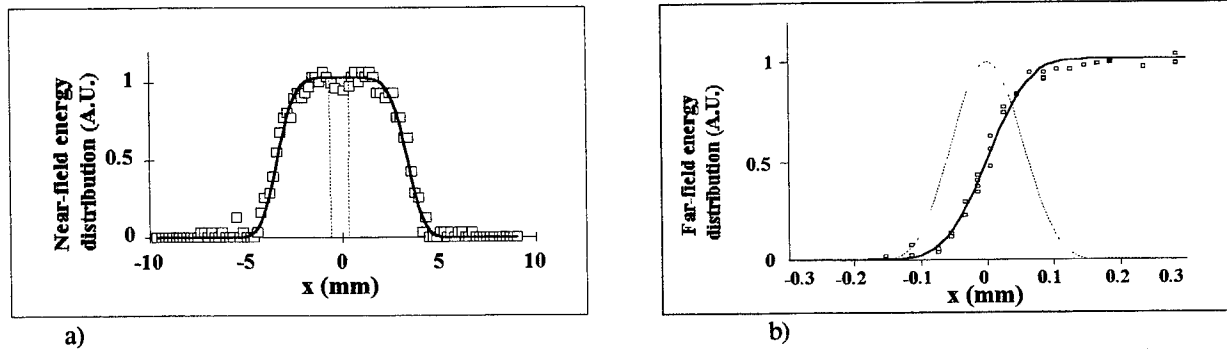


Fig. 2: a) near-field profile (at $y = 0$) of the Ianus GSFUR beam at 1.36 m from the output coupler; b) far-field integrated energy distribution of the beam measured by the knife-edge method (squares and solid line) and the corresponding far-field energy density distribution (dotted line).

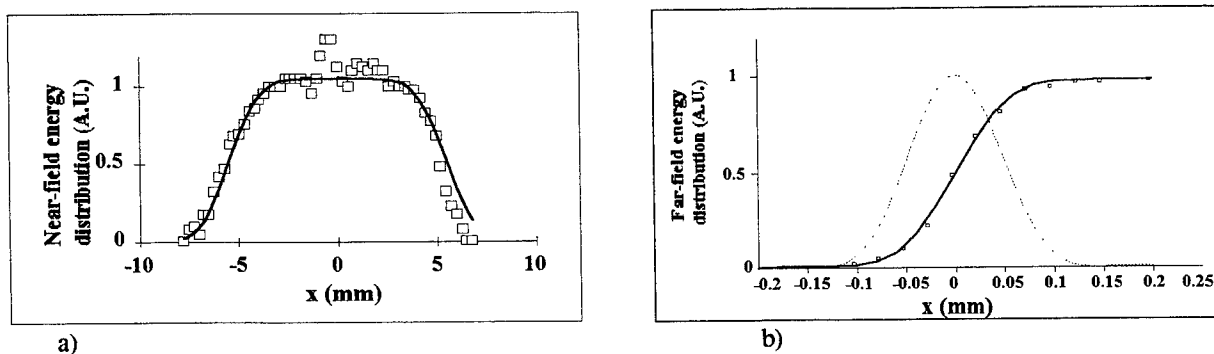


Fig. 3: a) near-field profile (at $y = 0$) of the Ianus POPA beam; b) far-field integrated energy distribution of the beam measured by the knife-edge method (squares and solid line) and the corresponding far-field energy density distribution (dotted line).

the single functions, the far-field profile of a supergaussian-like function is the product of a gaussian with an Airy function (in circular symmetry) or with a sinc function (in rectangular symmetry).

Figs. 1a, 2a and 3a show the experimental points of the NFED distribution together with the respective CP function with proper parameters, while in figs. 1b, 2b and 3b the unidimensional integral of the corresponding propagated (and properly widened) function is plotted (solid line). The presence of the hole in the near-field, due to the shadow of the output coupler in Hercules (see fig. 1a), is included in the calculation¹⁰. Figs. 1b, 2b and 3b also show the FFED profile of the Hercules and Ianus real beams (dotted line).

We compared the M^2 -factor with our TDL number, obtained by Eq. (1) either at a fixed k (in this case $k = 86.5\%$), and at θ taken at $1/e^2$ of the intensity maximum. The results are summarised in Table 2. The M^2 -factor is always larger than the TDL number, due to the non gaussian shape of the laser beams. However, when the beam has low spatial coherence, as in the case of Hercules, the difference between our TDL and the M^2 is small, about 12% for TDL at $1/e^2$ for the Hercules horizontal axis and less than 1% for the vertical one. The difference is remarkable when the beam has good spatial coherence, as in the case of Ianus, where the discrepancy is 18% for the GSFUR beam and 44% for the amplified beam.

LASER SYSTEM	TDL (Q 86.5%)	TDL (Q1/e ²)	M ²
IANUS GSFUR	1.1	1.1	1.3
IANUS POPA	1.6	1.6	2.3
HERCULES horizontal	16.8	17.6	19.7
HERCULES vertical	12.9	13.3	13.6

Table 2: Ianus and Hercules times-diffraction-limit-factors

4. BEAM-ANGULAR-STABILITY MEASUREMENT

We have checked the beam-angular-stability (BAS) of the Ianus beam by means of a novel technique¹⁷ which is simpler to be used than the method suggested by the ISO document¹⁹ even if it is less general. The beam was focused by a $f = 50$ cm lens on a $40 \mu\text{m}$ thick copper foil, until a hole was created, after a few shots. The irradiation was stopped when the transmitted energy fluctuation was of the same order of the total beam one (which was previously measured and equal to about 10%). By measuring the beam energy distribution in the focal plane and the hole dimension, it was possible to estimate the angular displacement corresponding to a 10%-transmitted-energy fluctuation. The BAS of the GSFUR beam resulted symmetrical and equal to $6 \mu\text{rad}$, about 1/10 of the full-beam divergence, whereas the amplified beam created an elliptical hole corresponding to a BAS of $9 \mu\text{rad}$ along the y direction and of $13 \mu\text{rad}$ along the x -axis. The larger value along the x direction could be partially due to thermal instability of the beam handling system.

5. CONCLUSION

We have presented a new method to estimate the TDL factor of a laser beam, including hard-edge, unstable resonator beams, which is only based on the phase distortion of the beam itself. We have tested this method on two high peak power excimer laser beams and the results have been compared with the corresponding M^2 -factor. It has been seen that the difference between our TDL and the M^2 -factor are larger when the beam is non gaussian and it has a good optical quality, like Ianus. This is because the TDL factor gives information on the spatial coherence of the real beam regardless of its amplitude shape which, on the contrary, may heavily affect the M^2 -factor.

Finally, we have presented a simple technique which is suitable to measure the beam angular stability of pulsed high peak power laser beams.

6. REFERENCES

1. See, e.g., H. Weber, "Some historical and technical aspect of beam quality", *Opt. Quantum Electron.* **24** S861-S864 (1992)
2. A.E. Siegman, "New Developments in Laser Resonators", *Proc. SPIE* **1224**, 2-12 (1990)

3. Document ISO/TC 172/SC 9/WG 1, Terminology and test methods for lasers. Manuscript for ISO/DIS 11146 Optics and optical instruments Lasers and laser related instruments Test methods for laser beam parameters: Beam widths, divergence angle and beam propagation factor "(February 15, 1995)
4. O. Svelto, *Principles of Lasers*, p. 397, Plenum Press, New York (1989)
5. C.M. Clayton, "Diagnostic for a developmental Iodine laser", *Laser Beam Radiometry Proc. SPIE 888*, 28-35 (1988)
6. P. Perlo, "Laser beam qualification and high power optical components design and testing", *Laser systems application in industry*, pp. 401-409, ed. ATA, Torino, Italy (1990)
7. M. Lurie, "Coherence and its effect on laser arrays", in *Surface Emitting Semiconductor Laser and Arrays*, pp. 435-465, G.A. Evans and J.M. Hammer eds., Academic Press (1993)
8. See, e.g., P.A. Belanger, Y. Champagne and C. Pare, "Beam propagation factor of diffracted laser beams", *Opt. Commun.*, **105**, 233-242 (1994)
9. M. Born and E. Wolf, *Principles of Optics*, pp. 460-462, 6th ed. Pergamon Press (1993)
10. S. Bollanti, P. Di Lazzaro and D. Murra, "How many times is a laser beam diffraction-limited?", *Opt. Commun.*, submitted for publication
11. P. Di Lazzaro, T. Letardi and C. E. Zheng, "Discharge medium influence on XeCl excimer laser beam quality", *Il Nuovo Cimento D* **14**, 41-48 (1992)
12. T. Letardi, S. Bollanti, P. Di Lazzaro, H. Fang, F. Flora, S. Fu, A. Gerardino, G. Giordano, N. Lisi, L. Mezi, G. Schina, A. Torre and C.E. Zheng, "Excimer laser development and applications at the ENEA Frascati Centre", *Proc. SPIE 1810*, pp.340-347, C. Fotakis, C. Kalpouzos, T. Papazoglou, Eds. (1993)
13. S. Bollanti, P. Di Lazzaro, F. Flora, G. Giordano, T. Letardi, D. Murra, C. Petrucci, G. Schina, O. Uteza and C. E. Zheng, "Experimental and theoretical results of high optical quality excimer laser beams", *High Power Lasers-Science and Engineering*, NATO-ASI vol. 3/7, pp. 191-198, R. Kossowsky, M. Jelinek and R.F. Walter, Eds., Kluwer Academic Publishers, The Netherlands (1996)
14. S. Bollanti, P. Di Lazzaro, F. Flora, G. Giordano, T. Hermesen, T. Letardi and C. E. Zheng, "Performance of a ten-liter electron avalanche-discharge XeCl laser device", *Appl. Phys. B* **50**, 415-423 (1990)
15. S. Bollanti, P. Di Lazzaro, G. Giordano, F. Flora, T. Letardi, G. Schina, M. Portaccio, A. Torre and C. E. Zheng, "High brightness large aperture excimer laser radiation", in *Proc. Int. Conf. on Lasers '91*, pp. 669-675, F. J. Duarte and D. G. Harris, Eds., STS Press, Mc Lean, VA (1992)
16. T. Letardi, S. Bollanti, P. Di Lazzaro, F. Flora, N. Lisi and C. E. Zheng, "Some design limitations for large-aperture high-energy per pulse excimer lasers", *Il Nuovo Cimento D* **14**, 495-507 (1992)
17. S. Bollanti, P. Di Lazzaro, F. Flora, T. Letardi, D. Murra, C. Petrucci, O. Uteza, "Study of a compact three-electrode oscillator-amplifier excimer laser system", *Opt. Commun.*, accepted for publication (1996)
18. P. Di Lazzaro, T. Hermesen and C. E. Zheng, "A generalisation of the self-filtering unstable resonator", *IEEE J. Quantum Electron.* **QE-24**, 1543-1547 (1988)
19. Document ISO/TC 172/SC 9/WG 1, Terminology and test methods for lasers. Provisional manuscripts for ISO/DIS 11 670 "Optics and optical instruments Lasers and laser related instruments Test methods for laser beam parameters: Beam positional stability" (August 31, 1994)

Improvement in the performance of a high average power XeCl laser

B.Lacour, H. Besaucèle*, H. Brunet, C. Gagnol and B. Vincent
CILAS, route de Nozay, 91460, MARCOUSSIS, FRANCE.

Tel.(1)64 54 49 16, Fax (1) 64 54 48 18

* SOPRA, 26 rue Pierre Joigneaux, 92270, BOIS-COLOMBES, FRANCE.

ABSTRACT

A 500 W, corona photo triggered XeCl laser has been upgraded up to 1100 W by increasing its input energy. Discharge efficiency in excess of 4 % has been demonstrated. The maximum average power was obtained at 440 Hz repetition rate.

Keywords : laser, excimer, XeCl, 1kW.

1. INTRODUCTION

Excimer lasers are known since a long time to be attractive U.V. sources usable for many applications. The development of them has been however slowed down by the lack of commercially available high average power Excimer lasers. Within the framework of the Eureka EU 205 European program, we have developed a high average power XeCl laser based on the concept of the "fast phototriggering". The "phototriggering" as it was proposed in 1982¹ is a simple and efficient way to operate reliably an Excimer laser since, by making the discharge be its own switch, it reduces considerably the stresses on the main switch of the laser. Efficient operation at high output energy has been demonstrated² and long pulses have been obtained³. A small one has been operated at high repetition rate⁴, but attempt to achieve high repetition rates with a larger device have shown that the spontaneous breakdown of the discharge was a limiting factor. As a way to overcome this difficulty, the concept of "fast phototriggering" has been proposed. It has been first tested on a laboratory device called "530" and found very efficient^{5,6}. A more industrial laser, the "635-1" has then been built. Its performances have been given recently⁷. An improved version, the "635-2" has been derived from it and is described in this paper. Fundamentals are the same but various improvements have been brought in order to improve the efficiency of the laser, the beam homogeneity and to make it easier to use and more reliable.

2. OPERATING PRINCIPLE

Every discharge excimer laser is operated with a preionization device that puts an initial electronic density in the gas, and a main discharge system that makes this density to increase up to breakdown thru avalanche processes.

In a "classical" photo triggered excimer laser, the voltage is set across the discharge on a μs time scale and it can be considered as constant during the avalanche grow. Then it is possible to define a avalanche time that will only depend on the gas mixture composition, on the reduced field and, to a less extent, on the preionization density and on the main electrical circuit impedance⁸.

In this case the only difficulty for the preionization device is to put electrons in the gas faster than collisional ionization does, in order to begin the discharge from a sufficiently high streamers density.

Unfortunately free electrons appearing between the electrodes due to natural radioactivity, corona parasitic discharge, field effect emission, left by the preceding discharge or created by the U.V. photons emitted by this preceding discharge can also start an avalanche process leading to an uncontrolled breakdown with arc formation.

Even a single free electron in the future discharge volume can produce such a non-controlled breakdown. Once the electronic density of the one electron initiated avalanche reaches the standard preionization value, it becomes impossible to control the discharge. The buildup time of this phenomenon is of the same order of magnitude than the preionization to discharge delay or slightly longer. (From 1 to 10^8 e/cm³ in the first case, from 10^8 to 10^{15} e/cm³ in the second).

This single initial electron can appear within the discharge volume at any time. Depending on the field value at

this time t_i and on the field time dependency, its avalanche will reach 10^8 e/cm^3 at the time t_p . In figure 1a and 1b⁹, we have plotted simultaneously all these points t_p as well as the time evolution of the charging voltage across the discharge for the two voltage rise times $10 \mu\text{s}$ and 400 ns . The best timing range for the preionization pulse is also shown. It is clear in these figure that 400 ns constitute a safe operating point with no risk of uncontrolled breakdown. It is possible to operate the laser at high repetition rate with longer charging time if one knows how to avoid gas ionization due to radiation from the preceding discharge. Actually in the 635 laser we have a charging time of the order of 400 to 600 ns .

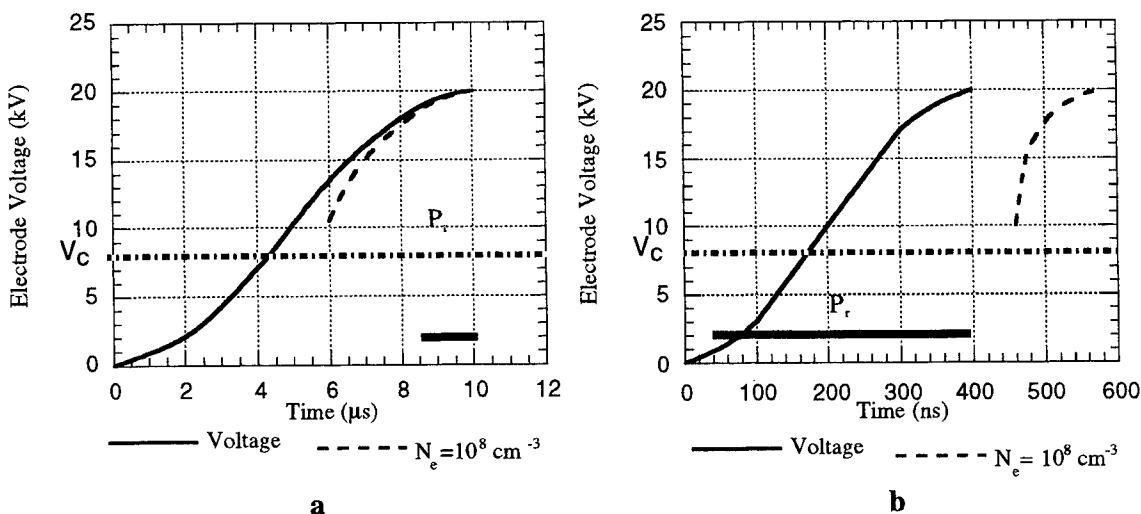


Figure 1. Laser voltage and correlated time of appearance of a 10^8 e/cm^3 electronic density due to randomly distributed ionizing events. Laser pressure 5 bar, $\text{Ne/Xe/Cl} = 998.3/1/0.7$, electrode spacing 3 cm. V_c = DC breakdown voltage, P_r = preferred preionization range.

3. DESCRIPTION

The "635" laser has been previously described elsewhere⁶. The design includes in the same stainless steel cylindrical vessel the complete gas circulation system, the discharge and the complete high current and high voltage circuitry. The overall volume, including gas bottles, vacuum pump, blowers motors and high voltage supplies is less than 4 m^3 .

The capacitors lay out and the geometry of the discharge current loop have been improved with respect to the 530 prototype. Hence, a very uniform field is achieved between the electrodes and along the insulators surfaces while keeping the inductance very low.

The discharge volume is $600 \times 35 \times 35 \text{ mm}^3$ (defining the name of this laser : "635") and the gas flow speed 35 m/s . The laser is usually operated at 4.5 bar with a typical gas mixture containing 0.7% HCl and 2% Xe in Ne buffer gas.

The electric scheme is of the charge transfer type but with a separate circuit to control the corona preionization device. The discharge loop inductance is only 8 nH , while the thyatron (or primary!) circuit inductance is much higher, 280 nH . Therefore no additional energy can be transferred directly from the primary capacitors to the discharge when the discharge breaks down.

For the first studies (635-1), the primary and discharge capacitors had the same value : 184 nF . The results described here on the "635-2" have been obtained with higher values, respectively 254 and 242 nF .

Preionization is based on a corona discharge (also called barrier discharge) that takes place between the rear face of the cathode and a ceramic surface. The first cathode we used had narrow slits and was 3 mm thick. The cathode used in this work on the "635-2" has wider slits and is only 2 mm thick and we have replaced the first vitrocereamics plate with an alumina plate. Preliminary measurements let us suppose that the preionization density is higher now.

4. EXPERIMENTAL RESULTS

4.1. Low repetition rate operation

4.1.1. Effect of preionization pulse width.

In a classical photo triggered laser, the preionization electrons are produced under high reduced field conditions and multiplication thru collisional ionization starts immediately. Thus the preionization must be short to be effective and not be drowned in the avalanche electrons. In a “fast photo triggered” XeCl laser, because of the shorter rise time and of ionization rate of the gas mixture, it is possible to preionize the gas at any time between the beginning of the voltage rise up to its maximum value, while keeping the same breakdown voltage. Therefore we can have the same preionization pulse in the presence of a multiplication rate ranging from a negative to a highly positive value.

Figure 2 shows how the output energy of the “530” and the “635” lasers depends on the voltage at the preionization time. As a comparison, we have plotted in this figure the effective preionization calculated value, assuming a 10 ns FWHM U.V. pulse (i.e. a 10 ns rise time for the electronic density due to preionization). It can be seen that this supposed rise time is in accordance with “530” laser output energy v.s. field. In the case of the “635” laser, it seems that the improvements brought to the preionization electrical circuit have led to a faster and more efficient preionization pulse.

4.1.2. Energy and efficiencies

The maximum single shot output energy obtained with this “635-2” laser was 3.5 J in a 70 ns FWHM pulse. The beam was square and very uniform, $\pm 7\%$ over more than 60% of the total beam cross section.

First, low repetition rate results with the “635-1” laser have been previously reported. Figure 3 shows the efficiencies obtained on the upgraded “635-2” laser. It is noteworthy that the intrinsic (or discharge) efficiency reaches very high values, comparable with best values obtained with spiker-sustainer circuits. (Energy and voltage measurement systems have been thoroughly verified !) The very good homogeneity of the discharge and the fact that we operate the laser at the reduced field that corresponds to the best efficiency can explain our results.

Concerning the overall (or C_1) efficiency (The electrical power for the blowers is not taken into account), its increase is due simultaneously to the improvement of the transfer circuit and to the above mentioned better discharge efficiency.

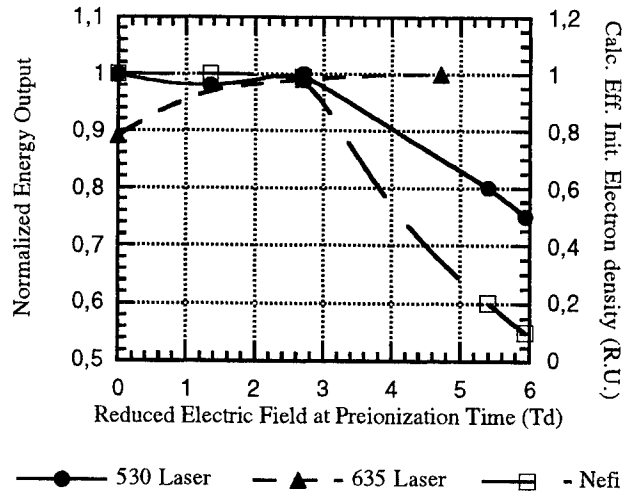


Figure 2. Laser output energies as a function of the reduced field value when the preionization pulse is applied. Total discharge voltage rise time: 400ns, preionization pulse width: 10ns.

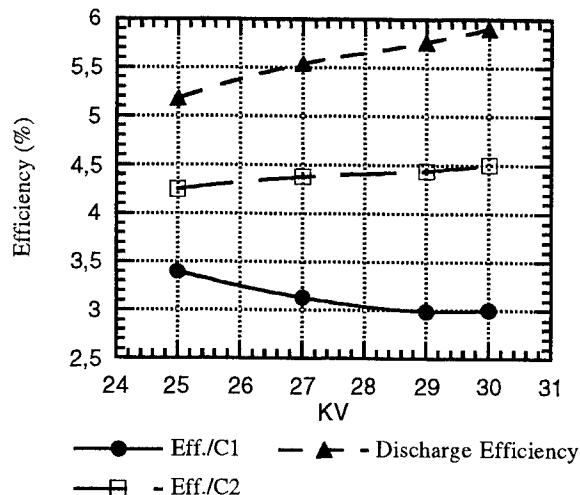


Figure 3. Efficiency v.s. energy put in C_1 , C_2 , or discharge as a function of the charging voltage. XeCl gas mixture pressure 4.5bar, capacitances: $C_1=254$ nF, $C_2=242$ nF.

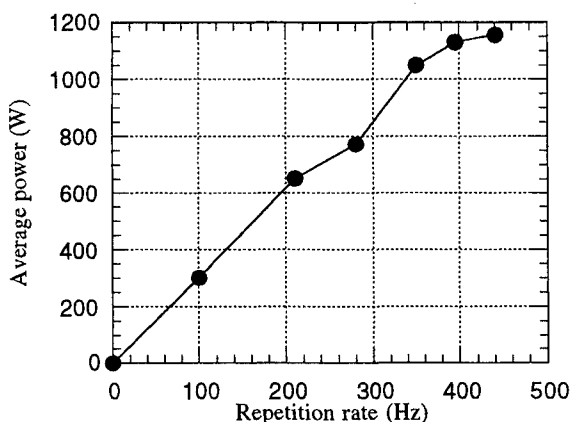


Figure 4. LASERDOT / CILAS 635-2 laser. Average power v.s. rep. rate frequency. XeCl, pressure : 4.5 bar, charging voltage : 30 kV, stored energy : 114J.

4.2. High repetition rate operation.

The laser has been operated at various repetition rate frequencies. Pulse to pulse temporal evolution was monitored with a fast U.V. photodiode and a digital oscilloscope operated in sequence mode. Average power was measured by accumulating 10 shots on a calorimeter. Due to the available charging power supplies (5×10 kJ/s), the maximum repetition rate was limited to 435 Hz at 30 kV charging voltage, corresponding to 114 J energy input per shot.

Figure 4 shows the average output power as a function of the repetition rate. In a 100 shot burst the energy per pulse is practically constant up to 350 Hz and shows no significant time dependency up to 400 Hz. At 435 Hz, however there is a marked decrease during the 10 first shots, clearly to be attributed to the on-set of a acoustical waves reverberation regime. There was no damping material inside the laser, but

we could easily install them and hence improve the high repetition rate operation.

5. CONCLUSION

-From the discharge physics point of view, it is noteworthy to see that a XeCl laser, operated on the so called "fast phototriggering" mode, with a simple charge transfer circuit, a very uniform field inside the cavity, and an optimized electrical circuit, is able to reach an efficiency that is, to our knowledge, the best ever achieved with an excimer laser.

-From a more practical point of view, we have, here, a high average power U.V. laser that is very compact and has been designed to be reliable, simple and easy to use. High productivity applications to many industrial processes ranging from the surface cleaning up to ceramics machining have been proved. They have now to be developed and to find their place.

6. ACKNOWLEDGMENTS

This work has been financially supported partly by the French Ministry of Industry.

7. REFERENCES

1. O. De Witte, B. Lacour and C. Vannier, Proc. CLEO'82, THQ2, 1982.
2. Y. I. Bychkov, M. L. Vinnik and M. K. Makarov, Sov. J. of Quant. Electr. **19**, pp. 542-543, 1992.
3. B. Lacour et al., Conf. LASER 88, HI 4, Lake Tahoe, Nevada, USA, 1988.
4. D. Beaupere et al., Proc. CLEO'88, TuH6, 1988.
5. B. Lacour et al., 9th G.C.L., SPIE Vol. 1810, pp. 368-371, 1992.
6. B. Lacour et al., SPIE Vol. 2206, pp. 41-45, 1994.
7. B. Lacour et al., Conf. UVX 94, Annales de physique, C1, N°5, Vol 19, pp. 205-212, 1994.
8. S. Mizzi, Thesis, Orsay, France, 1990.
9. H. Besaucèle, Thesis, Strasbourg 1, France, 1994.

Basic characteristic and application of KrF laser pumped by electric discharge

Koichi Kasuya*, Hiroyasu Sunami*, Chunlei Wu*, Eiki Hotta*,
Yuu Kawakita** and Sigeru Kato**

*Department of Energy Sciences, Interdisciplinary Graduate School of Science
and Engineering, Tokyo Institute of Technology,
Nagatsuta 4259, Midori-ku, Yokohama, Kanagawa, Japan 226

**High Voltage Research and Development Group, Research and Development Division,
Nissin Electric Company Limited, Umezu 47, Takase-cho, Ukyo-ku, Kyoto, Japan 615

ABSTRACT

A series of experiments were performed to investigate the fundamental characteristics of a KrF laser pumped by electric discharge. The mode patterns of the laser were observed by a high speed camera. A YBCuO target was irradiated by the same laser and the surface conditions were observed by a microscope. A model X-ray source for pre-ionization which used a wire-initiated plasma source was constructed.

Keywords: KrF laser, UV and X-ray pre-ionization, transverse modes, YBCuO surface irradiation

2.INTRODUCTION

We have presented a series of experimental results on a high repetition rate KrF excimer laser pumped by electric discharge.¹⁻³ UV light pre-ionization by arrays of small pin discharges was used in these experiments. We have also published numerical results of the same kind of laser.⁴ After these works, we were still continuing further research works in this field, and the results are presented here.

3.PREPARATION OF X-RAY SOURCE TO PRE-IONIZE KrF LASER

Although UV light is generally used for the pre-ionization, X-ray is superior to the UV light. X-ray well penetrates into the laser gas and enable us to form a uniformly distributed homogeneous discharge. So that, we have newly developed a X-ray pre-ionization apparatus based on a wire-ion-plasma source.

Fig.1 is a schematic diagram of the X-ray pre-ionization apparatus which shows the cross sectional view. The upper part is the wire-plasma ion source, and the downward extracted ions from the plasma source are accelerated by the negative high voltage electrode at the lower part. The secondary electrons produced by the ion bombardment are also accelerated upward to the uppermost heavy metal thin film (Ta), and X-ray is produced by this electron bombardment to the upper direction.

Two thin W-wires of 0.4mm diameter are used as the anodes, and a nearly coaxial SUS surrounding electrode is used as the cathode. These arrangement enable us to produce high density plasmas with rather low applied voltage. Two aperture electrodes at the both ends of the electrode system can confine electrons effectively, and the repetitive operation can be realized more easily. As the chamber gas is He of about several tens Torr, the coefficient of the secondary electron production by He ion is important for our case. The nominal value for 100keV energy He ion is about 10 or 15, for example.

The thickness of the top wall is decided under the compromise of two factors. The thinner wall is necessary for the smaller reduction of the X-ray, while the thicker wall is expected for the stronger mechanical structure. This compromise must be more strict at the counterpart wall of the laser chamber which contains the dangerous halogen mixture gas of the pressure of a few atmosphere.

The mechanical stress imposed on the upper Teflon window for X-ray of 2mm thickness was calculated. The transmitted X-ray through the Teflon sheet of 7mm thickness and the Cu thin film electrode of 0.5mm thickness on the laser main chamber was also calculated. The X-ray flux of about 30mR was estimated under the condition of the wire pulsed voltage of 7.5kV and the acceleration high voltage of -80kV.

4.BEAM CHARACTERISTICS OF KrF LASER

As the early experimental results of this subject are described in Ref. (3), the most recent results are

shown in this article. A wind tunnel type excimer laser apparatus with the UV light pre-ionization was also used here as before. The whole experimental arrangements are shown in Ref. (3). Although the main purpose was to measure the spatial and time-varying beam patterns, the laser power output and the gas constituents were measured at the same time.

The total gas pressure was set at 3 atm, and the continuous laser operation was tried with the repetition rate of 500 Hz and the CR value of 2.0. The transverse mode of the laser light was observed at the sequence of (1)1st, (2) 4×10^3 , (3) 1×10^4 , (4) 1×10^5 and (5) 1×10^6 shot. For example, the mode patterns and the intensity distribution are shown for the case of (1) and (5) in Fig.2.

The result of the laser power output is shown as a function of the laser shot number in Fig.3. To compare with this, the change of the gas constituent with the laser shot number is shown in Fig.4, where the H_2O history is shown separately from the others of O_2 , CF_4 , HF , F_2 . We can say that the rather rapid decrease of the power output in earlier time corresponds to the rather rapid increase of impurities, while the slow decrease of the power output in later time corresponds to the slow decrease of the F_2 . The gas constituent was measured with a mass spectrometer in our experiment. We did not use any gas purifier, and we did not make any injection to add F_2 gas in this experiment.

We also measured the temporal profiles of the laser light with a high speed streak camera. The streak photographs were also taken at the shot sequence of (1)1st, (2) 4×10^3 , (3) 1×10^4 , (4) 1×10^5 and (5) 1×10^6 , among which the results of (1) and (5) cases are shown in Fig.5 and 6. Together with the raw photos, the laser light intensity vs. time and the 3-dimensional plots of laser light intensity are shown here. We can see how the intensity changes with the continuous operation of the laser with high repetition rate. From these intensity history vs. time, we can get Fig.7, where the time duration of the laser light is shown as a function of the laser shot number.

5.ABLATION OF ROOM-TEMPERATURE SUPER-CONDUCTOR TARGET BY KrF LASER

The same laser light was used to irradiate a room-temperature super-conductor material, and the ablated surface was observed by a microscope. The experimental setup is shown in Fig.8, where the nominal experimental conditions are as follows. The laser energy per shot was 100mJ, the laser spot area was 4mm^2 , the laser flux was $0.2\text{--}2.5\text{J/cm}^2$, the repetition rate of the laser was 1Hz, the chamber background pressure was $1 \times 10^{-4}\text{Torr}$ and the target material was YBCuO.

The laser flux was changed as a parameter descretely from 0, to 0.2, 0.5, 1.0 and 2.5J/cm^2 . The solid YBCuO surfaces before (See Fig.9(a)) and after the single laser shot were observed by a microscope of 500 multiplication, and compared with each other. The surface was rotated along the axis, and the laser light was injected toward the renewed surface. The irradiated surface started to emit slight light at 0.5J/cm^2 and the microscope image started to change at this laser flux. At 1.0J/cm^2 the ablation plume became brighter, and the area of melted surface increased. At 2.5J/cm^2 the surface luminescence was brightest, and the solid surface was get rid of partially. Under the fixed laser flux of 1J/cm^2 , the irradiated surface was observed after 1, 5, 10 and 50 laser shots. The surface was melted non-uniformly even after the 25 shots, while it was melted uniformly after the 50 shots (See Fig.9(e)).

With these kinds of observations the preferable laser flux for the laser ablation of YBCuO etc. in the field of industrial application can be found.

6.FUTURE PLANS

Different kinds of pre-ionization methods with the UV light and the X-ray must be compared in the near future. Their effects on the laser gas flows are our main interests. We will make various kinds of flow and laser diagnostics to measure the density perturbations after the laser gas discharge, for example. The relation between the residual perturbations and the laser performances must be also investigated.

7.ACKNOWLEDGEMENTS

Supports by a Grant-in-aid for Scientific Research by the Ministry of Education, Sport, Science and Culture in Japan are acknowledged at first. Supports to promote the inland and international Cooperations by the Japanese Society for Promotion of Science are also acknowledged. Cooperation with Osaka University (Institute of Laser Engineering), The University of Electro-Communications (Center

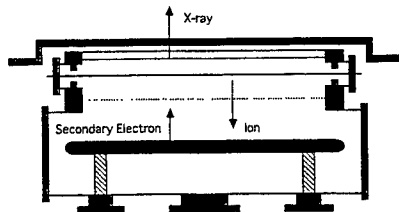


Fig.1. Schematic of X-ray pre-ionization apparatus.

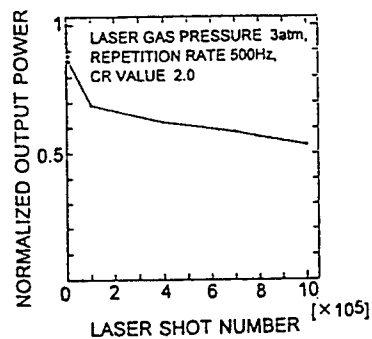


Fig.3. Laser power output vs. shot number.

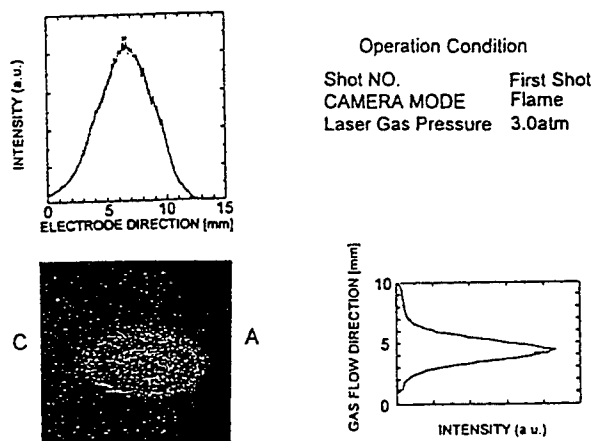


Fig.2(a). Beam profile and intensity distribution-1.

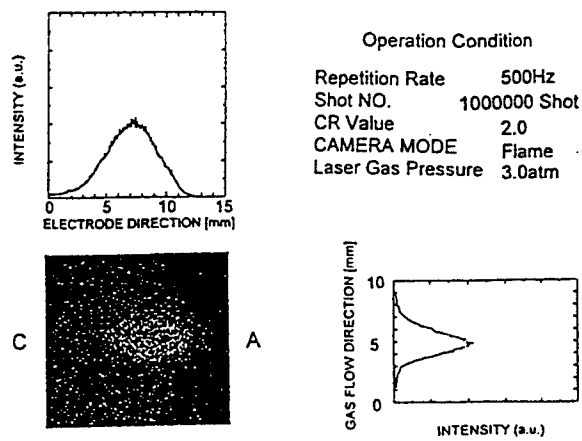
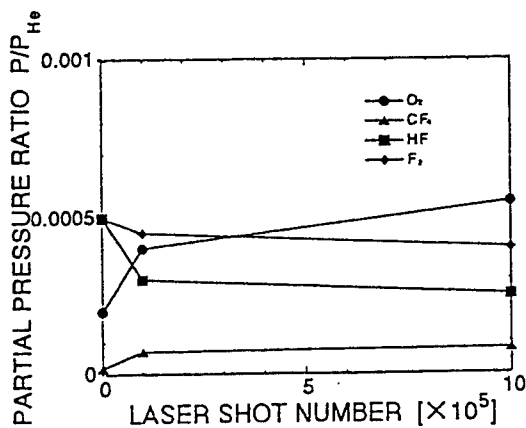
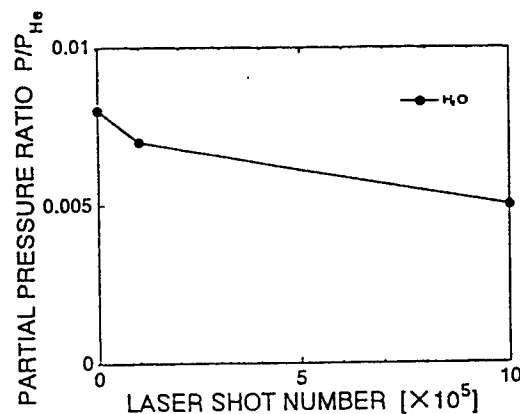


Fig.2(b). Beam profile and intensity distribution-2.



(a) O₂, CF₄, HF and F₂



(b) H₂O

Fig.4. Gas Constituent vs. shot number.

of Laser Science) and The Institute of Physical and Chemical Research must be thanked also. The authors acknowledge Dr.M.Watanabe, Mr.Y.Itoh and Mr.M.Abe for their technical supports.

8. REFERENCES

1.K.Kasuya et al., "Measurements of Gas Flow and Gas Constituent in a Wind-Tunnel Type Excimer Laser under High Repetition-Rate Operations," *Proc. of 8th GCL*, Vol.SPIE-1397, pp.67-70, 1991.

2.K.Kasuya et al., "Highly Sensitive Diagnostics of Particle Density Relaxation Process in KrF Laser," *Proc. of 9th GCL*, Vol.SPIE-1810, pp.388-391, 1993.

3.K.Kasuya et al., "Quality Measurements of KrF Laser Beams under High Repetition Rate Operation with Advanced High Speed Photography: Preparatory Experiments," *Proc. of 10th GCL*, Vol.SPIE-2502, pp.450-457, 1995.

4.K.Kasuya et al., "One-dimensional Computation of the Discharge Pumped Excimer Lasers under Repetitive Operations," *Laser and Particle Beams*, 12(4), pp.647-679 (1994).

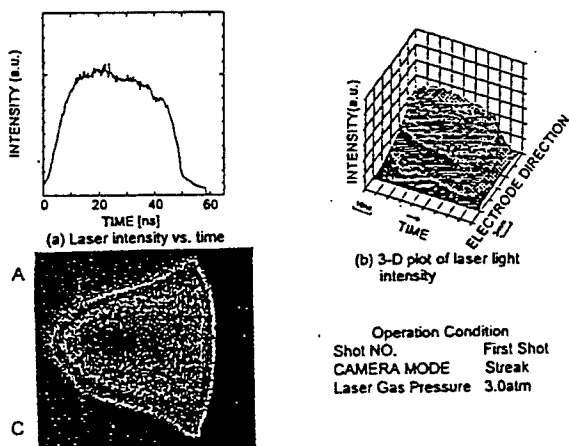


Fig.5. Time resolved laser intensity-1.

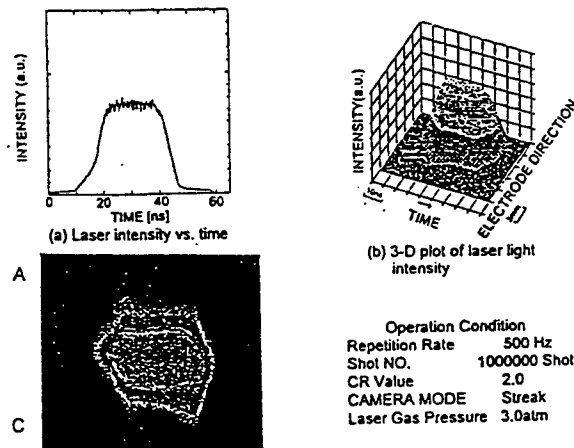


Fig.6. Time resolved laser intensity-2.

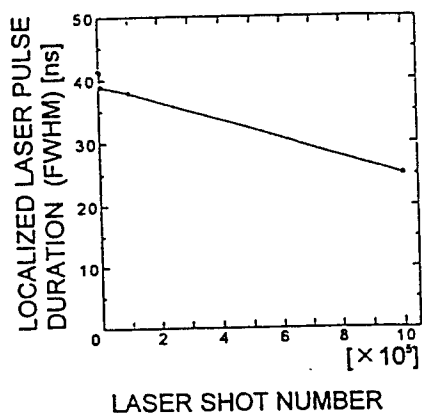


Fig.7. Pulse duration vs. shot number.

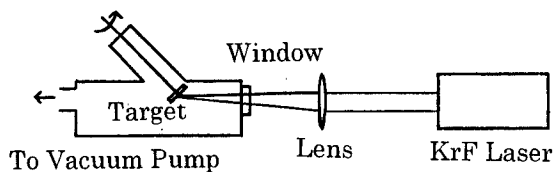


Fig.8. Ablation of YBCuO surface by KrF laser.

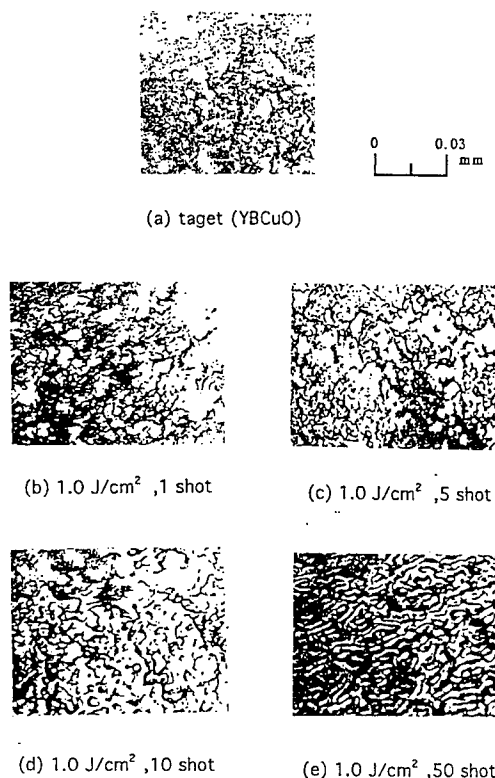


Fig.9. Microscope images of YBCuO after various number of shots of 1 J/cm^2 laser irradiation.

X-RAY PREIONIZED DISCHARGE PUMPED KrF LASER

J. BONNET, M. MAKAROV*, D. PIGACHE

ONERA - B.P.72 - 92322 Chatillon Cedex - France

Ph: +33 (1) 69.93.60.60. - FAX: +33 (1) 69.93.61.82

* - permanent address: HCEI, 4 Akademicheski ave., 634055, Tomsk, Russia

B. GODARD, M. STEHLE

SOPRA - 26, rue Pierre Joigneaux - 92270 Bois Colombes - France

Ph: +33 (1) 47.81.09.49. - FAX: +33 (1) 42.42.29.34

ABSTRACT

An X-ray preionized LC-inversion discharge pumped XeCl laser has been converted for KrF operation. The X-rays were produced by a long pulse (400 nsec FWHM) secondary emission electron gun. A KrF laser energy of 1.2 J is obtained, only slightly lower than those obtained in a XeCl regime at the same pumping conditions.

INTRODUCTION

The VEL laser, a 1 kW XeCl laser for industrial applications, has been realized in 1992¹. It is desirable to have the possibility to operate the laser at other wavelength with the minimum of re-equipment. The central point here is whether or not the long pulse X-ray generator made of a secondary emission electron gun currently used in the VEL laser is suitable for preionization of the strong-attachment fluorine-based active gas mixtures. The DENEb excimer laser, previously studied as a VEL prototype², has been converted for KrF operation by only changing the laser cavity mirrors. A parametric study is presented here.

EXPERIMENTAL SYSTEM

The DENEb laser pumping circuit as well as the X-ray generator design have been described elsewhere^{2,3}. Here is given a brief summary. A thyatron switched (two LS-4101 devices in parallel) LC-inverter with the arms of $C_1 = C_2 = 227$ nF is used for the 40/5.3/3 cm³ sized discharge. The preionizer was composed of a pulsed helium ion source (operating pressure of about 30 μ bar), a high-voltage cathode polarized up to -150 kV, and a gold coated aluminium output window. The X-ray pulse duration was about 400 nsec (FWHM). The interior of the laser chamber was coated with Ni. A gas purifier, GP2000XR (Oxford Lasers Ltd), operating at 110 K was applied.

EXPERIMENTAL RESULTS

Typical waveforms of the discharge current, thyatron current, and X-ray dose are shown in Figure 1. It is seen from the figure that a near-complete voltage doubling takes place before the discharge breakdown occurs. The current oscillations are indicative of the strong mismatch between the discharge and the pumping circuit in contrast to the XeCl operating regime realized previously³. This is partially due

to the degradation of the plasma micro-structure (filamentation) during the pumping pulse, though no glow-to-arc discharge transition has been detected.

Presented in Figure 2(a) is the laser energy versus the F_2 content of the active gas mixture Ne/Kr/ F_2 for different Ne/Kr ratio. Similar dependences on the Kr content are shown in Figure 2(b). A decrease in the laser energy with increasing F_2 or Kr content is due to discharge filamentation with more pronounced effect of the fluorine component. In contrast, the weak gas mixture do not provide the laser gain required. The optimum active mixture composition was found to be Ne/Kr/ $F_2 = 1000/20/0.7$.

No laser saturation has been achieved as the total gas pressure or the store charging voltage increase (Figures 3 and 4 respectively). And decline in the KrF laser efficiency is correspondingly not very strong (Figure 5). The maximum output of about 1.2 J per pulse has been obtained at the gas pressure of 3.5 bars and the initial charging voltage of 30 kV. This result compares well with the DENEb laser energy of about 1.5 J realized in the XeCl operating mode at the same pumping conditions. But the best total efficiency of about 0.9 % is only half the efficiency achieved with XeCl.

With a relatively uniform discharge structure, such a difference is most likely due to the mismatch between the pumping power density and the resonator configuration. An increase of the output coupler reflectivity from 7 % to 20 % caused a drastic increase in the laser energy (Figure 3, 4). Likewise, the discharge narrowing from 3 cm to 1.5 cm leads to an increase in the specific laser energy from 80 mJ/cm² to 160 mJ/cm².

The dependence of the laser energy on the delay time between the onset of preionization and the discharge breakdown has been studied (Figure 6). As one would expect, because of the strong attachment properties of the F_2 -molecule the allowable range of delay time is narrower than in XeCl lasers. The best results have been obtained when the discharge breakdown occurs just at the maximum of the X-ray pulse.

The X-ray dose has been varied by changing the electron-gun voltage. The results are presented in figure 7. The saturation is less pronounced than it was observed in XeCl operation regime³. Nevertheless, the preionization electron density created is quite sufficient for the KrF laser discharge initiation.

CONCLUSIONS

The DENEb excimer laser has been converted for the KrF operation by only changing the laser cavity mirrors. It has been demonstrated that the long pulse (400 nsec FWHM) X-ray generator made of a secondary emission electron gun currently used in the 1 kW VEL laser is suitable for the preionization of fluorine-based active gas mixtures. The maximum output of about 1.2 J per pulse (specific laser energy ~ 160 mJ/cm²) has been obtained at the gas pressure of 3.5 bars, only slightly lower than those obtained in a XeCl regime at the same pumping conditions.

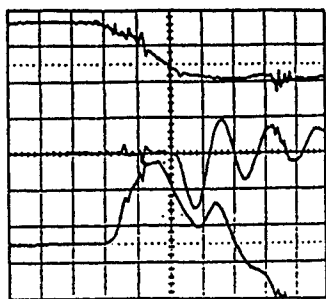
1. B. Godard et al, "Realization of a 1 kW XeCl laser," GCL IX, 1992, Crete, SPIE vol. 1810, pp. 372-375.

2. D. Pigache et al, "A secondary emission electron gun for X-ray preionization of high repetition rate XeCl lasers," ICPIG XIX, 1989, Belgrad.

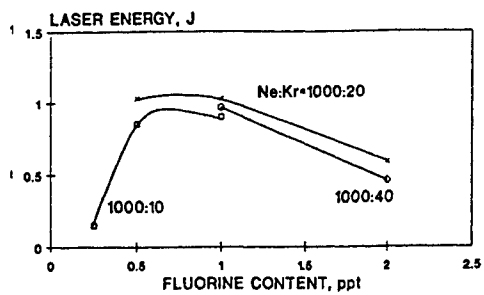
3. B. Godard et al, "Parametric study of an high average power XeCl laser," SPIE vol. 1503, pp. 71-77.

FIGURE CAPTIONS

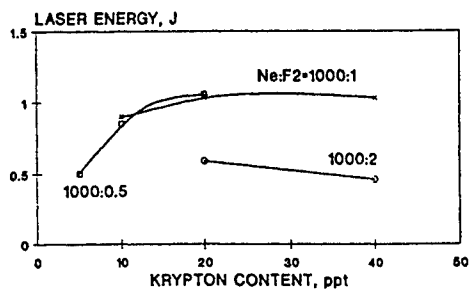
- Figure 1.** Typical waveforms of the X-ray dose (top, a.u.), the thyatron current (bottom, 6 kA/div), and the discharge current (50 kA/div). Ne:Kr:F₂ = 1000:20:0.7, p = 3.5 bars, U₀ = 25 kV; time scale: 200 nsec/div.
- Figure 2.** (a) Laser energy vs the F₂ content of the Ne:Kr:F₂ active gas mixture for different Ne:Kr ratio. p = 3.5 bars, U₀ = 25 kV; (b) Laser energy vs the Kr content of the Ne:Kr:F₂ active gas mixture for different Ne:F₂ ratio. p = 3.5 bars, U₀ = 25 kV.
- Figure 3.** Laser energy vs the total pressure of the active gas mixture for two different output coupler reflectivity. Ne:Kr:F₂ = 1000:20:0.7, U₀ = 25 kV.
- Figure 4.** Laser energy vs the initial store charging voltage for two different output coupler reflectivity. p = 3.5 bars, Ne:Kr:F₂ = 1000:20:0.7.
- Figure 5.** Laser efficiency vs the initial store charging voltage. Ne:Kr:F₂ = 1000:20:0.7, p = 3.5 bars.
- Figure 6.** Laser energy vs the time delay between the onset of preionization and the discharge breakdown. Presented on the inset are waveforms of the X-ray pulse (top) and the discharge current (bottom), time scale: 200 nsec/div. The time delay is indicated by the arrows. Ne:Kr:F₂ = 1000:20:0.7, p = 3.5 bars, U₀ = 25 kV.
- Figure 7.** Laser energy vs the electron gun voltage for two different initial charging voltage of the main energy store. Ne:Kr:F₂ = 1000:20:0.7, p = 3.5 bars, U₀ = 25 kV.



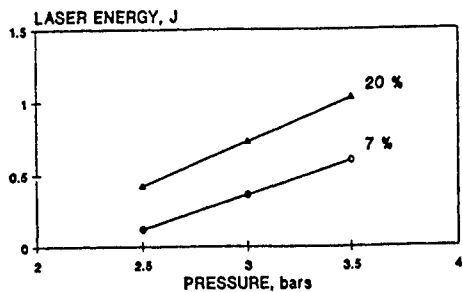
1



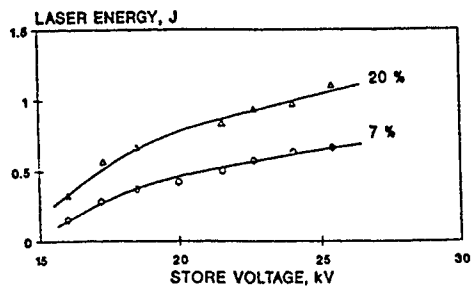
2(a)



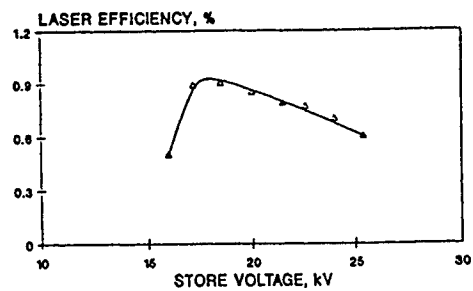
2(b)



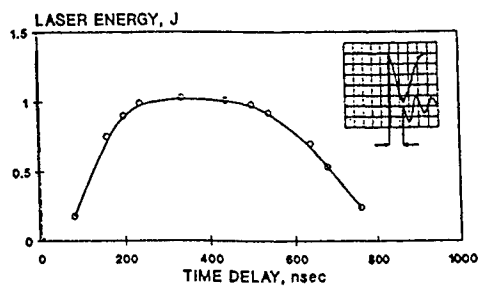
3



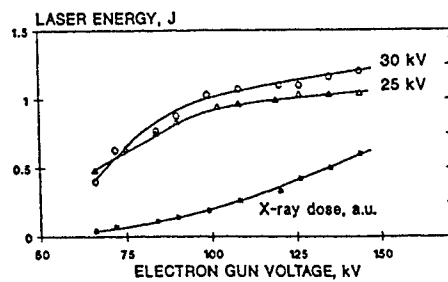
4



5



6



7

An X-ray pre-ionized molecular fluorine laser with a large discharge cross-section

H.M.J. Bastiaens, P.J.M. Peters and W.J. Witteman

University of Twente, Department of Applied Physics
P.O. Box 217, 7500 AE Enschede, The Netherlands
Fax: +31-53-4891102, E-mail: H.M.J.Bastiaens@tn.utwente.nl

ABSTRACT

High energy extraction from UV pre-ionized molecular fluorine lasers is hampered by the short period of discharge stability and the spatial inhomogeneity of the discharge. So far stable discharge operation is reported for small discharge cross sections with an area less than 0.8 cm^2 and efficiencies in the order of 0.15 %. To increase the energy extraction of the molecular fluorine laser the discharge cross section should be enlarged. Here we report on the successful operation of a molecular fluorine laser with a large discharge cross section of $1.5 \times 2.4 \text{ cm}^2$ (electrode spacing \times discharge width) which operates at a high intrinsic efficiency of 0.45 %. Crucial for obtaining this result is the development of a short pulse, high intensity X-ray pre-ionization source.

KEYWORDS: laser, gas discharge, molecular fluorine, X-ray pre-ionization

2. INTRODUCTION

The molecular fluorine laser which emits radiation at a wavelength of 157 nm can be excited by electron beam¹ and discharge pumping. Although the electron beam pumped systems give large absolute energy outputs they are not practical for applications due to their low repetition rate. Therefore in recent years attention is focused on discharge pumped molecular fluorine lasers^{2,3,4}.

To operate the molecular fluorine laser a high pumping power density is required⁵. The radiative lifetime of the upper laser level is only 3.7 ns. The lower laser level is bound but can be depopulated by collisions with the buffer gas. In helium the effective lifetime of the lower laser level is around 3 ns at a pressure of 5 bar. A fast build up of the intracavity laser field is required before the lower laser level is populated appreciably and laser output energy saturates. A rapid build up of the gain can be realized with a high pumping power density.

In UV pre-ionized discharge pumped fluorine lasers it is found that the stability of the discharge strongly depends on its geometric cross section. A stable discharge and an optimum output energy was reported for a discharge with a cross section of $0.8 \times 1.0 \text{ cm}^2$. However, an increase of the cross section did not lead to higher output energies².

In the present contribution we will discuss the successful operation of the molecular fluorine laser with a large cross section of $1.5 \times 2.4 \text{ cm}^2$ (electrode spacing \times discharge width). For this purpose we designed a laser head with a very low inductance. We also developed a new short pulse, high intensity X-ray pre-ionization source. It is found that the output energy scales with the discharge volume.

3. EXPERIMENTAL SETUP

The laser system is a charge transfer discharge device with a low inductance laser head in a high pressure vessel, as schematically illustrated in Fig. 1. The laser head consists of two metal plates holding two rows of capacitors in between. The lower plate is made of aluminum and forms the anode. The nickel plated, aluminum cathode is attached to the upper plate. The capacitors (type TDK UHV 5A/7A) are placed along the cathode and are as close as possible to the discharge gap. This construction ensures a low inductance of the discharge circuit. The inductance of the laser head is about 1.7 nH. The laser head is charged by a double stage Marx generator which has a total capacitance of 10 nF. The capacitance C_0 of the laser head can be easily varied and in this study amounts 14 nF and 30.6 nF respectively. The cathode has a length of 42 cm and a width of 2.2 cm. Setting the electrode spacing to 0.8 cm results in a discharge width of 1.4 cm and an excited volume of 46 cm^3 . When the electrode spacing is set to 1.5 cm, the discharge has a width of 2.4 cm and the excited volume of 153 cm^3 .

The necessary pre-ionization is provided by a short pulse, high intensity X-ray source. The X-ray source is built very compact as to fit into the laser vessel. It employs a corona plasma cathode⁶ which emits electrons. The electron accelerating voltage ranges from 40 kV and 110 kV. The electrons produce Bremsstrahlung when they are decelerated in the high Z-material which is attached to the vacuum housing of X-ray source.

The X-ray source is mounted under the anode. The X-rays emitted by the source penetrate the aluminum anode and ionize the laser gas. In the discharge volume they create the electron density necessary to ensure a homogeneous and stable discharge in a gas mixture of helium with up to 0.4 % fluorine at a total pressure of 5 bar. In the configuration as depicted in Fig. 1 the source can deliver up to 60 mRad in the discharge volume in a pulse with a length of 19 ns. The X-ray dose is measured with a pen dosimeter (Physiotechnie SEQ 6) and the time dependence with a plastic scintillator (NE102A) in combination with an optical fiber and a photomultiplier⁷ (Hamamatsu R763). In the longitudinal direction the X-ray source has a flat X-ray emission intensity profile ($\pm 6\%$) over a length of 46 cm.

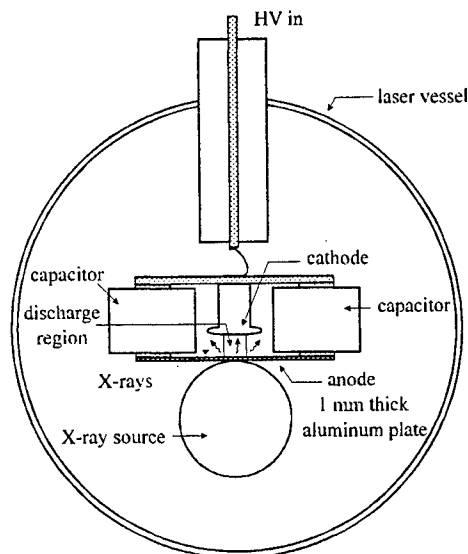


Fig. 1. Cross-section of the laser system

The laser is operated with a resonator formed by a dielectric total reflector ($R \approx 94\%$, Lambda Physik) and an uncoated MgF_2 output coupler. The length of the resonator is 70 cm. The mirrors are placed inside the laser vessel. The laser beam emerges from the vessel through a MgF_2 window. The window is tilted 5° to the axis of the laser to prevent back reflections into the laser medium. The laser energy is measured with pyroelectric energy meters which are calibrated versus a home made Joule meter⁸. The time history of the laser pulse is measured with a solar blind, vacuum photodiode (ITT F4115) in combination with an optical transmission filter for 157 nm. The optical paths to the detectors are evacuated to avoid strong absorption of the 157 nm laser light by the Schumann-Runge bands of molecular oxygen. The output energy of the red atomic fluorine emission which usually accompanies the 157 nm molecular fluorine emission is subtracted from the measured total energy.

The voltage, current and X-ray signals from the short pulse discharge system are measured with a Tektronix TDS 640 oscilloscope.

To remove absorbing impurities and to improve the lifetime of the laser gas a cryogenic gas purification system is connected to the laser system. It consists of a circulation pump, a liquid nitrogen cooled trap and a dust filter. The purification system is used during all the laser experiments.

4. EXPERIMENTAL RESULTS AND DISCUSSION

For the proper operation of the molecular fluorine laser with a stable glow discharge in a high pressure mixture of helium and fluorine the optimum conditions for X-ray pre-ionization are investigated. Fig.2 shows the time dependence of the X-ray pulse, the voltage on the electrodes, the current through the laser system, the input power and the laser pulse. The shown signals are an average of four shots. As for all the experiments reported here a gas mixture of 0.1% fluorine in helium at a total pressure of 5 bar is used.

After the Marx generator is fired the capacitors in the laser head are charged as can be seen from the voltage rise on the electrodes. During the voltage rise the X-rays are injected into the laser gas to pre-ionize the gas mixture. After typically 80

to 100 ns the gas breaks down and the discharge starts. While the voltage over the electrodes drops the current rises very fast and power is deposited in the laser gas. The voltage as shown in Fig.2 is corrected for $L di/dt$ due to the inductance of the laser head. The pump power deposition in the laser gas can be calculated from the measured voltage and current signals. The resulting pump power pulses are typically 6 ns to 9 ns wide (FWHM). The laser pulses have about the same width as the pumping pulse.

The optimum output energy as it depends on the timing of the pre-ionization is reached when the peak of the X-ray pulse falls in a time window between 90 ns and 50 ns prior to the discharge. The laser output energy is optimal and independent of the electron pre-ionization density when the X-ray dose is above 5 mRad.

The electron density generated with the X-ray source is measured with an ionization chamber. It is found that with a dose of 5 mRad an electron density of $1.5 \times 10^9 \text{ cm}^{-3}$ is generated in 5 bar argon. The electron density in helium is about 40 times lower⁸ and corresponds to a value of about $3.8 \times 10^7 \text{ cm}^{-3}$. This value is in the same order as reported by other authors for the proper pre-ionization of the XeCl lasers^{10,11}.

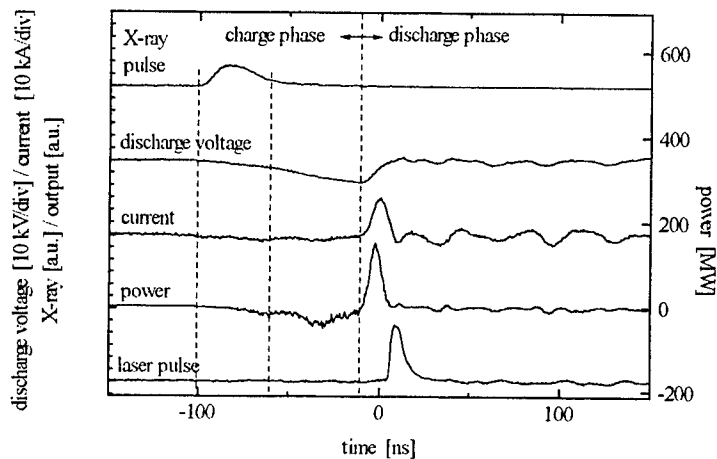


Fig. 2. The time dependence of the X-ray pulse, the voltage on the electrodes, the current through the laser, the input power and the laser pulse as measured for a charging voltage of the Marx generator of 20 kV, a capacitance of the laser head of 14 nF and an electrode spacing of 0.8 cm (config. I)

The laser output energy is plotted in Fig. 3a as a function of the charging voltage on C_1 for three different configurations. In configuration I the capacitance C_2 of the laser head is 14 nF, the inductance is 1.7 nH and the electrode spacing set to 0.8 cm. For configuration II the capacitance C_2 is raised to 30.6 nF, the inductance amounts 0.9 nH and the electrode spacing is kept at 0.8 cm. For configuration III the capacitance C_2 is 14 nF, the inductance is 1.9 nH and the electrode spacing is raised to 1.5 cm.

The laser is powered by the energy stored on capacitance C_2 and the output energy will thus depend on the voltage on capacitor C_2 . Increasing the charging voltage on C_1 leads to a higher rate of the voltage (dV/dt) on C_2 and a higher breakdown voltage of the gas. In this way the power deposition in the laser is varied. As can be seen in Fig. 3a the output energy increases for all three configurations with increasing charge voltage on capacitor C_1 . Increasing the capacitance in configuration I from 14 nF to 30.6 nF and keeping the electrode spacing at 0.8 cm (config. II) leads to an increase in stored energy on capacitor C_2 and an increase in output energy. Higher energy extraction can be reached by an increase of the electrode spacing from 0.8 cm to 1.5 cm with the capacitance C_2 at 14 nF (config. III). An increase in the electrode spacing results in a higher breakdown voltage and a higher energy stored on capacitor C_2 . A larger discharge volume is pumped and the output energy will increase. As can be seen in Fig. 3a the output energy increases by almost a factor of three.

The specific output energy is plotted in Fig. 3b as a function of the peak power pumping density for the three configurations used. As can be seen in Fig. 3b the specific output energy increases with increasing peak power pumping density for all three configurations. Although at higher pumping densities the rate of increase of the specific output energy decreases. At a pressure of 5 bar the saturation intensity will be in the order of 1 to 2 MW/cm^2 ¹².

The maximum output intensities for the different configurations range from 0.8 MW/cm^2 to 2 MW/cm^2 . As the output intensities are in the same range as the saturation intensity, saturation may play a role at higher pumping densities.

Electron quenching is the main loss channel for the upper laser level in the discharge pumped molecular fluorine laser⁵. With increasing peak power pumping density the current density is seen to increase. So also the electron density will increase resulting in stronger quenching of the upper laser level and a saturating specific output energy.

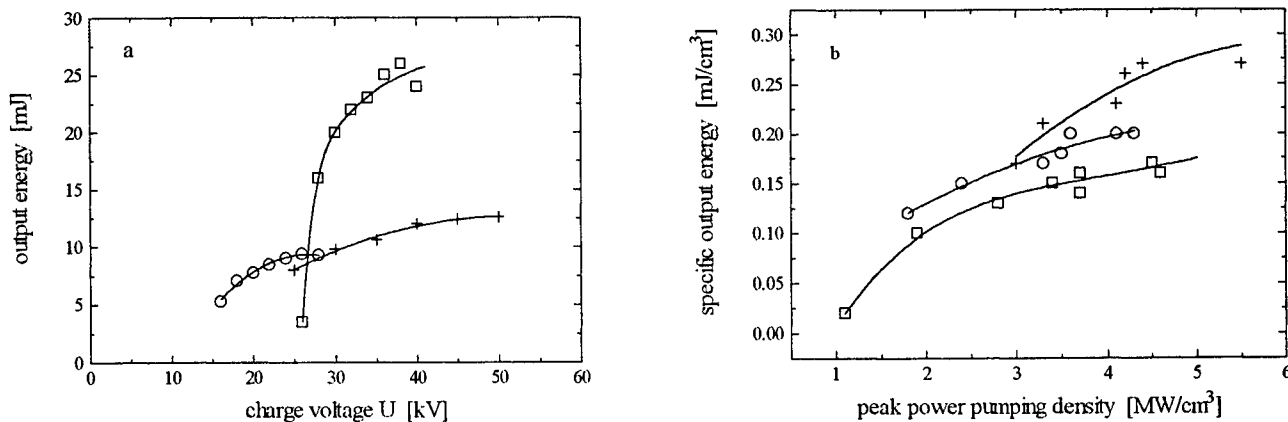


Fig. 3a. The output energy of the molecular fluorine laser as a function of the charge voltage on the Marx generator for the three different configurations of the laser head. (0: configuration I, +: configuration II, □: configuration III)

Fig. 3b. The specific output energy as a function of peak power pumping density for the three different configurations of the laser head. (0: configuration I, +: configuration II, □: configuration III)

The points plotted in Fig. 3a and Fig. 3b are an average of four shots.

Fig. 3b shows that with a higher laser head capacitance C_2 (config. II) the specific output energy is somewhat higher. With an increased electrode spacing the specific output energy is somewhat lower (config. III). The intrinsic efficiency defined as the output energy divided by the input energy amounts about 0.7% for configuration I and II.

For configuration III the intrinsic efficiency is somewhat lower and amounts 0.45% for the same range of peak power pumping density. The reason for this is not yet clear. Visual inspection of the discharge revealed no sign of streamers or other forms of instabilities over the whole range of experimental conditions reported here. As the discharge always looks homogeneous we expect it not to have a degrading influence on the specific output.

To increase the energy extracted from the laser system the length of the pump pulse may be extended. Preliminary results with a pulse forming network attached to the laser head show that pump and laser pulses can be made with a length of 50 ns.

5. ACKNOWLEDGMENTS

This project is supported by the Netherlands Technology Foundation (S.T.W.)

6. REFERENCES

1. F.T.J.L. Lankhorst, H.M.J. Bastiaens, H. Botma, P.J.M. Peters and W.J. Witteman, *J. Appl. Phys.* **77**, 399 (1995)
2. K. Yamada, K. Miyazaki, T. Hasama, and T. Sato, *Appl. Phys. Lett.* **54**, 597 (1989)
3. M. Kakehata, E. Hashimoto, F. Kannari, and M. Obara, *Appl. Phys. Lett.* **56**, 2599 (1990)
4. S.M. Hooker, A.M. Haxell, and C.E. Webb, *Appl. Phys. B* **55**, 54 (1992)
5. M. Kakehata, T. Uematsu, F. Kannari, and M. Obara, *IEEE QE-27*, 2456 (1991)
6. S.J. Scott, *Appl. Phys. B* **56**, 201 (1993)
7. F.A. van Goor, *J. Phys. D* **26**, 404 (1993)
8. J.G. Edwards, *J. Phys. E* **8**, 663 (1975)
9. K. Midorikawa, M. Obara, and T. Fujioka, *IEEE QE-20*, 198 (1984)
10. R.S. Taylor, *Appl. Phys. B* **41**, 1 (1986)
11. J. C. M. Timmermans, Thesis, Univ. of Twente, ISBN 90-0998674-9 (1995)
12. M. Kakehata, C.H. Yang, Y. Ueno, and F. Kannari, *Appl. Phys. Lett.* **61**, 3089 (1992)

Efficient VUV light sources from rare gas excimers and their applications

Wataru Sasaki, Shoichi Kubodera and Junji Kawanaka

Department of Electrical and Electronic Engineering, University of Miyazaki,
Nishi 1-1, Gakuen-Kibanadai, Miyazaki 889-21, Japan

ABSTRACT

Efficient VUV excimer lamps with two types of discharge configurations, expanding jet discharge and silent discharge (dielectric-barrier discharge) in a variety of rare gases and their mixtures, are presented. In the jet discharges VUV output power was 9 mW with an efficiency of 10^{-2} % at 126 nm for argon excimers. Output powers of other excimers were 300 mW with 1.0 % efficiency at 146 nm for krypton excimers and 500 mW with 1.6 % efficiency at 176 nm for xenon excimers. Simultaneous emissions from hetero-nuclear rare gas excimers (ArKr^* , 135 nm) as well as homo-nuclear rare gas excimers (Ar_2^* and Kr_2^*) were observed by using rare gas mixtures of argon and krypton. Output powers and efficiencies of the silent discharge excimer lamps were 500 mW and 1.6 % for argon, 5 W and 13 % for krypton, and 5 W and 20 % for xenon excimers. In the silent discharge extremely broad band excimer emissions were observed at the center wavelengths of 145 nm for an argon/krypton mixture and of 163 nm for a krypton/xenon mixture. A PMMA plate was photo-chemically etched at the rates of 1-2 nm/min by the irradiation of the 172 nm radiation in air and argon gas atmospheres.

Keywords: Rare gas excimer, Jet discharge, Silent discharge, Rare gas cluster, VUV lamp, Photo-chemical etching, Photon processing,

1. INTRODUCTION

Rare gas excimers have been known to be one of the most efficient VUV light sources. High power laser operation of 16 MW has been reported by electron beam pumping of pressurized argon of 40 atm.[1] High power excimer lasers in the VUV spectral region are suitable for many applications such as materials processing and semiconductor lithography.[2] Such lasers, however, require a large electron beam machine, which gives us some disadvantages for applications. In some applications neither monochromatic nor coherent radiation is required. For this reason incoherent VUV sources may become an interesting alternative to lasers, especially when large areas have to be irradiated. When rare gas excimer emission could be obtained by discharge excitation, such compact light sources would be useful for industrial applications.

In this paper we review the developments of rare gas excimer light sources excited by an expanding jet discharge and a silent discharge (dielectric-barrier discharge), and show a potential application of rare gas excimer lamps to photo-chemical processing of organic materials.

Rare gas excimer discharge lamps have been developed in quasi-cw jet discharges. It was experimentally verified that rare gas excimers were directly produced from relevant rare gas clusters in expanding jet discharges.[3] The jet discharge rare gas excimer lamps are ideally suited for semiconductors processing, because their emission geometry are quasi-point sources of

VUV radiation.

It has been reported that silent discharges were suited for efficient excitation of high-intensity VUV radiation from rare gas excimers.[4] Furthermore, by using rare gas mixtures in the silent discharges, extremely broad band excimer emissions were observed at the center wavelengths of 145 nm for an argon/krypton mixture and of 163 nm for a krypton/xenon mixture.[5] In an appropriate rare gas mixture, certain energy transfer processes between rare gases were possible, resulting in the simultaneous multi-excimer emissions in a single discharge tube. In the case of a krypton/xenon mixture, an emission spectrum of almost flat-top shape was obtained with wavelengths ranging between 150 nm and 175 nm.

Photon energies of rare gas excimer emissions were 9.8 eV for argon excimers, 8.5 eV for krypton excimers and 7.2 eV for xenon excimers. These high energy photons may dissociate most of the chemical bonds both in organic and inorganic materials. A PMMA plate was photo-chemically etched by irradiation of the 172 nm radiation from a xenon excimer lamp in air and argon gas with a pressure between 0.01 mmHg and 100 mmHg. Etching rates of PMMA under a constant intensity of 172 nm emission changed from 0.5 nm/min to 2.5 nm/min, depending on the gas pressure and the gas species. It was experimentally verified that those photo-chemical reactions (photon processing) had a great potential for applications to an extremely precise machining of optical elements and/or to surface cleaning of electronic devices.

2. JET DISCHARGE EXCIMER LAMPS

Since the detail of the experimental setup has been described elsewhere[3], only brief description is presented here. A Laval nozzle of 0.4 mm throat diameter was located inside a vacuum chamber, and a pair of iron electrodes were placed at 6 mm below the nozzle end and the distance between the electrodes was 5 mm. The electrodes were connected to a 0.53 mF capacitor, which was charged up to 2 kV. When a laboratory-grade rare gas was injected from the nozzle for 5 ms (FWHM), the discharge was initiated. To increase the excimer emission power, a magnetic field strength of about 0.1 T was applied parallel to the discharge current using a pair of solenoids.

As listed in Table 1, several excimer emissions were obtained by changing relevant rare gases. When the emission geometry was approximated as a point source, the output power was

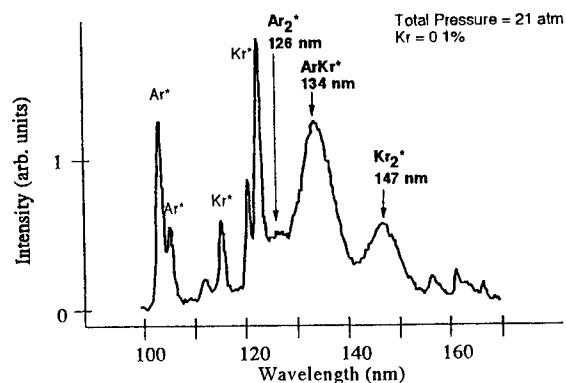


Fig. 1 Emission spectrum of argon/krypton mixture.

Table 1 Output characteristics of jet discharge excimer lamps.

	λ (nm)	$\Delta\lambda$ (nm)	P (mW)	η (%)
Ar ₂ *	126	8	9.1	8.6×10^{-3}
Kr ₂ *	147	8	300	0.89
Xe ₂ *	172	8	500	1.6
ArKr*	134 (130~138 nm)	8	6.1	5.7×10^{-3}

estimated to be 9 mW with an efficiency of 10^{-2} % at 126 nm for argon excimers. Outputs of other excimers were 300 mW with 1.0 % efficiency at 146 nm for krypton excimers and 500 mW with 1.6 % efficiency at 176 nm for xenon excimers.

Simultaneous emissions from hetero-nuclear rare gas excimers (ArKr^* at 135 nm) and homo-nuclear rare gas excimers (Ar_2^* and Kr_2^*) were observed by using rare gas mixtures of argon and krypton. Fig. 1 shows a clear ArKr^* excimer emission centered at 135 nm as well as Ar_2^* at 126 nm and Kr_2^* at 146 nm, when 0.07 % of krypton gas is mixed with 21 atm of argon gas in stagnation pressure. By further increase of krypton contents up to 35 mmHg (0.22%), the spectra of Ar_2^* excimer and ArKr^* excimer almost disappear and the only Kr_2^* excimer spectrum remains.

The jet discharge rare gas excimer lamps are ideally suited for semiconductors processing, because their geometry are quasi-point sources of VUV radiation.

3. SILENT DISCHARGE EXCIMER LAMPS

It has been reported that silent discharges (dielectric-barrier discharges) were suited for efficient excitation of high-intensity VUV radiation from rare gas excimers.[4] We also obtained rare gas excimer emissions by silent discharges in argon, krypton and xenon.

A discharge tube made of quartz with an inner diameter of 1.5 cm was sandwiched by a pair of aluminum electrodes with a length of 50 cm. A high frequency (20 kHz) voltage power supply provided voltages onto the aluminum electrodes with a peak voltage of 8 kV. In this case, output powers and efficiencies were 500 mW and 1.6 % for argon, 3.5 W and 13 % for krypton, and 5 W and 20 % for xenon excimers.

When rare gas mixtures such as argon/krypton or krypton/xenon were used in the discharge tube, extremely broadband emissions, which had emission bandwidths of about 30 nm with flat top spectral shapes, were obtained as shown in Fig. 2. Such broad band emissions consisted of hetero-nuclear excimers (ArKr^* for argon/krypton and KrXe^* for krypton/xenon mixtures) emissions as well as two homo-nuclear excimers from constituent rare gases. It was confirmed in a pulsed silent discharge that these broadband emissions were originated from hetero-nuclear rare gas excimers as well as homo-nuclear rare gas excimers.

The output powers and efficiencies of rare gas excimer lamps and mixed rare gas excimer lamps are listed in Table 2.

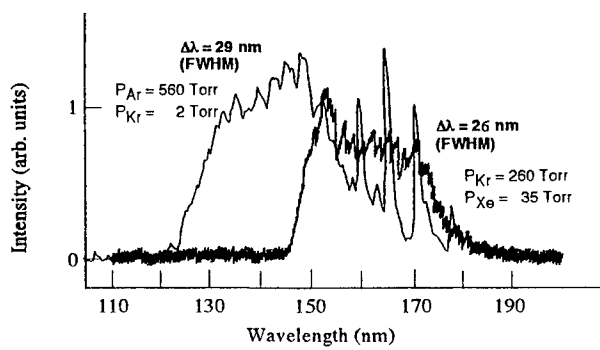


Fig. 2 Emission spectra of argon/krypton and krypton/xenon mixtures.

Table 2 Output characteristics of silent discharge excimer lamps.

	λ (nm)	$\Delta\lambda$ (nm)	P (W)	η (%)
Ar_2^*	126	9	0.9	3.4
Kr_2^*	147	12	3.4	13.1
Xe_2^*	172	13	5.3	20.4
$\text{Ar}_2^*/\text{Kr}_2^*$	145	30	0.54	2.2
$\text{Kr}_2^*/\text{Xe}_2^*$	162	30	3.4	13.6

4. PHOTON PROCESSINGS

A PMMA plate was photo-chemically etched by irradiation of the 172 nm radiation from a xenon excimer lamp in air and argon gas with a pressure between 0.01 mmHg and 100 mmHg. As shown in Fig. 3 etching rates of PMMA under a constant intensity of 172 nm emission changed from 0.5 nm/min to 2.5 nm/min by changing the pressure of air. The etch rates were measured with a Mach-Zender interferometer. Although mechanisms of such photo-chemical etching (photon processing) is not clearly understood, we consider that C-H chemical bonds were broken by the high energy photons (7.2 eV corresponding to 172 nm wavelength), together with by chemical reactions with some radicals such as N^* and/or O^* , which were generated by photo-dissociation of N_2 and O_2 .

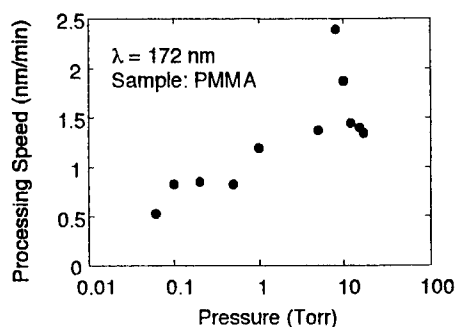


Fig. 3 Etch rates of PMMA as a function of air pressure.

5. CONCLUSIONS

We have developed efficient rare gas excimer lamps with a quasi-cw jet discharge and a silent discharge. When mixtures of rare gases were used, hetero-nuclear rare gas excimer emissions were obtained, together with homo-nuclear excimer emissions, which led to the spectra extension. From the practical view point of excimer lamps, the rare gas mixtures would have a great advantage, because the only small amount of expensive rare gases is needed when relevant excimer emissions are required. A PMMA plate was photo-chemically etched by the irradiation of the 172 nm radiation in air and argon gas atmosphere.

REFERENCES

- [1] K. Kurosawa, Y. Takigawa, W. Sasaki, M. Okuda, E. Fujiwara, K. Yoshida, and Y. Kato; IEEE J. Quantum Electron., 27, (1991) 71.
- [2] Y. Takigawa, K. Kurosawa, W. Sasaki, M. Okuda, E. Fujiwara, K. Yoshida, Y. Kato and Inoue; J. Non-Cryst. Solids, 125, (1991) 107.
- [3] J. Kawanaka, S. Kubodera, W. Sasaki, K. Kurosawa, K. Mitsuhashi, and T. Igarashi; IEEE J. Selected Topics in Quantum Electron., 1, (1995) 852.
- [4] B. Eliasson and U. Kogelchatz; Appl. Phys., B46, (1988) 299.
- [5] S. Kubodera, M. Honda, M. Kitahara, J. Kawanaka, W. Sasaki, and K. Kurosawa; Jpn. J. Appl. Phys., 34, (1995) L618.

Influence of electrode roughness on the discharge quality of a high PRF long pulse XeCl laser

I. Tassy, Ph. Delaporte, B. Fontaine, B. Forestier, M. Sentis and O. Uteza

Institut de Recherche sur les Phénomènes Hors Equilibre, U.M.R. 138 C.N.R.S. Université Aix-Marseille I & II
163, av. de Luminy, 13288 Marseille, cedex 9, FRANCE
Tél: 33 91 26 92 80; Fax: 33 91 26 92 89; E-mail: newlaser@mfmcas.univ-mrs.fr

ABSTRACT

The uniformity and stability of discharge process in a high Pulse Repetition Frequency (PRF) long pulse XeCl laser are investigated for three different copper electrode roughnesses versus PRF ($f \leq 500$ Hz; 10 shots). The discharge quality evolution is experimentally analyzed from discharge photographs obtained with a CCD video camera and pressure perturbation measurements achieved with a piezoelectric pressure probe placed very close to the discharge volume.

Keywords: excimer laser, high repetition frequency, discharge quality, electrode roughness.

1. INTRODUCTION

For many industrial applications, the achievement of reliable high Pulse Repetition frequency (PRF) and high average power excimer lasers is suitable. But the increase of the excimer laser average power through PRF increase is often limited by the development of strong non-uniform energy deposition processes which have deleterious effects on the laser output energy and laser beam quality. The discharge stability degradation origin, especially at high PRF and for long time laser operation, can result from aerothermodynamic phenomena¹, electrode characteristics (material, roughness), composition modification of the gas mixture, flow characteristics, dust contamination level, preionisation level, etc...

After a brief description of the main characteristics of the experimental setup, the uniformity and stability of the discharge process in a high PRF long pulse XeCl laser is investigated for three different copper electrode roughnesses versus PRF ($PRF \leq 500$ Hz). The other main experimental conditions are 10 shot bursts and a ~ 20 J/l.bar energy deposition.

2. DESCRIPTION OF THE LASER SYSTEM AND EXPERIMENTAL CONDITIONS

All the experiments have been performed on a UV preionized spiker-sustainer long pulse (~ 150 ns) XeCl laser which is shown in Fig.1. The laser system is composed of a fast flow subsonic closed cycle wind tunnel, a laser chamber and a high average power electrical system. The subsonic loop removes the gas between two successive shots and the flow speed (40 m.s^{-1}) is sufficient to ensure a clearing ratio of 3 at 1000 Hz. The electrical discharge circuit consists of a corona type UV preionizer system and a magnetic-spiker sustainer circuit using the overshoot mode². The sustainer capacitors ($C_s = 100$ nf) are pulsed charged to 11 kV in $\sim 1.1 \mu\text{s}$ from a 200 nf capacitor using a CX 1725 thyatron switch. The peaking capacitor bank is made up of ten 100 pf lumped capacitors ($C_{pk} = 1$ nf). Finally the spiker driver capacitor ($C_{sp} = 1.7$ nf) is continuously charged at 20 kV. The electrodes consist of a Ernst profile³ electrode and a perforated plate electrode. Both are 32 cm long with a gap of 3 cm and the discharge is ~ 1.5 cm wide and ~ 25 cm long. The mixture is made up of 99.44 % Ne, 0.47 % Xe, 0.092 % HCl at a total pressure of 3 bars. The laser resonator is equipped with plane-plane optics separated of 50 cm and composed of a high reflectivity rear reflector and a 40 % reflecting output coupler. The laser could be operated at PRF as high as 700 Hz in a burst mode (10 shots) with a laser output energy of ~ 200 mJ, a FWHM pulse duration of ~ 145 ns, a spot size of $\sim 1.3 \times 2.8 \text{ cm}^2$ and for an energy deposition of ~ 20 J/l.bar. For these laser working conditions, the laser efficiency is about 3.5 %.

An observation window set in one of the elbows of the subsonic flow loop allows the transverse visualisation of the visible light emitted by the discharge plasma (see Fig.1). The fast digitally controlled CCD video camera (PCO model Dicam 2) used in these experiments provides discharge photographs which exposure time was set to 400 ns in order to integrate the main part of the discharge process. The temporal evolution of the pressure perturbation amplitude is measured by a fast piezoelectric transducer (PCB 122A22) having the following characteristics: a $10^{-3} - 10^{+3}$ psi dynamic range, a $2 \mu\text{s}$

signal risetime and a resonance self frequency of 250 kHz. The pressure probe is inserted downstream the discharge volume in the R_{ext} innerwall at 6.5 cm of the centre of the optic (see Fig.1).

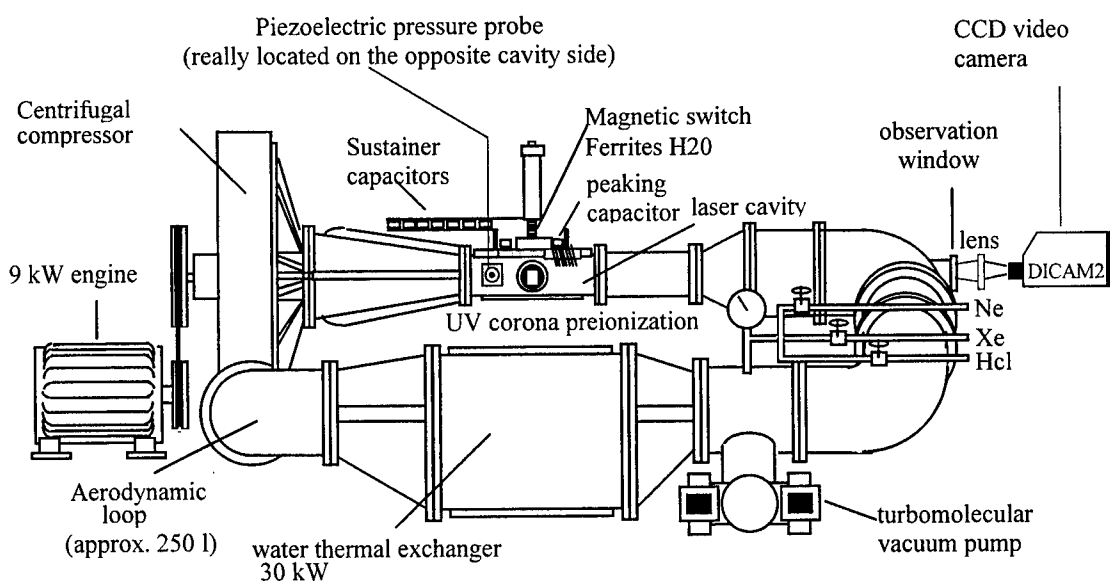


Figure 1: LUX test-bed scheme and main diagnostics.

3. INFLUENCE OF THE ELECTRODE ROUGHNESS ON THE DISCHARGE QUALITY IN SINGLE SHOT REGIME

To understand the electrode roughness influence on the discharge stability and uniformity, the same copper electrode (CuAl Electrolytic : Cu 99%, Ag 1%) has been prepared with three different roughnesses in accordance with the following process. Before each experiment, the copper electrode has been pounced with different sandpapers (3M inc. paper) providing to the electrode the following roughness characteristics: grits « 80 » (high roughness), grits « 320 » (medium roughness) and grits « 600 » (low roughness).

Previous studies⁴ have shown that the pressure perturbation signatures achieved with a pressure probe is a powerful means to evaluate the uniformity and stability of a discharge process. Fig.2 presents then the time evolution of pressure perturbations recorded in single shot mode operation (without flow) with the pressure probe for the three different copper electrode roughnesses. The discharge process is considered to be instantaneous and therefore determines the time origin ($t = 0$ ms) materialized in fig.2 by an artefact. This assumption is reasonable according to both pressure probe risetime and pressure signal dynamics, the sound speed in the active medium being approximated by the sound speed in pure neon ($v_{sound} \approx 460 \text{ m.s}^{-1}$).

The comparison of the three graphs shows that the medium roughness electrode develops a higher number of significant overpressures than both low and high roughness electrodes. The electrode of medium roughness presents surface non-uniformities whose dimensions promote the development of strong electric arcs probably appearing early during the discharge process and therefore inducing a lower discharge quality and a premature termination of the laser pulse⁵.

The main results obtained with the three different electrode roughnesses are summarized in table 1. They confirm that the medium roughness electrode does not allow an efficient extraction of the laser energy from the active volume.

Electrode roughness	high (grits 80)	medium (grits 320)	low (grits 600)
Output energy (mJ)	190	175	210
FWHM pulse duration (ns)	140	127	136
Efficiency (%)	3	2.7	3.5

Table 1: Main laser output characteristics obtained with the three electrode roughnesses.

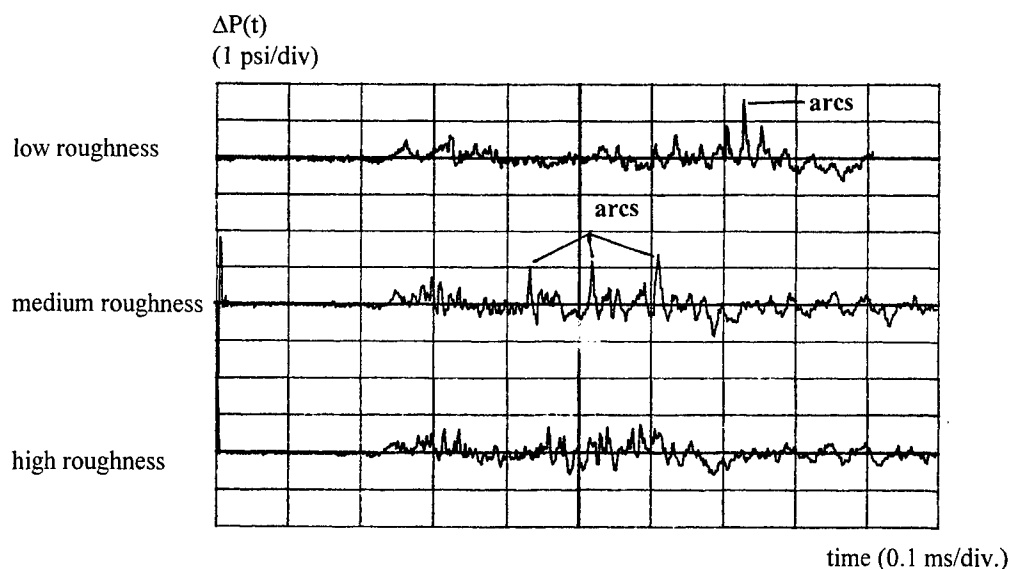


Figure 2: time evolution of pressure perturbations for the three copper electrode roughnesses (X: 0.1 ms/div; .Y: 1 psi/div).

4. INFLUENCE OF THE ELECTRODE ROUGHNESS ON THE DISCHARGE QUALITY IN HIGH PRF MODE OPERATION

Fig.3,4 respectively present the 10th shot output energy and FWHM pulse duration evolutions versus PRF for the three different electrode roughnesses.

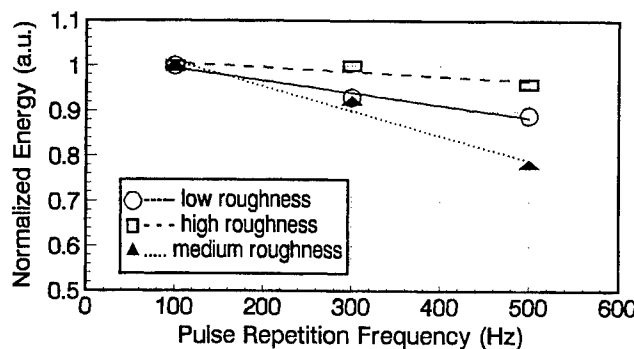


Figure 3: Output laser energy versus PRF for the three electrode roughnesses.

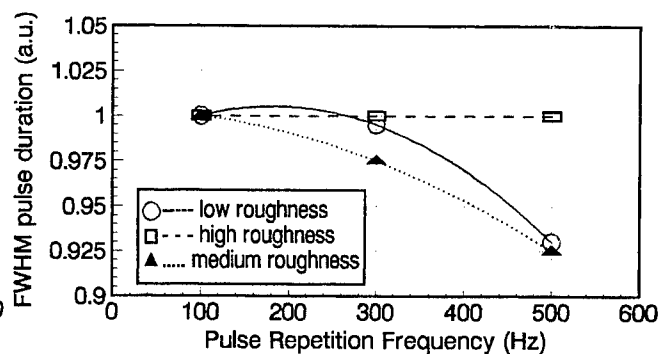


Figure 4: FWHM pulse duration versus PRF for the three electrode roughnesses.

The electrodes of high and low roughness allow to extract roughly the same laser energy versus PRF whereas the electrode of intermediate surface state (medium roughness) does not permit to maintain a ~ constant output energy for PRF ≥ 300 Hz. It can also be mentioned that the reduction of the FWHM pulse duration even occur at relatively low PRF ($f = 300$ Hz) for the medium roughness electrode. The bad laser performances obtained with this electrode can be related to the stronger spatial and temporal instability of the discharge process previously taken in evidence by the pressure probe measurements in the single shot regime and obviously amplified in the high PRF mode operation.

Better results have been obtained with the low and high roughness electrodes confirming the previous ones observed in the single shot regime. A possible explanation could be the following: the low roughness electrode contains surface non-uniformities presumably promoting the development of few electric arcs which induce a premature termination of the laser pulse (see fig.4) but delayed with respect to the one occurring in the case of the medium roughness electrode. On the other hand the high roughness electrode probably produces a lot of streamers ~ homogeneously distributed which do not affect the FWHM pulse duration as it can be seen on fig.4. As a result, a better control of the spatial and temporal

homogeneity of the current during the discharge process is achieved with both electrodes having a low and high roughness as shown by the following time-integrated discharge photographs taken at 500 Hz (see Figure 5).

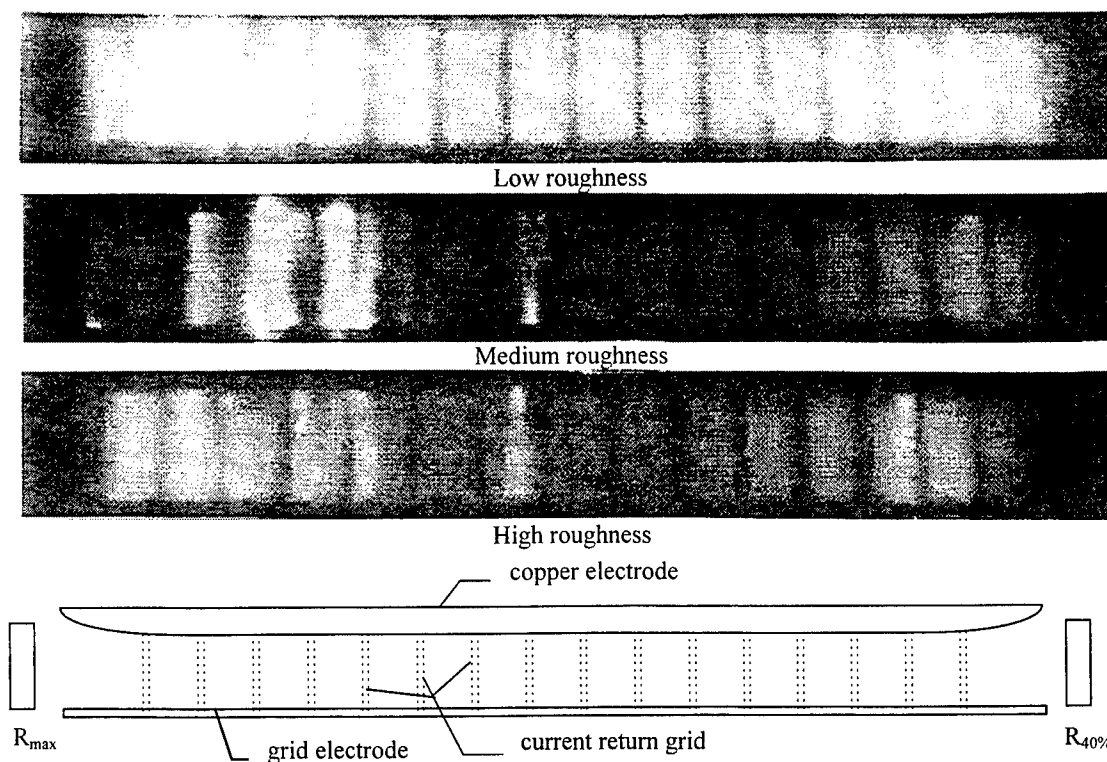


Figure 5: Time-integrated (exposure time = 400 ns) discharge photographs obtained at 500 Hz for the three electrode roughnesses.

5. CONCLUSIONS

The electrode roughness plays a leading role for the achievement of stable discharge processes. From our results, low and high electrode roughnesses seem suitable to high PRF mode operation because they promote more homogeneous and stable spatial distributions of the discharge current. However, further experiments have to be carried out to study precisely the occurrence time of the discharge quality degradation according to the different roughnesses. The behaviour of the different electrodes on longer bursts (a few hundreds and thousands of shots) has also to be studied to better determine the best electrode roughness for high PRF permanent mode operation.

6. REFERENCES

1. V.Y. Baranov, V.M. Borisov, A.Y. Vinokhodov, F.I. Vysikailo, A.V. Gubarev, Yu.B. Kiryukhin, I.E. Krayushkin, and S.A. Laptev, "Acoustic vibrations in the gas-discharge chamber of a fast-flow pulse-periodic laser," *Sov. J. Quant. Electronics*, **17** (6), 766-770, June 1987.
2. Ph. Delaporte, R.S. Taylor and K.E. Leopold, "Comparison of the diode, switch, and overshoot modes of magnetic-spiker excimer laser excitation," *J. Appl. Phys.* **73** (11), 7093-7101, June 1993.
3. J. Ernst, "Uniform-field electrodes with minimum width," *Optics communications*, **49** (4), 275-277, March 1984.
4. J.P. Truong, O. Uteza, M.L. Sentis, Ph. Delaporte, B. Forestier and B. Fontaine, "Aerothermodynamic and thermal phenomena in a high pulse-repetition rate XeCl laser," *Proc. of the 19th ISSW*, **3**, Springer-Verlag, 335-340, 1995.
5. M.J. Kushner, "Microarcs as a termination mechanism of optical pulses in electric-discharge-excited KrF excimer lasers", *IEEE Trans. on Plasma Science*, **19** (2), 387-399, April 1991.

Kr₂⁺Cs : a new class of triatomic excimer molecules

Ph. Delaporte, M. Voitik, Ch. Tarras, M. Sentis, O. Uteza, B. Fontaine, B. Forestier

Institut de Recherche sur les Phénomènes Hors Equilibre
U.M.R. 138 CNRS Aix - Marseille I & II universities
Pôle scientifique et technologique de Luminy
163 Av. de luminy, 13288 Marseille cedex 9
France
Tel. : (33).91.26.92.80; Fax. : (33).91.26.92.89
E. mail : newlaser@mfncalas.univ-mrs.fr

ABSTRACT

Alkali rare gas triatomic ionic excimers have been observed for the first time. These molecules have been produced by electron beam excitation of rare gas alkali mixtures at high pressure and high temperature. Emission spectra centred at ~159nm have been observed and attributed to Kr₂⁺Cs ions. Lifetimes and binding energies of the lowest excited states have been estimated. Simple kinetic considerations allowed us to propose two formation processes of these ions and to estimate their rate constant.

Keywords: ionic excimer, triatomic, kinetic, spectroscopy, alkali, rare gas

1. INTRODUCTION

There is only few possibilities to receive intense emission spectra in Vacuum UltraViolet (VUV) region from molecules. Rare gas excimers, molecular fluorine and diatomic ionic excimers are such sources. Particularly, diatomic rare gas (Rg) alkali (A) ionic excimers were theoretically proposed¹ and then intensively investigated²⁻⁷ to extend the gas laser performances towards the shorter wavelengths. These Rg⁺A molecules are efficient VUV sources and emission spectra have been observed from 66.5nm for He⁺Li to 189.9nm for Xe⁺Li.

In this paper, we present the first observation of triatomic ionic excimer such as Rg₂⁺A strongly emitting in the VUV spectral range. These molecules are of fundamental interest as a new short wavelength source, and as a new kind of excimer, giving informations on the binding energies of ligands to metal ions.

We investigated more precisely the Kr₂⁺Cs molecule. This ion was produced by electron beam excitation of argon/krypton/cesium mixtures at high pressure (>100mbar) and high temperature (>300°C). Observation of the VUV emission spectra of these ionic molecules allowed us to give some conclusions about the electronic structure and the formation kinetic processes of these excimers.

2. EXPERIMENTAL SETUP

The experimental setup used to investigate the triatomic ionic excimers was described in detail elsewhere⁸. So, only a brief description of the main features necessary for the understanding of the experimental results is given.

A cold cathode electron gun was used to excite transversally the gas mixtures. This electron gun, energized by a 300 kV- 1500 J Marx generator (MX 31 from Physics International Company), is separated from cell, with an active volume of 1.7 x 1.7 x 15 cm³, by a 25 µm thick titanium foil. For the experiments presented in this paper we worked with a current density of about 1 A/cm² during 800 ns, corresponding to a voltage of 210 kV applied to the diode. In these conditions, a typical energy deposition of a few hundred µJ/cm³ has been achieved in one bar of argon. The reproducibility of the signals from the electron gun was within 15%. In order to obtain a sufficient alkali vapor density inside the cell it is necessary to heat the gas up to 400°C. The measured temperature profile along the optical axis has a flat temperature distribution inside the active volume.

The gas inside the cell was separated from the detection apparatus by a magnesium-fluoride window. The spectra emitted from the excited zone are observed with a 0.2 m Seya-Namioka vacuum ultraviolet monochromator (VM 502 Acton Research Corporation) with a 1200 lines/mm grating. The fluorescence emissions are registered either time integrated by an optical multichannel analyser (IVUV 700 Princeton Instruments) with a spectral resolution of 0.4 nm or time dependent by a fast solar-blind photomultiplier photomultiplier (Thorn Emi VUV C640).

3. EXPERIMENTAL RESULTS

Experiments were performed by electron-beam excitation of krypton - cesium gas mixtures with and without argon as buffer gas. figure 1 presents some spectra observed for different conditions of gas mixtures. Before the introduction of cesium, the spectra observed in the 120nm - 180nm region after the excitation of pure krypton or argon-krypton mixture are only due to the broad second continuum of krypton (Kr_2^+) centred around 144nm (at $\sim 350^\circ C$). In presence of alkali vapor, the Kr_2^+ signal is strongly reduced and two other emission bands appear. As it is shown in figure 1, the spectra exhibit a narrow band (FWHM $\approx 1.5nm$) at 132nm, the Kr_2^+ emission and a new broad continuum centred around 159nm. The 132nm emission has been extensively studied⁷ and is clearly attributed to the ionic excimer Kr^+Cs . The other emission which appears only in presence of cesium, and for krypton pressure higher than 80mbar, is attributed by us to the triatomic ionic excimer Kr_2^+Cs .

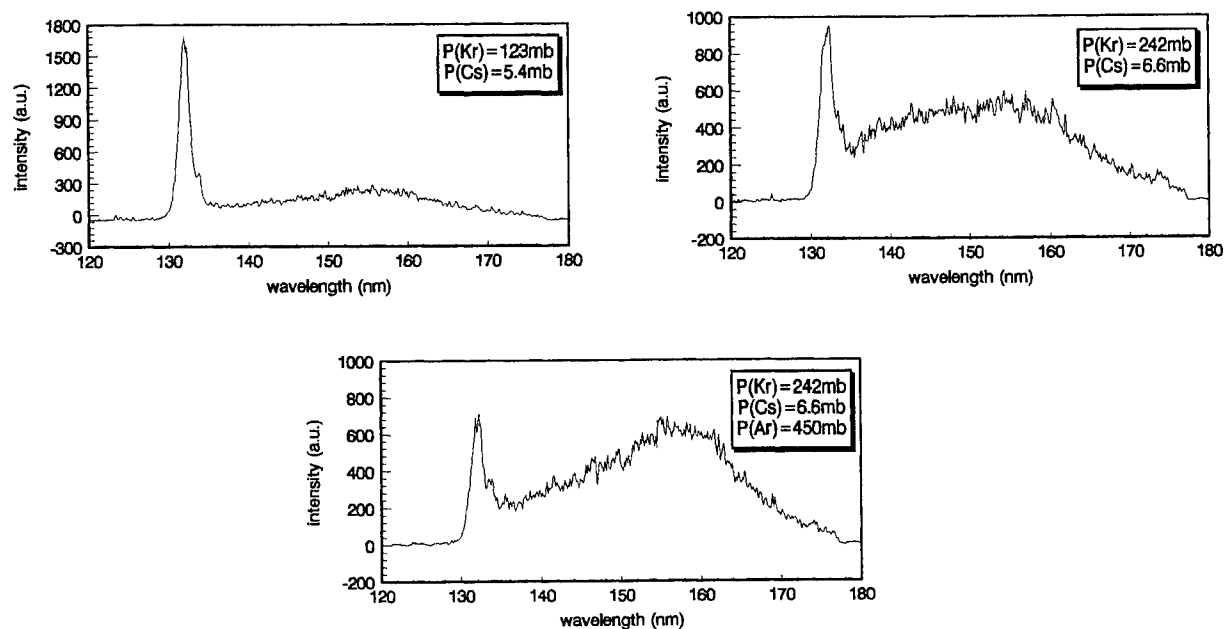


Fig. 1. Fluorescence emission spectra between 120nm and 180nm obtained by e-beam excitation of alkali rare gas mixtures

As it is shown by the figure 1, the intensities of the three emission bands have a strong dependence of cesium, krypton and argon pressures. To have a better understanding of the relative efficiency of the formation and competition processes involved in the kinetic, we studied the intensities of Kr_2^+ , Kr^+Cs and Kr_2^+Cs for a wide range of pressure of the three components. Figure 2 presents the most significant results of this study which allowed us to propose a simple kinetic scheme presented in § 4.2 and to evaluate some kinetic rate coefficients.

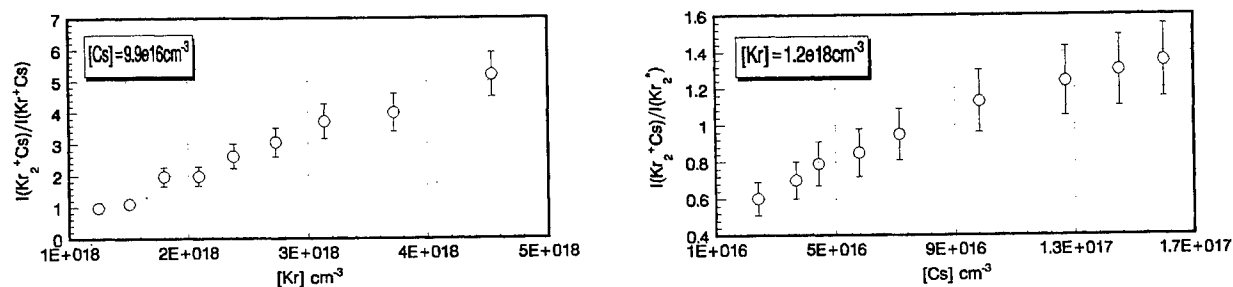


Fig. 2. Relative intensities of Kr_2^+ , Kr^+Cs , Kr_2^+Cs as a function of gas pressures. (a) $I(Kr_2^+Cs)/I(Kr^+Cs)$ as a function of Kr density, (b) $I(Kr_2^+Cs)/I(Kr_2^+)$ as a function of Cs density.

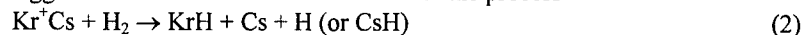
4. DISCUSSION

4.1 Spectroscopy

The central wavelengths of the two broad continua of Kr_2^+ and Kr_2^+Cs excimers are very close and it is impossible to precisely determine the center of the Kr_2^+Cs band from the spectra like those presented in figure 1. However, the addition of hydrogen to our mixture induced a complete quenching of Kr^+Cs and Kr_2^+ emissions due to the very fast charge exchange process



with a rate coefficient⁹ of $2 \cdot 10^{-10}$. And we suggest near the same coefficient value for the process



The Kr_2^+Cs emission was also strongly quenched, because of the quenching of its precursors, but not completely because the Kr_2^+Cs molecule has not enough energy to produce an efficient charge exchange process like (2), and it is still possible to observe this emission. The spectrum of figure 3 which has been recorded under these experimental conditions clearly shows that the Kr_2^+Cs emission band is centered at 159nm.

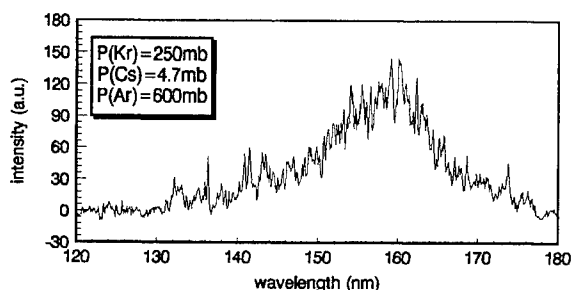


Fig. 3. VUV fluorescence emission spectrum obtained by e-beam excitation of alkali rare gas hydrogen mixture.

From simple energetic estimations taking into account the binding energy of 1.15 eV of a Kr_2^+ molecule and 0.89 eV of a Kr^+Cs one, it is clear that the binding energy for Kr_2^+Cs is about of ~ 0.9 eV, near the same as for a Kr^+Cs molecule. From the very broad, structureless, typically excimer character of the emission spectra, a repulsive behaviour of the ground state of Kr_2^+Cs , in difference for Kr^+Cs , is obvious. This experimental result is in a contradiction with calculations¹⁰. In this paper, the authors predict by ab initio calculations near the same binding energy for Rg_2M^+ (the $Rg - RgM^+$ bond) as for RgM^+ molecules, where M^+ is a metal ion, in particular, an alkali one. But the essentially repulsive character of a ground state is a plain fact for Kr_2^+Cs and for other triatomic rare gas - alkali molecules.

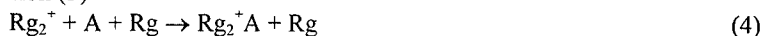
4.2 Kinetics

When an electron beam is used to excite an alkali rare gas mixture, the main formation process for diatomic ionic excimer Rg^+A is the three body reaction¹¹

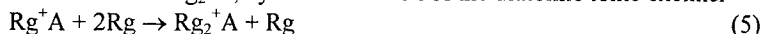


The rare gas ions are directly produce by collisions with the electrons of the beam or by charge transfert reactions beetwen the buffer gas ions (typically Ar^+) and the rare gas atoms.

Because of the very similar electronic structure of the rare gas ion Rg^+ and the molecular ion Rg_2^+ , we suggested to create the triatomic ionic excimer Rg_2^+A by electron beam excitation of alkali rare gas mixture. The first formation process proposed for these molecules is similar to reaction (3)



An other process has been also proposed for the formation of Rg_2^+A , by recombination of the diatomic ionic excimer



The efficiency of this last formation process is clearly improved by a high pressure of rare gas. Also, the two following reactions are more efficient at high rare gas pressures:



and



The first one is the competition process for the formation of Rg^+A (3) and induce an increase of the Rg_2^+ density, and the second one is a quenching process for Rg^+A emission and contribute also to the Rg_2^+ population. In both case, the higher Rg_2^+ density leads to a more efficient formation of Rg_2^+A through the reaction (4). These considerations allow to explain that for high rare gas pressures the relative intensity Rg_2^+A/Rg^+A increase, as it is shown on figure 2.a.

Rg_2^+ molecule is also the precursor of the second continuum of rare gas Rg_2^+ . So, to improve the production of the triatomic ionic excimer Rg_2^+A relatively to the Rg_2^+ molecule, at high rare gas pressure, it is necessary to increase the alkali pressure by working at higher gas temperature. The reaction (5) becomes efficient and, as we can see on figure 2.b, the relative intensity $\text{Rg}_2^+\text{A}/\text{Rg}_2^+$ increase with alkali pressure.

By consideration of a simple kinetic model including the formation and the main quenching processes of Kr_2^+ , Kr^+Cs and Kr_2^+Cs emissions, we estimated a value of the spontaneous lifetime of the Kr_2^+Cs excimers at $\tau_{s2} \sim 5$ ns, near the same as for Kr^+Cs . Previously, we determined the rate coefficient of the main reactions involved in the Kr^+Cs kinetic when argon/krypton/cesium mixture are excited by an electron beam⁷. With these values and the evolution of the relative intensity $\text{Rg}_2^+\text{A}/\text{Rg}_2^+$ as a function of alkali and rare gas pressures, we estimated the rate coefficients for Kr_2^+Cs formation to $k_5 \approx 5 \times 10^{-30} \text{ cm}^6/\text{s}$ for the reaction (5) and $k_4 \approx 10^{-30} \text{ cm}^6/\text{s}$ for the process (4).

5. CONCLUSION

In spite of the high Kr_2^+Cs emission intensity, it is impossible to consider this triatomic rare gas - alkali ionic excimers as a suitable candidates for a lasing. The reasons are the same than for Kr^+Cs ⁷, and this is due to strong competition processes and a high photoionization of alkali in a VUV region.

By electron beam excitation of other alkali rare gas mixtures, we observed also the emission spectra of Xe_2^+Cs (190nm), Kr_2^+Rb (160nm) and Ar_2^+Cs (135nm).

6. ACKNOWLEDGMENTS

The authors like to thank the French DRET for the financial support of this work.

7. REFERENCES

1. N. G. Basov, M. G. Voitik, V. S. Zuev, and V. P. Kutakhov, 'feasibility of stimulated emission of radiation from ionic heteronuclear molecules', *Sov. J. Quant. Electr* **15**, 1455 - 1460, (1985)
2. J. Fiedler et al, 'VUV-transitions in ionic rare-gas alkali molecules', *Z. Phys D - Atoms, molecules and clusters* **11**, 141 - 145, (1989)
3. Da Xing, Ken-ichi Ueda, and Hiroshi Takuma, ' Vacuum ultraviolet transitions from rare-gas alkali ionic excimers (XeRb^+ and $(\text{KrRb})^+$ by electron beam excitation', *Appl. Phys Lett.* **59**, 1028 - 1030, (1991)
4. H. M. J. Bastiaens, F. T. J. L. Lankhorst, P. J. M. Peters, and W. J. Witteman, 'Vacuum ultraviolet fluorescence of (XeRb^+) produced in an electron-beam-pumped gas mixture', *Appl. Phys. Lett.* **60**, 2834 - 2836, (1992)
5. P. Millar, G. Warwar, P. J. Wisoff, R. Sauerbrey, and K. Balasubramanian, 'Electron beam excitation of rare-gas alkali ionic excimaers', *Appl. Phys. Lett.* **55**, 2176 - 2178, (19 89)
6. D. Lo and J. Lawless, 'Fluorescence emissions of rare-gas - alkali ionic excimers in electrical discharges', *Optics communications*, **86**, 151 - 155, 1991.
7. H. Tischler, Ph. Delaporte, B. Fontaine, M. Sentis, 'Vacuum ultraviolet emissions from the ionic excimer molecules (KrCs^+ and $(\text{HeAr})^+$ by low-energy electron-beam excitation', *IEEE J. Selected Topics Quantum Electron* **1**, 877 - 885, (1995).
8. H. Tischler, Ph. Delaporte, B. Fontaine, B. Forestier, M. Sentis, 'Design and performance of a high-temperature fluorescence cell for discharge and electron-beam excited gas mixture', *Rev. Sci. Instrum.* **67** (7), July 1996.
9. D. L. Albritton. *Atomic Data & Nuclear Data Tables* **22**, 1 (1978).
10. CH. W. Bauschlicher Jr, H. Partridge, S. R. Langhoff, 'Comparison of the bonding between ML^+ and ML_2^+ ($\text{M}=\text{metal}$, $\text{L}=\text{noble gas}$)', *Chem. Phys. Lett.* **165** (2,3), 272 - 276, (1990)
11. M. Schumann, H. Langhoff, 'kinetic studies of ionic excimers', *J. Chem. Phys.* **101**, 4769 - 4777, (1994)

State and prospects of the XeF(C-A) optically pumped laser

S.V. Mitko, V.N. Ochkin,
Lebedev Physics Institute, Moscow.
F.A. van Goor, W.J. Witteman,
Univ. of Twente, The Netherlands.

ABSTRACT

Experimental and theoretical results are presented of a XeF(C-A) blue green laser driven by 5kJ energy. The laser was pumped by a ferrite induced discharge of 90 cm long. An output energy of 0.22J has been obtained with a plane - parallel resonator. A code to simulate the laser has been developed. Numerical results for a wide range of conditions are compared with experiments performed by us and other authors. It is found that the intracavity refractive losses limit the laser operation for XeF₂ pressures above 3 Torr. The laser output depends strongly on the discharge-cavity length ratio. Possible ways to increase the laser power and efficiency are discussed.

Keywords: XeF laser, C-A transition, optically pumped, surface discharge, ferrite

1. INTRODUCTION

The first XeF(C-A) optically pumped laser at 480nm was demonstrated in 1978 using the e-beam fluorescence of Xe⁺₂ at 172 nm to photodissociate XeF₂ [1]. Later [2,3,4] this laser was pumped by an open surface discharge allowing a pulse repetitive operating mode. Energies up to 117 J were obtained with an efficiency of about $1.3 \cdot 10^{-3}$. In this paper we consider two experimental situations using an open surface discharge both experimentally and theoretically [5].

2. THE PUMPING SOURCE

Experiments show that a bleaching wave proceeds from the discharge surface as an almost perfect hollow semi-cylinder [4]. It means that the pumping discharge is not optically thick and cannot be considered as a black body radiator. Actually, if we assume the black body radiator, the speed of the bleaching wave in the direction normal to the surface has to be two times greater than that in the tangential direction. So, it will not be the perfect semi-cylinder in the cross section of the wave, as assumed in [6]. The speed of the bleaching wave expansion is much higher than that of the discharge. For typical experimental conditions it equals to about 10 km/s compared to the discharge speed of about 1 km/s [2-4,7]. Thus, it is possible to consider the pumping discharge as an infinitely thin linear light source. This source is characterised by the number of photons emitted to the unit body angle and unit spectral region for the unit time interval from the unit length - $W(t)$ (phot/sec·cm·ster·nm). In this case, the equation of the XeF₂ photodissociation has the form:

$$\frac{dN}{dt} = -\frac{2N}{R} \int_0^{\pi/2} d\theta \int_0^\infty d\lambda W(t, \lambda, \theta) \sigma(\lambda) \exp - \left\{ \frac{\sigma(\lambda)}{\cos\theta} \int_0^R dr N(R, t) \right\} \quad (1)$$

We have determined the intensity of the pumping pulse, $W(t)$, assumed to be constant over the XeF₂ absorption band, by measuring the radius, $R(t)$, and the speed, dR/dt of the bleaching wave [5]:

$$W(t) = \frac{dR}{dt} \frac{(R N_0)^{\frac{1-k}{k}}}{k \pi \Delta\lambda} (\sigma_{\max})^{\frac{1-2k}{k}} \frac{1}{a^{\frac{1}{k}}} \quad (2)$$

with a and k fitted to the experimental data. When $k=0.5$, (2) gives the relation similar to that obtained analytically in [7] assuming a stationary profile of the bleaching wave:

$$W(t) = \frac{2}{\pi \Delta\lambda} R \frac{dR}{dt} N_0 \frac{1}{a^2} \quad (3)$$

3. ELEMENTARY PROCESSES IN THE XEF(C-A) LASER

Principal reactions and rate constants that are of importance in the kinetics of the XeF(C-A) optically pumped laser were taken from [6]. Only a few modifications were made:

- (I) One absorption band of XeF₂ centred at 158 nm was taken into account because the absorption of photons in the band at 230 nm doesn't result in the formation of XeF(B,C,D) excited states.

- (II) It was shown in [6] that the heating of the working mixture during photodissociation of XeF_2 doesn't exceed $\sim 100\text{K}$, so all temperature dependent constants were taken at room temperature.
- (III) Quenching of XeF(B,C) by binary collisions with Ar and N_2 was included in the kinetic model.

4. DYNAMICS OF THE LASER FLUX

The build-up time of the optical flux of our laser can be estimated using the relation [9]:

$$T \cong \frac{G L_c}{c g L_a} \quad (4)$$

where T - build-up time; G - amplification of the spontaneous emission up to the lasing level, L_a and L_c are the lengths of the active medium and the cavity respectively. It was shown in [9] that $G \approx 18 \pm 1$ for the lasers in the visible spectral region with $L_c \sim 0.5\text{-}2\text{m}$. The gain for C-A transition typically achieved in experiments is low ($\sim 0.3\% \text{ cm}^{-1}$) since the cross section for stimulated emission is low ($\sim 10^{-17} \text{ cm}^2$) and the linewidth is large $\sim 70 \text{ nm}$ [2]. Substituting $g = 3 \cdot 10^{-3} \text{ cm}^{-1}$, $G = 18$ and $L_c/L_a = 2$ into (4), one obtains $T = 0.4 \mu\text{s}$. Hence, the build-up time is compared to the pumping pulse duration of about $1 \mu\text{s}$, thereby limiting the laser efficiency. The build-up time depends on L_a/L_c and so does the laser output power. These factors haven't been taken into account in previous works.

5. INHOMOGENEITY OF THE ACTIVE MEDIUM

Experiments with plane-parallel and plane-concave resonators showed that gradients in the refractive index of the order 10^{-7} cm^{-1} [4, 7] are primarily responsible for internal losses [7]. There are two main reasons for the change of the refractive index in the bleaching wave in XeF_2 : The difference in the polarizability of the parent XeF_2 molecule and the combined polarizability of xenon and fluorine atoms. The chemical composition changes from XeF_2 before the front of the bleaching wave to the xenon atom and two atoms of fluorine behind it. This leads to a variation proportional to the initial XeF_2 concentration of the refractive index [7]. (about $1.5 \cdot 10^{-7}$ at a XeF_2 pressure of 2 Torr). The second reason is an increase in gas mixture pressure because of heat release during XeF_2 photodissociation. The rise in pressure results in gas density perturbations and a hence in a change of the refractive index [10]. Our experiments show that the speed of the bleaching wave, is about 14 km/s at these conditions. It can be shown that the gas dynamic component in the refractive index change is about $4 \cdot 10^{-8}$. Which is small compared to that related with the disruption of chemical bonds in XeF_2 . Therefore, it is possible to assume a linear dependence of Δn on the initial XeF_2 concentration, $[\text{XeF}_2]$. In general, the question about the optical inhomogeneities requires further studies. In our model we used for the intracavity losses:

$$\alpha = \frac{1}{w} \left[2 \Delta n \frac{L_a}{L_c} \right]^{1/2} \quad (5)$$

where w is the width of the lasing region defined as the width of the spatial distribution of dN/dt (Sec Sec. 2) at the half of its peak magnitude.

$$\Delta n = \varepsilon [\text{XeF}_2] \quad (6)$$

where ε was chosen such to get the best agreement between the calculations and the experimental results: $\varepsilon = 2.9 \cdot 10^{-7}$.

6. EXPERIMENTAL RESULTS, COMPARISON WITH COMPUTATIONAL RESULTS

6.1 XeF(C-A) laser with 5 kJ input energy

A detailed description of the device and experimental technique has been given in [11]. The laser was powered by 5 kJ energy stored in a capacitor bank. A pumping discharge was initiated by a ferrite rod of 90 cm long. The rod was positioned

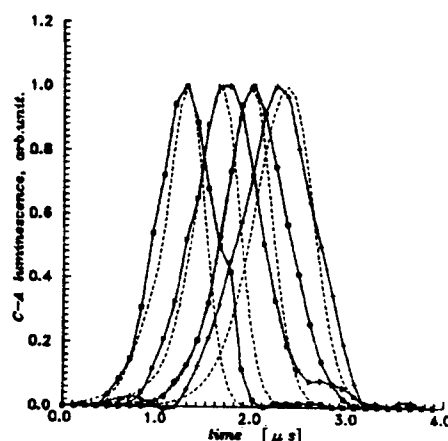


Figure 1 C→A luminescence at different distances from the ferrite surface versus time.
Solid lines: measured data.
Dotted lines: calculated.
□ 8.6 mm; ▴ 13.6 mm; ○ 18.6 mm; + 24.3 mm

at the edge of the clear laser aperture of 8.5 cm in diameter. The measurements to determine the pump source intensity, $W(t)$, were performed with a mixture of $N_2:Ar$ (1:3) at total pressure of 0.56 atm. Then, the waveforms of C-A luminescence at various distances from the discharge were measured in the same mixture with 2.1 Torr of XeF_2 added. The waveforms of C-A luminescence are shown in Fig. 1 by solid lines. To get the absolute value of the pumping flux, $W(t)$, we fitted the peak intensity of the experimental waveform to obtain the closest agreement between the observed and calculated luminescence waveforms. The calculated waveforms of C-A luminescence are shown in Fig. 1 by dashed curves. This yielded a peak value for $W(t)$ of $5.5 \cdot 10^{21}$ photons/sec-cm-nm-ster (6.91 kW-cm-nm-ster). The resulting intensity, $W(t)$, of the pumping discharge is shown in Fig. 2 by the curve 1. The results of calculations were then compared with the experiment when the device was operating as a laser with the same parameters of the working mixture. In this experiment a plane-parallel resonator consisted of two dielectric mirrors separated by a distance of 174 cm was used. One of the mirrors has a reflection of 99.9% and the other, the out-coupling mirror, had a transmission of 5%, both at the $XeF(C-A)$ emission wavelength. The transmission of the mirrors at the wavelength of the competing $XeF(B-X)$ transition was larger than 85%. Because the experimental conditions and the pumping source intensity were well defined, this comparison was used to obtain the proportionality coefficient, ϵ , between the refractive index change and the initial density of XeF_2 in the relation (6). Experimentally a laser energy of 225mJ was obtained while the calculation yielded 220mJ. To verify our method for a more wider range of experimental conditions we have simulated a more powerful laser.

6.2 $XeF(C-A)$ laser with 90 kJ input energy

As experiments with a small-scale laser were used to determine the ϵ coefficient in (6), the only fitting parameter in the numerical code, we were forced to compare our computational results with experiments conducted by other authors preferable with conditions far away from those in our experiments. One of the most detailed description of experiments with a large-scale laser is available in [3,4]. The laser was pumped by a surface creeping discharge of 190 cm long. The built-in optical resonator has a base of 280 cm long and consisted of two plane dielectrically coated mirrors with an optical diameter

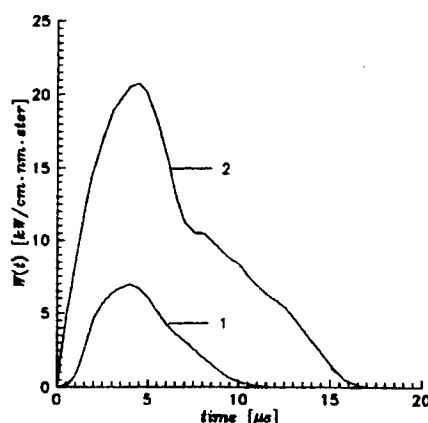


Figure 2 The intensity of the pumping pulse, W , versus time.

- 1 - energy input 5kJ
- 2 - energy input 90 kJ [4]

of 20 cm. One of the mirrors had a reflection of 0.99 and the other mirror with a reflection of 0.77 was used. The laser was filled by a mixture of $N_2:Ar$ (1:3) at a total pressure of 1.4 atm with varying amounts of XeF_2 . A pumping source was located on a side wall of a working chamber ($12 \times 20 \text{ cm}^2$). The distance between the optic axis of the resonator and the centre of the discharge was 6 cm. The discharge was powered by an energy of 90 kJ. To determine the pumping source parameters we used

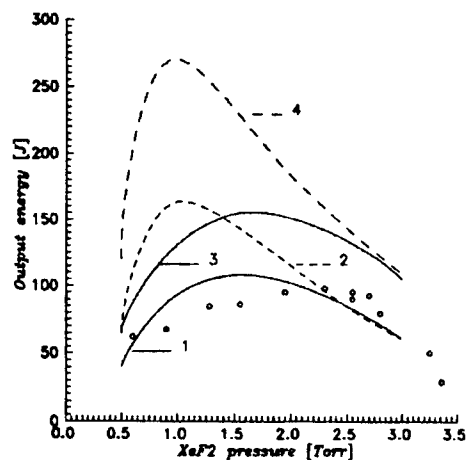


Figure 3 Dependence of the laser output energy on XeF_2 pressure.

- 270 Torr- N_2 ; 790 Torr-Ar. Mirror reflectivities: $R_1=0.99$; $R_2=0.77$
- 1- calculation for the conditions of [4].
- 2- the same as 1 but with an increased laser aperture.
- 3- the same as 1 but with $L_a=L_c=190 \text{ cm}$.
- 4- the same as 3 but with an increased laser aperture.
- oooooo experiment [4].

the waveform of the pumping pulse depicted in [4] taking into account that the efficiency of the open discharge slightly depends on its length, electric input and the surrounding gas pressure. Accordingly to [4] this efficiency is equal to about 10% in the pumping band of XeF_2 . Thus, we calculated the total quantity of dissociated XeF_2 molecules which corresponds to an efficiency of 10%. Then we fitted the peak intensity of the experimental waveform, $W(t)$, to obtain the amount of dissociated molecules. This gave a peak value for, $W(t)$, of $1.65 \cdot 10^{22}$ photons/sec-cm-nm-ster (20.7kW/cm-nm-ster). The intensity of the pumping pulse is shown in Fig. 2 by the curve 2. The dependence of the output laser energy on the XeF_2 initial pressure is shown in Fig. 3. Points are experimental results from [4] and the solid curve 1 is the result of our calculation. Calculations were made with the same coefficient ϵ used in formula (6). In view, that the accuracy of experiments is about 20%, and an accuracy of reaction rates is about 20-30%, the agreement between the calculations and experiments may be considered as good.

7. CONCLUSIONS

Calculations performed for the laser driven by 5 kJ energy showed that an energy of 1.3 J can be obtained with this device at a XeF_2 pressure of 1 Torr. When the limiting effect of the laser aperture is removed an energy of about 2 J can be obtained. A second option to increase the efficiency is to reduce the build-up time of the intracavity photon flux. To verify this assumption, we calculated the output energies that can be extracted when the cavity length L_c is equal to the discharge length L_a . Results of the calculation for the 90 kJ driven laser with $L_a=L_c=190$ cm are shown in Fig. 3. The solid curve 3 corresponds to the laser aperture reported in [4] while the case of an increased aperture is shown by the dashed curve 4. A significant increment of the output energy due to the reduction of the laser sizes is seen. Similar calculations for the laser driven by 5 kJ energy gave even more optimistic results. An output energy of 6 J can be extracted with the present laser aperture and 12 J with an increased aperture if $L_a=L_c=90$ cm. The output energies obtained to date with the optically pumped $\text{XeF}(\text{C-A})$ lasers are plotted in Fig. 4. versus the energy stored in the capacitor. The possible increase in the output energy is also shown for the two devices described above. The solid curves correspond to a constant efficiency. It is seen that under optimum conditions the efficiency of the laser with a small input is the same as that for the larger device.

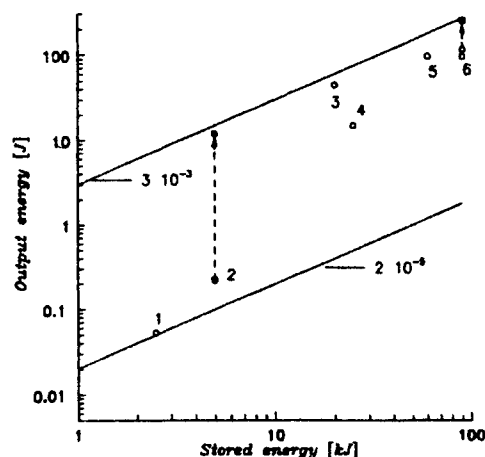


Figure 4 Output energy versus stored energy for the $\text{XeF}(\text{C} \rightarrow \text{A})$ laser.

1- Ref. 12; 2- Ref. 11; 3- Ref. 3; 4- Ref. 13; 5- Ref. 2; 6- Ref. 4. The dashed arrow is the possible increase in the output energy calculated in this work.

8. REFERENCES

- 1 W.K. Bischel, H. Nakano, D.J. Eckstrom, R.M. Hill, D.L. Huestis, and D.C. Lorents, "A new blue-green excimer laser in XeF ", *Appl. Phys. Lett.* **34**(9), 565 (1979); The same authors, Postdeadline Paper presented at *Int. Conf. on Lasers*, Orlando, Florida, (1978).
- 2 V.S. Zuev, G.N. Kashikov, N.P. Kozlov, S.B. Mamaev, V.K. Orlov, Yu. S. Protasov, and V.A. Sorokin, "Characteristics of an $\text{XeF}(\text{C-A})$ laser emitting visible light as a result of optical pumping by surface-discharge radiation", *Sov. J. Quantum Electron.* **16**(12), 1665 (1986).
- 3 V.S. Zuev, G.N. Kashnikov, V.V. Kirilenko, S.B. Mamaev, V.A. Sorokin, and V.F. Sukhorukov, "Photodissociation XeF laser emitting visible and ultraviolet radiation when pumped with radiation from a sectioned surface discharge", *Sov. J. Quantum Electron.* **19**(6), 748 (1989).
- 4 V.S. Zuev, G.N. Kashnikov, S.B. Mamaev, "Investigations of XeF laser optically pumped by radiation of surface discharges", *Preprint FLAN 23*, Moscow (1992).
- 5 S.V. Mitko, V.N. Ochkin, F.A. van Goor, W.J. Witteman, "State and Prospects of the $\text{XeF}(\text{C-A})$ Optically Pumped Laser", *Preprint 25*, Lebedev Physical Institute, Moscow (1996).
- 6 R.E. Beverly III, "Kinetic modeling of the photolytic $\text{XeF}(\text{C-A})$ laser", *Appl. Phys.* **B56**, 147-156 (1993).
- 7 L.D. Mikheev, D.B. Stavrovskii, and V.S. Zuev, "Photodissociation XeF laser operating in the visible and UV regions", *Journal of Russian Laser Research* **16**, 427 (1995).
- 9 E.L. Latush, G.D. Chebotarev, "On applicability of the maximum loss method for gain measurements in pulsed lasers", *Kvantovaya Elektron* **12**, 1480 (1985).
- 10 V.S. Zuev, A.V. Kanaev, and L.D. Mikheev, "Optical inhomogenities in the bleaching wave in the active medium of a photochemical laser", *Sov. J. Quantum Electron.*, **13**, 1232 (1983).
- 11 S.V. Mitko, F.A. van Goor, W.J. Witteman, V.N. Ochkin, "Optical pumping and ferrite flash discharges", *Proceedings of the NATO Advanced Research Workshop ARW 950443 on Gas Lasers-Recent Developments and Future Prospects*, Moscow, Russia, July 2-5, 1995. p. 185, Kluwer Academic Publishers, The Netherlands, 1996.
- 12 B.A. Knecht, R.D. Fraser, D.J. Wheeler, C.J. Ziektkiewicz, L.D. Mikheev, V.S. Zuev, "Compact $\text{XeF}(\text{C-A})$ and iodine laser optically pumped by a surface discharge", *Optics Letters* **20**(9) 1011 (1995).
- 13 V.S. Zuev, L.D. Mikheev, and D.B. Stavrovskii, "Efficiency of an optically pumped XeF laser", *Sov. J. Quantum Electron.* **14**(9) 1174 (1984).

Etching of organic optical materials by photo-material processing using an excimer lamp

Atsushi Yokotani, Noritaka Takezoe, Kou Kurosawa, Wataru Sasaki,
Tatsushi Igarashi*, Hiromitsu Matsuno*, Kunio Yoshida** and Takatomo Sasaki***

Miyazaki University, Department of Electrical and Electronic Engineering, Faculty of Engineering,
1-1, Gakuenkibanadai Nishi, Miyazaki, 889-21, Japan.

*Research and Development Center, USHIO Inc., 1194 Sazuchi, Bessyo-Cho, Himeji, 671-02, Japan

**Osaka Institute of Technology, Department of Electronic Engineering,
5-16-1, Omiya, Asahi-Ku, Osaka 535, Japan

***Osaka University, Department of Electrical Engineering, Faculty of Engineering,
2-1 Yamada-Oka, Suita, Osaka, 565 Japan

ABSTRACT

A dielectric barrier discharge type Xe excimer lamp has been used for etching of some organic materials which can be widely used for opt-electric applications. Using polymethylmetacrylate (PMMA) and polyimide (PI) resin as samples, they were irradiated at an intensity of 12 mW/cm². In both cases, etch rates could be varied by changing the species and pressures of gases in the chamber. The maximum etch rates for PMMA and PI were approximately 7 and 10 nm/min., respectively. The etched surface was found to be very smooth compared to the surfaces etched by the ArF excimer laser. Because the excimer lamp produces incoherent radiation, uniform irradiation over a large area without speckling or interference fringe has been obtained. Furthermore, because the peak power of the lamp is significantly lower than that of excimer lasers, effective quantum effects and photochemical effects without thermal effects has been observed. We applied this technique for etching single crystalline organic opt-electric materials such as L-arginine phosphate monohydrate and L-histidine tetrafluoroborate.

Keywords: excimer lamp, dielectric discharge Xe excimer lamp, vacuum ultra-violet light, photo-etching, polymer, Polymethylmetacrylate, polyimide

1. INTRODUCTION

Recently, various kinds of excimer lamps have been developed as a new light source in the vacuum ultra-violet (VUV) region¹⁻⁴, which can produce shorter wavelengths than conventional ArF excimer lasers. In particular, the Xe excimer lamp, in which the dielectric barrier discharge has been utilized, is very compact and has a high efficiency. These characteristics make it a promising light source for photo-material processing³⁻⁵. The Xe excimer lamp produces radiation at a wavelength of 172 nm, which corresponds to a photon energy of 7.2 eV. Energy of this level is higher than bonding energy of many covalent bonds, such as C-H (4.3 eV), N-H (4.1 eV), O-H (4.8 eV), C-C (3.5 eV), C-N (3.4 eV), C-O (3.9 eV), C=C (6.4 eV) and C=N (6.7 eV), which are the principal components in most organic materials. Only C=O (7.9 eV), C≡C (8.7 eV), C≡N (10.4 eV) *etc.* are higher. Therefore, most bonding in organic materials is broken when they absorb photons from the Xe excimer lamp. Furthermore, unlike lasers, because the lamp produces incoherent and quasi-continuous radiation, uniform irradiation over a large sample area without speckling or interference fringes can be expected. Besides, because the peak power of the light from the lamp is significantly lower than that of excimer lasers, effective quantum effects and photochemical effects without thermal effects can be observed. In this paper, we newly adopted the barrier discharge Xe excimer lamp as a light source of photoetching of some organic optical materials which can be widely used for opt-electric applications.

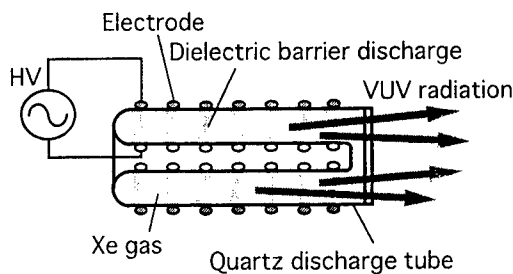


Fig. 1. A schematic drawing of a head-on type Xe excimer lamp.

2. EXPERIMENTAL SETUP AND PROCEDURE

2.1. DIELECTRIC BARRIER DISCHARGE XE EXCIMER LAMP

Fig. 1 shows a schematic drawing of the lamp (USHIO Inc., UER20H-172) used in the present experiment. It is referred to as a head-on type lamp, has an outer diameter of 40 mm and is 18 cm in length. The pressure of Xe in the tube was approximately 300 Torr. The input electric power was 20 W (20 kHz, 20 kV) and intensity at the end of the tube was approximately 12 mW/cm².

2.2. ETCHING EXPERIMENT

Fig. 2 shows a schematic drawing of the experimental setup for the etching experiment. The VUV radiation from the lamp was introduced into a vacuum chamber made of stainless steel through a MgF_2 window 2 mm thick. Polymethylmetacrylate (PMMA) and Polyimide (PI) resin were used as samples. Chemical formula of these materials were shown in Fig. 3. A 1 mm thick sheet-like sample was placed 25 mm below the window. Primarily, a metal mask with slits 100 μm apart was used for the experiment. The pressure of the gas in the chamber was monitored and regulated by a combination of a rotary vacuum pump and a pirani vacuum gauge. Either the air, N_2 , or Ar was used as a gas in the chamber. The irradiation period was varied from 10 to 60 min. in order to estimate the etching rate. The etched samples were characterized by the Talystep surface-roughnessmeter, scanning electron microscope (SEM), Fourier transformation infrared spectrometer (FT-IR), and an atomic force microscope (AFM). The technique was also applied to single crystalline organic opt-electric materials such as L-arginin phosphate monohydrate⁶ (LAP) and L-histidine tetrafluoroborate⁷ (LHBF).

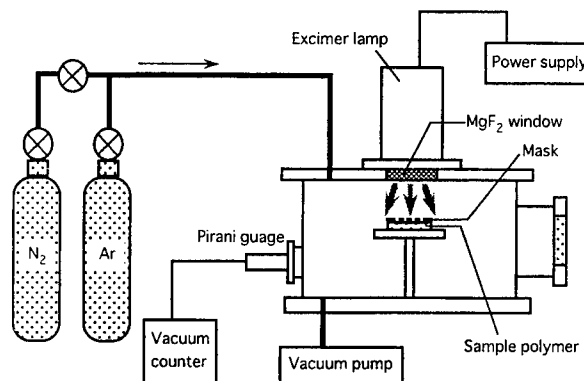


Fig. 2. A schematic drawing of the experimental setup for the etching experiment.

3. RESULTS AND DISCUSSION

3.1. ETCH RATE

The depth of the etched portions of the samples was measured from data taken by the roughnessmeter, as shown in Fig. 4. By changing the irradiation period, gas species and pressure, we were able to estimate the etch rate. The results are shown in Fig. 5. In the air and N_2 , the etch rate of both samples were maximum at a pressure around 10 Torr. The etch rate became smaller when the pressure became both larger and smaller than around 10 Torr. From these results, we concluded that the radicals of gases⁴ in the chamber which were activated around 10 Torr. by the VUV radiation, played an important role in the photoetching process. When the pressure around 0.75 Torr. and/or in the case of Ar gas, the etch rate was a few nm/min. Under these conditions, the number of radicals created was very small. Therefore we concluded that an etch rate of approximately 1 nm/min. was due to a quantum process, where the energies of the photon directly break the covalent bond in the polymers.

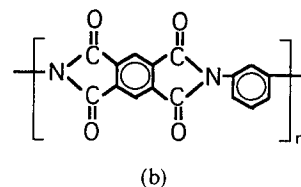
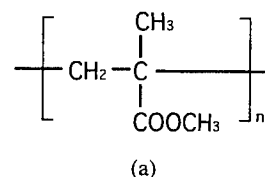


Fig. 3. Chemical formula of (a) PMMA and (b) PI.

3.2. SURFACE MORPHOROLOGY

Fig. 6 (a) and (b) show SEM images of the etched surfaces of PMMA and PI, respectively. In Fig. 6 (c) and (d) are SEM photographs of the same materials etched using a pulsed ArF excimer laser, for comparison. In Fig. 6 (c) and (d), the

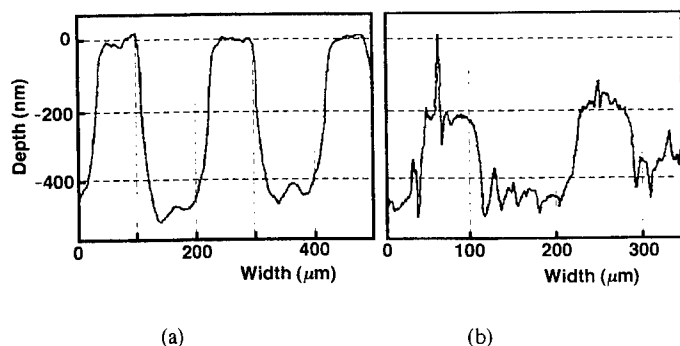


Fig. 4. Typical results from the measurement by the surface roughnessmeter. (a) PMMA. (b) PI.

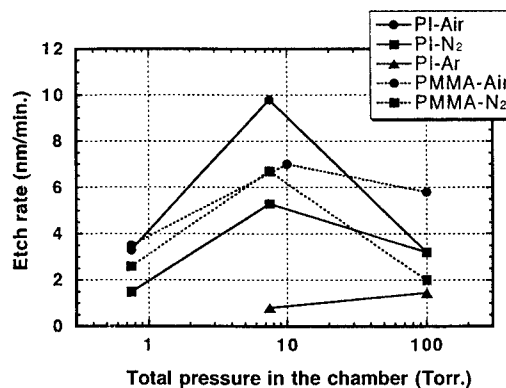


Fig. 5. Etch rate vs. total pressure in the chamber.

interference fringes and adsorbed debris, which are unsatisfactory for micro processing purposes, can be observed. In the case of PMMA, where the melting point is lower than for PI, traces of partial melting can be observed. In contrast, the surface etched by the lamp was found to be very smooth. No interference fringe was observed because of the incoherent light. Furthermore, neither adsorbed debris nor traces of partial melting were observed. This indicates that the thermal effects are very small or negligible in the process. The rising temperature calculated from the intensity of the lamp, thickness, absorption coefficient and thermal conductivity of the samples was as low as approximately 0.6°C .

Fig. 7 (a) and (b) show AFM images of PMMA before and after etching, respectively. In Fig. 7 (b), many cavities, which had not been present in the sample prior to etching, are observed. These cavities are considered to be etch-pits corresponding to the degree of crystallization in the polymers. Typical size of the pits was approximately 25 nm in diameter and 10 nm in depth. Unfortunately, a clear AFM image of the PI sample was not obtained because both the original and the etched surfaces were relatively rough, as shown in Fig. 4 (b).

3.3. POSSIBLE MECHANISM OF THE ETCHING

In the case of the etching using a single slit with width of $5\text{ }\mu\text{m}$, the width of etched part of PMMA became much wider than that of PI. To investigate this difference in etched width, FT-IR spectra of these samples were measured. The results are shown in Fig. 8. In the case of PMMA, a spectra near 3000 cm^{-1} and 1200 cm^{-1} changed after the irradiation process, whereas change in the spectrum of PI was very small. This indicates that a certain number of damaged molecules were present in the PMMA sample, whereas almost no damaged molecules were in the PI sample. As shown in Fig. 3 (a), in the case of PMMA, almost all bonds are single, of which energy is much lower than the photon energy. When the VUV is irradiated, damaged molecules should be distributed near the irradiated surface. As the breaking of the bonds proceeds, the molecules which become small enough to have a high evaporation pressure, leave the surface. On the other hand, in the case of PI, 35% of chemical bonding are double, with energies comparable or higher than the photon energy, as shown in Fig. 3 (b). In addition, the absorption coefficient of PI is larger than that of PMMA. Only the single bonds very near the surface are broken very effectively. Consequently, clusters including benzen rings and/or carbonyl groups should also leave the surface. The radicals mentioned above increase the rate leaving the clusters from the surface. At this moment, this is our hypothesis, and further investigation will necessary to identify the genuine process.

3.4. ETCHING OF SINGLE CRYSTALLINE ORGANIC OPTICAL MATERIALS

Fig. 9 (a) and (b) show optical micrographs of LAP and LHBf which have been etched by the Xe excimer lamp with the mask. The successful etching of these materials can be seen by observing the pattern of the mask on the surface. In the LHBf

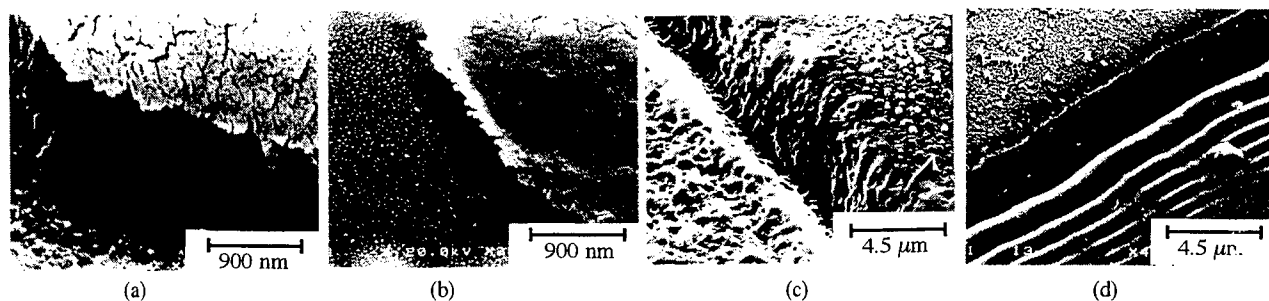


Fig. 6. Scanning electron micrographs of typical surface of (a) PMMA and (b) PI etched with the Xe excimer lamp, and (c) PMMA and (d) PI etched with a pulsed ArF excimer laser.

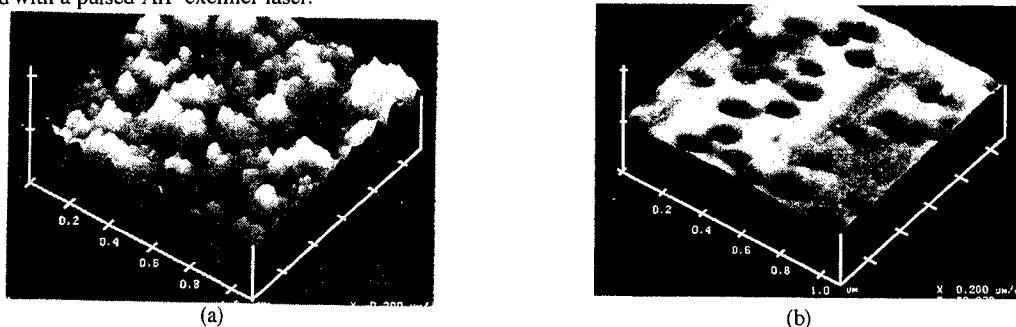


Fig. 7. Atomic force microscope images of surface of PMMA (a) before and (b) after etching. The scalings are $0.2\text{ }\mu\text{m/div.}$ along the x-y axes and 40 nm/div. along the z axis.

sample, wrinkle-like pattern and brawnish discoloration were observed on the surface of the etched parts. In the LAP crystal, similar pattern was observed soon after the etching had been completed. However the pattern disappeared after leaving in the air for a few days as shown in Fig. 9 (b). The reason of these phenomena might be that LAP contains phosphate group which has low evaporation pressure and very high deliquescency.

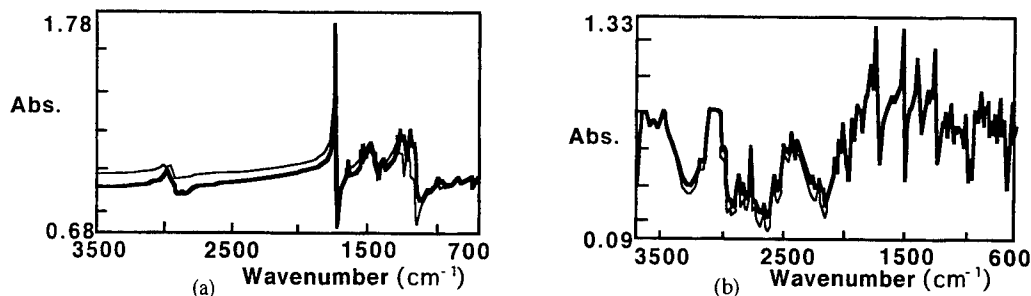


Fig. 8. FT-IR spectra of (a) PMMA and (b) PI, before and after the irradiation.

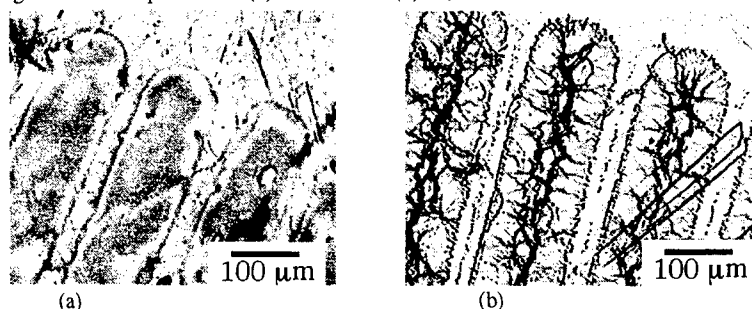


Fig. 9. Optical micrographs of surfaces of (a) LAP and (b) LHBF etched by Xe excimer lamp.

4. SUMMARY AND CONCLUSIONS

The dielectric barrier discharge type Xe excimer lamp has been used for etching of PMMA and PI, as well as LAP and LHBF. Because the radiation from the lamp was incoherent, a very smooth surface without speckling or interference fringe has been obtained. Furthermore, because the power of the lamp is significantly lower than that of excimer lasers, effective quantum effects and photo-chemical effects without thermal effects has been observed. In addition to these, it has been found that the etch rate can be controlled by changing the species and pressures of gases in the chamber. Also we considered the model in which radicals increased the rate at which molecules left the surface.

From these observations we can conclude that the Xe excimer lamp is very promising as a compact VUV light source for photo-material processing of organic materials in which thermal effect must be prevented.

6. REFERENCES

1. H. Kumagai and M. Obara, "New high-efficiency, quasi-continuous operation of KrF ($B \rightarrow X$) excimer lamp excited by microwave discharge," *Appl. Phys. Lett.* **54**(26), 2619-2621 (1989).
2. H. Kumagai and M. Obara, "New high-efficiency, quasi-continuous operation of KrF ($B \rightarrow X$) excimer lamp excited by microwave discharge," *Appl. Phys. Lett.* **55**(15), 1583-1584 (1989).
3. T. Igarashi, "Principle and applications of barrier discharge excimer lamps," *The Review of Laser Eng.* **23**(12), 1051-1055 (1995).
4. H. Esrom and U. Kogelschatz, "Modification of surfaces with new excimer sources," *Thin Solid Films* **218** 231-246 (1992).
5. A. Yokotani, N. Takezoe, K. Kurosawa, H. Matusno, and T. Igarashi, "A single precursor photolytic chemical vapor deposition of silica film by using a dielectric barrier discharge xenon excimer lamp," *Appl. Phys. Lett.* (1996) in press.
6. A. Yokotani, T. Sasaki, K. Yoshida, and S. Nakai, "Extremely high damage threshold of a new nonlinear crystal L-arginine phosphate monohydrate and its deuterium compound," *Appl. Phys. Lett.* **55**(26), 2692-2693 (1989).
7. H. O. Marcy, M. J. Rosker, L. F. Warren, C. A. Thomas, L. A. Deroach, S. P. Velsko, C. A. Ebberts, J.-H. Liao, and M. G. Kanatzidis, "L-Histidine tetrafluoroborate: a solution-grown semiorganic crystal for nonlinear frequency conversion," *Opt. Lett.* **20**(3), 252-254 (1995).

Gert Callies⁺, Henrik Schittenhelm⁺, George P. Pinho⁺⁺, Peter Berger⁺, Helmut Hügel⁺

⁺Institut für Strahlwerkzeuge (IFSW), University of Stuttgart, Pfaffenwaldring 43, 70569 Stuttgart, Germany

⁺⁺Department of Physics, University of Waterloo, Waterloo, Ontario N2L 3G1, Canada

e-mail: callies@ifsw.uni-stuttgart.de

ABSTRACT

In this contribution, the condensation theory of I.M. Lifshitz and V.V. Slyozov will be used to calculate the formation of metal clusters in the plasma/vapour regime above an aluminum target in a nitrogen atmosphere of 1 bar irradiated with 248 nm, 30 ns FWHM pulses. This theory takes into account formation of clusters by fluctuations in the supersaturated medium (plasma/vapour). It also accounts for both cluster growth due to atom-cluster-collisions (nucleation) and collisions between clusters (coalescence state). This condensation model is integrated in a gasdynamic code which calculates the flow field and the thermodynamic properties of the plasma/vapour. In addition, the density of electrons, clusters, and neutral particles are determined and, finally, with the appropriate polarizability the refraction index can be calculated. The theoretical data will be discussed together with the results of interferometric measurements.

Keywords: laser ablation, cluster formation, condensation, refraction index distribution

1 INTRODUCTION

The attenuation and absorption of the incident laser beam during treatment of material with CO₂-lasers is explicable by inverse bremsstrahlung. An interpretation of the attenuation during excimer laser ablation in terms of Rayleigh scattering of the incident laser beam by clusters in the plasma/vapour plume is given by Schittenhelm et al.¹ In this case the cluster growth was determined by effusion theory but the clusters density and the initial radius had to be assumed, and the essential thermodynamic properties were estimated by the Sedov blast wave theory. In contrast, Kar and Mazumder² derived the thermodynamic properties in the plume by solving the Euler equations, and the cluster size was calculated using a simplified model based on the condensation theory of I.M. Lifshitz and V.V. Slyozov.³ The procedure to determine the laser-induced processes in the present paper is similar to that one of Kar and Mazumder. However, the entire condensation theory has been taken into account and the cluster distribution, size, and density have been calculated considering the probability of fluctuation in dependence on the supersaturation in the plume as well as the cluster growth due to nucleation and coalescence.

2 THEORY

The flow of the evaporated material and the disturbed ambient gas above the Knudsen layer is described by the two-dimensional Euler equations with rotational symmetry. Mass, momentum, and energy are conserved and inverse bremsstrahlung is taken into account (the absorption coefficient is calculated after Mulser⁴). The coordinate system is fixed with the upper boundary of the Knudsen layer. The boundary conditions are given by the Knudsen layer mechanism. The finite-difference procedure is based on a modified McCormack algorithm which solves the equations with the predictor-corrector method including the time-splitting procedure. The simulation bases on prerequisites (e.g. constant specific heat etc.) and their improvements may lead to changes in the presented quantities.

In order to obtain the grain size from fluctuations in the supersaturated medium, a minimum energy $R_{min} =$

$4\pi a^2 \sigma - 8\pi a^3 \sigma / (3a_k)$ must first be expended on the formation of a grain¹. Here a , σ , and a_k are the radius of the grain, the surface tension, and the critical radius respectively. The critical radius is calculated by $a_k = 2\sigma / (kT\Delta(t))$ with the supersaturation of the vapour $\Delta(t)$. The probability of having grains with size a is given by the Boltzmann distribution function:

$$f_0(a) = n(t)4\pi a_k^2 \frac{\varrho_T}{m_a} \exp \left[-\frac{R_{min}(a)}{kT} \right] \simeq n(t)4\pi a_k^2 \frac{\varrho_T}{m_a} \exp \left[-\frac{4\pi\sigma a_k^2}{3kT} \right] \exp \left[\frac{4\pi\sigma}{kT} (a - a_k)^2 \right] .$$

Here $f_0(a)da$ is the number of grains with radius $[a \dots a + da]$ per unit volume, $n(t)$ is the particle density of the evaporated material, m_a is the atomic mass, and ϱ_T is the density of the atoms in a cluster. For a first approximation the density of the fluid itself was assumed. The function $f_0(a)$ has a strong minimum for $a_k = a$. Grains smaller than a_k dissolve after their formation (overcritical region), but, larger grains can increase unhindered (undercritical region). Grains from the overcritical region can, however, reach the undercritical region with a considerable probability. This is described by a diffusion equation in the space of grain dimension. The solution gives approximately the number of surviving grains per unit volume and time:

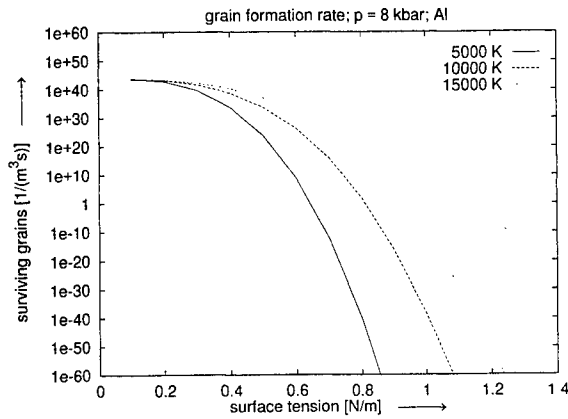


Figure 1: Surviving grains versus surface tension for Al at 8 kbar for different surface temperatures is given by the following equation:

$$\Gamma_n = \frac{1}{4}(n - n_a) \sqrt{\frac{8kT}{\pi m_a}} .$$

Here n_a is the number density corresponding to a cluster of radius a .² The particle flow onto the surface results in a rate of cluster growth:

$$\frac{da}{dt} = \frac{\sigma}{\varrho_T} \sqrt{\frac{2m_a}{\pi kT}} \left(\frac{1}{a_k} - \frac{1}{a} \right) .$$

This equation indicates that only for $a > a_k$ is growth of clusters possible. In the coalescence state the cluster sizes are increased due to cluster-cluster collisions. The formation of new clusters by fluctuations is negligible and the growth of clusters is determined by the process that larger clusters "eat up" smaller ones. The governing equations are:

$$a_k(t) = \left(\frac{8}{9} \frac{D\sigma m_a}{\varrho_T kT} t \right)^{1/3} , \quad n_{cl}(t) = 0.215 \Delta(0) a_k^{-3} \frac{m_a}{\varrho_T} , \quad \Delta(t) = \frac{2\sigma}{kT a_k(t)} .$$

The first equation describes the cluster growth, the second the evolution of the density of the clusters, and the third one the reduction of the supersaturation.

¹initial clusters are defined as grains

²The saturated vapour pressure for a curved fluid surface is higher than for a plane one. This leads to a higher saturation particle density at the surface of the grain if the temperature keeps constant.

3 RESULTS AND DISCUSSION

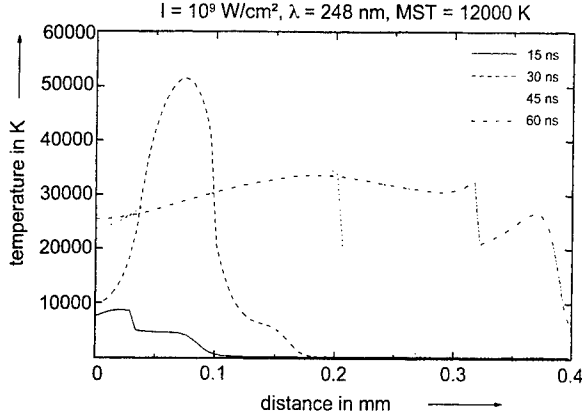


Figure 2: Temperature distributions along the optical axis for 15, 30, 45, and 60 ns.

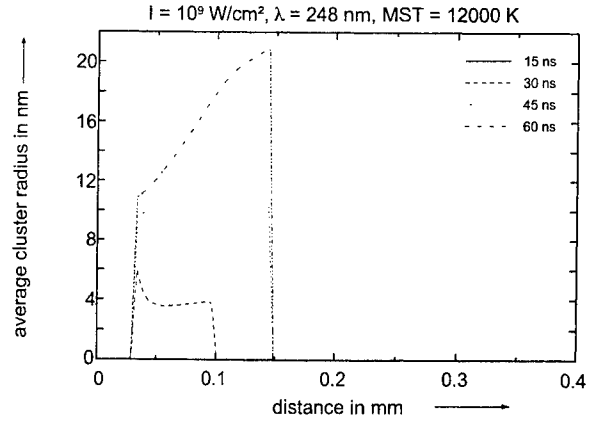


Figure 3: Cluster radii along the optical axis (at 15 ns the cluster growth is zero).

The temperature distribution along the optical axis and the corresponding cluster radii are presented in Fig. 2 and 3. The temperature profiles show a jump at the contact front due to a jump in the specific gas constant. The temperature is drastically increased in the region behind the contact front in the first 30 ns due to absorption by inverse bremsstrahlung. This leads to an acceleration of the contact front. Thus, the shock front is pushed forward, its velocity is increased, and a steeper temperature jump in the shock front occurs after 30 ns. This leads to a considerable electron density at the shock front as well. In a region between 25 μm and 150 μm above the target a condensation of clusters forms. After 60 ns they have a maximum average size of about 21 nm and the density of clusters amounts to 10^{20} m^{-3} . These studies from a theoretical point of view may lead to a modified interpretation of the earlier results of Callies et al.⁵

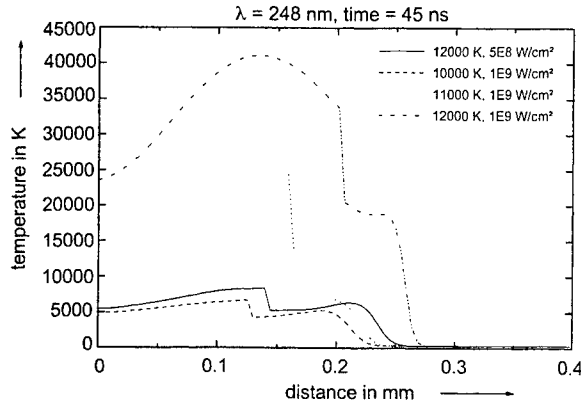


Figure 4: Temperature distribution along the optical axis for different intensities and MST.

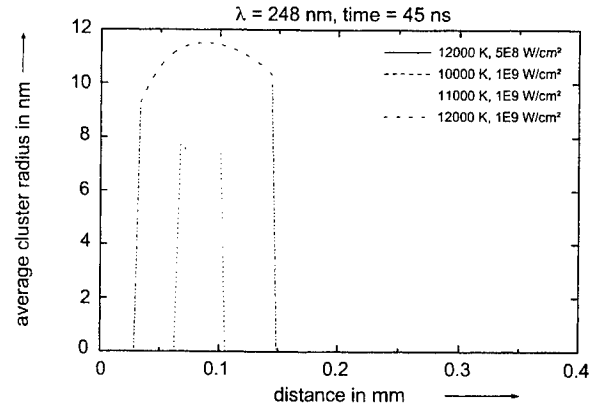


Figure 5: Avg. cluster radii. No cluster growth for $5 \cdot 10^8 \text{ W/cm}^2$ and 10,000 K respectively.

The cluster growth depends strongly on the intensity of the incident light and the maximum surface temperature (MST), see Fig. 4 and Fig. 5. The MST values are assumed from heat conduction calculations. No cluster growth occurs below 11,000 K MST or for an intensity of $5 \cdot 10^8 \text{ W/cm}^2$. In this case the initial number of free electrons in the plume is not large enough to increase the temperature in the plume by inverse bremsstrahlung and to force the cluster formation. In the case of 12,000 K MST and an intensity of 10^9 W/cm^2 the absorption is much higher which leads to a strong increase of the temperature and the cluster growth.

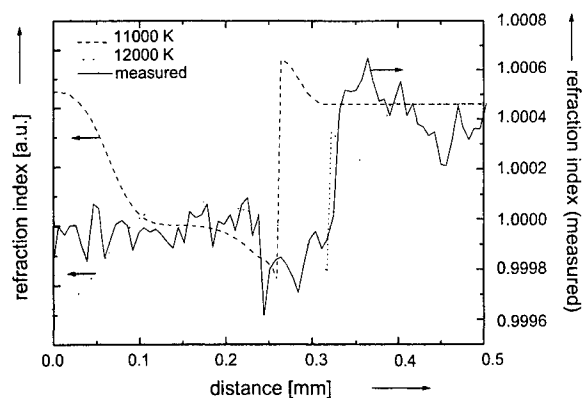


Figure 6: Calculated and measured refraction indices. The chosen parameters are described in the text.

The refraction index in the plume can be inferred from time resolved interferometric measurements.⁶ On the other hand it can be calculated if the electron density, neutral particle density and the density of clusters and their corresponding polarizabilities are known. In Fig. 6 calculated refraction indices are compared with measured ones. The parameters in the simulation are 11000 K and 12000 K MST respectively at an intensity of 10^9 W/cm^2 . The parameters in the experimental investigations are comparable except that copper was used instead of aluminum. The comparison shows a qualitatively good agreement. The distance of the ionization front in the case of 12000 K MST is in agreement with the measured values and even the calculated shock front position has almost the same distance. The simulation indicates that the strong decrease in refraction index closely behind the shock front is caused by the transition from disturbed ambient gas to material vapour.

The present calculations of the condensation phenomena lead to the following conclusions:

- The surface temperature alone is not high enough to produce cluster growth. The absorption by inverse bremsstrahlung, however, results in temperatures up to 40000 K in the plume. This is high enough to cause considerable cluster growth.
- Due to absorption of the laser energy the contact front is accelerated and pushes the shock front.
- The contact front is identical to the ionization front. The third discontinuity observed in earlier investigations⁵ may be a cluster front.
- The electron density is initially high in the metal vapour.
- The kinetic and internal energy of the ablated material is not high enough to cause an ionization of the compressed ambient gas behind the shock front.
- The comparison of calculated and measured refraction index shows a qualitatively good agreement.

The work is supported by the Deutsche Forschungsgemeinschaft (DFG) under code number HU 463/3 and by the Forschungszentrum Geesthacht GmbH under code number MPT 19.

4 REFERENCES

- [1] H. Schittenhelm, G. Callies, P. Berger, H. Hügel: Investigations of extinction coefficients during excimer laser ablation and their interpretation in terms of Rayleigh scattering." *J. Phys. D: Appl. Phys.* 29 (1996), pp. 1564.
- [2] A. Kar, J. Mazumder: "Mathematical model for laser ablation to generate nanoscale and submicrometer-size particles." *Phys. Rev. E* 49 (1994) Nr.1, pp. 410.
- [3] I.M. Lifshitz, V.V. Slyozov: "The kinetics of precipitation from supersaturated solid solutions." *J. Phys. Chem. Solids* 19 (1961) Nr. 1/2, pp. 35.
- [4] P. Mulser, R. Sigel, S. Witkowski: "Plasma production by laser." *Phys. Rep.* 6 (1973), pp. 187.
- [5] G. Callies, P. Berger, H. Hügel: "Time resolved observation of gasdynamic discontinuities arising during excimer laser ablation and their interpretation." *J. Phys. D: Appl. Phys.* 28 (1995), pp. 794.
- [6] H. Schittenhelm, G. Callies, P. Berger, H. Hügel: "Time-resolved interferometric investigations of the KrF-laser induced interaction zone." Poster on E-MRS Spring Meeting 1996 Symposium H (H-IX/P49).

Electron beams generation from a ferroelectric cathode induced by excimer lasers

J. Handerek^a, V. Nassisi and H. Riege^b

University of Lecce, Department of Physics, INFN, c.p.193-73100 Lecce-I

a) Institute of Physics, University of Silesia, 40007 Katowice-P.

b) AT Division CERN, 1211 23Genevra-CH

ABSTRACT

Results of experiments investigating the influence of the XeCl and KrCl laser beams on the generation of electron beams up to short threshold are reported. The cathode was a lead-lanthanum-zirconium-titanate PLZT ceramic having the emission side coated with 200 μ m large strips made up gold film. Under the laser irradiation the emission current increased more than 40%.

Keywords: excimer lasers, ferroelectric ceramic, electron emission

1. INTRODUCTION

Ferroelectric materials are a new class of electron generators. The highest value of electron generation has been observed when a fast polarising pulse was applied to the lead-lanthanum-zirconium-titanate (PLZT) cathode^{1,2}, whereas the mechanism responsible of the electron emission is due to the rapid internal electric field that appears during the polarisation change at temperatures near the antiferroelectric (AFE) ferroelectric (FE) phase transition. The polarisation change occurs applying a fast voltage pulse on the sample. The experimental results report electron emission variable from 10^{-9} to 100 A/cm².¹⁻⁴ It seems the ferroelectric electron emission (FEE) can be classified into two regimes⁵: the low current regime starts when the electric field applied by voltage between the electrodes is < 5kV/cm, while the high current regime, observed with PLZT ceramic, occurs under rapidly rising electric fields of more 20kV/cm applied across the dielectric with a time duration more than 100 ns.

Current densities resulted about two order of magnitude greater than the Child-Langmuir law. A such behaviour can be explained considering the high electron energy of emitted electrons⁶, the plasma formation during the electron emission⁷, and the presence of the exciting pulse in the propagation volume. The plasma can increase the accelerating field for the electrons but its expansion versus the collector limits the acceleration up the short threshold due to the short-circuits between the cathode-anode gap.

In the present work we shall give the experimental results relative to electron emission from a ferroelectric ceramic disc 4/95/5 PLZT under the influence of the laser radiation. We give also the measurements of the exciting pulse in the electron beam propagation volume.

II. EXPERIMENTAL SET-UP

Fig. 1 shows the vacuum chamber having the cathode holder and a quartz windows in order to permits the entrance of the laser beam. The emission current was accelerated by a polarised grid anode (A). It is made up a stainless steel grid with 4 meshes per mm² having an optical transmission of about 64%. The distance anode-cathode was 15 mm. The accelerating electric field was reached putting the emission electrode of the cathode to the ground and the grid anode to +5kV by a charging resistor higher than 50 Ω . The diagnostic system was composed by two Rogowski coils; the small one was utilised for the measurement of exciting current and its attenuation factor was 14.8 A/V, while the large one was utilised for the measurement of the electron current from the cathode and its attenuation factor was 30 A/V. This last current was monitored also with the grid anode which was able to detected only the 36% of total current. Its was measured by the voltage on the 50 Ω resistance connected to the anode by means a 4 nF capacitor, C.

The fast exciting voltage was realised by a fast transistor switch (TR1) Behlke HTS 30-06 and a discharging capacitor of 1nF. As trigger pulse was utilised the laser discharge pulse taken on the laser main electrodes by means a CuSO₄ voltage divisor. The trigger pulse started about 120 ns before the laser action so the trigger signal was transferred from the voltage divisor to the TR1 switch by a delay line such to counterbalance the laser beam delay. The

TR1 switch was fed with a positive power supplier as can be seen in Fig. 2. The pulse shape was accomplished connecting a second transistor switch (TR2) Behlke HTS 21-06 to a negative power supplier and 4nF capacitance. This last switched on a delay time due to the delay lines placed between the TR1 and TR2 trigger connectors. Specific voltage values and line lengths were necessary to get successful, namely to accelerate the beam without short-circuits.

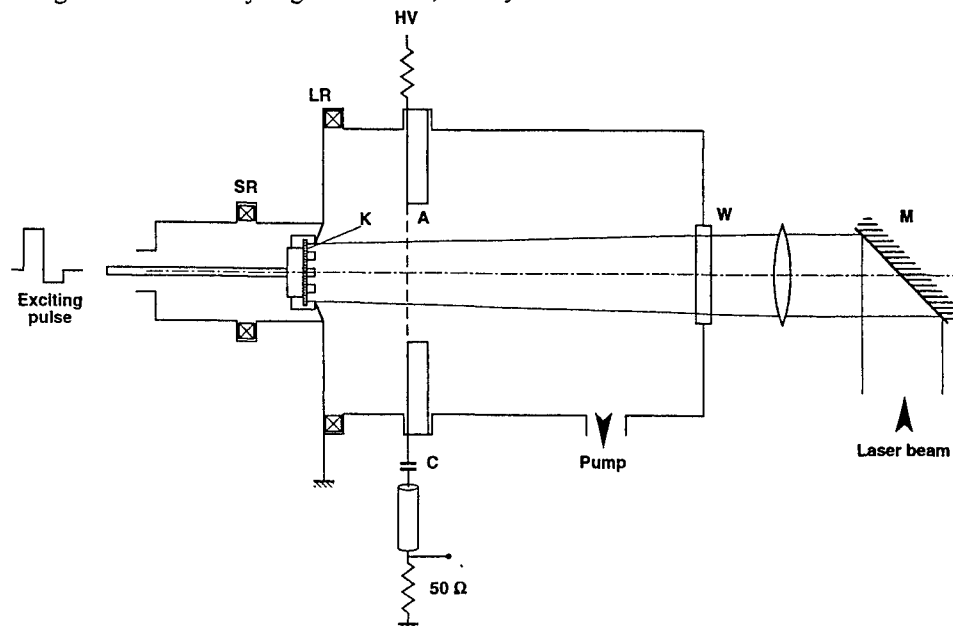


Fig. 1: Accelerating chamber. K: cathode, A: anode, LR: large Rogowski coil, SR: small Rogowski coil, C: 4nF separator capacitor, W: quartz windows, M: mirror.

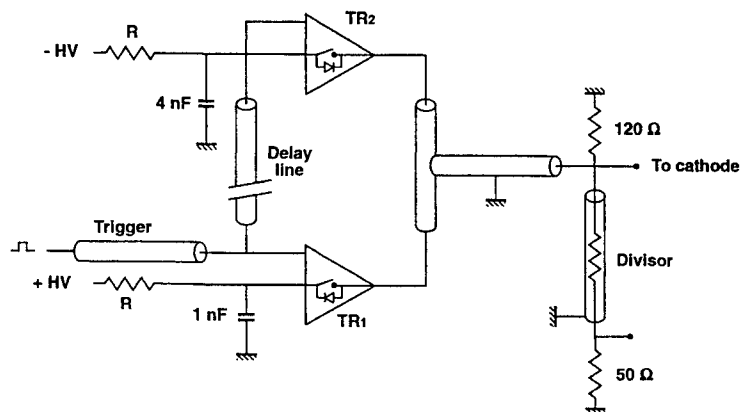


Fig. 2: Electric circuit of the pulser. TR1 (HTS 30-06) and TR2 (HTS 21-06) transistor switches, R: 5 k Ω charging resistors.

The connection between the exciting pulse and the cathode was realised by a short 50 Ω coaxial cable closed on a load resistance of 120 Ω . This solution was bound to variable cathode impedance during the excitation which did not allow to match the exciting pulse.

The exciting pulse was monitored with a fast resistive divisor having an attenuation of 100.

The laser device used in this experimental work was described in previous paper⁸. The standard mixtures for 308 nm (4.02 eV) and 222 nm (5.6 eV) were Xe/HCl/Ne and Kr/HCl/Ne, respectively. The output laser energy was 2mJ for the XeCl and 1 mJ for the KrCl. A vacuum of 10⁻⁶ kPa was maintained in the accelerating chamber by a turbo-molecular pump. The laser energy was measured with a joule-meter (Gentec ED200), while the laser pulse shape (temporal evolution) was recorded with a fast photodiode (Hamamatsu R1320U-02). Two digitising oscilloscope (Tektronix TDS 540, 1GHz and a LeCroy 9361, 2.5GHz) were used to record the signals

3. EXPERIMENTAL RESULTS AND DISCUSSION.

A 0.37 mm-thick, 16 mm-diameter ferroelectric ceramic, PLZT 4/95/5, disc coated with a thin uniform gold layer on the back and with 200 μm wide strips separated by a similar distance on the emission side was used. It was prepoled by applying a dc voltage of 2kV/cm with negative polarity on emission surface. The sample was maintained at 230 °C temperature for 15 min, reaching the FE phase and it was afterwards cooled down to room temperature reaching its AFE phase through the FE-AFE phase-transition temperature.

During the experiments the TR2 switch was fed with a fixed voltage corresponding to -1000V while the TR1 was led with a fixed voltage of 1900 V. These values were chosen up to short threshold, namely in order to avoid anode-cathode short-circuits with an exciting positive pulse width of 50 ns. Under these conditions the output current was of 1A.

Fig. 3 shows the generated current recorded with the grid anode.

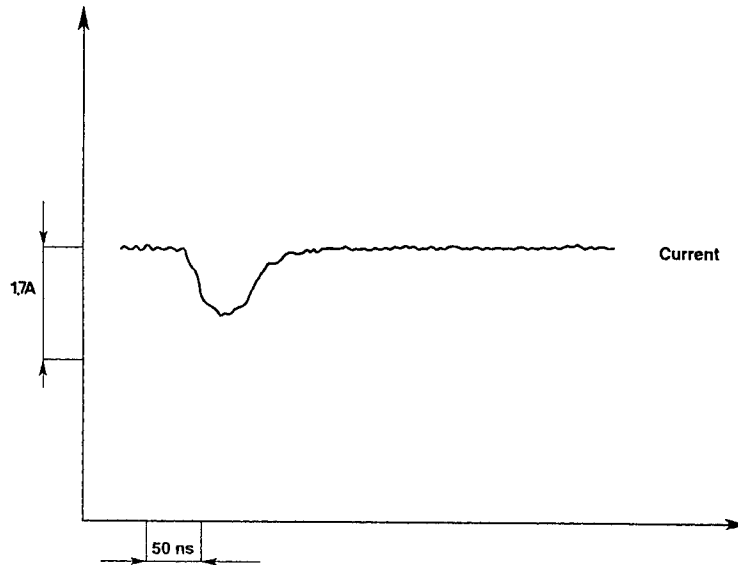


Fig. 3: Output current from the PLZT cathode without laser irradiation

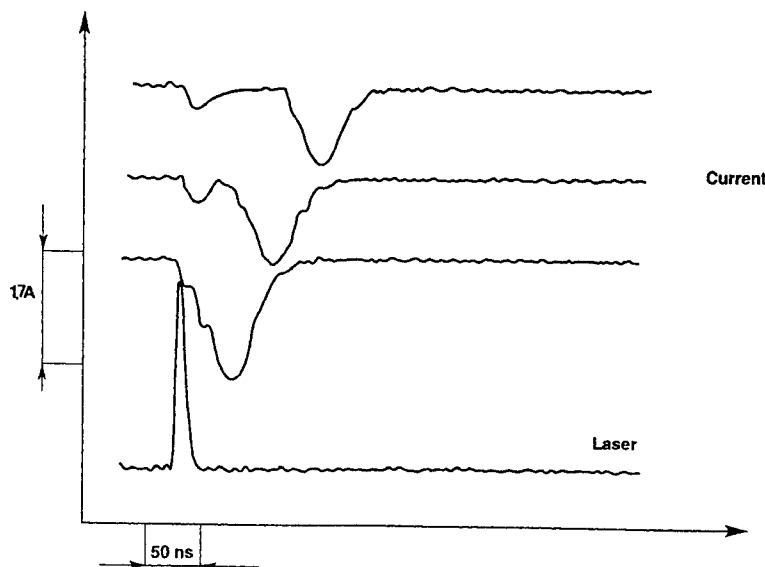


Fig. 4: Waveform of the output current and KrCl laser pulse at different delay times: 0, 50 and 100 ns between laser beam and output current.

Fig. 4 shows the results of emission current under the KrCl laser irradiation. The laser beam acted on the sample at different delay time with respect to the electron emission. From Fig. 4 it is possible to observe the presence of two peaks

in the electron emission. One peak is in correspondence with the laser beam and one peak is in correspondence with the exciting pulse. When the laser beam was applied at the onset time of the electron emission the output current became 80% higher than the current without the laser beam generating an output current of about 1.8 A. With the laser beam applied at 50 and 100 ns before the electron emission, the output current became 1.3 A and 1.2 A, respectively. In this case the current pulse observed with the laser action can be due to photoemission processes from the emission electrode present on the PLZT sample.

A different behaviour was observed with the XeCl laser irradiation. In this case the output electron beam was formed by a single pulse and the laser irradiation increased its intensity of about 40%.

Measurements were done applying the laser beam before the electron emission and as a consequence a output current pulse lower than 1.4 A was obtained. Fig. 5 shows the output current under the XeCl laser irradiation.

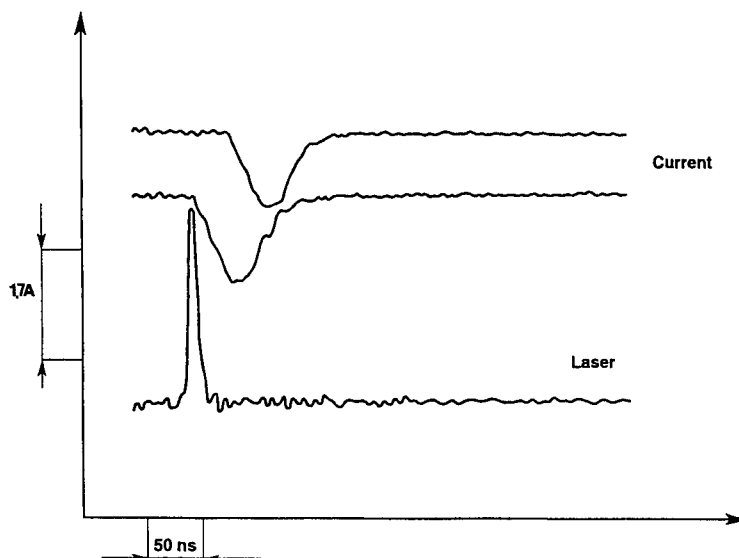


Fig. 5: Waveform of the output current and XeCl laser pulse at two delay times: 0 and 50 ns between laser beam and output current.

By theoretical calculations of the electron beam current, under our experimental conditions and using the Child Langmuir law a current density of 0.37 A/cm^2 was obtained. From our experimental results the maximum current density obtained was 0.74 A/cm^2 , value larger than the theoretical one. This discrepancy could be ascribed also to the electric field present in the propagation volume. In fact, putting a antenna probe near the emission electrode and annulling the accelerating voltage, a voltage pulse having a waveform similar to the exciting one was observed. Voltage signals propagating in the accelerating zone can penetrate only by the strip electrode. By comparing the voltage values measured with the ferroelectric cathode fixed into the holder and the voltage values measured with the insulating disc fixed into the holder we found a rate of 1/6. The percentage obtained (16%) was very meaningful. However, the penetrated field can strongly to modify the accelerating conditions and to generate electron beam of intensity very different from those calculated by the Child -Langmuir law.

4. REFERENCES

1. L.Schachter, J. D. Ivers, J.A. Nation, and G.S. Kersil, J. Appl. Phys. **73**, 8097 (1993).
2. H. Gundel, J. Handerek, and H. Riege, J. Appl. Phys. **69**, 975 (1991).
3. E. Sampayan, G.J. Caporaso, C.L. Holmes, E.J. Lauer, D. Prosnitz, D.O. Trimble, and G.A. Westenskow, Nucl. Instrum. Meth. **A340**, 90 (1994)
4. G. Rosenman, and I. Rez, J. Appl. Phys. **73**, 1904 (1993)
5. V.F. Puchkarev, and G.A.Mesyats, J. Appl. Phys. **78**, 5633 (1995).
6. V. Nassisi, A. Luches: Rev. Sci. Instrum. **50**, 900 (1979)
7. A. Beloglazov, V. Nassisi, and M. Primavera, Rev. Sci. Instrum., **66**, 3883 (1995)
8. A. Luches, V. Nassisi and M.R. Perrone, J. Phys. E: Sci. Instrum. **20**, 1015 (1987)

Time-of-Flight characterization of pulsed laser ablation plume from NbTe₄ target

F. Grangeon^a, H. Sassoli^b, W. Marine^b, M. Autric^a

^aU.M.R C.N.R.S 138 I.R.P.H.E / LP3

^bU.R.A C.N.R.S 783 Département de Physique

Parc Scientifique et Technologique de Luminy, 163 Avenue de Luminy 13009 Marseille France

ABSTRACT

The kinetic parameters of ejected species during excimer laser ablation of a NbTe₄ target are investigated by optical Time-of-Flight spectroscopy. Velocities of monoatomic neutrals, ions and molecules are calculated for different laser fluences.

Keywords : pulsed laser ablation, niobium tellurides, Time-of-Flight spectroscopy

1. INTRODUCTION

A large field of applications as microelectronics, micromechanics and optics needs to overcome the deposition of various materials showing dielectric, superconducting or piezoelectric properties under thin film form. Numerous methods were developed as Chemical Vapour Deposition, Sputtering, Thermal Evaporation. Since the early 1980's, a new process based on laser ablation is developed¹. The Pulsed Laser Deposition (P.L.D) method is based on the laser evaporation of a target and the subsequent deposition of the ablation plume on a substrate (see fig. 1). A wide variety of materials was successfully deposited in thin film form by this method².

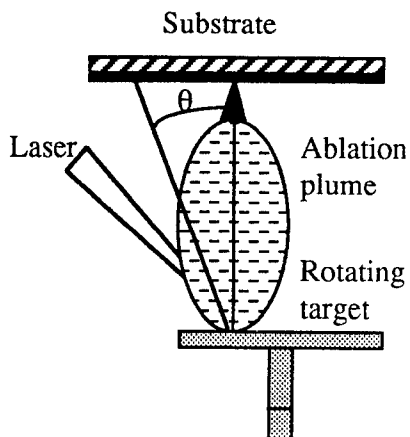


Fig. 1 : Typical Pulsed Laser Deposition set-up

Recently, thin films crystallized in the NbTe₂ phase were performed by using P.L.D process³. The NbTe₂ compound presents strong anisotropic properties and finds applications in microelectronics (2D conductors) and micromechanics (solid lubricant). These results shown the key role played by the laser fluence. The kinetic parameters of ablated species influence sharply the thin film formation processes. In order to understand the influence of the laser parameters on these mechanisms, it is necessary to study the ablation process and the expansion of the ablation cloud.

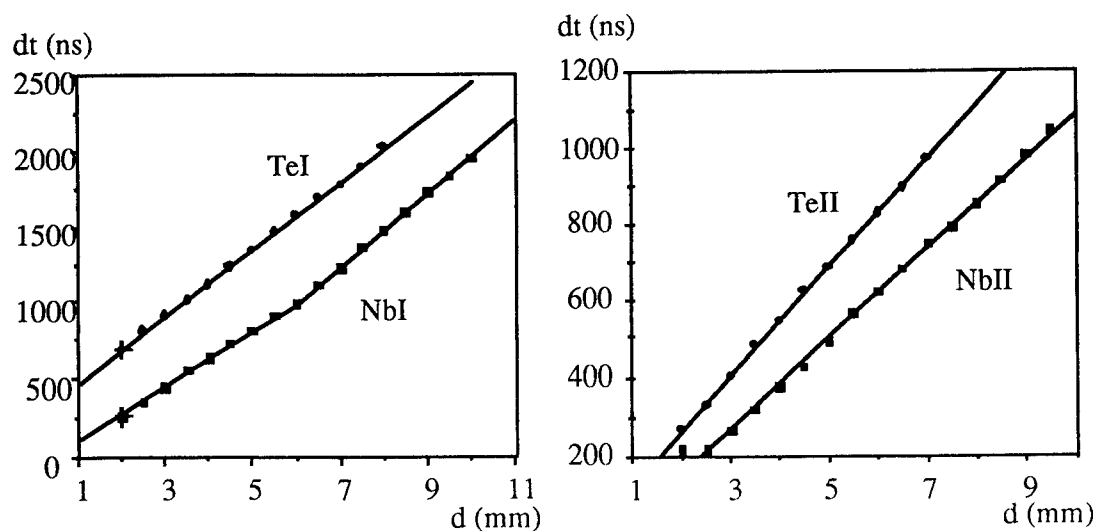
2. EXPERIMENTAL SET-UP

Ablation was performed in a stainless steel high vacuum chamber (pressure $2 \cdot 10^{-4}$ Pa). An excimer laser (Lambda Physics 220i KrF 248 nm) delivering 400 mJ in 20 ns pulse duration was used. The beam was focused onto a bulk NbTe₄ rotating target at 45°. The spot size was 1 mm². The energy density ranged from 3 to 8 J/cm². Targets were produced by direct preparation from the elements (Nb, Te) in stoichiometric proportion (solid state reaction in sealed quartz ampoule).

Characterization of the plume by Time-of-Flight (ToF) spectroscopy is based on the observation of the transient signal of the spectral lines of species present in the plume at different distances from the target. The time between the laser pulse and the maximum of the transient signal is the delay time. ToF measurements were made by using a 50 cm focal length MacPherson monochromator and a fast photomultiplier RCA 4837. We observed the following spectral lines : NbI 4058 Å, TeI 3175 Å, NbII 3194 Å, TeII 4866 Å and Te₂ 4957 Å. Velocities were calculated from the slope of variation of the delay time vs the distance.

3. RESULTS

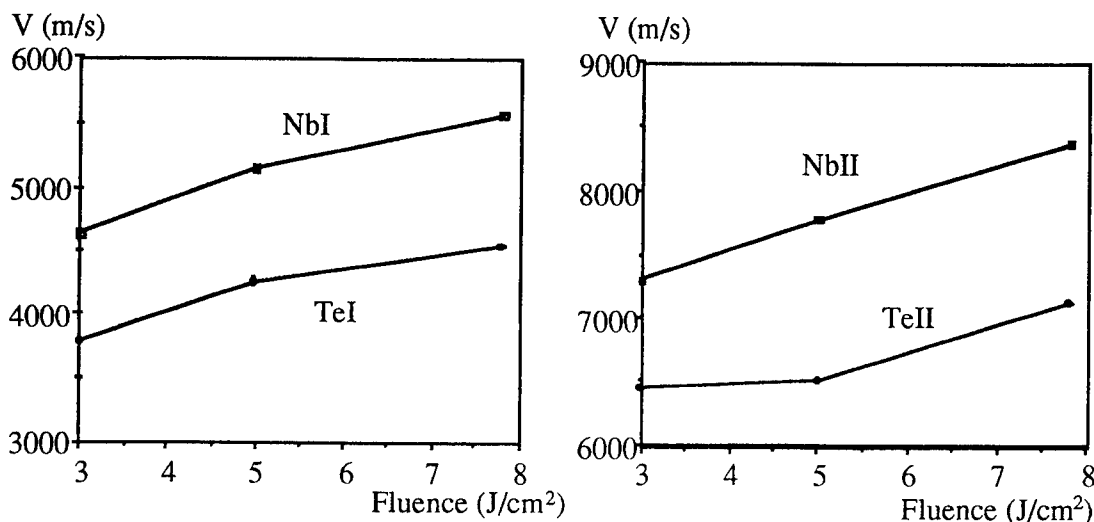
The ablation threshold of a NbTe₄ target is about 0.4 J/cm². Figures 2 and 3 show the evolution of the delay times of neutrals and ions, as a function of the distance to the target, at a fluence of 7.9 J/cm². Increasing the laser fluence induces a decrease of the delay times of all ablated species. It is noticeable that the delay times of neutral tellurium and both ionized species increase linearly with the distance on all the observed range (2 - 10 mm), for the TeI, TeII and NbII species. This indicates that these species move in the free expansion regime⁴ for distances up to 6 mm. At this distance, the slope of variation of the delay time increases, indicating that niobium atoms loose kinetic energy at this distance, probably during collisional processes. For distances higher than 6 mm, the delay time increases linearly again.



Figs. 2 and 3 : delay times of neutrals and ions vs the distance to the target ($\Phi = 7.9 \text{ J/cm}^2$)

Figure 4 and 5 show the evolution of the velocities of the neutrals and ions, as a function of the laser fluence. Increasing the fluence induces an increase of the velocities of all ablated species. We observed that the ratio of the velocity of a Nb atom by the one of a Te atom is closed to the square root of the ratio of the mass of a Te atom by the one of a Nb atom:

$$\frac{V_{\text{NbI}}}{V_{\text{TeI}}} = 1.2 \approx \left(\frac{M_{\text{Te}}}{M_{\text{Nb}}} \right)^{1/2} = 1.17$$



Figs. 4 and 5 : Velocities of neutrals and ions vs the laser fluence

The Te and Nb atoms movement follow the law of the conservation of the energy. This shows that neutral species are ejected from the target by the same mechanisms. The same observation concerning the ratio of velocities can be made for ionized species. We noticed that increasing the laser fluence from 3 to 5 J/cm² induces a weak increase of the velocity of TeII ions. Between 5 and 7.9 J/cm², the variation of velocity becomes important and close to the one of NbII ions.

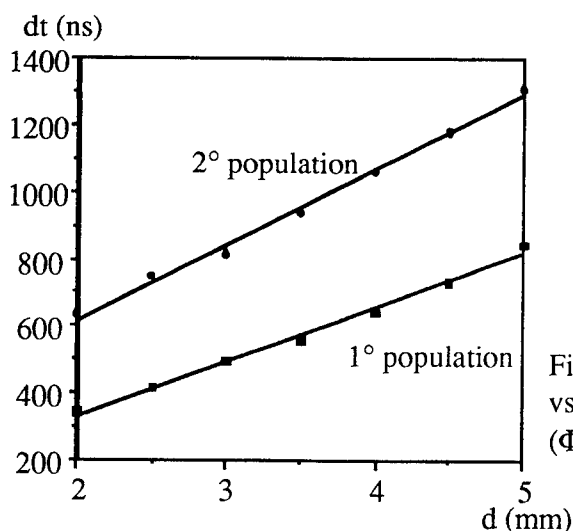


Fig. 6 : Delay times of Te₂ molecules vs the distance to the target (Φ = 7.9 J/cm²)

The observation of the transient signal of the Te_2 4957 Å shows two peaks related to two different populations of molecules, the second population appearing about 300 ns after the first one. The figure 6 shows the delay times of these two molecular populations as a function of the distance of the target, at a fluence about 7.9 J/cm². Figure 7 shows the velocities of the two populations vs the fluence. As for monoatomic species, increasing the laser fluence induces a decrease of the delay times and an increase of the velocities of both populations. Te_2 molecules move in a free expansion regime on all the observed range.

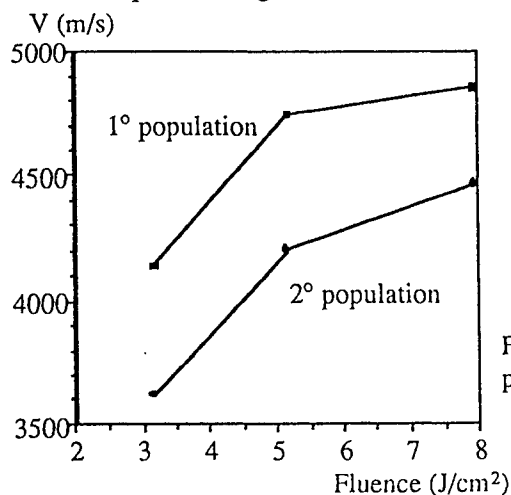


Fig. 7 : Velocities of molecular tellurium populations vs the laser Fluence

It is noticeable that the delay time of NbI atoms at 6 mm is very close to the one of the Te_2 molecules of the first population, extrapolated at 6 mm assuming a free expansion regime. This could indicate that niobium atoms loose kinetic energy during collisional transfert with Te_2 particles of the first population. Concerning the velocities of molecules, we noticed that the ratio of the TeII velocity to the first Te_2 population one is about 1.4 - 1.45. These species have very closed kinetic energies and are probably produced by the same mechanisms. We observed that the velocity of the second population of Te_2 molecules is very close to the one of TeI atoms. We can deduce that the second population is created by associative reactions from neutral tellurium :



4. CONCLUSION

Thin films properties depend strongly on the ablation process. The velocities of ablated species were deduced from the ToF spectra delay time and calculated for different fluences. The two different populations of Te_2 molecules were related to Te ions for the first one, and to association of Te atoms for the second one. The experiments showed the presence of collisional processes between NbI particles and molecules of the first population.

5. REFERENCES

1. See for example :
 - 1) Material Research Society Symposium Proceedings, V. 191 ed. by D.C. Paiene and J.C. Bravman, Pittsburg, 1990
 - 2) E-MRS Proceedings, V. 24, ed. by I.W. Boyd, Elsevier, 1992
2. K.L. Saenger, Processing of Advanced Materials 2, p1-24, 1993
3. H. Sassoli, F. Grangeon, Y. Mathey, M. Autric, D. Pailharey and W. Marine, to be published in Material Research Society Symposium Proceedings
4. W. Marine, M. Gerri, J.M. Scotto d'Aniello, M. Sentis, Ph. Delaporte, B. Forestier and B. Fontaine, Applied Surface Science, 54 (1991) 264

9. Laser Micromachining I

Laser Ablation: Processes and Applications

Peter E Dyer

Department of Applied Physics, University of Hull, Hull, HU6 7RX, UK

ABSTRACT

A brief review of laser ablation mechanisms and applications is presented. Topics covered include polymer ablation, thin film deposition, tissue ablation, and chemical analysis.

Key words: laser ablation, polymers, pulsed laser ablation deposition, cornea, chemical analysis

1. INTRODUCTION

The use of the term ablation to collectively describe phenomena related to material removal by a pulsed laser became common practice following Srinivasan's reports¹ of 193 nm ArF laser polymer ablation in 1982. Prior to this much work on pulsed laser-materials interactions in an irradiance regime intermediate to that of industrial welding, cutting and drilling and high-temperature plasma formation had been reported, but mainly restricted to longer wavelengths. The availability of commercial, deep UV, excimer lasers in the 1980's stimulated intense activity on ablation which continues to this day. Notable milestones include Srinivasan and co-workers studies of polymer¹ and biological tissue² and Dijkkamp et al's³ demonstration of the suitability of ablation-deposition for preparing thin films of the YBa₂Cu₃O₇ superconductor.

In this paper we will briefly review the current understanding of ablation mechanisms and the applications that have emerged in materials processing and analysis. Background concepts related to pulsed laser interactions are first introduced, followed by a brief overview of polymer ablation, pulsed laser ablation deposition, biological tissue ablation and the use of ablation in analysis.

2. ABLATION MECHANISMS

In laser ablation the basic physical process involves transferring a sufficiently high energy loading to a surface that a shallow layer of the material volatilizes. Interest may centre on the removal, as would be the case in micropatterning and micromachining, or on the volatilized materials itself, thin film deposition and chemical analysis by mass spectroscopy being typical examples.

We propose here a broad distinction in the ablation mechanism according to whether the material can undergo an irreversible step leading to volatile products within its volume or is dominated by a surface vaporisation mechanism. For polymers and probably certain biological materials, sufficient free volume exists for irreversible volatile product formation to occur within their bulk. In a thermal picture these products would arise through pyrolysis, the temperature rise induced being sufficiently large to produce volatile products during the heating timescale. For short wavelength lasers, where the photon energy exceeds bond energies, photochemical reactions can also be contributory or dominant (ablative photodecomposition¹). In either case, there will be an *apparent* threshold for ablation arising from the need to exceed some minimum volumetric energy loading to produce volatile products on the timescale of relevance. It can then be reasoned that material will be ablated to the depth to which this energy loading (and irreversible product formation) occurs.

In contrast, for a classical surface vaporisation process as would, for example, be encountered with a metal, the surface recession rate V_s found from kinetic theory is⁴

$$V_s = \frac{p}{\rho} \left[\frac{M}{2\pi RT_s} \right]^{1/2} \quad (1)$$

Here M is the molar mass, p the vapour pressure at the surface temperature T_s and ρ the density. Equation 1 neglects backscattering and condensation which act to reduce V_s . The net transport of material from a surface in this manner is an

intrinsically non-equilibrium thermodynamical process and the pressure on the surface can be shown to be lower than $p(T_s)$. Hence the material is superheated, ie. exists at a pressure lower than the equilibrium vapour pressure at T_s . The question then arises as to whether heat loss from within the *bulk* of the molten material can occur through the growth of vapour bubbles, ie. boiling. As the nucleation of bubbles from atomic scale voids within the melt requires very large vapour pressures, boiling in the transient interaction is suppressed and surface vaporisation dominates removal. Under pulsed, high irradiance, laser exposure the evaporative power flux can fall well short of that required to balance the incoming laser flux and very high temperatures are reached, ultimately approaching the critical temperature T_c . It has been postulated that at some maximum superheating temperature, $T_m \leq T_c$, the material can no longer sustain tensile forces and explosive boiling takes place causing its rapid disassembly⁵. This so called 'phase explosion'⁶ marks the transition from a surface to volume removal process.

Models for target heating are well developed⁷ but the requisite optical and thermodynamic properties are not always available over the temperature range encountered. A useful characterising parameter is the ratio of absorption length to thermal diffusion length obtaining over the laser pulse duration, τ , given by $\delta = 1/\alpha\sqrt{D\tau}$ where α is the absorption coefficient and D the thermal diffusivity.

For $\delta \gg 1$ negligible heat flow occurs during the pulse and the temperature rise profile ΔT is:

$$\Delta T = (1-R)\alpha F_e / \rho c \quad (2)$$

where F is the fluence, R the surface reflection coefficient, ρ the target density and c its specific heat. This usually provides a good description for polymers and biological materials under short pulse laser exposure.

For $\delta \ll 1$ heat flow dominates and in this limit the surface temperature rise ΔT_s is:

$$\Delta T_s = \frac{2I(1-R)}{k} \sqrt{\frac{D\tau}{\pi}} \quad (3)$$

where I is the irradiance and k the thermal conductivity. For $\delta \approx 1$ special treatment is needed although analytical solutions are available in complete [7] or approximate [5] form for rectangular pulses.

3. POLYMER ABLATION AND APPLICATIONS

The use of short pulse lasers, notably deep UV excimer devices, to ablate polymers has attracted much attention and effort since Srinivasan's first reports on this¹. This has been directed at understanding the underlying mechanisms and exploiting practical applications of the technique. Several detailed reviews^{8,9} have appeared describing the progress and developments in this field and only a brief overview is warranted here.

Polymers exhibit a fairly well defined ablation threshold that corresponds to a volumetric energy loading of typically $\sim 3-5 \text{ kJ cm}^{-3}$ ⁹. Threshold fluences may be as low as a few 10^5 mJ cm^{-2} in the ultraviolet and show an approximately inverse dependence on the absorption coefficient at the laser wavelength⁹.

Excimer laser ablation can produce exceptionally well defined patterning of polymers (Figure 1), a feature attributable to the high optical spatial resolution and strong polymer absorption in the UV (α can reach in excess of 10^5 cm^{-1}). On the basis of an absence of significant thermal damage it has been argued that the polymer decomposes principally via direct UV bond breaking without large temperature rise occurring (ablative photodecomposition¹). An alternative view is that rapid elevation of the temperature promotes thermal decomposition but confined to approximately the absorption depth (as $\delta \gg 1$, section 2) which can be very small in the UV. High absorption, and a concomitantly low threshold, also brings the advantage of low thermal loading⁹ which minimises thermal damage. The importance of attaining high absorption for effective ablation has been demonstrated by particulate doping of polymers for IR lasers¹⁰, dye doping for visible lasers¹¹ and line tuning TEA CO_2 lasers to match IR bands¹². TEA CO_2 laser-polymer ablation exhibits similar characteristics to excimers but with higher thresholds because of the lower absorption ($\alpha = \text{few } 1000 \text{ cm}^{-1}$ cf 10^5 cm^{-1} in the UV) and poorer spatial resolution because of the longer wavelength. Even so, well defined features of modest dimensions can be achieved (Figure 2).

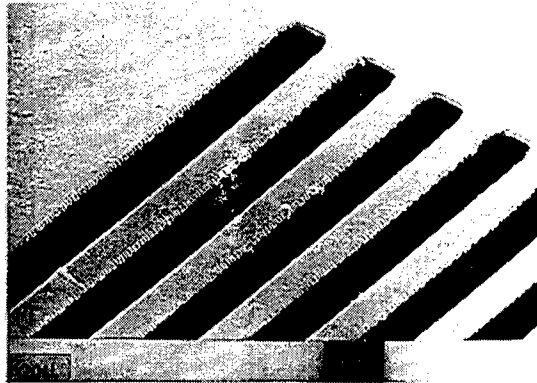


Figure 1 KrF laser ablatively etched grid in free standing 1.5μm thick polyethylene terephthalate film.

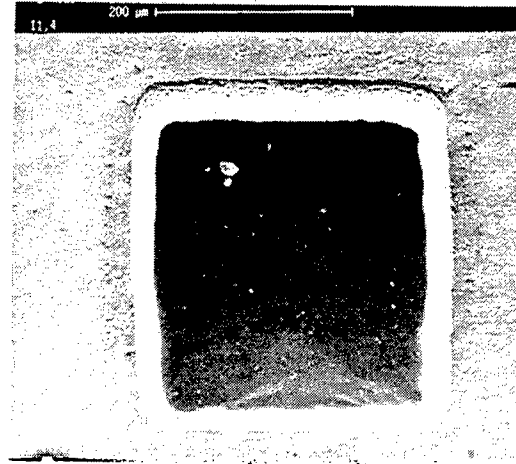


Figure 2 Via in Upilex polyimide produced using 9.2μm TEA CO₂ laser ablation.

The existence of a 'threshold' in the (UV laser) ablative photodecomposition model can be understood in terms of the need to break a sufficient density of bonds to produce volatile products which are in turn expelled rapidly enough from the surface to prevent bond 'remaking'. In a thermal picture a very sharp increase in the formation of volatile products with temperature T follows from Arrhenius decomposition rates which vary as

$$k = A \exp - E_A/RT \quad (4)$$

Here A is the frequency factor and E_A the activation energy. An apparent threshold then arises from the need to attain a sufficiently large value for k that decomposition can occur on the time-scale of the heating phase. If this corresponds to a temperature T_D then from equation 2, the depth to which ablation occurs can be found as:

$$x = \frac{1}{\alpha} \ln \left(\frac{F}{F_T} \right) \quad (5)$$

where $F_T = \rho c(T_D - T_R)/\alpha(1-R)$ is the threshold fluence and T_R the initial temperature. This familiar 'Beers Law' form for ablation indicates that F_T will vary inversely as the absorption coefficient.

Equation 5 neglects the fact that material undergoing the 'phase transition' to form ablation products may have different optical absorption to the parent solid. Taking this into account¹³

$$x = \frac{\mu}{\mu_p \alpha} \ln \left\{ 1 + \frac{\mu_p}{\mu} \frac{(F - F_T)}{F_T} \right\} \quad (6)$$

where $\mu = \alpha/\rho$ and $\mu_p = \alpha_p/\rho_p$ are the mass absorption coefficients of the solid and plume respectively.

When the plume retains the same mass absorption coefficient as the parent solid this reduces to equation 5. If $\mu \neq \mu_p$ then $x - \ln F$ plots will be non-linear, curving upwards or downwards depending on whether the plume has a lower or higher mass absorption coefficient (Figure 3). Changes in chemical composition, temperature induced broadening and shifts, and plasma absorption are possible mechanisms which will lead to the plume properties differing from those of the solid. Without clear information on these processes it is difficult to draw definite conclusions on the ablation mechanism simply from etch rate curves.

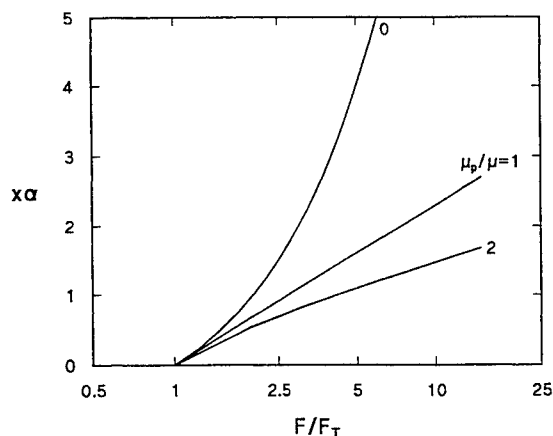


Figure 3 Variation of normalised etch depth, $x\alpha$, with fluence for various values of the ratio of mass absorption coefficients for plume and solid.

The very high heating rates attainable using lasers ($\sim 10^{11} \text{ K s}^{-1}$) has recently been invoked to explain the unusual spectra of decomposition products that appear in the ablation of various polymers¹⁴. Under rapid heating to high temperatures, decomposition pathways involving high activation energies and high frequency factors (equation 4) can be favoured over those with lower activation energy that predominate in conventional thermolysis. Lack of information on high temperature ($\geq 1000 \text{ K}$) thermolysis makes unravelling photochemical and photothermal steps in ablation a non trivial task.

Unhindered by an incomplete mechanistic understanding, applications of laser polymer ablation have continued to develop. Notable examples include excimer laser drilling of vias in polyimide layers¹⁵ and multilevel circuit boards¹⁶, catheters and fibres¹⁷ and hole drilling for ink jet nozzles. Micromachining for optoelectronic component fabrication¹⁸, the ablative recording of gratings on polymers¹⁹, surface modification⁹ and cleaning based on ablation have also been reported.

4. PULSED LASER ABLATION DEPOSITION

The use of lasers as an evaporation source for thin film deposition has a long history and up to the mid 1980's there was a steady stream of work reported on this topic. In 1987 Dijkkamp et al³ reported the successful application of a KrF laser to deposit thin layers of the high temperature superconductor $\text{YBa}_2\text{Cu}_3\text{O}_7$ (YBCO), initiating a major growth of activity on the use of pulsed laser ablation deposition (PLAD) for film growth. PLAD has proved to be extremely popular for the growth of layers and multilayers of, principally, inorganic materials and has been the subject of a detailed review by Beech and Boyd²⁰.

In the basic arrangement a pulsed laser (eg. excimer, fundamental Nd:YAG or harmonics, TEA CO_2) irradiates the source target in vacuo or a low pressure gas at a fluence which leads to volatilization of the target material. Expelled material in the form of an ablation plume is then directed to a suitable substrate where it condenses (Figure 4). Deposition rates are usually $\leq 1 \text{ Å/pulse}$ so that many thousands of laser pulses are needed to grow micron thick films. Epitaxial, crystalline and amorphous layers and multilayers have been grown in this way by suitable choice of the deposition conditions.

Attractive features of PLAD include: non contaminating photon source and compatibility for use in reactive atmospheres; stoichiometric transfer from complex multielement targets; energetic neutral and ion species (cf thermal source); versatile, flexible and simple. Against these must be set the disadvantages of the highly forward-directed nature of the plume which produces uniform coverage only over limited areas, and the propensity for droplets to become incorporated in the films. Efforts to understand and overcome these problems continue.

In the ablation of inorganic materials the concept of a threshold fluence is widely used to characterise the interaction. For materials exhibiting a well defined vapour pressure-temperature relationship this threshold is largely a measure of the fluence (irradiance) at which sensible ablation depths can be determined by the experimentalist. If equation 1 is integrated over the heating cycle, taking into account the p-T dependence, then some degree of removal is

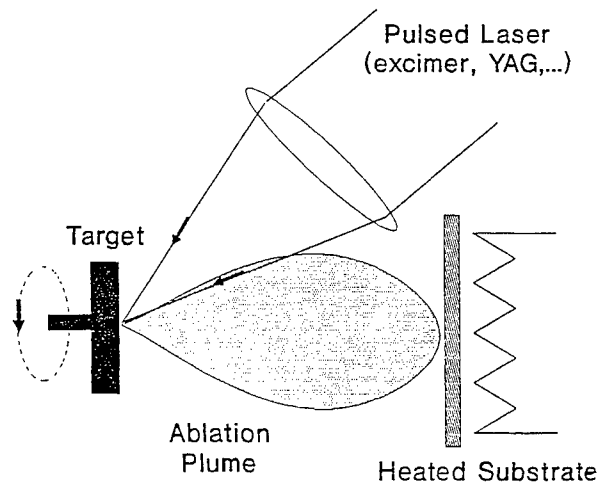


Figure 4 Pulsed laser ablation deposition geometry

some constant, there is a very strong temperature dependence and meaningful (measurable) removal only occurs above some relatively high temperature. As with polymers the 'threshold' marks a change to significant removal and is not a precise 'switching' point.

Stoichiometric transfer from target to substrate is an appealing aspect of PLAD and suggests a classical evaporation process may not apply as this would tend to lead to non-congruent evaporation for multielement targets. Stoichiometric films have been grown from complex oxides using PLAD, examples being the high temperature superconductors²⁰ (eg. YBCO); YIG²¹; YAG²²; the colossal magneto-resistance material $\text{La}_{60}\text{Ca}_{40}\text{MnO}_2$ ²³; and biocompatible hydroxyapatite, $\text{Ca}_{10}(\text{PO}_4)_6(\text{OH})_2$. This points to the possibility that explosive removal (ie. a phase explosion) occurs as outlined in section 2; being a volume rather than surface vaporisation process, this would act to preserve stoichiometry⁵.

For materials which exhibit significant spectral variation in their absorption (eg. glasses, some oxides) it is advantageous to work at a laser wavelength where the target exhibits strong absorption. This not only reduces the threshold but also the extent of droplet incorporation in films. Beam-plume interactions are also wavelength dependent and with, for example, long wavelength lasers (eg. $10\mu\text{m}$ CO_2) optical breakdown in the vapour above the surface may occur. High fractional ionisation and strong inverse bremsstrahlung absorption will then modify the plume dynamics. For UV lasers, although electron cascade breakdown is not expected at the irradiances used for deposition, a transition to plasma formation is observed at modest fluence²⁴. The fractional ionisation is higher than expected from thermal (Saha) ionisation and points to the likelihood that excited state photoionisation is an important route to charge species production in the UV.

Understanding the neutral and ion species dynamics ablation plumes and their influence on film properties form an important aspect of ongoing research.

5. BIOLOGICAL TISSUE ABLATION

Tissue ablation presents special problems in terms of gaining mechanistic understanding, the composite nature (involving protein, free and bound water) and heterogeneous structure of tissue bringing additional complexity. An interesting and important application which has emerged for the 193 nm ArF laser is its use for the removal of corneal tissue². Termed photorefractive keratectomy²⁶ this technique uses the ArF laser for highly controllable removal of the corneal surface (at the submicron level) allowing its reshaping to correct vision defects. Progress has been rapid, particularly at the technical and clinical level although questions remain as to the precise mechanisms involved in the ablation step. The status of this work has recently been reviewed by Pettit et al²⁵.

6. ANALYSIS

Ablation provides an effective means of volatilizing targets to produce a 'pulse' of products for subsequent analysis to ascertain their chemical composition or for use in neutral/ion beam experiments²⁶. The ablation of, for example, films of fullerenes (C_{60}) has been the subject of detailed study²⁷. In the technique of MALDI (Matrix Assisted Laser Desorption Ionisation) a laser absorbing semicrystalline organic matrix hosting a low concentration of protein molecules is ablated to produce intact protein ions for subsequent analysis by mass spectrometry²⁶. The matrices (eg. ferrulic acid) have low ablation enthalpies and high absorption in the UV and consequently exhibit low thresholds ($F_T \sim 10 \text{ mJ cm}^{-2}$) allowing use of compact 337 nm N_2 laser sources. Very large proteins ($> 500,000 \text{ u}$) have been analysed in this way and the technique has important applications in the biomedical sciences.

7. CONCLUSIONS

This brief, and necessarily restricted, review of laser ablation has attempted to provide a flavour of some of the important mechanistic aspects of the interaction process as well as various applications which have emerged. As a topic laser ablation is distinctly multidisciplinary with applicability in physics, chemistry, engineering and the biomedical sciences. Advances in understanding of the basic processes, cross-fertilisation between different areas, and improving laser technology should help spur an increasing uptake of ablation in the scientific and industrial environments and stimulate the emergence of new applications.

8. ACKNOWLEDGEMENTS

Thanks go to Dr P H Key for preparing the diagrams and to Mr G C Roberts for providing figure 2.

9. REFERENCES

1. R Srinivasan and V Mayne-Banton, "Self-developing photoetching of poly(ethylene terephthalate) films by far-ultraviolet excimer laser radiation", *Appl. Phys. Lett.* **41**, 576-578 (1982); R Srinivasan and W J Leigh, "Ablative Photodecomposition: Action of Far Ultraviolet (193 nm) Laser Radiation on Poly (ethylene terephthalate) Films *J. Am. Chem. Soc.* **104**, 6784-6785 (1982).
2. S T Trokel, R Srinivasan and B Braren, "Excimer Laser Surgery of the Cornea", *Am. J. Ophthalmolog.* **96**, 710-715 (1983); R Linsker, R Srinivasan, J J Wynne and D R Alonso, "Far ultraviolet laser ablation of atherosclerotic lesions", *Laser Surg. Med.* **4**, 201-206 (1984).
3. D Dijkkamp et al, "Preparation of Y-Ba-Cu oxide superconductor thin films using pulse laser evaporation from high T_c bulk material", *Appl. Phys. Lett.* **51** 619-621 (1987).
4. R Kelly et al, "Laser Sputtering, Part I, on the Existence of Rapid Laser Sputtering at 193 nm", *Nucl. Instr. Meth.* **B9**, 329 (1985).
5. P E Dyer, S R Farrar and P H Key, "Fast time-response photoacoustic studies and modelling of KrF laser ablated YBa₂Cu₃O₇", *Appl. Surf. Sci.* **54** 255-263 (1992).
6. A Miotello and R Kelly, "Critical assessment of thermal models for laser sputtering at high fluences", *Appl. Phys. Lett.* **67**, 3535-3537 (1995).
7. M von Allmen, *Laser-Beam Interactions with Materials*, Springer, Berlin, 1987.
8. R Srinivasan and B Braren, "UV Laser Ablation of Organic Polymers", *Chem. Rev.* **89**, 1303-1316 (1989).
9. P E Dyer, "Laser Ablation of Polymers", Chapter 14, in *Photochemical Processing of Electronic Materials*, eds. I W Boyd and R B Jackman, Academic Press, London, 1992.
10. X Wen, D E Hare and D D Dlott, "Laser polymer ablation threshold lowered by nanometer hot spots", *Appl. Phys. Lett.* **64**, 184-186 (1994).
11. S Preuss and M Stuke, "Single-shot micro-patterning of polymer surfaces by UV incubation/dye laser ablation using photochromism", *Appl. Surf. Sci.* **69** 253-257 (1993).
12. J H Brannon and J R Lankard, "CO₂ laser etching of polyimide", *Appl. Phys. Lett.* **48**, 1226-1228 (1986).
13. K Schildbach, "A simple analytic model including shielding by the plume during excimer laser ablation of polyimide", in *Proc SPIE Int. Congress on Optical Science and Engineering*, The Hague, 1990 (paper 1279.07).
14. G B Blanchet and C R Fincher, "Laser ablation: selective unzipping of addition polymers", *Appl. Phys. Lett.* **68**, 929, (1996).
15. J R Lankard and G Wolbold, "Excimer laser ablation of polyimide in a manufacturing facility", *Appl. Phys. A* **54** 355-359, (1992).
16. F Bachmann, "Excimer lasers in a fabrication line for a highly integrated printed circuit board", *Chemtronics* **4**, 149-152 (1989).
17. M Gower, *private communication*.
18. B L Booth, "Optical Interconnection Polymers", Chapter 9 in *Polymers for Lightwave and Integrated Optics*, ed. L Hornak, Dekker, New York, 1992.
19. P E Dyer, R J Farley, R Giedl, C Ragdale and D Reid, "Study and analysis of submicron-period grating formation on polymers ablated using a KrF Laser irradiated phase mask", *Appl. Phys. Lett.* **64**, 3389-3391 (1994).
20. F Beech and I W Boyd, "Laser Ablation of Electronic Materials", Chapter 15, in *Photochemical Processing of Electronic Materials*, eds. I W Boyd and R B Jackman, Academic Press, London, 1992.
21. H Kidoh, A Morimoto, and T Shimizu, "Synthesis of ferromagnetic Bi- substituted yttrium iron garnet films by laser ablation", *Appl. Phys. Lett.* **59** 237-239 (1991).
22. M Ezaki, H Kumagai, K. Koboyashi, K Toyoda and M Obara, "Crystal growth of Nd:YAG laser films on various substrates by pulsed laser deposition", *Jpn. J. Appl. Phys.* **34** 6838-6841 (1995).
23. S Gangopadhyay et al, "Colossal magnetoresistance in pulsed laser-deposited thin ceramic films", *J. Mag. Mag. Mats.* **147**, L225-L230 (1995).
24. P E Dyer, "Electrical characterization of plasma generation in KrF laser Cu ablation", *Appl. Phys. Lett.* **55**, 1630-1632 (1989).
25. G H Pettit, M N Ediger and R P Weiblinger, "Excimer laser ablation of the cornea", *Opt. Eng.* **34**, 661-667 (1995).
26. "Laser Ionization Mass Analysis", ed. A Vertes, R Gijbels and F Adams, *Chem. Analysis Ser.*, Vol. 124, Wiley, 1993.
27. R Mitzner, B Winter, Ch. Kusch, E E B Campbell and I V Hertel, "Coalescence reactions in laser-induced fullerene desorption: the role of fragments", *Z. Phys. D*, **37**, 89 (1996).

Q-switched CO₂ laser ablation of organic polymers

T. Sakai, N. Hamada, K. Minamida, and R. Yoshihara

Technical Development Bureau, Nippon Steel Corporation,
5-10-1 Fuchinobe, Sagamihara, Kanagawa 229, Japan.

ABSTRACT

The polymers ablation by a Q-switched CO₂ laser is demonstrated and compared with that of the conventional TEA laser ablation. The 20 - 100 μ m depth ablative etching of PET with well defined edge were successfully obtained when the strong absorbed 9R(20) line at 1078.57cm⁻¹ was irradiated. It was found the ablation characteristics by a Q-switched laser was almost same as that by a TEA laser.

Keywords: Q-switched CO₂ laser, Ablation, Organic polymers, Laser materials processing

1. INTRODUCTION

Since early works of laser ablation using excimer laser^{1, 2}, lot of studies focused on its mechanism have been reported. Many applications such as micro-machining of polymers, surface cleaning of solid and superconducting thin-film deposition are expected by using a laser ablation. Most of organic polymers show the strong absorption in IR region as well as in UV region, the pulsed CO₂ laser can also ablate these materials successfully. In order to avoid the thermal damage, a short duration and high peak power pulse is preferable for laser ablation. Therefore, TEA CO₂ laser was adopted for the IR laser ablation studies³⁻⁵. Werner and Schweizer reported the paint stripping of aircraft using commercially available TEA CO₂ laser of 2kW average power³. Brannon and Lankard studied the ablative etching of Polyimide, which is the insulating material for micro-electronic device, using a tunable TEA CO₂ laser. They pointed out that Polyimide can be etched clearly and precisely by selecting the proper CO₂ laser line at strong absorption band⁴.

For the industrial applications of the laser ablations, it requires a high average power (pulse repetition frequency \times pulse energy) pulsed CO₂ laser in order to ablate the large area with high speed. However, the average power of commercial TEA CO₂ laser was limited up to 2kW. On the contrary, a Q-switched oscillation based on a cw CO₂ laser has great potential especially in power scaling as well as high beam quality and low operating cost. The repetition frequency can easily reach over 10kHz. Therefore, a Q-switched CO₂ laser is an attractive tool for the industrial applications of organic materials processing, if the laser ablation could be realized by a relatively long duration and low peak power pulse of a Q-switched laser. From this point of view, there is a great interest in the ablation characteristics by a Q-switched laser. In this report, the polymers ablation by Q-switched CO₂ laser have been demonstrated and compared with that of TEA laser ablation.

2. EXPERIMENTAL SETUP

The experiment was carried out by using the grating-tuned Q-switched CO₂ laser based on a commercial cw CO₂ laser (Trumpf TLF2000SP). The average output power of original cw laser system is 2kW. The laser beam spatial mode is TEM₀₁* ring mode with diameter of 18mm. This laser system was modified to high peak and high repetition frequency pulsed Q-switched laser using the intense pulsed rf discharge and high speed mechanical chopper⁶.

The Q-switched laser pulse consists of an initial spike followed by a low power tail. The peak power of initial spike is 100 - 300kW with 250 - 300ns duration (FWHM). The pulse tail is terminated by closing the chopper slit. The duration of tail and total pulse energy, therefore, can be controlled by the slit width and rotating speed of the chopper. The Q-switched laser ablation experiment was performed at 5.3 μ s duration and 70mJ total energy at 5kHz. A TEA laser pulse also consists of an initial spike and a tail. The time duration is shorter than that of Q-switched laser. The characteristics of the Q-switched and the TEA laser pulse used in ablation experiments are summarized in Table 1.

3. RESULTS AND DISCUSSION

Ablation characteristics

The ablative etching experiments were carried out using the thin film (20 - 100 μ m) of PET (Polyethylene terephthalate), PP (Polypropylene) on the metal plate. The IR absorption characteristics was examined for each polymer film. Fig.1(a) and (b) are the absorption spectrum of PET and PP respectively. PET shows relatively strong absorption in CO₂ laser band.

The hole profiles of PET film ablated by Q-switched and TEA laser pulses were shown in Fig.2(a), (b). The 20 - 100 μ m depth holes with well defined edge and without thermal damage were ablated successfully when the strong absorbed 9R(20) line at 1078.57cm⁻¹ was irradiated. The hole profile was apparently affected by the laser beam mode. It was found the etching quality was almost independent on the laser pulse temporal shape. These results indicate that a Q-switched laser can successfully ablate the polymers with similar mechanism as TEA laser ablation in spite of its relatively long duration and low peak pulse.

Fig. 3 shows hole profiles of PP ablation. 10R(18) line at 974.61cm⁻¹ was selected for this experiment. Although PP shows relatively strong absorption at this line, the energy absorbed in polymer is much smaller than that in case of PET. As shown in Fig.3, the rim around hole was observed, which is probably due to the melting and the internal vaporization because the large part of laser energy penetrate the film.

The microscope photos of ablated edge are given in Fig.4. No thermal damage around the ablated area was observed for PET ablation, where the melted zone was observed for PP ablation. This is mainly attributed to the small thermal conductivity of PET (3.36×10^{-4} Cal sec⁻¹ cm⁻¹ K⁻¹)⁷. In addition, the heat transfer to around area can hardly melt the polymer due to the relatively high melting point of PET (538 - 544K)⁷. Therefore, PET is the suitable polymer for sharp etching by a CO₂ laser ablation.

Ablation rate

The ablated depth per pulse (= ablation rate) was examined and compared with that of TEA laser ablation. Fig.5 shows the ablation rate as a function of laser pulse fluence [J/cm²] for a Q-switched and a TEA laser, where the laser line was tuned at 9R(20) line. The experimental results indicate that the ablation rate was almost same in spite of the difference of pulse temporal shape. The threshold fluence was estimated 0.6J/cm², which corresponds to the value obtained for the other TEA laser experiment⁵. It is considered the irradiated laser line is more predominant factor for PET ablation than the pulse peak power or temporal duration of CO₂ laser pulse.

Since the ablation rate of PET is independent of the laser pulse temporal shape, the ablation speed, which is defined by the ablation area per unit time, is simply proportional to the average power of a laser system. A Q-switched CO₂ laser has a great advantage on this point. For example, the ablation speed for 10 μ m thick PET film by using a 10kW average Q-switch laser is estimated to be 900m²/hr., where the pulse repetition frequency is 20kHz, the pulse energy is 500mJ.

4. CONCLUSION

The ablative etching of polymers by a Q-switched CO₂ laser was examined. The ablation rate and its quality were almost same as that by a TEA laser. Considering the power scaling capability, a Q-switched CO₂ laser will be an attractive tool for the industrial applications of polymers ablation such as the paint stripping or machining of the micro-electronics device.

	Total pulse energy [J]	Initial spike peak power [W]	Total pulse duration [sec]	Pulse repetition frequency [Hz]	Average power [W]
Q-switched laser	7.0×10^{-2}	2.3×10^5	5.3×10^{-6}	5.0×10^3	3.50×10^2
TEA laser (Lumonics TEA-840)	2.5	2.0×10^7	2.0×10^{-6}	0.5	1.25

Table 1 Laser pulse characteristics of CO₂ lasers used in ablation experiment.

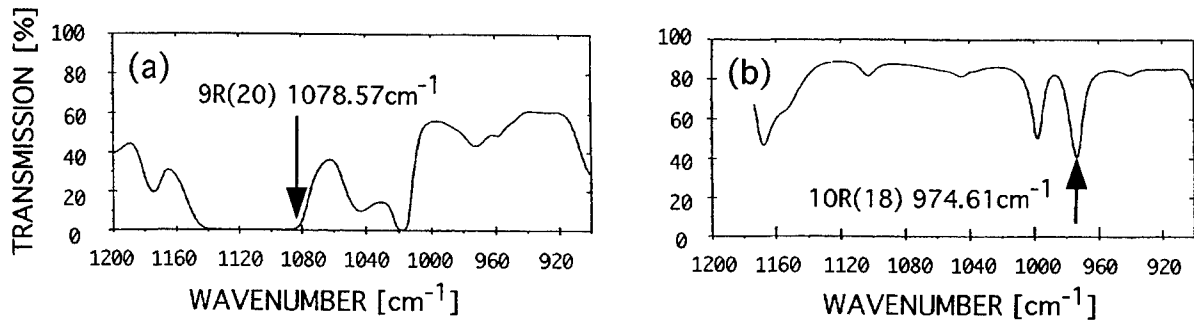


Fig. 1 Absorption spectrum of PET and PP.
(a) PET film: 30 μ m thick, (b) PP film: 25 μ m thick.

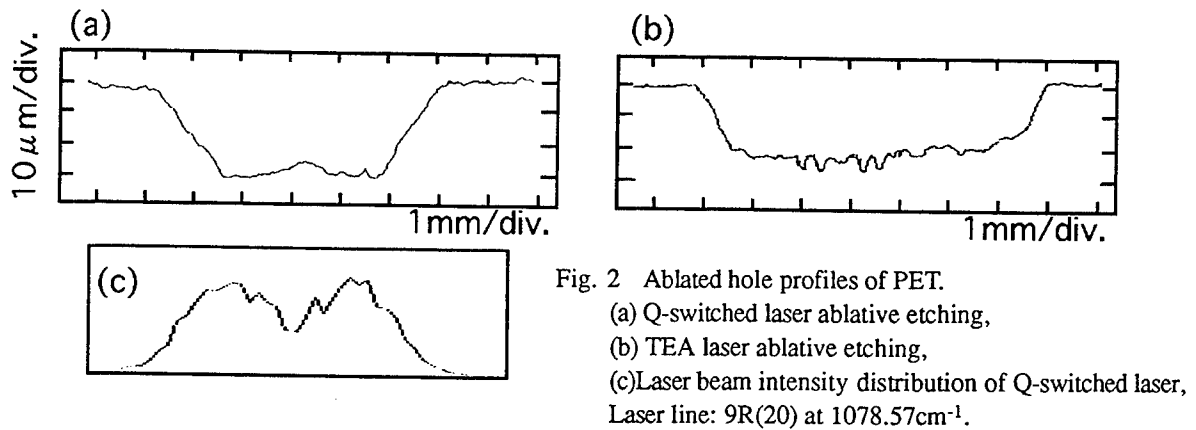


Fig. 2 Ablated hole profiles of PET.
(a) Q-switched laser ablative etching,
(b) TEA laser ablative etching,
(c) Laser beam intensity distribution of Q-switched laser,
Laser line: 9R(20) at 1078.57 cm^{-1} .

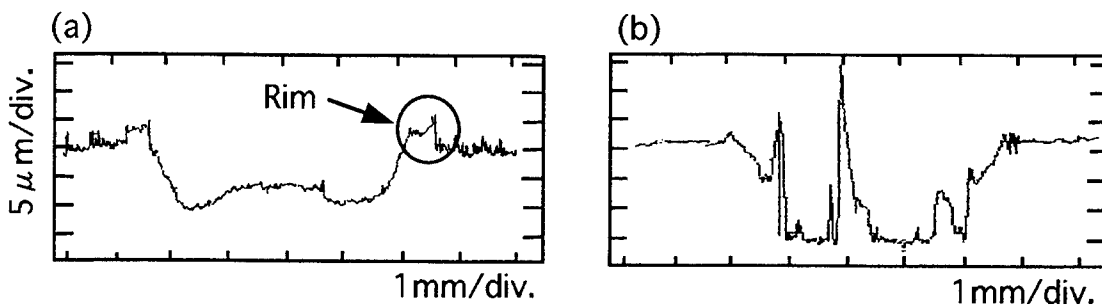


Fig. 3 Ablated hole profiles of PP.
(a) Q-switched laser ablative etching, (b) TEA laser ablative etching,
(c) Laser beam intensity distribution of Q-switched laser, Laser line: 10R(18) at 974.61 cm^{-1} .

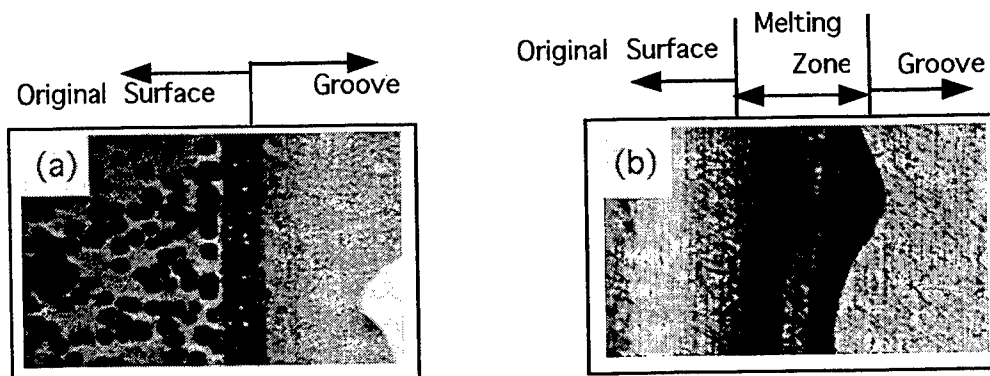


Fig. 4 Microscope photos of ablated surface by Q-switched laser.
(a) PET, Laser line: 9R(20) at 1078.57cm^{-1} , (b) PP, Laser line: 10R(18) at 974.61cm^{-1} .

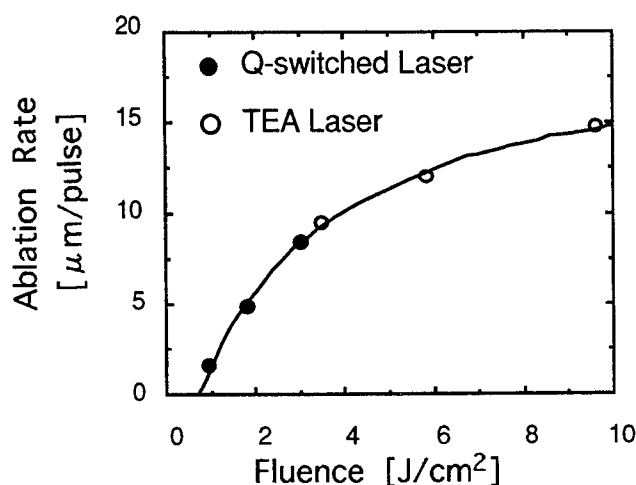


Fig. 5 Ablation rate of PET by the pulsed CO₂ lasers.
Laser line: 9R(20) at 1078.57cm^{-1} .

References

1. R. Srinivasan, V. Mayne-Banton, "Self-developing photoetching of poly(ethylene terephthalate) films by far-ultraviolet excimer laser radiation," *Appl. Phys. Lett.*, Vol.41, pp576-578, 1982.
2. J. E. Andrew, P. E. Dyer, D. Forster, P. H. Key, "Direct etching of polymeric materials using XeCl laser," *Appl. Phys. Lett.* Vol.43, pp717-719, 1983.
3. G. Schweizer and L. Werner, "Industrial 2kW CO₂ laser for paint stripping of aircraft," *Proc. 10th int. conf. Gas Flow and Chemical Lasers*, SPIE, Vol.2502, pp57-62, 1994.
4. J. H. Brannon and J. R. Lankard, "Pulsed CO₂ laser etching of polyimide," *Appl. Phys. Lett.*, Vol.48, pp1226-1228, 1986.
5. P. E. Dyer, G. A. Oldershaw, and J. Sidhu, "CO₂ laser ablative etching of Polyethylene terephthalate," *Appl. Phys. B*, Vol.48, pp489-493, 1989.
6. T. Sakai and N. Hamada, "A Q-switched CO₂ laser using intense pulsed RF discharge and high speed rotating chopper," *Proc. 10th int. conf. Gas Flow and Chemical Lasers*, SPIE, Vol.2502, pp25-30, 1994.
7. B. V. Petukhov, "Technology of Polyester Fibers," Macmillan Co., New York, N.Y., 1963.

Irradiation of fabrics of nylon and polyethylene terephthalate with short, frequency selected pulses from CO and CO₂ lasers

Andrei Ionin¹, Klaus Kleine², Henry Kobsa²

1. Lebedev Institute, Leninsky pr.53 Box 117924, Moscow

2. E. I. DuPont de Nemours and Co., Inc.

P O Box 80715, Wilmington, Delaware 19880-0715

Melt-spun fibers such as nylon and polyester offer many valuable features. They are stronger than natural fibers such as cotton or wool, so garments last longer. They provide superior wrinkle resistance and super wash-and-wear performance on fabrics. However, the aesthetics of nylon and polyester fabrics are inferior to those of cotton or wool fabrics. The smoothness of melt-spun fibers results in specular reflections from the fiber surface. This specularly reflected light is white which makes it more difficult or impossible to achieve deep, saturated shades. This effect is particularly noticeable when a garment is worn in highly directional light such as direct sunlight. In certain fabric constructions, this can lead to an undesirable "plastic" look. The smooth fiber surfaces also result in a large contact area with skin which is often perceived as a "plastic" feel.

By contrast, natural fibers, such as cotton or wool, have rough, scaly surfaces which diffuse the specular reflections in many directions, so they are not perceived. Their rough surfaces also have lower contact areas with human skin which results in preferred tactile aesthetics. Their problems have been well understood for half a century and there have been many, many attempts to roughen melt-spun fibers; but none have proven commercially feasible.

Bossmann and Schollmeyer (patent filed in Germany 1985, US Patent No. 5,017,423, 1991) discovered that irradiating fabrics of nylon or polyester with short, intense pulses of UV light from excimer lasers produced transverse ridges on the filaments which acted much like the scales on wool to break up the directional specular reflections and simultaneously reduce the contact area with the skin to improve both the visual and tactile aesthetics of the irradiated fabrics. In our hands, about 40 pulses of 50-100 mJ/cm² each produced the best results. Both KrF (248nm) and ArF (193nm) are effective for irradiating polyester; but only ArF works for nylon. It was clear from the beginning that the intense pulses of UV light, typically about 20 ns in duration, are absorbed in the outermost micrometer of the fiber which melts and often reaches temperatures of greater than 1000°K. However, the detailed mechanism by which the transverse ridges are formed was not understood in the early years.

Using excimer lasers in DuPont's laboratories in Wilmington, we showed that a wide variety of nylon and polyester fabrics can be successfully irradiated to produce fabrics which combine the attractive visual and tactile aesthetics of cotton or wool fabrics with the durability, wrinkle resistance, and wash-and-wear performance of fabrics of 100 percent nylon or polyester. Extensive wear tests in such demanding end uses as bicycle pants proved that the desired aesthetic improvements were retained in use.

Nevertheless, we were dubious about the feasibility of using this technology on a commercial scale. Excimer lasers have proven to be difficult to scale up to more than a few hundred watt, not enough for a commercial finishing line. Moreover, they are difficult to maintain, especially if operated with ArF. Fortunately, nylon and polyester have one or more strong absorption band(s) in the infrared. The CO laser can be tuned to the absorption band of the carbonyl group in these two polymers which occurs at 6.106 micrometer for nylon and 5.817 micrometer for polyester. In addition, polyester has a strong absorption band at the wavelength of the 9P48 line of the CO₂ laser at 9.15 micrometer.

Initial efforts to use IR radiation to surface texture nylon and polyester fibers proved frustrating because we did not understand the mechanism by which the surface textures is formed. To cut a long story short, the transverse ridges on the fibers form only if two conditions are met: the fibers are highly oriented; and the intensity of the radiation field varies spatially over distances of a few micrometers. While we did

not know it at the time, such short-range intensity fluctuations are characteristic of most excimer lasers; but rare in most other types of lasers. We obtained our first success with a TEA CO₂ laser in 1991 by removing the apertures from the laser cavity and producing a chaotic, multi-mode discharge similar to that in an excimer laser.

From that, it was a simple step to set-up interference patterns by splitting and recombining laser beams. With excimer lasers, this resulted in a reduction of the number of pulses required to produce the desired transverse ridge structure by an order of magnitude from 40 to just 4 pulses.

Figure 1 shows an unirradiated polyester fabric: the filaments are seen to be very smooth. Figure 2 shows nylon and polyester fabrics irradiated with an ArF laser. Figure 3 shows polyester fabrics irradiated with two interfering beams at the wavelength of the 9P48 line of the CO₂ TEA laser. Figure 4 shows a polyester filament irradiated with single 200 mJ/cm² pulse of the 9P48 line.

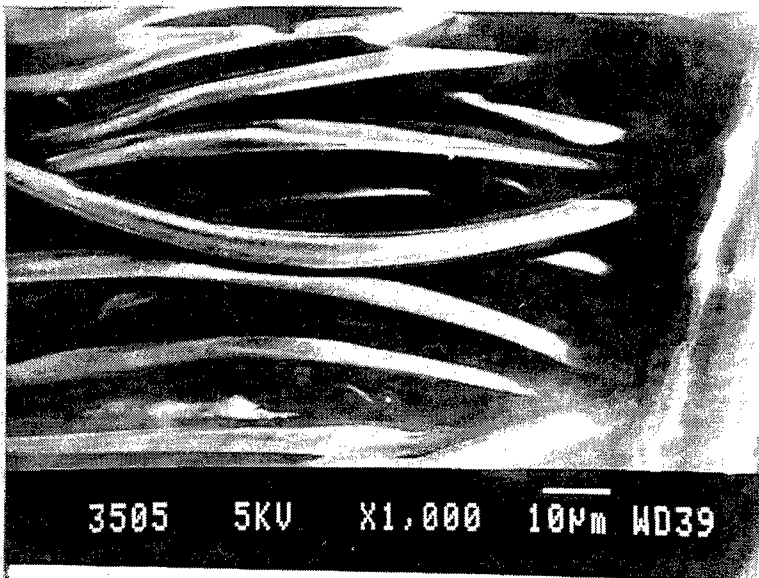


Fig. 1 unirradiated polyester fabric

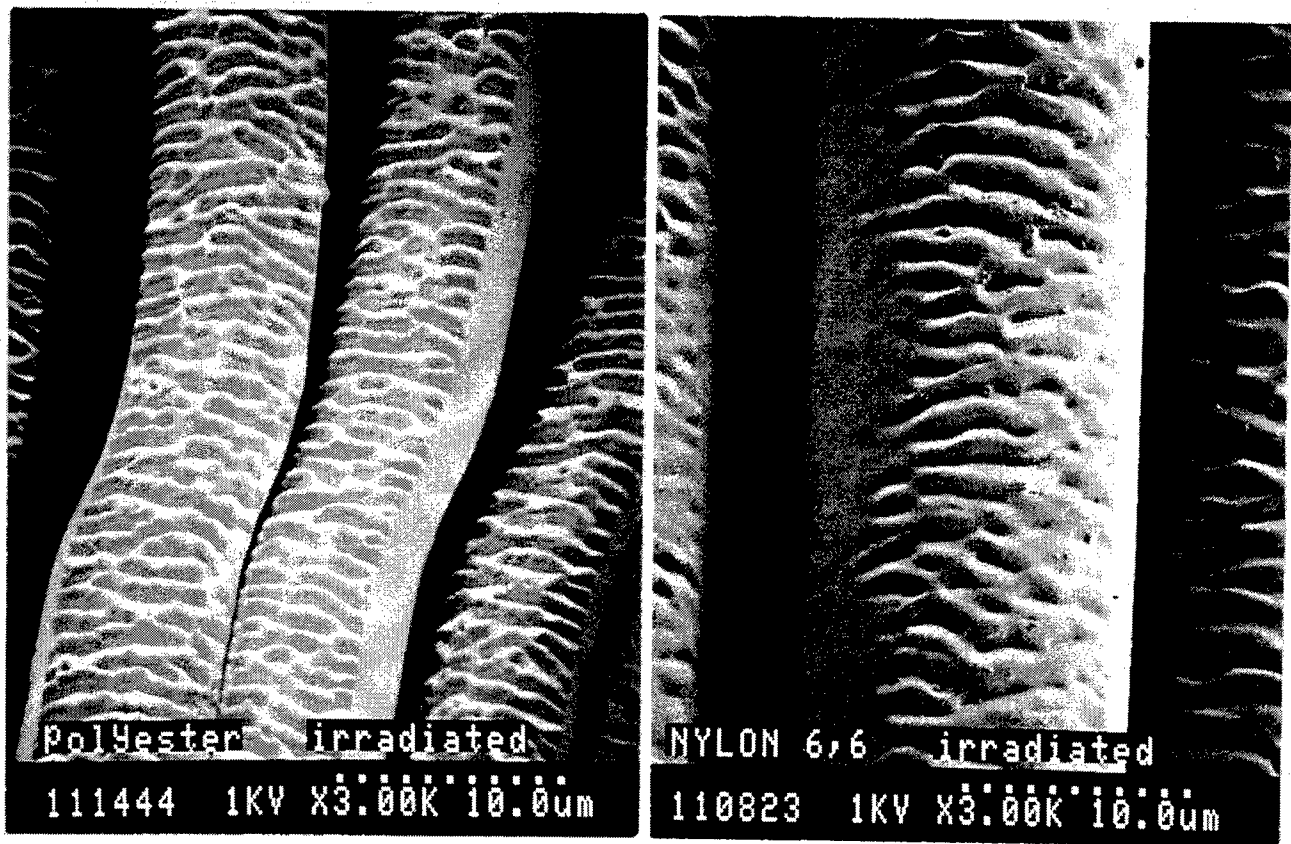


Fig. 2 nylon and polyester fabric irradiated by ArF Laser

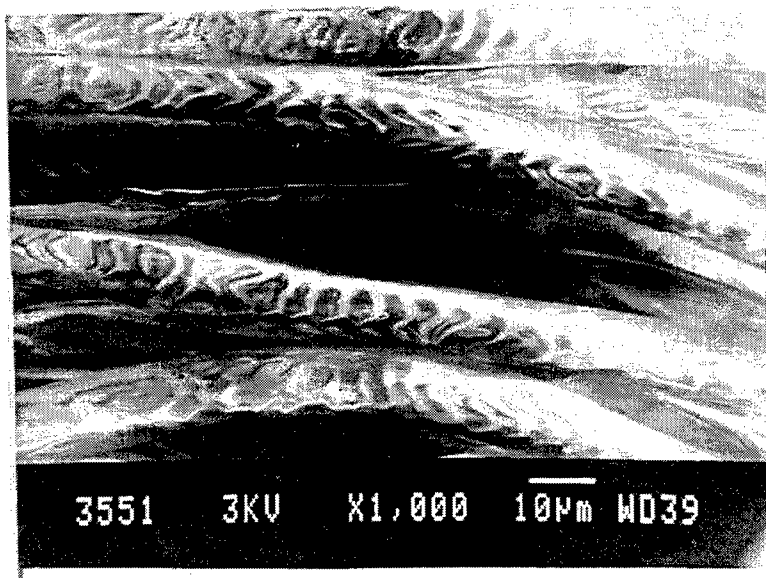


Fig. 3 polyester fabric irradiated by two interfering CO₂ TEA Laser beams of 9.15 micrometer wavelength (9P48 line)

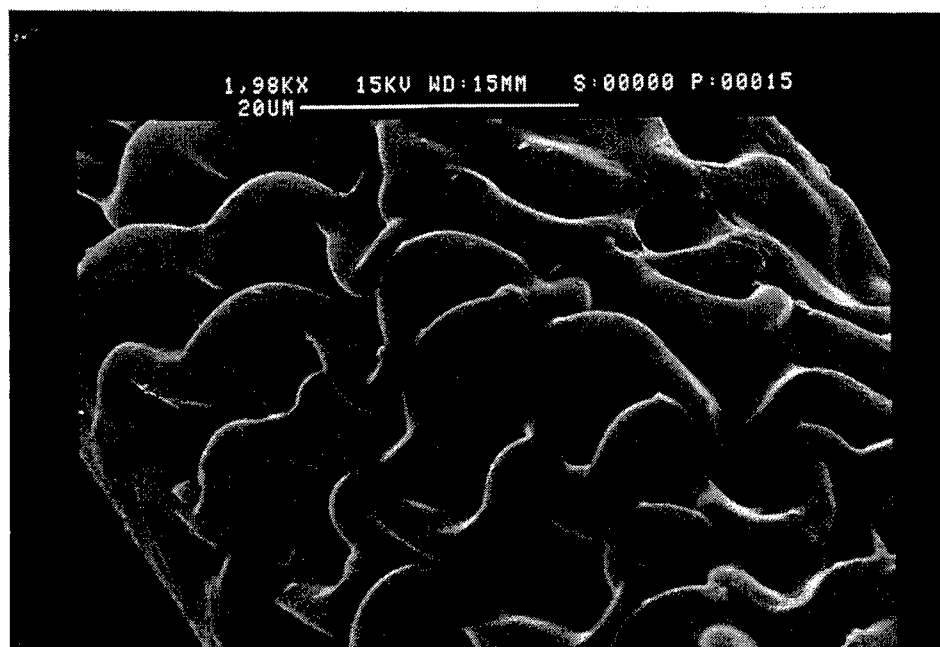


Fig. 4 polyester fabric irradiated by a single 200 mJ/cm² pulse of 9.15 micrometer wavelength

Micromachining with Copper Lasers

M. Knowles, A Bell, G Foster-Turner, G Rutterford, J. Chudzicki, A Kearsley
Oxford Lasers Ltd., Abingdon Science Park, Abingdon, OX14 3YR, U.K.

ABSTRACT

In recent years the copper laser has undergone extensive development and has emerged as a leading and unique laser for micromachining. The copper laser is a high average power (10 - 250W), high pulse repetition rate (2 - 32 kHz), visible laser (511nm & 578nm) that produces high peak power (typically 200kW), short pulses (30ns) and very good beam quality (diffraction limited). This unique set of laser parameters results in exceptional micro-machining in a wide variety of materials. Typical examples of the capabilities of the copper laser include the drilling of small holes (10 - 200 μ m diameter) in materials as diverse as steel, ceramic, diamond and polyimide with micron precision and low taper (<1 $^\circ$) cutting and profiling of diamond. Application of the copper laser covers the electronic, aerospace, automotive, nuclear, medical and precision engineering industries.

Keywords: micromachining, lasers, copper vapour lasers, laser systems, hole drilling, cutting, etching

2. RECENT DEVELOPMENTS IN COPPER LASERS

Whilst the copper laser has existed for thirty years, it is only in the last five years that it has been used for micromachining. Prior to this the beam quality of the lasers had been unsuitable. However, as a result of internal investment as well as co-operative programs such as Eureka and Brite-Euram, Oxford Lasers has developed a range of lasers and laser systems for micro-machining. In addition to this, in partnership with end-users we have developed many processing techniques and applications.

In terms of laser performance recent notable developments include industrial grade laser tubes, extended thyratron lifetime, feedback stabilized output power, diffraction-limited beam divergence. For example, the power stabilization locks the output power of the laser to within 0.5% of a user defined level. The latest resonator designs produce diffraction limited beams (about 50 μ rad for a typical copper laser). Thus focused spot sizes of a few microns can be readily achieved. The high optical quality of a copper laser amplifier enables the oscillator beam to be efficiently amplified to several hundred watts average power without significant degradation of the beam divergence.

Whilst laser development has been important in improving the fundamental processing performance, the integration of the laser into a machining system is of equal importance. The approach taken by Oxford Lasers is first to develop systems for use in-house and for our contract manufacturing service. This enables designs to be evaluated under realistic circumstances before offering the system on the market. Typical features include high magnification CCD camera for alignment and monitoring of the machining process, programmable laser exposure and high precision CNC systems. Early adopters of copper laser systems have been in the automotive and electronics industries.

3. DESCRIPTION OF MACHINING PROCESS

The material-removal mechanism is a complex process which depends on laser and material characteristics such as the absorption of the material, thermal properties, laser intensity, pulse width and average power. However, the material removal process with copper lasers can be generalized as ablative, that is, rapid surface vapourization. This ablative material removal assures a controllable effect with negligible heat affected zone.

4. BENEFITS OF COPPER LASERS FOR MICROMACHINING

The Copper Laser parameters have enabled it to add a totally new capability to the field of micromachining.

4.1 Wavelength

In radiation/material interaction the laser wavelength determines the type and degree of interaction. The reflectivity of many metals in the infra-red is typically $> 90\%$ and in some cases $> 98\%$. At the copper laser wavelengths the reflectivity is typically $50 - 60\%$. In contrast with other laser types, most of the material is ejected on the irradiated side at high velocities. This ejection of the material results from the sudden increase in pressure at the irradiation point from the very rapid heat input. The direction of ejection is away from the irradiated zone and the cone angle is quite narrow (this is important if material is to be ejected from the bottom of a very deep but narrow cut or hole). Thus it is not necessary to penetrate the material first before efficient cutting can commence.

4.2 Pulsewidth

The short pulsewidth of the CVL is advantageous in reducing heat affected zone. If the material is to be removed via evaporation or explosive melt ejection then it is necessary to create extremely high temperature gradients. High temperature gradients around the irradiated zone keeps the total heat absorption of the component

very low. At the same time it creates a very distinct and narrow barrier between the irradiated zone and the surrounding material. Thus the layer of material which melts but is not explosively ejected (recast layer) is very thin.

4.3 Repetition Rate

In many applications the repetition rate and average power of the laser determines the rate of material removal and therefore the process speed. The copper laser has the highest average power and pulse repetition frequency product of any visible or UV laser. When a low pulse energy is required to avoid an extended heat affected zone then it is clear that a high repetition rate laser is necessary to achieve a good process speed.

4.4 Beam Quality

The minimum size that a laser beam may be focused to is determined by its wavelength and the beam quality. The copper laser has significant advantages over CO₂, and Nd:YAG lasers in terms of the minimum spot size to which it may be focused as a result of its shorter wavelength. Copper lasers are commercially available in configurations with powers exceeding 100W with a large proportion of that power within the diffraction limit. Recent laboratory developments on copper laser resonators have increased the power within the diffraction limit to almost 100%. These resonators are now being used on Oxford Lasers products.

5. TYPICAL MICROMACHINING RESULTS

The copper laser produces excellent micro-machining results in a wide range of materials including metals, ceramics, metal-matrix-ceramics, diamond, glass, silicon, superconductors, composite fibre materials and polyimides.

5.1 Hole Drilling

The high peak power, good beam quality and short wavelength enables high precision drilling in metals and non-metals. The ablative nature of the material removal and low pulse energy permits drilling of small diameter through and blind-holes. The copper laser is capable of drilling holes as small as a few microns and as large as several hundred microns, larger holes are formed by CNC trepanning. The high coupling of the copper laser radiation into most materials enables the drilling of holes at an angle to the surface. Holes have been drilled at angles of 10° - 90° to the surface. Angled holes are used in the aerospace industry to improve the cooling of components.

5.2 Cutting and Profiling

The same properties that enable the copper laser to perform high precision drilling also facilitate high precision cutting and profiling. Kerf widths are typically in the range of 5 - 100 μm . One example of the difficult processes that have been successfully addressed is the cutting of 15 μm wide, 800 μm deep, blind slots in stainless steel. Ceramics are cut with speed and precision. The ablative processing of the copper laser results in a complete absence of glassification. Silicon shows strong absorption of copper laser radiation and this enables high precision cutting and drilling at speeds of up to 10 times higher than competing laser technologies. For example, accurate 125 μm diameter holes have been drilled through 1.75 mm thick silicon at a rate of 10 holes per minute. Recent work in CVD diamond has resulted in high precision cutting with taper angles less than 0.5° . Profiled diamond components are used in the electronics and tool-making industries.

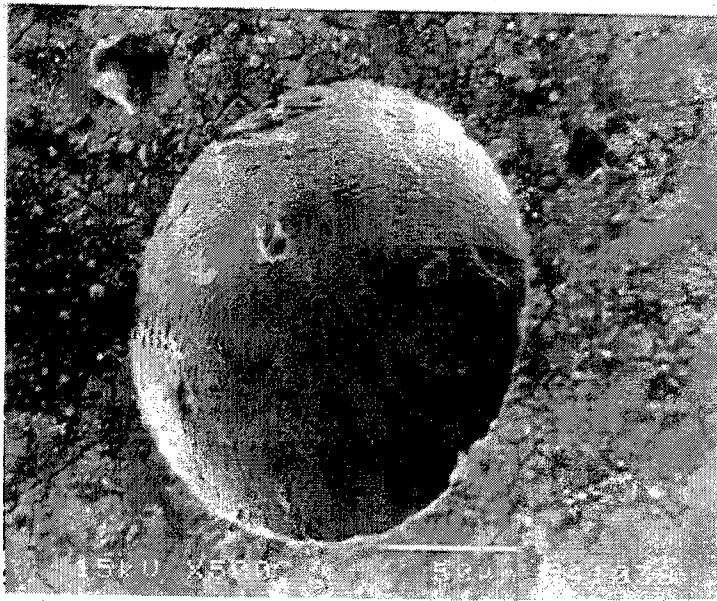


Fig. 1. Example of a 150 μm diameter hole drilled through 1mm thick stainless steel by a Copper Laser.

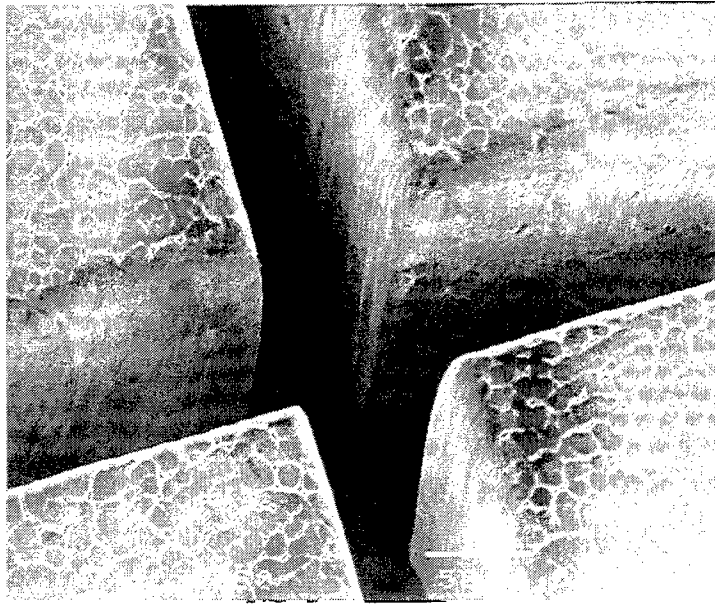


Fig. 2. Low taper, narrow kerf cutting of CVD diamond.

6. CONCLUSIONS

The copper laser is an emerging tool in micromachining. It demonstrates clear advantages over other processes in certain applications which have been addressed by the early adopters of this technology. The benefits of this laser seem to be especially applicable to small hole drilling and high precision cutting although as research continues new applications are being discovered.

Excimer Laser Beam Shaping and Material Processing using Diffractive Optics.

S.W.Williams, P.J.Marsden, N.C.Roberts, J.Sidhu and M.A.Venables

British Aerospace, Sowerby Research Centre
FPC 267, PO Box 5 Filton, Bristol BS12 7QW

ABSTRACT

Diffractive optical systems have been developed to allow high efficiency material processing using excimer lasers. These systems allow beam homogenising and shaping for surface treatment and parallel focusing for multiple hole drilling. Beam utilisation factors of 80% have been achieved.

(Excimer lasers, beam shaping, diffractive optics, drilling, surface treatment)

1 INTRODUCTION

With the advent of higher power excimer lasers new applications are becoming possible. Examples in the aerospace industry are manufacturing of porous panels (PP) for hybrid laminar flow control systems, drilling of carbon fibre composite (CFC) for acoustic damping panels and various surface treatments for bonding applications. However all of these applications require the processing of large areas (typically several square metres) so that highly efficient beam delivery systems are required. We have been investigating the use of diffractive optical elements (DOEs) for these delivery systems and have been testing them for the applications described.

2 DIFFRACTIVE OPTICAL ELEMENTS

For drilling of PPs the most appropriate DOE is a microlens arrays (MLA). The requirements of the MLA are a high fill factor to maximise the efficiency, long focal lengths for the correct processing conditions, good UV transparency and a high damage threshold. Square or hexagonal multilevel diffractive lenses manufactured in fused silica satisfy these requirements. For beam shaping and homogenising these MLAs have been evaluated directly. For drilling the acoustic dampers special arrays producing ring foci have been produced. The DOEs are computer designed and then reactive ion etched using photolithographic patterning. Substrates are generally 3mm thick and can be etched uniformly over an area with a diameter of about 50mm, sufficient to accommodate the beam size from most excimer lasers. Because of the short wavelength of the excimer laser etch depths are small, typically 314nm, but can be controlled to better than 3% accuracy (<10nm). If necessary AR coatings are applied to the flat side of the elements.

3 MULTIPLE HOLE DRILLING USING MICRO LENS ARRAYS.

The PP specification is currently 40-60 μ m diameter holes with 1-2% sheet porosity in 1mm thick titanium. Other materials such as aluminium and CFC are also of interest. The design of the MLA needs to be such that it optimises the drilling rate, achieves the correct hole profile and does not exceed the maximum diffraction angle. This means finding the optimum lens aperture and focal length for a specific laser source and material. Larger apertures give higher etch rates but there are less lens elements illuminated. Similarly shorter focal lengths provide higher rates but the aperture size is limited by the diffraction angle and short focal lengths can adversely affect the exit hole diameter for thick materials.

To define the lens array requirements studies of the metal drilling process were made using conventional imaging techniques¹. These studies showed that two regimes were present for drilling metals, vapourisation and melt expulsion (ME). In the vapourisation regime etch depths/pulse are <0.1 μ m but in the ME regime etch rates were >1 μ m per pulse for titanium. The transition from vapourisation to ME is dependent upon the depth of the hole but is usually in the range 20-50J/cm². In the ME regime etch rates depend on the image size at constant fluence which indicates the complex nature of the melt expulsion process¹. To study higher fluences focal plane drilling was studied. The etch rates were investigated as a function of the pulse energy to simulate the effect of changing the lens size in the MLA. The etch rates that were obtained under various conditions are shown in Table 1 for a pulse energy of about 5mJ.

Mat.	Gas	Pulse length	Etch Rate
Ti	Air	14ns	2-4 μ m/pulse
Ti	Air	150ns	8-10 μ m/pulse
Al8090	Air	14ns	>20 μ m/pulse
Al2014	Air	14ns	7 μ m/pulse
Al2014	He	14ns	12 μ m/pulse
Al2014	Air	150ns	>40 μ m/pulse
CFC	Air	14ns	1-2 μ m/pulse

Table 1. Etch rates for various materials.

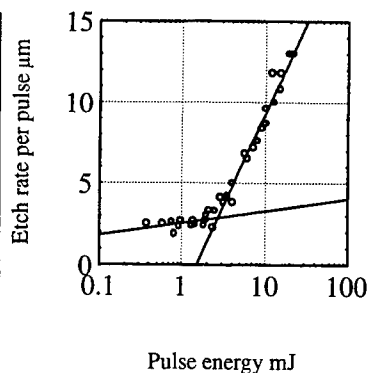


Figure 1. Etch Rates for CFC.

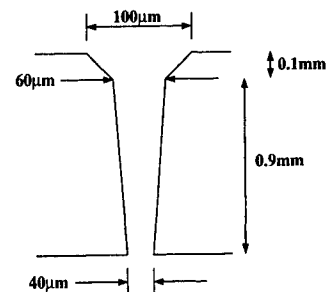


Figure 2. Schematic hole profile.

The beneficial effects of the helium environmental gas and, in particular, the extended pulse lengths are clear and are associated with a reduction in plasma screening. The significant difference in etch rates for the two aluminium alloys may be due to thermal or plasma effects. In all cases average fluences in the focal spots are estimated to be in the range 200-400 J/cm² with peak fluences even higher. To achieve the maximum etch rates it is usually necessary to focus below the surface of the sample to reduce the plasma absorption effects. These experiments have revealed a new processing regime for CFC with increased etch rates as shown in Figure 1. At pulse energies above 3-4 mJ the etch rate starts increasing dramatically up to 15 μ m/pulse at an energy input of 20 mJ. The lines indicate logarithmic etch rate dependencies for the two material removal mechanisms, they are based upon Beer law type absorption. The high etch rate regime may have application, particularly in cutting of CFC. Previously reported non metals ablation rates have saturated at about 1-2 μ m/pulse, however we are using much higher fluences or intensities (estimated at >1 kJ/cm² and 10¹¹-10¹² W/cm² respectively). The high etch rates could be derived either from a plasma etching or shock wave interaction mechanisms.

In addition to the process rate optimisation it is important to control the hole profile, both in the actual dimensions and in the variations across an array produced by the MLA. A typical hole profile produced by this process is schematically illustrated in Figure 2. Entrance hole diameters are in the range 60-120 μ m and are elliptical if the input beam has unequal divergences. The exit hole is always circular for metals. Figure 3 shows the effect of the laser pulse energy on the exit hole diameter for titanium metal. It can be seen that hole diameters in the region of 10-60 μ m can be produced with a high degree of control. The pulse energy was varied by inserting an attenuator in the beam so that the optical set up was constant. Hence the hole diameter is being controlled by the melt expulsion process and not by the optical arrangement. For lens focal lengths in the range 80-200 mm the hole diameter is independent of the optical arrangement. If larger hole diameters are required then these can be achieved by locally heating the metal using electromagnetic induction. Figure 4 shows that for an input pulse energy of 4.2 mJ the hole diameter can be increased from <40 μ m obtained at room temperature to >80 μ m using external heating. Similar results have been obtained with Nd-YAG drilling.

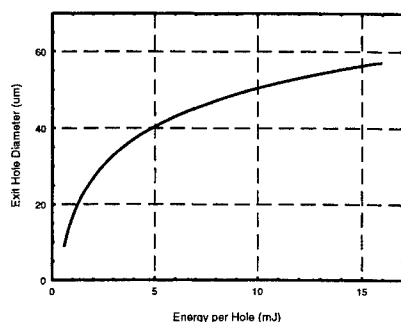


Figure 3. Ti exit hole diameter as a function of pulse energy.

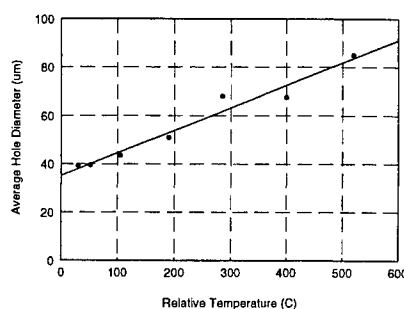


Figure 4. Al exit hole diameter as a function of substrate temperature.

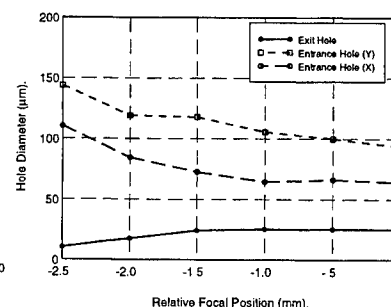


Figure 5. Ti exit and entrance hole diameters as function of focal position.

Several MLAs were designed, built and tested with a variety of lasers sources. The MLA is inserted directly into the laser output beam and the sample placed at the focus. The MLAs allowed up to 120 holes to be drilled simultaneously (depending on the laser pulse energy and lens aperture). A major advantage of this system is that because of the high f-numbers of the lenses (typically 50) the depth of field for the MLA is large as illustrated in Figure 5. The main problem associated in using the MLAs is in the non uniform laser beam profile and in matching the lens apertures such that the lenses on the outside are fully filled by the beam. This can lead to variations in hole diameter and drilling times across the array. If the beam profile is constant then this can be allowed for by using lenses with different apertures across the array but an MLA needs to be matched to a particular laser and delivery system for maximum efficiency. Tests have been carried out using a high power laser (450mJ @ 500Hz) with no adverse effects. Drilling rates up to 1 and 4 holes/sec/Watt for 1mm thick titanium and aluminium respectively are possible. Comparisons of the excimer laser drilling process with the conventional one of Nd-YAG laser drilling for the production of porous panels have been made². The excimer process has some significant potential advantages but, currently, at increased cost.

4 LARGE HOLE MACHINING.

For acoustic dampers holes with a diameters in the range 0.25-1mm and a pitch of a few mm are required in 1mm thick CFC. Using imaging techniques leads to long process times so we have investigated two techniques. The first is to use the MLAs described above but rotating the sample or MLA such that the array of spots trepan out the holes. Using this technique process rates of 0.5holes/minute/Watt are possible for 1mm hole sizes. The rate varies linearly with the circumference of the hole. The other technique uses specially designed DOEs which comprise elements that produce focused rings instead of spots. When processing CFC with excimer lasers wall angles will develop, the size of which is in inverse proportion to the incident fluence³. Hence the design of these elements has to be optimised with respect to focal length and aperture to ensure the ring will penetrate and also to maximise the number of illuminated elements. Figure 6 shows the profile provided by an element which is producing a ring with a diameter of 1mm. It can be seen that the ring has a half width of about 50 μ m. Figure 7 shows a multiple array of 250 μ m ring foci. Process rates for this type of system are about twice those of MLA trepanned holes but they are less flexible.

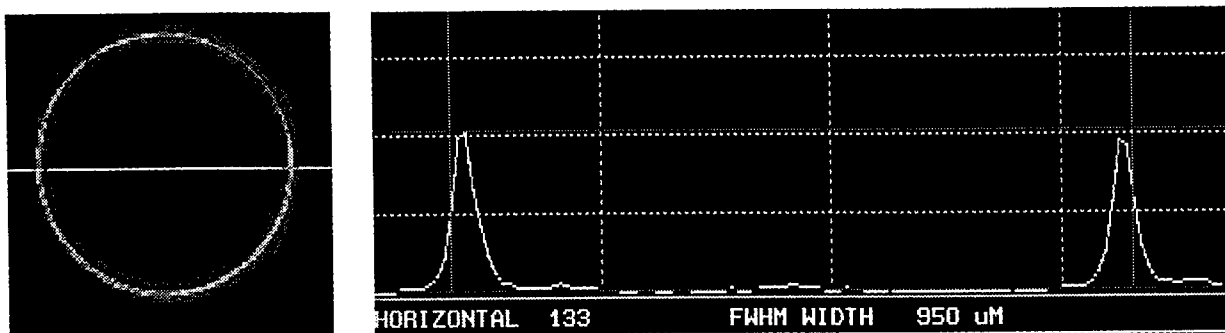


Figure 6. Profile of ring focus element with a diameter of 1mm.

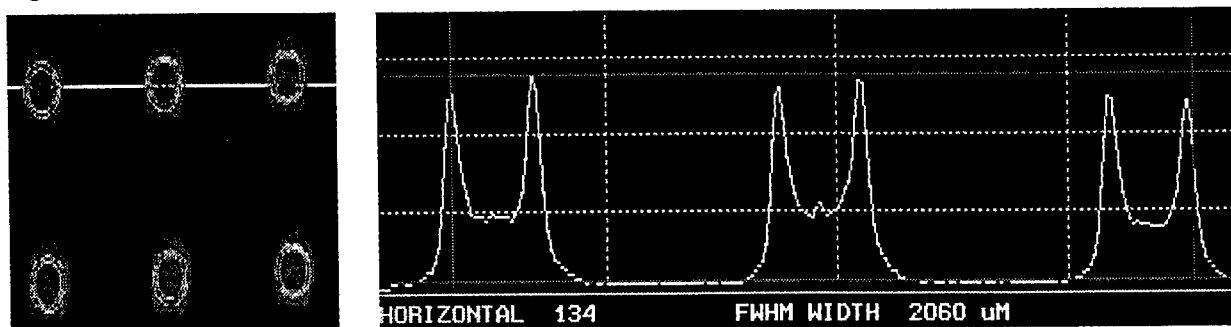


Figure 7. Profile of multiple ring focus elements.

5 DIFFRACTIVE MICRO LENS ARRAYS AS BEAM HOMOGENIZERS.

Combining an MLA with a conventional refractive lens produces a beam homogeniser and shaper, the homogenised plane being near the focus of the refractive lens⁴. In the homogenised plane the intensity is the superposition of three effects. Geometrically the beam takes the shape of the individual microlenses with the size being given by $W_{HP} = W_{MLA} \times F_{RL} / F_{MLA}$ where W_{MLA} is the width of the MLA elements, F_{MLA} is the focal length of the MLA elements and F_{RL} is the focal length of the refracting lens. By altering these parameters a variety of beam shapes and sizes can be obtained. The second effect is that the actual shapes are modulated by the Fresnel diffraction patterns at the edges. The third effect is multiple beam interference caused by the overlapping of the beams from individual lenses. These effects are illustrated by the intensity profile shown in Figure 8a. This shows the square beam shape provided by the square lenses, the Fresnel diffraction pattern superimposed on that and the high frequency modulation due to the interference. By increasing the lens element size the high frequency modulation is lost, as shown in Figure 8b for hexagonal lenses. The central spike is due to a DC component arising from etching errors. This can be reduced by moving slightly away from the focus of the lens, this also reduces interference and diffraction effects (with the penalty of slightly reduced edge definition)⁴. Obscuring part of the beam across the diagonal only has the effect of a general lowering of the overall fluence without significant changes to the homogenised profile as shown in Figure 8c. The MLAs are useful as beam shaping elements for surface treatment, for homogenising beams produced from unstable resonators with poor near field profiles and for correcting motion errors in moving beam gantry systems.

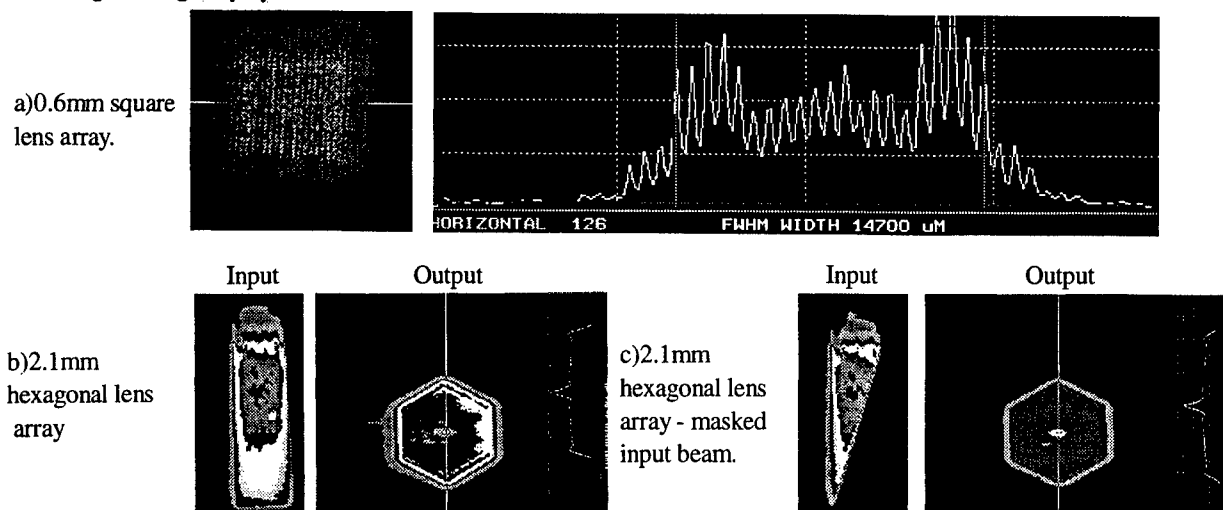


Figure 8. Beam profiles obtained using the MLAs as homogenising elements

ACKNOWLEDGMENTS.

The authors would like to acknowledge that the work was carried out under a collaboration with URENCO. They would also like to thank NCLR for allowing us access to the high power excimer laser to test them.

REFERENCES.

- 1 G.Scott and K.Henry, "Excimer Laser Processing of Aerospace Alloys," *Excimer Lasers SPIE 1835* pp 119-127 (1992).
- 2 S.W.Williams and P.J.Marsden, "New Laser Drilling Techniques for Porous Surfaces," Proc. 2nd European Laminar Flow Conf, to be published, Bordeaux June 1996.
- 3 P.H.Dyer, S.D.Jenkins and J.Sidhu, "Development and Origin of Conical Structures on XeCl Laser Ablated Polyimide," *Appl. Phys. Lett.* **49** 453-455 (1986).
- 4 X.Deng, X.Liang, Z.Chen, W.Yu and R.Ma, "Uniform Illumination of Large Targets using a Lens Array," *Appl. Opt.*, **25** (3), 377-381 1986.

10. Carbon Monoxide and Gas Dynamic Lasers

A room temperature operating pulse RF discharge excited CO laser

Minoru Uehara and Hirotaka Kanazawa

High Energy Technology Department, Ishikawajima-Harima Heavy Industries Co., Ltd.

3-1-15 Toyosu, Koto-ku Tokyo 135, Japan

ABSTRACT

A high power pulse CO laser operating at room temperature has been developed using the modulated pulse RF discharge excitation technique. The fast pulse response and the good reproducibility of laser pulse were obtained for pulse frequency up to 1 kHz with a stable and homogenous discharge. A maximum peak power of 920 W with a pulse width of 1.0 ms FWHM has been attained by the optimizing N₂ and CO concentration.

Keywords: CO laser, pulse characteristics, room temperature operation, RF discharge excitation

1. INTRODUCTION

It is well known that CO laser has the potential for providing high output power and high electric conversion efficiency at wavelength of 5 μ m band. The higher absorption coefficient for metals and smaller focus diameter caused by the difference of wavelength have resulted in superiority of CO laser to CO₂ laser in the field of the material processing, such as high speed sheet metal cutting,¹ aluminum welding² and surface treatment.³

Recently, radio frequency discharge excited CO laser at kilowatt output power level has been developed under room temperature operation. Sato et al.⁴ have reported fast-axial-flow apparatus with Xe gas addition. We attained 1 kW output power with 13.3 % conversion efficiency on a transverse flow RF discharge excited CO laser operating at room temperature without Xe gas addition.^{5,6} Moreover, we improved the beam quality and demonstrated the output power stabilization.

The objective of this work is to study the pulse characteristics of room temperature operating CO laser in order to develop a control technique for the adjustment of output power during the material processing. Especially, cutting of sharp edge and hardening of the edge required at higher pulse frequency regulation of the average laser power while keeping the higher peak power high by controlling the duty cycle. Deep penetration welding with narrow bead width required higher peak pulse operation. In case of CO laser, due to a cascade laser oscillation mechanism, the population inversion is formed slowly by the vibration to vibration energy exchange. So that it should be necessary for the industrial applications to improve the pulse response time faster. In this paper, the experimental results of pulse modulation with RF discharge excited CO laser under room temperature operating has been reported. The pulse performance has been experimentally investigated under various operating conditions.

2. EXPERIMENTAL SET-UP

The laser system was based on a transverse flow RF discharge excited CW CO laser.⁷ The experimental apparatus shows in Fig. 1. The optimum gas mixture for CW operation was made up of He, N₂, CO and O₂ in the ratio of 78.8 / 16 / 5 / 0.2 without Xe gas additions. The laser gas was circulated at around 30 m/s under typical operating conditions (80 hPa gas pressure, 290 K entrance gas temperature) by two axial blowers. CO₂ molecules were produced by the discharge induced plasma-chemical reaction during laser operation. A molecular sieve was installed in the flow loop, in order to trap CO₂ molecules and stabilize the output power.⁶ The loss of CO and O₂ due to the CO₂ formation was compensated by replacing the laser gas at a exchange rate of 5 l/min.

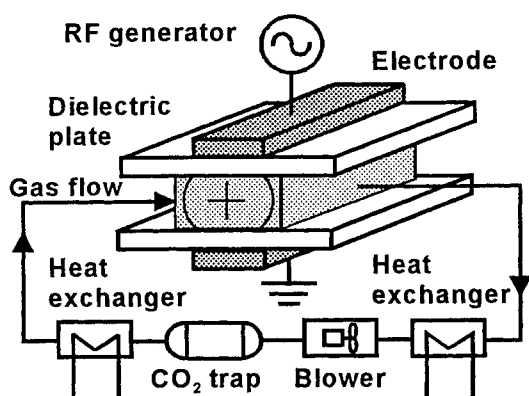


Fig. 1 Schematic diagram of RF excited CO laser.

was 50 %, which corresponded to the average discharge input of 2.5 kW and the average input power density of 6.4 W/cm³. The stable optical resonator was made up of a 20 m concave Si mirror and a plane ZeSe output coupler with 98 % reflectivity, where an effective diameter was 50 mm.

The discharge section consisted of dielectric plates (Al₂O₃) separated by a 40 mm discharge gap and had 392 cm³ discharge volume. The RF discharge input power was supplied from 10 kW, 13.56 MHz RF generator, via an LC impedance matching network which was adjusted to minimize the reflective RF power. Modulated pulse RF excitation is applied to gate continuous RF discharge, where the peak value of pulse RF discharge input was almost same as that of CW operation. The pulse frequency can be varied from CW to 10 kHz and the duty cycle is adjusted from 0 to 100%. On all experiments described here, the peak discharge input was 5 kW and the duty cycle

3. RESULTS AND DISCUSSION

Figure 2 shows shape of the discharge pulse and the laser pulse for various pulse frequency, operating at a gas pressure of 80 hPa and a gas temperature of 290 K. The average laser power and the laser pulse shape was measured by a Coherent Labmaster with sensor head of LM-1000 and a HgCdZnTe infrared photodetector whose response time was rated at 2 ns, respectively.

At a 100 Hz pulse frequency (Fig. 2 (a)), which corresponds to the discharge duration of 5 ms. A peak power of 810 W was obtained, which was 1.4 times higher than the CW output level and an average power of 270 W obtained. The laser pulse rises with a delay time of 0.7 ms after the discharge pulse starts then the peak power is increased rapidly, which forms on pointed peak output. After that the peak power decreases to the CW output power level due to a rise of gas temperature during the discharge pulse. It is considered that in the range of lower pulse frequency the discharge interval is sufficient for the convection gas cooling to the next discharge pulse. The laser pulse is terminated with a delay time of 1.2 ms after finishing of the discharge pulse. Tail of the laser pulse due to the energy transfer from N₂ to CO

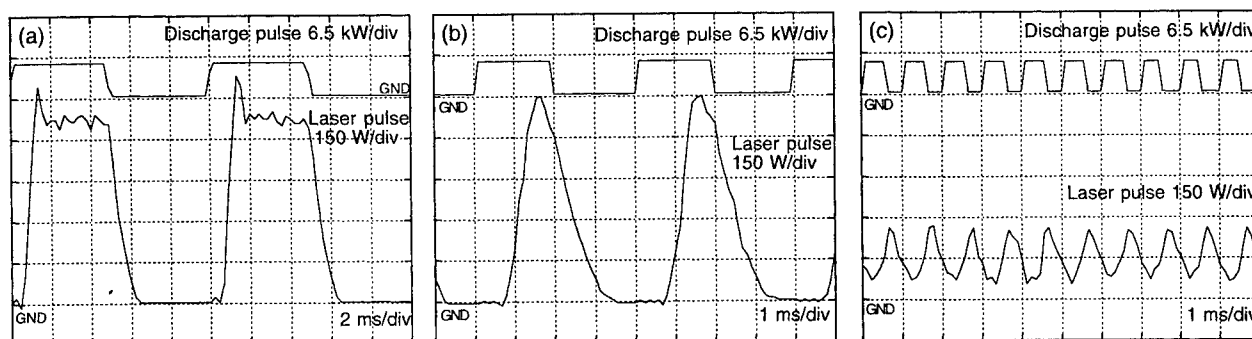


Fig. 2 Discharge pulse and laser pulse for various pulse frequency (a) 100 Hz, (b) 250 Hz, (c) 1 kHz. The upper trace shows discharge pulse and the lower trace shows laser pulse.

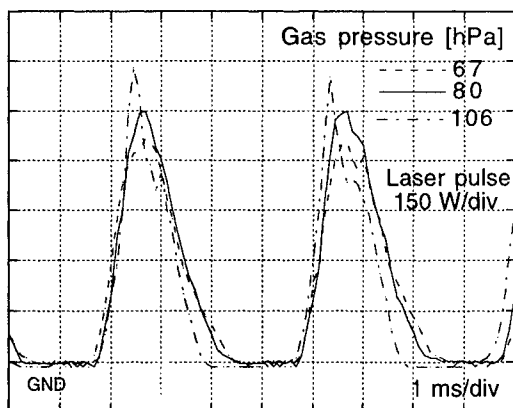


Fig. 3 Laser pulse shape for various gas pressure.

molecules are observed. A pulse width of 4.44 ms FWHM is somewhat shorter than the discharge pulse.

At a 250 Hz pulse frequency (Fig. 2 (b)), the pulse performance has a peak power of 750 W and the average power of 220 W with the pulse width of 1.22 ms. The rise and fall time of laser pulse are similar to a 100 Hz pulse frequency operation. However, the intense initial peak can not be seen from Fig. 2 (b). This is due to the insufficient convection gas cooling. At a 1 kHz pulse frequency (Fig. 2 (c)), a peak power of 260 W and an average power of 120 W is obtained. The laser pulse is merging into a quasi-CW performance. The reason is consider that the laser pulse was not following by the fast changing of discharge pulse, due to the cascade laser oscillation process.

The gas pressure dependence of the laser pulse performance at 250 Hz pulse frequency is shown in Fig. 3. It is seen that the peak power increases, also the pulse width and the pulse rise time are reduced with increasing gas pressure. This is considered to be mainly due to the increase of collisions among gas molecules, which causes the faster formation of population inversion and the greater loss of vibrational excitation energy. In case of higher gas pressure, the peak power is limited by the discharge instability process. On the other hand, at lower gas pressure, the peak power is limited by the overheating of laser gas during the discharge pulse. In case of cryogenic cooling operation, the pulse response is considered to be slower because of the lower optimum gas pressure, and also pulse width is longer due to the cascade laser oscillation from the higher vibrational excitation states, compared to the room temperature operation. Accordingly, it should be noted that the room temperature operation could realize the fast response pulse performance.

The pulse characteristics were also examined for various concentration of N_2 and CO, where 80 hPa total gas pressure was constant at 250 Hz pulse frequency. Figure 4 (a) and (b) show the dependence of the pulse characteristics on N_2 and CO concentration, respectively. The change of N_2 and CO concentration represented similar effects on the pulse characteristics. With increasing N_2 and CO concentration, the peak power is increased and the pulse width is

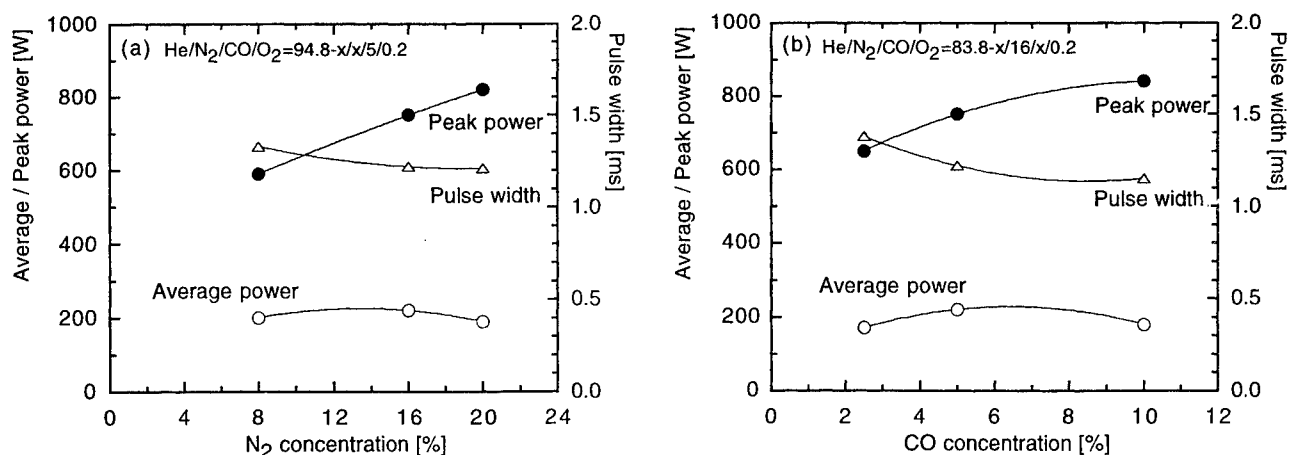


Fig. 4 Dependence of peak power, average power and pulse width on N_2 (a) and CO (b) concentration for 80 hPa gas pressure and 250 Hz pulse frequency.

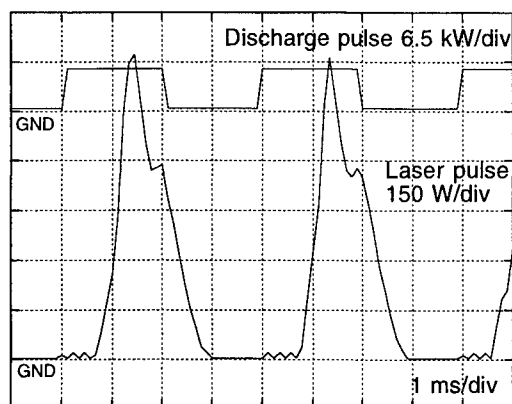


Fig. 5 Enhanced peak laser pulse for He / N₂ / CO / O₂ = 69.8 / 20 / 10 / 0.2, 80 hPa gas pressure and 250 Hz pulse frequency.

reduced, but the average power is not changed so much.

In order to obtain the enhanced peak laser pulse, the gas mixture was optimized to He / N₂ / CO / O₂ = 69.8 / 20 / 10 / 0.2 and 80 hPa gas pressure. A maximum peak power of 920 W in Fig.5 is factor of 1.6 times the CW output level at the same value of peak discharge input. In this case, the pulse width of 1.03 ms are attained for the fast response and the good reproducible pulse performance, without occurrence of the discharge instability. These results are attributed to raising of the frequent collisions between N₂ to CO molecules contributes to the fast and more efficient CO vibrational excitation under those operating conditions. Further increase of N₂ and CO concentration tends to occur the discharge instability.

4. CONCLUSIONS

The experimental results presented here with a room temperature operating pulse CO laser has demonstrated the modulated pulse RF discharge excitation technique. The faster pulse response and higher peak power of laser performance could be obtained with increasing N₂ and CO concentration and increasing gas pressure. A maximum peak power of 920 W was factor of 1.6 times the CW output level at the same value of peak discharge input. It has been confirm that the pulse performance is obtained good enough for the material processing. We believe that the room temperature operating high power CO laser will be used practically for industrial applications

5. REFERENCES

1. K. Kanazawa, N. Yamaguchi, Y. Hamano and M. Yuuki, "Comparison of cutting properties between CO laser and CO₂ laser," *Proc. LAMP '92 Nagaoka*, pp. 665-670, 1992.
2. T. Rudlaff, H. Dausinger, R. Satani, H. Kanazawa and N. Yamaguchi, "Surface hardening using CO laser," *Laser und Optronik* **23**, pp. 46-48, 1991.
3. M. Schellhorn, H. von Bülow: *Proc. 5th Int. Conf. on Laser Technologies '95, Industrial Lasers & Applications '95, Moscow, June, 1995*.
4. K. Shimizu, M. Taniwaki and S. Sato, "1 kW, room temperature, fast-axial-flow CO laser excited by a radio-frequency discharge," *OPTICS LETTERS* **21**, pp. 125-127, 1996.
5. M. Uehara and H. Kanazawa, "Experimental study on operation at room temperature of transverse flow carbon monoxide laser excited by radio frequency discharge," *Appl. Phys. Lett.* **65**, pp. 22-24, 1994.
6. M. Uehara, H. Kanazawa and K. Kasuya, "Recent studies of high power CO laser under room temperature operation," *Proc. 10th Int. Symp. on Gas Flow and Chemical Lasers, Friedrichshafen, 1994*, SPIE Vol. **2502**, pp. 38-43, 1995.
7. H. Kanazawa, M. Uehara, F. Matsuzaka and K. Kasuya, "Characteristics of a transverse-flow CO laser excited by RF-discharge," *IEEE J. Quantum Electron.* **30**, pp. 1448-1454, 1994.

A 3kW industrial CO laser operating at room temperature

W G McNaught¹, G Wlodarczyk²

¹Formely of: Laser Ecosse Ltd (currently Howden Laser Ltd),
Kings Cross Road, Dundee, DD2 3EL, U.K.

²T.W.I., Abington Hall, Abington, Cambridge, CB1 6AL, U.K.

ABSTRACT

An industrial CO laser with output powers in excess of 3kW and capable of operation at room temperature has been developed within a collaborative Eureka project. The design of this laser employs DC excitation and fast axial gas flow technology within a closed-circuit flow loop. The design and performance characteristics of this device are described.

Keywords: CO laser, industrial laser, room temperature operation.

1. INTRODUCTION

When compared with CO₂ multi-kilowatt lasers, CO lasers offer the prospect of improved materials processing because of their ability to generate high continuous optical powers at 5μm wavelengths with high conversion efficiencies (~10%). The theoretically predicted improvements in focusability and coupling to metallic workpieces may be expected to produce results which tend towards those of more expensive Nd:YAG lasers. Although CO lasers have been operated successfully at high powers, reports on investigations into their suitability as materials processing tools have been few. This is primarily due to the fact that such devices have had to be operated at cryogenic temperatures or by employing a gas-dynamic design approach¹. The practical difficulties which these associated laser support systems present to industrial laser manufacturers and users has meant that CO lasers have not been adopted for commercial materials processing applications. The development of a relatively compact, easily operable and maintainable device, capable of several kilowatts output at room temperature, is therefore seen as a pre-condition for evaluation trials directed at industrial materials processing.

Some degree of success in achieving room temperature operation of CO lasers has been reported in recent years^{2,3} although the output powers achieved in most cases have been well below 1kW. A variety of excitation and optical power extraction schemes have also been examined^{1,3}, each with its attendant benefits and limitations. From a laser manufacturing perspective, design factors such as electrical power source type, gas flow, gas handling, gas cooling sub-systems, as well as choice of optical resonator design need to be considered critically. An inappropriate selection and combination of these features could easily result in a device which is costly to build and maintain, as well as proving to be unreliable as a manufacturing tool.

A 3 year collaborative programme of work carried out within the Eureka initiative (Project EU113) has culminated in the successful operation of a 5μm wavelength CO laser capable of power outputs in excess of 3kW. This result is particularly significant in that no cryogenic cooling has been employed and the device is engineered along the lines of an industrial CO₂ laser.

Four organizations were involved in developing the laser source: Laser Ecosse Ltd (an industrial laser manufacturer taking on the role of laser source development), Farnell Hivolt Ltd (a power supply manufacturer who developed the electrical power source), Loughborough University (who undertook investigations into d.c. electrode design and gas flow behaviour) and T.W.I. (the evaluator of the laser's performance for materials processing applications).

2. DESIGN APPROACH

The design approach taken for this project was one which would most likely result in an operating laser which could be easily adopted for manufacture. To this end, a commercial CO₂ laser (AF5) from Laser Ecosse Ltd was selected and modified to operate at 5 μ m. The laser is, in its production form, a 5kW (at 10.6 μ m output), d.c. excited, fast-axial flow device employing a stable resonator. The latter is a multi-arm folded configuration which uses coated silicon reflectors and a ZnSe output window. The gas moving system is based on a twin-Rootes blower arrangement, required to transfer the laser gases through 20 300 \times 20mm diameter flow tubes at high velocity. Figure 1 shows the arrangement of tubes and mirrors. Heat exchangers are incorporated in series with the gas flow loop to remove excess thermal energy and maintain a gas inlet temperature of 20°C to the flow tubes.

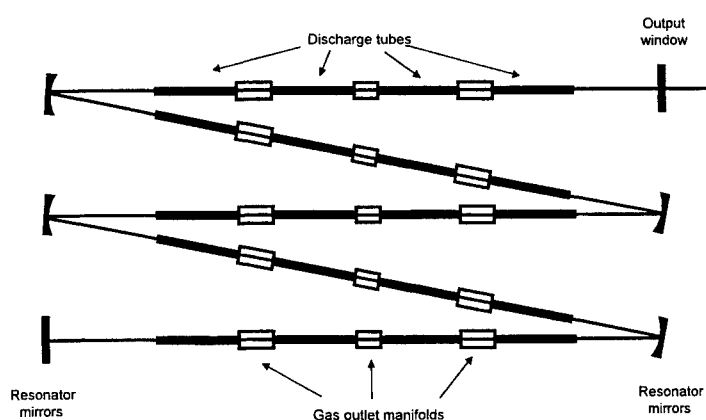


Figure 1 CO laser resonator configuration

For an effective transition to 5 μ m laser operation with a CO laser gas mix, a number of changes had to be made to this system. The Rootes blowers were replaced with higher swept volume units rated at 5000m³. hr⁻¹. This represents a 19% increase in mass flow. In order to minimize gas consumption, bakeable moisture traps were incorporated into the gas circulation path to allow long-term sealed-off operation. A gas mixing system which provided a mixture consisting of 1:20:1 CO:He:N₂ was used and was equipped with a facility to introduce Xe and O₂ at fractional partial pressures and flow rates. A target minimum gas temperature of -20°C was set for this device, to ensure that the required coolant temperature

could be attained using only commercially available refrigerated water chillers. A glycol-doped unit from Flowcool Systems Ltd was procured for this task. Additional improved design heat exchangers were also introduced into the gas system to provide more effective heat extraction and to assist in temperature reduction. The gas flow system is depicted in schematic form in figure 2. Considerable attention had to be paid to the prevention of air leaks into the system as CO laser operation is very sensitive to O₂ partial pressure and to the presence of water vapour. To ensure minimum optical losses within the resonator, the 10 μ m mirror and output window set was completely replaced with components coated for 5 μ m, using similar substrate materials. A window reflectivity of 65% was chosen, although some preliminary trials were undertaken with a 85% output coupler. In order to enhance controllability and electrical efficiency of the laser, a 50kW switched-mode power supply was developed for discharge excitation. This was evaluated in addition to a conventional d.c. resistive ballasted unit normally supplied with this laser.

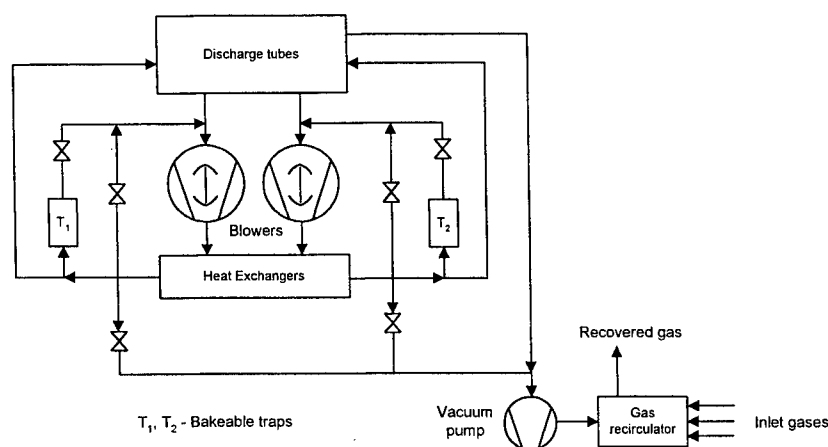


Figure 2 CO laser gas flow system

3. EXPERIMENTAL RESULTS

The system as described in the preceding section allowed gas inlet temperatures to the discharges to be maintained at -10°C . A maximum laser power of 4kW has been obtained with the 65% coupler, the higher output window proving to be unsuitable due to the buildup of excessive intra-cavity power. This had the effect of inducing significant thermal distortion in the optics and the risk of permanent damage was considered to be too great. Figure 3 indicates a reproducible laser output performance as a function of input power and corresponds to a discharge efficiency in excess of 8% at maximum power. The graph represents the behaviour of the laser under sealed-off, Xe doped conditions, higher powers being attainable with continuous gas purging. The effect of reducing gas temperature was also studied and revealed that the maximum output was relatively insensitive to this factor: an increase to 30°C resulted in a 30% power drop (figure 4). Sealed operation of the laser for periods of several hours has also been achieved. Air leaks into the system, which operated at a pressures between 120 and 130mbar, caused a reduction in laser output, an effect which could be associated with excessive O_2 content. A small amount of O_2 was found to be beneficial, however and an optimal level was set at 0.1 l.min^{-1} , using commercial grade gas. Laser action was similarly augmented by the introduction of Xe whose concentration showed a similar trend in its effect on output power. A 30% increase in laser power was noted when the Xe level was optimized at 1.5% of working pressure during sealed-off operation. Water vapour content was also found to be a significant factor in its effect on output. The best design of water vapour trap was experimentally confirmed to be one which incorporates 3A molecular sieve as the drying agent, producing a D.P. of -100°C ($\sim 10^{-5}$ mbar partial pressure H_2O). A total of 5 individual traps were employed in the final system to allow continuous operation. A comparison between the d.c.

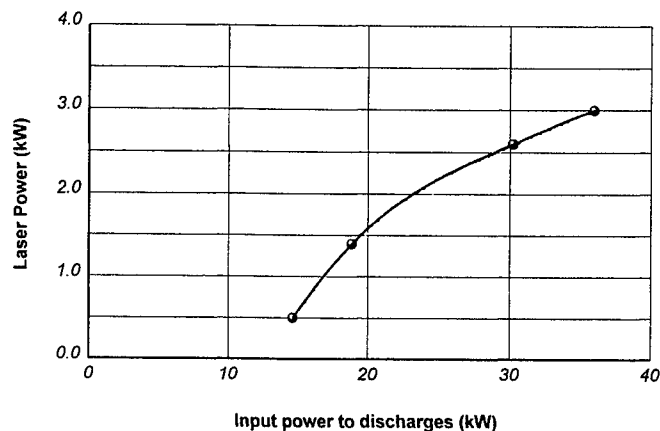


Figure 3 Laser output as a function of electrical input to discharges

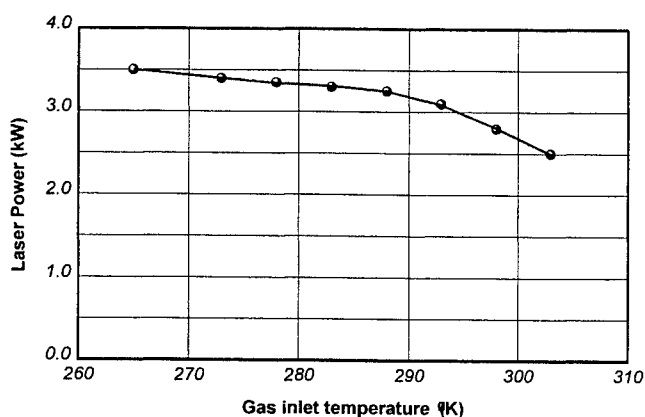


Figure 4 Laser output dependence on gas inlet temperature

resistive ballasted supply and the switched-mode unit showed no significant difference in laser performance.

The spectral composition of the output beam was investigated using an Optical Engineering CO_2 wavelength spectrum analyser, set to operate in its second diffractive order. The use of this equipment set an upper limit of $5.65\mu\text{m}$ for the measurements. With no Xe present in the gas mixture, at least 10 transition lines within a range $5.37\mu\text{m}$ to $5.64\mu\text{m}$ could be observed. The number of lines increased when Xe was added, 3 additional lines appearing, starting at $5.31\mu\text{m}$. Based on a knowledge of general CO laser oscillation characteristics, it is suspected that lines above this limit were also present. Confirmation of the absence of $10.6\mu\text{m}$ output was made by interposing a magnesium fluoride filter between the input beam and a

power meter. No significant output could be measured under normal operating conditions of the laser, although some $10.6\mu\text{m}$ radiation could be detected when the moisture content in the laser rose above partial pressure of 1.0 mbar.

An initial qualitative assessment of beam quality has indicated that low order mode output was being generated and this shows considerable promise for laser processing trials. Due to significant thermal lensing of the output window however, the output beam is strongly divergent and to some degree, output power dependent. Measures are currently underway to correct this problem. A fuller appraisal of achievable beam quality will follow in a future report.

4. CONCLUSION

This work has shown that a CO laser which meets the main design criteria important to industrial manufacturers and users can be developed. In addition, the general engineering design approach used for high power CO₂ lasers can be employed, albeit with some enhancements to the gas cooling system and to the maintenance of gas purity. The laser sub-systems needed to fulfil these functions can be easily constructed from commercially available materials and components.

5. ACKNOWLEDGEMENT

The authors wish to thank the Department of Trade and Industry for funding this project work under the Eureka EU113 programme.

6. REFERENCES

1. H. von Bülow, M. Schellhorn, "High power gasdynamically cooled CO laser with unstable resonator", *Proc. Tenth International Symposium on Gas Flow and Chemical Lasers*, SPIE Vol. **2502**, pp.63-68, (1994).
2. M. Uehara, H. Kanazawa and K. Koichi, "Recent studies of high-power CO laser under room temperature operation", *Proc. Tenth International Symposium on Gas Flow and Chemical Lasers*, SPIE Vol. **2502**, pp.38-43, (1994).
3. X. Luo, J.H. Schäfer and J. Uhlenbusch, "High power room temperature operating cw CO laser excited by microwave discharge", *Proc. Tenth International Symposium on Gas Flow and Chemical Lasers*, SPIE Vol. **2502**, pp.69-74, (1994).

Electrogasdynamic CO lasers with combustion products – a new scientific direction to the creation
of the industrial high-power lasers

I.Ya. Baranov

Baltic State Technical University
6, Gribalevoj St., Apt.15, St.-Petersburg, 194100, Russia
Phone: (812) 592-39-64, Fax: (812) 316-24-09, E-mail: komdep@bstu.spb.su

ABSTRACT

An industrial high-power laser is technical system to be characterized primarily by the Efficiency. For a high-power laser system to become as an industrial one the Efficiency must be more than 10%. As it is well known a steam-engine has such an Efficiency. In welding and in cutting thick materials to provide required power density in a spot for the device with long focus the value of output power of radiation must be no less than 100 kW at beam divergence 10^{-3} rad. At the present time there is a problem in concurrent fulfillment of the requirements on an output power, the divergence, and the Efficiency as well as the requirements on the stability of output parameters, total resource of operation, the safety of operation, and the use of standard components. A line of attack on this problem is proposed by the present author through the use of continuous formation of a CO laser mixture by combustion of a chemical fuel and the use of atmospheric air as a buffer gas (up to 80%), which is cooled in a supersonic nozzles followed by excitation in a radio-frequency (RF) electric discharge without an electron gun. A small-scale model system of electrodynamic CO laser was used by the present author and his colleagues to demonstrate for the first time the laser radiation was possible in a system with combustion products and air. A technical proposal for a multipurpose self-contained industrial cw high-power CO laser system is proposed. This laser system is based on standard electrical machinery with a gas-turbine drive without ejecting toxic CO into the atmosphere.

Keywords: industrial laser system, Efficiency, electrodynamic CO laser, radio-frequency discharge, combustion products, high-power

1. THE REQUIREMENTS TO INDUSTRIAL LASER SYSTEMS OF HIGH POWER

Laser technologies must be divided into two categories: technologies with lasers of low power and technologies with lasers of high-power. Such division is connected with the character of tasks to be solved and with character of heat exchange in a laser (heat-conduction process or convection process). In the latter case we should speak not about lasers but about laser systems because pumping device and regeneration device of a gas mixture much complicate a design and increase the overall dimensions of an industrial installation with laser of high power.

The requirements to industrial laser systems of high power follow from comparison of efficacy of laser technologies with efficacy of traditional technologies. The efficacy is defined by the relation of target final result to expenses. For example, in welding and in cutting thick materials the device with long focus and power density in a spot about 10^7 W/cm² are necessary to receive a result. At a focus of the order of 200 cm and at beam divergence (θ) about 10^{-3} rad the required output power of laser turns out about 100 kW.

Expenses of any technical system are characterized by the Efficiency. The Efficiency of an industrial laser system must be more than 10%. As it is well known a steam-engine has such an Efficiency. Because of this, it is used by people more than 100 years.

In result we have received the following requirements to industrial laser system of high power, which should satisfy:

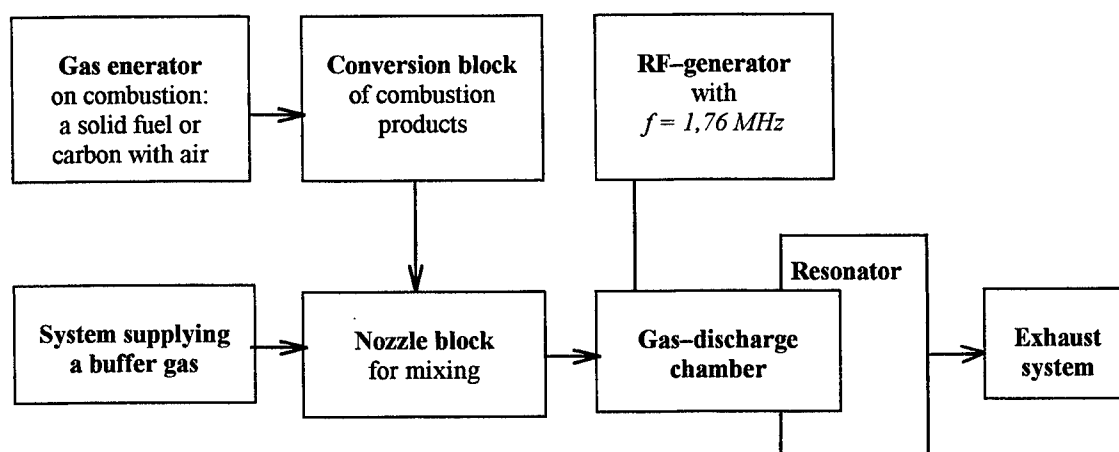
Output power: $P_{out} \approx 100$ kW, at beam divergence: $\theta \approx 10^{-3}$ rad and at Efficiency $\geq 10\%$,

plus of the requirement on the stability of output parameters at a level of 2%, total resource of operation more than 10 thousands hours, the safety of operation, and the use of standard components.

2. THE DIRECTION TO THE CREATION OF THE LASER SYSTEMS SATISFYING THE REQUIREMENTS

Hansen C.F., 1973	A electrogasdynamic laser as a combination of gasdynamic laser with Efficiency less than 1% and electric-discharge laser was proposed;
Bhaumik M.L., Lacina W.B., Mann M.M., 1972	Put ~100 kW and electric-optical Efficiency ~50% were obtained experimentally from quasi-cw electrogasdynamic CO laser installation with an electron gun (A unique properties of the CO molecule provide low divergence θ);
Monson D.J., 1976	Calculations of the closed working cycle and the open working cycle in an electrogasdynamic CO laser were made: Efficiency of closed cycle < Efficiency of open cycle;
Hertzberg A., 1978	Problem of a CO mixture recirculation was noted in the closed working cycle because of the high chemical activity of the CO molecules, the increase of contaminations in an active medium and attachment of beam electrons (A problems of the open working cycle cover release of a toxic CO mixture into the atmosphere, availability of an electron gun and prior formation of the mixture);
Baranov I. Ya. and his colleagues, 1993	Model installation of an electrogasdynamic CO laser was used to demonstrate practically that a laser radiation was possible in an installation with combustion products and air and with radio-frequency (RF) discharge in a supersonic gas flow. It makes possible continuous formation of a laser CO mixture during laser operation and excitation of this mixture without an electron gun;
Baranov I. Ya., 1994	Multipurpose industrial high-power laser system satisfying all requirements was proposed.

3. BLOCK DIAGRAM SHOWING THE COMPONENTS OF AN EXPERIMENTAL MODEL INSTALLATION¹



4. CONTINUOUS FORMATION OF A LASER CO MIXTURE

Continuous formation of a laser CO mixture can be made by the following processes:

(1) conversion of the combustion products into a CO mixture, for example, by the reaction of oxygen-containing

molecules with carbon² to remove CO₂ and H₂O molecules, because the rate of the VT relaxation of the vibrational energy of the CO molecules interacting with carbon dioxide and water is several orders of magnitude higher than the rate of relaxation of the vibrational energy by interaction with other components;

(2) preionization of the combustion products by expansion in nozzles¹, which ensures the maximum reduced electric field E/N in the discharge and the required eV-exchange rate;

(3) selection of the temperature in the combustion chamber to be below 1500 K (the cooled combustion products are then free of atomic hydrogen, which is a particularly strong relaxant of the vibrational levels of CO³) if preionization is adopted;

(4) addition to the combustion products, at their exit from the nozzles, of a cooling buffer gas, which is achieved by expansion in the nozzles of one's own and the mixing of supersonic flows, so that the necessary cryogenic temperatures are reached at relatively high pressures⁴ ensuring a high VV-exchange rate and conditions favorable for a partial inversion.

5. THE CONDITION OF EFFECTIVE LASER OPERATION ON A MIXTURE OF (CO:N₂:H₂:O₂)

$$\tau_{VV} \ll \tau_{eV_{CO}} < \tau_p < \tau_{eV_{N_2}} < \tau_{eV_{H_2}} \leq \tau_{eV_{O_2}} \leq \tau_{VT} \approx \tau_a \quad (1)$$

where τ with different indices are the times of excitation, VV-, VT-, eV-processes and electron attachment, respectively.

The condition (1) for the times is satisfied by selecting the values of E/N and the composition of a mixture.

$$E/N \approx 10^{-16} \text{ Vcm}^2, \quad \text{CO} > 10\%, \text{ N}_2 < 90\%, \text{ O}_2 < \text{CO}, \text{ H}_2 < 90\%$$

The feasibility of using the available electric-field energy in direct excitation of CO molecules in a mixture with N₂ molecules has been reported:

- Dolinina V.I., Koterov V.N., Pyatakhin M.V., Urin B.M.;
- Islamov R.Sh., Konev Yu.B., Kochetov I.V., Kurnosov A.K.;
- Hall R.J., Eckbreth A.S.;
- Iyoda M., Sato S., Saito H, et.al.

If the value of E/N [Vcm^2] is fixed and the density of energy deposition jE [W/cm^3] is limited by allowable heating, the value of current density j [mA/cm^2] is also limited:

$$j \approx 10 \text{ mA/cm}^2 \ll j_{\text{normal}} \quad (2)$$

The condition (2) is readily realized in a subnormal RF discharge with dielectric-coated electrodes. In this case, the losses by reactive load are not available, a field-strength in the electrode boundary layers is reduced, a secondary electron-emission coefficient is increased, and the contribution of an electron current to electrode is respectively increased⁵⁻⁸.

The discharge zone is tolerant to blow-off by high-speed gas flow. The discharge is uniform. The high-energy electrons, which are typical to use an electron gun, are unavailable. Because of this, in the discharge zone the electron losses are small owing to an electron attachment.

6. THE PROPOSAL OF MULTIPURPOSE INDUSTRIAL HIGH-POWER LASER SYSTEM BASED ON STANDARD COMPONENTS

At the present time the use of high-power laser in the industry is restricted because of substantial intricacy of laser units, their high cost, limits, deficient quantity of power density of focused laser radiation of CO₂ lasers. A wide range of special tasks, like stimulating of chemical reactions, isotope's separation, working of large surfaces of metal and

stone, cleaning of oil spills, etc., requires either high densities of laser radiation in the focal spot or large area of spot in given density in continuous regime. Theoretically, it is possible in going to high-power CO lasers⁹. A wide variety of problems arises in the context of the use of the high-power CO lasers of the closed cycle with supersonic and subsonic gas flow. These problems can be solved in using the open cycle of the work and the continuous making a laser CO mixture by combustion of the chemical fuel and use of air as buffer cooling gas¹⁰.

System design is necessary for developing such systems. The use of optimization of the main measurements (weight and overall dimensions) of a system, generalized scaling to define parameters of a laser^{11,12} and available standard component in working the technical offer¹³ at early stages of the design makes possible to reduce substantially expenditures on its performance. In this case each specific task to high-power laser requires technical solution of one's own. There is independent problem to find such tasks, in which the laser methods are of higher efficient than traditional ones. It is apparent that solved by high-power lasers' tasks will be limited fixed range. This range can be extended substantially only after the advent of these lasers on the market.

Proposed high-power CO laser is based on standard electrical machinery with a gas-turbine drive¹³. The combustion products and air are supplied by a combustion chamber and a gas-turbine compressor, respectively. The exhaust products of the laser, which contain CO, are directed to the compressor and are then additionally burnt in the combustion chamber: they thus become free of CO and are ejected into the atmosphere. This makes the laser ecologically acceptable and facilitates the operation of the diffuser. The proposed design can be used to construct mobile laser units¹³.

High-quality optical fiber is for the transmission of CO laser radiation¹⁴. This permits the use of adaptable fiber-optic cables and consequently optics manipulators and standard robots.

A technical proposal for a multipurpose self-contained ecologically acceptable cw CO laser with the formation of a CO mixture, without cryogenic equipments and an electron gun shapes a new scientific direction to the creation of the industrial high-power lasers.

7. REFERENCES

1. G.A.Baranov, I.Ya.Baranov, A.S.Boreisho, and I.V.Timoshchuk, "Supersonic CO combustion-product laser with a high-frequency excitation," *Quantum Electron.* **23**(3), 189-199 (1993).
2. A.S.Biryukov, V.M.Marchenko, and A.M.Prokhorov, "Gas-dynamic lasers utilizing carbon gasification," *Sov.J.Quantum Electron.* **15**, 449-454 (1985).
3. Y.M.Shmelev and A.D.Margolin, "Gas-dynamic CO laser utilizing hydrogen-containing active media," *Sov.J.Quantum Electron.* **11**, 487-494 (1981).
4. R.I.Soloukhin and N.A.Fomin, *Gasdynamic mixing lasers*, Nauka i Tekhnika, Minsk, 1984.
5. I.Ya.Baranov, "Effect of the velocity of molecular gas flow on the existence of the dark Faraday space in a moderate-pressure of discharge," *Plasma Phys. Rep.* **19**, 787-791 (1993).
6. I.Ya.Baranov, "Influence of the RF-discharge mode and electrode dielectric coating on gas flow blow off," *Plasma Phys. Rep.* **20**(4), 384-388 (1994).
7. Ya.Baranov, "Influence of dielectric coating of rf-discharge electrodes on the near-electrode sheath parameters," *Plasma Phys. Rep.* **21**(5), 431-434 (1995).
8. I.Ya.Baranov, "Controlling the parameters of the electrode boundary layers in a capacitive microwave discharge," *Plasma Phys. Rep.* **21**(6), 522-525 (1995).
9. M.M.Mann, "CO electric-discharge lasers," *AIAA J.* **14**, 549-567 (1976).
10. I.Ya.Baranov, "Method of CO laser active medium making," Russian Patent no.2.002.346, in *Inven. Bull.*, no.39-40, p.174, awarded Oct.30 1993.
11. I.Ya.Baranov, "Generalised scaling of an electrogasdynamic CO combustion-product laser," *Quantum Electron.* **24**(8), 673-676 (1994).
12. I.Ya.Baranov, V.D.Goncharov, I.V.Timoshchuk, "Calculation model of a CO laser with a high-frequency discharge in a supersonic stream of combustion products," *Quantum Electron.* **24**(2), 102-106 (1994).
13. I.Ya.Baranov, "Multipurpose high-power electrogasdynamic CO laser," *Quantum Electron.* **24**(6), 536-539 (1994).
14. Sato Sh., Watanase Sh., Fujioka T., "High power high intensity CO infrared laser transmission through As₂S₃ glass fibers," *Appl.Phys.Lett.* **48**(15), 960-962 (1986).

Multi-megawatt supersonic e-beam sustained CW CO lasers:
estimations of their energy characteristics and operating regimes.

B.M.Dymshits

LOK Co., 14, Dobrolubov Av., St-Petersburg, 197198, Russia

B.S.Alexandrov

Russian Scientific Centre "Applied Chemistry", 14, Dobrolubov Av., St-Petersburg, 197198, Russia

ABSTRACT

The calculations of energy characteristics, operating regimes and dimensions of the discharge zone of the supersonic e-beam sustained CO laser are presented. Calculations have been carried out for the laser modules with a power up to 40 megawatts.

Keywords: CO-laser, supersonic, e-beam sustained, energy efficiency, output power, operating parameters.

1. INTRODUCTION

A number of projects concerning the use of lasers in Earth-orbital space and some technologies (e.g. in production of ultrafine "laser" powders, isotope separation, etc) as well as the project of a radiatively driven wind tunnel¹ require using lasers of power units, tens and hundreds of megawatts. After a supersonic e-beam sustained CW CO laser (SSCO-EIL) operating with high efficiency appeared, such projects became feasible instead of being fantastic. The results of SSCO-EIL investigations presented in² were confirmed by the tests conducted with the participation of scientists from USA³. An analytical model of SSCO-EIL and a comparison of the results of analytical calculations (RAC) with the results of numerical calculations (RNC) obtained by solving the system of kinetic equations for vibrational levels of gas mixture components and one-dimensional gas dynamic equations were presented in² too.

In this paper the results of calculations performed for SSCO-EIL of multi-megawatt power are presented. RAC are compared with RNC. The RAC presented allow performing easily the engineering calculations for other output powers and initial data.

2. RESULTS AND DISCUSSION

The scheme of SSCO-EIL is shown in Fig.1. Lasers of this scheme offer the following advantages: 1.The system including a supersonic nozzle, a supersonic channel and a diffuser, is a very efficient, cheap, reliable and very compact refrigerating machine; 2.The coincidence of the resonator and the discharge zone allows to keep a low specific vibrational energy value in gas mixture. This leads to a low heat flow caused by V-T relaxation. This is very important in increase of the SSCO-EIL efficiency because of lower temperatures and energy expenditures for gas pumping in a closed-cycle system (the more input heat, the more total pressure losses); 3. High electro-optical efficiency, high specific output energy, high gas densities in a subsonic part of gas contour and small heat release lead to small values of the specific (per unit of output power) weights and sizes of power supply, compressor, pipelines, heat exchangers in a closed-cycle regime and to small volume (per unit of energy) of a tank for gathering the gas mixture and using it once more after clearing (a semi-closed cycle).

In all our estimations (we use symbols and relationships of analytical model from²) the gas mixture ratio, j_b , and E/N are the same as they were at testing the existing device. The ratio of the width B_b of the part of the supersonic channel where the bypassing gas flow takes place to the average height of the channel is the same as in the existing device, $2B_b=1.4(h_1+h_2)$. The bypassing gas is the operating gas mixture which flows outside the discharge zone; this gas is needed for preventing breakdowns to metal mirrors and other elements of the channel. In analytical calculations we used $B_3^0=4.2285\cdot 10^{-3}\text{ cm}^{-1}$, $E_{in}^0=82.9\text{ J/g}$. These values were obtained from the results of experiment No 9 (See Table 1 in²), which was conducted at $N_1/N_0=0.2$ (N_0 - Loschmidt number), $T_1=80\text{ K}$; $j_b=0.02\text{ mA/cm}^2$; $E/N=5.1\cdot 10^{-17}\text{ V cm}^2$. If the values of these parameters are changed to $(N_1/N_0)'$, T_1' , j_b' and $(E/N)'$, then

$$B_3' = B_3^0 \left[\frac{j_b'}{0.02} \cdot \frac{\sigma(E/N)'}{\sigma(5.1 \cdot 10^{-17})} \cdot \frac{(N_1/N_0)'}{0.2} \cdot \frac{\beta_r(5.1 \cdot 10^{-17})}{\beta_r(E/N)'} \right]^{1/2} \cdot \frac{V_e(E/N)'}{V_e(5.1 \cdot 10^{-17})} \cdot \frac{80}{T_1'} \cdot \frac{V}{V'} \cdot \frac{(E/N)'}{5.1 \cdot 10^{-17}}.$$

Consider the results of calculations. Plots of the efficiency of conversion of discharge energy into radiation $\eta_{T_1, E_{in}}$ and the ratio of the specific input energy E_{in} to E_{in}^0 are shown in Fig. 2-5. In numerical calculations for the same conditions

$E_{in}^0=104.6$ J/g for mixture CO:Ar=0.1:0.9 and $E_{in}^0=88.1$ J/g for mixture CO:N₂:Ar=0.05:0.15:0.8. It follows from Fig. 3,5 that experiment, RNC and RAC are different insignificantly for considered conditions.

The results presented reflect fully specific features of kinetic processes in SSCO-EIL. Further calculations for a particular device are engineering calculations in which the purely technical initial data such as allowable radiative flux density for optics, efficiency of resonator η_{res} , etc. should be taken into account. If the output power of SSCO-EIL is given, specific output energy $E_{out} = \eta_{res} \cdot \eta_{T_1, E_{in}} \cdot E_{in}$ allows determining the gas flow rate through discharge zone G_d and therefore the area of discharge zone cross-section $S_d=B_d \cdot h_1$.

In choosing of the cross section shape it is necessary to take into account that upon increasing the dimension of discharge zone along the beam B_d the area of e-beam gun window is increased and therefore its power consumption is increased, discharge current is increased and discharge voltage is decreased, the flow rate of bypassing gas is decreased. The height of channel is decreased too, which leads to the necessity to meet more exacting requirements to filling the channel, which height changes along the flow, with radiation.

The influence of changes in the gas mixture density and in the dimension of discharge zone along the flow on E_{in} and E_{out} is clear from the plots presented. If for one and the same SSCO-EIL the gas flow rate and therefore the gas density at the entrance to discharge zone are increased n times, the output power will rise more than $n^{3/2}$ times. It is obvious that acceptable areas of discharge zone cross-sections at high values of N_1/N_0 take place at output power level of units and tens of megawatts. It is necessary to note that at a steady-state operating conditions the heat removal from the output window is mainly due to the gas flow. As N_1/N_0 rises, heat removal rises too but not so fast as output power does. Estimations show that for all the variants of SSCO-EIL presented in Table 1 the steady-state regime with a gas tight output window is feasible. It is necessary to note that increasing N_1/N_0 increases the influence of optical non-uniformity of the flow on radiation divergence.

In order to estimate the volume of the tank of a semi-closed cycle and the energy expenditures on the gas pumping in a closed cycle, it is necessary to know the ratio of the Pitot pressure before the nozzle P_{01} to the pressure behind diffuser P_{0S} . We assumed that the pressure recovery in diffuser is in accordance with a formula that was obtained by approximating the experimental data presented in ⁴:

$$P_{01}/P_{0S} = \exp(0.3466M_2) \left[2 + (k-1)M_1^2 \right]^{k/(k-1)} / \left\{ 0.9 \left[2 + (k-1)M_2^2 \right]^{k/(k-1)} \right\},$$

where the coefficient 0.9 makes allowance for pressure losses in the contour. The plots of P_{01}/P_{0S} are presented in Fig. 6.

Table 1. Main initial data and calculation result of SSCO-EIL parameters

Parameter	1	2	3	4	5
1 Gas temperature at the entrance to discharge zone, T_1 , K	80	80	80	80	120
2 Loss coefficient of the resonator, k , m ⁻¹	0.35	0.25	0.35	0.25	0.20
3 Gas density at the entrance to discharge zone, N_1/N_0	0.2	0.2	1.21	1.21	1.21
4 Discharge zone length, X , cm	70	108	70	108	70
5 Specific input energy for gas in discharge zone, E_{in} , kJ/kg	82.9	124.3	187.4	278.0	229.1
6 Efficiency of discharge energy conversion, $\eta_{T_1, E_{in}}$	0.608	0.666	0.705	0.723	0.675
7 Resonator efficiency, η_{res}	0.769	0.870	0.769	0.870	0.769
8 Specific output energy for gas in discharge zone, E_{out} , kJ/kg	39.3	72.8	101.5	176.8	118.9
9 Discharge zone width, B_d , cm	50	250	50	250	50
10 Channel height at the entrance to discharge zone, h_1 , cm	5.4	6.64	5.4	9.25	5.4
12 Gas flow rate in discharge zone, G_d , kg/s	4.495	27.47	27.04	231.43	24.96
13 Total gas flow rate, G_d+G_b , kg/s	6.3	29.95	37.9	266.3	34.94
14 Output power, W_{out} , MW	0.177	2.0	2.74	40.5	2.97
15 Electro-optical efficiency, $\eta_{eo}=E_{out}/E_{in}$	0.474(0.468)	0.586	0.542	0.636	0.519
16 Discharge voltage, U_d , kV	1.490	1.830	9.0	15.4	9.0
17 Discharge current, I_d , A	251	1870	563	4174	635
18 E-beam gun cathode current, I_b , A	0.131	1.01	0.131	1.01	0.131
19 Pitot pressure before the nozzle, P_{01} , MPa	0.181	0.181	1.096	1.096	0.583
20 Pressure behind the diffuser, P_{0S} , MPa		0.0405	0.200	0.123	0.156
21 Vacuum tank volume for gas flow rate during 1 sec, m ³		65.2	17.4	170	

For some variants of SSCO-EIL principle initial data and RAC are presented in Table 1. In column 1 the parameters of the existing device and the results obtained in test No 9 (See Table 1 in ²) are presented. Presented in row 15 "electro-optical efficiency" are the experimental value and the calculated one (in brackets). In column 2 the calculated parameters of the 2 MW laser are presented. In this variant the operating parameters that are important for the discharge (gas mixture ratio, T_1 , N_1/N_0 , j_b , E/N) are the same as in the existing device. The dimension along laser beam is appreciably increased; increased a little are the height of channel at the entrance to discharge zone and the length of discharge zone along the flow. Calculated parameters of SSCO-EIL for the case where N_1/N_0 at the entrance to discharge zone is increased to 1.21 and all other parameters, including the geometric dimensions, are the same as in the existing device are presented in column 3. In this case, output power is increased to 2.74 MW. Results of calculation for the 40 MW SSCO-EIL are presented in column 4. In addition to increasing N_1/N_0 to 1.21, we increase the geometric dimensions. A comparison of the data of column 4 with those of column 2 shows that the module with the higher gas density, overall dimensions of which are insignificantly different and which requires the 9 times higher gas flow rate and the 2.6 times larger volume of vacuum tank, has the 20 times higher output power. Parameters of SSCO-EIL for a closed-cycle operation are presented in column 5. Its wall-plug efficiency is more than 26%. By using relationships of the analytical model other variants with other initial data can be calculated easily. RAC are in a satisfactory agreement with RNC. RNC and engineering calculations for the same variants are presented in ⁵.

Increasing the dimensions of discharge zone, both along the flow and along the laser beam axis, does not cause any problems, at least with regard to the stability of the e-beam sustained discharge. This is confirmed by the fact that the stable discharge taking place now has 70·50 cm² section. The theory of e-beam sustained discharge known to us does not limit increasing N_1/N_0 , with regard to the stability of the e-beam sustained discharge, if the values of E/N , j_b and gas mixture ratio are the same as in the case verified by experiment. However, in order to be absolutely sure, it is necessary to verify experimentally the possibility of providing the stability of the e-beam sustained discharge in supersonic flow with the same values of E/N as they were before and with the increased values N_1/N_0 .

3. CONCLUSIONS

Extremely high values of efficiency and specific energy output were predicted for a supersonic e-beam sustained CO laser 20 years ago ⁶.

An apt conjunction of the properties of operating gas mixture with the characteristics of the discharge sustained with e-beam, the understanding, more detailed than earlier, of the processes in SSCO-EIL and, as a consequence, the success in realization of such a laser that takes place at present - all this opens the way to create supereffective, supercompact and superpower lasers, including the lasers of multi-megawatt power. The advantages of SSCO-EIL show themselves at output power levels of hundreds of kilowatts and rise with increasing output power.

Many of the uncertainties could be resolved if the stable discharge were brought off (and if a successful work of the existing laser were shown) at the gas mixture density considerably exceeding the value that was used in our previous tests. Shall we be able under such conditions to maintain the same value of E/N as before?

4. ACKNOWLEDGEMENTS

The authors are grateful to GCL/HLP'96 Organizing Committee and Chairman Prof. D.R.Hall for financial support which made real their participation in Symposium.

5. REFERENCES

1. R.Miles, G.Brown, W.Lempert, D.Natelson, R.Yetter, J.Guest, G.Williams, and S.Bogdonoff, "Radiatively driven hypersonic wind tunnel", AIAA-94-2472 (18th AIAA Aerospace Ground Testing Conf., June 1994).
2. B.M.Dymshits, G.V.Ivanov, A.N.Mescherskiy, I.B. Kovsh, "CW 200 kW supersonic CO laser", *Proceedings of the Int. Symposium on High Power Lasers and Laser Application V*, SPIE, Vol.2206, pp.109-120, Vienna, April 1994.
3. R.O.Johnson, B.M.Dymshits, G.V.Ivanov, A.N.Mescherskiy, J.P.Reilly, M.L.Lander, "Laser-material test results from Russian high power carbon monoxide laser", *Proceedings of the 27 Annual Symposium on Optical Materials for High Power Lasers*, Boulder, CO, Oct.30-Nov.1, 1995.
4. A.Pope, K.L.Goin, *High-speed wind tunnel testing*, John Wiley and sons, Inc., NY-London-Sydney, 1965.
5. B. M. Dymshits, B.S.Alexandrov, V.A.Belavin, J. P. Koretskiy, "Numerical investigation of energy characteristics of the first overtone generation of a high power supersonic e-beam sustained CO laser", *Proc. of XI Int. Symp. GCL/HPL'96* (to be published).
6. D.J.Monson, "Potential efficiencies of open- and closed-cycle CO supersonic electric-discharge lasers", *AIAA Journal*, .14 (5), 614-620 (1976).

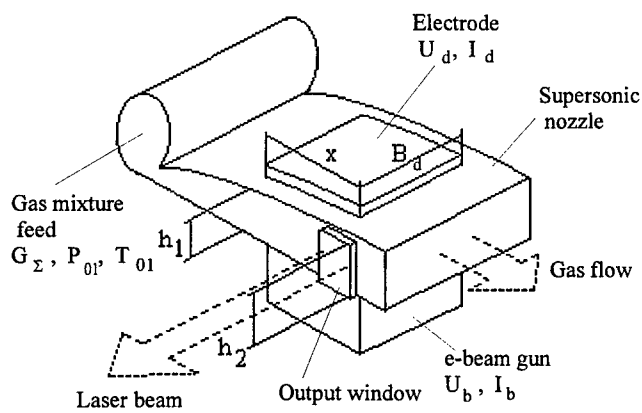


Fig.1. Scheme of SSCO-EIL

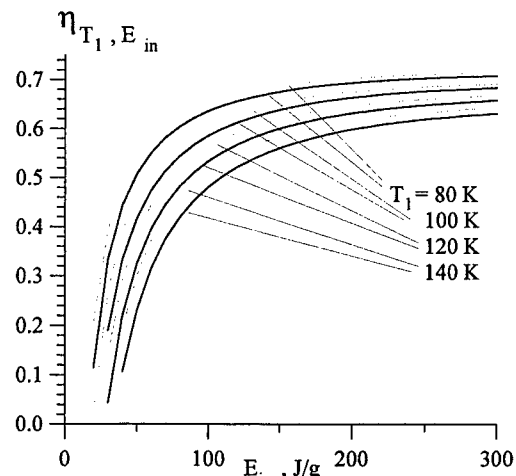


Fig.2. RAC for $\eta_{T_1, E_{in}}$

$$\frac{\eta_{T_1, E_{in}}(\text{RAC})}{\eta_{T_1, E_{in}}(\text{RNC})}$$

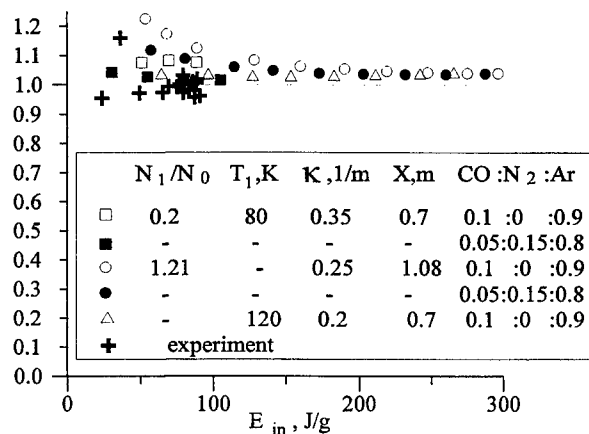


Fig.3. Comparison of RAC with experiment and RNC for $\eta_{T_1, E_{in}}$

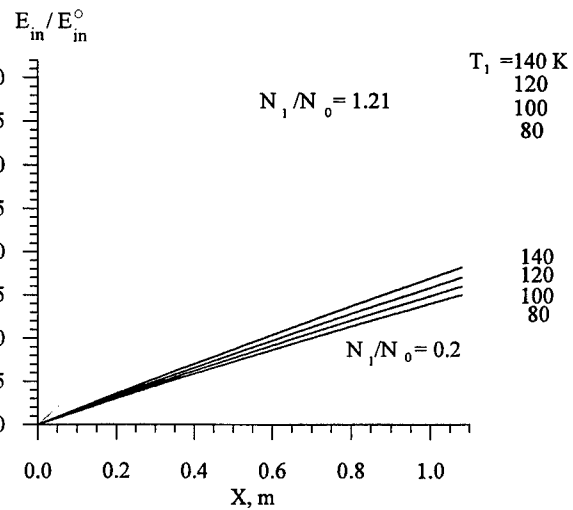


Fig.4. RAC for E_{in} / E_{in}^0

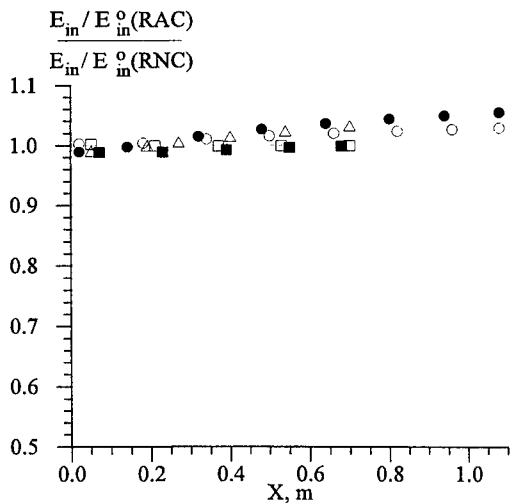


Fig.5. Comparison of RAC with RNC for E_{in} / E_{in}^0 ; the symbols are the same as in Fig.3.

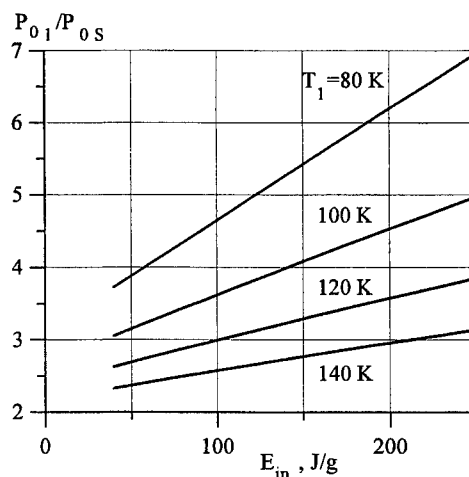


Fig.6. RAC for P_{01} / P_{0s}

A study on CO₂ gas dynamic laser driven by methane-air combustion

Yoshinori ITAYA, Yousuke KAWAMURA, Noriyuki KOBAYASHI*,
Chihomi TAKAMI** and Masanobu HASATANI

Department of Energy Engineering & Science, Nagoya University
Furo-cho, Chikusa-ku, Nagoya 464-01, Japan

*Research Center for Advanced Energy Conversion, Nagoya University
Furo-cho, Chikusa-ku, Nagoya 464-01, Japan

**Fundamental Research Department, Toho Gas Co., Ltd.
Shinpo-cho, Tokai, Aichi, 476, Japan

ABSTRACT

The CO₂ gas dynamic laser driven by methane-air combustion in an unsteady flame propagation combustor was proposed for the purpose of industrial application. The effect of coexisting H₂O with high concentration on the population balance between CO₂(001) and CO₂(100) levels of vibration-rotation modes was theoretically analyzed. The analysis showed that the population inversion between the two levels can take place with the methane-air combustion at stoichiometric ratio if the gas flow is accelerated to Mach number 5.0. The population inversion was confirmed by the experimental measurement of the small-signal gain carried out applying the unsteady flame propagation combustion. High emission power of about 2.5 kW with the path length of 0.3 m may be expected from the magnitude of the gain.

1. INTRODUCTION

A gas dynamic laser (GDL) is a promised technology that can generate high laser power driven directly by combustion energy. When a gas containing CO₂ with high temperature and pressure is expanded adiabatically through a supersonic nozzle, the population inversion between the two energy levels of (001) and (100) of CO₂ is achieved to emit laser of 10.6 μ m in the system. The GDL have been developed originally for the aims of military uses, and unusual fuels were used. The GDL is expected to be available industrially for energy applications so as energy transportation and precise heating processes because of its excellent power and energy utilization efficiency by recovering thermal energy. To lead this technology to industrial applications, however, there are several problems to be solved including use of more common fuels, development of high pressure combustor and a system design for the enhancement of total energy efficiency.

In this study, the applicability of natural gas or methane-air combustion to CO₂-GDL is examined. The combustion is carried out in the unsteady flame propagation combustor developed to achieve easily the methane-air combustion under a high pressure over 1 MPa.¹ The small-signal gain in the supersonic flow of the combustion gas through the nozzle is investigated experimentally to confirm the population inversion of CO₂ molecules. The theoretical analysis is also performed to predict the behavior of the population inversion. Laser emission power and efficiency are predicted from the magnitude of the gain.

2. EXPERIMENTAL PROCEDURE

Fig.1 shows the experimental apparatus used for the measurement of the small-signal gain in the methane-air combustion system of CO₂-GDL. The setup consists of a combustor of methane and air, a supersonic nozzle, a cavity with an optical system to measure the gain, and a diffuser. The combustor is the unsteady flame propagation combustion type. Methane and air are introduced to the combustor through fuel and air feed tubes. When the premixed gas flowing reaches an igniter in the combustion chamber and is ignited by electric spark, a flame propagates toward the upstream. But the flame blows off at the vicinity of gas inlet and then unburnt fresh gas pushes the burnt gas out. These combustion is repeated in the combustor. The inner diameter and the length of the combustion chamber are 60 mm and 756 mm. The inner wall of the chamber is lined with 41.6 mm thick castable refractory for high temperature and pressure resistance. Outstanding features of this combustor are 1) to have preheating effect of methane-air from the combustion chamber wall, 2) that flame stabilizers are not necessary, 3) that durability is desirable because the chamber wall is not continuously exposed to flame. The supersonic nozzle is a least length nozzle, and the throat area is 1.0mm high and 10.0mm wide. The area ratio of the nozzle (A/A^*) is 25.0. The combustion gas is adiabatically expanded through the supersonic nozzle and Mach number of the gas is about 5.0 at the cavity. To measure the small-signal gain, a CO₂ laser is used as a light source of stimulated emission. The CO₂ probe laser power is 5.7 W. Two anti-reflection-coated Zn-Se windows are installed at both sides of the cavity. The beam passes through the Zn-Se windows, and the output beam is reflected diffusely by the diffuse mirror. A part of diffused beam enters the MCT detector whose response time is 3 ms.

3. THEORETICAL CALCULATION

Prior to experiments for the confirmation of population inversion, the theoretical calculation on the inversion was performed. In the CO₂-GDL, the transmission between the two modes, (001) and (100) in CO₂ are used. The balance equations are derived to determine the population of the two modes here. It is assumed that the combustion gas flow immediately achieves the conditions of a constant temperature, a constant Mach velocity and a constant pressure after the gas is expanded adiabatically through a supersonic nozzle to simplify the problem.

The transient behavior of the population must be generally determined from the transition among all vibrational energy levels of CO₂. However, since the relaxation times are remarkably fast among the energy levels included in each mode when modes I and II are grouped as shown in Fig.2, the population in each mode can be approximated by an equilibrium state at individual temperature. Therefore, the balance equations are derived from the transition among the two modes and the base level. The formulas are obtained as follow,

$$dE_n/dt = -(\phi E_N - E_3)/\tau_1 \quad (1)$$

$$dE_3/dt = (\phi E_N - E_3)/\tau_1 - (E_3 - \bar{E}_3)/\tau_2 \quad (2)$$

where E_N and E_3 denote the vibrational energy of the N₂(v=1) and CO₂(v=3), respectively. ϕ is the mole fraction ratio of CO₂ to N₂. τ_1 and τ_2 are the relaxation times of (001) to (v=1) and (001) to (030), respectively. Using the dimensionless parameters defined by Eq.(3), finally Eqs.(1) and (2) become Eq.(4).

$$X_N = (E_N - \bar{E}_N)/E_N, \quad X_3 = (E_3 - \bar{E}_3)/E_3 \quad (3)$$

$$X_3 = A \cdot (\exp(-t/\tau_{1I}) - \exp(-t/\tau_{1J})) \quad (4)$$

where

$$1/\tau_I = (a+b)/2\tau_1, \quad 1/\tau_{II} = (a-b)/2\tau_1, \quad A = \phi X_{N,0} b, \\ a = \tau_1/\tau_2 + \phi + 1, \quad b = \left[(\tau_1/\tau_2 + \phi + 1)^2 - 4\phi\tau_1/\tau_2 \right]^{-1/2}$$

\bar{E}_N and \bar{E}_3 are the initial values and are determined by the assumption that the initial temperature of each mode is equal to the translation temperature of the molecules in the combustion chamber. When the Boltzmann distribution for the population in an equilibrium state is applied, the following equation is given,

$$N_{Ai} = N_{A0} \cdot \exp(-h\nu_i/kT_{vi})/Q \quad (5)$$

where N_{Ai} is a molecular density of the ν_i mode of A-molecule. N_{A0} is a total molecular density of A-molecule. The constant h denotes the Plank constant and k is the Boltzmann constant. T_{vi} is the vibration temperature of the ν_i mode and Q is the partition function. The relaxation times in the equations above are correlated by

$$(\tau_1)^{-1} = \frac{x_{CO_2}}{(\tau_c)_{CO_2-CO_2}} + \frac{x_{N_2}}{(\tau_c)_{CO_2-N_2}} + \frac{x_{H_2O}}{(\tau_c)_{CO_2-H_2O}} \quad (\tau_2)^{-1} = \left[\frac{x_{CO_2}}{\tau_a} + \frac{x_{N_2}}{\tau_b} \right] \frac{1}{x_{CO_2} + x_{N_2}} \\ (\tau_a)^{-1} = \frac{x_{CO_2}}{(\tau_a)_{CO_2-CO_2}} + \frac{x_{N_2-CO_2}}{(\tau_a)_{CO_2-N_2}} + \frac{x_{H_2O}}{(\tau_a)_{CO_2-H_2O}} \quad (\tau_b)^{-1} = \frac{x_{CO_2}}{(\tau_b)_{CO_2-CO_2}} + \frac{x_{N_2}}{(\tau_b)_{CO_2-N_2}} + \frac{x_{H_2O}}{(\tau_b)_{CO_2-H_2O}} \quad (6)$$

where x_i is a mole fraction of an i component. $(\tau_n)_{i-j}$ ($n=a,b,c$; $i,j=CO_2, N_2, H_2O$) denotes a relaxation time for a gas mixture of components i and j and are given from the experimental data.²

The results of the theoretical calculation are shown in Fig.3. Increasing the Mach number of the gas resulted in high molecular density ratio(N_{001}/N_{100}) of CO₂(001) to CO₂(100), and the maximum ratio is beyond 1.0 that means the achievement of the population inversion if the Mach number is faster than 4.0 as shown in Fig.3(a). Particularly the population

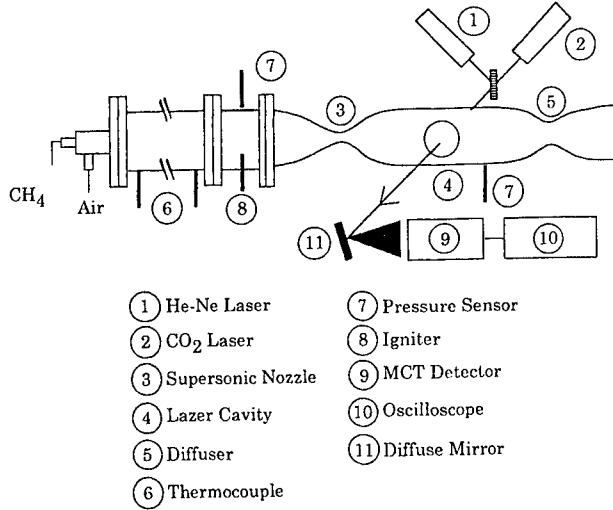


Fig. 1 Schematic drawing of experimental apparatus

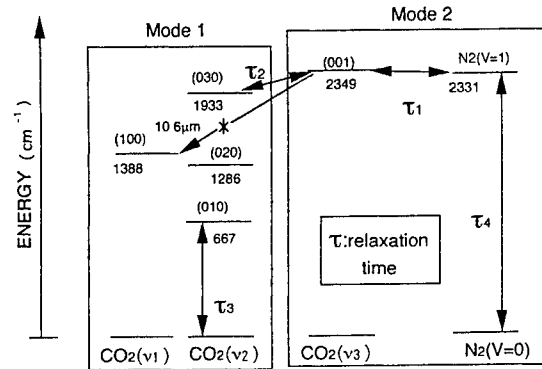


Fig. 2 The energy levels of each vibration mode of CO₂ and N₂

inversion becomes remarkable for $M=5.0$. Fig.3(b) shows the effect of H_2O concentration on the population balance. The ratio of H_2O to CO_2 is kept a constant at 2.0. The location of the peak of N_{001}/N_{100} sifted to the upstream with an increase in H_2O mole fraction while the peak magnitude of the ratio N_{001}/N_{100} became maximum when H_2O mole fraction is 0.4.

4. RESULTS AND DISCUSSION

4.1. Population inversion and small signal gains

All of the following experiments were carried out at the fuel-air ratio of 0.9 in combustion. Examples of pressure and MCT signals measured transiently are shown in Fig. 4. P_0 is the pressure in the combustion chamber, P_c is the pressure in the laser cavity, and MCT represents the output signal of the MCT detector. All the scales of the ordinate are arbitrary. The output power of the probe laser detected by MCT was equal constantly to the incident power to the cavity and neither absorption nor gain appeared in Fig.4(a) and (b). The MCT signal of the output power was raised periodically for the pressure $P_{0,ave}$ over 0.95 MPa. The increment was observed corresponding to the period when the methane-air mixture was ignited and the pressure rose in the chamber. This fact means that gain of the incident beam due to the stimulated emission could be obtained for the combustion gas produced from methane and air in the unsteady flame propagation combustor. However there was no increment of the probe laser power in the period of combustion gas exhaust after the blow-off of flame. Fig.5 shows the behavior of the magnitude of the small-signal gain plotted against the operating pressure $P_{0,ave}$. The small-signal gain G is determined by

$$G = (1/L) \cdot \ln(I_0/I) \quad (7)$$

where L [m] is the path length of a beam at the cavity, I is the peak output power of the beam detected by the MCT and I_0 is the incident beam power as seen in Fig.4(c). The gain rose from 0.22 to 0.68 m^{-1} against an increase in the pressure $P_{0,ave}$ from 0.90 to 1.18 MPa. The gain that has been reported in several works on the GDL^{3,4,5,6} was the order of 0.5 to 3.0 m^{-1} depending on the systems, and the gain obtained in the present work corresponds well to the conventional ones. Hence the present system may be available for development of the CO_2 -GDL with a sufficient achievement of the population inversion.

4.2. Estimation of laser power from the small signal gains

The laser power was calculated by Anderson's three-temperature model⁷ based on the small signal gain in Fig.5. This model adopted three temperature of T , T_{v1} , and T_{v2} . If the population inversion takes place within vibration-rotation modes, we can define often the following three temperature: the translation temperature T of CO_2 , the vibration temperature T_{v1} of v_1 and v_2 modes and the vibration temperature T_{v2} of v_3 and v_N modes which resonate with each other. v_1 , v_2 , and v_3 represent symmetrical elasticity vibration, the flexion

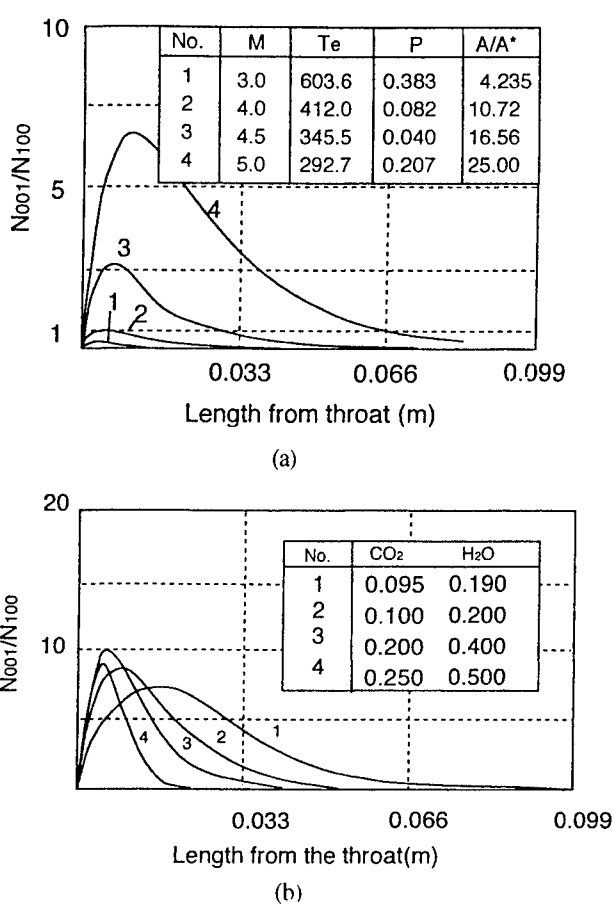


Fig.3 The Results of the theoretical calculation. (a): the effect of Mach number on the population balance. (b): the effect of H_2O concentration on the population balance

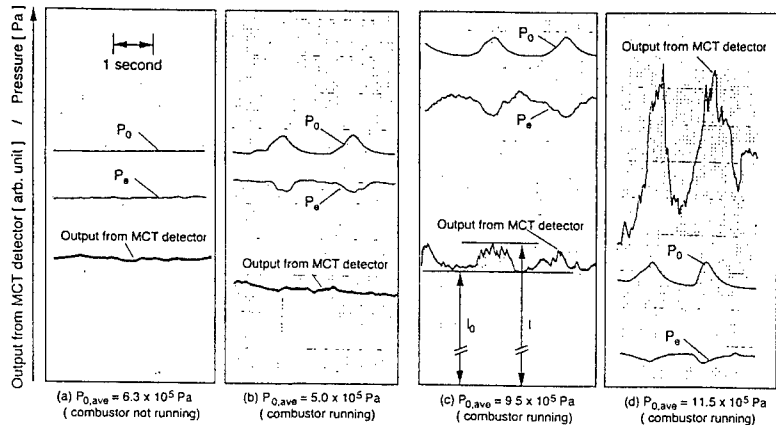


Fig.4 Examples of measurements

vibration, and the unsymmetric elasticity vibration of CO₂, respectively. v_N represents the symmetrical vibration mode of N₂.

The laser output that can extract from this system is expressed as

$$P_{out} = \dot{m} \cdot e_{max} \quad (8)$$

where \dot{m} [kg/s] is the mass flow rate of combustion gas, e_{max} [J/kg] is the increased vibration energy per unit mass. e_{max} is expressed as

$$e_{max} = 0.409 \{ e_{vII}(T_{vII}) - e_{vII}(T_{vII,e}) \} \quad (9)$$

where e_{vII} is the sum of energy of v_3 and v_N modes, and a constant 0.409 is the quantum efficiency. $T_{vII,e}$ is the vibration temperature at which the relaxation proceeds until N_{001} becomes equal to N_{100} . e_{vII} is expressed as function of T_v ,

$$e_{vII}(T_v) = C_{CO_2} R_{CO_2} \theta_3 \left[\exp\left(\frac{\theta_3}{T_v} - 1\right) \right]^{-1} + C_{N_2} R_{N_2} \theta_N \left[\exp\left(\frac{\theta_N}{T_v} - 1\right) \right]^{-1} \quad (10)$$

where C_i is the weight fraction, R_i [J/kg K] the gas constant, θ_i [K] the characteristic vibration temperature and i the sort of gas. From the approximate equation of gain,

$$G = \frac{\lambda^2}{4\pi Z} (N_{001} - N_{100}) \frac{45.6}{T} \exp\left(-\frac{234}{T}\right) \quad (11)$$

where λ [m] is the wave length of light, Z [s⁻¹] is the collision frequency. From Eq.(11), $N_{001} = N_{100}$ is equivalent to $G = 0$. N_i is expressed by

$$N_{001} = N_{CO_2} \frac{\exp(-\theta_3/T_{vII})}{Q}, \quad N_{100} = N_{CO_2} \frac{\exp(-\theta_1/T_{vI})}{Q} \quad (12)$$

where N_{CO_2} [m⁻³] is the particle density of CO₂ and Q is the partition function. When $G = 0$, T_{vII} becomes $T_{vII,e}$ from the definition. Hence, from eq.(12), $T_{vII,e}$ is expressed as

$$T_{vII,e} = (\theta_3/\theta_1) \cdot T_{vI} \quad (13)$$

Assuming $T_{vI} \cong T$, T_{vII} can be calculated from Eqs.(11) and (12). e_{max} and P_{out} are obtained from Eqs.(8), (9) and (10).

Fig.6 indicates the laser powers at pressure of 1.15 MPa. The solid line means the values calculated from the experimental data. The broken lines show the laser powers estimated from various amounts of gain for the comparison. The emission power is expected to be about 2.5 kW with the path length of 0.3 m from the magnitude of the gain.

5. CONCLUSIONS

The CO₂ gas dynamic laser driven by methane-air combustion in an unsteady flame propagation combustor was proposed for the purpose of industrial application. The population inversion was confirmed both by the analysis of the population balance and by the experimental measurement of the small-signal gain. The estimation revealed that a high emission power of about 2.5 kW with the path length of 0.3 m is expected from the magnitude of the gain.

6. REFERENCES

1. N. Kobayashi, Y. Itaya, and Masanobu Hasatani, "Development of flame propagation combustion applicable to driving gas generator for CO₂ gas dynamic laser", *Kagaku Kogaku Ronbunshu*, **20**(6), 894-901 (1994).
2. R.L. Taylor and S. Bitterman, "Survey of Vibrational Relaxation Data for Processes Important in the CO₂-N₂ Laser System", *Reviews of Modern Physics*, **41**(1), 26-47 (1969).
3. T. Hashimoto, S. Nakano, M. Hachijin, K. Komatsu, Y. Mine and H. Hara, "Characteristics of a downstream-mixing CO₂ gasdynamic laser caused by behavior of two supersonic flows in a laser cavity", *Applied Optics*, **32** (30), 5936-5943 (1993).
4. P. Cassady, J. Newton and P. Rose, "A new mixing gasdynamic laser", *AIAA J.*, **16**, 305-312 (1978).
5. W. Schall, P. Hoffmann and H. Hugel, "Performance of N₂/CO₂ gasdynamic mixing lasers with various injection techniques", *J. Appl. Phys.*, **48**, 688-690 (1970).
6. H. Hugel, W. Schall and P. Hoffmann, "Experimental investigation of gasdynamic N₂/CO₂ mixing lasers", *J. Phys. (Paris)*, **41**, 335-341 (1980).
7. Anderson, J. D. Jr., *Gasdynamic Lasers: An Introduction*, Academic Press, New York, 1976.

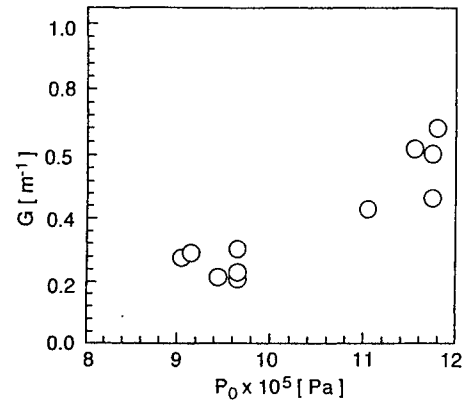


Fig. 5 Behavior of the magnitude of the small-signal gain for operating pressure $P_{0,ave}$

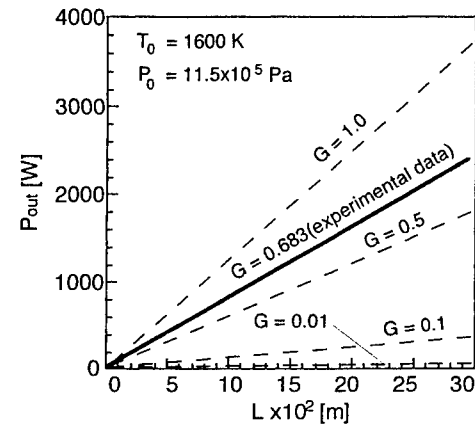


Fig. 6 Laser power of the CO₂-GDL estimated.

Anatoly S. Boreisho and Andrew G. Trofimovich

Baltic State Technical University, Department of Laser Technique
1-st Krasnoarmeyskaya 1, St.Petersburg 198005, Russia

ABSTRACT

The first purpose of combustion-driven CO₂-gas dynamic lasers (GDL) was military applications. Just these applications aimed to development of more and more powerful systems led to appearance of more and more expensive lasers using very dangerous and poison fuels. It is very hard to satisfy simultaneously both military and economy requirements, therefore, this idea could not be realized widely and successfully. On this way the lasers had no chance to be suitable for ordinary users. New approaches at the old idea of combustion-driven CO₂-GDL allow to open some ways to realize the lasers for education and research projects. The most inexpensive 10-15 kilowatt and 400 megawatt lasers are considered. Experimental results, technical and financial estimates are presented also.

Keywords: gas dynamic laser, solid propellant, liquid fuel, applications, estimations, efficiency

2. APPLICATIONS

GDL is one of oldest ideas to create a self-contained CW source of a high power light beam. Many various propellants and fuels were studied and many different lasers were built to search for the best way depending on real applications [1]. Nevertheless this idea was definitely given up more than ten years ago because efficiency of the lasers turned out to be too low in comparison with some other more effective and shorter wavelength laser systems.

As well as defense, some other possible applications for the lasers including of repairing in disaster areas, remote actions at inaccessible targets, entities, etc., were considered. Such lasers should be compact, mobile, harmless for users and friendly at environment. The most important criteria for the systems are low cost and economy efficiency. From this point of view an explosive and combustion chemical energy conversion remains a very attractive way and the combustion-driven GDL may become a reasonable solution thanks to their exceptional simplicity and minimal expenses both for their fabrication and operation. However, in this case just these parameters have to be defined as the most important and maximally motivated.

In spite of wonderful achievements in high power CW solid state and some other types of lasers, the electrical discharge fast flow CO₂-lasers remain the only type of industrial CW laser systems with output power 10-20 kW. Being cost-effective for mass-product lines these lasers are too expensive for mostly research and education labs.

Many more difficulties arise to provide studies of various technologies using of more powerful (20 - 100 kW) CW lasers. Each such laser is a unique and very expensive machine. Meanwhile all future technologies have to be developed today and than more groups of scientists and engineers are involved in the research processes today than more successful results may be expected tomorrow. It is very important from educational point of view also. Probably many universities and science centers would like to take part in such investigations, however, they cannot afford to apply today's high power lasers.

In these cases there is not necessary to apply the real long-time CW operation lasers. Mostly problems may be investigated and studied for shorter CW operation time experiments. Certainly such kind of lasers cannot be used directly for mass-product industrial and commercial applications. High power, continues wave, well focused, inexpensive gas dynamic lasers may turn out to be very helpful to develop various research and educational programs for modern materials processing, chemical, electronic and other high technologies.

3. ESTIMATIONS

Specific power for combustion-driven lasers may be up to 15 J/g if very special fuel components as N₂O, (C₂N₂)_n, etc., are applied to produce their active media [2]. Employment of much simpler, lower cost components provides as much as 6-8 J/g of the specific power.

Laser beam quality may be very high if to take into consideration usually good uniformity of the GDL active media. Multi-pass unstable resonators provide the lasers beam divergence close to some diffraction limits. The same time

depending on real applications much simpler stable resonators may be used also. In this case the beam divergence is worse by ten times than this one for an unstable resonator. Nevertheless they can provide maximal specific power as well as maximal output power for 10-20 kW lasers.

Dimensions - the gas dynamic lasers are very compact. Their dimensions may be estimated considering of the whole GDL as two independent parts: the same laser and working medium supply system.

1) The laser's dimensions depend on its efficiency and output power. The combustion-driven GDL output power of from the laser volume's unity is about 100 kW/m^3 .

2) Scale of working media supply systems are found out with the media efficiency, output power P and operation time τ . The propellant and/or fuel average density is about 1000 kg/m^3 , i.e. specific output energy may be presented as $10,000 \text{ kJ/m}^3$. Then the whole laser system volume V may be estimated as following: $V[\text{m}^3] \cong (1 + 0.01 \tau[\text{sec}]) \times P [\text{kW}] / 100$.

If full operation time of the laser is more than some minutes the laser's size is defined exceptionally with the laser working media supply system while for some seconds operation time the size is depended on a laser unit mainly.

Safety - The most important safety problem of the high effective gas dynamic lasers is the dangerous and poison components. Use of these materials leads to high expenses to provide enough safety both for technician and military staff as well as for environment. Meanwhile ordinary save components and/or whole propellant mixtures allows to apply the lasers anywhere without any extra actions and expenses.

Cost - It is very difficult to use a common approach for this very sensitive parameter. Our estimations are based on an existing experience for development of GDL with output power from some kW to some hundreds kW.

The cost of laser radiation power (energy) consists of two main parts - a cost of the laser and maintenance charges (wages, cost of fuels, propellants and additional energy, safety, protection of staff and environment). A simple 15 kilowatt uncooled GDL may be built today for \$75,000 USD, i.e., $\approx \$5 \text{ USD}$ per one watt of output power. This relative value is the same or lower for more powerful lasers. For example one 100 kilowatts combustion-driven gas dynamic laser may cost \$250,000 USD only ($\approx \2.5 USD per one watt of output power).

The maintenance charges are very different depending on used materials and components. Values of effective laser propellants may reach \$1.0 USD per one kilogram. It means this part of expenses has to be about \$0.1 USD for one kilojoule (kJ). Ordinary fuels and high pressure air cost at least by some tens times less, however, efficiency of the lasers is by two times less also, so and in this case that part of maintenance charges has not to exceed the value of \$0.1 per one kJ. The expenditures for safety, protection of staff and environment are also connected with the substances' values. For expensive poison explosive materials these expenses may be higher, while for ordinary wide-spread propellants they will be much less. Anyway the maintenance charges will not exceed \$0.1 USD per one output power kJ.

Ultimately the lasers' cost does not exceed \$5,000 USD for one kW output power, while their maintenance charges are expected on the level of \$0.1 USD for one kJ.

4. 10 kW COMBUSTION-DRIVEN GAS DYNAMIC LASER

The concept of a compact inexpensive combustion-driven CO_2 -laser including both solid propellant- and liquid fuel-air gas-generators as sources of the laser medium were developed in the Baltic State Technical University during several last years. Some such lasers (Fig.1) have been designed and built for various labs. The lasers utilize practically either solid propellants or liquid fuels (beginning of coal or kerosene) burned with air.

The working gas mixture (laser medium) of the laser presented on the Fig.1 is produced by burning of ordinary rocket double-base solid propellants and air, though such laser was tested with liquid fuel-air gas generators also. Combustion gas products of the solid propellants contain carbon monoxide (50 %), water vapor (16%), hydrogen (18%), nitrogen and carbon dioxide. The gas after-burning with air gives a new mixture that is suitable for the GDL.

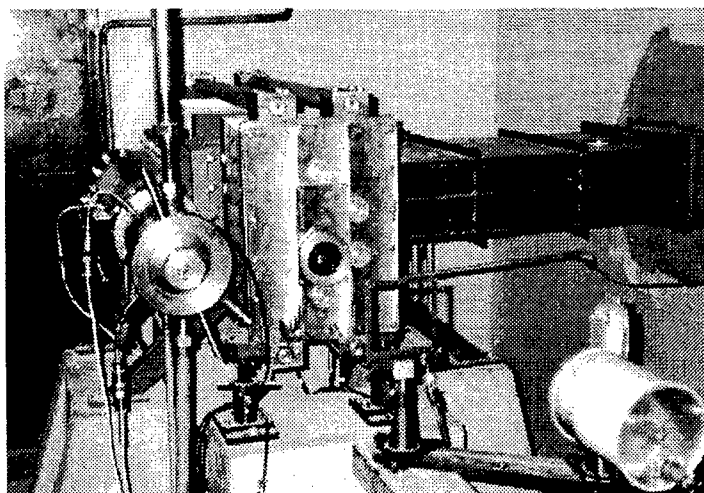


Fig.1

The laser specific power depends on the ratio β between the air and combustion products mass flow. For solid propellants-air combustion products the β optimal values are between 3.5 - 4.5 (Fig.2). The gas mixture consists of carbon dioxide (14%), nitrogen (68%), water vapor (9%) and oxygen (9%), temperature is 1700 - 2000 K. For liquid fuel-air mixtures combustion products are carbon dioxide (13%), nitrogen (76%), water vapor (7%) and oxygen (4%), temperature is 1800 - 2200 K while the optimal β values are 12-16.

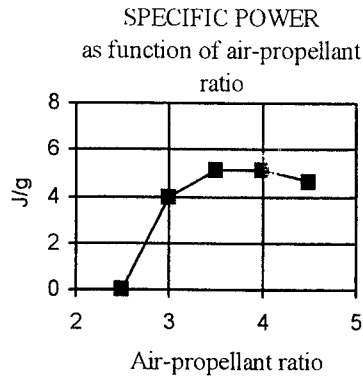


Fig.2

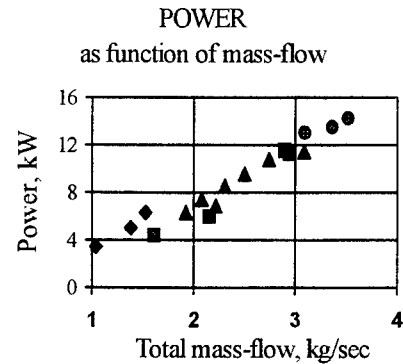


Fig.3

The GDL specific output power is 4,0 - 6,0 J/g for solid propellant-air gas generators, and 6,0 - 9,0 J/g for liquid fuel-air ones. One start duration of the CW operation is up to 5 s (it can provide some starts per hour), the laser overall dimensions are 150 × 130 × 67,5 cm. The solid propellant-air GDL tests results are presented on the Fig.3. Ordinary rocket double-base solid propellants stored sometimes more than 15 years were used for the experiments.

5. COMBUSTION-DRIVEN GAS DYNAMIC LASER FOR ENERGY ADDITION TO AIR FLOW

The general points. 400 MW output power CW laser is really fantastic system. Different kinds of high power lasers have been discussed as a possible source for energy addition to air flow of the hypersonic wind tunnel [3]. None of today's laser systems can satisfy directly this demand. Thinking about we try to estimate such laser's scheme, parameters, and cost based on our results [4]. In comparison with other chemical lasers GDL is less efficient, however a scale of a full chemical laser system of the same output power may be even larger. Besides of that the gas dynamic laser work medium is much more friendly at environment and (maybe the most important feature) this laser is more inexpensive both to built and to use it. On the Fig.4 the first preliminary scheme of the laser is presented as a part of the whole aerodynamic tube test site.

We assume that the operation time is one second. The specific output power as 8 kJ/kg may be obtained with applying of ordinary solid propellants and air enriched with nitrogen. The full flow rate of the laser is 50,000 kg/sec, i.e. it is necessary 10,000 kg of solid propellant and 40,000 kg of high pressure air for one second pulse. A vacuum system provides the full time operation collecting the laser work media in the tanks. Such way makes the experiments noiseless and saves both for people and environment. The same vacuum system may be used to collect hypersonic air flow from the tube. The volume of the vacuum system is 80,000 m³, i.e. 140 spheres of 15 m diameter each.

The first pumping up stage pressures gas from the vacuum volume up to 400 atm. 7,800 kg CO₂ and 4,500 kg H₂O become liquid and taken out from the system. Adding 4,000 kg O₂ at the mixture we get the best oxidizer for a new operation pulse of the laser. A part of the mixture (about 500 kg) under 400 atm pressure goes to the second pumping up stage to prepare gas for the hypersonic tube. Pressing the mixture up to 30,000 atm (?) and adding 50 kg O₂ the medium for the new operation pulse of the tube will be ready. In fact now we cannot imagine how this part of the system may operate, therefore this paragraph includes in the text only as a reference. However, using previous data we can estimate dimensions and expenses for the laser system. A preliminary design scheme of this system is presented on the Fig.4.

The scheme. The big laser consists of some equal units including both the master-oscillator and amplifiers and combined in the united system. A cross section of the wind tunnel is 8.5 m², therefore the best location of the output laser beams windows is around of the tunnel perimeter, i.e. on a diameter about five meters. The optimal nozzle blade's height is 15-20 cm. Directing of the laser units diffusers at the axes of the hypersonic wind tunnel to a collecting vacuum tube it is possible to place on the laser beams perimeter about 100 laser units. The output power of each laser unit is 4 MW. A

The cost. The laser volume without the work medium and vacuum system is about 2,700 m³. The laser can use some master-oscillators and amplifiers, so a main part of the work medium goes through the amplifiers. It may decrease the

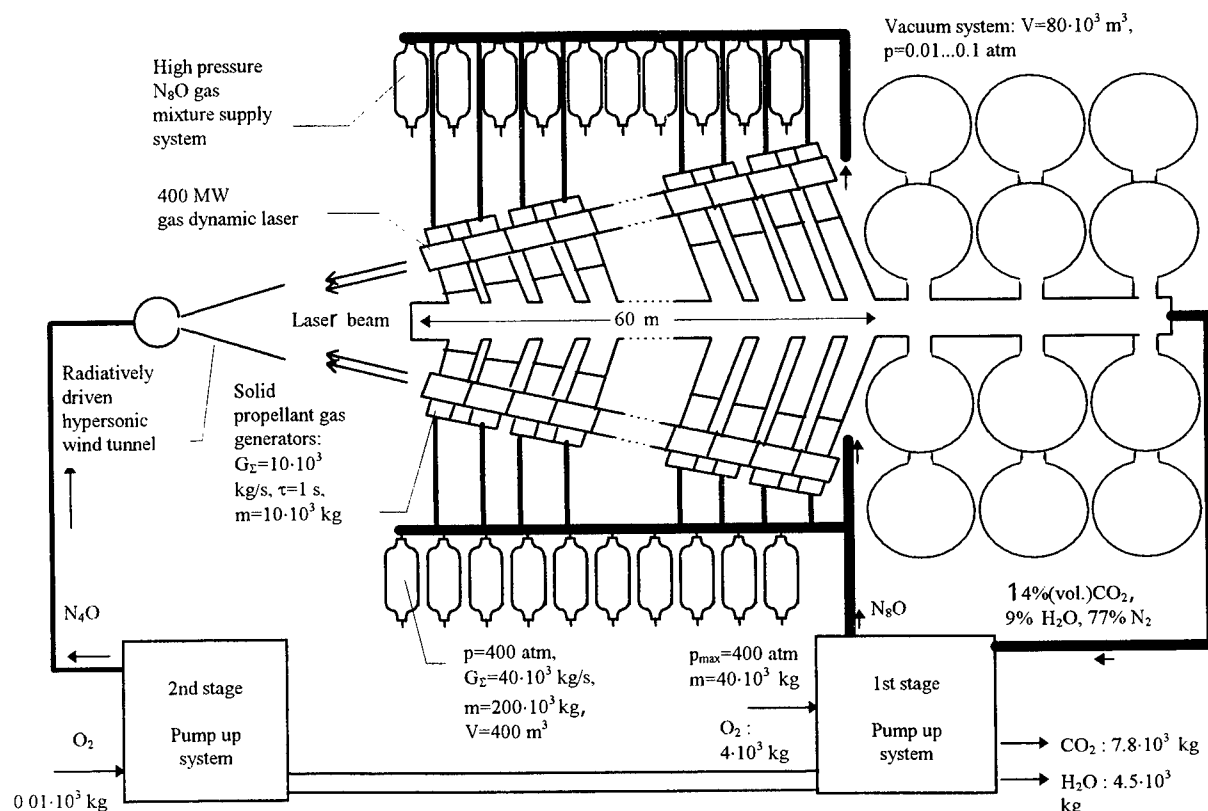


Fig.4

expenses for the optical systems that has to be simple enough for such kind of laser. Considering our today experience the cost for one mass product 100 kW gas dynamic laser module as part of the big 400 MW laser is about \$50,000, i.e. the whole laser system cost is about \$200,000,000.

The maintenance charges are \$ 0.0001 for one Joule according our previous estimate for such kind of lasers. Therefore the expenditure for one second operation time of the laser may be expected on the level about \$40,000 USD.

6. ACKNOWLEDGMENTS

The greatest thanks to our colleagues at the Laser Tech. Department of the Baltic State Technical University. Our contacts continue to have an important impact on the results.

We are also indebted to Staliy A.Losev, and Valeriy K.Ikonnikov for their attention and assistance.

At last only all our customers' interest, support and patience made these works possible.

7. REFERENCES

1. A.S.Boreisho, A.F.Leonov, V.L.Moshkov et al. "Active Media Inhomogeneties of Gas Flow Lasers", AIAA Paper 93-3166, 24th AIAA Plasmadynamics & Lasers Conference, Orlando, FL, 1993.
2. Cassady P.E. "A survey of advanced gasdynamic laser concepts", J.Energy, 1980, vol.4, p.145-161.
3. R.Miles, G.Brown, W.Lempert et al., "Radioactively Driven Hypersonic Wind Tunnel", AIAA Paper 94-2472, 18th AIAA Aerospace Ground Testing Conference, Colorado Springs, CO, 1994.
4. A.S.Boreisho, A.G.Trofimovich, "Combustion-Driven Gas Dynamic Laser for Energy Addition to Air Flow", BSTU 5590-95, St.Petersburg, 1995.

11. Laser Micromachining II

High Resolution Microlithography Applications of Deep-UV Excimer Lasers

F.K. Tittel¹, M. Erdélyi², G. Szabó², Zs. Bor², J. Cavallaro¹, and M.C. Smayling³

¹Department of Electrical and Computer Engineering and Rice Quantum Institute, Rice University, 6100 Main, Houston, TX 77005-1892, USA

²Department of Optics and Quantum Electronics, JATE University, H-6720, Szeged, Dom ter 9, Hungary

³Texas Instruments, Inc., 12201 S.W. Freeway, MS 735, Stafford, TX 77477, USA

1. Introduction

The recent trend in microelectronics towards patterning critical feature sizes of 0.25 μm and below has motivated the development of microlithography at the deep ultra-violet (DUV) laser wavelengths of 248 and 193 nm. In recent years the performance, reliability, and cost of ownership of excimer light sources have improved. Some key technologies needed for excimer lasers in microlithography include materials issues, gas lifetime, higher repetition rates and improved pulse-to-pulse energy repeatability.

As dimensions of circuit elements shrink, new wavefront engineering technologies such as phase shifting techniques, off-axis illumination, and other modifications to extend the lifetime of optical lithography are required [1-5]. Simultaneous improvement of the resolvable linewidth (CD) and the depth of focus (DOF) is an important issue. Both CD and DOF are limited by the familiar scaling laws $CD = k_1 \lambda / NA$ and $DOF = k_2 \lambda / NA^2$, where λ is the wavelength and NA the numerical aperture of the projection lens. The parameter k_1 depends upon the imaging technology and process control, while k_2 has been within range of 1-2 for many years. The key innovations required for microlithography are those that reduce k_1 . The 0.35 μm critical feature sizes required for the 64 Mb DRAM can be achieved with wavefront enhancement technology developed for i-line. Similarly, such techniques can be added to 248 nm DUV stepper systems to achieve the necessary resolution for 0.25 μm features needed for the production of the 256 Mb DRAM chip slated for initial production in 1998. The practical limit of optical lithography appears to be 0.12 μm required for the 4 Gb DRAM generation.

In 1987 Durnin [6] showed that the field described by $E(r, z, t) = A \cdot J_0(k_{\perp} r) \cdot e^{i(k_{\parallel} z - \omega t)}$ is an exact solution of the wave equation where $k_{\perp}^2 + k_{\parallel}^2 = \omega^2 / c^2$, and J_0 is the zero-order Bessel function of the first kind. This field represents a nondiffracting beam, because the transverse intensity distribution is independent of the propagation distance z . However, such an ideal beam cannot be realized experimentally over large values of z and r , because the

electric-field amplitude of the beam cannot be spatially integrated and would be rigorously exact only in infinite free space [6,8]. An experimental demonstration of a new method to generate nearly nondiffracting Bessel beams using a Fabry-Perot interferometer will be described. It was experimentally demonstrated that the *DOF* can be increased by a factor of 2 and simultaneously the transverse resolution improved by a factor of about 1.6, when using this technique to image contact holes.

2. Experiments and Results

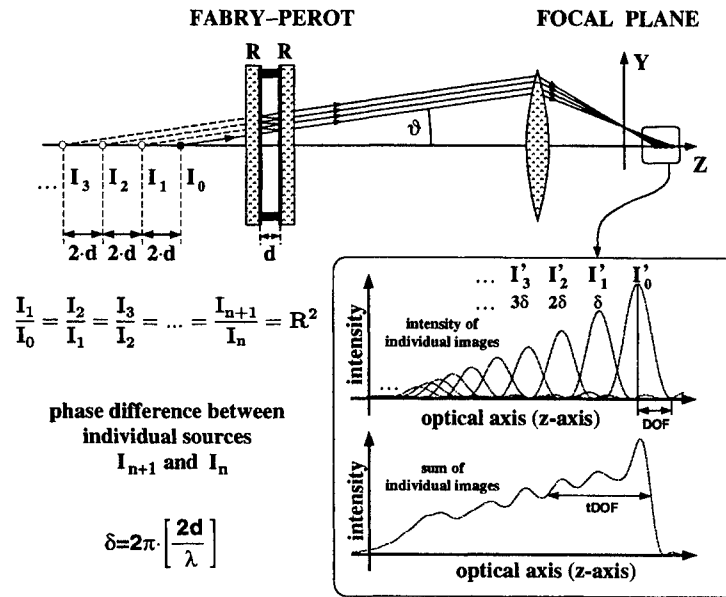


Figure 1: The image produced by the objective lens is the superposition of the images of the individual point sources.

Figure 1 shows the experimental arrangement used for generating nondiffracting Bessel beams. A point like source (I_0) generated by a microscope objective illuminates a scanning Fabry-Perot interferometer. Such a point like source plays the role of a contact hole on a mask. The aperture of the objective lens placed after the interferometer is adjusted so that it only transmits the first Fabry-Perot ring (at the rim of the aperture) and blocks all other rings. Due to multiple reflection in the interferometer, multiplied images ($I_1, I_2, I_3 \dots$) of the only one real point like source will be obtained beyond I_0 . The distance between these images is $2d$ and the intensity ratio is R^2 between adjacent individual sources where d is the separation and R is the reflectivity of the mirrors. The image produced by the objective is the superposition of the images of the individual point sources. The distance between these points is $2dM^2$, where M^2 is the longitudinal magnification of the objective lens. The intensity distribution on the optical axis strongly depends on the separation of the individual point like sources. It is possible to distinguish different cases depending on how many individual image points are in the range of one *DOF*. Let us define the relative image density (N) as

$$N = \frac{DOF}{2dM^2}. \quad (1)$$

N gives the number of image points in one DOF range. The image produced by the objective lens was magnified by two microscope objectives (the first was mounted on a precision translator to examine the axial intensity distribution) and monitored with a CCD camera (see Fig.2).

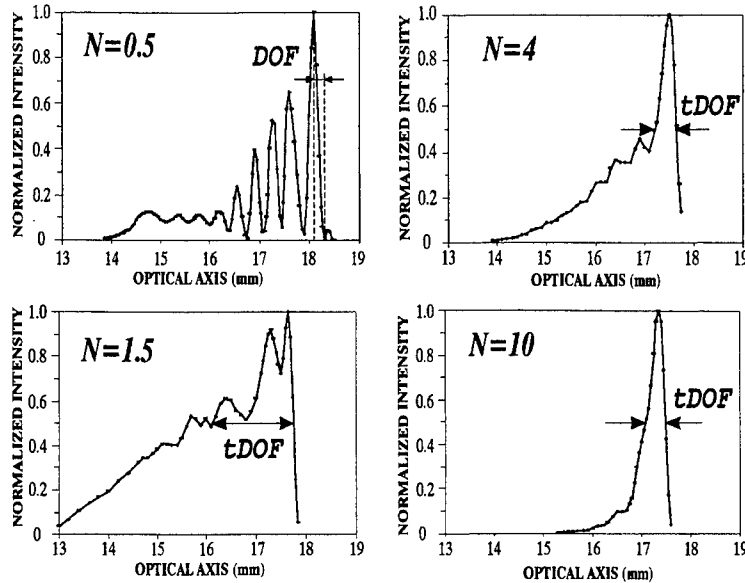


Figure 2: Measured intensity distribution on the optical axis for cases of different N values.

Four different experimental cases were studied ($N = 0.5, 1.5, 4$, and 10). In the first case ($N = 0.5$), the distance between the image points is twice the DOF , therefore the images can be observed separately. By decreasing the distance between the image points, the sharp peaks disappear and the intensity decreases faster on the optical axis. From a microlithographic point of view, oscillations in the intensity distribution are undesirable. By increasing the N ratio, the curves become smoother and the oscillations disappear. In the last case ($N = 10$), no oscillations occur. Since in case of superimposed images the first minimum is not zero, it is necessary to give a new definition of DOF so-called $tDOF$. $tDOF$ is defined as the range where the intensity is higher than the half of the main peak. The figures show normalized intensity, but in reality (due to the law of conservation of energy) by increasing the N ratio, the intensity of the main peak increases. The $N = 4$ case appears to be the optimum for microlithographic applications. The oscillations have already disappeared, and the $tDOF$ range is twice as large as without the Fabry-Perot interferometer.

The theoretically predicted intensity distribution in planes perpendicular to the optical axis is a J_0 function. The measured intensity distribution supports this prediction (Figure 3).

A comparison of the measured Bessel distribution and the Airy pattern showed that the FWHM of the Bessel beam is 1.6 times smaller than the FWHM of the Airy pattern. This decrease means an enhancement in the transverse resolution power.

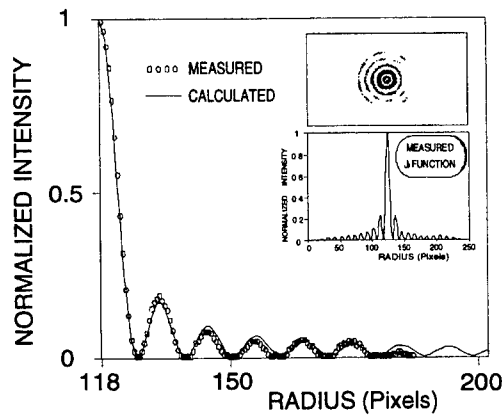


Figure 3: The measured intensity distribution perpendicular to the optical axis is quasi equivalent to a zero order Bessel function. The solid line shows the fitted curve to the measured intensity distribution (depicted by circles)

In microlithography it is often necessary to expose several contact holes simultaneously. To study the properties of imaging two contact holes (with special regard to the most critical case, when the first diffraction rings overlap), we placed a Michelson interferometer before the Fabry-Perot etalon. The experimental setup is shown in Figure 4.

The interferometer created two virtual point sources (P_1 and P_2) behind the mirror M_2 . By slightly turning the mirrors M_1 and M_2 , the relative transverse separation of P_1 and P_2 could be adjusted. Mirror M_1 was equipped with a PZT translator; thus, the relative phase difference between the virtual P_1 and P_2 could be arbitrarily adjusted. The inset of Figure 4 shows four different cases. In case *a* there is constructive interference between the first diffraction rings (the phase shift is 0), and the intensity between the two main peaks can reach 64%. Pictures *b* and *c* show intermediary cases, when the phase shift is in the range of 0 to π . In case *d* the phase difference is π and, due to the destructive interference, the intensity maximum between the main peaks is zero. These experiments, where the effect of a phase shift mask was simulated by a Michelson interferometer, show that even in the most critical case the undesirable effects of the interference of the diffraction rings can be considerably reduced with a phase shifting mask.

3. Discussions and Conclusions

Our experiments have demonstrated that for appropriate phase conditions the depth of focus could be increased significantly and that the transverse resolution improved by a factor of 1.6 when this technique is used to image isolated patterns such as contact holes. Although these experiments were performed with visible laser illumination, this method can be employed for I-line and deep UV lithography. For applications in a real optical stepper, further investigations are necessary to determine the appropriate insertion point, reflectivity and thickness of the Fabry-Perot etalon. Insertion of a thin Fabry-Perot layer between the lens and the wafer has several advantages (e.g. separation of the images is independent of

the magnification), however scattering may decrease the image quality.

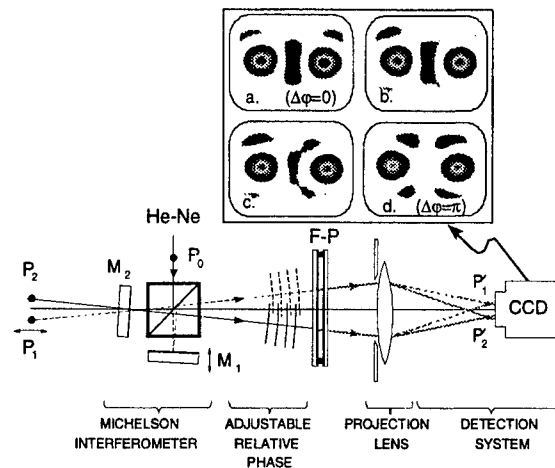


Figure 4: Imaging of two coherent point sources formed by a Michelson interferometer. The transverse distance and the relative phase difference between the sources was adjustable by translating and tilting the mirrors. The inset shows CCD images for different phase conditions.

Acknowledgment

This research was supported in part by Texas Instruments, NSF under grants DMI-9202639 and INT-9020541, and by the OTKA Foundation of Hungary (No. T20910).

References

1. M. D. Levenson, N. S. Viswanathan, and R. A. Simpson, *IEEE Trans. Electron Devices* **ED-29**, 1828 (1982).; M. D. Levenson, *Jpn. J. Appl. Phys* **33**, 6765 (1994).
2. H. Fukuda, N. Hasegawa and S. Okazaki, *J. Vac. Sci. Tech. B* **7**(4), 667 (1989).
3. M. Erdélyi, Zs. Bor, J. R. Cavallaro, G. Szabó, W. L. Wilson, C. Sengupta, M. C. Smayling and F. K. Tittel, *Jpn. J. Appl. Phys.* **34**, L1629 (1995).
4. F. K. Tittel, M. Erdélyi, Zs. Bor, G. Szabó, J. R. Cavallaro, M. C. Smayling, and W. L. Wilson, in *Gas Lasers – Recent Developments and Future Prospects*, ed. W. J. Witteman and V. N. Ochkin, 263-272 (1996).
5. M. Erdélyi, Z. L. Horváth, G. Szabó, Zs. Bor, F. K. Tittel, J. R. Cavallaro and M. C. Smayling, Generation of Diffraction-Free Beams for Applications in Optical Microlithography (submitted to *J. Vac. Sci. Tech. B*)
6. J. Durnin, *J. Opt. Soc. Am.* **4**, 651 (1987).
7. J. Durnin, J. J. Miceli, Jr., and J. H. Eberly, *Phys. Rev. Lett.* **58**, 1499 (1987).
8. G. Indebetouw, *J. Opt. Soc. Am.* **6**, 150 (1989).

Performance of 1 kHz KrF excimer laser for DUV lithography

Palash Das, Richard Morton, Igor Fomenkov, Bill Partlo, Rick Sandstrom, Cyndy Maley and Ray Cybulski
Cymer, Inc., 16275 Technology Dr., San Diego, CA 92127

ABSTRACT

In response to the requirement for higher wafer throughput and increased dosage accuracy in DUV lithography steppers and scanners, Cymer has developed a 1kHz KrF laser optimized for this application. We shall describe its performance and design features.

Keywords: KrF lasers, Deep Ultraviolet photolithography, SCR switched pulsed power

2. INTRODUCTION

Chip makers are gearing up for 686-class micro-processors and 64Mbit production. These require producing 0.35 μ m design rules. They are also focusing on 256Mbit DRAMs that require 0.25 to 0.35 μ m design rules (Figure 2.1). Therefore, the shift from mercury lamp based I-line to 248nm DUV steppers has begun in earnest. Current KrF laser models from several suppliers satisfy the optical/uptime requirements necessary for pilot production, and are beginning to compete well with I-line steppers.

3. LASER PARAMETERS AFFECTING STEPPER/SCANNER OPERATION

The parameters that affect the operation of a stepper or scanner are now well understood (Table 3.1)¹. A multifaceted relationship exists between the laser and stepper/scanner. Such is not the case with the mercury arc lamp and the stepper. As the move towards higher Mbit DRAMs and faster processors occur, the requirements for narrower linewidth KrF lasers increases, as shown in the table. Higher throughput and dose control accuracy require higher repetition rates and precise control of laser's energy reproducibility. Therefore, several laser sub-systems were re-examined during development of 1 kHz laser (Figure 3.1). Finally, the DUV lithography process has moved from the R&D laboratory to the pilot production line. Therefore, the lasers have to meet a host of international safety standards.

3.1 Chamber

By far, the most critical module in the laser is the chamber². The all-metal and ceramic chamber was re-designed to improve flow uniformity between electrodes and minimize blower power requirements (~30% of total input power). Flow guides introduced in the chamber eliminated flow non-uniformities, resulting in linear laser power with repetition rate. The linearity is required to achieve long gas life (100 M pulses between refills) and minimize peak-to-peak energy variations.

3.2 Pulsed Power

At 1kHz, the traditional approach of using a thyatron switched pulsed power system is inadequate (Table 3.2). An all solid-state pulsed power system³ was optimized for 1kHz operation. The energy-recovery feature in the pulsed power unit reduces energy into the discharge in the post-pulse period (Figure 3.2), resulting in increased chamber life and gas life.

3.3 Line Narrowing

The high NA steppers require narrow linewidths (<0.8pm, FWHM). The line narrowing technique utilizes an echelle grating in combination with beam expansion prisms. For short duration KrF laser, the final linewidth ($\Delta\lambda_f$) is related to the single pass linewidth ($\Delta\lambda_1$) via the equation:

$$\Delta\lambda_f = \frac{\Delta\lambda_1}{\sqrt{n}}$$

where n is the number of round trips. Since the number of round trips is small, 3 or 4, the single pass linewidth is designed to be a factor of two higher than the desired linewidth of 0.8 pm (Figure 3.3). This means that the magnification of the prisms is very high. However, this technique is susceptible to

deviations in material flatness or homogeneity which increases linewidth. The problem of small wavefront curvatures is corrected by introducing a small curvature ($R \sim 0.5$ to 10 km) in the grating.

3.4 Energy Stability in Stepper mode operation

The step-and-repeat lithography process has many steps, such as wafer loading, pre-alignment, exposure and stepping of die. Once in the ready state, the laser may be operated in short bursts (30 to 60 pulses), separated by rest periods (100 to 1000 ms). After exposure of one wafer, the wafer exchange step takes several tens of seconds, during which the laser remains idle. The burst mode makes laser operation unstable in energy & spectral performance at the beginning of few pulses of each burst. After few pulses, the energy is more well-behaved implying that the energy can be stabilized. Fortuitously, it has been observed that the energy behavior during the start of the burst is fairly repeatable. The laser's control system software is "trained" to compensate for this behavior. However, further investigation on the characteristics of the second laser pulse as a function of delay wrt the first pulse revealed interesting facts about the role of gas flow in controlling energy stability (Figure 3.4). The re-entrant gas during the second discharge retains some memory of the first discharge. The effects of re-entrant gas can be minimized by proper premixing of the gas prior to its re-entry into the electrode region. By a combination of software and gas flow engineering, the energy stability of the laser in the stepper mode can be improved significantly.

3.5 Energy Stability in Scanner mode operation

For scanner operation, the Energy Stability of laser impacts dose (which is the integrated energy over a burst) accuracy. The lasers are designed to operate in the range where dE/dV is the lowest (Figure 3.5), so that small fluctuations in the voltage do not create large fluctuation in energy. Therefore, lasers are designed such that they operate at or near 600V. With big improvements in manufacturing technology, today, Cymer can control the variability of the starting operating voltage to within 3%, i.e. all lasers operate at $600 \pm 3\%$. For scanners, the total dose is more appropriate than energy stability. The control software, therefore, attempts to minimize the deviation in the integrated dose during a burst by using a non-linear algorithm. Although the energy stability can be as much as 10%, the integrated energy can be controlled to within 1% for bursts as small as 50 pulses.

4.0 RELIABILITY AND COST-OF-OPERATION

Beam and system parameters have to be met throughout the life of the laser. Therefore, the laser is subjected to rigorous life/reliability tests. However, the present understanding of reliability goes beyond testing a laser for several billion pulses and documenting the failure mechanisms. Instead, Failure Reporting, Analysis and Corrective Action System (FRACAS) gathers reliability data. FRACAS is a SEMATECH created database program used to collect, record and analyze failures. Database logs and classifies all failures. It then tracks and monitors solutions to ensure closure of all problems. All laser failures starting with manufacturing build through system end of life are logged in FRACAS. Pareto analysis and other statistical reports generated by FRACAS help Cymer understand the reliability of ELS-5000. Therefore, reliability data is gathered from multiple sources, under multiple conditions to help Cymer track failures due to design, infant mortality, or lifetime.

5.0 CONCLUSION

After ten years of development, the stepper/scanner manufacturers, working in conjunction with excimer laser manufacturers have taken DUV lithography technology from R&D to pilot production. Simultaneously, the laser manufacturers have refined manufacturing techniques, introduced process controls and implemented reliability programs to effectively compete with I-line based steppers/scanners.

6.0 REFERENCES

1. U.K. Sengupta, "Krypton Fluoride Excimer Laser for Advanced Microlithography," Optical Engineering, Vol.32 No. 10, pp. 2410-2420, Oct. 1993.
2. R.G. Morton et. al., "Design considerations and performance of 1kHz KrF excimer lasers for DUV lithography", Proceedings SPIE Optical/Microlithography IX, to be published.
3. W. Partlo et. al. "Low cost of ownership KrF excimer laser using novel pulse power and chamber configuration", SPIE, Optical/Laser Microlithography VIII, Vol. 2440, pp. 90-100.

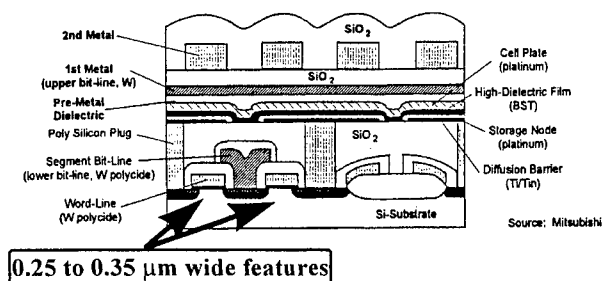


Figure 2.1 256 Mbit DRAM Structure

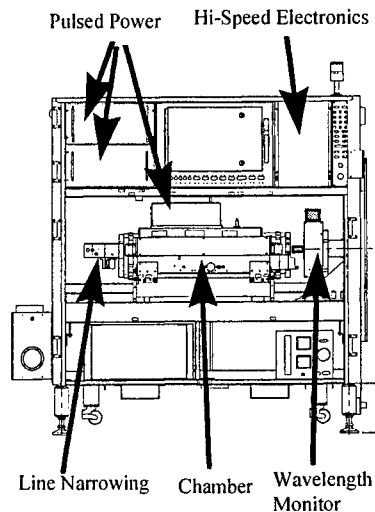


Figure 3.1 ELS-5000 and sub-systems

Table 3.1 Parameters that affect stepper/scanner operation

Spectral Bandwidth and Spectral Energy Distribution	⇒ (affects)	Resolution, Depth of Focus
Relative Wavelength Stability	⇒	Focal Plan Stability (long term) Resolution, D.O.F., (Short Term)
Absolute Wavelength Stability	⇒	Magnification, Distortion
Output Power	⇒	Throughput
Repetition Rate	⇒	Energy Dose Accuracy, Speckle Reduction
Pulse-to-Pulse Energy Stability	⇒	Energy Dose Accuracy
Beam Profile, Beam Pointing & Beam Divergence Stability	⇒	Exposure Uniformity, Illuminator Efficiency
Polarization Stability	⇒	Illuminator Efficiency
Spatial Coherence	⇒	Speckle, Exposure

Table 3.2 Differences in Thyatron and SCR-switched Pulsed Power

Thyatron Switched	Solid State Switched
<p>Advantages</p> <p>(1) Simple, with few components.</p> <p>Disadvantages</p> <p>(1) Thyatron dissipates significant energy due to its losses. Increased losses cause thyatron heating and unpredictable prefires.</p> <p>(2) Energy after Laser Pulse is dissipated in thyatron and laser electrodes, causing thyatron and electrode erosion.</p> <p>(3) 10 min. warm-up.</p>	<p>Disadvantages</p> <p>(1) Complex, many components</p> <p>Advantages</p> <p>(1) No unpredictable pre-fires. Very important for scanners.</p> <p>(2) Energy after Laser Pulse is recovered and used for subsequent pulse. This energy recovery increases system efficiency and laser chamber life. Scaling in repetition rate to 1 kHz is easier.</p> <p>(3) "Instant -on", no warm-up.</p> <p>(4) 15 times longer life than thyatron</p>

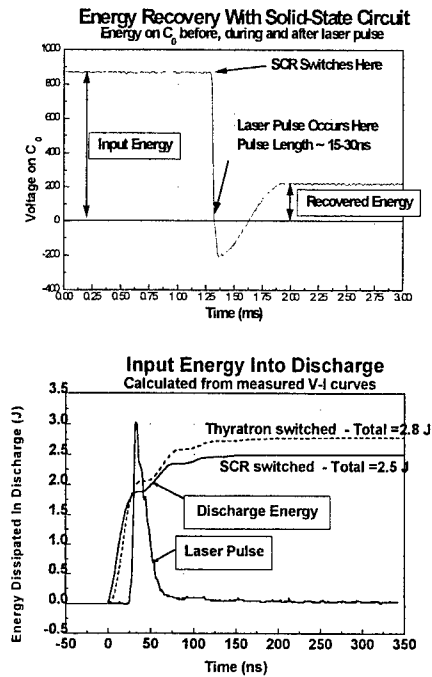


Figure 3.2 Energy recovery with SCR switched solid-state pulsed power system

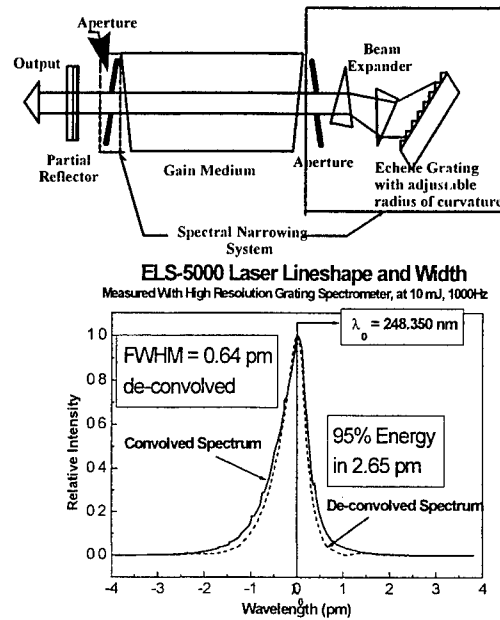
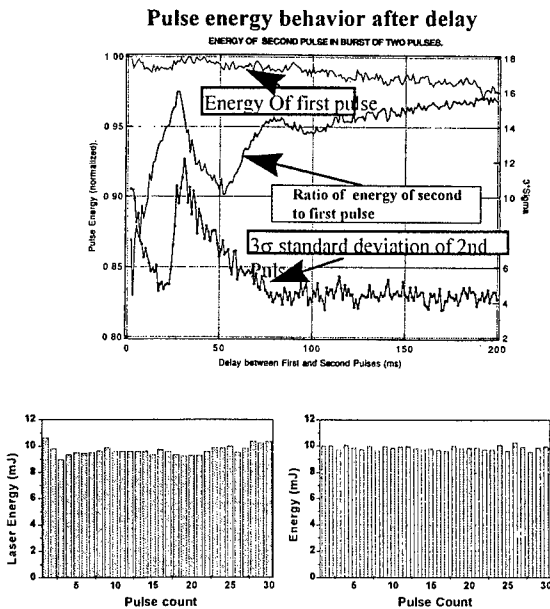


Figure 3.3 Line Narrowing system and spectral profile



Without software, $3\sigma = 10\%$ With software, $3\sigma = 6\%$

Figure 3.4 Energy Stability during stepper operation

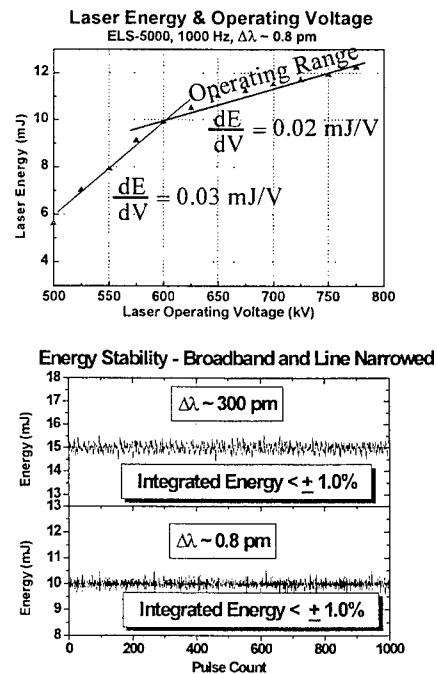


Figure 3.5 Energy Stability during scanner operation

High-resolution microlithography using a 193nm excimer laser source

Nadeem H. Rizvi, Dominic Ashworth, Julian S. Cashmore and Malcolm C. Gower

Exitech Limited

Hanborough Park, Long Hanborough, Oxford OX8 8LH, England

Tel: +44 1993 883324 Fax: +44 1993 883334

ABSTRACT

A 193nm excimer laser microstepper has been developed for deep UV photolithography research and development and system details are presented. The tool incorporates a x10, 0.5NA, 4mm field diameter, high-resolution imaging lens of either all-refractive or catadioptric design. An all-fused silica refractive lens has been used in the results reported here to carry out exposures in polymethylmethacrylate (PMMA) and polyvinylphenol (MX-P8) photoresists. Well-resolved images of 0.2 μ m dense lines and spaces have been produced in the PMMA and MX-P8 resists.

Keywords: 193nm lithography, silylation, top-surface imaging, photoresists, excimer lasers, line-narrowing.

1. INTRODUCTION

Much interest has recently been focussed on extending existing deep UV photolithography technology to produce sub-0.2 μ m features for future generations of >1Gbit DRAM semiconductor memory devices. Deep UV photolithography with an ArF excimer laser source at a wavelength of 193nm has been identified as a very attractive candidate for a potential process and as a tool capable of achieving these design rules^{1,2}. The emerging manufacturing implementation of 248nm lithography stepper tools serve as a guide for some of the problems that arise in the use of excimer laser exposure systems but many challenges need to be overcome before photolithography at 193nm can be seriously considered as a manufacturing process.

As is well known, the depth of focus (DOF) of optical projection systems is proportional to λ/NA^2 , where λ is the optical wavelength and NA is the numerical aperture of the imaging lens. For 0.2 μ m resolution at 193nm, the DOF falls to <1 μ m and so image enhancement techniques such as the use of phase-shift masks³ or top-surface imaging (TSI)⁴ need to be investigated. Other crucial areas also needing to be assessed and developed at 193nm include high quality fused silica and CaF₂ optical materials, high-NA lenses, lifetime testing of optical components, illumination issues such as beam homogenisation, off-axis imaging and development of suitable photoresists.

In this paper we report results using an Exitech Series 8000 ArF excimer laser microstepper designed for carrying out deep UV photolithography R&D at 193nm. TSI and single-layer imaging work is presented which demonstrates resolutions of <0.2 μ m. Some of the issues mentioned above are also addressed.

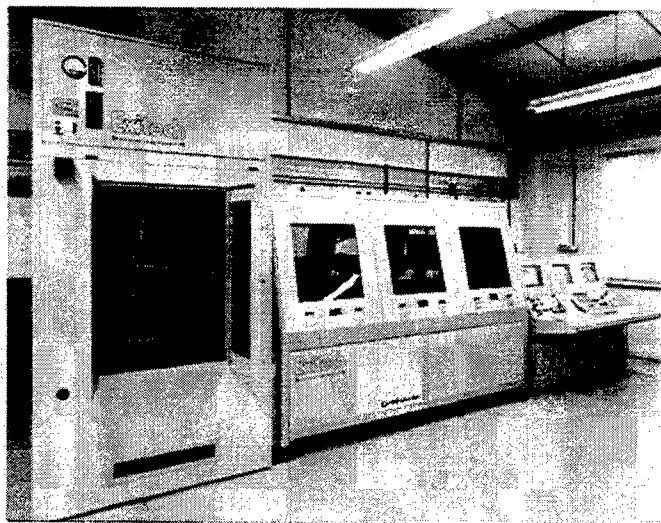


Figure 1. Exitech 193nm excimer laser microstepper system

2. EXPERIMENTAL

2.1 MICROSTEPPER SYSTEM

2.1.1 ArF Laser Source

The Exitech Series 8000 193nm microstepper, shown in Figure 1 and depicted schematically in Figure 2, incorporates a Lambda Physik LPX210i ArF excimer laser as the deep-UV source. When operated at 193nm, this laser produces 32W of average power at its maximum repetition rate of 100Hz within the full 370pm FWHM bandwidth of the ArF transition.

When modified using a specially developed line-narrowing module, the laser produces an average output power of ~0.5W in a minimum linewidth of <5pm FWHM. With this module, the laser may be tuned between wavelengths of 192.75 - 193.75nm and the bandwidth selected between 370-5pm FWHM.

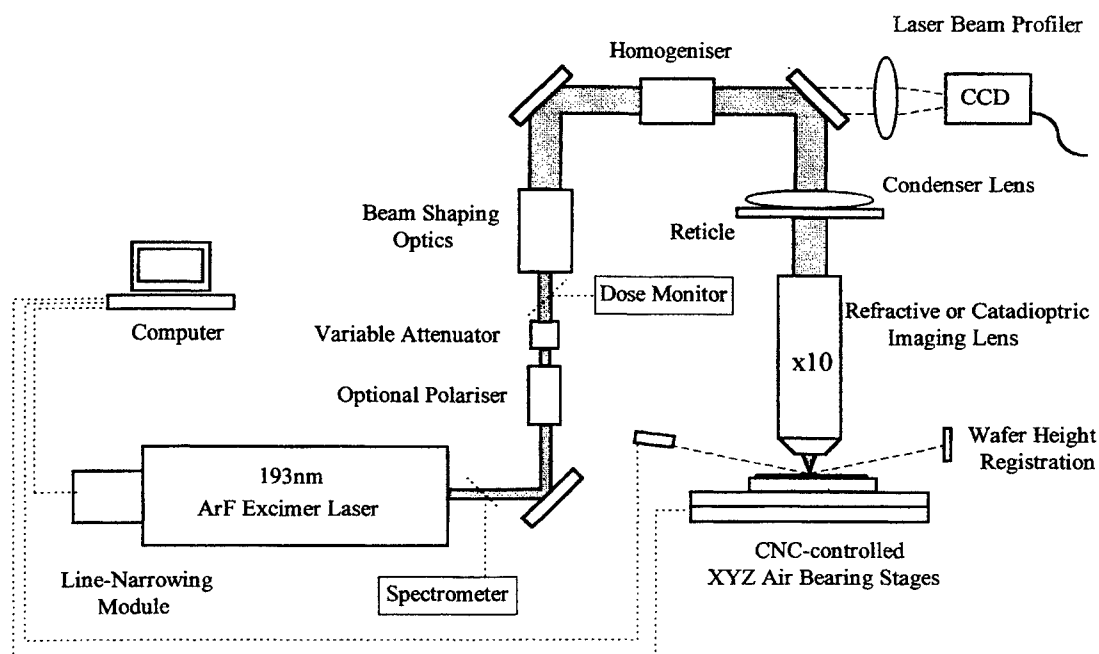


Figure 2 . Schematic diagram of 193 nm excimer laser lithography exposure system

2.1.2 Illumination optics

The beam from the laser is shaped to be 20mm x 20mm at the reticle plane and a double fly's eye homogeniser arrangement is used to produce a reticle illumination uniformity of $<\pm 5\%$ RMS/pulse. The degree of beam shaping and homogenisation depend on the type of lens objective being used. A CNC-controlled variable attenuator in the beam line is used to set the single pulse exposure dose on the wafer. For carrying out exposures with either s- or p-polarized 193nm radiation, a removable polarizer can be inserted into the beam train. All mirrors are coated with high damage threshold dielectric coatings while lenses and other transmissive optics are AR-coated to minimise Fresnel reflection losses. To reduce the absorption by atmospheric oxygen and to prevent the formation of ozone and contamination of the optical train, the entire system from the laser to the condenser lens is purged with dry nitrogen gas. Variable and fixed apertures incorporated in the beam homogeniser unit are used to adjust the partial coherence factor and provide off-axis illumination configurations.

The reticle, imaging lens and wafer stages are all mounted on a common granite block structure to provide precise mechanical stability. To allow comparative studies to be made between exposure work at 193nm and 248nm, the entire microstepper can be readily converted for use at either wavelength.

2.1.3 Imaging optics

The tool is designed to be used with either all-refractive or reflective catadioptric 0.5NA, x 10 193nm imaging lens objectives having image field diameters of 4mm. The lenses were designed using CODE V© and tested interferometrically during fabrication. Chromatic aberration of the ten element all-refractive fused silica lens was eliminated by reducing the bandwidth of the ArF laser to <5pm FWHM. All surfaces were coated with spun-on colloidal silica antireflection coatings and the mirrors of the catadioptric lens were coated with multilayer dielectric coatings having a reflectivity of >95% at 193nm. For this lens, seven fused silica corrective elements were used.

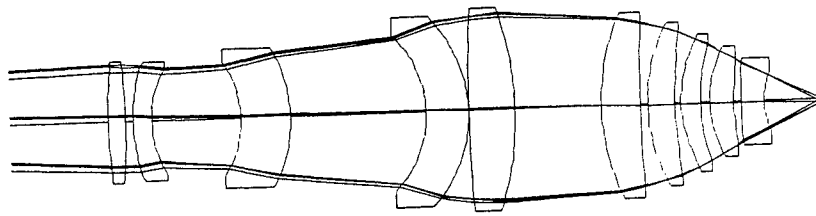


Figure 3. All-refractive, 0.5NA fused silica x 10 imaging lens

2.1.4 Wafer positioning and registration

Precision CNC-controlled air-bearing stages mounted on a granite base are used to provide both short- and long-term lateral stability of the wafer during an exposure. Using capacitive nanosensors, measurements from milliseconds to several minutes have shown that the wafer remains stationary to within $\pm 10\text{nm}$.

Either 6" or 8" wafers can be used with this microstepper system and these are held on a precision vacuum chuck. A CNC-controlled position-sensitive detection (PSD) system is used for focal registration and to provide an autofocus method for automated focal-dose exposure scans. Focal position and wafer surface height are registered and controlled to less than 100nm.

Coarse determination of the focal plane of the lens is made with an accuracy of $\sim 10\mu\text{m}$ using a microscope objective and CCD camera integrated in the wafer chuck. This allows a fluorescent image of the reticle, induced by the 193nm radiation in borosilicate glass wafers, to be brought into focus and the surface of the glass wafer registered with the PSD system.

2.1.5 Beam diagnostics

A CCD camera based Exitech P256NG 193nm laser beam profiling system is incorporated in the microstepper for monitoring the illumination profile at the reticle plane in real time during an exposure.

A high-resolution Exitech Minispec laser spectrometer ($\sim 1\text{pm}$ resolution at 193 and 248nm) is incorporated in the beam line to provide real-time monitoring of the laser wavelength, linewidth and stability. When line-narrowed, the centre wavelength of the laser output is maintained to within $\pm 1\text{pm}$ by a computer-controlled active feedback system developed by Exitech. This ensures stability and reproducibility of the laser spectral output during exposures and nullifies any thermally- or mechanically-induced variations in the laser wavelength. The temporal characteristics and energy of the laser pulses are measured using a silicon PIN photodiode and a joulemeter respectively.

To determine the refractive index and absorptive properties of developmental photoresists, the Series 7000 section of the tool (shown in the centre in Figure 1) can also be used to measure the reflectance of photoresists or thin films at 193nm (or other excimer laser UV wavelengths) as a function of angle of incidence under a computer-controlled environment.

A dose controller system monitors and controls the exposure dose at the wafer and thereby circumvents the fluctuations in the output energy pulse energy of the laser. The dose level can be controlled to better than 0.5% with this system.

2.1.6 System control

Functions such as the laser parameters, exposure dose setting, wafer-positioning and focussing are CNC-controlled from a single console operating under a PC Windows© platform enabling fully automatic exposures to be performed. The autofocus system checks and adjusts the focal position of the resist before each site on a wafer is exposed and conditions

such as dose, focal position, site identification, etc. for each site are stored in the system computer. A wafer map is produced after each exposure detailing the exact parameters of the exposed sites. After each exposure run, illumination beam profiles and the spectral characteristics of the laser can also be archived.

2.2. PHOTORESISTS

Currently there are very few photoresist candidates suitable for carrying out deep UV exposure work at 193nm. In the work reported here, we have concentrated on using two photopolymers - polymethylmethacrylate (PMMA) and polyvinylphenol (MX-P8).

The PMMA resist (Shipley 950PMMA C9) was spun to a thickness of $0.22\mu\text{m}$ onto a $0.3\mu\text{m}$ -thick layer of novolac (Shipley Microposit 2415) which acted as an anti-reflection layer between the substrate and the resist. Chlorobenzene was used as the solvent for the PMMA in a 1:1 mixture and baked for 1 min at 120°C prior to exposure. Post-exposure development was carried out in a 1:1 mixture (by volume) of isopropyl alcohol (IPA) and methylisobutyl ketone (MIBK) for 1 min followed by a standing rinse in IPA for 15 sec.

For top-surface imaging studies at 193nm, the MX-P8 resist (Microlithography Chemical Corp.) was spun to give a thickness of $0.3\mu\text{m}$. The same pre-exposure bake conditions were used as for PMMA. After exposure the resist was silylated in the vapour phase by injecting dimethylsilyldimethylamine (DMSDMA, Microlithography Chemical Corp.) at 15mbar pressure into a temperature-controlled oven at 120°C for 1 min. Reactive-ion etching was then performed using an Oxford Plasma Technology parallel-plate RIE80 system with O_2 gas (60W, 50sccm, 8 min). No skin etch was performed.

3. RESULTS

Results presented here were obtained using the all-refractive, 0.5NA fused silica x 10 imaging lens depicted in Figure 3. The laser was operated at a linewidth of $5\mu\text{m}$ with a typical fluence on the wafer of $\sim 300\mu\text{J}/\text{cm}^2$ per pulse. Since the sensitivity at 193nm of PMMA resist is $\sim 1\text{J}/\text{cm}^2$, operation at a laser repetition rate of 100HZ and these fluences give an exposure duration of around a minute. In contrast, the exposure dose for MX-P8 resist is only several tens of mJ/cm^2 so only a few seconds are required to expose each site. Exact exposure doses are set by CNC-controlling the integrated dose to the nearest integer number of laser pulses.

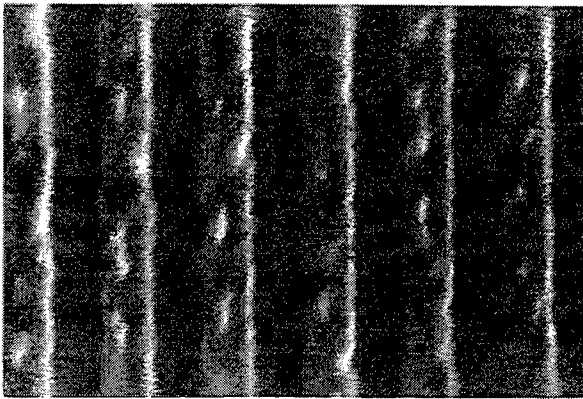


Figure 4. $0.2\mu\text{m}$ lines and spaces in PMMA

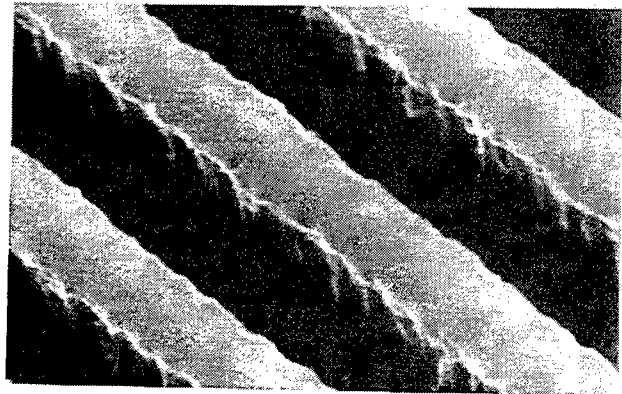


Figure 5. $0.2\mu\text{m}$ lines and spaces in MX-P8 imaged using top -surface imaging

SEM images of well-resolved $0.2\mu\text{m}$ lines and spaces imaged into PMMA photoresist are shown in Figure 4. The $0.2\mu\text{m}$ features were produced uniformly and reproducibly across the field for doses in the range of $1.1 - 1.3\text{J}/\text{cm}^2$ and the partial coherence factor was 0.55 for these exposures. We attribute the slight bubbling of the unexposed surface regions to the wet development process.

Figure 5 shows $0.2\mu\text{m}$ lines and spaces produced in MX-P8 using TSI. The modulations observed in the side-walls of the lines are thought to be due to defects in the reticle and are not optically-induced.

Contact holes were also imaged in MX-P8 resist. The partial coherence factor for the contact hole exposures was set to be 0.4 and focal dose scans were again conducted to determine the optimum conditions. $0.4\mu\text{m}$ and $0.35\mu\text{m}$ contact holes were imaged. $0.3\mu\text{m}$ contact have also been resolved but with lesser clarity. Further work is already underway to optimise the sub- $0.3\mu\text{m}$ imaging of contact holes structure.

Measurements of the process latitude in MX-P8 for lines and spaces ranging from $0.2\mu\text{m}$ to $0.35\mu\text{m}$ are shown in Figures 6 and 7. The exposure dose is plotted against the ratio of the width of the lines to the line/space period for different focal positions. These plots relate to the initial characterisation of the microstepper and were intended to give a broad indication of the overall performance of the exposure system and TSI photoresist. It can be seen that the optimum dose was $\sim 50\text{mJ}/\text{cm}^2$, though it appeared to be more critical than the focal position. This highlights one of the benefits of TSI in that this process is far more tolerant to defocussing since only a small portion of the top layer of the resist needs to be within the depth of focus of the lens for the image to be transferred well into the bulk of the resist⁵. The trend of requiring a higher dose for the imaging of smaller features is also observed.

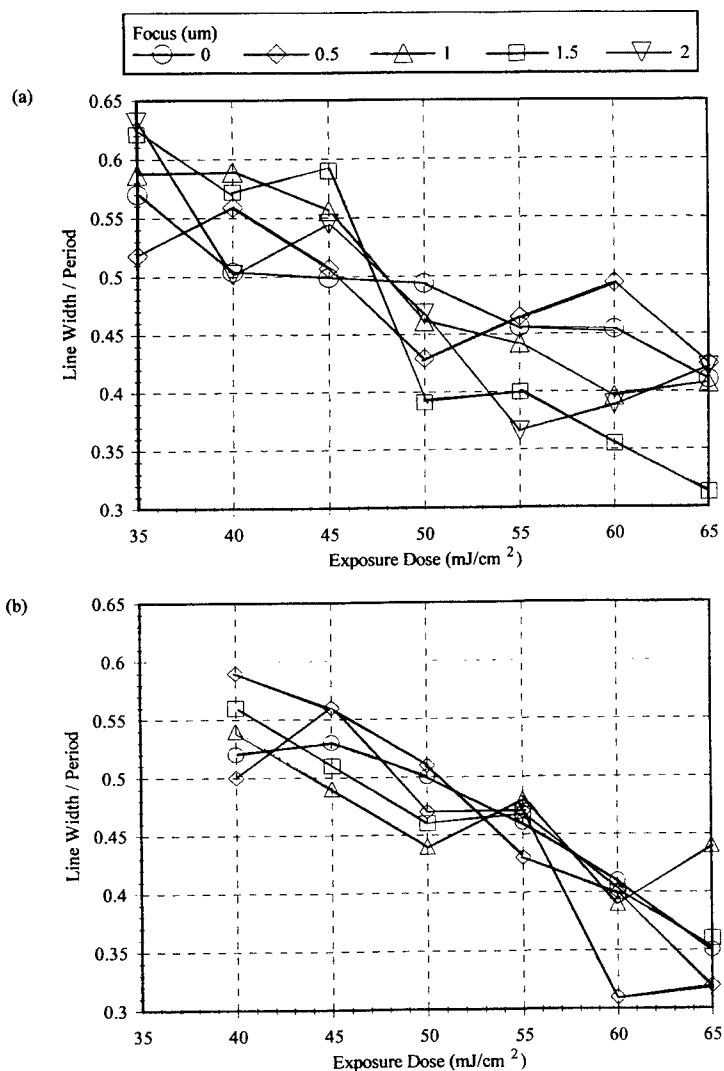


Figure 6 Exposure latitude for (a) $0.2\mu\text{m}$ and (b) $0.25\mu\text{m}$ lines and spaces

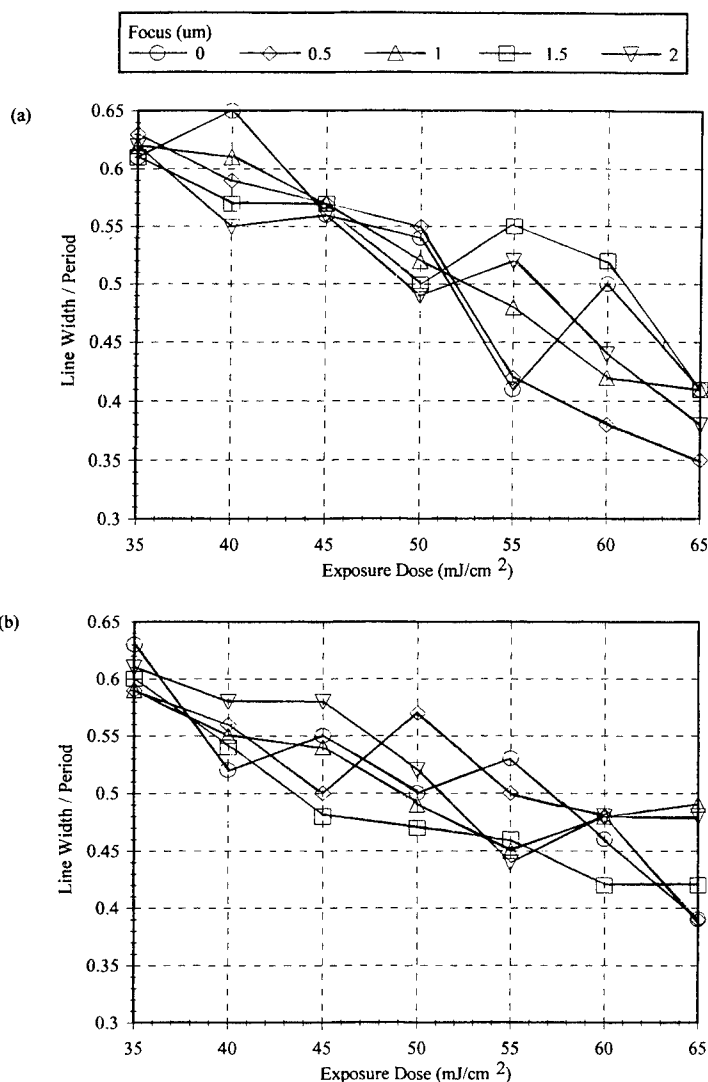


Figure 7 Exposure latitude for (a) 0.3 μm and (b) 0.35 μm lines and spaces

4. CONCLUSIONS

An ArF 193nm excimer laser R & D microstepper has been developed and used to image 0.2 μm lines and spaces in two separate photoresist materials. The overall performance of the system, including the line-narrowed excimer laser, beam diagnostics, wafer stage capabilities and the imaging lens has been characterised. Work is in progress to develop further the laser microstepper in terms of improving feature resolution by using off-axis illumination and suitable phase-shift masks at 193nm. Catadioptric imaging lenses will also be characterised and their performance compared to all-refractive designs. A fuller investigation of top-surface imaging techniques will also be undertaken to assess more fully the limits of the process at 193nm. As part of a continuing lens testing programme towards developing higher NA lenses for use at 193nm, aerial image measurements will be performed in the near future.

5. REFERENCES

1. M.D. Levenson, N.S. Viswanathan, R.A. Simpson, *IEEE Trans. Electron. Devices* 29, 1828 (1982)
2. M.A. Hartney, M. Rothschild, R.R. Kunz, D.J. Ehrlich, D.C. Shaver, *J. Vac. Sci. Tech.* B8 (6), 1476 (1990)
3. S.C. Palmateer, A. Forte, R. Kunz, M.W. Horn, M. Rothschild, *1st Intl. Symposium on 193nm Lithography*, Colorado Springs, Aug. 15-18 1995, Digest Session 4, Paper 9
4. B.W. Smith, A.E. Novembre, D.A. Mixon, *1st Intl. Symposium on 193nm Lithography*, Colorado Springs, Aug 15-18 1995, Digest Session 4, Paper 11
5. D.W. Johnson, M.A. Hartney, *Jpn. J. Appl. Phys.* 31, 4321 (1992)

Deposition of Diamond-like Carbon Films Using XeCl-Excimer Laser

Mau-Kuo Wei, Robert Queitsch, Adolf Lang, Karsten Schutte, Hans Wilhelm Bergmann

Applikations- und Technikzentrum ATZ-EVUS, Rinostraße 1, D-92249 Vilseck

1. ABSTRACT

Diamond-like carbon (DLC) films were deposited using the laser-assisted physical vapour deposition (LPVD) method. This work is dedicated to a XeCl-excimer laser PVD procedure. The influences of the power density, working distance, and substrate temperature on the DLC-deposition will be discussed. The propagation velocity of the laser ignited plasma was determined using short-time photography and time-of-flight (TOF) method.

Keywords: diamond-like carbon (DLC), thin films, PVD, pulsed laser evaporation (PLE), excimer laser, plasma dynamics

2. INTRODUCTION

Diamond and DLC films have recently become one of the most attractive materials due to their superior mechanical, optical, thermal and chemical properties. To produce DLC films, many techniques, such as chemical vapour deposition (CVD)¹, sputtering², ion-beam deposition³ and LPVD⁴⁻⁹, have been developed. Among these various techniques, the LPVD method is perhaps the most interesting due to a high deposition rate and a simple experimental set-up.

In this work, the influence of power density I , working distance d and substrate temperature T_s on the morphology and structure of the DLC-films have been determined. The propagation of the laser ignited plasma has been studied using two different methods: short-time photography and the TOF method.

3. EXPERIMENTAL

The experiments were carried out in a vacuum chamber with a set of a turbo-molecular pumps, as shown in Fig. 1, with the base pressure of this vacuum system set at approximately 1×10^{-5} mbar.

A carbon piece (purity 99.9%) was used as target, while steel, copper and Si (111) were used as substrate material. To obtain a uniform deposition and growth rate, the target and substrate were equipped with rotary transmittances and rotated at room temperature during deposition. For the deposition at higher temperatures a electrical heating was used. In this case the substrate was fixed.

The wavelength, pulse duration and frequency of the XeCl-laser (Siemens XP2020) was set at 308 nm, 55 ns and 8.0 Hz respectively. The laser beam was irradiated on the target at an incident angle of approximately 45° . The power density of the laser beam was varied using an attenuator.

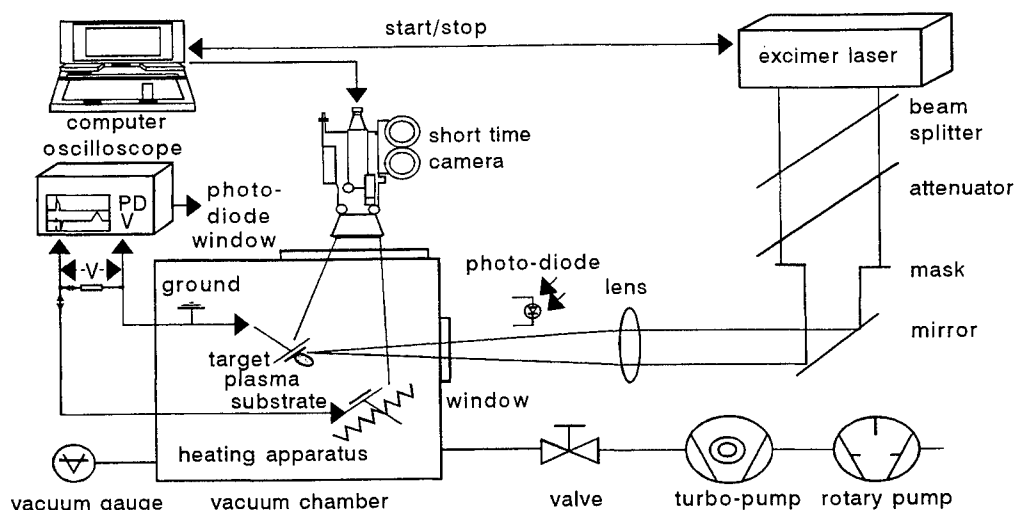


Fig. 1 Experimental set-up.

The velocity of the laser ignited plasma was measured using short time photography and the TOF method. The morphology of the films were then observed using a scanning electron microscope (SEM) (Zeiss DSM940). The refractive index n was measured with an ellipsometer at 632.8 nm. Finally, the Raman-spectrum was collected between 800 cm^{-1} and 2000 cm^{-1} wavenumbers using a 488 nm Ar^+ laser operating at 100 mW with a slit width of 200 μm .

4. RESULTS AND DISCUSSION

4.1 Velocity of the laser ignited plasma

Marquardt et al.⁴ had determined that the DLC films could only be produced at a high laser power density ($> 5 \times 10^{10} \text{ W/cm}^2$). Davanloo et al.⁷ had also pointed out that the internal stresses in the deposited films was found to be higher at lower power densities for target ablation. In addition, the interfacial layer, which is very important to the adherence of the films, was formed directly due to the bombardment of high energy ions on the substrate. Therefore, the kinetics of the laser ignited plasma seems to be very important in the explanation of the DLC-deposition. In the following the velocities of the ions and particles in the laser plume are illustrated.

4.1.1 Short-time Photography

The laser ignited plasma was recorded through a quartz window using a short time camera (PCO DuoCam2), as depicted in Fig. 1, with the delay of the photography determined by the coupling of the camera and the laser. The line scan intensity of the plasma was evaluated along the plasma propagation direction and normalized. If an arbitrary normalized line scan intensity of the plasma can be taken at different delays, the mean front velocity of the plasma propagation can be calculated.

As can be seen in Fig. 2(a), the velocity of the plasma at different laser power densities was constant in the delay range from 100 to 500 ns. In addition, the plasma propagation velocity increased with increasing laser power density, that is, the kinetic energy of the 'particles' in the plasma plume increased. Due to the low propagation velocity, it has been hypothesized that this detected velocity is a result of big carbon clusters or neutral particles.

4.1.2 The TOF method

The TOF measurement was obtained using an oscilloscope and a photodiode. This is the most elementary experimental set-up for the TOF measurement. Here, the photodiode receives the scattering laser light and is used as a zero reference for the delay measurement. As the laser light is obtained at the target, the plasma plume then forms perpendicular to the target and the ejected ions and neutral clusters impinged by the substrate. The target was grounded and the distance between the target and substrate was adjusted by moving the substrate. The electrical voltage between the target and substrate was recorded using an oscilloscope. The features of this method is very simple with the velocity measurement of ions, but the velocities of different ions could not be distinguished.

The measured ion velocities were 28 and 33 km/s at the power densities of 1.0×10^8 and $1.9 \times 10^8 \text{ W/cm}^2$ respectively, and were constant for the studied working distances of 22 to 42 mm between target and substrate, as shown in Fig. 2(b). The ion velocity increased with increasing power density for target ablation. Due to the high propagation velocity, it may be concluded that this detected velocity is due to small carbon ions.

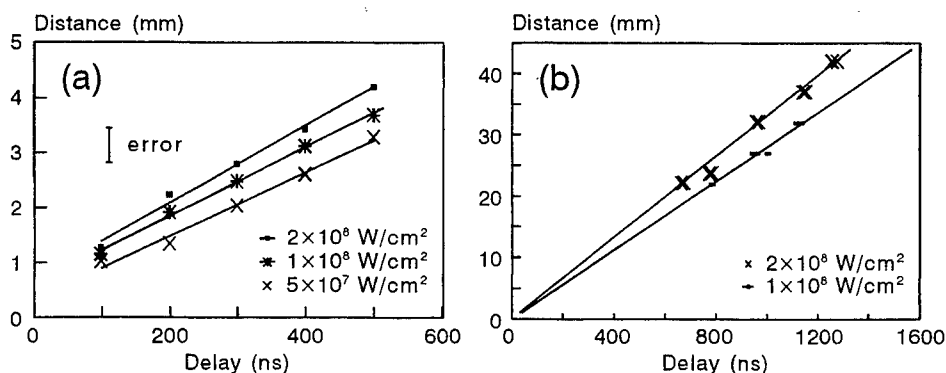


Fig. 2 Propagation velocity of the laser ignited plasma measured with (a) a short time photography, (b) the TOF method as function of the delay.

4.2 Morphology

The typical morphology of the DLC-film is very smooth. There were no significant changes in the morphology of the DLC-film with variations in the laser power density (6×10^7 to 5×10^8 W/cm²) or substrate temperature (RT to 300°C).

Figs. 3(a), 3(b) and 3(c) show the 'droplets' on the DLC-film surface at different laser power densities and working distances. The 'droplets' density on the film surface increased with increasing laser power density and with decreasing working distance.

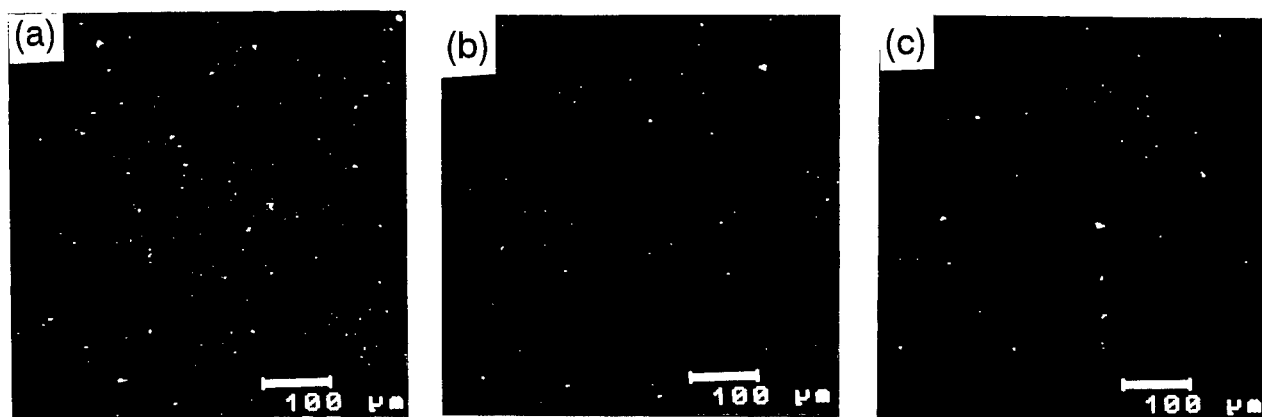


Fig. 3 Morphology of DLC-films deposited at (a) $I = 3.9 \times 10^8$ W/cm², $d = 30$ mm, (b) $I = 3.9 \times 10^8$ W/cm², $d = 40$ mm, (c) $I = 5.3 \times 10^7$ W/cm², $d = 30$ mm.

4.3 Structure

In another work⁸, the films deposited at room temperature with a power density in the studied range was characterized as DLC, which had a Raman band centered at about 1540 cm⁻¹. In addition, the FWHM (full-width-half-maximum) of the Raman band was broadened with decreasing laser power density for target ablation.

As shown in Fig. 4, all films deposited at various temperatures were identified as DLC with a Raman band centered at approximately 1540 cm⁻¹. However, the Raman signal had shifted to a lower wave number and the Raman band had broadened at a higher substrate temperature. This implies that the films had become more graphitic at higher substrate temperatures. The result is similar to those obtained by Sato et al.⁵ and Germain et al.⁶

4.4 Refractive index

The evolution of the refractive index with laser power density and with working distance is shown in Figs. 5(a) and 5 (b) respectively. The refractive index is strongly varied with laser power density. Except at the power density lower than 1×10^8 W/cm², the refractive index decreased with increasing power density. That is, the films deposited at higher laser power densities were more diamond-like. The result was similar to that obtained by Germain et al.⁶

The refractive index was decreased from 2.95 (graphite-like) down to 2.55 (diamond-like) with increasing working distance. This trend was similar to that obtained by Jelinek et al.⁹ As discussed above, the velocities of plasma propagation measured with two different methods were independent of the working distance. But the 'droplets' density decreased with increasing working distance. That is, the refractive index seems to be influenced not only by the plasma kinetics but also by the 'droplets' in the films.

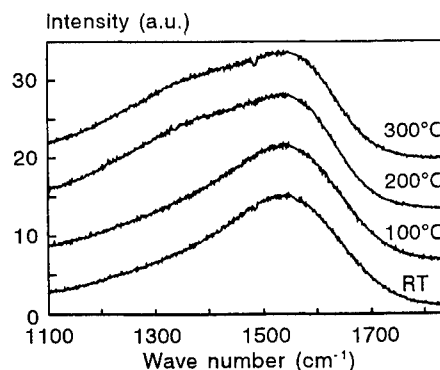


Fig. 4. Raman spectra of the DLC-films on Si at different temperatures ($I = 1.2 \times 10^8$ W/cm², $d = 30$ mm).

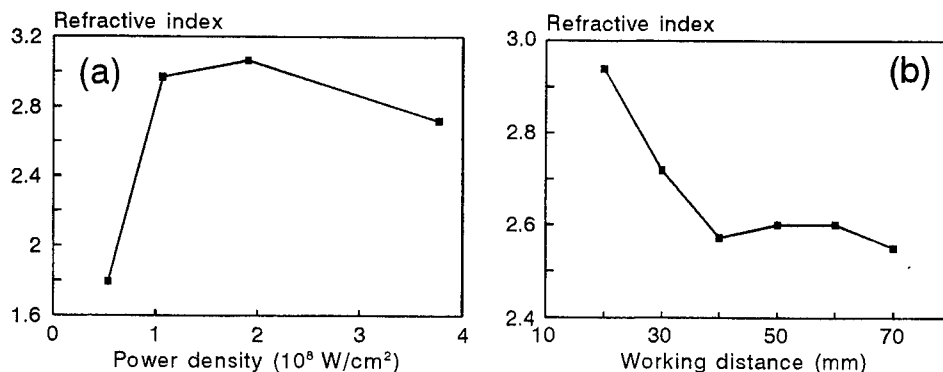


Fig. 5 The refractive index of DLC-films deposited (a) at different laser power densities ($d = 30 \text{ mm}$), (b) at different working distances ($I = 3.9 \times 10^8 \text{ W/cm}^2$).

5. Conclusion

At laser power densities between $6 \times 10^7 \text{ W/cm}^2$ to $5 \times 10^8 \text{ W/cm}^2$, DLC-films were deposited between room temperature and 300°C using a XeCl excimer laser. The films have a wider FWHM of Raman band if they were deposited either at lower power densities or at higher substrate temperatures ($\geq 200^\circ\text{C}$). The propagation velocity of small ions in the laser ignited plasma was determined to be about 30 km/s , while is lower for big carbon clusters (7 km/s). The refractive index was approached to diamond-like if the films deposited at higher laser power densities or at longer working distances.

6. Acknowledgements

This work was supported by the Bavarian Research Foundation (BFS) within the framework of the Bavarian Research Cooperation FOROB. The authors wish to thank M. Schreck (Department IV, Institute for Physics, University Augsburg) for the measurement of the Raman-spectra, and T. Sluneko and M. Hartmann (Department II, Institute for Materials Science, University Erlangen-Nürnberg) for the preparation of Si specimens cut with copper vapour lasers (CVLs). Thanks extend as well to G. Hinz (Institute for Experimental Physics, University Erlangen-Nürnberg) for his help in the evaluation of the line scan of the plasma propagation.

7. References

1. H. Vora and T. J. Moravec, "Structural investigation of thin films of diamondlike carbon", *J. Appl. Phys.* **52** (10), 6151-6157 (1981)
2. A. Hiraki, T. Kawano, Y. Kawakami, M. Hayashi and T. Miyasato, "Tetrahedral carbon film by hydrogen gas reactive rf-sputtering of graphite onto low temperature substrate", *Solid State Commun.* **50**, 713-716 (1984)
3. S. Aisenberg and R. Chabot, "Ion-beam deposition of thin films of diamondlike carbon", *J. Appl. Phys.* **42**, 2953-2958 (1971)
4. C. L. Marquardt, R. T. Williams and D. J. Nagel, "Deposition of amorphous carbon films from laser-produced plasmas", *Mat. Res. Soc. Symp. Proc.* **38**, 325-335 (1985)
5. T. Sato, S. Furuno, S. Iguchi and M. Hanabusa, "Deposition of diamond-like carbon films by pulsed-laser evaporation", *Jpn. J. Appl. Phys.* **26** (9), L1487-L1488 (1987)
6. C. Germain, C. Girault, R. Gisbert, J. Aubreton and A. Catherinot, "Laser ablation of graphite targets", *Appl. Surf. Sci.* **69**, 359-364 (1993); "KrF laser photo-ablation of a graphite target: application to the development of thin films", *Diamond Relat. Mater.* **3**, 598-601 (1994)
7. F. Davanloo, T. J. Lee, D. R. Jander, J. H. You, H. Park and C. B. Collins, "Mechanical and adhesion properties of amorphous diamond films", *Thin Solid Films* **212**, 216-219 (1992)
8. M.-K. Wei, R. Queitsch, A. Lang, K. Schutte, H. W. Bergmann and F. Qian, "Diamondlike carbon films deposited with excimer laser and their mechanical properties", Stuttgart, *ECLAT'96*, 16-18 Sept. 1996, in press
9. M. Jelinek, V. Olšan, L. Soukup, D. Charalabidis, E. Hontzopoulos and E. Georgiou, "Some properties of carbon films deposited by laser ablation", *Diamond Relat. Mater.* **3**, 1128-1131 (1994)

PICOSECOND IMAGING OF LASER-INDUCED ABLATION PROCESSES AND PRODUCTION OF MICROSTRUCTURES BY PICOSECOND LASER PULSES

J.Jandeleit¹, P.Rußbüldt¹, G.Urbasch¹, D.Hoffmann¹, H.-G.Treusch² and E.W.Kreutz¹

¹ Lehrstuhl für Lasertechnik, RWTH Aachen, Steinbachstraße 15, D-52074 Aachen,

² Fraunhofer-Institut für Lasertechnik, Steinbachstraße 15, D-52074 Aachen,
Federal Republic of Germany

ABSTRACT

Picosecond laser pulses were used for microstructuring metals, ceramics and diamond. Using 40 ps laser pulses line patterns with a minimum line width in the range of 7 μm were formed in diamond without destroying the crystallinity. In Si_3N_4 -ceramics holes were drilled with diameters smaller than 6 μm . Ultrathin copper and gold films of 1 μm thickness were removed from fused silica and silicon (100) without influencing the substrates. The ablation process was investigated by high-speed photography and pump & probe - measurements with a time resolution of 40 picoseconds. The measurements allow a detailed characterization of the melting, vaporization and solidification processes. Shock waves in the ambient atmosphere were detected and the energy in the shock wave was determined.

Keywords: microstructures, picosecond laser pulses, shock waves, ceramics, diamond, metals

1. INTRODUCTION

Pulsed Nd:YAG-laser radiation is a powerful tool for production of three dimensional microstructures, when it is used in combination with high-resolution optics and precision motion control systems. Different materials like metals, ceramics and diamond can be microstructured by laser radiation.^{1,2,3} Decreasing film thicknesses and sizes of microstructures show the limit of conventional nano- and microsecond laser pulses because the geometry of the heat-affected zones are of the same order of magnitude as the microstructures themselves. Picosecond laser pulses with a much lower heat load than nano- and microsecond laser pulses may produce heat-affected zones with geometries in the range of 100 - 200 nm. Therefore, they might be a promising tool for production of holes and grooves with dimensions smaller than 10 μm and for ultraprecise removal of thin layers.^{4,5}

Compared to nano- and microsecond laser pulses picosecond laser pulses change the physical conditions during material processing in different ways. Because of the short pulse length higher power densities can be reached and rapid heating can possibly lead to an earlier evaporation of the material and to a reduction of the thickness of the melt which resolidifies after the end of the laser pulse at the edges of the ablated area. For ultrashort laser pulses in the picosecond- and femtosecond-regime the deposition of optical energy in the material cannot be assumed to be instantaneous, as for nano- and microsecond laser pulses. The finite time needed to convert optical energy absorbed by the electrons of the material to internal energy of the lattice must be considered. Therefore, ultrafast laser heating of metals must be described by three processes: the deposition of optical energy in the electron-gas, the transport of energy by electrons and the heating of the lattice through electron-phonon interactions.^{6,7}

In the present work the production of microstructures in different materials by picosecond laser radiation is presented. Pump & probe - measurements are described which allow a detailed characterization of the ablation process including the feedback of the surrounding atmosphere to the processed microstructures.

2. EXPERIMENTAL

Picosecond laser pulses were generated by a diode-pumped modelocked Nd:YAG laser producing pulses with a length of 40 ps. The low energy pulses of the modelocked Nd:YAG laser were amplified by a diode-pumped regenerative amplifier leading to a maximum pulse energy of 200 μJ at the sample surface.⁸ The repetition rate of the amplified pulses was 750 Hz. The pulse length was measured with an autocorrelator. A single 40 ps pulse was separated from the pulsetrain by a Pockels cell, expanded and finally focused onto the sample surface by ULWD- (ultra large working distance) microscope objectives. The Pockels cell also suppressed pre- and post-pulses. For the second harmonic generation of the laser radiation ($\lambda = 532\text{nm}$)

an external KTP-crystal was used. The power density distribution of the laser radiation was monitored by a CCD-camera. A Gaussian distribution was detected. Depending on the different microscope objectives and the wavelength of the laser radiation a $1/e^2$ -focus radius of 3 - 18 μm was measured by the wedge method. The samples were mounted on an XYZ-stage allowing to expose each pulse to a virgin surface. All used samples had polished surfaces of optical finish. The integration of the focussing optic in an optical microscope permits the direct observation of the processed area. Optical and scanning electron microscopy (SEM) were used to characterize the processed microstructures.

In the pump & probe - measurements the interaction zone of the laser radiation and the sample surface is temporally and spatially resolved detected by photography using a CCD-camera. The fundamental wavelength of the Nd:YAG laser radiation is used for the material ablation while the second harmonic radiation serves as a flash lamp for the illumination of the interaction zone. The laser pulse length of the illumination pulse leads to a time resolution of 35 ps. A spatial resolution of 1 μm was achieved caused by the used microscope objectives. The first 20 nanoseconds of the ablation process in air at an ambient gas pressure of 1 bar were investigated. The delay Δt between the ablation and the illumination pulse was achieved by shifting the illumination pulse temporally against the ablation pulse.

3. MICROSTRUCTURES

3.1 Diamond

Using the second harmonic radiation of the Nd:YAG laser microstructures were produced in diamond. Line patterns with a line width b in the range of 7 μm were formed by moving the specimen under the focused laser beam (Fig. 1). The depth of the grooves were measured to be 15 μm . The grooves show sharp edges and no debris in the surrounding area. The crystalline quality of the diamond was checked by micro-Raman-spectroscopy before and after micromachining. In both cases a sharp peak at a relative wave number of 1334 cm^{-1} , corresponding to crystalline diamond, was detected.⁹ Hence, microstructuring by 35 ps laser pulses did not influence the crystallinity of diamond.

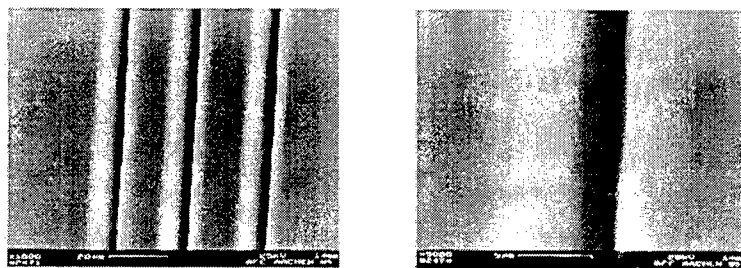


Fig. 1: SEM images of grooves in diamond, $\lambda = 527\text{ nm}$, $t_p = 35\text{ ps}$, $I = 4.6 \cdot 10^{11}\text{ W/cm}^2$, $f_p = 1\text{ kHz}$, $v = 0.25\text{ mm/s}$, $b = 7\text{ }\mu\text{m}$, magnification: left side: 1000x, right side: 5000x.

3.2 Ceramics

Using the fundamental wavelength of the Nd:YAG laser holes and grooves were produced in Si_3N_4 -ceramics. A minimal hole diameter of 5.5 μm was achieved and a groove with a width of 18 μm could be formed (Fig. 2). The structures are marked by sharp edges and steep walls. The recondensated particles in the surrounding area of the holes and grooves could, if necessary, easily removed by chemical or mechanical means.

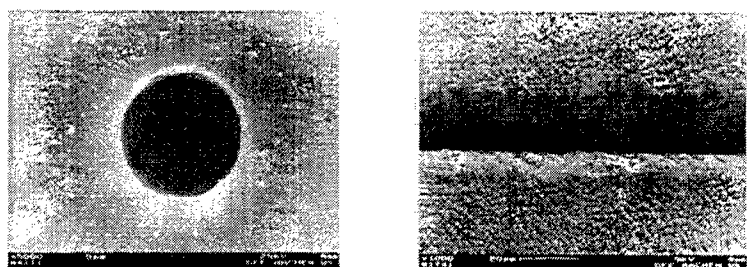


Fig. 2: SEM images of a hole and a groove in Si_3N_4 -ceramics, $t_p = 40\text{ ps}$, $\lambda = 1053\text{ nm}$, left side: $I = 2.6 \cdot 10^{11}\text{ W/cm}^2$, $d_m = 5.5\text{ }\mu\text{m}$, 10^3 pulses, right side: $I = 2.4 \cdot 10^{12}\text{ W/cm}^2$, $b = 18\text{ }\mu\text{m}$, $v = 0.25\text{ mm/s}$.

3.3 Metals

Thin gold and copper films (thickness < 1000 nm) on fused silica and crystalline silicon substrates can be removed precisely by 40 ps laser pulses. In accordance to the Gaussian power density distribution the holes show a circular geometry. At low power densities no redeposition of ablated material in the surrounding area of the laser drilled holes can be detected. The walls of the holes are covered by thin molten films with



Fig. 3: SEM images of holes in 1000 nm Au-films, $t_p = 40\text{ ps}$, $\lambda = 1064\text{ nm}$, $I = 9.8 \cdot 10^{10}\text{ W/cm}^2$, $d_m = 6.4\text{ }\mu\text{m}$, 1 pulse, left side: fused silica substrate, right side: Si(100)-substrate.

thicknesses in the range of 75 - 200 nm. These resolidified films indicate the existence of a sharp boundary between molten and non-molten material by picosecond laser processing of metals. Independent of the used substrate, holes drilled in 1000 nm thick gold films show for the same laser beam parameters the same processing results (Fig. 3). In the case of the silicon substrate micro-Raman-spectroscopy was used to check the crystalline quality of the substrate after the removal of the complete gold film. No changes in the crystallinity of the substrate could be detected at the ground of the holes. Therefore, thin metal films can be removed by 40 ps laser pulses without influencing the substrate.

4. PUMP & PROBE - MEASUREMENTS

Pump & probe - measurements offer the possibility of a detailed characterization of the ablation process. The investigations give information about the temporal onset of material ablation, the formation of the hole, changes in surface morphology and the feedback of the surrounding atmosphere to the processed microstructures. Two different illumination geometries were used. The first illumination geometry leads to the detection of reflexion changes of the sample surface while the second geometry leads to a detection of the transmission changes of the atmosphere in front of the sample. Figure 4 shows two images taken by the different illumination geometries at a delay of 600 ps after the ablation pulse has hit the sample surface. Different regions and discontinuities could be detected: I. a plasma region, II. a shock front, III. a ionization front. The plasma is marked by a high absorption of the illumination pulse in the region of the laser beam focus. The diameter of the plasma region increases with increasing pulse energy. A shock wave is build up in the ambient atmosphere. The shock front becomes visible through the step-like change of the refraction index distribution caused by the compressed air. The ionization front closely follows the shock front. This front represents an outer boundary to the plasma emission. Behind the ionization front the gas temperature increases rapidly, that ionization can occur.

The propagation of the shock wave can be analyzed by the Sedov theory¹⁰ describing the temporal and spatial propagation of a shock wave originating from a point source. If the propagation behaviour of the shock front is known, the Sedov theory can be used to determine the energy E in the shock wave. In the case of a spherical propagation the position of the shock front r can be calculated from

$$r = \lambda_0 * \left(\frac{E}{\rho} \right)^{0.2} * t^{0.4}, \quad (1)$$

with the density of the ambient atmosphere ρ , a dimensionless factor λ_0 and the time t . For 35 ps pulses ($\lambda = 1064$ nm) a energy of 10 - 20 % of the available laser pulse energy is detected in the shock front (Fig. 5). This result is in contrast to nanosecond-experiments where up to 80 % of the available laser pulse energy is deposited in the shock wave.¹¹

Pump & probe images taken by temporally overlapping illumination and ablation pulses show an increased absorption in the focal area of the ablation pulse. Therefore, material ablation starts for 40 ps laser pulses within the pulse length. This result was found for gold, copper and crystalline silicon even for the lowest used laser pulse energy of $E_0 = 4.1 \mu\text{J}$.

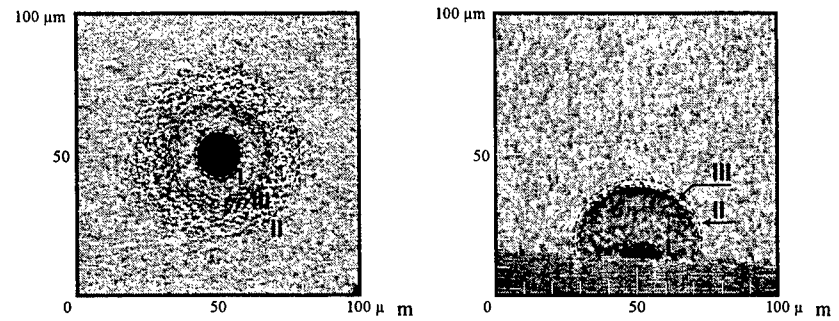


Fig. 4: Pump & probe measurements, copper, $\lambda = 1064$ nm, $t_p = 40$ ps, left side: reflexion measurement, right side: transmission measurement, $\Delta t = 600$ ps, I: plasma, II: shock front, III: ionization front.

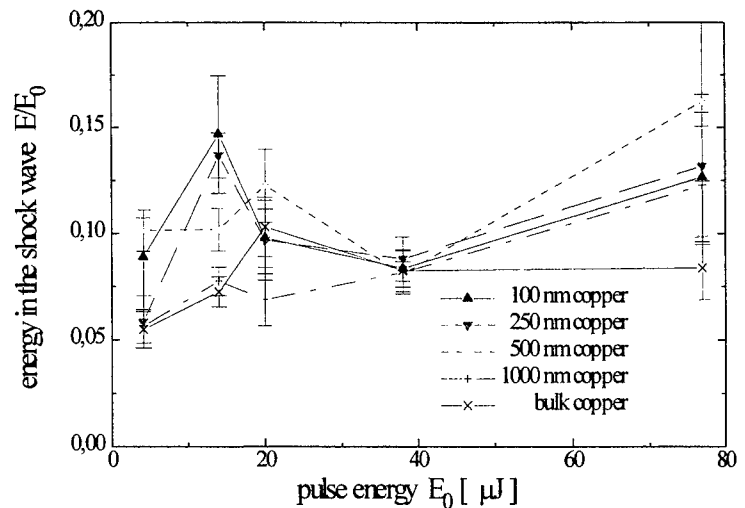


Fig. 5: Energy in the shock wave in air as a function of laser pulse energy for copper, $\lambda = 1064$ nm, $t_p = 40$ ps.

5. SUMMARY

Using 40 ps laser pulses line patterns with a minimum line width in the range of 7 μm were formed in diamond without destroying the crystallinity. In Si_3N_4 -ceramics holes were drilled with diameters smaller than 6 μm . Ultrathin copper and gold films of 1 μm thickness were removed from fused silica and silicon (100) without influencing the substrates.

The ablation process of different materials was temporally and spatially investigated by pump & probe - measurements. Different regions and discontinuities were detected: a plasma region, a shock front and a ionization front. The energy in the shock wave was calculated by using the measured propagation of the shock front according to the Sedov theory. For 40 ps laser pulses 10 - 20 % of the available laser pulse energy is deposited in the shock wave. The pump & probe - measurements also show, that the ablation process induced by 40 ps laser pulses always starts within the pulse length.

6. ACKNOWLEDGMENTS

The authors would like to acknowledge financial support by the BMBF within the framework PROBE, 13N6157. We are grateful to our colleague Dipl.-Phys. T. Klotzbücher for stimulating discussions and for his technical assistance in performance of the micro-Raman-spectroscopy.

7. REFERENCES

1. J. Jandeleit, G. Urbasch, H.D. Hoffmann, H.-G. Treusch, E.W. Kreutz, "Energiedissipation bei der Wechselwirkung ultrakurzer Laserimpulse mit Festkörpern," Proc. ECLAT 96, in press
2. B. Lässig, "Kontrollierter Formabtrag durch Sublimation mittels Laserstrahlung", dissertation RWTH Aachen, Verlag Shaker, 1995.
3. H.-G. Treusch, G. Herziger, "Metal precision drilling with lasers," SPIE Proc., Vol. 650, pp. 220-225, 1986.
4. J. Jandeleit, G. Urbasch, H.D. Hoffmann, H.-G. Treusch, E.W. Kreutz, "Mikrostrukturierung von Metallen und Halbleitern durch ultrakurze Pulse," Proc. Laser 95, Springer Berlin, Heidelberg, in press.
5. J. Jandeleit, G. Urbasch, H.D. Hoffmann, H.-G. Treusch, E.W. Kreutz, "Picosecond laser ablation of thin copper films," Appl. Phys., Vol. A63, pp. 117-121, 1996.
6. H. Kurz, L. A. Lompré, J. M. Liu, "Fundamentals of pulsed laser radiation of silicon," J. de Phys, Vol. C5, pp. 23-36, 1983.
7. H. Kurz, "Fundamentals of picosecond and femtosecond laser solid interactions," Mat. Res. Soc. Symp. Proc., Vol. 74, pp. 3-13, 1987.
8. H.D. Hoffmann, H.-G. Treusch, E.W. Kreutz, "Diodengepumpter, regenerativer Verstärker," Proc. Laser 95, Springer Berlin, Heidelberg, in press.
9. Ed. VDI-TZ Physikalische Technologien, "Präzise optische Bearbeitung von Festkörpern," VDI Verlag, 1996.
10. Y.B. Zel'dovich, Y.P. Raizer, "Physics of Shock Waves and High-Temperature Hydrodynamic Phenomena", Academic Press, New York, 1967.
11. G. Callies, P. Berger, H. Hügel, "Time-resolved observation of gas-dynamic discontinuities arising during excimer laser ablation and their interpretation," J. Phys. D: Appl. Phys., Vol. 28, pp. 794-806, 1995.

Recent developments in industrial excimer laser technology

Uwe Stamm, Rainer Pätzel, Igor Bragin, Jürgen Kleinschmidt, Frank Voß, Dirk Basting

Lambda Physik, GmbH
Hans-Böckler-Strasse 12, D-37079 Göttingen, Germany

ABSTRACT

The paper reviews recent developments in high power excimer laser technology driven by industrial requirements. Technological achievements as NovaTube™ laser tube technology and HaloSafe™ halogen generator technology are discussed. Experimental results are presented for various lasers at the most important excimer wavelengths 351nm (XeF), 308nm (XeCl), 248nm (KrF), 193nm (ArF) and 157nm (F₂) which have been designed for application in micromachining, thin-film-transistor annealing, marking as well as lithography.

Keywords: excimer laser, annealing, lithography, micromachining, marking.

1. INTRODUCTION

As powerful sources of deep ultraviolet light, excimer lasers are demonstrating unique efficiency in a variety of industrial and medical applications. Typically however, the process window for the laser beam parameters as power, pulse energy, stability, repetition rate and bandwidth depend on the particular application. For micromachining and TFT annealing for example high average power XeCl or KrF lasers with very homogeneous spatial beam profile are needed. In addition, because of the strong nonlinearity of the annealing process pulse energy, stability must be as good as possible. Marking applications at all wavelengths need either high pulse energy or high repetition rate to achieve the required throughput. In DUV lithography the development of new step-and-scan tools currently needs narrow band laser sources with kHz repetition rate at 248nm. Going below the 0.18μm design rule within the next years 193nm lasers are necessary and 157nm lasers are already entering the discussion. Of major general importance for all the industrial applications are long gas lifetime, extended maintenance cycles and finally low cost of operation.

The paper reviews recent developments in high power excimer laser technology driven by industrial requirements from micromachining, marking and lithography. General technological achievements are presented as well as results for the most important excimer gases XeF (351nm), XeCl (308nm), KrF (248nm), ArF (193nm) and F₂ (157nm).

2. NOVATUBE™ TECHNOLOGY AND HALOGEN GENERATORS

As general technological achievements there have been two major revolutionary developments during the last years. The first is NovaTube™ - a metal-ceramic excimer laser technology with optimized electrode and preionization materials. The second is the halogen generator - a device which enables the operation of excimer lasers without external gas installations for fluorine or chlorine gases.

The metal-ceramic excimer laser tube technology NovaTube™ is the key to achieve long gas and laser tube lifetimes at UV wavelengths especially for fluorine based excimers. The tube consists of optimized alloys and high density ceramics. Special chemical treatments have been developed to provide perfect surface passivation. Both electrode and pre-ionization materials are selected for minimum erosion. Electro-static dust precipitators in the gas circulation channel clean the gas from still remaining eroded materials. The result is a gas lifetime which is for fluorine based excimers approximately one order of magnitude longer than for the conventional predecessor of NovaTube™. Fig. 1 gives an example comparing the dynamic gas lifetimes of both technologies for an ArF laser and a F₂ laser. While for an ArF laser in the conventional laser tube design the gas lifetime is about 2 million shots, in the NovaTube™ design gas lifetime exceeds 20 million pulses. Even better is the improvement at the short 157nm F₂ laser: the gas lifetime increases more than 20-fold.

Because of the drastically reduced erosion the laser tube lifetime itself could be increased significantly. Laser tube lifetimes up to 4 billion pulses (KrF) and up to 10 billion pulses (XeCl) could be reached recently. Both the increased gas lifetime as well as the substantially longer tube lifetimes lead to the reduction of operational costs by half an order of magnitude in an industrial environment bringing production costs significantly down.

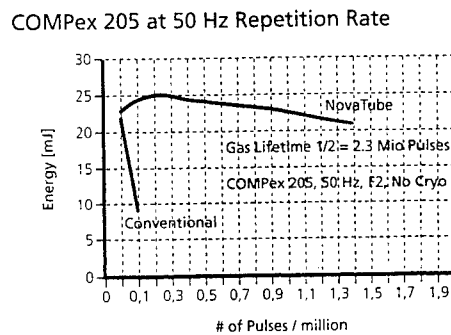
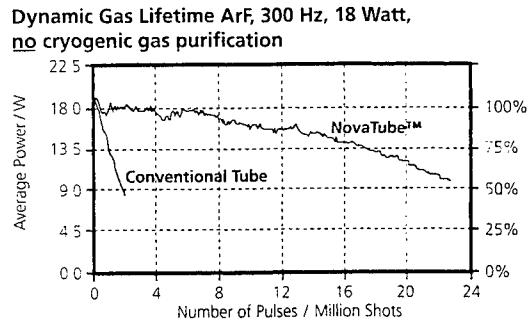


Fig. 1 : Comparison of the dynamic gas lifetime for ArF (upper) and F₂ (lower)

One of the drawbacks of excimer lasers in an industrial or medical environment is the need of external and often very expensive gas installations for the halogen gases fluorine and chlorine. Therefore the development of Halosafe™ halogen generators both for fluorine and chlorine which can be integrated directly into the laser is another important step to reduce cost and to improve safety. The principle of the halogen generator is shown for the example of a fluorine generator in Fig. 2. A closed can contains a solid non-hazardous fluorine compound. The container is normally at room temperature. To activate the fluorine generation the container is heated to a given temperature. Fluorine is released from the solid compound into gas phase. A valve is opened and the fluorine is filled into an accumulator. Switching off the heater of the first container stops the fluorine generation. To fill the laser tube with the necessary fluorine is diluted with buffer gas in a ratio of approximately 1:20. This mixture is then used to fill the laser chamber. The capacity of current halogen generators allows approximately 100 fills of the laser tube. Empty generators are exchanged in the field by new ones and are rechargeable in the factory. In addition to major cost savings one of the advantages of halogen generators is the equally high quality of the gas. The purity of the halogen gases from the HaloSafe™ fluorine generator is 99.98% in comparison to 99.60% from high quality gas bottles.

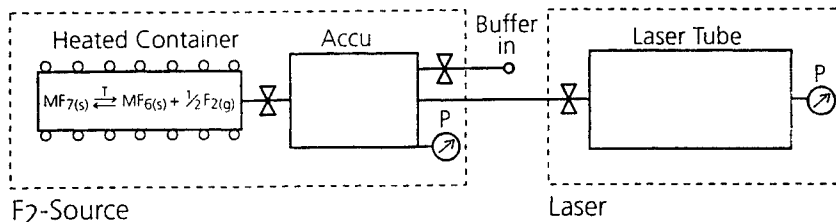


Fig. 2 : Schematic of the HaloSafe™ Fluorine generator

3. HIGH POWER EXCIMER LASERS FOR MICROMACHINING, ANNEALING AND MARKING

Several types of high power lasers for industrial use have been developed during the last years which feature high stability and long gas lifetime.

3.1 Industrial XeCl lasers

The industrial XeCl Laser LAMBDA 4308 has been especially developed for micromachining and TFT annealing applications. The laser features high average power (of up to 270W) and high pulse-to-pulse energy stability. Fig. 3a gives an example of the dependence of average output power on the repetition rate of the laser. Fig. 3b shows the stabilized average power at 200W over more than 50 million pulses gas lifetime. The high voltage in the diagram is for demonstration of the stabilization algorithm: an increase in high voltage compensates for the decrease in output power due to chlorine depletion. Jumps in the high voltage to lower values occur when a small amount of chlorine is injected into the laser tube. Recently due to improvement of gas circulation and discharge optimization the pulse to pulse stability of the output could be improved from 3% down to 2% (standard deviation). Peak to peak energy stability amounts today $\pm 7\%$. This is of special importance for TFT annealing applications since the energy stability of the laser directly translates into quality of the TFT displays.

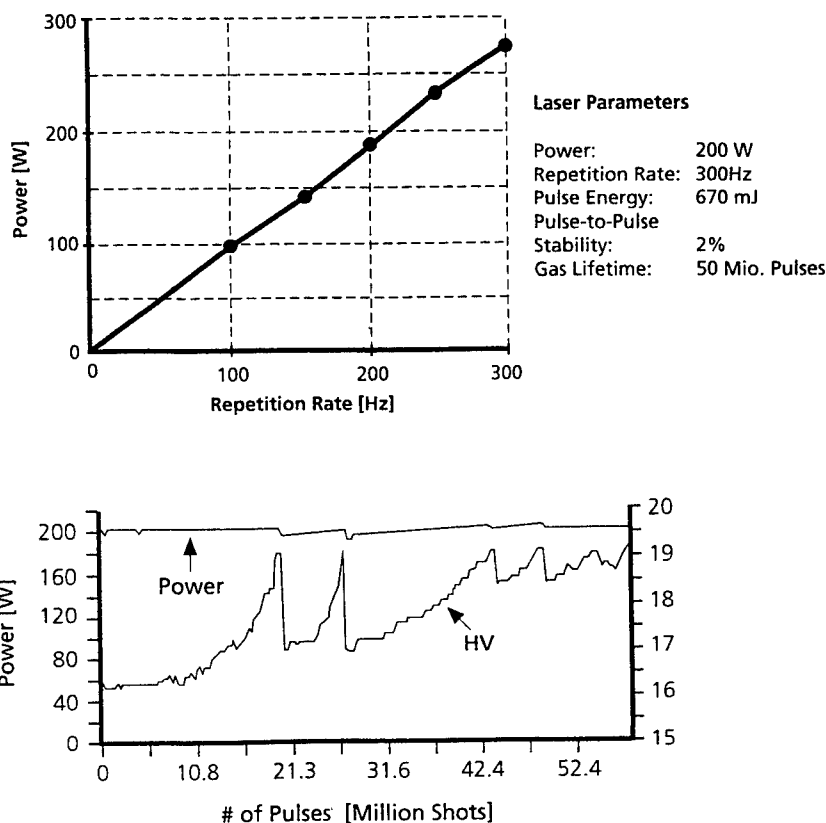


Fig. 3: a) Output power versus repetition rate for the industrial XeCl laser LAMBDA 4308
b) Stabilized output power and high voltage over more than 50 Million pulses.

3.2 Industrial XeF lasers

The industrial XeF laser LAMBDA 4351 has been developed in 1996 for marking, micromachining and annealing applications. While currently maximum average powers of about 100W have been achieved (see Fig. 4a) which is significantly less than available from XeCl lasers, the XeF laser has other advantages. First the spatial beam profile is more homogeneous than typically achievable for XeCl. Second the pulse energy stability is naturally better than with XeCl (see Fig. 4b). Pulse to pulse energy stability of about 1% (standard deviation) and peak to peak energy stability of better than $\pm 4\%$ are expected for the near future. While the gas lifetime of high power XeF laser is comparable to that of high power XeCl lasers window contamination plays only a minor role in XeF. Window cleaning intervals of more than 300 million pulses are realistic today.

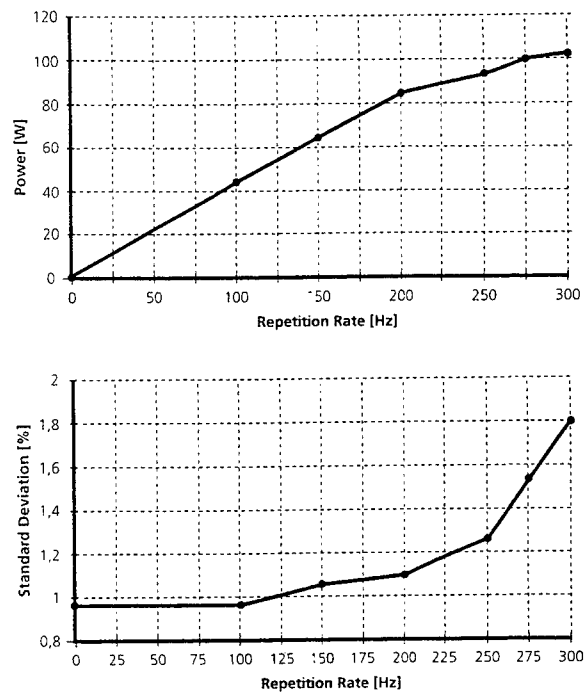


Fig. 4: a) Output power versus repetition rate for the industrial XeF LAMBDA 4351.
b) Pulse energy stability in dependence on repetition rate

3.3 High power KrF and ArF lasers

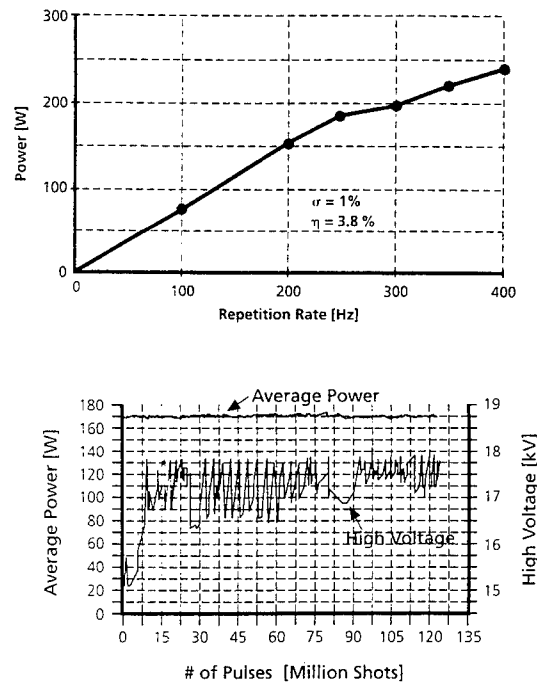


Fig. 5: a) Output power versus repetition rate for the industrial KrF laser NovaLine 100.
b) Stabilized output power and high voltage over 120 million pulse on a single fill

Currently under development is a new generation of high power KrF lasers for industrial use - the laser NovaLine™ 100 which is going to be released in October 1996. This high efficient laser (efficiency of 3.8%) has been developed for

micromachining applications with special emphasis onto stability and homogenous beam profile. Pulse to pulse energy stability of better than 1% (standard deviation) is achieved. Fig. 5a shows the dependence of output power on repetition rate. Fig. 5b gives a plot of the output power stabilized onto 170W versus number of pulses for a single gas fill. Again the high voltage during the run is shown for comparison. Gas lifetimes of more than 100 million pulses have been achieved.

The throughput in a production line is (as long as there is no process inherent limitation) directly proportional to the available average power. Therefore currently first investigations are made for the development of high power KrF lasers for industrial use in year 2000. Fig. 6 gives an example of the output power curve which has been recently achieved from an experimental KrF discharge module. This module is considered to be the basis for an industrial KrF laser with 300W stabilised output power. Major physical and technical issues still remain to be solved to achieve the required stability and gas lifetime of the laser.

Several materials require 193nm radiation for micromachining since at longer wavelength either the absorption is too low (several glasses) or other effects (thermal load) limit the micromachining quality. Recently we have demonstrated a 140W output from a 193nm laser (see Fig. 7). This laser is going to be developed into an industrial tool with above 100W stabilized average power for flexible machining of optical materials.

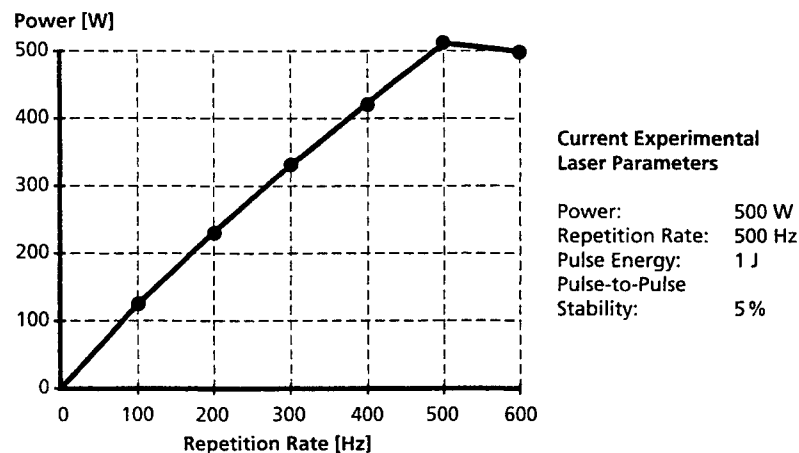


Fig. 6 Output power versus repetition rate for an experimental high power KrF discharge module

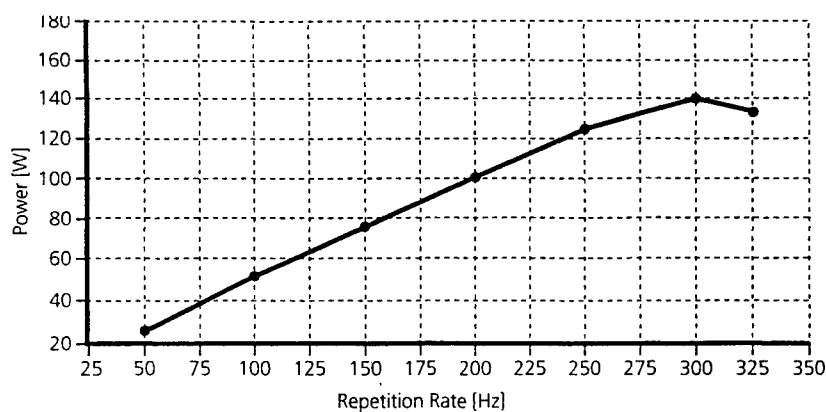


Fig. 7 Output power versus repetition rate for an experimental high power ArF module.

4. EXCIMER LASERS FOR DUV LITHOGRAPHY

For the next generation of DUV lithography step and scan tools, KrF lasers with a bandwidth of 0.8pm are needed with 1kHz repetition rate for exact dose control purposes. Therefore a 1kHz laser has been developed with 40W stabilized broadband output power and a pulse to pulse stability of about 1% (standard deviation). To obtain the required narrow bandwidth of the laser output a new resonator approach - the polarization coupled resonator - is employed. The principle of the polarization coupled resonator is depicted in Fig. 8. A polarizing beam splitter transmits one polarization component and reflects the perpendicular polarization component of the laser radiation. The line-narrowing resonator is formed between the line-narrowing module containing grating and etalon and the polarization coupling mirror for one polarization component. Due to the use of the entire gain volume the narrow band efficiency (narrow band output power/broad band output power) is as high as 25%. This results in narrow band average powers between 10W and 15W. A very low etalon coating load ensures sufficiently high optical components lifetime.

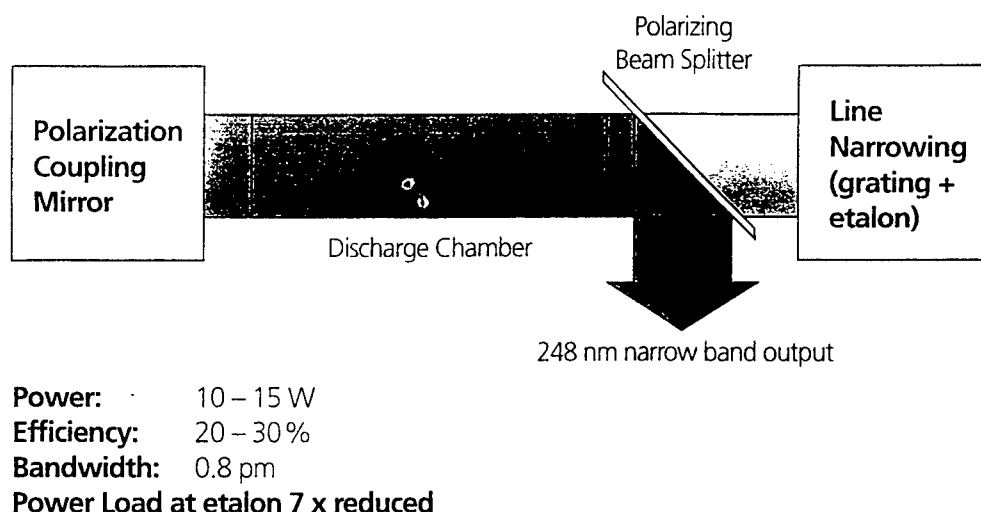


Fig. 8: Polarization coupled resonator for narrow bandwidth KrF lithography.

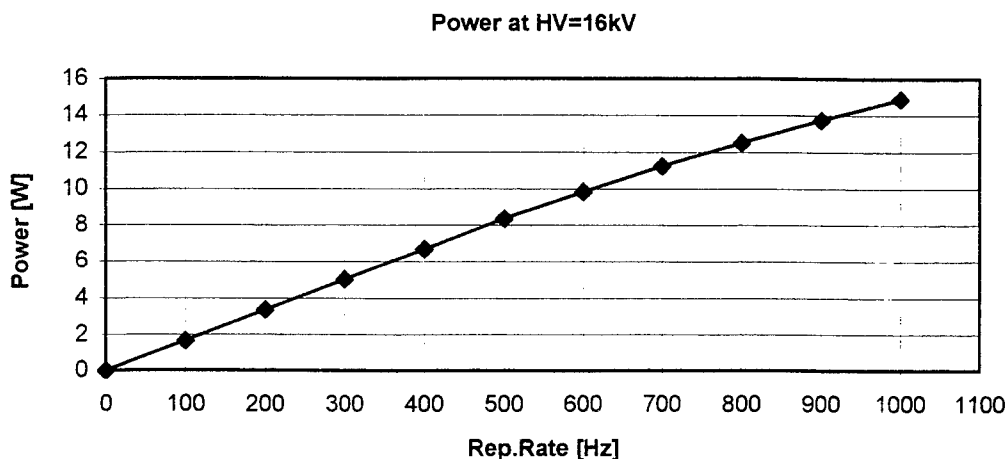


Fig. 9: Output power vs. repetition rate for the polarization coupled resonator based KrF lithography laser.

The dependence of the narrow band output power on repetition rate is shown in Fig. 9 and the characteristic output parameters of the extremely narrow bandwidth laser with the PCR resonator are summarized in Table 1

stabilized output power	10W (1 kHz)
repetition rate	0-1000 Hz
narrow-band efficiency	20-25%
bandwidth	0.8 μm
spectral purity (total energy within $\pm 2.0 \mu\text{m}$)	> 95%
beam size at 0.5 m (10%)	6 x 18 mm^2
beam divergence (10%)	1 x 2.5 mrad^2

Table 1: Characteristic parameters of the polarization coupled resonator KrF lithography laser

Looking onto the next after the next generation of DUV lithography tools for undergoing the 0.18 μm design rule, ArF lasers are expected to be the light sources in these devices. Requirements are similar as for the currently available KrF lasers: high repetition rate, high stability and a narrow bandwidth depending on the actual imaging system. We have developed a 1kHz ArF laser which achieves currently output powers of up to 1kHz. The power versus repetition rate curves as well as energy stability are given in Fig. 10. Several resonators for narrow bandwidth operation have been investigated containing different numbers of prisms and an etalon intra-cavity. The output energy for various bandwidths is shown in Fig. 11. The efficiency of all the resonators has to be improved in the future to make the laser parameters matching the 193nm lithography requirements.

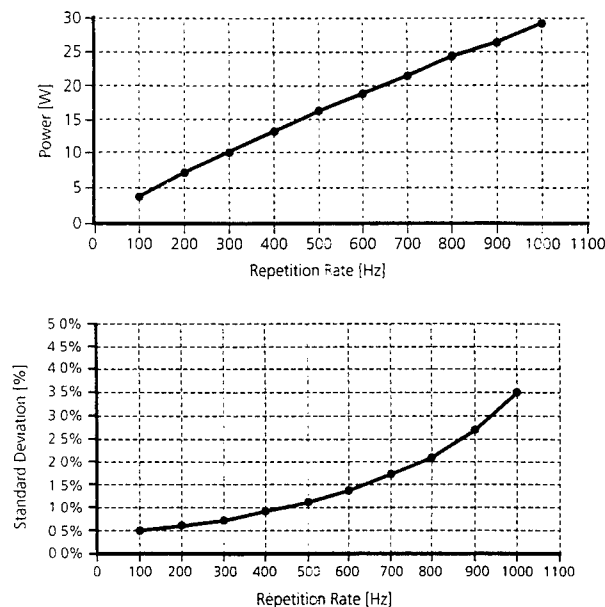


Fig. 10: Output power and stability for a 1 kHz ArF broadband lithography laser module.

5. CONCLUSIONS

We have reviewed the current status in high power excimer laser technology for industrial applications as micromachining, annealing, marking and lithography. While currently lasers with stabilized powers of up to 2000W are developed we expect the 300W class industrial excimer lasers until the year 2000. Special emphasis will be directed onto the improvement of the current power level lasers in stability beam uniformity as well as pulse shape stability. Reduction of maintenance and cost may be one of the driving forces to develop a sealed-off excimer laser in future. While currently industrial ArF lasers have started to be developed for the use in future lithography tools, we see a general trend onto new applications of shorter wavelengths in micromachining of special materials. The current performance of 157nm F₂ lasers in NovaTube™ technology (see Fig. 12) makes us optimistic that these lasers will find inroads into industrial applications in the next millennium.

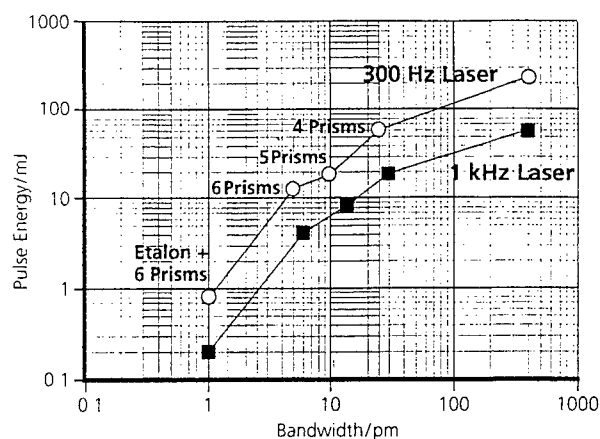


Fig. 11: Pulse energy in dependence on the bandwidth achieved with different ArF narrow band resonators.

Power Vs. Repetition Rate LPX 220i Nova Tube

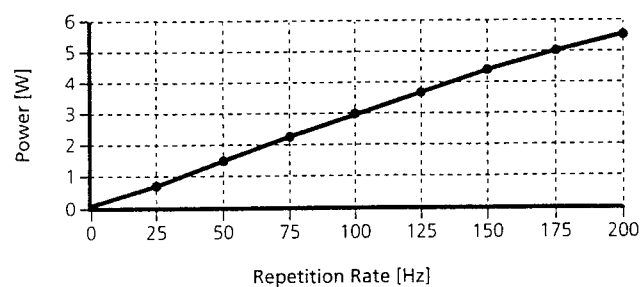


Fig. 12: Output power versus repetition rate of an F_2 laser for scientific application.

6. ACKNOWLEDGEMENT

Parts of this work are supported by the BMBF projects GOLD #01M2948C1 and PROMIS #02PV70055 as well as by the CEC projects ELIPSE #21760 and MATOC contract # BRPR-CT95-0103. We gratefully acknowledge the cooperation with Matsushita Research Institute, Tokyo, Japan, in the development of the polarization coupled resonator for KrF lithography lasers as well as the cooperation with V.M. Borisov, TRINITI, Troitsk, Russia in the investigation of high power KrF lasers.

12. HF/DF Lasers

Improved DF performance of a repetitively pulsed HF/DF laser using a deuterated compound

H. BRUNET

CILAS - Route de Nozay - 91460 MARCOUSSIS - FRANCE

ABSTRACT

The DF performance of the compact, repetitively pulsed HF/DF chemical laser, described at the last GCL, has been improved by using C_6D_{12} instead of D_2 as deuterium donor. The output energy previously achieved with D_2 was low, less than 3 J per pulse compared to the HF energy of 10 J obtained with C_2H_6 as hydrogen donor for the same experimental conditions. Unfortunately, it was not possible to employ C_2D_6 because of the excessive cost of this deuterated compound. Therefore we made a search for a not too expensive deuterated hydrocarbon and we found that C_6D_{12} could be an interesting product. We first tested C_6H_{12} as a hydrogen donor instead of C_2H_6 . Very good results were obtained on HF emission since the drop off in output energy was only about 5 %. Consequently, C_6D_{12} was ordered and tested. Output pulse energy up to 8 J was achieved at a charging voltage of 43 kV and a total pressure of 120 torr. In repetitive operation, typical average power of 450 W was achieved at a repetition rate of 65 Hz.

Keywords : HF/DF chemical lasers, phototriggered electric discharge. SF_6 gas mixture.

1. INTRODUCTION

HF and DF pulsed chemical lasers based on the electrical dissociation of SF_6 are very attractive because SF_6 is a non-corrosive gas easy to handle. Best HF laser performances are obtained by using C_2H_6 as hydrogen donor in the pumping reaction¹. In fact, replacement of H_2 by C_2H_6 leads to a laser energy more than 2 times higher than that achieved with H_2 .

Two main reasons can explain this behavior. The first one is related to the kinetics of the pumping reaction and the other to the discharge stability.

The product vibrational energy distribution of the $F + C_2H_6$ reaction is slightly different of that of $F + H_2$ and the reaction rate is fastest by a factor of about 7². Computer modeling shows that the two effects lead to an increase of about 30 % of the laser energy for typical discharge conditions.

On the other hand, recent work³ has shown that the electric discharge stability is increased by adding C_2H_6 to the SF_6 -Ne gas mixture. This is illustrated by a doubling of the duration of the current pulse, a similar increase of the laser pulse duration and an increase by more than a factor 2 of the laser energy compared to those observed with H_2 .

Theoretical investigations of the discharge show that the addition of a small amount of C_2H_6 to the gas mixture increases significantly the ionisation coefficient, especially at low E/N values. However, it is likely that more complex processes are involved in the discharge stability. In particular, the behavior of the plasma near the cathode seems to be carefully examined.

DF lasing was previously studied using D_2 as the deuterium donor. Poor laser performance was achieved with less than 3 J per pulse, at a charging voltage of 40 kV, for which a HF laser energy of about 10 J was observed¹.

It should be expected that efficient DF lasing could be achieved by using C_2D_6 instead of D_2 . Unfortunately, the cost of this deuterated hydrocarbon is very high and its use in our gas loop will be too much expensive. Therefore, we made a search for a not too expensive deuterated hydrocarbon. CD_4 is relatively cheap but gives poor laser performance. We found that C_6D_{12} could be an interesting candidate. Before ordering C_6D_{12} , we tested C_6H_{12} . Very good results were obtained since the laser energy was only slightly lower than that achieved with C_2H_6 . Consequently, C_6D_{12} was ordered and tested.

2. EXPERIMENTAL ARRANGEMENT

The device has been previously described in details ¹. Cyclo- C_6H_{12} / C_6D_{12} is a liquid at room temperature and is stored in a small glass bulb. It was flowed into the gas loop via a needle valve to achieve a convenient hydrocarbon partial pressure. Experiments were performed either on our standard laser head or on the enlarged one or on both the two.

3. RESULTS

A comparison of the HF laser energy achieved with C_6H_{12} , as a function of the charging voltage, is shown in Fig. 1. It is seen that there is only a small decrease of the laser energy when C_6H_{12} is used instead of C_2H_6 .

Before using C_6D_{12} as a deuterium donor, we tested D_2 and also CD_4 which is a relatively cheap product. Unfortunately, as shown in Fig. 2, DF laser output achieved with CD_4 was low. Energy measurements made with C_6D_{12} together with those achieved with D_2 and C_2H_6 are shown in Fig. 3. It can be seen that efficient DF lasing is achieved with C_6D_{12} , the output energy being close to 8 J/pulse at a charging voltage of 40 kV. The electrical efficiency is 2.2 % which is a very good result since it is equal to about 70 % of the HF efficiency.

In repetitive operation, the charging voltage had to be limited to 38 kV. The dependence of the DF energy as a function of the repetition rate is shown in Fig. 4. As seen, the laser energy decreases abruptly near 65 Hz due to an insufficient clearing ratio. The maximum average power achieved was about 450 W.

All the performances presented above were obtained using a stable optical cavity. However laser output achieved with an unstable cavity ($M=3.4$) was only slightly lower as shown in Fig. 5.

4. CONCLUSION

Efficient DF lasing has been achieved using C_6D_{12} as the deuterium donor. Laser output of 8 J/pulse has been observed from our device. In repetitive operation, a maximum average power of 450 W was achieved at a repetition rate of 65 Hz with an electrical efficiency of 2.3 %.

5. ACKNOWLEDGMENTS

This work was supported by DRET, Paris. The author wishes to thank M. MABRU and Ch. VANNIER who made these experiments in 1994.

6. REFERENCES

- [1] H. BRUNET, M. MABRU AND F. VOIGNIER, "High energy-high power pulsed HF/DF chemical laser", *Gas Flow and Chemical Lasers*, SPIE, 2502, 388-392, 1994.
- [2] D.J. SMITH, D.W. SETSER, K.C. KIM and D.J. BOGAN, "HF Infrared Chemiluminescence. Relative Rate Constants for Hydrogen Abstraction from Hydrocarbons, Substituted Methanes, and Inorganic Hybrides", *The Journal of Physical Chemistry*. 81(9), 898-905 (1977).
- [3] F. DOUSSET, M. LEGENTIL, S. PASQUIERS, C. POSTEL, V. PUECH, L. RICHEBOEUF "Correlation between laser performance and discharge dynamic in a photo-triggered HF laser", *Gas Flow and Chemical Lasers/High Power Laser*, Edinburgh, Scotland, UK, 1996.

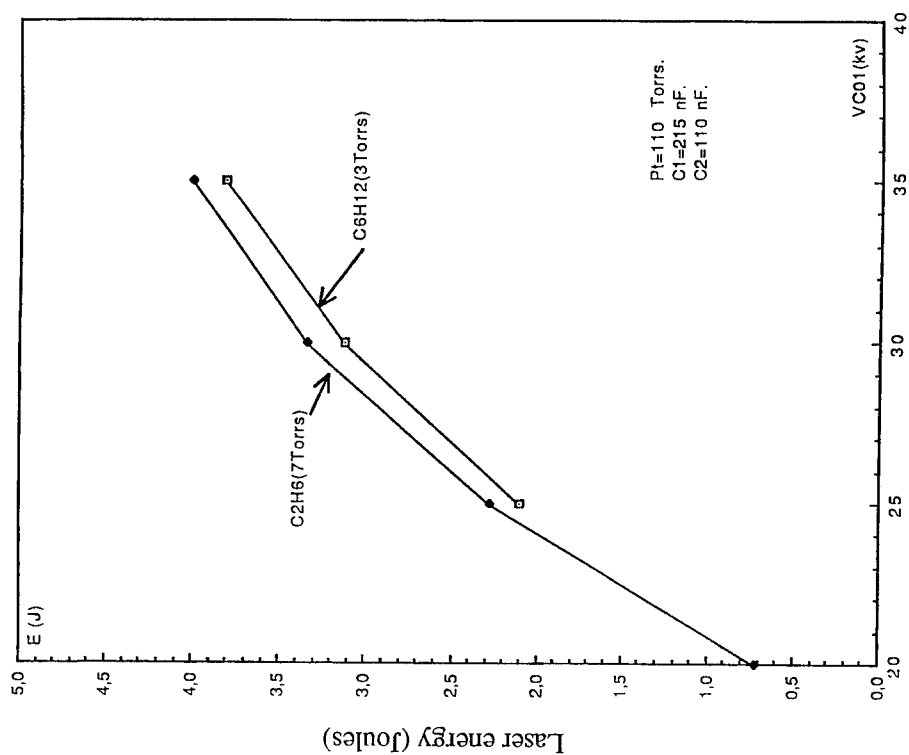


Fig. 1 - HF laser energy versus charging voltage

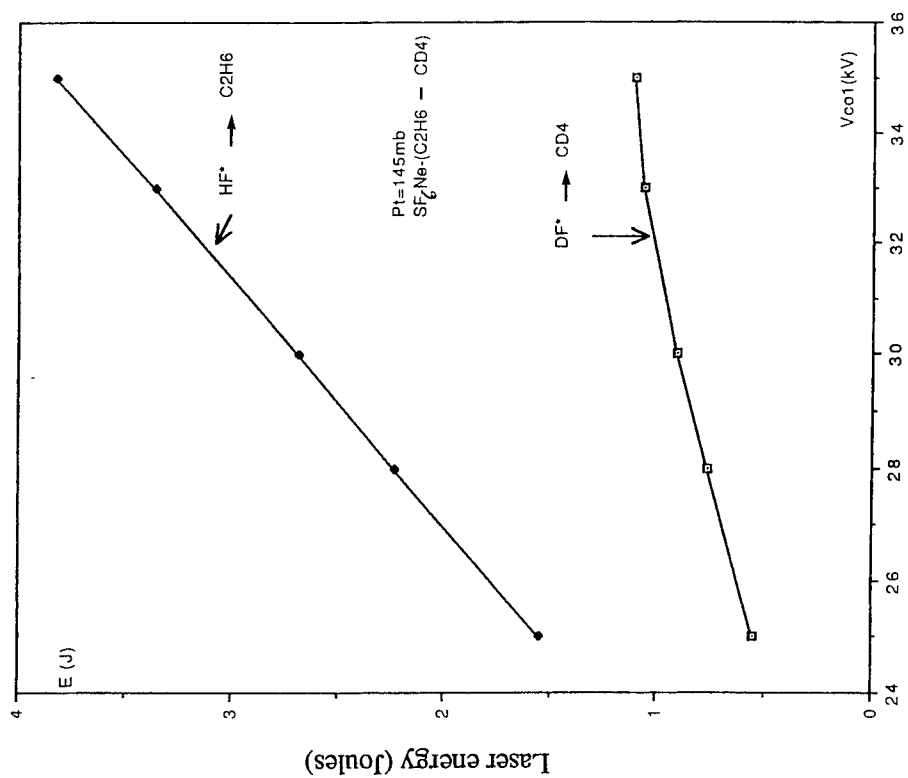


Fig. 2 - HF or DF laser energy versus charging voltage

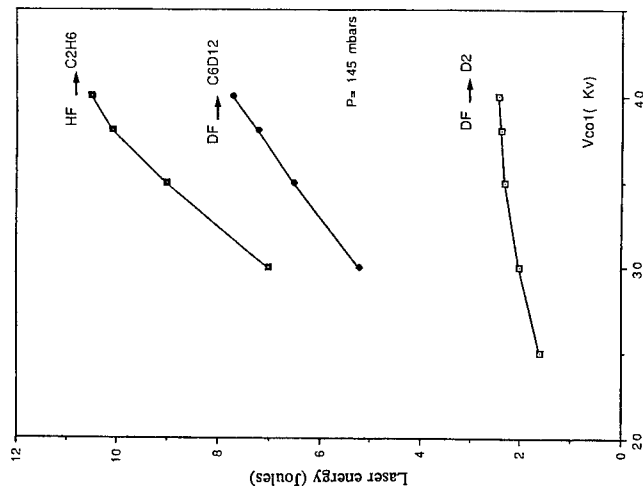


Fig. 3 - HF or DF laser energy versus charging voltage

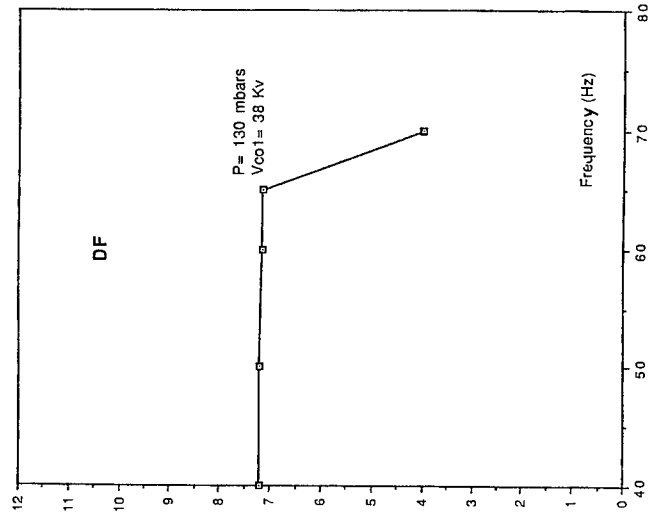


Fig. 4 - DF laser energy versus repetition rate

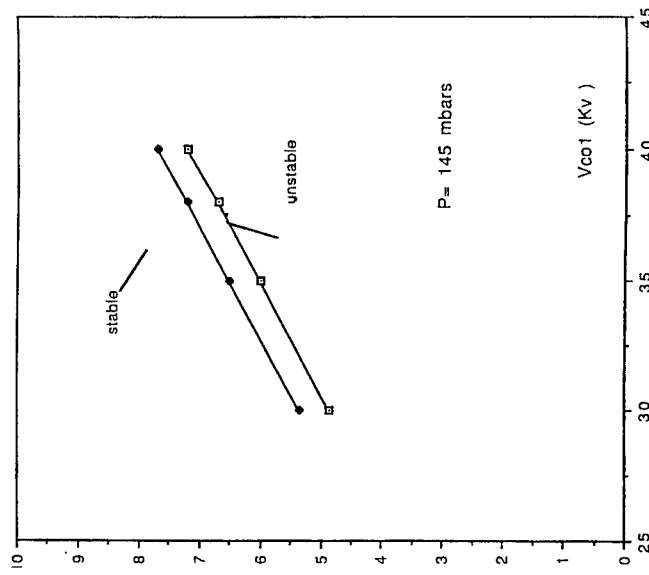


Fig. 5 - DF laser energy for stable and unstable optical cavity

A closed cycle high repetition rate pulsed HF laser

M R Harris, A V Morris and E K Gorton

Defence Research Agency
St Andrews Road, Malvern, Worcs WR14 3PS

Telephone: +44 168 489 4099

Fax: +44 168 489 4428

ABSTRACT

The design and performance of a closed cycle high repetition rate HF laser is described. A short pulse, glow discharge is formed in a 10 SF₆:1 H₂ gas mixture at a total pressure of ~ 110 Torr within a 15 x 0.5 x 0.5 cm³ volume. Transverse, recirculated gas flow adequate to enable repetitive operation up to 3 kHz is imposed by a centrifugal fan. The fan also forces the gas through a scrubber cell to eliminate ground state HF from the gas stream. An automated gas make-up system replenishes spent gas removed by the scrubber. Typical mean laser output powers up to 3W can be maintained for extended periods of operation.

Keywords: HF(DF) lasers, high repetition rate pulsed lasers, closed cycle HF(DF) lasers

1. DESIGN PHILOSOPHY

The HF(DF) laser exploits the chemical reaction between deuterium and fluorine to create excited state HF for the lasing process. The use of SF₆ to donate fluorine atoms is now a well established technique which overcomes the need to use fluorine which, particularly in conjunction with H₂, creates undesirable handling and containment problems.

The SF₆ is forced to donate fluorine atoms by means of high energy electron impact. The fluorine atoms so produced are available to react with deuterium to form excited state HF molecules. A glow discharge is essential to provide sufficiently energetic electrons to crack SF₆. In order to facilitate creation of such discharges, and to avoid voltages becoming excessively high, discharges transverse to the optical axis are commonly employed.

The operation of a transverse discharge gas laser at high repetition rate introduces the need to impose high transverse gas flow (mutually transverse to the optical axis and to the discharge) to remove "spent" gas from the discharge volume and replace this with fresh gas. Previous experience of operating pulsed carbon dioxide lasers at high repetition rate has shown that a minimum of 3 changes of the gas within the discharge volume between shots is essential. Since the stability of the discharge in the HF laser is more critical than the CO₂ laser it can be expected that more than 3 gas changes between shots will be required. The purpose of replacing the gas in this manner is to remove density perturbations arising from gas heating by the electrical discharge. In the HF laser it is also imperative that ground state HF molecules are swept out of the gain volume as they represent significant absorptive loss to the lasing process. If the laser is to be operated in closed cycle form so that the gas is recirculated for continuous use, then HF must be eliminated from the gas stream before it is recycled to the discharge region. The HF removal is performed in a cell commonly referred to as a "scrubber".

For the purposes of this discussion it is convenient to break down the high repetition rate HF laser into 4 separate but interactive sub-assemblies. These are the discharge structure, the gas flow and re-circulation system, the HF removal cell, and the optical resonator.

The discharge structure is designed to create suitable conditions for a pulsed glow discharge to be formed in SF₆ and H₂ gas mixtures. Glow discharges in SF₆ containing mixtures are difficult to form and maintain against collapse into arc discharge due to the highly electronegative nature of the gas. For this reason it is essential to utilise structures formed from carefully profiled electrodes, and the technology used here is based on that originally developed for CO₂ TEA laser use in which the glow discharge is struck between a pair of Rogowski profiled electrodes.

A pre-requisite for volume glow discharge formation is a background level of ionisation typically greater than about 10^7 electrons cm^{-3} . This pre-ionisation is created here by an intense pulsed UV source synchronous with the discharge pulse. Three variations of such pre-ionisation schemes were examined during the course of this work.

A final requirement for achieving stable glow discharges, particularly in these aggressive SF_6 containing gas mixtures, is that the energy should be deposited rapidly so that the discharge can be completed in a timescale shorter than that required for arc formation. This means that typical discharge pulse lengths are in the vicinity of 50 ns and attention must be paid to the selection of the rapid discharge circuit components and to the circuit layout.

The gas circulation system comprises a fan or blower to propel the gas around duct work and flow guides which direct the gas through the discharge structure and scrubber cell in turn. High repetition rate operation demands high flow velocity which limits the choice of blower. Since the pressure gradient induced by impedance to gas flow by the duct work and structures within the duct work increases as the square of flow velocity, high flow speeds require a blower capable of driving the gas flow against a high back pressure.

For purposes of experimental convenience the design of the laser has adopted the approach of separating the circulation fan, scrubber unit and discharge head and interconnecting them with sections of tubular ducting. This approach results in a large and cumbersome device but does allow the separate elements to be individually characterised and optimised, thus enabling maximum understanding and design information to be gleaned.

The role of the scrubber unit is to eliminate HF from the circulating gas stream. It is necessary to present the surfaces of the scrubber material to the gas stream so that good contact is made with all the gas without introducing an excessively high pressure differential.

The process of HF removal rapidly leads to significant loss of the SF_6 and H_2 fuel gases which then require replenishment. This can be readily performed by means of a pressure sensitive servo valve which automatically admits an appropriate mixture of SF_6 and H_2 as required.

The optical resonator is an essential component in any laser. The resonator has not been regarded as an issue in this study and has therefore not been subject to optimisation. A simple resonator has been provided to ensure that lasing takes place and to provide a laser output which can be used as a tool to monitor the performance of the other sub-assemblies.

2. CONSTRUCTION

The discharge structure was formed from a pair of Rogowski profiled electrodes defining a discharge volume $5 \times 5 \times 150 \text{mm}^3$. Assuming an SF_6 pressure of 100 Torr and an E/P of $120 \text{Vcm}^{-1} \text{Torr}^{-1}$ results in a discharge maintenance voltage of 6kV for the 0.5cm gap.

Once the discharge dimensions have been set the gas flow rate can be determined and a suitable circulation fan selected. The need to provide several gas changes between shots with an adequate allowance for gas by-passing results in a volumetric flow rate of about 2000lmin^{-1} . The high flow velocity through the discharge structure results in a large pressure gradient enforcing the selection of a centrifugal blower.

Measurements of flow impedance of 3mm zeolite pellets indicated that a scrubber cell of internal diameter 300mm holding a maximum depth of pellets of 120mm would introduce of pressure drop not greater than 0.5 Torr. This ensured that the maximum flow impedance is introduced by the discharge structure.

3. PERFORMANCE

The laser performance was examined using 3 types of preioniser (PI). Two PI schemes were arc array type whilst the third scheme was a silicon based distributed resistance corona PI. The first arc array scheme studied was a sliding spark array in which the arcs were fired in series between T pins capacitively coupled to ground. This scheme was rejected as the large voltage reversal encountered during running of the arc array tended to cause the thyatron to latch into a

conductive state. The other arc array approach, is one which is commonly adopted, involving running the arcs in series to charge coupling capacitors which also act as "peaking" capacitors in the rapid discharge circuit. This scheme worked well operating with a single array downstream of the main discharge volume. The distributed resistance silicon slice preioniser was constructed so that the slices lay in the plane of the gas flow to minimise flow impedance. This PI operated reliably although rather lower discharge energy loadings were permitted when compared with the arc array limiting the output power to about 1W.

The table below summarises the range of conditions explored and the performance obtained using the arc array PI arrangement. A 10 SF₆ : 1 H₂ gas mixture was used throughout since the output power was found to reach a broad optimum in the vicinity of this ratio.

SF ₆ Pressure (Torr)	Repetition Rate (kHz)	Output Power (W)
100	1.0	2.5
100	1.4	2.2
100	1.5	2.1
60	1.5	1.2
60	2.0	1.4
60	2.4	1.2
60	3.0	0.8
50	3.0	0.75

The fall off of output power and the need to reduce the SF₆ pressure with increased rep-rate indicates that the gas circulation rate is marginal. Figure 1 summarises a sealed run performed using this discharge configuration. The improving performance with accumulated number of shots arises from the improving pre-ionisation resulting from an increased arc length due to erosion of the tungsten arc pins. Over the course of the 3.5 million shot run the arc gap increased from about 1mm to almost 4mm. The silicon PI arrangement showed much less erosion than the arc array and appears to be a more promising candidate for very long life operation.

The rate of consumption of fuel gases was assessed by a combination of total gas pressure measurement and discharge maintenance voltage measurement. As the H₂ was consumed in the formation of HF, which was subsequently adsorbed onto the scrubber, the total gas pressure fell indicating the rate of H₂ usage. The SF₆ concentration could be monitored by measurement of the main discharge maintenance voltage providing a rate for SF₆ consumption. The SF₆ was found to be consumed at half the rate for H₂. If each H₂ molecule is assumed to contribute to the formation of 2 HF molecules the HF generation rate can be deduced from the H₂ usage rate. The HF generation rate was found to be close to 5×10^{19} molecules s⁻¹ W⁻¹.

4. CONCLUSIONS

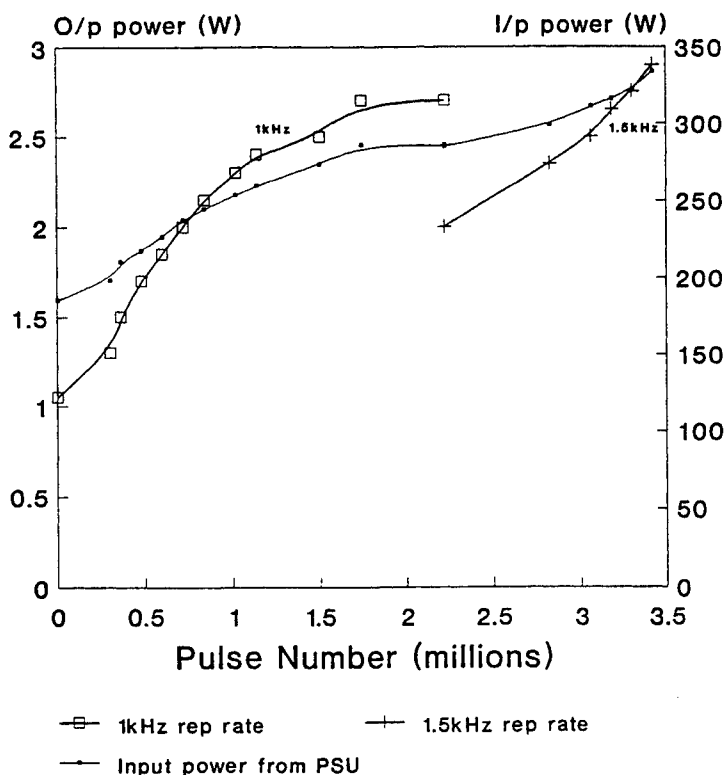
A pulsed HF (DF) laser generating a mean output power in the vicinity of 1W and operating at repetition rates around 1 kHz has been constructed and characterisation experiments performed. The principal findings are:-

- The rate at which HF (DF) is generated has been determined to be approximately 5×10^{19} molecules s⁻¹ W⁻¹.
- Ground state HF causes large reduction of the laser output power, severe power loss (~ 50%) is created at concentrations $\sim 10^{16}$ cm⁻³.
- The fuel gases SF₆ and H₂ (D₂) are shown to be consumed in the ratio 1 SF₆ : 2 H₂, i.e. each SF₆ molecule appears to donate 4 fluorine atoms. Gas make-up to replace the gas consumed in the formation of HF can be replaced from

a cylinder of SF_6 , H_2 mixture or from a separate supply of each gas. For long term closed cycle operation the latter technique might be preferable in case the above stoichiometry is not adhered to exactly. In this approach the discharge voltage has been demonstrated to provide a suitable measure of SF_6 concentration, whilst total pressure can provide adequate indication for H_2 addition.

- The primary limit to laser lifetime is the pre-ioniser. The semiconductor pre-ioniser having a lower rate of erosion shows advantage over arc array schemes. The laser efficiencies achieved with semiconductor and arc array PI schemes are similar although the arc arrays permit higher specific power density.
- The high gas velocity requirement resulting from high repetition rate operation forces selection of a centrifugal blower. Since the pressure drop which the circulation fan has to work against increases as the square of the gas velocity a few kHz appears to represent a practical limit to the repetition rate where the power drawn by the fan motor introduces a factor of 2 reduction in the overall laser efficiency.

**Fig 1. Arc array PI laser performance
in closed cycle with automated
gas make up.**



Line selected performance of a cw HF laser

Shawn J. Gordon, Lee H. Sentman, and David S. Jenkins

Aeronautical and Astronautical Engineering Dept.
University of Illinois at Urbana-Champaign, Urbana, Illinois 61801

ABSTRACT

A diffraction grating was used in the Littrow and off-Littrow configurations to select the lines in a cw HF stable resonator. The beam is outcoupled through a partially reflective mirror. Single line Littrow, single line off-Littrow, and off-Littrow line pair performance were measured. For the first time, as far as we know, in the operation of chemical lasers, Littrow and off-Littrow lines lased simultaneously. Two line (one Littrow line, one off-Littrow line) and three line (one Littrow line, two off-Littrow lines) Littrow/off-Littrow line combinations were demonstrated. The grating reflectivity was a strong function of the polarization of the laser beam. Data indicated that the grating generated a beam whose polarization was perpendicular to the grating grooves.

Keywords: line selection, Littrow, off-Littrow, cw HF laser

1. INTRODUCTION

The HF chemical laser is a multiline device. Because of this, and the density variations in the supersonic flow field, phase front aberrations occur. The phase front aberrations limit the far field focus that can be obtained. One process for correcting the phase front aberrations in the output beam uses the Stimulated Brillouin Scattering (SBS) process. Since there is a threshold input power for the SBS process to occur, each line in the multiline beam must be above this threshold. Because the HF laser is a multiline device and typically has several lines below this threshold, it is desirable to operate the HF laser on only a few lines so that all of them will have the requisite threshold power to utilize the SBS process. This requirement brings to the forefront a question that has been of interest ever since it was shown that the HF laser operated on many lines simultaneously: what fraction of the multiline performance can be achieved when a cw HF laser is operated on a selected number of lines? The purpose of this work is to investigate line selected performance experimentally and with computer simulations to understand the underlying physical processes responsible for line selected performance and to determine the conditions required to optimize line selected performance.

2. THE CW HF LINE SELECTED RESONATOR

2.1 Littrow and off-Littrow line selection

The arc driven cw, supersonic HF chemical laser (SSL) can be operated with only one or two lines lasing using the line selected resonator demonstrated by Chodsko^{1,2}. In this application, a diffraction grating is used to select the lines. The fundamental equation that describes the direction of diffracted radiation is the "grating equation"^{3,4}:

$$\sin\theta_{\pm m}^{\lambda} = \pm [(m\lambda/d) \pm \sin\theta_i] \quad (1)$$

where $\theta_{\pm m}^{\lambda}$ is the angle of the diffracted order m , λ is the wavelength, d is the groove spacing, the $+$ sign is used for the positive order, the $-$ sign for the negative order, and θ_i is the angle of incidence at which the radiation strikes the grating. All angles are measured from the normal to the plane of the grating.

For each wavelength that strikes the grating, there are three beams associated with each diffracted order: the positive m^{th} order, negative m^{th} order, and zeroth ($m=0$) order. The direction of the zeroth order diffraction is the same for each wavelength. Thus, the zero order beam contains all of the same wavelengths as the incident beam.

The grating efficiency determines the strength of the zeroth and negative m^{th} order diffractions. Since the energy in negative m^{th} and zero orders is a loss that cannot be eliminated, the energy in these orders should be minimized.

In the Littrow configuration, which occurs when the positive m^{th} order diffracted angle is equal to the incident angle, the positive m^{th} order diffracted beam is reflected back on the same path as the incoming beam. The incident angle at which this occurs is called the Littrow angle. To select a line using the Littrow configuration, the grating is rotated to the Littrow angle for that line⁴. Since each wavelength has a different Littrow angle, only one Littrow line can be selected at a time. Lasing occurs between the diffraction grating and a partially reflective mirror, denoted the "outcoupler".

In the off-Littrow configuration, lines are selected by the appropriate placement of feedback mirrors. In this configuration, the angle of the m^{th} order diffracted beam is related to the incident angle by Eq. (1). To select an off-

Littrow line, a feedback mirror is placed at the location of the first order diffraction of that line. Due to space limitation, a maximum of two off-Littrow lines can be selected in the cw HF line selected resonator.

Although simultaneous lasing in the Littrow and off-Littrow orientations had not been reported in the operation of chemical lasers, grating theory indicates that it should be possible. To obtain the Littrow line, the grating is rotated to the Littrow angle for that line. To obtain the off-Littrow lines, the feedback mirrors are placed at the locations of the first order diffractions of the desired lines.

2.2 Grating selection

To minimize losses and cavity length, a 600 lines/mm ($d=1.667 \mu\text{m}$) grating diffracting into the first order ($m=1$) was chosen. The line selected resonator was designed to operate for different combinations of the lines $P_1(3-11)$ and $P_2(3-11)$. The lines that are likely to give the largest fraction of multiline performance are the peak gain lines. Since the intensity of a line depends on how close it is to the grating's blaze wavelength (λ_{Blaze}), λ_{Blaze} was chosen close to the center of the peak gain line wavelength range (between $P_1(4)$ and $P_2(8)$), $2.7755 \mu\text{m}$.

2.3 Description of the diffraction gratings used in the cw HF line selected resonator

Three diffraction gratings have been used in the line selected resonator. The coating of Grating 1 continuously degraded over time. Grating 3, which was manufactured in the same way as Grating 1, degraded almost immediately after it was first used. This is the same behavior that was noted with Grating 1. It was thought that the degradation of Grating 1 was due to a long term exposure to the atmosphere. Grating 3 was stored in a desiccator to avoid this problem. The degradation of Gratings 1 and 3 was caused by heating due to the intracavity flux.

The Grating 2 manufacturing process was designed to prevent coating degradation due to incident heat flux. To protect Grating 2 from the moisture in the atmosphere, it was stored in a desiccator when not in use. Repeatable data were obtained with Grating 2 for approximately 9 months. Recently, Grating 2 has shown signs of degradation.

Prior to degradation, Gratings 1 and 3 were more efficient than Grating 2. Thus, a grating that is capable of producing repeatable data (i.e. one that does not rapidly degrade) and that has the efficiency of Gratings 1 and 3 is desired. The grating manufacturer has suggested a new manufacturing process that should produce such a grating.

2.4 Experimental layout of the line selected resonator

In order to eliminate Brewster window losses, the entire resonator was placed in vacuum boxes (VB) specifically designed for the line selected stable resonator. To measure the power diffracted into the zeroth and negative first orders, these orders are transmitted through a CaF_2 window. Figure 1 shows the experimental setup of the line selected resonator. A HeNe laser is used to align the resonator. One power meter is placed on the partially reflective mirror side to measure outcoupled power. A second power meter is used to measure the power in the negative first and zero order beams. A Monolight scanning monochromator is used on the outcoupled side to determine the lines that are present in the beam. Translation stages inside each VB allow the optical axis position to be easily varied. The outcoupler, grating, and feedback mirror mounts are all water cooled. Horizontal and vertical alignment of the outcoupler and vertical alignment and rotation of the grating under vacuum were accomplished with motorized micrometers. To prevent the laser flow from leaking into the VB and getting trapped there, a pair of purge ducts were attached to the side of the laser body inside the VB.

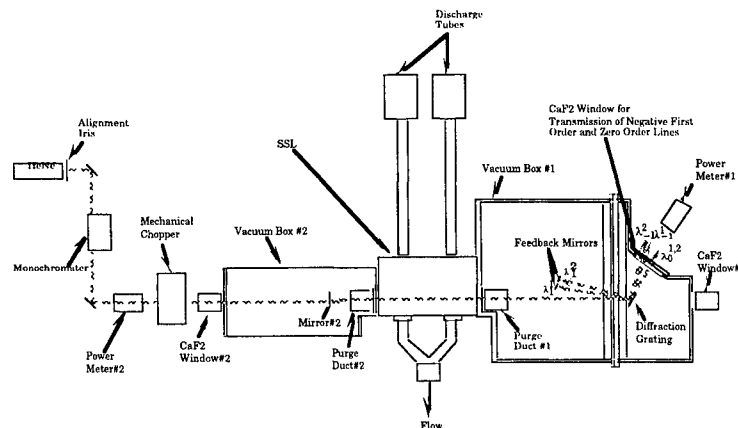


Figure 1. Experimental Layout of the Line Selected Resonator

3. EXPERIMENTAL RESULTS

All of the following data were measured on the SSL. The resonator consisted of the 2 meter concave (2mCC) 73% reflective outcoupler, the diffraction grating, and, for off-Littrow lines, Si Enhanced Total Reflector (ETR) feedback mirror(s) (99.5% reflective). Grating 2, prior to degradation, was used to obtain Littrow, off-Littrow, and multiple line selected data. Grating 3, prior to degradation, was used to obtain Littrow data.

The zero order diffraction was detected for all of the measured lines. The negative first order diffraction was detected for all of the measured off-Littrow lines. $P_{V,L}(J)$ denotes a Littrow line and $P_{V,OL}(J)$ denotes an off-Littrow line.

3.1 Single line Littrow results

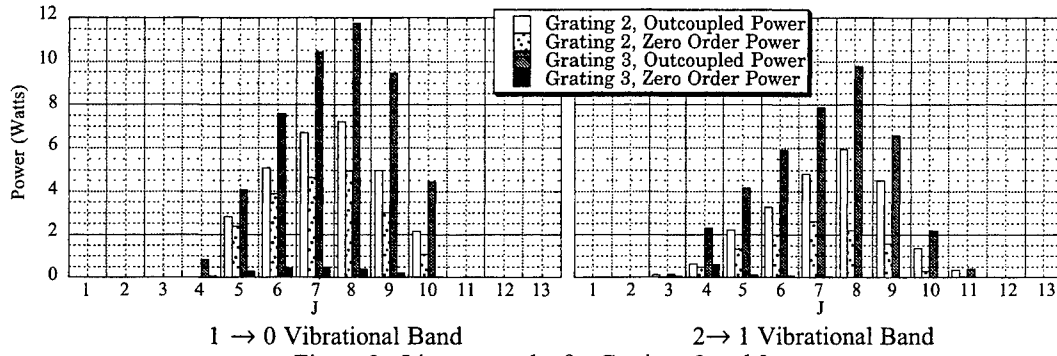


Figure 2. Littrow results for Gratings 2 and 3.

For Grating 2, the zero order power was 16%-85% of the outcoupled Littrow power, Fig.2. For Grating 3, the zero order power was 0.8%-45% of the outcoupled Littrow power, Fig.2. Since the zero order beam powers are much smaller for Grating 3 than for Grating 2, the pristine Grating 3 was much more efficient than the pristine Grating 2.

There is very little difference between the measured total (outcoupled + zero order) powers for the two gratings. Since the zero order power for Grating 3 is much smaller than that for Grating 2, this means that the outcoupled power for Grating 3 is almost equivalent to the total power for Grating 2. Thus, the more efficient Grating 3 places the majority of the total Littrow power in the useful outcoupled beam.

3.2 Single line off-Littrow results

Single line off-Littrow data were measured with Grating 2 for $P_1(7)$, $P_1(8)$, $P_2(6)$, and $P_2(7)$. The incident angle of the grating was chosen so that the angle between the input beam and the first order diffraction was 10° . For each line, the total off-Littrow power was smaller than the corresponding total Littrow power for that line. The total powers in $P_{1,OL}(7)$ and $P_{1,OL}(8)$ were 51% and 48% of the total powers in $P_{1,L}(7)$ and $P_{1,L}(8)$, respectively. The total powers in $P_{2,OL}(6)$ and $P_{2,OL}(7)$ were 67% and 81% of the total powers in $P_{2,L}(6)$ and $P_{2,L}(7)$, respectively. In the off-Littrow experiment, the beam strikes the grating twice. Thus, the effect of an inefficient grating is cumulative in the off-Littrow experiment.

3.3 Multiple Line Selected Results

Off-Littrow/off-Littrow (OL/OL) line combinations were measured with Grating 2, Table 1. For the first time in the operation of chemical lasers, simultaneous lasing of Littrow and off-Littrow lines were demonstrated. Littrow/off-Littrow (L/OL) and Littrow/off-Littrow/off-Littrow (L/OL/OL) line combinations were measured, Table 1.

Littrow	Line 1 (OL)	Line 2 (OL)	$P_{out}(Watts)$	$P_{nf1}(Watts)$	$P_{nf2}(Watts)$	$P_{zero}(Watts)$	$P_{tot}(Watts)$
	$P_2(6)$	$P_1(7)$	0.68	0.25	0.49	0.70	2.12
$P_2(8)$	$P_1(7)$		10.37	2.13		6.62	19.11
$P_2(8)$	$P_1(7)$	$P_1(6)$	10.58	1.72	1.08	6.64	20.02
$P_2(9)$	$P_1(8)$		6.27	0.82		3.19	10.28
$P_2(9)$	$P_1(8)$	$P_1(6)$	6.27	0.53	0.14	3.35	10.29
$P_2(7)$	$P_1(8)$		10.45	2.23		6.91	19.59
	$P_2(7)$	$P_1(8)$	3.92	1.06	0.49	2.55	8.02
$P_2(7)$	$P_1(7)$		8.88	1.94		5.85	16.67

Table 1 - Multiple Line Selected Results

The addition of $P_{1,OL}(6)$ to the L/OL line pairs $P_{2,L}(8)$, $P_{1,OL}(7)$ and $P_{2,L}(9)$, $P_{1,OL}(8)$ had very little effect on the total power.

The same cascade pair, $P_2(7)$, $P_1(8)$ was obtained for both the L/OL and OL/OL cases, Table 1. The $P_{2,OL}(7)$, $P_{1,OL}(8)$ OL/OL pair total power was 59% smaller than the $P_{2,L}(7)$, $P_{1,OL}(8)$ L/OL pair total power. Thus, the L/OL pair had a substantially higher performance than the OL/OL pair.

4. DIFFRACTION GRATING REFLECTIVITY

To make a proper comparison between line selected and multiline performance, the reflectivity of the outcoupler must be the same for the multiline and line selected resonators. The reflectivity of the other mirror in the multiline resonator must be the same as that of the diffraction grating. Thus, the reflectivity of the grating must be determined.

Reflectivity measurements were performed on Gratings 2 and 3, prior to their degradation, with the following types of single line probe beams: polarization vector parallel to the grating grooves ("parallel probe beam"), polarization vector perpendicular to the grating grooves ("perpendicular probe beam"), and unpolarized ("unpolarized probe beam"). The first order reflectivity (R_1) and zeroth order reflectivity (R_0) of the gratings for the single line $P_1(8)$ were measured as a function of incident angle. Measurements were made within $\pm 10^\circ$ of the Littrow angle for $P_1(8)$. The negative first order diffraction was not detected. Within $\pm 10^\circ$ of the Littrow angle, both R_1 and R_0 are fairly constant. The results of the reflectivity measurements, averaged over incident angle, are summarized in Table 2.

Grating	Parallel Polarization		Perpendicular Polarization		Unpolarized	
	R_1	R_0	R_1	R_0	R_1	R_0
2	3.74	89.8	67.2	22.2	38.5	50.3
3	4.38	89.2	79.3	3.16	44.0	43.0

Table 2 - Reflectivity Results for Gratings 2 and 3 (averaged over incident angle) for $P_1(8)$.

Both gratings are least efficient when the polarization vector is parallel to the grooves and most efficient when the polarization vector is perpendicular to the grooves. For the unpolarized probe beam, the efficiency of both gratings falls in between the parallel and perpendicular polarization results. The reflectivity results obtained for both gratings with the parallel probe beam are similar. The reflectivity measurements for the perpendicular polarized and unpolarized probe beams clearly show that Grating 3 is more efficient than Grating 2, Table 2.

Measurements made with an unpolarized single line probe beam have shown that the reflectivities of Gratings 2 and 3 are a strong function of wavelength. For both gratings, R_0 decreased and R_1 increased as the wavelength increased. For wavelengths less than the blaze wavelength, R_0 was larger than R_1 . Among the measured lines, the one with the wavelength closest to the blaze wavelength ($\lambda_{\text{Blaze}} = 2.7755 \mu\text{m}$) was $P_1(8)$ ($\lambda = 2.7826 \mu\text{m}$). For both gratings, R_0 was slightly larger than R_1 for $P_1(8)$. For wavelengths greater than that of $P_1(8)$, R_0 was smaller than R_1 . The more efficient Grating 3 had a larger R_1 and a smaller R_0 than the less efficient Grating 2 for each of the measured lines.

5. POLARIZATION OF THE LINE SELECTED OUTPUT BEAMS

Since the grating reflectivity is a strong function of the polarization, the reflectivity of the grating when it is in the line selected resonator depends on the polarization of the output beam. To investigate the polarization of the laser in line selected mode, the outcoupled beam was passed through a parallel plate polarization analyzer. Preliminary results indicate that both gratings polarize the outcoupled beam so that its polarization vector is almost perpendicular to the grating grooves. Thus, the reflectivity of the grating in the line selected resonator is given by the perpendicular probe beam measurement. Preliminary results also indicate that the degree of polarization is a function of wavelength.

6. ACKNOWLEDGMENT

This work was supported by BMDO through W.J. Schafer Associates subcontract SC-92C-04-04.

7. REFERENCES

1. R.A. Chodzko, "Multiple-Selected-Line Unstable Resonator," *Applied Optics* 13(10), pp.2321-2325, 1974.
2. R.A. Chodzko, "Multiple Line Selection in cw HF/DF Chemical Lasers," *Aerospace Report No.ATR-92(2732)-1*, Draft., July 1, 1993.
3. M.C. Hutley, *Diffraction Gratings*, pp.1-5, 198-201, 156-157, Academic Press, London, 1982.
4. L.H. Sentman, S.J. Gordon, J.W. Otto, and D.L. Carroll, "A Study of the Effect of Line Selection on HF Oscillator Performance," AAE TR 93-10, UILU Eng. 93-0510, Aeronautical and Astronautical Engineering Dept., University of Illinois, Urbana, IL, July, 1993.

Correlations between laser performance and discharge dynamic in a photo-triggered HF laser

S.Pasquiers, L.Richeboeuf, F.Doussiet, M.Legentil, C.Postel, V.Puech

Laboratoire de Physique des Gaz et des Plasmas
(laboratoire associé au C.N.R.S.)
Université Paris-Sud, 91405 Orsay cedex, France

ABSTRACT

The non-chain reaction HF laser energised by an X-ray photo-triggered discharge has been studied for Ne/SF₆/C₂H₆ and Ne/SF₆/H₂ gas mixtures. For an active volume of 312 cm³, a high specific output energy of 10 J/l has been reached with an electric efficiency of 4.7% for the mixture with ethane, whereas only 6 J/l is obtained with an efficiency of 3.1% for the mixture with hydrogen. It is shown that discharge instabilities are responsible for the laser emission disruption in the case of the H₂-mixture. However, addition of C₂H₆ to Ne/SF₆, in place of H₂, induces the discharge stabilization. The higher laser performance obtained with the C₂H₆-mixture, compared with the performance of the H₂-mixture, is a direct consequence of this stabilization effect.

Keywords: HF laser, pulsed electric discharge, discharge instability, high pressure SF₆ plasma.

1. INTRODUCTION

Performance of the electrically initiated HF lasers using Ne/SF₆/RH gas mixtures are very sensitive to the nature of the RH molecule. The use of ethane allows to achieve high output energy and efficiency, whereas the use of H₂ leads to lower performances¹⁻⁴. In order to understand these differences, we have investigated the X-ray photo-triggered laser discharge for Ne/SF₆/H₂ and Ne/SF₆/C₂H₆ mixtures.

For a discharge volume of 312 cm³ an output laser energy as high as 3.0 J has been obtained in the C₂H₆-mixture⁴ with an electrical efficiency of 4.7 %, whereas the maximum energy achieved with the H₂-mixture is only 1.75 J with an efficiency of 3.1 %. Recent experimental and theoretical works⁴⁻⁵ have shown that the F-atom density growth during the development of the discharge, as well as the total HF-molecule density, weakly depend on the RH molecule type, so that the differences on the laser performance cannot be ascribed to different F-atom productions. A spatially and temporally resolved CCD camera diagnostic has been implemented on the laser structure in order to study the discharge stability, correlated with the temporal evolution of the laser power.

2. EXPERIMENTAL DEVICES AND MEASUREMENTS

Both the experimental devices and measurements have been detailed in references 4 and 5, and a complete description of the X-ray photo-triggered laser has been previously given⁶. They will not be revisited here. The discharge cell of the "X525" laser studied in this work has an electrode gap $d=2.5$ cm. The cathode is 50 cm in length and is flat over 2.5 cm width, whereas a plate works as the anode. The charging voltage of the energy storage line can be chosen so that the corresponding reduced field $(E/N)_0$ can reach 300 Td across the electrodes at the time of the pre-ionization; $(E/N)_0 = V_0/(N \cdot d)$, where N is the total mixture density. All the results presented thereafter have been obtained for a storage capacitance $C=144$ nF. The laser cell has been filled with a Ne/SF₆ (1/1) mixture at a total pressure of 118 Torr, with addition of hydrogen or ethane at a partial pressure ranging from 4 up to 15 Torr.

3. DISCHARGE DYNAMIC AND LASER EMISSION

For a C₂H₆ or a H₂-pressure of 4, 7.5, and 15 Torr, figure 1 presents the laser energy plotted against $(E/N)_0$. In the case of ethane the energy weakly depends on the C₂H₆-pressure and monotonously increases when $(E/N)_0$ increases. The maximum energy seems to be only limited by the field value which can be applied across the electrodes. On the contrary, the laser energy obtained with hydrogen strongly depends on the field and H₂-pressure values.

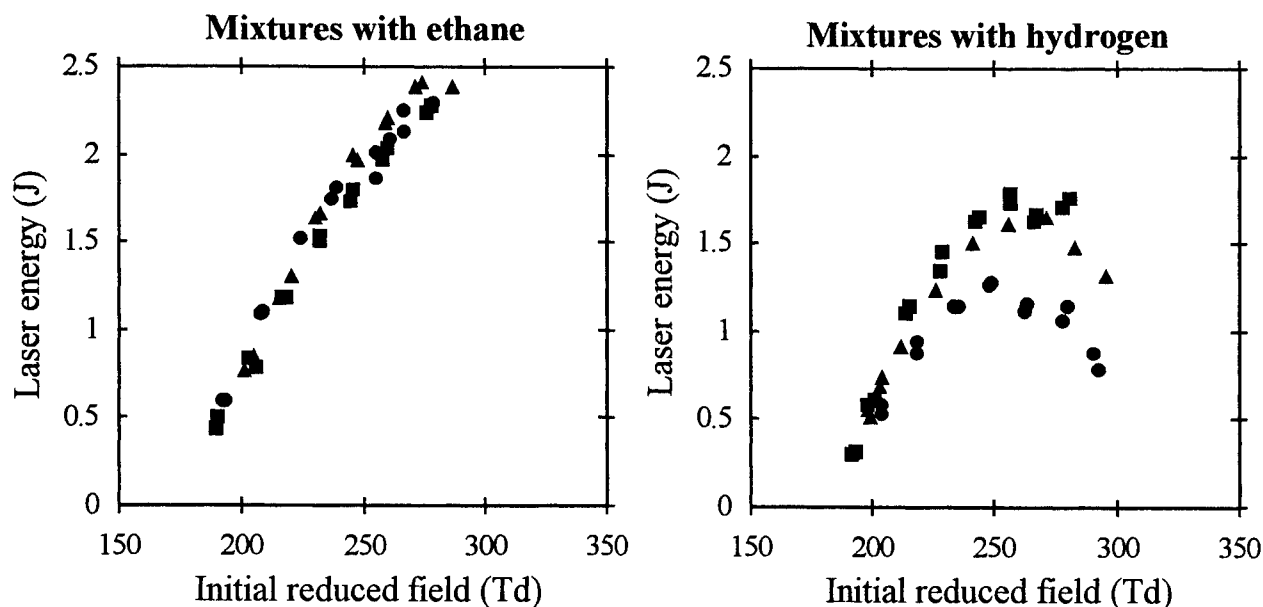


Fig.1 - Laser energy plotted against the initial reduced electric field. $C=144$ nF.

Ethane or hydrogen partial pressure: (●): 4 Torr, (▲): 7.5 Torr, (■): 15 Torr.

At 4 Torr of hydrogen the energy first increases as $(E/N)_0$ increases up to 250 Td, and thus decreases for higher $(E/N)_0$ values. At 15 Torr the laser energy obtained with the two mixtures are equals for $(E/N)_0$.

less than 250 Td, but for a higher field it remains constant in the case of H_2 . As a result the laser energy obtained with hydrogen cannot raise above 1.8 J.

For a low partial pressure, 4 Torr, figure 2 presents the temporal evolution of the current, of the voltage, and of the laser power obtained at an initial field of 263 Td, for the mixture with H_2 or with C_2H_6 . For that field value we measure a laser energy $E_L=1.15$ J and a peak power $P_e=50$ MW in the case of hydrogen, whereas $E_L=2.20$ J and $P_e=70$ MW for ethane. Camera frames acquired at the time of the peak power are given below. The intensity scale ranges from black, which corresponds to areas where there is no plasma fluorescence, to white which corresponds to saturation of the detector. Optical attenuations used in front of the CCD camera are given below the corresponding frames. The cathode is located at the top of the frames, and is seen in perspective on more than three quarter of its length.

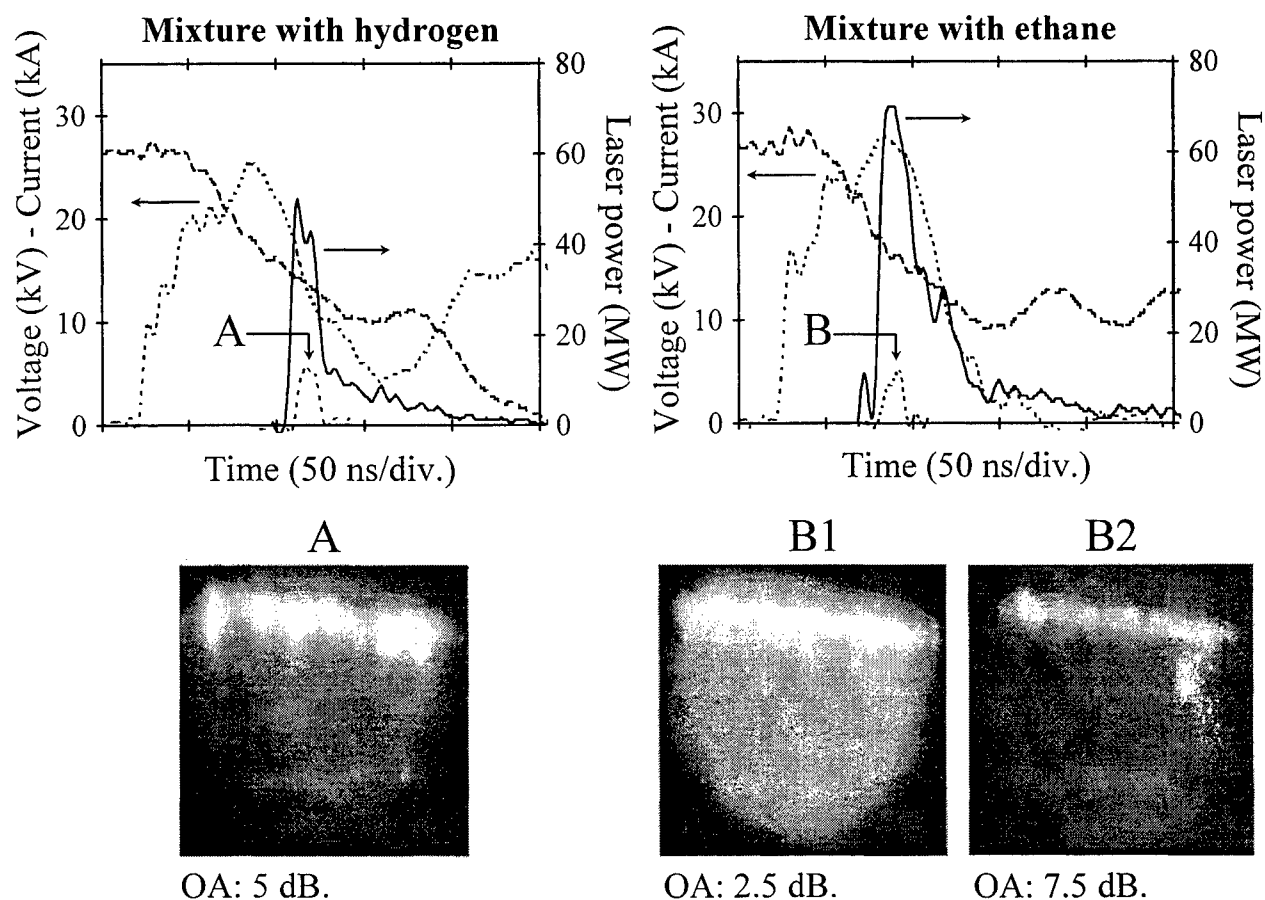


Fig. 2 - Time and spatially resolved diagnostic of the inter-electrodes space. $C=144$ nF, $(E/N)_0=263$ Td. Hydrogen or ethane partial pressure: 4 Torr. The temporal evolution of the current (...), of the voltage (---), and of the laser power (—), and the camera opening (---) are given on each diagram. OA: optical attenuation.

For the H_2 -mixture in the conditions of figure 2, the laser emission occurs about 20 ns after the peak

current. At that time a discharge instability has began to develop: an intense and inhomogeneous cathodic luminescence is measured, with hot spots connected to plasma inhomogeneities in the discharge volume. At a later time a second current pulse is detected, which is characteristic of a completely inhomogeneous discharge⁵. At a higher $(E/N)_0$ value, 290 Td, the laser emission delay time with respect to the voltage drop is unchanged with respect to the time measured at 263 Td, but the instability onset is closer to the first peak current. As a result the laser emission is much strongly affected by the instability: the peak power is only 35 MW, and the output energy is 0.75 J. In fact, at 4 Torr of hydrogen, the decrease of the energy for $(E/N)_0$ above 250 Td is due to the unstable discharge behaviour in the Ne/SF₆ mixture⁵; addition of H₂ does not change the discharge dynamic. However an increase of the H₂-pressure leads to a decrease of the time delay between the peak current and the laser peak power, owing to the increase of the HF molecule production frequency. Thus, at high concentration of H₂, the laser emission can appear before the instability onset. This explains that, at fixed $(E/N)_0$, the laser energy is an increasing function of the hydrogen pressure.

For the C₂H₆-mixture, frames B1 and B2 on figure 2, which have been acquired at the same time but for a different optical attenuation, emphasize that the active medium is homogeneous (B1) during the laser emission, and that the cathodic luminescence (B2) is homogeneously distributed along the electrode length without significative spatial gradient of intensity. Such results are obtained for any ethane pressure higher than 2 Torr: an ethane concentration above 3% induces the discharge stabilization. In that case, contrary to the H₂-mixture, the laser energy is only determined by the value of the electrical energy which can be transmitted to the active medium, and by the intrinsic kinetic of this medium such as the fluorine atoms production rate and the quenching rates of the HF ro-vibrational levels.

4. ACKNOWLEDGMENTS

The authors wish to thank the DRET for its financial support through contract No. 93/34092.

5. REFERENCES

1. T. Jacobson and G. Kimbell, "Transversely pulse-initiated chemical lasers: atmospheric-pressure operation of an HF laser", *J.Appl.Phys.* **42**, 3402-3405 (1971).
2. H. Brunet, M. Mabru, J. Rocca-Serra and C. Vannier, "Pulsed HF chemical laser using a VUV photo-triggered discharge", *Proc.SPIE* **1397**, 273-276 (1990).
3. V. Puech, P. Prigent and H. Brunet, "High-efficiency, high-energy performance of a pulsed HF laser pumped by photo-triggered discharge", *Appl.Phys.B* **55**, 183-185 (1992).
4. F. Doussiet, M. Legentil, S. Pasquiers, C. Postel, V. Puech, L. Richeboeuf, "Investigations of a photo-triggered HF laser", *Proc.SPIE* **2702**, 179-190 (1996).
5. L. Richeboeuf, F. Doussiet, M. Legentil, S. Pasquiers, C. Postel, V. Puech, "Study of the chemical HF laser pumped by a photo-triggered discharge", to appear in *Proc. SPIE* **2788** (1996).
6. R. Riva, M. Legentil, S. Pasquiers and V. Puech, "Experimental and theoretical investigations of a XeCl photo-triggered laser", *J.Phys.D* **28**, 856-872 (1995).

**Pulsed-periodical chemical laser based on chain reaction of fluorine and hydrogen
with pulse energy near 5 kJ and repetition rate near 1Hz**

S.D.Velikanov, G.A.Kirillov, M.V.Sinitzyn, V.D.Urlin, V.V.Shchurov

Russian Federal Nuclear Center (VNIIEF), 607190, Sarov, Nizhni Novgorod Region, Russia
Fax: (831) 30 54565; Phone: (831) 30 56646, e-mail: velikan_2566@rfnc.nnov.su

ABSTRACT

The characteristics of 45 litres active volume chemical laser, which chain reaction was initiated by two contrary electron beams with 1 Hz repetition rate, have been investigated. Maximum single pulse energy was about 5 KJ, radiation divergence - near 10^{-4} rad.

Keywords: chemical laser, electron beam, pulsed-periodical regime, divergence of radiation, energy of radiation.

1. INTRODUCTION

The hopefulness of pulsed chemical lasers using the chain reaction of fluorine with hydrogen to create the inversion of population, from the point of view of obtaining the high specific output energy and physical efficiency, has been performed already in 70th for the small pilot models by many investigators [1, 2].

Laser pulses of several kilojoules energy can be obtained only under the next four conditions:

- use of an actuating mixture with a large volume;
- use of a gas mixture with high concentrations of fluorine and hydrogen;
- use of a high power source for initiation of the chemical reaction;
- use of an actuating mixture with the optimum composition, for which the maximum population inversion occurs after the initiation and chemical reactions.

The results of the experimental investigation of pulsed-periodical chemical laser with near 45 litres volume and electron beam initiation of a chain reaction of fluorine with hydrogen, are performed in this paper.

The difficulties of the preparation of a high pressure hydrogen fluoride mixture, at first rate in a large volume, have hindered many investigators to make a laser with high output power.

We together with the employees of the Russian Scientific Centre of Applied Chemistry (St. Petersburg) have developed the technology for preparation of high-concentrated hydrogen fluoride mixtures ($P_{F_2} = 1$ atm) in a large volume. This serve as a basis for making up a high power laser.

An electron beam is one of the most available methods to initiate the chemical reaction in a laser volume. Accelerators possess a high intrinsic technical efficiency (near 60...70%) [3], that is promising for obtaining the high efficiency of a laser. We used the large cross section electron beams propagating across the optical axis of the laser. Such method is more advantageous than axial initiation [4] in energy respect, because of there is no necessity to make an external magnetic field, confining the electron beam, and, consequently, the high technical efficiency of laser can be reached.

In the paper [5] we have determined experimentally an optimal composition of the actuating mixture of the laser from the point of view of achieving the maximum output energy. This composition is: $F_2:H_2:O_2:SF_6 = 4:1:x:5$, where x is a maximum possible value, conditioned by the mixture preparation technology.

2. EXPERIMENTAL SET-UP

The scheme of the pulsed-periodical chemical laser is performed on the Fig.1. The steady pulsed-periodical operation regime was achieved by such a choice of method to change the mixture, for which the combustibles flow is interrupted after each initiation. The portions of combustible ($H_2 + SF_6$) mixture and inert substitute ($He + SF_6$) mixture were brought alternatively from the special containers by means of valves, switching on with driving block according to certain algorithm, into the continuous flow of oxidiser ($F_2 + O_2 + SF_6$). This method of supplying the mixture components prevented up-flow movement of combustion [6].

The system of flow formation was destined for mixing the components and organising the homogeneous flow with required structure and pressure and with a minimum level of optical nonuniformities.

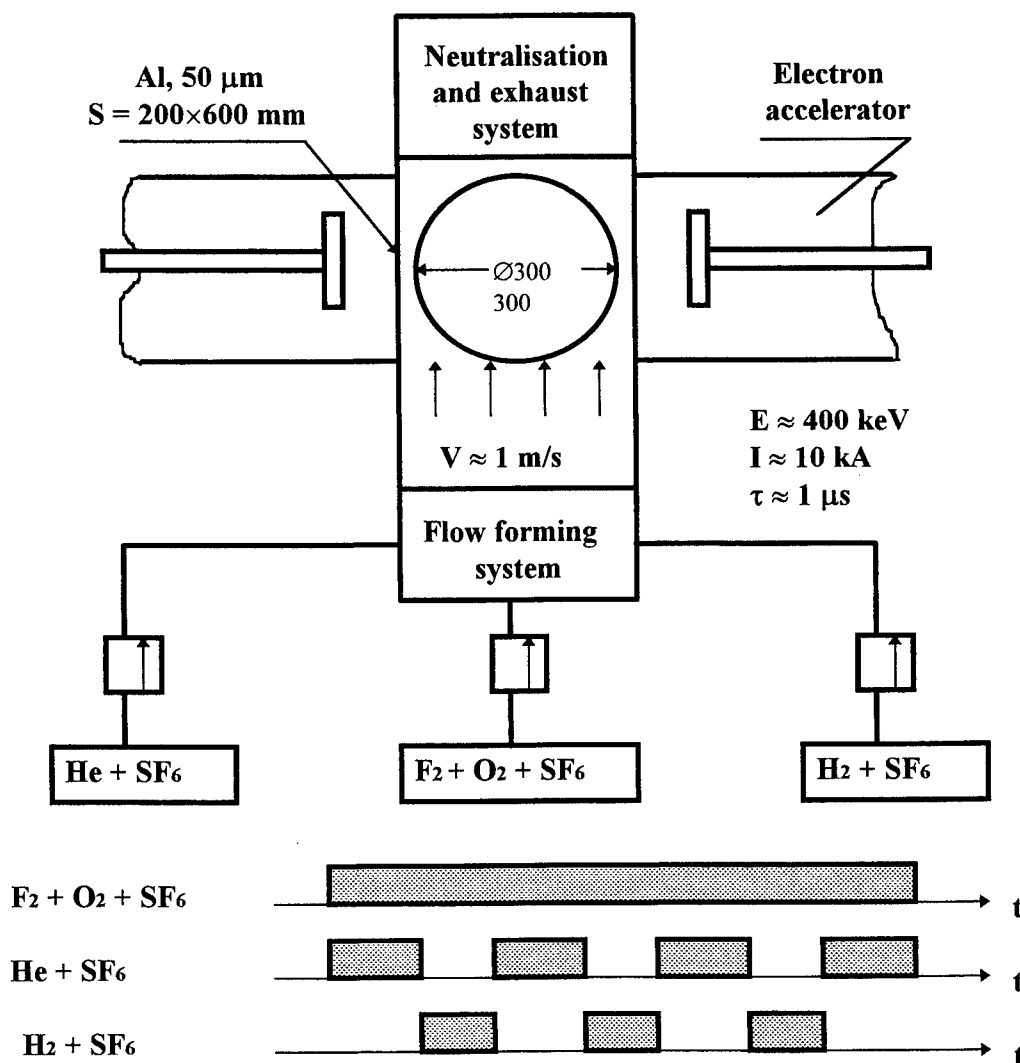


Fig.1. Scheme of pulsed - periodical chemical laser

Flow velocity from 0,7 to 1,0 m/sec in the resonator volume permitted to remove with high efficiency the postreaction mixture from resonator volume between the initiation pulses repeating with the 1 Hz rate.

The chemical reaction was initiated by two contrary beams obtained with two accelerators, that emitted the electron beams with (20*60) sq.cm cross section. The duration of the electron current pulse was near 1 μ s and the maximum energy of the electrons of beam was near 400 keV.

The optical aperture of laser was equal to 300 mm, and active volume constituted near 45 liters. Both resonator of plano configuration and unstable telescopic one were used in the experiments.

After initiation, the waste mixture entered the system of exhaust and neutralisation, where toxic and aggressive components were treated.

During the preliminary experiments the composition of the actuating mixture, which is optimum for the achieving maximum output energy parameters of laser, has been determined as: $F_2 : H_2 : O_2 : SF_6 = 4 : 1 : x : 5$ [5]. This composition was used in all described herein experiments. The density of mixture was varied by changing the pressure and oxygen contents.

The resonator of plano configuration was arranged by the pile of three fluorite plates (output mirror) and copper mirror. The effective reflection coefficients of mirrors were $R_1 = 0,16$ and $R_2 = 0,94$.

3. EXPERIMENTAL RESULTS

Series of experiments was carried out on determination of the influence of mixture density upon the laser energy. The results are performed on the Fig.2. As the electron beam energy, deposited in gas, is proportional to the medium density, along with an increase of the latter should occur the increase of the laser output energy. The maximum of energy of generation was obtained in our experiments for the mixture density $\rho \approx 2$ g/l. A further density increase produced the decrease of the output energy, because of the appearance of the space charge in the medium resulting in the electron beam locking. This phenomenon has been investigated by us in details [7], and was confirmed by the character of the near-field distribution of the laser energy.

Further experiments, aimed to increase the specific output energy and total output energy in the given apparatus at the expense of the decrease of the oxygen content, were carried out at the $\rho \approx 2$ g/l density of the actuating mixture. The dependence of laser per pulse energy upon the oxygen contents in the mixture is shown on the Fig.3 (curve 1).

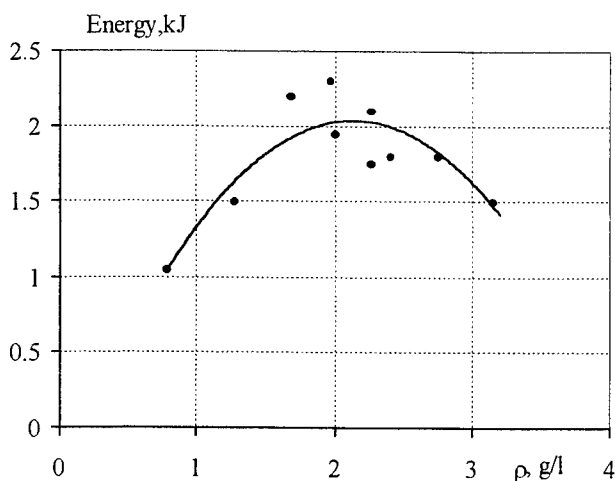


Fig.2. Dependence of laser energy on the mixture density ($F_2 : H_2 : O_2 : SF_6 = 4 : 1 : 0,4 : 5$)

The technological polishing of the mixture change system enabled us to reduce the oxygen contents in the mixture flow up to $\xi = [O_2]/[F_2] = 1\%$ and to obtain the $E = 5,9$ kJ per pulse energy for the average specific output energy $\varepsilon \approx 130$ J/l.

Energy distribution for the end face of laser, received in one of the experiments performed with the oxygen contents $\xi = 1\%$, is shown on the Fig.4.

Experimental data have shown, that for near 75% of the area of the laser end face, the value of the specific output energy exceeded 150 J/l. Zones with the specific output energy in 2 or more times lower than the average value occupied the peripheral areas of the aperture, and their area was less than near 10% of the total one. The highest specific output energy, equal to $\varepsilon \approx 223$ J/l, was achieved near the anodes of the accelerators.

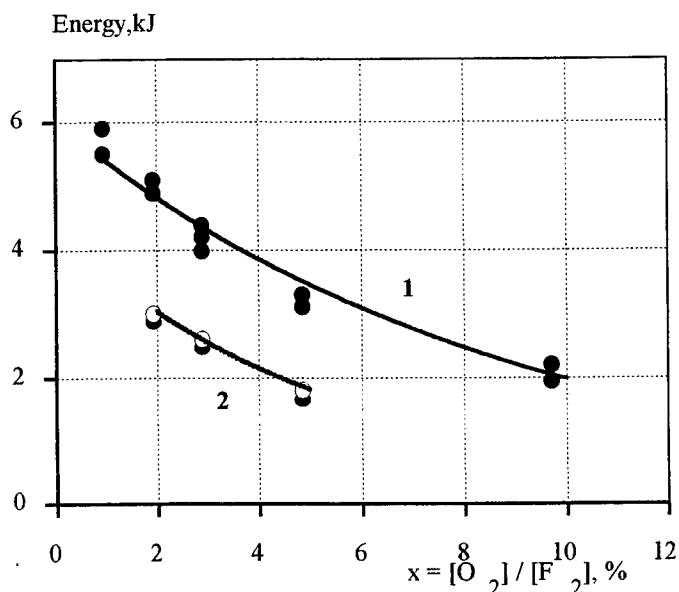


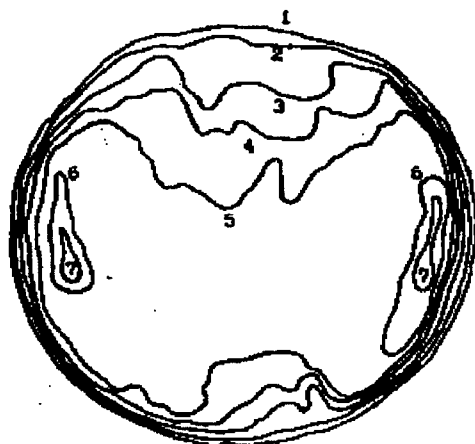
Fig. 3. Dependence of laser energy on the oxygen contamination in mixture $\rho = 2\text{g/l}$; 1 - resonator of plano configuration; 2 - unstable resonator

divergence of the laser radiation for an unstable resonator is a sum of the divergence resulting from the diffraction losses (θ_d) and the divergence stipulated by optical nonuniformities (θ_{ou}):

$$\theta_{ur} = \theta_d + \theta_{ou} = \frac{2,44 * \lambda}{D} + \frac{2 * La * \text{grad}(n)}{1 - 1/M}, \quad (2)$$

where λ - wave length of radiation, D - diameter of actuate volume, $\text{grad } n$ - gradient of refractive index, M - multiplicity of the resonator telescope magnification.

Experiments have shown, that gradient of a refractive index for our apparatus didn't exceed $\text{grad } n \leq 5 * 10^{-7} \text{ cm}^{-1}$ in the course of initiation and chemical reactions. Consequently, for the $M = 4$, $D = 300 \text{ mm}$ and $D = 640 \text{ mm}$ one could expect to obtain the divergence $\theta_{ur}^{\text{calc}} \cong 1 * 10^{-4} \text{ radn}$.



Isolevel numbers	Output area, %	Laser energy, %	Extracted energy, J/l
1 - 2	4.6	0.9	25.4
2 - 3	9.7	4.8	64.5
3 - 4	12.5	9.4	98.3
4 - 5	26.6	25.9	127.6
5 - 6	43.9	54.4	162.8
6 - 7	2.7	4.6	223.4

Fig. 4. Output end energy distribution

Besides energy, there is another important parameter of laser, namely - divergence. For the resonator of plano configuration it is determined by the value of mixture refractive index (Δn) and the ratio of the lengths of the actuating medium (La) and of the resonator (Lr) [8]:

$$\theta_{\text{fr}} = 2 * \sqrt{2\Delta n La / Lr} \quad (1)$$

The values of above parameters under our experimental conditions were $\Delta n \cong 6 * 10^{-7}$, $La/Lr = 0.3$, so the calculated quantity of divergence constitutes $\theta_{\text{fr}}^{\text{calc}} = 1,2 * 10^{-3} \text{ rad}$. The angular distribution of the output energy is shown on the Fig. 5 (curve 1). Some excess of the experimentally recorded divergence over the calculated one can be attributed to an error of manufacturing and tuning of mirrors of resonator.

Use of unstable telescopic resonator instead of that of plano configuration is an effective method of laser radiation divergence improving. The

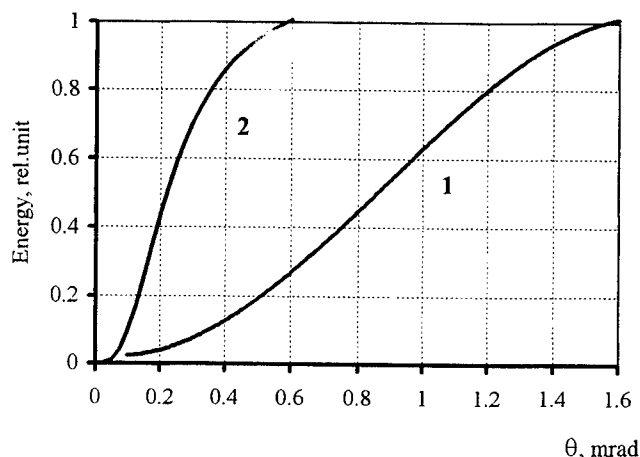


Fig.5. Dependence of laser energy on the divergence

Series of experiments was carried out using an unstable resonator, made of the copper mirrors with the radii of curvature, first, of the concave mirror $R=8017$ mm and, second, of the convex mirror $r = 2014$ mm ($M = 3,98$). It was found that for the optimum mixture density ($\rho = 2,0$ g/l) the laser energy decreased by near 40% as compared with energy, obtained with the resonator of a plano configuration (Fig.3, curve 2).

Angular dependence of laser energy is shown on the Fig.5 (curve 2). It is seen, that transit from the resonator of plano configuration to the unstable one decreased the divergence by a factor of near 4, and the latter constituted $\theta_{ur} \approx 3 \cdot 10^{-4}$ radn. The brightness of radiation increased, approximately, by an order at that.

4. CONCLUSION

So, as a result of performed investigations of the operational regime and output characteristics of a pulsed-periodical chemical laser with an active volume near 45 liters, initiated by two contrary electron beams with a large cross section, we have obtained:

- the stable pulsed-periodical operational regime of the chemical laser with the 1 Hz repetition rate.
- dependencies, governing the laser energy characteristics, as the mixture density and contents of oxygen were varied.
- the laser energy near $E \approx 5,9$ kJ achieved for the average specific output energy $\varepsilon \approx 130$ J/l.
- the angular characteristics of laser radiation were studied. It was shown, that use of unstable resonator with multiplicity of telescope magnification $M \approx 4$ instead of that of plano configuration produced near 4-times decrease of divergence and near one order increase of brightness of laser radiation.

REFERENCES

1. A.S.Bashkin, A.N.Oraevsky, V.N.Tomashov, N.N.Yurishev, "A study into feasibility of high specific parameters of the chain-reaction HF laser action", *Quantum Electronics*, **9**, N3, 628-630 (1982).
2. J.A.Mangano, R.L.Limpaecher, J.D.Daugherty, F.Russel, "Efficient electrical initiation of HF chemical laser", *Appl. Phys. Lett.*, **27**, N5, 293-295 (1975).
3. F.Ya.Zagulov, V.Ya.Borisov, G. Ya. Vlasov et al, "Pulsed high-current nanosecond electron accelerator operating with repetition rate 100 Hz", *Pribory i tekhnika eksperimenta (Devices and technique of experiment)*, N5, 18-21, (1975).
4. R.A.Gerber, E.L.Patterson, L.S.Blair, N.R.Greiner, "Multi-kilojoule HF laser using intense-electron-beam initiation of HF-DF mixtures", *Appl. Phys. Lett.*, v.25, 281 (1974).
5. S.D.Velikanov, S.B.Kormer, M.V.Sinitzyn et al, "Influence of multi-atomic gases on the efficiency of operation of photoinitiated chemical HF laser", *Pisma v ZTF (Letters to JTF)*, **9**, v.3, 34 (1983).
6. V.V.Burtzev, S.D.Velikanov, Yu.N.Frolov, "Propagation of combustion in mixtures of pulse-periodic chemical lasers based on the reaction of fluorine with hydrogen", *Quantum Electronics*, V.22, N2, 123-126, (1995).
7. Bashurin, S.D.Velikanov, A.Ya.Dovgiy et al, "On propagation of electron beam through electronegative gases", *Doklady AN SSSR (Reports of Scientific Academy of SSSR)*, **287**, N3, 614-618 (1986).
8. G.A.Kirillov, S.B.Kormer, G.G.Kochemasov et al, "Investigations on divergence for an output of the photodissociated optical parametric oscillator with nonuniform active medium", *Quantum Electronics*, v.2, N4, 666-671 (1975).

13. Laser Welding

Invited Paper

Laser welding of aluminium

H. Hügel, M. Beck*, J. Rapp, F. Dausinger

Universität Stuttgart, Institut für Strahlwerkzeuge (IFSW),
Pfaffenwaldring 43, D-70569 Stuttgart, Germany

*Current address: Daimler Benz AG,
Forschungszentrum F4P/P, D-89013 Ulm, Germany

ABSTRACT

The role of laser beam parameters and material properties in establishing a stable deep welding process is investigated, experimentally and theoretically. Particular emphasis is placed on the mechanisms involved in the energy coupling. It will be shown that high quality welds are achieved by a proper choice of parameters and a sophisticated process conduction.

Keywords: laser welding, laser weldability of aluminium, energy coupling, process stability

1. INTRODUCTION

Requirements such as the reduction of weight and cost or the possibility to recycle materials have led to novel approaches for light-weight construction. In this context, aluminium and its alloys are facing increasing interest in the automotive and rail vehicle industry. Laser welding as a joining technique brings along many advantages compared with conventional technologies. In particular, it allows an economical realisation of design and production concepts based on tailored blanks and space-frame constructions. In order to be accepted for industrial mass production, the process has to demonstrate maturity regarding efficiency and quality of its results. Some investigations aimed at this goal will be reported herein.

Compared to the welding process of steel that of aluminium turns out to be much more complex due to material properties such as a low absorptivity, high heat conductivity as well as the effect of various alloy components on vaporisation temperature. In addition, the achievable weld quality - assessed in terms of porosity or hot cracks, strength etc. - strongly depends on the material composition. Since the particular alloy will be chosen according to the requirements stemming from a specific application, it is, therefore, absolutely necessary to handle the weldability of aluminium alloys in an integral approach incorporating aspects of the process, metallurgy and design at the same time, see Ref. 1, 2 (as well for a detailed discussion of static and dynamic strength). Here, the discussions will be focused on the welding process itself.

In the experimental studies, both modern CO₂- and Nd:YAG-lasers were used and have proven to be adequate tools. The results not only provide applicable data for a variety of welding tasks but also give useful indications regarding the potential of the particular laser type.

2. ENERGY COUPLING

2.1 Threshold conditions

The mechanisms involved in the formation of a keyhole as the precondition of the deep penetration welding process and the ways by which laser energy is deposited at its wall are relatively well understood, today. Along the ideas elaborated in e.g. references 3 to 8 (the latter also giving a good summary of the relevant literature), the primary energy coupling is due to Fresnel absorption as the beam penetrates into the material by multiple reflections. The fraction of heat that is conducted from the keyhole plasma to the wall strongly depends on the keyhole geometry (which in itself is a result of the interacting process parameters), the material properties and the laser beam's wavelength^{6,8}.

Keyhole formation will set in when the material under the irradiated spot has reached vaporisation temperature. From a balance between absorbed and dissipated energy the useful relation can be found (approximately valid also for not too high welding speeds) $P/d_f \propto T_v k/A$, with P the incident laser power, d_f the spot diameter at the surface, T_v the vaporisation temperature, k the heat conductivity, and A the absorptivity. The calculated and experimentally found threshold behaviour as depicted in Figs. 1 and 2 fairly well reflects these dependencies. In addition, for a variety of aluminium alloys a direct proportionality between the threshold intensity and the product $T_v k$ is evident, see Fig. 3. In this representation, the measured data (obtained with CO₂-laser) is taken from Ref. 9 whereas the material properties (in particular the reduction of T_v by volatile elements, such as Mg, Zn, Li) were calculated by means of a theoretical model^{10,11}.

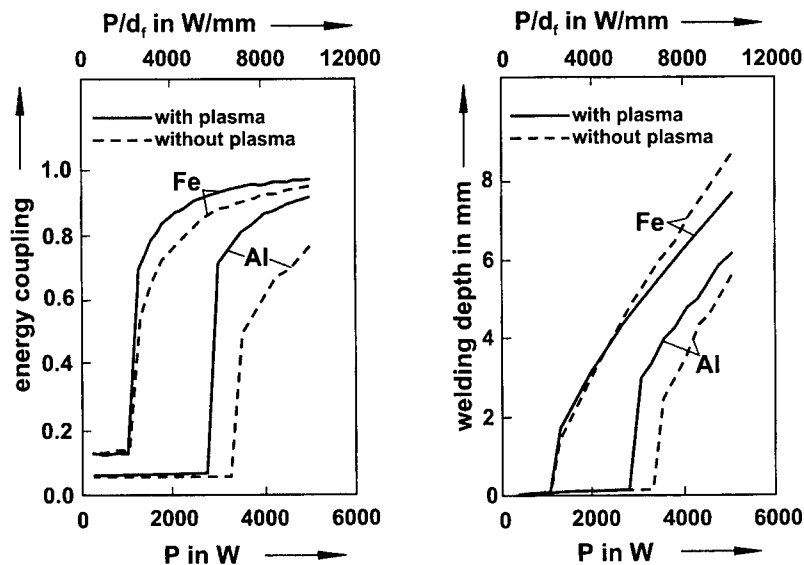


Fig. 1. Calculated energy coupling and welding depth as a function of incident laser power; Laser: CO₂, TEM₀₁; $d_f=0.48$ mm, $v=2$ m/min.

It is seen from Fig. 1 that the laser induced plasma in the case of aluminium lowers the threshold via enhanced energy coupling. Furthermore, it should be born in mind that different surface conditions (roughness, oxide layer) modify the absorption and, above all, the „effective“ spot diameter is not known because of refraction effects within the plasma plume above the workpiece^{8,11,12}. This means that with the Fresnel absorptivity in the above relationship can be expected qualitative agreement with experiments only. Nevertheless, this scaling yields useful first estimations regarding the required laser parameters.

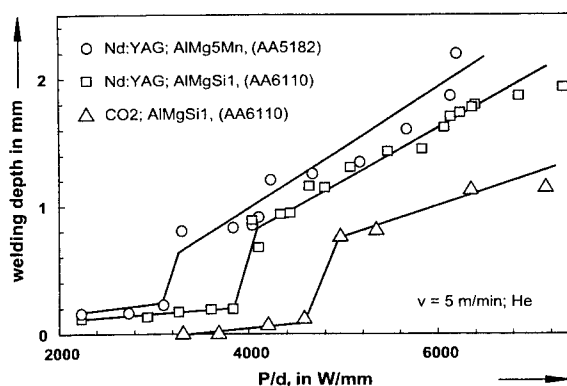


Fig.2. Experimental welding depth; the threshold depends on wavelength and material composition.

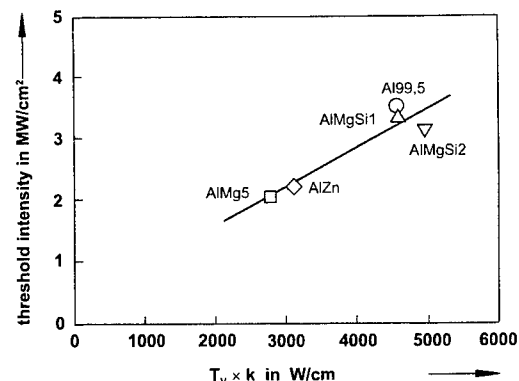


Fig.3. Experimentally determined (Ref. 9) threshold values of aluminium alloys as a function of calculated material properties.

2.2 Efficiency considerations

The favourable effect of a slender keyhole with respect to high energy coupling is demonstrated in Fig. 4. The theoretical curve for a cone-shaped keyhole^{8, 13} is obtained utilising and modifying an expression given in Ref. 14 for the total absorption in a spherical hole; the result agrees remarkably well with that of the self-consistent model described in Ref. 6. Herefrom a clear demand for lasers with high beam quality (small spot diameters and large Rayleigh length achievable with reasonable F-numbers) can be inferred.

Further has to be considered the thermal efficiency of the process, namely that fraction of absorbed energy which was utilised to achieve the weld seam intended; Fig. 5 presents typical data. The theoretical curves are based on a model¹⁵ assuming uniform heat release (P/d) along a line-source being moved through the material. It is seen that more than twice the absorbed (!) power is needed for aluminium in comparison to steel in order to obtain the same thermal efficiency. In view of the required equipment for performing a given task, the data in Fig. 5 provide an useful hint.

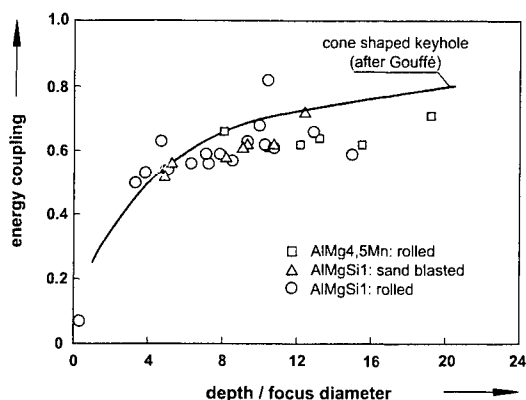


Fig.4. Energy coupling depending on the slenderness of the keyhole; CO₂, P_L ≈ 4 kW.

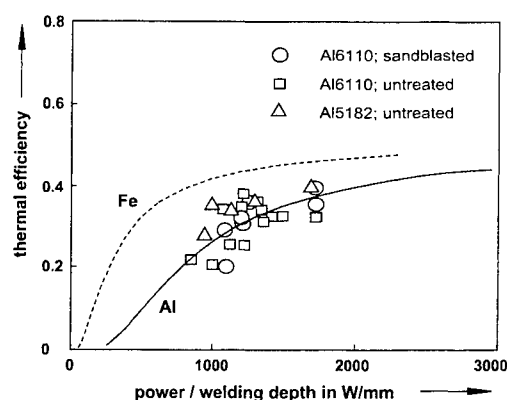


Fig.5. Thermal efficiency as function of power per unit penetration depth.

3. PROCESS STABILITY AND QUALITY OF THE WELD SEAM

3.1 Possible causes of instability

It is generally agreed that process instabilities give rise to imperfections of the weld seam. Due to the complexity of the welding process as a whole, there is neither complete understanding of the possible causes leading to the results observed nor exists a theory that would explain the phenomena in their entirety. A number of models has been developed instead, addressing particular aspects such as e.g. keyhole/plasma interaction¹⁶, keyhole/melt pool dynamics¹⁷ or fluid dynamic phenomena associated with the melt flow around the keyhole and induced by surface tension^{18, 19}. Here, some qualitative lines of reasoning shall be presented that explain cavities/pores (not hydrogen pores which are due to metallurgical causes) and blowholes originating from instabilities of the keyhole²⁰.

The higher sensitivity of the aluminium welding process (compared to that of steel) to fluctuations in laser power or plasma induced variations of the spot diameter¹¹ is easily understood in view of the messages given in Figs. 1, 2 and 4: If the welding process is conducted with parameters yielding conditions not well above threshold, then relatively small perturbations in P and/or d_f lead to drastic changes in energy coupling. Hence, the energy balance in the keyhole as well is disturbed with all the consequences for the rate of vaporisation, keyhole geometry, momentum balance etc. A wavelength of 1.06 μm in comparison to 10.6 μm does enlarge the processing window in two respects, namely the threshold is lowered as a consequence of the higher Fresnel absorptivity and effects of the plasma above the keyhole (refraction, absorption) are less severe because the absorption coefficient in the plasma approximately scales at λ^2 , see references 8, 13 and 21.

Following the ideas developed in Ref. 8, a keyhole geometry with a cross section increasing from bottom to the surface is favourable for a stable process. In Fig. 6 the pressure distribution for two different keyhole forms (type 1 and 2) is presented. It results from a model calculation taking into account momentum and mass conservation and (instead of using the energy equation), the vapour temperature as a parameter. The physical reason for the pressure rise in the region of the keyhole's constriction is the fact that here the pressure exerted on the wall as a consequence of the surface tension in the melt is higher ($\propto r^{-1}$) and has to be compensated by a higher pressure within the keyhole. The corresponding vapour velocities in Fig. 7, considering friction effects at the wall, among others reflect the temperature dependency of the viscosity and because ionisation has been taken into account as well, the sensitivity of the vapour-plasma to the wavelength. As is seen for the type 2 geometry both effects, the pressure rise due to the constriction and the friction decelerate the flow and, in case of high temperature even might lead to a complete choking and flow reversal. If the vapour does not condense fast enough, the keyhole volume must increase. This will occur in regions with least energy expenditure, i.e. down of the constriction, and at the same time, the constriction's radius decreases leading to an increased pressure rise due to surface tension. It is well conceivable that such a mechanism with positive feedback of events is the cause for process instabilities producing cavities/pores, blowholes and irregular roots.

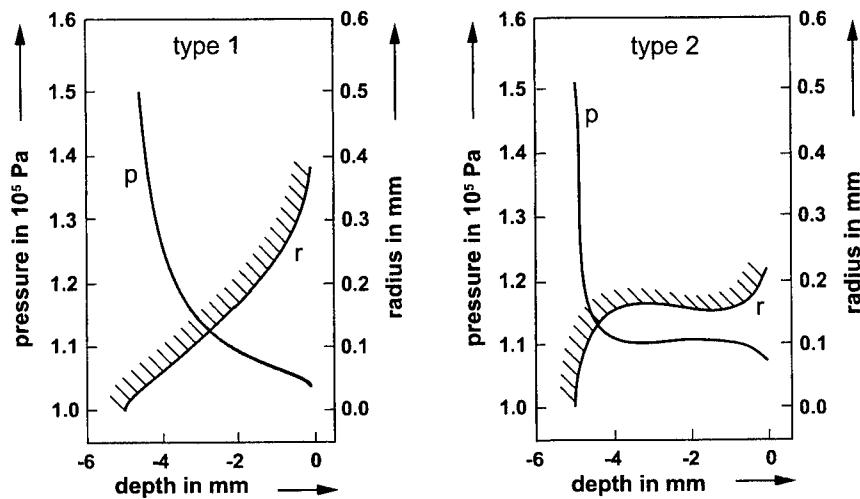


Fig.6. Pressure distribution in keyholes (Fe) with different geometry $r(z)$.

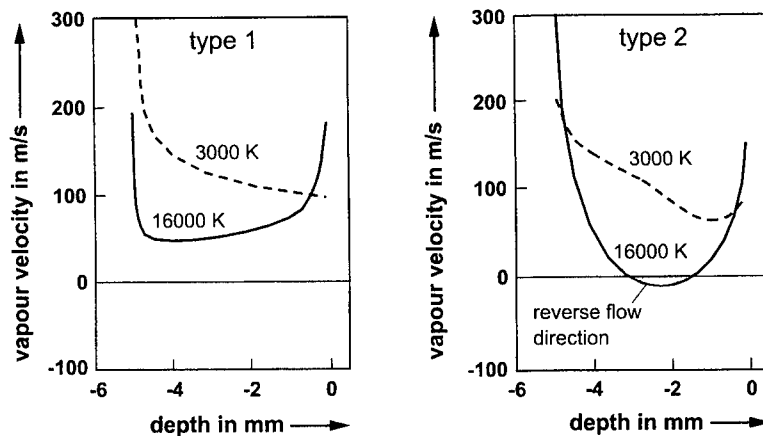


Fig.7. Velocity of metal vapour in dependence of keyhole geometry (Fig. 6) and vapour temperature.

3.2 Measures to improve process stability

In view of the above argumentation, two straight forward measures appear to be evident for improving the process stability. One measure has already been mentioned, i.e. the use of lasers with shorter wavelength which, in fact, has proven to be a most promising approach²⁰. Here, due to a far lower absorption coefficient of the plasma for $1.06\text{ }\mu\text{m}$, its temperature will be lower as compared to welding with $10.6\text{ }\mu\text{m}$ ^{22, 23} allowing for an undisturbed vapour/plasma flow out of the keyhole (see dashed curves in Fig. 7). The other one is a „shaping“ of that kind of keyhole where the type 1-like geometry is realised.

This can easily be done by utilising two laser beams^{2, 20, 24} (remember the requirement of a high value P/d_f) focused on to the workpiece surface with spot diameters and distance between their centres depending on the particular task. By this technique, a stable and in welding direction enlarged keyhole is established yielding weld seams of high quality¹. It is applicable for both CO_2 - and Nd:YAG-lasers and can be modified by beam splitting provided a sufficient power level is available.

It is further experienced that the use of filler wire - primarily applied because of metallurgical reasons - also exerts a stabilising effect on the process^{2, 20, 25}. Some speculations of possible causes are to be found in Ref. 25.

Fig. 8 summarises the results of achieving high-quality weld seams; it represents the average of a seam length between statistically occurring blowholes. It is seen that the twin focus technique yields the best results, by far. Further investigations to this aspect are still in progress.

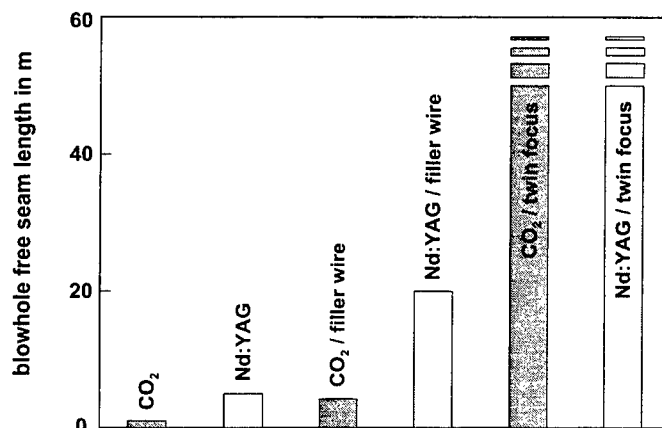


Fig.8. Effect of possible measures to improve seam quality via enhanced process stability.

4. CONCLUSIONS

Laser welding of aluminium alloys requires a careful choice and adaptation of laser beam properties with respect to the specific requirements stemming from material and design. Lasers with high power (resp. high value P/d_f) and high beam quality (small d_f and slender focal geometry) are favourable in view of efficiency and stability. A short wavelength is favourable for reducing threshold conditions and enhancing the process stability. The use of filler wire and, above all, the application of the twin focus technique are efficient means to produce weld seams of high quality.

5. REFERENCES

1. J. Rapp, *Laserschweißbeignung von Aluminiumwerkstoffen für Anwendungen im Leichtbau.*, Forschungsberichte des IFSW, Teubner, Stuttgart, 1996.
2. J. Rapp, C. Glumann, F. Dausinger and H. Hügel, "Laser welding of aluminium lightweight materials: problems, solutions, readiness for application", *Opt. and Quantum Electronics* **27**, 1203 (1995).
3. C. Banas, "High power laser welding", *The Industrial Laser Annual Handbook*, 1986, Penn Well Publ. Corp., 1986.
4. I. Miyamoto, H. Maruo, Y. Arata, "Beam absorption mechanism in laser welding", SPIE, Vol. 668, p. 11, 1986.
5. M. Schellhorn, "Mathematical simulation of welding processes", *Proc. Europ. Scientific Laser Workshop on Math. Simulation*, p. 225, Sprechsaal Publishing Group, 1989.
6. M. Beck, F. Dausinger, H. Hügel, "Studie zur Energieeinkopplung beim Tiefschweißen mit Laserstrahlung", *Laser und Optoelektronik* **21**, p. 80, 1989.
7. A. Kaplan, "A model of deep penetration laser welding based on calculation of the keyhole profile", *J. Phys. D: Appl. Phys.* **27**, 1805 (1994).
8. M. Beck, *Modellierung des Lasertiefschweißens*, Forschungsberichte des IFSW, Teubner, Stuttgart, 1996.
9. H. Sakamoto, K. Shibata, F. Dausinger, "Laser welding of different aluminium alloys", *Proc. ECLAT'92*, DGM, p. 125 (1992).
10. J. Rapp, M. Beck, F. Dausinger, H. Hügel, "Fundamental approach to the weldability of aluminium- and copper-alloys", *Proc. ECLAT '94*, DVS-Bericht 163, p. 313 (1994).
11. M. Beck, M., P. Berger, H. Hügel, "The effect of plasma formation on beam focusing in deep penetration welding with CO₂ lasers", *J. Phys. D: Appl. Phys.* **28**, p. 2430 (1995).
12. R. Duchanne, P. Kapadia, J. Dowden, "A mathematical model for the deforming of laser light above a workpiece in laser material processing", *Proc. ICALEO '92*, Laser Institute of America, p. 187 (1992).
13. F. Dausinger, *Strahlwerkzeug Laser: Energieeinkopplung und Prozeßeffektivität*, Forschungsberichte des IFSW, Teubner, Stuttgart, 1995.
14. A. Gouffé, "Corrections d'ouverture des corps-noirs artificiels compte tenu des diffusions multiples internes", *Rev. Optique* **24**, p. 1 (1945).
15. D.T. Swift-Hook, A.E.F. Gick, "Penetration welding with lasers", *Welding Research Supplement* **493-s**, p. 492 (1973).
16. T. Klein, M. Vicanek, J. Kroos, I. Decker, G. Simon, "Oscillations of the keyhole in penetration laser beam welding", *J. Phys. D: Appl. Phys.* **27**, p. 2023 (1994).
17. J. Griebisch, *Grundlagenuntersuchungen zur Qualitätssicherung beim gepulsten Lasertiefschweißen*, Forschungsberichte des IFSW, Teubner, Stuttgart, 1996.
18. M. Beck, P. Berger, F. Dausinger, H. Hügel, "Aspects of keyhole/melt interaction in high-speed laser welding", *Proc. 8. Int. Conf. on Gas Flow and Chemical Lasers 1990*, SPIE 13977 (1991), p. 769.
19. N. Pirch, H. Schmidt, B. Ollier, E. Kreutz, D. Becker, "Die Humping Instabilität beim Schweißen und Laserstrahlung", *Proc. of LASER '91*, p. 552, Springer (1992).
20. F. Dausinger, H. Hügel, "Prozeßadäquate Systemtechnik als Schlüssel für das Aluminiumschweißen", *Proc. 12. Int. Cong. LASER '95*, p. 211, Meisenbach-Verlag, Bamberg (1995).
21. P. Mulser, "Hydrogen plasma production by giant pulse laser - A theoretical study", Inst. f. Plasmaphysik, Internal Study IPP3/95 (1969).
22. H.C. Peebles, R.L. Williamson, "The role of the metal vapor plume in pulsed Nd:YAG laser welding of aluminium 1100", *Proc. LAMP '87*, vol. 1, p. 19.
23. T.J. Rockstroh, J. Mazumder, "Spectroscopy studies of plasma during cw laser materials interaction", *J. Appl. Phys.* **61**, p. 917 (1987).
24. C. Glumann, J. Rapp, F. Dausinger, H. Hügel, "Welding with a combination of CO₂-lasers - advantages in processing and quality", *Proc. ICALEO '93*, Laser Institute of America, p. 672, 1993.
25. Ch. Binroth, "Beitrag zur Prozeßstabilität beim CO₂-Laserstrahlschweißen von Aluminium mit Zusatzwerkstoff", *Strahltechnik* Vol. 1, BIAS, 1995.

M. Schellhorn and A. Eichhorn

Deutsch-Französisches Forschungsinstitut ISL
5, rue du Général-Cassagnou
F-68301 Saint-Louis, France

ABSTRACT

Average electron densities and temperatures were measured for both CO and CO₂ laser induced aluminum welding plasmas using spectroscopic techniques. The plasma temperature is smaller in the case of CO laser welding, whereas the electron density is slightly higher. Therefore the absorption length (inverse bremsstrahlung) of the CO laser radiation in the welding zone is a factor of 2 to 7 longer. This is the reason for the better weld seam quality obtained with the CO laser.

Keywords: CO laser, CO₂ laser, aluminum laser welding, plasma spectroscopy

1. INTRODUCTION

Up to now carbon monoxide (CO) lasers have not yet found a place in industrial applications although they offer with their wavelength around 5 μm an attractive compromise between the attributes of CO₂ and Nd:YAG lasers, particularly through their potential for very high power and efficiency¹, possibly high power transmission through chalcogenide glass fibres^{2,3} and improved processing⁴. Especially in laser welding of aluminum which is a major research subject in industry the processing range for the CO₂ laser is small^{5,6}. The maximum usable process intensity is limited by the onset of a statistically appearing shielding plasma leading to weld defects, such as porosities and crater formation. Since the plasma absorption coefficient for the laser radiation is proportional to the square of the wavelength the use of a Nd:YAG laser seems to be appropriate but it suffers from an inherent bad beam quality. Therefore the application of Nd:YAG lasers in aluminum welding is limited to a sheet thickness of 2 mm because of the poorer focusability, i.e. the shorter Rayleigh length of the beam⁷. The advantages of the CO laser refer to the better focusability, the higher absorptivity of metals and lower plasma absorption by inverse bremsstrahlung. The better focusability of the CO laser results in deeper penetration in aluminum welding compared to CO₂ and Nd:YAG lasers⁸. The higher absorptivity of metals by CO laser radiation leads to a lower threshold for deep penetration welding, i.e. the CO laser can initiate a keyhole at substantial lower powers than the CO₂ laser⁹. The consequence of the lower plasma absorption of the CO laser radiation was demonstrated the first time in deep penetration welding of mild steel: no difference in welding depths was observed using helium or argon in case of the CO laser, whereas the penetration depth obtained with the CO₂ laser was drastically reduced when argon was used as the process gas¹⁰. Due to the reduced beam-plasma interaction the CO laser weld seams are characterized by a homogeneous and smooth surface⁸. First spectroscopic comparison of CO and CO₂ laser induced aluminum welding plasmas indicates lower plasma temperatures in the case of CO laser welding¹¹. In this paper we will present measured values of the average electron density and temperature for both CO and CO₂ laser induced aluminum welding plasmas. From these quantities the absorption length of the laser radiation by the effect of inverse bremsstrahlung has been calculated.

2. EXPERIMENTAL SETUP

2.1. Characteristics of CO and CO₂ laser system

The resonator of the gasdynamically cooled CO laser system^{12,13} is formed by a triple pass unstable resonator with a magnification of $M = 2$. An annular mode of approximately 28 mm outer diameter is extracted. The Strehl ratio of 0.5 and the M^2 -value of 5.8 were measured at a maximum power level of 4.5 kW.

A commercial industrial CO₂ laser (Rofin Sinar RS6000) has been used for comparison. This laser is equipped with a stable resonator and runs in the TEM₂₀ mode with a beam diameter of 24 mm ($M^2 = 4.3$).

The focus radii obtained with a $f = 125$ mm welding were measured with a beam diagnostic system (Prometec) using a rotating hollow needle and are summarized in Tab. 1. Due to the shorter wavelength of the CO laser the focus radius is

smaller resulting in a higher peak intensity. The mode of the stable CO₂ laser resonator is characterized by a steep intensity slope at the edges of the beam radius resulting in a ratio of only 1.5 between the maximum intensity and the average intensity in the focus. On the other hand the intensity distribution of the unstable CO laser mode (ring mode) shows widespread wings at the peripheric of the beam resulting in a ratio of approximately 7 between the maximum intensity and the average intensity in the focus.

2.2. Spectroscopic methods

Timeintegrated emission spectra from laser induced plasmas were measured with a prism spectrograph, a 500 mm focal length (SPEX 500) and a 156 mm focal length spectrograph (MonoSpec 18) with 1200 grooves/mm gratings and a silicon diode array detector (2048 pixels). The spectra were taken with a total accumulation time of about 1s, thus smoothing short fluctuations of the line intensities. The apparatus widths of the SPEX 500 and MonoSpec 18 are 1 Å and 2.5 Å, respectively. The light was fed into the spectrograph by means of a fibre optic with a core diameter of 1 mm. Spectra of aluminum laser welding plasma were taken at a power level of 2.5 kW and 4 kW at a feed velocity of 6 m/min for CO₂ and CO laser welding of AlMgSi1. Either helium or argon gas was used as the process gas at a flow rate of 30 and 20 l/min, respectively. A copper tube of 6 mm inner diameter mounted at an angle of 20° with respect to the surface produced a tangential flow opposite to the weld direction. The focal length of the welding head were $f = 125$ mm or $f = 200$ mm.

The electron density was estimated by the Stark-broadening method using the Al (II) line at 5593.2 Å. Assuming that the laser induced plasma is in local thermodynamic equilibrium (LTE) the temperatures can be estimated from the relative line intensities of subsequent ionization stages of the same element whereby the electron density must be known as well as from the relative line intensities from the same element and the same ionization stage. These methods are described in detail in Ref. 14. For the first method the intensity ratio of the Al (III) line at 5696.5 Å and the Al (II) line at 5593.2 Å was used. For the second method the Al (II) lines of the ³P-³D multiplet (6226.2 Å, 6231.7 Å and 6243.4 Å) and the Al(II) lines of the ³S-³P multiplet (7042.1 Å, 7056.7 Å and 7063.7 Å) was used. The energy gap between the upper levels of those spectral lines is 2 eV, thus the calculation of the temperature from the ratio of the sum of the intensities of the separated lines of each multiplet could be done with sufficient accuracy. The transition propabilities were taken from Ref. 15. The resulting temperatures using these two different methods agree within a factor of 10 %.

3. EXPERIMENTAL RESULTS

Fig. 1 shows the overview spectra of CO₂ and CO laser induced aluminum spectra at a power level of 4 kW. Helium is used as the process gas. The spectra were taken with the prism spectrograph. The CO₂ laser induced plasma consists mainly of lines of Mg (I), Mg (II), Al (II) and Al (III) transitions. In the case of the CO laser the intensities of the Al (II) lines are drastically reduced, there is no appearance of Al (III) lines and the intensity of the resonance Al (I) line is higher. This indicates that the degree of ionization in the CO laser induced plasma should be lower. Fig. 2 (a) shows a high resolved spectrum taken with the SPEX 500 spectrograph at a power level of 4 kW of the CO₂ laser (helium). Fig. 2 (b) shows the CO laser induced welding spectrum at the same power level but argon is used as process gas. In this case the Al (III) lines at 5696.5 Å and 5722.7 Å are observed, however at very weak intensities. Helium lines do not appear as in the case of CO₂ laser welding, e.g. the He (I) line at 5875.6 Å (Fig. 7a). Argon lines were observed also in CO laser welding but compared to CO₂ laser welding at much lower intensities.

Tab. 1: Measured focus radii, maximum and average intensities obtained with the $f=125$ mm focusing optic.

Laser	Power (W)	Radius r_s (μm)	I_{\max} (W/cm ²)	I_{average} (W/cm ²)
CO ₂	1750	146	$3.5 \cdot 10^6$	$2.2 \cdot 10^6$
CO ₂	3300	148	$6 \cdot 10^6$	$4.1 \cdot 10^6$
CO	2500	81	$6 \cdot 10^7$	$1 \cdot 10^7$
CO	3600	94	$7.8 \cdot 10^7$	$1.1 \cdot 10^7$

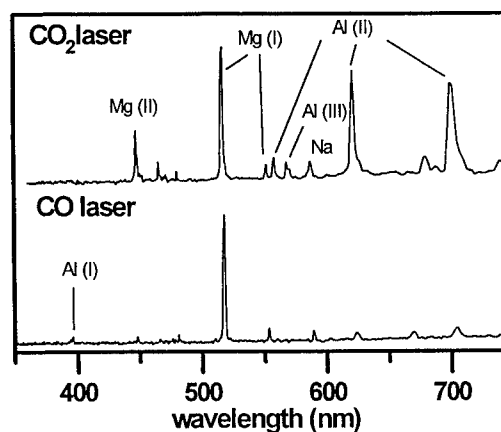


Fig. 1: Overview spectra of CO₂ and CO laser induced aluminum welding plasmas at a power level of 4 kW (helium).

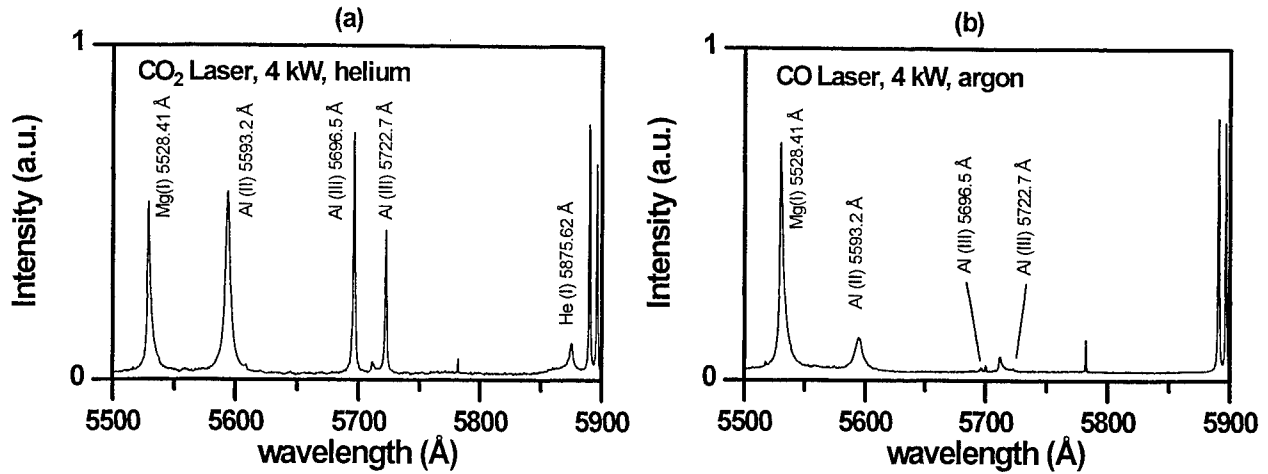


Fig. 2: Timeintegrated emission spectra of (a) CO₂ (process gas: helium) and (b) CO (process gas: argon) laser induced aluminum plasmas at a power level of 4 kW ($f = 125$ mm optic).

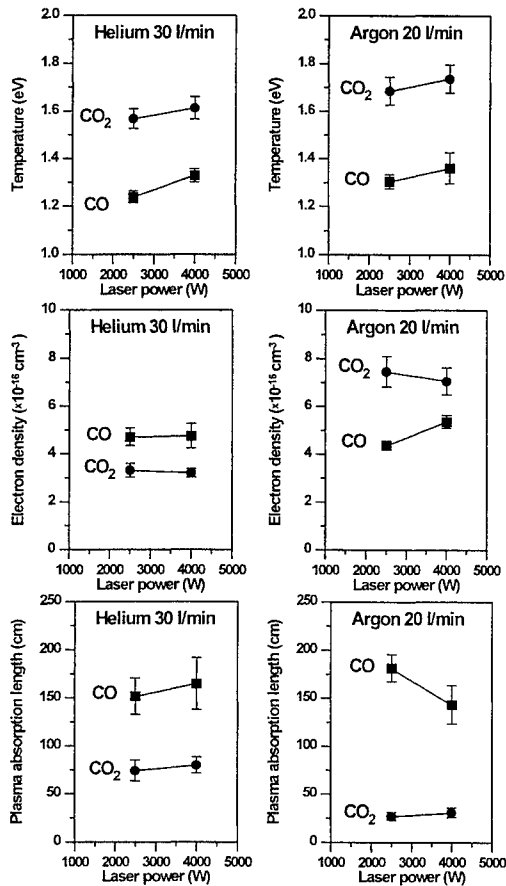


Fig. 3: Measured temperature, electron density and calculated plasma absorption length for CO and CO₂ laser induced aluminum plasmas as function of the laser power using helium or argon as the process gas ($f = 125$ mm focusing optic).

The results of the temperature and electron density measurements as well as the calculated plasma absorption length for CO and CO₂ laser induced aluminum plasmas as function of the laser power using helium or argon as the process gas are shown in Fig. 3. In the CO₂ laser induced plasmas the temperatures are in the range of 1.6 eV and the electron densities in the range of $3 \times 10^{16} \text{ cm}^{-3}$ if helium is used as process gas and 1.7 eV and $7-8 \times 10^{16} \text{ cm}^{-3}$ if argon is used. The better plasma cooling in the case when helium is the process gas is well known in the literature^{16,17} and refer to its smaller molecular mass as well as its higher heat conductivity. The energy transfer between the electrons and the process gas atoms is proportional to their mass ratio. Higher conductivity increases the heat flux from the plasma to the ambient gas. Both these factors result in the decrease of the plasma temperature which in turn causes recombination and decreases the electron density. In the CO laser induced aluminum plasmas the temperatures are considerable lower in the range of 1.3 eV (helium) and 1.35 eV (argon). The electron density is nearly independant of the nature of the process gas at a value of $5 \times 10^{16} \text{ cm}^{-3}$. From the temperature and the electron density the value of the plasma absorption length was calculated for the two laser wavelengths¹⁸. For the CO laser radiation the absorption length is a factor of 2 higher when helium is used as the process gas and a factor of 6-7 higher when argon is used. Due to the higher transparency of the laser induced plasma a smaller amount of the laser power is absorbed resulting in smaller plasma temperatures. A surprising fact is that in the case when helium is used as the process gas the electron density is higher in the CO than in the CO₂ laser induced plasma. This could be explained by the fact that at smaller temperatures the particle density is higher (assuming a plasma pressure of 1 bar) and therefore the electron density could be higher although the degree of ionization is lower. In Fig. 4 the plasma temperature is shown as a function of the peak intensity in the focus. Lower temperatures could be expected when the peak intensity will be reduced using a CO laser system with a stable resonator.

4. SUMMARY

Spectroscopy of CO and CO₂ laser induced aluminum welding plasmas was carried out. In CO₂ laser welding the average electron density increases from $3 \times 10^{16} \text{ cm}^{-3}$ (helium) to $7 \times 10^{16} \text{ cm}^{-3}$ if argon is used as process gas, whereas the average electron density in the case of CO laser welding is $\sim 5 \times 10^{16} \text{ cm}^{-3}$, independent of the nature of the process gas. The average electron temperatures are smaller in CO laser welding (1.2 - 1.3 eV) compared to CO₂ laser welding (1.6 - 1.7 eV). The calculated plasma absorption length is 2 times longer (helium) and 6-7 times longer (argon) for the CO laser radiation compared to the CO₂ laser radiation. No differences in weld performance has been observed using argon instead of helium as process gas, although the maximum intensity of the CO laser radiation in the focus region has been measured one order of magnitude higher than the intensity of the CO₂ laser radiation. Therefore the CO laser offers interesting prospects in laser welding, especially of aluminum alloys. The results are significantly better than using commercial CO₂ as well as Nd:YAG lasers.

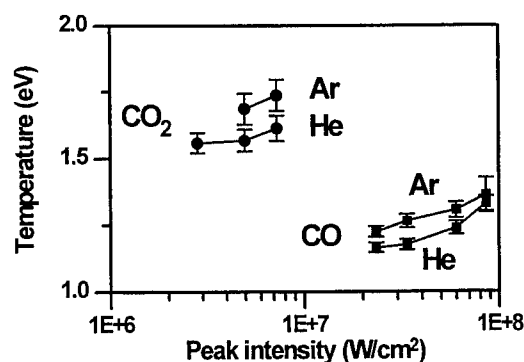


Fig. 4: Measured temperatures of CO and CO₂ laser induced aluminum plasmas as a function of the peak intensity in the focus.

5. REFERENCES

1. B.M. Dymshits, G.V. Ivanov, A.N. Mescherskiy and I.B. Kovsh, "Continuous wave 200-kW supersonic CO laser", *Proc. SPIE* **2206**, 109 (1994).
2. S. Sato, K. Igarashi, M. Taniwaki, K. Tanimoto and Y. Kikuchi, "Multihundred-watt CO laser power delivery through chalcogenide glass fibers", *Appl. Phys. Lett.* **62**, 669 (1993).
3. S. Somkuampanit, D. Su, F. Villarreal, A.D. Colley, H.J. Baker, J.D.C. Jones and D.R. Hall, "Beam delivery characteristics of optical fibres for carbon monoxide lasers", *Optics and Lasers in Engineering* **23**, 221-231 (1995).
4. F. Maisenhlder, "Material Processing by CO lasers", *Proceedings of the International Conference of Laser Advanced Material Processing (LAMP)*, Nagaoka, Japan (High Temperature Society of Japan, Osaka, 1992), Vol.1, p. 43.
5. G. Shen, G. Roth and F. Maisenhlder, "Laserschweien von Aluminium-Magnesium-Legierungen", *Laser und Optoelektronik*, **25**, 96 (1993).
6. R. Schfer, K. Behler and E. Beyer, "Improvements of energy coupling of welding aluminum by CO₂ lasers", *Proc. of the 9th Int. Congress, LASER 89*, Springer Verlag (Berlin), 544 (1989).
7. J. Rapp, C. Glumann, F. Dausinger and H. Hgel, "Laser welding of aluminium lightweight materials: problems, solutions; readiness for application", *Optical and Quantum Electronics* **27**, 1203-1211 (1995).
8. M. Schellhorn, "Application of a high power CO laser in aluminum welding", *Proc. SPIE* **2713**, 287-292 (1996).
9. B.A. Mehmetli, K. Takahashi and S. Sato, "Comparison of aluminum alloys welding characteristics with 1 kW CO and CO₂ lasers", *Journal of Laser Applications* **8** (1), 25-31 (1996).
10. M. Schellhorn and H. v. Blow, "Deep penetration welding using a CO laser with an unstable resonator", *Opt. & Las. Techn.* **27** (3), 191 (1995).
11. M. Schellhorn and A. Eichhorn, "Spectroscopic comparison of aluminum welding plasmas produced by high power CO and CO₂ lasers", *Opt. & Las. Techn.* **28** (5), 405-7 (1996).
12. M. Schellhorn and H. v. Blow, "Improvement of the beam quality of a gasdynamically cooled CO laser with an unstable resonator by use of a cylindrical mirror", *Opt. Lett.* **20** (12), 1380 (1995).
13. M. Schellhorn and H. v. Blow, "Multi-kW supersonic CO laser with high beam quality", *Proc. SPIE* **2773**, 9-15 (1996).
14. H.R. Griem, *Plasma Spectroscopy*, McGraw-Hill Book Company, New York (1964).
15. "Kurucz data base", World Wide Web: <http://leanda.pmp.uni-hannover.de/projekte/kurucz/sekur.html>.
16. W. Sokolowski, G. Herziger and E. Beyer, "Spectroscopic study of laser induced plasma in the welding process of steel and aluminum", *Proc. SPIE* **1132**, 288-295 (1989).
17. Z. Szymanski and J. Kurzyna, "Spectroscopic measurements of laser induced plasma during welding with CO₂ laser", *J. Appl. Phys.* **76** (12), 7750-6 (1994).
18. P. Mulser, R. Sigel and S. Witkowski, "Plasma production by laser", *Physics Reports* **6** (3), 187-239 (1973).

Process stabilising potential of shielding gas mixtures in laser welding with CO₂ lasers

M. Kern, M. Beck*, P. Berger and H. Hügel

Universität Stuttgart, Institut für Strahlwerkzeuge (IFSW),
Pfaffenwaldring 43, D-70569 Stuttgart, Germany

*Current address: Daimler Benz AG,
Forschungszentrum F4P/P, D-89013 Ulm, Germany

ABSTRACT

A numerical beam propagation model has been developed to calculate the absorption and defocusing of a CO₂ laser beam by the laser induced plasma plume during deep penetration welding. By directly solving the paraxial wave equation with a finite difference scheme, the model allows to calculate the laser beam propagation through the plasma plume and to determine the "effective" intensity distribution in the focal plane. In combination with a previously published model that takes into account Fresnel absorption at the keyhole walls and plasma absorption inside the keyhole, now a calculation of the welding depth as function of the process parameter becomes possible. In particular, the propagation model clarifies the role of plasma absorption above the workpiece. The calculations identify the defocusing of the laser beam by the plasma plume as the main mechanism that degrades the laser deep welding process. Absorption by the plasma is shown to be of little importance. Additionally, the propagation model elucidates the process stabilising potential of shielding gas mixtures, especially of helium and argon mixed in a ratio of 3:1; a result also of phenomenological investigations that is used frequently in practice.

Keywords: laser welding, absorption, defocusing, optical properties of plasma, shielding gas, process stability

1. INTRODUCTION

A narrow and deep weld seam is characteristic for the laser welding process. Due to the high energy density in the focused laser beam the material is not only melted but vaporised. The back pressure of the vaporised material forms a keyhole in the melt pool and keeps it open against the surface tension. Inside the keyhole two energy-coupling mechanisms come into effect. In the first case the energy is deposited by direct (Fresnel) absorption at the keyhole walls during the laser beam's multi-reflection controlled penetration into the workpiece. In the second case the energy is absorbed through free electrons in the laser induced plasma and transferred by heat conduction to the keyhole walls. In addition to the absorption mechanisms inside the keyhole the laser induced plasma above the surface reduces the energy coupled into the workpiece and causes refraction of the laser beam. Particularly, in the case of welding with a CO₂ laser, with its wave length of 10.6 µm, the beam would be well absorbed in a pure material-vapour plasma plume and the energy coupling in to the workpiece would be significantly disturbed or completely interrupted. To prevent such a "plasma shielding" a gas with a high ionisation potential is applied for diluting the plasma plume.

These effects have been experimentally investigated to estimate the absorption coefficient and the refraction index. All experiments confirm that the plasma absorption length greatly exceeds the typical size of the plasma plume and therefore the plume has to be considered transparent as long as the metal vapour content in the plume can be diluted less than 10% with a shielding gas. Additionally, some theoretical investigations explained (by using a ray-tracing model) the defocusing effect of the plasma caused by refraction as being due to a local variation of optical properties within the plume.¹⁻³ Since the ray-tracing method is not applicable in the focal area of a laser beam, the intensity distribution in the focal plane can not be exactly derived.

To describe the intensity distribution in the focal plane and hence the "effective" focus diameter the paraxial wave equation has to be solved and combined with calculated optical properties of the plasma plume which depends on plasma pressure and temperature as well as on shielding gas composition and laser wavelength. In combination with a model for laser deep welding⁴, the interaction mechanisms in the plasma plume above the workpiece and inside the keyhole will be separately estimated and directly compared.

2. LASER BEAM PROPAGATION IN THE PLASMA PLUME

The propagation of an electromagnetic wave through the plasma is described by the wave equation:

$$\left(\nabla^2 + \mathbf{k}^2 \cdot \hat{n}^2 \right) \cdot \mathbf{E} = 0 \quad (1)$$

E: phasor amplitude of the electromagnetic field
k: propagation vector of the optical field

where \hat{n} is the complex index of refraction. The index of refraction and the absorption coefficient are calculated by the dispersion relation :

$$\hat{n} = 1 - \frac{\omega_p^2}{\omega \cdot (\omega_p + i \cdot \omega_c)} \quad (2) \quad \omega: \text{laser frequency}$$

where ω_c and ω_p are the electron collision frequency and plasma frequency.

2.1 Optical properties of the plasma

To calculate the values of the plasma frequency and the electron collision frequency the density of atoms, ions and the electron density in the plasma had been derived⁵. The resulting absorption coefficient α as well as the refraction index n_r for shielding gas and pure metal vapour plasmas are presented in Fig. 1. It is obvious that if the metal vapour mixes with the ambient air or the shielding gases applied, the optical properties of the plasma change. The absorption coefficient of the plasma resulting from a mixture of metal vapour with a helium or argon shielding gas is shown in Fig. 2. Using a helium shielding gas, the absorption coefficient can be reduced in the temperature range up to 30000 K. The temperature dependence of the absorption coefficient is less for a metal vapour/shielding gas mixture than for just a pure metal vapour. With an argon shielding gas, the reduction of the plasma absorption coefficient is limited to temperatures less than 15000 K. In the range above, the ionisation level of the argon atoms determines the plasma properties. In this temperature range, the resulting absorption coefficient of the Ar-Fe plasma mixture is much higher than that of the He-Fe mixture.

Due to the optical properties of the plasma and their dependence on the electron collision frequency ω_c and density it is evident that the absorption coefficient is a function of the ambient pressure. Fig. 3 shows the dependence of the absorption coefficient α on pressure and approximately on the square of the wavelength. Note that α is linearly proportional to the pressure. This connection emphasises the advantage of using a shorter wavelength and low ambient pressure for laser welding.

2.2 Propagation through the plume and results

To calculate the propagation of a laser beam in a medium with spatially varying optical constants, the wave equation has to be solved numerically⁶. To determine the absorption and defraction of the laser beam within the plasma plume, the temperature distribution and the shielding gas content within the plume have to be exactly known - properties, that are extremely difficult to obtain experimentally. In the following study, therefore, these properties are pre-set for calculation. They are parametrically varied to demonstrate the possible effects of the plasma plume upon laser focusing.

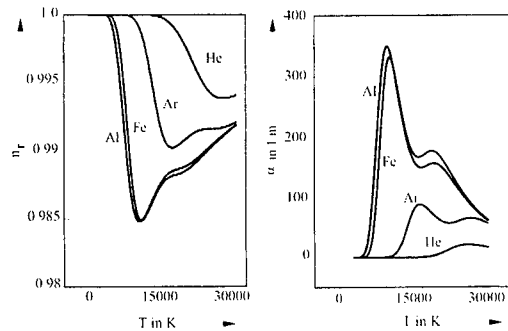


Fig 1. Optical properties of various plasmas; p=1 bar.⁵

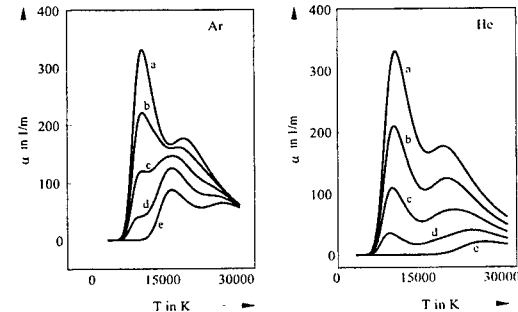


Fig. 2. Absorption coefficient of Fe-Ar, Fe-He plasma mixtures; p = 1 bar; shielding gas content: a = 0, b = 0.25, c = 0.5, d = 0.75, e = 1.⁵

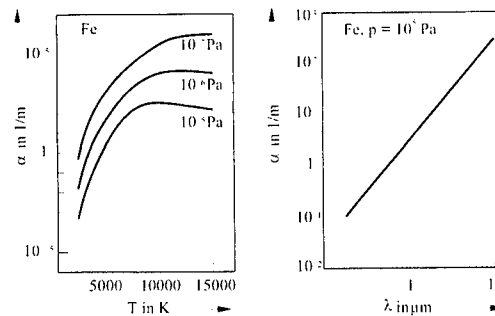


Fig. 3. Absorption coefficient dependent on plasma temperature, pressure and laser wave length.

The plasma plume is assumed to be elliptically shaped (Fig. 4) with a Gaussian like temperature distribution according to:

$$T(r, z) = T_{plmax} \cdot \exp \left[-2 \cdot \left(\frac{r^2}{r_{pl}^2} + \frac{(z - h_{pl})^2}{z_{pl}^2} \right) \right] \quad , \quad (3)$$

and the shielding gas is assumed to be homogeneously distributed within the plume.

The effect of plasma temperature and shielding gas content is shown in Fig. 5. For all shielding gas compositions a dependence of the focus diameter on the plasma temperature is noticeable. Thinning the iron plasma by applying He as shielding gas limits the enlargement of the focus radius. For 80% shielding gas content, the enlargement is less than 2 within a temperature range up to 22000K. In contrast, absorption is hardly effected by the plasma temperature (for plasma temperatures of more than 10000 K) but mainly dependent on the shielding gas content.

2.3 Process stability

Experimental investigations show a high frequent modulation of the plasma temperature⁷. Since the plasma affected focus diameter depends on this temperature, it obviously fluctuates as well during processing. Whenever the plasma temperature varies within a temperature range between 12000 K and 22000 K, the focus diameter can temporarily change by a factor of 2 - even at a shielding gas content of 80% He (Fig. 5 curve e). This might be one cause for process instabilities. To increase process stability, therefore, the temperature dependence of the focus diameter should be suppressed as in a range wide as possible. This can be achieved by applying appropriate shielding gas mixtures to reduce the temperature dependence of the plasma's optical properties. The resulting temperature dependence of the focus diameter in a metal vapour plasma thinned by a particular process gas mixture is shown in Fig. 5 curve (d). Whereas pure gases lead to a focal spot size strongly dependent on plasma temperature, the optimised shielding gas mixture (especially helium with argon by a ratio of 3:1) reduces this dependence. This ensures an almost complete decoupling of the intensity distribution in the focal plane from plasma temperature fluctuations. Since the dependence of the plume absorption on plasma temperature is additionally reduced, the laser intensity coupled to the workpiece is almost independent of plasma temperature. Because of these effects He-Ar shielding gas mixtures are favourable for obtaining stable welding.

Beside the theoretically discussed process stabilising potential of the shielding gas mixture, it has to be mentioned that the way in which the mixture is applied in practice is of particular importance for obtaining an improved process stability by using an appropriate shielding gas mixture (Fig 6).

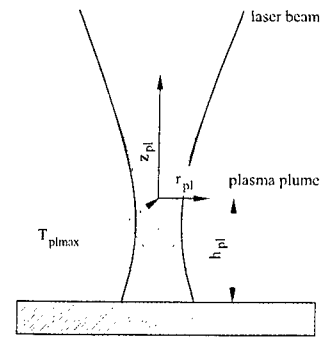


Fig. 4. Definition of the plume characteristic magnitudes

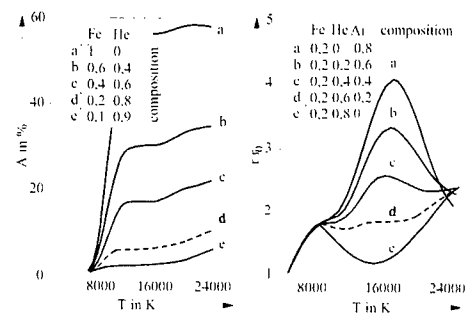


Fig. 5. Shielding gas mixture of helium and argon by a ratio 3:1 reduces the dependency of the disturbed focus radius on the plasma temperature; ambient pressure: $p = 1$ bar.

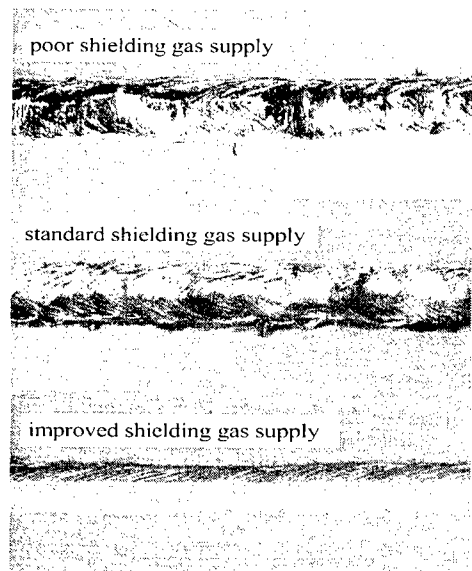


Fig. 6: The shielding gas effect is not only a question of the gas mixture. To obtain the advantage of a He/Ar mixture in a ratio of 3:1, an improved shielding gas supply is necessary.⁹

2.4 Energy coupling

This contribution was concentrated on the influence of the plasma plume above the keyhole on the focused laser beam. Earlier published models^{4,7} considered only the energy coupling mechanisms inside the keyhole.

In addition to the energy coupling mechanisms inside the keyhole it is now possible to discuss their specific effects and their effects as a whole respectively on the welding depth. In a model which now takes into account all three mechanisms it can be shown that the plasma inside the keyhole can be an advantage for the coupled energy e.g. welding of aluminium with its a low Fresnel absorption⁸, Fig. 7. On the other hand, the plasma plume simultaneously increases the focus diameter and therefore increases the threshold power for the deep penetration effect and also reduces the welding depth by laser power values above threshold. It is therefore obvious that local varying optical properties in the plume cause process instabilities especially when welding aluminium with CO₂ lasers up to 5kW: the discussed mechanisms have a hyper-sensitive impact on the welding process particularly in the threshold range.

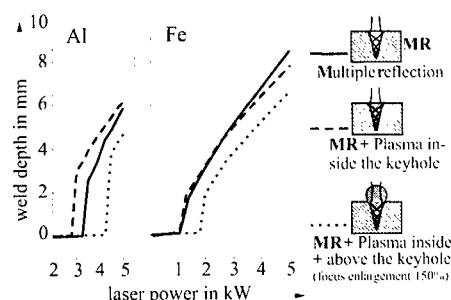


Fig. 7. Influence of interaction mechanisms on the coupled and simultaneous effect in the process; not effected by the plasma plume: $r_f = 0.24$ mm, effected by the plasma plume: $r_f = 0.36$ mm, $u_0 = 2$ m/min, $z_f = 0$ mm. Mode: TEM01*.

3. CONCLUSION

The focusing characteristics of a high power CO₂ laser beam in laser welding is strongly deteriorated due to refraction and absorption by the plasma plume. These negative effects can be minimised by applying appropriate shielding gases. From experiments it is known that a shielding gas mixture of helium and argon in a ratio of 3:1 applied for diluting the metal-vapour plasma shows a process stabilising potential.

The discussed effects can be explained by a numerical beam propagation model. The model accounts for the absorption and defocusing of a CO₂ laser beam by the laser induced plasma plume in deep penetration welding. By directly solving the paraxial wave equation with a finite difference scheme, the model allows to calculate the laser beam propagation through the plasma plume and to determine the "effective" intensity distribution in the focal plane.

It was found that a metal-vapour plasma plume diluted by shielding gases has to be considered as highly transparent. Nevertheless, a considerable amount of refraction is present. Plasma defocusing and not plasma absorption, therefore, is identified to be the main effect for the so-called "plasma shielding" observed in laser welding.

Additionally, defocusing by a plume diluted by a pure shielding gas depends on the plasma temperature. Since the plasma temperature has a high frequent modulation, the plasma-effected focus diameter fluctuates as well. Applying an appropriate shielding gas mixture reduces the dependency of the focus diameter on the plasma temperature and, therefore, dampens the plasma induced intensity fluctuations of the focused laser beam. A mixture of helium and argon by a ratio of 3:1 is found to be favourable to enhance process stability.

4. REFERENCES

1. T.J. Rockstroh and J. Mazumder, "Spectroscopic studies of plasma during cw laser materials interaction," *J. Appl. Phys.* **61**(3), 1987.
2. A. Poueyo et. al., "Study of laser induced plasma in welding conditions with continuous high power CO₂-lasers," In: Matsunawa, A., Katayama, S. (Editoren): *Laser Advanced Materials Processing (LAMP'92)*, Vol.1, pp. 323.
3. R. Ducharme et. al., "A mathematical model for the defocusing of laser light above a workpiece in laser material processing," *Proc. of ICALEO'92* (Orlando: Laser Institute of America), pp. 187.
4. M. Beck, F. Dausinger and H. Hügel: "Studie zur Energieeinkopplung beim Tiefschweißen mit Laserstrahlung," *Laser und Optoelektronik* **21** Nr. 3, S.80-84, 1989.
5. M. Beck, P. Berger and H. Hügel, "The effect of plasma formation on beam focusing in deep penetration welding with CO₂ lasers," *J. Phys. D: Appl. Phys.* **28**, pp. 2430, 1995.
6. Hecht, Zajac: *Optics*, Addison-Wesely Publishing Company, 7th printing, 1982.
7. W. Sokolowski, *Diagnostik des laserinduzierten Plamsas beim Schweißen mit CO₂-Lasern*. Dissertation, *Achener Beiträge zur Lasertechnik, Band 2*, Aachen: Verlag der Augustinus- Buchhandlung, 1991.
8. M. Beck, *Modellierung des Lasertiefschweißens*, Dissertation, Universität Stuttgart. In: *Laser in der Materialbearbeitung, Forschungsberichte des IFSW*. Stuttgart: B. G. Teubner-Verlag, 1996.
9. M. Kern, P. Berger and H. Hügel, "Optimiertes Querjetkonzept zur effizienten Spritzerablenkung und gesicherten Schutzgaszufuhr beim Laserschweißen," *Laser und Optoelektronik* **28** Nr.4, S.62, 1996.

Effects of different shielding gas compositions on the process of cw CO₂ laser welding in the hyperbaric range.

R. Ducharme, P. Kapadia

Physics Department, University of Essex, Colchester, Essex CO4 3SQ, United Kingdom

C. Lampa, A. Ivarson, J. Powell, C. Magnusson

Division of Materials Processing, Lulea University of Technology, Lulea, Sweden

ABSTRACT

A continuous CO₂ laser of 1.35 kW has been used to study the welding of 5mm thick stainless steel for pressures ranging from 0.1 to 0.8 MPa in increments of 0.1 MPa. Experimental data including penetration depths, weld widths, and in some cases weld pool profiles has been obtained for each value of the pressure using different mixtures of argon and helium shielding gases. In a previous paper it has been reported that keyhole welding could not be carried out for pressures significantly in excess of atmospheric pressure using pure argon and nitrogen shielding gases, but that the process was possible at pressures up to 0.8 MPa using helium. In the present paper the critical pressure for keyhole welding is determined as a function of the mixed shielding gas composition. The laser material interaction is analysed by solving the heat conduction equation with line and point heat sources representing the keyhole and plume respectively. The line source strength is itself calculated from consideration of the inverse bremsstrahlung and Fresnel absorption processes in the keyhole. It is concluded that successful laser welding in the hyperbaric range crucially hinges on good plume control through the effective delivery of an appropriate shielding gas mixture.

keywords: hyperbaric, laser welding, thermal modelling, shielding gases

1. INTRODUCTION

Laser welding of 5mm thick sheets of stainless steel has been carried out in a hyperbaric chamber using a cw CO₂ laser. The purpose of this study has been to determine the effects of pressure on the laser material interaction. In a previous paper¹ based on a similar experimental setup it has been reported that keyhole welding was not possible for pressures significantly in excess of atmospheric pressure using pure argon and nitrogen shielding gases due to the blocking effect of the plume, but that the process was possible at pressures up to 0.8 MPa using helium. In the present paper this existing study has been extended to include mixtures of argon and helium shielding gases. Two further differences from the original paper are as follows. Firstly, the F number of the near Gaussian laser beam used in the experiments has been increased from 4.0 to 6.0 and this has been found to produce a marked reduction in the penetration depths of the welds at corresponding pressures. Secondly, the point and line source model employed to analyse the experimental weld pool profiles in the original paper has been extended to include formula for both the strength and length of the line source. These are shown to give good agreement with experiment.

The experimental configuration has been described in detail in our earlier paper. The laser beam is admitted into the hyperbaric chamber through two Zinc-Selenide windows designed to minimise the effects of distortion at the elevated pressures. It is then directed through the shielding gas nozzle and downwards onto the workpiece by a system of reflecting and focussing mirrors. The shielding gas nozzle is situated about 10mm above the translating workpiece. In the interests of maintaining control over gas dynamic effects in the weld zone the rate of mass flow through the chamber was kept constant for the range of gases and pressures used at a value of 550 g/h. The welding speed throughout the trials was 2.5 m/min and the stainless steel test pieces were all of the same dimensions i.e. 160 x 20 x 5 mm.

2. MATHEMATICAL MODEL

One of the simplest methods of analysing experimental weld pool cross-sections is to make use of line and point sources^{1,2,3} to represent the thermal influence of the laser generated keyhole and plume respectively. The steady

state heat conduction equation is solved using these point and line sources and their strengths are adjusted until the calculated weld pool profiles matches the experimental weld. Three constants, the point source strength as well as the strength and length of the line source, are therefore needed in order to calculate the temperature distribution in the workpiece for each weld. In the present paper the line source strength and length are both calculated from consideration of the absorption processes in the keyhole. The number of arbitrary parameters that need to be fixed for each weld is therefore effectively reduced from three to one.

The formula for the line source strength Q_L (ie. the power deposition per unit depth in the keyhole) is based on the integrated keyhole and weld pool model of Ducharme² *et al.* The model assumes that Q_L is made up of contributions from inverse bremsstrahlung absorption in the keyhole plasma and Fresnel absorption on the keyhole wall. For weld translation speeds less than a certain critical value U_c the plasma contribution by itself will be sufficient to maintain a keyhole radius larger than the radius r_0 of the incident laser beam. Under these conditions

$$Q_L = (LP_0)^{1/2} \quad (U \leq U_c)$$

where P_0 is the incident laser power and $L = 8150 \text{ W/m}^2$ is the linking intensity for the action of a cw CO_2 laser beam on steel. At weld speeds greater than U_c , however, the radius of the keyhole will be smaller than r_0 forcing a direct interaction to take place between the laser light and the wall of the keyhole. From analysis of the experimental data^{2,3,4} it appears that the Fresnel contribution arising from this direct interaction is proportional to the weld translation speed but effectively independent of the laser power. This result finds expression in the form

$$Q_L = (LP_0)^{1/2} + A.(U - U_c) \quad (U > U_c)$$

where $A = 10^7 \text{ J/m}^2$.

The critical velocity U_c is calculated by equating the line source strength to the power per unit depth needed to maintain a uniform circular keyhole of radius r_0 assuming that the keyhole wall is at the boiling temperature T_V of the metal being welded. This condition gives

$$(LP_0)^{1/2} = 2\pi k(T_V - T_0) \text{cyl} \left(\frac{U_c r_0}{2\kappa} \right)$$

with

$$\text{cyl}(x) = \frac{I_0(x)}{K_0(x)} + 2 \sum_{n=1}^{\infty} (-1)^n \frac{I_n(x)}{K_n(x)}$$

where I_0 and K_0 are modified Bessel functions of the first and second kinds, k and κ denote the thermal conductivity and diffusivity of steel and T_0 is the ambient temperature. This equation is readily solved using a binary chop algorithm.

The line source length d is calculated from the expression

$$d = \frac{(1 - \epsilon)P_0 - Q_P}{Q_L}$$

where ϵ is the proportion of the energy in the laser beam which is not absorbed in the workpiece. Typically ϵ falls in the range 0.1 to 0.3 for partially penetrated keyhole welds, so that $\epsilon = 0.2$ is usually a good default value.

3. DISCUSSION OF RESULTS

Experimental weld pool cross-sections have been obtained using a near Gaussian cw CO_2 laser beam with F numbers of 4.0 and 6.0. Table 1 lists the focal spot radii⁵, the critical velocities, the line source strengths and the width of the parallel sided stem part of the welds produced using each of these F numbers. Table 2 compares the experimental and calculated values of both the weld width at the top of the workpiece and the penetration depth for 28 different welds. In each case the line source strength has been taken from table 1. The point source strength has then been varied until the calculated weld pool profile is a reasonably good match to the experimental profile.

Welds 1 to 13 have been obtained using pure helium shielding gas and an F number of 4. It can be seen that as the pressure rises the point source strength increases and the weld penetration depth decreases. The

F no.	beam radius (mm)	critical vel.(mm/s)	line source (W/mm)	stem width (mm)
4.0	0.055	45.0	270	0.38
6.0	0.080	33.0	350	0.53

Table 1: Laser beam radius and line source strength.

increasing strength of the point source is due to the enhanced inverse bremsstrahlung absorption in the plume with rising pressure. The effect attenuates the available power in the laser beam and is therefore responsible for the reduction in the weld penetration depth. Notice above 0.55 MPa that both the experimental and theoretical top weld widths become insensitive to the point source strength. This is because the weld penetration depth has become significantly shorter than the top weld width. Under these conditions the top weld width asymptotically approaches the maximum possible value of 1.8 mm corresponding to a pure point source of 1080 W.

Welds 14 to 17 show that at atmospheric pressure shielding composition has very little effect on the weld pool profile. It is, however, interesting to compare welds 1 and 14. The only difference in operating conditions between these welds is that the F number has been increased from 4.0 to 6.0. It is clear that this has had little effect on the point source strength but has produced a significant reduction in the penetration depth. This is because the larger diameter laser beam interacts more strongly with the keyhole wall. Since the total power in the laser beam is fixed a greater power dissipation per unit depth in the keyhole leads to a corresponding reduction in its length.

Welds 18 to 21 have been obtained using 10% argon in helium shielding gas mixture and an F number of 6.0. The results show similar trends to those discussed in connection with welds 1 to 13. The point source strengths are similar at corresponding pressures but the penetration depths are shorter as might be expected given the increase in the F number. It appears that pure helium shielding gas and the 10% argon in helium mixture behave similarly. The presence of the argon would make a difference, however, if an attempt were being made to use the shielding gas to disrupt the plume. This is usually achieved by delivering a high flow rate of shielding gas from the side rather than from above. The gas mixture containing 10% argon can be expected to perform better under these circumstances given that this mixture is approximately twice as dense as pure helium and therefore more able to dislodge the plume. It is, of course, the growth of the plume that determines the critical pressure for the failure of keyhole welding. Consequently, disruption of the plume is clearly one method by which the critical pressure for keyhole welding might be increased.

Welds 22 to 28 illustrate the failure of keyhole welding at different critical pressures depending on the absolute pressure. The critical pressure for keyhole welding is less than 0.2MPa in a pure argon shielding gas environment. This is increased to above 0.3MPa if the proportion of argon is reduced to 40%, 0.4MPa if it is reduced to 20% and 0.7 MPa if pure helium is used. It is notable that the failure of keyhole welding involves more than just the disappearance of the line source. In particular, there is also a sudden drop in the top weld width indicating that a much smaller proportion of the laser power is absorbed in the workpiece once keyhole welding fails.

REFERENCES

1. R. Ducharme, P. Kapadia, C. Lampa, A. Ivarson, J. Powell and C. Magnusson, "A point and line source analysis of the laser material interaction in hyperbaric keyhole laser welding" Proc. ICALOE'95. LIA, Orlando, 1996.
2. W.M. Steen, J. Dowden, M. Davis and P. Kapadia, "A point and line source method of laser keyhole welding" J. Phys. D: Appl. Phys. 21, 1255-1260 (1988).
3. W.K. Hamoudi and R. Ducharme, "Keyhole welding of C/Mn steel using a 10 kW CO₂ laser" Int. J. Joining of Materials 8 (1) 30-36 (1996)
4. R. Ducharme, K. Williams, P. Kapadia, J. Dowden, W.M. Steen and M. Glowacki, "The laser welding of thin metal sheets: an integrated keyhole and weld pool model with supporting experiments" J. Phys. D: Appl. Phys. 27, 1619-1627 (1994).
5. W.M. Steen, *Laser Materials Processing*, Springer, London, 1980.

weld no.	pressure (MPa)	%Ar	F no.	exp. top width (mm)	exp. pent. depth (mm)	theo. top width (mm)	theo. pent. depth (mm)	Q_p (W)
1	0.1	0.0	4.0	1.2	2.6	1.2	2.8	310
2	0.15	0.0	4.0	1.3	2.5	1.3	2.7	350
3	0.2	0.0	4.0	1.3	2.4	1.3	2.5	400
4	0.3	0.0	4.0	1.4	2.1	1.4	2.3	450
5	0.35	0.0	4.0	1.4	2.0	1.5	2.1	490
6	0.4	0.0	4.0	1.5	1.9	1.5	2.0	510
7	0.45	0.0	4.0	1.5	1.8	1.6	1.9	550
8	0.5	0.0	4.0	1.6	1.6	1.6	1.7	630
9	0.55	0.0	4.0	1.7	1.5	1.7	1.5	680
10	0.6	0.0	4.0	1.7	1.4	1.7	1.4	700
11	0.65	0.0	4.0	1.7	1.2	1.7	1.2	750
12	0.7	0.0	4.0	1.7	1.1	1.8	1.1	770
13	0.8	0.0	4.0	1.7	1.0	1.8	1.0	790
14	0.1	100.0	6.0	1.4	1.7	1.4	1.9	400
15	0.1	80.0	6.0	1.4	1.7	1.4	1.9	400
16	0.1	20.0	6.0	1.3	1.6	1.4	1.9	400
17	0.1	0.0	6.0	1.4	1.7	1.4	1.9	400
18	0.1	10.0	6.0	1.4	1.7	1.4	1.9	400
19	0.3	10.0	6.0	1.6	1.5	1.6	1.5	540
20	0.4	10.0	6.0	1.7	1.3	1.7	1.2	650
21	0.5	10.0	6.0	1.8	1.0	1.8	1.0	760
22	0.7	10.0	6.0	1.8	0.8	1.8	0.9	800
23	0.3	40.0	6.0	1.8	1.6	1.6	1.7	650
24	0.4	40.0	6.0	0.8	0.3	-	-	-
25	0.4	20.0	6.0	1.8	1.2	1.7	1.2	650
26	0.5	20.0	6.0	0.9	0.4	-	-	-
27	0.7	10.0	6.0	1.8	0.8	1.8	0.9	770
28	0.8	10.0	6.0	1.0	0.3	-	-	-

Table 2: Comparison of experimental and predicted weld geometries.

Full penetration detection in Nd:YAG laser welding by analysis of oscillatory optical signals: application to overlap weld seam tracking

[†]D. P. Hand, [†]F. M. Haran, [‡]C. Peters, [†]J. D. C. Jones

[†]Physics Department, Heriot-Watt University, Edinburgh EH14 4AS

[‡]Lumonics Ltd., Cosford Lane, Swift Valley, Rugby CV21 1QN

ABSTRACT

We describe a non-intrusive optical sensor for process monitoring of Nd:YAG laser welding, using light returned through the core of the power delivery optical fibre. This sensor is referred to as the core power monitor (core PM), and uses the delivery fibre to collect the broadband light generated in the process, which is then divided into spectral bands (designated as UV/visible and IR). These optical signals exhibit a characteristic oscillatory intensity modulation within the frequency range 2 - 5 kHz, which is believed to arise from a combination of keyhole and weld pool oscillations. The frequency content may be related to the size and shape of the welding keyhole, and an alarm system for overlap welding has been developed based on this principle. This can detect both misalignment of the focused laser spot off the seam, and any excessive gap between the plates.

Keywords: laser welding, process monitoring, seam tracking

1. INTRODUCTION

Laser welding is becoming a more widely used joining technique in many applications in, for example, the aerospace and automotive industries. As with all welding techniques, the relationship between process parameters and ultimate weld quality is complex, and so in-process monitoring of the welding process is advantageous to avoid time-consuming post-process analysis. Closing the loop to give real-time process control will greatly aid the development of reliable and flexible automated systems, particularly important when welding very large structures (e.g. aerospace) where scrapped parts can prove very expensive.

In this paper we describe an optical sensor which detects the radiation generated in laser welding, and which can be used as an alarm system for overlap seam welding, using a 2 kW Nd:YAG laser with fibre delivery. This alarm system operates by analysing the intensity modulation of the detected optical signals, which is dependent on the size and shape of the welding keyhole. In particular, there is a significant change in signal at the transition between a partial and fully penetrating keyhole, which generates the alarm. We have previously used this optical sensor as the basis of a focus control system for laser welding, which can operate in parallel with the alarm. In addition to ensuring constant focus, this combined operation will also allow the direction of any seam tracking error.

Many authors have attempted to detect events in the welding process by observing the optical radiation emitted. Various techniques have been used to monitor this radiation including direct pick-up with photo-diodes in various positions², using an optical fibre to collect the radiation³, and monitoring the light returned either through the cladding⁴ or core⁵ of the power delivery fibre. In this paper the light returned through the core of the delivery fibre is detected at the rear of a laser turning mirror; this sensor is referred to as the core power monitor (PM).

2. THEORY

Laser welding is known to generate oscillatory optical and acoustic signals. There are many theoretical papers appearing in the literature dealing with the establishment of the welding keyhole and the origins of these oscillatory signals. There are two main hypotheses. Firstly it has been argued that the oscillations are due to instabilities in the keyhole. It has also been proposed that there are oscillations in the weld pool due to the propagation of capillary waves. It is unlikely that these two phenomena are mutually independent. The keyhole created during laser welding is held open by a pressure balance combined with an energy balance. The pressure balance requires that the surface tension is compensated by the sum of the recoil pressure of particles ablated at the keyhole surface, and excess pressure due to gas flow out of the keyhole. The transport of a small amount of metal vapour across the keyhole has also been proposed as a further possible keyhole-

sustaining pressure. It can be argued that weld pool oscillations are established due to varying surface tension $\Lambda(r)$ depending only on the radial coordinate r . The surface tension of the molten weld pool depends on temperature, and because of the variation of the temperature of the weld pool with distance from the laser it is expected that the surface tension in turn depends on r . This effect establishes the capillary waves within the weld pool.

3. EXPERIMENTS AND RESULTS

The experimental arrangement is shown in fig.1 The core PM is incorporated into a Lumonics MultiWave™ 2000 Nd:YAG laser, and welds are produced by translating the workpiece under the effector optics. The optical radiation emitted from the laser/work-piece interaction zone is partially collected by the effector optics and imaged into the core of the power delivery fibre. The fibre guides this light back to the laser head, where a portion of it is transmitted at a dielectric turning mirror outside the laser cavity. After the turning mirror the process radiation is split into two spectral bands: 0.3 - 0.7 μm , described as UV/visible, and 1.1 - 1.6 μm , described as IR. The detected signals were sampled at 20 kHz and stored digitally for subsequent analysis.

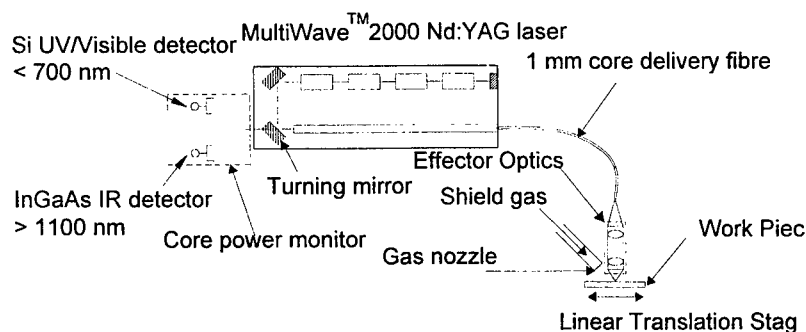


Figure 1: Experimental set-up.

3.1 Effect of changing material thickness

To explore the effect of material thickness on the optical signals a bead-on-plate weld was produced across a mild steel wedge with a 0.3° angle at a traverse speed of 3 m min^{-1} . The wedge was 0.7 mm thick at its thin end and 200 mm long, and orientated such that optimum focus was maintained on the top surface. The laser was operated at 2 kW in continuous wave (CW) mode, and an argon gas shield was used to prevent oxidation in the weld bead and surrounding material.

A Gabor spectrogram was derived from the captured signals using a 512 point sliding Hanning window. The UV/visible spectrogram is plotted in figure 2, and shows the frequency content of the time series as a function of time. This spectrogram shows that for a fully penetrating keyhole there is a very distinct peak, at decreasing frequencies as the material gets thicker. The peak vanishes during the transfer from the fully penetrating to partially penetrating regimes, and the modulation spectrum becomes broad-band. The IR spectrogram is very similar to the UV one.

3.2 Application to overlap welding

The distinct frequency peak which is apparent in the above results may be exploited as a lap welding alarm signal. The usual practice when lap welding with Nd:YAG lasers is to weld as fast as possible whilst maintaining a fully-penetrating weld bead through both sheets. Despite the weld bead being fully penetrating, however, the *keyhole* is not, so a broadband signal is observed. However, if the laser beam moves off the seam, or the gap between the sheets becomes too large, welding only occurs in a single sheet. In this case the keyhole will be fully penetrating, creating a distinct frequency peak.

As shown in fig 3(a), overlapping pieces of 1 mm thick mild steel sheet were used as a workpiece in the experimental arrangement described above to produce a simulated lap-weld. The signals of importance are those produced when the Nd:YAG laser moves off the seam, so we welded across rather than along it. The effect of varying the gap between the plates was also investigated using the work-piece configuration schematically shown in figure 3(b).

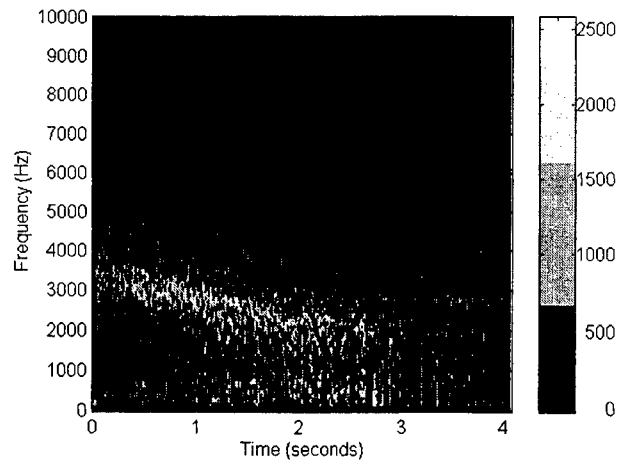


Figure 2: Spectrogram of UV/visible signal produced when welding mild steel wedge in the direction from thin to thick

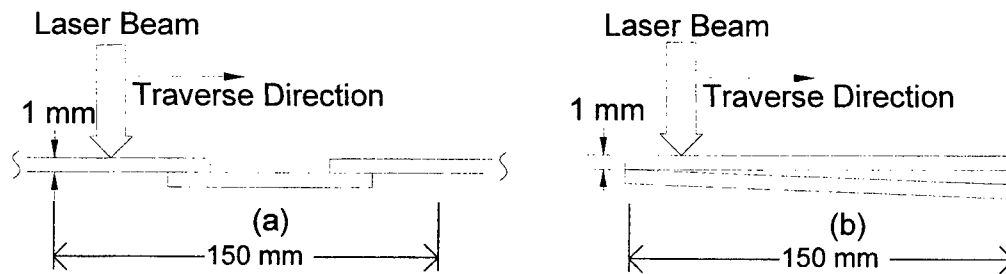


Figure 3: (a) Mild steel stepped work-piece, (b) lap-weld with gap.

The UV/visible Gabor spectrogram generated when welding across the simulation lap weld is shown in figure 4. As expected, when the laser moves off the seam (i.e., the laser is directed at the single-thickness material, rather than an overlapping region) then a distinct frequency peak appears. In addition, the amplitudes of this frequency peak are different to the left and right of the seam. On one side of the seam the laser beam remains in focus on the surface of the work-piece, and on the other it is 1 mm out of focus. This asymmetry is potentially exploitable to yield directional information in seam-following. Probably a more practical fail-safe method of obtaining directionality is to use this system in conjunction with the previously developed closed-loop focus control system which uses the same sensor but different signal processing¹.

To generate the alarm signal, a computer with an A/D card is used to sample the detected signal. An FFT is taken, and if a frequency peak above a certain threshold exists in a predefined frequency bin around 3 kHz then an alarm signal is generated. The appropriate threshold level and frequency bin are defined by the sheet thickness.

Figure 5 shows the intensity signal obtained from the core PM as well as the alarm signal which is obtained when seam tracking alignment is lost when welding at 3 m/min. There is a slight delay in the alarm signal due to the time it takes to capture the data and perform an FFT of 1024 data points. Figure 6 shows the intensity signal obtained from the core PM as well as the alarm signal which is obtained when welding a work-piece like that shown in figure 3 (b) in the direction from zero gap to a gap of 1 mm between the plates, again welding at 3 m/min. Figure 9 shows the spectrogram of the intensity signal shown in figure 8. We only detect the peak in the frequency signal once the gap exceeds a certain threshold leading to full penetration on the top plate, unaffected by the bottom plate. From figure 8 it can be calculated that this gap threshold is approximately 0.7 mm.

4. DISCUSSION AND CONCLUSIONS

We have described an optical sensing technique which can be used to collect the optical radiation emitted from a laser welding process. Initial experiments have been conducted to investigate the effect of the material thickness on the signals. For a fully penetrating keyhole the signals obtained by the core PM show a distinct frequency peak between 2 - 4 kHz depending on the material thickness, with lower frequencies for thicker material. The peak disappeared when the material was too thick to allow a fully penetrating keyhole. This phenomenon was used as the basis of a lap-welding alarm system which detects both seam tracking errors and excessive gaps.

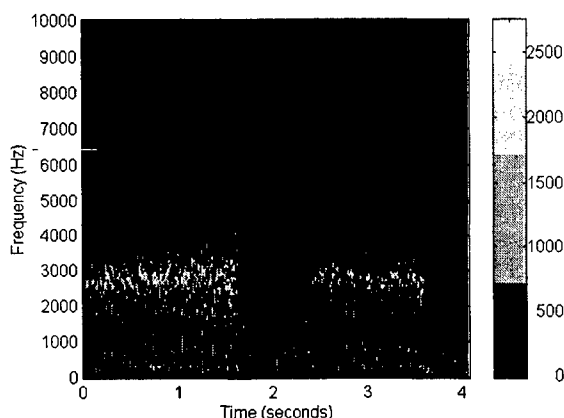


Figure 4: Spectrogram of UV/visible signal obtained when welding stepped work-piece.

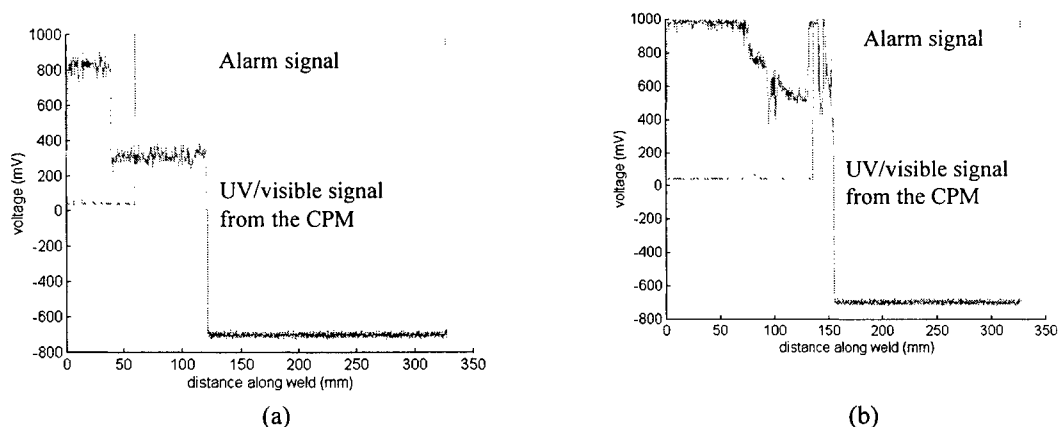


Figure 5: Alarm signal indicating (a) seam mistracking and (b) excessive gap between the plates

5. ACKNOWLEDGEMENTS

The authors gratefully acknowledge support under the Laser Engineering for Manufacturing Applications Programme, by the Engineering and Physical Sciences Research Council, UK, and Lumonics Ltd.

6. REFERENCES

- [1] F. M. Haran, D. P. Hand, C. Peters, J. D. C. Jones, "Real-time focus control in laser welding", *Meas. Sci. Technol.* 7 1095-1098 (1996)
- [2] Y-L. Mao, G. Kinsman, W. W. Duley *Jnl. of Laser Applications* 5 17-22 (1993)
- [3] A. Otto, G. Deinzer, M. Geiger 1994 Symposium on Laser Materials Processing: Industrial and Microelectronics Applications 2207 282-288
- [4] A. A. P. Boechat, D. Su, J. D. C. Jones *Meas. Sci. Technol.* 3 897-901 (1992)
- [5] T. Ishide, Y. Nagura, O. Matsumoto, T. Nagashima, A. Yokoyama 1992 European Conf. on Treatment of Materials 110 81-86

Remote optical power and focus monitoring in pulsed Nd:YAG laser welding

Cheol-Jung Kim, Sung-Hoon Baik, Min-Suk Kim and Chin-Man Chung

Korea Atomic Energy Research Institute
P.O.B 105, Yusong, Taejeon, Korea 305-600

ABSTRACT

The thermal radiation from the weld-pool is measured at two wavelengths through the laser delivery fiber between Nd:YAG laser pulses. The chromatic aberration of delivery optics has been optimized to detect the variation of weld bead width. The design of optics and the signal processing algorithm for optical monitoring is described. Furthermore, the applications of optical monitoring to the detection of power variation and focus shift are shown.

Keywords : Weld Process Monitoring, Chromatic Aberration, Nd:YAG laser, Thermal Radiation, Focus Shift

I. INTRODUCTION

Laser welding is becoming a common tool in industry. The process monitoring of laser welding has been attracting many researcher's interests due to its importance in the optimization of laser welding parameters¹. However, due to its complex nature, the monitoring has been quite qualitative and the sensitivity of it was not mentioned.

Since the advent of laser, the remote materials processing by laser beam delivery was considered to be pertinent for nuclear applications due to the limited human accessibility in nuclear facilities. The laser welding has also been used in repair welding of steam generator heat exchange tubes in nuclear power plants as soon as the kW class Nd:YAG lasers became available in industry. For this repair welding, Nd:YAG laser is delivered through a fiber and focused on the inside of sleeve tube and a tilted mirror is rotated for the circumferential welding of sleeve and heat exchange tubes. The soundness of welding has to be investigated by ultra-sonic or eddy-current test after welding. To make sure the sound welding, one has to monitor if the laser is being kept on focused along the circumference. Furthermore, the power failure due to the damage of delivery optics has to be detected before the disaster. Also, the full-penetration welding or excessive deep welding has to be located for rewelding or tube-plugging because they can not be considered to be resistant enough for corrosion anymore. An optical monitoring was invented, but it could detect the power failure only².

The objective of this paper is to demonstrate the performances of optical monitoring which measures on thermal radiation at two or three wavelengths. The multi-wavelength thermal radiation was also measured for weld process monitoring³. However, the main features of this paper are the chromatic aberration introduced in the delivery optics, the measurement of delayed thermal radiation and the special signal processing algorithms. Due to the spherical aberration of delivery optics, the transmittance of thermal radiation through the fiber varies over the weld-pool area and also, due to the chromatic aberration, this transmittance distribution over the weld-pool area depends on the wavelength. Therefore, the effects of the variation of weld-pool size or the change in the distribution of weld-pool surface temperature are different for each wavelength and the change in weld-pool surface status can be detected by measuring the thermal radiation signals at two wavelengths. Furthermore, the thermal radiation signals measured after various delays can give information on the inside status of weld-pool such as the weld depth, gap between the weld metals, full-penetration, etc. The decay of thermal radiation is getting slower as the weld-pool depth becomes deeper. Furthermore, the decay of weld-pool is not uniform if some part of the weld-pool is getting closer to the air. The decay of that part becomes slower than the remaining weld-pool. In other words, the status of whole weld-pool, surface and deep inside, can be monitored from the thermal radiation signals. This optical weld process monitoring can be used in the optimization and evaluation of welding process.

To obtain the information on the weld-pool status, the ratio of the thermal radiation signals at two wavelengths and also the ratio of the decay of thermal radiation signals are used. It is better than the direct use of the thermal radiation signals which are easily affected by environmental parameters. The effects of environmental parameters can be compensated in the division of two similar signals. The main advantage is that the thermal radiation is being detected during the welding process in real-time where the radiation signal not only depends on the laser parameters and focus position but also is affected by the environmental parameters such as weld metal temperature, shielding gas flow, spattering, depth of weld-pool, deep cooling inside of weld-pool, etc. Therefore, the multi-wavelength thermal radiation signals have some information

related on these environmental parameters and can give more realistic information for the evaluation of welding status in real-time.

II. OPTICAL ANALYSIS

Fig.1 shows the schematic of fiber delivery system for remote laser welding. Due to the spherical aberration of the collimating and focusing lenses, the focused laser spot is larger than the geometrical image of the fiber aperture. Furthermore, the size of weld-pool is larger than the focused laser spot due to the thermal conduction. Now, the thermal radiation from the weld-pool has to be reimaged by the focusing and collimating lenses and has to pass the fiber to get to the detector. Due to the spherical and chromatic aberrations of the lenses, the transmittance of the thermal radiation through the fiber depends on the position of thermal radiation source and the wavelength. The dependence is illustrated in Fig.2. Two plano-convex SF6 lenses with 25 mm focal length are used for 1 to 1 imaging of 1 mm diameter fiber. The f number of the focusing lens is assumed as F/3.1.

The 950 nm wavelength is chosen because the 1.064 μm Nd:YAG laser can be cut off with optical filter to protect the Si detector, but it is close enough to the 1.064 μm to maintain the same chromatic property. The other 532 nm is chosen because it is far from the 950 nm to show the chromatic aberration such that each wavelength can see the weld-pool of different radius and the transmittance has the different profile at each wavelength. Now, even if we measure the thermal signal integrated from the whole weld-pool aperture, we can find the local change on the weld-pool surface. Furthermore, the thermal radiation signal at 532 nm is large enough to detect and the 532 nm band-pass filter is commercially available.

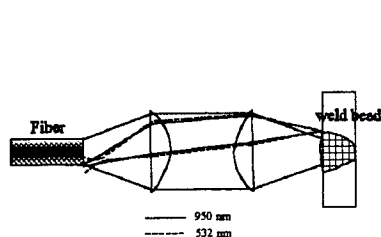
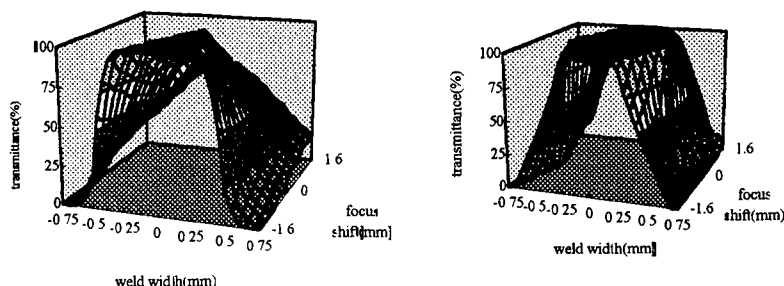


Fig.1 Laser Delivery Optical System



(a) at 532 nm
(b) 950 nm
Fig.2 Transmittance Distribution vs. Position of Thermal Source

III. EXPERIMENTAL SETUP

The schematic of optical monitoring system is shown in Fig.3. Three Si detectors (Thor Labs, DET2-Si) are used to monitor up to three wavelengths of thermal radiation, but only two channels are used in this experiment. The laser pulse is also monitored for synchronization of trigger pulse. An interface is designed to capture the two thermal radiation signals five times at every fixed amount of delay after the end of each laser pulse. Then, the ratio of two thermal radiation signals and the ratio of the decays of the same signals are calculated and displayed for analysis. The decay of each thermal radiation signal is calculated either by the difference or the ratio between one signal and the next delayed signal.

VI. APPLICATIONS and RESULTS

The feasibility of optical monitoring was investigated in laser welding of Inconel 600 plates. Fig.2 (b) shows that if the weld bead width is smaller than 1.5 mm, the 950 nm signal can be used for the monitoring of focus shift up to ± 1.5 mm. The 950 nm signal for 2 mm focus shift at 225 W average power is shown in Fig.4. It shows 10 % signal drop for 0.5 mm focus shift near the best focus. Therefore, it can be used in locating the absolute position of focus with accuracy of 0.5 mm. The 225 W power is not enough for the welding, but is large enough for preheating. So, the optical monitoring can check the focus status before main welding.

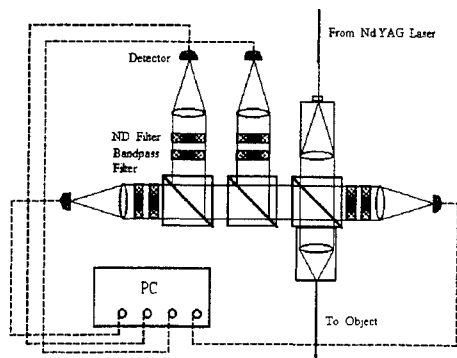


Fig.3 Schematic of Optical Monitoring System

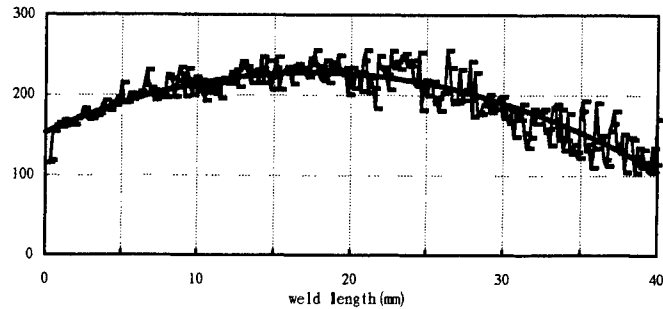


Fig.4 Variation of 950 nm signal vs. Focus shift (at 225 W)

Fig.2 also shows that if the weld bead width is larger than 1.5 mm, the ratio of 532 nm and 950 nm signals can be used for monitoring of the weld bead width. The ratio increases as the width is getting wider. If we vary the delay to measure 532 nm and 950 nm signals, we can monitor the variation of weld width and depth. The weld depth can be estimated from the measured values for the power variation between 350 W and 260 W. The accuracy of estimation is about 10 % for both width and depth. The focus was not shifted during the power variation in Fig.5. However, we have to be cautious in estimating the weld depth. Because it uses the delayed signals the result depends on the decay pattern. It is accurate, but the range of accurate estimation is rather narrow. The same estimation at the front of weld and at the end does not mean the same depth because the temperature of the plate rises during the welding and the decay pattern has been changed at the end. Likewise, the estimation in deep weld is not linear to that from the shallow weld. However, the estimation near each area is linear.

Now, how can we monitor the focus shift during laser welding? We can see the ratio of 532 nm and 950 nm signals is not any more constant during focus shift for constant weld width. Fig. 6 shows the ratio of 532 and 950 nm signals for 2 mm focus shift at constant 350 W average power. The ratio increases linearly about 20 % for 1 mm outward focus shift (weld length 20 to 40 mm). The ratio does not show the linear dependence for inward focus shift (weld length 0 to 20 mm). This kind of tendency can be expected from Fig.2. We have to monitor one more wavelength such as 1.5 μm to determine the sign of the focus shift. The focus shift as small as 0.5 mm can be easily detected. Furthermore, the weld width varies little even for a considerable amount of focus shift. The weld width, which is much larger than the size of defocused laser, mainly depends on the average input that is constant during focus shift. On the other hand, the weld depth varies a lot during focus shift. The weld depth depends on the size of the focused laser beam that varies much during focus shift. Therefore, the ratio of 532 and 950 nm signals varies much with delay in focus shift. However, the same ratio does not vary much during the power variation. So, we can distinguish focus shift and power variation easily with optical monitoring. The main difference is that the smaller laser spot means deep weld in focus shift, but shallow weld in power variation.

The fluctuation in 532 and 950 nm signals is noticeable if the weld pool temperature is close to the boiling temperature and shows the surface quality. For weld process control, we have to detect the gap and also the full-penetration. The edge of weld pool decays slowly compared to the center of weld pool near the gap due to the non-effective cooling through the gap. On the other hand, for full-penetration weld or excessive deep weld, the effect is reversed compared to the gap. Fig.7 shows the change in the ratio of decays for 532 and 950 nm signals along 40 mm long weld with 150 μm gap between plates. It can be easily detected. Fig.8 shows the same ratio of decays for full-penetration. There is a large fluctuation near full-penetration due to the sudden large amount of cooling by spatter. The spatter means a fast cooling in the center of weld pool. The full-penetration can also be monitored from the weld depth estimation that is also shown in Fig.8.

V. CONCLUSIONS

A remote optical weld processing technique has been implemented by optimizing the chromatic aberration of delivery optics. It can monitor the weld bead width and depth, warn the excessive deep weld before full-penetration, detect the gap between the weld metals, and estimate the surface quality of weld bead. It can also locate the focus with minimum spot size

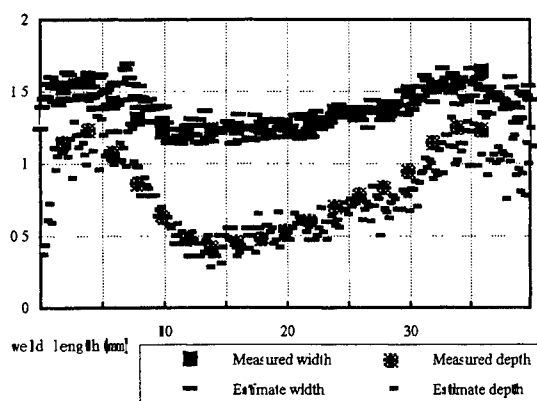


Fig.5 Correlation between weld width and depth and ratios of thermal signals at 1 and 5 msec delays during power variation

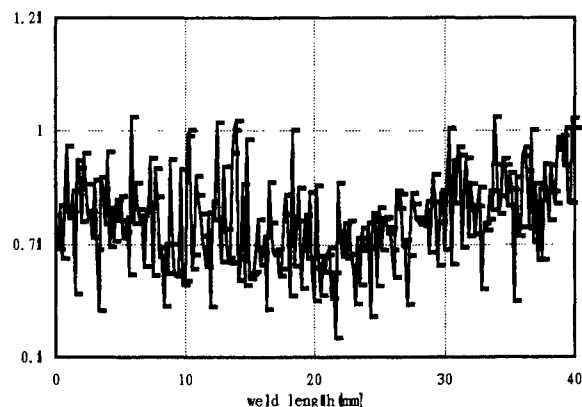


Fig.6 Ratio of 532 and 950 signals vs. Focus shift (350 W)

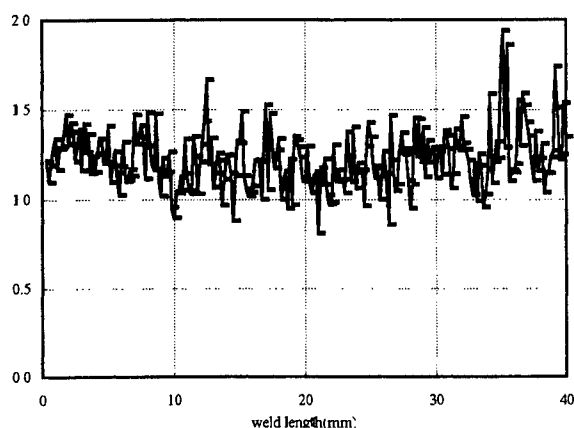


Fig.7 Ratio of decays of 532 and 950 signals (1 msec delay) with 150 um gap between plates

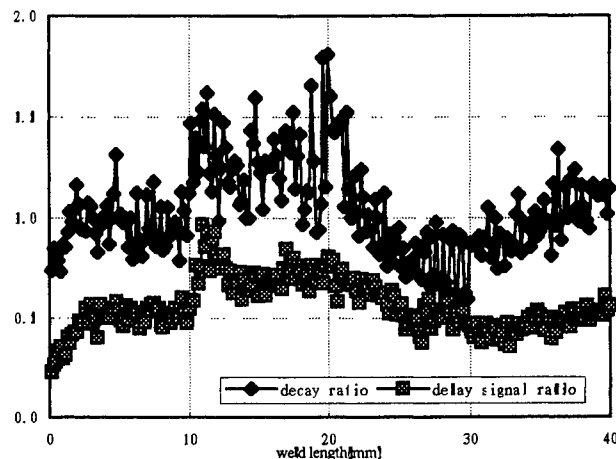


Fig.8 Ratio of decays of 532 and 950 (1 msec delay) near full-penetration and ratio of 532 and 950 (5 msec delay)

and monitor the focus shift from that position. The main feature is that all these information can be obtained in real-time and non-intrusively.

Furthermore, the accuracy of measurement was shown accurate enough for weld process monitoring. It can investigate the status of weld-pool while the weld process is on going. It is quite important for optimization of weld process. It does not investigate the results after welding where it is quite difficult to decide what to do. Now, we can find what to vary in the optimization of weld process. One simple application can be the optimization of pulse-shaping which has been thought that there are too many variables in pulse-shaping. The auto-focusing with three wavelengths measurements would be another application for industrial use.

V. REFERENCES

1. D.Hand,C.Peters, and J.Jones, "Nd:YAG laser welding process monitoring by non-intrusive optical detection in the fiber optic delivery system," Meas.Sci.Technol. 6,1389-1394 (1995).
2. US patent 5,155,329
3. H.Chen,L.Li,D.Brookfield, and W.Steen, "Multi-frequency fibre optic sensors for in-process laser welding quality monitoring," NDT & E International, 26(2), 67-73 (1993).

Poster Session II

Extraction efficiency of a 5-cm gain length supersonic chemical oxygen-iodine laser

C.A. Helms, T.L. Rittenhouse, S.P. Phipps, K.A. Truesdell, G.D. Hager

USAF Phillips Laboratory, LIDB
3550 Aberdeen Ave SE
Kirtland AFB, NM
87117-5776, USA

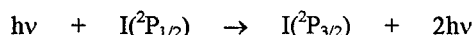
ABSTRACT

Gain saturation and diffractive loss data have been collected on the Phillips Laboratory's VertiCOIL laser. These data have been applied to the COIL simplified saturation model to estimate the optical extraction efficiency of VertiCOIL.

Keywords: chemical oxygen-iodine laser, chemical laser, oxygen iodine laser

1. INTRODUCTION

The chemical oxygen-iodine laser (COIL) is an electronic transition transfer laser first demonstrated at the Air Force Weapons Laboratory (now the Phillips Laboratory) in 1978. It is the shortest wavelength high energy chemical laser in existence today and is the first chemical laser to operate on an electronic rather than a vibrational transition. COIL laser output at 1.315 μm is achieved by stimulated emission on the magnetic dipole transition in atomic iodine:



The population inversion on this transition is maintained by near resonant collisional energy transfer ($\Delta E = 279 \text{ cm}^{-1}$) from metastable excited $\text{O}_2(^1\Delta)$ to the I atom ground state ($\text{I}(^2\text{P}_{3/2})$).

$\text{O}_2(^1\Delta)$ is produced by chemical reaction between gaseous chlorine and aqueous basic hydrogen peroxide (BHP). The reaction is extremely exothermic (approximately 110 KJ/mol) and yields 100% of the oxygen in the excited $\text{O}_2(^1\Delta)$ state. However, deactivation processes limit the useable amount of $\text{O}_2(^1\Delta)$ to approximately 60% of the total oxygen, typically referred to as the yield.

COIL technology has potential application in both the military and commercial sectors. The usefulness of COIL for military application is evidenced by the current Air Force Airborne Laser program. Features that make COIL attractive for industrial application include the ability to transmit high powers efficiently through standard fiber optics, focusability, and the fact that construction of medium power lasers (10-40 kW) is relatively straightforward. Also, the COIL wavelength of 1.3 μm couples well into metals, making metal cutting and welding more efficient. The VertiCOIL device was designed to address issues of interest to both military and commercial applications, such as run time, high efficiency operation, and compact design.

The VertiCOIL device was designed with several goals in mind. The most important goal was to demonstrate stable power for long times (tens of minutes) from a rotating disk generator. A secondary goal was to design the laser to be as compact as possible. An additional goal was to achieve high efficiency operation at relatively high subsonic pressure (>75 torr) by minimizing the transport loss of $\text{O}_2(^1\Delta)$. This was done by minimizing the subsonic gas volume.

As part of the development of the VertiCOIL device, we wish to understand the performance of various aspects of the device that lead to the reported chemical efficiency of 26.7%¹. Analysis of COIL performance is often done with the aid of an energy bookkeeping methodology such as the COIL heuristic equation². The most critical inputs to the heuristic equation are the plenum yield, cavity gas temperature, and the optical extraction efficiency. The other terms are either relatively straightforward to measure or can be estimated without having a major impact on the results. Since VertiCOIL does not have a diagnostic amenable to sophisticated measurements of oxygen yield, we have focused instead on obtaining a good

estimate of the optical extraction efficiency at the high efficiency operating condition. The approach taken to calculate the extraction efficiency was to measure as many quantities as possible to use as input to the COIL simplified saturation model published previously³.

Quantities that have been measured are mirror reflectivity, mirror transmission, small signal gain (from saturation data), and diffractive spill from the cavity during lasing. Some direct measurements of small signal gain have also been made, but these results are considered preliminary and are used only to re-enforce the small signal gain inferred from saturation data. The preliminary gain measurements also provide linewidth information that suggest cavity temperatures, but these results are also preliminary.

2. EXPERIMENTAL

The VertiCOIL device has been described previously¹, but a brief description will be given here for completeness. VertiCOIL is a 1 kW class supersonic COIL driven by a 10 inch diameter rotating disk generator. In order to maximize run time with a minimum amount of BHP, the BHP is cooled and reintroduced into the generator forming a closed-loop system. Run times of greater than one hour have been achieved in this manner.

The oxygen flow exiting the generator travels through a 1.27 cm by 5 cm diagnostic duct and enters the iodine injection plenum. VertiCOIL does not have a water condensation trap, and therefore relies solely on thermal management of the BHP to control water vapor in the flow. Iodine is injected into the oxygen flow transversely through 2 rows of holes on each side of the flow duct. Following iodine injection, the duct narrows to 0.89 cm by 5 cm, forming the sonic throat. The nozzle then expands by a factor of 2 producing approximately mach 2 flow in the lasing cavity. The nozzle ramps limit the multi-mode output beam size to 3.2 cm by 1.8 cm.

The resonator used on VertiCOIL consists of 2" optics with a mirror separation of 86.7 cm and an active gain length of 5 cm (fig. 1). The mirrors are isolated from the device by ducts which are purged with He (50 mmol/sec total) to protect the mirror coatings from BHP contamination and prevent ground state iodine atoms from occupying the ducts. The resonator consists of a maximum reflector with a 2 meter radius of curvature and a flat outcoupling mirror with a reflectivity of 97-99%. Because VertiCOIL utilizes such a high reflectivity for its outcoupler, a significant amount of power is transmitted through the maximum reflectivity mirror. The power transmitted through the maximum reflector has been measured at 3% to 8% of the total power, depending on the mirror set. Laser power on the outcoupler side was measured with an Ophir model 100 5 kW water-cooled power meter. Power transmitted through the maximum reflector was measured with a Coherent model 213 power meter. Reported values for power and efficiency reflect the sum of the powers transmitted through both mirrors.

Intensity saturation data were taken by changing the reflectivity of the flat outcoupler and measuring the power transmitted through both mirrors. Diffractive spill data were collected by installing one of two limiting apertures in the resonator (1.5 x 1.5 and 1.5 x 3 cm, see fig. 1). The apertures were located near the curved mirror to ensure that the beam footprint was limited by the aperture. The apertures were manufactured from a copper alloy and oxidized for maximum absorption. The absorptivity of the apertures at 1.315 μm was measured to be 93% \pm 1%. The apertures were outfitted with 4 thermocouples on the four quadrants of the back side of the aperture (on the opposite side from where the diffracted beam impinged on the aperture).

Preliminary gain measurements have also been made using a 1.315 μm distributed feedback diode laser developed by Physical Sciences Inc. for the Air Force⁴. The diagnostic was used in a 2 pass configuration using a flat maximum reflector to reflect the diagnostic beam, with the beam launch and detector mounted together, separated by 5 mm. This configuration facilitated obtaining a 2-D gain map of the entire region accessible by the 2" optics.

Diffractive spill was calculated from the average temperature rise of the apertures, using the mass and heat capacity of the copper alloy. Each condition was tested five times and the results averaged. The data were reproducible within 10%.

Mirror reflectivities and transmissions were measured using a 1.315 μm diode laser and an International Light model ILX 700 InGaAs detector. All measurements were taken 3 times to ensure reproducibility. The repeatability of the measurements was approximately $\pm 0.2\%$. The flow condition selected for analysis is shown in table 1.

Table 1. Flow conditions for high efficiency test.

Total average power	1750 watts
Chlorine flowrate	69.5 mmol/sec
Chemical efficiency	26.7%
Primary He diluent	280 mmol/sec
Generator pressure	70 torr
Chlorine utilization	.94
I ₂ /O ₂ ratio	.017
BHP flowrate (7 M O ₂ H-)	6 GPM
Diskpack rotation rate	45 RPM

Table 2. Required inputs to COIL saturation model.

Input parameter	value
Mirror reflectivities	.997/.982
mirror scattering loss	.0025/.0025
mirror absorption loss	$10^{-5}/10^{-5}$
cavity inlet yield (assumed)	.54
small signal gain	.014 cm^{-1}
cavity temperature	200 K
diffractive loss per round trip	0.00083
gain length	5 cm
mode length	3.2 cm
gas velocity in cavity	1×10^5 cm/sec

3. RESULTS AND DISCUSSION

The chemical efficiency as a function of outcoupling (saturation) for the nominal 70 mmol/sec condition is shown in figure 2. The maximum efficiency occurred at a reflectivity of $R=0.982$. Extrapolation of the curve to zero power suggests a small signal gain of approximately .014 cm^{-1} . Mode footprints collected at high outcoupling fraction reveal that the laser is operating near single mode on the optical axis, so the gain inferred from the intensity saturation applies along the optical axis. The average gain over the aperture is almost certainly somewhat lower.

The 1.315 μm gain diagnostic was used to collect small signal gain directly for various flow conditions. The interpretation of these measurements is presently incomplete, but the gain is consistent with gain inferred from the saturation curves. The diagnostic was developed to also have the capability of determining temperature from linewidth. Preliminary indications are that the cavity temperature is considerably higher than previously thought.

The diffractive spill data for the 1.5 x 1.5 cm and 1.5 x 3 cm apertures are shown in figures 3 and 4, respectively. The diffractive spill is plotted as a percentage of the measured power. At the reflectivity of interest ($R=0.982$), the diffractive spill for both the 1.5 x 1.5 cm and 1.5 x 3 cm apertures was approximately 5% of the power.

A simple model has been developed to describe how the yield and gain are related in a COIL, and how they are affected by the presence of a cavity³. This model, the COIL simplified saturation model, uses the properties of the resonator along with flow properties to calculate the optical extraction efficiency. The required inputs to the model are listed in table 2.

3.1 Inputs to model

The mirror reflectivities, scattering losses (calculated as $1-R-T$), small signal gain, diffractive loss, gain length, and mode length shown in table 2 are measured quantities. The gas velocity is calculated and the absorption loss term is estimated. The rationale for the selection of other quantities is shown below, along with a discussion of the diffractive loss term.

As input to the simplified saturation model, a diffractive loss needs to be assigned to the high efficiency test, even though the high efficiency test did not include an instrumented limiting aperture. Based on the observation that the two apertures tested had very similar losses, a loss of 5% of the measured power will be assumed for the calculation. This is probably an upper bound due to the fact that the boundary layers along the walls transverse to the optical axis act as a gain aperture without clipping the beam.

Assuming a scattering loss on the outcoupler mirror of 0.0025, and a reflectivity of $R=0.982$ (and neglecting absorption), 0.0155 of the one-way circulating power was measured by the power meter. Since the measured diffractive spill was 5% of the power and 93% of the diffraction was absorbed, the round trip diffractive loss was $(.05/.93)*.0155 = 0.00083$.

The assumed cavity yield is based on an assumed detachment yield of $Y_{det} = 0.7$, transport χ of 0.088 torr-sec ($Y_{plen} = .623$), and a measured iodine/oxygen ratio of .017 with an assumed dissociation² n of 5.

Cavity temperature is also required as input to the model. It is straightforward to calculate the isentropic temperature of a non-reacting flow based purely on expansion ratio, resulting in temperatures of approximately 120 K. However, heat release in the flow due to gas phase quenching of I^* increases the actual temperature to perhaps 160 K. It has also been proposed that the process of water condensation in the cavity may account for even higher temperatures. However, premixed equilibrium COIL gain models suggest that the cavity temperature must be well below 200 K to be consistent with measured gain⁵. Preliminary linewidth data from gain measurements taken on VertiCOIL indicate temperatures well above 200 K. For the purpose of modeling the high efficiency case, since we have a direct measure of the gain (from saturation data), and a reasonable estimate of the yield, the cavity temperature does not have a large impact on the extraction efficiency, although it does have a large impact on chemical efficiency.

A variety of temperatures have been used in the model to study the impact of temperature. The model does prefer low temperatures in the following sense. The iodine atom concentration in the cavity can be calculated independently from the model quite simply from pressures and flowrates and a cavity temperature. The iodine atom number density can also be calculated from gain, yield, and cavity temperature. The temperature must be near 180 K for these two calculations to agree.

Using the values shown in Table 2, the optical extraction efficiency predicted by the simplified saturation model is approximately 0.67, surprisingly high for a short gain length device. Low scattering optics, low diffractive loss, and good medium saturation ($g_u/g_o=.15$) combine to produce relatively good extraction. The results of an analysis such as this must be viewed with caution. The model neglects boundary layers that cause gain and temperature nonuniformities across the aperture.

The extraction efficiency of 0.67 can now be used in the heuristic equation to determine how the predicted chemical efficiency compares with the measured chemical efficiency of 26.7%. Using $Cl_2 = .07$ mol/sec, $Util = .94$, mixing efficiency = .9, and geometric efficiency = 1, the heuristic model predicts an efficiency of 26% assuming the cavity temperature is 200 K. The cavity temperature has a strong impact on overall efficiency (a 20 K increase in temperature decreases the predicted chemical efficiency to 25%), so the overall performance prediction is uncertain until the cavity temperature is better known.

4. SUMMARY

A number of experimental parameters and flow properties affecting optical extraction efficiency on Phillips Laboratory's VertiCOIL laser have been measured. The laser extraction efficiency has been modeled using the COIL simplified saturation model. The model predicts an extraction efficiency of approximately 0.67. The relatively good extraction is due to low mirror scattering, low diffractive loss, and good medium saturation. This extraction efficiency allows the laser to operate with an overall chemical efficiency of nearly 27%.

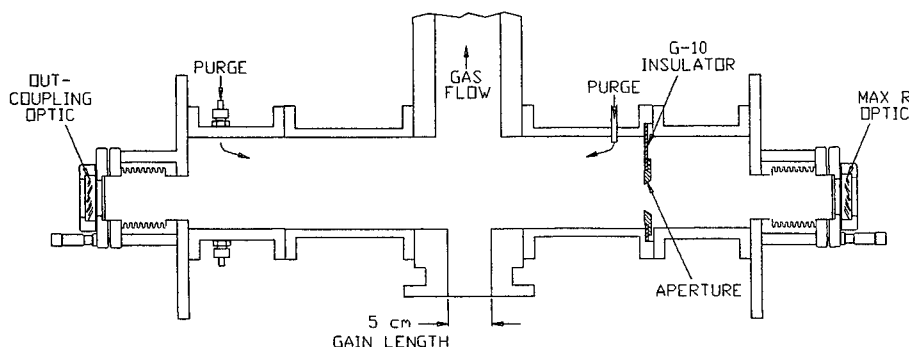


Figure 1. Experimental set-up for diffractive spill measurement.

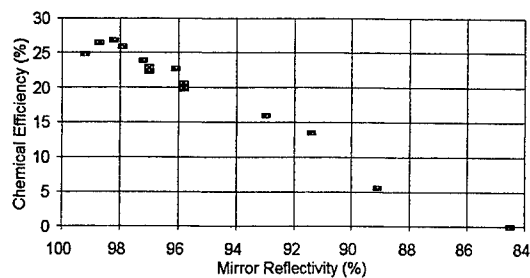


Figure 2. Chemical efficiency as a function of mirror reflectivity at the conditions listed in table 1.

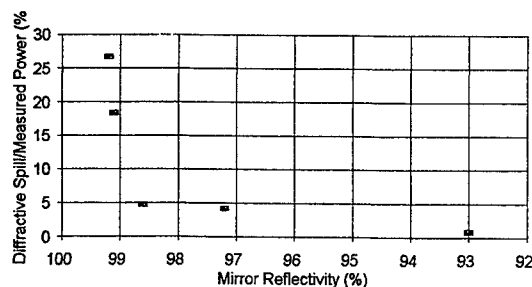


Figure 3. Power diffracted into the 1.5 x 1.5 cm aperture as a percentage of the total power at the conditions listed in table 1.

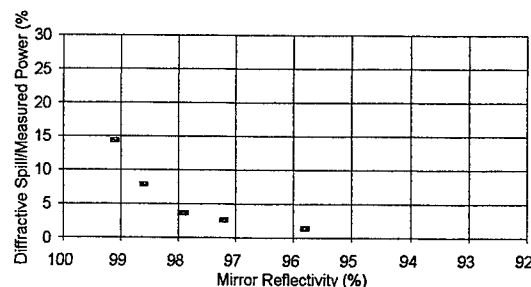


Figure 4. Power diffracted into the 1.5 x 3 cm aperture as a percentage of the total power at the conditions listed in table 1.

5. REFERENCES

- ¹T.L. Rittenhouse, S.P. Phipps, C.A. Helms, K.A. Truesdell, "High efficiency operation of a 5-cm gain length supersonic chemical oxygen-iodine laser," in *Gas and Chemical Lasers*, Robert C. Sze, Editor, Proc. SPIE 2702, 333-338 (1996).
- ²J. Hon, D.N. Plummer, P.G. Crowell, J. Erkkila, G.D. Hager, C.A. Helms, K.A. Truesdell, "Heuristic method for evaluating COIL performance," *ALAA J.*, **34**, no. 8, pp 1595-1603, 1996.
- ³G.D. Hager, C.A. Helms, K.A. Truesdell, D. Plummer, J. Erkkila, P. Crowell, "A simplified analytic model for gain saturation and power extraction in the flowing chemical oxygen-iodine laser," *J. Quant. Elec.*, in press, 1996.
- ⁴S.J. Davis, M.G. Allen, W.J. Kessler, K.R. McManus, M.F. Miller, P.A. Mulhall, "Diode laser-based sensors for chemical oxygen iodine lasers," in *Gas and Chemical Lasers*, Robert C. Sze, Editor, Proc. SPIE 2702, 195-201 (1996).
- ⁵R.F. Tate, B.S. Hunt, C.A. Helms, K.A. Truesdell, and G.D. Hager, "Spatial gain measurements in a chemical oxygen-iodine laser (COIL)," *J. Quant. Elec.*, **31**, no. 9, pp 1632-1636, 1995.

Slit nozzle jet $O_2(^1\Delta)$ generator

Yuko Hoshino, Shunsuke Takahashi, Tomoyuki Sekiguchi and Taro Uchiyama

Department of Electorical Engineering, Faculty of Science and Technology, Keio University,
3-14-1, Hiyoshi, Kouhokoku, Yokohama, Japan

ABSTRACT

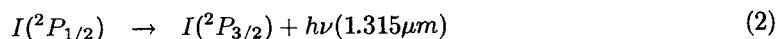
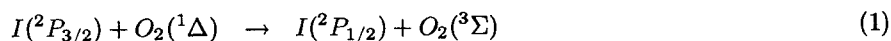
The supersonic chemical oxygen iodine laser (SCOIL) is full of promise as the industrial laser due to its high power and efficiency. The most important part of the SCOIL is a singlet oxygen generator (SOG) which produce energy source of the laser system. Although there are several types in SOG, a jet type SOG (JSOG) is expected to be the most suitable for the SCOIL. We conducted tests of a slit nozzle JSOG that is a new type JSOG and compared with generally used round nozzle JSOG.

Keyword: chemical oxygen iodine laser, singlet oxygen generator, slit nozzle

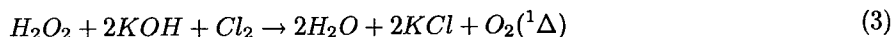
1. INTRODUCTION

The chemical oxygen iodine laser (COIL) was firstly realized in 1978¹ and was studied by many research institutes after that time. Recent development of the COIL is remarkable and an output power over 30KW has been already achieved using a supersonic flow². Because of its high power and applicability of transmission through optical fiber, the SCOIL is very promising in the field of material processing.

The COIL is pumped by energy transfer from singlet molecular oxygen to iodine



The most important part to realize the SCOIL is a singlet oxygen generator (SOG) which produce $O_2(^1\Delta)$ by chemical reacting gaseous chlorine with a basic hydrogen peroxide (BHP) solution



Several types of SOG, such as bubbling type, wetted disk type³, porous pipe type⁴ and jet type⁵, have been developed. But we think jet type is the most suitable SOG for the SCOIL because it is possible to get a large specific surface area of the BHP.

Generally the jet type SOG has many small round nozzles and the BHP solution passes through nozzles into the reaction zone. The key of designing the high pressure JSOG is increasing the specific surface area of the BHP solution within the generator in order to get a large reaction area of the BHP with Cl_2 gas. So we thought of using slit nozzles instead of round ones. It is easily shown that the slit nozzle can make a much larger specific surface area of the BHP than the round nozzle with the same cross sectional area.

2.EXPERIMENTAL APPARATUS

The schematic drawing of the experimental apparatus employed is showed in Figure.1 and Figure.2. It consists of a reaction chamber, a jet nozzle plate, a BHP solution reservoir, a BHP solution tank, Cl_2 injectors, a heat exchanger and a circulating system of refrigerant.

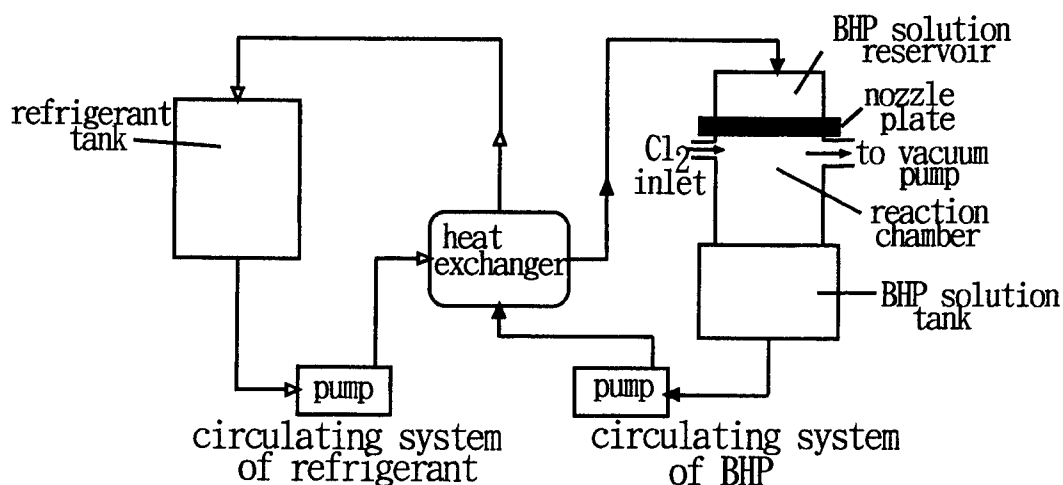


Figure.1 Schematic drawing of the experimental apparatus

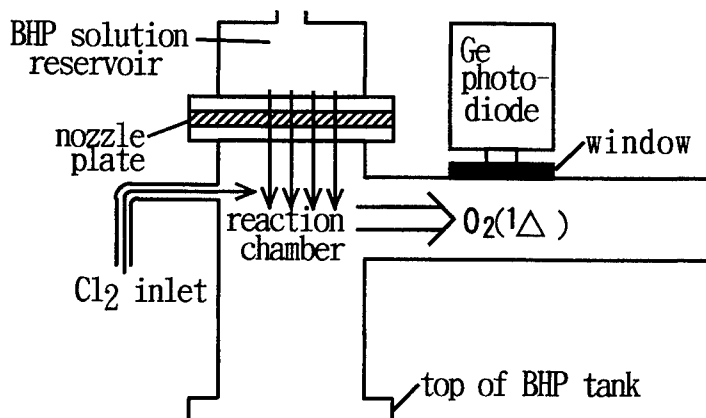


Figure.2 Cross sectional drawing of the SOG

The reaction chamber made of scleroid polyvinyl chloride resin had the inside diameter of 79mm, the outside diameter of 89mm and the height of reaction zone of 100mm. The BHP solution (18% of H_2O_2 and 35% of KOH) precooled under $-10^{\circ}C$ by the heat exchanger using ethylene glycol as refrigerant was injected downward from the solution reservoir located at upper part of the chamber through the jet nozzle plate into the reaction chamber. The Cl_2 gas was crossflowed to it through many orifices that are 2mm in diameter. A germanium photo diode was used to detect the fundamental emission of $O_2(^1\Delta)$ at 1270nm. The residual

BHP solution was collected at the BHP tank located at lower part of the chamber and was repumped into the upper reservoir by a circulating pump.

In this test in order to investigate the influence of the specific surface area of the BHP solution within the reaction zone, two different jet nozzle plates were employed; a slit nozzle plate and a round nozzle plate. The drawings of these plates are showed in Figure.3. Each plate made of scleroid polyvinyl chloride resin was 130mm in diameter and was 6mm thick. The slit nozzle plate had rectangular orifices of $0.13 \times 10 \text{ mm}^2$ and the round nozzle plate had circular orifices of 1.3mm in diameter. These two orifices have almost same cross sectional areas but the specific surface area of the BHP solution passed through the slit shape is much larger than the one passed through the round shape within the reactor.

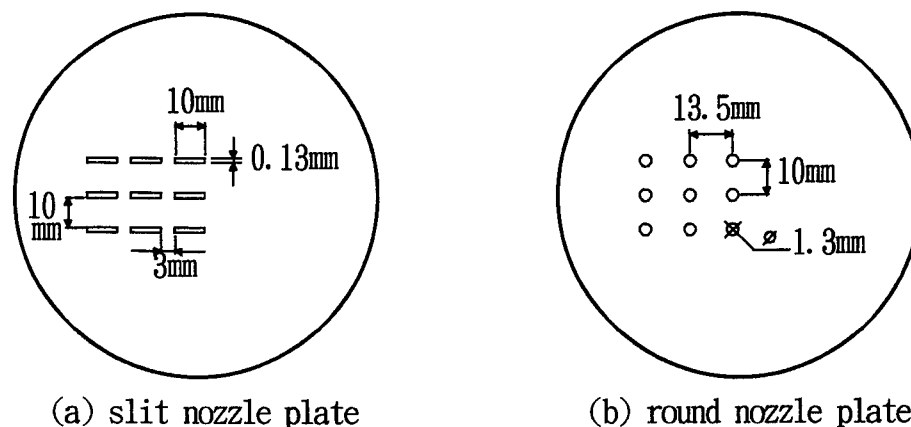


Figure.3 Drawings of Nozzle plates

3.RESULTS

Tests of $O_2(^1\Delta)$ generation using the slit nozzle plate and the round nozzle plate were conducted. Results of these tests are showed in Figure.4. The Cl_2 mass flow rate was controlled by changing secondary pressure of the Cl_2 cylinder. In each test $O_2(^1\Delta)$ generation was in proportion to secondary pressure of the Cl_2 cylinder.

The slit nozzle produced higher $O_2(^1\Delta)$ generation than the round nozzle in the tests but the results fell short of our expectation. The slit nozzle should be able to produce much higher $O_2(^1\Delta)$ in comparison with the round nozzle in theory. The cause is thought that there was a problem about the shape of the BHP solution in the reaction chamber. Observation of the jet within the reactor showed that the solution was laminar film form in the length of a few centimeters just after passing through the slit nozzle but gradually converged and finally became column form. That's why the specific surface area of the BHP solution became small and $O_2(^1\Delta)$ generation was reduced. If laminar film form of the BHP becomes longer by means of making the pressure of pushing the BHP stronger and using more narrow slits and so on, there is a possibility of producing higher pressure $O_2(^1\Delta)$.

So far, only $O_2(^1\Delta)$ pressure was calibrated. So it is necessary to investigate the relative $O_2(^1\Delta)$ pressure in this equipment compared with the $O_2(^3\Sigma)$ pressure, the residual chlorine pressure and the water vapor pressure.

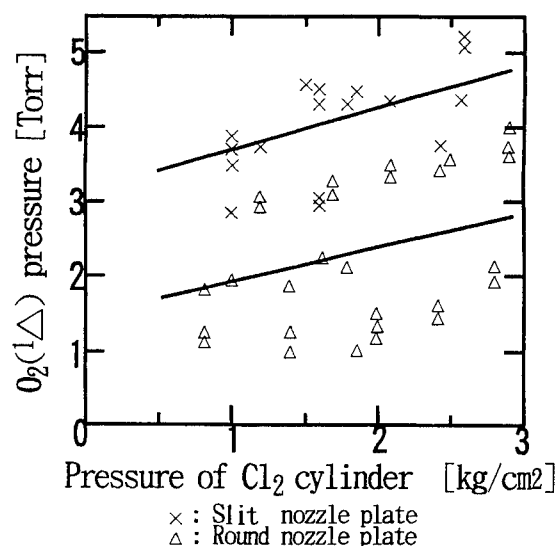


Figure.4 $O_2(^1\Delta)$ pressure vs secondary pressure of Cl_2 cylinder

4.CONCLUSION

Tests of $O_2(^1\Delta)$ generation were conducted using the slit nozzle and the round nozzle. Results presenting the advantage of the slit nozzle were obtained but these fell short of our expectation. We think the slit nozzle should be able to produce much higher pressure $O_2(^1\Delta)$ if the region of laminar film form of the BHP becomes much longer.

REFERENCES

- [1] W.E. McDermott, N.R. Pchelkin, D.J. Benard, and R.R. Bousek, "An Electronic Transition Chemical Laser", *J. Appl. Phys.* 70, pp. 5211 (1991).
- [2] P.V. Avizonis, G. Hasen, and K.A. Truesdell, "The Chemically Pumped Oxygen-Iodine Laser", *Proc. SPIE* 1225, pp. 448 (1990).
- [3] R.J. Richardson, C.E. Wiswall, P.A.G. Carr, F.E. Hovis, and H.V. Lilenfeld, "An Efficient Singlet Oxygen Generator for Chemically Pumped Iodine Lasers", *J. Appl. Phys.* 5, pp. 4962 (1981).
- [4] K. Takehisa, N. Shimizu, and T. Uchiyama, "Singlet Oxygen Generator Using a Porous Pipe", *J. Appl. Phys.* 61, pp. 68 (1987).
- [5] M.V. Zagidullin, A. Yu. Kurov, N.L. Kupriyanov, V.D. Nikolaev, M.I. Svistun, and N.V. Erasov, "Highly Efficient Jet $O_2(^1\Delta)$ Generator", *Sov. J. Quant. Electern.* 21, pp. 747 (1991).

INVESTIGATIONS ON THE EFFICIENCY OF A ROTATING DISK TYPE OXYGEN GENERATOR

K.Grünewald, J.Handke, L.v.Entreß-Fürsteneck, W.L.Bohn*, W.O.Schall*

DLR - Institut für Technische Physik, Langer Grund D-74239 Hardthausen, Germany

*DLR - Institut für Technische Physik, Pfaffenwaldring 38-40, D-70659 Stuttgart, Germany

ABSTRACT

For a rotating disk type generator the dependencies of utilization and yield on the generator operating mode are experimentally investigated. The fundamental effects of rotational speed, reduced gas volume, gas flow and liquid phase composition on the efficiency of singlet delta oxygen generation are discussed together with theoretically predicted generator performance from literature.

KEYWORDS: COIL, rotating disk generator, singlet delta oxygen, utilization, yield, efficiency

1. INTRODUCTION

Since the provided singlet delta oxygen is substantially affecting the achievable laser output power¹, high power operation of chemically pumped oxygen iodine lasers requires efficient singlet delta oxygen generation.² In the intention to achieve fast and reliable scaling arguments with respect to most efficient laser operation, utilization and yield have been tested over a wide operating range of a rotating disk type generator, as implemented in the multikilowatt oxygen iodine laser of the DLR.^{3,4} The demonstrated dependencies of singlet delta oxygen production on disk rotation, gas phase and chemistry are in good agreement with the theoretical predictions^{5,6,7,8}. So, a combined, theoretically and experimentally deduced, data set can be used to determine reproducible high efficient generator operating mode.

2. GENERATOR CONFIGURATION AND EXPERIMENTAL SET-UP

The investigated oxygen generator is of the conventional rotating disk type, developed and mounted at the Phillips Lab in Albuquerque⁹. Compared to the original version, the present generator configuration, as shown in Fig. 1, has been changed by additional fittings to reduce the gas volume of the exit side. The singlet delta oxygen molar flow is measured by emission diagnostics in the duct, directly attached to the generator exit.³ Including the pooling losses along the distance between generator exit and measuring point, the yield does underpredict the generator performance. So, the measured efficiency data can be interpreted as a lowest limit of the true generator efficiency. The molar flow of residual chlorine is derived from absorption diagnostics, the molar flows of initial chlorine and buffer gases are measured by gasdynamic methods.

The present generator configuration allows reproducible hot runs on a time scale of up to 60 sec with little decrease in effi-

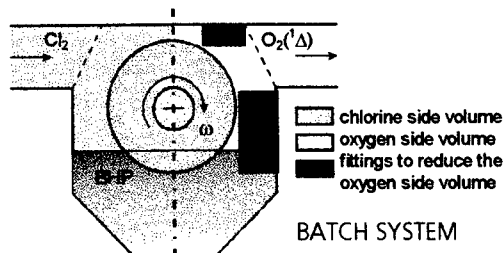


Fig. 1: Generator configuration

ciency. The run time is limited by effects due to temperature rise and BHP depletion during hot flow. Figure 2 shows 30-sec-hot-run-histories of utilization and yield and, as the product of both, the efficiency. The data are recorded for standard operating conditions of the test series: 24 rpm, 0.55 mol/s initial chlorine flow and a supply gas ratio of He:Cl₂ of 3:1. Since the chlorine flow is constant during the hot run, the molar flow of excited oxygen follows the shape of the efficiency, multiplied by a constant factor. In the following, the hot run typifying utilization and yield are measured after one disk round plus one additional second (=3.5 sec for 24 rpm) after hot run start (emission signal) to avoid the transient phase and to represent stable generator operating conditions.

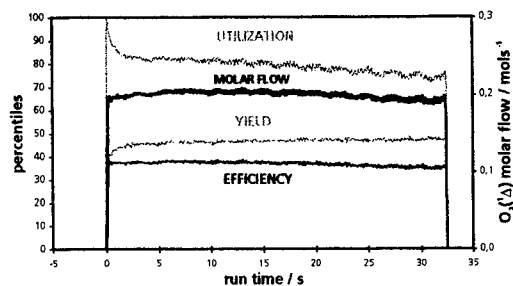


Fig. 2: Generator performance

3. THEORETICAL BACKGROUND

Based on the theoretical studies of McDermott^{5,8} and Copeland et al.^{6,7} the limitations of utilization and yield have been calculated. Besides, the thermal balancing at the interface in progressing hot run has been roughly approximated.

A near optimum rotation speed was found by Copeland et al.⁶ in verifying the range of validity of the perturbation solution to approximate the utilization in the case of decreasing surface concentration of hydroperoxy anions (O_2H^-). The achievable efficiency data were found to saturate at rotation speeds little above this validity criterion.

Two limitations of singlet delta oxygen generation have directly been derived from the BHP molarity.^{5,6} If the surface concentration of O_2H^- is assumed to be constant, the singlet delta oxygen generation is liquid phase limited only by the finite rate k_1 of the reaction of Cl_2 with BHP. The reduced description leads to the absolute maximum of utilization for a given operating mode. Independent of the liquid exposure time, this limitation is based on the assumption of infinitively fast O_2H^- diffusion in the liquid and/or extremely high rotational speeds. For 24 rpm the maximum utilization exceeds the exact theoretical solution by about 10 %.⁶ The second limitation is given by the finite O_2H^- diffusivity in the BHP⁴, followed by a linear decrease of achievable utilization when reducing the O_2H^- surface concentration.

To approximate the thermal processes at the interface, the energy balancing is serially calculated considering the heat transfer by chlorine reaction, the singlet delta oxygen deactivation in the liquid phase, the water vaporization⁸, the thermal conduction to the disks and the temperature balancing with the bulk BHP.

4. EXPERIMENTAL RESULTS AND THEORETICAL PREDICTIONS

4.1 Gas phase considerations

In the intention to reduce the pooling losses within the generator by reducing the oxygen residence time, Teflon fittings have been installed mainly into the gas volume on the exit side of the generator. At a BHP level of 60 mm below the generator axis, this volume has been reduced by about 50 %. At test series standard conditions, the new configuration leads to yields of 5 % to 10 % higher than without fittings. Since the threshold and dissociation losses remain constant, a large part of the increase of the yield can directly be converted into laser power.

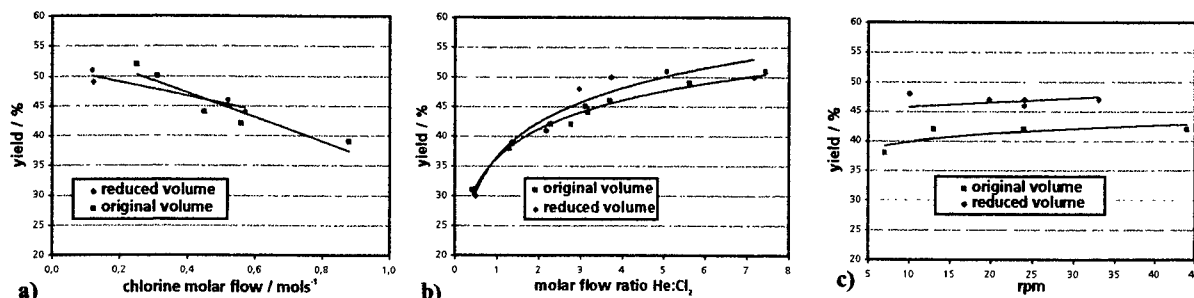


Fig. 3: Yield increase by reduced generator volume due to a.) chlorine molar flow, b) molar flow ratio, c) rotation rate

For low chlorine molar flow, the yield measured at reduced volume is lower than that of unchanged generator, see Fig. 3a. Beside of the acceleration of the gas flow, the fittings also cause a better penetration of chlorine into the disk spacing, leading to a little higher utilization. This effect is negligible at high chlorine molar flows, but it becomes important for small ones, where the higher $O_2(^1\Delta)$ flow is subjected to distinctly higher pooling losses. At increasing molar flows of buffer gas, the improvements of the yield values increase, too, Fig. 3b. This trend is limited, when the excited oxygen lifetime at the actual gasdynamic conditions exceeds the oxygen residence time. The improvements are most clearly shown in Fig. 3c, when relating the yield to the rotational speed.

For a given rotational speed, the utilization and yield are decreasing by increasing the chlorine molar flow, while they show a slight rise at increasing molar flow of buffer gas. In Fig. 4, the measured utilization and yield of both variations are related to the product of chlorine molar flow and gas transit time. At diminishing values of this product, utilization and yield are increasing, independent of which factor of the absciss is reduced. It can be seen that the effi-

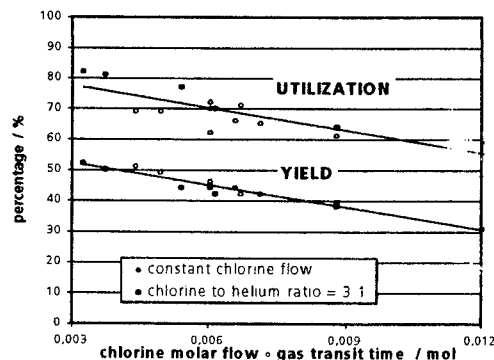


Fig. 4: Gas phase affecting utilization and yield

ciency here only depends on the amount of moles of chlorine provided at the reactive surface. Each value of moles of chlorine can be adjusted either by varying the chlorine molar flow or by a matching of the buffer gas flow.

The relations presented in Fig. 4 are only valid for constant liquid exposure time. A variation of the rotational speed for a constant gas phase mode yields completely different relationships.

4.2 Liquid phase induced limitations

For the standard test conditions the near optimum rotation speed is displayed as black lines in Fig. 5. The two lines reflect two different values of reaction rate k_1 .^{4,5} The white contour lines show the smoothed values of measured utilization. Even when the courses of contours and calculated rotation speeds are not exactly parallel because of mavericks, the calculation gives a good idea of the relevant rotational speeds for different BHP mortalities at a given operating mode. For small O_2H molarities, both calculated curves show a rapid increase of the desired rotational speed up to 1000 rpm. Since rotational speeds above 50 rpm involve the risk of liquid overflow into the duct, O_2H molarities less than 5 mol/l are not practical to gain high efficiency performance at the discussed operating conditions.

Fig. 6 shows the measured utilization resulting from hot runs of different test series at standard operating conditions. The utilization is related to the actual O_2H molarity at hot run start. Additionally, the calculated utilization limitations by O_2H diffusion and reaction rate k_1 are outlined. The BHP mortalities at the start of each test series are described by the starting BHP molarity of KOH and the excess molarity of H_2O_2 . Since the stand-by phase between two hot runs lasts several minutes due to cooling requirements, the molarity of the film BHP on the disks at hot run start is estimated to be the same as in the bulk. For O_2H molarities above 5.5 mol/l, the measured values of utilization lay inside the area of reaction limitation. Lower molarities lead into the region, where the achievable utilization is roughly limited by O_2H diffusion. Because of the drastic descend of the utilization limit in this area, small BHP mortalities have to be avoided. In the reaction limited area, the measured utilization achieves about 86 % of the theoretical limit, which is in good agreement with the exact theoretical solution.^{6,7} The increase of the molarity above 7 mol/l, does not result in much higher utilization but enables stable generator performance. This fact could be proven in single hot runs on a time scale of up to 1 minute as well as in a series of short runs of a few seconds of run time, showing comparable performances, despite of growing salt accumulation. An experimentally implied limitation is coming up at O_2H molarities of about 8 mol/l by the foam which is cropping up after a few runs and is of a

nearly crusty and very stable kind.

From the measured duct yield, the detachment yield has been calculated "backwards", only considering the pooling losses.³ The values obtained by this simplification differ by a factor of 1.6 from the theoretical detachment yield, calculated from the O_2H surface concentration^{5,6}, see Fig. 7. The increase of both results by increasing O_2H molarity is faster than the rise of the measured duct yield. So, because only pooling losses are considered, the delay has to be interpreted as a measure for the increase in pooling losses due to higher O_2H concentration resultant from increasing utilization. As shown in [5], the dependencies of utilization and yield on BHP molarity are caused by the dependencies of chlorine lifetime and nascent yield on the surface concentration of O_2H .

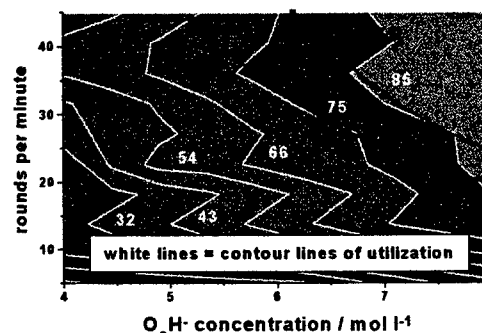


Fig. 5 : Near optimum rotation speed

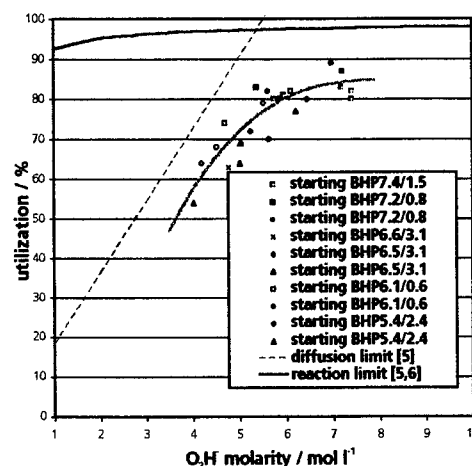


Fig. 6: Utilization limitations

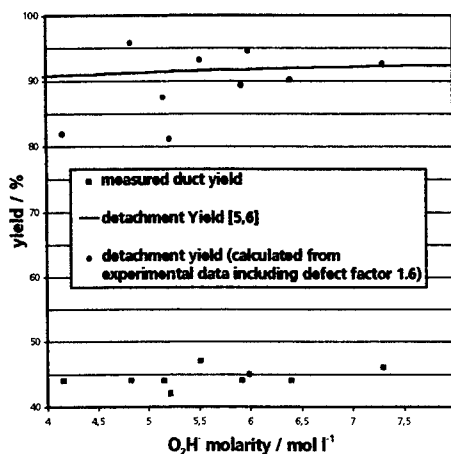


Fig. 7: Detachment yield

In the same manner as the utilization of the hot run series has been investigated, now, the progress of single hot runs will be examined. In Fig. 8, the measured utilization is outlined for two hot runs at rotational speeds of 8 rpm and 24 rpm respectively, at the same operating conditions. In the case of the low rotational speed, the utilization is plotted after every quarter of a round and for the high speed after every full round. Filled points show the molarity dependence, when the decrease in O_2H^- anions is related to the bulk BHP, empty points when related to the film BHP on the disks.

At fast rotation, the bulk values follow the diffusion limitation, while the film values exceed this limit. At low speed, the values show the opposite behaviour. While the shape of bulk values is far from the diffusion limitation, the film values are leaning on this limit. Additionally, BHP temperatures measured in the disk spacing during hot run show a faster increase for high rotation speeds, even of shorter exposure times, than for low ones, according to the higher oxygen generation. In a rough approximation of thermal balancing, the chlorine reaction could be verified as the dominant heat supply process which is not to be compensated by temperature dependent cooling processes such as water evaporation and heat conduction. As a consequence high efficiency operating conditions like near optimum rotational speed and/or high BHP molarity are always accompanied by strong temperature increase during hot run. The rotational speed dependent expansions of utilization and temperature in progressing hot run indicate differences in the film BHP refreshing process and are requiring more detailed investigations of the interface conditions.

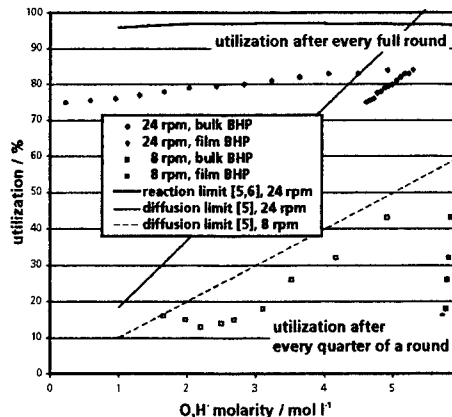


Fig. 8: Utilization in progressing hot flow

5. CONCLUSIONS

The results of theoretical studies and experimental investigations are in good agreement. In a combination of both, a set of optimization criteria has been obtained with regard to high efficient generator operating mode.

High efficiency performance and stable conditions are primarily achieved by high BHP molarities in the liquid and by reducing the residence time of excited oxygen in the gas. The increase of BHP concentration is limited by growing difficulties of foam handling. The provided moles of chlorine at the interface are to relate to the liquid exposure time. The liquid exposure time itself is to orient to the near optimum rotation speed, in order to gain high utilization and to avoid liquid overflow into the duct caused by unnecessary fast rotation.

6. REFERENCES

1. J.Handke, W.O.Schall, W.L.Bohn, L.v.Entress-Fürsteneck, K.Grünwald, R.Kwirandt, A.Werner, "Multikilowatt Supersonic Chemical Oxygen Iodine Laser", *Proc. Forth Int. Workshop on Iodine Lasers and Applications*, SPIE Vol. 2767 (1995), p. 195.
2. P.V.Avizonis, G.Hasen, K.A.Truesdell, "The Chemically Pumped Oxygen-Iodine Laser", *High Power Gas Lasers, Proc. GCL 8th Int. Symp.*, SPIE Vol. 1225 (1990), p. 448.
3. J.Handke, K.Grünwald, L.V.Entress-Fürsteneck, W.L.Bohn, W.O. Schall, "Supersonic COIL Operation at DLR Germany", to be presented at this conference.
4. J.Handke, A. Werner, W.L.Bohn, W.O.Schall, "Multikilowatt Supersonic Oxygen Iodine Laser", *Proc. GCL 10th Int. Symp.*, SPIE Vol. 2502 (1994), p.266.
5. McDermott, "The Generation of Singlet Delta Oxygen - A Technology Overview", *Intense Laser Beams and Application*, SPIE Vol 1871 (1993), p.135.
6. D.A.Copeland, W.E.McDermott, V.Quan, A.H.Bauer, "Exact and Approximate Solutions of the Utilization and Yield Equations for $O_2(^1\Delta)$ Generators", *Intense Laser Beams and Applications*, SPIE Vol. 2119 (1994), p.27.
7. D.A.Copeland, V.Quan, J.A.Blauer, S.E.Rogriguez, "Two-Phase Model of $O_2(^1\Delta)$ with Application to Rotating Disk Generators", *Intense Laser Beams and Applications*, SPIE Vol 1871 (1993), p.203.
8. W.E.McDermott, "Thermal Effects in Singlet Delta Oxygen Generation", *Intense Laser Beams and Appl.*, SPIE Vol 1628 (1992)
9. K.A.Truesdell, S.E.Lamberson, "Phillips Laboratory COIL technology overview", *Proc. GCL 9th Int. Symp.*, SPIE Vol.1810 (1992), p476.

Pulsed iodine photolytic laser system PERUN

B. Králíková, J. Skála, J. Krása, L. Láška, K. Mašek, K. Rohlena, P. Straka

Institute of Physics, Acad. Sci. of the Czech Rep., Na Slovance 2, 18040 Praha 8, Czech Republic
Tel/Fax:: +422 66052623 / +422 821227 E-mail: kralik@fzu.cz

ABSTRACT

The photolytic pulsed iodine system PERUN has already been described^{1,2}. This contribution presents its improvements within the last few years according to an increasing demand of interaction experiments. As examples of its use a short description of some interaction experiments currently being performed with the system PERUN - self-smoothing effect of double-pulse laser plasma, production of highly charged ions for particle accelerators, passage of laser light through a hole (plasma shutter) - are given.

Keywords: iodine laser, laser plasma

1. DESCRIPTION OF THE PERUN PRESENT STATE

The present arrangement is given in Fig. 1. As reported^{1,2}, the system consist of an oscillator and four amplifiers. There are a few new elements recently included. Two Faraday rotators placed behind both the third and the fourth amplifiers, which protect the optical elements from the laser beam reflected from the target and amplified by a residual inversion population remaining in amplifiers. A spatial filter placed behind the third amplifier improves the quality of the beam which depends on the diameter of its pinhole.

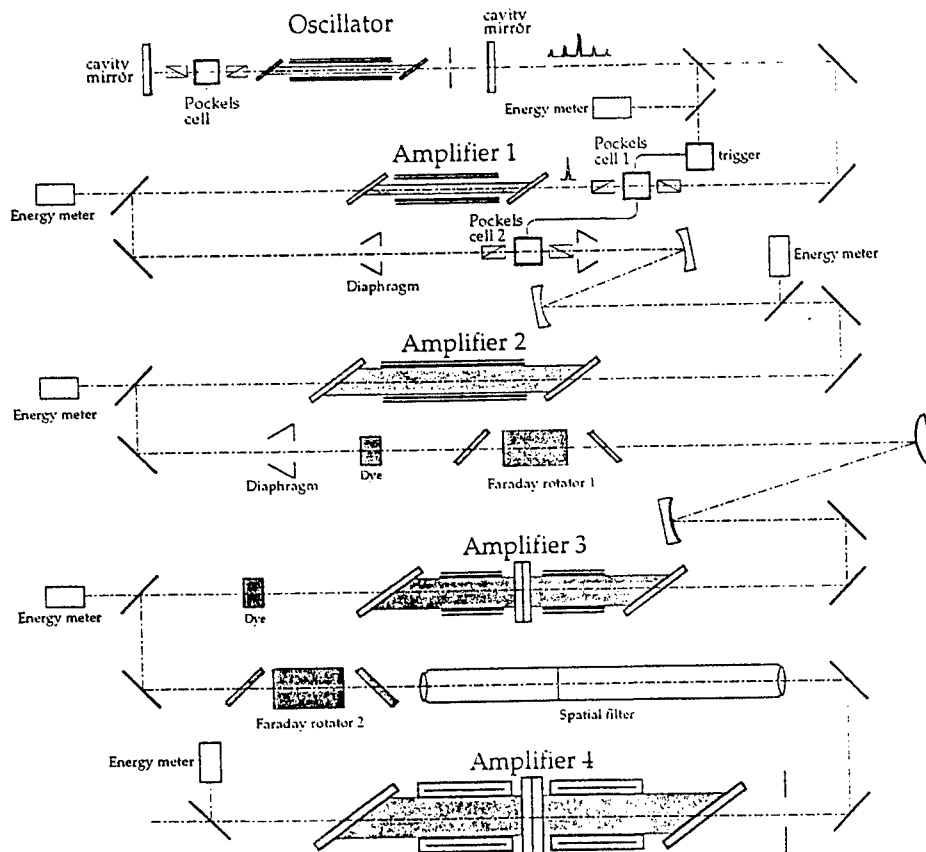


Fig. 1. Present arrangement of the laser PERUN

Basic output parameters of the laser are given in the table:

WAVELENGTH	1.315 μm	ENERGY	50 J
	0.657 μm		25 J
	0.338 μm		20 J
NOMINAL PULSE LENGTH	300 ps		
BEAM DIAMETER	84 mm		
MAXIMUM INTENSITY IN FOCUS	$5 \times 10^{15} \text{ W/cm}^2$		

2. IMPROVEMENTS OF THE SYSTEM

2.1. The frequency up-conversion

The frequency doubling and tripling makes our laser system more versatile. For non-linear frequency conversion to the second and the third harmonics of the laser beam the large size monocrystals of DKDP fabricated in the Institute of Applied Physics of the Russian Academy of Sciences in Nizhni Novgorod were used. Maximum conversion efficiency to the second harmonic ($\lambda = 0.657 \mu\text{m}$) of 55% was attained at the laser energy 40 J³. The laser beam full angle divergence was determined to be $4 \cdot 10^{-4}$ rad. For the generation of the third harmonic ($\lambda = 0.438 \mu\text{m}$) the sum-frequency mixing scheme of type II - II was applied with a couple DKDP crystals were combined as doubler and mixer. In this case the conversion efficiency was 50%, which represents the energy of the blue radiation 20 J⁴.

2.2. Beam space-time intensity distribution

Due to demands of interaction experiments on uneven timing of the various parts of the laser beam profile (fractions of nanosecond) it was necessary to deal with the space-time intensity distribution (STID) of the beam. The radial dependence of the pulse propagation speed can lead not only to an uncertainty of the pulse timing but also, after focusing, the interaction time is prolonged and the power density in the focus is decreased. That was why attention was paid to a determination of STID of the system PERUN. We found out that the propagation speed of the laser pulse showed a radial dependence; local pulse duration (resulting mainly from the saturation shortening of the original pulse) varied from 300 to 400 ps and the total pulse length integrated per the cross-section was from 700 to 1000 ps. After a detailed study of the STID profile evolution of the beam passing through the amplifier chain we modified the optical arrangement of the laser system⁵. The local pulse length remained unchanged, but the length of the focused pulse approached the local one (Fig. 2).

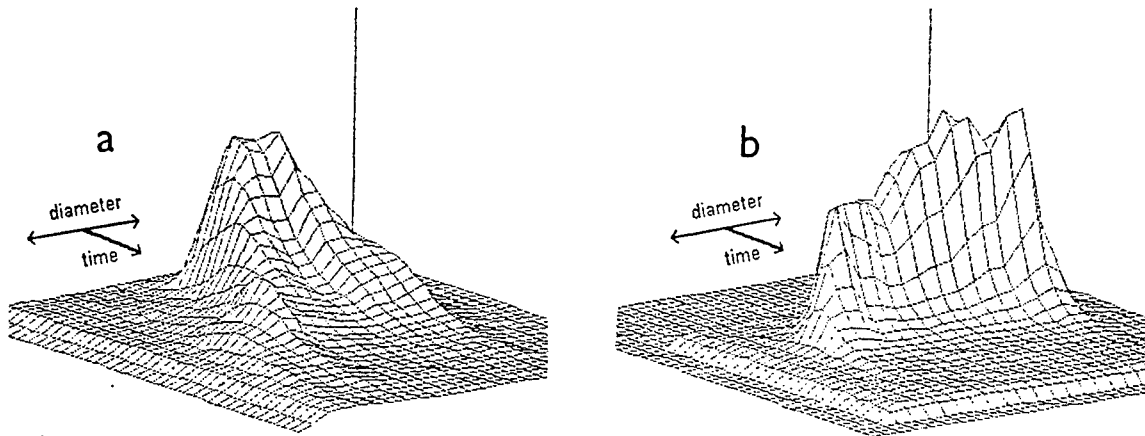


Fig. 2. Space - time distribution of the laser pulse intensity a) before and b) after the modification of the laser system

2.3. Maintaining the constant beam divergency

In the system PERUN the flashlamps with a long pulse ($\sim 300 \mu\text{s}$) are used as a pumping source. It has a consequence in the form of an acoustic wave, which propagates through the active medium, perturbing its optical homogeneity, and impairing the beam divergency and/or focussability. These variations are of the order 10^{-4} rad. The influence of this phenomenon can be reduced by increasing the proportion of He in the laser active medium ($\text{C}_3\text{F}_7\text{I} + \text{SF}_6 + \text{He}$)². Some interaction experiments are very sensitive⁶ to the change in the beam divergency because in such a case the focus length in the interaction chamber varies. That's why a special attention to continual beam divergency check is needed. The arrangement follows: Behind the output amplifier a part of the beam is separated and is led on a spherical mirror ($f = \sim 1\text{m}$) with a mask having four holes in the same distance from the center. A burn paper is placed 15 mm in front of the focus. The distance of spots on the paper is now the measure of the beam divergency and in our arrangement it is proportional to the relative position of the focus in the interaction chamber. The focus position can be determined with an accuracy of $50 \mu\text{m}$. This value is satisfactory for all practical purposes since it is well within the caustic length.

3. EXAMPLES OF THE LASER PERUN USE FOR INTERACTION EXPERIMENTS

3.1. Self smoothing effect of double pulse laser plasma

In these experiments we decided to test the idea of smoothing the ablation pressure inhomogeneity by increasing the distance between the critical and ablation surfaces and allowing thus the lateral thermal conductivity to wash out the spatial inhomogeneities occurring on the critical surface due to an uneven illumination⁷. The position of the critical versus ablation surface can be controlled by driving the main heating pulse through a prepulse plasma. The prepulse weakens the density gradient and prolongs the distance which the heat deposited at the critical surface must cross to power the ablation. A plasma is first formed by a weaker prepulse using the second harmonic of the laser and about one nanosecond later the main, third harmonics pulse is introduced. After passing through the DKDP crystals - frequency converters - the beams with different wavelength are separated by special selective mirrors. The target chamber is fitted with an aspherical optics which can be adjusted to either of the three harmonics ω , 2ω , 3ω of the iodine laser wavelength. The focusing optics was set to the third harmonics and the separated second harmonics beam was passing through an auxiliary lens to achieve about a $200 \mu\text{m}$ focus. Optionally a random phase element could be added for further homogenization. The delayed main pulse (3ω) was split by a wedge in two beams which were then focused onto the larger 2ω focal spot to form two separated blue foci of about $40 \mu\text{m}$ in diameter each. The effect of the smoothing was evaluated from x-ray pinhole pictures of the focal spot.

3.2. Highly charged ion production

The production of highly charged heavy ions is of great importance for the present and future accelerators at the European Organization for Nuclear Research and at other heavy ion facilities. It was presented⁸ that CO_2 lasers have the potential of producing tens of miliamperes of heavy ions (e.g. Pb, Ta) of a similar charge state like in electron cyclotron resonance ion sources but within a pulse of several microseconds. An iodine laser represents an alternative approach by giving a short and intense pulse (0.5 ns , $10^{14} - 10^{15} \text{ W/cm}^2$) in a near infrared region and simultaneously provides a complementary experimental information to that obtained by CO_2 lasers.

The principal diagnostic techniques for studying Ta laser-produced plasma were based on the time-of-flight method. A cylindrical ion energy analyzer and an ion collector were used for the determination of the charge state distribution as well as of the total number of ion species in a large distance from the target. The aim of this experiment was to test the optimum conditions for obtaining a maximum current of highly charged Ta ions at a fixed laser pulse energy, i.e., the focus position versus the target surface and the target tilt angle with respect to the laser beam were varied. The highest charge state of Ta ions which can be safely recognized was $46+$. Later experiments confirmed the occurrence of Ta ions with the charge state up to $54+$ ⁸.

3.3. Passage of laser light through a hole - plasma shutter

Passage of focused laser light through a small hole placed in the region of the laser focal point is of primary interest in microcavities („hohlraum“) or the problems relating to spatial filtering of high power beams. When the focused laser light passes through a hole with a diameter comparable to that of the laser beam, its finite intensity on the aperture material produces a plasma on the hole periphery. This plasma expands inwards and screens the hole, which results in a reduction of the hole transmission. The goal of this work⁹ was a temporal characterization of the phenomenon and the comparison of the experimental results with 1-D computer simulations as well as a simple analytical model. The laser beam with energies 8-15 J at the first harmonics and with the pulse duration of $\sim 0.5 \text{ ns}$ was focused by a $f/2$ ($f = 20 \text{ cm}$) aspheric lens system to produce a spot focus $\sim 80 \mu\text{m}$ in diameter. The passing light was collected with another $f/2$ lens. A target pointing system made possible the pointing of the laser focus into the pinhole with a precision of $5 \mu\text{m}$ in the transversal and $\sim 40 \mu\text{m}$ in the

longitudinal direction. Both the experimental and theoretical results show the effect of pulse shortening of the transmitted laser light. Obtained experimental data were in a good agreement with the 1-D hydrodynamic simulations.

4. CONCLUSION

It can be said that the pulsed iodine photolytic laser system PERUN offers for interaction experiments specific advantages of a medium scale experimental facility such as a large degree of experimental flexibility, high shot rate and a simple laser interaction geometry.

5. ACKNOWLEDGMENTS

Presented results were performed partially under sponsoring of the Grant Agency of the Czech Republic and Grant Agency of the Academy of Sciences.

6. REFERENCES

1. M. Chvojka, V. Hermoch, B. Králíková, J. Krása, L. Láška, K. Mašek, J. Musil, S. Polák, K. Rohlena, J. Schmiedberger, J. Skála and J. Sulek, "100 GW pulsed iodine photodissociation laser system PERUN I," *Czech J. Phys.* **B38**, pp. 1337-1356 (1988).
2. J. Beránek, M. Chvojka, V. Hermoch, B. Králíková, J. Krása, L. Láška, K. Mašek, J. Musil, K. Rohlena, B. Rus, J. Schmiedberger, J. Skála, O. Štirand and P. Trenda, "A pulsed iodine photodissociation laser with slow pumping," *Laser and particle beams* **10**(4), pp. 871-890 (1992).
3. V.I. Bespalov, V.I. Bredichin, M. Chvojka, B. Králíková, L. Láška, K. Mašek, A.V. Ryadov, K. Rohlena, J. Skála, S.A. Sukharev, O. Štirand, I.N. Voronich and A.I. Zaretskii, "Conversion to the second harmonic of high power iodine photodissociation laser system PERUN," *Czech J. Phys.* **45**(9), pp. 757-759 (1995).
4. V.I. Bespalov, V.I. Bredichin, D.G. Efimov, B.I. Katsman, B. Králíková, L. Láška, K. Mašek, K. Rohlena, J. Skála, S.A. Sukharev, P. Trenda, I.N. Voronich and A.I. Zaretskii, "Conversion to the third harmonic of the iodine photodissociation laser PERUN," *Czech J. Phys.* **45**(9), pp. 761-765 (1995).
5. B. Králíková, K. Rohlena, J. Skála and P. Straka, "Improvement of the space-time intensity of the pulsed iodine photodissociation laser PERUN," 24th ECLIM, Madrid (SPAIN) June 3-7, 1996.
6. L. Láška, J. Krása, K. Mašek, B. Králíková, T. Mocek, M. Pfeifer, J. Skála, P. Straka, K. Rohlena, E. Woryna and J. Wolowski, "Influence of laser beam focusing on production of highly charged ions from laser plasma," 4th Int. Workshop on Iodine lasers and applications, Třešt' Castle (Czech Rep.) September 18-22, 1995, pp. 142-149.
7. B. Králíková, J. Krása, L. Láška, K. Mašek, S. Přeučil, K. Rohlena, J. Skála, A.V. Bessarab, S.G. Garanin, G.A. Kirillov, Yu.F. Kiryanov, G.G. Kochemasov, L.V. Lvov, A.B. Ryadov, S.A. Sukharev, N.A. Suslov and A.I. Zaretskii, "Imprint removal by a prepulse plasma," 24th ECLIM, Madrid (SPAIN) June 3-7, 1996.
8. L. Láška, K. Mašek, B. Králíková, J. Skála, K. Rohlena, E. Woryna, J. Wolowski, K. Langbein and H. Haseroth, "Highly charged Ta ions produced by the photodissociation iodine laser with subnanosecond pulses," *Appl. Phys. Lett.* **65**(6), pp. 691-693 (1994).
9. K. Mašek, B. Králíková, J. Krása, L. Láška, K. Rohlena, B. Rus, J. Skála, O. Štirand, P. Trenda, V.A. Bessarab, S.G. Garanin, G.A. Kirillov, Yu.F. Kiryanov, G.G. Kochemasov, A.B. Ryadov, S.A. Sukharev, N.A. Suslov and A.I. Zaretskii, "Passage of Laser Light through a Hole - Plasma Shutter," *Laser and Particle Beams* **12**, pp. 445-454 (1994).

Intracavity Second Harmonic Generation of Chemical Oxygen Iodine Laser with a Brewster cut LBO Crystal

Tomohiro SHIMIZU , Takeo TEZUKA , Kuntetsu CHEN ,
Katsuki HASHIMOTO and Taro UCHIYAMA

Department of Electrical Engineering, Faculty of Science and Technology, Keio University, 3-14-1, Hiyoshi
Kouhokuku, Yokohama, Japan

ABSTRACT

Second Harmonic Generation of Chemical Oxygen Iodine Laser was investigated with a Brewster cut LBO crystal. By utilizing a Brewster cut LBO crystal the loss in the resonator can be suppressed. Further, by reducing crystal absorption, the crystal can't be heated and go off phase match or even crack due to thermal stress. We could obtain 16.4 W of second harmonic power and keep out the crystal from being destroyed by the damage of thermal stress.

1 INTRODUCTION

Chemical Oxygen Iodine Laser (COIL) is the chemical laser which operates by consuming singlet delta state molecular oxygen $O_2(^1\Delta)$ for dissociating iodine molecule and exciting iodine atom. The energy source of COIL, $O_2(^1\Delta)$ gas at near 100 % yield in the Torr range is generated easily by chemical reaction of Cl_2 gas with basic hydrogen peroxide solution. The merit of COIL lies in high power electric input is not necessary for lasing. Additionally, the merit lies in the $1.315 \mu m$ lasing wavelength, because it is on the least loss wave range of the quartz fibre. This enables COIL to be applied for the industrial processing use and controllable cutting machine. For industrial use the shorter wavelength laser is requested because it means the higher processing efficiency and quality. And second harmonic of COIL has characteristics of the $0.658 \mu m$ wavelength of visible laser.

On second harmonic generation, conversion efficiency η_{SHG} of the nonlinear optical crystal is given by:

$$\eta_{SHG} \equiv \frac{P_{2\omega}}{P_{\omega}} = 2(\epsilon_0)^{1/2}(\mu_0)^{3/2} \frac{\omega^2 d^2 l^2 \sin^2(\Delta k l / 2)}{n^3 (\Delta k l / 2)^2} \frac{P_{\omega}}{A} \quad (1)$$

where $P_{2\omega}$ is the second harmonic power, P_{ω} is the fundamental power, l is the crystal length, n is the index of refraction, d is the nonlinear optical coefficient, A is the cross section area¹. In equation (1), conversion efficiency is proportional to the fundamental amplitude and the square of crystal length, but in the case of 10 mm LBO crystal the second harmonic output and intracavity SHG conversion efficiency as a function of the chlorine flow rate had saturated because of the competition of fundamental Gaussian mode with high degree Gaussian mode. So the crystal length was decided for 5 mm to keep off this saturation.

2 EXPERIMENTAL SETUP

A schematic drawing of the laser system is shown in Fig.1. The COIL apparatus is divided into three parts, singlet oxygen generator (SOG), vapor trap and laser cavity. In SOG $O_2(^1\Delta)$ is generated by passing Cl_2 gas through liquid mixture of 35 % H_2O_2 and 50 % KOH in the ratio of 10:1. SOG is the bubbler type because it can maintain stable $O_2(^1\Delta)$ yield. In water vapor trap water vapor is removed from $O_2(^1\Delta)$ flow since it quenches I^* significantly. The $O_2(^1\Delta)$ is introduced into laser cavity and mixed with I_2 . In the laser cavity molecular iodine is dissociated and inverted by $O_2(^1\Delta)$ flow by the energy transfer reaction. Laser output is converted to second harmonic from fundamental output.

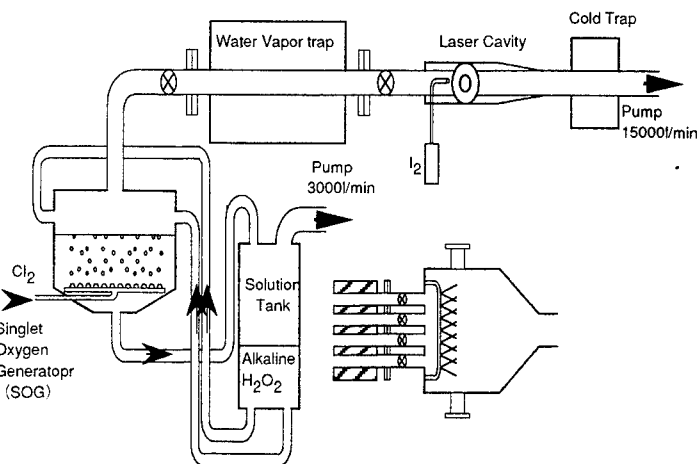
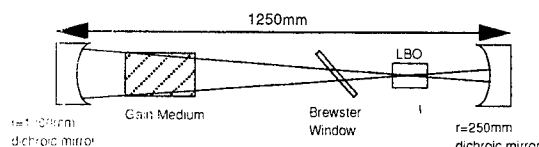
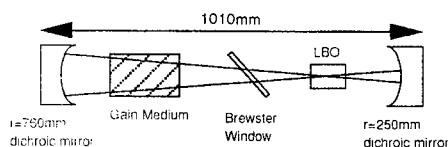


Fig.1 Schematic drawing of experimental device

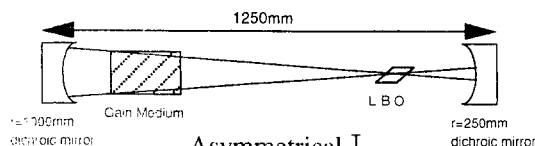


Asymmetrical I

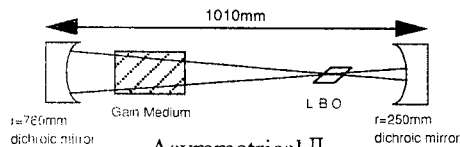


Asymmetrical II

(a) Cubic LBO crystal



Asymmetrical I



Asymmetrical II

(b) Brewster cut LBO crystal

Fig.2 Schematic drawing of experimental resonator

LBO (LiB_3O_5 : Lithium Tri Borate) was selected as the nonlinear crystal because of the characteristics of the large acceptance angle and the small walk off angle. Two types of LBO crystal were used. One was a cubic LBO crystal whose surface were AR coated and the other was a Brewster cut LBO crystal which was not used AR coating and cut for Brewster angle.

We used two types of concentric asymmetric resonators (Fig.2) whose length were different each other. One was the laser cavity consisted of a 1000 mm radius of curvature mirror (99.98% reflecting at $1.315 \mu m$, 97 % transmitting at $0.658 \mu m$) and a 250 mm radius mirror (99.98% , 97%) separated by 1250 mm , the other was consisted of a 760 mm radius mirror (99.99% , 97%) and a 250 mm radius mirror separated by 1010 mm. Experimental study were made to measure the second harmonic output power, intracavity fundamental power, to determine the extraction efficiency and the conversion efficiency. Investigation about these were conducted on each resonator and crystal.

3 MEASUREMENT

Fig.3 shows the measurement system. In order to measure the second harmonic output power from the inside mirror, power meter (OPHIR OPTICS L-150A) is used. In order to estimate the intracavity fundamental power, we use germanium photodiode (HAMAMATSU B1920-01). This measures the leaking fundamental beam from inside mirror. From this measured value and the transmittance of the inside mirror and beam splitter at $1.315\ \mu\text{m}$ (93% fundamental-wave transmittance and 99.9% reflectivity for the second-harmonic wave at an angle of 45°), the intracavity fundamental power is estimated.

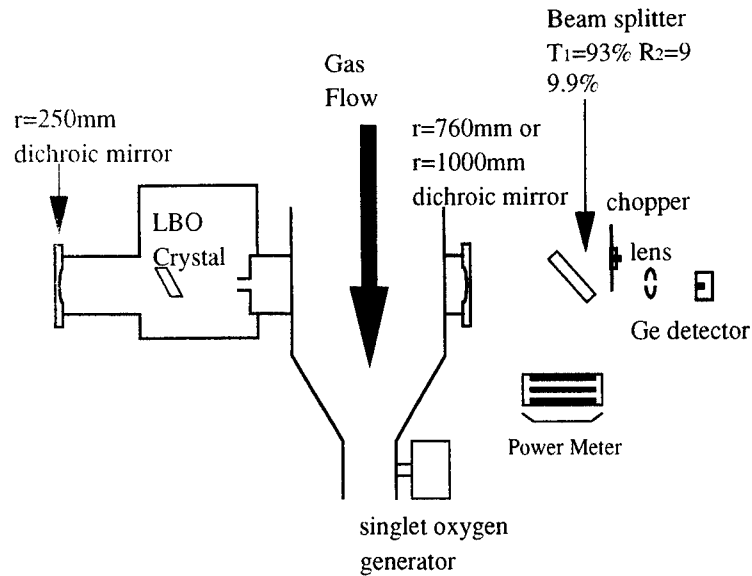


Fig.3 Laser cavity and Measurement system

4 RESULT

Conversion efficiency η_{con} is calculated by:

$$\eta_{con} = \frac{\text{second harmonic output [W]}}{\text{intracavity fundamental [W]}} \quad (2)$$

where intracavity fundamental power ($P_{\omega(int)}$) is measured as the fundamental wavelength leak power from dichroic mirror by Ge detector when second harmonic generation is done.

Extraction efficiency η_{ext} is calculated by:

$$\eta_{ext} = \frac{\text{second harmonic output [W]}}{\text{fundamental output [W]}} \quad (3)$$

where the fundamental power is the maximum output of the measurement of fundamental lasing experiment in the case of same cavity length. The result of second harmonic generation by cubic LBO crystal is shown by Table I.

	$P_{2\omega}$	$P_{\omega(int)}$	conversion efficiency	fundamental output	extraction efficiency
asymmetric resonator I	12.8W	970W	0.66%	8.0W	160%
asymmetric resonator II	2.9W	390W	0.37%	9.4W	30.9%

Table I SHG experimental result by cubic LBO crystal

The second harmonic maximum output power of 12.4 W were obtained by using a cubic LBO crystal, but it was found that an influence of loss of AR coating was exercised. By using a Brewster cut LBO crystal the loss in the resonator become very small because not only AR coating but also CaF_2 Brewster window was not needed.

	$P_{2\omega}$	$P_{\omega(int)}$	conversion efficiency	fundamental output	extraction efficiency
asymmetric resonator I	16.4W	1630W	0.51%	8.0W	205%
asymmetric resonator II	12.6W	1402W	0.45%	9.4W	134%

Table II SHG experimental result by Brewster cut LBO crystal

The second harmonic maximum output of 16.4 W were obtained and the conversion efficiency was 0.51% when the resonator length is 1250 mm, utilizing a Brewster cut LBO crystal. This output power is much higher than that obtained utilizing a cubic LBO crystal and that obtained using different type of concentric resonator(1010 mm).

In intracavity second harmonic generation it can be achieved the value of 100 % extraction efficiency since we can extract as the same output as the fundamental laser output power by the same resonator fundamental lasing experiment. And asymmetrical resonator is suitable for second harmonic generation on the point of loss in the resonator is low and mode volume in the laser medium can be made large. In this measurement we obtained extraction efficiency of more than 100 %. This means the quality of dichroic mirror is different from fundamental transmit mirror. Additionally, the outcoupler of the laser cavity is suitable for second harmonic generation compared with fundamental laer.

In the cubic or Brewster cut LBO experiment we can get the higher power of second harmonic output in the asymmetric I than in the asymmetric II. This is because the intracavity fundamental amplitude is higher in the case of asymmetric I ,both experiments. Asymmetric II has the good point of small fundamental beam weist than in asymmetric I, but in this case beam weist is so small that conversion efficiency is controlled by crystal length ,so asymmetric I has the advantage of larger mode volume in the laser medium.

5 SUMMARY

This study confirms the effect of the Brewster cut LBO crystal that suppress loss of resonator. And from result of analysis of transverse mode profile we found that second harmonic was effectively extracted in case of single mode fundamental wave. Obtained total second harmonic power was maximum of about 16.4 W. Then the internal conversion efficiency was estimated at 0.51 % and the effective extraction efficiency was 205 %. The 100 % extraction efficiency were obtained at every asymmetric resonator.

6 REFERENCES

1. D.E.Johnson,R.H.Humphreys,Jr.,P.Keating,and G.D.Hager," A Frequency Doubled Chemical Oxygen Laser" ,Appl .Phys.B,48,339(1989).

Optimization of jet singlet oxygen generator for chemical oxygen-iodine laser

Otomar Špalek*, Jarmila Kodymová, Marcelle V. Zagidullin**, Valery D. Nikolaev**

Institute of Physics, Academy of Sciences of the Czech Republic

Na Slovance 2, 18040 Prague 8, Czech Republic

Tel/Fax: (42) 2 6605 2699 / (42) 2 821227, e-mail: kodym@fzu.cz

*Institute of Inorganic Chemistry, Academy of Sciences of the Czech Republic

Pelléova 24, 16000 Prague 6, Czech Republic, e-mail: spalek@iic.cas.cz

**Lebedev Physical Institute, Russian Academy of Sciences, Samara Branch

Novosadovaya 221, Samara, Russia

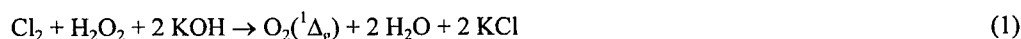
ABSTRACT

Experimental investigation of a jet singlet oxygen generator for a supersonic chemical oxygen-iodine laser was performed aimed to evaluation of the effects of BHP temperature and composition on the water content and other output generator parameters. Laser experiments on a small-scale system were realized to prove the obtained results.

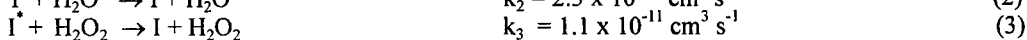
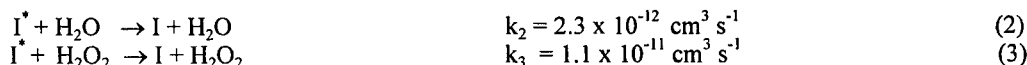
Keywords: chemical oxygen-iodine laser, singlet oxygen generators, jet generator

1. INTRODUCTION

The electronically excited molecular oxygen in delta state, $O_2(^1\Delta_g)$, for pumping an atomic iodine in a chemical oxygen-iodine laser (COIL) is produced in required concentrations by a chemical reaction between gaseous chlorine and alkaline solution of hydrogen peroxide



Besides $O_2(^1\Delta_g)$ and $O_2(^3\Sigma_g)$, the gas flowing from the singlet oxygen generator (SOG) contains the detrimental impurities for lasing as water and hydrogen peroxide vapours, and residual chlorine. Particularly the first two compounds quench very efficiently the excited atomic iodine in the reactions



A dissipation of energy by these processes is determined by relative concentrations of these molecules to $[O_2(^1\Delta_g)]$.¹ According to calculations, a relative content of water and peroxide vapours should not exceed 5 % in generated oxygen to attain high values of small signal gain in COIL.^{1,2}

Most generators of singlet oxygen hitherto used in COIL installations were equipped with a water vapour trap (WVT) placed in front of laser body to reduce partial pressure of water to a reasonable level. However, a WVT included in the system causes an increase in the hydraulic losses and $O_2(^1\Delta_g)$ loss in the pooling reaction



which becomes serious mainly in a COIL with supersonic flow.³ A reduced water vapour content in these systems can be efficiently achieved by a SOG operation with basic hydrogen peroxide (BHP) solution of very low temperature in which saturated vapour pressure is lower. According to calculations¹, the partial pressures of water and peroxide corresponding to their saturated vapour pressures above the water solutions of H_2O_2 -KOH (NaOH) at temperatures of -20 to -30 °C are low enough to achieve high gain values in COIL. However, it was proved experimentally that the pressure of water and peroxide

vapour in gas can be much higher than corresponds to their saturated vapour pressure at the given temperature of BHP.⁴ This effect depends on the type of SOG, and can be caused partly by a surface overheating of liquid during extremely high exothermic reaction (1) and partly by entraining liquid droplets by gas flowing from SOG.

In the case of a jet SOG, which is very effective and high pressure source of $O_2(^1\Delta_g)$ for a supersonic COIL systems, it could be presumed that the content of water vapour in oxygen is meaningfully suppressed by a gas cooling with cold liquid jets and the surface overheating of jets is small (up to 3.6 °C only as follows from the modeling of JSOG⁵). On the other hand, liquid droplets created by a jets disintegration can be escaped from the generator with the gas flow to active zone of laser where they enhance the partial pressure of water (peroxide), and in the form of aerosol they can increase substantially the inner losses of resonator. As these factors influence considerably the laser output power and the water concentration has not been systematically evaluated for jet SOGs, the present contribution is devoted above all to this problem.

2. EXPERIMENTAL

The jet SOG including the geometry of jets and chlorine diagnostics is described in the previous paper.⁶ In the experiments performed, a jets velocity was 6.8 m s⁻¹ for 0.8 mm, 6.3 m s⁻¹ for 0.5 mm, and 3.5 m s⁻¹ for 0.3 mm of jet diameter. A gas flow velocity counterflow liquid jets was in the range of 12 - 18 m s⁻¹.

A 40 mm long cylindrical optical cell of inner diameter 30 mm was equipped with Germanium photodiode (Judson JS 01, 1 mm in diameter) to detect the fundamental emission of $O_2(^1\Delta_g)$ at 1270 nm, and Silicon photodiode (Hamamatsu, S2387-1010R, 10x10 mm active area size) for $O_2(^1\Sigma_g)$ detection by fundamental emission at 762 nm. The amplified signals from both photodiodes were processed by on-line PC. The absolute calibration of $O_2(^1\Delta_g)$ optical detection was made by means of ESR method and confronted with a proposed numerical method.⁷ A reasonable agreement of both methods was obtained ($\pm 15\%$). A light-band filter was used to suppress the radiation of shorter wavelength than 762 nm not to interfere the signal of Silicon photodiode. Transmission of this filter was 93.5 % at 762 nm and 0.9 % at 634 nm ($O_2(^1\Delta_g)$ dimolar emission). The absolute calibration of $O_2(^1\Sigma_g)$ spectral detection was performed by the same numerical method⁷ including the photodiode detectivity and the filter transmission.

Water vapour concentration was evaluated by the method based on a rapid quenching of $O_2(^1\Sigma_g)$ formed in the reaction (4) by water molecules



Issuing from the mass balance of $O_2(^1\Sigma_g)$, the total concentration of water vapour was evaluated by the equation

$$c_{H_2O} = k_4 c_A^2 / k_5 c_\Sigma \quad (6)$$

Most of generator and diagnostics parameters was processed by on-line PC.

Some tests of jet SOG with the same jet orifice geometry and in the same conditions like in our laboratory (however with the generator cross section 5.7 cm²) were performed on a small-scale supersonic laser in the co-operation with the Russian COIL group in Samara. Downstream the generator output a gaseous nitrogen was admixed into the oxygen flow in the ratio 2:1. The supersonic nozzle of COIL system was rectangular 5 x 0.5 cm and iodine was injected just in front of the critical cross section through the orifices 0.6 mm in diameter. The average Mach number 1.5 was evaluated in the supersonic part of the duct.

3. RESULTS AND DISCUSSION

The experimental results on the jet SOG concerning the measurements of water content in oxygen, were obtained for the chlorine molar flow rates in the range of 0.8 to 4 mmol/s and the corresponding pressures in generator up to 5.5 kPa (40 Torr). Fig. 1 shows the example of two dependences which document that a relative content of water in gas substantially decreases with increasing pressure in generator while the partial pressure of water in gas moderately increases. The values of partial pressure of water correspond approximately to the saturated water vapour pressure, which was calculated for the

solution used (4 l H_2O_2 (34%) and 0.8 l KOH (54%)). In these calculations based on published gas-liquid equilibrium data for peroxide-water system, also water produced by H_2O_2 dissociation by KOH and pressure reduction by KOH content were considered. An increase in partial pressure of water with the pressure in generator (or with chlorine flow rate) is a result of increasing temperature of jets caused by the strong exothermic reaction (1). A correlation between the partial pressure of water and the jet temperature is evident from Fig.2. These measurements were performed with jets of 0.5 and 0.8 mm in diameter and provided nearly the same water concentration in gas for both jet thicknesses.

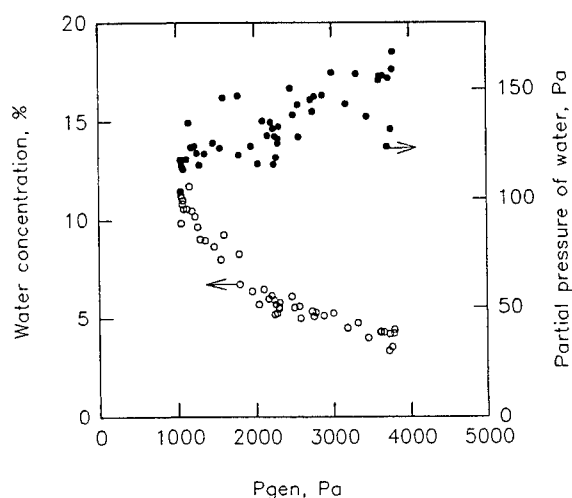


Fig.1. Relative water concentration and water pressure vs. generator pressure. Corresponding jets temperature is given in Fig.2.

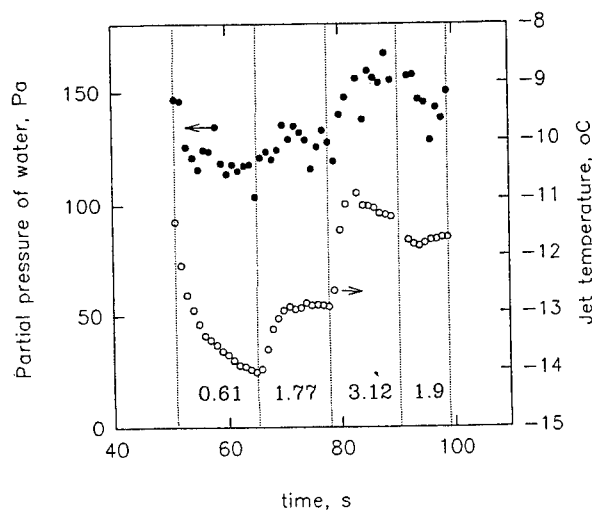


Fig.2. Water vapour pressure and jet temperature at different chlorine flow rate (given in $\text{mmol cm}^{-2} \text{s}^{-1}$).

In the experiments, in which BHP was prepared from more concentrated peroxide (3.2 l H_2O_2 (70%) and 2 l KOH (42%)), the partial pressure of water was lower by 30 Pa approx. as compared with the above BHP composition (at the same temperature). In the experiments with this BHP, the relative water concentration in gas was decreasing from 9% to 3.5% in the pressure range of 1 to 3 kPa and the liquid temperature - 18°C. An increase in liquid temperature by 5 °C resulted in the water partial pressure higher by 30 Pa.

The jet SOG with liquid jets of 0.3 mm in diameter provided higher partial pressures of water by 30 - 40 Pa, or relative water content higher by 3% approx.. It was caused probably by escaping small liquid droplets into gas due to a strong disintegration of these jets.

In the next set of experiments, the influence of BHP composition and temperature on the output parameters of the jet SOG and laser output power was investigated. As follows from the phase diagram of the system H_2O_2 -KOH- H_2O , the freezing point of a BHP is lower at higher content of alkali. Therefore, we added sequentially 0.4 litre portions of KOH (54 %) to 4 litres of H_2O_2 (34%). The results of these experiments are presented in Tab. 1.

The values of the output power of the supersonic small-scale laser with the jet SOG generator are in the last row of the table. They were obtained at chlorine molar flow rate of 11 mmol s^{-1} , iodine molar flow rate of 0.1 mmol s^{-1} and resonator mirror transmissions of 0.1 and 0.8 %. The gas pressure in generator was around 3.3 kPa, in the resonator 0.13 kPa.

It follows from the Tab. 1 that the water content slightly decreases with increasing KOH concentration in BHP and more rapidly with lowering of liquid temperature. The both courses coincide with the dependences of the saturated water vapour pressure. The $\text{O}_2(^1\Delta_g)$ excitation efficiency dropped from 90% to 55% with the gas pressure. The content of residual chlorine in gas was increasing simultaneously from 4 % to 25 %.

The laser experiments have shown that in the conditions when the water content was reduced, the laser output power was higher, while the oxygen excitation efficiency remained unchanged. This fact documents a detrimental effect of water in the concentration range of 4.7% to 8 % on lasing, which confirms the results of modeling.^{1,2}

Tab 1 Effects of BHP composition and temperature in upper reservoir (t_{ur}) on jet temperature (t_{jet}), water vapour concentration (c_{H_2O}), partial pressure (P_{H_2O}), $O_2(^1\Delta_g)$ excitation efficiency (η_{Δ}), and laser output power (P_L) at the total pressure 3 kPa						
$c_{H_2O_2}$, M	7.4	6.8	6.3	5.9	5.5	5.2
c_{KOH} , M	2.5	3.5	4.3	5.0	5.6	6.2
t_{ur} , °C	-11.9	-11.5	-11.7	-12.6	-17	-21.7
t_{jet} , °C	-9.2	-9	-9	-8.9	-13	-17
c_{H_2O} , %	7.2	6.6	6.5	6.1	4.5	3.5
P_{H_2O} , Pa	230	207	200	190	145	130
η_{Δ} , %	52	53	57	56	55	54
P_L , W	51	53	62	-	70	74

4. CONCLUSIONS

1. Water vapour concentration in the gas flowing from the jet singlet oxygen generator was measured. It was found that the relative content of water decreases with increasing total pressure, while the partial pressure of water slightly increases. This dependence was explained by increasing jet temperature, proved experimentally, which results in increasing saturated water vapour pressure. The measured partial pressure of water in gas corresponds to the calculated value of saturated vapour pressure of water above the BHP used. The water pressure in gas is descending with increasing both KOH and H_2O_2 concentrations in BHP solution, and with decreasing liquid temperature.

2. Experiments performed with a small supersonic COIL proved a detrimental effect of water in the concentration range from 7.2 % to 3.5 % on the laser output power.

5. ACKNOWLEDGEMENTS

This work was done with the financial support of the Grant Agency of the Czech Republic and the Grant Agency of the Academy of Sciences of the Czech Republic.

6. REFERENCES

1. N.G. Basov, M.V. Zagidullin, V.I. Igoshin, V.A. Katulin, N.L. Kupryanov, „Active medium of chemical oxygen-iodine laser“ *Quantum Electronics (in Russian)* **13**, 787-796 (1986).
2. Yu.A. Kulagin, L.A. Shelepin, V.N. Yarygina, „Kinetics of active medium of oxygen-iodine lasers“, *Trudy FIAN (Lebedev Institute Papers) (in Russian)* **212**, 123-143 (1991).
3. M.V. Zagidullin, V.I. Igoshin, N.L. Kupryanov, „Water vapour content in active medium of chemical oxygen-iodine laser“, *Quantum Electronics (in Russian)* **14**, 516-523 (1987).
4. T. Kikuchi, T. Tsuruyama, T. Uchiyama, „Performance characteristics of a chemical oxygen-iodine laser without a water vapour trap“, *Proc. 7th Int. Symp. Gas Flow and Chemical Lasers*, SPIE Vol. **1031**, 287-293 (1988).
5. V.D. Nikolaev, „Current research of COIL in Samara“, *Proc. 4th Int. Workshop on Iodine Lasers and Applications*, SPIE Vol. **2767**, 185 - 191 (1995).
6. O. Špalek, J. Kodymová, „Influence of arrangement of liquid jets on operation of jet singlet oxygen generator“, *Proc. 4th Int. Workshop on Iodine Lasers and Applications*, SPIE Vol. **2767**, 237-244 (1995).
7. V. Bálek, O. Špalek, J. Kodymová, „Numerical method for calibration of optical methods for $O_2(^1\Sigma_g)$ and $O_2(^1\Delta_g)$ detection“, *Czech. J. Phys. B* (in preparation).

A 1D kinetic model of COIL applied to experimental data

Jaroslav Beránek, Karel Rohlena, Jarmila Kodymová, Otomar Špalek

Institute of Physics, Acad. Sci. of the Czech Republic,
Na Slovance 2, 180 40 Prague 8, Czech Republic
Tel/Fax: (42) 2 6605 2792/(42) 2 821227
e-mail: rohlena@fzu.cz, kodym@fzu.cz

ABSTRACT

A 1D kinetic model of COIL performance based on the concept of mixing length is described. The results of calculations are compared with the experimental data measured on the COIL device in the Institute of Physics, Prague.

Keywords: iodine lasers, metastable oxygen, kinetics, modelling

1. INTRODUCTION

A realistic COIL model should involve the process of mixing, since the diffusion of the injected components proceeds at a final rate. Without the mixing, a so called pre-mixed model is obtained (as discussed in¹), which would correspond to a very fast diffusion. This is usually not the case in the pressure range of interest $1 \div 10 \text{ torr}$. A consistent approach would require solving the equation of the perpendicular diffusion. Instead, in the literature the concept of mixing length L_s is sometimes encountered.² It simply assumes that following the injection point any component enters the chemical reactions only gradually, after being mixed to the molecular level with the medium, into which it was injected. This gradual mixing is described by an exponential law, so that the concentration of a component which does not react chemically (such as Ar as a carrier gas) is given by $[Ar] = [Ar]_0(1 - \exp(x/L_s))$, where $[Ar]_0$ is the average concentration at the injection point. Such a relation originates from a phenomenological term of the type

$$([Ar]_0 - [Ar])/L_s \quad (1)$$

added to the purely chemical part of kinetic equation. The presence of these phenomenological terms in selected equations of the kinetic set modifies in a certain measure the results. In the following we shall try to find the most favourable configuration of these terms by testing the computational results against experimental data. The chemical part of our model involves a reduced reaction scheme,^{1,3} more general schemes⁴ lie beyond the scope of our purpose. Thermal dependencies of the reaction rates were included as long as they were available, see Table 1.

2. KINETIC EQUATIONS

The laser output power is given by the relation

$$P = Ah\nu_{ac} \frac{c}{2l_{res}} |\ln R_1| u \frac{F_I - g_2^T/g_1^T F_I}{(\kappa + \zeta)g_2^T(1/g_1^T + 1/g_2^T)} \quad (2)$$

provided the threshold condition $(2l_{ac}\sigma/l_{res})([I^*] - g_2^T/g_1^T[I]) - (\kappa + \zeta) = 0$ is met.

Designation: $\kappa = (c/2l_{res})|\ln R_1 R_2|$ are the losses through the end mirrors (R_1, R_2 are the reflectivities, c light velocity, l_{res} resonator length), A beam cross-section, $h\nu$ photon energy, l_{ac} active length of the amplifying medium, u velocity of the stream, ζ coefficient of internal loss, $g_1^T = 24$, $g_2^T = 12$ are the total degeneracies of the lower and upper laser level, $\sigma = 7.5 \times 10^{-18} \sqrt{300/T} [cm^2]$ is the cross-section of the stimulated emission (temperature dependent), $[]$ designates the number density of a component. F_I and F_{I^*} are the rates of the chemical production of the ground level $I(^2P_{3/2})$ and $I(^2P_{1/2})$ upper level of the iodine atoms, which also enter the kinetic equations

$$d[I]/dx = F_I + \frac{1}{u}[c\sigma([I^*] - g_2^T/g_1^T[I])W] \quad (3)$$

$$d[I^*]/dx = F_{I^*} - \frac{1}{u}[c\sigma([I^*] - g_2^T/g_1^T[I])W] \quad (4)$$

where $W [cm^{-3}]$ is the photon number density. The kinetic equations for the remaining species are constructed analogically. For instance, the production rate of the molecular iodine I_2 including the mixing term of the type (1) is given by

$$d[I_2]/dx = F_{I_2} + ([I_2]_0 - [I_2])/L_s \quad (5)$$

with the mixing term of the type (1) was added describing the fact that the molecular iodine injected with the average concentration $[I_2]_0$ must first be mixed to the molecular level over the length L_s to become available for the chemical reactions. The rate equations are still supplemented by a thermal balance equation for the mixture temperature T

$$dT/dx = F_T \quad (6)$$

The expression for the chemical rates $F_I, F_{I^*}, F_{I_2}, \dots$ (the rate equations not written explicitly apply to $O_2, O_2(^1\Delta_g)$, etc.) as well as for the heating rate F_T are constructed in a usual way from the known reaction rates of the chemical reactions considered. They are summarized in a table (reaction rates in the 2nd column are in $[cm^3 s^{-1}]$ for the binary or in $[cm^6 s^{-1}]$ for the triple reactions; reaction energies in the 3rd column are in $[eV]$)

$2O_2(^1\Delta_g) \rightarrow O_2(^1\Sigma_g) + O_2$	$9.5 \times 10^{-28} T^{3.8} \exp(700/T)$ Ref. ⁵	0.33 Ref. ³
$O_2(^1\Sigma_g) + I_2 \rightarrow O_2 + 2I$	4.0×10^{-12} Ref. ⁶	0.087 Ref. ³
$O_2(^1\Delta_g) + I \rightarrow O_2 + I(^2P_{1/2})$	$2.3 \times 10^{-8}/T$	0.034 Ref. ⁷
$O_2 + I(^2P_{1/2}) \rightarrow O_2(^1\Delta_g) + I$	$3.1 \times 10^{-8} \exp(-403/T)/T$ Ref. ⁸	0.034 Ref. ⁷
$O_2(^1\Delta_g) + I(^2P_{1/2}) \rightarrow O_2(^1\Sigma_g) + I$	$4.0 \times 10^{-24} T^{3.8} \exp(700/T)$ Ref. ⁵	0.29 Ref. ³
$2I + I_2 \rightarrow 2I_2$	3.0×10^{-30} Ref. ³	1.5 Ref. ³
$2I + O_2 \rightarrow I_2 + O_2$	5.0×10^{-32} Ref. ³	1.5 Ref. ³
$2I + Ar \rightarrow I_2 + Ar$	1.0×10^{-32} Ref. ⁹	1.5 Ref. ³
$O_2(^1\Delta_g) + I_2 \rightarrow O_2 + I_2(v > 0)$	7.0×10^{-15} Ref. ⁶	0
$O_2(^1\Delta_g) + I_2(v > 0) \rightarrow O_2 + 2I$	3.0×10^{-10} Ref. ⁶	0
$I(^2P_{1/2}) + I_2 \rightarrow I_2(v > 0) + I$	$1.6 \times 10^{-11} \exp(272/T)$ Ref. ⁷	0
$I_2(v > 0) + O_2 \rightarrow I_2 + O_2$	5.0×10^{-11} Ref. ⁶	0

3. TESTING THE MODEL AND CONCLUSIONS

The set of kinetic equations (3-6) and the analogous ones for other components of the mixture occurring in the table are solved numerically aiming at the conditions described in the experiment.¹⁰ These are briefly as follows

- total molar flow rate $11.8 mmol/s$ ($[Cl_2] = 0$), pressure $0.75 torr$ ($98 Pa$)
- O_2 about 60%, pressure $0.45 torr$ ($60 Pa$)

Molecular iodine injection rate $50\mu\text{mol/s}$, pressure 0.005torr (0.7Pa)

Ar pressure 40Pa

Geometry: distance injector-resonator 2.05cm , resonator width 3.7cm , height 2.5cm , optical length $l_{re} = 80\text{cm}$, active length $l_{ac} = 40\text{cm}$

Reflectivity of the output mirror $R_1 = 98.1\%$ or 97.8%

Velocity of the flow $u = 30\text{m/s}$.

The model includes the mixing length L_s as a free parameter, see Fig. 1. Fairly uncertain is also the internal loss ζ , though it is possible to make an estimate using the experimental data $\zeta = 5.6 \times 10^{-4}\text{cm}^{-1}$.¹⁰ We were trying to map the solution changing L_s and ζ , for $L_s = 2\text{cm}$ the internal loss coefficient $\zeta = 7 \times 10^{-5}\text{cm}^{-1}$ appeared to be the best fit for the laser output power 58W , see Fig. 2. Equally, the mixing term (1) was alternatively switched on and off for various components. It is not difficult to show that unless it is either present or absent for all the components involving a specific particle species (e.g., iodine atoms bound or free), the local conservation of number of the particles may be breached for very short mixing lengths.

In conclusion an important consequence of the flexibility in the mixing term application will be demonstrated on the example of the laser power dependence on the I_2 injection rate. With an asymmetric mixing (the mixing term is switched on for I_2 only, (Fig. 3) the dependence is monotonous as noticed also in.¹ However, with a symmetric mixing involving also the O_2 and $O_2(^1\Delta_g)$ the dependence passes through a maximum corresponding to the experimental finding, Fig. 4.

4. REFERENCES

- [1] B. D. Barmashenko, A. Elior, E. Lebiush and S. Rosenwaks, "Modeling of mixing in chemical oxygen-iodine lasers: Analytic and numerical solutions and comparison with experiments," *J. Appl. Phys.* **75**, 7653-7665 (1994).
- [2] L. G. Vinogradova, M. V. Zagidullin, V. I. Igoshin, V. A. Katulin and N. L. Kupryanov, "Analysis of energetics of chemical oxygen-iodine laser (in Russian)," *Kvant. Elektr.* **9**, 1193-1198 (1982).
- [3] N. G. Basov, M. V. Zagidullin, V. I. Igoshin, V. A. Katulin and N. L. Kupryanov, "Active medium of chemical oxygen-iodine laser (in Russian)," *Kvant. Elektr.* **13**, 787-796 (1986).
- [4] Yu. A. Kulagin, L. A. Shelepin and V. N. Yarygina: "Kinetics of processes in gaseous media containing the metastable oxygen (in Russian)," *Trudy FIAN (Lebedev Institute Papers)* **218**, 166-226 (1994).
- [5] E. Lebiush, B. D. Barmashenko, A. Elior and S. Rosenwaks, "Parametric study of the gain in a small scale, grid nozzle, supersonic chemical oxygen-iodine laser," *IEEE J. Quant. El.* **31**, 903-909 (1995).
- [6] S. Churassy, R. Bacis, A. J. Bouvier, C. P. Mery, B. Erba, J. Bachar and S. Rosenwaks, "The chemical oxygen-iodine laser: Comparison of a theoretical model with experimental results," *J. Appl. Phys.* **62**, 31-35 (1987).
- [7] A. I. Didukov, Yu. I. Krasnoshchekov, Yu. A. Kulagin, V. A. Morozov, S. A. Reshetnyak and L. A. Shelepin, "Kinetics of physical processes in oxygen-iodine medium (in Russian)," *Kvant. Elektr.* **9**, 645-655 (1982).
- [8] G. D. Hager, D. Kopf, B. S. Hunt, B. Anderson, C. Woolhiser and P. Crowell, "The chemical oxygen iodine laser in the presence of a magnetic field I: Gain measurements and polarization effects," *IEEE J. Quant. El.* **29**, 933-943 (1993).
- [9] M. V. Zagidullin, V. I. Igoshin, V. A. Katulin and N. L. Kupryanov, "Numerical modelling of chemical oxygen-iodine laser (in Russian)," *Kvant. Elektr.* **9**, 1899-1901 (1982).
- [10] J. Schmiedberger, J. Kodymová, O. Špalek and J. Kovář, "Experimental study of gain and output coupling characteristics of a CW chemical oxygen-iodine laser," *IEEE J. Quant. El.* **27**, 1265-1270 (1991).

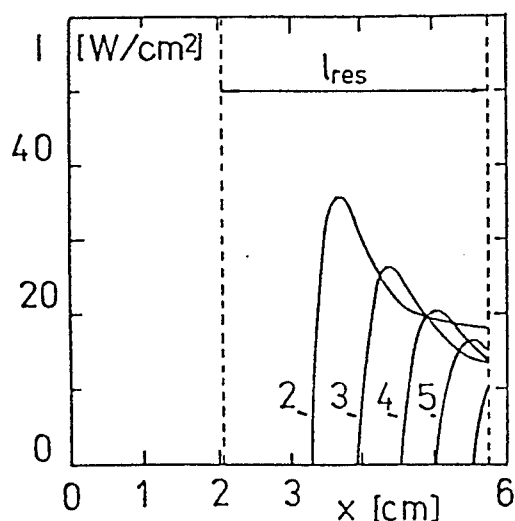


Figure 1: Computed laser intensity across the resonator. Parameter: mixing length L_s , reflectivity $R_1 = 98.1\%$. The internal loss coefficient $\zeta = 2.7 \times 10^{-4} \text{ cm}^{-1}$ was fitted to the experimental output power 58 W for $L_s = 2 \text{ cm}$.

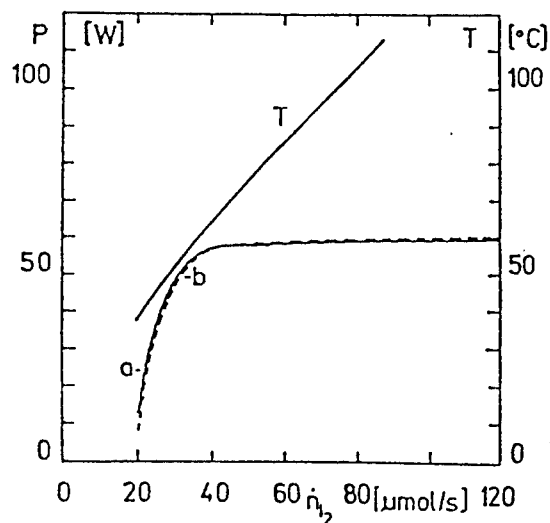


Figure 3: Calculated dependence of the laser output power and of the mixture temperature T on the molecular iodine injection rate. $a - R_1 = 98.1\%$, $b - R_1 = 97.8\%$, $L_s = 2 \text{ cm}$. Internal loss coefficient $\zeta = 7 \times 10^{-5} \text{ cm}^{-1}$. The asymmetric mixing renders a monotonous dependence.

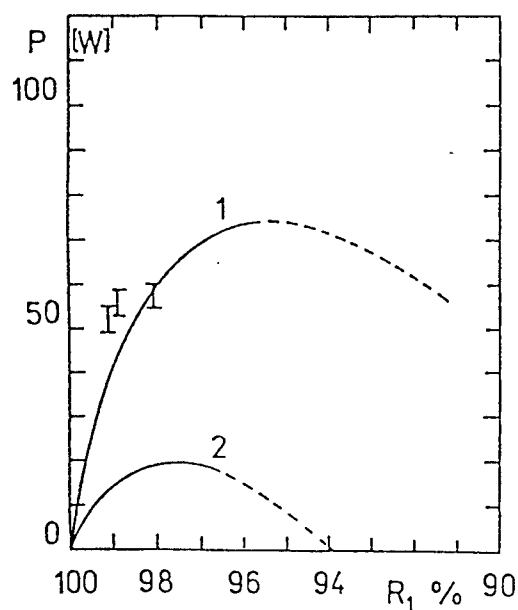


Figure 2: Computed laser power as a function of the output mirror reflectivity R_1 for two values of the mixing length 1 - $L_s = 2 \text{ cm}$ and 2 - $L_s = 4 \text{ cm}$. Internal loss coefficient $\zeta = 7 \times 10^{-5} \text{ cm}^{-1}$. The experimental points are shown.

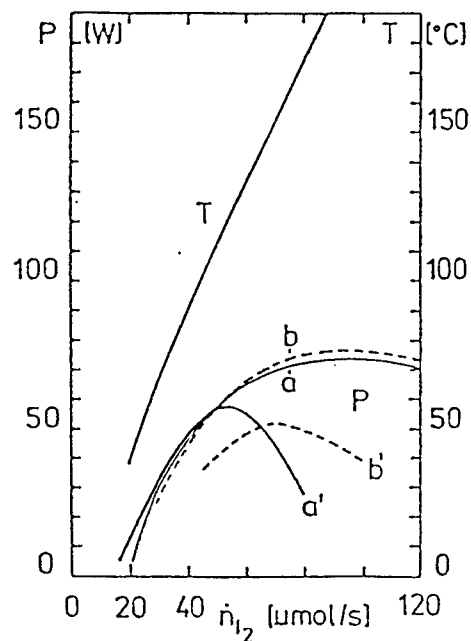


Figure 4: Calculated dependence of the laser output power and of the mixture temperature T on the molecular iodine injection rate. $a - R_1 = 98.1\%$, $b - R_1 = 97.8\%$, $L_s = 2 \text{ cm}$. The internal loss coefficient $\zeta = 7 \times 10^{-5} \text{ cm}^{-1}$. The symmetric mixing causes a maximum on the power curves to appear

Mixing/Reacting Zone Structure and Small Signal Gain Coefficient of a Supersonic Flow Chemical Oxygen-Iodine Laser

Wataru MASUDA, Manabu HISHIDA, Naoki AZAMI,

Faculty of Engineering, Nagaoka University of Technology,
1603-1 Kamitomioka, Nagaoka 940-21, Japan.

Hiroo FUJII and Toshio ATSUTA

Kawasaki Heavy Industries Ltd, 118 Futatsukasa, Noda 118, Japan

ABSTRACT

The flow field of a supersonic flow chemical oxygen-iodine laser is simulated solving three-dimensional Navier-Stokes equations, and the dependence of the mixing/reacting zone structure and the resulting gain region on the effective velocity ratio of I_2 jet to the primary flow is studied. It is assumed that the flow is laminar and the water vapor condensation due to the supersonic cooling is ignored. A chemical kinetic model encompassing 21 chemical reactions and 10 chemical species is used to determine the chemical composition of gas mixture. The I_2/He ratio and plenum pressure of the secondary flow are varied in order that the amount of iodine injected into the primary flow is kept constant in each effective velocity ratio. The present results demonstrate that a pair of contrarotating vortices generated behind the I_2 jet greatly enhances the mixing and the simultaneous chemical reaction of I_2 and $O_2(^1\Delta)$. It is shown that the optimum condition for the secondary I_2 jet momentum exists. The I_2 jet which causes the high gain penetrates into the primary flow moderately deeply and does not collide with the counter one.

Key Words : Supersonic Flow, Reactive Flow, Chemical Laser, Iodine, Oxygen, Numerical Simulation

1. INTRODUCTION

In most supersonic flow chemical oxygen-iodine lasers (S-COILs), the molecular iodine I_2 is injected transversely into the subsonic primary flow of the singlet delta oxygen $O_2(^1\Delta)$ from the chemical oxygen generator, as shown in Fig.1. Then, the flow in which I_2 mixes and reacts with $O_2(^1\Delta)$ is choked and expanded through supersonic nozzle blades in order to create a favorable gain region from which the optical energy is extracted. Therefore, performance characteristics of S-COIL depend significantly on the mixing/reacting zone structure.

The penetration and properties of a jet injected transversely into a primary flow depend mainly on an effective velocity ratio which is defined as the square root of the ratio of the momentum flux across the jet orifice to that of the primary flow,¹

$$\Gamma = \sqrt{\rho_s U_s^2 / \rho_p U_p^2}, \quad (1)$$

where ρ is the density, U denotes the velocity, and the subscripts p and s represent the primary and secondary flows, respectively. In the present study, the flow field of S-COIL is simulated solving the three-dimensional full

Navier-Stokes equations and the dependence of the mixing/reacting zone structure and the resulting gain region on Γ is discussed.

2. MATHEMATICAL MODELING AND NUMERICAL METHOD

In the previous papers,^{2,3} the authors demonstrated that the condensation of water vapor due to the supersonic cooling reduces the small signal gain coefficient. For simplicity, however, the condensation is ignored in the present simulation. It is reasonable to assume that the flow is laminar, since the Reynolds number of S-COIL based on the nozzle throat conditions and the throat height is at most 10^4 , and one based on the orifice diameter of I_2 injector and the injection condition is only of the order of 10^2 . Moreover, the compressibility and the rapid acceleration by the nozzle tend to stabilize the flow. The steady state solution is obtained using Lower-Upper Symmetric Gauss-Seidel (LU-SGS) method with local time steps for time-integration of the governing equations. Details of the numerical method used in the present calculation were described elsewhere.⁴

Figure 1 shows the configuration of nozzle blades and iodine injectors adopted for the present calculation. The nozzle blade is one which was used in the previous experiment.⁵ A cylindrical I_2 injector is located upstream of each nozzle blade. In the previous experiment,⁵ the secondary I_2 gas was injected into the primary flow through 4 rows of circular orifices drilled in each cylinder. In the present calculation, however, only 2 rows of orifices are used for injection in order to investigate the basic characteristics of the mixing/reacting zone structure clearly.

The plenum conditions of the primary flow from the chemical oxygen generator and the secondary flow supplied by the I_2 injector are shown in Table 1 where the subscript 0 represents the plenum condition. The I_2/He ratio and P_{0s} of the secondary flow are varied in order that the amount of iodine injected into the primary flow is kept constant in each case.

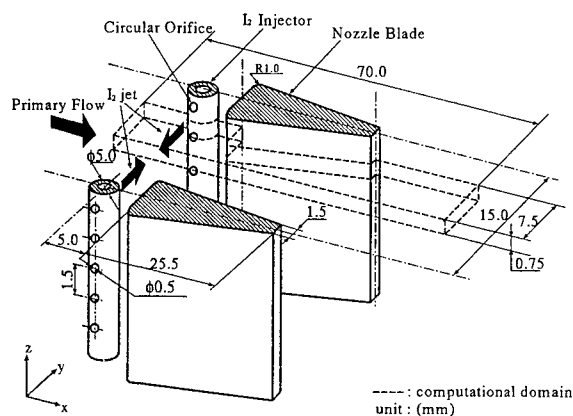


Fig. 1. Schematic diagram of nozzle blades and I_2 injectors.

Table 1. Plenum conditions of the primary and secondary flows.

primary flow				
P _{0p} (torr)	T _{0p} (K)	molar fraction		
		O ₂ (¹ Σ)	O ₂ (¹ Δ)	O ₂ (³ Σ)
39.6	273	3.34 × 10 ⁻⁵	0.179	0.060
		H ₂ O	Cl ₂	He
		0.012	0.026	0.723

secondary flow					
case	P _{0s} (torr)	T _{0s} (K)	Γ	molar fraction	
				I ₂	He
1	55.4	376	4.0	0.323	0.677
2	121		7.5	0.075	0.925
3	214		11.6	0.030	0.970

3. RESULTS AND DISCUSSIONS

Figures 2(a) and 2(b) show the stream lines and the cross-sections of the I_2 jet issuing from the upper half of the orifice with the effective velocity ratios $\Gamma = 4.0$ (case 1) and 11.6 (case 3), respectively. The jet centerline shown in Fig.2 is defined as the stream line issuing from the orifice center. It can be seen that the secondary I_2 jet penetrates more deeply as Γ becomes larger and that the jet centerline of the case 3 reaches close to the counter I_2 jet at the nozzle inlet. In all cases, the cross-section of the jet is stretched significantly due to the strong shear force near the side boundary of the jet and a pair of contrarotating vortices are formed behind the curved jet. These figures indicate that the vortices behind the curved jet greatly enhances the mixing and the simultaneous chemical reaction of I_2 and $O_2(^1\Delta)$.

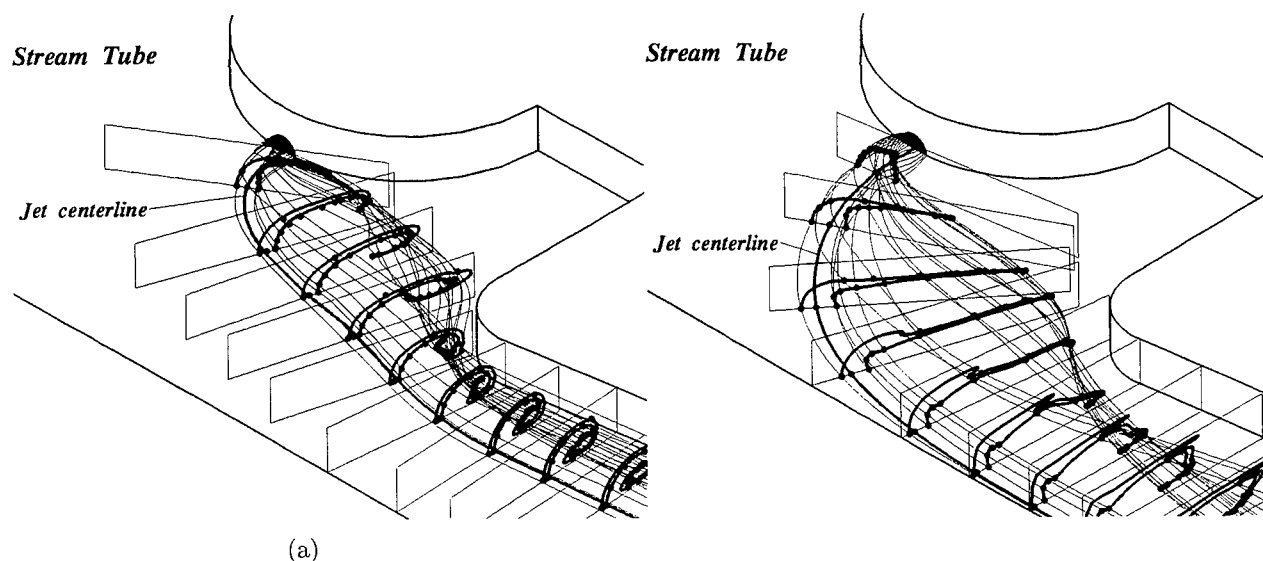


Fig. 2. The stream lines and the cross-sections of the I_2 jet issuing from the upper half of the orifice on planes perpendicular to the jet centerline with the effective velocity ratios (a) $\Gamma = 4.0$ (case 1) and (b) $\Gamma = 11.6$ (case 3).

Figure 3 shows the distributions of molar fractions of I_2 and the small signal gain coefficient downstream of the nozzle inlet. The mixing/reacting zone structure induced by the vortices near the injector is preserved even in the downstream region of the nozzle blade. These results clearly demonstrate the important effect of the vortices behind the iodine jet upon the laser performance. The calculated small signal gain coefficient of the case 3 is distributed more widely and uniformly than that of the case 1. The excessively shallow penetration of the I_2 jet, as shown in Fig.3(a), leads to the lack of iodine near the flow axis. It is also pointed out that some amount of I_2 remains in the central portion of the I_2 jet because the singlet oxygen $O_2(^1\Delta)$ sufficient to dissociate I_2 completely cannot intrude into the jet. Consequently, the small signal gain coefficient in these portions of flow cannot attain the positive value.

The small signal gain coefficients 25 mm downstream of the nozzle exit \bar{G} which are averaged over the plane perpendicular to the flow axis are plotted in Fig.4. The averaged small signal gain coefficient of the case 2 is largest in the present calculation. These results indicate that the optimum condition for the secondary I_2 jet momentum exists, and that the jet which causes the high gain penetrates into the primary flow moderately deeply and does not collide with the counter one.

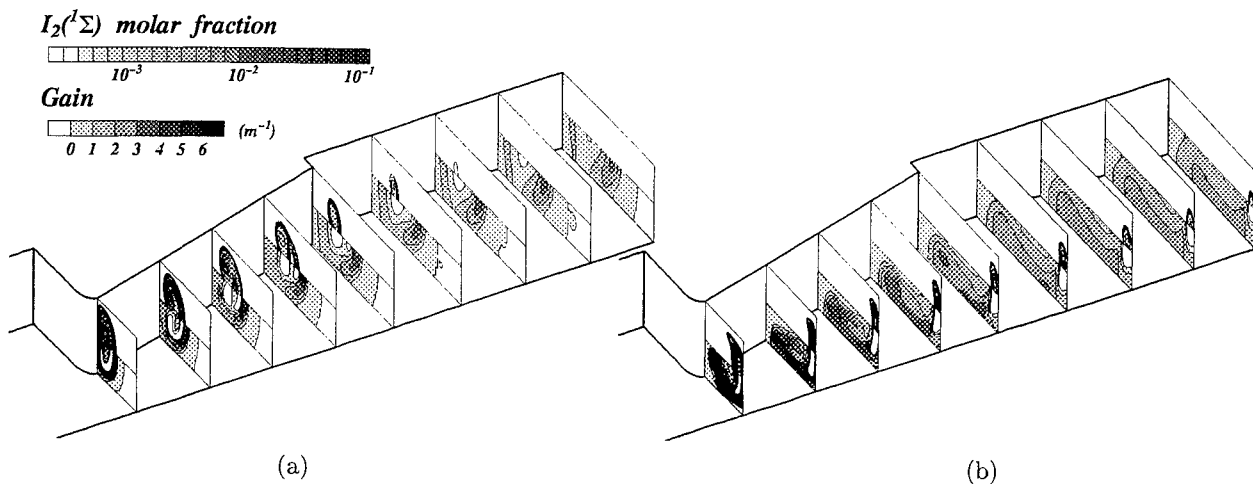


Fig. 3. The distributions of I_2 molar fraction (upper part) and small signal gain coefficient (lower part) on planes perpendicular to the flow axis with the effective velocity ratios (a) $\Gamma = 4.0$ (case 1) and (b) $\Gamma = 11.6$ (case 3).

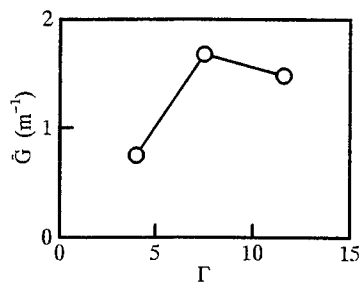


Fig. 4. The small signal gain coefficients 25 mm downstream of the nozzle exit \bar{G} which are averaged over the plane perpendicular to the flow axis.

4. REFERENCES

- [1] Fearn, R. and Weston, R. P., Vorticity Associated with a Jet in a Cross Flow, AIAA J., Vol.12, No.12(1974), p.1666.
- [2] Masuda, W., Satoh, M. and Yamada, H., Effects of Water Vapor Condensation on the Performance of Supersonic Flow Chemical Oxygen-Iodine Laser, JSME Int. J., Series B, Vol.39, No.2 (1996), p.273.
- [3] Masuda, W., Satoh, M., Fujii, H. and Atsuta, T., Numerical Simulation of a Supersonic Flow Chemical Oxygen-Iodine Laser Solving Navier-Stokes Equations, JSME Int. J., (to be published).
- [4] Masuda, W., Hishida, M., Hirooka, S., Azami, N. and Yamada, H., Three-Dimensional Mixing/Reacting Zone Structure in a Supersonic Flow Chemical Oxygen-Iodine Laser, JSME Int. J., (to be published).
- [5] Masuda, W., Yamada, H., Naitoh, H., Fujii, H. and Atsuta, T., Theoretical and Experimental Investigation on a Supersonic Flow Chemical Oxygen-Iodine Laser, SPIE Vol.2502 (1995), p.244.

Liquid breakup studies for jet type singlet oxygen generators

Wolfgang O. Schall and Ina Plock

DLR - Institut für Technische Physik, Postfach 80 03 20, D-70503 Stuttgart, Germany

ABSTRACT

The instability of the liquid jets in a jet singlet oxygen generator for oxygen-iodine lasers may limit the operational conditions and the scalability of such generators. Therefore the type of instability and the breakup behaviour of jets is investigated experimentally for varying operational conditions. Jets of basic hydrogen peroxide are simulated by the use of glycerin solutions with different viscosities. Transition from laminar to turbulent jets, the associated breakup modes and the beginning of jet dissolution by surface spraying are observed. Jet lengths have been measured for various parameters, including gas counter-flow.

Keywords: Chemical oxygen-iodine laser, singlet oxygen generators, jet generators, jet breakup.

1. INTRODUCTION

Jet singlet oxygen generators (jet SOG) were first suggested by Balan et al.¹ in 1989 as a new source for the production of $O_2(^1\Delta)$ for Chemical Oxygen-Iodine Lasers (COIL). Basically a jet SOG consists of a multitude of thin jets of basic hydrogen peroxide (BHP) flowing through an atmosphere of chlorine. With these generators very high yields of $O_2(^1\Delta)$ at comparatively high partial pressures have been obtained². Jet SOGs have been implemented in a subsonic laser device and more recently in 2 supersonic devices as well^{4,5}. However, depending on the operating conditions jet SOGs may suffer from early jet breakup and from spraying. Small droplets may be entrained into the laser gas flow in significant amounts to disturb the laser process in various ways. It is therefore of great importance to know in advance what kind of behaviour of the jets is to be expected in a generator and what the scaling possibilities of jet SOGs are. While Spalek et al. have made parametric performance investigations of various types of BHP jet arrays⁶, this work is dedicated to the establishment of the stability limits of individual jets under conditions relevant for jet and drop generators.

The basic parameters that control the intact jet length are the orifice diameter, the driving pressure (liquid pressure) with which the liquid is forced through the jet forming orifices, and the viscosity of the liquid. Various modes of jet structure and breakup can be observed. A laminar flow has a smooth, unwrinkled jet surface. Due to the inherent axial instability these jets form regular contractions with decreasing waste diameter. The jets finally break up into regularly sized drops (Rayleigh break-up). If the driving pressure is raised, the jet surface begins to wrinkle due to turbulent motions of the liquid inside the jet. The contractions become irregular and therefore the breakup also. Spraying occurs, once the turbulent motion inside the jet is so strong that the jet surface breaks up locally and ejects liquid radially in the form of small droplets. - First investigations of the length and structure of intact jets and the mode of breakup for liquid with BHP-like fluid properties are reported in references 7 and 8. In the meantime, the method of observation has been improved significantly and the range of operating parameters has been extended.

2. EXPERIMENTAL SET-UP

The jet generator simulating device is shown in Fig. 1. The storage tank on top contains the liquid prior to the test at a pressure of up to 10 bar (= 1 MPa). The run tank is separated from the storage tank by a magnetically driven valve. The volume of the run tank is kept as small as possible (25 cm³) and fills within a fraction of a second. The liquid flows through an interchangeable plate with orifice holes that define the jet diameters in the low pressure jet chamber underneath. The cross-section of the jet chamber is 15 x 15 mm and the observable jet length is 25 cm. Gas can be introduced into the jet chamber from ports at two opposite sides in 10, 15 and 20 cm distance from the orifice plate and pumped out 2 cm below the orifice plate. In every run four identical jets are produced, which are separated by 2 mm centerline distance. The jets are continuously photographed with a video camera by illuminating them in backlight with a stroboscope of very short flash duration (order of 100 ns). The flash frequency is matched to the framing rate of the video camera. This method avoids all motion blur completely, even for close-up pictures with considerable magnification. The breakup length can usually be identified and repeated to within +/- 0.5 cm. Because droplets from spraying attach to the walls of the chamber, the visibility through the viewing windows can be strongly reduced.

In order to avoid complications with BHP, which needs continuous cooling, solutions of glycerin in water have been used as a liquid to simulate BHP. The viscosity of BHP can be easily matched by the concentration (and temperature) of the glycerin and

has been varied from 1 to 30 mPa s. Other parameters that have been varied were: driving pressure p , chamber pressure p_c , orifice diameter d , orifice length l , and gas flow velocity v_g . The jet velocity can be estimated to within about 10% from the pressure and density of the liquid using an appropriate discharge coefficient or can be inferred from the measurement of the flow duration of a defined amount of liquid. Air has been used for the counter-flowing gas and v_g was adjusted by injecting a defined flow rate of air.

3. EXPERIMENTAL RESULTS

3.1 Flow modes and start-up phenomena

The transition from a laminar to a turbulent jet is not a discontinuous process. It is therefore difficult to associate the transition with a definite Reynolds number $Re = \rho v d / \eta$ (ρ , v , η are the density, velocity and viscosity of the liquid and d is the jet diameter). At first the strongly symmetric axial instability with Rayleigh breakup starts to become irregular, but the jet surface remains smooth. The resulting drops are no more round but rather elongated and irregular in shape. From the observation of the jet surface structure we have associated "full turbulence" with the appearance of irregular wrinkles on the before smooth jet surface. As the Reynolds number is further increased the wrinkles increase in number and depth and their size decreases. The contractions from the wrinkles become more and more significant for the breakup mechanism. At higher pressures intermediate breakup states have been observed for the liquids with higher viscosities: The jet breaks up and forms a series of drops and reconnects then again. As the turbulence in the jets increases the straightness of the jets is lost. The jets may curl up (sinusoidal jets) and change their direction (wandering). Eventually spraying starts from the jet surface with an increasing number of ejected droplets. In some occasions an instantaneous, explosion like, complete destruction of a jet has been observed.

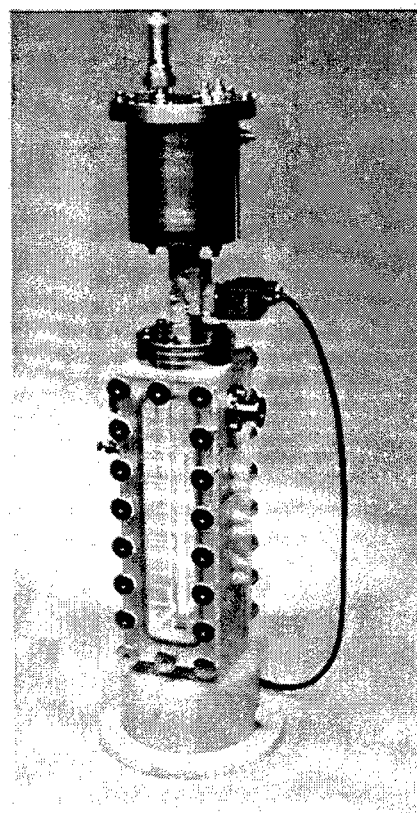


Fig. 1. Jet generator simulator

As the analysis of the first video frames after start of the experiment shows, the final jet mode is not established instantaneously. The jet formation begins with a dripping process lasting for about 100 μ s until the jets appear as solid cylinders with a smooth surface. During the next 40 μ s the surface of the jets exhibits a few occasional bulbs and then begins to wrinkle rapidly. Along with this wrinkling process spraying from the jet surface sets in and achieves a maximum rate approximately 250 μ s after flow start. The jet surface is now very rough. However, the spraying can cease within seconds, depending on liquid pressure and viscosity. Although it is assumed that these transient phenomena are initiated by the

establishment of an undisturbed flow from the storage tank through the run tank (see Sect. 3.3), the observed stabilizing times are much longer than for instance the filling time of the run tank. For a 45%wt. glycerine solution spraying starts at about 3 bar and for a 65% glycerine is only observed at pressures of 4 bar and higher. It should be emphasized at this point, that such transient phenomena may influence the oxygen generation during that time as well. Therefore, short-time laser experiments with jet SOGs may not be representative for a continuous longterm operation.

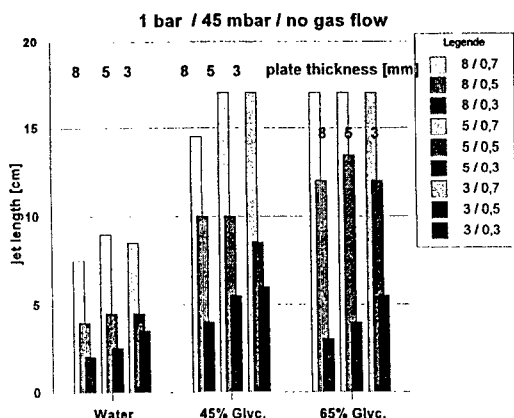


Fig. 2. Jet lengths for various orifice dimensions at a liquid pressure of 1 bar, a chamber pressure of 45 mbar and no gas flow. (The upper limit of 17 cm is set by the generator height).

3.2 Jet lengths

In a first series of experiments the intact jet length has been measured for water ($\eta = 1$ mPa s), 45 %wt glycerine (5 mPa s), and 65 %wt glycerine (15 mPa s), for 3 orifice diameters (0.3, 0.5, and 0.7 mm) and for 3 orifice lengths (3, 5, and 8 mm, defined by the thickness of the plate into which the orifices were drilled). At 1 bar jets from the two thinner plates were generally found to be longer by up to 2.5 cm than for the 8 mm thick plate (Fig. 2). However, in some cases the jets from the 3 mm plates were also shorter (max. 1.5 cm) than those from the 5 mm plate. The shortening of the jets with increasing orifice length can be explained by a larger friction loss and therefore a reduced jet velocity. A reduction of the jet length for thin

plates might be explained by an incomplete development of the velocity profile in too short an orifice. Yet, the influence of the orifice length is only a minor one, compared to the effect of the other two parameters, jet diameter and viscosity; the jet length increases roughly proportional with the jet diameter. A reduction in jet length is also found, if the pressure in the chamber is raised above 0.1 bar.

Jet length measurements have been carried out for a pressure range from 0.5 bar to 8 bar. The result for the 8 mm /0.5 mm orifice and for two of the tested liquids are shown in Fig. 3 with no gas flow in the chamber. It is seen that at first there exists a clear trend of increasing jet length with increasing pressure. While the already turbulent water jets continue to grow over the whole pressure range, there appears a reversal of this trend for the glycerine jets at pressures higher than 3 bar. The turnover in the jet length is associated with the onset of surface spraying, which then increases with the pressure. Also an increasing tendency to curl up and wander is observed. In the laminar flow range of 65% glycerine the situation is somewhat different. Independent of gas velocity and liquid pressure the jets show first breaks without the formation of drops after a flow length of 4 to 7 cm. Further downstream breaks occur successively more frequent and an increasing number of drops appears in these breaks. Finally, within less than a centimeter the jet turns completely into a chain of drops. This limit is also a strong function of the pressure, but drops only were never observed when the pressure was higher than 2 bar.

In an extension of this parameter study, air has been introduced into the jet chamber 20 cm below the orifice plate and pumped out 2 cm below the orifice plate. The velocity was adjusted from 0 to 50 m/s by varying the gas flow rate. After changing the flow rate the chamber pressure was adjusted by a regulating valve in the pump line. For *water* and $p_c = 45$ mbar jet lengths for liquid pressures higher than 1 bar are almost universally reduced by 2 to 3 cm when a gas flow is applied. Above 10 m/s this reduction is independent of the gas flow velocity to within the experimental uncertainty and the jet lengths do not exceed 8 cm. The same jet length values are found for a chamber pressure of 200 mbar, with the exception that already in the quiet environment the jets are reduced to these values and thus appear to be independent of any gas flow. However, gas velocities higher than 30 m/s could not be applied for $p_c = 200$ mbar. At these higher velocities the drops were destroyed at the gas inlet. The water was blown to the chamber walls, driven upwards to the gas exit and entrained in large amounts into the pump line. For *glycerine solutions* a reduction of the jet length (transition to a pure drop flow) of up to 50% is found with increasing gas velocity, irrespective of the chamber pressure. For the 65% glycerine this decrease occurs over the whole pressure range. At a fixed gas velocity (i.e. 30 m/s) the jet length increases roughly with the square root of the liquid pressure. If the pressure is not too high (≤ 4 bar), a similar decrease in jet length with increasing gas velocity is found for the 45% glycerine, as Fig. 4 shows. However, at pressures of 6 and 8 bar the influence of the gas flow becomes notably less.

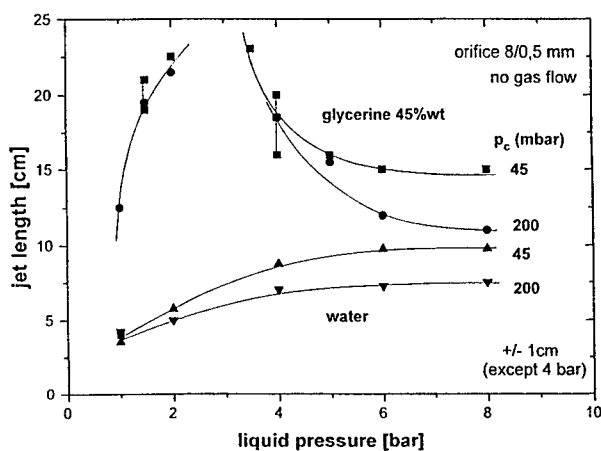


Fig. 3. Jet length variation with the pressure of the liquid for water and 45% glycerine and two chamber pressures

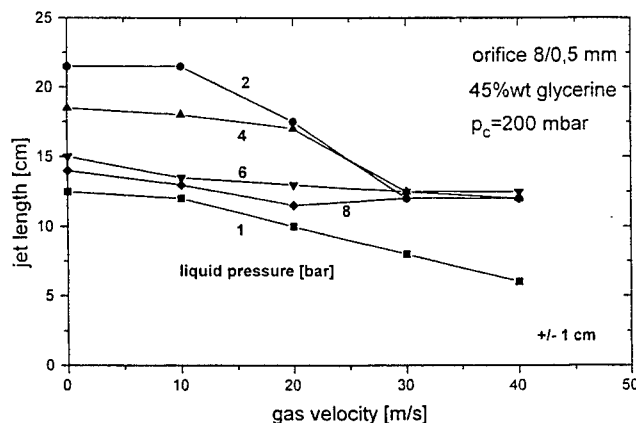


Fig. 4. Jet length variation with the velocity of the gas flow for different pressures on 45% glycerine.

3.3 Orifice effects

By observing the jet structures it has been found, that in some cases the jet diameter is shrinking with increasing liquid pressure. Causes may be searched in nozzle inlet effects and cavitation like mechanisms inside the orifice, which prevent a proper matching of the flow to the orifice walls. Gills et al. have reported about such effects⁹. This speculation has lead us to a separate

investigation of the flow inside the orifice. For that purpose a 1 mm diameter and 10 mm long bore had been drilled into lucite to view the interior flow. The same videographing and lighting technique had been applied with a magnification up to 30 for recording the flow features. Initially the edge of the bore entrance had been kept sharply rectangular.

In the first experiments with water it became immediately apparent, that a cavitation type process is occurring at the inlet indeed. The filling of the bore with liquid downstream of the inlet was found to be a strong function of the pressure on the liquid. While at a driving pressure of 1 bar, the bore filled after a flow distance of about half of its length, already at 2 bar these cavitation features were dragged all the way down to the bore end and at even higher pressures the bore was never filled with liquid. In all cases the flow was clearly turbulent at the exit. Increasing the viscosity to 2.5 mPa s (30% glycerine) reduced this cavitation effect considerably: At 1 bar the bore filled after 20% of the bore length and the cave reached to the bore end only at 4 bar. A further increase in viscosity to 5 mPa s initiated a reduction of the cavitation length at high pressures: With 25 mm it was maximum at the pressure of 2 bar and disappeared entirely for pressures of 6 bar and higher. Finally, for viscosities of 15 mPa s and higher (65% and 73% glycerine) the bore remained filled at all times. In an attempt to improve the situation, the inlet edge of the bore has been rounded with a radius of 2 mm. Now, cavitation could not be observed anymore. - In order to show a possible deficit in mass throughput as a consequence of an incomplete filling of the bore, the flow rate has been measured for both cases, unrounded and rounded inlet edge. As expected, it increased almost $\propto \sqrt{p}$ (exact power is 0.52 to 0.57), but turned out to be roughly a factor of 2 below the theoretically expected values⁸ in either case. The ratio of the measured to the theoretically ideal flow rate is nearly independent of the pressure for water and 30% glycerine and approaches a limiting value of 0.38 at the higher pressures. Checking the Reynolds no. shows, that this is the case when Re becomes larger than $Re_{crit} = 12000(l/d)^{0.3}$, a value given by Sande and Smith¹⁰. This means turbulent flow and corresponds with the observed appearance of the cavitation mechanism.

4. CONCLUSIONS

Basically the jets are found to follow the general laws layed out in ref. 7. For higher pressures the instabilities of the jets increase quite rapidly. Low viscosity jets show considerable surface spraying and a reduced jet length. As expected, a counter-flowing gas does shorten the jet length and this effect is independent of the pressure in the jet chamber. For short term operations of the generator transient phenomena did occur which exhibited strong spraying for at least several seconds. Low viscosity of the liquid, together with a sharp inlet into the orifice bore may give rise to cavitation features, which limit the flow rate and increase turbulence effects.

5. REFERENCES

1. N.F.Balan, M.V. Zagidullin, A.Yu. Kurov, V.D. Nikolaev, and M.I.Svistun, "Source of high pressure $O_2(^1\Delta)$," *Sov. Tech. Phys. Lett.*, Vol. 15, pp. 731-732, Sept. 1989.
2. V.N.Azyazov, M.V. Zagidullin, V.D. Nikolaev, M.I.Svistun, and N.A.Khvato, "Jet $O_2(^1\Delta)$ generator with oxygen pressures up to 13.3 kPa," *Quantum Electronics*, Vol. 24, pp. 120-123, Febr. 1994.
3. V.N.Azyazov, M.V.Zagidullin, V.D. Nikolaev, M.I.Svistun, and N.A.Khvato, "Oxygen-iodine laser with a drop-jet generator of $O_2(^1\Delta)$ operating at a pressure up to 90 Torr," *Quantum Electronics*, Vol. 25, pp. 423-425, May 1995.
4. I.Blavvas, B.D.Barmashenko, D.Furman, S.Rosenwaks, M.V.Zagidullin, "Power optimization of small scale chemical oxygen-iodine laser with jet-type singlet oxygen generator", to appear in *IEEE J.Quant.Electron.*, 1996.
5. H.Fujii and T.Atsuta, "COIL activities in Japan: industrial COIL development", *Fourth Int. Workshop on Iodine Lasers and Applications*, Proc. SPIE Vol. 2767, pp170-184, 1996.
6. O.Spalek and J.Kodymova, "Influence of arrangement of liquid jets on operation of jet singlet oxygen generator", *Fourth Int. Workshop on Iodine Lasers and Applications*, Proc. SPIE Vol. 2767, pp.237-244, 1996.
7. C.C.Franck and W.O.Schall, "Fluid mechanic investigations for $O_2(^1\Delta)$ jet generators," *Proc. Gas Flow and Chemical Lasers*, SPIE Vol.2502, pp.297-303., Sept. 1994.
8. W.O.Schall and D.Kraft, "Liquid breakup studies for singlet oxygen generators," *Fourth Int. Workshop on Iodine Lasers and Applications*, Proc. SPIE Vol. 2767, pp.229-236, 1996.
9. V.V.Gil', R.Goshi, V.L.Kolpashchikov, S.A.Kuleshov, O.G.Martynenko, A.I.Shnip, "Intrachannel dispersion of rapid jets of low viscosity liquids", *Ing. Phys. Journal*, Vol.54, No. 1, 1988 (in Russian).
10. E.van de Sande and J.M.Smith, "Jet break-up and air entrainment by low velocity turbulent water jets," *Chem. Eng. Sciences*, Vol. 7, pp. 219-224, 1976.

Oxygen - Iodine Laser Capacity at the Elevated Pressure.

Adamenkov A.A., Vyskubenko B.A., Gerasimenko N.N., Deryugin Yu.N., Zelensky D.K., Ilyin S.P.,
Krukovsky I.M., Kudryashov E.A.

Abstract:

The present paper describes the experimental results for aerosol-jet singlet oxygen generator with a twisted flux to separate the aerosol effectively. It was demonstrated that at 50 Torr pressure and 30 m/s velocity, there does not exist the aerosol in the flux at the reactor output, and singlet oxygen contribution constitutes 70%, not less. The numerical simulations results are given for supersonic COIL up to 50 Torr pressure in the nozzle input with and without inertia diluent in the main flux.

Key words: singlet oxygen generator, iodine-oxygen laser, aerosol, jet and dropped regimes, laser cavity.

1. Introduction.

Further trends in chemical oxygen-iodine laser (COIL) development assume higher pressure in the gas path as it provides for reduced energy consumption to sustain a working vacuum. Moreover with increased pressure laser dimensions and weight decrease for a specified power, if one manages to preserve the efficiency. The advance in singlet oxygen generator (SOG) studies facilitated the pressure range of 30 - 100 Torr at the SOG output, provided oxygen excitation being high [1,2,3,4]. This allowed to reach lasing of 10% efficiency for subsonic flow in the cavity and over 25% for supersonic COIL (SCOIL) without a water vapour trap to be used in COIL experiments [1,5]. In SCOIL experiments the SOG oxygen flow was deluted drastically with helium. It is evident that on one hand, helium present eases substantially the achievement of high efficiency of lasing, on the other, increases its cost considerably, and thus is not desirable in practical applications. Recent publication of Samara physics show that a jet SOG facilitates up to 100 Torr in the gas mixture at the output without helium (or argon) at 60% singlet oxygen concentration. Meanwhile still unclear is the capability of COIL lasing section proper, to convert effectively the stored energy in SOG flux in laser radiation if there is no buffer gas. Special research is needed to identify optimal pressure achievable without a notable loss in the efficiency. First, one has to identify a key component of a COIL limiting its energy permeability: a SOG or a lasing section proper.

The present work is a certain step in the solution of the problem. The paper consists of two parts. The first part gives the experimental results for a SOG of VNIIEF proposed scheme [6] implementing an aerosol-jet reactor in which an basic solution of hydrogen peroxide (BHP) is fed as condensed jets across the gas flux twisted to separate the liquid drops from oxygen at the early stages. To shorten the name, the reactor is named as TASOG. The TASOG design aimed at higher pressures of singlet oxygen and its velocity at the reactor output compared with the exciting reactors. The second part of the paper presents the calculation of lasing power results at higher pressures of singlet oxygen when there is no neutral diluent in the prime energy carrying flux.

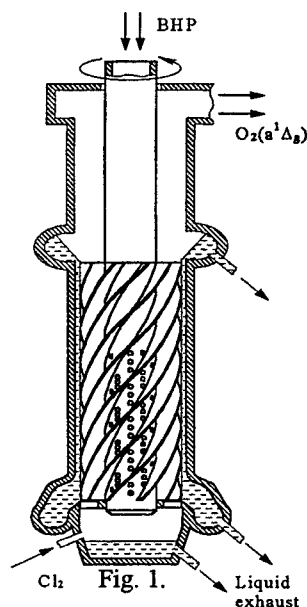
2. Twisted Aerosol SOG Experiments.

As it is known, by now the highest SO pressure was recorded in jet SOG shots which design was proposed and studied by Samara physics [3,4,5]. Currently, the advantages of this reactor provided the higher energy characteristics of a gas at lower water concentration in the output flux: at 70-100 Torr and 30-40 m/s for the gas in the basic cross section of the reactor the SO contribution constitutes 70-50%, partial water pressure is less than 2 Torr. Unfortunately the high SO flux at high gas pressure and velocity was accompanied by aerosol carry-over from the reactor and residual chlorine increase in output flow. The published experimental data showed that the boundary velocity and pressure ranges are 15-20 m/s and 30-50 Torr, correspondingly, which, when increased, cause aerosol removal.

We have tried with our SOG scheme [6] to perfect the arrangement of gas and liquid flows as well as aerosol separation with a hope to achieve higher pressure, velocity and SO contents at low water and aerosol concentration at the output. Present state of the work is shown below.

TASOG reactor (fig. 1) is a cylinder of 4.2 cm inner diameter and 25 cm height. BHP in the form of drop jets of 10 m/s velocity is delivered through the holes in a central tube of 1.6 cm outer diameter perpendicular to the wall, and the gas is blown through a system of these jets along the cylinder axis. Holes diameter was 0.03 cm. The central tube rotates and is equipped with a feeder to collect and remove a spent

liquid. Provided the gas passing along the screwed channels of the feeder, acquires an angular velocity which exceeds substantially the velocity of feeder rotation that allows to remove aerosole from the gas flux effectively. A transversal arrangement of the short jets provides for fresh solution along the path of interaction and allows to choose a length for the working zone needed for complete chlorine utilization at any gas velocity.



The first TASOG experiments showed a conceptual feasibility of the proposed scheme and high utilization of chlorine characteristic of aerosole reactors [6]. The directions for gas fluxes and liquid removed over cylinder wall coincided with the force of gravity, thus partially the liquid got in the measuring tract in these shots. The present design was slightly changed to avoid this drawback causing high water concentration in the output flux. Mainly, these shots aimed at the conditions to be developed under which the gas at the reactor output is free from the aerosole. Also, the measuring tract geometry was changed, as the old edition had the measuring points for singlet oxygen glow taken unjustly too far from the SOG output. The measuring tract simulated the COIL subsonic nozzle section and was completed with the supersonic nozzle. Varied relationships of the areas of chlorine washer and a supersonic nozzle allowed to change the reactor pressure and velocity. Pressures were measured in the reactor bottom and in the measuring section, as well as radiation rates at 2 wavelengths: 0.76 and 1.27 μm . Chlorine consumption was measured on the calibrated washer, its concentration - in the measuring section by light absorption on 0.334 μm wavelength. The velocity was measured with Pitot tube in the measuring section. During the onset gas was sampled from the flux by

which its chemical composition was identified. Thermocouples measured the flux temperature. In the shots we chose the design parameters which facilitated aerosole precipitation prior to their release from the reactor, as well as the cylinder wall geometry and collector location which prevent from liquid film ablation from the cylinder walls in the measuring tract. Visually the aerosole presence or absence was recorded. Table 1 shows the experimental measurements when the SOG output flux did not contain the liquid. We had some difficulties in interpretation of the singlet oxygen radiation intensity measurements because of gas density uncertainty in such experiments. It is caused by unreliable temperature measurement by means of thermocouples in rare gas at SO relaxation. So we tried to rationalize the obtained experimental results on the basis of one-dimensional engineering model presented below.

EXPERIMENTAL RESULTS

Table 1.

Press.	Veloc. react.	Cl ₂ flow rate		Cl ₂ density		O ₂ (¹ Δ)		ΔP on Pitot tube		Temperat.		Cl ₂ utiliz.	O ₂ (¹ Δ) lot	Temp.	Veloc.
	m/sec	mmol/sec		10 ²³ part./m ³		10 ²³ part./m ³		Torr		K		%		K	m/sec
		exp.	Calc.	exp.	Calc.	exp.	Calc.	exp.	Calc.	exp.	Calc.	Exit reactor parameters			
4	22	16	15,7	0,4	0,3	2,79	2,78	0,8	0,25	350	352	91	0,93	334	22,5
24	26,4	33	33,3	0,8	0,82	3,34	3,75	1,05	0,7	370	385	85	0,85	344	28,2
44	14,7	35	34,5	0,8	0,87	3,95	4,44	0,55	0,45		467	90	0,76	445	20,3
22	14,2	16	16,3	0,7	0,73	3,05	3,17	0,45	0,18		395	85	0,85	373	16,2
67	15,6	57	56	1,6	1,64	4,5	6	0,9	0,75		444	88	0,72	477	23,2
48	20,8	52	52,8	1,4	1,2	4,9	5,08	1,2	1,05	470	476	87	0,8	418	27
34	35	52	52,2	1,4	1,3	4	4,8	1,1	1,35	410	416	83	0,88	363	33
42	30	79	67,2	2	1,8	4,5	5,3	1,2	1,65	410	372	82	0,72	345	32
62	25	87	83,8	1,8	1,7	4,8	4,9	1,2	1,4	467	348	90	0,38	327	25
62	21	87	69,3	1,8	1,5	4,8	5,1	1,2	1,4	467	491	87	0,61	401	26

The interpretation using one-dimensional code results is presented in emphasis cells. There are two different interpretation cases of the same experiment in the last two rows.

The calculated form of the SOG output and measuring section was taken from experiment. Gas velocity and oxygen excitation degree at reaction zone exit were selected to reach the sonic velocity at exit nozzle and to

ensure maximal correspondence of the measured and calculated parameters. Table 1 provides the results of numerical experiments interpretation. The measured and calculated values are shown to be close primarily but the highest pressure experiments. Besides that we did not manage to describe the tube Pitot reading, that requires the additional study.

The gas sample analyzing shows water concentration became vitally lower compared to the first shots. It must be mentioned that these results were obtained without additional cooling of the reactor and with -10°C solution. If more concentrated solutions are used and the temperature is reduced to $-15 \div -20^{\circ}\text{C}$, water concentration can be made even lower. It must be stressed that for all table pressures and velocities in the reactor, the aerosol was not trapped from the reactor. The SO lot also can be seen a little decreasing at pressure increasing up to 60 Torr. Velocity is to be increased to keep the high SO content at the high pressure. To prevent aerosol carry-over from SOG some modifications are necessary to implement. In the experimental model mentioned, the separation section of the reactor had to be prolonged by a shortened working zone so the chlorine utilization was reduced compared to the first experiments, nevertheless even at 6 cm working zone of the reactor, chlorine was utilized at 85-90% level, not less. Further advance to higher pressures and velocities of the gas demands the next model of a reactor with longer working zone filled with jets.

The numerical estimates revealed that the input of COIL supersonic nozzle replacing the measuring section, the TASOG even in the present arrangement is capable of producing a flux of 70-80% oxygen excitation under 50 Torr.

3. Calculation model.

To assess the COIL efficiency under higher pressures a mathematical model was used which was presented in the previous work [6]. The model includes the 2-D or 3-D supersonic gasdynamic equations with account of turbulent mixing, chemical kinetics and energy exchange and interaction with radiation in the cavity, including basic energy exchange channels as well as calculations of lasing power in the cavity. This numerical model with a kinetics block for gasdynamic CO_2 laser was verified in detail via the comparison with experimental data in a wide range of conditions and has shown a good agreement with the experiment that testifies for a correct description of the flow gasdynamic processes and choice of turbulence models in mixing [9,10]. In the COIL model the kinetics block was replaced for the block describing the kinetics of chemical reactions and energy exchange for COIL mixtures. The kinetics model was borrowed from FIAN work [11] with certain additions to the reactions accounted and slight changes in the choice of constants [6].

Prior to numerical research we have numerically modeled VERTYCOIL facility to check its validity. Initial data was taken from the experiment published in ref.[1]. The calculated laser power constituted 1.76 kW in 1-D model and 1.66 kW - in 2-D model that is close enough to experimental 1.75 kW.

4. COIL Calculations under Elevated Pressure.

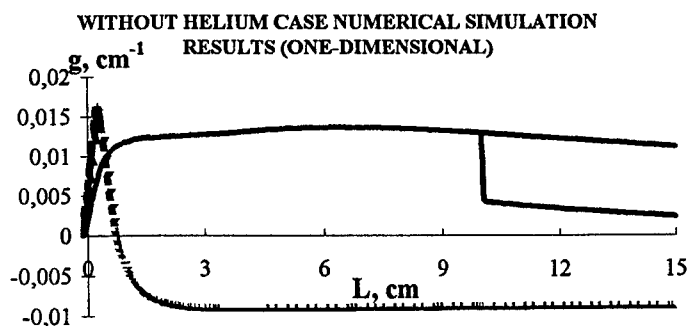


Fig. 2.

1. Main energy carrying flow: $P_0 = 0.066 \text{ atm}$, $T_0 = 300\text{K}$, composition: $0.46 \text{ O}_2 + 0.5 \text{ O}_2^* + 0.02 \text{ Cl}_2 + 0.02 \text{ H}_2\text{O}$
2. Injecting flow: $P_0 = 0.066 \text{ atm}$, $T_0 = 370\text{K}$, composition: $0.01 \text{ J}_2 + 0.99 \text{ N}_2$
3. Mixing points coordinates: $X_m = 0.025\text{cm}$, $X_m = -0.15\text{cm}$ (subsonic case).

Figures 2 and 3 show the basic parameters of the calculated design with main calculations. One has to note that reliable data obtained in numerical modeling requires thorough verification of the code via calculated and experimental result comparison in a wide range. This is to be done yet, so the obtained results, most probably, must be specified. Nevertheless, certain features revealed in calculations attract the attention. First, with no helium for energy compensation released in the flux, especially in the cavity, we had to increase the geometrical expansion degree to 6 and the expansion angle to 5° after the shaped section. At smaller expansion in the cavity a supersonic flux can not be preserved. Second, higher pressure of the synglet oxygen in the nozzle input and no

helium require a mixing point shifting in the supersonic region, otherwise the supersonic flux is not realized in the cavity. Fig. 2 illustrates the parameters of the flow occurred in case of small shift of injection point to subsonic side. One can see that the available laser energy is all but lost yet before the cavity to be reached. Supersonic injection results in the fact that the production of atomic iodine and maximum gain factor shift downstream. If this fact is confirmed in the experiments, then the best results are to be expected for the mixing scheme we had used for the mixed gasdynamic laser in which the mixed gas is delivered in the

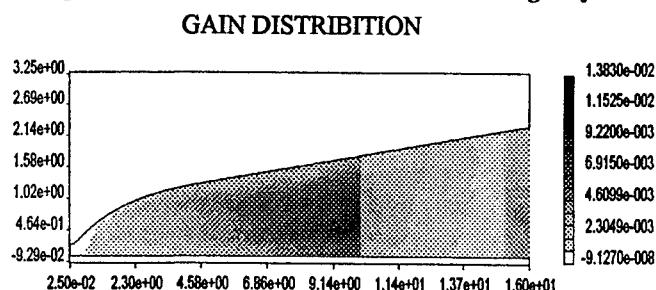


Fig. 3.

supersonic nozzle section in the form of jets parallel to the basic flux [6,9,10]. Our experiments with mixing gasdynamic laser which had been performed earlier proved this mixing system provided sufficiently homogeneous mixing under minimal gasdynamic disturbances caused in flow. The last factor becomes especially important when SO high pressure because it provides the more stable supersonic flow under the less geometrical expansion degree of the nozzle.

5. Conclusion.

The main results obtained can be formulated in the following way:

- It was experimentally showed that we managed to achieve over 30 m/s velocities under 40 Torr in the SOG scheme with the twisted flux without solution removal from the reactor. The obtained numerical estimates demonstrate TASOG is able to provide the SO flux at the supersonic COIL input under the pressure of 50 Torr and higher and oxygen excitation at the reactor output constituting 70%, not less.
- The comparison of the calculated power values with the published experiments showed a satisfactory agreement that speaks for applicability of the mathematical model for COIL parameters study.
- The calculations done for 50 Torr input pressure in the supersonic nozzle showed the need for supersonic iodine mixing in the basic flux if the main flux lacks the inertia diluent.

6. References.

1. T.L.Rittenhouse, S.P.Phipps, C.A.Helms and K.A.Truesdell. "High efficiency operation of a 5 cm gain length supersonic chemical oxygen-iodine laser", Conference in San Jose, January 1996.
2. Jay A.Blauer, S.A.Munjee, K.A.Truesdell, E.C.Curtis, and J.F.Sullivan, "Aerosol generators for singlet oxygen production." J. Appl. Phys. 62 (6), 15 September 1987, pp.2508-2517.
3. V.N.Azyazov, M.V.Zagidullin, V.D.Nikolaev, M.I.Svistun, N.A.Khvatov "Jet $O_2(^1\Delta)$ generator with 13.3 kPa oxygen pressure". *Quantum electronics*, 21, 129 (1994).
4. M.V.Zagidullin, V.D.Nikolaev, M.I.Svistun, Ufimtsev. "Predicted and measured parameters of high pressure jet SOG". *Fourth International Workshop on Iodine Lasers and Applications*. SPIE Vol. 2767/221.
5. Nikolaev V.D. "Current Research of COIL in Samara". *Fourth International Workshop on Iodine Lasers and Applications*. SPIE Vol. 2767/185.
6. Adamenkov A.A., Vyskubenko B.A., Gerasimenko N.N., Eroshenko V.A., Deryugin Yu.N., Zelensky D.K., Ilyin S.P., Krukowsky I.M., Kudryashov E.A. "High Pressure COIL Problem". *Fourth International Workshop on Iodine Lasers and Applications*. SPIE Vol. 2767/209.
7. Wolfgang O. Schall and Daniela Kraft. "Liquid Breakup Studies for Singlet Oxygen Generators". *Fourth International Workshop on Iodine Lasers and Applications*. SPIE Vol. 2767/229.
8. Otomar Spalek and Jarmila Kodymova. "Influence of Arrangement of Liquid Jets on Operation of Jet Singlet Oxygen Generator". *Fourth International Workshop on Iodine Lasers and Applications*. SPIE Vol. 2767/237.
9. B.A.Vyskubenko, Yu.N.Deryugin, G.A.Kirillov, Yu.V.Kolobyandin, S.B.Kormer, V.D.Nikolaev, B.P.Tikhomirov. "Comparison of 2-D calculations results for mixed GDL with the experiments.", VANT, series: techniques and codes of numerical solutions, vyp. 3(14), p. 18-22, 1983.
10. B.A.Vyskubenko, Yu.N.Deryugin, Yu.V.Kolobyandin, S.B.Kormer, B.P.Tikhomirov. "Comparison of 2-D calculations results for mixed GDL with the experiments." Part II. 3-D grid. VANT, series: techniques and codes of numerical solutions, vyp. 1(15), p. 59-61, 1984.
11. Yu.A.Kulagin, L.A.Shelepin, V.N.Yarygina. "Kinetics of active media. Oxygen-iodine laser." FIAN proceedings, 1991, v.212, p. 123-143.

HF laser initiated by an intense electron beam

M. Gastaud , J. Bouesc , M. Autric

CNRS - IRPHE / LP3

Parc scientifique et technologique de Luminy
163 avenue de Luminy - 13009 Marseille -FRANCE

Tel: 33- 91 26 92 90 fax: 33- 91 26 92 89

E-mail: gastaud @mfmcaldas.univ-mrs.fr

ABSTRACT

A 400-keV electron beam has been used to initiate HF chemical laser pumped by the nonchain reaction. Parametric studies of the energy deposited and laser performance were performed to determine optimum pressure and composition of SF₆/ H₂ or C₂H₆ mixture.

1 - INTRODUCTION

Previous investigators have used high-energy electron beams to produce HF chemical lasers operating either on the chain reaction [1-4] with high specific energy (100J / l) or on the nonchain reaction [5, 6] with lower specific energy (10J / l). This initiation is usually performed by injection of a beam along the cavity axis or perpendicular to this axis.

In the present experiment an intense electron beam was injected into the laser mixture and a pressure transducer was used to infer energy deposition. In our investigation we found that an increase in the pressure of SF₆ to p~ 500mb increase the energy deposition linearly. For higher gas density, the spatial ionization region contracted and the energy deposition remain constant.

Laser output energy dependence on the H₂ and C₂H₆ concentration was investigated for a gas mixture with a constant SF₆ pressure of 550 mb. The maximum laser energy measured was 7 J with a H₂ partial pressure included between 8 and 70 mb. With C₂H₆ the energy initially increases rapidly with increasing ethane pressure up to a maximum of 6 J at 10 mb ; then, the energy decreases quickly for pressures greater than 20 mb.

2 - EXPERIMENTAL APPARATUS

Figure 1 shows a schematic representation of the experimental apparatus. The laser initiation is made by two counterpropagating electron beams delivered by two accelerators. The high voltage to apply across the anode and cathode of the diode is produced by a six-stage Marx generator. The maximum charging voltage is 100 kV and the stored energy is 36 kJ. Typical electron beam parameters is 400 keV , 28 kA at the e-beam diode for a pulse duration of 500 ns. The e-beam is injected into the laser gas mixture through a 15 cm high - 100 cm long - 75 µm thick aluminized kapton anode foil supported by a steel grid whose geometric transparency is ≅90%. The laser cell has an over-all length of 120 cm and a cross section of 20x20 cm².

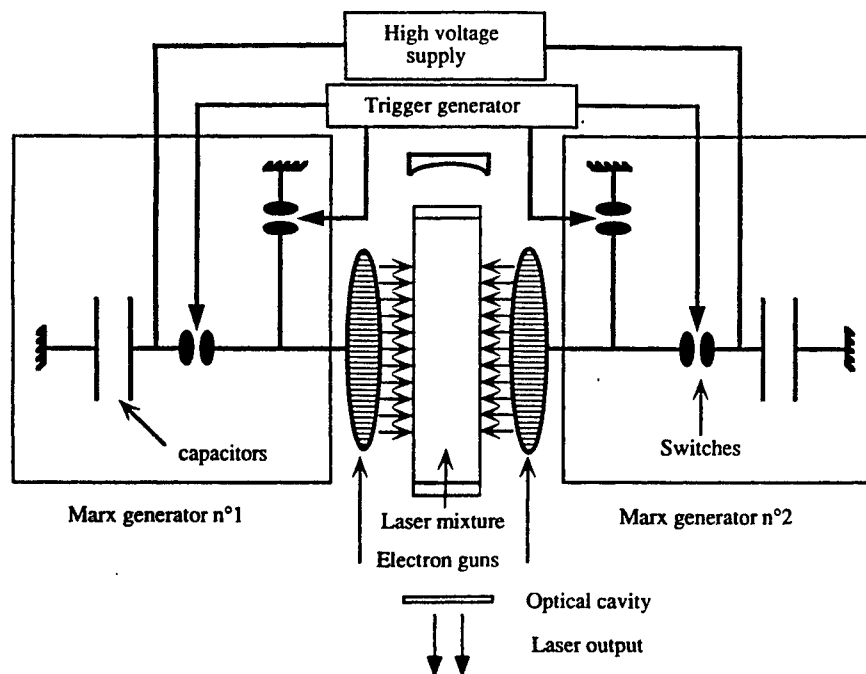


Figure 1: schematic of the experimental apparatus

Output HF laser performance has been investigated by using a 5 cm diameter optical cavity made of 10 m radius total reflector and a flat CaF_2 window. The optical axis is located at 3 cm from the anode in the beam transport direction.

3 - EXPERIMENTAL RESULTS AND DISCUSSION

Experimental results has been obtained by using only one electron beam.

A pressure transducer was used to infer energy deposition from the increase in pressure due to electron beam heating and dissociating of the pure SF_6 gas. Figure 2 shows the energy deposited in SF_6 for three different values of the diode voltage.

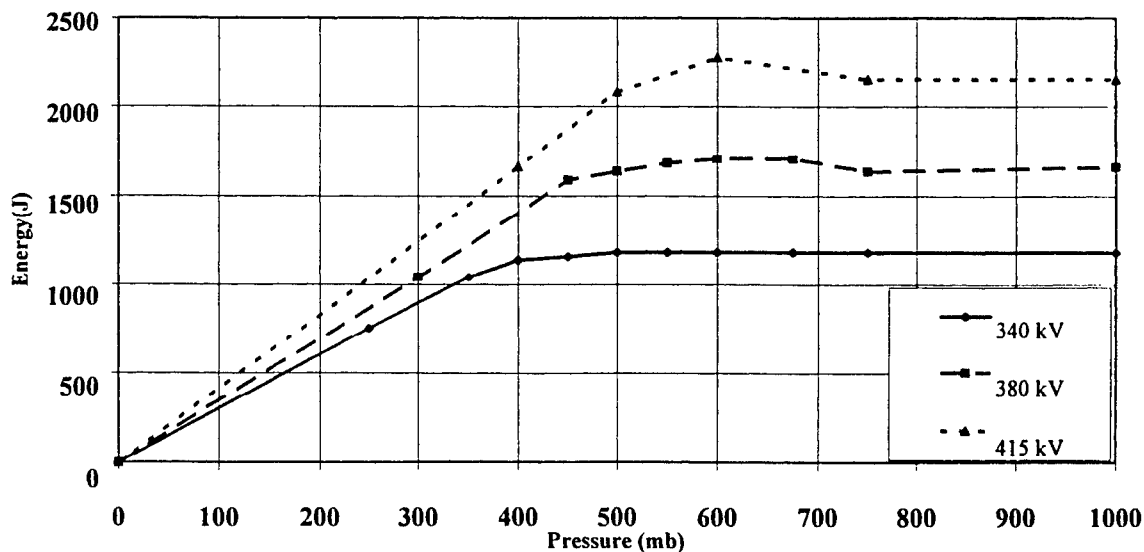


Figure 2: Energy deposited in SF_6 for a gas chamber length of 20 cm

In our investigation we found that an increase in the pressure of SF_6 to $p \sim 500\text{mb}$ increase the energy deposition linearly. For higher gas density, the spatial ionization region contracted and the energy deposition remain constant. This optimum value of the energy deposited is only about one-third to one-half of the energy available at the cathode level. In SF_6 the e-beam is locked in by the space charge and a large amount of the electron energy is lost in the work against the electric space-charge field.

Laser investigation was conducted by using a laser cavity of 5 cm in diameter located at 3 cm downstream the electron beam foil. Laser output energy dependence on the H_2 and C_2H_6 concentration was investigated for a gas mixture with a constant SF_6 pressure of 550 mb. Figure 3 shows the dependence of the HF laser energy on the H_2 or C_2H_6 partial pressure. The maximum laser energy measured is 7 J with a H_2 partial pressure included between 8 and 70 mb. This result corresponds to a specific energy output of 4 J/l. With C_2H_6 the energy initially increases rapidly with increasing ethane pressure to a maximum of 6 J at 10 mb, then the energy decreases quickly for pressures greater than 20 mb.

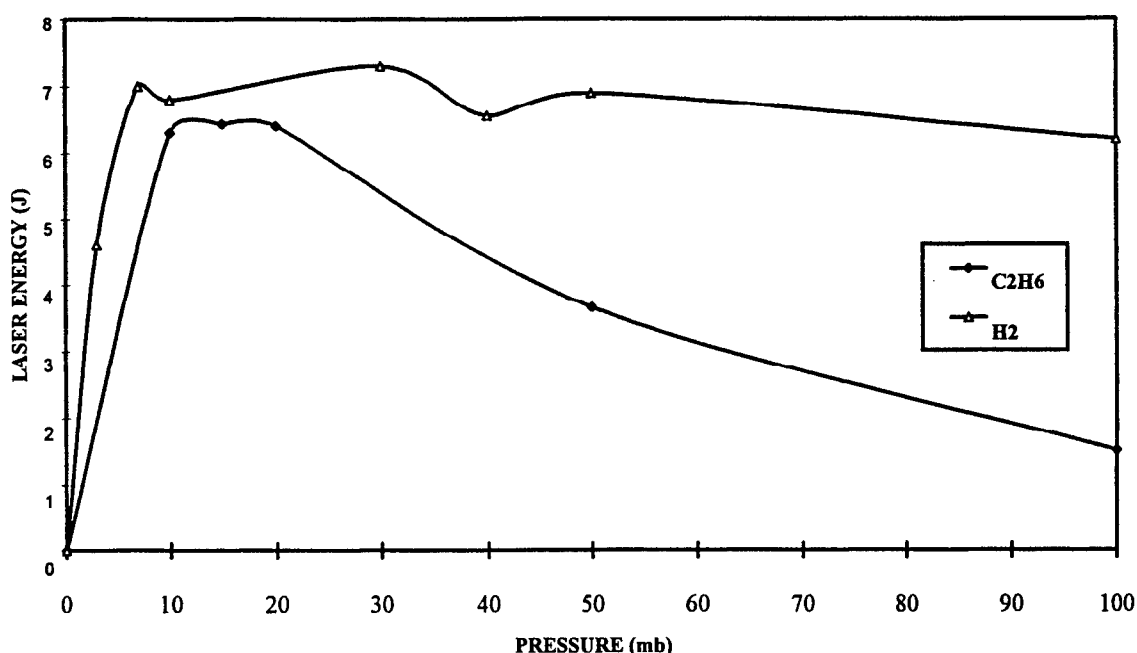


Figure 3: HF laser energy Vs H_2 or C_2H_6 partial pressure

The spatial distribution of the laser radiation was measured by the 'footprint' left on thermal paper. The zone with the maximum output energy was located near the anode; the output energy decreased in the beam transport direction in agreement with measurements on the electron beam energy absorbed by SF_6 .

Tests of laser functioning using the two electron guns pumping mode will be carried out in a near future in the laboratory using all the active volume ($20 \times 20 \times 100 \text{ cm}^3$). The output energy expected in this configuration has been evaluated at more than 100 Joules in less than 500 ns pulse duration.

For optimizing the laser functioning, small-signal gain measurements will be realized on various transitions (typically P_4 , P_5 on 3-2; 2-1; 1-0 bands).

Quantitative chemical analysis of the HF production (ie F-atom) in the product gases will be performed by aqueous titration for different mixtures and for different gun voltage.

4 - ACKNOWLEDGMENTS

The research work leading to this paper was supported by DRET, Paris
The authors would like to thank G. INGLESAKIS for helpful discussions through the course of these experiments

5 - REFERENCES

- 1 - A.S. Bashkin, A.F. Konoshenko, A.N. Oraevskii, V.N. Tomashov, N.N. Yuryshev: Sov. J. Quantum Electron. 8(7), 922, July 1978
- 2 - S.T. Amimoto, J.S. Whittier, M.L. Lundquist, F.G. Ronkowski, R. Hofland Jr., P.J. Ortwerth: Appl. Phys. Lett. 40(1), 20, January 1982
- 3 - H. Inagaki, F. Kannari, A. Suda, M. Obara: J. Appl. Phys. 59(2), 324, January 1986
- 4 - V.P. Borisov, V.V. Burtsev, S.D. Velikanov, A.Y. Dovgii, A.M. Podavalov, S.N. Sin'kov, Y.N. Frolov, Y.N. Sheremet'ev, V.V. Shchurov: Quantum Electronics 26(2), 115, 1996
- 5 - R.W.F. Gross, F. Wesner: Appl. Phys. Lett. 23, 559, 1973
- 6 - E.L. Patterson, R.A. Gerber: IEEE J. QE-11, 642, 1975

Experiments on optically pumped HF and DF transitions by
a Cr^{4+} :Forsterite laser

Pascale Prigent, Geneviève Girard, Annick Lavenant, Henri Brunet and Pierre Lemaiguen

Cilas, Route de Nozay, 91460 MARCOUSSIS - FRANCE

ABSTRACT

We describe results of experiments on optically pumped HF(0-2) and DF(0-3) transitions using a tunable and narrow-line Cr^{4+} :Forsterite laser. Cascade lasing transitions on 2-1 band of HF and on 3-2 and 2-1 bands of DF have been obtained. A computer modelling on DF has been also developed in conjunction with experiments to predict and compare the results obtained.

Keywords: mid-IR lasers, gas lasers, optical pumping, tunable Cr^{4+} :Forsterite laser.

1. INTRODUCTION

Optical pumping of vibrational transitions in molecules is a convenient mean for producing laser radiation at wavelengths that solid-state lasers cannot directly generate, especially beyond 3 μm . The hydrogen and deuterium halide molecules (HCl, DF, HBr) are of interest because they are the source of laser lines in the 3-5 μm regions. Their wavelengths are well suited for applications that require long range beam propagation through the atmosphere.

Recently, tunable nonlinear optical sources driven by Nd:YAG or dye lasers have been used to pump the 0-2 transitions of hydrogen and deuterium halide lasers. Energy conversion efficiencies (output energy versus absorbed energy) ranging from about 20 to 30% have been obtained¹⁻². Laser effect on the P(5) line of the DF(3-2) transition has been also reported by pumping the 0-3 transition with a Raman-shift Alexandrite laser³.

In this type of laser source, a short laser pulse is used for pumping the overtone transitions of the hydrogen halide molecules contained in a gas cell. A cascade inversion of population is then created between a high vibrational level ($v = 3$ or 2) and the lower unpopulated levels resulting in the emission of several rovibrational laser lines in the 3-2 and 2-1 bands. Depending upon the gas and the pump source used, various spectral regions between 3 and 5 μm can be covered.

Nevertheless, the main difficulty is to find the appropriate laser source for pumping the discrete and narrow lines of the overtone transition. At the moderate pressures (due to kinetics effects) generally used to obtain laser action in hydrogen halide molecules, the absorption lines present a very narrow linewidth (< 1 GHz). Therefore the pump source must have the same narrow spectral properties and must be exactly tuned to an absorption line for efficient pumping.

In this paper, we describe results of experiments on optically pumped HF(0-2) and DF(0-3) transitions using a tunable and narrow-line Cr^{4+} :Forsterite laser.

2. OPTICAL PUMPING EXPERIMENTS

2.1 Experimental set-up

The overall experimental arrangement is shown in Fig.1. The Cr^{4+} :Forsterite crystal was 23 mm long with a $4 \times 6 \text{ mm}^2$ cross-section. Its end-faces were cut at Brewster angle. The crystal was longitudinally pumped by a Q-switched Nd:YAG laser at 1.064 μm . This latter produced 10 ns pulses with an energy up to 130 mJ at 10 Hz repetition rate. A 70 cm focal length lens was used to adapt the Nd:YAG output beam to the crystal dimensions. The wavelength selection was accomplished by passing the forsterite laser beam through three dispersive prisms and by rotating the Rmax mirror. In order to reduce the spectral bandwidth of the laser emission, two Fabry-Perot étalons were inserted in the cavity. The first Fabry-Perot (FP1) and second one (FP2) were respectively 0.2 mm and 2 mm thick; both were 50% coated. The forsterite laser cavity length was 65 cm. The narrow-line radiation produced by the Cr^{4+} :forsterite laser was then coupled into the gas cell through a curved (5 mcd) dichroic cavity mirror which was highly transmissive at the pump wavelength and highly reflective at the DF lasing wavelengths. Two stainless steel cells equipped with CaF_2 Brewster windows were employed. The HF cell was 15 cm long, and the DF one, 50 cm. A ED-100 A Gentec pyroelectric detector was used to measure the radiation energy and a fast Ge: Au (SBRC) detector was employed to monitor the temporal behavior of the laser pulses. A 700 mm monochromator provided with a 300 grooves/mm grating blazed at 3 μm and coupled to a Ge: Au or an InSb detector was used to spectrally resolve the emission output.

2.2 Performances of the Cr⁴⁺:Forsterite laser

The emission spectrum of the Cr⁴⁺:forsterite laser was analysed using a 1.15 m monochromator coupled to a Ge:Au detector. The monochromator was provided with a 1200 grooves/mm grating blazed at 500 nm which allowed wavelengths detection up to 1.4 μm . The forsterite laser was smoothly tunable from 1.16 μm to 1.33 μm . The peak of the tuning range was centered at 1.25 μm . A maximum laser energy of 13 mJ per pulse was obtained at 1.25 μm with 130 mJ pump energy into the crystal, corresponding to a 10% optical conversion efficiency. The bandwidth of the forsterite laser was typically 20 Å (FWHM). By adding the first Fabry-Perot, the bandwidth was reduced to 0.6 Å. With the second Fabry-Perot the upper limit of the linewidth was estimated to be 0.06 Å. This value was deduced from results on the optical pumping of a narrow absorption line of the HF molecule. However, the addition of these optics reduced the efficiency of the laser. Output energy decreased and pulse duration increased at wavelengths where the gain was low. Table 1 resumes the performance of our narrow-line and tunable Cr⁴⁺:forsterite laser for the pumping wavelengths of the 0-2 and 0-3 HF and DF transitions, respectively.

2.3 Results with HF

Due to its strong absorption coefficient, the HF(0-2) R(3) line was detected easily by absorption measurements (without the Fabry-Perot). At 10 Torr HF pressure, with the prisms and the two Fabry-Perot centered on this line, we observed a complete absorption of the pump laser beam by the gas cell and a simultaneous infrared fluorescence signal around 2.8 μm . The forsterite energy at 1.268 μm was 6 mJ in a 50-70 ns (FWHM) pulse duration and for a 2 mm beam diameter. Under these conditions, due to the high gain produced on the 2-1 transition, infrared superfluorescence was detected along the axis of the gas cell for HF pressures ranging from 1 to 100 Torr which was the maximum value used. A maximum superfluorescence energy of 250 μJ was then measured without any mirrors for a 30 Torr HF pressure. The emission spectrum observed is represented in Fig.2 with also the energy levels involved. Only P branch lines, P(3), P(4), P(5) and P(6) of the 2-1 transition around 2.8 μm were observed. The strongest was the P(5) which emanates from the pumped level ($v=2$, $j=4$). At pressures higher than 10 Torr, temporal analysis of the lines shows that the P(3), P(4) and P(5) lines are nearly coincident in time with the peak of the pump pulse. The P(6) line appears about 10 ns after. This behavior indicates that the rotational relaxation is very fast and thermalizes the populations according to the Boltzmann statistics.

2.4 Results with DF

For these experiments, the Cr⁴⁺:forsterite laser output was tuned to the P(3) line of the DF(0-3) transition at 1.193 μm . The 50 cm long gas cell was used. Due to the low absorption cross-section of this line, it was not possible to locate it on the monochromator by absorption measurements as previously for the HF absorption line. Lasing action was directly searched and obtained with 10 Torr of DF by scanning the spectral region around the calculated position of the P(3) line. The forsterite laser energy was 3 mJ in a 70 ns (FWHM) pulse duration. The experiments described thereafter were performed with a 95% output coupler that reflected in addition 80% of the pump beam into the DF gas cell. Under these conditions the DF laser emission was analysed for pressures ranging from 3 to 50 Torr. Between 3 and 6 Torr, we have observed a cascading laser emission on the 3-2 and 2-1 transitions. Between 3.64 μm and 3.85 μm several laser lines are emitted simultaneously. Fig.3 shows the spectrum obtained at a pressure of 5 Torr. The laser lines are the P(3), P(4), P(5) and P(6) of the 3-2 band and the P(3), P(4) and P(5) of the 2-1 band. At low pressure, the P(3) line of the 3-2 band emanating from the $j=2$ pumped level is always the most intense. Its build-up time with respect to the peak of the pump pulse is 20 ns. The other lines occur about 100 ns after. Fig.4 shows the temporal behavior of the pump and DF laser pulses at 5 Torr. It is clear that there is a transient nonequilibrium between the rotational levels. The energy emitted by the DF laser lines was about 10 μJ . When the pressure increases, the laser emission on the 2-1 band disappears and the relative intensities of the P lines of the 3-2 band are modified according to the Boltzmann distribution. P(4) and P(5) lines tend to dominate. DF lasing action has been observed up to 50 Torr but the laser intensity was about ten times lower than at 5 Torr pressure.

3. DF MODELLING

A computer modelling which includes the thermochemical, spectroscopic and kinetics properties of the DF molecule was constructed for simulating the optical pumping of the 0-3 transition. This model calculates for each P rotational transition ($j=1$ to 15) of the 3-2 and 2-1 bands, the gain and the laser intensity as a function of the DF pressure, the temperature in the gas cell and the pump intensity. It includes the V-T relaxation and V-V exchange ($\Delta v = \pm 1$) processes and line broadening parameters based on values given in the literature^{4,5}. The first seven vibrational levels are considered. In order to limit the number of differential equations and the computation time we assumed that the rotational populations are distributed following the Boltzmann law. The spatial dependence of the absorption process is also neglected. This is justified since the laser intensity does not change appreciably over the length of the cell due to the low absorption.

Fig.5 shows the evolution of the calculated DF laser energy output as a function of the pressure for operating conditions similar to those of the experiment. The DF laser energy is maximal around 4-8 Torr and falls down rapidly with the increase of the pressure which reduces the gain on the rotational lines by collisional effect. For a 2 mm pump beam diameter, the theoretical maximum energy is about 15 μ J close to the experimental value of 10 μ J.

The model predicts that at pressures where the gain is maximum (4 to 8 Torr), lasing action occurs in cascade on the 3-2 and 2-1 bands and that at higher pressures laser effect only occurs on the 3-2 band. These theoretical results are in good agreement with the experimental observations. However, our modelling is not able to describe correctly the temporal evolution of the individual laser lines because it does not take into account the rotational relaxation processes. Fig.6 shows the evolution of the predicted DF laser energy as a function of the pressure for a higher theoretical pump intensity. For 10mJ pump energy in a 10 ns pulse duration, the calculated DF laser energy is about 160 μ J near 3.8 μ m at 5 Torr. The theoretical efficiency is 1.6% which corresponds taking into account the 5.8% absorption at 5 Torr to a conversion efficiency around 27%.

4. CONCLUSIONS

We have developed a narrow-line and tunable Cr^{4+} :forsterite laser to pump the discrete lines of the HF and DF overtone transitions. We then have studied experimentally the HF and DF optical pumping. We have demonstrated cascading laser emission on the 3-2 and 2-1 bands of DF at pressures ranging from 3 to 6 Torr. Seven laser lines have been generated between 3.64 μ m and 3.85 μ m with an output energy of 10 μ J. The experimental DF laser results have been reasonably well reproduced by the computer simulations. An other issue is that rotational and vibrational relaxation processes play an important role in the laser performance.

5. ACKNOWLEDGMENTS

This work was supported by " Direction des Recherches, Etudes et Techniques ", Paris.

6. REFERENCES

1. H. Miller and G. Hager, " Experiments on Gas-Phase Optically-Pumped Infrared Lasers", *SPIE Proceeding*, Vol. 2502, pp. 475-482, 1994.
2. H. C. Miller, D. T. Radzykewycz, Jr and G. D. Hager, " Gas phase optically pumped infrared lasers ", *SPIE Proceeding*, Vol. 1871, pp. 591-596, 1993. " An optically pumped Mid-Infrared HBr laser ", *IEEE J. of Quant. Electron.*, Vol. 30, No. 10, pp. 2395-2400, 1994.
3. S. J. Davis, W. J. Kessler and K. W. Holtzclaw, " Laser-pumped gas phase mid-IR lasers ", *SPIE Proceeding*, Vol. 2502, pp. 469-474, 1994.
4. R. W. F. Gross and J. F. Bott, *Handbook of chemical lasers*, John Wiley and Sons, New York, 1976.
5. S. R. Leone, " Rate coefficients for vibrational energy transfer involving the hydrogen halides ", *J. Phys. Chem. Ref. Data*, Vol. 11, No. 3, 1982.

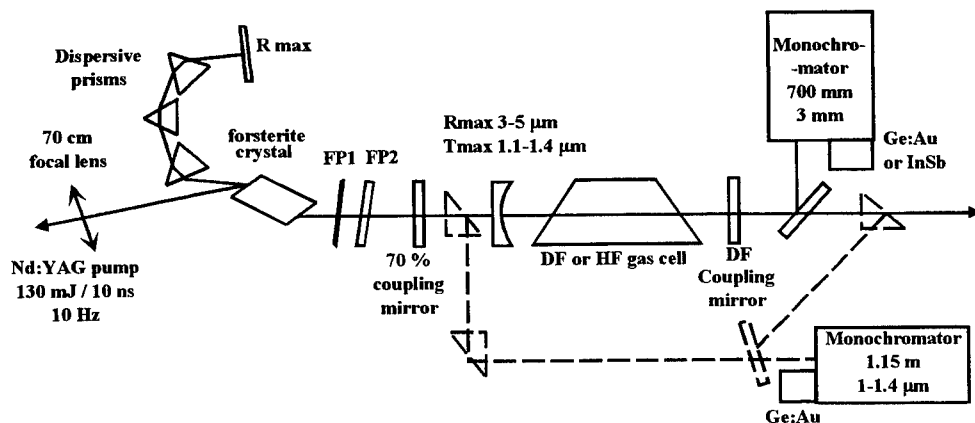


Fig.1: Overall experimental arrangement

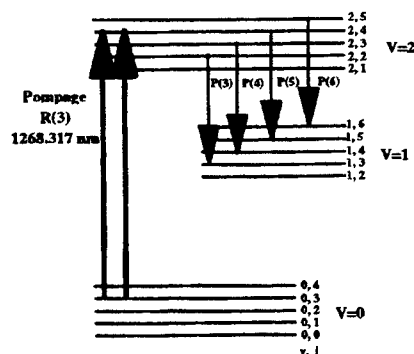
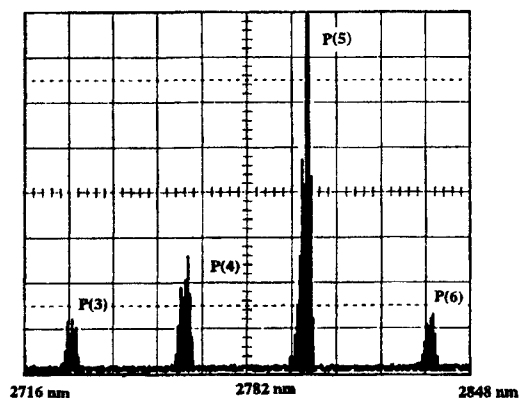


Fig.2: Spectrum of the infrared superfluorescence of HF(2-1) at 30 Torr pressure in the 15 cm gas cell. Involved energy levels.

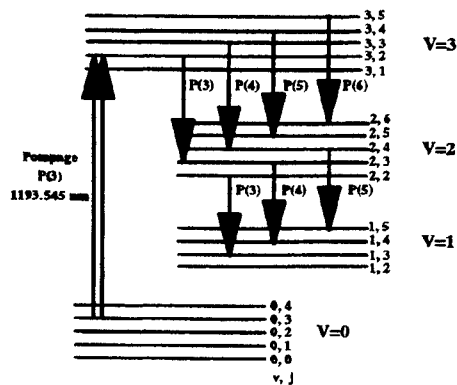
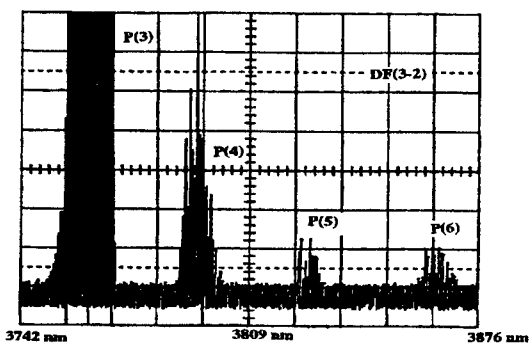
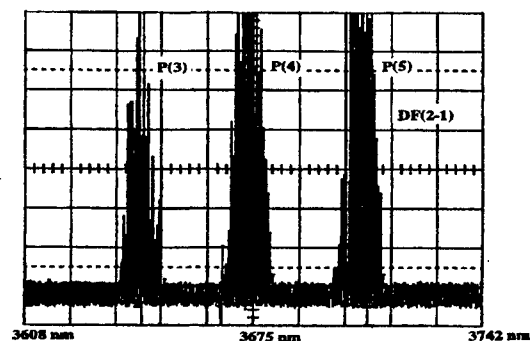


Fig.3: Spectrum of the DF(3-2) and DF(2-1) laser emission at 5 Torr pressure in the 50 cm gas cell. Involved energy levels.

Energy:	
1.268 μm R(3) line of HF(0-2)	6 mJ
1.193 μm P(3) line of DF(0-3)	3 mJ
Beam diameter	
2 mm	
Pulse duration (FWHM)	
50-70 ns	
Linewidth (FWHM)	
0.06 \AA	

Table 1: Performances of the forsterite laser at the HF and DF pumping wavelengths, with the prisms and the Fabry-Perot étalons.

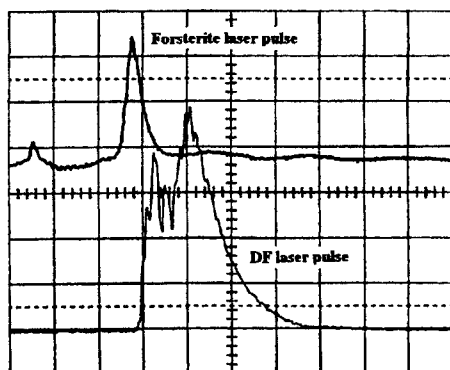


Fig.4: Delay between the forsterite pump pulse and the DF laser one.
P = 5 Torr, 100 ns/div.

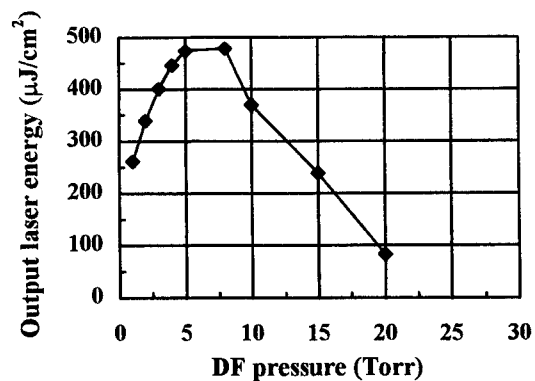


Fig.5: Theoretical evolution of the DF laser energy density as a function of DF pressure for conditions similar to the experimental ones.

Pump energy = 3 mJ - 70 ns - $\phi = 2$ mm
R1 = 99% R2 = 95% L = 50 cm

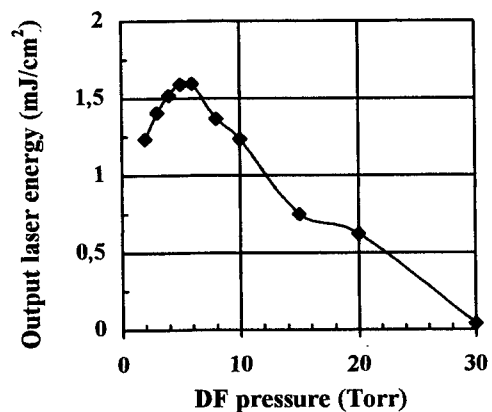


Fig.6: Theoretical evolution of the DF laser energy density as a function of DF pressure.

Pump energy: 10 MW/cm² en 10 ns
R1=99% R2=80% L=50 cm

Performance and spectral characteristics of sliding-discharge excited UV-IR laser

P.A. Atanasov, Z.Y. Peshev, G.I. Furlinski and K.A. Grozdanov

Institute of Electronics, Bulgarian Academy of Sciences,
72 Tsarigradsko Shose, Sofia 1784, Bulgaria

ABSTRACT

A sliding-discharge excited SF_6 :propane-butane: N_2 laser emitting simultaneously in the UV and IR region is investigated experimentally. The shapes of the voltage, current and laser (UV and IR) pulses are obtained and shown in their sequence. The IR laser spectrum consisting of more than 20 separated lines is registered and their intensity redistribution is found out when the N_2 pressure increased.

Keywords: sliding discharge; gas laser; chemical laser; nitrogen laser; UV and IR emission.

1. INTRODUCTION

The HF lasers, emitting in the $2.5\div 3.5\ \mu\text{m}$ spectral range, are promising sources for such applications as an ecological monitoring, delicate surgery, spectroscopy, investigation of semiconductor structures, etc.¹⁻³ The prevalent ecologically important substances and compounds have absorption spectra lying in the UV and IR spectral regions. So, it is of great practical interest to develop compact, high power and low divergence pulsed lasers providing simultaneous emission in the UV and IR range.

Discharge sliding along the surface of a dielectric has been previously used as a preioniser⁴, plasma electrode⁵ and for direct laser pumping.⁶⁻⁸ The sliding-discharge excited lasers possess such advantages as low divergence, uniformity and possibility to work at high repetition rates.⁶ Recently, a work is reported⁸ in that simultaneous UV and IR emission is achieved in sliding-discharge excited laser using SF_6 :propane-butane: N_2 mixture.

In this work we report on the study of the energy, spectral, and temporal characteristics of the UV-IR laser.

2. EXPERIMENTAL LAYOUT

In order to enhance the UV- part of laser output, as well as to minimise the formation of arcs a steep discharge-leading-edge is required. With regard to this, a charge-transfer electric circuit is used in our experiments. Its scheme is

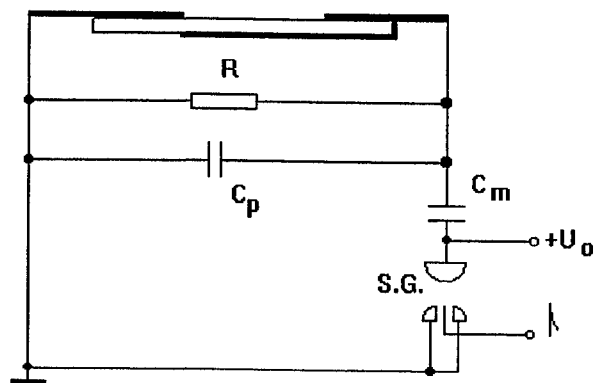


Figure 1. Cross section of the laser channel with the electrical excitation circuit.

shown in Fig. 1. The head of the UV-IR laser is vacuum tight Plexiglas chamber containing the 1.5 mm thick epoxy-fiberglass circuit board (dielectric constant $\epsilon=5$) with copper electrodes 2.6 cm apart. The values of the main capacitor C_m and the peak one C_p are 18 nF and 6 nF, respectively. The maximum charging voltage for free of arcs discharge is 25 kV.

The laser active area is $(2.6\times 26)\ \text{cm}^2$. The chamber has two CaF_2 windows mounted at Brewster angle for the horizontal polarisation. The non selective and non optimised optical cavity is formed by a flat gold-coated total reflector and BaF_2 flat output coupler. The active laser medium consists of SF_6 :propane-butane: N_2 (71%:5%:24%) mixture flowing continuously through the laser chamber.

The output energy measurements are performed using PRJ-D (GenTec) energy-meter equipped with ED-200 pyroelectric probe. The temporal parameters are monitored by a Tektronix-406 storage oscilloscope and a 2 ns resolution fast photodiodes (p-i-n and avalanche "Radec" for UV and IR, respectively). The spectral characteristics are followed by SPM-2 monochromator (Carl Zeiss Jena) with an LiF₂ 82° prism.

3. RESULTS AND DISCUSSION

The experimental results for the dependence of the UV and IR output energies on the N₂ and propane-butane pressure are shown in Fig.2 (a) and (b), respectively. The maximum output energy achieved for the UV radiation is 1.1 mJ. The addition of nitrogen to the SF₆:propane-butane mixture decreases the IR pulse energy from 80 mJ without N₂ to less than 20 mJ at optimum for the UV generation conditions. This behaviour is logical, since the optimum average electron energy for the HF laser is about 3.1 eV (the dissociation energy for the SF₆ molecule)⁹ and the excitation energy of the C³Π_u state of the N₂ molecule is about 11 eV. This means that the optimal discharge conditions for the N₂ generations are different from those of the HF generation. The UV output energy increases slightly when small amount of propane-butane is added to the N₂:SF₆ mixture. One possible explanation of this effect can be the improved discharge uniformity.

The voltage and current pulse shapes, as well as the temporal shapes of both N₂ and HF laser pulses are presented in Fig. 3.

The voltage shape has a typical pulsing form with three fading main peaks and rise time of 30 ns. The first peak duration is 58 ns (FWHM) and the entire pulse duration is about 100 ns at the 0.1 of maximum level. The current pulse appears after about 30 ns, compared to the voltage one.

The N₂ laser pulse appears first at the current leading edge and is 12 ns long (FWHM), while the HF one arises with about 40 ns delay and is 35 ns long (FWHM) (100 ns at the 0.1 level of the maximum). It corresponds to the maximum pulsed power of about 2 MW for the pure HF laser operation (without N₂).

The HF pulse duration is not affected considerably when discharge or pressure conditions are varied. The variation of N₂ pressure, for example, from 0 to 30 mbar causes a decrease of HF pulse width of only about 5 ns, while the HF output energy drops drastically (see Fig.2 a). However the HF-pulse shape evolves significantly, for the same N₂ pressure variation. The reasons of the mentioned HF-shape redistribution are not clarified yet.

Considerable changes in HF emission spectrum are observed as a result of the HF pulse shape redistribution discussed above. Figure 4 presents the spectra of HF laser with 20 mbar N₂ in the chamber (a) and without N₂ (b). More than 20 separate spectral lines are registered in the 2.6-3.1 μm spectral range. One can see that the addition of the N₂ causes also a spectral redistribution. For example, only amount of 5 mbar N₂ causes significant decrease of the 2.64 μm-line intensity. This line disappears when the N₂ pressure reaches 20 mbar (i.e., 2.4%). As a rule, the intensity of all lines decreases when the N₂-pressure raises, but the factor of this decreasing is different. Some of the lines, such as 2.9529 μm and 2.9542 μm, as well as 3.0628 μm and 3.0644 μm are very close one to another and the

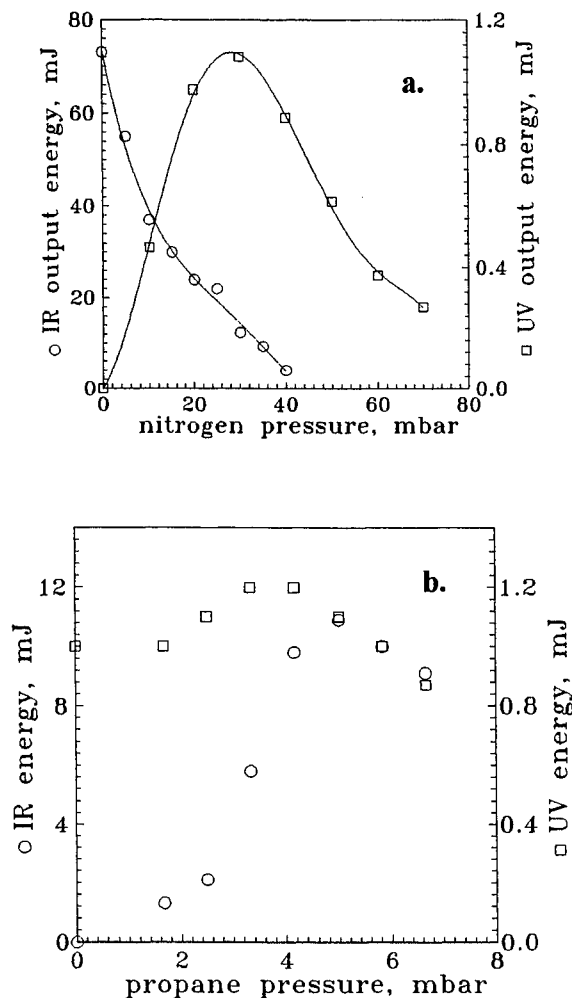


Figure 2. Dependence of the UV and IR output energy on the N₂ (a) and propane-butane (b) pressure.

monochromator's spectral resolution is not enough to separate them. So, their common intensity is given in Fig. 4.

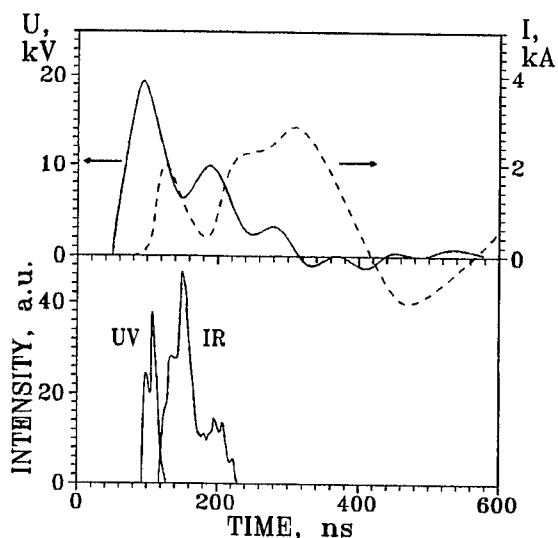


Figure 3. Waveforms of voltage, current and laser pulses.

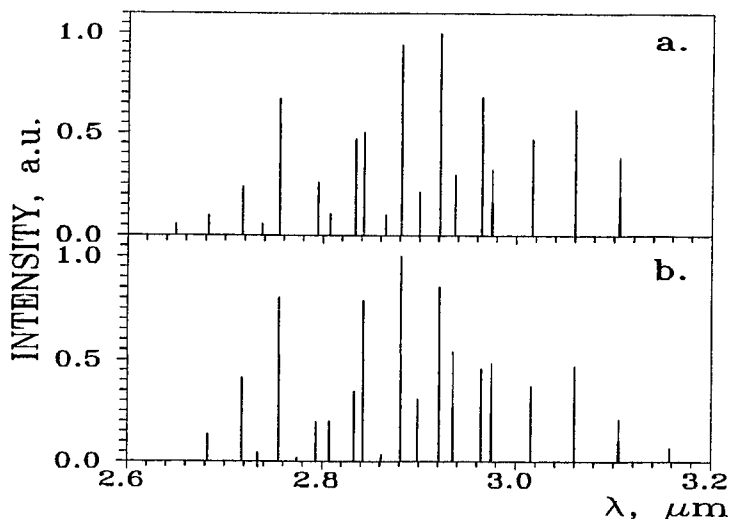


Figure 4. IR laser spectra.
a. - without N_2 ; b. - with 20 mbar N_2 .

A feature of the UV-IR laser described is also the fact that the time duration of the separate lines is only slightly shorter compared to the duration of the entire pulse i.e., during the HF pulse practically all lines oscillate. More detailed investigation of the emission spectrum of the UV-IR laser will be made in next experiments.

4. CONCLUSIONS

A sliding-discharge excited SF_6 :propane-butane: N_2 laser emitting simultaneously in the UV and IR is investigated experimentally.

The shapes of the voltage, current, and laser (UV and IR) pulses are obtained and shown in their sequence. It is found that the N_2 -pulse appears first at the current leading edge and the HF pulse appears with about 40 ns delay after N_2 one. The HF pulse width of 35 ns (FWHM) and maximum pulsed power of 2 MW are achieved. The time duration of the separate lines is only slightly shorter than this of the entire pulse, i.e., during the HF pulse practically all lines oscillate.

The laser spectrum consisting of more than 20 IR separated lines is registered and an intensity redistribution is found out when the N_2 pressure increased. The realisation of a tunable UV-IR emission will be an object of forthcoming work.

5. ACKNOWLEDGMENTS

This work is supported financially by the Bulgarian National Science Fund under contract F-434. The authors are very grateful to Dr. G.V. Kolarov for the helpful collaboration.

6. REFERENCES

1. M.L. Wolbarsht, "Laser Surgery: CO_2 or HF", *IEEE J. Quantum Electron.* Vol. QE-20, p. 1427, 1984.
2. A.A. Serafetinides, "Improved performance of TEA HF lasers suitable for delicate surgery", *private communication*, 1989.

3. C.V. Hatch, "A compact resistive electrode HF laser suitable for optical studies of semiconductors", *J. Phys. E: Sci. Instrum.* **Vol. 13**, p. 589, 1980.
4. G. Włodarczyk, "A photo-preionised atmospheric pressure HF laser" *IEEE J. Quantum Electron.* **Vol. E-14**, p. 768, 1978.
5. D.Yu.Zaroslov, G.P.Kuz'min and V.F.Tarasenko, "Sliding discharge in CO₂ and excimer lasers", *Radio Eng. Electr. Phys.* **Vol. 29**, p. 1, 1984.
6. P.P.Branzalov, B.O.Zikrin, N.V.Karlov, I.O.Kovalev, A.V.Korablev, G.P.Kuz'min and V.F.Perov, "UV nitrogen laser excited by sliding discharge" *Sov.Tech.Phys.Lett.*, **Vol. 14**, p. 419, 1988.
7. P.A.Atanasov and A.A.Serafetinides, "TEA gas lasers excited by a sliding discharge along the surface of a dielectric", *Opt. Commun.*, Vol.72, p. 356, 1989.
8. P.A.Atanasov and K.A.Grozdanov, "Simultaneous ultraviolet and infrared emission in a sliding-discharge excited laser", *IEEE J. Quantum Electron.*, **Vol. 32**, p. 1122, 1996.
9. B.K. Deka and P.E Dyer, "Mode control and performance studies of a pulsed unstable resonator HF/DF laser", *IEEE J. Quantum Electron.* **Vol. QE-14**, p. 661, 1978.

Computer modelling of the pulsed DF-HBr optical resonance transfer laser (ORTL)

M. A. Azarov, V. A. Iskhakov, V. I. Mashendzhinov, V. E. Revich and A. P. Vorobjev

Russian Scientific Centre "Applied Chemistry"

14, Dobrolubov Av., St. Petersburg, 197198, Russia

Tel: (812) 238-94-48, Fax: (812) 238-92-51, E-mail: rotinian@sovam.com

ABSTRACT

The aim of the present investigation is to forecast a principle opportunity of a pulsed DF to HBr laser frequency conversion and to evaluate an efficiency of that process. Computer modelling of the pulsed DF-HBr optical resonance transfer laser (DF-HBr ORTL) is performed and output characteristics of the system are predicted. The ORTL gas mixture contained DF at 10 Torr, HBr at 10 Torr and He at 100 Torr. It was considered as a multiline pumping. The pump radiation flux was varied from 0.02 to 2 J/cm². Depending on conditions the length of an ORTL gas media must be between 2 and 30 cm at using the longitudinal pump geometry. When DF-HBr gas mixture is pumped by a pulsed flash-initiated chemical DF laser, it is feasible to produce HBr lasing with a specific output energy over 100 mJ/cm³ and efficiency of 40 % relative to absorbed radiation energy. When used for pumping, a pulsed electrical discharge chemical DF laser can provide HBr lasing with specific energy up to 20 mJ/cm³ and efficiency up to 25 %. Therefore one will anticipate that a highly efficient laser system of the 4.2 - 5.2 μ m spectral region can be developed.

Key words: chemical laser, pulsed laser, optical pumped laser, HF, DF, HBr, ORTL, optical resonance pumping, computer modelling.

1. INTRODUCTION

Laser systems operating on the HF or DF molecules have shown the highest energetic performances among all of the chemical lasers.¹ At present a flash initiated chain chemical laser and an electrical discharge nonchain chemical laser are the most technologically advanced pulsed chemical laser devices. Existing flash initiated chain chemical lasers make available to produce single laser pulses with several kilojoules of energy.² Pulsed discharge chemical lasers produce up to several hundreds millijoules per pulse at the repetition rates up to several hundreds of pulses per second.³ At present developed closed gas cycle devices allow the discharge lasers to operate in such mode for a long period of duration (about 1 hour at repetition rate of 100 pulses per second³). However a spectral range of the considered lasers is bounded over two wave bands: $\lambda_{\text{HF}}=2.6 - 3.5 \mu\text{m}$ and $\lambda_{\text{DF}}=3.5 - 4.2 \mu\text{m}$ (up to 5 μm under particular conditions).^{2,3} It is possible to expand or shift a spectral range of the laser radiation to longer wavelengths by means of the optical resonance transfer laser method.⁴

Pulsed HF or DF ORTL were investigated both theoretically and experimentally.^{4,5} At optical resonance pumping a partial inversion can be achieved on some vibrational-rotational levels with higher rotational quantum numbers J than those of the pump. Therefore the lasing spectrum of these systems was red-shifted as compared with the pump spectrum. However the shift was relatively small. Significantly more extending laser spectrum can be produced in systems with a V-V energy transfer from absorbing to lasing molecules.

One of these systems is ORTL with DF molecules to be pumped and HBr molecules to lase (DF-HBr ORTL). The HBr lasing have been produced by a pulsed chemical laser.^{6,7} However these systems have relatively low performance, and the closed cycle gas devices are not developed for them yet. Therefore the DF-HBr ORTL with pumping by the pulsed chemical DF laser may be preferable. Moreover the DF-HBr ORTL can in principle operate in the 3.5 - 4.6 μm wavelength region due to simultaneous DF and HBr lasing.

A literature information on investigations of the pulsed DF-HBr ORTL is not available. Yet the DF-HBr ORTL pumped with a continuous wave (CW) DF chemical laser was described.⁸ Recently a pulsed mode DF ORTL has been obtained with a high conversion efficiency of a pumping energy (about 37%).⁵ Also it has been reported about the pulsed HBr lasing due to solid state laser pumping with overtone band transitions.⁹ Therefore one will anticipate that a pulsed DF-HBr ORTL can be developed. A high conversion efficiency may be expected due to nearly resonance coupling of vibrational levels of DF and HBr.

The present investigation was aimed to forecast a principle opportunity of a pulsed DF to HBr laser frequency conversion and evaluate an efficiency of that process. A theoretical simulation DF-HBr ORTL is reported for the first time, though similar theoretical studies were early carried out for the pulsed HF and HF-DF ORTL.^{4,10}

2. ORTL MODEL

The following processes were included in the computer model of the pulsed DF-HBr ORTL: resonance optical pumping; vibrational-vibrational, vibrational-translational, and rotational relaxation; and lasing. Gas mixture of the ORTL cavity was considered to consist of DF, HBr and some diluting gas such as He. In the modelling of vibrational relaxation kinetic all the vibrational molecular levels were taken into consideration. The rotational structure ranging at 30 sublevels was taken into account only for the first five vibrational levels. Optical transitions between these vibrational-rotational terms were considered at pumping (in DF molecules) and lasing (in DF and HBr molecules). Such description of the processes is analogous with one, which was used to model the HF dissociation at resonance optical pumping.¹¹ The rotational relaxation rate was set to be proportional to the deviation of the rotational sublevel population from one, which appropriate to a thermal rotational distribution. Such an approach to describe a rotational relaxation corresponds with the model "of strong collisions" used to simulate CW HF ORTL.¹²

In the optically thin layer approximation the mathematical model of ORTL is reduced to a system of ordinary differential equations for vibrational and rotational populations and radiation densities. The lasing is defined by nonstationary equations for average radiation density in the optical cavity.¹³

An important feature of the model is that the task has been divided into two independent parts. In the first part the modelling of DF pumping and lasing was performed taking into consideration the DF-HBr V-V energy exchange. In the second part the modelling of the HBr lasing taking place for a reason of the same V-V transfer was conducted. The advantage of such approach is to enable us to make an independent study of problems concerning absorption of the pump radiation and the HBr lasing, and to simplify the computer program.

Unfortunately the information available on elementary processes in the system considered is rather incomplete. Therefore we had to use some assumptions and analogies. In the modelling a considerable attention was focused on possibly complete use of all known experimental data on elementary processes. In the lack of suitable data the constants and the coefficients for HBr were assumed to be the same as for DF, and for DF as for HF.

The Einstein coefficients for DF were taken out from handbook¹, and for HBr were calculated on the basis of published data.^{14, 15} The spectral line profile was approximated by the Voigt function. The collision broadening data for DF and HBr were found in the literature sources^{1, 16, 17} and^{15, 18} respectively.

The resonance optical pumping allows a deposition of extremely high pump energy densities into vibrational mode of the absorbed molecule.^{5, 19} As a consequence, one may obtain a very strong excitation of the molecules. Yet little is known on the behaviour of highly excited molecules and a special attention must be given to this problem. We used the results of the experimental investigation²⁰ in which the channels of V-T and V-V relaxation processes in the HF molecule have been divided as well as the experimental data²¹ on relaxation of the high vibrational levels of DF. Accordingly a very abrupt dependence on the vibrational level number was assumed for the V-T relaxation rates in the ORTL model. The rate coefficients for DF and HBr were taken to be proportional to V^α , where α was varied between 2.1 and 3.6 for different vibrational numbers V . If we had used traditionally a harmonic oscillator approximation to treat the vibrational relaxation we would have over-estimated the ORTL calculated output by reason of $\alpha=1$. The rate coefficient for the intramode V-V energy exchange was represented by the equation that had been proposed in the theoretical paper¹¹. This formula has a power function dependence on V and an exponential dependence on the vibrational energy defect. The power of 3.8 was chosen to meet the requirements of the V-V energy exchange data of HF.²⁰ The exponential dependence parameter was determined from empirical correlation between a V-V exchange probability of hydrogen halides and energy defect.²²

The temperature dependencies and the absolute magnitudes of vibrational relaxation rate coefficients were set on the basis of the published data.^{1, 22} The rotational relaxation both DF and HBr was treated by an identical way, as it was done in the paper¹² using HF data.

3. RESULTS OF MODELLING

The absorption of pump radiation of the chemical DF laser by working gas mixture in the DF-HBr ORTL cavity was calculated under the following conditions. The ORTL gas mixture contained DF at 10 Torr, He at 100 Torr and HBr at the partial pressure p_{HBr} var-

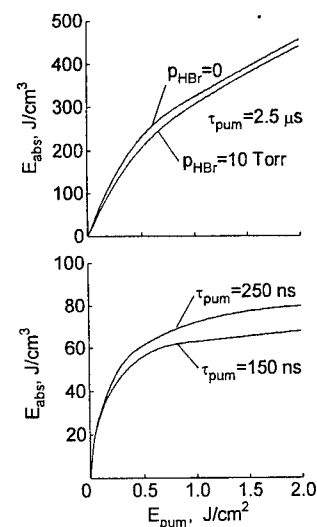


Fig. 1. The specific absorbed energy as a function of the pump energy density.

ied between 0 and 10 Torr. It has been considered a multiline pumping with the rectangular pulse of radiation. The pulse duration τ_{pump} had a series of values: 0.15, 0.25 and 2.5 μs . The first two are the characteristic of a discharge chemical laser, and the last magnitude is typical for a flash-initiated one. The pump radiation flux was varied between 0.02 and 2 J/cm^2 . The pump spectrum consisted of 9 lines with identical intensities. These were P (6), P (7) and P (8) transitions in the first three fundamental bands of DF.

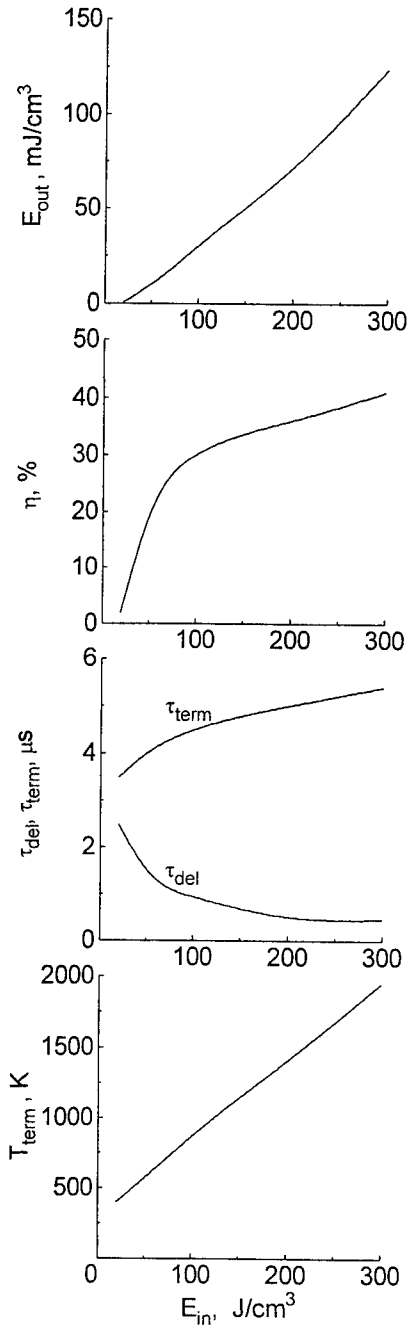


Fig. 2. Characteristics of ORTL as a function of the specific input energy:

E_{out} is the specific output energy; η is the efficiency; τ_{del} is the delay time of lasing; τ_{term} is the terminal time of lasing; T_{term} is the temperature at the lasing termination.

According to the simulation results a dependence of the radiation absorption on the HBr added quantity can be ignored at $p_{\text{HBr}} \leq 10$ Torr (Fig. 1). The specific absorbed energy can be as high as several tens or hundreds of millijoules per 1 cm^3 of the ORTL working gas media volume for the pumping by discharge ($\tau_{\text{pump}} \approx 0.25$ μs) or flash ($\tau_{\text{pump}} \approx 2.5$ μs) initiated chemical laser, respectively. The ratio $E_{\text{pump}}/E_{\text{abs}}$, where E_{pump} is the incident energy per 1 cm^2 , and E_{abs} is the absorbed energy per 1 cm^3 , allows to roughly evaluate the distance where the pump radiation is completely absorbed. The optical path sufficient for the radiation absorption at $E_{\text{pump}} = 0.2 - 2$ J/cm^2 was estimated to be between 2 and 4 cm at $\tau_{\text{pump}} \approx 2.5$ μs and between 10 and 30 cm at $\tau_{\text{pump}} \approx 0.25$ μs . These data indicate that a longitudinal pumping of the ORTL media can be carried out while the pump flux is directed under a small angle with the resonator optical axis.⁵

The calculation of DF-HBr ORTL operation was carried out at the input energy E_{in} up to 300 mJ/cm^3 (Fig. 2). In the absence of the DF lasing the input parameter E_{in} equals to the absorbed energy E_{abs} . The pump pulse duration ($\tau_{\text{pump}} \leq 2.5$ μs) has practically no influence on energetic performances of the HBr lasing, but affects significantly the HBr lasing pulse duration at a relatively low pumping energy ($E_{\text{abs}} < 100$ mJ/cm^3).

The HBr lasing appears at rather moderate contributions of the pumping energy: 20 - 50 mJ/cm^3 (Fig. 2). The input results from a low pump flux: $E_{\text{pump}} < 0.1$ J/cm^2 (Fig. 1). The figures show the results, which have been performed at the following parameters: $p_{\text{HBr}} = 10$ Torr, $\tau_{\text{pump}} = 2.5$ μs and $K_r = 10^{-3}$ cm^{-1} , where K_r is a coefficient of optical cavity losses. The DF-HBr ORTL had shown no critical dependence on the cavity losses because of a high gain of the laser media. The variation of K_r from 10^{-3} to 10^{-2} cm^{-1} causes a minor increase of the lasing threshold pumping and a small decrease of the output of the pump energy, which is well over the threshold. The threshold value of E_{in} is shifted from 20 to 30 mJ/cm^3 , yet at $E_{\text{in}} = 300$ mJ/cm^3 the output energy E_{out} is changed only by 3%.

At the energy contributions about 300 mJ/cm^3 the output specific energy is over 100 mJ/cm^3 and the radiation conversion efficiency, which is determined as $\eta = E_{\text{out}}/E_{\text{abs}}$, is 40% (Fig. 2). This energy deposition may be achieved at $\tau_{\text{pump}} \approx 2.5$ μs and $E_{\text{pump}} = 1$ J/cm^2 (Fig. 1). Pumping with such parameters may be easily real-

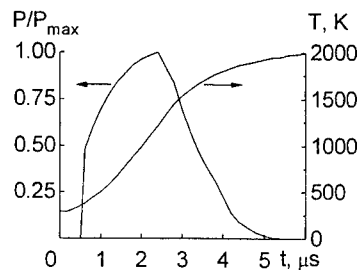


Fig. 3. Time histories of the output power P and the gas temperature T at $E_{\text{in}} = 300$ mJ/cm^3 .

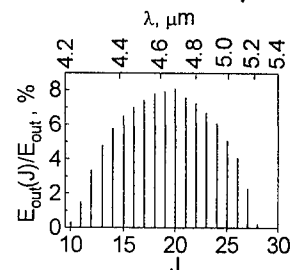


Fig. 4. The output spectrum at $E_{\text{in}} = 300$ mJ/cm^3 .

ised by using a flash-initiated chemical DF laser. At energy contributions obtained using a discharge chemical DF laser ($E_m \leq 80 \text{ mJ/cm}^3$) the specific energy output of 20 mJ/cm^3 and conversion efficiency of 25% may be achieved (Fig. 1, 2).

A typical shape of a laser pulse is shown on Fig. 3. The fast rise of the gas temperature promotes a suppression of lasing. The pulse delay τ_{del} and the laser terminal time τ_{term} from a start of the pump pulse are shown on Fig. 2. The HBr lasing begins after a pronounced delay (0.5-2.5 μs) with respect to the pump start and continues for several microseconds soon after the pumping of DF has terminated. In accordance to the calculations the DF lasing in DF ORTL begins with a considerably shorter delay and terminates within several tenths of microseconds after the pump pulse termination. A distinction in the time dependencies of HBr and DF lasing may be explained by a relatively slow rate of the intermolecular vibrational energy exchange. Yet a transfer of energy to HBr allows to use the DF vibrational energy more efficiently. The HBr ORTL operates even under conditions when the DF gain is less than the threshold value.

The HBr lasing is produced on fundamental 1-0 band transitions in the 4.2 - 5.2 μm spectral region (Fig. 4). The lased spectral lines are P(10) - P(28). At a high absorbed energy the most part of the output radiation falls on the lines with high rotational quantum number J. It is due to a fast rise of the gas temperature during the laser action (Fig. 3) and to a high temperature value at a moment of the lasing termination (Fig. 2).

The above energetic performances of the pulsed DF-HBr ORTL are not to be treated as the maximal characteristics until optimising calculations were conducted.

4. CONCLUSION

Computer modelling of the pulsed DF-HBr ORTL has been carried out. That simulation has forecast a principle opportunity of a conversion of pulsed DF to HBr laser frequency. Pumping of DF-HBr ORTL may be carried out using a longitudinal pump geometry. Pump radiation may be obtained by advanced and practical pulsed chemical lasers such as a flash initiated chain chemical laser and an electrical discharge nonchain chemical laser. Under those conditions it has been predicted a high efficiency and a high specific output in the 4.2 - 5.2 μm wavelength region. If DF-HBr ORTL had been developed it could be a preferable system for the mentioned above spectral region.

5. REFERENCE

1. *Himitscheskie lasery (Chemical lasers)*, Russia, Editors R. Gross and J. Bott, "World," Moscow, 1980.
2. M. A. Azarov, et al., *Proc. SPIE*, Vol. 2502, p. 382, 1994.
3. N. V. Baranov, V. A. Eller, V. I. Mashendzhinov, V. E. Revich, "Discharge chemical laser with lasant recirculating," 8-th Laser Optics Conference ("LO'95"), June 27 - July 1, 1995, St. Petersburg, Russia, *Technical Digest*, Vol. 1, pp.163-164, (*Proc. SPIE*, to be publ.).
4. S. Yamaguchi et al., *J. Appl. Phys.*, Vol.54, p.1675, 1983.
5. V. I. Mashendzhinov, V. E. Revich, V. V. Sudarikov, A. P. Vorobjev, "Pulsed HF (DF) ORTL," 8-th Laser Optics Conference ("LO'95"), June 27 - July 1, 1995, St. Petersburg, Russia, *Technical Digest*, Vol. 1, pp. 161-162, (*Proc. SPIE*, to be publ.).
6. K. Tayoda et al., 3rd International Symposium on Gas-Flow & Chemical Lasers, Sept. 8-12, 1980, Marseille, France, *Suppl. J. Phys.*, FASC11, 1980.
7. P. Arrosmith, et al., *Appl. Optics*, Vol. 22, p. 2716, 1983.
8. K. K. Hui et al., *Appl. Optics*, Vol. 19, p. 831, 1980.
9. H. Miller, G. Hager, *Proc. SPIE*, Vol. 2502, p. 475, 1994.
10. K. Kumamoto et al., *IEEE J. Quantum Electron.*, Vol. QE-20, p. 515, 1984.
11. U. Schmailzl et al., *J. Phys. D: Appl. Phys.*, Vol. 11, p. 111, 1978.
12. A. S. Bashkin et al., *Trudy FIAN (Proceedings PIAS)*, Russia, Vol. 194, p. 45, 1989.
13. M. O. Bulanin et al., *Optika i spektroskopija (Optics and spectroscopy)*, Russia, Vol. 48, p. 94, 1980.
14. R. N. Stocker, A. Goldman, *J. Quantum. Spectrosc. Radiant. Transfer*, Vol. 16, p. 375, 1967.
15. H. J. Babrov., *J. Chem. Phys.*, Vol. 40, p. 831, 1964.
16. P. A. Bonczik, *Phys. Rev. A*, Vol. 11, p. 1522, 1975.
17. P. A. Bonczik, *Phys. Rev. A*, Vol. 13, p. 251, 1976.
18. B. Seaidi et al., *Mol. Spectrosc.*, Vol. 112, p. 88, 1985.
19. M. Fürsich, K. L. Kompa, *J. Chem. Phys.*, Vol. 75, p. 763, 1981.
20. L. S. Dzelzkalns, F. Kaufman, *J. Chem. Phys.*, Vol. 79, p. 3363, 1983.
21. L. S. Dzelzkalns, F. Kaufman, *J. Chem. Phys.*, Vol. 81, p. 4975, 1984.
22. S. Ormonde, *Rev. Modern Phys.*, Vol. 47, p. 193, 1975.

Chemical laser emitting simultaneously from excited HF^* and DF^* molecules

S.D.Velikanov, A.S.Elutin, A.F.Zapolsky, D.V.Konkin,
S.M.Kulikov, V.N.Novikov, M.V.Synitsin, S.A.Sukharev.

Russian Federal Nuclear Center (VNIIEF), 607190, Sarov, Nizhni Novgorod Region, Russia
Fax: (831) 30 54565; Phone: (831) 30 56646, e-mail: velikan_2566@rfnc.nnov.su

ABSTRACT

Performance has been investigated of a broadband chemical laser utilizing chain and nonchain reactions and emitting simultaneously from excited HF^* and DF^* molecules. Simultaneous stimulated emission of radiation in the spectral ranges of 2.7-3.0 μm and 3.7-4.1 μm has been obtained. Theoretical dependencies are presented of laser energy characteristics on the ratio of initial H_2 and D_2 concentrations in a working mixture.

Keywords: spectrum, spectral energy distribution.

INTRODUCTION

It is known that the chemical lasers work successfully, when the structure of an actuating mixture enters H_2 or D_2 molecules. However, among the extensive literature, devoted the researches of HF and DF lasers, there are only two mentions of researches of chemical lasers emitting simultaneously from excited HF^* and DF^* molecules. In paper [1] this effect was observed by work of photoinitiated laser acting with SF_6 -HD and SF_6 -HD- D_2 mixtures. In paper [2] the data are presented on a spectral structure of laser radiation, indicative about simultaneous excitation of molecules HF and DF in the laser acting with SF_6 - H_2 - D_2 mixture.

However, the questions of such lasers energetics are not practically investigated. At the same time the lasers, having such wide spectrum of radiation - 2.5÷3.4 microns and 3.5÷4.4 microns, can find wide practical application. Therefore the researches of the characteristics of chemical lasers present doubtless interest.

The results of researches of the energy characteristics of pulsed chemical lasers, operating on the basis of chain and nonchain reaction in mixtures, containing simultaneously the H_2 and D_2 molecules, are performed in the present report.

The researches of the laser acting with nonchain chemical reaction were conducted using the described in [3] electric-discharge chemical laser (EDCL) and applying the system of discharge formation offered in [4]. Stored electric energy of the initiating system constituted $E_{\text{stored}} = 16 \text{ J}$. Actuating mixture was SF_6 - H_2 - D_2 . Molar correlation of sulfur hexafluoride with hydrogen isotope in all experiments was constant ($\text{SF}_6 : (\text{H}_2 + \text{D}_2) = 9 : 1$) at total pressure of a mixture $P_{\text{mix}} = 51.5 \text{ torr}$.

In experiments the flat-parallel resonator from mirrors with dielectric interference covers, put on substrates from fluorite was used. Factors of reflection of mirrors in 2.7-4.0 microns spectral range were $R_1=0.95$ and $R_2=0.48$ accordingly. Active volume of resonator amounted to 600 cm^3 . Energy of laser radiation for the pulse of 1.5 μs duration constituted 0.5-0.8 J.

1. EXPERIMENTS

Two series of experiments were conducted, the optical schemes of which are performed on fig.1. In the first series of experiments total energy of radiation ($\text{HF} + \text{DF}$) and energy of radiation in the range of 2.7-3.0 microns (HF) was measured. The extraction of energy of HF radiation was carried out with the help of filter, consisting of four quartz plates

with total thickness of 70 mm. Factor of transmittance of filter in 2.7-3.0 microns spectral range (HF) was equal to $T_{HF}=0.56$ and for 3.6-4.0 microns range it was $T_{DF}=5 \cdot 10^{-3}$. In experiments weakening HF radiation by water vapors in the measurement path was taken into account. The DF radiation was determined as a difference of total energy and HF radiation energy. In the second series of experiments radiation of laser with the help of a LiF prism was splitted into two beams of the radiation appropriate to spectral ranges of the radiation of HF and DF molecules (2.5-3.0 microns and 3.6-4.0 microns), which were directed onto separate calorimetric detectors. Thus total energy of radiation was supervised too.

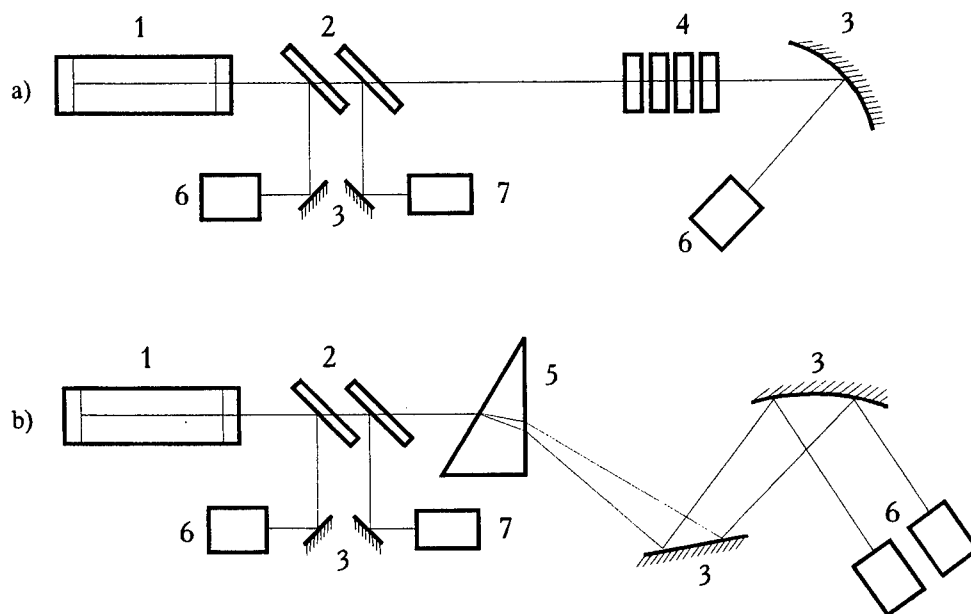


Fig. 1. Optical schemes of experiments:

1 - EDCL; 2 - CaF₂ plates; 3 - mirrors; 4 - quartz plates; 5 - LiF prism; 6 - calorimetric detectors; 7 - tuning He-Ne-lasers.

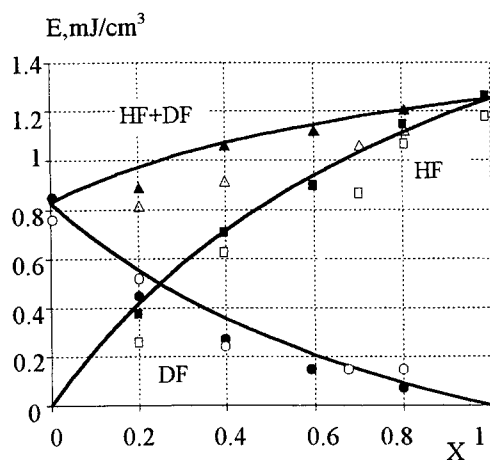


Fig. 2. Energy distribution on spectral ranges for different isotopic composition of hydrogen in actuating mixture at nonchain reactions for 1st (dark points) and 2nd (light points) experimental series. Solid curves - calculation.

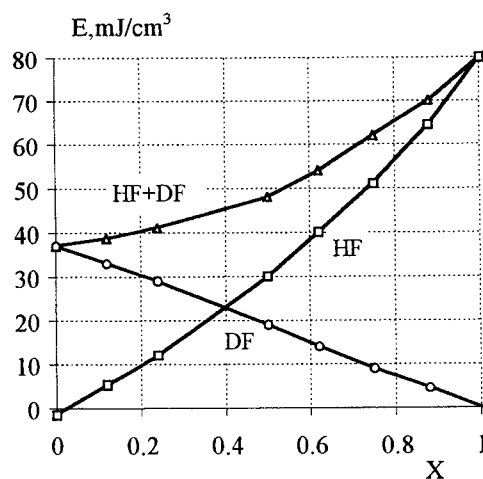


Fig. 3. Energy distribution on spectral ranges for different isotopic composition of hydrogen in actuating mixture at chain reactions. Solid curves - calculation.

The results of experiments are indicated on fig. 2 as a kind of dependence of energy of radiation on a share of xH_2 in $H_2 + D_2$ mixture ($x = [H_2]/([H_2] + [D_2])$).

From the above graphs follows, that the generation of radiation in both spectral ranges is observed, practically, at any correlations of D_2 and H_2 , besides, probably, significances of x close 0 and 1, where at small concentration of H_2 and D_2 should be displayed threshold effects. The energy of generation for pure HF about in 1.5 times is higher, than for pure DF.

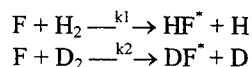
Researches of the laser on the basis of chain reaction of fluorine with hydrogen were carried out with flashlamp initiation. The mixture of F_2 : $(H_2 + D_2)$: O_2 : $He = 1$: 0.33 : 1.67 : 9.046 : 0.3 was used as an actuating one. Reaction was initiated by a xenon flashlamp during the discharge of capacitor battery with 7.5 kJ stored energy. The resonator of the laser was formed by a flat-flat BaF_2 plate and flat cooper mirror. The energy of generation for separate pulse of 1.5 microsec duration constituted the value 25...50 J. Experiments were carried out with use of optical scheme performed on fig. 1b.

The experimental results are indicated on fig. 3. The energy of radiation for pure HF is, about, two times higher, than that for pure DF. We shall note, that comparison of dependences, indicated on fig. 2 and fig. 3 demonstrates their difference for lasers based on chain and nonchain reactions.

2. DISCUSSION OF RESULT OF EXPERIMENTS

The analysis of received experimental dependences shows the processes, determining population inversion of energy levels of HF and DF molecules, influencing each other in conjointly running. This is determined by both a competition of reactions causing the formation of the excited HF and DF molecules, and a competition of deactivating processes of these molecules [5,6].

Apparently, the main processes determining formation of received dependences for the laser based on nonchain reaction are the following ones:



where $k_1/k_2 = \gamma = 1.8 \div 2$ [5,6]

The deactivating processes, apparently, are not of large significance because of small concentration of ground state HF and DF molecules.

Decision of the system of kinetic equations:

$$\begin{aligned} \partial[HF^*]/\partial t &= k_1 [H_2] [F], \\ \partial[DF^*]/\partial t &= k_2 [D_2] [F], \\ \partial F/\partial t &= - (k_1 [H_2] + k_2 [D_2]) [F] \end{aligned}$$

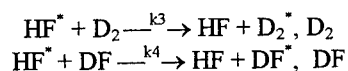
carried out on the assumptions of instantaneous ejection of fluorine atoms and constant H_2 and D_2 concentrations, which meet the conditions of experiment, results in following simple dependences:

$$\begin{aligned} E_{HF}(x) &= E_{HF}^0 \gamma x / [1 + (\gamma - 1)x] \\ E_{DF}(x) &= E_{DF}^0 (1-x) / [1 + (\gamma - 1)x] \\ E(x) &= [E_{DF}^0 + (\gamma E_{HF}^0 - E_{DF}^0)x] / [1 + (\gamma - 1)x], \end{aligned}$$

where E_{HF} and E_{DF} - are energies of radiation in 2,6...3,1 microns and 3,5...4,0 microns spectral ranges, correspondingly, E_{HF}^0 and E_{DF}^0 - are energies of radiation for pure HF^* and DF^* , $E(x)$ - is energy of radiation of EDCL.

Obtained calculated dependencies are drawn on the fig. 2 for the case of $E_{HF}^0 = 1.25 \text{ mJ/cm}^3$, $E_{DF}^0 = 0.83 \text{ mJ/cm}^3$ and $\gamma = 2$. It is seen, that there is a good agreement with experimental data. For chain reaction the complete account of interaction of elementary processes of reactions, determining formation of excited HF^* and DF^* molecules is very

combined. Therefore in result of the analysis of experimental dependencies (see fig. 3), constants of reactions rates and deactivation processes [5, 6], we were limited by consideration only of two processes:



The backward influence of elementary processes of reaction, causing to formation of excited HF^* molecules on processes of formation of excited DF^* molecules, apparently, is small, as the dependence of radiated energy of laser based on DF is linear from x.

Proceeding from above performed one can made the simple assumptions. As a result of reactions the excited HF^* and DF^* are formed in amounts proportional to the concentrations of H_2 and D_2 , correspondingly. The interactions of chains of reaction is described by characteristic for chemical kinetic expression: $\exp(-A[\text{D}_2])$, where $A = (k_3 + \alpha k_4)t$, t - time of generation, $\alpha = [\text{DF}]/[\text{D}_2]$ - the relation of formed during generation DF to initial concentration of D_2 .

As a result it is possible to write down the obvious dependencies for energy of radiation in various spectral ranges:

$$\begin{aligned} E_{\text{HF}}(x) &= E_{\text{HF}}^0 \times \exp[-A N_0 (1-x)], \\ E_{\text{DF}}(x) &= E_{\text{DF}}^0 (1-x), \\ E(x) &= E_{\text{DF}}^0 (1-x) + E_{\text{HF}}^0 \times \exp[-A N_0 (1-x)], \end{aligned}$$

where N_0 - initial total concentration of H_2 and D_2 .

From experimental dependence of $E(x)$ the values $E_{\text{HF}}^0 = 82 \text{ mJ/cm}^3$ and $E_{\text{DF}}^0 = 38 \text{ mJ/cm}^3$, $AN_0 = 0.69$ were determined. Taking into account these received parameters the calculated significances are in good agreement with experimental ones (see fig. 3).

The obtained calculated and experimental results show an opportunity of creation of the laser based on mixtures, containing H_2 and D_2 with a beforehand given correlation of energy of generation in 2,7...3,0 microns and 3,6...4,0 microns spectral ranges.

REFERENCES

1. K. L. Kompa, G. C. Pimentel, "Hydrofluoric acid chemical laser", *J. Chem. Phys.*, 47, 857 (1967).
2. R. L. Rudko, Z. Drozdovich, S. Linhares, "Hi rap rate recirculating HF/DF laser", *Rev. Sci. Instr.*, 53, 452 (1982).
3. S. D. Velikanov, A. F. Zapol'sky, M. V. Sinitzyn, "Chemical electric-discharge HF laser with technical efficiency above 100%", *Izvestiia AN SSSR, ser. fizicheskaya (News of Scientific Academy of USSR, Physics Series)*, 52, 318 (1988).
4. A. I. Pavlovsky, V. S. Bosamykin, V. I. Karelin, V. S. Nikol'sky, "Electric-discharge laser with initiation in the active volume", *Kvantovaya elektronika (Quantum Electronics)*, 3, 601 (1976).
5. A. S. Bashkin, V. I. Igoshin, A. N. Oraevsky, V. A. Shcheglov, in *Khimicheskie lasery (Chemical lasers)*, ed. by Basov N.G., Nauka, Moscow, 1982.
6. Imanuel J., "Numerical simulation of chemical lasers" in *Khimicheskie lasery (Chemical lasers)*, ed. by Gross R., Bott N.G., Mir, Moscow, 1980.

Ways and conditions of achieving extreme energy characteristics
of pulsed chemical DF and HF lasers.

M.A.Azarov, B.S.Alexandrov, V.A.Drozhdov, G.A.Troshchchenko

Russian Scientific Centre " Applied Chemistry ", 14 Dobrolubov av., St.-Petersburg, 197198, Russia

ABSTRACT

Ways of achieving extreme energy characteristics of pulsed DF/HF lasers were determined as results of theoretical and experimental (at energy up to 5 kJ) investigations of generator and amplifier. The close output energies of DF and HF lasers and higher efficiency of the cascade circuit relative to an equivalent generator were obtained.

Keywords: pulsed HF/DF laser, master generator-amplifier, active medium, CO₂ impurity, spectrum, energy.

1. INTRODUCTION

Results of experimental and theoretical investigations of pulsed chemical DF/HF lasers with photoinitiation were partly presented before.¹⁻³ In this paper the results are added and generalised. The main purpose of our investigations was to study the ways and to define the conditions of achieving top energy characteristics. Special attention was paid to problems not resolved till now during the development of DF lasers generating radiation in the atmospheric transmission window:

- studying reasons of the fact that lower specific output energy from the active medium of DF in comparison with HF lasers is observed in experiment in spite of that during the chain reaction $D_2(H_2)+F_2$ the same energy of chemical interaction is spent on excitation of vibrational-rotational levels of DF and HF molecules;
- investigating the structure of energy losses in non-uniform chemically reacting active media in order to bring out the main types of spatial-temporal non-uniformity limiting growth of radiation density ;
- investigating a cascade circuits " master generator- amplifier" (MG-A) to determine conditions for the most effective work of the amplifier with energy characteristics exceeding those of the equivalent generator.

2. EXPERIMENTAL SETUP

The procedure and diagnostics of experiment were stated before.¹⁻³ In the experiments the modular design of chemical reactor and initiation system were used, which allowed to conduct the investigations of the pulsed chemical DF and HF lasers that worked as a generator or as an amplifier, with common length (L_a) on the active medium up to 8 m and volume (V) up to 100 l. MG and A had the same construction. The cylindrical geometry of the illuminated volume of the chemical reactor, and the application of a teflon reflector ensured high efficiency of using UV-light initiating chemical reactions in hydrofluoric mixtures. The resonator is formed by plane mirrors with refraction effective coefficient of $R_{1,2}=0.0036-0.98$ and circle aperture of 132 mm. CO₂ impurity was fed in the active medium and absorption cavity placing inside the resonator. As a result of optimisation of the mixture composition, of the initiation system parameters and resonator the following experimental condition was chosen:¹⁻²

- mixture composition - $F_2 : D_2 (H_2) : O_2 : He = 3 : 1 : 0.3 : 6.7$ up to pressure 0.11 MPa;
- capacitor energy ($CU^2/2$) of photoinitiation system per unit of the active medium $E_i = CU^2/2V = 105$ J/l.

3. RESULTS AND DISCUSSION

For theoretical study the nonequilibrium model of pulsed chemical laser was developed that takes into account the final velocity of rotational relaxation and enables to conduct the calculation of energy and spectral-temporal characteristics of the radiation. By calculated investigations it was shown, that for achieving the maximum specific output energy it is necessary to use a high quality resonator ensuring more than 100-fold excess (M) of the unsaturated gain (K_0) above threshold ($K_r = -\ln(R_1R_2)/2L_a$): calculated maximum was observed at $R_1=0.06$, $R_2=0.98$, $L_a=20$ m (Fig.1). Such high values of the excess parameter required for achieving maximum efficiencies, are peculiar only to pulsed chemical lasers generating on a large number of vibrational-rotational transitions which gains differ by a factor of more than 10^2 . It leads to the fact that for excitation of generation on transitions in high bands between levels with comparatively small populations inversion but with large energy store, a high quality resonator with the excess parameter $M>50$ is required. In experiment the maximum specific output energy was received at excess parameter $M=50$ ($L_a=5$ m).

The main distinction between DF and HF lasers lies in the fact that during the chain reactions $D_2 + F_2$ and $H_2 + F_2$ the equal energy of chemical interaction is spent on exciting different numbers (N) of vibrational-rotational levels of the DF and HF molecules ($N_{DF} > N_{HF}$). Therefore the gains on the transitions of the DF molecule are lower than those of HF molecule, and for excitation of DF laser generation a higher quality resonator is required. However, as a result of intracavity losses, the equality of maximum values of efficiency (ϵ) from the active media of the DF and HF lasers is not reached. The $\epsilon_{DF}/\epsilon_{HF}$ ratio achieved in the first experiments¹ at $M=50$ was only 0,7 (Fig.1). At $M>50$ ($L_a>5m$) in spite of the fact, that the energy characteristics of DF and HF lasers became more alike, further growth of a number of generating transitions, and occurrence of high bands up to 10-9 for DF and 7-6 for HF lasers in the laser spectra, considerable decrease of specific output energy was observed. The decrease of energy characteristics corresponded to high intracavity losses $\rho=0.07\text{ m}^{-1}$ (Fig.1), that cannot be explain by nonequilibrium model. Therefore the following stage of our work consisted in detailed theoretical and experimental investigations of the structure of intracavity losses.

The main reason of the discrepancy lies in the fact that this model does not consider the effects connected with the spatial-temporal non-uniformity of chain processes. The inclusion of non-uniformity required considerable complication of the calculation program, that in turn would result in excessive increasing the machine time. Therefore for the investigation of the power losses structure in non-uniformly reacting active medium a semiempirical model of chemical laser was developed. The model was based on the approximate analytical solution of differential equations for the power density. The beam propagation inside the resonator was simulated on the basis of the geometrical optic laws. The temporal dependence of the refraction coefficient of the active medium obtained in the experiment, was approximated by analytical function. The best coincidence of experimental and calculated dependences of the energy characteristics of the laser radiation on the resonator loss factor was observed when taking into account all real types of the spatial-temporal non-uniformity of chain processes caused by the non-uniform photoinitiation, and introducing into calculation the distributed losses caused by absorbing impurities in the resonator volume (Fig.1). For initiation system used in the experiment the types of spatial-temporal non-uniformity lay at $M>50$ in the following sequence according to the growth of their influence on laser energy: the own-temporal non-uniformity of the development of chain processes, longitudinal spatial and temporal non-uniformity, transverse non-uniformity of initiation.²

To determine to what degree the CO_2 impurity effectively absorbing radiation over the wavelength range of 4,2-4,3 μm influences the energy and spectral characteristics of the DF/HF lasers, the experimental investigations were conducted. It was shown, that the sensitivity ($S=\Delta E C_0 / \Delta [CO_2] E_0$, where E -laser energy, C_0 -mixture concentration) of energy characteristics of the DF laser to the CO_2 impurity within laser medium depends on the generation regime. At CO_2 concentration more than 0.1% and M less than 10 the generation over the wavelength range of 4.2-4.3 μm fails (Fig.2), and sensitivity is determined by relaxation processes. In this case the sensitivity is $100 < S_{DF} < 300$. At CO_2 concentration less than 0.1% and M more than 20 over the absorbing radiation wavelength range of 4.2-4.3 μm the DF laser generates up to 25% of total energy (Fig.2). In this case the sensitivity is determined basically by absorption processes, and S_{DF} reaches the value of 1000 (Fig.1). The increase of the CO_2 concentration from 0,01% (that corresponded to the standard experiment) up to 0,067% caused the 30% energy decrease (Fig.1), and the failure of generation on about 20 lines (Fig.2). At further increase of CO_2 concentration from 0.1% up to 0.6% the 5-fold decrease of energy generation and suppression of generation on about 50 spectral lines of DF laser's six high bands were observed. Using F_2 with CO_2 concentration of 0.01% allowed to reach the value of maximum specific output energy ratio $\epsilon_{HF}/\epsilon_{DF}$ more than 0,9. The sensitivity for HF laser³ is only 13. Such strong distinction is due to two reasons: high values of the relaxation rate constants of excited molecules DF^* by CO_2 molecules, and strong CO_2 absorption.

It is known that for obtaining extreme energy characteristics the use of cascade circuit "MG-A" is more preferable. Then the losses in the active medium caused by refraction and absorption of the radiation, can be considerably reduced. In our experiments at increasing active length of cascade circuit up to 8 m, the continuum growth of specific output energy was observed. The theoretical and experimental investigations showed that for the most effective work of the cascade circuit a stringent spatial-temporal synchronisation of processes in active media of MG and A is required. In our experiments the strongest change of the HF/DF laser energy characteristics is observed at change of MG spectrum, and the variations of delay in initiation between MG and A (Fig.3). At increase of input energy density by 10^3 the amplifier specific output energy only doubles. The conditions at which energy characteristics of the amplifier exceed the corresponding characteristics of the equivalent MG (of the same length), are determined as follows:

- the high bands must be present in the MG spectrum, which is achieved at $M>50$ ($L_a>4m$) (Fig.2,3);
- the value of the input energy density must provide high saturation of the active medium of the amplifier with the parameter $M>50$; in experiments at the active length of the amplifier of 4 m the output energy of HF laser was 2.8 kJ at the input energy density of 5 J/cm² (2.5 MW/cm²) (Fig.3);

- the initiation delay of the amplifier relative to the generator must be optimised; for example, the optimum delay in the experiment and calculation with the cascade circuit MG(2m)-A(4m) of the HF laser was 0,1 μ s (Fig.3).

4. CONCLUSIONS

Firstly, the ways and conditions of achieving the extreme energy characteristics of the pulsed chemical DF/HF lasers are determined. These conditions consist in following:

- use of the cascade circuit;
- removing CO₂ impurity from optical channel between master generator and amplifier in DF laser;
- use of the high quality resonator ensuring more than 50-fold excess of unsaturated gain above the threshold for the excitation of generation on transitions of high bands in master generator;
- the value of energy density at the amplifier inlet must provide high saturation of the active medium with the parameter $M > 50$;
- high uniformity of active medium and low losses on the absorbing molecules; for achieving the level of e_{DF}/e_{HF} more than 0.9 the content of CO₂ impurity in the active medium of DF laser must not exceed 0,01%;
- optimisation of the initiation delay of the amplifier relative to the generator is necessary.

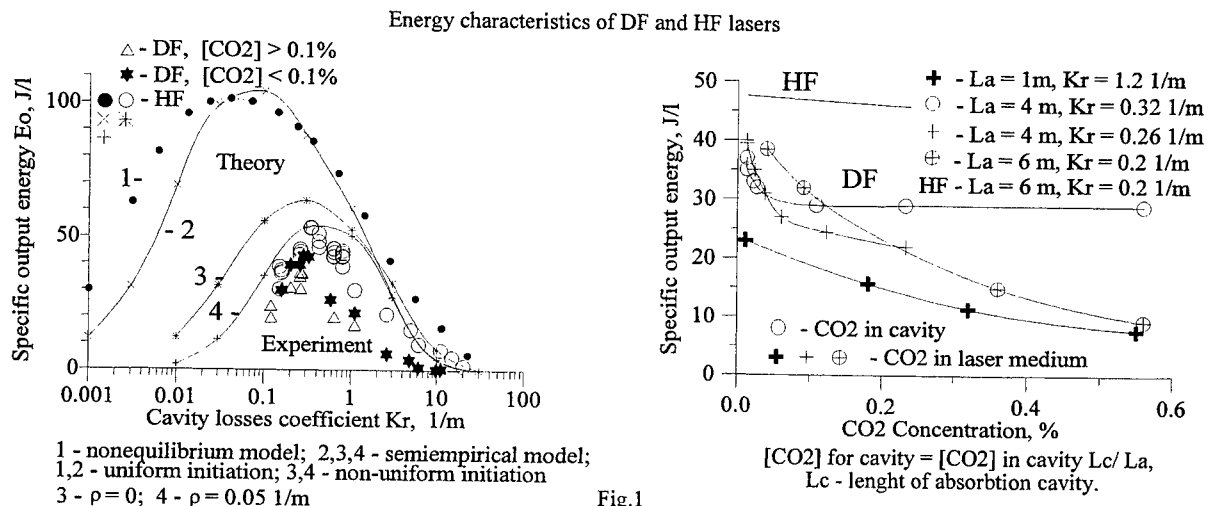
Secondly, the realization of these conditions has allowed to observe for the first time:

- the close values of the specific output energies with DF and HF molecules ($e_{DF}/e_{HF} > 0.9$ at $M > 50$);
- the fullest spectra of DF and HF lasers consisting of 10 and 7 vibrational bands over the wavelength range 2.7-3.5 and 3.6-5.0 μ m, respectively;
- higher efficiency of the cascade circuit relative to the equivalent master generator;

and to achieve the best energy characteristics of DF/HF lasers with flashlamp initiation: specific output energy - 45/50 J/l, technical efficiency - 35/40 %, total laser energy of cascade circuit MG(4 m)-A(4 m) - 4/5 kJ.

5. REFERENCES

1. M.A.Azarov, V.A.Drozov, Yu.A.Malyshev, "High-efficiency pulsed chemical HF and DF laser with flashlamp initiation", Fluid and Gas Mechanics, Chemistry and Lasers, *Proceedings of the 20-th Scientific Conference of the NPO GIPH*, Leningrad, Russia, 1991, pp 120-127.
2. M.A.Azarov, B.S.Alexandrov, V.A.Drozov, G.A.Troshchinenko, "Energy and spectral characteristics of pulsed chemical HF and DF lasers", *Proceedings of the 10-th International Symposium on Gas Flow & Chemical Lasers*, Friedrichshafen, Germany, 1994, SPIE, Vol. 2502, pp 382-387.
3. M.A.Azarov, V.A.Drozov, G.A.Troshchinenko, "Influence of CO₂ impurities within laser medium on energy and spectral characteristics of HF and DF lasers", *Proceedings of the 15-th International Conference on Coherent and Non-linear Optics & 8-th Laser Optics Conference*, St-Petersburg, Russia, 1995, (to be publish by SPIE).



on the DF and HF laser spectrum



Fig. 3



Influence of aerosols on gas-breakdowns, induced by high power pulsed infrared laser radiation

Patrick Bourgeois, Marion Althaus, Manfred Hugenschmidt

French-German Research Institute of Saint-Louis, ISL
P.O. Box 34, 68301 St.-Louis, France

1. ABSTRACT

Atmospheric aerosols can limit laser beam propagation and reduce energy transfer to work-pieces by creating shielding plasmas. The purpose of this paper is to get results for plasma ignition thresholds depending on incoming laser power density, kind and density of impurities in the interaction volume.

Keywords: Aerosols, gas breakdown, chemical laser, interferometry, streak recordings, plasma transmission.

2. INTRODUCTION

Aerosols exist all over the atmosphere. The source of aerosols can be of natural origin (fog and dust) or they can be created by industrial applications (exhaust). These fluid or solid based microparticle clouds can influence the spreading of the laser beam by interacting with the incident radiation and thus creating shielding plasmas. These so-called gas-breakdowns seriously affect the transmission capability by limiting the atmospheric propagation of the laser radiation. As a consequence, energy transfer to work-pieces, for example in the case of material processing, is also reduced.

3. EXPERIMENTAL SETUP

For initiation of gas-breakdowns we use a chemical laser at a wavelength of $2.7\text{ }\mu\text{m}$ working in single-shot-mode. This hydrogen-fluoride (HF) gas-laser with variable output energy (up to 12 Joules) produces power densities up to 74 GW/cm^2 by t_{FWHM} of 330 ns pulses.

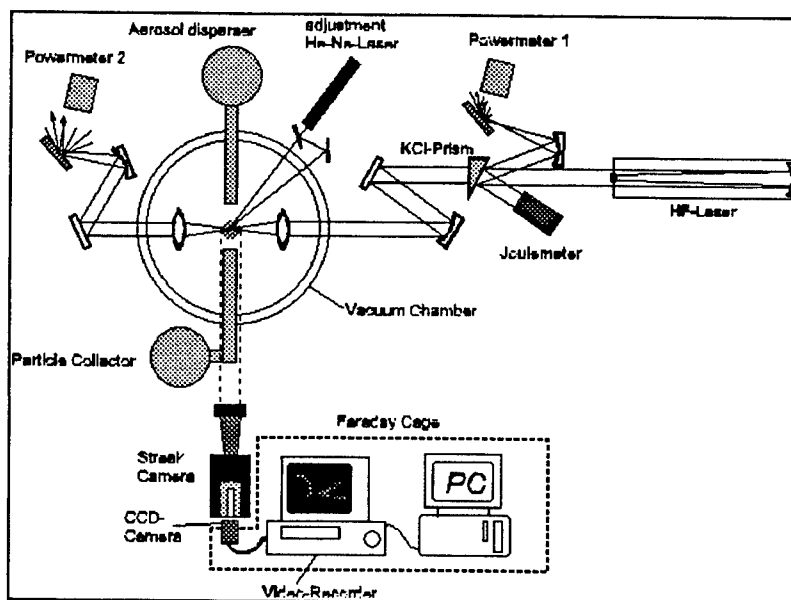


Fig. 1: Experimental Setup

Based on different high-speed diagnostic techniques (streak recordings, interferometer) we have not only the possibility to investigate the non-linear dynamic plasma formation in pure gases but also in gases seeded by the injection of micro-particles. Caused by the variation of the power density transferred into the polluted atmosphere, we are able to get results for air-breakdown thresholds. These are depending e.g. on the density of particles in air. Furthermore, we investigate ignition and expansion of these plasmas depending on the type of aerosol and also the propagation of the incident laser pulse through the plasma.

Due to the high laser power, threshold densities may be achieved already in front of the focal plane. It is therefore important to register physical parameters of the plasma as well as the geometrical conditions: location of ignition centres or shape of detonation-wave fronts.

4. RESULTS

In our studies we disperse four basic materials, TiO_2 as a ceramic, cigarette smoke, water and DEHS (sebacic acid di(2-ethylhexylester)), an oil-based fluid, into aerosols for imitating industrial and natural existing pollution. By using different generators for seeding particles and aerosols, designed and developed at ISL, we are able to import well-known impurities into the volume of interest. For determining the output of these particle generators we use different techniques: particle counter and Laser-Doppler-Anemometry (LDA). As results of these measurements we obtain size and volume density of the ejected particles.

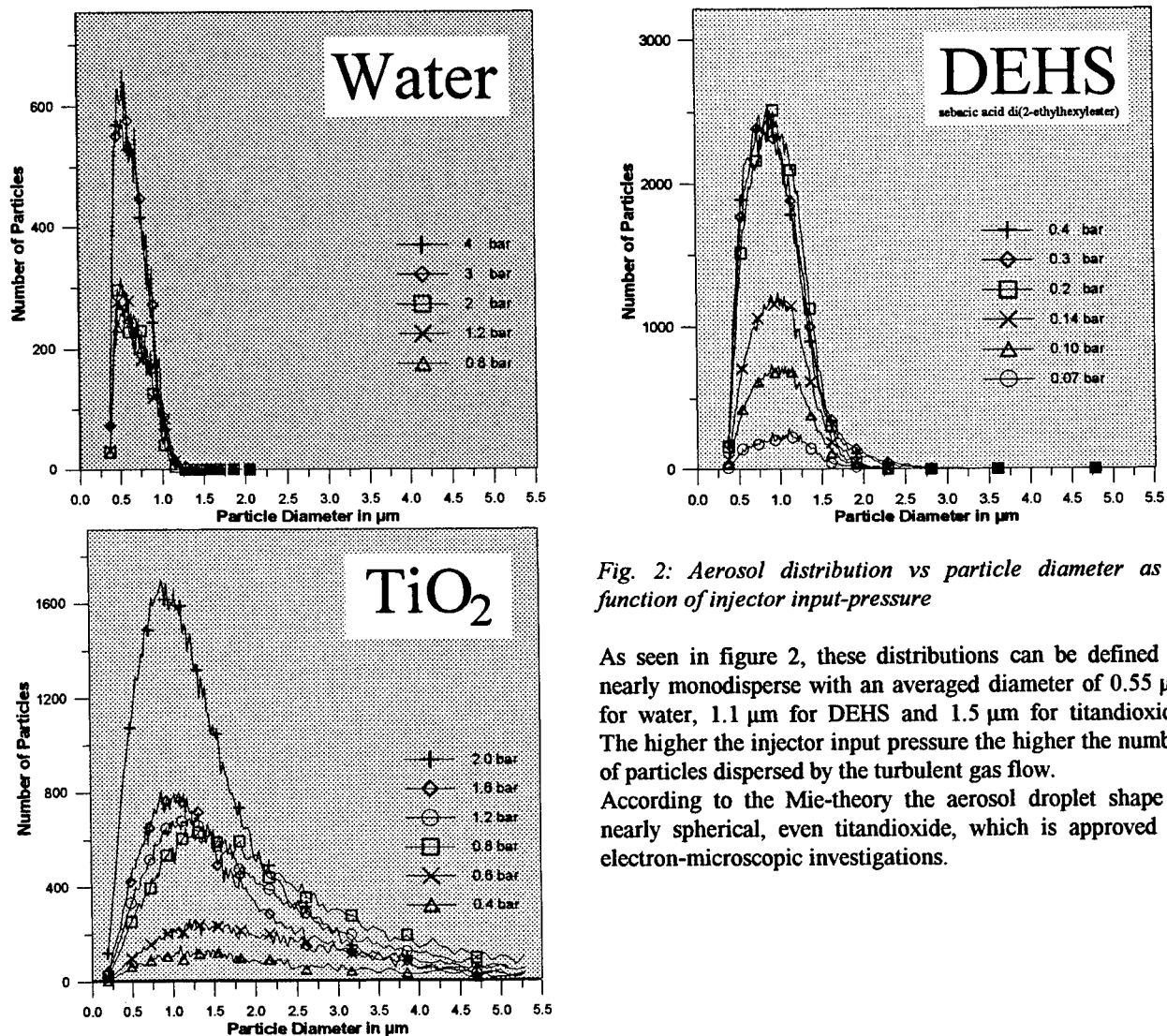


Fig. 2: Aerosol distribution vs particle diameter as a function of injector input-pressure

As seen in figure 2, these distributions can be defined as nearly monodisperse with an averaged diameter of $0.55 \mu\text{m}$ for water, $1.1 \mu\text{m}$ for DEHS and $1.5 \mu\text{m}$ for titandioxide. The higher the injector input pressure the higher the number of particles dispersed by the turbulent gas flow. According to the Mie-theory the aerosol droplet shape is nearly spherical, even titandioxide, which is approved by electron-microscopic investigations.

With one Wollaston-prism we are able to implement an easy adjustable Mach-Zehnder-Interferometer. For visualising the refraction-index variations inside the plasma spark we use a frequency-doubled Nd:Ylf-laser at $\lambda=523 \text{ nm}$ with a t_{FWHM} of 10 ns orthogonal to the plasma creating HF-laser beam and orthogonal to the direction of streak recordings. Figure 3 shows typical results of sparks in water haze at early plasma life times.

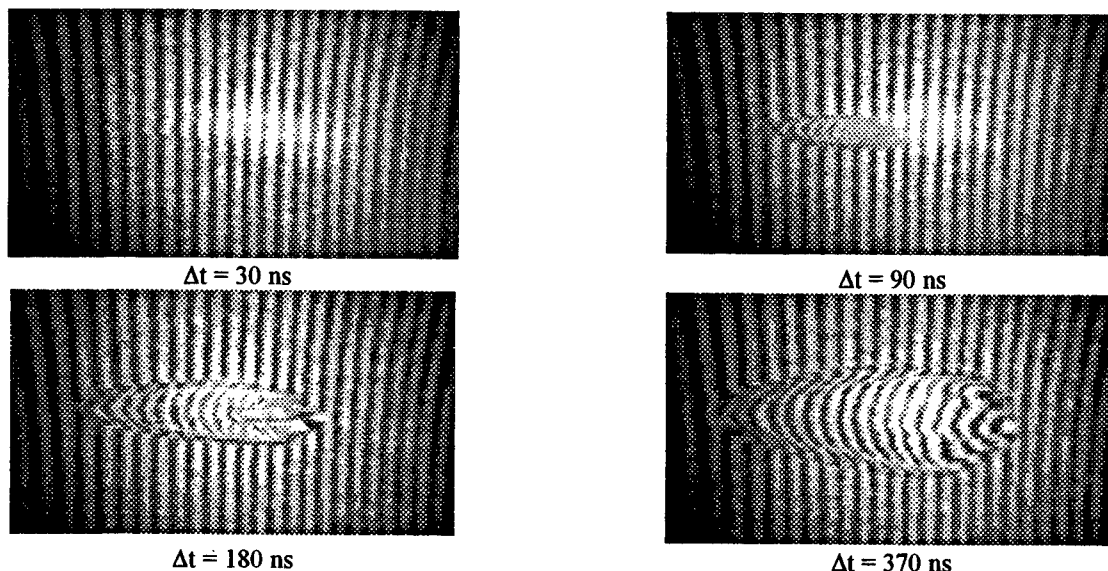


Fig.3: Water, injector input-pressure: 1 bar, incident laser intensity 23,5 GW/cm²
 ─────────── 2 mm

The high dense detonation front expands as a spherical wave with different velocities axial and radial to the plasma generating HF-laser beam. The origin of plasma ignition could be several separated particles, leading to an asymmetrical detonation shape. The optical thickness, shape and expansion velocities are strongly material dependent.

By using a Beckman-Whitley streak camera with a beryllium mirror, rotating by compressed air flow, we observe the plume of the plasma spark directly time resolved. Observing the streak image plane with a CCD-camera we store the results by using vidoe-tapes, which can be transferred to PC by a frame grabber card. This technique enables us to show several detonation fronts even at early plasma life times.

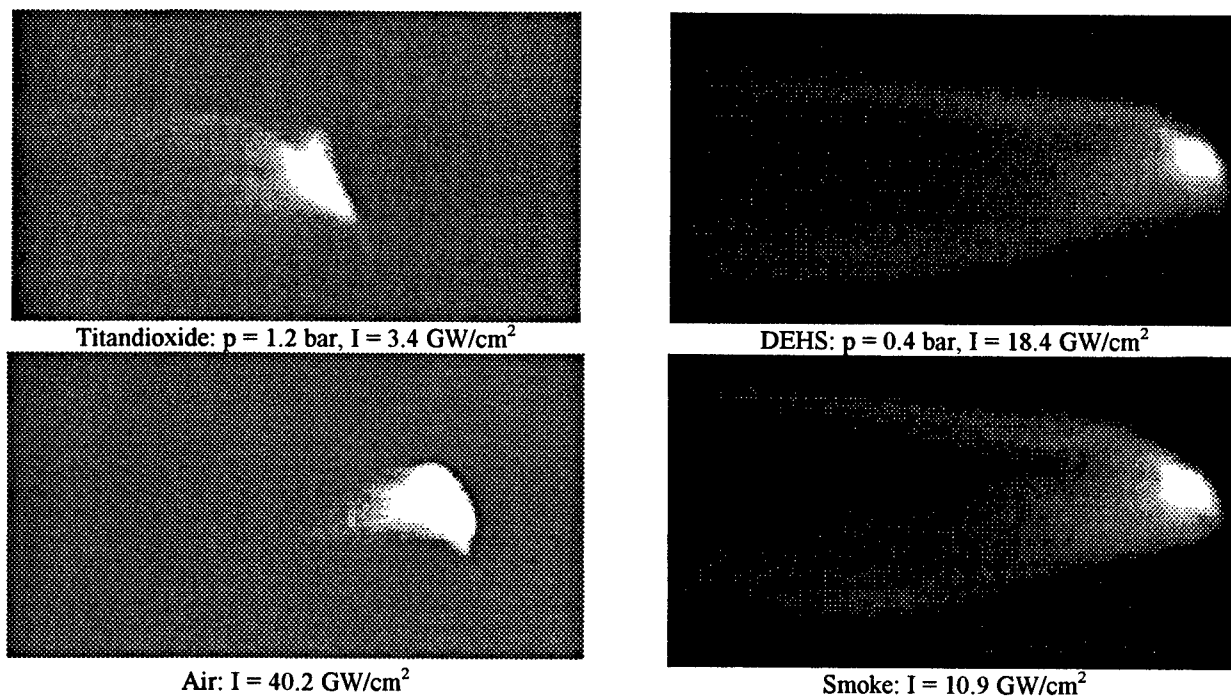


Fig. 4: Streak recordings of different seeding materials at nearly the same incident laser intensity (laser beam propagates from the top, time scale from the right to the left side)
 ─────────── 1 μs ─────────── 1 cm

The aerosol is vaporised instantaneously by the incident laser pulse. The detonation fronts of the exploding particles propagate with up to 50 km/s along the laser beam, and as a retonation front with up to 120 km/s towards it.

By the aid of transient recordings we are able to determine some special plasma effects as the drastically decrease of the laser pulse, which is transmitted through the plasma plume, the plasma shielding by the fast growing of the absorbing detonation wave fronts and the time development of plasma luminosity depending of the incoming energy. Hereby, we detect an immediate dependence of these plasma effects on the material and density of the injected aerosol and laser intensity.

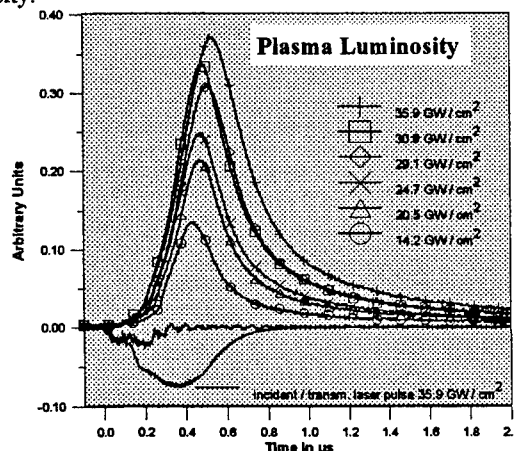


Fig. 5: (Titandioxide, injection pressure 1.2 bar), time resolved plasma luminosity compared at different laser intensities, time reference for the highest luminosity are incident and transmitted laser pulses

The time delay between plasma spark ignition and the time dependent shape of the luminosity are strongly material dependent. The maximum of the luminosity is always reached at the end of the laser pulse. The ignition starts, when the transmitted pulse begins to break down. For titandioxide, the time delay of the plasma ignition ranges from 170 ns at 8.9 GW/cm² up to 280 ns at 3.6 GW/cm².

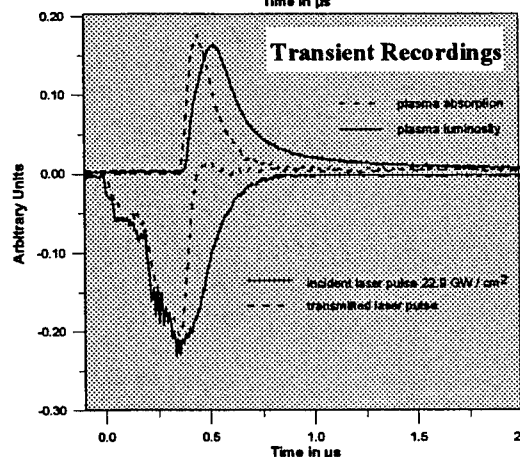


Fig. 6: (Water, water injector input-pressure 4 bar, laser intensity 11.7 GW/cm²), transient recordings

The incident laser beam heats up until the threshold intensity is reached, and vaporises the aerosol particles instantaneously (1 to 3 ns). The explosion generates high dense spherical detonation waves, which reduce the propagation of the laser radiation. The detonation front still heats up by absorbing the laser beam and a bright spark appears several tens ns (in this case 40 ns) later and the transmitted laser pulse is completely blocked.

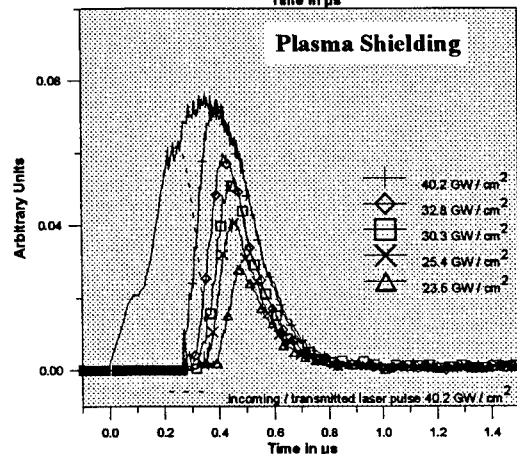


Fig. 7: (DEHS, injector input pressure 0.3 bar), plasma shielding as a function of laser intensity

The enveloping curve refers to the incident laser beam, the shielding effect is strongly dependent on the incoming intensity. It starts for lower intensities several nanoseconds later. The increasing front velocity is strongly material dependent. The higher the incident laser intensity and the number of particles inside the focal volume, the faster the aerosol plasma becomes opaque for the incoming laser radiation.

5. SUMMARY

As shown in table 1 the laser threshold intensity for initiation gas breakdowns is drastically reduced when polluting aerosols are inside the interaction volume. This lowering is strongly dependent on the particle material properties.

	max. front velocity [km/s]		plasma size [cm]	reached after [ns]	aerosol diameter [μm]	threshold intensity [GW / cm ²]
	return	deton				
TiO₂	55	30	1.3	560	1.5	< 3.4
DEHS	100	50	1.1	950	1.1	6.7
H₂O	110	30	0.8	690	0.55	7.1
Fume	40	10	1.1	890	< 0.1	3.8
Air	120	60	1.0	440	unfiltered	14

Table 1: Results

Natural or artificial genuine aerosols exist everywhere in the atmosphere. These impurities reduce the laser-induced air breakdown threshold eminently. The aerosol-initiated breakdown strongly limits the propagation of high-power laser pulses through the atmospheric gas medium. When the air breaks down due to an intense laser pulse, the generated high-pressure, high-density plasma fast absorbs the incident laser radiation. The plasma plume expands along the laser beam and towards it, fills the laser beam inside the interaction volume and subsequently blocks off the incident laser energy. This plasma shielding effect is of great disadvantage to all laser manufacturing processes. Even the smallest number of seeding particles reduces the energy transfer to the work-piece drastically.

In industrial laser applications both, the energy transfer mechanisms and the energy transmission conditions through the plasma have to be understood. Plasmas building up ahead of the work-piece can shield incident radiation and reduce treatment efficiency. A contribution to this problem can give a profound knowledge of the breakdown mechanisms in polluted gas atmospheres.

6. REFERENCES

1. R. L. Armstrong, *Laser induced droplet heating*, Optical effects associated with small particles, World Scientific, Singapore, p.203, 1988
2. M. Autric et al., *Study of a high power infrared laser beam through the atmosphere. Influence of metrological conditions* Proceedings, 7th GCL, SPIE Vol. 1031, p. 564, 1988
3. A.A. Lushnikov et al., *Aerosols in strong laser beams*, J. Aerosols Sci., 24, p. 707 - 735, 1992
4. D. C. Smith et al., *Laser radiation induced gas breakdown*, R04-63-9, 1976
5. M. Hugenschmidt, M. Althaus, *Recent developments in high-resolution optical diagnostics of repetitively pulsed laser-target effects*, Proceedings, 21st Int. Cong. on High-Speed Photo. and Phot., Korea, 1994

Investigation into the absorptivity change in metals with increased laser power.

M.Sc. Kristian Blidegn and Dr. Flemming O. Olsen.

Institute of Manufacturing Engineering, Thermal Processing of Materials, Laser Group, The Technical University of Denmark, DK-2800, Lyngby Denmark

Abstract

At a first glance the low absorptivity of metals in the infrared (IR) makes the use of YAG or CO₂ lasers in metal processing very inefficient. However, it has been demonstrated that the absorptivity can reach significantly higher levels during the high power laser interaction. An increase which cannot be explained by the increase in temperature only. The interaction between laser light and metals is a major physical phenomena in laser material processing and when modelling processes the Drude free electron model or simplifications, such as the Hagen-Rubens relation, have often been used. This paper discusses the need to extend the Drude model taking into account interband transitions and anormal skin effect at low light intensities and a multiphoton absorption model in order to describe the increase in the absorptivity at high intensities. The model will be compared with experimental results carried out at low power, and tested on experimental absorptivity measurements at high power YAG laser pulses, found in literature.

Keywords: metals' absorptivity , ,intraband transition, interband transition, multiphoton absorption.

1. Model for absorption in metals

1.1 Drude free electron model

The Drude model [1] is based on the assumption that in metals the energy absorption proceeds through the intermediary of the electrons (intraband transitions), which then transmit, through collisions, their energy to the crystalline lattice. Collisions will occur over a period

$$\tau = \frac{1}{\Gamma} \quad \text{eq 1}$$

Where $\Gamma = \Gamma_{ep} + \Gamma_{ee} + \Gamma_{ed}$, where Γ_{ep} , Γ_{ee} and Γ_{ed} correspond to electron collisions with phonons, other electrons and impurities (defects), respectively. The equation describing the electron movement in the electrical field will then be:

$$m^* \frac{d^2 y}{dt^2} + m^* \Gamma \frac{dy}{dt} = -e |E_i| \exp(-i\omega t) \quad \text{eq 2}$$

$$m^* = m \frac{n_0}{n_e} \quad \text{eq 3}$$

y is the electron position, ω the circular freq. of radiation, and m^* is the effective mass defined by m , the mass of the electron, n_0 the density of valence electrons, e the charge of the electron, E_i the amplitude of the electrical field and n_e the density of free electrons.

The theory connects Γ with the complex dielectric permittivity ϵ_c via conductivity (σ) (defined as the ratio of the electric current density oscillating in phase with the electric field), and polarisability, α_p , (defined as the current component outphased at 90° with respect to the electrical field):

$$\epsilon_c \cong 1 - \frac{\omega_p^2}{\omega^2 + \Gamma^2} - i \frac{\Gamma \omega_p^2}{\omega(\omega^2 + \Gamma^2)} \quad \text{eq 4}$$

$$\omega_p^2 = \frac{4\pi n_e e^2}{m^*} \quad \text{eq 5}$$

1.2 Interband transitions

For transitions metals interband absorption begins at arbitrarily low energy [2], and i.e., it is impossible to separate the intraband - and interband transitions.

The model for interband transition is an extend of the free electron model with a restoring force f .

$$m \frac{d^2 y}{dt^2} + m \Gamma \frac{dy}{dt} + f y = -e |E_i| \exp(-i\omega t) \quad \text{eq 6}$$

The interband model gives a contribution to the complex dielectric permittivity :

$$\epsilon_c = 1 + \frac{N e^2}{m \epsilon_0} \frac{1}{\omega_0^2 - \omega^2 + i \Gamma \omega} \quad \text{eq 7}$$

Where N is the density of bound electrons with resonance frequency ω_0 .

1.3 Anormal skin effect

Since Γ decreases with the temperature, one can expect that at very low temperatures the absorptivity will approach a zero limit. However, experiments performed in the 1930s indicated that even at the transition to superconductivity did not result in a substantial decrease in absorptivity. This behaviour, called the anormal skin effect, cannot be explained within the classical theory and occurs whenever the free mean path of the electrons become comparable with the radiation wavelength and the penetration depth. In other words, the motion of the electron becomes dependent of the value of the electric field in locations not exceeding the free electron path. This effect originates changes in the penetration depth, reflectivity and absorptivity calculated from the Drude theory [4]. The effect on the absorptivity of the anormal skin effect can be derived to an additional absorption A_A [4][5] :

$$A_A \cong 3 \frac{v_F}{4 C_0 (1 + \Gamma^2 \omega^2)} \quad \text{eq 8}$$

Where v_F is the electron speed on the fermi surface (for metals $\approx 10^8 \text{ cm s}^{-1}$), C_0 is the light velocity in vacuum and Γ origins from the free electron model.

2. Model versus Real Metallic Surfaces

The Drude free electron model is often used when modelling the interaction between laser light and metal in the infrared. However, the need of extending the model with interband transitions and anormal skin effect is illustrated in the case of aluminium in Figure 1.

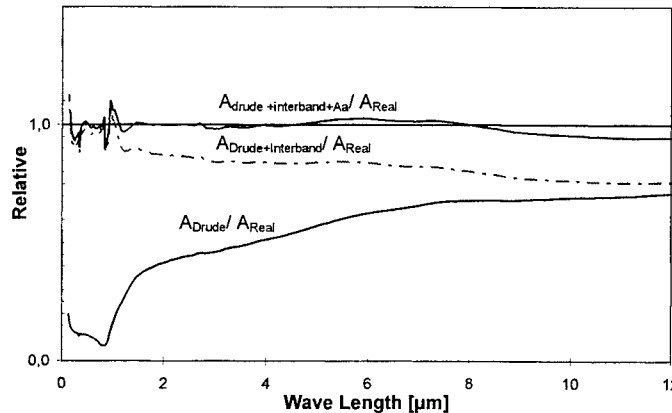


Figure 1 Absorption models divided by measured absorption values for Al at normal incidence, vs. Wave Length.

The Drude (free electron) model is based on values found in literature (see Table 1). It is possible to obtain a better agreement in the infrared (IR) by fitting a ω_p value, however such values, not found from the plasma edge, should not be taken to seriously [2].

In the case of aluminium there is more than 200 interband transitions (valence I,II and III) in the region from 150nm to 2.2μm. To implement all transitions would make a model too complicated therefore four ω_0 have been selected to represent all transitions giving a contribution to the complex dielectric permittivity:

$$\epsilon_c = \sum_k \frac{N_k e^2}{m \epsilon_0 \omega_{0k}^2 - \omega^2 + i \Gamma_k \omega} \quad \text{eq 9}$$

Three of the four interband resonance frequencies have been selected from accumulated strength of interband transition (valence I,II and II) [6], the last ω_{0k} is a fitted value in the IR, since the interband absorption in transitions metals begins at arbitrarily low energy [2]. The values of Γ_k are obtained by numerical fitting to $\epsilon_c(\omega)$, $A(\omega)$, $n(\omega)$ and $k(\omega)$ (see table below).

Intraband coefficients :				Interband coefficients :				
n_0/n_e	$\sigma (\omega=0)$	ω_p	Γ	k :	1	2	3	4
2.11	3.61e7	1.66e16	6.77e13	$\omega_{pk} [\text{rad s}^{-1}]$	3.43e15	2.99e15	2.33e15	3.77e14
[7]	[8]			$N_k [\text{m}^{-3}]$	1.47e29	7.60e27	1.92e28	2.11e27
	$\Omega^{-1} \text{m}^{-1}$	rad s^{-1}	s^{-1}	$\Gamma_k [\text{s}^{-1}]$	3.59e15	6.93e14	8.18e14	6.8e14

Table 1 Coefficients for the combined Intraband-, Interband-, and Anormal skin effect model.

3. Multiphoton absorption

The experimental absorption data found in literature is carried out at low light intensities. With increasing intensity the absorptivity of metals shows a significant increase [10]. This increase cannot be explained by temperature dependency alone [3].

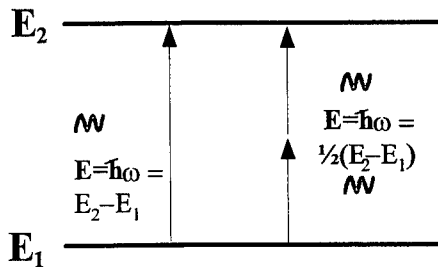


Figure 2 Illustration of one- and two-photon absorption.

In the following the increase in absorptivity measured by Zavecz and Saifi [3] on copper is explained by a simple model for multiphoton absorption.

Multiphoton transitions or absorption occur, if two (or more) photons arrive at the atom and initialise a transition that takes twice (or n times, $n \in \mathbb{N}_+$) the incoming photon energy, as illustrated in Figure 2. The atom or molecule will in the case of two-photon absorption see the two incoming photons as one with half the wavelength and will therefore show a higher absorptivity.

With increasing intensity it is well known that the energy levels of the atom or molecules are broadened, shifted and/or split up. Less known is the fact that the probability of multiphoton transition increases with increasing intensity[9].

A simple model assuming that the possibility of a three-photon absorption follows an exponential distribution in the intensity (Laser Power) gives the probability of one- two- and three-photon absorption as given below.

$$\begin{aligned} P_1 \text{ photon absorption(Laser Power)} &= e^{-\alpha \text{ LaserPower}} \\ P_2 \text{ photon absorption(Laser Power)} &= e^{-\beta \text{ LaserPower}} - e^{-\alpha \text{ LaserPower}} \\ P_3 \text{ photon absorption(Laser Power)} &= 1 - e^{-\beta \text{ LaserPower}} \end{aligned} \quad \text{eq 10}$$

This results in an absorption coefficient in the case of YAG laser as shown below:

$$\begin{aligned} A_{\text{tot}}(\text{Laser Power}) &= P_1 \text{ photon absorption(Laser Power)} * A_{\lambda=1.06\mu\text{m}} + \\ &P_2 \text{ photon absorption(Laser Power)} * A_{\lambda=0.503\mu\text{m}} + \\ &P_3 \text{ photon absorption(Laser Power)} * A_{\lambda=0.265\mu\text{m}} + \end{aligned} \quad \text{eq 11}$$

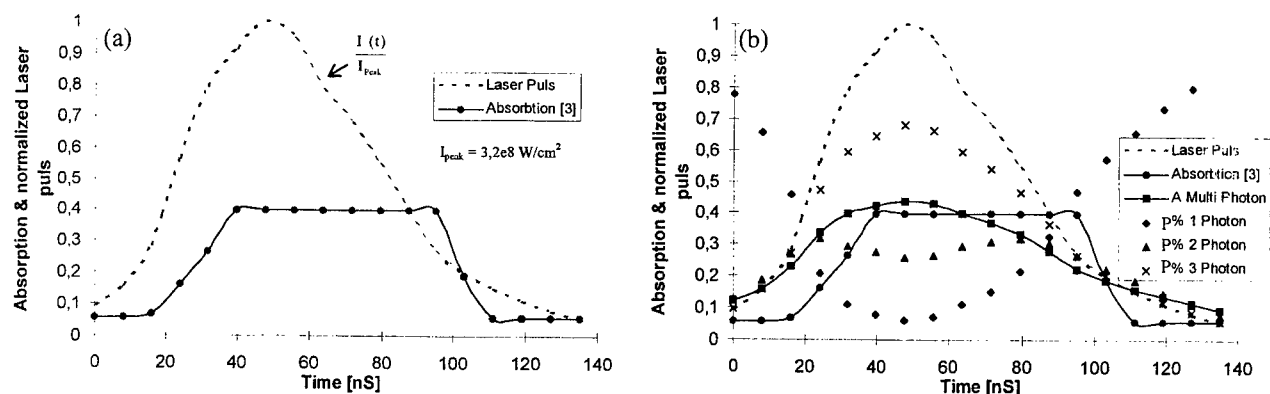


Figure 3 (a) Absorptivity behaviour of an oxide-free copper surface (no melting) illuminated with a YAG laser [3]. (b) Simulation of (a) with one- to three-photon absorption.

Figure 3 (a) shows the absorptivity behaviour of a copper surface irradiate by a YAG laser. Next to (in Figure 3(b)) the coefficients α and β are fitted to describe the increase in absorptivity. It is clear that the model is too simple, when the delay due to change in perturbation is not considered, assuming that the optical constants for the used wavelengths are unaffected by the intensity of the lasers light and not including the change in temperature. The model shows that it is reasonable to assume that three-photon absorption takes place (at least two-photon when using absorption coefficients at melting temperature).

4. Conclusions

In this paper the modelling of metals' absorptivity has been discussed with focus on the necessity of expanding the most used model, the Drude free electron model to obtain a good accordance with the actual absorptivity at low and high light intensity.

Through comparison with measurements found in literature, a model including the Drude as well as four interband terms and the anormal skin effect has been made for aluminium. This model has in the wavelength range from 1 to 10 μm a deviation within the accuracy of the measurements (5%) and less than 10% deviation in the range from 150nm to 1 μm , which is a significant improvement of the Drude free electron model.

A multiphoton model has been introduced in order to describe the increase in the absorptivity at high light intensities. This model has by comparison with measurements of the absorptivity behaviour of an copper surface performed by T.E. Zavecz and M.A. Saifi [3] made probable that two-photon and probably three-photon absorption takes place.

5. References

- [1] Drude Paul, "The Theory of Optics" Dover Publications, INC. New York, 1959
- [2] Weaver J. H., Krafka C., Lynch D. W., Koch E. E., "Physik Daten" "Optical Properties of Metals", Fach-informations-zentrum Karlsruhe GmbH, 1981
- [3] T.E. Zavecz and M.A. Saifi, "Metal reflectivity under high-intensity optical radiation", App. Phys. Letters, Vol. 26, No.4 15 February 1975
- [4] A.M. Prokhorov, V. I. Konov, I. Ursu & I.N. Mihailescu, "Laser Heating of Metals", The Adam Hilger Series on Optics and Optoelectronic, Adam Hilger Bristol, Philadelphia and New York, 1990
- [5] B. Donovan "THE INTERNATIONAL ENCYCLOPEDIA AND CHEMICAL PHYSICS", Pergamon Press London, 1967.
- [6] R. C. Weast, "CRC Handbook of Chemistry and Physics", 63rd Edition, CRC Press, Inc. Boca Raton, Florida, 1982.
- [7] E. D. Palik, "Handbook of Optical Constants of Solids", ISBN 0 12-544420-6.
- [8] J. Bass, K.H. Fischer "LANDOLT-BÖRNSTEIN" "Numerical Data and Functional Relationships in Science and Technology", New Series Volume 15 Subvolumen a, Springer-Verlag Berlin, 1982.
- [9] H. Walter, "Topics in Applied Physics" Springer-Verlag, New York, 1976.
- [10] F.O.Olsen "Theoretical Investigations in the Fundamental Mechanisms of High Intensity Laser Light Reflectivity", Spie Vol. 1020, 1988.

Model-based Process Planning and Control - Laser Beam Welding with CALAS

M. Dahmen¹, B. Fürst¹, S. Kaierle¹, E.W. Kreutz¹, R. Poprawe¹, G. Turichin²

¹Lehrstuhl für Lasertechnik der Rheinisch-Westfälischen Technischen Hochschule Aachen
Steinbachstrasse 15, D-52074 Aachen, Germany

²Technical University of Sankt Petersburg
Belgradskaya 32 - 144, 192212 Sankt Petersburg, Russia

Abstract

Software supported process planning and quality assurance are of main importance for the realization of a manufacturing method in laser beam welding. A novel software tool for process planning and prediction of the properties of laser welded seams named CALAS, i.e. Computer Aided LASering, is presented. Its structure and performance are described in detail. The software tool connects a physical model of welding by CO₂ laser radiation to an interactive man/machine-interface by simulation and visualization. The model considers five fundamental physical processes, absorption of laser radiation at the keyhole surface including multiple reflexion, heat conduction in liquid and solid phase, melt flow, gas flow and heat conduction in the vapor phase, and absorption of laser radiation inside the keyhole volume (plasma absorption). The effect of processing parameters and the resulting geometry of the welded seam are calculated and displayed. The interface provides a three dimensional visualization of the keyhole and the melt pool. Cross sectional views and longitudinal sections may be displayed two-dimensional. Besides typical parameters the beam characteristics, such as power density distribution, and material properties, such as temperature dependent surface tension and heat conductivity, are included in the calculation, too. Due to direct and fast prediction of process parameters and seam geometry CALAS serves as a controlling tool for the operator at the machine tool, and in a more genral view, it serves as tool for processing planning and quality assurance in industry.

Keywords: laser beam welding, process planning, simulation, modelling, analytical approach, software tool

1. Introduction

In computer aided tools engineering of laser beam welding the features of the process are accessible to process planning by modelling. The main aim is to interconnect general task planning, path planning, and process simulation and to link these functionalities to the sensors for process control. Fundamental for this is a process model which computes the parameters relevant for processing and supplies information for the setup of the sensors. Requests for information have to be treated fast to keep the planning procedure as short as possible. Especially in re-planning a fast response is necessary, in order to minimize number and duration of deadlocks between two machining operations. Hence, the speed of calculation has to be optimized at simultaneously high accuracy of the results. To this end a model-based simulation software, named CALAS (Computer Aided LASering) has been developed and tested. This contribution describes the fundamentals of a process model and the physical processes required for modeling. Realization of the program and the performance data are reported.

2. Fundamentals

CALAS describes the process of deep penetration welding with continuous wave CO₂-laser radiation. Due to the interaction of radiation and material a capillary is formed by evaporating and ionizing the metal. Material is then evaporated at the front and sides of the capillary. The dimensions of the keyhole are determined by the equilibrium between the pressure of the vapor, the surface tension and the static pressure of the molten material. To describe the process the following partial processes are applied:

- transport and absorption of radiation by the mechanism of multiple reflexion
- heat conduction in liquid and solid phase
- melt convection
- convection and heat transfer in the vapor/plasma phase in the keyhole
- absorption of radiation in the vapor/plasma in the keyhole.

The description of the deep penetration welding process is based on two assumptions:

- the process is stationary in a system of coordinates fixed to the axis of the laser beam
- heat and mass transfer perpendicular to the surface of the workpiece are neglected.

Thus, the three-dimensional problem is reduced to a two-dimensional one. For discretization the workpiece is virtually split up into layers. In each layer the energy coupling, heat conduction in solid and liquid phase, and mass transfer are calculated independently. After determining the dimensions of the keyhole, the heat flow, the melting isotherms and hence, the geometry of the melt pool, are calculated by solution of the heat conduction equation.

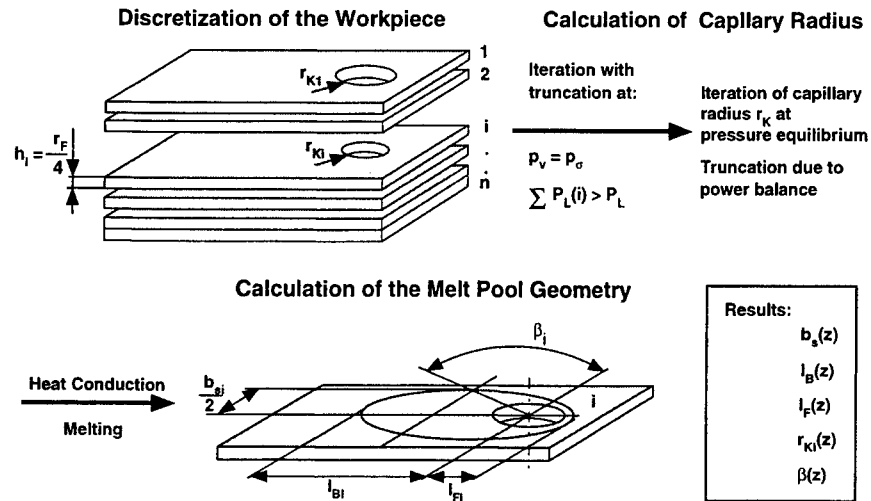


Figure 1: Discretization of the workpiece and calculation of the melt pool geometry

Absorption by the laser-induced plasma is described by the Lambert-Beer's law

$$P(z) = P(z = 0) e^{-\alpha z}$$

where $P(z=0)$ is the incident power and α is the plasma absorption coefficient.

Absorption of radiation at a metallic surface approximately takes place within the optical penetration depth which is small compared to the thickness of the material. No transmission of radiation takes place at material thickness greater than absorption length, i.e. the absorptivity A can be calculated from $A = 1 - R$. The reflectivity $R(\varphi=0)$ at perpendicular incidence is determined by the Hagen-Rubens relation

$$R(\varphi = 0) = 1 - \sqrt{\frac{8\omega_L\epsilon_0}{\sigma}}$$

where $\omega_L = 2\pi\nu$ and σ denotes the electrical conductivity of the material.

The absorptivity and their dependence on the angle of incidence φ of laser radiation follows from the Fresnel formulas. For perpendicular (s) and parallel (p), polarization the absorptivity is given by

$$A_s = 1 - \left(\frac{\cos\varphi - \sqrt{n_c^2 - \sin^2\varphi}}{\cos\varphi + \sqrt{n_c^2 - \sin^2\varphi}} \right)^2 \quad \text{and} \quad A_p = 1 - \left(\frac{n_c^2 \cos\varphi - \sqrt{n_c^2 - \sin^2\varphi}}{n_c^2 \cos\varphi + \sqrt{n_c^2 - \sin^2\varphi}} \right)^2$$

The propagation of the beam is described by means of geometrical optics. In each layer the power density is determined by ray tracing and superposition. The calculation is carried out for the s- and p-polarized parts of the radiation separately. Reflexions originating from deeper layers are neglected.

Heat transfer is considered as conductive and convective energy transport. Using temperature-averaged values of the thermal properties it is described by

$$\underline{u}\nabla T = \kappa \Delta T.$$

The boundary conditions at the surface of the capillary are given by the energy absorbed. This condition leads to

$$\frac{\partial T}{\partial n} = -\frac{I_L(\varphi)}{K} \text{ at } r = r_K \text{ and } T(r \rightarrow \infty) = T_0.$$

The melt flow is assumed as a stationary potential flow around a cylinder. After transforming the polar coordinates (r, φ) to the streamlines of the flow by conformal mapping (η, ζ) the two-dimensional temperature field results to

$$T(\zeta, \eta) = \frac{a}{\pi \lambda} \exp(Pe \zeta) \int_{-1}^1 \frac{I_L(-\xi') \exp(-Pe \xi')}{\sqrt{1-\xi'^2}} K_0(Pe \sqrt{\eta^2 + (\zeta - \xi')^2}) d\xi',$$

i.e. the temperature profile becomes only dependent on the power density and the Péclet number.

3. Mode of operation

Operation of CALAS requires the following input parameters

- beam parameters: focal radius, aperture, focusing number, and power density distribution
- thermo-physical properties of the material: melting and boiling temperatures, latent heats of melting and boiling, plasma absorption coefficient, and reflectivity.
- processing parameters: beam power, feed rate, and relative focal position.

Beam and processing parameters are dependent on the laser machine tool. They can be varied by moving the scrollbars on the user interface. From a parameter set an initial seam geometry is calculated. This step is called

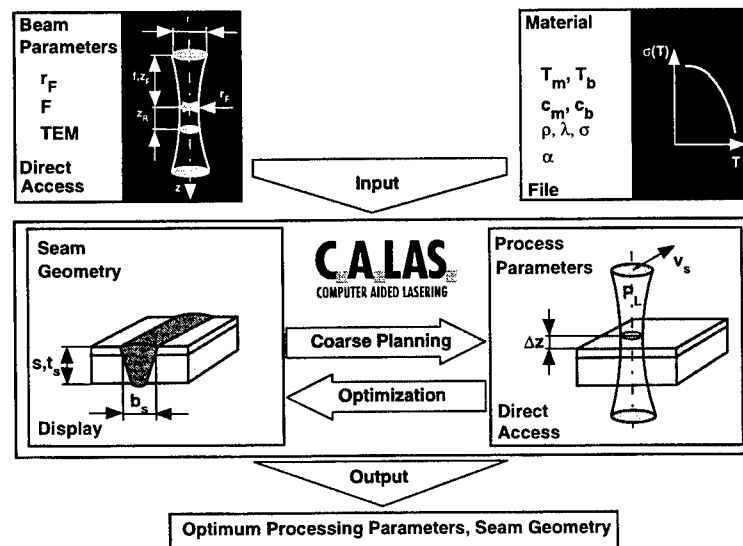


Figure 2: Information flow chart

"coarse planning". The second step "fine planning" consists of altering the processing parameters at fixed beam parameters (Fig. 2). The latter remain constant because they are properties of a special machine tool configuration. Iteration leads to the desired shape of the seam cross section. If the result is satisfactory the resulting parameter set and the geometrical data either are printed as a worksheet or transferred to the quality test station and, after post processing, to the laser machine.

These function are enabled by working of CALAS as TCP/IP server. By this the simulator is linked to an autonomous production cell which covers all functions necessary for planning and control of the laser beam welding process on line. CALAS supplies processing parameters to a CAD system for path planning and generation of NC data. Furthermore simulated data are utilized for adjusting and initializing control devices.

4. Performance

To estimate the calculation speed, the features of the software physical model, graphics display, and TCP/IP interface have to be regarded as separate parts. The time of computation amounts to 0.1 s each complete calculation. Displaying the results requires about 0.2 s. The transfer of the data depends on the utilization ratio of the network to which CALAS is coupled. Therefore the time for transfer can be quoted in an order of magnitude of several seconds. Typical computation times of models utilizing FEM or FVM amount to several hours. Empirical approaches lack of universality since they are based on experimental results. Qualitative results of the benchmark test are shown in Fig. 3. One result of the comparison between experimental and calculated results by regarding the welding depth is shown in Fig. 3. Bead on plate welds were carried out in a flat sheet of mild steel with a carbon content up to 0.2% (St 52-3, 1.0570). The beam parameters were fixed to $F = 7.1$, $r_F = 175 \mu\text{m}$, and $P_L = 3000 \text{ W}$ at a mode TEM_{10+} . In the range of medium feed rates $1 \text{ m/min} \leq v_s \leq 6 \text{ m/min}$ a good agreement is

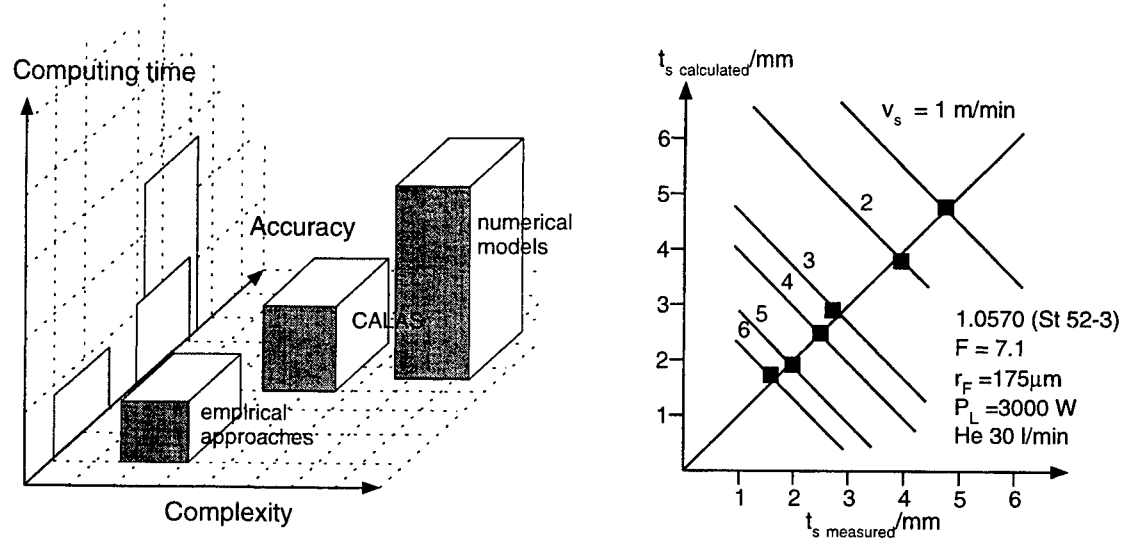


Figure 3: Results of the program test by benchmarking and comparison between measurement and calculation

obvious. The maximum deviation amounts to $\pm 5\%$. Further tests revealed a higher deviation at high feed rates up to 12 m/min. This error is caused by the model assumption that the capillary is circular and perpendicular to the surface of the workpiece. In real processing the change of shape and inclination of the keyhole will lead to an altering of the optical energy absorbed.

5. Conclusion

A simulation software CALAS for process planning and optimizing is presented. It utilizes a model of deep penetration laser beam welding in an analytical formulation which is linked to a graphics display and a data transfer interface to the machine tool. Due to applications in production planning at the workbench it offers high performance data. The time required for one computation amounts 1/10 of a second. Results are displayed on screen after 200 ms. Since CALAS works as a TCP/IP server data transfer to every system in a network is possible. The modularity of the program enables a quick and easy extension of its functionalities. Future work will concentrate on extending the simulation capabilities by adding process models of other techniques of laser materials processing, i.e. cutting and transformation hardening. Furthermore the scope of materials will be enhanced. Also the use of Nd:YAG laser radiation will be implemented to meet the requirements of today's industrial applications.

Acknowledgement

The work presented is carried out within Sonderforschungsbereich (SFB 368) supported by the German Research Association (DFG).

Propagation and shielding effects of surface plasmas on coated and uncoated materials due to pulsed CO₂-laser radiation

Rüdiger Schmitt, Manfred Hugenschmidt, French-German Research Institute of Saint-Louis (ISL)
5 rue du Général Cassagnou, F-68300 Saint-Louis, France, or: P.O. Box 1260, D-79574 Weil am Rhein, Germany
Tel. +33-89 69 5171, FAX +33-89 69 5077, E-mail: schmitt@decu1x.ba-loerrach.de

Abstract

The thermo-mechanical coupling of pulsed laser radiation with matter is affected by surface plasmas and ablation. Studies concerning these transient effects were carried out at ISL with a pulsed CO₂-laser.

In thin layers, depending on the skin depths and absorptivities, the transformation or vaporisation temperatures can be reached even within a single pulse. In the initial stage the ignited plasmas are partially transparent for the laser radiation and enhance the coupling due to energy transfers from this plasma to the target. At a later time the rapidly expanding plasmas tend to shield the target. The temporal development of these plasmas and the ablation of material from the surface were recorded with a high-speed video camera. The dependencies of the shielding effects on laser parameters and material properties were investigated additionally by plasma transmission measurements.

Keywords: CO₂-laser, interaction laser-matter, surface plasma, plasma propagation, plasma shielding.

1 INTRODUCTION

For materials, which are not transparent at the wavelength of the laser radiation, the skin depth is in the range of a few μm and below. Energy, absorbed in thin surface layers, is transferred into the underlying material due to thermal conductivity.

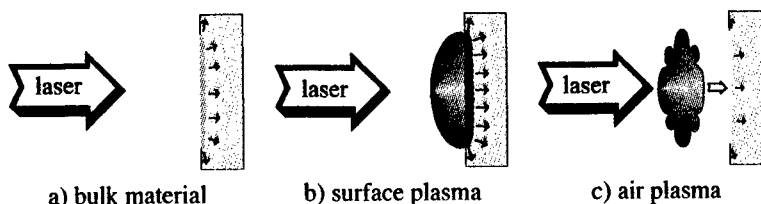


Figure 1: Coupling mechanisms and plasma formation

For metals with their low absorption coefficient the energy transfer is limited to a few percent and the heating is rather low (figure 1). Above a material dependent power threshold, plasmas with a higher absorption than the bulk material are ignited on the surface. Due to continued absorption these plasmas expand along the inverse laser direction. This laser supported absorption wave (LSA) can be divided into two kinds, the laser supported combustion wave (LSC) and the laser supported detonation wave (LSD) [1]. Indirect energy transfer from the surface plasma to the bulk material causes an enhanced heating of a thin surface layer (figure 1b) [2]. Besides this thermal effect a mechanical momentum is transferred to the target, affecting the ablation of molten material.

For power densities in the range of GW/cm^2 the ignition of plasmas can occur in the atmosphere in front of the target [2]. Due to their low transmittance the target is nearly shielded from the laser radiation. As a consequence the surface heating is rapidly decreased (figure 1b).

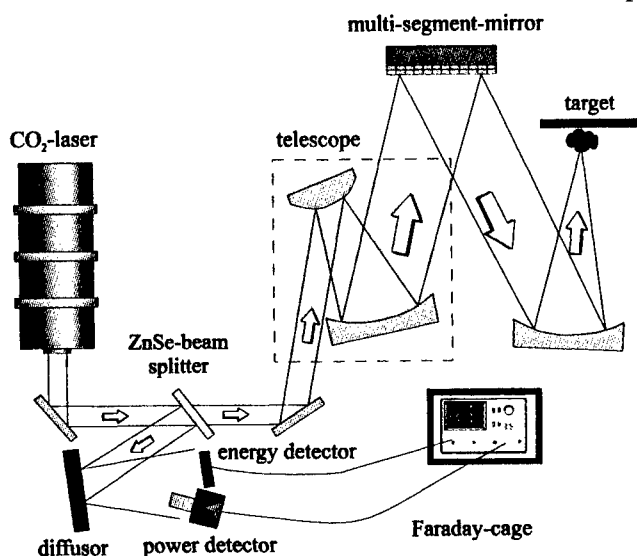


Figure 2: Schematic setup

2 EXPERIMENTAL SETUP

The setup scheme is given in figure 2, the temporal pulse shape in figure 3 [3]. The ZnSe beam splitter (reflectivity 3%) splits the laser radiation for power and diagnostic purposes. The telescope and the right concave mirror improve the initial poor spatial laser beam quality.

For a gas pressure of 196 mbar and a gas mixture $\text{CO}_2 : \text{He} : \text{N}_2 = 1 : 10 : 4$ the pulse energy was 24 J at a pulse length of 20 μs and a peak power of 3.4 MW.

The average power of the system at the maximum repetition rate of 100 Hz was 2.5 kW. The spot size on the target were adjusted to 1 cm * 1 cm.

3 PROPAGATION OF THE SURFACE PLASMAS AND SHIELDING EFFECTS

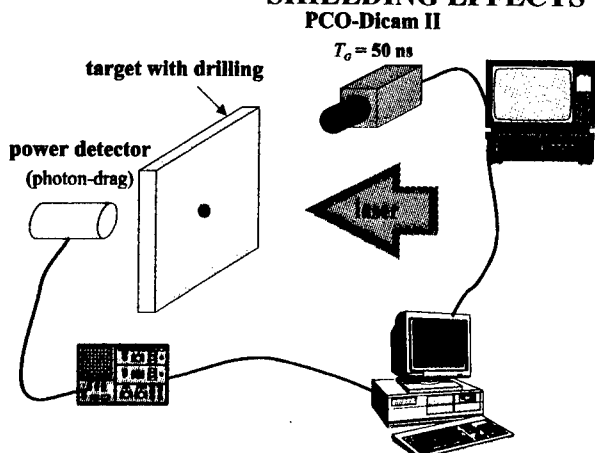


Figure 4: Registration setup

The processes on the target surface like plasma ignition and expansion were registered with a PCO-DICAM II video camera. The amplification time of the multi-channel tube, which is a governing factor of the exposure time of the camera, was chosen to $T_G = 50$ ns as a compromise of noise and sharpness. A photon-drag detector mounted at the rear of the target registered the transmitted laser signal through a hole with a diameter of 1 mm, which was drilled into the target. This setup shown in figure 4 allowed the drawing of conclusions concerning the shielding properties.

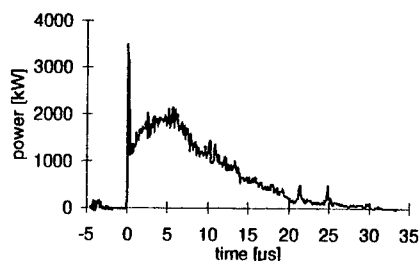


Figure 3: Temporal pulse shape

3.1 PMMA

Laser irradiation of PMMA is attended with a light zone as can be seen in figure 5. Their brightness is small compared to the plasma brightness in the examples below. The laser pulse energy was 24 J. The time Δt is measured from the beginning of the laser pulse.

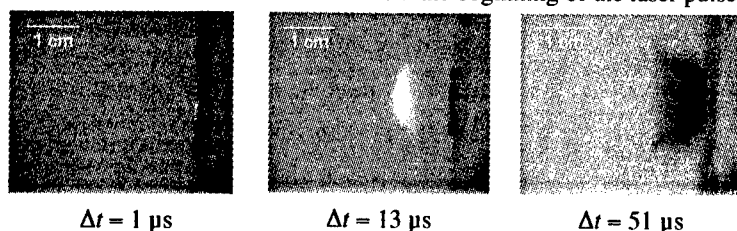


Figure 5: Expansion of the light zone and material ablation

shape in both cases is different from the original undisturbed signal. The peak is transmitted nearly undisturbed, temporal late parts of the pulse become weakened mostly due to vaporised material.

3.2 Varnished sheet metal

In figure 7 recordings from the short-time exposure camera of pulses with an energy of 24 J on a target of varnished sheet metal are shown. The upper row shows the interaction of the first laser pulse on the undisturbed varnishing, the lower a second pulse on the same target.

During the first pulse the plasma is attached to the surface only in the initial phase of the laser pulse. The plasma expansion velocities in this case reached values up to 4000 m/s as can be seen from figure 9.

After this pulse the varnish with its high absorption in the infrared is removed and for subsequent pulses the plasma is attached to the surface during the total time of the laser radiation. The expansion velocity of the plasma front is in the range of the velocity of the first pulse.

The fast expanding light zone reaches initial maximum velocities up to 1400 m/s and is propagating in the inverse laser direction despite the orientation of the target. The material ejection with maximum velocities of about 280 m/s is observed with a delay to the laser pulse and occurs perpendicular to the target surface [1, 4].

The registered transmitted signals are shown in figure 6 for two different pulse energies. The pulse

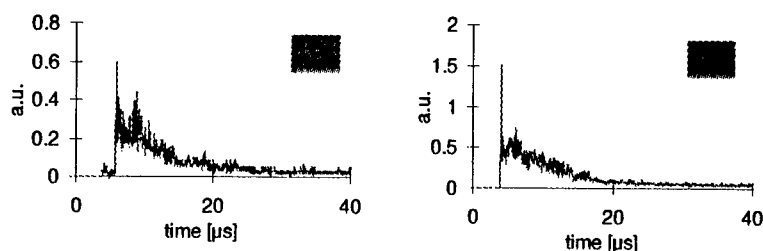


Figure 6: Transmitted signals

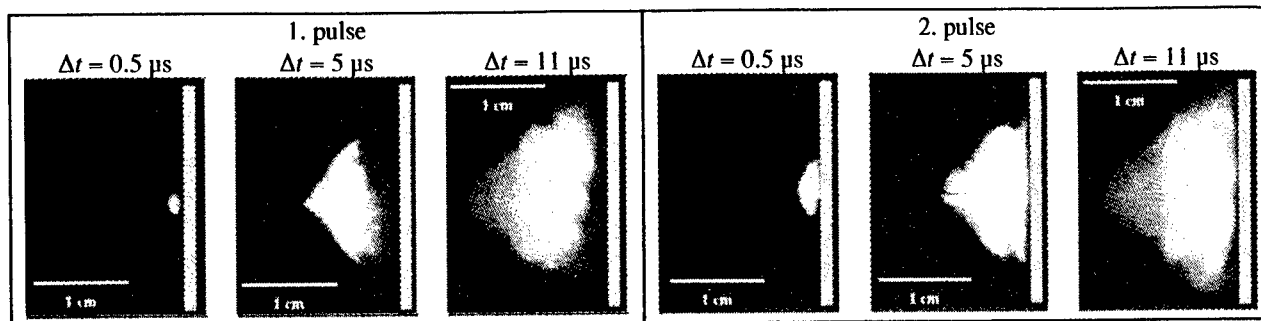


Figure 7: Plasma expansion

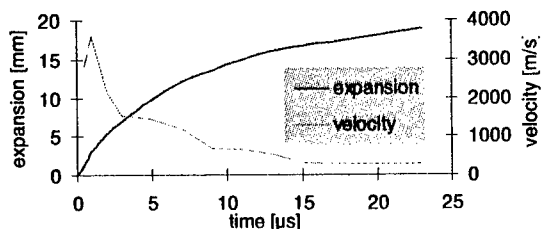


Figure 9: Propagation of the plasma front

The influence of the paint coating on the transmission can be seen from figure 8. The laser peak is transmitted undisturbed through the hole. The surface plasma becomes opaque after some μs

leading to a rapid decline of the transmitted power signal. The beginning of this decline decreases with the removal of the varnish and the shielding becomes more abrupt. As can be seen from the right diagram in figure 8, an increased pulse energy augments the built-up of the plasma and the shielding tends to previous moments.

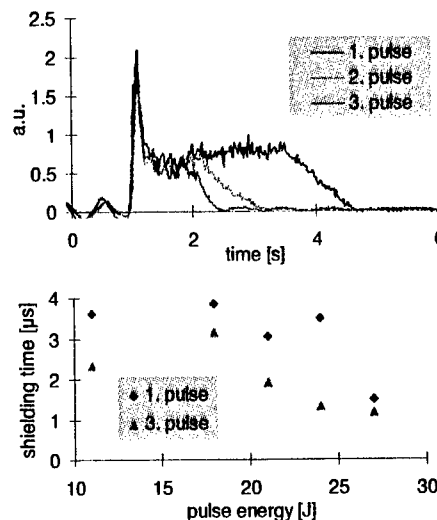


Figure 8: Transmitted signals and energy dependency of the shielding time

3.3 Varnished copper

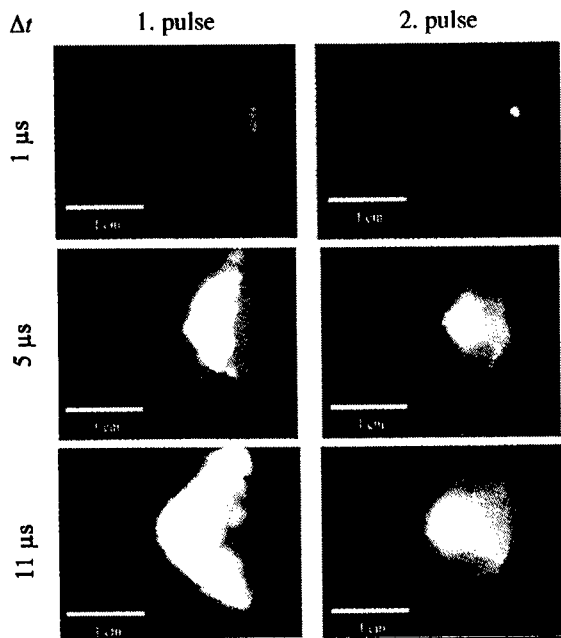


Figure 10: Short-time exposure camera recordings

The results for copper varnished with a black paint layer at a pulse energy of 24 J are shown in figure 10.

The observations are similar to the result obtained with sheet metal mentioned in the section before. During the first pulse the plasma is attached only for a short time to the surface. During the second pulse the rear side of the plasma is attached to the surface for the total pulse length. The plasma front expands with velocities up to 1800 m/s for pulse energies of 24 J. With decreasing pulse energy the expansion velocity

declines to 1100 m/s for a pulse energy of 11 J.

In figure 11 results from an energy reflection measurement are shown for two different energy values.

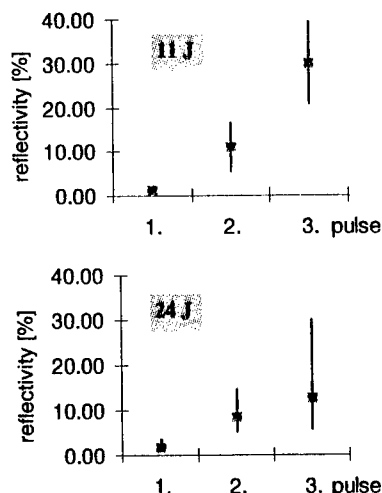


Figure 11: Energy reflectivity

For the first pulse the high absorbing varnish effects only a low reflection. As the coating is removed the reflectivity of the bare metal is increased. The ignition of surface plasmas after removal of the varnish has an opposite effect on the reflectivity due to their high absorption.

3.4 Mirror coated with a gold layer

Instead of a high absorbing surface layer mirrors are topped with a high reflectance coating. Nevertheless, due to strong laser radiation, the mirror surface can be damaged [5]. The short-time exposure camera recordings for a mirror coated with a gold layer are shown in figure 12 at a pulse energy of 2 J.

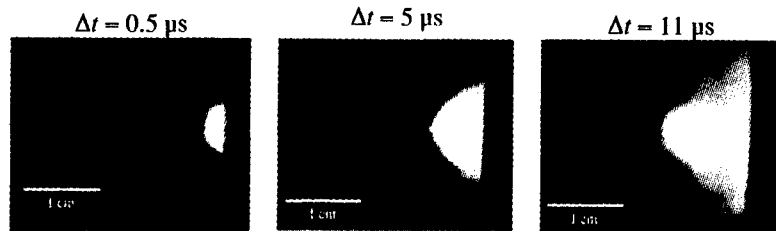
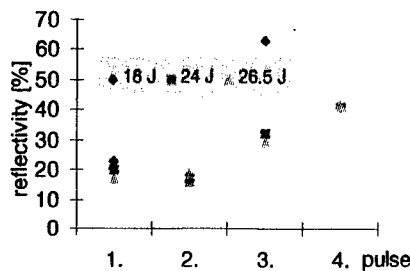


Figure 12: Short-time exposure camera recordings



The surface attached plasma again propagates along the inverse laser direction. The corresponding energy dependency of the reflectivity and the shielding time are shown in figure 13.

For low pulse energies no plasmas were ignited, the incident laser radiation was mainly reflected. At higher pulse energies surface plasmas were ignited early resulting in a reduced reflectivity.

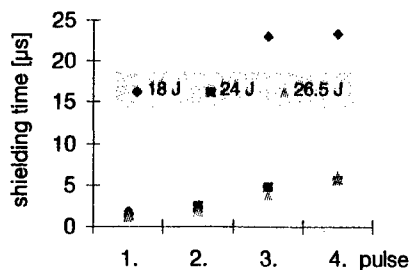


Figure 13: Energy reflectivity and shielding time

3.5 Brass

The plasma ignition threshold in this case was rather high and so the reduced reflectivity due to plasma absorption occurs only for high energy densities. Even for a pulse energy of 24 J only the first pulse ignited a plasma at impurities on the surface. Subsequent pulses on the bare surface are nearly reflected for 100 %. Pulse energies above 25 J causes the recurrent ignition of surface plasmas resulting in the reduction of the reflectivity shows an

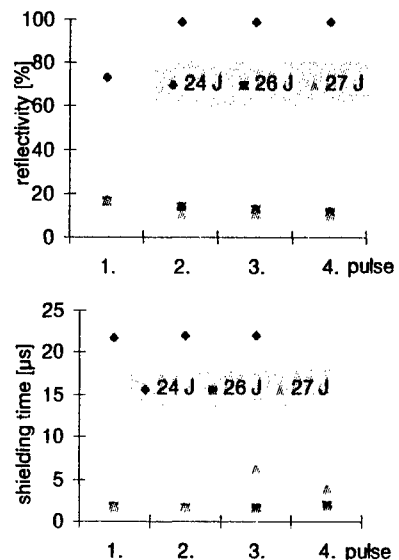


Figure 14: Energy reflectivity and shielding time

4 ACKNOWLEDGMENTS

The authors wish to thank L. Geiss, E. Stechele, M. Christen and D. Walgenwitz for their helpful work.

5 REFERENCES

- [1] J. Lu, X. Ni, A. He, „An interferometric investigation of ignition and propagation of laser-supported-detonation wave at the initial stage“, Interferometry VI: Applications, SPIE Proceedings, volume 2004, p. 100-106, 1993.
- [2] Ch. Boulmer-Leborgne, J. Hermann, B. Dubreuil, „Plasma formation resulting from the interaction of a laser beam with a solid metal target in an ambient gas“, Plasma Sources Sci. Technol., vol. 2, p. 219-226, 1993.
- [3] R. Schmitt, M. Hugenschmidt, L. Geiss, E. Stechele, „Interaction of pulsed CO₂-laser radiation with optical materials“, Proceedings of the tenth international symposium on gas flow and chemical lasers, Friedrichshafen, SPIE, volume 2502, p. 712-719, 1994.
- [4] R. Schmitt, M. Hugenschmidt, „Visualization of transient phenomena during the interaction of pulsed CO₂-laser radiation with matter“, in Proceedings of ICONO '95, St. Petersburg, Russia, SPIE, volume 2796, p. 260-266, 1995.
- [5] E. Bliss, D. Milam, R. Bradbury, „Dielectric mirror damage by laser radiation over a range of pulse durations and beam radii“, Applied optics, vol. 12, p. 677-689, 1973.

Optimisation of the Laser Cutting Process

Birgitte Dragsted, Flemming Olsen

Department of Manufacturing Engineering
Building 425, Technical University of Denmark, 2800 Lyngby, Denmark

ABSTRACT

The problem in optimising the laser cutting process is outlined. Basic optimisation criteria and principles for adapting an optimisation method, the simplex method, are presented. The results of implementing a response function in the optimisation are discussed with respect to the quality as well as the productivity.

Keywords: laser cutting, multicriteria optimisation, weighted response, simplex method, 2.5 mild steel, roughness, burr.

1. INTRODUCTION

In [1] the problem of optimising the laser cutting process is explained. In the paper we argued that the optimisation of the laser cutting process can be categorised as a multicriteria type, and that the following order of priority should be used in the optimisation process:

1. Obtain a satisfactory quality , and
2. optimum productivity,

as a cut with a poor quality performed under high productivity is useless. An adapted version of a modification of the simplex method was implemented in a number of optimisation series. The only quality characteristic that was used to evaluate the laser cut items was the roughness. When a satisfactory roughness (field 1 according to DIN 2310 [3]) was obtained, the cutting speed was maximised. The optimisations were carried out in 2mm Mild Steel, 2mm AlMg3 and 3mm AISI316. For all series a remarkably better roughness (decreases up to 67%) as well as higher productivity (up to 135 % increases in the cutting speeds) were achieved. But for the optimisation in 2mm Mild Steel some dross attachment appeared, which emphasis that the quality should be evaluated by more characteristics than the roughness. In [2] it was demonstrated that it is possible to obtain a satisfactory quality of the cut only by comparing the samples when using the optimisation algorithm. This is important, as it shows it is possible to find a parameter combination which result in a cut where all relevant quality characteristics are satisfactory. Indicating that if the right quality characteristics are chosen it must be possible to make a quantitative response that reflects the overall quality. The response should be calculated based on a combination of the measured values of the quality characteristics, as a quantitative judgement speeds up the time spent on the optimisation as well as it result in a more objective evaluation of the laser cut.

Therefore the main purposes of this paper are to 1) create response functions for some of the main quality characteristics, 2) advance different strategies of how various optimisation series should be carried out in order to reach the wanted quality as well as a high productivity, and 3) test and evaluate one of the strategies experimentally.

2. CREATION OF A RESPONSE FUNCTION FOR THE QUALITY

Table 1 Classification of the roughness according to DIN2310 (where 'a' is the material thickness)

Roughness	Field
$0 \leq R_z \leq 10+2a$	1
$10+2a < R_z \leq 30+3a$	2
$30+3a < R_z \leq 60+4a$	3

Since the optimisation in 2mm Mild Steel [1] had resulted in a satisfactory roughness but not a satisfactory burr height, it was decided to include both the burr height and the roughness as quality characteristics in the optimisation. The following is a presentation of how the quality functions for the two characteristics were created, and suggestions of how to combine them in a response function so a quantitative estimate of the cut quality can be determined.

In DIN 2310 [3] instructions of how to classify the quality of a laser cut surface are given. As shown in Table 1 the standard divides the roughness into three groups depending on the material thickness. Though the standard deals with classification of the quality, no guidelines for the classification of the appearance of burr are presented. In

Table 2 a suggestion of how to classify the burr height in three different fields based on the recommendations in [4] is presented. Contrary to the classification of the roughness it appears that the burr height does not depend on the material thickness.

The demands on the quality may vary depending on the purpose of the laser cut item. If the best quality must be obtained,

$$f(R_z) = \begin{cases} \frac{R_z}{10+2a} & , 0 \leq R_z \leq 10+2a \\ \frac{R-(10+2a)}{(30+3a)-(10+2a)} \cdot 3 + 1 & , 10+2a < R_z \leq 30+3a \\ \frac{R-(30+3a)}{(60+4a)-(30+3a)} \cdot 7 + 4 & , 30+3a < R_z \leq 60+4a \\ \frac{R-(60+4a)}{(60+4a)-(30+3a)} \cdot 10 + 11 & , 60+4a > R_z \end{cases} \quad (1)$$

it means that the both the roughness, R_z , as well as the burr height should be in field 1.

The creation of the quality functions, is based on some basic

$$g(\text{burr height}) = \begin{cases} \frac{\text{burr height}}{0.05} & , 0 \leq \text{burr} \leq 0.05 \\ \frac{\text{burr height}-0.05}{0.5-0.05} \cdot 3 + 1 & , 0.05 < \text{burr} \leq 0.5 \\ \frac{\text{burr height}-0.5}{2.5-0.5} \cdot 7 + 4 & , 0.5 < \text{burr} \leq 2.5 \\ \frac{\text{burr height}-2.5}{2.5-0.5} \cdot 10 + 11 & , 2.5 > \text{burr} \end{cases} \quad (2)$$

principles in operational research. Interested readers may find more about the subject in [7]. The quality function, f , for R_z was created as a penalty function as it appears in equation 1. Meaning that a roughness in field 3 is given a relatively higher value than a roughness in field 2, so the optimisation is "forced" in the right direction.

In order to impose the same weight on the quality characteristics, the quality function for the burr height, g , in equation 2, was created. In this way a burr height or a roughness situated relatively the same place in one of the fields would be given the same value, when using its quality functions.

Since the simplex method only deals with one response the two quality functions have to be combined. A way to do this is by weighting the quality functions in the following way:

$$\text{Quality response} = \alpha \cdot f(R_z) + \beta \cdot g(\text{burr height}), \text{ where } \alpha + \beta = 1 \quad (3)$$

3. OPTIMISATION METHOD

In the following a very brief introduction to some of the basic principles in the modified and adapted simplex method are presented, as this is important for the evaluation of the optimisation afterwards. The method is described in [5] and the original computer programme of the algorithm the adapted method is based on is presented in [6]. Some of the principles that have been introduced to fit the method for the laser cutting process can be found in [1].

The optimisation is initialised with a simplex design. A simplex design consists of $k+1$ parameter combinations when k parameters are to be optimised. Consequently the initial design in the simplex method consists of three laser cuts (performed with three different parameter combinations) when two parameters take part in the optimisation, and five laser cuts when four parameters are to be optimised as it was the case in these experiments.

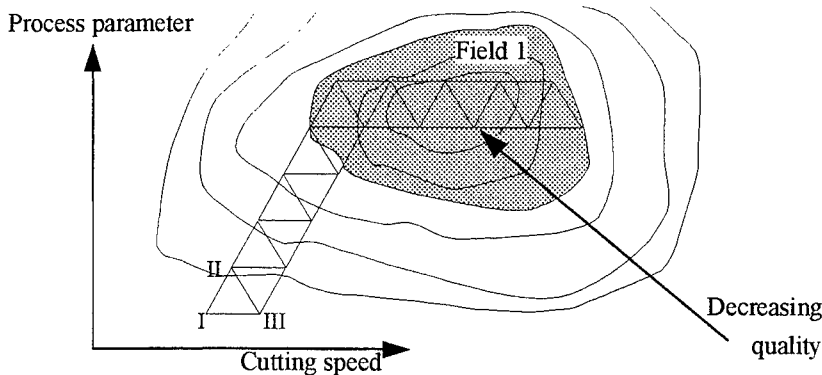


Figure 1 Illustration of the optimisation procedure

Table 2: Classification of the burr height based on the recommendations in [4].

Burr height	Application	Classification
1)	Corners with permitted burr chamfer/rounding	Above field 3
+2.5		Field 3
+1		
+0.5		Field 2
+0.3		
+0.1		
+0.05	Sharp corner	Field 1
+0.02		
1) Additional sizes according to requirement		

When all experiments in the design have been carried out, the responses are compared and the one with the worst response is substituted by its image. In this way a new parameter combination (corner) is found and an experiment with this combination shall be carried out. This corner, together with the remaining corners form a new simplex design, which then is evaluated as explained above. In this way the algorithm proceeds until a maximum or a minimum is reached.

As explained previously a satisfactory quality should be obtained. Therefore the quality response function is used as response until both the roughness as well as

the burr height, for all the corners in the simplex, are in field 1. When this is achieved, the responses in all the corners of the simplex are replaced by their parameter setting of the cutting speed. The optimisation algorithm then continues with the cutting speed as response.

In Figure 1 the principle of an optimisation with two process parameters, is illustrated. The quality response is considered as a mountain scenery (please note that this obviously just is an illustration of how the quality response is connected with the process parameters, in order to facilitate the understanding of the optimisation). It appears that until all corners in the triangle are in field 1 (the grey area) the quality response is used as response, hereafter the cutting speed is used as response. In this way the experiments are forced towards the minimum until all corners are in field 1. Hereafter the experiments are forced in the direction of an increased cutting speed as long as the both quality characteristics belongs to field 1.

Another question that need to be investigated is when the optimisation process should be stopped. In the original computer programme [6], the simplex is contracted when the optimisation gets nearer to an optimum, that is the distance between the corners in the simplex design is reduced. The optimisation is stopped when

$$2 * \frac{|highest\ response - lowest\ response|}{|highest\ response| + |lowest\ response|} \leq ftol, \quad (4)$$

where the highest response refers to the corner with the highest response in the last simplex design. Analogously the lowest response refers to the corner with the lowest response. In the adapted optimisation programme ftol=0.1.

4. EXPERIMENTAL PROCEDURE

All experiments have been carried out with a 3kW CO₂-laser PRC 3001. The variable process parameters, shown in Table 3, were chosen as only quantitative variables can take part in the simplex method. In the table the weighting of the quality functions is also shown. It appears that the quality functions for the roughness and the burr height were equally weighted. This weighting was chosen as it was the first optimisation series with a multiresponse for the quality.

Before the actual simplex optimisation was started, a preliminary design of experiments was carried out, so sufficient information was gained in order to create the initial simplex design. For this purpose a 2⁴⁻¹-factorial design (that is 8 experiments) was carried out. The experiments were evaluated by using the quality response in Table 3.

Table 3 Optimisation conditions.

Material	2.5mm Mild Steel
Variable ¹ process parameters	Cutting speed Power (CW) Gas pressure Focus point position
Goal	R _z ≤ 15µm Burr height ≤ 0.05mm Max. cutting speed
Quality response ²	0.5*f(R _z)+0.5*g(burr height)

5. DISCUSSION OF THE OPTIMISATION

The parameter combination in the preliminary experiments with the best quality response fulfilled the demands to the quality as well as it had a higher cutting speed (3.4 m/min) than the one suggested by the operator (for that parameter combination the cutting speed was 2.4 m/min and a satisfactory cut quality was not obtained). Consequently already the goal of reaching a satisfactory cut quality as well as an increase in the cutting speed of 42% was achieved in the preliminary 8 experiments. Based on these experiments the simplex optimisation was started and 39 experiments were carried out.

The maximum cutting speed during the optimisation is shown in the Figure 2. It appears that the maximum cutting speed, which also had a satisfactory cut quality, increased until experiment number 24. None of the following parameter combinations in the optimisation that had a higher cutting speed resulted in a satisfactory cut quality. By examining Figure 3, it appears that the variety of the measured burr heights increases drastically at about 5 m/min. The figure also shows that the roughness decreases when the cutting speed is increased, though at about 5 m/min the observed roughnesses are more spread. These tendencies indicates that the maximum limit of the cutting speed has been reached. In Figure 2 the relatively difference between the corner with maximum and the one with the minimum cutting speed in the latest simplex is shown. As this difference nearly stops decreasing even though the cutting speed has reached a maximum, it indicates that changes should be add to the stop criterion in the programme for in this way prevent that too many useless experiments are carried out.

¹ Only quantitative process parameters can take part in the simplex optimisation

² The quality functions for the roughness and the burr height are found in page 2

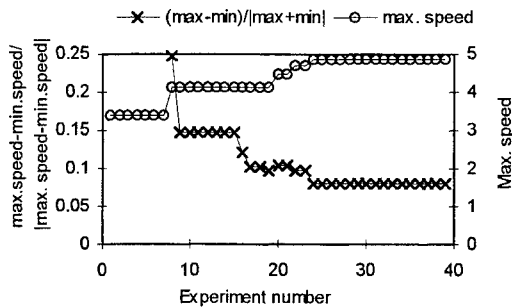


Figure 2 The relatively difference between the maximum and minimum response in the simplex, and the maximum cutting speed achieved during the optimisation.

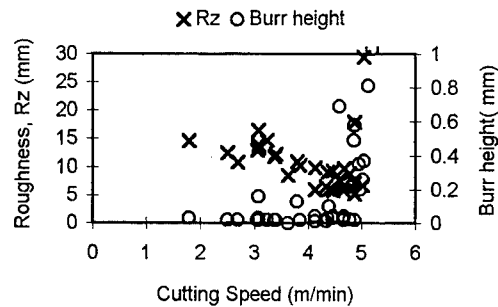


Figure 3 Connection of the two quality characteristics and the cutting speed plotted for all measurable experiments in the optimisation.

6. CONCLUSION

Response functions for the roughness, $f(R_z)$, and the burr height, $g(\text{burr height})$, have been developed. It has been suggested that a quality response $= \alpha \cdot f(R_z) + \beta \cdot g(\text{burr height})$, where $\alpha + \beta = 1$, should be used as quality response until a satisfactory cut quality has been obtained. An

optimisation series for $\alpha = \beta = 0.5$ has been carried out in 2.5mm Mild Steel. The optimisation turned out successfully, as it resulted in a satisfactory cut quality as well as an increased cutting speed which was an increase in the productivity of about 100%. In Table 4 the results of the optimum parameter combination is shown. This parameter combination was reached in approximately 2.5 hours, and could be handled by a trained laser operator as the method had been developed for a computer programme. The evaluation of the results showed that it may be possible to improve the method even more by changing the stop criterion. In this way it can be avoided that the optimisation proceeds despite the maximum limit of the cutting speed has been reached.

Table 4 Optimum parameter combination (reached after 32 experiments (incl. the 8 preliminary experiments))

2.5mm Mild Steel	Starting point	Optimum parameter combination	Changes
Cutting speed	2.4 m/min	4.87 m/min	103%↑
Burr height	0.04 mm	0.02 mm	50%↓
Roughness Rz	18μm	7.2μm	60%↓

7. ACKNOWLEDGEMENTS

The authors wish to thank Ph.D. Steen Skytte Jensen at Danfoss A/S in Nordborg, Denmark, for making it possible to perform all the experiments at Danfoss.

8. REFERENCES

- [1] Dragsted B., Olsen F.O. "Multi Criteria Optimisation of the Laser Cutting Process". 5th NOLAMP Conference, pp 13-22 SINTEF Forum Post-box 124 Blindern 0314 Oslo Norway 1995.
- [2] Dragsted B., Olsen F. O. "Computer based optimisation routines" to be published in ECLAT'96 6th European Conference on Laser Treatment of Materials, AWT IFSW Institut für Strahlwerkzeuge, Universität Stuttgart, 1996
- [3] DIN 2310: Termisches Schneiden, Beuth, Berlin 1990 (in German).
- [4] DS/ISO 13715 Technical drawings-Corners-Vocabulary and indication on drawings, DANSK STANDARD in Danish and English 1995-10-31.
- [5] Spendley, W., Hext, G.R., Heinsworth F. R., Sequential Application of Simplex Designs in Optimisation and Evolutionary Operation, Technometrics, Vol. 4, No. 4, 1962.
- [6] Press W.H., Flannery B.P., Teukolsky S.A., Vetterling W.T., Numerical Recipes, The Art of Scientific Computing, University Press. 1990.
- [7] Carlos Romero, HANDBOOK OF Goal programming in goal programming, Pergamon press.

Control of the surface plasma during pulsed laser cutting

U. Bielesch, M. Napp, J.H. Schäfer, J. Uhlenbusch

Heinrich-Heine-Universität Düsseldorf, Institute for Laser- and Plasmaphysics
Universitätsstr. 1, 40225 Düsseldorf, Germany

ABSTRACT

During pulsed laser cutting of aluminum with a repetitively pulsed CO₂ laser a strong correlation between quality of the cut judged by the burr height and electron density of the laser induced plasma on the surface and in the kerf occurs. The electron density is supervised by an absorption experiment and can be adjusted by the pulse duration. A feedback loop based on a comparison between the actual absorption signal and an absorption set point on the one hand and a variation of the laser pulse duration on the other hand is developed to provide an in situ control of the quality of the cut. The system works suitable for different sheet thicknesses and for outlined cuts. The results of optimized cuts are introduced.

Key words: laser cutting, quality of the cut, feedback loop system, burr reduction, outlined cutting

1. INTRODUCTION

The realization of an optimum quality in laser material processing of metals is still basing on expensive, time wasting trial and error methods. Aim of this work is a systematic investigation of the dependences of some parameters influencing the process quality. A quality saving feedback loop is developed utilizing the results of these investigations. With a microwave-excited pulsed oscillator amplifier CO₂ laser system the opportunity is given to reach high maximum pulse power < 900 kW, high pulse repetition rates < 200 kHz, average power < 4,5 kW and a good beam quality near K=1. The pulses are formed with a mechanical chopper wheel performing pulse durations from minimum 2 μs to cw. For more details see [1,2]. Varying one of the parameters like pulse duration τ, focus position z_F and rate of feed of the sheet v and keeping constant the others we study the influence on the quality of the cuts judged by the burr height. To develop a feedback loop it is important to know a process variable, which is coupled to the burr height and can be modified directly by the experimenter. Such a quantity is the absorption of a probing laser beam due to the laser induced surface plasma. Therefore the time resolved measurement of the plasma absorption is a useful mean to control the surface plasma during laser cutting.

2. ABSORPTION EXPERIMENT

A reasonable mean to investigate the plasma absorption due to inverse bremsstrahlung is to use a probing IR HeNe laser at λ = 3,39 μm. Free electrons gain energy during a three-body collision by absorbing a photon. To assume the conservation of momentum a third particle has to receive the residual momentum. Such particles can be ions or neutrals. In a laser produced plasma electron-ion collisions are of major relevance, much more than collisions between electrons and neutrals. To calculate the energy absorption we have to know the collision rate for electron-ion collision ν_{ei}, which follows from:

$$\nu_{ei} = \frac{4}{3(4\pi\epsilon_0)^2} \frac{\sqrt{2\pi} Z^2 e^4 n_e \ln \Lambda}{m^2 \left(\frac{k_B T}{m} \right)^{\frac{3}{2}}}, \quad (1)$$

with the Coulomb logarithm ln Λ.

If ω_p and ν_{ei} << ω, the frequency of the probing laser beam, the absorption coefficient can be written:

$$\alpha_{ei} = \frac{\omega_p^2 \nu_{ei}}{c\omega^2} = \frac{4}{3(4\pi\epsilon_0)^2 \epsilon_0} \frac{\sqrt{2\pi} \lambda^2 Z^2 e^6 n_e^2 \ln \Lambda}{4\pi^2 c^3 \left(m k_B T \right)^{\frac{3}{2}}}. \quad (2)$$

The absorption coefficient is proportional to λ^2 . So it is useful for attaining a reasonable absorption level to choose a light source with a comparatively long wavelength. Restrictions for the wavelengths are due to the wanted small beam diameter.

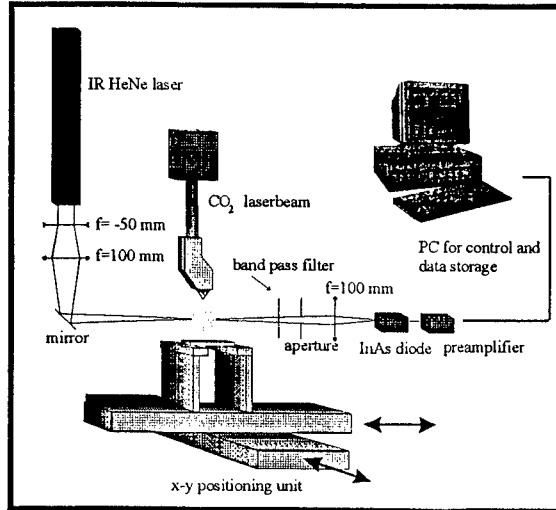


Fig. 1. Plasma diagnostic unit

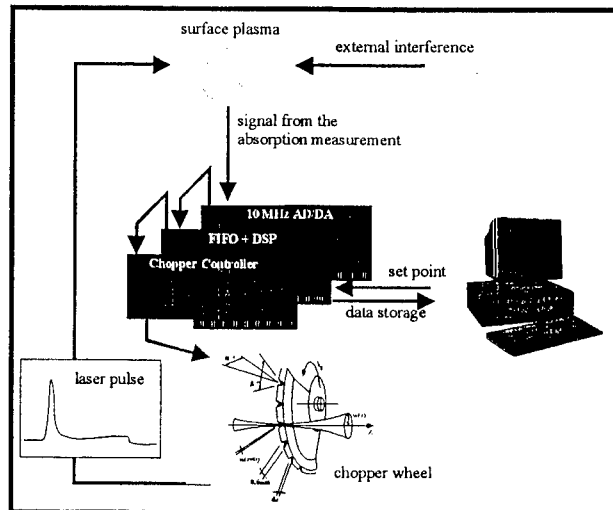


Fig. 2. Setup of feedback loop

The schematic of the absorption experiment is shown in Fig. 1 and in [3,4,5]. The use of an IR HeNe laser represents a good compromise between high enough absorption level and spatial resolution. The probing laser beam is focussed into the surface plasma, which has a typical size of 400 μm . The diameter of the focus ($d = 150\mu\text{m}$) is small enough to deliver a spatial resolution of the plasma. The transmitted radiation is selected from the emission spectrum of the plasma utilizing a narrow bandpass filter and is detected with a InAs diode.

3. EXPERIMENTAL SETUP OF THE FEEDBACK LOOP

The diode signal S is proportional to the transmitted intensity. Measuring the signal in the case of a free passing and a chopped beam the setup can be calibrated in order to avoid errors due to temperature drift of the diode. The provided diode signal is digitized by a fast AD converter with a sample rate of 10 MHz. A digital signal processor (DSP) picks up the digitized signal and computes an average absorption value, which is compared with a set point provided by the PC, see Fig. 2. If the absorption signal $S \propto I_0 n_e^2$ is too large, this means that the electron density is too large. The actual electron density is strongly correlated to the pulse peak power. To decrease the pulse peak power the pulse duration has to be increased. With a pulse repetition rate $f = 22,5 \text{ kHz}$ kept constant, $S(\tau)$ behaves as shown in Fig. 3. The actual pulse duration can easily be adjusted by means of a mechanical chopper wheel, which contains 90 triangular slots on its circumference. Moving the wheel perpendicular to the laser beam the pulse duration can be changed. The displacement of the wheel is realized by a linear motor, which moves forward 100 μm in 25 ms. The difference between set point and mean absorption to be found is a measure for the displacement of the chopper wheel required to minimize this difference.

4. EXPERIMENTAL RESULTS

To obtain a realistic set point of absorption for the feedback system it is necessary to investigate experimentally the influence of pulse duration, focus position and rate of feed of the workpiece on the formation of the burr. The experimental results for different sheet thicknesses are shown in Fig. 4-6. From Fig. 4 one may obtain the optimum value of the pulse duration leading to a minimum burr plotted here for different sheet thicknesses. At low pulse duration (below say 7 μs) no metal will be molten, because the electron density in the plasma has become too large. So the metallic surface is shielded against the laser irradiation. If the laser is working continuously, only a weak plasma will be ignited on the metal surface or in the kerf, so that the release of molten metal will only be insufficiently or not be supported. There also exists an optimum rate of feed belonging to a minimum burr depending on the sheet thickness as

shown in Fig. 5. The optimum rate of feed decreases with growing sheet thickness. If the rate of feed is larger than the optimum value, the metal melts incompletely,

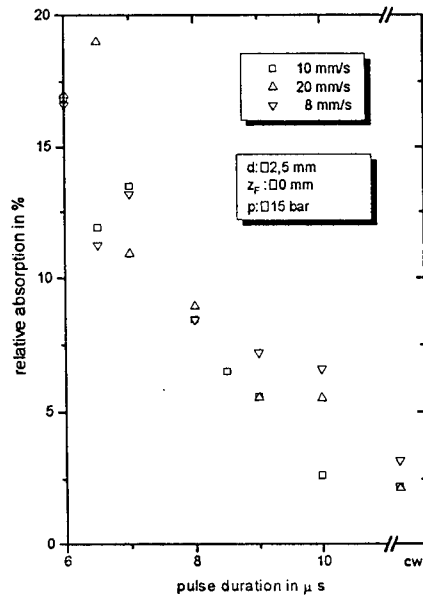


Fig. 3. Dependence of the rel. absorption on pulse duration for different rates of feed

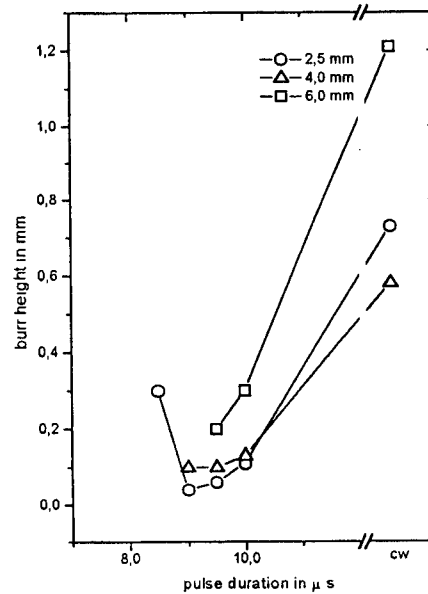


Fig. 4. Dependence of burr height on pulse duration for different sheet thicknesses

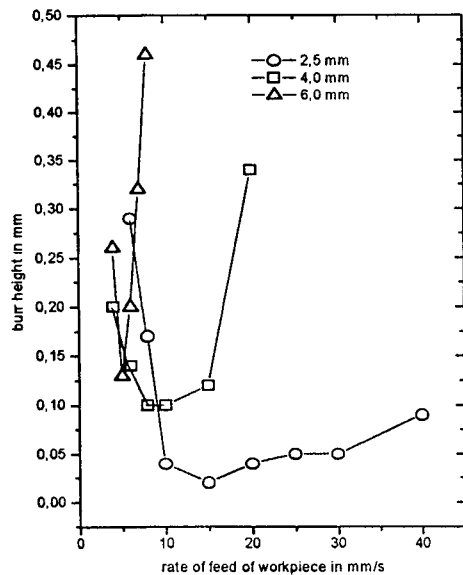


Fig. 5. Dependence of burr height on rate of feed for different sheet thicknesses

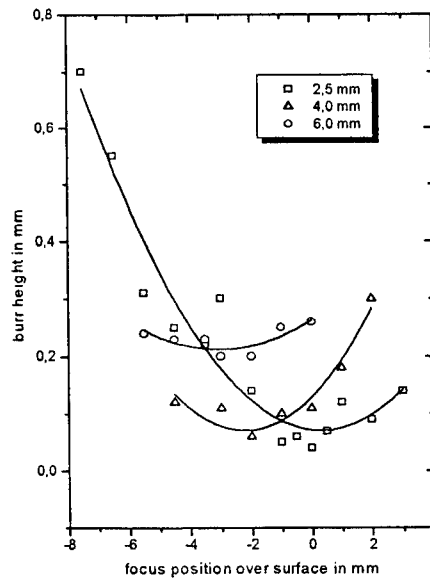


Fig. 6. Dependence of burr height on focus position for different sheet thicknesses

whereas at lower rates of feed the influence of probably superheating or gas flow instabilities become noticeable. The focus position should lie in the middle of the sheet, see Fig. 6. If the focus position is aligned too high, the kerf surface becomes more and more grainy because the surface oxidizes due to an increased admixture of oxygen to the inert process gas. The kerf reaches a minimum dimension if the beam waste is positioned to the middle of the sheet. With these experimental results it is possible to choose an optimized set of parameters for a given sheet thickness and to stabilize the quality of the cut by controlling the absorption of the surface plasma.

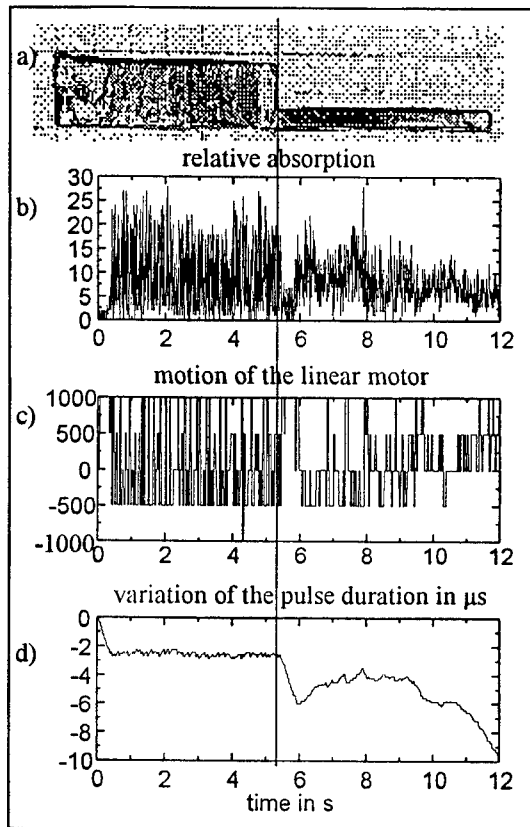


Fig. 7a-d visualizes the result of a controlled cut of a sheet having a step, whereby the thickness decreases from 8 mm to 2,5 mm. On the left side of Fig. 7a the cutting process starts uncontrolled. The relative absorption is comparatively low. At $t=0$ s a trigger starts the feedback system, see Fig. 7b. Because the absorption set point is fixed to 10%, the feedback system detects an actual absorption signal, which is too low. Therefore the pulse duration is decreased until the averaged absorption signal reaches 10%, see Fig. 7b+d. When the step is reached, there is a sudden decrease of the actual absorption, so that the feedback system reacts by reducing the pulse duration in order to hold the absorption set point. Fig. 7c displays the motion of the linear motor. A positive number of steps means a displacement of the chopper wheel into the CO_2 laser beam to decrease the pulse duration. A negative number of steps means a displacement out of the beam, respectively. The rate of feed of the workpiece is $v=4\text{mm/s}$.

Fig. 7 a-d: The quality control system cutting a step

5. ACKNOWLEDGEMENTS

The authors are indebted to the Deutsche Forschungsgemeinschaft for supporting our work by a grant.

6. REFERENCES

- [1] U. Bielesch, M. Budde, M. Fischbach, B. Freisinger, J.H. Schäfer, J. Uhlenbusch, W. Viöl, 9th Int. Symp. On Gas Flow and Chemical Lasers, Proc. SPIE 1810, 1992, 57-60
- [2] U. Bielesch, S. Klein, M. Napp, J.H. Schäfer, J. Uhlenbusch, *Recent Developments in Metal Processing with Pulsed Laser Technology*, in press, Appl. Surface Science 1996
- [3] M. Fischbach, A. Michaelis, J. Uhlenbusch, W. Viöl, Proc. 5th Int. Symp. on Laser-Aided Plasma Diagnostics, Konferenzen des Forschungszentrums Jülich 9, 1991, 86-91
- [4] E. Heidecker, J.H. Schäfer, J. Uhlenbusch, W. Viöl, J. Appl. Phys. 64, 1988, 2291-2297
- [5] U. Bielesch, J.H. Schäfer, J. Uhlenbusch, W. Viöl, ECLAT Bremen, 1994

Some applications of the powerful CO₂-lasers.

F.K.Kosyrev, A.G.Krasjukov, V.G.Naumov, A.V.Rodin

Troitsk Institute for Innovation and Fusion Research (TRINITI)
Troitsk, Moscow Reg. 142092, Russia

ABSTRACT

It is known that comparatively small beam divergence and sufficiently high beam intensity of CO₂ lasers give possibility of their application in various technological processes, that demand distant interaction. The results of some technological applications of continuous wave (CW) and high repetition rate (HRR) CO₂-lasers with average power up to 50 kW are presented. It is shown that these lasers can be used in the field of nuclear power.

Keywords: CO₂-laser, laser cutting, laser welding, laser treatment of the concrete.

1. HIGH-POWER CO₂-LASERS FOR TECHNOLOGICAL APPLICATIONS.

The TRINITI devotes much effort to scientific and engineering studies of low-temperature plasma that have resulted in creation of the fast-flow gas discharge lasers. The first soviet technological CW CO₂-laser LT-1 produced up to 5 kW of the output power. This laser has been commercially available since 1989 and successfully applicable in more than 10 different industrial fields. The parameters of the family of these lasers are shown in Table 1.¹

Table 1

	LT1-2	LT1-3m
Max. output power, kW	5.5	9
Cavity type	unstable	unstable
Output spot pattern	ring	ring
Beam divergence, rad	0.6-1·10 ⁻³	1·10 ⁻³
Gas mixture N ₂ :CO ₂ :He	9:1:6	
Operation mode	continuous or pulse-periodic	continuous
Size, m	2.2 x 4.2 x 3.5	

They feature a triple mixture circulation through the entire loop, active-medium low pressure (30-60 Torr) and resonator alignment with the discharge area. Lasers with a closed loop have a decrease in output power because of changes in mixture composition due to chemical processes. The solution to this problem resides in partial renovation of the working gas mixture (0.5-1%) or in addition of stabilizing substances to the laser mixture. The best experimental results were obtained with the additive: 1.7% CO₂ + 1.4% H₂.

Table 2

PARAMETERS	Gas mixture	
	CO ₂ - N ₂ - He 0.06 : 1 : 0.5	CO ₂ - air 0.05 : 1
Output radiation power, kW	50	35
Electrooptical efficiency %	10 - 12	6 - 9
Gas pressure in the discharge chamber, mmHg	50 - 120	30 - 80
Radiation divergence, 10 ⁻³ rad	0.5 - 1.0	0.5 - 1.0

There are also two open-cycle fast-flow pilot industrial CO₂-lasers with average power of about 50 kW in TRINITI, namely CW CO₂-laser pumped by self-sustained discharge and high repetition rate CO₂-laser pumped by e-beam controlled discharge. The main parameters of these lasers are shown in Tables 2-3.²

Table 3

PARAMETERS	Gas mixture	
	CO ₂ - N ₂ - He 1 : 6 : 3	CO ₂ - N ₂ - H ₂ O 1 : 9 : 0.06
Output radiation power, kW	50	40
Electrooptical efficiency, %	13	10
Gas pressure in the discharge chamber, mmHg	760	760
Radiation divergence, 10 ⁻³ rad	0.5 - 1.0	0.5 - 1.0
Pulse duration, μs	50 - 100	50 - 100
Pulse repetition rate, Hz	100	100

2. LASER CUTTING

Here are some possible examples on the powerful laser application. Available applications of the powerful lasers described above are mainly based on three technological processes, including cutting, welding and surface treatment.³

The advantages of laser cutting were the following: the opportunity of the remote interaction, the opportunity of cutting the bulky construction, high quality of cut surface, high cutting speed and the minimum zone of the thermal influence.

Critical cutting thickness depends not only on laser beam power but also on the cutting beam velocity. The plot shown in Fig.1 represents dependence of the thickness of a steel plate to cut on the cutting velocity for the laser average power of 25 kW. In the cutting technology in question, an additional gas flow (N₂, Ar or He) is used to increase a cutting efficiency due to removal of a molten metal. As to dependence of the maximum cut thickness on the laser beam power, one may roughly estimate the maximum thickness in mm as a half of the beam power above 5 kW and cutting velocity about 1.5-2 m/min.

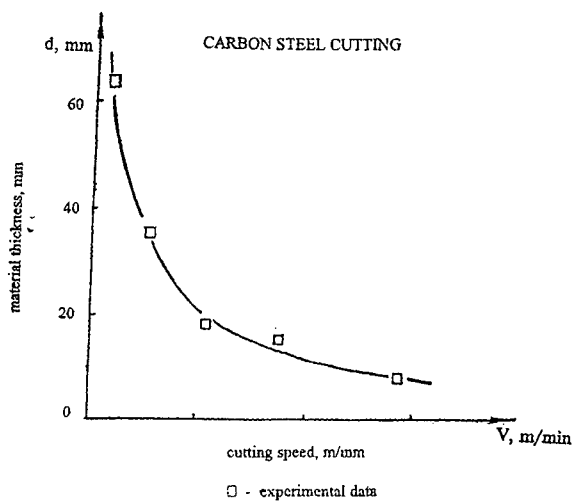


Fig. 1 Dependence of the material thickness d on the cutting speed V

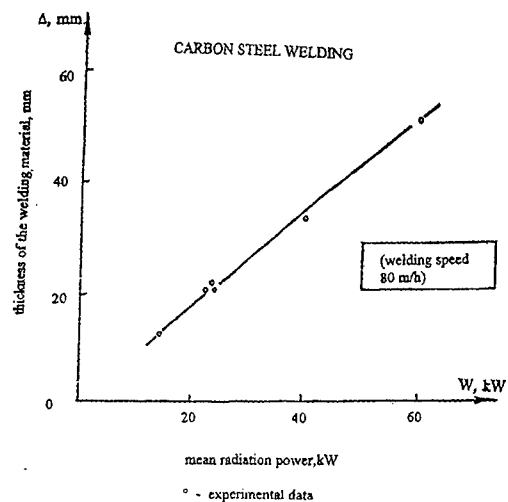


Fig. 2 Dependence of the thickness of the welding material Δ on the mean radiation power W .

We have also carried out experiments on distant remote cutting of pipeline components made of a stainless steel with the diameter of 80 mm and wall thickness of 4 mm typical for atomic power plant. Using the 30 kW CW laser we were able to cut the pipe at the rate of 0.6 m/min with external inert gas flow without the tube rotation.

The investigations of the possibility of laser cutting of used reactor fuel were made because the remote mechanical cutting is rather complicated and has a low lifetime. The experimental setup was built in radiochemical department of Radium institute. This setup consists of LT-1 laser, compartment for cutting with positioning system, system for analyzing of volatile products and aerosols, beam delivery and adjustment system. Three used fuel elements were exposed to laser cutting. Their weights were 126, 115 and 132 g and lengths were 235, 218 and 242 mm. 16 cuts on the first fuel element and 10 cuts on the second and third were made. For used fuel elements the main parameters of laser cutting irradiated heat-generating elements WWER-365 with burning out 11600 MW days/T and exposition of about 3 years are shown in Table 4.

Table 4

Diameter of heat-generating element	9.1 mm
Rotation speed	3 revs/s
Technological gases consumption	3 l/s
Laser radiation power	3 kW
Time of one cut	≤1.5 s
Cut width	≤0.9 mm
Conversion of material into melt	~0.35 g/cut
Conversion of material into aerosol	~1.5 g/cut
Gas output by laser opening	~3 %
Aerosol concentration	~50 g/m ³
Specific activity of gaseous phase	~5.10-2 Ci/m ³

3. LASER WELDING

Laser welding has several advantages over commonly used welding techniques: the welding is done by only one pass without additional edge treatment, high welding speed, minimum zone of the thermal influence, absence of the weld strength and the increasing of the weld corrosion resistance.

Critical welding thickness of a carbon steel versus average laser beam power is shown in Fig.2. The dependence is close to a linear one. We have also welded a stainless plate with the thickness of 20 mm with a laser beam of 25 kW.

The main parameters of laser welding of holders of safety system of RBMK reactors as well as argon shielded arc welding are shown in Table 5.

Table 5

Welding parameters	Laser welding	Ar-arc welding
Beam (arc) power, kW	3	6
Welding velocity, m/hr	90	12.5
Welding time, s	6.2	140
Protective gas consumption, l/weld	3.1 (He)	64 (Ar)
Electric energy consumption, k Whr/weld	0.05	0.23

The welding pool has a form of a "flute", wide near the surface and narrow near the bottom. The welding depth was about 3.5-4 mm. Testing showed that the joint strength in the case of laser welding is not less then in the case of arc-welding. The laser welded joint satisfies the requirements of exploitation. 440 articles for atomic power plant were welded with the use of our technology. All these articles were tested and used on the Ingalsinskaya atomic power plant.

During number of years joint efforts of specialists of TRINITI and one of the shipbuilding plants were directed on the development of the technology of pipe welding in pipe lattices of Ti-alloy heat exchangers. The main requirements of the process are high degree of reliability and hence necessity of achieving of welding depth 4 mm in the case of pipe wall thickness 1 mm. Using all our experience and making experiments on welding special samples we succeeded in developing the technology fitting all necessary requirements.

4. LASER TREATMENT OF THE CONCRETE

The removing of surface layers of concrete with the thickness of 5-10 mm was made by the pulsed beam. Laser beam pulsed power density was varied between 10^5 and 10^6 W/cm² at the pulse duration of 40 μ s and at the repetition rate of 100 Hz. As you can see (Table 6), there exists the mode when efficient concrete surface shelling and falling off occur. The surface destruction depth is proportional to the number of laser pulses, it reaches 8 mm when the number of pulses is about 200. This means that the process can be efficiently used to deactivate rooms in the course of dismantling and emergency works at nuclear power plants.

Table 6

Laser radiation power density, W/cm ²		EFFECT OF INTERACTION
Average	In pulse	
$< 10^3$	$< 2 \cdot 10^5$	The essential change of the surface properties is not observed
$(1.5 - 3.0) \cdot 10^3$	$(3 - 6) \cdot 10^5$	Destruction of the concrete surface is observed. The destruction depth is proportional to the number of radiation pulses
$> 5 \cdot 10^3$	$> 10^6$	The concrete melting with the glass like layer appearing is observed.

5. CONCLUSION

The results of the investigations allow to conclude that powerful CW and HRR CO₂-lasers can be used in different industries including atomic industry.

6. ACKNOWLEDGMENTS

The materials presented appeared as the result of the activities of large group of specialists from TRINITI. The authors wish to thank all participants of this work.

7. REFERENCES

1. F.K.Kosyrev, N.P.Kosyreva, A.P.Leonov, V.A.Timofeev, "LT1-2 5 kW commercial process laser unit", *Avtomaticheskaya Svarka*, № 10, pp.51-52, 1978.
2. V.G.Naumov, A.V.Rodin, "Physics of low temperature plasma and CO₂-laser with average power up to 50 kW for industrial application", *Proc. of Int. Conf. on Laser'94*, Quebec, Canada, pp.171-175, 1994.
3. V.G.Naumov, R.A.Dmiterko et al., "CO₂-lasers with average power up to 50 kW and their industrial applications", *Proc. of Sov.-Amer. Symposium "Research, technology and trade"*, San Francisco, USA, pp.21-25, 1991.

Studies of high average power pulsed CO₂-laser-radiation -material interaction phenomena

M. Hugenschmidt, R. Schmitt

German-French Research Institute Saint-Louis
5, rue du Général-Cassagnou; P.O. box 34
F-68301 Saint-Louis CEDEX, France

ABSTRACT

Basic laser processes involved in high average power laser target interaction include nonlinear optical effects. Energy transfer rates are largely influenced by surface induced plasma phenomena. Current investigations are related to plasma enhanced energy coupling mechanisms by using repetitively pulsed CO₂-laser radiation. The laser system, presently available at ISL, provides bursts of pulses with energies of 20 to 30 J/pulse. Repetition rates can be set arbitrarily up to 100 pps. Peak powers of the individual pulses in the multi-MW-range are attained with average powers, determined by the repetition rate up to 3 kW. According to the type of material under investigation, the required power densities have been adapted by suitably chosen focussing conditions. Experimental results are reported and discussed concerning the behaviour of various target materials. Emphasis was put on the study both of dielectric and semiconducting materials. A few examples have been chosen which are of common technical interest for laser protective devices in an industrial environment or in other fields of high power-density laser applications.

Keywords: High power lasers, laser-target interaction, laser induced plasmas, laser generated mechanical stresses, high speed photography, laser diagnostics, shadowgraphy, interferometry.

1. INTRODUCTION

In order to achieve efficient energy transfer in laser beam target interaction, laser beam parameters have to be optimized and adapted to the material dependent requirements. Laser characteristics include the overall power or energy capability to be extracted, the emission wavelength, as well as the maximum achievable energy densities or power densities, respectively in any target plane. In the mid-infrared spectral range considered, most dielectric materials, even those with high transparency in the visible, are optically opaque. In contrast to metals, these materials are strongly absorbing in most cases and only partially reflecting the incident radiation. Optical transparencies of this type are therefore frequently termed "out of band"-materials with respect to the infrared laser-wavelengths. Typical penetration depths are of the order of several tens of μm . In contrast, so-called "in-band"- materials (optical components for the visible or infrared spectral ranges or optronical devices) are characterized by high transparencies at the considered wavelengths. A few examples of this class of materials shall be considered as well. Process optimization for the given wavelength (10.6 μm) was shown in the past to be achievable by temporally modulating the radiation and by adapting power and repetition rates, correspondingly the ratios of peak power densities to average power densities, to the special type of target.

2. BASIC PHYSICAL PROCESSES

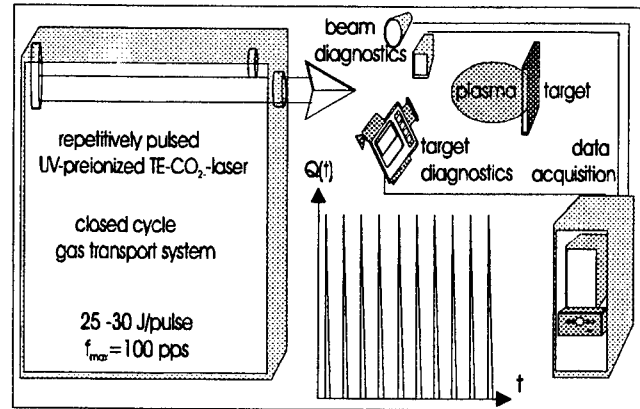
The heating rates of any type of material are determined by absorbed power densities or energy densities, respectively. An increase of incident flux conditions provides faster thermal target response^{1, 2}. Quasi-explosively developing plasma processes are observed at intensities typically above the multi-MW- to GW-range which are easily achievable, even with current, commercially available pulsed lasers. Plasma ignition thresholds depend both on laser wavelengths and material characteristics. Below „cut-off“- electron densities ($n_{\text{ec}} \approx 10^{19} \text{ cm}^{-3}$ at 10.6 μm) increased thermal coupling is provided by largely thermalizing the incident radiation with electron temperatures of the order of 20 000 to 40 000 K, as small-scale measurements have revealed under similar flux and fluence conditions

Additionally mechanical effects have to be taken into account. They are rapidly built up, even in the lower fluence range due to thermomechanically induced processes. At power densities above plasma ignition threshold, further contributions are provided by absorption wave induced mechanical shocks of the so-called LSC- or LSD-type^{3, 4}. If sufficient laser energy is provided to achieve surface temperatures above the transformation temperatures or vaporization temperatures, respectively, recoil momenta due to the ejection of material are additionally acting mechanically on the bulk of any material.

3. EXPERIMENTAL SET UP AND DIAGNOSTICS

The experimental set-up is shown schematically in fig.1. Laser beam diagnostics include simultaneous measurements of energies and temporal pulse shapes, both of single pulses and bursts of arbitrary lengths. The various diagnostics methods used for studying the plasma controlled thermal and mechanical effects on targets are not shown explicitly. Special schemes for this purpose were developed in the past and have been currently used in the meantime. Visualization has been obtained by using fast streak or framing cameras and image converters, as well as by applying various laser diagnostic optical methods (photographic and videographic imaging).

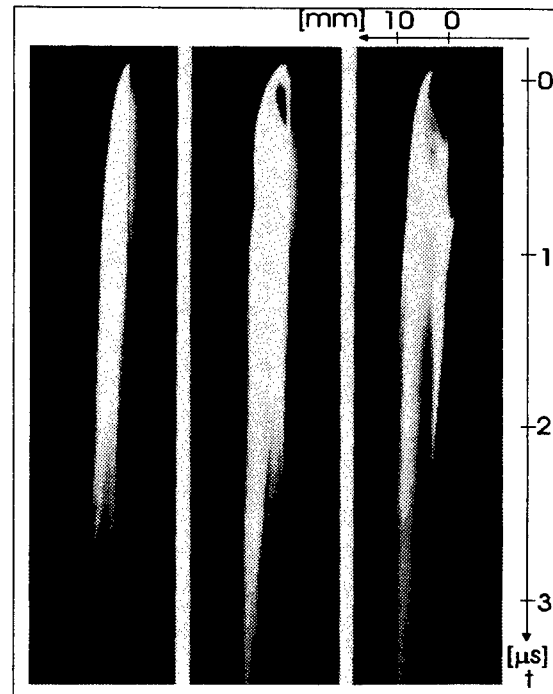
Figure 1. Experimental set-up



3.1 High-speed photographic recording

Recordings of this type provide the necessary information on thermodynamic plasma parameters, established after the ignition of absorption waves, during their fast expansion and subsequent decay. Three rotating mirror streak camera recordings of absorption wave plasmas, induced by CO₂-laser pulses on quartz windows are shown as a first example in fig. 2. Fluences, above the plasma ignition threshold, in a range of several tens of J/cm², are stepwise increasing from left to right. Efficient energy transfer both requires plasmas to be optically thin and not to be detached from the surface. This last stringent condition is violated in the case of the highest of the three fluences shown. There, breakdown already occurs in front of the target in the surrounding air. From the ignition center, two plasma fronts are then seen to propagate in opposite directions, one towards the incident laser beam and the other one towards the target surface which is only reached after a considerable lack of time.

Figure 2. CO₂-laser induced plasmas on quartz windows



3.2 Laser diagnostic techniques

The basic interest in the present investigations has been in studying dielectric materials (transparent in the visible, opaque in the infrared) by using various optical diagnostic methods. An interesting result, referring to plexiglass (PMMA) windows, is shown in fig. 3. A properly synchronized frequency doubled Nd-laser has been used as a light source for shadowgraphic recordings. Due to the transparency of PMMA, simultaneous information is provided by this method both on plasma effects in the surrounding air (ignition, expansion velocity, opacity) and on acoustic waves and shockwaves inside the target. Further results for polycarbonate (PC), see fig. 4 were obtained with a slightly modified experimental set-up, comprising additionally two crossed polarizers. This polarizational-optical method allows for direct visualization of thermo-mechanical stresses inside the PC, suitable for subsequent quantitative evaluation with nanosecond temporal resolution half-widths (15 to 20 ns) of the diagnostic laser pulses. Excellent spatial resolution has been obtained as well in spite of the rather poor optical quality of the PC-samples. Further results, for a few specific materials and laser irradiation conditions, have been worked out recently by M. Althaus⁵. These measurements were aimed at determining spatial distributions and temporal developments of electron temperatures and electron densities inside surface induced plasmas by means of spectroscopic and interferometric methods.

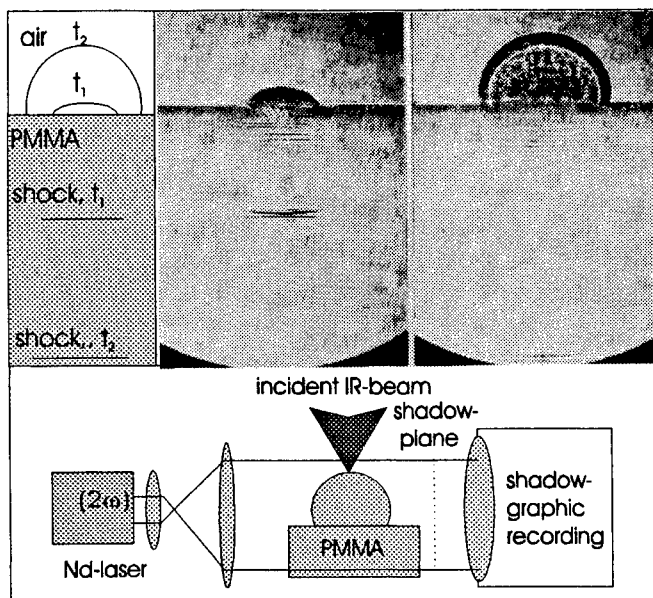


Figure 3. CO₂-laser impact on PMMA, plasma ignition and mechanical compression waves formation

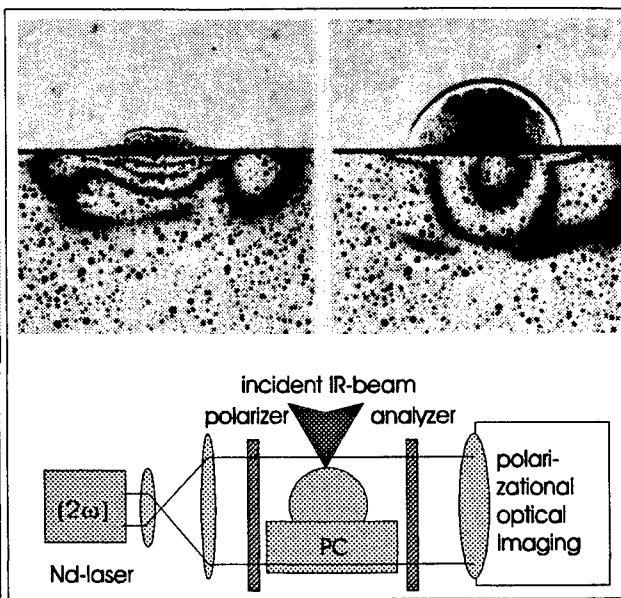


Figure 4. CO₂-laser impact on polycarbonate, visualization of external plasmas and internal mechanical stresses

4. REPETITIVELY PULSED TARGET EFFECTS

It has to be stated that plasma controlled energy transfer in the mode at high repetition rates cannot be understood without a detailed knowledge of the above-mentioned single pulse effects. In fact, basically similar processes are occurring repeatedly, allowing an accumulation and transfer of large amounts of laser energy at high average power levels. Depending on repetition rates, on time constants and/or relaxation times during interaction, the total energy consists of the sum of the individual pulse contributions. To demonstrate some different possible target responses, two materials under various experimental conditions shall be discussed briefly in the following.

As a first example, damage effects of plastic windows (PMMA), subject to high average power density pulse trains are shown in Fig. 5. For pulse trains, fast heating and quasi-explosive boiling, resulting in fast structural changes of transparencies, are observed at lower fluences than in the single pulsed mode (which are typically of the order of 4 to 5 J/cm²). The optical quality of such types of plastic components (windows, filters, lenses) is strongly affected. The transmission losses are caused by rapid thermal outgassing close underneath the surface (in a skin layer corresponding to the penetration depth of the laser radiation) within a few tens of nanoseconds. Due to the fast heating and cooling, resulting bubbles cannot escape from the highly viscous surface. Different mechanisms, however, are responsible for other dielectrics transparencies, such as for glass, quartz or other optical substrates. Thermally induced stresses and subsequent surface microcracks are building rapidly up in these cases, resulting in the observed roughness and changes of the modulation transfer function. For visualization, an interferometric method has been set up and used which yields information, both on damage threshold intensities and on spatial frequency dependent optical contrast variations. The interferograms of the PMMA-samples in Fig. 5 reveal the losses, induced even by short bursts of five pulses only, at rather low fluences below 2.5 J/cm², as well as the dependency on the repetition rate. For comparison, an interferogram prior to the impact has been included.

- The second example chosen gives the response of infrared transparent materials. In this "in-band"-case, energy deposition occurs inside the volume. Some results, concerning germanium shall briefly be discussed. Fig. 6 shows two photographs of effects which have been induced by bursts of 16 and 32 pulses at repetition rates of 100 pps and fluences of 44 J/cm² per pulse which is above the surface plasma ignition threshold. A slight increase of the surface roughness is even provided by single pulses at these fluence levels. Noticeably stronger deteriorations, however, are found by increasing the number of pulses, as can be seen for the two pulse trains in the upper part and lower part of fig. 6. Even the shorter pulse train induced degradation would be capable of introducing strong scattering losses, if these materials were used in an IR-optical measuring device or imaging system. For longer bursts, the thermo-mechanical stresses are rapidly leading to an increased crack formation and to macroscopic fragmentation of the samples, as shown in Fig. 6.

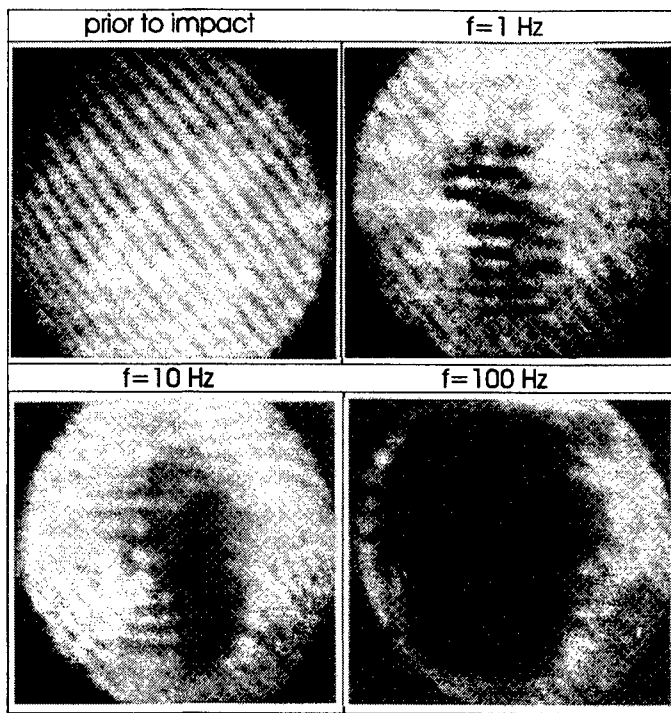


Figure 5. laser induced transparency changes of PMMA
5 pulses, 22 J/pulse, 2.5 J/cm², 1 / 10 / 100 pps

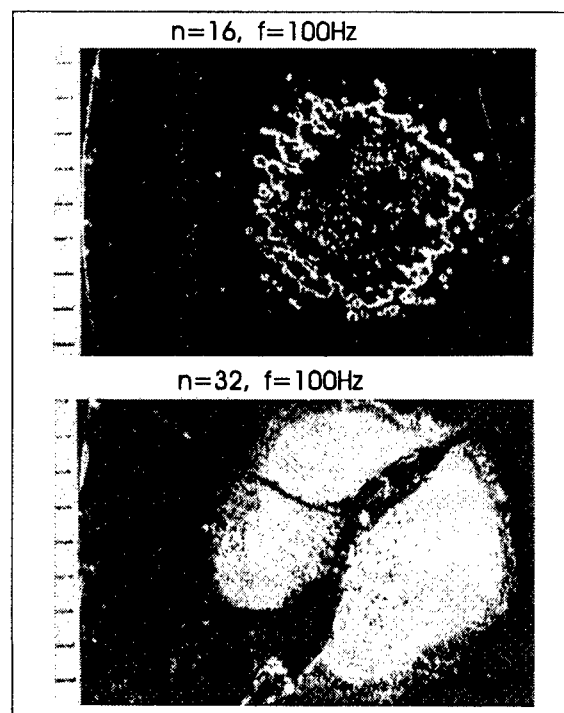


Figure 6. laser induced transparency changes of Ge
16 / 32 pulses, 22 J/pulse, 44 J/cm², 100 pps

5. CONCLUDING REMARKS

The experiments performed at ISL give a valuable insight into the physics of the transient processes of pulsed laser target interaction, both on surface effects in case of opaque ("out-of band")-materials and on volume effects for ("in-band") transparent materials. For most plastics, strong degradations of optical qualities are generated by fluences down to a few J/cm², causing transmission losses, if used in optical systems or windows. Different mechanisms were found responsible for infrared materials such as Ge, ZnSe, MgF₂ which are frequently used in high power lasers, in laser diagnostic systems or in optronic imaging devices. Specific results were given for Ge. The few examples discussed, reveal the interest and the importance for many fields of industrial, medical and defense related laser applications.

6. ACKNOWLEDGMENTS

The authors gratefully acknowledge the support of the work by German and French government contracts, as well as the help given by W. Baca, L. Geiss and E. Stechele in carrying out experiments and in discussing results.

7. REFERENCES

1. C. R. Phipps, R. W. Dreyfus, "The high laser irradiance regime, laser ablation and plasma formation" in Laser Ionization and Mass Analysis, edited by Akos Vertes et al., Chem. Analysis Series, 124, pp. 369, (1993)
2. M. Hugenschmidt, R. Schmitt, "Pulsed laser-target effects and high resolution process diagnostics", Optical and Quantum Electronics, special issue, vol. 27, pp. 1231, (1995)
3. M. Hugenschmidt, W. Baca, L. Geiss, E. Stechele, "Beeinflussung der optischen Eigenschaften transparenter Materialien durch IR-Hochenergie-Laserimpulse", ISL-report SR-917/93, (1993)
4. L. Marty, "Etude numérique et expérimentale d'une onde de choc induite par impact laser dans une cible solide" Thèse de doctorat, présentée à l'ENSMA de Poitiers, (1988)
5. M. Althaus, "Untersuchungen zu laserinduzierten Prozessen der Wechselwirkung zwischen IR-gepulster Laserstrahlung und Materie im Hinblick auf die Optimierung der Energieübertragung", ISL-report R 105/96, (1996)

J.P. Hayes, H.V. Snelling, D. Sands, A.G. Jenner and R.D. Greenough
Department of Applied Physics, University of Hull, Hull, U.K. HU6 7RX.

ABSTRACT

TEA CO₂ laser ablation deposition of iron and zirconium elemental layers has been investigated for the production of the FeZr magnetic system. Measurement of the individual deposition rates has allowed the production of bilayers on borosilicate glass substrates. The magnetic response and structure of these films has been measured using a vibrating sample magnetometer (VSM) and x-ray diffraction (XRD) respectively. Using a numerical heat flow model, the temperature profile within the layered system under laser irradiation has been calculated. Films heat treated in this way have shown significant changes in their magnetic behaviour.

1. INTRODUCTION

Magnetoelastic materials have been studied extensively over the years with the aim of exploiting their properties in devices^{1,2}. Magnetoelastic devices fall into either active or passive categories depending whether the magnetomechanical effect (k) or magnetostriction (λ) is utilised³. In crystalline materials, structural order imposes constraints both on the physical and magnetic characteristics of metals and alloys. However, the use of rapid quenching techniques has led to the synthesis of solids with disordered atomic structures whose properties, magnetic or material, are not dependent on the crystal structure. It is the unique combination of physical and magnetic properties found in amorphous materials that opens up the potential of sensor applications. In general, it has been demonstrated that the disordered state produces materials that can be mechanically robust (very high tensile strengths), and yet retain very soft magnetic properties (relative magnetic permeabilities of 100,000 have been quoted), have relatively high electrical resistances and a strong resistance to corrosion.

Work on the metal-metal system, Fe-Zr is presented here. In this alloy system, zirconium possesses a deep eutectic at the composition Fe₉₀Zr₁₀ and has been produced in amorphous form; as such it is used as an alternative glass former to the metalloid Boron. The fabrication of these field and stress sensitive materials, including processing to optimise their metallurgical structure and magnetic responses, in a form ready to use in devices is of great current interest.

2. EXPERIMENTAL DETAILS

A conventional TEA CO₂ laser ablation deposition system was used to irradiate metallic targets in the fluence range 25 - 65 J cm⁻² as described earlier⁴. In all the experiments presented here the substrates used were 12mm diameter borosilicate glass disks which were masked so as to produce 10mm diameter films. The thickness of films deposited from elemental targets of iron and zirconium was measured using a mechanical stylus instrument (DekTak) as a function of incident laser fluence for a fixed target to substrate separation of 15mm.

Layered or composite films were produced using one of three different targets. Firstly, a zirconium disk surrounded by a concentric ring of iron allowed deposition of one element followed by a layer of the other by simply repositioning the target under vacuum to give a different radius of laser irradiated track. In this way, and by reference to the deposition rate results, bilayer films of predicted ratio 9:1, Fe:Zr, were produced. Secondly, a target was manufactured of one half iron and one half zirconium so that during rotation Fe and Zr are alternately ablated. The deposition rate of both elements are such that less than one atomic monolayer is produced per revolution and therefore the resultant film cannot be thought of as a layered structure. Lastly, a third target was used in a similar way to the previous one with the proportion of Fe and Zr adjusted by area and deposition rate to give a 9:1 Fe:Zr non-layered film.

The laser deposited films were characterised in addition to thickness measurements by XRD for structure and magnetically by VSM. Post-production annealing was performed using the TEA CO₂ laser at normal incidence at fluence levels to be discussed in the next section in a background of helium at a pressure of 700 torr.

3. RESULTS AND DISCUSSION

The deposition rates for iron and zirconium are shown in figure (1). It can be seen that at this laser wavelength, the high reflectivity (Fe = 98%, Zr = 55%) results in incident fluences in excess of 40 J cm⁻² being required for film deposition over practicable timescales. At high laser fluence the surface quality of the films becomes poor due to a large number of droplets of target material. Subsequent layered and "mixed" films were produced using an incident laser

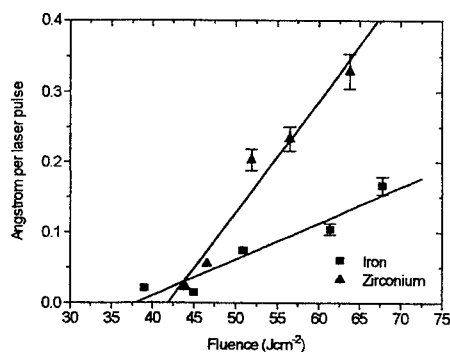


Figure 1. Deposition rates of iron and zirconium as a function of incident TEA CO₂ laser fluence for a target/substrate separation of 15mm and 10⁻⁵ mbar He.

fluence of 50 J cm⁻² which resulted in films of good surface quality in reasonable deposition times at a laser pulse repetition rate of 10Hz. X-ray diffraction studies of these elemental films shows a strong preferred texture along with some oxide phases possibly due to post-deposition oxidation (figure 2). For films deposited as bilayers (40nm Zr followed by 160nm Fe) a substantial reduction in the XRD signal was observed with only the α -Fe peak remaining (figure 3). Magnetic moment measurements (figure 3) indicate that this is not as a result of a large amount of the film

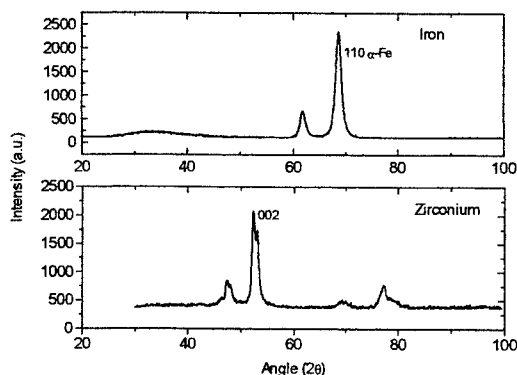


Figure 2. XRD measurement with a Cr source for elemental films (\approx 200nm) of Fe and Zr.

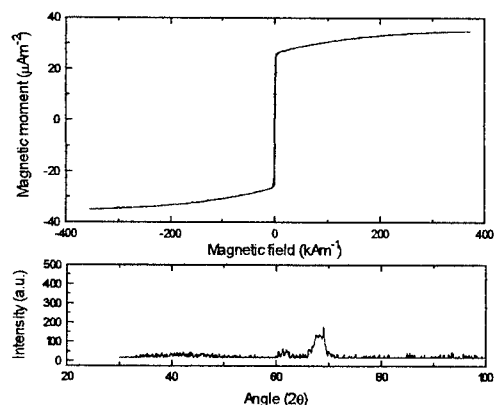


Figure 3. As deposited Fe/Zr bilayer. Upper graph shows VSM data, lower, XRD trace showing only reduced Fe structure

being amorphous as the expected resultant FeZr composition would be paramagnetic at room temperature and show no hysteresis⁵. The decrease in the peak height is more likely to result from finely dispersed crystallites⁶. The absence of both the Fe and Zr phases in the XRD result also indicates a degree of intermixing as is to be expected during the energetic deposition process.

The effect of laser heating on the mechanical and magnetic properties of the bilayer system was investigated. In order to calculate the laser irradiance required to cause a temperature rise approaching melting in both the iron and zirconium when bonded to a poor thermal conductor (the glass substrate) the following equations were solved numerically. Firstly, the heat diffusion equation

$$F = \frac{dQ}{dt} = -k \frac{dT}{dx} \quad (1)$$

where k is the thermal conductivity and also the continuity equation

$$\text{div} F + \alpha I_0 t e^{-\alpha x} = \rho C \frac{dT}{dt} \quad (2)$$

In this case C is the specific heat capacity, ρ is the density of the material and $\alpha I_0 t e^{-\alpha x}$ represents the exponential absorption of the laser irradiance I_0 for an absorption coefficient of α . The material properties were spatially dependent to allow for the bilayer structure and substrate. The laser irradiance terminates at $t=t_p$ where t_p is the laser pulse duration, in this case 90ns for the TEA CO₂ laser used. For each time interval Δt the temperature rise in an element $x + \Delta x$ was calculated. This element length must be sufficiently shorter than the thermal diffusion length during a time Δt for the assumption of an unperturbed temperature, which is implied in equation (1), over the time interval considered, to be valid. This criterion is ensured by the application of equation (3):

$$\Delta x = 0.2 \sqrt{\frac{k}{\rho C} \Delta t} \quad (3)$$

Typically, Δx is set to the order of 10nm. A typical calculated temperature profile at the end of the laser pulse is shown in figure(4). It can be seen that although the thermal properties of iron and zirconium differ from each other the temperature gradient is very small. This is as a result of the poor thermal conductivity of the substrate and is only seen to become appreciably sloped for total film thicknesses in excess of 300nm. By calculating sets of these curves as a function of absorbed laser fluence it was possible to generate a straight line fit for the surface temperature rise (figure 4)

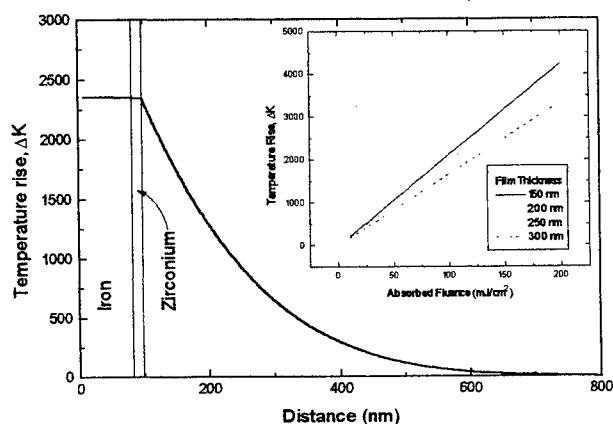


Figure 4. Calculated temperature profile for an absorbed fluence of 125 mJ and (inset) surface temperature rise.

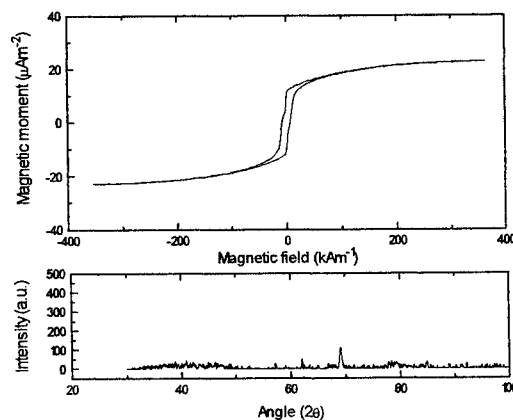


Figure 5. Post anneal VSM and XRD data for the sample shown in figure 3.

as a convenient way to find the required laser fluence for various thickness of samples.

The bilayer film was irradiated normal to the surface at an incident laser fluence of 3.4 Jcm^{-2} ($\approx 58 \text{ mJcm}^{-2}$ absorbed) giving a surface temperature of $\approx 1350\text{K}$. The laser beam was scanned manually so that the whole area of the film was covered. The resultant XRD and VSM data are shown in figure (5). There is a significant increase in the coercivity and a reduction in the magnetic moment. This is thought to be as a result of the addition of zirconium to iron as the iron-iron coupling will be reduced. A complete amorphous film is not generated as mixing due to solid state reaction is only expected to a thickness of 2nm ⁷. Films produced from the composite targets showed no structure under preliminary x-ray measurements and are the subject of further study.

4. CONCLUSIONS

Deposition rates for TEA CO_2 laser ablation deposition of iron and zirconium have been measured. Knowledge of these parameters has allowed the production of bilayer iron zirconium structures on glass substrates. X-ray diffraction studies of these films do not show a superposition of the elemental structure and it is thought that the energetic deposition process causes substantial intermixing at the interface. The predominance of the $\alpha\text{-Fe}$ peak is to be expected as the iron layer is four times thicker than the zirconium to achieve an average composition of $\text{Fe}_{90}\text{Zr}_{10}$. Laser heating of the films has been shown to modify their magnetic response and may be applied to "write" a magnetic structure during post deposition processing. Production of amorphous FeZr will require the production of thinner layers ($\sim 2\text{nm}$) in a multilayer "stack" and is the subject of current study.

5. ACKNOWLEDGEMENTS

The authors would like to thank the EPSRC for financial support, Lumonics (Hull Operations) Ltd for the use of the laser and P.Wilson for preparation of the targets.

6. REFERENCES

1. F.Claeyssen, N.Lhermet and G.Grosso, "Giant magnetostrictive alloy actuators," *Magnetoelastic effects and applications*, L.Lanotte, 153-159, Elsevier science pubs, 1993.
2. H.T.Savage and M.Wan-Fogle, "Amorphous magnetoelastic materials," *Materials research society symposium proceedings*, **360**, 201-212, (1995)
3. C.Modelzelewski, H.T.Savage, L.T.Kabacoff and A.E.Clark, *IEEE Trans. Mag.* **19**(6), 2837, (1981)
4. J.P.Hayes, H.V.Snelling, A.G.Jenner, R.D.Greenough, "Thin magnetoelastic films prepared by pulsed TEA CO_2 laser ablation deposition," Accepted for publication, *Journal of magnetism and magnetic materials*.
5. J.H.Purdy, PhD Thesis, "The magnetic and magnetoelastic properties of amorphous rare earth metal metal alloys," University of Hull, (1992).
6. Yu.A.Bykovskii, V.M.Boyakov, V.T.Galochkin, A.S.Molchanov, I.N.Nikolaev and A.N.Oraevskii, "Deposition of metal, semiconductor, and oxide films with a periodically pulse CO_2 laser," *Sov. Phys. Tech. Phys.* **23**(5), 578-581, (1978).
7. W.Kiauka, W.Keume, T.Shinjo and N.Hosoito, "Mossbauer investigation of the magnetic properties of amorphous FeZr interface layers formed by solid state reaction," *J.Mag.Mat.*, **93**, 494-498, (1991).

Christophe PRAT *, †, Kazuo MAENO†, Michel AUTRIC*.
Hiroshi ASANUMA†, Hao DU†

† Chiba University - Department for Mechanical Engineering
Faculty of Engineering
1-33 Yayoi, Inage, Chiba #263, Japan.
tel : (81) 43 290 3220
fax : (81) 43 290 3039
e-mail : chris@shock.tn.chiba-u.ac.jp

*Institut de Recherche sur les Phenomenes Hors d'Equilibre
Laboratoire Laser, Plasma et Procédés Photoniques
Parc Scientifique et Technologique de Luminy
163, Avenue de Luminy-Case 918 - 13009 Marseille, France.
tel : (33) 91 26 92 83.
fax : (33) 91 26 92 89
e-mail : autric@mfmcalas.univ-mrs.fr

ABSTRACT

A composite material including optical fibers is submitted to the mechanical effects induced by a high-power CO₂ laser radiation in order to test its behaviour when undergoing repetitive stress. The experiments pointed out that such a new material could be used to monitor the stress to which it is submitted.

Keywords : high-power laser, interaction, shock-wave, composite material, smart material.

1. INTRODUCTION

Among the so-called "new- materials", the composites are now widely considered as some of the most promising. To the properties usually expected from these materials, such as mechanical resistance and lightness, for instance, one try to add the faculty to provide informations like a sensor. Then a sensitive element must be included in the composite as one of its components. The material used in our experiments is a aluminium matrix reinforced by SiC fibers embedded along with optical fibers. The process developed to make this material is thought to be safe for the optical fibers which do not suffer any damage neither to their structure nor to their optical properties¹. The composite is expected to be used as structural material as well as stress or damage detector, since the mechanical perturbations to which it is submitted, induce changes in the optical signal conveyed by the fibers. Bending test performed on this composite pointed out clearly, through the time-history of the loss in the optical fibers, the successive stages of damaging process of the sample.

Once fractured, the fibers still transmit light; cracks can then be made intentionally for the composite to be more sensitive to the stress. The optical properties of the interface of the fracture, however, is thought not to be constant, especially when undergoing repetitive stress. In the present study, the material is submitted to shock waves induced by a pulsed CO₂ laser. At intensity greater than 1 MW/cm², the irradiation of a solid material results in a mechanical effect (shock wave) due to the formation of a high temperature and high pressure plasma at the surface of the target².

The mechanical effect of laser radiation is used here to excite samples of the composite material in order to test the behaviour of fibers previously fractured.

2. EXPERIMENTS

The sample consists of single-mode SiO₂ optical fibers (diameter : 125 µm - Fujikura Co.Ltd.) embedded in a composite metallic matrix of aluminium. Fibers are placed in grooves made in an aluminium plate and then covered with a second plate and hot-pressed. The resulting composite is 2 mm thick (Figure 1).

As a matter of convenience only one fiber has been tested in each sample. In fact the fiber sticks out each side of the sample of few centimeters ; for the experiments it must be connected to longer fibers by means of glass capillaries and maintained by resin . One extremity of the fiber is connected to a stabilized light source (Ando - AQ 4141B - wavelength : 0.67 µm) and the second one to a photodiode.

Cracks can be induced in the fiber by stretching the sample or by indentation using a hardness tester. The latter one was chosen for the experiments presented here in so far as the stretching is known to induce irregular fracture . The transmission of the fiber is monitored during the process in order to ensure that it is broken (Figure 2).

The experiments have been performed using a pulsed-CO₂ laser (Lumonics 100-2) able to emit 8.6 J in a 17 μ s-pulses (duration during which 90% of the total energy is delivered)(Figure 3). This allowed the irradiation of the samples with an energy density of about 93 J/cm² to 260 J/cm². The radiation is focussed onto the sample by a ZnSe lens of 250 mm of focal-length. The energy is measured by a joulemeter (Gentec ED500).

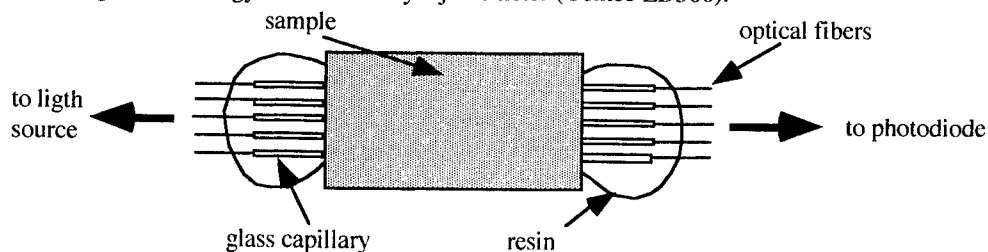


Figure 1 : composite sample connected to longer fiber by means of glass capillaries

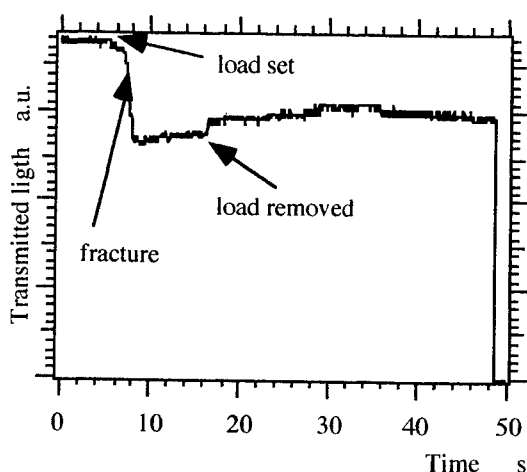


Figure 2 : Fracture of the fiber by indentation

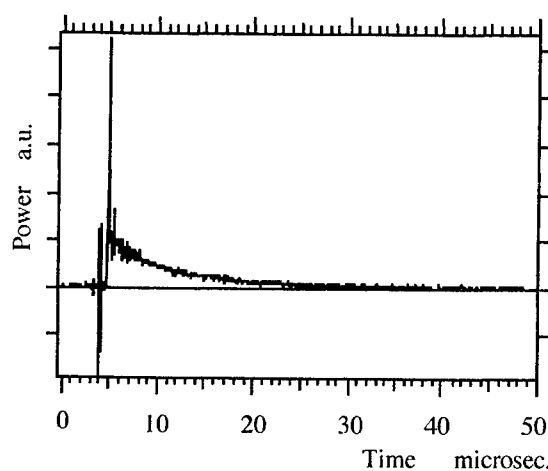


Figure 3 : Laser pulse shape. Peak duration 60 ns.

3. RESULTS AND COMMENTS

A typical series of tests is presented in figure 4. The peak of figure 4a has been obtained by irradiating a metallic screen placed just before the sample. This noise, picked up by the photodiode, is induced by the electric discharge in the laser and the plasma initiated in front of the screen. This is used as reference signal. The laser pulse is delivered at the beginning of this peak. Direct irradiation of the sample induces a loss in the transmission leading to a recess in the optical signal visible in figure 4b just after the peak. The reflectivity of aluminium at 10.6 μ m is known to be greater than 90 %. Then, in an attempt to enhance the signal, a polymer film has been pasted on the target in order to improve the absorption of the laser radiation and the mechanical effect. That leads to a permanent change of the transmission (Figure 4c).

Two main processes can be responsible for such a change. The relative displacement of the two parts of the fiber due to deformation of the surrounding metal is highly improbable since the laser-induced shock is far from the elasticity limit of the metal. A displacement is however possible if a gap remains around the fiber after the fabrication process. A new fracture of the fiber is also possible. Direct irradiation of fibers placed on a metallic plate pointed out that the fiber can hardly be broken that way. Indeed several laser shots do not induce any change in the transmission. Nevertheless in many cases the fiber or even the glass capillary broke at the limit of the resin used to maintain them. Vibrations propagate from the irradiated spot and result in shear stress at the boundary between the embedded part of the fiber and the free one. If a gap is left between the fiber and the metallic matrix, such stress may exist along the groove where the fiber is placed. Moreover, the indentation process may also initiate several cracks that could gradually stretch across the fiber on the expense of the transmission, when the sample is irradiated.

In addition to that, the stability of the connections with glass capillaries is also questionable. Indeed the vibrations propagating across the sample until its extremities can cause the fiber to move in the glass capillary. The inner diameter of the glass capillary, however, fit well the core of the fiber and when the laser irradiation is performed elsewhere than at the indentation point, no change in the transmission can be observed. Therefore the changes in the transmission are really induced in the sample. Moreover the response seems to depend on the location where the mechanical perturbation is applied.

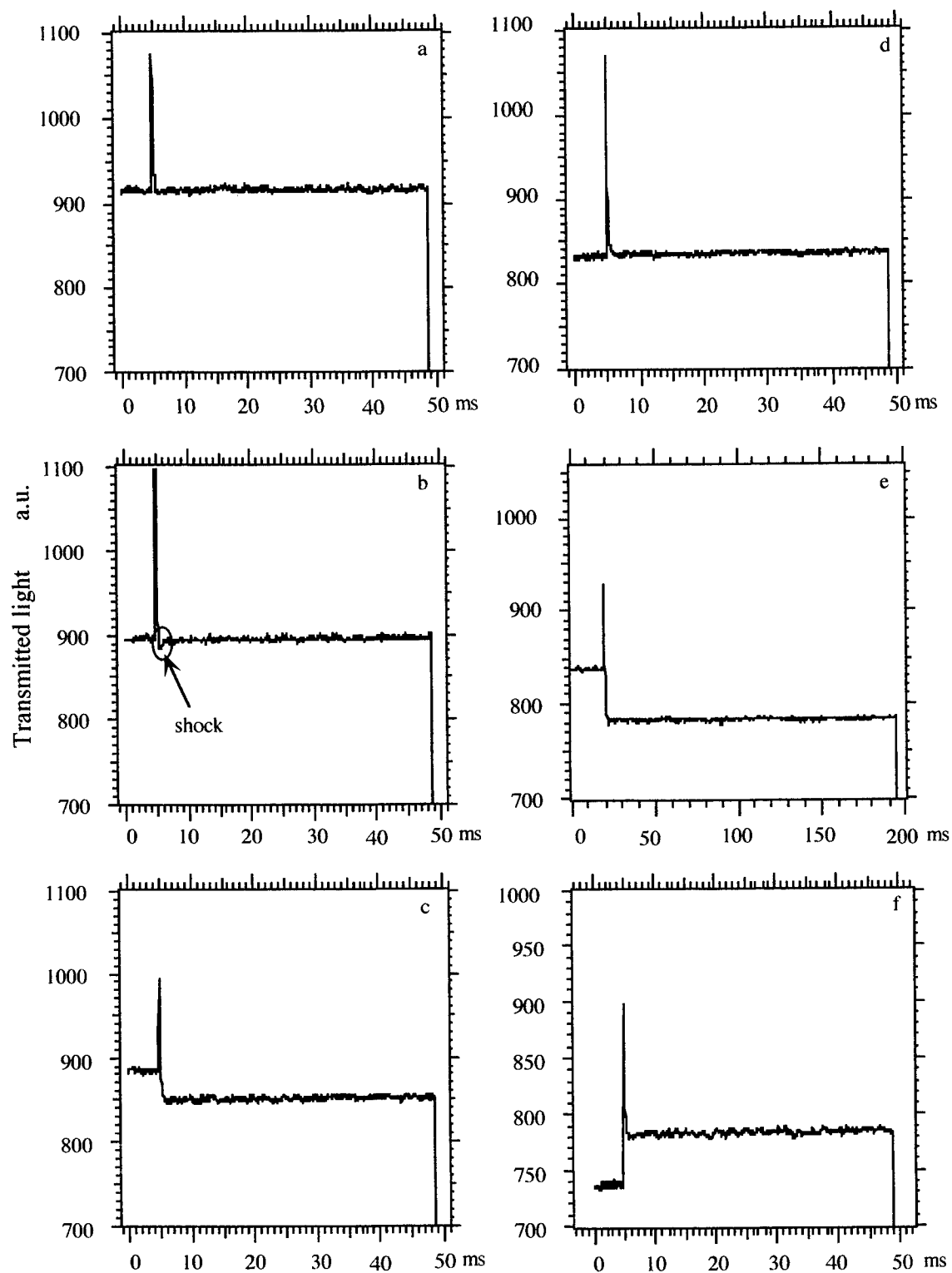


Figure 4 : Changes in the transmission of embedded optical fibers due to laser induced shock wave. a) noise, b) direct irradiation, c) irradiation with polymer film, d) direct irradiation, e) and f) irradiation with polymer film. Several laser shots have been done between e and f, inducing a step by step decrease in the signal.

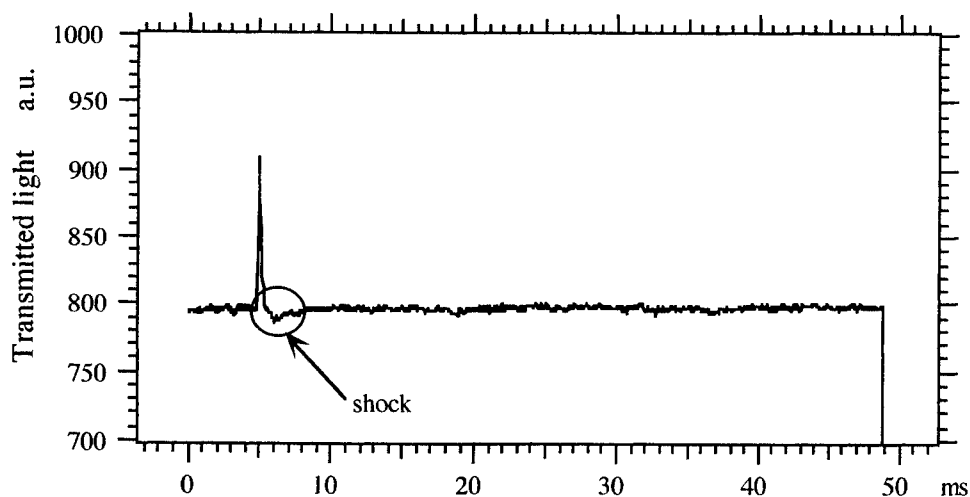


Figure 5 : Signal obtained subsequently to 4f by direct irradiation without polymer film.

After this first drop of the transmission the fiber seems not to be sensitive any more to the shock induced by a direct irradiation (Figure 4d) but to the stronger one obtained with polymer film (figure 4e). Looking at the figure 4f the hypothesis of the displacement of the fiber appears to be the most suitable since the cracks formation is irreversible. After several shots that makes the transmission of light to decrease step by step, it suddenly recovers a higher level. Further irradiation performed without any polymer film on the sample showed that the material is again sensitive to weak shocks (figure 5).

4. CONCLUSION

A new composite material has been tested by an original and flexible method using the mechanical effect induced by a high-power laser radiation. This technique allowed to excite the sample repetitively at a precise location and it pointed out that the material is sensitive to the shock applied at the location of the fracture of the fiber and not anywhere else. In addition it is possible to carry out the testing and to check continuously the optical signal transmitted through the fibers in order to detect long-term changes in the properties of the sample.

Since the material could withstand the stress (within a range that should be defined), it is reasonable to use it as a gauge being able to estimate the perturbations induced in the structure which it is included in. Moreover the optical diagnostics is known to be rather insensitive to the electro-magnetic noise in contrast with piezoelectric and piezoresistive pressure gauges. This advantage can be valuable for the measurement of laser-induced shock wave, in so far the plasma and the laser itself are known to be strong sources of noise.

5. ACKNOWLEDGMENTS

The authors are thankful to JSPS for supporting these studies and greatly appreciate the contribution of Fujikura Co. Ltd that offered the optical fibers.

6. REFERENCES

- 1) Asanuma H., Hirohashi M., Ichikawa K., Du Hao.
"Fabrication of fiber reinforced aluminium smart composites with optical fiber by the interphase forming/bonding method."
1995 North American Conference on Smart Structures and Materials, San Diego, February 1995.
- 2) Ch. Prat, J.E. Montagne et al.
High power laser radiation induced shock waves in solids.
Shock Waves in Condensed Matter and Heterogeneous Media. vol.III. p.255
R. Brun and L.Z. Demitrescu ed. Springer Verlag 1995.

Numerical simulation of viscous shock layer with carbon ablation : preparatory research works for future reentry experiment with high-power laser and target

Masato Funatsu*, Hiroyuki Shirai** and Koichi Kasuya*

**Department of Energy Sciences, Interdisciplinary Graduate School of Science and Engineering, Tokyo Institute of Technology,
4259 Nagatsuta-machi, Midori-ku, Yokohama, Kanagawa,
226 JAPAN*

***Department of Mechanical System Engineering, School of Engineering, Gunma University
1-5-1 Tenjin-cho, Kiryu, Gumma, 376 JAPAN*

Key Word : Carbon Ablation, Shock layer, Jupiter entry, Radiative heating, High enthalpy flow

ABSTRACT

This simulation included mass injection, radiative transfer, diffusion, and viscous effects. The radiations included were molecular bands, atomic lines, and continuum processes. It was found that carbon ablation materials were effective in reducing the radiative flux.

1.INTRODUCTION

If we can irradiate sample solid targets with high power lasers of a few kW level, fundamental ablation processes of space vehicles during the reentry can be clarified. From the point of view of doing this kind of experiment in the near future, we tried to make some numerical calculations in this field. The purpose of the current research work is to make clear the ablation processes which use high power lasers, to estimate the heat flux toward the target surfaces.

As a first step, we calculated the flow-field and surface response conditions of a planetary probe entering the Jupiter atmosphere. Within the region behind a detached shock wave, the blunt nose is heated to high temperature. So that, the numerical results were obtained under a viscous-shock-layer analysis. The shock layer temperature and pressure were 16000K and 0.5MPa, for example. To protect the probe against this high temperature condition and to reduce the heat flux, which includes convectional and radiative heat transfer, we used the ablation of C/C (Carbon/Carbon phenols) composite materials. Along the stream-line through the stagnation point, the probe was subjected to the most hostile environment. The shock layer must be handled to be chemically active plasmas. Radiative characteristics of carbon ablation layer were as follows¹;

The absorption coefficient of carbon plasmas was calculated for two cases of temperature of 5000 and 7000K, thickness from 0.0 to 7.5mm, pressures from 0.1 to 1.0MPa. The carbon plasmas were assumed to be isothermal and in local thermodynamic equilibrium. The radiations included were molecular bands, atomic lines, and continuum processes. The absorption coefficient thus calculated was applied to a simplified model of the ablation layer for Jupiter entry probe. It was found that the molecular carbon bands were effective in reducing the radiative flux to the vehicle at low ablation-layer temperature (5000K), while the photo-ionization process in atomic carbon was effective at high ablation layer temperature (7000K).

After the calculations mentioned above, a viscous-shock-layer analysis including carbon ablation was tried. In this analysis the shock boundary layer was thickened by the carbon ablation, and the distribution of temperature, chemical species and velocity depended on the carbon mass injection. It was also found that the carbon ablation materials were effective in reducing the convectional and radiative heat flux.

2.THEORY

We assumed a free-stream gas composition which is called as a nominal model with the volume ratio H_2/He of 85 / 15. A viscous-shock-layer was assumed to be in chemical equilibrium. In this work, a viscous-shock-layer analysis was tried to calculate the stagnation flow field for a condition near to the peak radiative heating of a entry

probe into Jovian atmosphere (Table.1). We considered chemical species,

$H_2, He, H, H^+, e^-, C, C_2, C_3, C_2H, C_3H, C_4H, C^+, C_s$. Here C_s was the solid carbon species.

The shock layer equations were derived from the governing equations for reacting gas mixtures and were written for a body oriented coordinate system as shown in Fig. 1. The viscous shock layer equations were obtained from the steady Navier-Stokes equations. These equations are shown below^{2,3},

Continuity Equation:

$$\frac{\partial}{\partial s} [(r + y \cos \phi) \rho u] + \frac{\partial}{\partial y} [(1 + \kappa y)(r + y \cos \phi) \rho u] = 0$$

S-moment Equation:

$$\begin{aligned} & \frac{1}{1 + \kappa y} \rho u \frac{\partial u}{\partial s} + \rho u \frac{\partial u}{\partial y} + \rho u v \frac{\kappa}{1 + \kappa y} + \frac{1}{1 + \kappa y} \frac{\partial P}{\partial s} \\ & = \varepsilon^2 \frac{\partial}{\partial y} \left[\mu \left(\frac{\partial u}{\partial y} - \frac{\kappa u}{1 + \kappa y} \right) \right] + \varepsilon^2 \mu \left(\frac{2\kappa}{1 + \kappa y} + \frac{\cos \phi}{r + y \cos \phi} \right) \left(\frac{\partial u}{\partial y} - \frac{\kappa u}{1 + \kappa y} \right) \end{aligned}$$

Y-moment Equation:

$$\frac{\partial P}{\partial y} = \frac{\kappa}{1 + \kappa y} \rho u^2$$

Energy Equation:

$$\begin{aligned} & \frac{1}{1 + \kappa y} \rho u C_p \frac{\partial T}{\partial s} + \rho v C_p \frac{\partial T}{\partial y} - \frac{1}{1 + \kappa y} u \frac{\partial P}{\partial s} - v \frac{\partial P}{\partial y} = \\ & \varepsilon^2 \frac{\partial}{\partial y} \left(k \frac{\partial T}{\partial y} \right) + \varepsilon^2 \left(\frac{\kappa}{1 + \kappa y} + \frac{\cos \phi}{r + y \cos \phi} \right) k \frac{\partial T}{\partial y} - \varepsilon^2 J_r C_p \frac{\partial T}{\partial y} + \varepsilon^2 \mu \left(\frac{\partial u}{\partial y} - \frac{\kappa u}{1 + \kappa y} \right)^2 \end{aligned}$$

Species Conservation Equation:

$$\rho \left(\frac{u}{1 + \kappa y} \frac{\partial \tilde{C}_i}{\partial s} + v \frac{\partial \tilde{C}_i}{\partial y} \right) = \frac{\varepsilon^2}{(1 + \kappa y)(r + y \cos \phi)} \left\{ \frac{\partial}{\partial y} \left[(1 + \kappa y)(r + y \cos \phi) \frac{\mu}{N_{sc}} \frac{\partial \tilde{C}_i}{\partial y} \right] \right\}$$

Here the parameter Q in the energy equation is the divergence of the radiative heat flux. The Navier-Stokes equations were nondimensionalized by variables with their shock values. The s-moment and the energy equation were transformed into the finite-difference equations. Therefore we obtained the tangential velocity component and temperature distribution. The pressure distribution was derived from integrated y-moment equation. The normal velocity distribution and shock stand off distance could be obtained by the integration of the continuity equation.

3. RADIATIVE CHARACTERISTICS OF THE HYDROGEN-CARBON PLASMAS^{1,4}

In general, the radiative and absorption characteristics have been discussed by the inherent radiative and absorption coefficients. The absorption coefficient was the function of the particle number density and absorption cross-section for chemical species in the gases.

In this work, the spectrum absorption coefficient with the viscous shock layer was taken into account as follows;

In hydrogen: bound - bound transition (b-b), free - bound transition (f-b), free - free transition (f-f), where b-b transition included 14 atomic hydrogen lines as Balmer, Lyman.

In carbon: b-b, f-b, f-f transition of carbon atoms, the seven band systems as Swan, Ballik-Ramsay of C_2 . Data for C_3 and C_2H are shown in Ref. 4.

4. RESULTS AND DISCUSSION

Fig. 2 and 3 shows the distribution of the shock layer mass fraction with and without carbon ablation. The horizontal axis is the distance Y normalized by the shock stand off distance Y_{sh} . The vertical axis is mass fraction

in a log scale. $Y/Y_{sh} = 0$ and 1 correspond to the probe wall and the shock wave locations. As is shown in Fig. 2, the carbon is blasted upward from the carbon ablation surface and the carbon ablation layer nearby the wall is formed. Therefore the thickness of the boundary layer increases and the layer has more effect on the physical variables.

Fig. 4 shows the distribution of the shock layer temperature. With the carbon ablation, the temperature is reduced immediately after the shock. The temperature difference of 2000K is calculated with and without the carbon ablation. As the temperature gradient nearby the wall is flat, the heat flux flow into the wall reduces because of the carbon absorption effect.

Fig. 5 shows the distribution of the shock layer normal speed. With the carbon ablation, the speed is reduced by the carbon injection effect nearby the wall. Therefore in the nearest region of the wall, the speeds indicates negative values.

Fig. 6 shows the absorption coefficient to the representative shock layer temperature ($T = 5000, 1000, 16000K$). The hydrogen Lyman lines are very bright. The distribution is dominated by the carbon species at low temperature. The contribution by the carbon species decreases as the temperature becomes high.

Fig. 7 shows the distribution of the radiative intensity at the INTERFACE and WALL for the stagnation point. Here the INTERFACE is the carbon ablation layer edge, the WALL is the probe wall, θ is the angle measured from normal (see Fig. 7). During the INTERFACE flux reached the probe wall, the flux was absorpt by C_2 Swan band system ($h\nu \cong 2-3[eV]$), C_3 UV band system ($h\nu \cong 8[eV]$) and photoionization of carbon atoms ($h\nu \geq 11[eV]$).

Fig. 8 shows the angular distribution of the radiative heat flux. The flux at the wall reduces about 60% compared with the INTERFACE at the angle of the maximum flux. And the total flux integrated by the angle reduces about 60% from the INTERFACE flux. Without carbon ablation, the flux at the wall reduced about 40% by the carbon ablation effect.

5.CONCLUDING REMARKS

- 1) The carbon ablation had influence on the distribution of the shock layer temperature, chemical species and speed.
- 2) The carbon ablation layer had very large absorption effect which depended on the carbon species.

- 3) The stagnation heat flux from the shock layer was reduced by the carbon ablation markedly.

6.REFERENCES

- 1.M. Funatsu, H. Shirai, "Radiative Characteristics of Carbon Ablation Layers," *Symposium on Flight Mechanics and Astrodynamics*, Tokyo, pp83-86, 1994.
- 2.E. W. Miner, C. H. Lewis, "Hypersonic Ionizing Air Viscous Shock-Layer Flows over Nonanalytic Blunt Bodies," *NASA CR-2550*, 1975.
- 3.J. N. Moss et al., "Viscous-Shock Layer Solutions with Radiation and Ablation Injection for Jovian Entry," *AIAA PAPER No.75-671*, 1975.
- 4.J. O. Arnold et al., "Line-By-Line Transport Calculations for Jupiter Entry Probes," *AIAA PAPER No. 79-1082*, 1979.

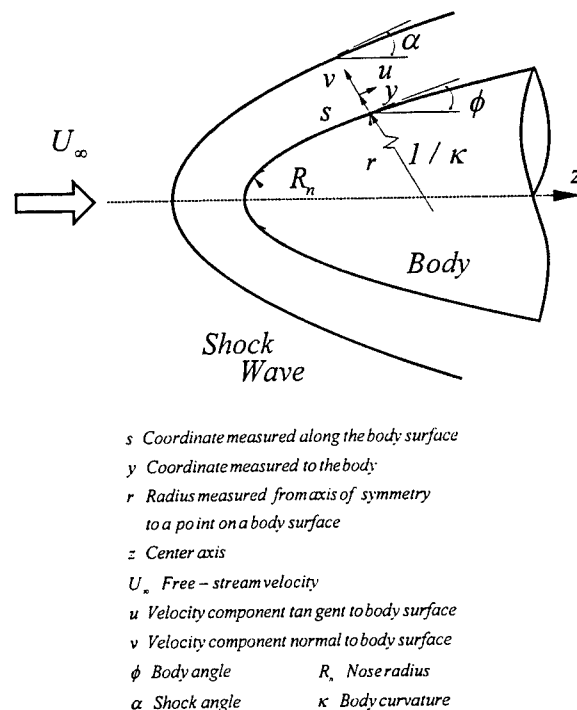


Fig. 1 Coordinate system

Table. 1 Free-stream condition

Altitude [km]	Temperature T_∞ [K]	Density ρ_∞ [kg / m ³]	Velocity U_∞ [km / sec]	Pressure P_∞ [MPa]
131.90	154.0	3.38E-04	41.16	1.875E-04

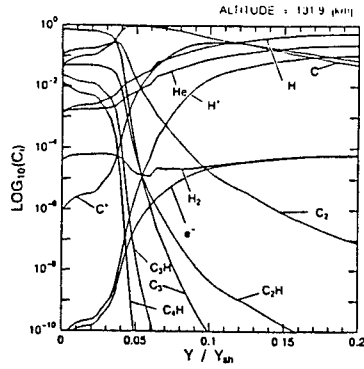


Fig. 2 The distribution of the shock layer mass fraction (nearby the wall)

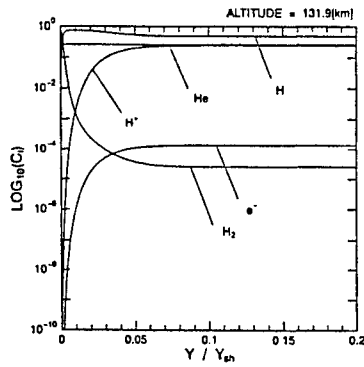


Fig. 3 The distribution of the shock layer mass fraction (nearby the wall)

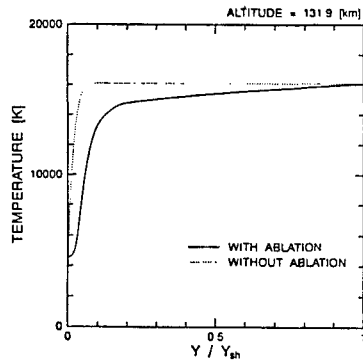


Fig. 4 The distribution of the shock layer temperature

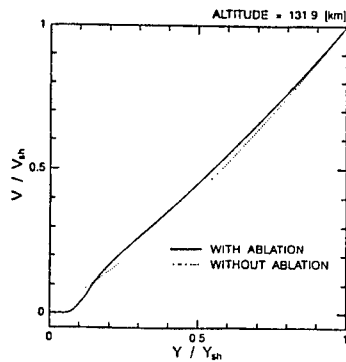


Fig. 5 The distribution of the shock layer normal speed

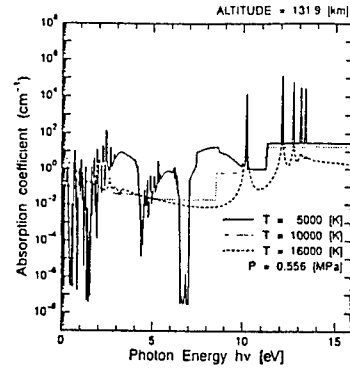


Fig. 6 The shock layer absorption coefficient

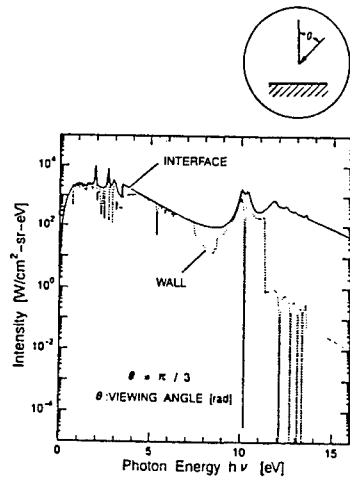


Fig. 7 The radiative heat flux from the shock layer

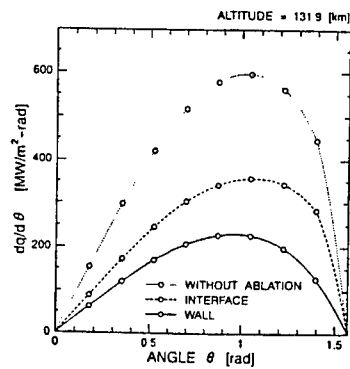


Fig. 8 The angular distribution of the radiative heat flux

Novel optical techniques for remote water column temperature measurement

B.Cresswell, E.Hodgson, C.Wakefield

Department of Physics, University of Salford, Salford, M5 4WT

ABSTRACT

This paper assesses novel optical techniques for the remote measurement of water column temperatures, using non-linear effects such as stimulated Raman scattering. Results are presented from a modelling programme to predict water flow patterns produced by an underwater heat source. **Keywords:** Remote sensing, water column, temperature.

2. INTRODUCTION

At present, there is no accurate way to make remote measurements of the subsurface temperature distribution of a body of water^{1,2}. Only the surface temperature can be determined by remote sensing techniques³, and underlying currents must be traced by thermometers. The difficulty lies in the strong absorption of long wavelength electromagnetic radiation by water, limiting conventional thermal imaging techniques to the surface. Visible light does penetrate through water, with the best transmission in the blue-green⁴. However, to exploit visible light it is necessary to identify suitable temperature-sensitive physical effects. The work described here is part of a project to establish an accurate method of measuring subsurface temperatures, by optical remote sensing techniques. Existing methods have been surveyed, and the possibility of using non-linear optical techniques assessed. To provide a test-bed for experimental work, a water tank has been set up in which controlled underwater currents can be generated by heated cylinders, and a mathematical model has been developed that predicts the temperature and velocity profiles of such currents.

3. EXISTING REMOTE SENSING TECHNIQUES

The most widely-explored to date has been spontaneous Raman scattering^{5,6}. There is a well-documented⁷ shift with temperature in the relative intensity of the Gaussian components that make up the first Stokes peak, albeit quite small, 1 % per degree K. Several groups^{2,8} have demonstrated this technique at sea, but the accuracy was limited to ± 1 K by noise effects. The Raman scattering cross-section in water⁹ is low compared to many materials, being only $0.0002 \text{ m}^2 \text{sr}^{-1}$, and the broad-band signals are easily swamped by daylight, fluorescence etc. The Raman signal is also affected by the salinity of the water. The only other optical technique tested experimentally^{9,10} is spontaneous Brillouin scattering, which needs a Fabry-Perot interferometer with ≈ 500 MHz resolution to detect the signal. The very narrow bandwidth of the signal allows better discrimination against background, but the overall performance is no better than the Raman systems.

4. NON-LINEAR OPTICAL PROCESSES

Stimulated Raman scattering¹¹ (SRS) should offer a much better signal-to-noise ratio, as the scattering cross-section is much higher, and the directional nature of the scattering means that a much higher fraction of the scattered light can be captured by a telescope. SRS will only occur in regions of high laser intensity, ie in the focal plane of the projection optics, so depth resolution could be provided simply by altering the focal plane, avoiding constraints on the laser pulse length and the detector response time. To date, only a limited amount of experimental work¹² has been carried out on SRS in water. The effects of temperature are quite different from the spontaneous case. There are significant amounts of light generated at the first anti-Stokes line and the second Stokes, as well as the first Stokes, and the ratio between these alters with temperature. However, the stimulated process is very unstable shot-to-shot, and it remains to be demonstrated as a means of temperature sensing.

5. MODELLING OF WATER HEATING

The first stage was to generate a known water flow pattern for the optical system to measure, using a heating element submersed in a water tank. A model was developed to predict the temperature and velocity profiles of the turbulent currents produced. Consider a hot cylinder, temperature T_h , of height L_c and radius R_c sitting in a large tank of water at temperature T_a (see figure 1). Water in contact with the sides of the cylinder will be heated and rise, forming a cone of convective flow around the cylinder. At the top of the cylinder, the rising cone will converge to form a buoyant plume. Both the cone and the free plume will entrain cool water from the surroundings. The value of the entrainment coefficient K_c has been determined experimentally to be ≈ 0.1 .

Assume a) Friction at cylinder wall is not important

b) Heat is transmitted only at the cylinder surface

c) Heat flux density is averaged over wall and top surface

d) Average values of velocity U and excess temperature T in horizontal plane at any height x .

There are two zones to the model; the lower section around the cylinder itself, and the free plume above the top of the cylinder. There is a minimum "waist" of the flowing region just above the top of the cylinder, at height $x_w = L_c + R_c/2$. Let A be the horizontal cross-section area of the convective flow, and S be the perimeter of the outer boundary of the flow. For thermal expansivity E , liquid density ρ , and specific heat capacity per unit mass C_p , then the starting equations are as follows:

Flow continuity:

$$\frac{\partial}{\partial x}(AU) = SK_e U$$

Momentum:

$$\frac{\partial}{\partial x}(AU^2) = EgAT$$

Heat flux:

$$AUT = \frac{q}{\rho C_p}$$

where q is the total heat input at height x . Define $Q' = \text{total power}/\rho C_p$. Then at the waist height x_w ,

Average vertical velocity :

$$U_w = \left[\left(\frac{3}{5} Eg \right) \left(\frac{4}{3K_e} \right) \left(\frac{Q'}{2\pi x_w r_w} \right) \right]^{\frac{1}{3}} x_w^{\frac{1}{3}}$$

Average excess temperature:

$$T_w = \left(\frac{4}{3K_e} \right)^{\frac{2}{3}} \left(\frac{Q'}{2\pi x_w r_w} \right)^{\frac{2}{3}} \left(\frac{5}{3Eg} \right)^{\frac{1}{3}} \frac{1}{x_w^{\frac{1}{3}}}$$

where r_w is an effective mean radius defined as $r_w = R_c + 3/8 K_e x_w$

5.1 On the cylinder wall

Outer radius of rising layer :

$$R = R_c + \frac{3}{4} K_e x$$

Mean radius of rising layer:

$$r = R_c + \frac{3}{8} K_e x$$

Average velocity of rising layer :

$$U = U_w \left(\frac{r_w}{r} \cdot \frac{x}{x_w} \right)^{\frac{1}{3}}$$

Average excess temperature of rising layer:

$$T = T_w \left(\frac{r_w}{r} \right)^{\frac{2}{3}} \left(\frac{x_w}{x} \right)^{\frac{1}{3}}$$

5.2 For the detached, buoyant free plume

Define effective outer radius $R_{eff} = R_c + 3/4 K_e x_w$

Starting radius of the plume :

$$R_w = (R_{eff}^2 - R_c^2)^{\frac{1}{2}}$$

Plume radius at height x :

$$R_p = R_w + \frac{6}{5} K_e (x - x_w)$$

Plume velocity at height x :

$$U_p = U_w \left(\frac{R_w}{R_p} \right)^{\frac{1}{3}}$$

Plume excess temperature at height x :

$$T_p = T_w \left(\frac{R_w}{R_p} \right)^{\frac{5}{3}}$$

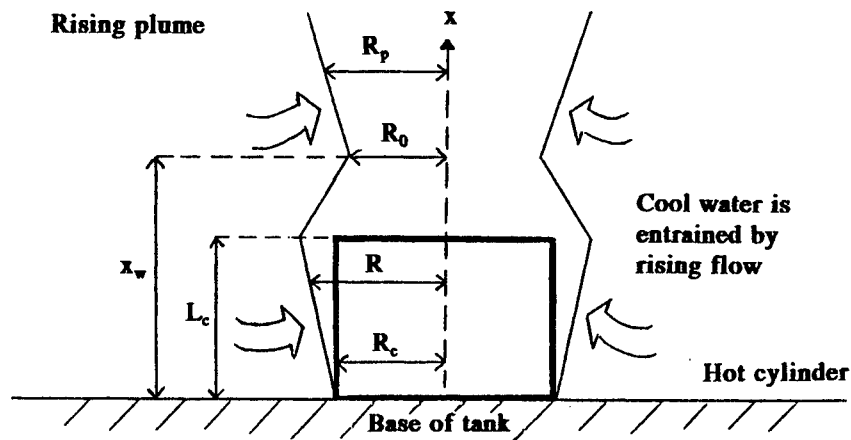


Figure 1 : Rising plume of water forming around heated cylinder

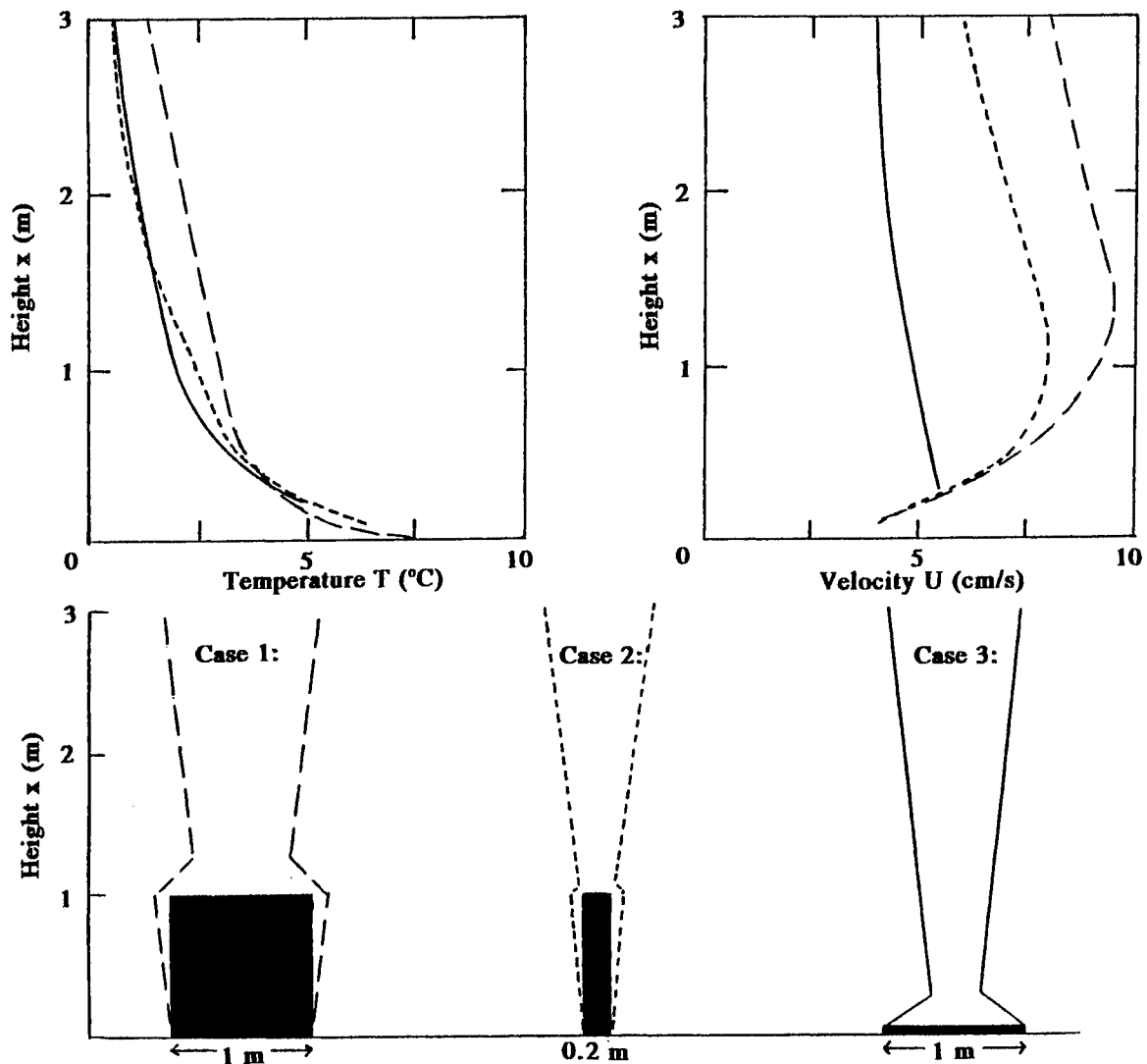


Figure 2 : Average temperature, velocity and diameter of water plume as a function of height for different heat sources.

6. EXAMPLES OF THE MODEL

Using the parameter values averaged over 20-80°C,

density $\rho = 1000 \text{ kgm}^{-3}$

expansivity $E = 4.2 \times 10^{-4} \text{ K}^{-1}$

viscosity $\mu = 6 \times 10^{-4} \text{ Pas}$

thermal conductivity $k = 0.6 \text{ Wm}^{-1}\text{K}^{-1}$

the model was run for three very different shapes of cylinder, all 80 °C above the ambient water temperature. Case 1 is a cylinder 1 m high and 1 m in diameter ($Q=344 \text{ kW}$). Case 2 is also 1 m high but only 0.2 m diameter ($Q=58 \text{ kW}$). Case 3 is 0.1 m high and 1 m in diameter ($Q=72 \text{ kW}$). Figure 2 shows the physical dimensions, excess temperature and average velocity of the heated water in each case. For scaling to other shapes, the average velocity is proportional to $Q^{1/3}$, and the average temperature is proportional to $Q^{2/3}$.

7. CONCLUSION

The model shows that the temperature of water rising from a submersed hot object is only a few degrees above the ambient water temperature, even where the heat deposited from the object is hundreds of kilowatts. Such small temperature differences are very hard to measure accurately by remote techniques. The velocity of the rising plume is several centimetres per second, and could be measured by laser Doppler velocimetry. In still water, a combination of these techniques might provide a useful guide to the degree of underwater heating.

8. ACKNOWLEDGEMENTS

The University of Salford wishes to gratefully acknowledge the encouragement and financial support provided by BNFL, and in particular the assistance of Dr Andrew Whitehouse and Mr Chris Madin, of BNFL Sellafield.

9. REFERENCES

1. G.D.Hickman et al, "Aircraft laser sensing of sound velocity in water: Brillouin scattering", *Remote Sens.Environ.* **36**, 165-178 (1991)
2. V.Raimondi and G.Cecchi, "Lidar field experiments for monitoring sea water column temperature", *EARSeL Advance.Rem.Sensing* **3**(3-VII), 84-89 (1995)
3. M.Arbelo et al, "Determination of sea surface temperature using combined TOVS and AVHRR data..", *Int.J.Remote Sensing* **17**(2), 359-371 (1996)
4. R.Smith and K.Baker, "Optical properties of the clearest natural waters (200-800nm)", *Appl. Optics* **20**(2), 177-184 (1981)
5. K.Cunningham and P.A.Lyons, "Depolarisation ratio studies on liquid water", *J.Chem.Phys.* **59**(4), 2132-2139 (1973)
6. G.E.Walrafen, *Water - a comprehensive treatise* ed.F.Franks, Plenum, New York (1972)
7. J.R.Scherer, M.K.Go and S.Kint, "Raman spectra and structure of water from -10 to 90°", *J.Phys.Chem.* **78**(13), 1304-1313 (1974)
8. D.Leonard, B.Caputo and F.Hoge, "Remote sensing of subsurface water temperature by Raman scattering", *Appl. Optics* **18**(11), 1732-1745 (1979)
9. D.Leonard and H.Sweeney, "Remote sensing of ocean physical properties: a comparison of Raman and Brillouin techniques", *Proc.SPIE* **925** Ocean Optics IX, 407-414 (1988)
10. J.G.Hirschberg et al, "Speed of sound and temperature in the ocean by Brillouin scattering", *Applied Optics* **23**(15), 2624-2628 (1984)
11. M.Sceats, S.Rice and J.Butler, "The stimulated Raman spectrum of water and its relationship to liquid structure", *J.Chem.Phys.* **63**(12), 5390-5400 (1975)
12. V.Parkash, M.K.Dheer and T.S.Jaseja, "Stimulated Raman spectrum of water", *Phys.Lett.* **29A**(5), 220-221 (1969)

The finding of the time-dependent Resistance and Inductance of the laser discharge in a Pulsed Gas laser through their waveforms of the voltage and the current

P. Persephonis, A. Ioannou and J. Parthenios

University of Patras, Department of Physics 26500 Patras GREECE

ABSTRACT

A new method of finding the time histories of the resistance and inductance of a discharge in the laser chamber of a pulsed gas laser is described. This method exploits simultaneously the voltage across the laser channel and the flowing current in the laser discharge while the knowledge of the entire circuit is not required. The mathematical model used is simple and the results show strong variations of the resistance and inductance during the formation phase of the discharge while in the main phase these quantities fluctuate around constant values.

Keywords: Discharge, Plasma, Gas Laser

1. INTRODUCTION

In any pulsed gas laser two electric discharges take place. The first in the switch system (spark-gap or thyatron) and the second in the laser channel. These two discharges introduce in the electric circuit time dependent parameters whose the knowledge of their time histories is very useful for the study of these laser systems.

In two previous works of ours, a method of determining the time dependent resistance and inductance of the electric discharges was presented. This method was based on the exploitation of the voltage waveforms across the discharges¹, or the exploitation of the current waveforms through the discharges.² The mathematical model used in this method depends on the type of the electric circuit of the pulsed gas laser. However, this method presents a serious disadvantage, namely its application requires the knowledge of all the electrical parameters of the circuit of the laser system.

In the present work a modified and simplified method of determining the resistance and inductance of the laser discharge is presented. This simple method utilizes simultaneously only the voltage across the discharge and the current which flows the laser channel. These two quantities are combined through the differential equation governing the performance of the laser channel. This method is independent on the electrical circuit and requires only the knowledge of the voltage across the discharge and the current which flows through it.

2. DESCRIPTION OF THE METHOD

When the electric discharge of a pulsed gas laser takes place in the laser channel, the differential equation governing the electric behavior of the laser channel is given. This is

$$V = L \frac{dI}{dt} + \left(R + \frac{dL}{dt} \right) I \quad (1)$$

where V is the voltage across the laser channel, I is the current which flows through the laser channel and L , R are the time dependent inductance and resistance respectively of the electric discharge (It is mentioned that an electric discharge can be described through a resistance and inductance in series combination). It is noted that the voltage V and current I waveforms can be easily measured through very fast voltage and current probes. After the measuring of these quantities they are digitized and filtered for noise elimination. Then, the first derivative of the current can be easily calculated. Afterwards the values of the voltage, current and its derivative are substituted into the differential equation (1) at a certain time instant. Thus, an algebraic equation between the resistance R and inductance L is produced for this time instant. In the same way, algebraic relationships between R and L can be obtained for every time instant during the discharge in the laser channel. Finally, we consider that for four extremely close adjacent time instants the resistance R and inductance L are varied linearly in time. So the differential equation (1) gives the four following relationships

$$V = (L + n\Delta L) \frac{dI}{dt} + I \left(R + n\Delta R + \frac{\Delta L}{\Delta t} \right) \quad (2)$$

$$n = -1, 0, 1, 2$$

for four close adjacent time instants, where ΔL and ΔR are the differences of the inductance and resistance between two successive time instants. Then solving The system of the above algebraic equations (2) we can find the values of R and L which correspond at the middle of the time period covering the four adjacent time instants. Scanning the entire time region of the discharge, the time histories of the resistance R and inductance L of the laser channel can be calculated.

3. Experimental Verification, Measurements

The above mentioned method of finding the time histories of the inductance and resistance of the laser discharge was verified through a typical charge transfer circuit (C-to-C) Nitrogen laser with capacitors $C_1 = 18$ nF (Storage Capacitor) and $C_2 = 12$ nF (Peaking Capacitor). This is shown in fig. 1.

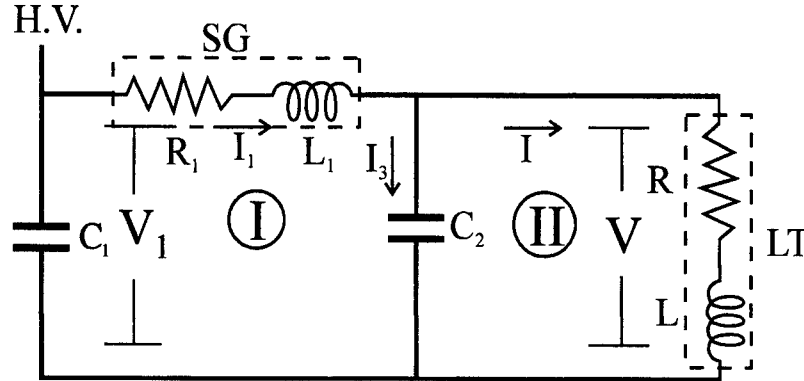


fig. 1 The equivalent electric circuit of a 'C-to-C' pulsed gas laser

Details on the description of the above laser system is given in a previous paper of ours.³ The waveform of the voltage V was taken through a high voltage probe (Tektronix P6015) and a fast oscilloscope (Tektronix 7104 rise time 350ps). The waveform of the current I has also been measured through a fast rise time viewing resistor (T&M INC. W-2-0005-18FC, with resistance 0.0005 Ω). These waveforms of the voltage V and current I are shown in fig. 2. Afterwards, These waveforms were filtered with a Butterworth filter 5th order and the cut-off frequency was 2.25×10^9 Hz. This filtering eliminated the small distortions of the waveforms and gave more accurate derivatives (fig.3).

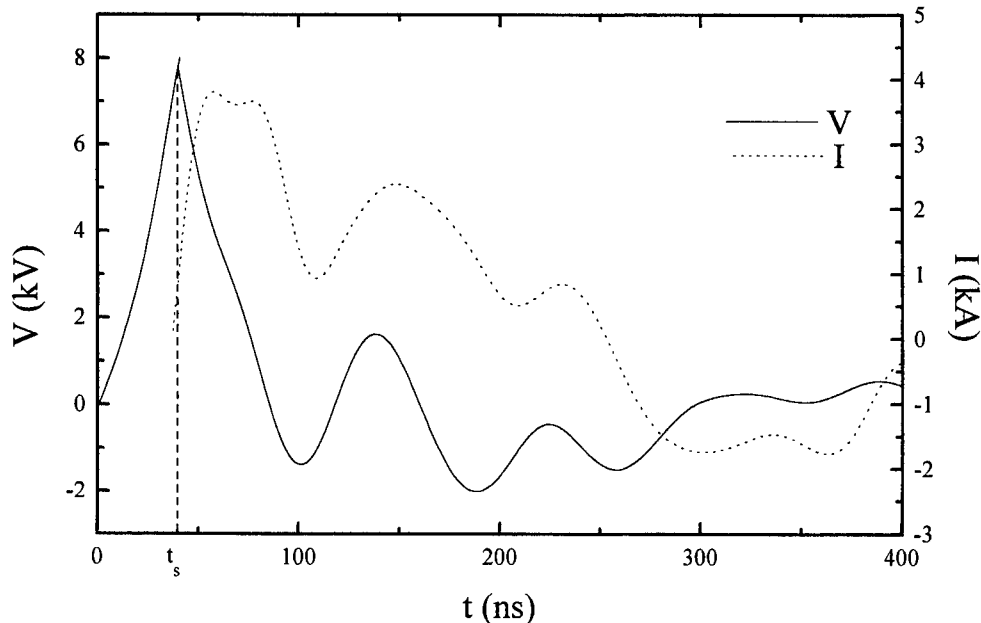


fig. 2 The voltage V and current I waveforms

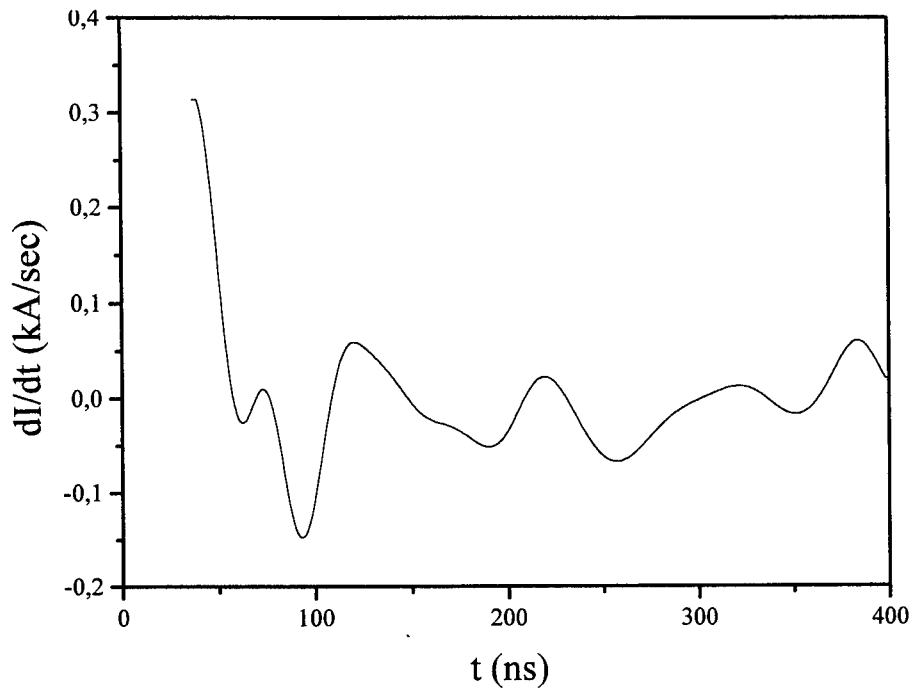


fig. 3 The first derivative of the current waveform I

The first derivative of the current I was calculated through the '5th point' difference formula^{4,5} (fig.3). This calculation verified by the Savitzky-Golay smoothing filters, which do best at preserving feature heights and widths⁵. Substituting the values of the voltage V , the current I and its first derivative dI/dt into equation (1) we form similar algebraic relationships between the resistance R and inductance L of the laser discharge for every time instant. Combining these relationships for four adjacent time instants we can find the values of R and L for the time period covering the four adjacent time instants. Scanning the entire time region of the laser discharge the time histories of the resistance R and inductance L of the laser discharge are revealed. These are shown in fig. 4.

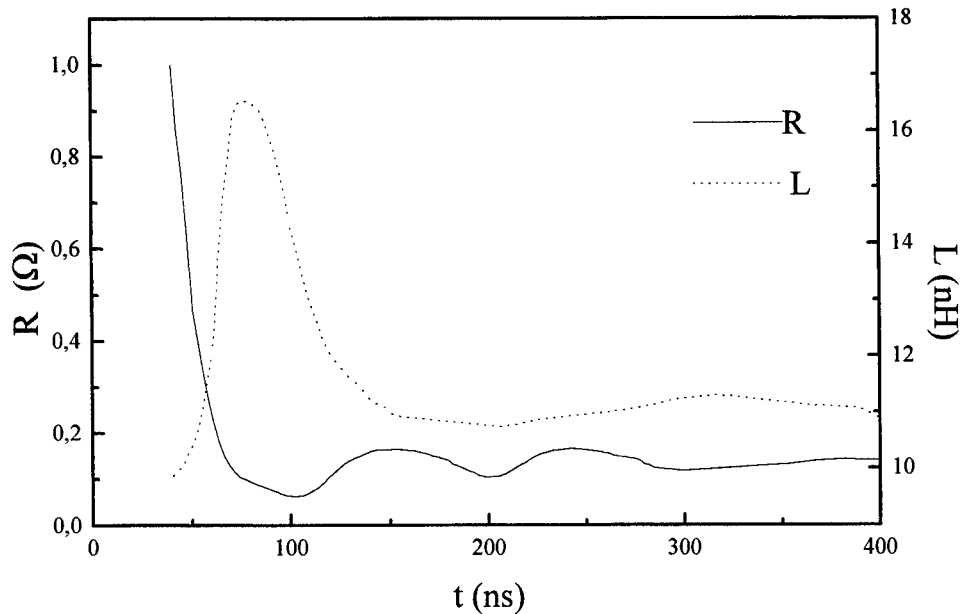


fig.4 The time history of the resistance R and inductance L , of the laser channel

4. Discussion

The time dependence of these electric quantities shows strong variations in the formation phase of the discharge (first 45 ns). Concretely, The resistance R (fig.4) of the laser discharge drops exponentially from a very high value, because of the electron avalanche multiplication.

On the other hand the inductance L of the laser discharge shows an abrupt high peak which is attributed to the temporary plasma constriction.⁶ This is due to the attractive electromagnetic forces (Laplace force) because of the parallel motion of the electrons. The following expansion of the plasma results from the finite time required for the electric field to penetrate into plasma. This is due to the well known skin depth effect.^{7,8} This phenomenon is derived from Maxwell's equations

$$\nabla \times \mathbf{E} = -\frac{\partial \mathbf{B}}{\partial t}, \quad \nabla \times \mathbf{B} = \mu_0 \mathbf{J} + \mu_0 \frac{\partial}{\partial t} \epsilon_0 \mathbf{E} \quad (3)$$

$$\nabla(\nabla \cdot \mathbf{E}) - \nabla^2 \mathbf{E} = \mu_0 \frac{\partial \mathbf{J}}{\partial t} + \mu_0 \frac{\partial^2}{\partial t^2} \epsilon_0 \mathbf{E} \quad (4)$$

Assuming $\nabla \cdot \mathbf{E} = 0$ and $\frac{\partial}{\partial t} \epsilon_0 \mathbf{E} \ll \mathbf{J}$ then one obtains

$$\nabla^2 \mathbf{E} - \mu_0 \frac{\partial}{\partial t} (\sigma \mathbf{E}) = 0 \quad (5)$$

This diffusion-like equation for the electric field in a plasma is the basis of inductance. Finally, after the formation phase of the discharge, the inductance and resistance of the laser discharge present small fluctuations around constant values.

5. CONCLUSION

In this work a simple and accurate method of finding the time dependent resistance and inductance of a laser discharge is described. This method uses only the voltage across the laser channel and the current which flows through the laser discharge. The method is independent on the type of the used electric circuit and their electrical parameters are not required. The differential equation governing the laser discharge is very simple and we use only the values of the voltage across the laser discharge, the current and its first derivative. Thus, mathematical model is simpler than the model proposed in another paper of ours^{1,2} and the numerical and experimental errors are smaller.

The resistance and inductance of the laser discharge vary strongly in the formation phase of the discharge while in the main phase they fluctuate around constant values.

6. REFERENCES

1. P. Persephonis, V. Giannetas, A. Ioannou, J. Parthenios and C. Georgiades, "The Time Dependent Resistance and Inductance of the Electric Discharges in Pulsed Gas Lasers," IEEE J. Quantum Electron. **31**, 1779-1784 (1995).
2. P. Persephonis, V. Giannetas, A. Ioannou, J. Parthenios and C. Georgiades, "The Time Evolution of the Resistances and Inductances of the Discharges in a Pulsed Gas Laser through its Current waveforms," IEEE T. Plasma Sci. **24**(4), August 1996.
3. P. Persephonis, V. Giannetas, J. Parthenios, A. Ioannou and C. Georgiades, "Optimization of the Optical Output in a C-to-C Pulsed Gas Laser," IEEE J. Quantum Electron. **31**, 1059-1063 (1995).
4. Steven E. Koonin, *Computational Physics*, CA: Benjamin/Cummings, 1986.
5. W. H. Press, S. A. Teukolsky, W. T. Vetterling, and B. P. Flannery, *Numerical Recipes: The Art of Scientific Computing (Fortran Version)*, New York: Cambridge Univ. Press, 1990, 1992.
6. Martin Bahr, Woldemar Botticher, and Stefan Choroba, "The Time-Dependent Development of the Macroscopic Instability of a XeCl* Laser Discharge," IEEE T. Plasma Sci. **19**(2), 369-378 (1991).
7. L. F. Champagne, A. J. Dudas, N. W. Harris, "Current rise-time limitation of the large volume x-ray preionized discharge-pumped XeCl laser," J. Appl. Phys. **62**(5), 1576-1584 (1987).
8. Pinhas Blau, "Analysis of the Impedance of a Coaxial, Large-Bore Copper-Vapor Laser," IEEE J. Quantum Electron. **30**(3), 763-769 (1994).

Electrical behaviour of laser damaged silicon photodiodes

Jean-Pierre Moeglin, Bernard Gautier and René Joecklé

Institut Franco-Allemand de Recherches de Saint-Louis (ISL)
5 rue du Général-Cassagnou 68301 SAINT-LOUIS CEDEX (France)

ABSTRACT

A measurement of the electrical parameters degradation of Si photodiodes irradiated by laser visible light has been performed. The laser is a Q-switched Nd:YAG, frequency doubled, operated in single pulse mode of 4 ns duration. The applied fluence levels range up to 90 J/cm^2 . Two kinds of irradiation process have been applied : either a part of the detector active area has been irradiated in single pulse mode, or a scanning of the whole detector active area has been performed with successive identical pulses. It has been shown that the fluence necessary to induce significant changes (local decrease of 35%) in responsivity is several times the surface melting threshold fluence (0.5 J/cm^2). Conversely, the dark current is the most sensitive parameter, it increases by about four magnitudes for high irradiation. The in-depth dopant distribution is altered by high fluence irradiation in a way that cannot be explained by simple thermal modelization.

Keywords : visible laser, silicon photodiode, detector, laser induced damage, responsivity, junction capacitance, dark current, dopant diffusion

1. INTRODUCTION

Silicon photodiodes are the most common detectors used to measure near-infrared and visible optical radiation. Many applications such as radiometry, photometry and colorimetry require these devices to be operated in laser environments where radiation overloads are likely to be produced (if for example, the laser beam is focused on the active area of the detector). It becomes important to understand the laser induced permanent modification in the electrical parameters. Morphological damage for silicon material has been extensively studied¹, and a threshold fluence for melting surface (0.5 J/cm^2 for a 4 ns laser pulse) has been established. Moreover, the morphological damage and its influence on the response of a detector has been studied by Watkins et al². The purpose of this paper is to extend this investigation in order to get a better knowledge of the damage process.

2. EXPERIMENTAL RESULTS

2.1 Experimental set-up

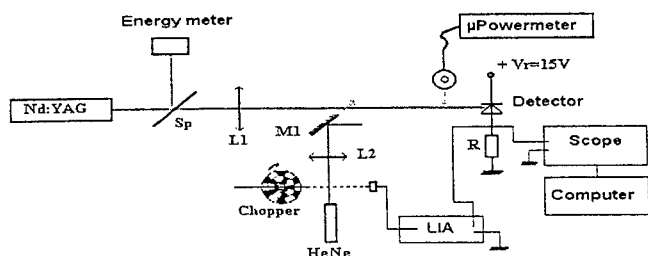


FIG. 1. Experimental system used for laser irradiation

An experimental set-up (Fig. 1) has been used to perform the irradiation of the detectors. The laser beam is focused to a spot radius of about 1 mm. Two kinds of commercial Si detectors have been used for test. The laser source was a Q-switched Nd:YAG laser, frequency doubled ($\lambda=532 \text{ nm}$) with a 4 ns pulse width duration (FWHM) and a pulse energy of 0.4J per pulse (BMI 502). The radial profile of laser intensity is nearly Gaussian, as well as the temporal distribution. Electrical parameters were measured before and after irradiation. Each detector was irradiated with a single pulse shot ; for the small detectors (7 mm^2 -BWP 34), the irradiated area was roughly 11% of the active area, whereas for the large ones (41.3 mm^2 -995), it was about 2%. For the latter, a series of tests has been performed by scanning the entire active surface irradiation with successive pulses, in order to obtain a uniform 90 J/cm^2 fluence on the whole detector.

2.2 Junction Capacitance (JC) measurement

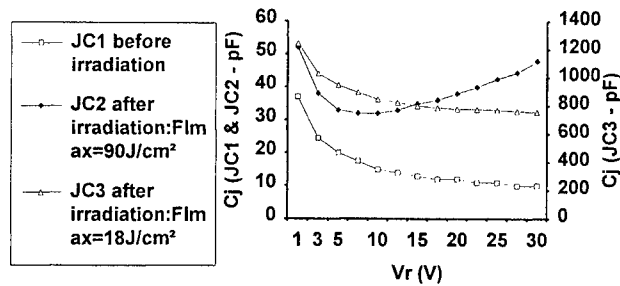


FIG. 2. JC measurement - BPW34 detector - $f = 1$ kHz.

voltage of 7V ($f=1$ kHz) under a 90 J/cm^2 fluence. This phenomenon has not been observed for a 18 J/cm^2 fluence. For the large 995 detectors, the JC remains unaffected after a single pulse 90 J/cm^2 fluence irradiation; however, if the whole sensitive area is irradiated, the measured variations of the main electrical parameters are in good agreement with those obtained with type BPW34 detectors. Furthermore, we noticed that the JC exhibits an inflexion point dependent on the frequency.

2.3 Dark current

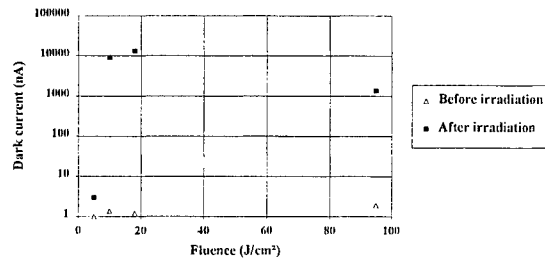


FIG. 3. Variation of the dark current with fluence

The detector is 15 V biased and placed in darkness. Fig. 3 shows how the dark current varies with the fluence. It increases by three to four orders of magnitude as soon as the fluence is higher than several J/cm^2 . The dark current has been less modified for large area type 995 detectors than for small area type BPW34 ones : the dark current increases by 150% after a 90 J/cm^2 one-pulse irradiation. For the entirely irradiated "large" detector, the dark current increases from 20 nA to 10 μA after irradiation. According to the above measurements, the variation of the main electrical parameters is mainly dependent on the ratio of the damaged area to the total active area. This increase has been pointed out qualitatively by Watkins et al^{2,3}.

2.4 Overall sensitivity

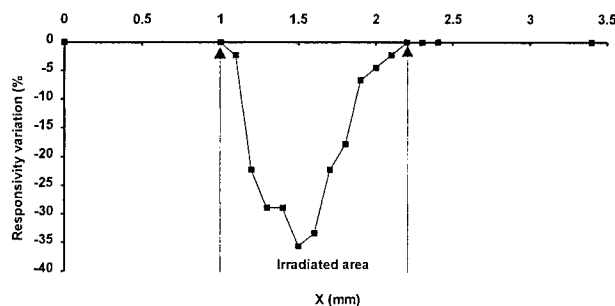


FIG. 4. Local responsivity variation of the irradiated detector.

2.5 Local sensitivity variation on large detector

The "local" sensitivity of partially irradiated detectors has been measured as follows : the entire active area is scanned with a probe beam (HeNe) focused in order to get a small spot; the beam is mechanically chopped at the frequency $f=4$ kHz, in order to measure the signal of the HeNe laser beam. Figure 4 shows that the local responsivity of the detector exhibits a drop of 35% at the center of the damaged area ; this effect can be attributed to the AR coating removal. Indeed, the unaffected surface does not reflect the HeNe beam, whereas a diffuse reflection can be seen at the location of the damaged site.

2.6 Reverse current, Short Circuit Current (SCC) and Open Circuit Voltage (OCV)

The reverse voltage V_r ranges from zero volt (included) to the breakdown voltage (excluded). It has been shown that the SCC drops of 16% under a 90 J/cm^2 fluence and of 27% under 18 J/cm^2 , whereas the OCV decreases by 12% under 90 and 18 J/cm^2 . According to the above measurements, the variation of the main electrical parameters is mainly dependent on the ratio of the damaged area to the total active area. For large detectors irradiated by scanning the whole active area, the SCC and OCV have decreased by 39% and 15% respectively. This increase of the leakage current of the detector after irradiation has been noticed by Watkins^{2,3} and Borch⁴. Furthermore, Watkins² noticed that the leakage current increases when a sufficiently large quantity of defects is introduced in the depletion region.

2.7 SIMS experiments

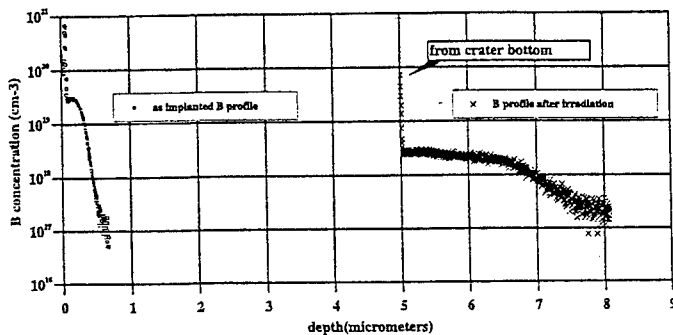


FIG. 5. Profiles of the boron concentration given by SIMS of a detector before and after irradiation ($F_{\text{max}}=90 \text{ J/cm}^2$)

Several SIMS (Secondary Ion Mass Spectroscopy) experiments have been made at the Centre de Recherches Nucléaires (CRN-PHASE) of Strasbourg. This experiment yields the in-depth concentration of dopants in a semiconductor. Typical results are shown on Fig. 5 : before irradiation, the junction depth is about $0.6 \mu\text{m}$ deep; after a 90 J/cm^2 irradiation, it increases up to $5.5 \mu\text{m}$ measured from the bottom of the crater. Taking into account the depth of ablated material, it can be assumed that the melting pool reaches a depth of $10 \mu\text{m}$.

3. THEORY

3.1 Thermal model description

Thermal models are useful to predict the time history and the extent of the heat affected zone (the shape of the melting pool). For short laser pulses, the dopant diffusion takes place mainly in the liquid phase of the material. Purely analytical solutions⁵ of the thermal diffusion equation are available in some limit cases including constant thermal properties and in the case of a phase change in the vicinity of the steady state solution⁶. These analytical solutions are not suitable in the present case : thermal and optical properties of silicon are strongly temperature dependent. As an example the volume absorption coefficient α ranges from 10^4 cm^{-1} at room temperature to 10^6 cm^{-1} at the vaporization temperature¹ (at $\lambda=0.532 \mu\text{m}$). The deposition of laser energy cannot be considered spatially uniform and constant in time. Furthermore, it can be shown that, due to the short irradiation time, the thermal diffusion length remains of the same order of magnitude as the absorption coefficient length ($1/\alpha$). Therefore, silicon cannot be considered to be a purely opaque material as suggested by the high values of α ($\approx 10^6 \text{ cm}^{-1}$). Temperature profiles exhibit an "in-depth" overshoot well above the

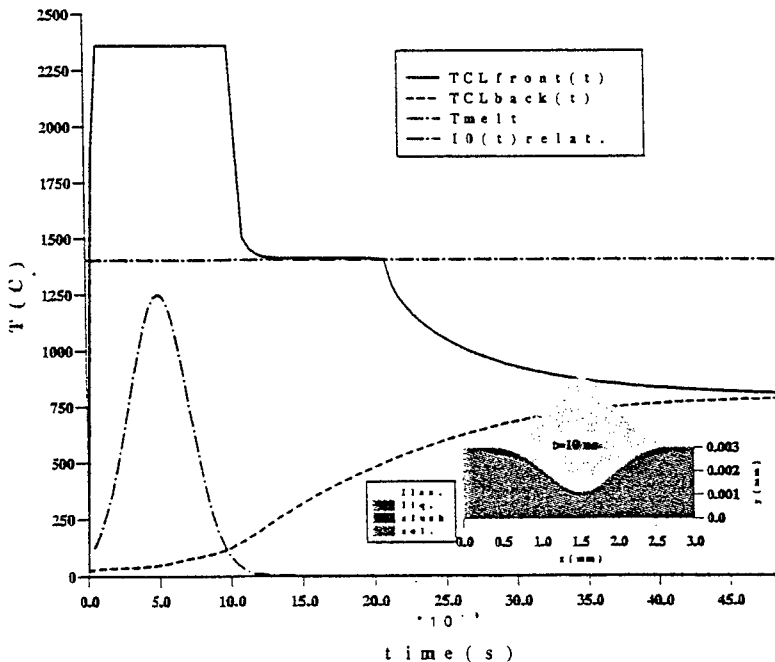


FIG. 6. Numerical application Silicon disk. 3 mm diameter, $3 \mu\text{m}$ thick; laser pulse duration = 5 ns ; pulse energy = 0.3 J

surface temperature which remains fixed at the vaporization value. In order to properly predict the time history of the melting pool, with data close to our experimental conditions, a more sophisticated 2D axisymmetric thermal model has been used⁸.

This model solves the general form of Fourier equation in a 2D axisymmetric space limited by a time dependent free boundary. The "source" term takes into account the large variation of the volume absorption coefficient as a function of temperature. Two interfaces defined by solidus and liquidus temperatures limit a "slush" phase in which the specific heat is increased by the latent heat of fusion. This assumption does not strictly apply to pure materials with single melting temperature. Nevertheless, it has been kept for computational purposes provided this temperature difference is reduced to a few degrees. The heat input (laser beam absorption) can be specified in both space and time (here, $I_0(r)$ and $I_m(t)$ are Gaussian). Fig. 6 shows the temperature evolution of the front and back faces (located at the center line). Also depicted is the shape of the three above defined interfaces at the end of laser irradiation. It can be noticed that a large part of the material has been vaporized and that the liquid layer remains very thin during the whole interaction process.

4. DISCUSSION AND CONCLUSION

The sensitivity decrease due to laser irradiation can be explained in the two following ways : first, the appearance of a diffuse reflexion resulting from the removal of the AR layer under the laser impact and/or secondly, the increase of the density of surface states⁹. In that case, the surface recombination velocity increases, thus inducing a drop of the photocarriers (minority). The measurement of the crater profile is in relative agreement with the predicted mass removal through surface vaporization given by the numerical model. However, SIMS experiments show an extended zone of boron diffusion (up to 10 μm in depth). Assuming that, for such short duration laser pulses, dopant diffusion takes place only during the liquid phase lifetime, such a deep diffusion cannot be explained on the basis of computed liquid layer thickness and duration. The electrical parameters such as the OCV, SCC and the Dark Current (DC) are substantially modified if the laser affected surface covers almost the whole of the detectors sensitive area. The DC has been increased by a factor of 10^3 to 10^4 thus inducing a noise increase which merges the output signal. The irradiated detector will be unable to detect small light signals. The measured increase of the JC is due to the creation of defects acting as recombination centers, thus decreasing the minority carriers lifetime. Laser irradiation induces the migration of these defects toward the depletion region, thus rising the JC as pointed out by several authors^{7,2,3} (they state that an increase of the DC by a factor of 4 produces an increase of the JC). This is in agreement with the fact that our experiences conducted with a single partial irradiation of large active area detectors do not exhibit JC modification, emphasizing the effect of the laser spot size / active area ratio. The measured electrical parameters variation of irradiated detectors stresses that there is no single "destruction threshold", but a progressive decrease in performances as the applied fluence is increased.

5. ACKNOWLEDGEMENTS

The authors are grateful to Pr. Stück (PHASE laboratory, CRN Strasbourg) who performed SIMS analysis, for his help.

6. REFERENCES

1. O. Muller, *Etude des effets d'irradiations pulsées intenses sur des cibles de silicium considéré en tant que matériau de base pour détecteurs optiques* (Study of the effects of laser irradiation on silicon target as bulk material for optical detectors), Ph. D. Thesis, University of Strasbourg, France, 1994
2. S.E. Watkins, Chen-Zhi Zhang, R.M. Walser and M.F. Becker, "Electrical performance of laser damaged silicon photodiodes," *Appl. Optics*, Vol. 29, No. 6, pp. 827-835, February 1990
3. S.E. Watkins and C.Z. Zhang, "Laser-induced electrical parameter degradation in silicon photodiodes," *20th Symposium on Optical Materials for High Power Lasers*, NIST Special Publication # 775, pp. 288-310, NIST, Boulder CO 1989
4. E. Borch, R. Macii, C. Leroy, C. Manoukian-Bertrand, C. Furetta et al, "Leakage current, annealing, and deep defect production studies in neutron irradiated n-type Si detectors," *Nuclear Instruments and Methods in Physics Research*, Vol. A301, No. 2, pp. 215-218, March 1991
5. H.S. Carslaw and J.C. Jaeger, *Conduction of heat in solids*, Clarendon Press 2nd ed. 1959
6. F.W. Dabby and Un-Chul Paek, "High intensity laser induced vaporization and explosion of solid material," *IEEE Journal of quantum electronics*, QE 8, No 2, p. 106, 1972
7. J. Walter, W. Garber, R. Wunstorff, W. Bugg, J. Harvey and W. Casson, "Bulk defects and radiation damage in detector grade silicon," *Mat. Res. Soc. Symp. Proc.*, Vol. 302, pp. 515-526, 1993
8. B. Gautier, J.P. Moeglin and F. Lacroix, "Le phénomène de rochage induit par irradiation laser des matériaux germanium et silicium (Laser-induced protuberance growth on germanium and silicon)," ISL report R104/96, 1996.
9. M.S. Tyagi, *Introduction to semiconductor materials and devices*, J. Wiley & Sons, New-York, 1991

V.V.Ryzhov, I.Yu.Turchanovsky

High Current Electronics Institute,
Russian Academy of Sciences,
4, Akademicheskoy Ave., 634055, Tomsk, Russia
Tel: (3822) 25-84-71, Fax: (3822) 25-94-10, E-mail: tur @hcei.tomsk.su

ABSTRACT

To study the performance of high power lasers with a many-sided electron beam injection, MUFLON-code has been developed. This code was used to choose and design optimum injection schemes for the excitation of the high-power gas lasers developed at the High Current Electronics Institute.

Keywords: high power lasers, many-side electron beam excitation, computer modeling.

1. MUFLON-CODE

Electron beams of hundreds of kiloelectron-volts are used for pumping high-power gas and chemical lasers having a large active gas volume. For a uniform excitation of such a volume, pumping schemes using several beams injected sym-

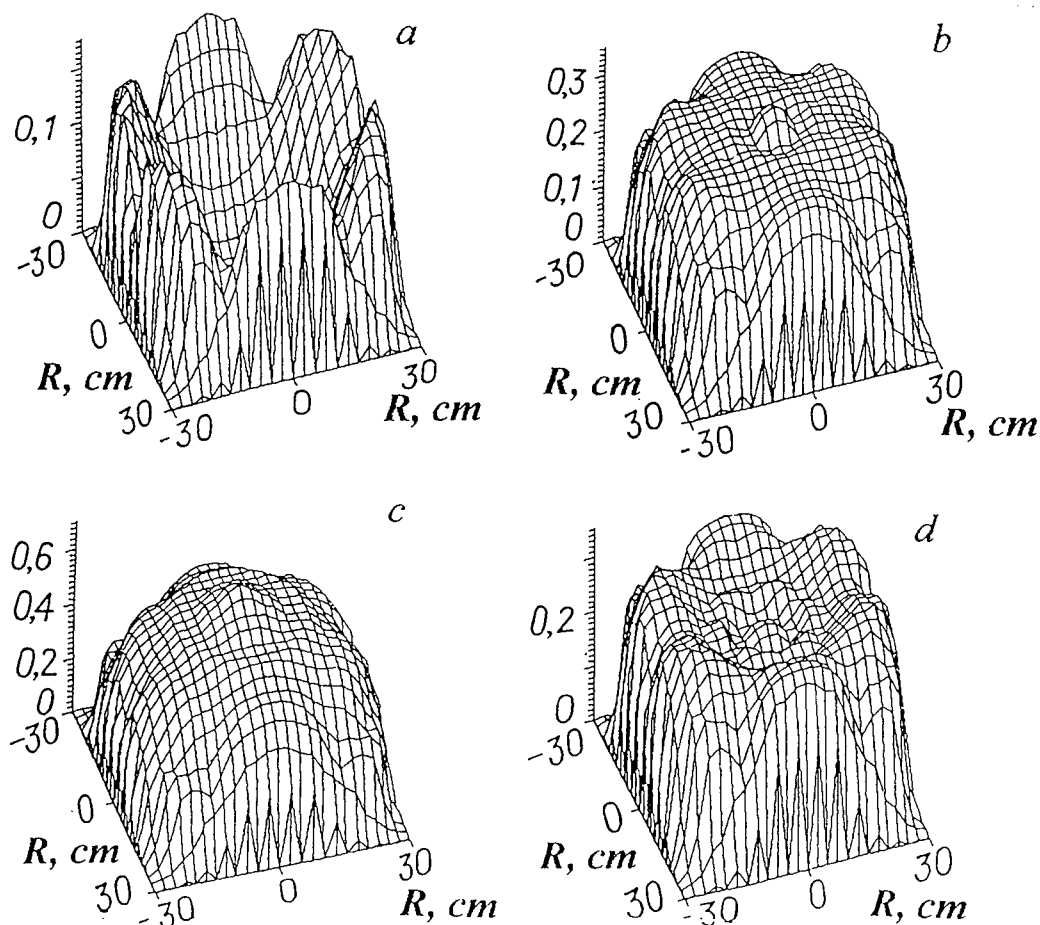


Fig. 1. Spatial distribution of the pumping power over the active volume of the output module filled with argon at 2 atm in 30 (a), 90 (b), 200 (c) and 400 ns (d)

metrically on the laser chamber sides have been suggested.

To study the performance of high-power lasers with many-sided electron beam injection, the MUFLON code has been developed. This code is based on a self-consistent solution of problems concerning the electron beam energy deposition and the plasma chemical reaction kinetics and the Boltzmann equation for the plasma electron energy distribution function and of the equations for photon fluxes. MUFLON includes Monte-Carlo code VOLPUM to calculate the spatial electron energy distribution in a gas mixture for any electron beam injection scheme¹.

2. CALCULATION RESULTS

Using the codes developed, computations were performed to investigate the uniformity and efficiency of the excitation of the active volume of a high-power laser system with many-sided injection of monoenergetic radially convergent beams. To pump this type of laser system, accelerators with the voltage pulse amplitude stabilized by vacuum lines are commonly used. These units substantially increase the mass and overall dimensions of the system, which is a disadvantage of such systems².

An electron accelerator powered from a vacuum-insulated voltage pulse generator was developed at the High Current Electronic Institute and used as a base for the creation of compact laser modules with many-sided injection beam pumping, capable of producing 100–1000 J of output energy³. A feature of the excitation of laser modules with the use of this type of accelerator is a time-varying special distribution of the pumping power which is related to the time-varying voltage pulse amplitude. We have analyzed theoretically the capabilities of many-sided nonmonoenergetic electron beam injection schemes for excitation of large gas volumes and have shown this excitation method shows a rather high efficiency and provides good azimuth uniformity of the pumping power.

Figure 1 shows the evolution of the pumping power spatial distribution in the active volume of the output module (OM) of a cascade laser system rated at several kilojoules of the pulse output energy. The active volume of the output module has the shape of a cylinder of radius 30 cm. and length 200 cm. Used to excite it, 12 accelerators arranged symmetrically by six in two rows were used. This injection scheme was chosen after a preliminary investigations of the deposited energy distribution using the VOLPUM code. The investigation has shown (Fig. 1) that for this system operated with argon-based gas mixtures the energy disposition is most uniform and efficient at a pressure of about 2 atm. With that, up to 60% of the beam energy is deposited in the uniform excitation mode. At high pressures, although the azimuth uniformity is kept good, a large fraction of the energy is absorbed near the foils, which results in a nonuniform radial energy distribution.

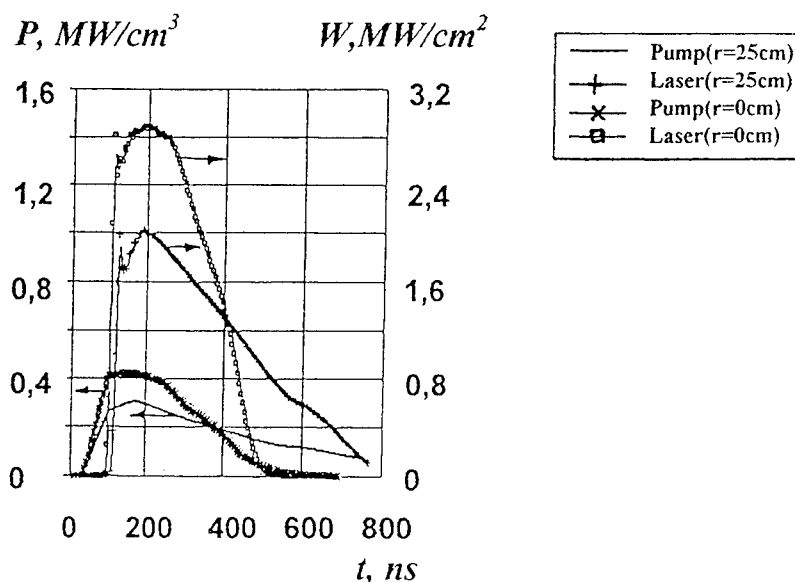


Fig 2 Time-varying pumping power P and output power density W at the axis of the output module ($r = 0$) and near the foil ($r = 25$ cm.)

We have performed a detailed simulation of the OM operating in the mode of laser oscillation with a plane-parallel resonator through the transitions of the XeCl molecule occurring on the excitation of the Ar-Xe-Cl mixture.

The kinetics model used to simulate the plasma processes is described in detail elsewhere¹. The calculated time-varying laser radiation power density at the system axis and at $r = 25$ cm is presented in Fig. 2.

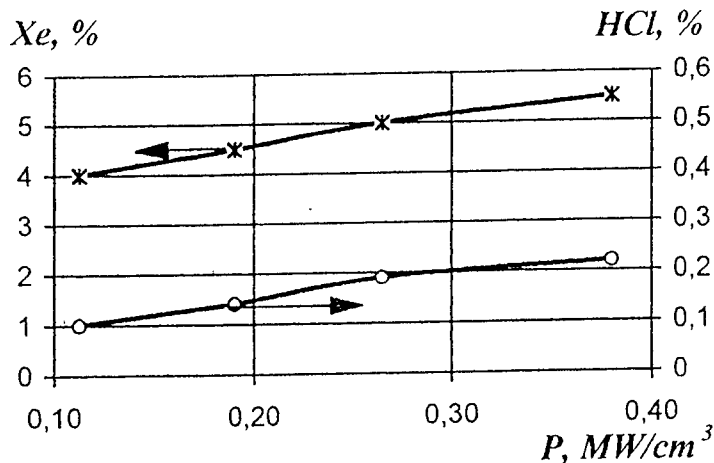


Fig. 3. Optimum concentration of Xe and HCl as functions of the average pumping power at a gas mixture pressure of 2 atm.

Having analyzed the results of the calculation of the laser output, we have arrived at the conclusion that the optimum composition of the gas mixture strongly depends on the average pumping power that varies over the cross section of the operating chamber of the system. From Fig. 3 it can be inferred that for low pumping powers the mixtures with a low content of HCl are optimum. As the pumping power is increased from 0.1 to 0.4 MW/cm³, the concentration of HCl increases in optimized mixtures, and so does the concentration of Xe, the rise rate of the former being higher than that of the latter. Thus, at low pumping powers the optimum proportion of the components is Xe : HCl = 40 : 1, while at high pumping powers it is 25 : 1. The change in the optimum concentration component ratio is related to the energy transfer processes and to the formation of XeCl molecules.

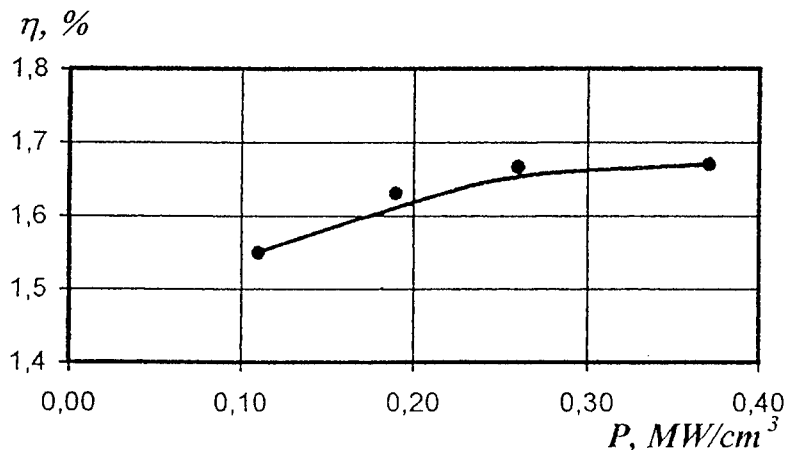


Fig. 4. Laser oscillation efficiency as function of the average pumping power for the output model with an optimized gas mixture pressure at 2 atm.

It has been predicted that as the pumping power is increased from 0.1 to 0.4 MW/cm³, the laser oscillation efficiency increases insignificantly (Fig. 4) remaining below ~3%, the highest value achieved for the given gas mixtures at high gas

pressers. Thus, for the output module operating in the laser oscillation mode at a mixture pressure of 2atm. the expected efficiency is 1.6–1.7%, which agrees with experimental data to within experimental error.

3. REFERENCES

1. V.V. Ryzhov, "Laser-gas-pumping by an electron beam", Ch.4 in G.A.Mesyats, V.V.Osipov, and V.F.Tarasenko, *Pulsed Gas Lasers*, pp. 65-108, SPIE, NY, (1994).
2. D. Craddock, C.B. Edwards, F.S. Gibbert, F. O'Neill, D.J. Nicholas, P. Roccett, and M.J. Shaw, "Development of pulsed e-beam system for large volume, high power KrF lasers", *Proc. III IEEE Inter. Pulsed Power Conf.*, p. 399-402, New Mexico, 1981.
3. G.A. Mesyats, V.V. Osipov, and V.F. Tarasenko, *Pulsed Gas Lasers*, SPIE, NY, (1994).

Solitonic approach to the wave of reflection and conduction mechanism

E. Kudriavtsev*, M. Autric**.

* P.N. Lebedev Physical Institute of Russian Academy of Sciences, Division of Optics,
117924 Moscow Leninsky Pr. 53, RUSSIA

** Institut de Recherche sur les Phenomenes Hors d'Equilibre, Laboratoire LP3
Luminy Parc Scientifique et Technologique 163, Avenue de Luminy-Case 918
13009 Marseille, FRANCE.

ABSTRACT

The possibility of the wave of reflection and conduction mechanism as interaction of soliton and heat flows is discussed on the base of our groups experimental results and published data of soliton motion computer modelling.

Keywords: photoinduced wave, soliton - like behaviour, reflection, conduction, pressure variations, IR laser excitation, solitonic mechanism.

1. INTRODUCTION

The heat energy produced by IR laser pulse is the ground reason of the Wave of Reflection and Conduction (WRC) appearance; part of that energy is transported later by WRC in the manner different from usual heat diffusion [1]. WRC has a number of specific features that characterised solitary wave or soliton.

The question about possible roll of solitons in transfer of heat energy has up to now a rather long story. Solitary wave was discovered by J.S. Russell on Union Canal in Edinburgh, Scotland, in 1834, but second rediscovery of it was made by N.G. Zabusky and M.D. Kruskal in 1965 [2]. They were investigated the ergodic problem of E. Fermi - J.R. Pasta - S. Ulam, which showed [3] that energy in coupled harmonic oscillators did not equally distributed as it is supposed to be. E.A. Jackson [4] and M. Toda [5] devoted special articles to the solitons and lattice thermal conductivity relation. They pointed out that non adequacy of the ergodic hypotheses following from soliton solutions of nonlinear equations poses the question about nonvalidity of the Fourier law established in 1822. M. Toda formulated in [5] that in nonlinear lattices the energy is mainly transported by solitons, which play important roles in the heat conduction in the disordered non-linear lattices (that was one - dimensional in his calculations for simplicity).

As soon as we know nearly all investigations in this area were made theoretically or by means of numerical solutions of nonlinear equations by help of computers. There exist also the published opinion of R.E. Peierls [6] that even close to the melting point the close to the melting point the magnitudes of excitations in real three - dimensional systems are so small that soliton - like contributions can surely be neglected.

This opinion could be disputed. For the case of non stationary conditions the input of energy transfer by solitons could be entirely determining during some period of time and for the some distance from pulse heat source. It happens because of the grate difference in the velocity of heat transfer due to heat diffusion (realised mainly by phonons at high temperatures) and heat transfer due to soliton - like wave processes.

2. RESULTS OF EXPERIMENTAL WRC STUDYING

It has been used the non stationary measurements method for setting up an experiment which was realised in series of our works including [1,7-14]. Effect of non diffuse soliton - like energy transfer is also small in such an experiments: $(5 \div 50)$ K of heating as evaluated from changing of reflection coefficient $\Delta R \cong (0,5 \div 5)\%$. But this effect was entirely determining the sample transient heating in the area of WRC maximum at the $(4 \div 1)$ mm distances from IR laser focal point.

It is important that the heat energy can be translated by WRC through the samples of any of 4 main crystal types and also of some amorphous solids or glasses as it was shown in experiments [1,7-14]. WRC has following solitary wave features in mentioned our experiments: 1) the WRC amplitude is of one sign (all the time or above or below abscissa so its shape differs from sinusoidal one) and it is changing much more slowly than by diffusion law. 2) The WRC is very stable and its velocity (or velocity of its mentioned components) states nearly constant. 3) The WRC reflects from the sample surfaces without changing the sign of pulse amplitude. 4) At some conditions it may lose the stability when the only one parameter changed. For example WRC could degrade after short distance of travelling if DC electrical field will be imposed on the conducting HT SC sample [15].

3. APPROACH TO SOLITONIC MECHANISM OF THE WRC

Taking in to account this soliton - like behaviour of WRC it is naturally to try to develop the solitonic mechanism of this wave.

The heat equation

$$\frac{du}{dt} - v \frac{d^2 u}{dx^2} = 0 \quad (1)$$

does not have soliton solution as a linear one. To have a chance to make some of comparison with theoretical results in area of solitonic research we choose "Toda lattice" [16] as a very rough model of the solid state substances where WRC is travelling. Toda lattice is one - dimensional lattice with exponential interaction of the closest neighbours. It has following equation of motion (with a and b constants such that $ab > 0$):

$$m \frac{d^2 y_n}{dt^2} = a (e^{-b(y_n - y_{n-1})} - e^{-b(y_{n+1} - y_n)}), \quad (2)$$

which has at some limit the following soliton solution:

$$e^{-b(y_n - y_{n-1})} - 1 = \frac{m}{ab} \beta^2 \operatorname{sech}^2(\alpha n \mp \beta t), \quad (3)$$

with $\beta = \sqrt{\frac{ab}{m}} \sinh \alpha$. As one can see in [16], "The two last equations represent a pulse - like wave of compression for $b > 0$ with width h/α , height β^2 and speed

$$c = \beta h / \alpha, \quad (4)$$

where h is the lattice spacing. The higher the pulse, the smaller the width and the larger its speed". It is important for us here that lattice spacing h is included in expression of soliton speed c : $c = \beta h / \alpha = (h/\alpha)(ab/m)^{1/2} \times \sinh \alpha \rightarrow h(ab/m)^{1/2}$ at small α , because in this case $\sinh \alpha \rightarrow \alpha$.

One can see from expression for the c - value that it is possible to fulfil the comparison of the results for taken theoretical model with measured velocity of WRC using two parameters, namely $c \sim h/\sqrt{m}$. Such a comparison gives a kind of agreement for 10 different sample materials studied in [17].

For additional experimental support of general soliton - like model of heat transfer it would be very important to check whether the mentioned before rigid Toda lattice soliton wave velocity expression (4) is satisfying all the time when WRC is travelling along the sample. For such a control one needs to measure carefully such WRC component parameters as: height of pulse amplitude, its width and its velocity. In our case it needs fulfilment an additional experiments on scheme different from one used before; we hope to get the results of such an experiments later.

One can see from data presented in [17] that WRC velocity does not follow any dependence on heat diffusion coefficient that was changing in a very broad (4 orders of magnitude) region for solid state samples especially chosen for such investigation.

4. ABOUT KINETICS OF WRC APPEARANCE

It is important also to understand the kinetics of the WRC appearance processes following the time of laser irradiation of the sample. The following WRC creation scenario agrees with set of our different experiments and published data of soliton motion computer experiments.

The local laser excitation of the sample causes production of the solitons which distribute with approximately sound velocity, c , through all over the sample. If our explanation of WRC experiments is correct they reflect from the sample boundaries and keep moving during a time of the order of few seconds gradually losing the energy. For comparison time of lattice ions vibrational relaxation typically is equal to 10^{-12} s. When it registered at some distance from focal spot, WRC has many components with velocity at least in the range of $30 \div 1.0$ cm/s [11]. One of the slowest component has a $10^{-5} \times c$ velocity that corresponds to the speed of heat flow for the first moments of usual heat diffusion (as it was found for NdCeCuO). The interaction of the wave components with soliton flow causes nonlinear heat diffusion behaviour. In combination with sample wave dispersion it may produce the conditions of stable solitary wave existence for WRC. WRC will slowly degrade all along with solitons.

The crystal sugar results of pressure variation measurements made with $1 \mu\text{s}$ resolution at different sweep speed of oscilloscope [12] are in reasonable agreement with mentioned WRC creation scenario.

5. CONCLUSION

As an conclusion, our experimental results support the possibility of non stationary soliton - like heat transfer in different three - dimensional solid states samples, and Toda lattice model gives solution that looks like being in a kind of agreement with experimental results.

6. ACKNOWLEDGEMENTS

This work was partially sponsored by Russian Foundation of Fundamental Investigations (Project No 94-02-06489-a).

7. REFERENCES

- [1] E.M.Kudriavtsev, Yu.I.Rybalko, S.D.Zotov, M.Autric, G.Inglesakis. "IR laser induced reflection and conduction wave unlike heat diffusion process in HTSC ceramics", Proc. SPIE, vol. 1810, pp. 740-743, 1992.
- [2] N.J.Zabusky and M.D.Kruskal, *Phys.Rev.Lett.* 15,240 (1965).
- [3] E.Fermi, J.P.Pasta, S.M.Ulam, Los Alamos Report No LA-1940 (1955), published in *Collected Papers of Enrico Fermi* (University of Chicago Press, Chicago, 1965), Vol.II,p.978.
- [4] E.A.Jackson. "Nonlinearity and irreversibility in lattice dynamics", *Rocky Mountain J.Math.*,8,127(1978)
- [5] M.Toda "Solitons and heat conduction", *Physica Scripta*,20, 424-430 (1979).
- [6] p.273 In: "Solitons. (Topics in current physics: v.17)", R.K.Bullough,P.J.Caudrey Editors, 1980, p.273, Springer-Verlag, Berlin Heidelberg New York.
- [7] E.M.Kudriavtsev, S.D.Zotov, V.V.Krivov, E.N.Lotkova, Yu.I.Rybalko, " Reflection and conductance wave in HTSC after IR laser irradiation ", MRS Fall,92, Book of abstracts, H3.25, Boston,USA,1992.
- [8] Preprint FIAN No 133, Moscow, 1992; *Kvantovaya Elektronika*, No 8, s.725 (1996), (in Russian).
- [9] E.M.Kudriavtsev,S.D.Zotov,V.V.Krivov,M.Autric."Reflection and conduction wave in ceramic HTSC after IR irradiation pulse", *Physica C*, 234-240, pp.1439-1440 (1994).
- [10] E.M.Kudriavtsev, S.D.Zotov, V.A.Batanov, A.I.Demin, M.Autric, G.Inglesakis, "Study of the appearance of IR pulsed laser generated wave of reflection and conduction as detected in polycrystal high temperature superconductors," in *Gas Flow and Chemical Lasers: Tenth International Symposium*, Willy L.Bohn, Helmut Hugel, Editors, Proc. SPIE 2502, p.720-723 (1995)

- [11] E.M.Kudriavtsev, E.N.Lotkova, S.D.Zotov, M.Autric. "RCW in crystals including transparent in visible region", Proc. SPIE (will be published).
- [12]. E.Kudriavtsev, E.Lotkova, S.Zotov, K.Maeno, C.Pratt, N.Amrul, "Measuring of the pressure and reflection variation in crystal sugar samples undergoing wave of reflection and conduction", submitted to *The Review of Laser Society Engineering (The Laser Society of Japan)*, 1996.
- [13]. E.Kudriavtsev, E.Lotkova, S.Zotov, F.Guignard, G.Inglesakis, M.Autric. "Cylindrical wave of reflection and conduction in IR transparent BaF₂ single crystal excited by 2,5 μ s duration pulse of CO₂ laser", Preprint FIAN (to be published).
- [14]. E.M.Kudriavtsev, M.Autric. "Solitonic approach to the WRC mechanism", in *Advance Programme*, XI International Symposium on Gas Flow and Chemical Lasers and High Power laser Conference, P2 - 43.
- [15]. E.M.Kudriavtsev, V.V.Krivov, S.D.Zotov, M.Autric "DC electrical field influence on the behaviour of the reflection and conduction wave in polycrystal HTSC sample NdCeCuO at room temperature", Preprint FIAN No 20, p. 16, Moscow, 1996.
- [16]. M.Toda, "On a nonlinear lattice (the Toda lattice)". In: "Solitons. (Topics in current physics: v.17)", R.K.Bullough, P.J.Caudrey Editors, 1980, pp.143-155, Springer-Verlag Berlin Heidelberg New York.
- [17]. E.M.Kudriavtsev, E.N.Lotkova, S.D.Zotov, M.Autric, "Velocity of the wave of reflection and conduction propagated in different types of solid states (collected velocity data up to Jan.1996). Preprint FIAN, Moscow (to be published).

14. Chemical Oxygen-Iodine Lasers I

COIL performance modeling and recent advances in diagnostic measurements

K. A. Truesdell, C. A. Helms, S. Frerking, and G. D. Hager
3550 Aberdeen Ave SE
Phillips Laboratory, Kirtland AFB, NM 87117

D.N. Plummer and R.J. Copland
Logicon RDA, 2600 Yale Blvd, Albuquerque NM 87106

ABSTRACT

This paper describes the analysis of power extraction from a chemical oxygen iodine laser (COIL) using a Simplified Saturation Model (SSM). Previously our COIL modeling efforts have been limited by an inability to accurately measure $O_2(^1\Delta)$ concentrations which in turn is a measure of the power available in the laser. Earlier application of the SSM to RotoCOIL data implied that our measured $O_2(^1\Delta)$ could not be correct. In this paper we show how a new method for experimentally inferring $O_2(^1\Delta)$ by measuring $O_2(^3\Sigma)$ leads to better agreement between experiment and theory. These results strongly imply that if a COIL model is anchored to literature $O_2(^1\Delta)$ measurements, caution needs to be applied when using the model for predicting performance.

Keywords: Chemical oxygen iodine laser, chemical laser, chemical laser diagnostics

I. INTRODUCTION

The basic concept for a simple method of describing gain saturation and power extraction in COIL devices was developed about a decade ago at the Phillips Laboratory and is documented in an unpublished report¹. The same approach was developed independently in 1990 by Copeland et. al.² and an abbreviated description of the model was presented in 1993³. More recently Barmashenko and Rosenwaks developed simple expressions for the extraction efficiency from COIL devices for both stable and unstable resonators⁴. Finally a generalized version of the model was presented in 1996 and the model was compared to the RotoCOIL experimental data base⁵.

The initial application of SSM to RotoCOIL data relied on $O_2(^1\Delta)$ concentrations inferred from a three-dimensional Navier-Stokes calculation⁶. Here we will justify using the inferred $O_2(^1\Delta)$ concentration for the RotoCOIL modeling by directly measuring $O_2(^3\Sigma)$ in the RADICL device⁷. The direct measurements are made using a diode laser to probe an oxygen absorption line [$O_2(^1\Sigma)$ - $O_2(^3\Sigma)$] at 760 nm⁸. In addition to $O_2(^3\Sigma)$ concentrations, the absorption line width also contains gas temperature information. These type of measurements verify the usefulness of the SSM method and should improve all COIL modeling efforts.

II. EXPERIMENTAL

The oxygen diagnostic measures the R7Q8 band of the $O_2(^1\Sigma) - O_2(^3\Delta)$ absorption near 760 nm. This diagnostic was developed by Davis et. al. and its operation is described in reference 8. This wavelength region was selected because there is no absorption by other gases in the flow. Since the absorption by $O_2(^3\Sigma)$ is very weak (absorption cross section = $2.73 \times 10^{-22} \text{ cm}^2$ at 300 K), better results are obtained by using a multipass configuration.

Figure 1 shows a schematic of the oxygen diagnostic. The diode laser current is scanned at 1 kHz and the beam is carried to the RADICL laser diagnostic duct by a single mode fiber optic cable. A Herriot cell (M1 & M2 in Figure 1) is positioned around the laser diagnostic duct AR coated windows (W1 & W2 each have a 3 degree wedge) and the diode laser beam is injected with a fiber collimator (FC) into the cell through a slot in mirror M1. Typically 16 passes of the 25 cm diagnostic duct are used before the diode laser beam exits a slot in mirror M2 and impinges onto a silicon detector (SD in Figure 1). The voltage from the silicon detector is monitored with a balanced ratiometer detector (BRD) circuit along with the reference beam from the laser diode. The output from the BRD is processed by a computer where the absorption scans are averaged and stored. A typical averaging time is 1 sec (1000 scans). The diagnostic is calibrated in situ by metering bottled oxygen through a control orifice and into the laser at the beginning of each test day. Typically oxygen pressures of 0.5 to 10 torr are used for calibration.

The gas temperature in the diagnostic duct is measured with 0.005" and 0.010" diameter Type-T thermocouple coated with Teflon. Water concentration is also measured with an absorption diagnostic⁸, and the residual chlorine is measured with a He-Cd laser absorption diagnostic⁹. The total oxygen and helium pressures in the diagnostic duct are deduced from input flowrate measurements (measured with sonic orifices), total pressure measurements (using MKS Model 122 1, 10, & 100 torr barotrons), and the above water and residual chlorine measurements. Ideal gas law behavior is assumed. The $O_2(^1\Delta)$ yield in the nozzle plenum (Y_{PLEN}) is calculated from the total oxygen pressure and $O_2(^3\Sigma)$ pressure assuming [$O_2(^1\Sigma)$] = 0.

III. SIMPLIFIED SATURATION MODEL (SSM) FOR COIL LASERS

The SSM for COIL lasers is intended to explain the experimentally observed saturation curve shown in Figure 2. The key to interpreting this data is understanding the relationship between the power available (P_A), the zero loss power (P_0), and the output power, P (see Figure 3). In order to accomplish this goal mathematical expressions must be developed for P_A , P_0 , and P . This was accomplished in reference 5 with the aid of the following assumptions:

1) The dissociation of iodine has occurred upstream of the laser cavity, the flow is premixed, and deactivation in the cavity during the lasing process is negligible.

2) The concentration of $O_2(^1\Sigma)$ is assumed negligible so that the total oxygen concentration is given by:

$$O_2 \text{ total} = [O_2]_0 = [O_2(^1\Delta)] + [O_2(^3\Sigma)]$$

3) The temperature, gas density and flow velocity are assumed constant. It is common practice in COIL devices to provide area relief [i.e. increase the flow area, $(A_E/A_0) > 1$, where the cavity cross sectional area at x at the downstream mirror edge is A_E and at x at the upstream mirror edge is A_0]. Here we assume $(A_E/A_0) = 1$.

4) The power extraction can be modeled as a single frequency plane wave. This is justified even though the COIL gain medium is inhomogeneously broadened because there are many modes operating (for the large apertures of interest) and the gain is pulled down to threshold over the entire absorption line.

5) The gain saturation process can be adequately described using a Fabry-Perot resonator.

The resulting expressions⁵ for P_A , P_0 , and P are given in Equations 1-3:

$$P_A = \epsilon \dot{x}(O_2) (Y_0 - Y_{th}) \quad (1)$$

where $\epsilon = 90956.0$ Joules/ mole $I^* \rightarrow I$ photons, $\dot{x}(O_2)$ is the molar flowrate of oxygen, U_{cl_2} is the chlorine utilization, and $\dot{x}(Cl_2)$ is the molar flowrate of chlorine into the oxygen generator. The yield ($Y = [O_2(^1\Delta)]/[O_2(\text{Total})]$) is the fraction of oxygen that is in the $O_2(^1\Delta)$ excited state at any specified location. Y_0 is the oxygen yield entering the cavity and is defined by

$$Y_0 = Y_{plen} - Y_{diss}$$

where Y_{plen} is the yield just upstream of iodine injection, and Y_{diss} represents the singlet delta oxygen lost in dissociating the iodine. Y_{diss} is in turn defined as

$$Y_{diss} = N \cdot (I_2 \text{ flowrate}) / (O_2 \text{ flowrate})$$

where N is number of $O_2(^1\Delta)$'s required to dissociate one I_2 (energetically must be at least 2). The term Y_{th} represents the oxygen yield that is in equilibrium with zero gain at the cavity temperature and is given by

$$Y_{th} = 1 / (1 + 2k_{eq}(T))$$

where $k_{eq}(T) = 0.74 e^{401.4/T}$ is the equilibrium constant for the I atom/ $O_2(^1\Delta)$ energy transfer reaction.

$$P_0 = \epsilon \dot{x}(O_2) (Y_0 - Y_{sat}) \quad (2)$$

$$Y_{sat} = \frac{2g^* + \sigma [I]_0}{\sigma (1 + 2k_{eq}) [I]_0 + 2g^* (1 - k_{eq})}$$

where σ = cross section in cm^2 ($1.3 \times 10^{-16} x T^{-1/2}$). The loaded gain g^* is

$$g^* = g_T + \mathcal{L} - \frac{\ln(1-\delta)}{2L_g}$$

where L_g = gain length, \mathcal{L} = distributed non-saturable loss, and δ is the aperture diffraction loss. g_T is the threshold gain and is defined by:

$$g_T \equiv \frac{-\ln R_1 R_2}{2L_g}$$

where R_1 = outcoupler reflectivity, and R_2 is the maximum reflector.

$$P = \frac{\epsilon \dot{X}(O_2) \Omega (Y_0 - Y_{sat})}{2L_g g^*} \quad (3)$$

where:

$$\Omega \equiv \frac{(1 - R_1 - S_1) \sqrt{R_2} (1 - \delta) \ln [R_1 R_2 (1 - \delta)]}{\left[\sqrt{R_2} + \sqrt{(1 - \delta) R_1} \right] \left[\sqrt{R_1 R_2 (1 - \delta)} - 1 \right]}$$

and S_1 = mirror scattering loss. The medium extraction efficiency is defined as:

$$\eta_{med} \equiv \frac{P_0}{P_A} = \frac{(Y_0 - Y_{sat})}{(Y_0 - Y_{TH})} \quad (4a)$$

or in terms of small signal gain:

$$\eta_{med} = \frac{(g_0 - g_T)}{(g_0 - \phi g_T)} \quad (4b)$$

where g_0 and ϕ are given by

$$g_0 = \frac{\sigma [I_0] (2Y_0 k_{eq} - 1 + Y_0)}{2(1 + Y_0 k_{eq} - Y_0)}$$

and

$$\phi \equiv \frac{(k_{eq} - 1) (Y_0 - Y_{TH})}{1 + Y_0 k_{eq} - Y_0}$$

The optical resonator efficiency is defined as:

$$\eta_{opt} = \frac{P}{P_0} = \frac{\Omega (g_0 - g^*) (g_0 - \phi g_T)}{2L_g g^* (g_0 - g_T) (g_0 - \phi g^*)} \quad (5)$$

With the medium and optical extraction efficiencies defined by Equations 4 and 5, the output power may be expressed as:

$$P = P_A \eta_{med} \eta_{opt} = P_A \eta_{ext} \quad (6)$$

Note that this expression is exactly what is referred to in Reference 6 as the heuristic power equation for a premixed flow (i.e. $\eta_{mix} = 1$), assumption 1. The final equation for output power is:

$$P = P_A \eta_{med} \eta_{opt} \eta_{mix} \quad (7)$$

$$= 91 \dot{X}(Cl_2) U_{Cl} (Y_{PLEN} - Y_{DISS} - Y_{TH}) \eta_{med} \eta_{opt} \eta_{mix}$$

where η_{mix} has been added as a multiplicative correction to the power available to account for oxygen that is not accessed by iodine in the cavity, and η_{geo} is a factor that accounts for the fact that not all of the flow is interrogated by the resonator. Departures of η_{med} , η_{opt} , and η_{mix} , from values of unity represent losses which are characterized as medium, resonator, and mixing losses. The medium and optical losses are shown schematically in Figure 3 where the zero loss power and output power are plotted versus transmission. The medium loss is a consequence of extracting the power at a non zero value of threshold gain which is a result of

the optical losses forcing the maximum power to occur at a finite value of transmission. As discussed in References 5 and 6, COIL laser data for RotoCOIL and RADICL under consideration here are assumed to have η_{mix} near unity.

We refer to the expressions 1 through 7 as the COIL Simplified Saturation Model (SSM). As indicated, the cavity flow conditions (temperature, velocity and density) were assumed constant to obtain these results [Assumption 3]. If this assumption fails it is a straightforward matter to relax the constant density assumption and still obtain analytical results for the power extraction process (Reference 5, Appendix A). The generalized version contains (A_E/A_0) the ratio of the cross-sectional areas (A_E at $x = \ell$, the down stream resonator edge and A_0 at $x = 0$, the upstream resonator edge) as a parameter and degenerates to Equations 1-3 for unity values of the area ratio.

A study of the details of the SSM reveals the following. First, the yield is not driven to the threshold value (Y_{TH}) during gain saturation, but instead approaches its own saturation value (Y_{sat}), thus the accessible $O_2(^1\Delta)$ energy is the difference between Y_0 and Y_{sat} . Second, the energy difference between Y_{sat} and Y_{TH} cannot be accessed in the presence of diffraction, mirror scattering, or medium losses because the losses prevent reduction of the out coupling fraction. This behavior is illustrated in Figure 4.

IV. RESULTS AND DISCUSSIONS

In this section, we compare the simplified saturation model with experimental power data for the RotoCOIL laser device¹² and more recent data taken with the Phillips Laboratory RADICL device⁷. Table 1 lists the inputs conditions and results from the simplified saturation model for the RotoCOIL and RADICL devices. The RotoCOIL data is taken from reference 5.

Table 1. Measurement and Calculation Summary.

Parameter	source*	RotoCOIL	RADICL
Y_{PLEN} - Plenum Yield	M	0.34 (wang)	.6 ($O_2(^3\Sigma)$ probe)
Y_{DISS} - Iodine Dissociation Loss (N=5)	C	0.075	0.10
T_{CAV} - Cavity Temperature	C	167 K	170 (assumed)
k_{eq} - I - $O_2(^1\Delta)$ Equilibrium Constant	C	8.2	7.8
Y_{TH} - Threshold Yield	C	0.058	0.060
R_1 - Outcoupler Reflectivity	M	0.91	0.90
R_2 - Max R Reflectivity	vendor	0.995	0.999
small signal gain g_0	M	.0068	.012
L_g - Gain Length	M	54 cm	25 cm
g_T - Threshold Gain	C	0.0009	0.0021
\mathcal{L} - Distributed non-saturable loss (ref 5)	E	0	0
δ - Aperture diffraction loss	M	.015	0.011
g^* - Loaded Gain	C	0.0009	0.0023
$[I]_0$ - I atom concentration	C	$1.1 \times 10^{15}/cm^3$	$2 \times 10^{15}/cm^3$
Y_{SAT} - Saturation Yield	C	0.072	0.082
S_1 - Mirror Scattering Loss	M	0.0025	0.0025
η_{med} - Medium Extraction Efficiency	C	0.88	0.91
η_{opt} - Optical Extraction Efficiency	C	0.81	0.87
$x(O_2)$ - Chlorine Input Molar Flowrate	M	1.56 mole/s	0.53 mole/s
U_{cl} - Chlorine Utilization	M	0.89	0.86
η_{mix} - Mixing Extraction Efficiency	C	0.95	0.9
η_{geo} - geometric interrogation efficiency	M	1	1
power calculated using SSM and measured yield	C	17.3 kW	12.6 kW
Experimentally Measured Power	M	31.5 kW	10.7 kW

* M=measurement, C = calculation, E = estimate

For the RotoCOIL case, perusal of Table 1 clearly shows that the measured power is inconsistent with the power predicted by the SSM using the measured plenum yield of 0.34. Application of 3-Dimensional computational fluid dynamics modeling (MINT) to the RotoCOIL case indicates the required plenum yield for self consistency is $Y = 0.50$. The result of using the MINT yield value of 0.50 in the SSM is shown in Figure 5, along with RotoCOIL measured powers. The result for the constant density assumption (Assumption 3, $A_E/A_0 = 1.0$) is seen to over-predict the data somewhat. Since the mirror length for the RotoCOIL device is relatively large (eight centimeters), the gas density changes by about thirty percent over the cavity length and the generalized version of SSM is required for the RotoCOIL case under consideration here (curve $A_E/A_0 = 1.3$ in Figure 5). This result is seen to improve the agreement with the experimental results (34 kW compared to 31.5 kW).

For the RotoCOIL case, perusal of Table 1 clearly shows that the measured power is inconsistent with the power predicted by the SSM using the measured plenum yield of 0.34. Application of 3-Dimensional computational fluid dynamics modeling (MINT) to the RotoCOIL case indicates the required plenum yield for self consistency is $Y = 0.50$. The result of using the MINT yield value

V. CONCLUSION

The COIL simplified saturation model (SSM) provides a set of simple expressions for the extraction efficiencies for the constant gas density assumption and somewhat more complicated (and more accurate) expressions for a variable gas density case. The successful comparison of the model with a recently developed method for "measuring" singlet delta yield has important implications for COIL yield data. Although a great deal of effort and care has been devoted to measuring singlet delta yield in COIL devices using the 1.27 micron $O_2(^1\Delta) \rightarrow O_2(^3\Sigma)$ emission¹²⁻¹⁴, the correlation to measured power through various modeling efforts has been less than satisfactory^{1-3,5,6,15}. This casts doubt on using yields obtained with this experimental method to anchor COIL models. A great deal of care needs to be exercised when selecting COIL yield data to anchor models. This study, the SSM study of reference 5, along with the 3-D Navier-Stokes COIL mixing study of reference 16 shows that good singlet delta yield data and good I_2/O_2 mixing models are required before the chemical kinetics of I_2 dissociation and $O_2(^1\Delta) - I$ atom energy transfer can be thoroughly unraveled for COIL lasers.

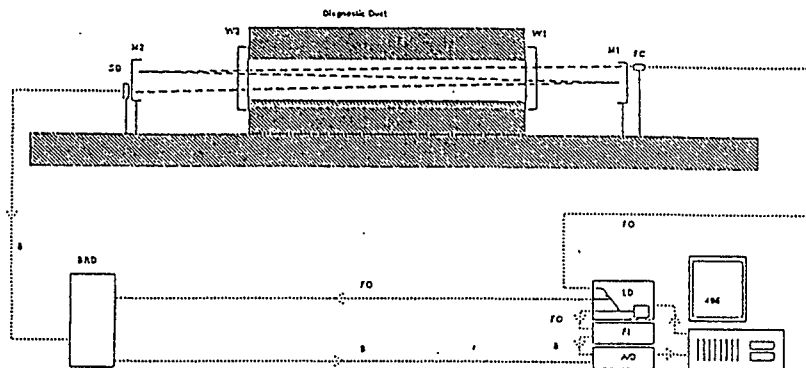


Fig. 1 Schematic for $[O_2(^3\Sigma)]$ concentration measurements.

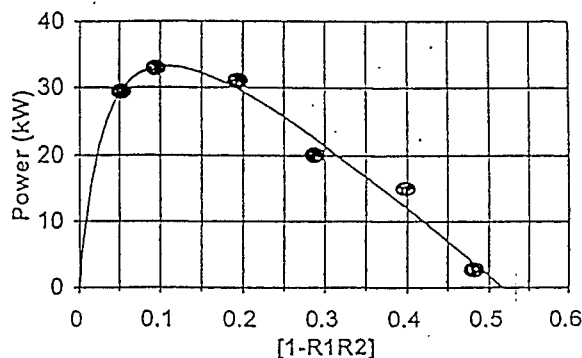


Fig. 2 RotoCOIL Isat Data

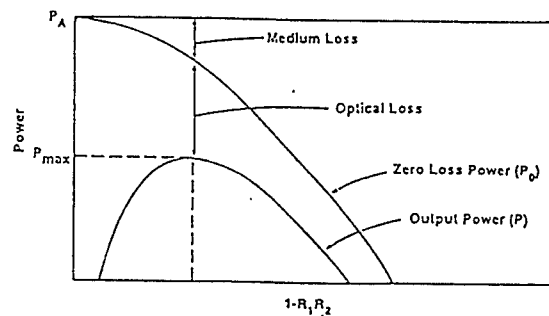


Fig. 3 Schematic Representation of medium and optical losses for power versus out coupling fraction

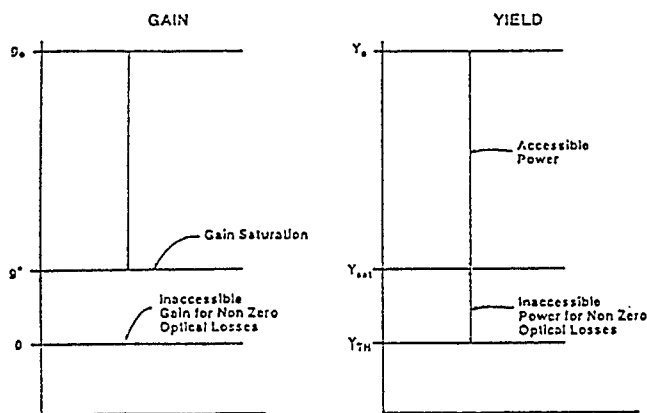


Fig. 4 Schematic Representation of Gain and Yield Saturation

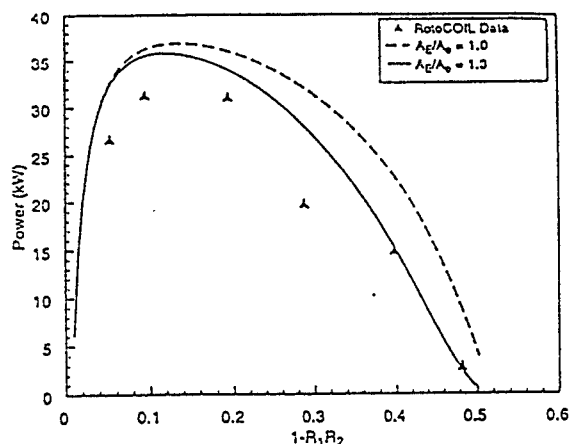


Fig. 5 Comparison of COIL simplified saturation model with RotoCOIL power saturation data

VI. References

- ¹G.D. Hager and R.H. Humphreys Jr., "Simple analytic model for gain saturation and power extraction in the chemical oxygen-iodine laser," AFWL-TR-86-117, August 1987.
- ²D.A. Copeland, C. Warner, and A. H. Bauer, "Simple model for optical extraction from a flowing oxygen-iodine medium using a Fabry-Perot resonator," *Optical Resonators*, SPIE Vol. 1224, pp 474-499, 1990.
- ³P.G. Crowell and D.N. Plummer, "Simplified chemical oxygen-iodine laser system model," *Intense Laser Beams and Applications*, SPIE Vol. 1871, pp 148-180, 1993.
- ⁴B.D. Barmashenko and S. Rosenwaks, "Simple analytical expressions for the optical extraction efficiency from COILs with different kinds of resonators," *AIAA 26th Plasmadynamics and Laser Conference*, AIAA Paper 95-1925, San Diego, CA, 1995.
- ⁵G. D. Hager, C. A. Helms, K. A. Truesdell, D. Plummer, J. Erkkila, and P. Crowell, "A simplified analytic model for gain saturation and power extraction in the flowing chemical oxygen-iodine laser," *J. Quant. Elec.*, in press, 1996.
- ⁶J.F. Hon, D.N. Plummer, P.G. Crowell, J. Erkkila, G.D. Hager, C.A. Helms, and K.A. Truesdell, "A heuristic method for evaluating COIL performance," *AIAA 25th Plasmadynamics and Laser Conference*, AIAA Paper 94-2422, Colorado Springs, CO, 1994.
- ⁷R.F. Tate, B.S. Hunt, C.A. Helms, K.A. Truesdell, and G.D. Hager, "Spatial gain measurements in a chemical oxygen-iodine laser (COIL)," *J. Quant. Elec.*, **31**, no. 9, pp 1632-1636, 1995.
- ⁸M.G. Allen, K.L. Carleton, S.J. Davis, W.J. Kessler, and K.R. McManus, "Diode laser-based measurements of water vapor and ground state oxygen in chemical oxygen-iodine lasers," *AIAA 25th Plasmadynamics and Laser Conference*, AIAA Paper 94-2433, Colorado Springs, CO, 1994.
- ⁹K.A. Truesdell, et. al., "The design and construction of a 25-kW rotating disk chemical oxygen-iodine laser (RotoCOIL)," PL-TR-92-1035, p 83, 1992.
- ¹⁰W. Rigrod, "Homogeneously broadened CW lasers with uniform distributed loss," *J. Quant. Elec.*, **14**, no. 5, pp 377-381, 1978.
- ¹¹K.A. Truesdell, C.A. Helms, and G.D. Hager, "COIL development in the USA," *AIAA 25th Plasmadynamics and Laser Conference*, AIAA Paper 94-2421, Colorado Springs, CO, 1994.
- ¹²P. Keating, L. Hanko, and G.P. Perram, "Absolute detection of O₂(¹Δ) concentrations," PL-TR-90-85, Phillips Laboratory, Kirtland AFB, NM, 1992.
- ¹³J.O. Berg, et. al., "Chemical oxygen-iodine laser advanced technology," AFWL-TR-82-51, Air Force Weapons Laboratory, Kirtland AFB, NM, 1982.
- ¹⁴S. Hurlock, et. al., "Engineering development of singlet delta oxygen generator," AFWL-TR-80-153, Air Force Weapons Laboratory, Kirtland AFB, NM, 1982.
- ¹⁵R.C. Buggeln, S. Shamroth, A.I. Lampson, and P.G. Crowell, "Three-dimensional (3-D) Navier-Stokes analysis of the mixing and power extraction in a supersonic chemical oxygen-iodine laser (COIL) with transverse I₂ injection," *AIAA 25th Plasmadynamics and Laser Conference*, AIAA Paper 94-2435, Colorado Springs, CO, 1994.

Analysis of lasing in COILs with wide aperture of the mirrors in the resonator

B. D. Barmashenko and S. Rosenwaks

Department of Physics, Ben-Gurion University of the Negev, Beer-Sheva 84105, Israel

ABSTRACT

Optical extraction efficiency of the COIL is calculated for (transverse) multimode oscillation. The effects of hyperfine and velocity cross-relaxation and changes of the gain and intracavity intensity in the flow direction are taken into account.

Keywords: optical extraction efficiency, chemical oxygen-iodine lasers, stable optical resonator.

1. INTRODUCTION

In order to extract most of the energy stored by $O_2(^1\Delta)$ in the supersonic chemical oxygen iodine laser (COIL) the dimension of the aperture of the mirrors in the resonator in the flow direction l_{res} should be 3 - 10 cm.^{1, 2} Lasing in resonators with wide aperture has some specific features. In the case of stable or Fabry-Perot resonators many transverse modes oscillate. As a result the power and spatial distribution of the output radiation differ from those for single mode oscillation. These issues are analyzed theoretically in the present paper.

2. CW MULTIMODE LASING IN THE CASE OF STABLE OR FABRY-PEROT RESONATORS

Different transverse modes have different frequencies and spatial distributions in the flow direction. As a result both the lasing power and spatial distribution of the output radiation strongly depends on the mode structure of the resonator. The influence of the mode frequency spectrum and nonuniform spatial distribution of the radiation along the flow on the power is analysed in the following sections.

2.1. Influence of the mode frequency spectrum on the optical extraction efficiency

Consider the mode frequency spectrum at a fixed position inside the resonator taking into account the processes of hyperfine and velocity cross-relaxation. Here we do not take into account the changes of the intracavity intensity and gain along the flow. Assume that the Lorentzian linewidth $\Delta\nu_L$ is much less than the Doppler linewidth $\Delta\nu_D$ which is always the case for the COIL.¹ The output power P of a laser can conveniently be presented as ²

$$P = P_{av} \eta_{ext}, \quad (1)$$

where η_{ext} is the extraction efficiency; P_{av} is the maximum available power expressed by the Doppler saturation parameter I_{SD} , the small signal gain g_0 , the gain length L and the beam cross section S as

$$P_{av} = I_{SD} g_0 L S. \quad (2)$$

It is convenient to represent η_{ext} as a product of the extraction efficiency of the resonator, η_r , and the extraction efficiency for extracting power from the gain medium, η_m : $\eta_{ext} = \eta_r \eta_m$, where

$$\eta_r = \frac{t}{t + a} = \frac{g_{th} 2L - a}{g_{th} 2L}, \quad (3)$$

t and a are the transmission and loss of the mirrors, respectively; $g_{th} \equiv (t + a)/2L$ is the threshold gain of the resonator. The most important parameter η_m depends on the mode frequency spectrum and the rates of hyperfine and velocity cross-relaxation. In the case of single mode lasing η_m can be found using results obtained in ³:

$$\eta_m = 1 + \frac{1}{2 f (g_0/g_{th})} - \left[\frac{1}{(g_0/g_{th})^2} + \frac{1}{f (g_0/g_{th})} + \frac{1}{4 f^2 (g_0/g_{th})^2} \right]^{1/2}, \quad (4)$$

where $f = I_{SL}/I_{SD}$ is the cross relaxation factor³ and I_{SL} is the Doppler saturation parameter (the values of I_{SL} and I_{SD} are presented in³). If the rates of hyperfine and velocity cross-relaxation are very large $f \rightarrow \infty$ and η_m reaches its maximum value given by the Rigrod model² $\eta_{m, Rig} = 1 - g_{th}/g_0$.

Consider multimode lasing assuming that the following condition for the distance between the modes Δv_m holds: $\Delta v_L < \Delta v_m \ll \Delta v_D$. The latter inequality means that many modes are oscillating, whereas the former means that the modes are well separated. In this case, performing analysis similar to that described in³ we find that η_m is given by

$$\eta_m = [1 - \exp(x^2)(g_{th}/g_0)], \quad (5)$$

where $x = 2(\ln 2)^{1/2} \Delta v / \Delta v_D$ and Δv is the half width of the lasing spectrum. The value of x is found from the algebraic equation:

$$\begin{aligned} & [\operatorname{erf}(\sqrt{2}x)e^{x^2} + 1]e^{x^2} - \frac{2x}{\sqrt{\pi/2}} \frac{\varepsilon}{g_{th}} = \frac{g_0}{g_{th}}, \\ & \varepsilon = f \frac{\Delta v_D}{\Delta v_m} \frac{1}{\sqrt{\ln 2}}. \end{aligned} \quad (6)$$

Fig. 1 shows dependencies of η_m and x on the parameter ε which is inversely proportional to the distance Δv_m between the modes. As the number of modes increases and the distance Δv_m between them decreases, the dimensionless half width x of the lasing spectrum also decreases resulting in increase of the efficiency η_m .

For very large number of modes, when $\Delta v_m < \Delta v_L$, the above analysis is incorrect. In this case η_m is still given by Eq. (5), but x is found from the algebraic equation presented in Refs. 4 and 5, both η_m and x being independent of Δv_m . In this case η_m is the maximum extraction efficiency and x is the minimum width of the lasing spectrum that can be achieved by decreasing the distance Δv_m between the modes.

Eqs. (4) - (6) can be used to estimate the extraction efficiencies of different COILs. The effects of the hyperfine and velocity cross-relaxation are especially important for supersonic COILs operating without primary diluent and tested in our laboratory. For these lasers the pressure in the resonator is 1 Torr, $\text{He}/\text{Cl}_2 = 0.5$ (only secondary He is used), and the temperature $T = 250$ K. In this case the parameter f is small and equal to 0.18. Hence, in the case of single mode lasing η_m found from Eq. (4) is also small and equal to 0.35 for $g_0/g_{th} = 5$ (the maximum possible efficiency $\eta_{m, Rig} = 0.8$ is much greater than η_m). In the case of multimode lasing η_m increases, e.g., for $\Delta v_D/\Delta v_m = 4$ (5 modes inside the Doppler profile) $\eta_m = 0.53$. Further decrease of Δv_m makes it possible to obtain the maximum possible efficiency and minimum width of the spectrum: for $\Delta v_D/\Delta v_m = 8$, $\eta_m = 0.7$ and $x = 0.61$. For the COILs developed at the Phillips laboratory⁶ the pressure is about 7 Torr and $\text{He}/\text{Cl}_2 = 4$. In this case $f = 3.2$ and even in the case of single mode lasing $\eta_m = 0.7$ is close to $\eta_{m, Rig} = 0.8$ ($g_0/g_{th} = 5$). Hence the influence of hyperfine and velocity cross-relaxation is small and increase in the number of modes does not affect η_m .

2.2. Influence of variation of the intracavity intensity and gain in the flow direction on the optical extraction efficiency

In the COIL both the gain and intracavity intensity I change in the flow direction. In what follows we consider the influence of these changes on the optical extraction efficiency of stable resonators. As shown above in the case of multimode lasing the spectrum is narrow, hence we assume that the gain for any mode is close to that in the center of the line. Besides, we do not take into account the effects of hyperfine and velocity cross-relaxation assuming that the saturation of the local gain is homogeneous.

The rate of change of the $O_2(^1\Delta)$ yield $Y \equiv [O_2(^1\Delta)]/[O_2]$ with distance x is equal to the stimulated emission rate,

$$U \frac{dY}{dx} = - \frac{g}{[O_2]} \left(\frac{I}{h\nu} \right), \quad (7)$$

where U is the flow velocity,

$$g = \sigma \frac{[I]_0}{2} \frac{(2K_e + 1)Y - 1}{(K_e - 1)Y + 1} \frac{1}{1 + I/I_{SD}} \quad (8)$$

is the gain,

$$I_{SD} \approx h\nu \frac{2 k_f [O_2]}{3 \sigma K_e} [(K_e - 1)Y + 1], \quad (9)$$

$\sigma \equiv (7/12)\sigma_{34}$, $\sigma_{34} = 1.29 \times 10^{-17} (300/T)^{1/2} \text{ cm}^2$ being the stimulated emission cross section for the $I(^2P_{1/2}, F=3) \rightarrow I(^2P_{3/2}, F=4)$ transition, $[I]_0 \equiv [I^*] + [I]$, k_f is the forward rate constant of the reaction $O_2(^1\Delta) + I(^2P_{3/2}) \leftrightarrow O_2(^3\Sigma) + I(^2P_{1/2})$ and $K_e = 0.75 \exp(402/T)$ is the equilibrium constant of this reaction.

Assuming that number n of transverse modes participate in lasing,

$$I(x) = \sum_{i=1}^n I_i f_i(x), \quad (10)$$

where $f_i(x)$ is a known function vanishing as $x \rightarrow \pm\infty$ and $\int_{-\infty}^{\infty} f_i(t) dt = 1$, $i = 1, \dots, n$. The mode intensities I_i can be found from the conditions

$$\int_{-\infty}^{\infty} g f_i(x) dx \begin{cases} = g_{th}, & I_i > 0 \\ \leq g_{th}, & I_i = 0 \end{cases} \quad (11)$$

Consider the so called case of fast $O_2(^1\Delta)$ energy extraction² when the residence time of the gas in the resonator, $t_g \equiv l_{res}/U$, is much greater than the $O_2(^1\Delta)$ extraction time, $t_e \equiv 1/(k_f[I]_0)$. Only in this case the extraction efficiency is high. The spatially averaged intensity I in this case is much less than I_{SD} defined by Eq. (9). If we assume that $I(x)$ does not have peaks then $I(x) \ll I_{SD}$ for any x . In this case the total intensity $I = \sum_i I_i$ and hence the lasing power can be found analytically from the system of Eqs. (7) - (9) and (11). For any set of modes participating in lasing the power is given by Eq. (1), where $P_{av} = h\nu [O_2] S U [Y_i - 1/(2K_e + 1)]$, whereas η_m is a solution of the algebraic equation

$$\eta_m + (1 - \eta_{m,F-P}) \ln(1 - \eta_m) = 0, \quad (12)$$

where

$$\eta_{m,F-P} = (1 - \frac{g_{th}}{g_0}) / \left[1 - \frac{g_{th}}{g_0} \frac{Y_i - \frac{1}{2K_e + 1}}{Y_i + \frac{1}{K_e - 1}} \right] \quad (13)$$

is the extraction efficiency for a COIL with a Fabry-Perot resonator in the case of fast $O_2(^1\Delta)$ energy extraction, Y_i is the initial value of Y before the resonator. Fig. 2 shows the dependencies of η_m , $\eta_{m,F-P}$, and $\eta_{m,Rig}$ on g_{th}/g_0 . It is

seen that $\eta_m > \eta_{m,F-P} > \eta_{m,Rig}$ for any g_{th}/g_0 . These inequalities can be obtained analytically from Eqs. (12) and (13).

The intensities I_i of different modes were calculated in the simplest case of plane mirrors when $f_i(x) = \sin^2(i\pi x/2l_{res})/l_{res}$. Calculations show that only high order transverse modes participate in lasing. The maximum number of oscillating modes depends on diffraction losses. In particular, if the diffraction losses $\delta_{dif}(i) = 10^{-3} g_{th} i^2 L$ and $g_{th}/g_0 = 0.4$ only the modes with $i = 3, 4$ and 5 oscillate ($I_3/I_4/I_5 = 0.34/0.007/1$). Although the diffraction losses strongly affect the energy distribution between the modes, the total power is almost independent of the losses. Also in the case of stable resonators with spherical mirrors, only the high order Hermitean modes totally filling the resonator cross section oscillate. As a result $I(x)$ near the resonator edges is higher than in the center which is in line with experimental observations. In this case the above approximation $I(x) \ll I_{SD}$ is not always correct; numerical estimates show that η_m still can be calculated using Eq. (12) (in fact η_m is a little lower than that given by Eq. (12)).

3. CONCLUSIONS

The above analysis suggests formulas for calculating the optical extraction efficiency η_m in COILs with stable resonators in the case of multimode lasing. Eqs. (4) - (6), taking into account the effects of the hyperfine and velocity cross-relaxation, should be used in the case of slow $O_2(^1\Delta)$ energy extraction or for calculating the power at a fixed position inside a Fabry-Perot resonator. In the case of fast $O_2(^1\Delta)$ energy extraction Eq. (13) should be used to calculate η_m . In the latter case the efficiency of stable resonator is higher than that of a Fabry-Perot resonator. It is shown that only high order transverse modes participate in the lasing.

REFERENCES

1. D. A. Copeland and A. H. Bauer, *IEEE J. Quantum Electron.* **29**, 2525(1993).
2. B. D. Barmashenko and S. Rosenwaks, *AIAA* **95-1925**.
3. M. V. Zagidullin, V. I. Igoshin and N. L. Kupriyanov, *Sov. J. Quantum Electron.* **14**, 930 (1984).
4. G. C. Valley, *IEEE J. Quantum Electron.* **17**, 1292(1981).
5. M. V. Zagidullin, A. P. Zaikin and V. N. Igoshin, *Kratkie soobshchenia po fizike*, No. 10, 3 (1987) (in Russian).
6. C. A. Helms, J. Shaw, G. D. Hager, K. A. Truesdell, D. N. Plummer, and R. J. Copland, *SPIE*, **2502**, 250(1995).

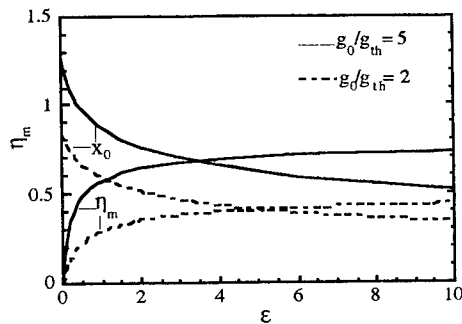


Fig. 1. Dependencies of η_m and x on the parameter ϵ which is inversely proportional to the distance Δv_m between the modes.

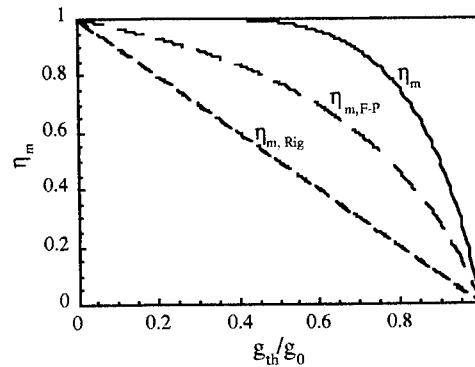


Fig. 2. Dependencies of η_m , $\eta_{m,F-P}$, and $\eta_{m,Rig}$ on g_{th}/g_0 , $Y_i=0.4$ and $T=150$ K.

A new type of rotating disk singlet oxygen generator

Wolfgang O. Schall and Frank Duschek

DLR - Institut für Technische Physik, Postfach 80 03 20, D-70503 Stuttgart, Germany

ABSTRACT

A small rotating disk generator, particularly suited for closed cycle operation has been built and operated successfully. The generator has no external drive for the disks, but is rather driven by the momentum of the injected basic hydrogen peroxide. The rotation rate and the submergence of the disks in the liquid pool can be adjusted independently by the liquid flow rate, the size of the injection nozzle, the height of the outlet for the liquid, and also by the amount of injected gas. The closed cycle comprises a liquid reservoir for the cooling of the liquid and for the sedimentation of crystalized salt, and a gear pump for circulation of the liquid. First results for utilization and yield have been gained as a function of total pressure, rotation rate, and gas flow rate and composition. The performance of the generator shows a remarkable improvement over a sparger type generator for equal flow rates.

Keywords: Chemical oxygen-iodine laser, singlet oxygen generators, rotating disk generator

1. INTRODUCTION

Rotating disk type generators for chemical reactors, in which a gaseous species is to react with a liquid on the surface of the disks, are known at least since the thirties of this century¹. Their use for the generation of singlet oxygen by the reaction of chlorine gas with basic hydrogen peroxide (BHP) has first been mentioned in public in a study of the American Physical Society² and elaborated by Harpole et al³. Disk type generators have been used successfully and extensively at Phillips Laboratory, Kirtland, USA^{4,5} and also at DLR, Lampoldshausen, Germany^{6,7}. The idea of the rotating disk generator is to provide a continuously replenished liquid surface and expose it to an also continuously flowing gas. A series or stack of disks is partially submerged into the BHP. As the disks rotate the surfaces that emerge from the liquid are covered with a thin layer of the BHP which reacts with the chlorine gas. After the reaction the surface dives again into the liquid pool and it is assumed that the used-up and warm liquid dissolves from the surface in the bath and fresh BHP attaches to the surface. The short residence time of the oxygen in the generator enables the production of singlet oxygen at high partial pressures (>1 kPa) and high efficiency and therefore makes rotating disk generators particularly suitable for supersonic chemical oxygen iodine lasers.

In conventional rotating disk generators the shaft of the disk pack is led through the generator housing and connected to an electric motor, which turns the disk pack with a rate of up to 60 rpm (1 Hz). The sealing of the feed-through for the shaft from atmospheric pressure to the low-pressure generator interior requires careful maintenance. If the residence time of the BHP in the generator is long an active cooling of the BHP inside the generator is highly indicated to prevent excessive evaporation of water (which is detrimental to the laser kinetics) and also a dangerous run-away effect of spontaneously decomposing peroxide.

2. EXPERIMENTAL APPARATUS

2.1 Generator

A new type of rotating disk generator (called "Autodisk") has been designed, built, and tested with the special emphasis on simplicity and suitability for long-time continuous operation. Continuous operation requires the flowing of the BHP through the generator. In the Autodisk-concept the momentum of the flowing liquid is used for keeping the disk pack in continuous rotation. The experimental device (Fig. 1) has been designed for a small total gas flowrate of up to 10 mmol/s chlorine + buffer gas (He, Ar or N₂). The housing is made from lucite and has only inlets and outlets for the liquid and the gas (and some diagnostic devices), but no feed-through for a wheel drive. The wheel consists of a stack of 10 nickel disks on a shaft with 3 mm spacing, each disk being 1 mm thick ($A/V \approx 3 \text{ cm}^{-1}$). The disks have a diameter of 80 mm. Twelve blades around the circumference of the same sheet material are sticking through the disk pack radially in the outer half of the disk radius. These blades serve several purposes: Beside holding the disk pack together they transfer the momentum of the liquid onto the wheel and bring it into motion. In addition, the reactive gas (chlorine and some buffer gas), flowing in from the top of the housing, is forced to penetrate into the narrow inner space between the disks. The high flow drag there may otherwise prevent a large part of the gas from reaching this space. The disk pack wheel is suspended on a simple slide bearing in the housing walls and can be easily removed from the top.

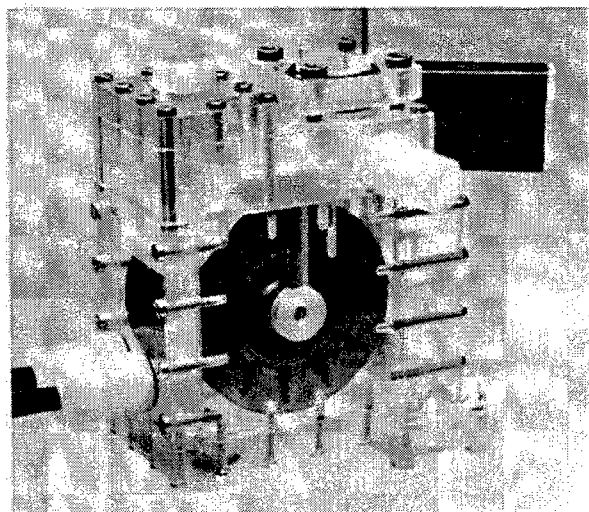


Fig. 1. Auto Disk generator

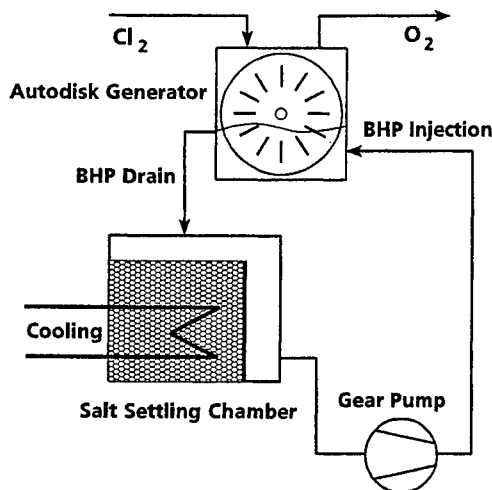


Fig. 2. BHP flow loop for closed cycle operation

The BHP enters the housing interior 18 mm above and parallel to the floor via two injection nozzles at the small side of the housing. On the opposite side the lower part of the wall is replaced by a plate with adjustable height. It forms a spill and allows the variation of the liquid level independent of the liquid flow rate (rotation rate). Behind the spill the BHP flows down vertically into a tank. The introduced unreacted gas is equally distributed across the housing depth by a multitude of inlet orifices. A bending of the wheel blades or an angle to the gas flow can give rise to an aerodynamical force on the plate which acts or counteracts the turning direction imposed by the liquid flow. The reacted gas leaves the housing on the other side vertically up through the top cover. The flow direction of the gas relative to the rotation direction of the disks can be selected by a turning of the cover by 180° .

2.2 Closed BHP circuit

Fig. 2 shows the principle arrangement of the flow loop. The collection tank immediately below the generator is equipped with a cooling coil for removing the heat of reaction from the BHP. The volume of the tank is filled with Raschig rings to slow down the flow and allow the settling of crystallized salt, which eventually accumulates at the bottom. To prevent entrainment of large amounts of salt into the pump, the BHP flows over a spill to remove only the top layers of the liquid volume. The gear pump for circulation requires a minimum pressure head for proper operation and is therefore installed 1 m below the collecting tank. The outlet of the pump is directly connected to the liquid inlet of the generator. The rotation speed of the pump and thus the flow rate of the liquid can be controlled. The rotation rate of the disks is monitored by a light barrier. The lowest rotation rate of the nickel disks is about 1/3 Hz. A lower flow speed cannot overcome the inertia of the relatively heavy disk pack and leads to a jerky motion of the wheel. The upper limit of the applicable rotation rate is set by a trapping of the liquid between the wheel blades at rotation rates of 3 to 4 Hz. The standard liquid content of the whole system is 2.2 l BHP.

2.3 Diagnostic equipment

The 21 mm inner diameter glass tube for conducting the oxygen extends 15 cm in vertical direction above the generator outlet before it is bend into horizontal direction. A V-shaped liquid separator is attached in case liquid is carried downstream. A cold trap may be added, but has not been used with this generator. One meter downstream of the bend is the $O_2(^1\Delta)$ detection tube, which can be calibrated by a blackbody source. Also connected to the glass tube is a mass spectrometer for measuring the water vapour content of the flow. Finally, there is an absorption cell directly after the singlet delta detection tube for measuring the residual chlorine in absorption at a wavelength of 330 nm. The gas flow rates of chlorine and the buffer gas are measured with conventional flow meters before mixing. Pressure and temperature can be measured inside the generator and at two locations along the flow tube. The temperature in the collection tank is continuously surveyed and is usually kept steady at -15°C . The degree of reaction can be monitored by a pH-electrode inserted into the collection tank.

3. EXPERIMENTAL RESULTS

First experiments were carried out with water only in order to characterize the liquid level as a function of liquid flow rate, rotation rate and the height of the spill. The main goal of the investigations is to prove the feasibility of the concept and to find out the laser relevant performance data, i.e. the chlorine utilization ($U = [\text{O}_2]/[\text{Cl}_2]$) and the yield of singlet oxygen ($Y = [\text{O}_2(^1\Delta)]/[\text{O}_2]$) as a function of gas flow rate and gas composition, BHP composition, rotation rate and the coverage of the disks with BHP. The gas flow rate defines the generator pressure, but can also modify the rotation rate. The generator pressure can also be adjusted by throttling the volume flow rate of the vacuum pump. Utilization and yield are a measure for the efficiency of the generator and can directly be compared to similar investigations with a sparger type generator for the same parameter range⁸. Other important aspects of the investigation are the long term behaviour of the closed cycle, including questions of temperature and chemical stability of the BHP. Typical run times are 10 to 30 minutes before the BHP is largely degraded. Problems to be solved are the extension of these run times by continuous replenishment of the BHP through the adding of KOH, and the management of the salt production.

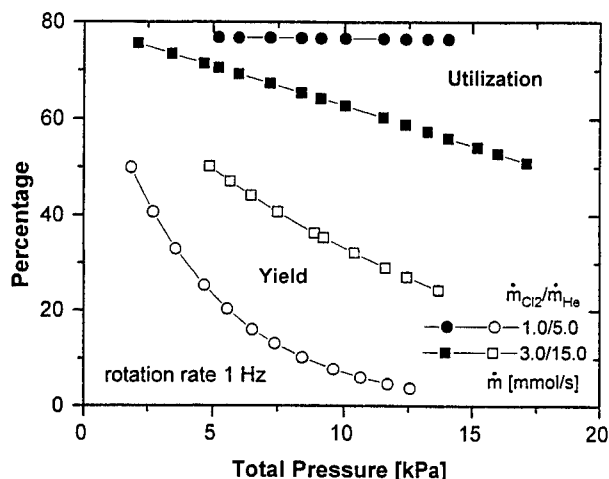


Fig. 3. Utilization and yield vs. generator pressure for two different gas flow rates but equal composition.

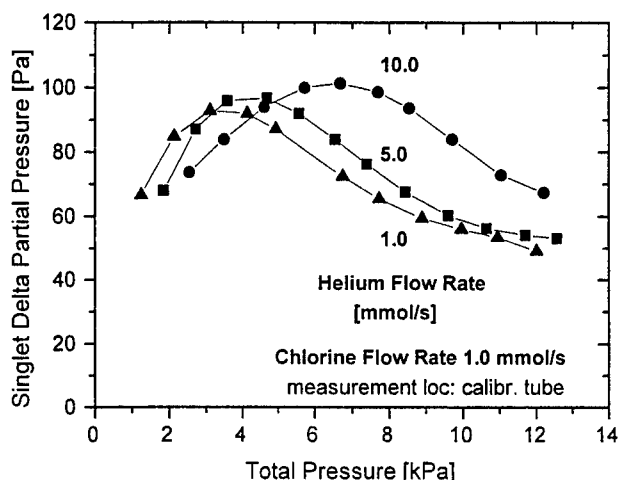


Fig. 4. Partial pressure of $\text{O}_2(^1\Delta)$ vs. total pressure for three mixture ratios with helium.

Test runs have been made with helium and with argon as the buffer gas. Fig. 3. shows utilization U and yield Y as a function of the total pressure for two gas flow rates: $\text{Cl}_2 + \text{He} = 1.0 + 5.0$ mmol/s and $3.0 + 15.0$ mmol/s, thus keeping the mixture ratio constant. The BHP composition is 7.4 mol/l KOH with 0.6 mol/l H_2O_2 in excess. The rotation rate of the disks was kept steady at 1 Hz. The difference for U and Y for the two flow rates is remarkable. The utilization decreases linearly with pressure for the high flow rate only, in contrast to the nearly independent behaviour at the low gas flow rate. Because for the high flow rate the gas velocity in the generator is 3 times higher at the same total pressure, it is assumed that the supply of O_2H^- ions to the reactive BHP surface layer is too slow and we are thus operating in a diffusion controlled mode. On the other hand the yield is much higher. Comparing the chemical efficiency of the generator, $U \cdot Y$, gives a four times better value at 10 kPa in spite of the lower utilization at the high flow rate. The absolute yield values at the generator exit are still higher, because especially at higher total pressures a significant fraction of the singlet delta molecules is lost due to the various quenching mechanisms in the rather long flow tube. Taking into account pooling losses only, the generator exit yield at this pressure is at least 26%. As expected, large amounts of helium shift the partial singlet delta pressure towards higher total pressures, as seen in Fig. 4. The optimum moves from 3 to 4 kPa at helium contents of less or equal 5 times the chlorine amount to over 6 kPa with $\text{He}:\text{Cl}_2 = 10:1$. It must be stated however, that the yield remains largely unaffected by the amount of helium. The same is true if helium is replaced by argon, a finding comparable to results with a sparger generator⁸. In a particular test series the pressure has been kept constant and the rotation rate of the disks has been varied by changing the flow rate of the BHP (Fig. 5). In this case the utilization decreases and the yield increases with growing rotation rate. In essence, the efficiency remains nearly constant. It is noteworthy to mention that this behaviour does not agree with findings in the large rotating disk generator at our Lampoldshausen site⁷. The test runs with argon at flow rates of 1 mmol/s $\text{Cl}_2 + 3$ mmol/s Ar allow a direct comparison with former results gained with a sparger type generator. It is seen from Fig. 6 that the new Autodisk generator is superior of the sparger generator, which becomes particularly prominent at higher total pressures. Measurements of water vapour in the flow yielded comparable results to those of a sparger generator filled with Raschig rings and is about a third lower than from an ordinary sparger generator.

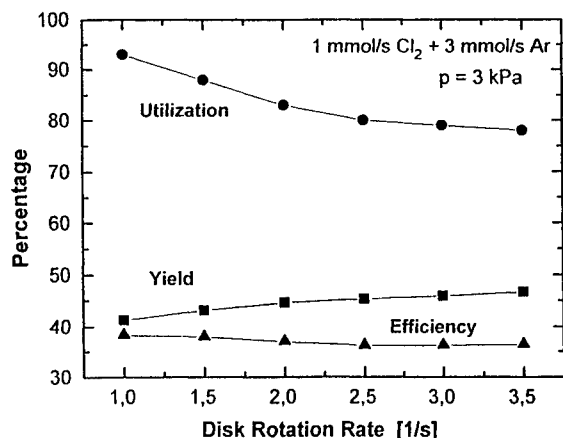


Fig. 5. Utilization, yield and efficiency vs. disk rotation rate for argon as the buffer gas.

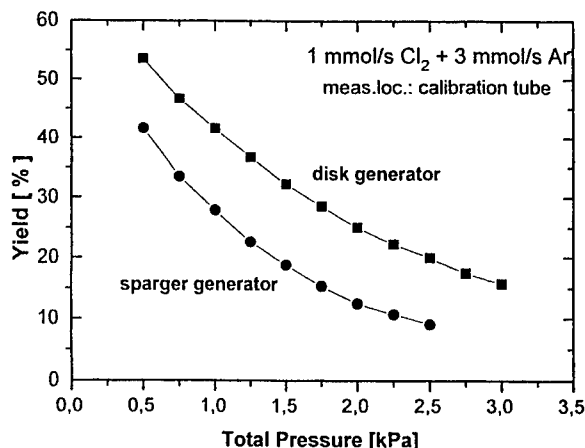


Fig. 6. Comparison of yield for the Autodisk and a sparger generator at equal flow conditions.

Beside the establishment of operational limits to the generator, in particular with respect to high pressures, future investigations will look into more general questions, such as the effects of the rotation direction relative to the gas flow, of disks made from other materials (i.e. plastics) and with modified surfaces, and of the packing density of the disks (specific area A/V).

4. CONCLUSIONS

A small rotating disk generator, which is internally driven by the flowing BHP of a closed flow circuit has been built and operated successfully and is a feasible concept for a simple oxygen generator. This generator is particularly appropriate for high generator pressure operation in a closed BHP flow loop. The results are superior to those of a sparger generator of comparable design data, although the generator proper assumes only a small fraction of the sparger.

5. ACKNOWLEDGMENTS

Special credit is given to R. G. Kwirandt, who has set up the closed circuit, made it work and gained the very first results.

6. REFERENCES

1. German patent no. 614 175, 1935
2. "Science and Technology of Directed Energy Weapons", *Reviews of Modern Physics*, Vol. 59, No. 3, Part II, July 1987.
3. G.M.Harpole, W.D.English, J.O.Berg, and D.J.Miller, "A rotating disk oxygen generator", *AIAA 23rd Plasmadynamics and Lasers Conference*, 92-3006; 6 July 1992, Nashville TN, USA.
4. K.A.Truesdell, C.A.Helms and G.D.Hager, "A history of COIL development in the USA", *Gas flow and Chemical Lasers: 10th Int. Symposium*, Proc. SPIE Vol. 2502, pp. 180-203 (1994).
5. S.P.Phipps, C.A.Helms, K.A.Truesdell, and K.P.Healey, "A compact cw supersonic chemical oxygen-iodine laser (COIL)", *Gas flow and Chemical Lasers: 10th Int. Symposium*, Proc. SPIE Vol. 2502, pp. 314-320 (1994).
6. J.Handke, A.Werner, W.L.Bohn, and W.O.Schall, "Multikilowatt supersonic chemical oxygen-iodine laser", *Gas flow and Chemical Lasers: 10th Int. Symposium*, Proc. SPIE Vol. 2502, pp. 266-271 (1994).
7. K.Grünwald, J.Handke, L.v.Entress-Fürsteneck, W.L.Bohn, and W.O.Schall, "Investigations on the efficiency of a rotating disk type oxygen generator", this conference.
8. G.R.Kwirandt and W.O.Schall, "Basic Experiments on the production of $O_2(^1\Delta)$ ", *Gas flow and Chemical Lasers: 10th Int. Symposium*, Proc. SPIE Vol. 2502, pp. 331-337 (1994).

Experimental study of a small scale COIL using a jet type generator of singlet oxygen

S. Rosenwaks, I. Blayvas, B. D. Barmashenko, D. Furman and M. V. Zagidullin*

Department of Physics, Ben-Gurion University of the Negev, Beer-Sheva 84105, Israel

*Present address: P.N. Lebedev Physical Institute, Samara Branch, Novosadovaya 221, Samara 443125, Russia

ABSTRACT

We report on studies of a 5 cm gain length chemical oxygen-iodine laser (COIL) energized by a jet-type singlet oxygen generator (JSOG) are presented. For 10 mmole/s of Cl_2 flow rate, output power of 132 W with chemical efficiency of 14.5% were obtained without a water vapor trap. 163 W and 18% were achieved when cooled (173 K) He was introduced downstream of the JSOG; under these conditions the small signal gain was estimated to be $0.32\% \text{ cm}^{-1}$. 190 W and 10.5% were obtained for 20 mmole/s of Cl_2 flow rate. Replacing He by N_2 as a buffer gas resulted in a 13% power decrease only. The main key for increasing the chemical efficiency of a COIL without a water vapor trap for a given iodine-oxygen mixing system is found to be high oxygen pressure and low water vapor pressure inside the reaction zone of the JSOG. The last goal was achieved by optimizing the composition and temperature of the basic hydrogen peroxide solution (BHP). The experimental results are discussed and related to the composition and flow conditions of the gaseous reactants and of the BHP. We also report on preliminary results of efficient COIL operation without primary buffer gas using rectangular nozzles with iodine injection in the throat.

Keywords: supersonic COILs, chemical oxygen-iodine lasers.

I. INTRODUCTION

A 5 cm gain length COIL was developed at Ben-Gurion University for operation at maximum chlorine flow rate of 20 mmole/s under laboratory conditions.¹ Maximum power of 60 W for chlorine flow rate 15 mmole/s with chemical efficiency of 4.4% was obtained with a sparger-type SOG and WVC. In the present paper the operation and power optimization of this small scale COIL, but with jet-type SOG (JSOG) and without WVC are studied. This JSOG was designed, manufactured and tested at the P.N. Lebedev Physical Institute (Samara Branch) and is similar to that described in ². It is shown that optimization of the JSOG operation and laser cavity conditions result in both power and chemical efficiency increase. The results are discussed and related to the composition and flow conditions of the gaseous reactants and of the BHP solution.

II. EXPERIMENTAL SETUP

The experimental setup is presented in Fig.1. The JSOG (1) was manufactured of Plexiglass for visual observation of the BHP/ Cl_2 reaction zone. The reaction zone is 20 cm long with 12 x 50 mm cross section. The BHP is prepared in a mixing, double jacket, stainless steel tank (2) with a volume of 7.5 liter and delivered into the reaction zone under atmospheric pressure through two 1 cm i.d. polyethylene tubes. The BHP jets are generated in the reaction zone through a perforated plate (3) mounted in the upper part of the JSOG. Two kinds of perforated plates are used. Jet plate # 1 has 74 tubes of 10 mm length and 0.6 mm i.d., and 17 tubes of 23 mm length and 0.8 mm i.d. It is used when 10 mmole/s of chlorine flow rate is applied, the BHP flow rate being 0.2 liter/s. Jet plate #2 has 86 holes of 2.5 mm length and 0.7 mm i.d. and 20 tubes of 23 mm length and 0.8 mm i.d. For this plate both the BHP flow rate (0.32 liter/s) and the gas/liquid interfacial area are greater than those for plate #1. Plate #1 was replaced by #2 for chlorine flow rate of 20 mmole/s. The row of 23 mm long tubes is located closer to the output slit valve (4). The chlorine is delivered into the reaction zone through two perforated stainless steel tubes (5) mounted on the walls of the JSOG. The chlorine inlet position is at 10 or 15 cm from the output slit valve. The cross section of the slit in the valve controls the linear velocity of the gas flow in the JSOG reaction zone. The primary buffer gas can be mixed with chlorine upstream of the chlorine inlet (5) or with oxygen downstream of the slit valve. In the latter case the buffer gas is delivered into gas injectors (6) located in the upper and lower walls of an intermediate cell (7) and admixed through number of holes drilled in walls of the cell. The intermediate cell is 20 cm long (in the flow direction) with 5 cm wide, 1 cm high cross section.

Downstream of the intermediate cell iodine mixing nozzles (8) and a laser cavity (9) are located. Detailed description of the nozzles, laser cavity and molecular iodine vapor generator are given in ¹. The iodine mixing system consists of 5 nozzles with iodine injector holes in both sides of each nozzle; the injection occurs 8 mm upstream of the nozzle throat. The laser section, starting at the nozzle exit plane, is a $5 \times 1 \text{ cm}^2$ flow duct; 3 cm from the nozzle exit plane, the floor and the ceiling of the duct open at an angle of 2° . At the end of the section, 18 cm downstream of the nozzle exit plane, the height of the duct reaches 2 cm. The optical resonator is 26 cm long, has 5 cm active length and consists of one flat mirror and one of 1 m curvature. Two optical axis positions are available: 7 cm and 15 cm downstream of the nozzle exit-plane. The vacuum pumping system provides a volumetric pumping rate of 450 liter/s.

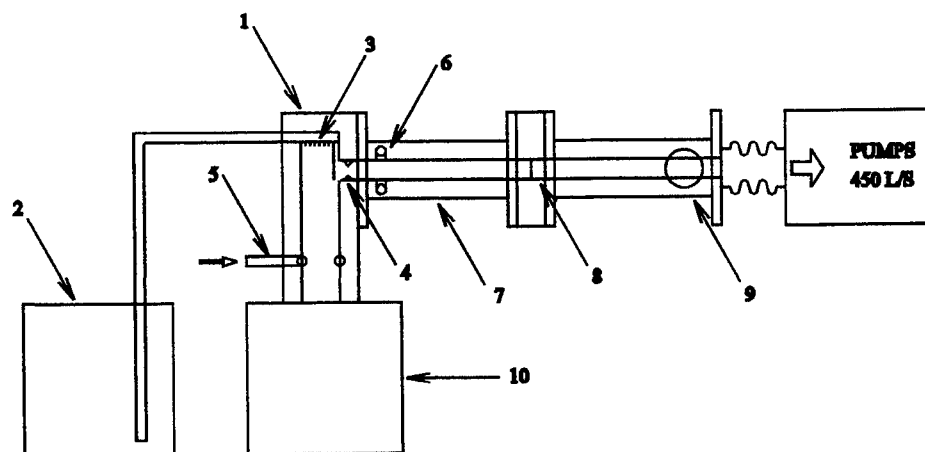


Fig. 1. The chemical oxygen-iodine laser/jet-type singlet oxygen generator (JSOG) setup. (1) JSOG, (2) mixing tank, (3) perforated plate, (4) slit valve, (5) chlorine inlet, (6) gas injector, (7) intermediate cell, (8) nozzles, (9) laser cavity, (10) collecting tank.

During the experiments the molar flow rate of He, Cl_2 and I_2 and the pressure in the reaction zone (P_0), the intermediate cell (P_1), the nozzle exit plane (P_2) and at the end of the laser section (P_3) (18 cm downstream of the nozzles) were measured as described in ¹. The output power from one of the mirrors (that with the higher transmission) was measured with a powermeter (Ophir-Nova 150 W). The total output power is assumed to be equal to $W \approx W_1(T_1 + T_2)/T_1$ where T_1 and T_2 are the mirror transmissions and W_1 the output power from the T_1 mirror. The time duration of a single COIL run was 20 s for 10 mmole/s of chlorine flow rate and 10 s for 20 mmole/s. After each run the BHP was collected in tank (10) and delivered back into tank (2).

III. RESULTS

The operation parameters of the JSOG were initially tested at the P.N. Lebedev Physical Institute (Samara Branch). For chlorine flow rate 10 mmole/s typical values of the $\text{O}_2(^1\Delta)$ yield and chlorine utilization are 65% and 90%, respectively. The measurements were performed with BHP prepared from 3 liter, 32% wt H_2O_2 and 1.5 liter, 46% wt (12M) aqueous KOH solution at -10°C . For decreasing the water vapor partial pressure the COIL experiments at Ben-Gurion University were performed with BHP prepared with 50% wt H_2O_2 . For COIL without WVC the water vapor fraction at the exit of the JSOG is a very important parameter because of its quenching role in the iodine mixing and dissociation zone. The water vapor pressure inside the JSOG is close to the saturated water vapor pressure and the BHP temperature should be as low as possible to decrease quenching of $\text{O}_2(^1\Delta)$. However, the BHP temperature decrease is bounded by the freezing point. The freezing point strongly depends on the BHP composition³. In the present series of experiments three BHP solutions were tested:

BHPa: 3 liter 50% wt H_2O_2 + 1.5 L 46% wt KOH at -15°C (4M HO_2^- , freezing point = -16.5°C),

BHPb: 3.5 L 50% wt H_2O_2 + 1L 55% wt KOH at -20°C (3.3M HO_2^- , freezing point = -21.5°C),

BHPc: 3.75 L 50% wt H_2O_2 + 0.75 L 67% wt KOH at -20°C (3M HO_2^- , freezing point = -25°C).

For BHPb and BHPc the saturated water vapor pressure is expected to be lower than for BHPa.

In the first experiments the optimal optical axis-nozzles distance and iodine molar flow rate were found. In these experiments BHPa was jetted in the reaction zone using jet plate # 1. Chlorine at flow rate of 10 mmole/s and primary He at 20 mmole/s were delivered into an inlet 15 cm from slit valve; the gas pressure in the reaction zone of the JSOG was 90 Torr. The He flow rate through the iodine generator (secondary He) was 8 mmole/s. A maximum power of 68 W was achieved for optimal iodine flow rate, approximately 0.1 mmole/s, and optical axis position 7 cm downstream of the nozzles (mirror transmissions were $T_1 = T_2 = 0.6\%$); in all further experiments, COIL runs were done under these optimal conditions.

Using BHPb instead of BHPa at the 0.1 mmol/s iodine flow rate resulted in power increase from 68 to 90 W at 90 Torr of overall pressure in the JSOG. This is most probably due to the decrease of the partial water vapor pressure because of lower temperature which results in reduced quenching of iodine atoms in the laser and hence in losses of $O_2(^1\Delta)$.

The next step was the optimization of gas flow conditions in the reaction zone of the JSOG. In this series of experiments a $Cl_2:He$ 1:2 mixture at 10 mmole/s of chlorine flow rate was delivered to the inlet at 15 cm from the slit valve and BHPb was used. The change of the cross section of the slit valve resulted in a change of the gas pressure and velocity in the JSOG reaction zone. An optimum of ~ 60 Torr overall pressure and approximately 15 m/s of gas velocity were found. The maximum power was 108 W.

In all the above mentioned experiments the buffer gas was premixed with chlorine before the generator. However, JSOGs of high pressure also can operate with injection of pure chlorine into the reaction zone of the generator and addition of the buffer gas downstream of the slit valve. In this case the extent of mixing between the buffer gas and oxygen flow upstream of the nozzles is very important for efficient COIL operation. For checking this extent, two experiments were performed with BHPc and for mirror transmission $T_1 = T_2 = 0.6\%$. In the first experiment a $Cl_2:He$ = 1:2 mixture at 10 mmole/s of chlorine flow rate was delivered into the JSOG (inlet position 15 cm from the slit valve, working pressure 60 Torr) and in the second pure chlorine at 10 mmole/s was delivered into the JSOG (inlet position 15 cm, pressure 20 Torr) and 20 mmole/s of He was delivered into the gas injector downstream of the slit valve. In the former experiment the output power was 95 W and in the latter 108 W. Thus, it seems that the mixing of He and O_2 in the intermediate cell is good under these conditions and it is preferable to operate the laser with pure chlorine inside the reaction zone of the JSOG. In the next experiment the He flow was passed through a copper tube spiral immersed in liquid nitrogen and through a thermoinsulated pipeline and then injected into the intermediate cell. This procedure was continued for 5-10 minutes until the temperature of the pipeline outside surface reached 163 K. At this point the COIL was operated and the output power reached 120 W. In these runs condensation of water vapor was observed on the walls of the intermediate cell. For a longer time of pipeline cooling the condensation of water vapor and iodine also was observed on the walls of the laser cavity.

The dependence of the output power on mirror transmission is presented in Fig. 2. For this series of experiments the JSOG operated at 10 mmole/s of pure chlorine (20 Torr in the reaction zone) and 20 mmole/s of primary He delivered into the gas injector. By linear extrapolation to zero power (see solid line in Fig. 2) it can be estimated that the threshold gain is 3.2% and the distributed small signal gain $3.2 \times 10^{-3} \text{ cm}^{-1}$ under these conditions. Linear extrapolation to zero mirror transmission gives 200 W extractable power in the absence of nonresonant radiation losses. The highest power, 163 W, and chemical efficiency, 18%, were obtained for mirror transmissions $T_1 = 0.6\%$, $T_2 = 0.1\%$.

The influence of buffer gas species and dilution on the output power is presented in Fig. 3. In all these tests the buffer gas was introduced into the gas injector (6) (Fig. 1). It is seen that just as in Ref. 4, the power is a nonmonotonic function of the He flow rate. Substituting He by N_2 resulted in 13% power decrease under the same experimental conditions. The power decreases strongly when the flow rate of the primary diluent gas is equal to zero. The dilution of oxygen with buffer gas was accompanied by a change of the pressure in the intermediate cell. For example, for zero buffer gas flow $P_1 = 9$ Torr, for 20 mmole/s of He flow $P_1 = 13.5$ Torr and for 20 mmole/s of N_2 , $P_1 = 18$ Torr.

Several COIL runs were performed with 20 mmole/s of pure chlorine flowing into the JSOG for inlet position 15 cm from the slit valve. In these runs BHPc was jetted in the reaction zone using jet plate # 2. The working pressure in the

reaction zone was 27-28 Torr. 40 mmole/s of primary He at room temperature were delivered through the gas injector (6) (Fig. 1). The secondary He flow rate was 10 mmole/s and the iodine flow 0.1 mmole/s. Output power of 190 W for $T_1 = 0.6\%$, $T_2 = 0.6\%$ mirrors was achieved, i.e., 1.8 times more than for the same mirrors at 10 mmole/s of chlorine and 20 mmole/s of primary, uncooled He.

Very recently we have carried out experiments using rectangular nozzles with iodine injection in the throat. In preliminary tests output power of 122 W and chemical efficiency of 12% were obtained without primary buffer gas for mirror transmissions $T_1 = 0.85\%$ and $T_2 = 0.2\%$.

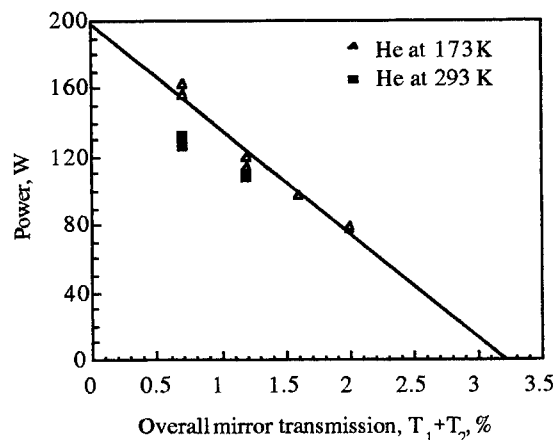


Fig. 2. Output power versus mirror transmission. The Cl_2 molar flow rate is 10 mmole/s, the He flow delivered into the gas injector (6) (Fig. 1) is 20 mmole/s, secondary He flow is 8 mmole/s and I_2 flow rate is about 0.1 mmole/s. BHPc is used.

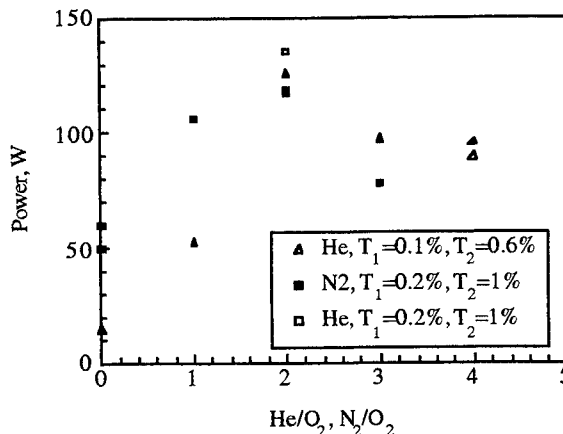


Fig.3. Influence of buffer gas dilution of oxygen on output power. The Cl_2 molar flow rate is 10 mmol/s, the secondary He flow is 8 mmole/s and the I_2 flow rate is about 0.1 mmole/s. BHPc is used. The buffer gas is delivered at 293 K.

IV. CONCLUSIONS

Output power of 132 W and chemical efficiency of 14.5% were obtained without WVC. 163 W and 18% chemical efficiency were achieved with introduction of cooled (173 K) He downstream of the JSOG. 190 W at 10.5% efficiency were obtained for a 5 cm gain length COIL for 20 mmole/s of chlorine flow rate. The estimated small signal gain was about $0.32\% \text{ cm}^{-1}$. Using nitrogen as a buffer gas instead of helium resulted in a 13% power decrease only. However, replacing helium by nitrogen allows to decrease the cost of laser operation. The main key for increasing the chemical efficiency of a COIL without water vapor trap for a given iodine-oxygen mixing system is high oxygen pressure and low water vapor pressure inside the reaction zone of the JSOG. The last goal is achieved by adjustments of the BHP composition and temperature. This adjustment is limited by the freezing point of the BHP and by slower kinetics processes when the BHP temperature decreases. Possible ways to overcome these problems are increasing of the partial oxygen pressure inside the JSOG and using BHP prepared with highly concentrated H_2O_2 . Preliminary experiments where rectangular nozzles with iodine injection in the throat were applied have shown that output power of 122 W and chemical efficiency of 12% can be obtained without primary buffer gas.

REFERENCES

1. A. Elior, B.D. Barmashenko, E. Lebiush and S. Rosenwaks, *Appl. Phys. B.*, **61**, 37(1995).
2. M.V. Zagidullin, V.D. Nikolaev, M.I. Svistun, *Quantum Electronics*, **24**, 21(1994).
3. N.P. Vagin, D.G. Karapetyan, A.F. Konoshenko, P.G.Kryukov, V.S. Pasyuk, V.N. Tomashov and N.N. Yuryshv, *Journal of Russian laser research*, **15**, 213(1994).

Improved RF plasma jet generation of singlet delta oxygen

Josef Schmiedberger¹, Sanyo Takahashi² and Hiroo Fujii³

¹ Department of Gas Lasers, Institute of Physics, Academy of Sciences of the Czech Republic
Na Slovance 2, 180 40 Prague 8, Czech Republic

² Energy Conversion Division, Department of Energy Engineering, Mechanical Engineering Laboratory
Namiki 1-2, Tsukuba, Ibaraki, 305 Japan

³ Opto Engineering Laboratory, Kanto Technical Institute, Kawasaki Heavy Industries, Ltd.
118 Futatsuzuka, Noda City, Chiba, 278 Japan

ABSTRACT

RF oxygen plasma jets were studied experimentally as an alternative source of molecular singlet delta oxygen for an oxygen-iodine laser. The relative yield of singlet delta oxygen was measured under a wide variety of experimental conditions. The RF frequency range was 27.2-99.9 MHz and the RF power was up to 200 W. The oxygen output pressure was 0.05-0.40 Torr and the oxygen flow rate was 195-1000 sccm. High purity oxygen or its mixtures with Ar, N₂, NO and Hg at the pumping velocity of 250 m³/h were used. The plasma jet was produced in nozzles, having the inner diameter of 1-6 mm and the length of 1-16 mm. The nozzle materials Al, Ti, Ta and W gave significantly better results than Pt and Ni. The dependence of singlet delta oxygen production on the radiofrequency was increasing monotonously. Other dependencies were not monotonous and exhibited an optimum. The cw mode of operation gave usually better results than a pulsed mode. The most effective admixture was N₂, which gave the highest enhancement. This resulted in the relative yield of singlet delta oxygen exceeding 15 %.

Keywords: radiofrequency plasma, plasma jet, hollow cathode, molecular oxygen, singlet delta oxygen, metastables generation, molecular nitrogen, oxygen-iodine laser.

1. INTRODUCTION

Our previous study¹, utilizing the device DSOG-1 (Discharge Singlet Oxygen Generator 1), was continued by more extensive investigation of the RF hollow cathode discharge using an improved experimental apparatus DSOG-2. The new device DSOG-2 was designed to enable more stable performance under well defined conditions and to avoid such technical problems of DSOG-1 as the residual thermal continuum background at 1.27 μ m or the fast erosion of hollow electrode. Some of the latest results of such effort are included in this paper.

Our previous results had been reconsidered and it resulted in a correction of calibration. The main change was due to substantially improved determination of optical fiber coupling to the diagnostic chamber where the fundamental emission of singlet delta oxygen was measured. The previous results became 3.8 times lower and the best of them amounted to 4.2 % yield of singlet delta oxygen.

2. EXPERIMENTAL

The experimental set up of DSOG-2 is schematically shown in Fig. 1. It consisted of two parts - a discharge chamber and a diagnostic chamber. Both of them differed from that of DSOG-1.

The discharge chamber consisted of two electrodes with an insulation in coaxial arrangement. The outer grounded electrode was made of pure aluminium and it was water cooled. The RF nozzles were made of Al, Ti, Ta, W, Pt and Ni, respectively. The nozzles had a cylindrical shape, having the inner diameter 1-6 mm and the length of 1-16 mm. The nozzle holder was made of stainless steel and it was water cooled. Gas was fed through the holder into the nozzle. High purity oxygen or its mixtures with Ar, N₂, NO and Hg were used. The pumping velocity was 250 m³/h. The oxygen partial pressure downstream the discharge was 0.05-0.40 Torr. The oxygen flow rate was 195-1000 sccm. The pressure and the temperature of gas upstream the nozzle was measured at the inlet of holder. The RF power was supplied via a matching network. The RF frequency range was 27.2-99.9 MHz and the RF power was up to 200 W. Under usual conditions

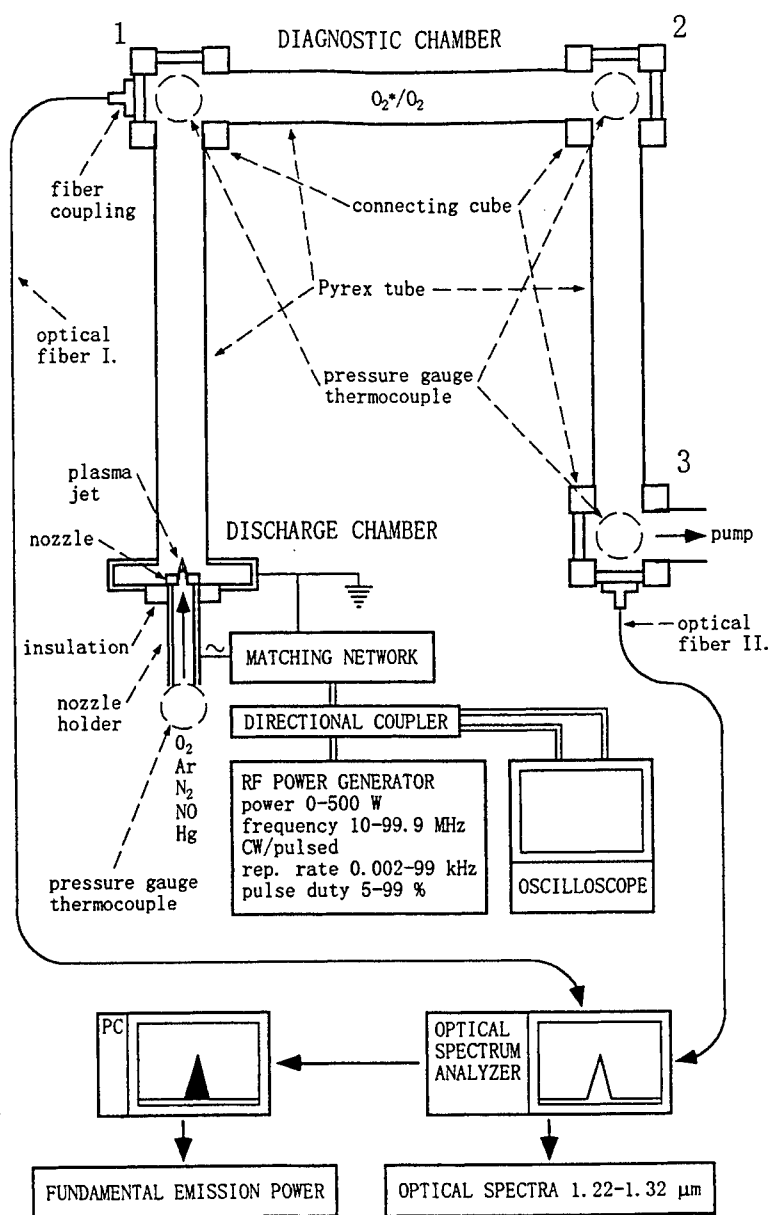


Fig.1 The experimental set up of DSOG-2

surrounding the fundamental emission band was monitored - the range 1.22-1.32 μm . This spectrum gave sufficient information about the band itself and, at the same time, about an optical noise, if any occurred. There was no problem with the residual thermal continuum background at 1.27 μm , however, some optical noise was detected in cases of mixtures containing nitrogen. This noise originated from the airglow chemiluminiscent reaction of O and NO. The personal computer integrated only the true fundamental emission band. These data together with the pressure and temperature data measured in the diagnostic chamber at the cubes 1, 2 or 3, were used for the determination of singlet delta oxygen yield.

Gases were mixed upstream the nozzle holder. Mercury was added to the gas stream when it passed through a glass vessel partially filled with Hg. This vessel was placed between the nozzle holder and the point, where gases were mixed. All gases had high grade purity 99.95 % or 99.9995 %. Premixed mixtures of nitrogen contained 2 % or 10 % of NO and they were supplied from the bottles commercially available. Other mixtures were prepared continuously.

(radiofrequency 99.9 MHz, pure oxygen flow rate 195 sccm) the threshold of plasma jet initiation inside nozzles was about 2 W only. A typical pressure upstream the nozzle was about 10 Torr.

The diagnostic chamber consisted of 3 Pyrex tubes connected by aluminium cubes. All was arranged at "U" shape geometry having the inner length of all the three parts 50 cm. The inner diameter of the whole duct was 51 mm. Each of the cubes had two glass windows and two inlets for a pressure gauge and a thermocouple. This arrangement increased the signal to noise ratio significantly, compared to the "T" case¹ and it enabled to separate optically the far afterglow region from discharge, plasma decay and near afterglow regions. The far afterglow region was in the third tube namely. A typical pressure downstream the nozzle, measured at positions 1,2 or 3 was about 0.1 Torr.

Significant features of such RF plasma jet system are: a high pressure ratio of upstream and downstream pressures (typically about 100) and a very short residence time of the order 10-100 μs . This differs the RF plasma jet system from other types of discharges used in the past for generation of singlet delta oxygen (e.g. microwave discharges). The other typical phenomena are strong plasma inhomogeneities (both radial and axial) and significant influences of wall effects and space charge sheath effects.

The diagnostics of singlet delta oxygen remained in principle the same as earlier¹. The emission from the diagnostic chamber was coupled into the step index optical fiber with a core diameter of 0.8 mm. The fibers were 2 m long and guided the radiation to the optical spectrum analyzer. Usually, only a narrow part of the near infrared spectra,

3. RESULTS AND DISCUSSION

Preliminary experiments with pure oxygen at the conditions (the Al nozzle, the inner diameter 3 mm, the length 4mm, the CW discharge, the radiofrequency 99.9 MHz, the flow rate 300-1000 sccm) showed that singlet-delta oxygen yield measured at the cube 3 was a little bit higher than that in cube 1. This enhancement was about 10 % relatively and was caused probably by recombination of atomic oxygen on Pyrex walls directly to the singlet delta state of molecular oxygen in accordance with the paper². That is why all the following dependencies were measured at the cube 3, i.e. 150 cm downstream the discharge. The preliminary tests included also pulsed mode experiments, however, under conditions of

DSOG-2 experiments there was no case of enhancement due to the pulsed mode. That is why all the following dependencies refer to the CW mode only.

The dependence of singlet delta oxygen yield on radiofrequency is shown in Fig. 2. The dependence was increasing monotonously. There seemed to be no signs of saturation at the highest frequencies. It might be expected, however, on the other hand it may be noted that the same yield was usually obtained with microwave discharges, which usually had 25 times higher frequency than the highest frequency of DSOG-2. The data in Fig. 2 were obtained with Al nozzle, having the inner diameter 2 mm and the length 3 mm. The flow rate of pure oxygen was 195 sccm. All the following dependencies were measured at the radiofrequency 99.9 MHz.

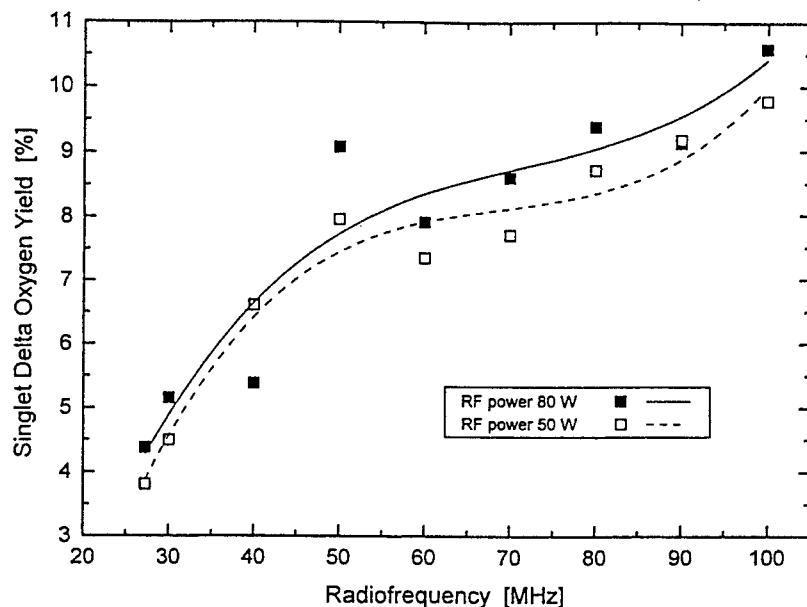


Fig. 2 $O_2(a^1\Delta_g)$ yield vs radiofrequency

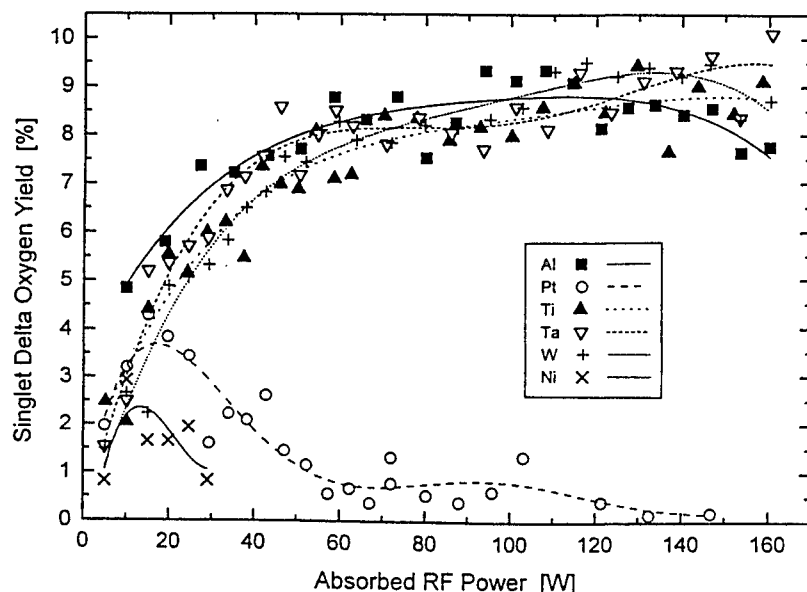


Fig. 3 $O_2(a^1\Delta_g)$ yield vs RF power for different nozzle materials

phenomena. All the nozzles had the inner diameter 2 mm and the length 3 mm. The flow rate of pure oxygen was 195 sccm. An erosion of the nozzles by oxygen plasma was the most significant in the case of platinum.

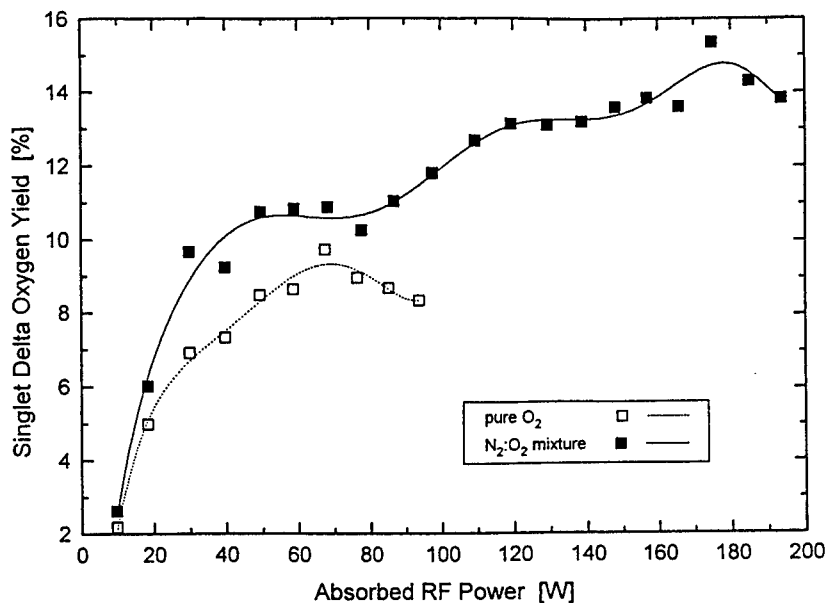


Fig. 4 O₂(a¹Δ_g) yield vs RF power for pure oxygen and N₂:O₂ mixture

was used, keeping all other parameters the same, an additional enhancement at a low RF power (below 60 W) was observed, however, it disappeared at a higher power (above 60 W). It may be assumed that the additional enhancement was caused by a collisional energy transfer from the state NO(a⁴Π_i) to molecular oxygen. The disappearance of this effect at the higher power may be caused by dissociation of NO molecule. The admixture of argon to pure oxygen resulted in negligible enhancement, compared to nitrogen. The admixture of mercury caused nearly no enhancement in case of pure oxygen and in case of oxygen nitrogen mixture it caused even measurable degradation in DSOG-2 performance. This could confirm that atomic oxygen had little chance to quench delta oxygen because of the short residence time in the nozzle and low pressure downstream the nozzle. Mercury could quench excited metastable nitrogen.

4. CONCLUSION

The performance of the experimental apparatus DSOG-2 was significantly better than that of DSOG-1 both in the relative yield of singlet delta oxygen and in the electrical efficiency. This holds up our hope for achieving a sufficiently high yield of singlet delta oxygen to pump an oxygen-iodine laser.

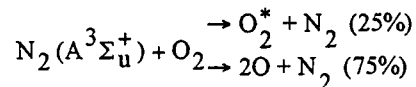
5. ACKNOWLEDGMENTS

This research work has been supported by the Japan International Science and Technology Exchange Centre and by the Kawasaki Heavy Industries, Ltd.. The authors also wish to thank to Mr. Tooru Nagai from the Opto Engineering Laboratory of Kawasaki Heavy Industries, Ltd. for the careful recalibration of optical fiber coupling.

6. REFERENCES

1. Schmiedberger J., Fujii H., "RF Hollow Electrode Discharge Generator of Singlet Delta Oxygen", *10th International Symposium on Gas Flow and Chemical Lasers*, Friedrichshafen, Germany, Proceedings of SPIE, Vol. 2502, 338-343, 5-9 September 1994.
2. Black G., Slanger T.G., "Production of O₂(a¹Δ_g) by oxygen atom recombination on a Pyrex surface", *J. Chem. Phys.* **74**(11), 6517-6519, 1 June 1981.
3. Sharpless R.L., Slanger T.G., "Surface chemistry of metastable oxygen. II. Destruction of O₂(a¹Δ_g)", *J. Chem. Phys.* **91** (12), 7947-7950, 15 December 1989.
4. Iannuzzi M.P., Jeffries J.B., Kaufman F., "Product channels of the N₂(A³Σ_u⁺)+O₂ interaction", *Chem. Phys. Lett.* **87** (6), 570-574, 16 April 1982.

Experiments with gas mixtures brought about an enhancement of singlet delta generation, compared to the pure oxygen case. The example of such enhancement may be seen in Fig. 4. The mixture N₂:O₂ had the ratio of volumetric flow rates 10:195 sccm. Using the A1 nozzle (the inner diameter 3 mm and the length 2 mm), the highest yield of singlet delta oxygen was achieved. This enhancement was probably caused by the reaction⁴:



with the rate coefficient $k=3 \times 10^{-12} \text{ cm}^3/\text{s}$. The excited state of molecular oxygen may be ascribed to one of singlet states with possible subsequent cascade depopulation to the singlet delta state. The above reaction made an additional creation channel for singlet delta oxygen. When 2 % or 10 % admixture of NO in nitrogen

15. Chemical Oxygen-Iodine Lasers II

Industrial Chemical Oxygen Iodine Laser

Hiroo FUJII and Toshio ATSUTA

*Opto Engineering Department, Kanto Technical Institute
Kawasaki Heavy Industries, Ltd., 118 Futatsuzuka, Noda, Chiba, 278 Japan*

ABSTRACT

Having succeeded the oscillation of 6 kW output power by a supersonic flow, the chemical oxygen iodine laser (COIL) is now going to be realized as a new industrial laser by adopting various leading technologies.

Keywords: iodine laser, chemical laser, COIL, industrial laser, high power laser, optical fiber, singlet oxygen generator, SOG, material processing, decommissioning

1. INTRODUCTION

Since the first oscillation of the Chemical Oxygen Iodine Laser (hereafter referred to as COIL) in the USA was achieved in 1978, major stress has been laid on the COIL research for the purpose of military utilization because of its high power output capability. Kawasaki has been developing COIL, on the contrary, aiming at the industrial application since 1986 because it has excellent characteristics of a high power, a high beam quality and a good transmission through optical silica fibers.

The subsonic COIL development was fulfilled in our laboratory from 1986 to 1992. During this term, a duration time of 3 hours operation with the output power of 100 W was achieved by continuously replenishing the chemical fuels. An output power of 1 kW was attained by investigating the key technologies to scale up. As the results, the first commercial COIL in the world was demonstrated installed in a material processing machine.¹ But the size of this system was still large in comparison with its output power.

The supersonic COIL(SCOIL) development has been conducted since then. In 1994, 1 kW oscillation was achieved with a new type singlet oxygen generator under the supersonic gas velocity of Mach 2. A length of the laser medium was only 9 cm, though the one of subsonic was 100 cm. Aiming at the thick steel cutting, a scaling up of this system was carried out and the higher

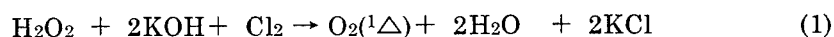
power up to 6 kW was achieved in 1995.² This SCOIL has a folded stable resonator and obtained a high quality beam with a stable power for about 5 minutes.

For the industrialization of SCOIL, the cost performance becomes very important. Some of the break through technologies for the industrial COIL such as no water vapor trap, no helium gas and so on, have already been achieved in our laboratory with no degradation of the efficiency. It will not be the far future that the industrial SCOIL are running in various fields as the automobile production line with processing robots connected by optical fibers, the wide processing yard in the ship building factory which requests the capability of thick plate cutting, the decommissioning in the nuclear factory which needs the remote control operation for the personnel safety with the high energy transmission through optical fibers.

2. COIL DEVELOPMENT

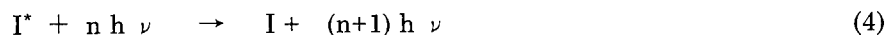
2.1 Basic composition of COIL system

The basic composition of the subsonic COIL system consists mainly of a singlet oxygen generator(SOG), a water vapor trap(WVT) and a laser resonator in Figure 1. The pressure of these components are retained at 1-3 torr by a vacuum pump. The SOG generates excited oxygen $O_2(^1\Delta)$ through the chemical reaction of Cl_2 and aqueous solution of H_2O_2 and KOH:



$O_2(^1\Delta)$ is led to the WVT together with vaporous H_2O in which the water vapor is removed by frozen on the cooled wall.

In the laser cavity, iodine molecules I_2 are dissociated and activated by the $O_2(^1\Delta)$ and after achieving the population inversion, a near-infrared laser beam of 1.315 μm in wavelength is emitted. These reactions in the cavity are as follows:



The atomic iodine is pumped up by a resonant energy pooling reaction and reaches equilibrium (4) in less than 10 μs . This powerful pumping of iodine atoms is primarily the base of the high power of COIL.

2.2 Subsonic COIL development

The 1 kW COIL for material processing which Kawasaki has delivered to ALEC in Figure 2 has some specific facilities for long term stable oscillation, such as the fuel recirculation system, pressure control system at the cavity, the iodine evaporator with the radiant heater of a halogen lamp for coping with quickly to the laser power variation, and the water vapor trap of rotating disk type. In the fuel recirculation system, the alkaline H_2O_2 composition and the temperature are controlled automatically for stabilizing the excited oxygen generation. And the waste solution of after reaction is utilized to melt the ice which scraped off from the disk surfaces of the water vapor trap. This molten water is continuously discharged to outside the vacuum line by means of the ice discharge pump. Thus the operation could be continued stably for long time.

Figure 3 shows the main construction of this COIL. The performance of the laser is over 1 kW output power within $\pm 2\%$ power fluctuation with 30% chemical efficiency. Using this equipment, 5 mm thick stainless steel was cut at the speed of 2 m/min by 1 kW beam which led through a 0.3 mm diameter optical silica fiber. The power density on the focusing point reached to over $1.4 \times 10^6 \text{ W/cm}^2$ which satisfied for achieving the laser cutting phenomenon.

2.3 Supersonic COIL development

The supersonic cavity is divided into three parts, iodine injectors, supersonic nozzles and a folded type stable resonator. To obtain good mixing of the iodine to a primary flow of the excited oxygen, the iodine is injected both transversally and obliquely by the injectors in a subsonic flow region upstream of a supersonic nozzle throat. Then the laser gas which is composed of the oxygen and iodine is expanded to about Mach 2 through the supersonic nozzles in which an area ratio of the nozzle throat to the nozzle exit plane is 1 to 2.3, so as to decrease a gas temperature. Figure 4 shows the main construction of supersonic COIL (SCOIL).

A stable resonator of folded type is applied to the SCOIL. In a case of the stable resonator which composed of a concave reflector mirror and a plane output mirror, a full divergence angle θ of a multi mode beam is defined as follows;

$$\theta = 2a / [L(R - L)]^{1/2} \quad (5)$$

Where $2a$ is a beam diameter on the output mirror, L is a distance between both mirrors and R is a curvature radius of the concave mirror. The test data shows the good agreement with this theoretical value. The folded resonator has an effect to have a smaller θ not only by lengthening L but also shortening diameter a to the direction of the gas flow. Thus the output beam can be

focused on the optical fiber core of its diameter 0.3 mm.

The SCOIL has been running with the stable power 5-6 kW in the laboratory of Kawasaki Kobe Works.

3. INDUSTRIAL COIL

Table 1 indicates main differences of the COIL between for military and for industry.

Suitable output power for the industrial COIL can be estimated from 10 kW to 100 kW approximately. Because not so many users would request more than 100 kW even they want to cut 300 mm thick plate and only few manufacturers try to produce less than 10 kW COIL because of the difficulties to compete with the other lasers as YAG or CO₂ in price at such low power region. The most desirable performance of the industrial COIL would be the cost per photon, though higher power per unit weight of laser facility is requested for the military COIL because it is usually used on the airplane. Beam quality would be enough for the industrial use if the output beam can be focused on the optical fiber core with its energy density over $0.5-1.0 \times 10^7$ kW/cm² for evaporating steel instantly when cutting. And, of course, this beam should be come out of the oscillator stably for a long time.

For achieving these requests, many developments on the industrial COIL have been carrying out, such as no helium dilution, no water vapor trap, higher exhaust pressure for vacuum pump, recyclable system of the basic hydrogen peroxide (BHP) and so on. The 10 kW industrial COIL installed the above leading technologies is now under construction in Kawasaki, Noda Works.

Table 1 Comparison of desirable specification on the COIL
for military and for industry

ITEM	Military COIL	Industrial COIL
Power	MW	KW
Performance	Power/Weight	Cost/Photon
Operation	Peak power on duty	Long duration
Beam quality	Brightness	Optical fiber
Pollution	loose	strict(Cl ₂ , COD)

4. CONCLUSION

In 1992, the world first industrial COIL was demonstrated installed in a material processing machine. But the performance value(P.V.) which is defined in table 1 as [Cost/Photon] could not be sufficient as the commercial one.

The oscillation of 1 kW COIL under the supersonic gas flow has succeeded in 1994. A length of the active medium became 10 times smaller than the one of subsonic COIL.

Inspired by the achievement of 6 kW oscillation by the scaling up SCOIL in 1995, 10 kW DEMO SCOIL is now under construction in Kawasaki, Noda Works. This P.V. of the SCOIL can be estimated 10 times better than the COIL's and is reaching to the commercial level.

5. REFERENCES

1. H.Fujii and T.Atsuta,"Current Status of industrial COIL Development", SPIE Vol.1980, p.148-152, 1992
2. Hiroo FUJII, Toshio ATSUTA and Wataru MASUDA," COIL Activities in Japan", SPIE Vol.2767, p.170-184 , 1995

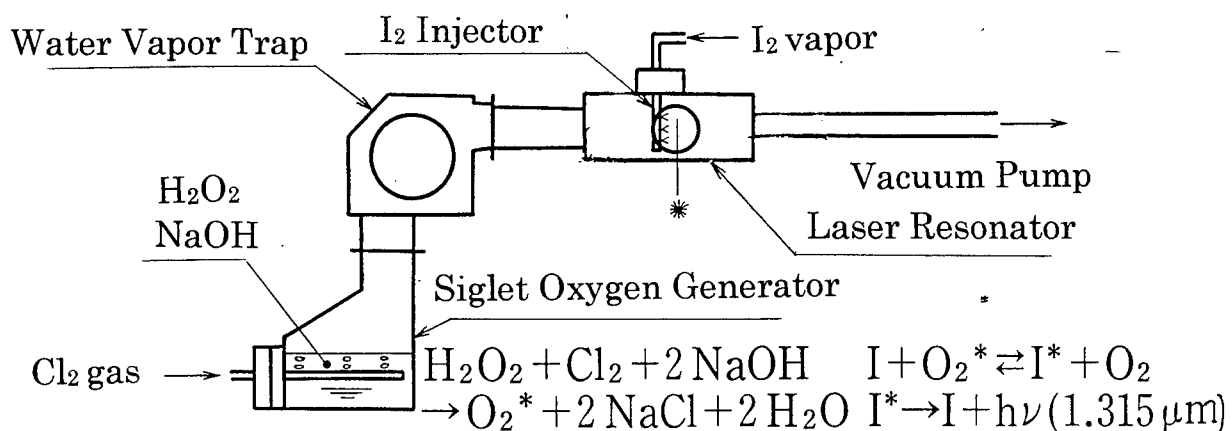


Fig.1 The basic design of COIL

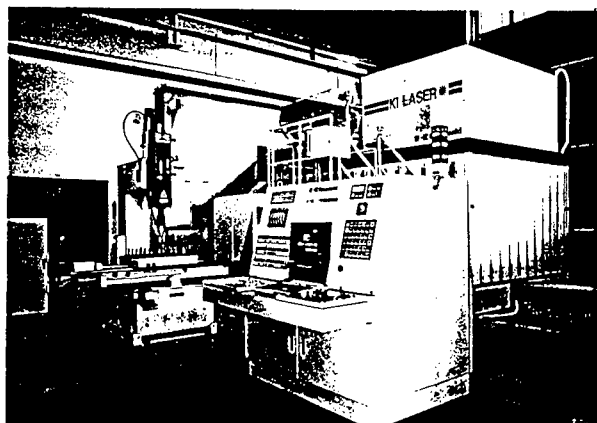


Fig.2 A 1-kW COIL device delivered to ALEC in 1992

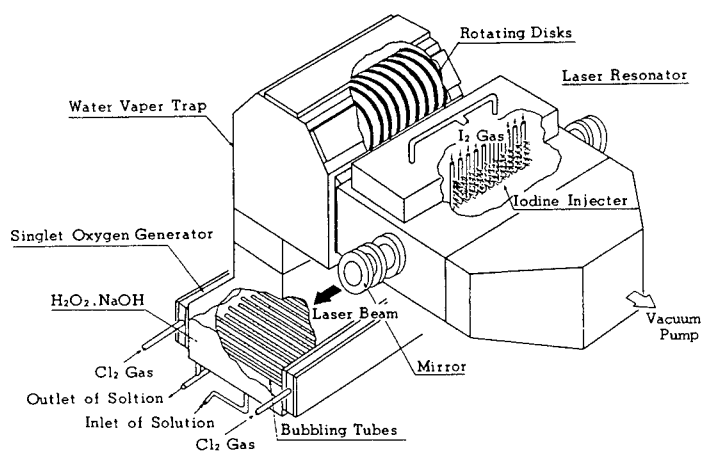


Fig.3 Schematic construction of a subsonic COIL

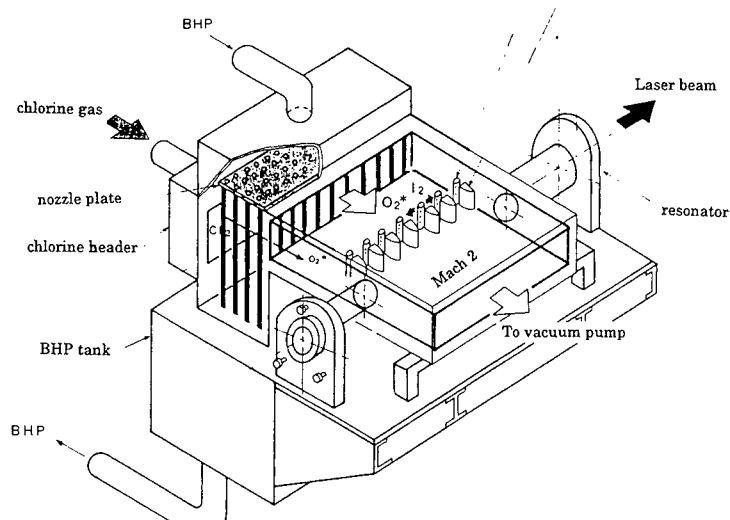


Fig.4 Schematic construction of a supersonic COIL

Supersonic COIL Operation at DLR Germany

L.H.von Entress-Fürsteneck, J.Handke, K.Grünwald
W.L.Bohn*, W.O.Schall*

DLR-Institut für Technische Physik
D-74239 Lampoldshausen / *D-70659 Stuttgart, Germany

ABSTRACT

The German Aerospace Research Establishment (DLR) is routinely operating its supersonic chemical oxygen-iodine laser^{1,2} (COIL). Meanwhile over 200 single tests have been performed at run times extending to 1 minute. Power levels of 5 KW have been exceeded. Parametric studies were performed resulting in chemical generator efficiencies of about 43% for the baseline operation with high power output. The BHP molarity was found as one of the most important parameters for a stable and reproducible operation. Yield measurements revealed lower numbers than expected from theoretical calculations. The paper gives an overview of the COIL device and discusses the experimental and calculated results of the investigations.

Keywords: chemical laser, supersonic flow, oxygen, iodine, utilization, yield

1. INTRODUCTION

The German COIL activities are concentrated on the development and investigation of a supersonic multikilowatt class laser device. These are supported by small scale basic research on selected COIL topics like BHP chemistry, advanced generator technology and development of diagnostic tools and methods. We demonstrate reliable, safe and reproducible handling in short and long run operation. Subsystems have been improved in order to optimize generator efficiencies and to reduce transport losses in the duct. Further improvements with special emphasis on aspects concerning long run operation have been started.

2. SYSTEM SETUP

The general system setup is displayed in Fig.1. A separate BHP preparation system is used in order to premix hydrogen peroxide and KOH before it is transferred to the oxygen generator. In this generator, the BHP is brought into contact with gaseous chlorine in order to produce electronically excited oxygen $O_2(^1\Delta)$. The oxygen is transported to the laser head that consists of the iodine mixing region, the supersonic expansion nozzle and the laser cavity with the optical resonator. Before the gas is recompressed and exhausted to atmosphere corrosive and toxic components are removed by a scrubber system.

A special feature of the whole setup is the extended use of plastic materials wherever it is possible. Within the BHP preparation system all containments, tubes and valves are manufactured out of polyethylen. The generator is a rotating disk type generator on loan from the Phillips Lab at Albuquerque, NM. The data of this generator are extensively reported⁴. Currently the laser is operated without a water vapor trap between generator and laser head. Several ports along the duct between generator and laser head allow optical measurements of singlet delta oxygen as well as of residual chlorine concentrations. The nozzle array consists of sixteen two-dimensional expansion nozzles for supersonic expansion to an isentropical mach number of 1.8. In the subsonic region the iodine is transversely injected from the nozzle walls into the oxygen flow through a row of 0.5 mm diameter orifices. In the present configuration a stable resonator is placed directly at the nozzle exit plane. The free aperture in flow direction is 44 mm. The resonator length is 0.82 m with a gain length of 0.21 m. The pumping system consists of three parts: the cryogenic trap, the vacuum system and a scrubber. The intention of the cryogenic trap is to remove iodine and residual chlorine from the exhaust gas in order to prevent corrosion of the vacuum pumps. The vacuum

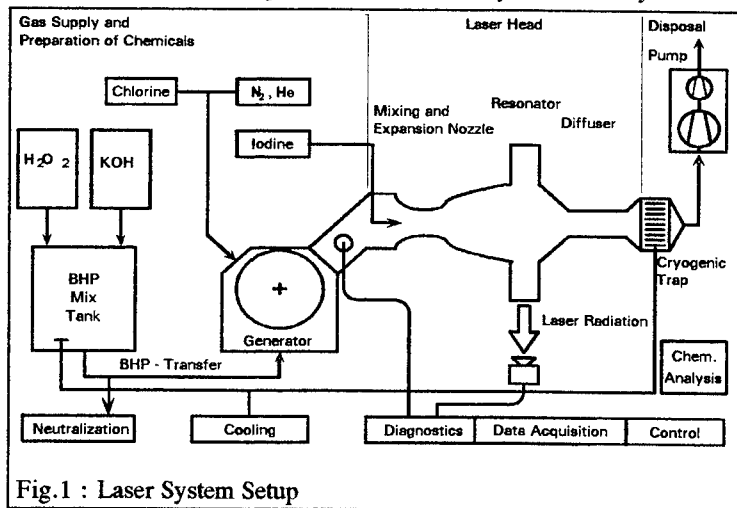


Fig.1 : Laser System Setup

aperture in flow direction is 44 mm. The resonator length is 0.82 m with a gain length of 0.21 m. The pumping system consists of three parts: the cryogenic trap, the vacuum system and a scrubber. The intention of the cryogenic trap is to remove iodine and residual chlorine from the exhaust gas in order to prevent corrosion of the vacuum pumps. The vacuum

system itself is a three stage pumping system with a capacity of $16,000 \text{ m}^3/\text{h}$. It consists of a large roots stage on the vacuum side, followed by three units of a second roots pump and a rotary valve pump in parallel.

3. AUTOMATIC CONTROL & DATA ACQUISITION

A sketch of the main automatic control and data acquisition systems of the COIL device is shown in Fig.2. Several sequences like BHP preparation or hot flow are controlled by the interactive system control Simatic S5-135U. It is charac-

terized by 488 digital input and 248 digital output channels as well as by 104 analog input/output channels at a cycle time of about 45 ms. Three graphical displays are installed on the supervisor desk. Valve signals are directly connected to the S5 system. Some of these valve signals, as well as all pressure and temperature values and signals from optical measurements are connected to the amplifier system. Other important functions like safety and online monitoring of pressures and temperatures are executed from the supervisor desk. The temperatures of important subsystems are controlled by a separate thermal management system. As an option the valves of the whole device can be set directly by using the manual valve control board. Its priority of access to the valve positions is higher than that of the automatic control system. Another important aspect is the graphical online monitoring of values like molar flows of helium, chlorine, iodine, singlet delta oxygen and residual chlorine by a special PC-based software. A data acquisition system with 220 channels at a sampling rate of 1 Hz to 1 kHz is used.

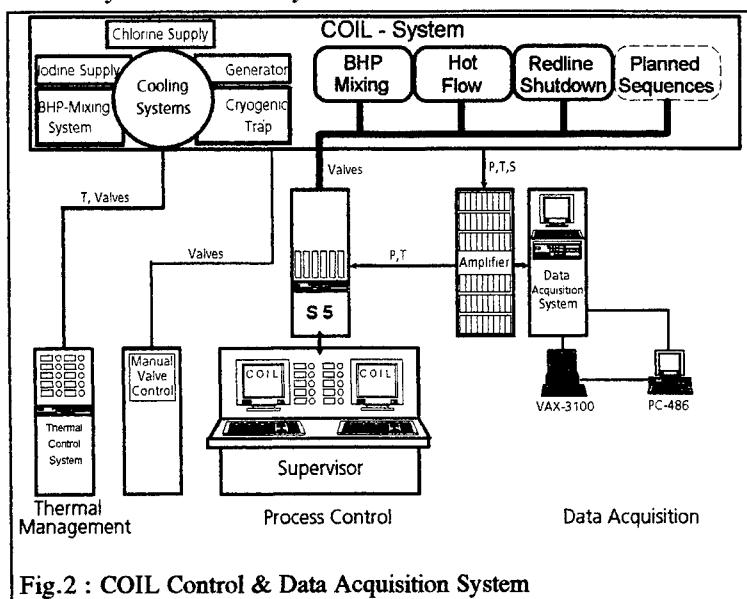


Fig.2 : COIL Control & Data Acquisition System

4. TYPICAL PERFORMANCE DATA

Fig. 3 shows the typical time history of a short-run experiment with a run time of about 7.5 seconds. Plotted are the molar gas flows and the measured output power. The chlorine rate is deduced from the sonic condition at the supply orifice. The spiking results from switching conditions. The time difference of 0.7 seconds between the onset of the chlorine supply and the residual chlorine results from the flow time between the chlorine orifice and the optical port in the duct. The residual chlorine is inferred from the absorption signal of a halogen lamp at 330 nm and the local gas parameters. It is cross-checked by an experiment without BHP in the generator. Singlet oxygen is derived from emission spectroscopy at $1.27 \mu\text{m}$, which is calibrated by the emission of a piston light source. The time evolution of the power is measured by a fast photodetector coupled to an integrating optical sphere.

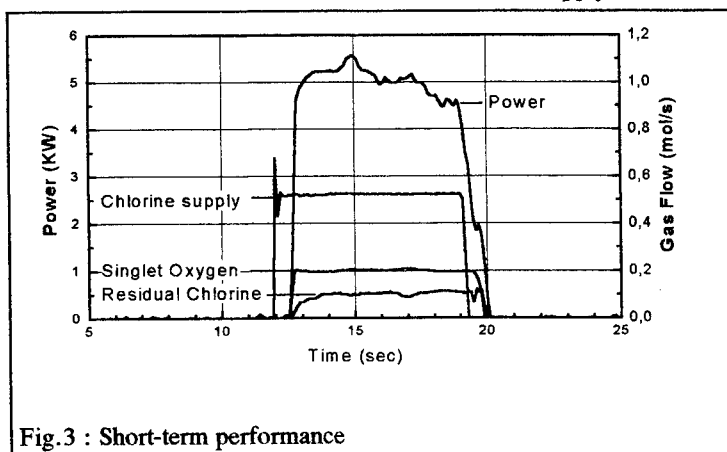


Fig.3 : Short-term performance

In the present setup the BHP inside the generator is only cooled by rather slow heat transfer to the housing. Therefore the BHP temperature increases as long as chlorine is fed into the generator, leading to an increased amount of water in the flow. This may explain the power decrease in Fig.3. In addition the temperature increase also limits the capability for long run operation. Maximum continuous run time at baseline flow rates is approximately one minute.

5. PARAMETRIC INVESTIGATIONS OF UTILIZATION AND YIELD

The laser power is largely determined by the efficiency at generator exit which is defined as the product of utilization ($[O_2]/[Cl_2]_0$) and yield ($[O_2(^1\Delta)]/[O_2]$). Therefore attempts have been made to characterize and optimize the generator conditions. For these tests the iodine supply was disconnected. The experimental results were analysed and compared with theoretical models^{5,6}.

Fig.4 compares the utilization measured in two test series with different BHP molarities, i.e. standard molarity BHP with 6.5 mol/l O_2H^- at a 3.1 mol/l excess of peroxide and high molarity BHP with 7.2 mol/l O_2H^- .

All single tests were performed with a molar chlorine gas flow of 0.55 mol/s and a molar helium flow of 1.6 mol/s at a BHP starting temperature of about $-20^\circ C$ and a disk rotation speed of 24 rpm. The run time was limited to three disk revolutions or 7.5 seconds.

The initial spike of the utilization in the diagrams of Fig.4 is an artifact due to flow time as discussed above. Therefore, the calculated utilization is not reliable for the first 0.7 seconds. At the standard starting condition of 6.5 mol/l O_2H^- the utilization decreases continuously during the hot run. The decrease is even stronger if some salt (1.2 mol/l) has already accumulated. In comparison, the high molarity BHP of 7.2 mol/l O_2H^- provides a higher and more stable utilization without and with salt accumulation. Thus, stable and reproducible laser operation is obtained. The experimental results may be explained as follows: For the high molarity BHP the oxygen production is reaction limited while for lower molarities it is limited by O_2H^- diffusion⁵.

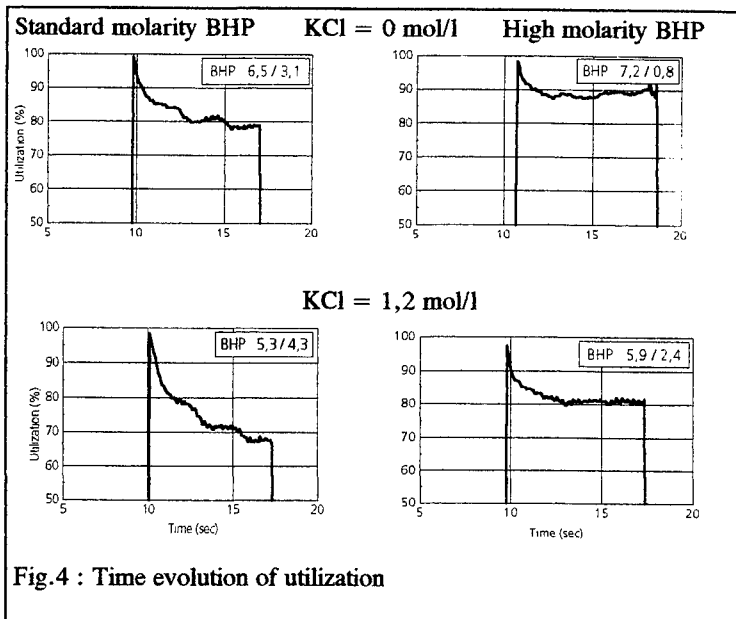


Fig.4 : Time evolution of utilization

The second important parameter describing the generator efficiency is the generator exit yield. Experimental results are displayed in Fig.5 as a function of the diluent ratio of He/Cl_2 , while the molar gas flow of chlorine is fixed to 0.5 mol/s. The increase of the helium diluent results in an enhanced flow velocity and thereby in a reduced residence time for the excited oxygen in the system. Assuming that pooling is the most important loss mechanism for $O_2(^1\Delta)$ the yield will increase accordingly. A further decrease of the singlet delta residence time was obtained by reducing the duct volume by 18% and in a second step by reducing the generator gas volume by another 7%. As a consequence the yield increased by about 40% for the base line flow ($He/Cl_2 = 3$) and by more than 20% for higher molar helium flows.

Using the available theoretical models we have calculated the detachment yield (90%) and the pooling losses at different locations of the laser system, using an effective rate constant $k_p = 6.1 \times 10^{-17} \text{ cm}^3/\text{molecule sec}$ ⁷. We assume that excited oxygen is produced homogeneously over the disk package.

Therefore pooling losses in the disk package can be attributed to one half of the gas volume between the plates. The remaining volume up to the optical port is divided into three parts: the gas volume from the end of the disk plates to the generator exit, the gas volume of the liquid separator, and finally the duct volume up to the optical port. The results of the calculation at the end of each subvolume are plotted in Fig.6. The highest losses arise within the disk package with a decreasing significance at higher diluent ratios.

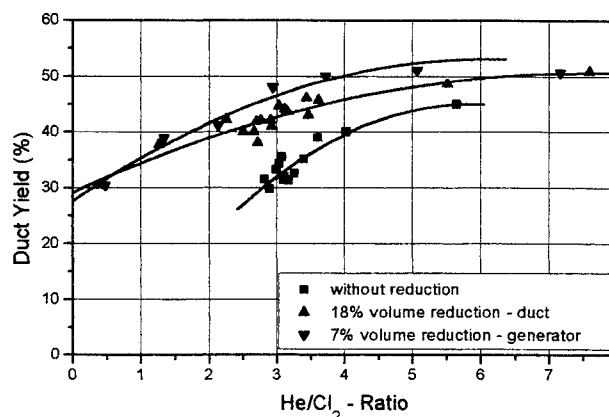


Fig.5 : Yield increase by volume reduction

For comparison the measured yield is also shown in Fig.6. The values are distinctly lower than the calculated results by a constant factor of 1.6.

In a different investigation the increase of the gas flow energy between the generator and the optical port in the duct was calculated from the measured temperature increase between both positions. This temperature increase corresponds with the calculated pooling losses, but it cannot explain a singlet delta loss from the assumed detachment yield to the measured yield. According to a model calculation a higher yield should also lead to a much higher laser power than measured.

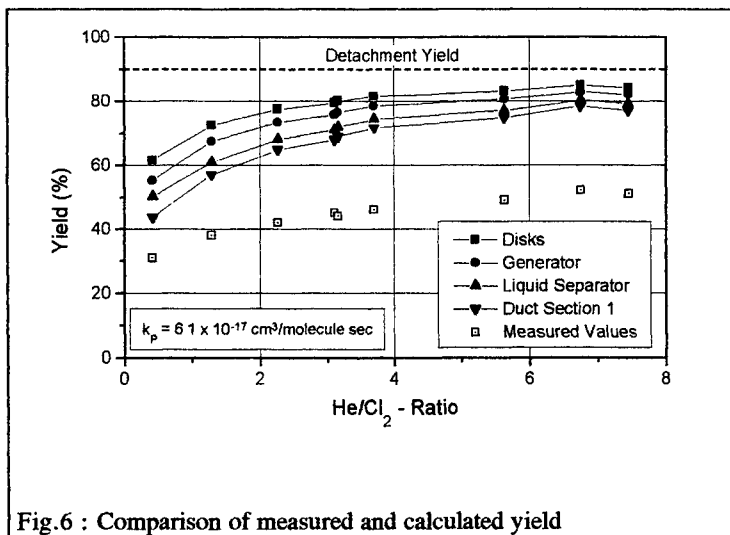


Fig.6 : Comparison of measured and calculated yield

6. CONCLUSIONS

We have demonstrated the successful operation of a supersonic COIL with a reproducible output power exceeding 5 KW and operation times up to one minute. The experimental investigations showed that a high and stable utilization demands a high molarity of the O_2H^+ in the BHP and that the reduction of generator and duct volume leads to a higher yield. The optimization of utilization and yield resulted in a measured increase of the generator exit efficiency from 26% to 42% for a fresh BHP. There remains an uncertainty factor of 1.6 between calculated and measured yield. This major discrepancy requires further investigations.

7. REFERENCES

1. J.Handke, W.O.Schall, W.L.Bohn, L.H.von Entref-Fürsteneck, K.Grünwald, R.Kwirandt, A.Werner, "Multikilowatt supersonic chemical oxygen iodine laser", Proc. 4th Int. Workshop on Iodine Lasers and Applications, Trest'Castle, CR, SPIE Vol. 2767 (1996), p.195
2. J.Handke, A.Werner, W.L.Bohn, W.O.Schall, "Multikilowatt Supersonic Oxygen Iodine Laser", Proc. GCL 10th Int. Symp., SPIE Vol.2502 (1994), p.266
3. W.L.Bohn, "The chemical oxygen-iodine laser: achievements, problems and future perspectives", Proc. GCL 9th Int. Symp., SPIE Vol.1810 (1992), p.168
4. K.A.Truesdell, S.E.Lamberson, "Phillips Laboratory COIL technology overview", Proc. GCL 9th Int. Symp., SPIE Vol. 1810 (1992), p.476
5. K.Grünwald, J.Handke, L.H.von Entref-Fürsteneck, W.L.Bohn, W.O.Schall, "Investigations of the efficiency of a rotating disk type oxygen generator", to be presented at this conference
6. D.A.Copeland, W.E.McDermott, V.Quan, A.H.Bauer, "Exact and Approximate Solutions of the Utilization and Yield Equations for $O_2(^1\Delta)$ Generators", Intense Laser Beams and Applications, SPIE Vol.2119 (1994), p.27
7. K.A.Truesdell, C.A.Helms, T.Longergan, C.Wisniewski, J.E.Scott, K.P.Healey, "COIL Thermal Management", Proc. GCL 10th Int. Symp., SPIE Vol.2502, p.321

MODE LOCKING OF A CW SUPERSONIC CHEMICAL OXYGEN IODINE LASER

by

Stephen P. Phipps, Charles A. Helms, R. James Copland, Wolfgang Rudolph,
Keith A. Truesdell, and Gordon D. Hager

Abstract- This paper presents the results of the first mode locking experiments on a supersonic Chemical Oxygen Iodine Laser (COIL). Mode locking has been achieved using an acousto-optic modulator (AOM) and lasing demonstrated on the TEM₀₀ modes with a small intracavity aperture. A DC magnetic field was used increase the number of axial modes and a peak power of 2.5 kW has been reached with a pulse width of 2.1 ns at a repetition rate of 43.68 MHz.

I. INTRODUCTION

Photolytic iodine lasers have been mode locked at Alkyl-iodide pressures above 80 torr [1]. Recent experiments by Tate et al. using axial pumping to photolyze CF₃I report mode locking at pressure of 1-30 torr [2]. Successful mode locking of a pulsed low-pressure photolytic iodine laser suggested that mode locking could also be demonstrated on a low-pressure cw supersonic Chemical Oxygen Iodine Laser (COIL) operating at a cavity pressure of 7 torr.

II. EXPERIMENT

The mode locking experiments were conducted at the USAF Phillips Laboratory on a 5-kW class supersonic COIL (RADICL) using a rotating-disk oxygen generator coupled to a Mach-2 single-slit supersonic nozzle. A general description of the RADICL laser has been given elsewhere [3]. The laser's standing-wave stable resonator was housed in mirror boxes attached to the laser body. Resonator optics inside the boxes rested on floating tables to reduce vibration from the ground and nearby laser hardware. Figure 1 shows a diagram of the experimental setup.

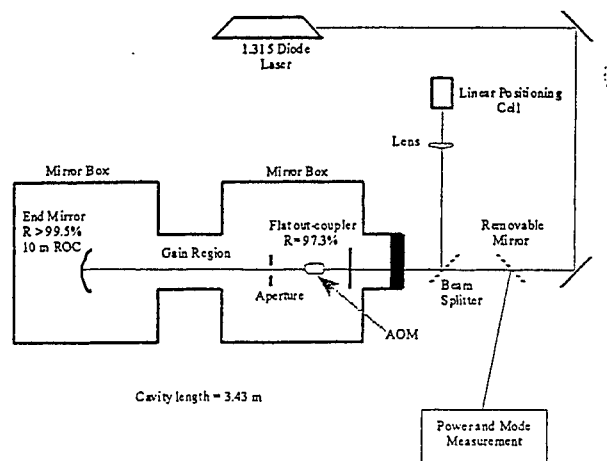


Figure 1. Overall experimental set-up and resonator parameters for the mode-locking experiment.

Gas pressures in the resonator were typically less than 10 torr so that Doppler broadening was the dominant line-broadening mechanism. During the experiment the Doppler-broadened line width was 180 MHz and the pressure -broadened line width was 60 MHz (based on flow conditions given in Table 1). The resulting Voigt line shape has a FWHM width of 230 MHz.

Table 1. Flow Rate and Cavity Conditions

Flow Rates	
Cl ₂	0.52 mol/s
Cl ₂ utilization	92.6%
I ₂	8.7 mmol/s
He (primary)	2.04 mol/s
He (secondary)	1.10 mol/s
H ₂ O [†]	73 mmol/s
Cavity Conditions	
Temperature [†]	170 K
Pressure	7.7 torr
Pressure Broadening Coefficient	7.74 MHz/torr

[†] calculated value

A linear positioning cell and a diode laser operating at 1.315 microns were used to align the RADICL resonator with an intracavity acousto-optic modulator (AOM). Final alignment with an intracavity AOM is typically performed while the laser is running. A small circular aperture placed in front of the AOM restricting lasing to TEM₀₀ modes. Figure 2 shows the arrangement used to measure power and gauge the number of oscillating modes. A known fraction of the COIL beam was sent to an uncoated fused silica window where Fresnel reflections off the front and back surfaces were directed into a 20-kHz bandwidth germanium detector and a 100-Joule calorimeter respectively. The calorimeter measured total energy delivered while the germanium detector traced relative power as a function of time. A 1-GHz bandwidth InGaAs detector was used to register mode beats. The detector's signals were recorded by a 2-Gigasample/s, 1-GHz bandwidth digitizing oscilloscope. Fast Fourier transforms (FFTs) of the data revealed the mode beat frequencies, allowing one to infer the number and spacing of resonator modes. To increase the number of axial modes, a 180 gauss DC magnetic field was applied to the gain region [4]. The field broadened the gain by weakly splitting the zeeman components of the $I(^2P_{1/2})_{F=3}$ to $I(^2P_{3/2})_{F=4}$ hyperfine transition.

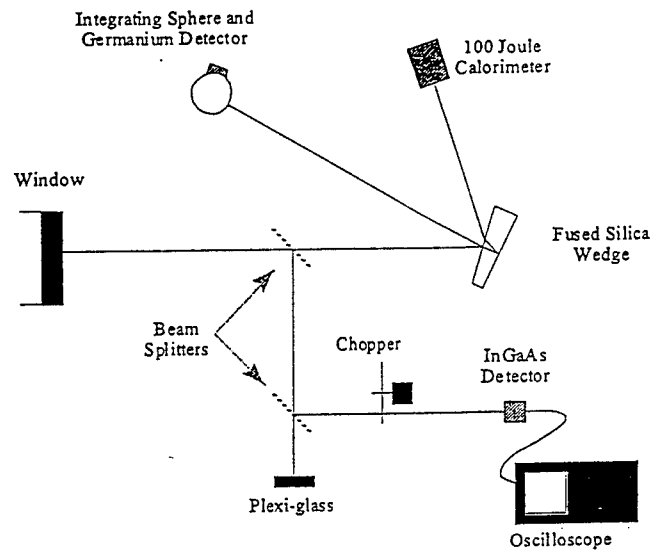


Figure 2. Experimental set-up for measuring power and modes.

Figure 3 shows mode-locked pulses when the 7.1 mm diameter aperture was in place. Peak pulse powers of 2 kW and FWHM pulse width of 2.4 ns were measured. The measured pulse width was 1.5 times the predicted transform-limited value derived when one assumes the mode intensities fall under a Gaussian envelope [5]. The frequency bandwidth used to predict pulse widths was the product of the number of modes counted and the axial mode spacing. The FFT in Figure 4 shows the presence of 10 axial and 1 transverse mode.

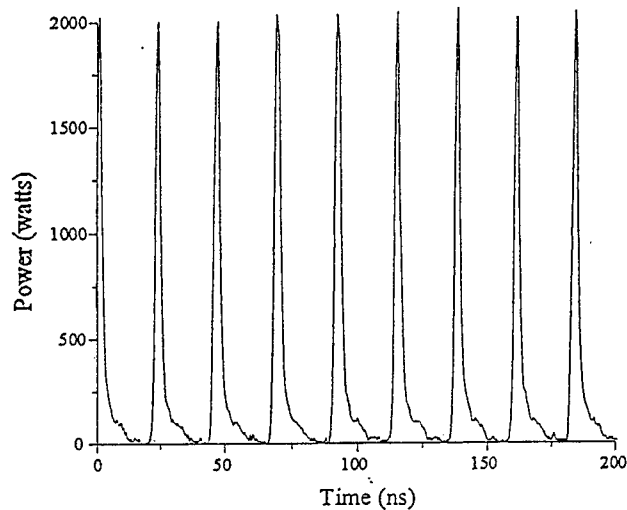


Figure 3. Mode-locked pulses from the 7.1mm diameter aperture. A 180-Gauss magnetic field was applied.

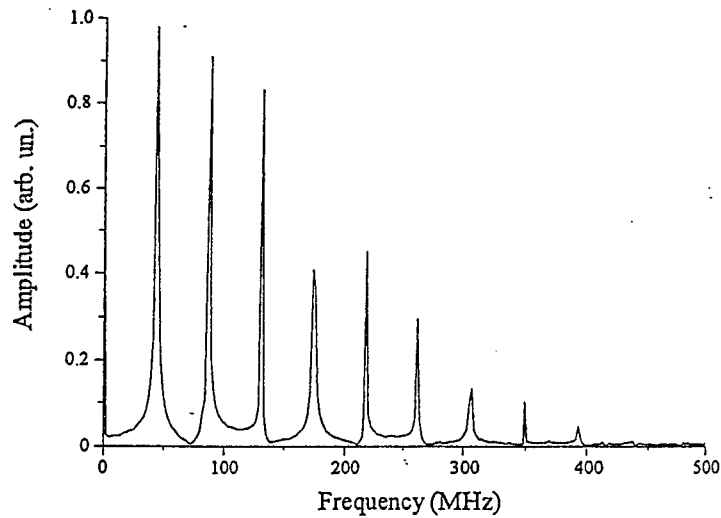


Figure 4. FFT of the signal in Figure 3.10 axial and 1 transverse mode are present.

Figure 5 shows mode-locked pulses for the 10.1 mm aperture case. Measured pulse width were 2.1 ns, again 1.5 times the predicted value. The larger aperture increased peak powers to 2.5 kW and allowed a second transverse mode to lase (see the FFT in Figure 6). The oscillation in the pulse train envelope in Figure 5 is the result of this second transverse mode.

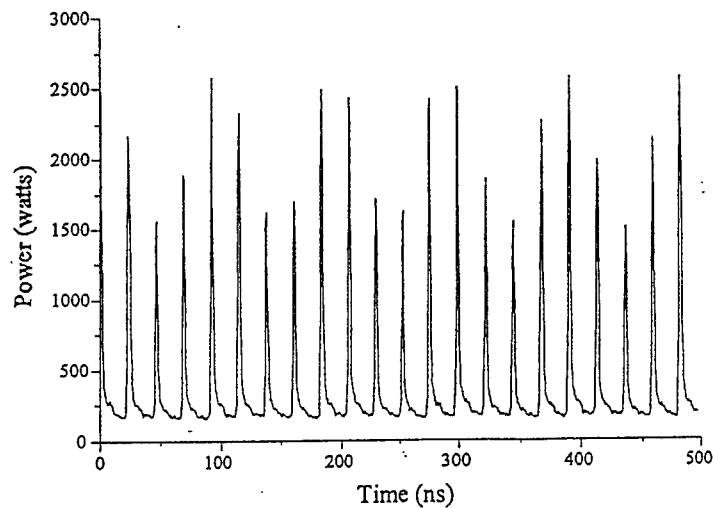


Figure 5. Mode-locked pulses from the 10.1mm diameter aperture. A 180-Gauss magnetic field was applied.

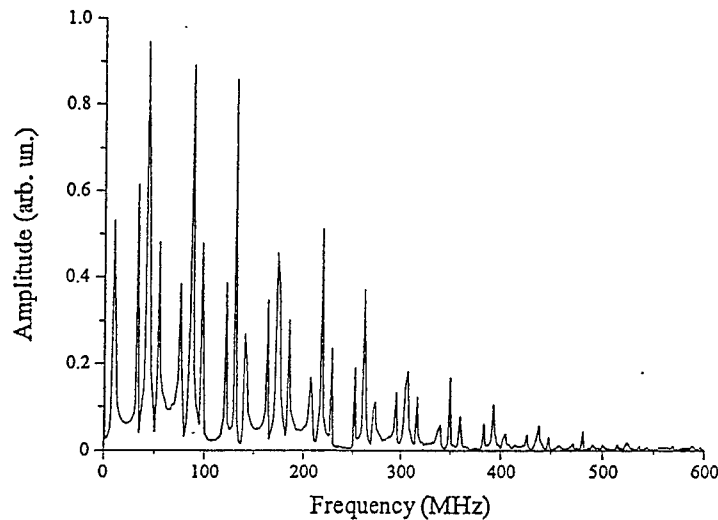


Figure 6. FFT of the signal in Figure 5.12 axial and transverse modes are present.

IV. Summary

A small intracavity aperture was used to confine lasing to TEM₀₀ mode operation on a 5-kW class supersonic Chemical Oxygen Iodine Laser. By applying a 180-Gauss DC magnetic field and inserting an acousto-optic modulator, mode-locked pulses with 2.5 kW peak power and a 2.1 ns width were achieved representing a factor of 10 increase in peak power over cw power for the same aperture size. This is the first demonstration of mode-locking on a COIL.

References:

1. Y. S. Kim and S. S. Lee, "Small acousto-optic modulation for active mode locking in the iodine photo-dissociation laser and the effect of supplementary saturable absorber," *Rev. of Scientific Instrum.*, Vol. 56, pp. 208-210, 1985.
2. R. Tate, et al., "Dynamics of a mode-locked low pressure photolytic I* laser," *IEEE J. Quantum electron.*, Vol. 31, No. 11, p. 1910-1912, November 1995.
3. R. F. Tate, et al., "Spatial Gain Measurements in a Chemical Oxygen Iodine laser," *IEEE J. Quantum Electron.*, Vol. 31, No. 9, September 1995.
4. G. D. Hager, et al., "The Chemical Oxygen Iodine Laser in the Presence of a Magnetic Field I: Gain Measurements and Polarization Effects," *IEEE J. Quantum Electron.*, Vol. 29, No. 3, p. 933-943, March 1993.
5. J. T. Verdyen, *Laser Electronics* (Englewood Cliffs, NJ: Prentice-Hall, Inc., 1989), p. 277.

Forward-Backward Mode Coupled Unstable Resonator

Katsuhiko Sunako, Tadashi Kakinuma, Osamu Sato and Tomoo Fujioka

Department of Physics, School of Science, Tokai University

1117 Kitakaname, Hiratsuka-shi, Kanagawa, 259-12, JAPAN

Tel. +81-463-58-1211 (Ex. 3718) & Fax. +81-463-50-2013

ABSTRACT

We proposed a new unstable resonator, in which forward-mode and backward-mode coupled each other, for low gain large bore laser media such as COIL. The calculations showed that the new unstable resonator can be useful for COIL, which does not oscillate with the usual unstable resonators. The parameters of the resonator for the best performance are also gotten for COIL and CO₂ laser medium.

Keywords: chemical laser (COIL), new unstable resonator, Fresnel-Kirchhoff integration equation

1. INTRODUCTION

Many types of the optical resonators have been proposed since Shawlow and Townes proposed to use Fabry-perot interferometer as an optical resonator, and almost of them are categorized into two types, that is, the stable resonator and the unstable one. Stable resonators are usually used for many lasers, because they can be used for any type of laser medium and easy to oscillate. However, because the diameter of fundamental mode is narrow, they oscillate in multi-modes in the large bore laser and the focusability is not good. So stable resonator is not suitable for large bore lasers.

On the other hand, unstable resonators^{1),2),3)} can have large volume and oscillate in single-like mode, so can be used for large volume laser such as industrial high power lasers. But the output of the unstable resonators is ring-shaped and the large amount of the energy are spread out into the side lobe in the far field pattern. And also the high-gain is necessary for the oscillation, so it should be difficult to use for low-gain laser bore medium such as the chemically pumped oxygen-iodine laser (COIL).

So we proposed new unstable resonator, in which these disadvantages are improved, and showed that COIL can oscillate for with it. And now we need to obtain optimum conditions of configuration of the resonator, so calculated the characteristics of the new resonator, changing the parameters to obtain the suitable condition.

2. CALCULATION

a) RESONATOR CONFIGURATION

In Fig. 1, we show schematically the resonator configurations. Fig. 1 (a) is the positive-branch confocal unstable resonator proposed by Siegman⁴⁾. The output beam is ring-shaped because the beam is extracted around the edge of the M₂ mirror as the diffraction loss. The improved resonator is shown in Fig. 1 (b). The diffracted beam is reflected back to the opposite direction in the resonator by the plane mirror, so the forward mode are coupled with the backward mode of the resonator. As the result, the optical path length in the resonator is nearly twice of that in the normal unstable resonator, and the output is taken out from a hole at the center of the concave mirror. By this improvement, the non-ring shaped beam can be extracted from the center

hole after full amplification, and the low-gain lasers can oscillate in a non-ring-shaped mode.

b) CALCULATION

The beam patterns in the resonator was calaculated using Fresnel-Kirchhoff integration equation. This was showed by Fox and Li⁹⁾ at the first time to calaculate the beam patterns in the resonator by the iterative computer calculation of Fresnel-Kirchhoff integration equation. The iterative computer calculation is easier, but the higher order modes cannot be separated with this analysis. The higher-order modes can be analyzed by the fast Fourier transform method(FFT), but the calaculations are rather complicated and the cost of the working time for the computer is expensive. In addition, the resonator with laser medium is difficult to analyze by this method, because the modes couple each other in the laser medium. In any laser medium, especially in the high-power laser, the distributions of gain, reflective indexes, etc. are not uniform and fluctuating, and the precise comparison between the analysis and the experiment is very difficult. So we do not need to persuade the complicated calaculation such as FFT method.

In calaculation, we defined the magnification $M=a_1/a_2$, where a_1 and a_2 are the radius of cocave and convex mirrors, and the ratio of output hole with the concave mirror diameter as $K=h/a_1$. The calculation were carried out by changing the three parameters K, M, and Fresnel number $N_0=a_1^2/\lambda L$ for COIL ($1.32\mu\text{m}$) as low gain laser, and CO_2 ($10.6\mu\text{m}$) as medium gain laser. We assumed that all laser medium were in thin sheets near the resonator mirrors because of the simple calaculation.

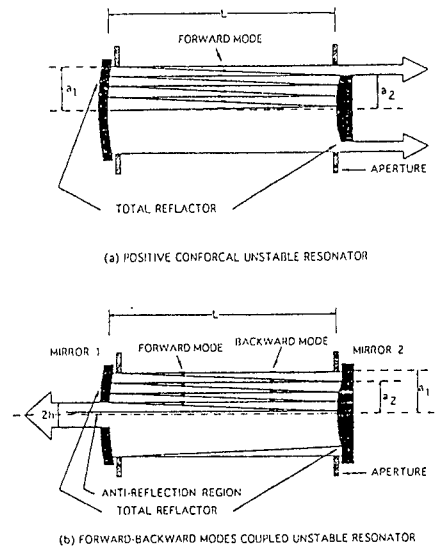


Fig 1 Resonator Configuration

3.THE RESULT OF THE CALCULATION

a) COIL

We assumed in the case of COIL with sub sonic gas flow, the small signal gain g_0 and the saturation parameter I_s are taken to be 0.2%/cm and $5.0\text{kW}/\text{cm}^2$ as example. The resonator length is taken to be 1m which is normal size for industrial lasers. The calaculation were carriedout by changing K and M value. The output power and internally stored power changing K value are shown in Fig.2 for the case of $N_0=15.0$ with $M=1.2-2.0$. The output power have a peak for K, so the optimum K value exist for a given N_0 .

And the output power also have a peak for M as shown in Fig.3. So the

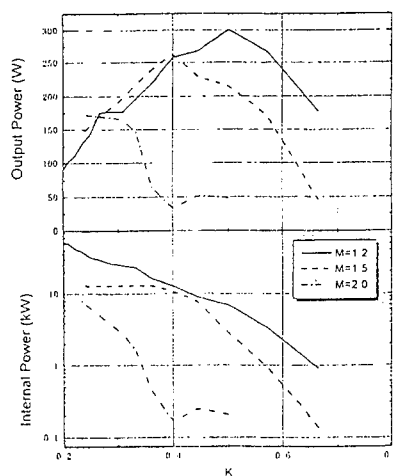


Fig 2 Output and internally stored power versus K for various M value in COIL laser with $N_0=15.0$

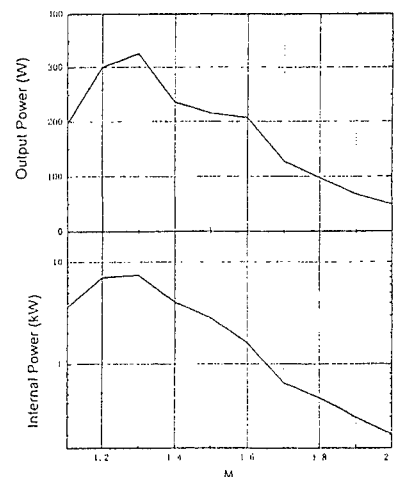


Fig 3 Output and internally stored power versus M in COIL laser with $N_0=15.0$

suitable resonator condition are determined by K and M for a given N_0 .

The near-field beam profile (a), near-field phase distribution (b) relative distance x/h , the far-field beam profile (c), the cumulative power (d) versus relative beam angle θ/θ_0 ($\theta_0 = \lambda/2a_1$) at $K=0.5$ and $M=1.2$ is shown in Fig.4 at which condition 0.3kw is gotten. The far-field beam pattern are not uniform but if K is taken to be small, Gaussian-like beam profile can be taken out, though the extracted power is rather lower, as shown in Fig.5.

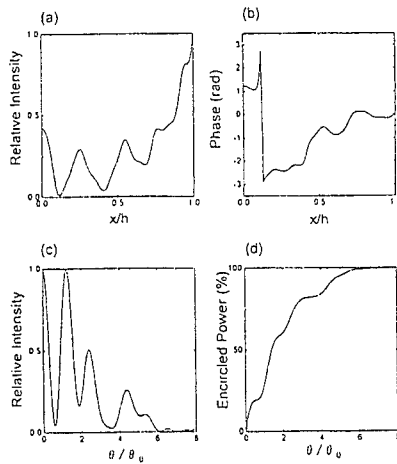


Fig 4 (a) Near-field intensity distributions, (b) phase distributions, (c) far-field intensity distributions, (d) encircled power distributions for resonators with $N_0=15.0$, $M=2.0$, $K=0.5$

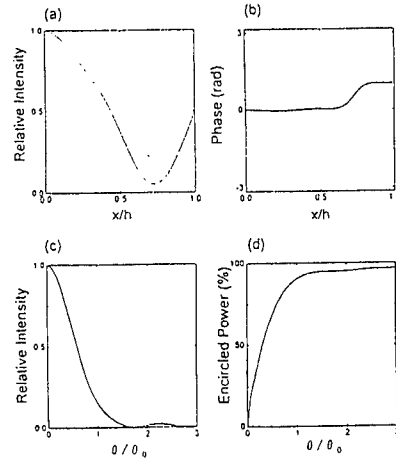


Fig 5 (a) Near-field intensity distribution, (b) phase distributions, (c) far-field intensity distributions, (d) encircled power distributions for resonator with $N_0=10.0$, $M=1.3$, $K=0.20$

b) CO₂ LASER

For CO₂ laser, the small signal gain g_0 and the saturation intensity I_s are taken to be 1.0%/cm and 1kW/cm². We assumed the resonator length to be 0.74m and filling factor at 49%, which is the ratio of resonator and electrode length. The calculation were carried out for CO₂ laser with $M=1.2-2.0$ changing K . The output power and the stored power for CO₂ laser are shown in Fig.6 for the case of $N_0=18.4$. The peak power, where the expected maximum power is about 1kW, is taken with $K=0.55$ and $M=1.2$ in this case, and the near-field beam profile (a), near-field phase distribution (b) versus relative distance x/h which were obtained at the output hole, and far-field beam profile (c), cumulative power (d) versus relative beam angle θ/θ_0 ($\theta_0 = \lambda/2a_1$) are shown in Fig.7. And the peak power is rather lower to be 0.5kW, Gaussian-like beam profile can be taken out at $K=0.2$ and $M=2.0$ as shown in Fig.8.

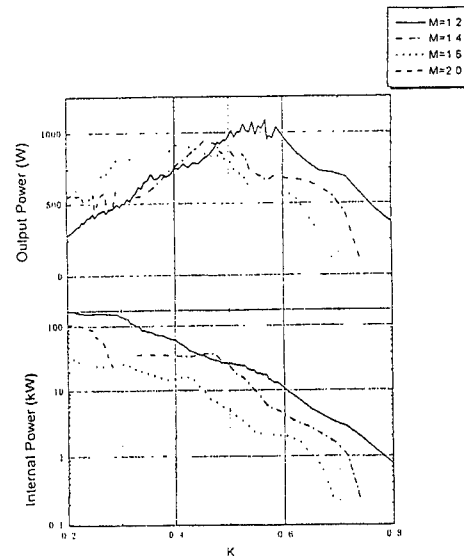


Fig 6 Output and internally stored power versus K for various M value in CO₂ laser with $N_0=18.4$

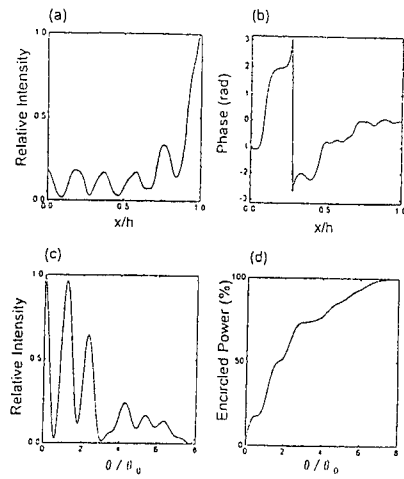


Fig 7 (a) Near-field intensity distributions, (b) phase distributions, (c) far-field intensity distributions, (d) encircled power distributions for resonators with $N_0=18.4$, $M=1.2$, $K=0.55$

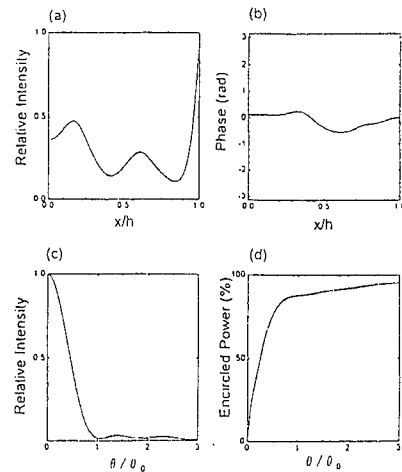


Fig 8 (a) Near-field intensity distribution, (b) phase distribution, (c) far-field intensity distribution, (d) encircled power distribution for resonator with $N_0=18.4$, $M=2.0$, $K=0.25$

4. CONCLUSION

This resonator is clearly shown to be effective for low gain large bore laser such as COIL, which can not oscillate with usual unstable resonator, because of full amplification by forward-mode coupled with back-ward mode, and we find the factors for the best performance of the aperture are shown as functions of K and M for N_0 . We are now preparing the experiment in the best performance condition.

5. REFERENCES

1. Joseph T. Verdeyen, LASER ELECTRONICS, Chap 12.6-8, Prentice-Hall International Inc. (1995)
2. D.R. Hall and P.E. Jackson, The Physics and Technology of Laser Resonators, Chap 2, Adam Hilger Bristol and New York, (1989)
3. K. Nanri, K. Mabuchi and T. Fujioka, "The Unstable Resonator with a Stable Resonator Core", Jpn. J. Appl. Phys. **35**(3), 1744-1750 (1996)
4. A.E. Siegman, "Unstable Resonator", Appl Opt. **13**(2), 353-367 (1974).
5. A.G. Fox and T. Li, "Resonant modes in a maser interferometer", Bell Syst. Tech. J. **40** (3), 453-488 (1961)

A. Kar, Center for Research & Education in Optics & Laser (CREOL), Mechanical and Aerospace Engineering Department, University of Central Florida, 4000 Central Florida Blvd., Orlando, Florida 32816-2700, USA

J. Rothenflue, Phillips Laboratory, Applied Laser Technology Branch (PL/LIDB), 3550 Aberdeen Avenue SE Kirtland AFB, New Mexico 87117-5776, USA

W. P. Latham, Phillips Laboratory, Lasers and Imaging Directorate (PL/LI), 3550 Aberdeen Avenue SE Kirtland AFB, New Mexico 87117-5776, USA

Abstract

This paper examines the use of Chemical Oxygen-Iodine Laser (COIL) for depositing ceramic coating on a substrate. The cladding experiments were conducted in the environment of nitrogen gas, and the laser beam was focused to a rectangular spot with large aspect (length to width) ratio. The beam was scanned by keeping the length of the spot aligned to the transverse direction. Optical micrographs are presented for the morphology of the clad surface and the cross section of the cladding zone.

Keywords: chemical oxygen-iodine laser, COIL, laser cladding, ceramic coating, stainless steel substrate, zirconium oxide (ZrO_2) and aluminum (Al) coating, thermal barrier coating, high temperature coating.

Introduction

CO_2 and Nd:YAG lasers are used extensively for various types of materials processing. The Chemical Oxygen-Iodine Laser (COIL) is of wavelength 1.315 μm with a very high output power which makes it suitable for materials processing. The principles of COIL have been discussed briefly by Kar et al.¹ Atsuta, et al.² used COIL to cut stainless steel up to 5 mm thick, and reported that the cutting capability of a 1 kW COIL is equivalent to a 1 kW Nd:YAG laser and about 2.5 times better than a 1 kW CO_2 laser. This improved cutting performance of COIL can be explained by noting that the absorptivity for COIL is larger than that for CO_2 laser because of the shorter wavelength of the former laser than the latter. This means that COIL is expected to have improved performance for other types of laser materials processing.

The ability of a laser beam to induce localized heating is utilized extensively to perform various types of materials processing. However, a large area of the substrate surface can be melted in a single pass of a scanning laser beam of very high power. For instance, a 10 kW laser beam with a rectangular spot of size 10 mm \times 1 mm gives rise to an intensity of 10^5 W/cm² that can be used to produce a melt pool of width 10 mm in a single pass of the laser beam. Therefore, high power lasers can be used for large-area processing such as laser hardening, surface alloying, thin film deposition, coating, cladding and materials removal. This paper presents some results concerning large-area cladding of substrates using ceramic powders.

Laser cladding is used to improve the oxidation, corrosion and wear resistant properties of an engine part or any other structure. This technology provides a means of utilizing inexpensive materials for high temperature applications such as aircraft engines by depositing materials of improved properties on the workpiece. Due to rapid cooling inherent in laser materials processing, the molten clad material solidifies rapidly leading to the formation of nonequilibrium alloys with metastable microstructures. These novel microstructures enhance the properties of the clad material.

Kar and Mazumder^{3,4,5,6} studied the formation of nonequilibrium alloys during laser cladding. Singh and Mazumder⁷ investigated the increase in solid solubility of the reactive element Hf in the binary alloy of Ni-Hf which was obtained by cladding a nickel-based superalloy substrate with a power mixture of Ni and Hf. Weerasinghe and Steen⁸ used a powder delivery system and a reflective dome near the cladding zone to carry out laser cladding, and claimed that the reflective dome recovers 40% of the delivered power. Yang et al.⁹ performed large-area cladding by using NiCrSiB as the cladding powder, and showed that 1.3 cm, 4 cm and 5 cm wide cladding can be achieved in a single pass of the scanning laser beam for laser power and scanning velocity of 1.68 kW and 2.5 mm/s, 7 kW and 3 mm/s, and 7.5 kW and 2.5 mm/s, respectively. Besides metal cladding, ceramic coatings are also applied to improve the surface properties of the workpiece. Thermal barrier coating, which is a duplex layer consisting of a MCrAlY (M = Ni or Co) bond coat and a partially stabilized zirconia coating, is applied to the low risk regions in

the turbine section of certain aircraft engines by using the plasma spraying or physical vapor deposition technique¹⁰⁻¹². Jasim et al.¹³ examined the structure of laser-cladded zirconia on mild steel, and found distinct regions of different crystal sizes. Gassmann et al.¹⁴ produced thick coatings of 7% yttria-stabilized zirconia on metals as well as composite materials containing up to 45 vol% high-melting-point carbides within a metal matrix. Gassmann and Modest¹⁵ investigated the laser cladding of partially yttria-stabilized zirconia on titanium, nickel and steel alloy substrates. This paper is concerned with the experimental studies of cladding stainless steel substrates with ceramics using COIL.

Experimental procedure

Laser cladding experiments were conducted using the RADICL (Research Assessment, Device Improvement Chemical Laser) device located at the U.S. Air Force's Phillips Laboratory in Albuquerque, New Mexico. The output laser beam of this device was focused into a rectangular spot of length and width 4 mm and 1 mm respectively on the surface of preplaced cladding powder mixture. For all experiments, stainless steel substrates of dimension 87 mm × 49 mm × 6.5 mm were used and the mixture of ZrO₂ and Al cladding powder was preplaced on the substrate in the form of a rectangular layer of dimension 25 mm × 4 mm × 2 mm. The compositions of ZrO₂ and Al are specified in Figs. 1 - 4. The substrate with this cladding powder mixture was placed on a translation stage that was moved at a speed of 0.5 cm/s relative to the laser beam for all experiments. The laser beam was kept stationary and it was so aligned that the length of the spot was in the transverse direction. The experiments were conducted in the environment of N₂ gas whose pressure was slightly above 1 atm.

Results and discussion

Ceramic coatings were deposited on stainless steel substrates by carrying out experiments under the above-mentioned conditions. Optical micrographs for two coatings are presented in Figs. 1 - 4. Figures 1 and 2 represent results for the incident laser power 4.65 kW and a cladding powder mixture of nominal composition 95.08 wt% ZrO₂ and 4.92 wt% Al. Figures 3 and 4 are for the incident laser power 4.72 kW and a cladding powder mixture of nominal composition 80.04 wt% ZrO₂ and 19.96 wt% Al. Figure 1 shows fish-scale-like morphology while Figure 3 shows relatively smoother texture although it has a few cracks. The smooth texture in Fig. 3 may be due to excessive Al that melts and redistributes in the clad melt pool and provides a binding mechanism for the ceramic grains. However, the presence of the cracks, which may be due to thermal and metallurgical transformation stresses, is unknown at present. Further studies are needed to understand the effects of the Al content on the surface morphology and cracks.

Figures 2 and 4 show the cross section of the clad, clad-substrate interface and the substrate melt pool. The sharp clad-substrate interfaces in these two micrographs indicate that the substrates are diluted very little by the ceramic cladding material. This means that the properties of the substrate will be unaffected by the cladding material due to ceramic coating. However, the size of the substrate melt pool is fairly large. This is because the ceramic powder has higher melting temperature than the stainless substrate and therefore, a large amount of heat is lost to the substrate during the melting and solidification of the cladding material. Large melt pool in the substrate can alter the substrate properties near the clad-substrate interface due to rapid heating and cooling of the fusion zone. Further studies are needed to minimize the change in substrate properties near the clad-substrate interface.

Conclusions

Results are presented for the cladding of stainless steel substrates with ceramics using COIL. Low Al content in the initial cladding powder mixture produces crack-free coating with fish-scale-like surface morphology. High Al content in the initial cladding powder mixture produces relatively smooth surface but the surface has a few cracks. The dilution of the substrate by the cladding powder mixture is found to be very little. Further studies are needed to understand the effects of Al on the surface morphology and cracks. Also, oxidation tests are needed to determine the improvement in the oxidation-resistant properties of the substrate.

Acknowledgments

This work was accomplished when A. Kar was at the Phillips Laboratory, Applied Laser Technology Branch (PL/LIDB), at Kirtland Air Force Base, Albuquerque, New Mexico under the 1996 Summer Faculty Research Program sponsored by the Air Force Office of Scientific Research (AFOSR). Testing was contributed by the Applied Laser Technology Branch of the Phillips Laboratory. The authors thank Jun Cheng and Jian Xie, who are graduate students in the Mechanical, Materials and Aerospace Engineering Department and CREOL at the University of Central Florida, for preparing the optical micrographs for this paper.

References

1. A. Kar, J. E. Scott and W. P. Latham, "Theoretical and Experimental Studies of Thick-Section Cutting with a Chemical Oxygen-Iodine Laser (COIL)," *J. Laser Applications*, Vol. 8, 1996, pp. 125-133.
2. T. Atsuta, K. Yasuda, T. Matsumoto, T. Sakurai and H. Okado, "COIL and the Material Processing," in *Conference on Lasers and Electro-Optics (CLEO)'94*, Vol. 8, 1994, OSA Technical Digest Series (Optical Society of America, Washington D. C.), P. 351, 1994.
3. A. Kar and J. Mazumder, *J. Appl. Phys.* **78**, 6353 (1995).
4. A. Kar and J. Mazumder, *J. Appl. Phys.* **61**, 2645 (1987).
5. A. Kar and J. Mazumder, *Metall. Trans.* **20A**, 363 (1989).
6. A. Kar and J. Mazumder, *Acta Metall.* **36**, 701 (1988).
7. J. Singh and J. Mazumder, *Acta Metall.* **35**, 1995 (1987).
8. V. M. Weerasinghe and W. M. Steen, Laser cladding with pneumatic powder delivery, *Proc. 4-th Int. Conf. on Lasers in Materials Processing*, edited by E. A. Metzbowser, (American Society of Metals, Metals park, Ohio, 1984), pp. 166-175.
9. X. C. Yang, B. Q. Wang, Y. S. Wang, X. Zhao, H. K. Cha, B. R. Su and W. J. Fang, "Laser cladding by 10 kW CO₂ laser wide-band scanning pyramid mirror," in *Laser Materials Processing*, *Proc. ICALEO'94*, Vol. 2500, T. D. McCay, A. Matsunawa and H. Hugel, Editors, (Laser Institute of America and The Society of Photo-Optical Instrumentation Engineers - The International Society for Optical Engineering, Orlando, Florida), 1994, pp. 155-163.
10. R. A. Miller, "Current status of thermal barrier coatings - an overview," *Surf. Coatings Tech.* **30**, 1 (1987).
11. D. J. Wortman, B. A. Nagraj and D. C. Duderstadt, "Thermal barrier coatings for gas turbine use," *Mater. Sci. Eng.* **121A**, 433 (1989).
12. R. Taylor, J. R. Brandon and P. Morrell, "Microstructure, composition and property relationships of plasma-sprayed thermal barrier coatings," *Surf. Coatings Tech.* **50**, 141 (1992).
13. K. M. Jasim, R. D. Rawlings and D. R. F. West, "Thermal barrier coatings produced by laser cladding," *J. Mater. Sci.* **25**, 4943 (1990).
14. R. C. Gassmann, S. Nowotny, A. Luft and W. Reitzenstein, "Laser cladding of hard particle rich alloys," in *Proc. Int. Conf. on Applications of lasers and Electro-Optics (ICALEO): Laser materials Processing*, Vol. 75, (Laser Institute of America, Orlando, Florida, 1993), pp. 288-300.
15. R. C. Gassmann and M. F. Modest, "Laser cladding of partially yttria stabilized zirconia on titanium, nickel and steel alloys," in *Laser Materials Processing*, *Proc. ICALEO'94*, Vol. 2500, T. D. McCay, A. Matsunawa and H. Hugel, Editors, (Laser Institute of America and The Society of Photo-Optical Instrumentation Engineers - The International Society for Optical Engineering, Orlando, Florida), 1994, pp. 125-134.

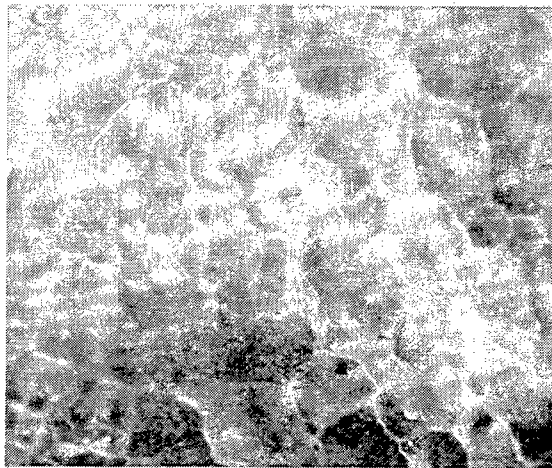


Figure 1. Surface morphology of a laser ceramic clad. Magnification: 25. Cladding mixture: 95.08% ZrO_2 and 4.92 % Al by wt. Substrate: Stainless steel. Laser parameters: Incident power = 4.65 kW, Scanning speed = 0.5 cm/s, 4 mm \times 1 mm rectangular spot.

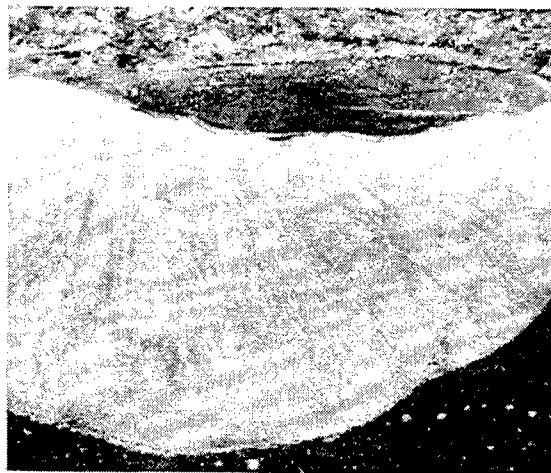


Figure 2. Cross sectional view of the ceramic clad, clad-substrate interface and substrate melt pool. Magnification: 18. Cladding mixture: 95.08% ZrO_2 and 4.92 % Al by wt. Substrate: Stainless steel. Laser parameters: Incident power = 4.65 kW, Scanning speed = 0.5 cm/s, 4 mm \times 1 mm rectangular spot.

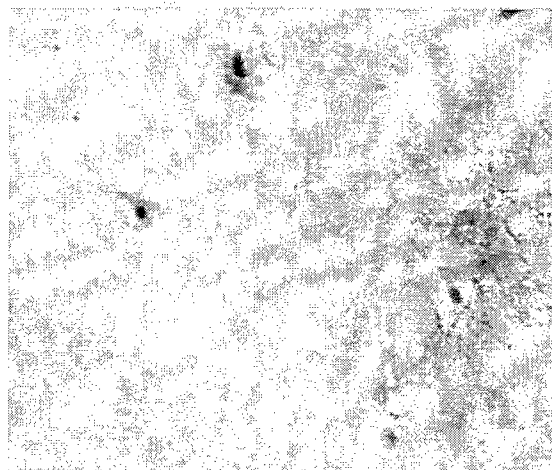


Figure 3. Surface morphology of a laser ceramic clad. Magnification: 35. Cladding mixture: 80.04% ZrO_2 and 19.96 % Al by wt. Substrate: Stainless steel. Laser parameters: Incident power = 4.72 kW, Scanning speed = 0.5 cm/s, 4 mm \times 1 mm rectangular spot.



Figure 4. Cross sectional view of the ceramic clad, clad-substrate interface and substrate melt pool. Magnification: 18. Cladding mixture: 80.04% ZrO_2 and 19.96 % Al by wt. Substrate: Stainless steel. Laser parameters: Incident power = 4.72 kW, Scanning speed = 0.5 cm/s, 4 mm \times 1 mm rectangular spot.

Prospects for an Industrial Chemical Oxygen-Iodine Laser

John Vetrovec

Rocketdyne Division, Rockwell International Corp., 6633 Canoga Avenue, Canoga Park, California, 91309, U.S.A.
(818) 586-3101, (818) 586-3074 (fax), email: jvetrove@rdyne.rockwell.com

ABSTRACT

This work evaluates the prospects of developing a chemical oxygen-iodine laser which could be used for cutting, welding, and other material processing applications that can benefit from a high-power, high-brightness, fiber-delivered laser beam. It shows how application-specific requirements drive the technological and economic considerations of the iodine laser.

Keywords: COIL, iodine laser, industrial laser, chemical laser

1. INTRODUCTION

It is well known that the chemical oxygen-iodine laser (COIL) has the capability of delivering high power output with excellent beam quality [1, 2]. At the 1.315 μm wavelength, the COIL beam is compatible with optical fibers and can be efficiently delivered to remote application areas [3]. These characteristics make COIL a candidate for a variety of industrial applications in material processing, where high power, high-brightness, and delivery by optical fiber can provide economic and/or technological advantages over existing industrial lasers such as CO_2 and Nd:YAG. Although COIL has been the subject of laboratory investigation and technology development for almost two decades, much of that effort was motivated by high energy laser weapons rather than industrial applications [4]. Key challenges to an industrial COIL were its dependence on chemical fuel, difficulty of integration into industrial operations, and economic considerations. In recent years, as COIL and related laser technologies have become more mature, the prospects for an industrial COIL are becoming brighter.

2. TRENDS IN INDUSTRIAL HIGH-POWER LASERS: CASE FOR HIGH-BRIGHTNESS

Use of high-power lasers in material processing, namely metal cutting and welding, is enjoying rapid growth [5,6], Figure 1. Introduction of lasers thus far has been due primarily to a technology push which offered better tools for traditional applications. Now that lasers are accepted as standard manufacturing equipment and new applications start to emerge, this environment is changing to a market pull characterized by an increasing demand for laser systems engineered to meet specific material processing needs [7].

The key requirements for industrial lasers are economy, process quality, system reliability, and easy integration into manufacturing operations [5]. In particular, economy of operation is sought through increased device utilization by time sharing and beam splitting [8]. Figure 2 shows how material processing needs are translated into laser requirements, namely high-power, good beam quality, and beam delivery via optical fibers. Process quality is reflected in a small heat affected zone, in the continuity and penetration consistency of welds, and precision cutting that produces clean edges, Figure 3. Reliability becomes an extremely important factor on production lines where a laser system failure can cause costly downtime.

Often, the laser application workstation is part of a production process in which floor space is at a premium and the laser beam is preferably generated at another location and remotely delivered. The requirement for remote delivery and timesharing is conveniently met with a laser beam that can be delivered through optical fibers. Flexibility in remote delivery is particularly critical where the production process configuration changes frequently, such as in the flexible manufacturing concept. In addition, high-brightness lasers are also critical to certain emerging applications such as aluminum cutting and welding, thick section cutting for dismantlement of nuclear installations [9], laser driven x-ray lithography [10], and pulsed laser deposition [11]. Aluminum cutting and welding by lasers is especially important to the automotive industry which plans to reduce vehicle weight and to increase gas mileage by introducing aluminum car bodies [12].

3. PROGRESS TOWARD AN INDUSTRIAL COIL

Today, the gas CO_2 and the solid state Nd:YAG are the principal high-power industrial lasers for material processing. While the CO_2 devices are available in higher power and better beam quality, compatibility with optical fibers is making the Nd:YAG increasingly popular [13]. The major limitation of commercially available Nd:YAG lasers is their relatively poor beam quality, caused by cooling problems in the arc lamp-driven laser rods [14]. There is an ongoing effort to remedy this problem by configuring the laser media into slabs and by replacing the lamps with more efficient laser diodes [15]. While Nd:YAG (and glass) diode pumped lasers generating about 1 kW of near diffraction-limited beams have been reported [16, 17], production models are many years away and, even then, will be largely unaffordable, unless the cost of diodes is significantly reduced. COIL is thus the only near term candidate for an industrial high-power, high-brightness laser with fiber-compatible output. Power and beam quality performance demonstrated by laboratory devices are stimulating interest in industrial COIL at the Phillips Laboratory [18] and Rocketdyne in the U.S.A., Kawasaki Heavy Industries in Japan [19], DLR in Germany [20], and other laboratories [21]. Figure 4 shows the comparative performance of leading and emerging industrial lasers.

The basic science and technology required for efficient operation of COIL have been established in previous efforts. Chemical efficiencies of 26.7% have been reported [22] and 40% projected [23]. Recent breakthroughs in compact, high-pressure oxygen generators [24] make it possible to reduce the size and cost of the vacuum plant. Efficient transmission of COIL beam by optical fibers has been already demonstrated at the 1 kW level [3] and analysis indicates that over 20 kW of power could be transmitted through commercially available fibers with 1 mm ϕ [18, 25]. Commercial availability of hydrogen peroxide electrosynthesizers [26] promises in-situ regeneration of COIL fuels. In the author's opinion, key challenges to the development of industrial COIL are no longer in science but in product engineering. First steps toward construction of a practical, safe, and integrated COIL system have already been taken by Kawasaki and Rockwell, Figure 5.

4. FUEL CYCLES IN COIL

Unlike other industrial lasers, in which the lasing media are generated either in electric discharges or with radiation produced by electric light sources, the lasing medium in COIL is produced by reacting chemical fuels. The raw fuels for COIL are potassium hydroxide, hydrogen peroxide (which are mixed to prepare basic hydrogen peroxide or BHP), chlorine, and iodine. First, chlorine gas is brought into contact with the BHP in an oxygen generator to produce singlet delta oxygen. Then, iodine vapor is mixed with the singlet delta oxygen to produce the lasing medium [1].

Past research in COIL was motivated by military applications, in which the laser produced only short bursts of energy and the cost of fuel and supply logistics were of little concern. However, for the continuous operation required for most industrial applications, the cost of fuel, fuel logistics, and management of laser effluents have significant impact. This suggests two approaches in the design of an industrial COIL. First is the traditional "open loop" fuel cycle, in which fresh fuels are obtained in bulk form and reaction products are disposed of. An alternate approach is to regenerate and recycle the laser fuels in-situ. Regeneration of BHP and chlorine from COIL reaction products (potassium chloride and water) can be accomplished by adapting and integrating two commercially available electrochemical technologies: (1) brine electrolysis, to produce hydroxide and chlorine [27], and (2) electrolytical synthesis of hydrogen peroxide in an alkaline electrolyte [26]. As seen in Figure 6, the overall process is continuous and consumes only electricity and atmospheric oxygen.

5. ECONOMIC CONSIDERATIONS

Since economic considerations are among the leading factors in the purchase of a material processing laser system, the industrial COIL must be cost competitive. Competitiveness can be judged by the cost of acquisition, cost of operation, and the life cycle cost, which is the sum of the first two. The typical purchase price of a multi-kilowatt fiber-fed cw Nd:YAG laser is about \$100/watt [28]. The price for a comparable CO₂ system is about \$60/watt. Pulsed systems are typically somewhat more expensive. The cost of the industrial COIL based on the concepts presented here is estimated at about \$120/watt for the "open cycle" and \$210/watt for the regenerative version.

The very low cost of electricity (~\$0.10/kWh in the U.S.) keeps the operating cost of CO₂ and Nd:YAG in the range of \$2-6/kWh of laser power. The open cycle COIL requires a continuous supply of chemical fuels which (based on the prices of bulk chemicals in the U.S.) bring the cost of operation to about \$33/kWh. The regenerative COIL can be operated at about \$7/kWh, which is quite comparable to that of a Nd:YAG [28]. Amortizing the cost of acquisition over a system lifetime, e.g. 10,000 hours (5 years of 8 hours/day operation) yields the life cycle cost of the system, which, for the open cycle COIL, is almost 3x higher than that of a comparable Nd:YAG and almost 4x higher than CO₂ lasers. The lifecycle cost of the regenerative COIL is comparable to that of the Nd:YAG but higher than the CO₂. However, the life cycle cost should also take into account laser effectiveness for specific applications. For example, the CO₂ laser effectiveness is reduced due to its long wavelength which is susceptible to reflection from the workpiece and is also strongly absorbed by the plasma. Taking these effects into consideration indicate that COIL could potentially be the the best cost-performer [29].

6. CONCEPT DESIGN EXAMPLE

Economic considerations dictate device configuration, choice of technologies, and engineering design. The overall industrial COIL concept configuration is comprised of Fuel Supply, Laser Assembly, and Beam Delivery Assembly systems, Figure 7. Two versions of the fuel supply were considered: open loop and regenerative. The choice of power was set at 20 kW, based on the average 5 kW requirement for individual applications and simultaneous supply of four beams to multiple work stations. Chemical efficiency is estimated at about 20%. The wall plug efficiency for the regenerative system is about 3%.

A supersonic cavity and high pressure flow throughout the Laser Assembly are favored by a tradeoff between hardware cost, operating cost and beam quality. This approach allows reduction of the vacuum plant size to a single stage. Nitrogen, which is used as a diluent in 3:1 molar ratio to chlorine, is provided either by evaporation of liquid nitrogen, which is used as a refrigerant for the open cycle system, or from an air separation unit, which also generates oxygen required for electrosynthesis of BHP. Iodine is recycled internally within the laser by condensing the iodine vapor downstream of the diffuser, then vaporizing it and feeding the vapor back to the nozzle. Any small amount of iodine leaking through the condenser and unreacted chlorine (<5%) are removed from the flow in a conventional concurrent scrubber, which also chills the flow and

provides minor compression. The vacuum plant consists of conventional water ring pump(s). An unstable negative branch resonator with uncooled optics is used for high extraction, good beam quality, and low sensitivity to misalignment. Nominal operation is cw but pulsed mode operation could be achieved by magnetic gain switching [30].

Fuel Assembly for the open cycle system operates in a batch mode. A suitable quantity of BHP is prepared from commercial grade H_2O_2 and NaOH and the laser is operated until the molarity drops to the threshold level for efficient operation. NaOH is used in lieu of KOH because of its lower cost and the higher salt solubility. At \$0.10/gallon and almost 400 kJ/kg refrigeration effect, liquid nitrogen is the most economical choice for refrigeration and source of cavity diluent. Liquid chlorine is flash vaporized in a standard commercially available vaporizer. The regenerative fuel supply integrates cells for brine electrolysis and electrosynthesis of BHP based on established technologies. A salt separator is employed to extract KCl from the BHP flow and to feed it into the brine cell. A commercially available air separator generates oxygen for BHP electrosynthesis and nitrogen diluent for the laser. A standard compression type refrigerator is used for thermal management.

The Beam Delivery Assembly splits and multiplexes the 20 kW beam according to a timesharing protocol and delivers it to application workstations using commercially available optical fibers. Preservation of beam quality is of particular concern for long fibers with multiple and sharp bends. Previous effort [31] suggests that graded index fibers are less detrimental to beam quality. It is conservatively assumed that delivered beam quality (M^2) will be about 10, which is still about an order of magnitude better than current Nd:YAG's [32]. The corresponding COIL beam peak intensity is in the range of 10^9 W/cm².

7. CONCLUSION

The need for high-power, high-brightness lasers for existing and emerging applications has been established. It was shown that COIL uniquely meets the power, brightness, and beam delivery requirements. COIL science and technology are sufficiently mature to enable initiation of product development. Economic comparisons indicate that COIL could be a cost competitive industrial laser for material processing. Concepts presented illustrate how various COIL and commercial technologies can be integrated to yield an economically viable product.

8. REFERENCES

1. K.A. Truesdell, et al, "A history of COIL development in the USA," 10-th GCL Conf., SPIE vol. 2502, p. 217 (1994)
2. P.V. Avizonis and K.A. Truesdell, "The Chem. Oxygen-Iodine Laser," 10-th GCL Conf., SPIE vol. 2502, p. 180 (1994)
3. H. Fujii, "COIL development in Japan," 25-th AIAA Plasmadynamics & Laser Conf., Colorado Springs, U.S.A. (1994)
4. S. Lamberson, "The airborne laser,," SPIE vol. 2702, p. 208 (1996)
5. D.A. Belforte, "Improving laser system productivity through production line integration," SPIE vol. 2207, p. 4 (1994)
6. D.A. Belforte, Belforte Associates, Sturbridge, Mass., communications (1996)
7. R. Kryger, "Laser material processing viewpoint," Workshop on Laser Applic. in Automotive Industry, Detroit, (1995)
8. W. Moon, "Defining an optical energy distribution system....," Industrial Laser Review, February 1994
9. J. Vetrovec et al, "High-power iodine laser application for remote D&D cutting," presented at this conference
10. T. Roltsch, "Cost effective X-ray lithography," E-Beam, X-Ray, & Ion Beam Litho. for Mfg., SPIE vol. 1465 (1991)
11. B.E. Warner, et al, LLNL, presented at Workshop on Pulsed Metal Vapor Lasers, U. of St. Andrews, Scotland, 1995
12. B. Irving, "Blank welding forces automakers to take notice," Welding Journal **71** (9), p. 39-41, (1991)
13. H.K. Tonshoff et al, "New possibilities in material processing with kW-solid state lasers," SPIE vol. 1277, p.199 (1990)
14. U. Wittrock, "High power rod, slab and tube lasers," in Solid State Lasers: New Devel. & Applic, Plenum, NY (1993)
15. R.L. Byer, "Diode pumped solid state lasers," in Solid State Lasers: New Devel. & Applic, Plenum, NY (1993)
16. M. Seguchi and K. Kuba, "1.4 kW Nd:YAG slab laser with diffusive coupled....," Opt. Letters, **20** (3) p. 300 (1995)
17. S. Basu and R.L. Byer, Appl. Opt. **12**, 1765 (1990)
18. J.E. Scott et al, "The use of COIL for high-speed cutting of thick steel," SPIE vol. 2702, p. 339 (1996)
19. H. Fuji, and T. Atsuda, "Current status of industr. COIL devel.," Iodine Lasers & Applic., SPIE vol. 1980, p.148 (1992)
20. H. von Bulow and Schall, W.O., "Oxygen iodine lasers for ind. applic.," 10-th GCL Conf., SPIE vol. 2502 p.258 (1994)
21. V.V. Kalinovskiy et al, "High-power oxygen iodine laser," Iodine Lasers & Applic., SPIE vol. 1980, p. 138 (1992)
22. T.L. Rittenhouse et al, "High efficiency operation of a 5 cm gain length supersonic ...," SPIE vol. 2702, p. 333 (1996)
23. W.E. McDermott, "Generation of singlet delta oxygen - a survey update," SPIE vol. 2702, p. 239 (1996)
24. M. Zagladullin, et al, Sov. J. Quantum Electron. **21**, (7) p. 747 (July 1991)
25. S. Takeda, "Industrial and reverse-industrial applications of COIL," SPIE vol. 2702, p. 191 (1996)
26. The Dow Chemical Co., Midland, MI 48674: "On-site alkaline peroxide generation system," product brochure (1995)
27. D. Pletcher and F.C. Walsh, "Industrial Electrochemistry," chapter 3, 2nd ed., Chapman and Hall, New York (1986)
28. T. Weber, Hobart Laser Products, Livermore, Calif., communications (1995)
29. W.L. Bohn, "Current status of COIL research in Germany," SPIE vol. 2702, p. 368 (1996)
30. G.D. Hager et al, IEEE J. Quant. Electronics, **29**, March issue, p. 933 and 944 (1993)
31. H. Haferkamp et al, "Cutting with high power Nd:YAG lasers and fiber for beam delivery, SPIE vol. 2207
32. R. Joeckle, "Laser processing with high-power gas lasers," 10-th GCL Conf., SPIE vol. 2502, p. 597 (1994)

Area	Application	User Industry				Requirements		Market (\$M)	
		Auto	Ship-building	Heavy Equip	Other	Power	Beam Quality	1996	2000
Current Applications	Cutting	●	●	●	●	●	●	~60*	~190*
	Welding	●	●	●	●	●	○		
	Drilling	●	●	○	●	●	●		
	Cladding	○	○	○	○	●	●		
	Cleaning	○	○	○	○	●	●		
	Heat Treating	○	○	○	○	●	●		
	Other	○	○	○	○	●	●		
Emerging Applications	Alum. Proc.	●	○	○	○	●	●	?	?
	Pulsed Las. Depos.	○	○	○	○	●	●		
	X-Ray Litho	○	○	○	○	●	●		
	Nuclear D&D	○	○	○	○	●	●		

● = Strong need ○ = Some need *) Based on ref. [6]

Figure 1: Uses and users of high-power industrial lasers

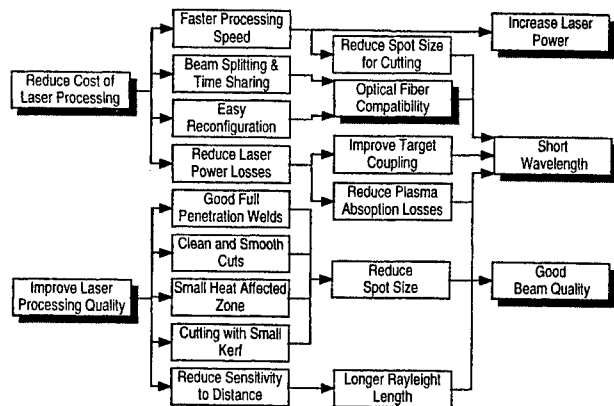


Figure 2: Application needs translate into laser parameters

	Beam Features		Impact on Processing Quality	
	Intensity Profile	Depth of Field	Cutting	Welding
High Brightness Beam	High Peak Intensity 	Long Depth of Field 	Sharper cut, small kerf, less burr, faster processing 	Faster production of high quality full penetration welds
Low Brightness Beam	Low Peak Intensity 	Short Depth of Field 	Large heat affected zone, uneven edge, burr 	Large heat affected zone, meniscus, weaker weld

Figure 3: High-brightness beams for material processing

High Power Industrial Laser Class	Wave-length [μm]	Optical Fiber Compat.	Demonstr. BQ (M ²)	Acquisition Cost # [\$ / Watt]	Demon'd Power** [kW]	Commerc. Availab'ity	Comments
Nd:YAG-Rod Lamp pumped	1.06	Yes	~80	100	4	Now	Inherently poor BQ, poor scaling in power
Nd:YAG-Slab Lamp pumped	1.06	Yes	<2	NA	~1	No plans	No thrust for product development
Nd:YAG-Slab Diode pumped	1.06	Yes	<2	1000*	~1	2-3 years?	Major thrust for product development
COIL	1.315	Yes	<2*	120* (op cyc) 210* (regen.)	39	3-5 years	Excellent power scalability, BQ not affected by power
CO ₂	10.6	No	<2	~60	45	Now	Poor BQ at high power
CO	5.3	No	9	NA	20	No	Poor BQ at high power

*) Projected, **) Best achieved to-date, #) CW

Figure 4: Performance comparison of high power lasers

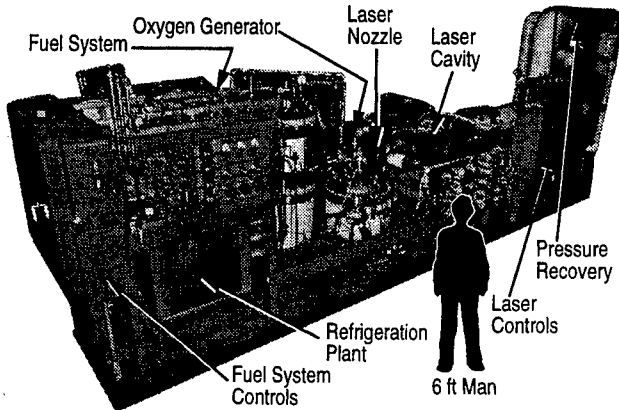


Figure 5: Rockwell's self-contained high-power TSS COIL

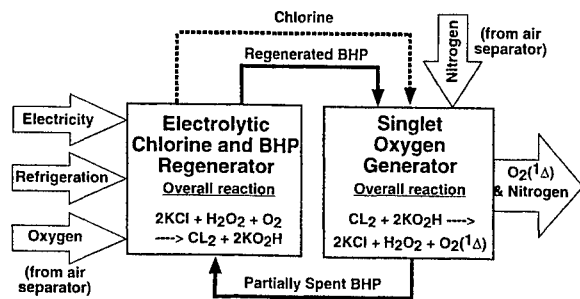


Figure 6: BHP and chlorine regeneration for COIL

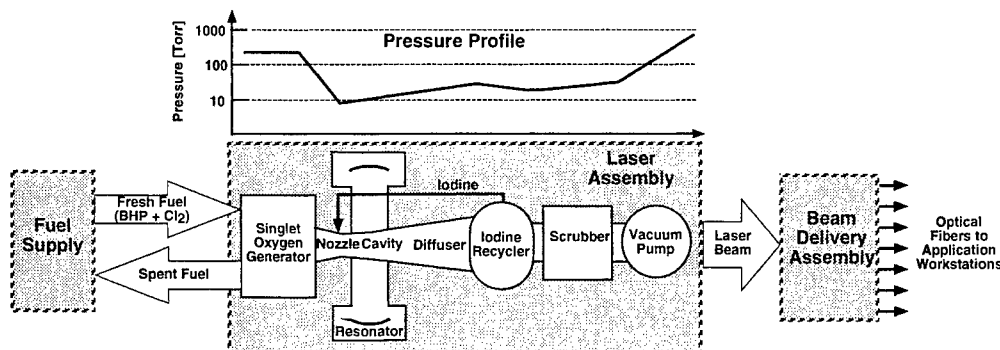


Figure 7: Industrial COIL concept

16. Laser Applications

ORION: Clearing near-Earth space debris in two years using a 30-kW repetitively-pulsed laser

C. R. Phipps

Photonic Associates

1621 Calle Torreon, Santa Fe, New Mexico 87501, USA

J. P. Reilly

Northeast Science and Technology

117 Northshore Boulevard, East Sandwich, Massachusetts 02537, USA

Key words: debris, photoablation, high power neodymium laser, iodine laser

ABSTRACT

Nearly 200,000 pieces of debris in the 1–20-cm range in low-Earth orbit (LEO), a legacy of 35 years of spaceflight now threaten long-term space missions. An economical solution to the problem is to use a ground-based laser to create a photoablation jet on the objects and cause them to re-enter the atmosphere and burn up. A sensitive optical detector is required to locate objects as small as 1 cm at 1500 km range. Applied when the object is rising and between about 45 and 15-degree zenith angle, the necessary Δv is of order 100m/s. A laser of 30 kW average power at 5-ns pulsewidth and a 4–6-m mirror with adaptive optics can clear near-Earth space of the 1–20-cm debris in 2 years of operation. A high altitude site minimizes turbulence correction, interference from nonlinear optical effects, and absorption. We discuss the effect of nonlinear optical processes in the atmosphere as boundaries on propagation, and how to choose system parameters to guarantee optimum conversion of laser energy to target momentum. The laser might be Nd:glass ($1.06\mu\text{m}/530\text{nm}$), or iodine ($1.3\mu\text{m}$).

1. DEBRIS

Thirty-five years of space activity have produced several hundred thousand pieces of space debris larger than 1 cm in near-Earth orbit [Phipps, *et al.* 1996] (Fig. 1). Debris objects are now sufficiently numerous to pose a significant threat to the International Space Station Alpha (ISSA). For ISSA, the impact velocity spectrum of these objects peaks at 10–12 km/s, for which a 1-cm-diameter aluminum object has kinetic energy ≈ 100 kJ. The size range of greatest hazard to spacecraft is 1.5–20-cm. It is possible to shield against objects smaller than 1.5 cm. Larger objects are few, and can be seen and avoided. Cumulative debris flux in the 800–1100-km altitude band in this size range (meaning impacts from objects with size $\geq d$) is about $9\text{E-}5/\text{m}^2$ cross-section per year [Kessler 1995a]. Today, space debris in low-Earth orbit (LEO) threatens any mission in the $h = 1000$ km vicinity which has a product of exposed area and on-station lifetime of the order of $10^4 \text{ m}^2\text{-years}$. For example, a fleet such as that planned by Teledesic Corp. with orbit-average projected cross-section of $8.3\text{E}4 \text{ m}^2$ is expected to experience a hit once every 2 months. These hits are not necessarily catastrophic, but 3–4 satellites in this constellation will be lost to debris at a cost of \$30–\$40M in a decade [Stewart 1996].

There is still substantial uncertainty amounting to factors of 3 or 4 in the 1–20-cm flux because only the 7900 objects larger than 10 cm have been catalogued. Density of smaller objects is based on sampling [see, e.g., Stansbery, 1996]. A pernicious aspect of the debris arises from the possibility that collisions between these objects will produce many smaller objects. Some authors suggest the critical debris density for this effect has been achieved in this band [Kessler 1995b]. This process is irreversible in the popular 800–1100-km altitude band where lifetime is of order 10k yr.

2. WHY DEBRIS MITIGATION IS IMPORTANT

2.1 Protecting the Space Environment

Space is a commons. This last and most pristine frontier is being polluted.

2.2 Insurance policy

Presently, the users of space have mostly decided to assess the threat of space debris in terms of their individual assets. On the basis of the threat to an individual satellite, one can ignore the risk. Instead, we believe it is logical to look at the collective risk, since the total threat to World installed space assets (of order \$60B) is significant, but may be mitigated, as in

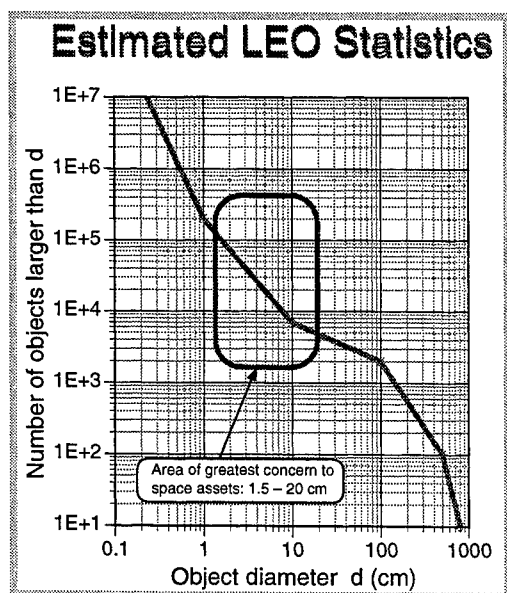


Figure 1

Estimated number of debris vs. size

e.g., Stansbery, 1996]. A pernicious aspect of the debris arises from the possibility that collisions between these objects will produce many smaller objects. Some authors suggest the critical debris density for this effect has been achieved in this band [Kessler 1995b]. This process is irreversible in the popular 800–1100-km altitude band where lifetime is of order 10k yr.

the case of the threat of collision to a fleet of automobiles, by pooling the risk in an insurance policy. That insurance policy is ORION, and its construction can be completed for a premium of about 0.2% of the installed capital investment.

2.3 Technology base

This project is the first opportunity to build a high average power, high peak power laser system. Its technical requirements also stretch existing capabilities in pointing, tracking, acquisition, detection, and adaptive optics.

2.4 Debris database

Small objects in the threatening 1-20-cm size range have mostly not been characterized, leading to unacceptable uncertainties in number density, flux, and orbital parameters of the objects.

3. PREVIOUS MITIGATION EFFORTS

Mitigation of debris has been discussed by Metzger, *et al.* 1989, Loftus & Reynolds 1993, Monroe 1994, Phipps 1993, and Phipps *et al.* 1996. A major policy document in this area is the Interagency Report on Orbital Debris [OSTP 1995].

The approach of Metzger, *et al.* is space-based, featuring a nuclear-powered spaceborne debris sweeper powering a neutral particle beam or a 10-kJ, 1-Hz krypton fluoride laser ($\lambda = 248$ nm). The advantage of this concept is that the photoablation thrust vector averaged over many laser shots can be directed exactly opposite to the momentum of the object for maximum efficiency, which cannot be done from the ground. The disadvantages are that mass costs \$10 – 20/g to put in low Earth orbit, plus the fact that the complexity of a space-based debris sweeper far exceeds that of the Hubble Telescope, which was a multi-billion-dollar effort both to install and to service. Also, because of the 1000-km depth of the debris band, space-based debris sweeper needs a range of action which turns out to be not dramatically different from that of its ground-based counterpart to be effective in a reasonable time. Finally, a space-based system discards a “free” advantage of the ground-based system since, from the ground, interesting objects are all moving against a fixed background, whereas, in space, velocity discrimination must be used, leading to complicated detection schemes involving 4-wave mixing. Monroe 1994 proposes a ground-based system featuring a 10-m-diameter beam director with adaptive optics correction and a 5MW reactor-pumped 1.73- μ m wavelength laser. Loftus and Reynolds 1993 catalog forces available for removing objects from orbit, including direct propulsion, enhanced aerodynamic drag, solar sails, electromagnetic drag, and solar/lunar orbit perturbations. They also mention valuable efforts at international cooperation and improved spacecraft design to dramatically reduce the rate of increase of debris.

4. THE ORION SYSTEM

4.1 Overview

A ground-based, repetitively pulsed laser system with about 30kW average power (Nd:glass at 1.06 μ m is assumed but frequency-doubled Nd:glass, or iodine at 1.3 μ m have not been ruled out) is focused on the debris object by a 6-m diameter beam director fitted with adaptive optics capable of correcting atmospheric turbulence well enough to achieve a Strehl ratio of 0.5. Pulse energy is 30kJ. The system is installed at a high altitude, low-latitude site with good seeing to minimize the difficulty of attaining this goal. The laser pulse intensity on the debris object is adjusted so that a photoablation jet is created. Since most irregularly-shaped debris objects were created by explosion or collision, they will be tumbling about 3 axes, and this tumbling combined with operation near the photoablation threshold intensity will produce a net thrust averaged over many laser shots which is approximately parallel to the laser propagation vector. If the system only addresses objects which are rising with zenith angle $45^\circ < \theta_z < 0$ the object's perigee will be lowered sufficiently (200 km) to produce rapid re-entry and burnup. For many of the objects, this can be done in one pass. In order to send the ORION laser beam through the atmosphere, beam intensity must be low enough to avoid driving nonlinear processes at the pulsewidth employed. Those of primary concern are Stimulated Raman scattering (SRS), Stimulated Thermal Rayleigh Scattering (STRS) and nonlinear index (n_2). The system can clear near-Earth space of the primary threat debris population in about two years.

4.2 Pulsed laser format is preferable to CW

Our studies have shown that a CW laser (1.3–3.8 μ m) would require a power of 5–10 MW to achieve good momentum coupling to a debris target at 1500 km range. We will show that only 30kW average power from a repetitively-pulsed $\approx 1\mu$ m laser is sufficient to clear near-Earth space debris in less than 2 years.

4.3 Momentum coupling coefficients are well known

By convention, the momentum coupling coefficient C_m is defined as the ratio of target momentum produced by photoablation to incident laser pulse energy:

$$C_m = \frac{m\Delta v}{W} \quad \text{dyne-s/J.} \quad [1]$$

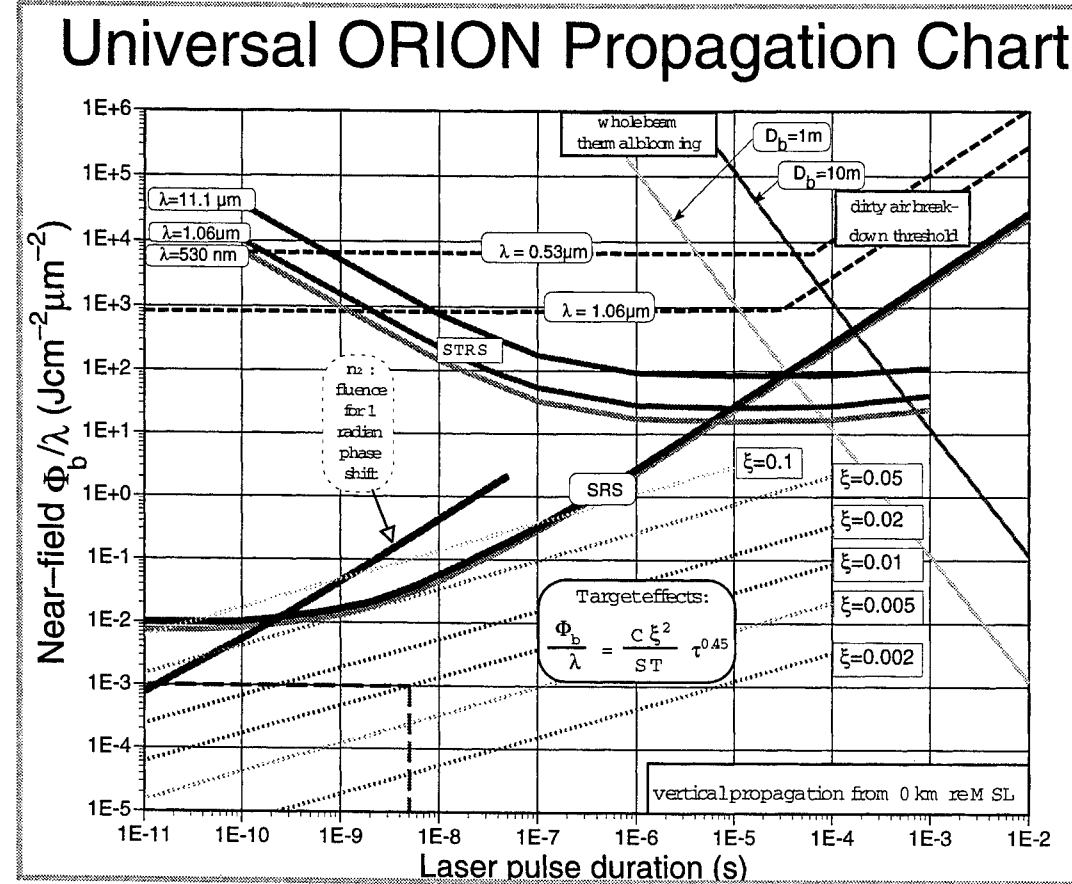
As incident pulsed laser fluence increases past threshold, C_m for a wide variety materials rises rapidly to a peak value in the

range 2–8 dyne-s/J, declining slowly for higher fluence as ejecta velocity increases. We surveyed the results of 46 experiments in which the fluence Φ_{opt} for optimum coupling was measured, and determined that for a wide variety of possible debris surfaces, wavelengths ranging from 0.25 to 10.6 μm , and pulsewidths $100\text{ps} < \tau < 1\text{ms}$, Φ_{opt} can be best fit by:

$$\Phi_{\text{opt}} = C \tau^{\alpha} \quad \text{J/cm}^2 \quad [2]$$

with $\alpha = 0.45$ and $C = 2.3\text{E}4$. Thermal transient theory would, of course, give $\alpha = 0.5$.

4.4 Pulsed laser energy and pulsewidth are determined



'SRS and n_2 in the atmosphere are the limiting factors for beam pulse intensity. On the other hand, achieving optimum thrust at the distant target requires that a minimum fluence be delivered at range. Cost and agility set limits to the mirror diameter which can be used, and, hence, to beam diameter in the atmosphere. Given a wavelength, these effects together determine combinations of pulse energy and duration which satisfy both limits. That solutions exist is shown by Fig. 2. With laser pulse energy and beam diameter W_b and

Figure 2. Graphical Solution to Target Physics and Nonlinear Atmospheric Transmission Limits D_b , range z , wavelength λ , Strehl ratio S and atmospheric transmission T , fluence (J/cm^2) in each pulse Φ delivered to the debris is given by:

$$\Phi = \frac{\pi W_b T S}{4} \left(\frac{D_b}{z \lambda} \right)^2 \quad \text{J/cm}^2 \quad [3]$$

Equating [2] and [3] gives

$$\frac{\Phi_b}{\lambda} = \frac{C \xi^2}{S T} \tau^{\alpha} \quad \text{for the necessary beam fluence at the ground.} \quad [4]$$

In Eq. [4], $\xi = z/\lambda/(\pi D_b^2/4)$. In the Figure, we have plotted lines of constant ξ (with D_b in m, λ in μm and z in Mm for convenience). It is seen that $\xi = 0.05$ pushes the nonlinear limits as hard as one dares in the 100ps–100ns range. This choice then fixes maximum system slant range z , once λ and D_b are picked. Note that the target effects lines move downward in proportion to the 4th power of D_b .

4.4 Number of targets, Δv for de-orbit and time for clearing debris determine laser average power

The present debris database cannot tell us the detailed composition of the 1–20-cm debris cloud. However, we have constructed a hypothetical [except for column A], representative 5-component cloud [Table I], and conclude from it that 30kW average power is sufficient to clear the population below 1500km in 2 yr. Average power is, of course, inversely related to clearing time. A 4–6-m diameter mirror is assumed. The laser might be a derivative of the DoE/Livermore National Lab de-

TABLE I: 30kW Average Power is Sufficient to Clear Hypothetical Debris Population in 2 Years

Target	A	B	C	D	E
Hypothetical Debris Item:⇒	Na/K sphere	Carbon phenolic fragment	MLI (plastic/Al surfaces)	Crumpled Al	Steel tank rib support
System Parameter:					
Inclination (deg)	65	87	99	30	82
Apogee (km)	930	1190	1020	800	1500
Perigee (km)	870	610	725	520	820
A/m (cm ² /gm)	1.75	0.7	25	0.37	0.15
Actual size (cm)	1.0	1x5	0.05x30	1x5	1x10
Bond albedo	0.4	0.02	0.05/0.7	0.05/0.7	0.5
Optimum C _m (dyne-s/J)	6±2	7.5±2	5.5±2	4±1.5	4±1.5
Δv required (m/s)	190	110	140	90	160
Est. number of targets	50k	20k	60k	10k	10k
Laser re-entry effort:					
Shine time/item [30kW](min)	5	6	0.3	13	9
Retargeting time (min)	0.5	0.5	0.5	0.5	0.5
Total time all targets (yr)	0.5	0.3	0.1	0.3	0.2
Down time all targets (yr)	0.2	0.1	0.05	0.1	0.1
Total (yr)	0.7	0.4	0.15	0.4	0.3
[Grand Total (yr)]					[1.95]

sign for 1 of 64 arms of the National Ignition Facility (NIF) laser.

4.5 Acquiring/tracking debris

Probably the most difficult aspect in ORION is acquiring and tracking objects as small as 1cm at ranges up to 1500km. To clear 150k objects in 2 years, it is only necessary to acquire 17 objects /hr. Ho *et al.* [1993] have designed and tested a unique imaging, photon-counting detector which can see 1.3-cm objects with a geometric albedo of 8% at 400km range (or 100% at 1400 km) in solar illumination during dawn and dusk within a 1° field of view. Their detection algorithm is based on identifying linear tracks of single photons in x-y-t space containing, e.g., 16 photons during a 1-s interval. Even if 150k debris objects were uniformly distributed, acquisition rate within a 1° field of view would be 2.9/s. At this

rate, a single detector operating only during the 3 hours of twilight can acquire the entire population in about 5 days. Using a slightly smaller field of view, background can be reduced sufficiently to acquire all targets of interest to ORION with a more-than-adequate data rate. As has been suggested [Phipps *et al.* 1996], a small, short-pulse tracking laser can develop an ephemeris for each object in 3 dimensions sufficiently accurate for the ORION laser to later find and act on the object in the dark (after a few orbits). This final process involves expanding the ORION beam footprint to match the few-m track uncertainty, using its beam as target illuminator, then progressively narrowing the footprint with the aid of a quadrant detector, computed relativistic lead angle, sodium beacon and adaptive optics. A polychromatic guidestar [Foy, *et al.*] may be of assistance.

5. PROBABLE SYSTEM COST

The 1500-km range all-optical system should cost of order \$100–200 M, based on costs of systems already built, as well as operating costs for manpower and consumables over a 2 – 3-yr operating life.

Acknowledgments

The authors gratefully acknowledge Mr. Ivan Bekey and Dr. John Rather, NASA headquarters for making possible portions of our work reported here, and Dr. Jonathan Campbell, NASA/MSFC. We also had useful discussions with Drs. Herbert Friedman, John Murray, David Eimerl, Lloyd Hackel, and Brent Dane, Lawrence Livermore National Lab (LLNL), Dr. Cheng Ho, Los Alamos National Lab, Dr. Joseph Loftus, NASA/JSC, and Dr. Robert Fugate, USAF Starfire Optical Range.

References

- FOY, R., *et al.*, 1995 *Astron. Astrophys. Suppl.* **111**, 569
HO, C., PRIEDHORSKY, W. & BARON, M 1993 in "Space Debris Detection and Mitigation", *Proc. SPIE* **1951** pp. 67 *et seq*
KESSLER, D. *et al.*, 1995a, paper IAA6.3-93-744, *Proc. 44th Cong. Int'l Astronautical Federation (Graz, Oct. 16-22, 1993)*
KESSLER, D. *et al.*, 1995b, paper AIAA 95-0662, *Proc. 33rd Aerospace Sciences Meeting, 1/9-12/95, Reno, NV*
LOFTUS J. AND REYNOLDS, R., 1993 *SPIE* **1951** pp. 147-8
METZGER, J. D., *et al.*, 1989 *J. Propulsion & Power* **5** pp. 582-90
MONROE, D. K., 1994 "Space debris removal using a high-power...", in *Laser Power Beaming, SPIE* **2121**, pp. 276-83
PHIPPS, C. R. *et al.*, 1996 *Laser and Particle Beams* **14**, 1-44; PHIPPS, C. R., 1993 *AIP Conf. Proceedings* **318** pp. 466-8
STANSBERRY, E. G. 1996, *et al.*, NASA report JSC-27436, "Haystack Radar Measurements of Orbital Debris Environment."
STEWART, J., private communication
U.S. OFFICE OF SCIENCE & TECHNOLOGY POLICY 1995, *Interagency Report on Orbital Debris*

High-Gain Double-Pass Pulsed Dye Amplifiers For Laser Guide Stars

D. Kapitan, H. Booth, G.J. Murray, G.P. Hogan and C.E. Webb

Department of Atomic & Laser Physics, Oxford University
Clarendon Laboratory, Parks Road, Oxford OX1 3PU, United Kingdom
Telephone: +44 - (0)1865 - 272216 • *Fax:* +44 - (0)1865 - 272400 • *E-mail:* g.hogan@physics.ox.ac.uk

ABSTRACT

The design issues for a scaleable sodium laser guide star are discussed, involving cw frequency lock of a dye laser using polarisation spectroscopy, pulse multiplexing techniques and high power pulsed dye amplifiers. A numerical model and results from preliminary measurements on a double-pass dye amplifier are presented. The possible integration of an unsaturated, high gain pre-amplifier, and a saturated, low gain power amplifier into a single dye amplifier cell are investigated for pulsed amplification of a cw master oscillator.

Keywords: sodium laser guide stars, adaptive optics, frequency lock, polarisation spectroscopy, phase modulation, copper vapour lasers, pulsed dye amplifiers

1. SODIUM LASER GUIDE STAR SYSTEM DESIGN

1.1 Introduction

Laser guide stars (LGS) are required to obtain greater sky coverage for astronomical telescopes incorporating adaptive optics. Resonant scattering of a high power pulsed laser from atomic sodium in the mesosphere is the most promising technique for the production of a LGS. However, due to saturation of the sodium, the efficient generation of a bright LGS using pulsed excitation is difficult. We are devising a modular system where the brightness of the LGS can be increased linearly by adding more laser units¹. The main elements of the intrinsically scaleable sodium LGS system are as follows:

- Frequency locked cw dye master oscillator (DMO)
- Pulse multiplexing mechanism
- Pulsed dye amplifiers (PDA)

1.2 Frequency locked cw dye master oscillator

The DMO provides a low power cw seed beam to be sequentially injected into an array of pulsed dye amplifier sub-units. With polarisation spectroscopy² the DMO can be locked to a hyperfine peak of the sodium D₂ transition, as is schematically depicted in Fig. 1. A linearly polarised pump beam is propagated through an atomic sodium vapour cell, creating significant changes in the population densities of the hyperfine upper levels of the sodium D₂ transition by optical pumping. Due to the induced birefringence, a counter-propagating circularly polarised probe beam experiences a dispersion which is different for the polarisation components parallel and perpendicular to the pump beam. The transmitted probe beam is split into two polarisation components at $\pm 45^\circ$ to the pump polarisation, the intensity difference between which is used to generate the error signal for the frequency stabilisation.

The spectral bandwidth of the DMO output, which has a linewidth of 1 MHz, must be spectrally broadened in order to reduce saturation and to obtain efficient excitation of the sodium layer. The optimum laser linewidth for efficient photon return from the sodium layer has been shown to be approximately 600 MHz³. It is possible to broaden the effective linewidth of the cw DMO beam by electro-optic phase modulation (EOPM). If the frequency of the laser is modulated on a time scale much shorter than the lifetime of the sodium D₂ transition (16.1 ns), the laser will appear to the atomic sodium to have a broadened linewidth. Initially, a standing wave EOPM which is commercially available will be used to broaden the cw DMO beam. A travelling wave EOPM will enable more control over the spectral profile of the DMO output and is currently under development.

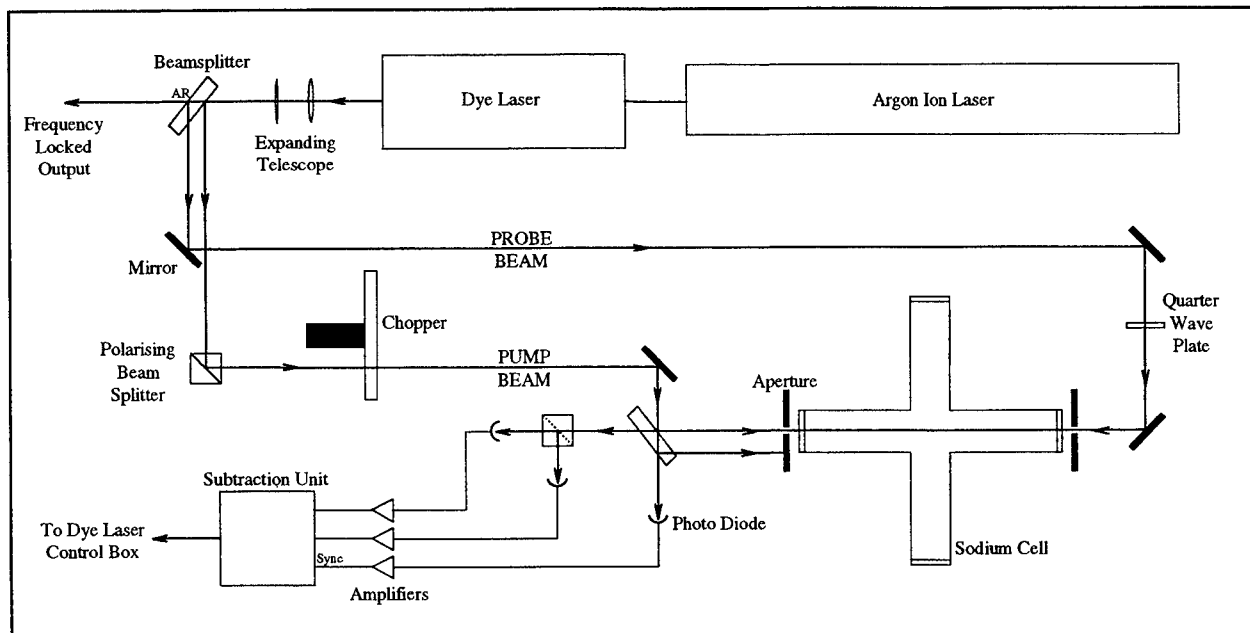


Figure 1: Experimental set-up for atomic sodium frequency lock

1.3 Pulse multiplexing mechanism

A pulse multiplexing mechanism is used to seed each of the pulsed dye amplifier sub-units in turn with the DMO beam, and to recombine the amplified output beams. This approach gives rise to the pulse train format shown in Fig. 2. Power scalability is achieved by adding dye amplifier sub-units to increase the *average* output power without increasing *peak* power. This means the photon return from the LGS will scale linearly with the number of dye amplifier sub-units in the system as the level of saturation of the sodium remains constant. To create such a multiplexed macro pulse, different time-multiplexing arrangements will be investigated using either spinning mirrors, or Pockels-cells in conjunction with $\lambda/4$ -plates and polarising beamsplitters¹.

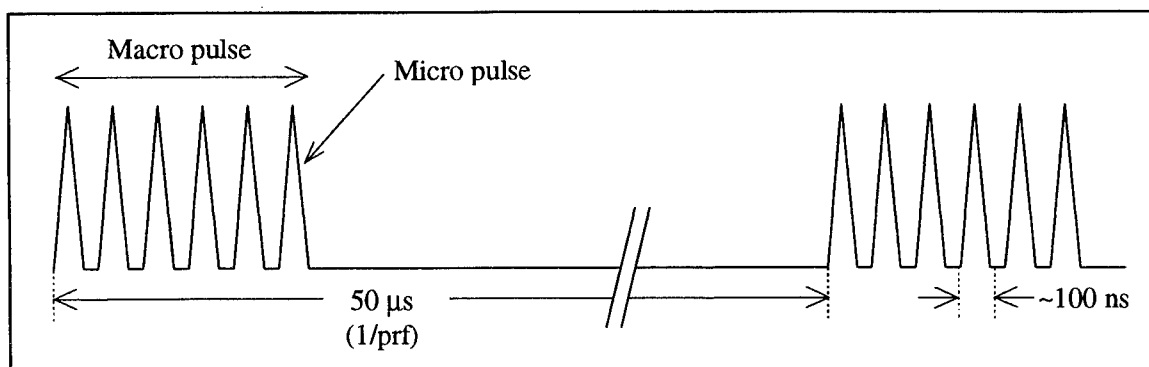


Figure 2: Pulse format of sequentially multiplexed output

1.4 Pulsed dye amplifier

The choice of a cw DMO has the advantage that it facilitates time-multiplexing and only requires frequency stabilisation of one laser unit. The corollary of this is that the available peak power to seed the PDAs is decreased by three orders of magnitude compared with conventional pulsed dye master oscillators, thus requiring the use of high-gain PDAs. At the same time, high optical conversion efficiencies are needed to minimise the pump power required. To match both these requirements we set out to investigate the possibility of using a double-pass dye amplifier arrangement.

2. DOUBLE-PASS DYE AMPLIFIERS

2.1 Introduction

To achieve high amplification and efficient power conversion, multi-stage amplification systems are usually used which consist of high-gain pre-amplifiers and efficient, saturated power amplifiers. Due to technological constraints, however, the number of amplifier cells for the sodium LGS system needs to be kept to a minimum. We have investigated the use of a double-pass geometry where a single side-pumped dye amplifier cell operates as both pre- and power amplifier. In this approach (see Fig. 3), the degree of amplifier saturation varies along its length providing a region of high gain (low efficiency) at the mirror end, while the gain medium near the input/output end operates in the saturated (high efficiency) regime. Double-pass dye amplifier stages have been successfully employed as high-gain pre-amplifiers⁴, resulting in enhanced conversion efficiency compared to a single-pass arrangement.

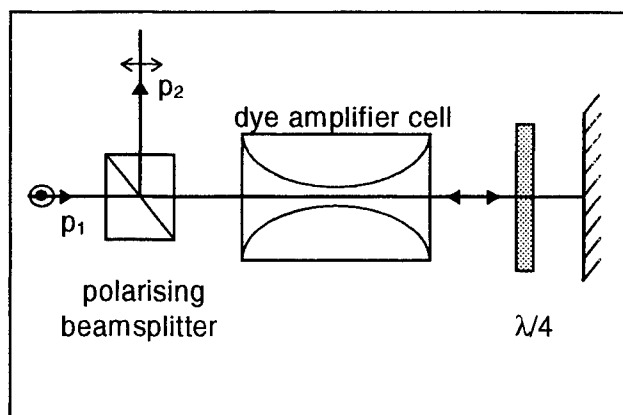


Figure 3: Double pass dye amplifier set-up

2.2 Numerical modelling

To give reasonable estimates for typical operating parameters, a one-dimensional numerical simulation was performed, using a rate-equation model for the amplifier medium. The effect of excited state absorption, which is known to limit the performance of high-power dye amplifiers⁵, is accounted for. The build up of amplified spontaneous emission (ASE) in the medium is modelled using source terms resulting from spontaneous emission originating at the end-faces of the amplifier medium, following investigations by Ganiel *et al.*⁶. The optical field is taken to consist of five components: two counter propagating oscillator signals, two single-pass ASE fluxes from either end of the gain medium, and one double-pass ASE signal which originates from feedback of one single-pass ASE component at the rear mirror.

Results from the numerical modelling show that due to the low seed signal from the cw DMO, the laser gain medium will be saturated by ASE, especially by the double-pass ASE signal. Spatial and spectral filtering at the rear mirror are required, to suppress ASE and prevent loss of power.

From the numerical simulations it can be concluded that, in order to saturate the amplifier on the second transit in a double-pass arrangement, the incoming oscillator intensity needs to be at least $\sim 10^{-2}$ times the saturation intensity of the medium. Presently, with around 0.1 W of cw DMO input, the incoming signal intensity is $\sim 10^{-4}$ times the saturation intensity.

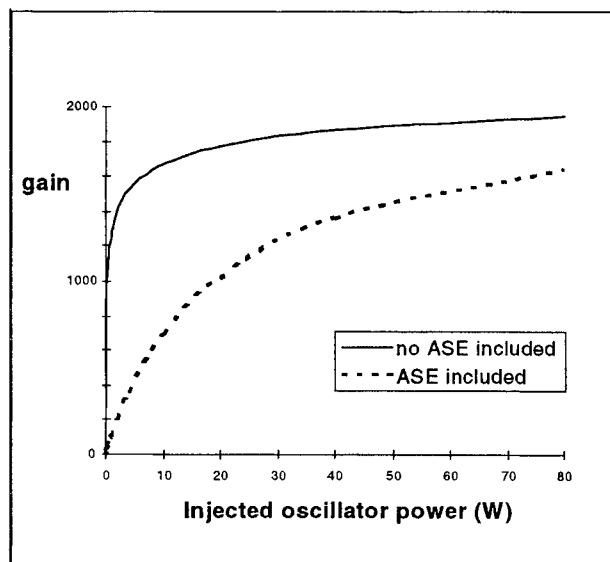


Figure 4: The calculated effect of amplified spontaneous emission on amplifier performance

2.3 Preliminary experiments

In preliminary experiments, the DMO was approximately tuned to the sodium wavelength with a birefringent filter to give 175 mW cw output with a linewidth of ~ 1 nm. The gain medium containing 0.7 mM of Rhodamine B dissolved in ethanol, was transversely pumped with 10 W of green pump light from a single copper vapour laser. The DMO was focused to match the diameter of the gain volume (0.5 mm), the length of which was 5 mm. The measured gain was $5 \cdot 10^4$, corresponding to a conversion efficiency of 2.3%. The ASE component present in the amplified signal was found to have been reduced by $\sim 20\%$ compared with the output from the unseeded PDA.

2.4 Discussion

From the calculated and measured double-pass amplifier gains, it can be concluded that in the present arrangement the PDA is operating in the non-saturated regime. Although the oscillator signal is starting to be sufficiently high to compete with the ASE signal, saturation is not attained even on the second transit through the gain medium. By optimising the pumping geometry it is expected that stage gains of $\sim 10^5$ can be achieved with efficiencies of 5-10%. However, this is not sufficient for production of a sodium LGS, and pre-amplification will still be required to boost the signal by two orders of magnitude. Future experiments will investigate various pre-amplifier arrangements for further development of the scaleable sodium LGS system.

3. REFERENCES

1. G.P. Hogan and C.E. Webb, "Proposed design for a scalable dye laser for use in sodium laser guide star generation," Proceedings OSA/ESO Conference on Adaptive Optics, 2-5 October 1995 Garching, Germany.
2. J.W. Thomsen, N.C.R. Holme, U. Müller and J.O.P. Pedersen, "Modulation-free frequency stabilisation of a dye laser by polarization spectroscopy," *Meas. Sci. Technol.* **6**, pp. 170-173, 1995.
3. B.M. Welsh and C.S. Gardner, "Nonlinear resonant absorption effects on the design of resonance fluorescence lidars and laser guide stars", *App. Opt.* **28**(19), 19, 1989.
4. S. Lavi, G. Bialolanker, M. Amit, D. Belker, G. Erez and E. Miron, "Characterization of a pulse amplifier for cw dye lasers," *Optics Commun.* **60**(5), pp. 309-313, 1986.
5. K. Dasgupta, S. Kundu and L.G. Nair, "Extraction efficiency of saturated-gain high-power dye amplifiers: effect of nonlinear signal absorption", *Appl. Opt.* **34**(12), pp. 1982-1988, 1995.
6. U. Ganiel, A. Hardy, G. Neumann and D. Treves, "Amplified spontaneous emission and signal amplification in dye-laser systems", *IEEE J. Quant. Elec.* **11**(11), pp. 881-892, 1983.

YAG Laser System with Combined Beams from Three Oscillators and Its Application to Materials Processing

Hiroshi Miura, Shigeki Fujinaga, Toru Narikiyo, Akira Ohmori, Keiji Okino * and Syuichi Watanabe *

Research and Development Dept., The Advanced Materials Processing Institute Kinki Japan,
Amagasaki Hyogo, Japan

* NEC Corporation Laser Equipment and Mechatronics Div., Shimokuzawa Sagamihara
Kanagawa, Japan

ABSTRACT

We constructed a system in which a newly developed pulse excited YAG laser oscillator of 1.5kW average power and an integration optics were incorporated, together with two CW YAG laser oscillators of 2kW average power, a 6-axes articulated robot and a PC. The integration optics summed up three laser beams transmitted through optical fibers and condensed to a focused spot at the focusing point. We could obtain the following results using the system. (1) The focused spot diameter for good welding quality with the integration optics could be available without changing the distance between the specimen and the optics. (2) The delay time between the pulse excited YAG laser beam and the rectangularly modulated CW YAG laser beams should not exceed the time of keyhole formation with the CW laser beams to obtain the maximum penetration depth. (3) The deepest penetration depth and the largest volume of welding could be obtained by the overhead position welding compared with the flat, horizontal and vertical position welding.

1. INTRODUCTION

Heavy industries are demanding the YAG laser with higher brightness to apply the laser materials processing to their works which are thicker than the ones of electric or automotive industries. A YAG laser output power can be scaled up by increasing YAG rod volume and a input power of an exciting lamp. The thermal lens effect of a YAG rod, however, prevents from increasing the output power with a small beam divergence angle ¹. Several new lasers, for example, slab laser ², laser-diode pumped YAG laser ³ and tube laser ⁴ have been studied to overcome the disadvantage. Another method to increase a laser power is to sum up the laser beams from laser oscillators at a position on an optical path between the laser output mirrors and the work, although the methods increase a beam parameter product and processing characteristics with the method is inferior to the one with the same output power from a single oscillator ⁵. There are many methods using an optical fiber owing to the high flexibility of it. We have been studying the summing-up methods and the processing characteristics with them ^{6, 7, 8}. We would report here about a newly developed YAG laser processing system and its application to welding. The purposes of the study are to reveal the superimposed relation for the optimum welding quality between CW YAG laser beams and a pulse excited one and to obtain the fundamental information for all position welding. For this purpose, we constructed a system in which a newly developed pulse excited YAG laser oscillator of 1.5kW average power and integration optics were incorporated, together with two CW YAG laser oscillators of 2kW average power, a 6 axes articulated robot and a PC. The integration optics summed up three beams from laser oscillators which have been transmitted through optical fibers respectively, and condensed the beams into a spot diameter larger than the core diameter of optical fibers. The similar system was reported ⁹ in which, however, three beams from the same kind of oscillator were summed up and condensed spot diameter could not be variable. The details of the developed system and some welding results using the system would be reported in the paper.

2. DEVELOPMENT OF THE SYSTEM

One of two elements to be developed in the system is the pulse excited YAG laser oscillator with 1.5k W average power. The maximum average power of the rod type pulse excited YAG laser products has been 1kW ⁹ until now. The another element to be developed is the integration optics with variable condensed spot diameter. Using the optics we can

vary the focused spot diameter and have the optimum condition for many kinds of laser materials processing. We would describe the details of the developed system in the chapter.

2.1 YAG laser oscillators in the system

The newly developed pulse excited YAG laser oscillator consists of an oscillator and following two amplifiers. The sizes of the rods are $8 \phi \times 200\text{mm}$ in the oscillator and $10 \phi \times 200\text{mm}$ in the amplifiers. The rods were set at the common focal axes of the double elliptic cylinders and excited by the two Xenon flash lamps of the maximum input power of 10kW at the other focal axes. The rods of the oscillators and the two amplifiers were excited by the same input power and were set at the equal spaces in order to obtain the same focal length with the thermal lens effect and hence the stable oscillation. The maximum repetition rate and pulse width is 200pps and 20ms respectively. Figure 1 shows the dependence of an average laser output power transmitted through the optical fiber with core diameter of 1mm, 10m length and the step index refractive profile on an input electric power. The repetition rate and the pulse width are 10pps and 10ms respectively. Four $8 \phi \times 200\text{mm}$ rods were used in a CW YAG laser resonator, set in the equal spaces and excited by the same input power per rod for the same reason in the pulse excited laser. The CW laser oscillator have a sinusoidal or rectangular quasi-CW mode of the maximum frequency of 200Hz by modulating the current of the exciting Krypton arc lamp. In the rectangular quasi-CW mode the peak power can be enhanced twice as high as the average power at the duty ratio smaller than 50 % .

2.2 Optical fibers and integration optics

The beams from the three oscillators were transmitted through the optical fibers, collimated respectively, condensed by a large aperture lens enough to cover the three collimated beams and summed up to the maximum average power of 5.5 kW at the focal point of the lens. The schematic diagram of the integration optics is shown in Figure 2. The collimator lenses were movable and their position could be set at the appropriate position from outside the lens holder so that a suitable spot diameter and hence a suitable power density for any materials processing could be obtained without changing the work distance between the surface of the specimen and the lowest edge of the integration optics. The integration optics can image the cores of the optical fibers with the ratio of 1:1 at the focal point of 100mm and then achieve the spot diameter of 1mm with 5.5kW average power of YAG laser beams. Figure 3 shows the shapes of the focused beams for six positions of collimator lenses at the focal point using a Laserscope UFF100. It was found from the results that any spot diameter of laser beams larger than the core diameter of the optical fiber are obtainable. Figure 4 shows the shapes of the focused beams for three caustic positions in the region of the focal point at the position (d) of the collimator lenses in the Figure 3. The focused spot is splitted into each beam of laser oscillator.

3. EXPERIMENTAL RESULTS OF LASER WELDING

We conducted the bead-on-plate welding of SUS 304 using the newly developed system for evaluating the system, revealing the superimposed relation between CW YAG laser beams and the pulse excited one for the optimum welding quality and obtaining the fundamental characteristics for all position welding. All position welding is the big application for the developed system with an optical fiber beam delivery. The integration optics was held and moved by the articulated robot irradiating the focused laser beams on the specimen. Figure 5 shows the dependence of welding characteristics on the position of collimator lenses. We would report the delay effect of different kinds of oscillations on welding characteristics and all position welding using the developed system. Figure 6 shows an example of all position welding.

4. CONCLUSIONS

We could sum up the results through the study as follows.

- (1) The appropriate focused spot diameter for good welding quality with the integration optics of three beams is available without changing the distance between the specimen and the optics.

- (2) The delay time between the pulse excited YAG laser beam and the rectangularly modulated CW YAG laser beams should not exceed the keyhole formation time not to crush the keyhole and to obtain the maximum penetration depth.
- (3) The deepest penetration depth and the largest volume of welding are obtained by the overhead position welding compared with the flat, horizontal and vertical position welding because of the removal of the molten metal at the bottom of the keyhole with the gravitational force.

5. ACKNOWLEDGEMENTS

We are grateful to Dr. Y.Arata, general manager of the institute and Prof. Dr. A. Matsunawa of Joining and Welding Research Institute for their encouragement about the study.

6. REFERENCES

1. W.Koechner, Solid State Laser Engineering, 4th Edition, p.394, Springer-Verlag, Berlin, 1996.
2. W.S.Martin and J.P.Chernoch, " Multiple internal reflection face-pumped laser " U.S.Patent No.3,633,126, (1972)
3. A.Giesen,H.Hügel,A.Voss,K.Wittig,U.Brauch and H.Opower, " Scalable concept for diode-pumped high-power solid-state lasers " Appl. Phys. Vol. B5, pp.365-372, 1994.
4. U.Wittrock and H.Weber, " Inside-pumped Nd:YAG tube laser " Optics Letters, 16, pp.1092-1094, 1991.
5. F.Dausinger,F.Faisst,C.Glumann,R.Hack und R.Ifflaender, " Effiziente Strahladdition zum Laserschweissen " Laser und Optoelektronik, 27(4), pp.45-50, 1995.
6. H.Miura,S.Fujinaga and T.Narikiyo, " Consideration on summing-up methods of YAG laser beams into optical fiber for materials processing " Proceedings of ICPE '95, pp.155-158, Singapore, 1995.
7. T.Narikiyo,S.Fujinaga,H.Miura,A.Ohmori and Y.Arata, " YAG laser welding with combination system of three oscillators " Proceedings of ICALEO '95, pp.885-894, Laser Institute of America, San Diego, 1995.
8. S.Fujinaga,H.Miura,T.Narikiyo,S.Katayama and A.Ohmori, " Development of integration system of high power three Nd:YAG lasers for materials processing " to be published in the Proceedings of ICLAT '96.
9. I.Norris,C.Peters and P.Wileman, " Welding with a 3kW Nd:YAG laser " Proceedings of ICALEO '92 pp.53-62, SPIE, Florida, 1992.

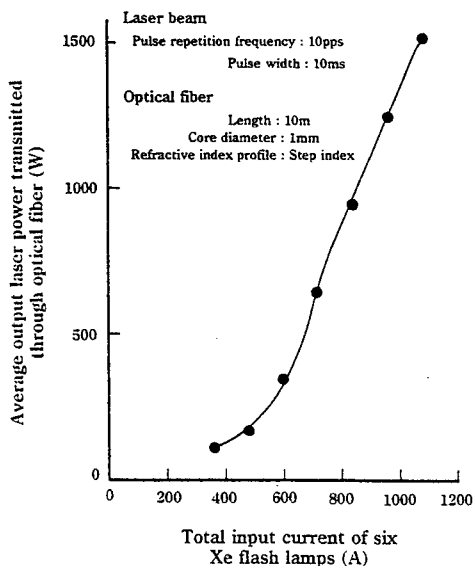


Fig. 1 Output versus input energy for the newly developed pulse excited YAG laser oscillator

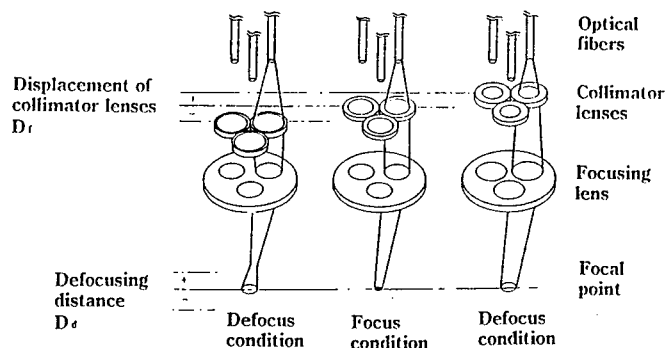


Fig. 2 Schematic diagram of integration optics

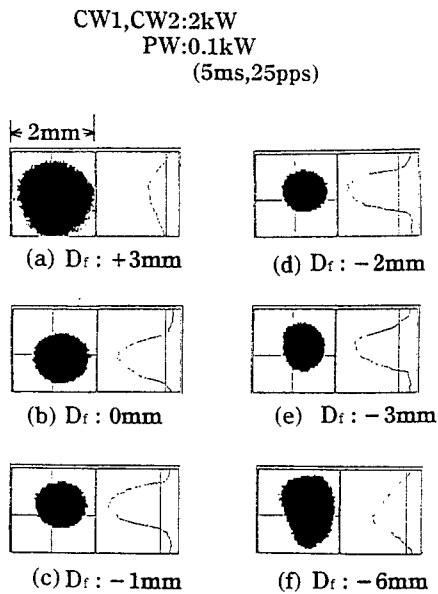


Fig. 3 Focused laser beam shapes by the integration optics for six displacement positions D_f of collimator lenses

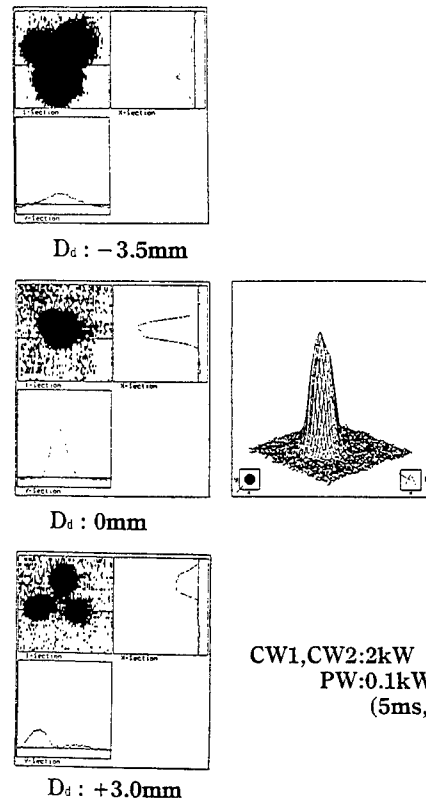


Fig. 4 Focused laser beam shapes by the integration optics for three caustic positions D_d in the region of the focal point

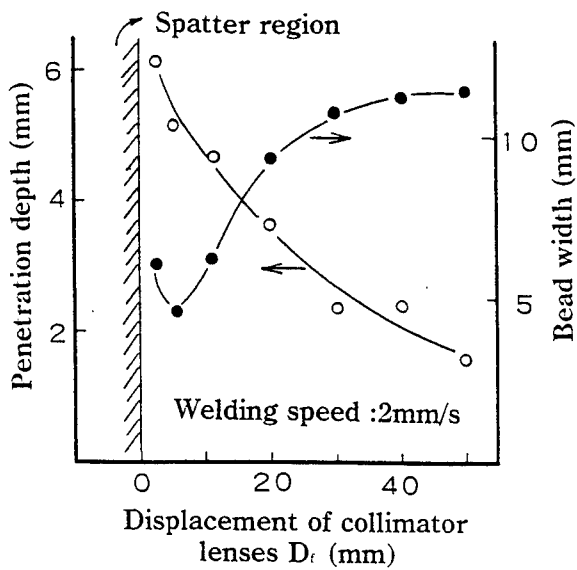


Fig. 5 Dependence of penetration depth and bead width on the displacement of collimator lenses

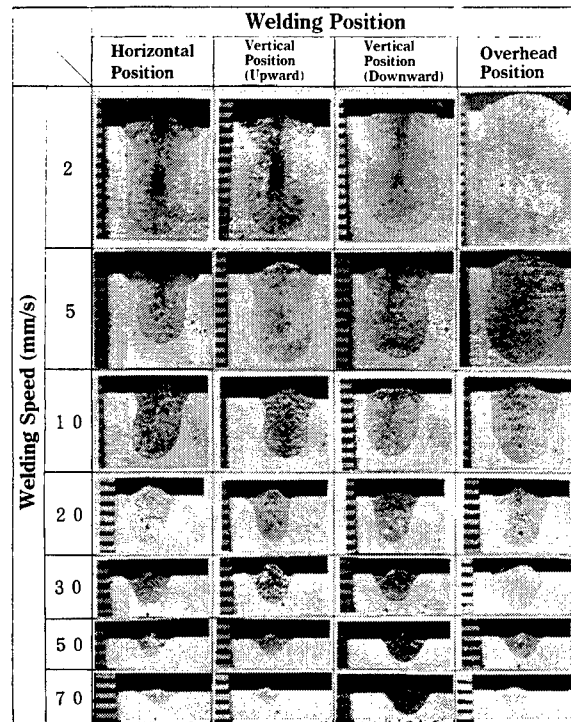


Fig. 6 Cross-sectional photographs of horizontal, vertical and overhead position welding

Rust and paint stripping from power transmission towers with a pulsed Nd:YAG laser

Shuichi Ashidate

Power Electronics Department, Power Engineering R&D Center, Tokyo Electric Power Company
4-1 Egasaki-cho, Tsurumi-ku, Yokohama 230 JAPAN

Minoru Obara

Department of Electronics and Electrical Engineering, Faculty of Science and Technology, Keio University,
3-14-1 Hiyoshi, Kohoku-ku, Yokohama 223 JAPAN

ABSTRACT

The possibility of the rust and paint removal from the power transmission towers was investigated with the pulsed Nd:YAG laser for the first time. The red rust and paint were successfully removed without damaging underlying Zn(zinc) galvanized steel substrates. The optimum irradiated laser fluence for the red rust was found from $0.3\text{J}/\text{cm}^2$ to $0.4\text{J}/\text{cm}^2$ for 9ns short pulses, from $1.0\text{J}/\text{cm}^2$ to $4.4\text{J}/\text{cm}^2$ for 200ns long pulses, respectively. For the paint stripping the optimum ranged from $3.3\text{J}/\text{cm}^2$ to $4.4\text{J}/\text{cm}^2$ with the pulse width of 200ns.

Key words: rust stripping, paint stripping, Nd:YAG laser, pulsed laser

1. INTRODUCTION

The towers for the power transmission lines are constructed of Zn galvanized steel frames against corrosion. Some of them are coated with red and white striped colors for the safety of the flights of the air planes. The Zn galvanized and painted frames have gradually eroded by aging. The repainting cycle depends on the constructed place of towers such as a mountain or an industrial area, for instance. The perfect removal of rust and unwanted paint is expected to prolong the cycle of the repainting and then reduces the cost of maintenance dramatically. The existing stripping process which is usually made by hands with brushes, grinders and the like, takes much time to remove and cannot strip completely as the towers have complicated structures. The easy, efficient, and automated surface cleaning system is eagerly required in the electric power companies. As the laser stripping process is expected to be one of the promising process, we have investigated the rust and paint removal from the power transmission towers by lasers.

2. EXPERIMENT

In more recent years lasers have been used to remove the coating from the airplanes¹, to clean eyesores from graffiti.² Most works have been made with excimer lasers, or with the pulsed CO₂ laser which is one of the most efficient and cost effective lasers. They are not suitable for energy delivery by optical fibers. As the stripping process for the towers are made in the open air, the flexibility of the laser beam delivery is required. The Nd:YAG laser which could deliver the high laser energy with high efficiency, was used in the experiment. The laser pulse width was 9ns and 200ns in FWHM. The pulse repetition frequency was 50Hz. The laser was set at a constant energy per pulse. The average peak power was determined from the irradiated laser energy divided by the beam area and pulse width. The test pieces used were Zn galvanized steel(SS400) plates without any strain, with red rust, with polyurethane coating, and with epoxy coating. The completeness of the coating removal was measured by the roughness analyzer (Tencor Instruments: α lpha-step200).

2.1. Measurement of reflectivity

In the laser stripping process it is required that the irradiated laser energy is sufficiently and selectively absorbed by the coating material. We measured the reflectivity of the used Zn substrate, rust, and paint with the spectrophotometer (JASCO:V-570). Figure 1 shows the relative reflectivity as a function of the wavelength. The reflectivity of the coatings was about 6~9% smaller than that of the substrate. The laser energy may be sufficiently absorbed in the rust and paint. These results roughly show that the laser is able to remove the unwanted rust and paint selectively.

2.2. Removal of red rust

One of the most important factors for the stripping process is not to damage the underlying substrates in addition to the complete removal of the coating material. We investigated a maximum irradiated laser energy for stripping by varying the laser fluence to the Zn substrate. The upper limit of the laser fluence was found at $0.4\text{J}/\text{cm}^2$ in a 9ns pulse width and $4.4\text{J}/\text{cm}^2$ in 200ns. The colored beam patterns were visually observed on the Zn substrate when the laser energies beyond the threshold were applied. The detailed analysis of the damaged surface was studied by X-ray photoelectron spectroscopy (XPS). XPS has been used to analyze the chemical bonding of the elements in the surface. The XPS analysis was performed with the electron analyzer (Nippondenshi:JPS-90SX). The applied voltage was 10kV. Figure 2 shows the obtained spectra around the O 1s spectra. When the laser pulses were irradiated on the Zn substrate, both the peak energy and the shoulder of the spectra at higher energy decreased. The different chemical bonding of the elements shifted. Two peaks were reported.³ The observed spectra were the combination of two different bonding. The lower energy peak located at 530eV corresponds to bulk oxygen in ZnO while the higher energy peak located at 532eV is related with the surface chemisorbed oxygen. As the total peak energy is shifted to the lower energy after the high energy laser irradiation, the increase of the oxidation would be shown.

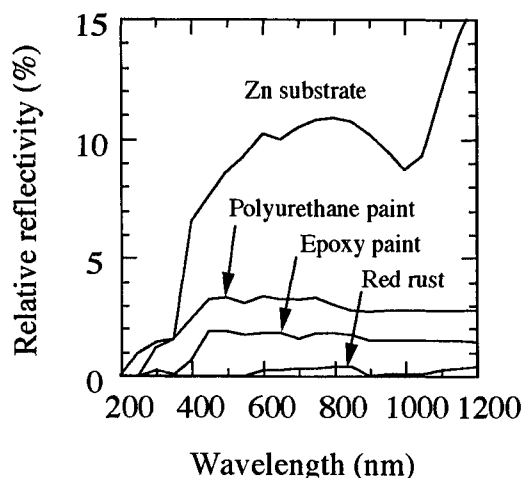


Fig.1. Measured relative reflectivity of the Zn substrate, red rust, and paint.

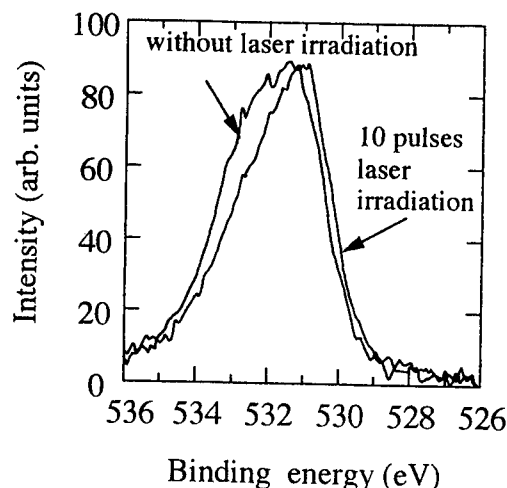


Fig.2. Measured binding energy spectra of the damaged Zn substrate.

Figure 3 shows the optimum range of the laser energy for the red rust stripping. The optimum removal was defined as the case in which there were no beam patterns or rust visible on the substrate. The average thickness of the rust was about $4\text{ }\mu\text{m}$. The threshold of ablation was found at $0.3\text{J}/\text{cm}^2$ in a 9ns laser pulse and $1.0\text{J}/\text{cm}^2$ in 200ns . From the results previously achieved at the Zn galvanized steel substrate, the optimum laser fluence ranges between $0.3\text{J}/\text{cm}^2$ and $0.4\text{J}/\text{cm}^2$ at 9ns . For the long pulse operation, the optimum laser fluence ranged from $1.0\text{J}/\text{cm}^2$ to $4.4\text{J}/\text{cm}^2$. The obtained roughness of the surface was $0.89\text{ }\mu\text{m}$ at $0.35\text{J}/\text{cm}^2$ with 9ns and $1.2\text{ }\mu\text{m}$ at $3.3\text{J}/\text{cm}^2$ with 200ns . As the typical removal process by brushes gives the roughness of $2\text{ }\mu\text{m}$ at the best, these results show that the Nd:YAG laser stripping can effectively remove the red rust without damaging the underlying substrate.

2.3. Removal of paint

The relatively higher towers for the high voltage transmission lines are painted with red and white striped colors by air regulations. The coating usually consists of two layers. The epoxy paint is coated on the substrate and secondly white or red polyurethane coating is covered on it. The depainting of each white colored paint was evaluated respectively. The thickness was about $100\text{ }\mu\text{m}$ and the white colored paint was used. The dependence of the energy density is shown in Figure 4. As far as the energy density was concerned, the same results were obtained in each paint. Regardless of pulse width, the single shot irradiation was hard to remove it. The accumulation of the pulse energy was necessary to completely remove the painting. The short laser pulse was able to depaint the coating at about $1.7\text{J}/\text{cm}^2$ per pulse. As the fluence was beyond the threshold for damaging the Zn substrate, the short laser pulse was not suitable for the paint stripping. As for the 200ns long pulses, it was found that the threshold pulse energy density for the paint stripping should be higher than $3.3\text{J}/\text{cm}^2$. As the substrate was damaged at in excess of $4.4\text{J}/\text{cm}^2$, the paint stripping was found optimal between $3.3\text{J}/\text{cm}^2$ and $4.4\text{J}/\text{cm}^2$. These results confirm that the long pulsed Nd:YAG laser with 200ns can remove the paint for red and white striped colored towers.

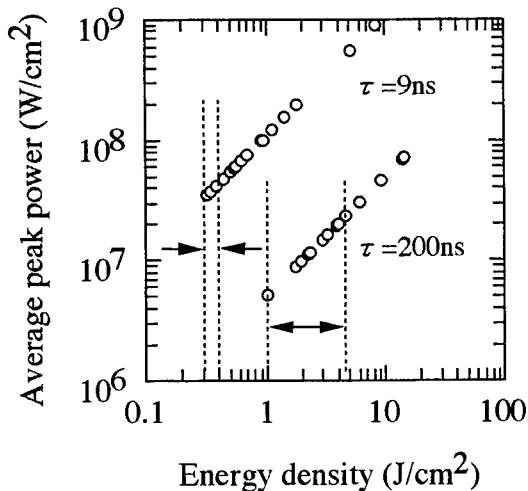


Fig.3. Optimum energy density for the red rust stripping. The laser pulse width is 9ns and 200ns in FWHM.

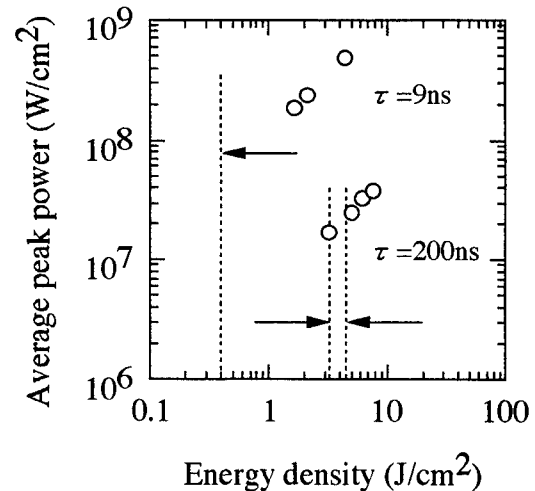


Fig.4. Optimum energy density for the paint stripping. The laser pulse width is 9ns and 200ns in FWHM.

3. CONCLUSION

The possibility of the rust and paint stripping for the transmission towers was investigated. The rust and paint stripping by the pulsed Nd:YAG laser has the potential to replace the conventional method.

4. REFERENCES

1. J.A. Woodroffe, "Laser removal of poor thermally-conductive materials," U.S. Patent, 4,756,765 (July 1988).
2. E. Hontzopoulos, C. Fotakis, and M. Doulgeridis, "Excimer laser in art restoration," Proceedings of SPIE vol. 1810, pp. 748-751, September 1992.
3. J. Rodriguez and J. Hrbek, "Decomposition of NO_2 on metal surfaces: Oxidation of Ag, Zn, and Cu films," J. Vac. Sci. Technol. A 12(4), 2140-2144 (1994).

ABSTRACT

In addition to the well established processes of laser hardening of steel and laser remelting of cast iron, the laser surface modification of light metals finds more and more interest in the research community. While a lot of work concentrates on aluminium and titanium, only a few investigations on the laser treatment of magnesium are published¹⁻¹⁷. In this work the laser surface alloying of magnesium base alloys with aluminium, copper, nickel, silicon and combinations of these elements was carried out. In all cases the laser alloying process led to an increase of hardness caused by the formation of intermetallic compounds. This resulted in improved wear resistance and in some cases additionally in improved corrosion resistance.

Keywords: laser surface alloying, magnesium alloys, wear resistance, corrosion resistance

1. INTRODUCTION

Except laser welding and cutting, today the industrial application of high power lasers in material treatments is only wide spread in the field of laser surface hardening of steel and laser surface remelting of cast iron. In laser treatment of light metals the laser nitriding of titanium and the surface remelting of cast Al-Si-alloys have found some industrial applications.

In the last years magnesium alloys became very interesting for structural applications in the field of automotive and aerospace industries because of their low specific densities of 1.75 - 1.85 g/cm³. But the poor wear and corrosion resistance are one of the greatest restrictions for further applications. This work investigates the possibilities of laser surface alloying of magnesium base alloys to increase the wear resistance without having a negative effect on the corrosion resistance.

With laser remelting a very fine and homogenous structure occurs in the laser tracks due to the rapid solidification. A medium increase of hardness (max. 50 %) and a slightly better corrosion resistance can be achieved, but a further improvement can only be achieved by alloying. For this investigations commercial pure magnesium (99.9 %) and several magnesium base alloys were used as substrates. These alloys were laser alloyed in a one step process with aluminium, known to improve the corrosion resistance and to cause solid solution hardening, as well as with copper, nickel and silicon which are forming hard and stable intermetallic compounds with magnesium. Additionally mixtures of these alloying elements were used to combine the alloying effects.

2. MATERIALS AND LASER PROCESSING

2.1 Substrate materials and alloying elements

Table 2.1 lists the compositions of the magnesium base alloys used as substrate material in the form of sheets with a thickness of 10 mm. For general investigations on the wear and corrosion behaviour cp Mg was used as substrate. Alloying elements were aluminium, copper, nickel and silicon in the form of powders with a particle size < 45 µm. The general feasibility of laser surface alloying with pure alloying elements to magnesium base alloys has been shown elsewhere¹⁴⁻¹⁷. This work is focused on of the alloying of pure magnesium with combinations of two alloying elements. The former results showed a strong increase of wear resistance by laser alloying of magnesium with copper and nickel, whereas the corrosion resistance was only increased by aluminium or high nickel contents. This led to investigations on alloying with combinations of aluminium with copper (50 at.% each) and aluminium with nickel (75 at.% Al and 25 at.% Ni).

Alloy	Condition	HV _{0.1}	Al	Zn	Mn	Y	Zr	RE	Mg
cp Mg	as cast	30							99.9
Al 80	extruded	50	0.8						rem.
AZ 61	extruded	60	6.0	1.0	0.3				rem.
WE 54	cast, T6	95				5.1	0.5	2.9	rem.

Table 2.1: Condition and chemical composition (wt%) of the substrate alloys

2.2 Laser processing

The laser treatment in this work was carried out with a Heraeus 5 kW CO₂-laser with a rectangular beam shape in combination with a Perkin-Elmer Metco powder feed unit. Depending on the melting point of the alloying elements a defocused beam within a power range from 2.5 to 3.5 kW was used at working speeds from 0.5 to 1.5 m/min. The protection of the reactive molten magnesium and of the alloying powders was realised by using argon as powder feed gas.

Figure 2.1 shows the principle of the one step laser alloying process. The alloying elements were fed directly into the molten pool during laser treatment. The alloy content and the resulting hardening effects of the intermetallics formation and solid solution hardening were controlled by the powder feed rates. As for laser remelting, the rapid cooling during the laser alloying process led to a much finer microstructure compared to conventional cast alloys. The structure and the phase composition of the laser alloyed surface layers were investigated by light and electronic microscopy and by X-ray diffraction.

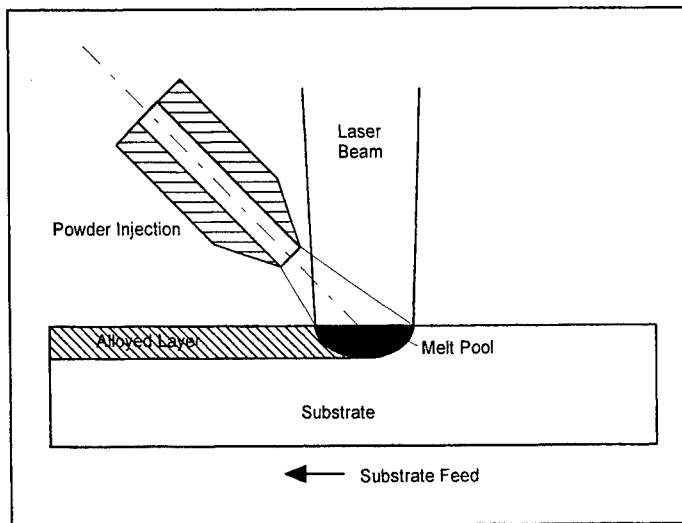


Figure 2.1: Principle of laser surface alloying

2.3 Investigations of the wear resistance using the scratch test method

The wear resistance of the laser alloyed layers was examined with a Teer Coating multiscratch tester. The principle of this test method is shown in figure 2.2. A fixed hardened steel ball is moved within a measuring length of 3 mm over the surface layer with an applied load of 20 N for a number of 250 cycles. As a result of the applied load in combination with the small contact point of the steel ball, a high hertzian pressure occurs in the contact zone. Compared to several other wear tests, this combination of sliding wear and hertzian pressure is more realistic in respect to industrial applications. Under a high hertzian pressure the deformation of a softer material under a hardened surface layer can cause crack formation and spalling of the layer. The result of the multiscratch test is a groove-like wear track. The depths of these tracks, indicating the material loss, were measured by a Perthometer roughness tester and compared for all untreated and laser alloyed materials.

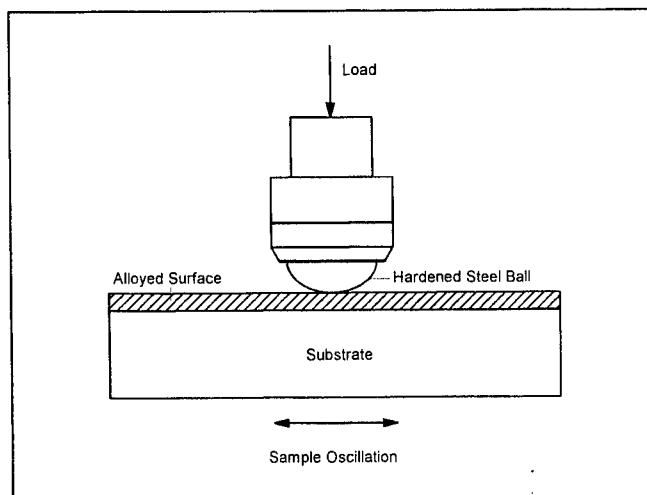


Figure 2.2: Principle of the multiscratch test

2.4 Corrosion tests

Investigations on the corrosion resistance of the laser alloyed surface layers were carried out by the salt water immersion test. The samples were cut to a size of 15 x 15 mm and mounted in polymer resin to cover the untreated substrate material and subsequently ground up to 2400 grit abrasive paper to realise a comparable surface finishing. Then the samples were immersed in 1000 ml of 3% NaCl solution for 16 hours at room temperature. After the test, the corrosion attack on the surface was inspected by microscopic investigation. To compare the laser alloyed layers to untreated material, samples of cast cp Mg were also tested under the same conditions.

3. RESULTS AND DISCUSSION

3.1 Results of the laser alloying process

As for laser alloying with one element, the formation of intermetallic compounds occurred in the Al+Cu and the Al+Ni alloyed layers. Table 3.1 lists the formed intermetallics and their melting points. For laser alloying with Al and Cu a ternary compound $\text{Mg}(\text{Al,Cu})_2$ with magnesium is formed for element contents of 38 at.% Cu and 25 at.% Al in the layers. The intermetallic showed a dendritic structure with a compact short armed form of the dendrites. The formation of the ternary phase increased the hardness to values above 300 $\text{HV}_{0.1}$, but strong embrittlement led to crack propagation during grinding. Laser alloying of magnesium with aluminium and nickel led to the formation of the binary intermetallic Al_3Ni_2 in the form of long oriented grown dendrites in a mainly of Mg and Al consisting eutectic matrix for alloying contents of 45 at.% Al and 26 at.% Ni. Hardness values of 280 $\text{HV}_{0.1}$ were achieved, whereas neither embrittlement nor crack formation was observed. Due to the fact that larger surface areas had to be alloyed for producing the samples for wear and corrosion testing, a stronger distortion of the laser treated sheets occurred as a result of the high thermal expansion of magnesium.

Alloying element	Melting point [°C]	Intermetallic compound	Melting point [°C]
Al	660	$\text{Mg}_{17}\text{Al}_{12}$	402
Cu	1083	Mg_2Cu	568
Ni	1453	Mg_2Ni	760 (peritectic)
Si	1410	Mg_2Si	1085
Al + Cu	---	$\text{Mg}(\text{Al,Cu})_2$	*)
Al + Ni	---	Al_3Ni_2	1133 (peritectic)

*) dependent on composition

Table 3.1: Magnesium intermetallics^{18,19}

3.2 Results of the wear and corrosion tests

As reported earlier¹⁴⁻¹⁷ the laser alloying with copper showed the strongest increase of wear resistance for the pure elements. But the corrosion resistance of these layers was decreased dramatically. The former work showed also a strong influence of the substrates alloying elements on the structure of the formed intermetallic compound, resulting in a different wear resistance of the alloyed layers. This new results of the investigations on laser alloying of pure magnesium with combinations of two elements showed an additionally increase of wear resistance. Compared to alloying only with copper the combination of Al and Cu resulted in a slightly lower wear rate, whereas the corrosion resistance of these layers was strongly increased. The only visible corrosion effect was a slight darkening of the surface, no pitting corrosion occurred.

The highest wear resistance was achieved by the Al + Ni alloyed samples. The wear depth was decreased to values of 11% compared to the untreated pure magnesium. Figure 3.1 summarises the results of the wear tests on laser alloyed layers on pure magnesium (alloyed with Al, Al+Cu and Al+Ni) respectively Al 80 (alloyed with Ni, Cu and Ni). As for alloying with pure nickel or the combination Al+Cu, the corrosion resistance of the samples was increased due to a low amount of magnesium solid solution crystals in the layers. Additionally to the bonding of nickel in the Al_3Ni_2 -phase, the surplus aluminium is dissolved into the magnesium solid solution, resulting also in an increased corrosion resistance of the remaining Mg. Compared to the Al+Cu alloyed samples the corrosion attack led also to a slight darkening but additionally to the formation of a thin grey layer of corrosion products.

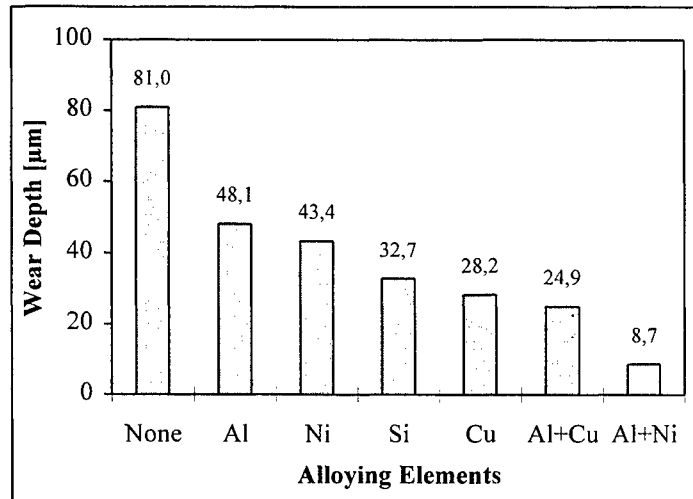


Figure 3.1: Results of multiscratch test, 20 N, 250 cycles, on laser alloyed surface layers on cp Mg (respectively Al 80)

4. CONCLUSIONS

The investigations demonstrated the possibilities of increasing the wear resistance of magnesium base alloys without loss of corrosion resistance. The one step laser alloying of commercial pure magnesium with combinations of two elements was carried out successful with the element combinations Al+Cu and Al+Ni. Compared to laser alloying with one element, the alloying with a mixture of aluminium and nickel resulted in a further increase of wear resistance. No strong decrease of corrosion resistance, as observed for alloying with copper, was found. The reason for the strong increase of wear and corrosion resistance was the formation of a magnesium-free intermetallic compound of the used alloying elements. Whereas the corrosion resistance was increased by the additional alloying of the remaining magnesium solid solution crystals with aluminium. Due to the fact that the actual work was carried out only on pure magnesium, further investigations should examine the laser alloying of different magnesium base alloys with this combinations of two alloying elements. Additionally investigations on laser alloying of cp Mg with other combinations of alloying elements like Al+Si or Al+Zn should be carried out.

5. REFERENCES

1. F.C. Grensing, H.L. Fraser: „Structure and Properties of Rapidly Solidified Magnesium-Silicon Alloys“, *Materials Science and Engineering*, **98**, 313-319, 1988.
2. K. Schemme, E. Hornbogen: „Rapidly Solidified Mg-Li Base Superlight Alloys“, *Proceedings of the International Conference on Advanced Aluminium and Magnesium Alloys*, Amsterdam, 797-803, 1990.
3. E. Hornbogen, K. Schemme: „Prospects of Superlight Metals and Their Laser Surface Alloying with Ceramic Phases“, *Proceedings of the Thermal Structures Conference*, Charlottesville, USA, 95-111, 1990.
4. K. Schemme, E. Hornbogen: „Erste Untersuchungen laserbehandelter Mg-Li-Al Legierungen“, *Metall*, **45**, (10), 1007-1010, 1991.
5. K. Schemme, G. Huppert: „Laseroberflächenveredeln von Mg-Li-Legierungen durch Legieren und Dispergieren“, *Metall*, **47**, (6), 541-546, 1993.
6. K. Schemme: "Entwicklung superleichter Magnesium-Werkstoffe", *Fortschritt-Berichte VDI*, **Reihe 5**, (Band 293), VDI-Verlag, Düsseldorf, 1993.
7. P.L. Hagans: „Surface Modification of Magnesium for Corrosion Protection“, *Proceedings of the 41st World Magnesium Conference*, London, 30-38, 1984.
8. R.K. Kalimullin, Y.Y. Kozhevnikov, I.A. Faizullin, V.V. Valuev: „Influence of Laser Treatment on the Structure and Mechanical Properties of MA21 Alloy“, *Metal Science and Heat Treatment*, **26**, (9-10), 684-687, 1984.
9. R.K. Kalimullin, Y.Y. Kozhevnikov: „Structure and Corrosion Resistance of an Mg-Li Base-Alloy After Laser Treatment“, *Metal Science and Heat Treatment*, **27**, (3-4), 272-274, 1985.
10. R.K. Kalimullin, A.T. Berdnikov: „Increasing the Corrosion Resistance of MA21 Magnesium-Lithium Alloy by Surface Laser Treatment“, *Protecting of Metals*, **22**, 223-225, 1986.
11. R.K. Kalimullin, V.V. Valuev, A.T. Berdnikov: „The Effect of Surface Laser Treatment on the Creep of the Magnesium-Lithium Alloy MA21“, *Metal Science and Heat Treatment*, **28**, (9-10), 668-670, 1986.
12. R.K. Kalimullin, V.B. Spiridonov, A.T. Berdnikov, A.A. Romanov, G. Pautkina: „Properties of Alloy MA21 After Laser Treatment“, *Metal Science and Heat Treatment*, **30**, (5-6), pp 338-348, 1988.
13. V.V. Shibaev, T.V. Gulayeva, L.A. Shimchenyuk, N.A. Siulina: „Study of the Effect of Pulsed Laser Heat Treatment on the Corrosion Properties of Magnesium Alloy VMD10“, *Protection of Metals*, **26**, (5), 606-609, 1991.
14. A. Weisheit, R. Galun, R. Haude: „Laserrandschichtbehandlung von Aluminium- und Magnesiumwerkstoffen“, *Metall*, **48**, (6), 455-460, 1994.
15. R. Galun, A. Weisheit, B.L. Mordike: „Surface Treatment of Magnesium Alloys With Laser Melting and Laser Alloying“, *Proceedings of the 5th European Conference on Laser Treatment of Materials (ECLAT '94)*, DVS-Berichte Bd. 163, DVS-Verlag, Düsseldorf, 421-426, 1994.
16. R. Galun, A. Weisheit, B.L. Mordike: „Laser Surface Alloying of Magnesium Base Alloys to Improve the Corrosion and Wear Properties“, *Proceedings of the 14th International Congress on Applications of Lasers & Electro-Optics (ICALEO '95)*, 69-77, 1996.
17. R. Galun, A. Weisheit, B.L. Mordike: „Improving the Surface Properties of Magnesium by Laser Alloying“, *Proceedings of the 3rd International Magnesium Conference*, Manchester, 1996, in print.
18. A. Prince, G. Effenberg and S.B. Prima: in *Ternary Alloys*, VCH Verlag, Weinheim, Germany, different volumes, 1992
19. G. V. Raynor: *The Physical Metallurgy of Magnesium and its Alloys*, Pergamon Press, London, 1959.

2 kW cw Nd-YAG laser surface hardening.

G.DUFFET*, P.KIRAT*, H.ANDRZEJEWSKI*, A.B.VANNES**

*Laboratoire Laser et Traitement des Matériaux / Université de Bourgogne / Institut Universitaire de Technologie 12 rue de la Fonderie 71200 Le Creusot (France) Tel 85803030 / FAX 85803615

**IFOS-Ecole Centrale de Lyon 36, Av. Guy Collongue BP163 69131 Ecully cedex (France)

Introduction

Some classical surface hardening methods require a new machining after treatment or a break in line machining. The laser surface hardening allows to avoid these disadvantages. Moreover the associated Nd:YAG laser optical fiber enables to become independent of the piece geometry : in our case, an extrusion screw.

In order to control the depth quenched by Nd:YAG laser beam, a temperature-field fast calculation based on the knowledge of the laser-material interaction parameters, of the laser power, of the scanning speed and of the material thermal diffusivity and conductivity is proposed. The method is applied to iron-chromium and to iron-nickel-chromium alloys. Quenched depth measurements on four steels lead to experimental results in good agreement with the proposed model.

The hardening zone is characterized by hardness, structure, Young's modulus and yield stress. Notably an original way is used to know thermal affected zone Young's modulus and yield stress : hertzian hardness.

1-Materials :

Four steels are tested : three iron-chromium alloys and one iron-nickel-chromium alloy :100Cr6, 42CrMo4, 50CrV4 and 45NiCrMo17. These steels are in quenched-tempered state before laser treatment.

chimical analysis	C %	Cr %	Ni %	Mo %	Mn %	Si %	V %
42CrMo4	0.4	1	0	0.2	0.75	0.25	0
100Cr6	1	1.5	0	0	0.3	0.25	0
50CrV4	0.5	1	0	0	0.85	0.25	0.15
45NiCrMo17	1.7	1.7	4	0.4	0	0	0

2-Used Nd:YAG laser :

It is a two kilowatt continuous Nd:YAG laser equipped with a 600 μm optical fiber and with a 75 mm focal distance lens. The beam energy distribution is a 2.8 mm diameter flat hat.

To be able to use in the future a three kilowatt laser with two beams, a 1.3 kW incident power is chosen. With this incident power, eleven scanning speeds are tested (1m/min to 2m/min) to obtain a 300 μm treated depth. 1.2m/min scanning speed is selected because this speed gives the required affected depth.

3-Proposed model :

Built on the resolution of the fundamental heat conduction equation dependent on time for a half infinite medium, the following model is used [1]:

$$T(x, y, z) = \frac{AP_{inc}}{k(\pi)^{3/2}} \int_0^\infty \exp \left[-\frac{(x + vt)^2 + y^2}{2a + 4\alpha t} - \frac{z^2}{4\alpha t} \right] / \left[\sqrt{\alpha t} (2a^2 + 4\alpha t) \right] dt$$

whereas α is the thermal diffusivity, k is the thermal conductivity, A is the absorptivity, P_{inc} is the incident power, v is the scanning speed, a is the equivalent laser spot and the (x, y, z) is the cartesian coordinates.

Thermal parameters are invariable in the considered temperature -field. The absorbed laser energy is equivalent to a surface source at $z = 0$.

Finally, the depth at which the AC1 temperature is reached can be predicted

4-Comparison between test and model results :

Laser parameters are the incident power, the scanning speed and the laser beam diameter. Absorptivity A is measured by a powermeter and its value is 0.33. The mean diffusivity and conductivity for the considered temperature-field, 850°C-1150°C, are used [2]. Then the measured penetrations on specimen and the calculated thermal affected zone are in agreement within 20%.

model-test	α	k	exp.d.	calc.d.
comparison	mm ² /s	W/mmK	micron	micron
42CrMo4	5	0.035	290	240
100Cr6	5	0.035	290	240
50CrV4	5	0.035	290	240
45NiCrMo17	5.5	0.025	360	420

5-Structural and mechanical affected depth characterization

5-1-Structure

After laser treatment, structure is a homogeneous martensite.

5-2-Hardness

treated zone hardness	maximum	minimum	observation
	Hv50	Hv50	
42CrMo4	875	775	flat
100Cr6	975	620	decrease
50CrV4	900	570	decrease
45NiCrMo17	810	610	decrease

Maximal and minimal affected depth hardness are given in the preceding table. The shape of the hardness curve is flat or decreasing with a 300 Hv variation. Only the 42CrMo4 alloy answers the purpose of 800 Hv on a 300µm depth.

5-3-Young's modulus and yield stress

The treated zone Young's modulus and yield stress are obtained by hertzian hardness, a method developed by V. Malau and A.B. Vannes [3]

5-3-1-Hertzian hardness apparatus principle

The diagram of the hertzian hardness apparatus is given in appendix.
A scale pan supports weights (ten to two thousand grams). Loading and unloading of the indenture apparatus (the small ball) is provided by an electric motor with a good reproductibility. The capacitive sensor allows to know loading and unloading displacement with a practically infinite resolution. A loading and unloading cycle is given in appendix.

5-3-2-Young's modulus determination [3]

From Hertz's theory concerning static plane-sphere contact, a relation exists between a the contact radius and F the applied load :

$$a^3 = \left(\frac{3R}{4E_0} \right) F \quad (1)$$

whereas

a is the contact radius

R is the ball radius

F is the applied load

E₀ is the equivalent Young's modulus

$$E_0 = \frac{E_1}{1 - \nu_1^2} + \frac{E_2}{1 - \nu_2^2} \quad (2)$$

whereas E_1 is the ball Young's modulus (310 GPa), ν_1 is the ball Poisson's coefficient (0.27)
 E_2 is the studied material Young's modulus and ν_2 is the studied material Poisson's coefficient

now F is proportional to T the recorded tension from capacitive sensor

therefore a^3 is proportional to T

so $a^3 = CT$ whereas C is a proportionality constant

first, C is obtained with a reference material : $a_{ref}^3 = CT_{ref}$

secondly, C is used for the studied material : $a_{stud}^3 = CT_{stud}$

finally, the (1) and (2) relations allow to calculate the studied material Young's modulus E_2

The mean E_2 value for the laser treated 42CrMo4 alloy is 220 GPa

5-3-3-Yield stress determination [3]

The relation (1) is linear up to a limit value (a_{lim}, F_{lim}). That corresponds to an elastic behavior.

From the relation (1) we obtain the relation : $E_0 = \frac{3R}{4} \left(\frac{F_{lim}}{a_{lim}^3} \right) \quad (3)$

Above this limit a new curve exists and corresponds to an elastoplastic behavior.

In the case of a plane-sphere contact with an infinitely rigid sphere from Hertz's theory and with a Tresca's criterion, a linear relation exists between the elastic limit σ_y and the contact radius a :

$$\sigma_y = \frac{4E_2}{3\pi R(1 - \nu_2^2)} a \quad (4)$$

The relations (2), (3) and (4) allow to calculate the material yield stress σ_y .

With this method, the measured 42CrMo4 σ_y value is about 1100 MPa.

Conclusion :

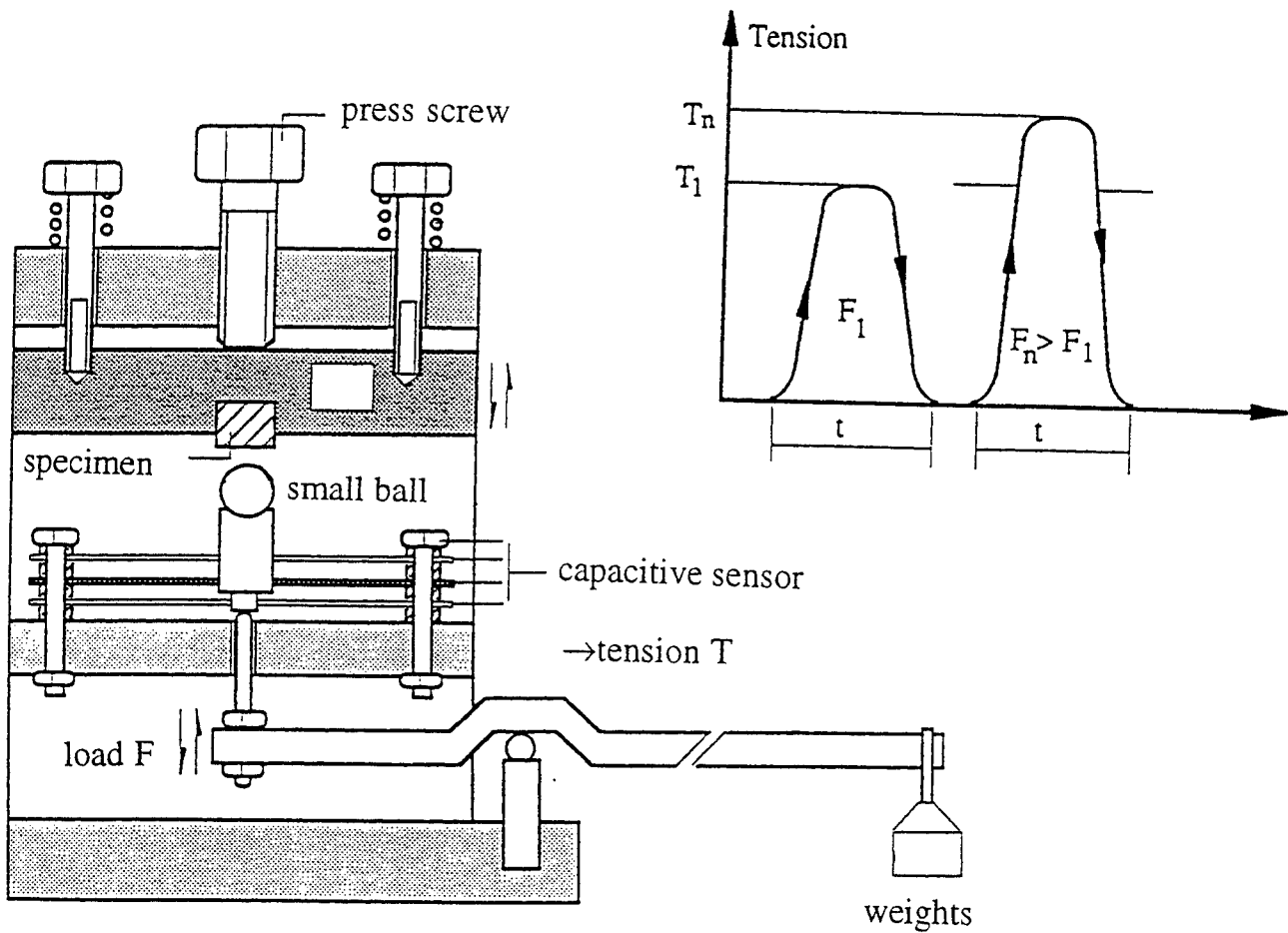
Nd:YAG laser surface hardening brings solutions to industrial problems, for example treatment in line machining and treatment of not easily accessible zones.

Therefore we pay particular attention to show that :

- a fast temperature-field calculation allows to estimate the treated zone depth (within 20%)
- the required hardness is obtained (800 Hv on a 300µm depth)
- the Young's modulus and the yield stress of the 300µm treated zone is measurable by an experimental method, hertzian hardness.

- [1] P.KIRAT, Ph.D. Thesis, N°ISAL 0030, Lyon, 1992.
- [2] Y.S.TOULOUKIAN. Thermal Physical Properties of Matter, TPRC Data Series, I.F.I./Plenum, New York, 1973.
- [3] V.MALAU. Ph.D. Thesis to be upheld, Ecole Centrale de Lyon, september 1996.

Appendix : diagram of the hertzian hardness apparatus



Laser generating metallic components

M. A. McLean, G. J. Shannon & W. M. Steen

Laser Laboratory, Department of Mechanical Engineering
University of Liverpool, Liverpool, L69 3BX

ABSTRACT

Recent developments in rapid prototyping have led to the concept of laser generating, the first additive manufacturing technology. This paper presents an innovative process of depositing multi-layer tracks, by fusing successive powder tracks, to generate three dimensional components, thereby offering an alternative to casting for small metal component manufacture. A coaxial nozzle assembly has been designed and manufactured enabling consistent omni-directional multi-layer deposition. In conjunction with this the software route from a CAD drawing to machine code generation has been established. The part is manufactured on a six axes machining centre incorporating a 1.8 kW CO₂ laser, providing an integrated opto-mechanical workstation. The part build-up program is controlled by a P150 host computer, linked directly to the DNC machining centre. The direct manufacturing route is shown, including initial examples of simple objects (primitives -- cube, cylinder, cone) leading to more complex turbine blade generation, incorporating build-up techniques and the associated mechanical properties.

Keywords: laser generating, laser cladding, rapid prototyping, powder deposition

1. INTRODUCTION

The principle of laser cladding has led to the development of Laser Direct Casting (LDC). Injecting metallic powder into a laser generated melt pool on a moving substrate produces a solidified metal track. Deposition of successive tracks produces a multi-layer build. Originally, powder was delivered through a single pipe into the melt pool. This was difficult to align and only provided unidirectional processing. LDC incorporates a novel coaxial nozzle that delivers an annulus of powder around the laser beam thus permitting omni-directional movement. The powder can be focused into the melt pool by varying the axial, powder and shrouding gas flows. Scanning the melt pool by moving the substrate about the laser produces the build path. To achieve a 'down-hand' weld orientation the LDC nozzle remains vertical as the system positions the component. Initial three axes multi-layer build paths have produced simple objects (i.e., primitives -- cube, cylinder, cone, pyramid). Data obtained proves that a three axes system is not capable of producing multi-layered walls with an incline greater than 30° to the vertical. This presents the need for five or six axes to generate complex geometry. The process is ideally suited for industrial manufacturing applications such as rapid manufacture of metallic components, complex form tools or as a corrective/alternative process to casting.

2. EXPERIMENTAL PROCEDURE

A 1.8kW CO₂ laser was used in conjunction with the omni-directional coaxial cladding technology developed at Liverpool University. An omni-directional nozzle, consisting of three annular sections (figure 1), delivered fluidised metal powder coaxially into the melt pool on the surface of the substrate. A motor controlled Archimedes screw feed mechanism was used to regulate the flow of metal powder to the process. A *Cybaman* three axes positioning system, placed on a Matrix Churchill machining centre was used to provide the 2½D and 3D part manipulation.

Invented by Cybomatic, the *Cybaman*¹, allows unique articulation about a fixed datum in space. The *Cybaman* positioning system comprises three rotational axes. The datum position occurs at the intersection of all rotational axes, the 'Null point' (figure 1). The base axis supports all rotational axes and provides full 360° rotational movement about the vertical axis. The inclined axis, offset at 45°, supports the table axis. This facilitates presentation of the component at any angle between the horizontal and vertical. By use of three additional linear axes, in the principle planes (X, Y and Z), it is possible to present any surface vector parallel to the tool axis. System control software incorporates an intelligent mathematical algorithm² that uses 3D rotational matrices to generate six axis simultaneous interpolation³.

Vector tool paths generated by AutoCADR13 are translated into DNC codes. The controller then moves the component to the laser axis with the predetermined path.

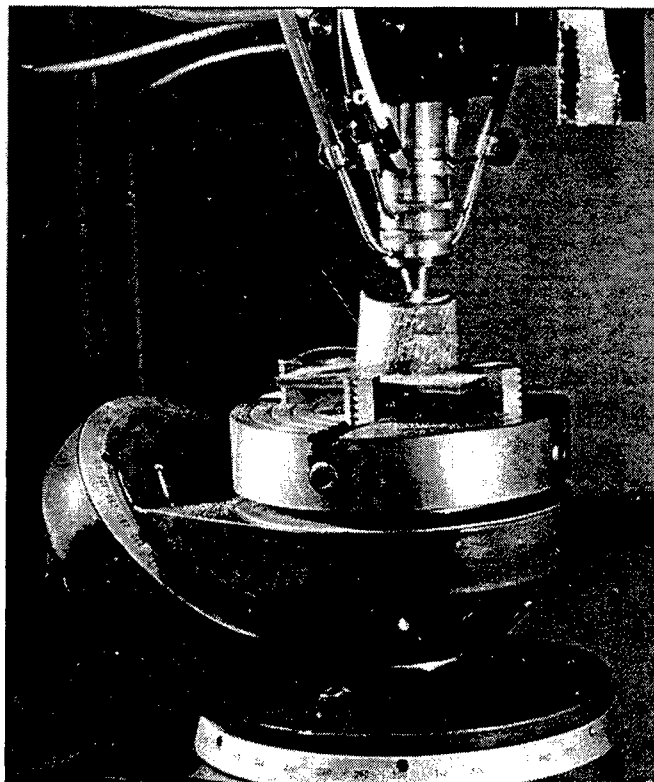


Figure 1. Laser Direct Casting an aerofoil with the omni-directional nozzle on the six axis Cybaman

3. RESULTS

Mild steel was used as the substrate material in all experiments. Stainless steel powder (316L) was used for the process characterisation. Using the DNC system single and multi-layer cladding trials were performed to optimise the process. The deposited structure is affected by processing parameters such as process speeds, laser power, powder flow rates, shielding gas (argon) flow rates, laser spot size and substrate stand-off. Experiments to produce single clad tracks were performed to establish the process window and clad geometry necessary for multi-layer build strategies. The clad geometry is strongly influenced by the laser power, powder flow rate and processing speed. Nominally within the ranges of 0.5-1.5 kW, 0.1-0.3 g/s and 500-1000 mm/min respectively to obtain individual layer dimensions within 0.5-1.5 mm. The width of the clad is mainly determined by the laser spot size.

Multi-layer clads were produced and gave representational results of the single clad tracks. Figure 2(a) and (b) show typical multi-layer builds from stainless steel powder. The interface region between layers is identified by a white strip. The circular geometry of each layer is modified to a shallower curve due the effect of depositing the next layer. The clad structure is typical of cast components, directional solidification occurs with epitaxial grain growth through the interface region and successive layers. The length of the grains increases significantly as the depth of build increases. On this micrograph there are no visible pores within the structure.

Further experiments were performed with other metal powders including cobalt and high nickel alloys. Extensive oxidation problems were solved by a high degree of gas shielding. All powders were used in the generation of components to demonstrate the limitations of three axis generation.



Figure 2(a). Cross section of a 10 layer stainless steel 316L build, showing epitaxial grain growth.



Figure 2(b). Longitudinal section of a 10 layer stainless steel 316L build.

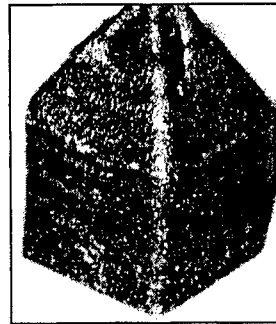


Figure 2(c). Limitations of three axes system when generating a stainless steel 'house' with roof inclined at 45°.

4. DISCUSSIONS

The clad geometry is strongly affected by the process parameters, ideally a clad aspect ratio (height : width) of 1 : 2 should be achieved. In addition the temperature of the melt pool is indirectly responsible for the layer size. A temperature rise on the process path, due to poor heat dissipation will increase the powder catchment and therefore the layer size. A solution is to use a closed-loop power control system to maintain a constant melt pool temperature.

High nickel alloy powders are considered to be more realistic materials for industrial component requirements. Oxidation problems were rectified by increased inert shrouding. Sample components were successfully generated, as shown in figure 3(a). Typical surface roughness value of $R_a = 40 \mu\text{m}$ was achieved for the specimens after the residual powder was brushed from the surface. A Vickers hardness value of $HV_{\text{nickel}} = 478$ was obtained.

Multi-layer walls were generated to test the maximum degree of inclination possible on a three axes system. By depositing the successive layers at a slight overhang a sloped surface can be generated. Data obtained proves that a three axes system is not capable of producing multi-layered walls with an incline greater than 30° to the vertical. In the example, figure 2(c), the overhanging layers do not fuse, resulting in reduced height and eventually loss of desired shape. Any complex geometry will only be possible by using five or six axes systems.

Simple objects were produced in stainless steel, cobalt and nickel (figure 3(a)). Figure 3(b) shows a post processed aerofoil component generated in stainless steel 316L. The component was manufactured in 25 minutes having a wall thickness of 2mm and overall height of 50mm.

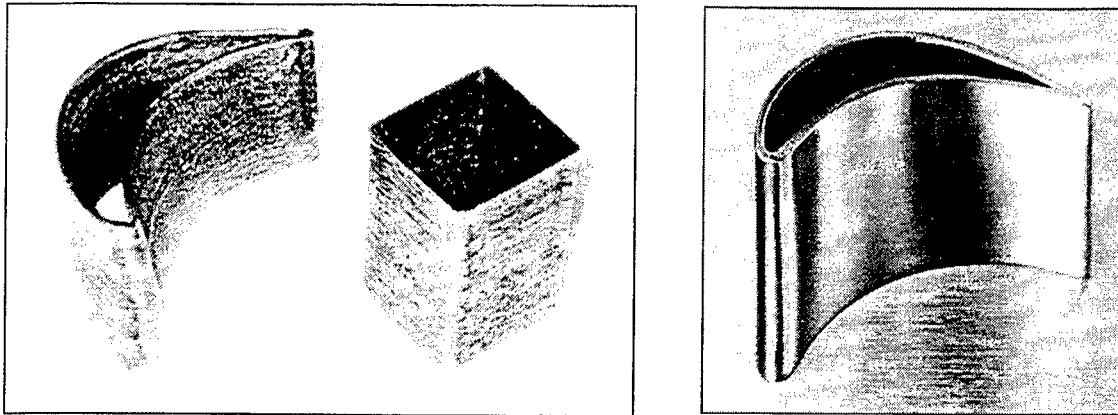


Figure 3. (a) Simple nickel alloy components, (b) Aerofoil manufactured by LDC from stainless steel (316L) powder.

5. CONCLUSIONS

Predictability of clad geometry is of great importance to the dimensional accuracy of a finished component. This is possible by the closed-loop control of the process parameters by monitoring the melt pool temperature. As a result there will be an improved surface finish. The manufacture of true 3D components is only achievable with a five/six axis system. Further research into 3D LDC is progressing. An example is shown below.

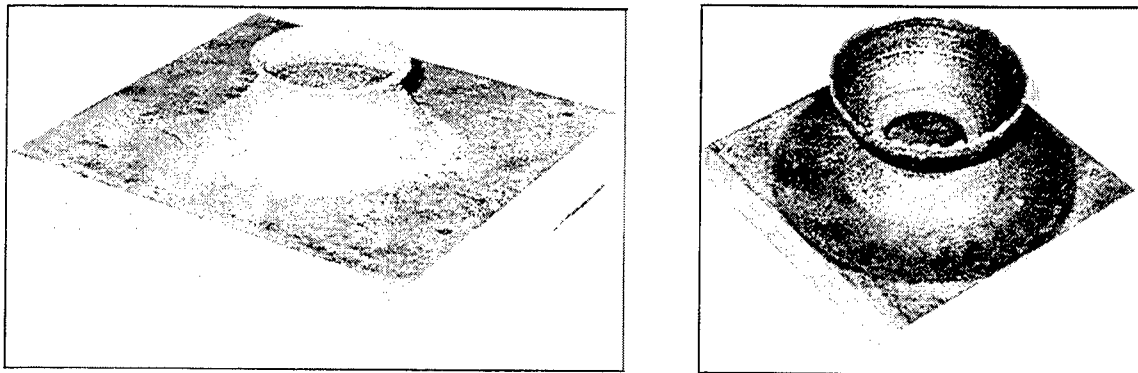


Figure 4(a)&(b). A LDC 'bowl' manufactured from cobalt using the six axes Cybaman system. Base - 100x100mm

6. ACKNOWLEDGEMENTS

The authors would like to thank Cybomatic Ltd. for their collaboration during the course of this work.

7. REFERENCES

1. McLean, J.G. European Patent No. 0123433. "Articulated Assembly of Members". 1984.
2. McIntyre, H.A.J. "Control of the New Cybaman Positioning System". Salford University Business Services Ltd. 1992.
1. Rogers, P.A. and McIntyre, H.A.J. "Feasibility Study into the Control of a Variable Geometry fixture for Robotic Applications". Salford University Business Services Ltd. 1984.

17. Laser Cutting

Invited Paper

Experimental study of cutting thick aluminum and steel with a chemical oxygen-iodine laser using an N₂ or O₂ gas assist

David L. Carroll

Mechanical and Industrial Engineering Department
Aeronautical and Astronautical Engineering Department
University of Illinois at Urbana-Champaign, Urbana, Illinois 61801

James A. Rothenflue

Phillips Laboratory, Applied Laser Technology Branch (PL/LIDB)
Kirtland Air Force Base, New Mexico 87117-5776

ABSTRACT

A chemical oxygen-iodine laser (COIL) was used for cutting aluminum and carbon steel. Cut depths of 20 mm were obtained in aluminum and 41 mm in carbon steel using an N₂ gas assist and 5-6 kW of power on target. The same laser at the same power level produced a cut depth of 65 mm in carbon steel with an O₂ gas assist; a low quality cut to a depth of nearly 100 mm in carbon steel was demonstrated. These data are compared with existing COIL and CO₂ laser cutting data. COIL cuts carbon steel and stainless steel at approximately the same rate. For a given cut depth, power and spot size, COIL cuts steel approximately three times faster than a CO₂ laser using an inert gas assist. COIL cutting speeds in carbon steel are improved by approximately a factor of three when an O₂ assist is used in lieu of an N₂ gas assist. With an N₂ gas assist, COIL cuts aluminum at approximately the same rate as CO₂ cuts steel. To improve the agreement between data and an existing theoretical cutting model, an empirical correction factor was added to the model; this modification provides excellent agreement with data.

Keywords: laser cutting, materials processing, thick-section cutting, chemical oxygen-iodine laser, COIL

1. INTRODUCTION

Lasers made their debut for materials processing in 1965. Since that time, materials processing with CO₂ and Nd:YAG lasers has evolved into a mature technology.¹ Other laser technologies which are still evolving for materials processing applications are CO, excimer, HF/DF and the chemical oxygen-iodine laser (COIL).²⁻⁴ Of these other laser technologies, COIL is of particular interest because of its short wavelength (1.315 μ m), high scalable continuous wave (cw) power, and excellent beam quality (due to very small density gradients in its laser cavity).

The short wavelength has three primary advantages over CO₂. First, the shorter wavelength of COIL can be focused to a smaller spot size. Second, the COIL wavelength couples better (higher absorption) with materials such as steel and aluminum.¹ Third, the COIL wavelength can transmit through SiO₂ fiber optics with a loss of only around 0.5 dB/km.¹ While the capital and operating costs of today's COIL devices may make them economically uncompetitive with CO₂ devices in the low to mid power level markets, COIL has considerable potential for high power (> 5 kW) applications. Further, while Nd:YAG effectively has the same wavelength advantages as COIL, there are presently no Nd:YAG devices with average power levels in excess of 5 kW; this makes Nd:YAG a non-competitor in the high power market.

The chemical oxygen-iodine laser was first demonstrated in 1977.⁵ Briefly stated, a chemical laser is a device which uses a series of chemical reactions to obtain excited atoms (or molecules) for subsequent lasing. The chemical oxygen-iodine laser (COIL) utilizes an energy transfer from the singlet delta electronically excited state of oxygen [O₂(¹ Δ)] to I₂ to dissociate the iodine molecule. This process is followed by an energy transfer from other O₂(¹ Δ) molecules to the liberated iodine atoms, thus providing the energy for the atomic iodine laser transition of interest. A block diagram of a typical COIL system is illustrated in Fig. 1. Since its first demonstration, COIL technology has evolved and matured to a sophisticated state for military applications. Good summaries of military COIL technological development are provided by Truesdell *et al.*⁶ and Avizonis and Truesdell.⁷ Meanwhile, research towards making COIL an industrial device began in the latter half of the 1980's.⁸ Long duration, high power industrial COIL operation has been addressed in several papers.⁹⁻¹⁴ General issues associated with the industrialization of COIL were discussed by Scott and Truesdell.¹⁵

Recently, COIL cutting data has appeared in the literature. Atsuta *et al.*¹⁶ obtained the first results for cutting stainless steel which were quite promising. Kar *et al.*¹⁷ produced a more complete data base for stainless steel cutting with an inert gas assist. This work extends the COIL cutting data base to include data for cutting aluminum and carbon steel with

an N_2 gas assist, and for carbon steel with an O_2 gas assist. These data are compared with existing COIL and CO_2 laser cutting data as well as to Kar *et al.*¹⁷ cutting theory.

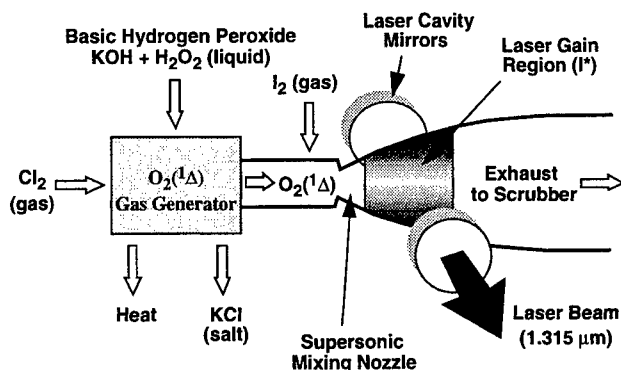


Fig. 1 Block diagram illustrating the major components of a typical COIL system.

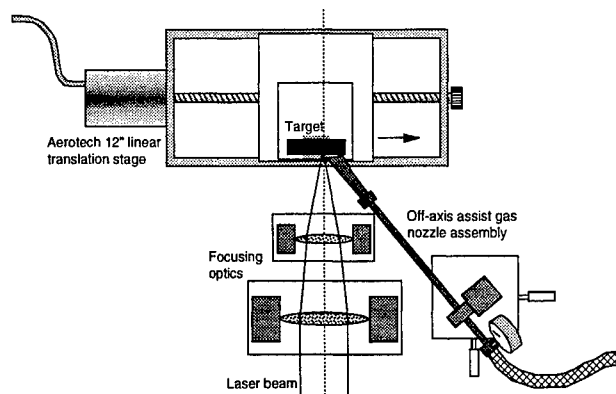


Fig. 2 The experimental set up for the thick section metal cutting experiments with RADICL.

2. EXPERIMENTAL SETUP

The Research Assessment, Device Improvement Chemical Laser (RADICL), located at the U.S. Air Force's Phillips Laboratory, was used for all of these cutting tests. To maximize power output, a stable resonator was used on RADICL which consisted of a highly reflective 10 m radius of curvature feedback mirror and a partially reflective flat outcoupler spaced 3 m apart. Because of the use of a stable resonator, a large number of transverse modes were present in the outcoupled beam; this prevented the beam from being focused to a diffraction limited spot. A combination of lenses was used to focus the beam on the target, Fig. 2. The target was situated so that the focal point was located 1 mm into the workpiece. The rectangular multimode focal spot was 1.8 mm wide by 3.0 mm long. The spot was horizontally oriented such that the leading edge of the spot was the smallest dimension. The power on target ranged from 5 to 6.5 kW.

The gas assist nozzle for all tests was the same large nozzle used by Kar *et al.*¹⁷ The nozzle was made from 19.1 mm (0.75 inch) diameter stainless steel tubing that was flattened and shaped to form a rectangular nozzle. The nozzle exit dimension was approximately 1.0 mm by 22.9 mm. The gas assist nozzle was oriented horizontally so the long dimension was lined up with the cut direction (or kerf) and was fixed at a 45 degree angle from normal to the target, Fig. 2. The gas assist consisted of either nitrogen at a pressure of 793 kPa (115 psia) or oxygen at a pressure of 310 kPa (45 psia).

The targets for the tests consisted of metal plates which were mounted on a stepper motor-controlled, horizontal translation stage (capable of speeds up to 3.0 m/min) and scanned through the focal region at constant speed. Scans were conducted at various speeds and the cut depth was measured later. The aluminum targets were 38.1 mm (1.5 inches) thick and the carbon steel targets were 76.2 mm (3 inches) thick. For one test, a 101.6 mm (4 inches) carbon steel target was used. None of the data reported in this work actually cut through the entire thickness of the target. Since it is possible that slightly higher cut speeds might be obtained when a complete cut is made and molten material is allowed to blow out the back of the cut, these data may represent a slight underestimate of COIL cutting speeds.

3. ALUMINUM AND CARBON STEEL EXPERIMENTS AND COMPARISON WITH OTHER CUTTING DATA

Before any aluminum or carbon steel cutting tests were performed, two cuts were made in stainless steel to verify that the experimental setup and conditions were comparable to those of Kar *et al.*¹⁷ The two tests gave results which fall directly on Kar's cutting data, Fig. 3. Six cutting tests were then made in carbon steel (A36) with a nitrogen gas assist at various cutting speeds v , Fig. 3. The cut speeds varied from 0.03 to 1.0 m/min. As expected, for a relatively constant power level (5.7-6.5 kW) and spot size, as the scanning speed increases, the cut depth decreases. The average kerf widths were 1.65-2.54 mm with the larger kerf widths occurring for the slower cutting velocity cases. It is clear from Fig. 3 that COIL cuts carbon steel and stainless steel at approximately the same rate; this result is most likely a tradeoff between the effects of a higher absorption coefficient (more power absorbed) and a higher thermal conductivity (more energy dissipated) in carbon steel than in stainless steel. Figure 3 presents a comparison of inert gas assist steel cutting with a COIL versus that with a CO_2 laser.¹⁸ Most importantly, this figure shows that COIL cuts steel faster than CO_2 by approximately a factor of 3 for a fixed d/P and w_k .

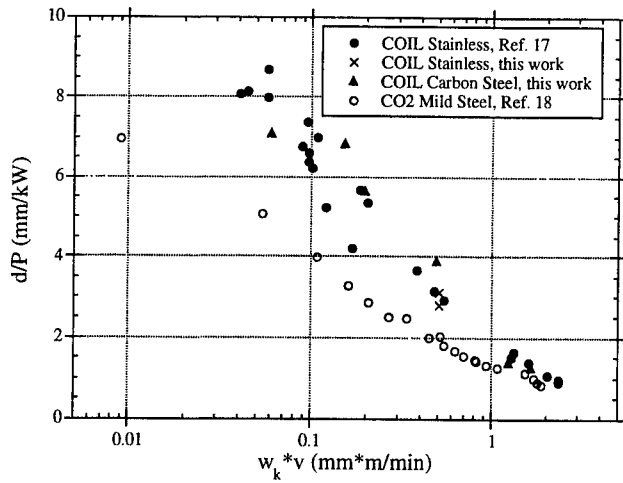


Fig. 3 Comparison of inert gas assist steel cutting data with a COIL device and with a CO₂ laser.

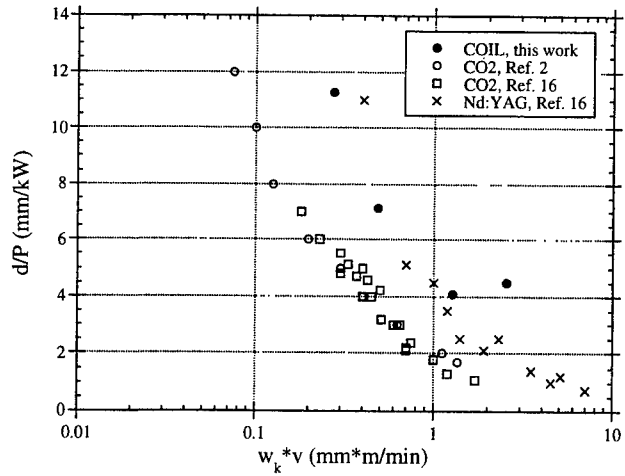


Fig. 4 Comparison of O₂ gas assist carbon steel cutting data with a COIL device and with a CO₂ laser.

A comparison of these data with Nd:YAG cutting data from Ref. 18 indicates that COIL and Nd:YAG cut steel at approximately the same rate (not shown). Since the wavelength of COIL (1.315 μm) and Nd:YAG (1.06 μm) are roughly the same, this is not a surprising result.

Four cutting tests were then made into carbon steel (A36) with an oxygen gas assist at various cutting speeds v , Fig. 4. For safety reasons, the assist pressure was reduced to 310 kPa (45 psia) to reduce the amount of reaction with oxygen. The cut speeds varied from 0.12 to 1.0 m/min. Again, as expected, for a relatively constant power level (5.7-7.2 kW) and spot size, as the scanning speed increases, the cut depth decreases. The kerf widths at the front face of the workpiece were notably larger (2.0-2.5 mm) when the O₂ assist was used. For the O₂ assist tests, the cut quality was significantly reduced from that of the inert gas experiments. The use of more sophisticated oxygen assist technology would probably result in a higher quality cut. A comparison of Figs. 3 and 4 shows that the O₂ gas assist substantially improves the cutting speed for a given power, cut depth, and kerf width; for a fixed d/P and w_k , there is approximately a factor of 3 increase in cutting speed with the O₂ gas assist above that when using an inert gas assist. A comparison of O₂ gas assist steel cutting with a COIL versus that with a CO₂ laser^{2,16} and an Nd:YAG laser¹⁶ is shown in Fig. 4. With an oxygen gas assist and for a fixed d/P and w_k , COIL cuts approximately 2 to 3 times faster than a CO₂ laser. As found for an inert gas assist, COIL and Nd:YAG also cut carbon steel at approximately the same rate when using an oxygen gas assist.

A long duration test was performed to cut a 4"x4"x4" block of carbon steel at a speed of 0.107 m/min. Because of thermal management issues associated with the long run time of the RADICL laser, the power level for this test was only 5.4 kW. The O₂ gas assist pressure was increased to 483 kPa (70 psia) to improve the momentum transfer through the workpiece. While there was a significant amount of melting of the workpiece during this test (making it difficult to adequately judge a kerf width), the beam cut to a depth of 96.5 mm. The amount of melting was most likely enhanced by the increase in the oxygen assist pressure. Despite the low quality of the cut, this test demonstrates the ability of COIL to cut fairly thick steel.

Six cutting tests were made into aluminum with a nitrogen gas assist at various cutting speeds v , Fig. 5. The cut speeds varied from 0.03 to 1.50 m/min. As anticipated, for a relatively constant power level (5-6.3 kW) and spot size, as the scanning speed increases, the cut depth decreases. All of the kerf widths were 1.65-1.78 mm (approximately the beam spot width). Figure 5 shows that COIL cuts aluminum nearly as fast as CO₂ cuts steel.¹⁸ This finding may have important implications for COIL as an excellent laser for aluminum cutting/welding/drilling applications.

4. COMPARISON AND MODIFICATION TO THEORETICAL MODEL

A simple mathematical model of laser cutting was developed by Kar *et al.*¹⁷ The general form of the theory is given by

$$\frac{d}{P} = \frac{\alpha}{w_k v + \beta \sqrt{w_k v}} \quad (1)$$

where d is the kerf depth given in units of mm, w_k is the kerf width given in units of mm, v is the velocity of the scanning laser beam in m/min, and P is the power of the incident laser beam in kW, Fig. 6. The α term represents the ratio of energy absorbed to the energy required for melting the solid material. The β term describes the ratio of the heat energy conducted into the solid substrate to the energy required for melting the solid material.

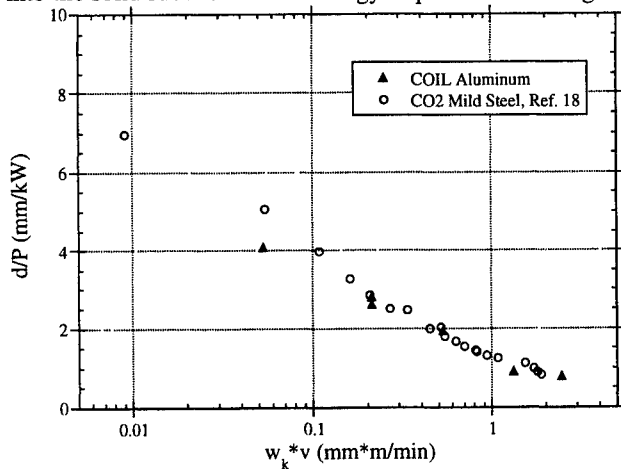


Fig. 5 Comparison of COIL cutting of aluminum with CO₂ cutting of steel. These data were taken with an inert gas assist.

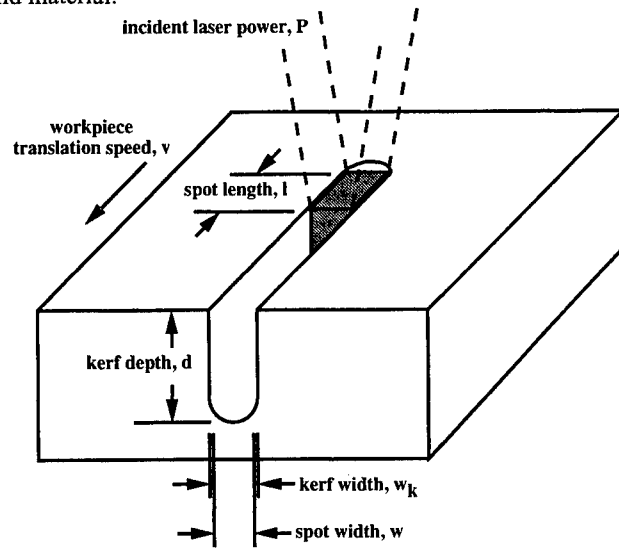


Fig. 6 Laser processing parameters.

Using thermophysical properties found in Refs. 19-21 and an absorption coefficient A of 0.25, the constants α and β are computed to be $\alpha = 2.08$ and $\beta = 0.57$ for stainless steel. For comparison, Eq. (1) is plotted in Fig. 7 for stainless steel using two values of the absorption coefficient A , 0.25 and 0.40 ($\alpha = 3.33$). Depending upon the surface roughness of the workpiece, absorptivities of 0.29 to 0.54 for steel have been measured at $1.06 \mu\text{m}^4$ (near the COIL wavelength of $1.315 \mu\text{m}$). Regardless of the absorption coefficient, it is clear from Fig. 7 that Eq. (1) models the data reasonably well, but tends to curve upwards too steeply for lower values of $w_k v$ [this effect is a consequence of the fact that Eq. (1) goes to infinity as $w_k v$ goes to zero]. Thus, it appears that there is an effect unaccounted for in Kar's theory which becomes more significant at smaller values of $w_k v$.

An empirical modification to the theory is to simply add a constant γ to the denominator of the right hand side of Eq. (1),

$$\frac{d}{P} = \frac{\alpha}{w_k v + \beta \sqrt{w_k v} + \gamma} \quad (2)$$

Using an absorptivity of 0.40 ($\alpha = 3.33$) and setting $\gamma = 0.22$, Eq. (2) provides an excellent fit to the stainless steel data, Fig. 7. Of course, the drawback to such a modification is that γ is an empirical constant which will change from material to material and probably change for different wavelengths. The physical significance of such a term may be a more accurate treatment of the conduction term in Kar's model. Other possibilities are the inclusion of convection, radiation or plasma absorption, which were all assumed negligible in the derivation of Eq. (1). A more formal derivation of the γ term will be left as the subject of another paper.

For carbon steel, using thermophysical properties found in Refs. 19-21 and an absorption coefficient A of 0.40, the constants α and β are computed to be $\alpha = 3.40$ and $\beta = 1.28$. When Eq. (1) is plotted (not shown) for carbon steel using two values of the absorption coefficient A , 0.40 and 0.55 ($\alpha = 4.68$), the character of the curves are very similar to those of Fig. 7. Joecklé *et al.*⁴ found that the absorptivity of iron was approximately 3% higher than stainless steel at $1.06 \mu\text{m}$. Therefore it is reasonable to assume that a likely absorptivity range for carbon steel (similar to iron) will be a few percent higher than stainless steel, probably in the range 0.30 to 0.55. The actual workpieces of carbon steel which were used did have a dark iron-oxide layer which may increase the absorptivity; therefore, a reasonable absorption coefficient for the carbon steel data should be around 0.40-0.55. Eq. (1) models the data reasonably well, but again tends to curve upwards too steeply for lower values of $w_k v$. Using Eq. (2), an absorptivity of 0.55 ($\alpha = 4.68$) and setting $\gamma = 0.15$ provides a better fit to the carbon steel data (not shown). From a theoretical standpoint, the fact that COIL cuts carbon steel at approximately the same rate as

stainless steel is primarily a tradeoff between the effects of a higher absorption coefficient (more power absorbed) and a higher thermal conductivity (more energy dissipated) in carbon steel than in stainless steel.

Using thermophysical properties found in Refs. 19-21 and an absorption coefficient A of 0.13, the constants α and β are computed to be $\alpha=2.97$ and $\beta=2.40$ for aluminum. For comparison, Eq. (1) is plotted in Fig. 8 for aluminum using two values of the absorption coefficient A , 0.13 and 0.18 ($\alpha=4.11$). Fujioka² indicates an absorption coefficient of roughly 0.18 for aluminum with a commercial roughness at the COIL wavelength. It is clear from Fig. 8 that Eq. (1) models the data reasonably well, but again tends to curve upwards too steeply for lower values of $w_k v$. A better fit to the aluminum data is obtained with Eq. (2), an absorptivity of 0.18 ($\alpha=4.11$) and setting $\gamma = 0.22$, Fig. 8. Since there are only six aluminum data points, it is difficult to establish a better overall fit to the data.

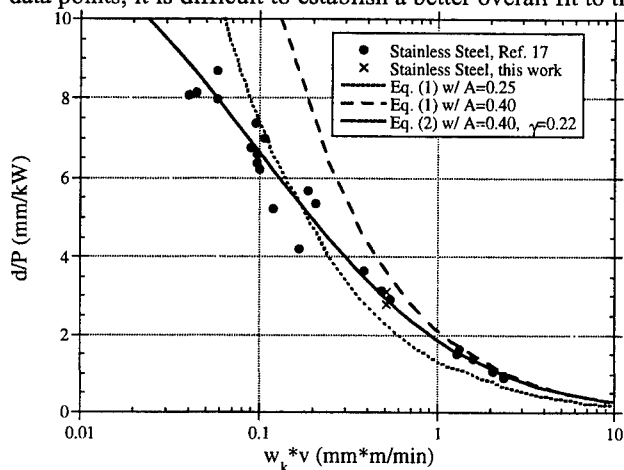


Fig. 7 Comparison of inert gas assist stainless steel COIL cutting data with theory.

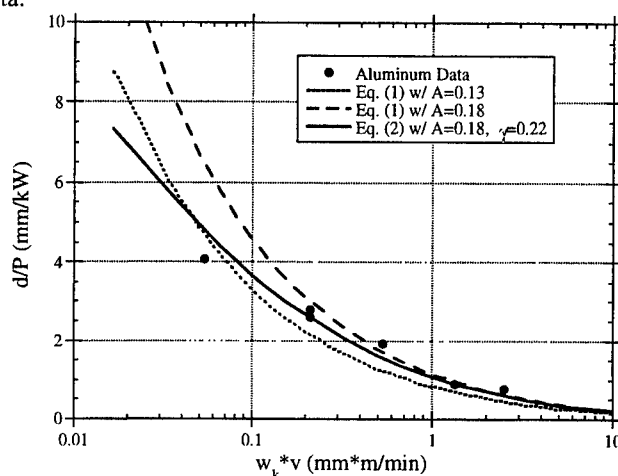


Fig. 8 Comparison of inert gas assist aluminum COIL cutting data with theory.

5. SUMMARY AND CONCLUDING REMARKS

A chemical oxygen-iodine laser (COIL) was used for cutting aluminum and carbon steel; these data represent an addition to the minimal COIL cutting database which exists for stainless steel. Cut depths of 20 mm were obtained in aluminum and 41 mm in carbon steel using an N_2 gas assist and 5-6 kW of power on target. The same laser at the same power level produced a cut depth of 65 mm in carbon steel with an O_2 gas assist; a low quality cut to a depth of nearly 100 mm in carbon steel was demonstrated.

COIL cuts carbon steel and stainless steel at approximately the same rate. When these data are compared with existing CO_2 laser cutting data, it is found that for a given cut depth, power and spot size, COIL cuts steel approximately three times faster than a CO_2 laser using an inert gas assist. COIL cutting speeds in carbon steel are improved by approximately a factor of three when an O_2 assist is used in lieu of an N_2 gas assist. With an N_2 gas assist, COIL cuts aluminum at approximately the same rate as CO_2 cuts steel. This finding may have important implications for COIL as an excellent laser for aluminum cutting/welding/drilling applications.

COIL and Nd:YAG cut steel at approximately the same rate when using either an inert or an oxygen gas assist. Since the wavelength of COIL and Nd:YAG are roughly the same, this is not a surprising result. However, Nd:YAG has power levels which are limited to roughly 5 kW or less (at the present time) and as such it is difficult (if not impossible) for Nd:YAG to cut very thick steel. Since COIL cuts metal faster than CO_2 lasers, and Nd:YAG lasers are presently limited in power level, COIL has considerable potential as a high power (> 5 kW) industrial laser.

These data were compared with an existing laser cutting model. Using thermophysical data for stainless steel, carbon steel and aluminum, this theory agrees reasonably well with the data. However, there is some divergence between the model and data for low values of $w_k v$. To improve the agreement between the model and data at lower values of $w_k v$, an empirical correction factor was added to the existing cutting theory; this modification produced excellent agreement with the data. A more formal derivation of this additional term will be left as the subject of another paper. The theory still needs to have a reactive term added to model O_2 gas assist data.

To obtain a better value for the empirical correction factor γ as a function of the material being cut, more carbon steel and aluminum data should be taken. The acquisition of more data using a shorter focal length lens arrangement and a beam with fewer transverse modes is desirable. Improvements to the oxygen assist technique should be made and more data taken

with an O₂ gas assist. Undoubtedly, much can be learned from existing CO₂ reactive gas assist cutting technology. One possibility is to use an air gas assist with around 1000 kPa (145 psia) plenum pressure. Such a high pressure air assist would provide roughly the same amount of oxygen as used in these tests, but would provide a larger momentum with which to blow molten material out of the cut, as well as increase the convective heat loss; these effects should reduce the amount of reactive melting in the workpiece and improve the quality of the cut. Another possible improvement is the commonly used practice of cutting downwards (rather than horizontally); this allows gravity to help pull molten material out of the cut region.

6. ACKNOWLEDGEMENTS

This work was supported by STI Optronics through COIL STTR AFPL contract F29601-95-C-0204. Testing was contributed by the Applied Laser Technology Branch of the Phillips Laboratory. The authors would like to thank A. Kar for useful conversations and L. Rothenflue for some of the thermophysical properties information.

7. REFERENCES

- ¹ D. Belforte and M. Levitt, *The Industrial Laser Annual Handbook, 1990 Edition*, PennWell Books, Tulsa, Oklahoma, xvi (1990).
- ² T. Fujioka, *Infrared Phys.*, **32**, 81 (1991).
- ³ I. J. Spalding, T. Stamatakis, G. Wlodarczyk, and J.H.P.C. Megaw, "Industrial Laser Developments in the UK," AIAA Paper 93-3152 (1993).
- ⁴ R. Joecklé, B. Gautier, J. Nett, M. Schellhorn, A. Sontag, and G. Stern, "Laser-Material Interactions with Short-Wavelength Infrared Lasers," AIAA Paper 95-1921 (1994).
- ⁵ W.E. McDermott, N.R. Pchelkin, D.J. Benard, and R.R. Bousek, *Appl. Phys. Lett.*, **32**, 469 (1978).
- ⁶ K.A. Truesdell, S.E. Lamberson, and G.D. Hager, "Phillips Laboratory COIL Technology Overview," AIAA Paper 92-3003 (1992).
- ⁷ P.V. Avizonis and K.A. Truesdell, "Historical Perspectives of the Chemical Oxygen-Iodine Laser (COIL)," AIAA Paper 94-2416 (1994).
- ⁸ S. Yoshida, H. Fujii, T. Sawano, M. Endo, and T. Fujoka, *Appl. Phys. Lett.*, **51**, 1490 (1987).
- ⁹ H. Fujii, S. Yoshida, M. Iizuka, and T. Atsuta, *J. Appl. Phys.*, **66**, 1033 (1989).
- ¹⁰ K. Shimizu, T. Sawano, T. Tokuda, S. Yoshida, and I. Tanaka, *J. Appl. Phys.*, **69**, 79 (1991).
- ¹¹ F. Wani, N. Naitou, T. Nagai, M. Iizuka, H. Tsuji, and H. Fujii, "Development of 1 kW CW Iodine Laser for Industrial Use," *Proceedings of Laser Advanced Materials Processing (LAMP '92)*, Niigata, Japan, 127 (1992).
- ¹² K.A. Truesdell, T. Lonergan, C. Wisniewski, K. Healey, J. Scott, and C. Helms, 1994, "COIL Thermal Management," AIAA Paper 94-2441 (1994).
- ¹³ S. Phipps, C.A. Helms, and K.A. Truesdell, 1994, "Compact CW Supersonic Chemical Oxygen Iodine Laser (COIL)," AIAA Paper 94-2453 (1994).
- ¹⁴ T.L. Rittenhouse, S.P. Phipps, C.A. Helms, and K.A. Truesdell, "High efficiency operation of a 5 cm gain length supersonic chemical oxygen-iodine laser," *Gas and Chemical Lasers*, International Society for Optical Engineering, Vol. 2702, 333 (1996).
- ¹⁵ J.E. Scott, and K.A. Truesdell, "Industrialization of the Chemical Oxygen-Iodine Laser," *Space Instrumentation and Dual-Use Technologies*, International Society for Optical Engineering, Vol. 2214, 188 (1994).
- ¹⁶ K. Yasuda, T. Atsuta, T. Sakurai, H. Okado, A. Hayakawa, and J. Adachi, "Study on material processing of Chemical Iodine Laser," in *Proceedings of the 3rd JSME/ASME Joint International Conference on Nuclear Engineering*, 1769 (1996).
- ¹⁷ A. Kar, J. E. Scott and W. P. Latham, "Theoretical and experimental studies of thick-section cutting with a chemical oxygen-iodine laser (COIL)," *J. Laser Applications*, **8** (3), 125 (1996).
- ¹⁸ R. Hack, F. Dausinger, and H. Hügel, "Cutting and Welding Applications of High Power Nd:YAG Lasers with High Beam Quality," in *Laser Materials Processing, Proceedings of ICALEO '94*, edited by T.D. McCay, A. Matsunawa and H. Hügel, International Society for Optical Engineering, Vol. 2500, Orlando, Florida, 210 (1994).
- ¹⁹ D.R. Lide, editor, *CRC Handbook of Chemistry and Physics, 74 Edition*, CRC Press, Ann Arbor, 12-134 (1993).
- ²⁰ F.P. Incropera and D.P. DeWitt, *Fundamentals of Heat and Mass Transfer, 3rd Edition*, John Wiley and Sons, New York, A4 (1990).
- ²¹ D. R. Gaskell, *Introduction to Metallurgical Thermodynamics, 2nd Edition*, Hemisphere Publishing Corporation, New York, 142 (1981).

Comparative Studies of Metal Cutting with High Power Lasers

J. Xie and A. Kar, Center for Research and Education in Optics and Lasers (CREOL), Department of Mechanical and Aerospace Engineering, University of Central Florida, Orlando, FL 32816-2700

J. Rothenflue and W.P. Latham, Philips Laboratory, LIDB and LI, 3550 Aberdeen Avenue SE, Kirtland Air Force Base, Albuquerque, New Mexico 87117-5776

ABSTRACT

The most widely used high power industrial lasers are Nd:YAG and CO₂ lasers. Chemical Oxygen Iodine Laser (COIL), whose wavelength (1.315 μm) is between that of YAG (1.06 μm) and CO₂ (10.6 μm) lasers, is another high power laser for industrial applications. The cutting capability of these lasers is investigated. The cut depth depends strongly on the absorptivity of materials, kerf width and cutting speed. Absorptivity is an unknown parameter for which experimental data at high temperatures are unavailable. Theoretical values of the absorptivities of various metals are obtained using Hagen-Rubens's relation. It is found that the absorptivity of metals is linearly proportional to the square root of resistivity and inversely proportional to the square root of the wavelength. The absorptivities of COIL and YAG lasers are 2.84 and 3.16 times larger than that of CO₂ laser, respectively. Based on the theoretical values of absorptivity, the cut depth of metals are analyzed for various laser powers, cutting speeds for these lasers. Due to the wavelength dependence of absorptivity, the cut depths for COIL and YAG lasers are expected to be 2.84 and 3.16 times deeper than that for CO₂ laser.

Keywords: absorptivity, cutting capability, CO₂ laser, COIL, YAG laser, high power

1. INTRODUCTION

Laser cutting is one of most popular applications of high power lasers [1-3]. CO₂ and YAG lasers are recognized as major lasers for metal cutting [2-3]. Chemical Oxygen-Iodine Laser (COIL) invented by McDermott et al. in 1977 [4] has the advantage of both the high power of CO₂ laser and short wavelength of YAG laser. COIL can generate power as high as a CO₂ laser and its wavelength (1.315 μm) is close to that of YAG laser. Since COIL and CO₂ are flowing gas lasers, they can have near diffraction-limited optical quality at very high powers. That is, they are not limited by thermal defocusing as the power increases. A COIL beam can be focused to a smaller spot than a CO₂ laser beam to produce higher intensity for a given power because of the shorter wavelength. Also, due to shorter wavelength, the absorptivity of a materials at the wavelength of COIL is higher than that at the wavelength of CO₂ laser. In comparison to a Nd:YAG laser, the absorptivity of a material for COIL is slightly less than that for the Nd:YAG laser due to the shorter wavelength. Also, a Nd:YAG laser beam can be focused to a smaller spot and therefore, it can produce higher intensity than a COIL beam for a given power.

The material processing capability of COIL was investigated by Atsuta et al. [5] using the ALEC COIL to cut stainless steel up to 5 mm thick. They demonstrated that the cutting capability of a 1 kW COIL is equivalent to that of a 1 kW Nd:YAG laser and about 2.5 times better than a 1 kW CO₂ laser. Other studies on cutting with COIL can be found in Refs. [6-9]. This paper is concerned with the cutting capability of the CO₂, COIL and YAG lasers.

2. ABSORPTIVITY OF METALS

The absorptivity of materials, which is an important parameter in laser materials processing, depends on the temperature, phase of the material and the surface conditions of the workpiece. However, the surface condition has little effect on the absorption of laser energy in the case of cutting and welding because the surface

of the workpiece melts in a very short time after the high power laser irradiation begins. In this study, the absorptivities for CO₂, COIL and YAG lasers are obtained by using the Hagen-Ruben relation as given below

$$A_{CO_2} = 112.2\sqrt{\rho} \quad (1)$$

$$A_{COIL} = 318.43\sqrt{\rho} \quad (2)$$

$$A_{YAG} = 354.67\sqrt{\rho} \quad (3)$$

For aluminum,

$$\rho = 10^{-8}(-1.0 + 1.25 \times 10^{-2}T) (\Omega\cdot m) \quad \text{for } 273K \leq T \leq 933K \quad (4)$$

$$\rho = 10^{-8}(10.7 + 1.45 \times 10^{-2}T) (\Omega\cdot m) \quad \text{for } 933K \leq T \leq 1473K \quad (5)$$

and for stainless steel,

$$\rho = 10^{-8}(60 + 5 \times 10^{-4}T) (\Omega\cdot m) \quad \text{for } 273K \leq T \leq 1700K \quad (6)$$

Using Eqs. (1) and (4-8), the absorptivity for aluminum is found to be 1.86, 5.28 and 5.88 at the room temperature and 6.4, 18.2 and 20.2 at the melting temperature for CO₂, COIL and YAG lasers respectively. Similarly, the absorptivities for stainless steel are 9.72, 27.57 and 30.72 at the room temperature and 14.0, 39.7 and 44.2 at the temperature of solid phase change (phase β) for CO₂, COIL and YAG lasers respectively.

3. RESULTS AND DISCUSSION

The values of ρ_0 , c_p , L_b , L_m , T_m , k , α are 2.7×10^3 kg/m³, 8.99×10^2 J/kgK, 1.13×10^7 J/kg, 9.7×10^4 J/kg, 633 K, 92 W/mK, 3.8×10^{-5} m²/s respectively for aluminum, and the values of ρ_0 , c_p , L_b , L_m , T_m , k , α are 7.9×10^3 kg/m³, 5.02×10^2 J/kgK, 6.95×10^6 J/kg, 3×10^5 J/kg, 1700 K, 30.4 W/mK, 4.9×10^{-5} m²/s respectively for stainless steel. Kar et al. [6] presented the following expression to predict the cutting capability of high power lasers.

$$\frac{d}{P} = \frac{A_0}{v w_k + A_3 \sqrt{v w_k}} \quad (7)$$

where the coefficients A_0 and A_3 are defined as

$$A_0 = \frac{10^6 A}{a_0} \quad (7a)$$

$$A_3 = 4.08 \times 10^{-3} \times \frac{l}{a_0} \frac{w_k + 2l}{\sqrt{l w_k}} \frac{k(T_m - T_0)}{2\sqrt{\alpha}} \quad (7b)$$

$$\text{and} \quad a_0 = 1.67 \times 10^{-5} \rho_0 [c_p(T_m - T_0) + L_m + \beta L_b] \quad (7c)$$

Here, d , l and w_k are given in units of mm, v is in m/min and P is in kW. All other variables are in SI units. The mathematical model is based on the rectangular cross-section of COIL beam. To compare the cutting capabilities of COIL, CO₂ and YAG lasers, it is assumed that the CO₂ and YAG laser beams are focused to rectangular spots by using appropriate focusing lens. It should be noted that A_3 is the coefficient of the conduction heat loss term. Although A_3 can be calculated using Eq. (7b), it can be used as an adjustable parameter to approximately account for all heat losses.

Figures 1-4 show the increase in absorptivity and the improvement in cutting capability of the COIL and YAG lasers compared to the CO₂ laser for various metals. These figures also show the variation of conduction heat loss with temperatures. The absorptivities of COIL and YAG lasers are 2.84 and 3.16 times higher than that of CO₂ laser, respectively. The cut depths of COIL and YAG lasers are also expected to be 2.84 and 3.16 times deeper than that of CO₂ laser since the cut depth expressed in Eq. (6) is linearly proportional to absorptivity. This is based on the assumption that the incident laser beam is normal to the surface of the workpiece and is reflected by the flat surface. However, it should be noted that the total absorption of laser energy by the workpiece depends on (i) the absorptivity, and (ii) the effect of the geometry around the cut region. For large cut depth in thick-section workpieces, the total absorption of laser energy will increase due to multiple reflections of the incident beam in the kerf. For example, the absorption can be very high (almost 100%) in laser key-hole welding irrespective of the thermophysical and optical properties of the workpiece. Because of this increase in the absorption of laser energy due to the geometrical effect, the cut depth, in practice, will be a little higher than that

derived from this model for thick-section workpieces. For thick-section cutting, the increase in the absorption of laser energy may improve the cutting capability of CO₂ laser more than that for COIL and YAG lasers. This is because the absorption will become 100% for all lasers and for thick-section due to multiple reflections of the laser beam around the cut region. Therefore, the cutting capability of COIL and YAG laser are expected to be smaller than 2.84 and 3.16 times that produced by the CO₂ laser respectively [5].

4. CONCLUSIONS

The absorptivity of materials is linearly proportional to the square root of resistivity and inversely proportional to the square root of wavelength as expressed by the Hagen-Ruben relation. The variation of absorptivity with the wavelength of the incident radiation and the temperature and phase of the workpiece indicates that the absorptivities of metals for COIL and YAG laser are 2.84 and 3.16 times higher than that for CO₂ laser respectively. For identical cutting parameters, the cut depths produced by COIL and YAG laser are almost identical and are, respectively, 2.84 and 3.16 times deeper than that for CO₂ laser. The differences in the cutting capability of the COIL, CO₂ and YAG lasers decrease at high speed cutting, and for thick-section cutting due to multiple reflections around the cut region.

Nomenclature: A - Absorptivity of metals, A_{CO_2} , A_{COIL} , A_{YAG} - Absorptivities for CO₂, COIL and YAG lasers, c - Speed of light in vacuum, c_p - Specific heat of metals at constant pressure, d - Kerf depth, k - Thermal conductivity, l - Length of the rectangular laser beam, L_b - Latent heat of boiling, L_m - Latent heat of melting, P - Power of the incident laser beam, T_0 - Initial temperature of metals, T_m - Melting temperature of metals, T_b - Boiling temperature of metals, v - Velocity of the cutting, w_k - Kerf width

Greek Symbols: α - Thermal diffusivity of the metals, β - Boiling coefficient, the fraction of the kerf width above the boiling temperature (assuming $\beta=0.1$), ϵ_0 - Permittivity of free space, $\epsilon_0=1/(36\pi\times 10^9)$ F/m, λ - Wavelength of laser in vacuum, ρ - DC resistivity of the metals, ρ_0 - Density of the materials, ω - Angular frequency of the monochromatic radiation, $\omega=2\pi\nu/\lambda$

5. ACKNOWLEDGMENT

This work was done at the Center for Research and Education in Optics and Lasers (CREOL) in the University of Central Florida under AFOSR contract number: F49620-93-C0063.

6. REFERENCES

- [1] D. Schuocker, Laser Cutting, in The Industrial Laser Annual Handbook, D. Belforte and M. Levitt, Editors, (PennWell Books, Tulsa, Oklahoma), 1986, pp.87-107.
- [2] J. Powell, Guidelines and Data for Laser Cutting, in The Industrial Laser Annual Handbook, D. Belforte and M. Levitt, Editors, (PennWell Books, Tulsa, Oklahoma), 1990, pp.56-57.
- [3] W. M. Steen, Laser Materials Processing, Springer-Verlag, New York, 1991, p. 47.
- [4] W. E. McDermott, N.R. Pchelkin, D. J. Benard and R. R. Bousek, An Electronic Transition Chemical Laser, Appl. Phys. Lett., 32, 1978, pp.469-470.
- [5] T. Atsuta, K. Yasuda, T. Matsumoto, T. Sakurai and H. Okado, COIL and the Material Processing, in Conference on Lasers and Electro-Optics (CLEO)'94, Vol. 8, 1994, OSA Technical Digest Series (Optical Society of America, Washington, D. C.), 1994, p.351.
- [6] A. Kar, J. E. Scott and W. P. Latham, Theoretical and Experimental Studies of Thick-section Cutting with a Chemical Oxygen-Iodine Laser (COIL), J. Laser Applications, Vol.8, 1996, pp. 125-133.
- [7] A. Kar, J. E. Scott and W. P. Latham, Effect of Mode Structure on Three-dimensional Laser Heating due to Single or Multiple Rectangular Laser Beams, J. Appl. Phys., Vol. 80, 1996, pp. 667-674.
- [8] J. Xie and A. Kar, Analysis for the Laser Welding of Copper, Proc. ICALEO'95, Edited by J. Mazumder, A. Matsunawa and C. Magnusson, (Laser Institute of America, San Diego, California, 1995).
- [9] D. L. Carroll and J. A. Rothenflue, Experimental Study of Cutting Thick Aluminum and Steel with a Chemical Oxygen-Iodine Laser Using an N₂ or O₂ Gas Assist, XI Inter. Symp. Gas Flow and Chemical Lasers and High Power Laser (GCL/HPL'96), Edinburgh, Scotland, UK, 25-30 August, 1996.

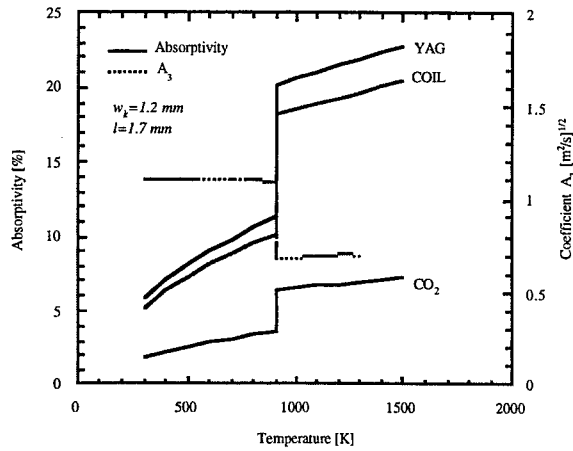


Fig. 1. Absorptivity of CO₂, COIL and YAG lasers and coefficient A_3 for aluminum.

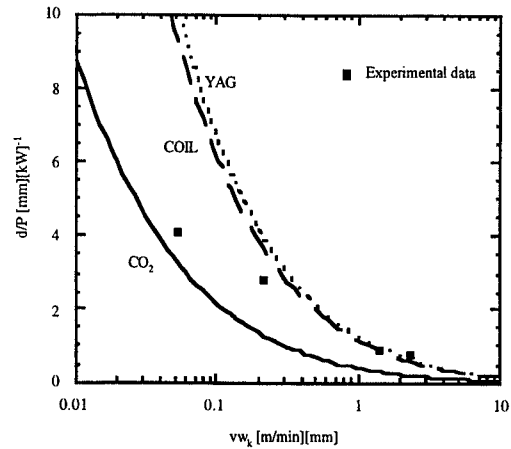


Fig. 2. CO₂, COIL and YAG laser cutting of aluminum. The experimental data are for cutting aluminum using COIL and N₂ as the cutting gas [6].

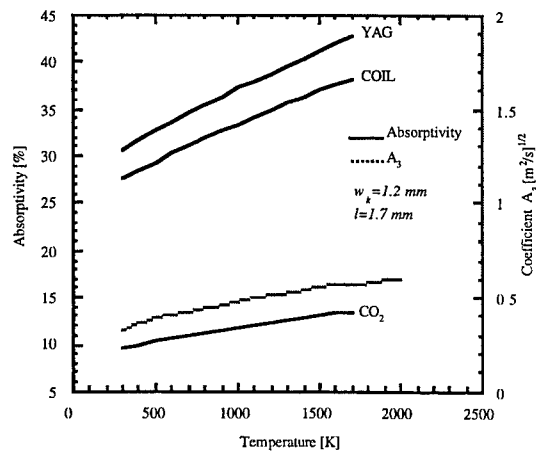


Fig. 3. Absorptivity of CO₂, COIL and YAG lasers and coefficient A_3 for stainless steel (AISI 304).

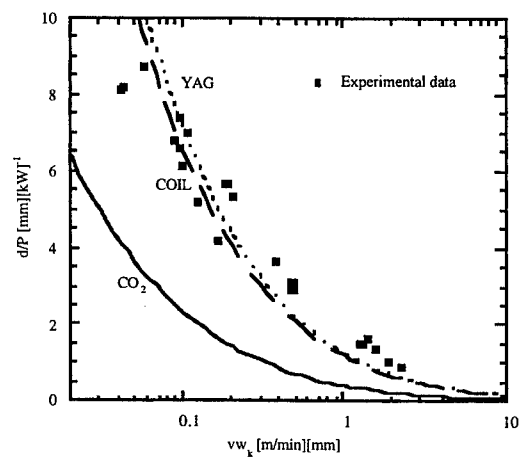


Fig. 4. CO₂, COIL and YAG laser cutting of stainless Steel (AISI 304). The experimental data are for cutting 400-series stainless steel using COIL and N₂ as the cutting gas.

Laser system technology for an improved workpiece tracking in 3D-CO₂-laser beam cutting

Norbert Neubauer¹, Peter Hoffmann¹

Manfred Geiger²

¹Bayerisches Laserzentrum
Schallershofer Straße 108
91056 Erlangen

²Lehrstuhl für Fertigungstechnologie
Egerlandstraße 11
91058 Erlangen

ABSTRACT

The integration of adaptive optics into the working head of a CO₂ laser machine allows the variable adjustment of the focus position in relation to the workpiece. The parallel gas flow produced by Laval nozzles allows the laser cutting with a nozzle distance of up to 15 mm. A new method for laser cutting of three dimensional workpieces is possible by a specially designed working head with adaptive optics and Laval nozzles.

Keywords: CO₂ laser, laser cutting, Laval nozzle, adaptive optics, 3D processing, production systems

1. INTRODUCTION

The technology of three-dimensional laser cutting is applied in short-run productions as well as mass productions for example in applications of the automotive industry. Modern laser systems have devices for the adjustment of the process parameters. Focus position and working distance are usually kept constant by a capacitive closed loop control. A common solution for the cutting of edges is the reduction of the cutting speed and laser output power and the inclination of the cutting head against the normal of the workpiece surface.¹ Nevertheless there remains a category of workpiece elements, where conventional laser system technology is not sufficient. Examples are crimps and the inner contour of edges: the geometry of the workpiece doesn't allow the processing as required for optimum cut quality. For the cutting of the inner contour of an edge the nozzle cannot be kept at the required distance in order to avoid collisions with the workpiece. A new method for the laser cutting of these workpieces is possible with a system with variable focus position and nozzle distance. The setup of a focussing head with variable focus position through the integration of adaptive optics is discussed. The characterisation of Laval nozzles for the laser beam cutting with variable working distances allows the demonstration of this method for contoured workpieces and inner edges.

2. SETUP OF THE WORKING HEAD

In laser materials processing so called adaptive optics are copper mirrors with a variable focal length. The deformation of the mirror plate can be mechanically controlled by the variation of the coolant pressure² or by an piezoelectric actuator which is placed centrally at the backside.³ Adaptive optics have been successfully used in laser beam cutting for the compensation of varying beam paths length between laser source and focussing optics in systems with flying optics.⁴ Another application is the variable focus shift which is achieved by integrating the adaptive optics into the working head.^{5,2} In the following setup adaptive optics from Diehl (Nuremberg, Germany) are used. The mirror plate is deformed by a piezoelectric actuator which allows frequencies of up to

200 Hz. With actuator strokes from $-20\text{ }\mu\text{m}$ to $+20\text{ }\mu\text{m}$ this type of adaptive optics has a focal length from $+2.5\text{ m}$ to ∞ to -2.5 m .

The system was designed to achieve a variable focus shift with minimum aberrations in the focussed laser beam. Parameters of the setup as the angle between incident and reflected laser beam at the adaptive optics have been optimized by wave optical simulations of the beam propagation. If the angle is too wide, astigmatism distorts the focus. A maximum angle of 36° was calculated in accordance with experimental results. Another important parameter is the laser beam diameter on the adaptive optics. As result of the principle of the deformation of the mirror plate only the central part of the mirror surface is spherical. A Shack-Hartmann sensor was used for the measurement of the wavefront of a HeNe laser beam reflected by an adaptive optics. By wave optical simulations the maximum laser beam diameter for an acceptable distortion of the reflected laser beam was calculated as 12 mm. Nevertheless larger beam diameters are possible: experiments in laser beam welding and laser beam cutting of mild steel DC04 showed that a beam diameter of up to 17 mm is allowed without a substantial reduction of the processing speed.

A new processing head was constructed and built for the laser machine TLC105. The machine consists of a rf-excited 5kW CO_2 -laser and a five axis gantry handling system. The adaptive optics is integrated in the beam guiding system at a reflection angle of 36° with a distance of 200 mm to the focussing optics. The adaptive optics can be combined with the standard focussing heads for laser beam welding and laser beam cutting. Fig. 1 shows an photograph of the processing head. The diagram plots the characteristic curve of the focus shift as a function of the actuator stroke of the adaptive optics. With a focal length of 7.5" a focus shift in the range of 24 mm is possible.

Laval nozzles have been proposed for laser cutting because of higher possible cutting speeds and a reduction of dross.^{6,7} If used at design pressure a Laval nozzle produces a supersonic gas flow with low lateral expansion which is able to transport a high momentum into the cut kerf. But a further feature of this nozzle type was not used before: Laval type nozzles produce a parallel supersonic gas beam over a working distance of several millimetres. The combination with a variable focus shift using adaptive optics makes a new method for 3D laser beam cutting possible.

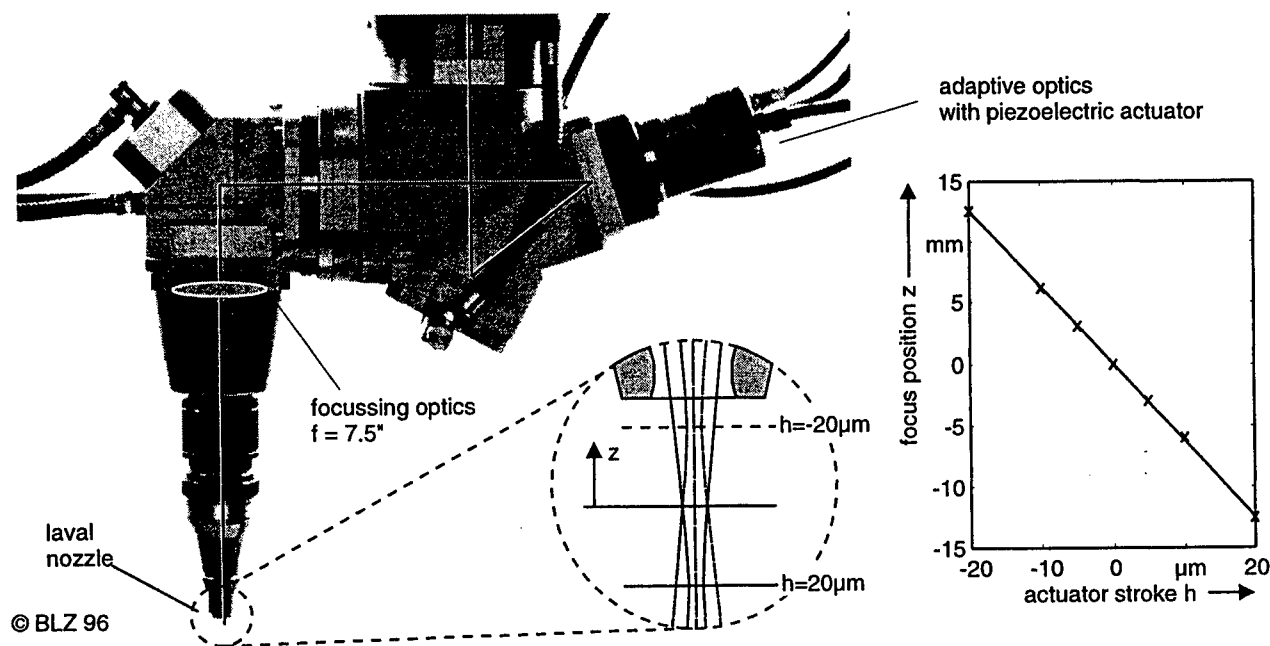


Figure 1: Focussing head for a 3D system with integrated adaptive optics, Laval nozzle and height sensor. The diagram shows the characteristic curve for the focus shift as a function of the actuator stroke.

Laval nozzles with a design pressure of 0.25 MPa and 0.50 MPa were examined in combination with a variable focus position by using the working head shown in fig. 1. The investigation of the gas flow characteristics of the nozzles with a Schlieren setup showed that a working distance of up to 15 mm is possible. Mild steel DC04 with a thickness of 1 mm was cut for nozzle distances from 1 to 15 mm with a laser power of 1.7 kW. For a distance of up to 10 mm between nozzle and workpiece a dress free cut at 9 m/min could be obtained. For larger distances from 10 to 15 mm the speed had to be reduced to 6 m/min. For the cutting of three-dimensional workpieces an inclination between the working head and the normal of the workpiece is often necessary. The maximum angle for an inclination of the working head in the direction of the cut was found at 25° for nozzle distances of up to 15 mm. An inclination of up to 45° against the direction of the cut is possible. The same results could be obtained for the cutting of the workpiece with a linear ramp from a nozzle distance of 1 mm to a distance of 15 mm and a simultaneous focus shift by the adaptive optics.

3. ADVANCES IN 3D-LASER BEAM CUTTING

Laser beam cutting with conventional system technology is problematic for workpieces as shown in Fig. 2. For cutting a contoured workpiece the nozzle cannot follow the workpiece in the crimps because of danger of collision. Identical problems occur for the cutting of an inner edge of workpieces where the outer edge cannot be accessed. The new system technology with adaptive optics and Laval nozzle as described above allows a new method for an improved workpiece tracking. The machine is programmed with a smoothed path for the nozzle while the focus is kept on the surface by the adaptive optics. The constant gas flow produced by the Laval nozzle allows the variation of the distance between nozzle and workpiece. Fig. 2 shows the beam entrance and exit side of

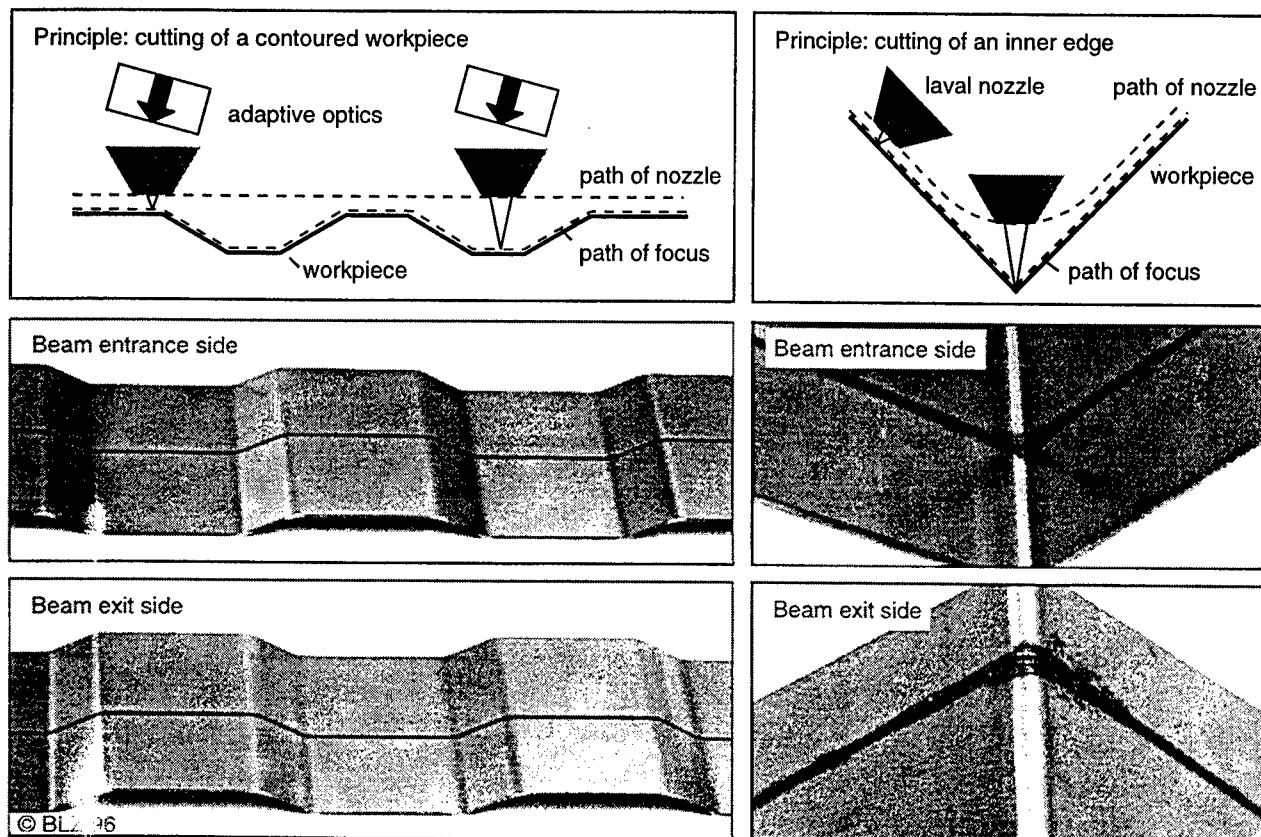


Figure 2: Test workpieces showing the possibilities of laser cutting with adaptive optics and Laval nozzles: beam entrance and exit side of the laser cut of a contoured workpiece and an inner edge.

two workpieces. The contoured workpiece was cut with a laser power of 1.25 kW at a speed of 3 m/min. The nozzle distance varied between 1 and 9 mm, the angle of the sides is 30°. The inner contour of a 90° edge was cut with a laser power of 1.6 kW at a speed of 3 m/min. In the edge which was bend with a radius below 1 mm a small zone of heat influence can be observed at the beam exit side. For larger radii starting at 2 mm a cut with constant quality can be achieved.

4. SUMMARY

Combining adaptive optics for the adjustment of the focus position with Laval nozzles which produce a parallel gas flow leads to a new method for three dimensional laser beam cutting. The cut quality can be improved for contoured workpieces and for inner edges. A height sensor can be used for the automatic adjustment of the focus position resulting in a system which can be programmed very easily because the required accuracy of the distance between nozzle and workpiece is in the range of ± 5 mm. The concept can easily be transferred to the laser beam welding where the gas flow characteristics are easier. The laser induced plasma requires new concepts for a distance sensor as already presented with the same laser system.⁸

5. ACKNOWLEDGEMENT

The investigations are supported by Diehl GmbH & Co., Nuremberg, Trumpf GmbH & Co., Ditzingen and the "Bayerische Forschungsförderung" within the FORLAS program.

6. REFERENCES

- [1] Kallies, B.: *Laserstrahlschneiden von Blechformteilen*. München: Hanser (1995).
- [2] Bea, M.; Glumann, C.; Grünwald, B.; Rapp, J.; Giesen, A.; Hügel, H.: Flexible beam delivery for improved laser applications. Proc. SPIE Vol. 2207 (1994), pp. 111-124.
- [3] Bär, K.; Freisleben, B.; Kozlik, C.; Schmiedl, R.: Adaptive Optics for industrial CO₂ laser systems. *Lasers in Engineering* 4 (1995), pp. 233-242.
- [4] Neubauer, N.; Hoffmann, P.: Enlarged productivity in laser material processing by the use of Adaptive Optics. In: Ahlers, R.-J.; Hoffmann, P.; Lindl, H.; Rothe, R. (Hrsg.). *Laser Materials Processing and Machining*. Proc. SPIE Vol. 2246 (1994), pp. 198-205.
- [5] Geiger, M.; Neubauer, N.; Hoffmann, P.; Hutfless, J.: Adaptive beam delivery for CO₂ laser material processing. In: Mazumder, J. (ed.). *Laser Processing: Surface Treatment and Film Deposition (Proceedings of the NATO ASI 1994 in Sesimbra)* (1994) to be published.
- [6] Edler, R.; Berger, P.; Hügel, H.: Performance of various nozzle designs in laser cutting. In: Mordike, B. (ed.). *Laser Treatment of Materials*. Proc. ECLAT'92: Göttingen DGM Informationsgesellschaft mbH Oberursel, (1992), pp. 111-116.
- [7] Leidinger, D.; Penz, A.; Schuöcker, D.; Deinzer, G.; Geiger, M.; Hänsel, A.; Herbig, N.: Nozzle Design and Simulation of Gas Flow For The Laser Cutting Process. In: *Laser Materials Processing: Industrial and Microelectronics*. Proc. SPIE Vol. 2207 (1994), pp. 469-479.
- [8] Hoffmann, P.; Schuberth, S.; Zuber, M.: Quality control loops for precision laser beam welding. In: Proc. ECLAT 96 Stuttgart, to be published.

CW CO₂ laser cutting of plastics

P.A. Atanasov

Institute of Electronics, Bulgarian Academy of Sciences
72, Tsarigradsko Shose Blvd., Sofia 1784, Bulgaria

M.G. Baeva

Department of Physics, Technical University of Varna, Varna 9010, Bulgaria

ABSTRACT

CW CO₂ laser cutting of plastics is studied experimentally and theoretically. Cutting of plates of PMMA, teflon-PMMA-teflon sandwich structure, and Si-rubber is presented. A three dimensional heat transfer model of laser cutting with a moving Gaussian heat source is elaborated and applied here. The model is based on the energy balance for a given small volume in the material. The maximal scanning speed as a function of the incident laser power and the material thickness is investigated. A very good agreement between the theoretical and experimental data is observed.

Keywords: CO₂ laser; cutting; plastics; modeling; technology.

1. INTRODUCTION

The laser material processing is nowadays a problem of great interest from the view points of its experimental investigation and theoretical simulations. Laser cutting of plastics is commonly used for machining of complex geometric form^{1,2}, combining the capabilities of automatic process control and CAD programming. Several papers concerning CO₂ laser cutting are published.³⁻⁶ In theoretical aspect the general aim is to describe the process as closer to reality as possible in order to obtain a good agreement with the experiment. Of course, the full physical picture is rather complicated and some simplifications are needed. Most of the works solve the heat conductivity equation for a stationary or a moving with respect to the laser beam solid. A review of works concerning laser technology and analysis of the interaction of laser radiation with materials can be found in Ref. 7. The fundamental heat and hydrodynamic processes in the laser material processing and electron beam treatment are given in Ref. 8. Some methods and solutions for the temperature field are considered. Another approach to the problem is the numerical modeling. A number of authors have considered models of the laser cutting process. Modest et al. have studied evaporative cutting of solid with a moving cw laser beam.^{9,10} A three-dimensional quasi-steady state model of heat transfer is developed by Mazumder et al.¹¹

The purpose of the present work is to present the results obtained for cw CO₂ laser cutting of several materials as plexiglass (PMMA), teflon-PMMA-teflon sandwich structure, and Si-rubber plates. A three-dimensional model, based on the energy balance is elaborated and applied here. The results of the model are compared to the experimental data for the first two materials. The dependencies of the maximal cutting speed as a function of the laser power and the material's thickness are given.

2. PHYSICAL AND MATHEMATICAL DEFINITION OF THE PROBLEM

We consider a Gaussian laser beam, striking the surface of a substrate, having semi-infinite thickness and infinite length, moving in the positive x -direction with a uniform velocity u . The laser power P_L is absorbed at the surface. The material properties (thermal conductivity coefficient K , specific heat capacity C , mass density ρ) we assume not dependent on the temperature. Once the material reaches the temperature T_r (removal temperature), it consumes some heat L_m (specific heat of removal). The evaporated material does not interact with the incoming laser beam.

The derivative of full energy with respect to time in a control volume V having a surface area S results from a transfer of full energy of the entering and the leaving the volume mass, internal heat sources and heat conductivity:¹²

$$\frac{\partial}{\partial t} \int_V \rho \left(\frac{u^2}{2} + \varepsilon \right) dV = - \int_S \rho \left(\frac{u^2}{2} + \varepsilon \right) \vec{u} \cdot d\vec{S} + \int_V Q_i dV - \int_S \vec{q} \cdot d\vec{S}, \quad (1)$$

where ε is the internal energy, Q_i is the power of internal energy sources and \vec{q} is the vector of the heat flow density. Taking into account the mass variation equation the Eq.(1) yields:

$$\frac{\partial}{\partial t} \int_V \rho C T dV + \int_S \rho C T \vec{u} \cdot d\vec{S} + \int_S \vec{q} \cdot d\vec{S} + \int_V \theta (T_r - T) \rho L_m dV = 0, \quad (2)$$

where $Q = Q_i - \frac{u^2}{2} Q_m = \theta (T - T_r) \rho L_m$. Here, Q_m is the mass sources power, $\theta(x)$ is the Heaviside's function¹³, and $\varepsilon = CT$. The last term on the left hand side of Eq.(2) presents the heat energy loss due to evaporation. It occurs only for the upper wall of the volume V . The heat energy flux through the other walls may be written as follows:

$$\frac{\partial}{\partial t} \int_V \rho C T dV + \int_S \vec{f} \cdot d\vec{S} = 0. \quad (3)$$

In Eq.(3) $\vec{f} = \rho C T \vec{u} + \vec{q} = \rho C T \vec{u} - K \nabla T$. The total energy absorbed by the surface is:

$$f_s = \frac{2aP_L}{\pi\omega^2} \exp \left[-2 \frac{(x-ut)^2 + y^2}{\omega^2} \right], \text{ where } \omega = \omega_0 \left[1 + \left(\frac{W+z}{\pi\omega_0^2 / \lambda} \right)^2 \right]^{1/2}. \quad (4)$$

Here, ω_0 is the effective radius at the focal plane, W is the distance between the focal plane of the beam and the material surface, a is the material absorption coefficient, and x, y, z are the Cartesian coordinates, respectively. The boundary conditions to the problem are:

$$x=x_{min}, y=y_{max} : T=T_{in}, \text{ and } x=x_{max}, y=y_{min}, z=z_{min} : \frac{\partial T}{\partial x} = 0, \text{ for } T_{in} - \text{the initial temperature.}$$

3. EXPERIMENTAL SET UP.

The laser system used in the experiments consisted of a cw 120 W TEM₀₀ mode CO₂ laser (BLS 120C - C.B.Lasertechnik GmbH), and two work stations. The first had a XYZ table, an Anorad Automatic II CNC controller with a pulse generator unit. The 17 mm diameter Gaussian laser beam was focused using a 127 mm ZnSe lens on the upper surface of the material. The nozzles fitted to the beam delivery system had exit borers of $\Phi_n=(1.2-1.8)$ mm. The nozzle-workpiece stand-off distance was (0.4-0.6) mm. Compressed air or N₂ were assisted during the cutting. Some cuttings (especially teflon-PMMA-teflon and Si-rubber) were performed by Comp II controlled galvanometer-based optical scanners - the second work station. Here, the laser beam was focused by a ZnSe-plane field lens with focal length of 100 mm and no assisted gas was applied.

4. RESULTS AND DISCUSSIONS

Fig. 1 presents the experimentally obtained maximum cutting speed as a function of thickness of the PMMA plates at 3 given values of the laser power. Here, some air was blowing out of the nozzle only to protect the focusing lens. The laser beam was focused on the surface of the work piece.

Important input parameters to the model providing its successful application are the material properties. They are taken or estimated by the description given in Ref. 14. The relevant material properties are summarized in Table. Of course, they should not be considered as absolute, because usually their values in the literature are available in an interval. The absorptivity a is found experimentally to be 0.92 for PMMA and 0.65 for teflon, respectively.

Material parameters	PMMA	Teflon
Removal temperature - T_r , K	433	600
Thermal conductivity - K , W/(m.K)	0.139	0.234
Density - ρ , kg/m ³	1180	2150
Heat capacity - C , J/(kgK)	1435	1050

Table. Values of the material properties used in the model

The model developed is applied to investigate the laser cutting parameters for Plexiglas and sandwich structure consisting of 3 layers: Teflon - Plexiglas - Teflon. The latter has fixed thickness of 500 μm (20 μm -460 μm -20 μm , respectively). The scanning speed and the laser power are varying parameters in the numerical simulation.

Fig.2 presents the results obtained for laser power of 90 W for Plexiglas. The maximal cutting speed is plotted as a function of the material thickness. Also, the experimental data are given for comparison. It is seen that the experimental points are close to the model's curve. It is worth noting that the agreement is very good nevertheless an assistant gas is not taken into account. Its role, however, is included indirectly. We assume that once the removal temperature in an elementary volume is reached, the volume is evaporated and it is not considered in the further calculation.

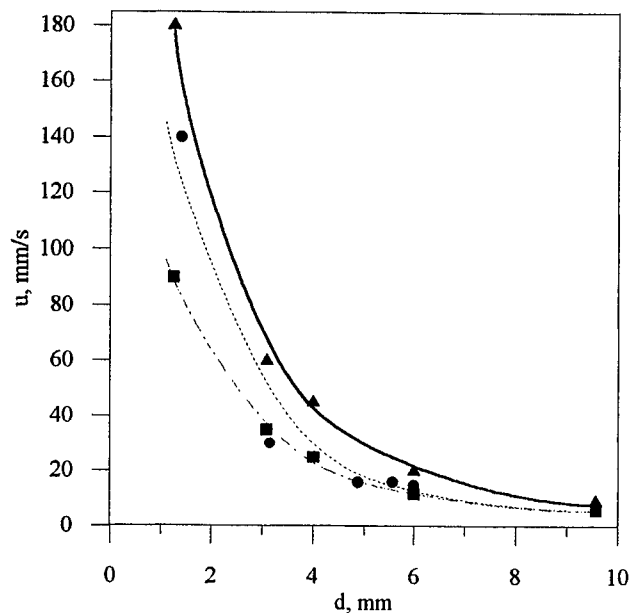


Fig.1 The dependence of the experimentally obtained maximum cutting speed on the material thickness for PMMA at different values of CO_2 laser power: \blacktriangle - $P_L = 120$ W; \bullet - $P_L = 90$ W; \blacksquare - $P_L = 60$ W.

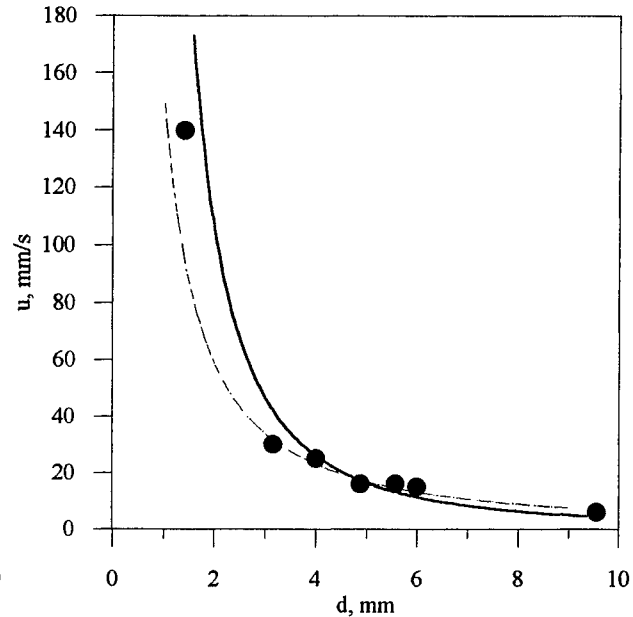


Fig.2 The maximum cutting speed versus the material thickness for PMMA. $P_L = 90$ W. Black circles - experimental data; solid line - modelling curve; dashed line - forecasting function.

It is interesting to expand the comparison by adding the standard processing curve, described by the simple equation¹⁵:

$$u = P_L Q d^{-B}, \quad (5)$$

where u is the maximal cutting speed (m/min), P_L is the laser power (W), d is the material thickness (mm), and Q and B are experimentally derived constants, which depend on the laser-focusing optics combination and the material, respectively. Experimental work¹⁶ shows that the value of B can be taken as 1.35 over a wide range of polymers. The average value of Q found by our experiment is estimated to be 0.0995. The forecasting function $u = u(d)$ is presented by a dashed curve on the Fig.2. This curve should not be accepted as absolute true, but it gives a kind of information about the model's reliability.

The results obtained for the sandwich structure mentioned above are shown on Fig.3. Here, the thickness is constant and the laser power is a varying parameter. The maximum scanning speed reached as a function of the laser power is investigated. The results demonstrate a linear behavior of this function which agrees with the empirical relation (5). It is

seen also, that the model's curve fits well the experimental data pointed on the graph.

Very delicate and precise gaskets are cut with high quality from Si-rubber. For thickness of 0.51 mm and 0.35 mm the best quality was achieved at the following cutting parameters: $P_L=17$ W at $u=30$ mm/s, and $P_L=85$ W at $u=160$ mm/s, respectively. No gas was assisted.

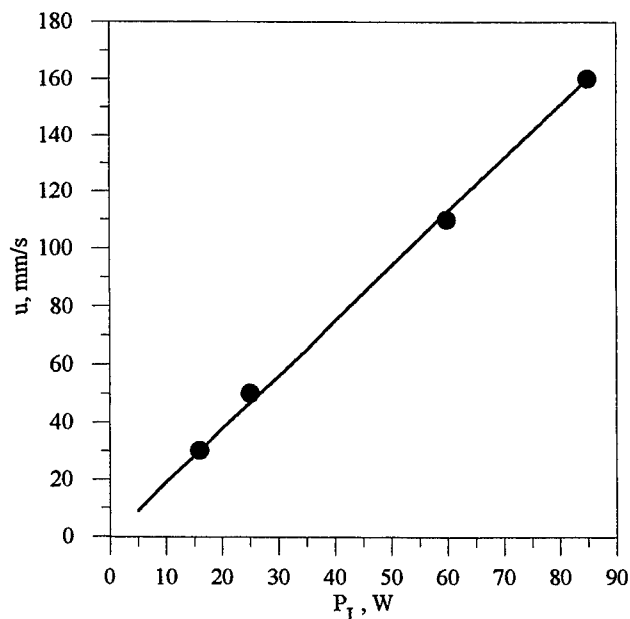


Fig.3 The dependence of maximum cutting speed on the laser power for teflon-PMMA-teflon sandwich structure. Circles - experimental data; solid line - modeling curve.

5. CONCLUSIONS

The three-dimensional model of the laser cutting process presented in this work could be used to predict maximum cutting speeds and thickness achieved for a given scanning speed. Also, the groove shape, the temperature distribution around the evaporated zone are available as output results. The effect of absorption, thermal conductivity or other parameters could be investigated, too.

Applied to polymers the model for laser cutting shows a very good agreement with experimental data. It is possible from the model to obtain the conditions such as the maximum cutting speed as a function of substrate thickness, or laser power and to use them as processing characteristics.

6. ACKNOWLEDGMENTS

This work is supported by the Bulgarian National Scientific Fund under Grants No. F-548/95 and No. F-425/94.

7. REFERENCES

1. Fr-J Trasser, *Laserstrahlschneiden von Verbundkunststoffen*, VDI-Verlag GmbH, Dusseldorf, **238**, 1992.
2. W. Konig, Fr-J Trasser, and W. Wetzels, "Using CAD/CAM-systems for process optimization during laser beam cutting and surface treatment", *Laser and Optoelektronik*, **23**, 62-66, 1991.
3. W. Konig and Fr-J Trasser, "Cutting of plastics using lasers: conflict between cut and quality and hazardous by-products", *Laser and Optoelektronik*, **25**, 37-42, 1993.
4. J. Powell et al., "Laser cutting of polymeric materials: an experimental investigation", *Proc. of LAMP*, Osaka, 273-278, 1987.
5. D. Schuocker, "Laser cutting", in *The industrial laser. Annual handbook*, ed. D. Belfore and M. Levitt, 87-107, 1986.
6. P. A. Atanasov, "Laser processing of plastics", *Proc. of SPIE*, **2502**, 632-637, 1994.
7. W.W.Duley, *Laser processing and analysis of materials*, Plenum-Press, NY-London, 1983.
8. N.N.Rykalina et al., *Laser and electron beam processing of materials*, Handbook, Moscow, 1985. (in Russian).
9. M.F.Modest, H.Abakians, "Evaporative cutting of a semiinfinite body with a moving cw laser", *J.Heat Transfer*, **108**, 602-607, 1986.
10. S.Ramanathan, M.F.Modest, "Cw laser cutting of composite ceramics", *Proc. of LAMP'92*, **1**, 625-632, Japan 1992.
11. J.Mazumder, W.M.Steen, "Heat transfer model for cw laser material processing", *J.Appl.Phys.*, **51**, N2, 941-947, 1980.
12. L.Landau, E.Lifshitz, *Course of theoretical physics. Fluid mechanics*, **6**, Pergamon Press, Moscow, Nauka, 1988.
13. M.Reed, B.Simon, *Methods of modern mathematical physics. Functional analysis*, **1**, Acad.Press NY-London, 1972.
14. D.W.Van Krevelen, *Properties of polymers, correlations with chemical structure*, Elsevier, Amsterdam-London-New York, 1972.
15. J.Powell, *CO₂ laser cutting*, Springer Verlag, 1993.
16. J.Powell, et al., in: *Proc. Int. Conf. Lasers in Manufacturing (LIM 4)*, W.M.Steen (ed), Birmingham UK, 69-82, 1987.

A semi quantitative approach to the effect of anodized layer thickness on laser cutting of an aluminium alloy

A P Hoult, M Y Shan, B Bryden, I R Pashby

Warwick Manufacturing Group, Department of Engineering,
University of Warwick, Coventry CV4 7AL, UK

ABSTRACT

Experimental laser cutting work has been performed on a commonly used sheet aluminium alloy to establish an approximate relationship between maximum laser cutting speed and the thickness of an anodized layer on the surface of the material. Results show a very significant increase in maximum speed, which is maintained even with increasing thickness of the anodized layer well beyond that at which maximum beam absorption is thought to occur.

Keywords: laser cutting, aluminium alloys, anodized layer, optimum cutting speed, cut quality.

1. INTRODUCTION

An increase in usage of aluminium in road transport and other areas, combined with recent advances in high power industrial lasers and laser processing has increased interest in laser processing of aluminium and its alloys. Various authors have identified the problems involved with laser processing of aluminium and its alloys, and useful information has been generated^{1,2}. This has highlighted the importance of surface finish to both laser cutting and welding processes, more specifically, the effect of surface oxides⁴. There are a wide variety of surface finishes available for aluminium and its alloys and in the case of anodizing, various depths of treatment are used commercially to achieve a variety of surface properties and effects, both functional and aesthetic. A conventional CO₂ gas laser has therefore been used to cut 6016 aluminium alloy sheet, which has been anodized to produce a range of oxide thickness. Maximum cut speeds for a particular set of laser parameters have been determined from a number of straightforward readily available techniques for measuring cut quality.

2. STRUCTURE AND PROPERTIES OF ALUMINIUM SURFACES

A layer of aluminium oxide (Al₂O₃) forms rapidly on any aluminium surface in the atmosphere. This layer is both adherent and relatively impervious, so that once formed, it protects the underlying metal from further oxidation⁵. Under normal atmospheric conditions the natural oxide layer remains rather thin, less than 100 Å or 10 nm (typically around 40 Å) and if damaged, immediately re-forms⁶. The high resistance of aluminium and its alloys to corrosion is due to the presence of these dense, adherent films. These films provide excellent protection to pure aluminium but are less protective on many strong alloys which have a high alloy content. During prolonged exposure the film thickens and becomes rough, the aluminium losing its characteristic appearance and assuming a dull grey finish. The thickness of the surface layer depends strongly on the sample structure and history, and the process of anodizing is simply a method of artificially increasing the thickness of this oxide layer by chemical means. The porous outer layer of the surface is typically a few microns thick, but for certain external applications can be up to 20µm or above. It is composed of a cellular like structure which increases the effective surface area enormously and can be considered a very rough surface. The important properties in this context include reflectivity, image clarity and refractive index. Reflectivity, (or its complement, absorptivity,) being by far the most important, as this property largely determines the initial reaction of the material surface to the beam. Various authors⁷ have calculated theoretical values from basic principles for reflectivity, refractive index and extinction coefficient for 10.6 µm laser light, for optical quality aluminium surfaces. All determine a figure of close to 100% at room temperature^{8,9}.

3. REAL ALUMINIUM SURFACES

Touloukian⁹ has looked at rough impure samples, and the data, though sparse, does indicate that at 10.6 µm wavelength, absorptivities (at Rt) of anything up to 30% are possible. The absorptivity of the oxide however is likely to be very different to that of the base metal, and despite the difficulty of experimental determination of reflectivity, Arata⁸ has shown that the thicker oxide layers absorb almost 100% of a 10.6µm wavelength beam. It is widely accepted that reflectivity of the base metal drops dramatically, even in the case of 10.6µm if melting or evaporation of the target occurs. It should also be noted that not only do the optical properties change but the thermal properties of target materials also change with temperature. In the case of anodized aluminium, the situation is further complicated by the fact that the

thermal diffusivity of the high melting point Al_2O_3 surface layer is an order of magnitude less than that of the base metal¹⁰. Arata⁹ has also shown that an increase in surface roughness can cause a reduction in reflectivity, although most real engineering surfaces are already macroscopically rough when compared to optical surfaces and this effect has been demonstrated especially if the surface roughness is greater than $\frac{1}{4} \lambda$ ¹¹, certainly true for most engineering finishes.

4. FACTORS AFFECTING CUT SPEED

Along with aluminium, other non-ferrous metals such as copper, combine high reflectivity with a high thermal conductivity and diffusivity. Laser cutting of aluminium has been considered difficult because of the combination of the high thermal reflectivity, high conductivity and diffusivity, of all aluminium base materials.

Thermal diffusivity, κ , is defined as;

$$\kappa = \frac{K}{\rho C_p} \quad (1)$$

where K , C_p and ρ are thermal conductivity, specific heat capacity and density of the material respectively. This term, κ , represents the rate at which thermal energy diffuses through the material when a temperature gradient exists, and is therefore relevant in transient heat flow situations. In common with thermal conductivity, it also has a marked temperature dependence. It is important to note that typical figures for aluminium are $97 \times 10^{-6} \text{ m}^2\text{s}^{-1}$, almost as high as that of copper, but a factor of 7 greater than mild steel, and a factor of 22 greater than stainless steel¹⁰. Hence the considerable heat loss from the cut zone, particularly at the low cut speeds and high specific heat inputs associated with low average powers.

However, a review of recent literature and practical experience with laser cutting of aluminium and its alloys has shown that there are three main process variables which determine the maximum laser cutting speed for a given laser power and set up. It has been shown that both the type of assist gas¹² and the composition of the alloy, in particular, the magnesium content¹², and the presence of an oxide layer can produce an increase in cut speed. The best estimate⁴ is a cut speed increase of up to 30%, attributed to the presence of anodised surfaces. Of these three variables, it is the surface condition which is the least understood from both a practical and an analytical viewpoint, hence the requirement for this current work.

4.1 Purpose of current work

There is evidence therefore that the actual reflectivity of anodised engineering aluminium surfaces to $10.6\mu\text{m}$ radiation is controlled by the characteristics of the anodised film and is far lower than might be expected from results concerned with high quality optical surfaces, especially if the thickness of the anodised layer is greater than $5\mu\text{m}$. It has also been noted⁴ that the presence of an anodised layer has other beneficial effects, the material is easier to pierce by laser and the cutting process window is wider. This work therefore attempts experimentally to improve understanding by assessing the contribution made by the oxide layer thickness to cut speed.

5. EXPERIMENTAL TECHNIQUE.

A single sheet of 1.2 mm thick AlMgSi, (designated 6016) aluminium alloy¹³ was used throughout. It is widely used commercially and is known as Anticorodal-120 ®. It has a magnesium content of 0.25-0.6 wt %¹³. The initial surface finish of each sample was a conventional mill finish. Samples were then treated as follows;

Batch 1: NaOH alkaline etch / clean, assumed zero oxide layer.

Batch 2: Degreased only, standard mill finish, normal oxide layer only.

Batches 3 - 7: Sulphuric acid anodised for increasing times to give increasing anodised layer thickness. Bath conditions were carefully controlled so that although the anodised layer is rather thicker than would normally be produced commercially, a consistent structure was produced up to the maximum thickness of $35 \mu\text{m}$, table 1, each thickness being measured optically.

These sheets were then laser cut using a Photon Sources VFA 1200 CO_2 Fast Axial Flow (FAF) laser at 1 kW average power output, as measured at the workpiece. Beam mode was approaching TEM 00. Despite a circular polariser being used to reduce directional effects, the further precaution of making all cuts along the rolling direction of the sheet was employed. A 127 mm focal length ZnSe lens was used with a conventional machining head employing nitrogen as an inert assist gas. Other processing precautions taken prior to each processing session were; a standard warm up period,

flushing of the machining head and delivery pipes with gas and regular checks on power output. Samples were cooled to room temperature between cuts.

Ranging trials on gas pressures and power settings considered appropriate for this thickness of material produced approximately optimised cuts at 2 bar gas pressure and 1 kW average power at the workpiece. These speeds were close to those given in the literature under similar conditions. A maximum cut speed was determined for a control sample of the standard mill finished 6016. Cut speeds for the treated panels were then determined by increasing or decreasing cut speed in increments of 5 mms^{-1} for each sample to cover a wide range of cut speeds. Maximum cut speed was taken to be the speed close to the point of cut failure, but giving the optimum cut quality. The cut quality criteria measured for each cut were: upper and lower kerf width, cut surface roughness and Heat Affected Zone (HAZ) depth and area.

6. RESULTS

<i>Treatment</i>	<i>Speed in mms^{-1}</i>
NaOH etch	15
standard mill finish	30
3 micron anodize & seal	50
6 micron anodize & seal	60
12 micron anodize & seal	60
24 micron anodize & seal	70
35 micron anodize & seal	80

Table 1. Cut speed v oxide layer thickness

Optimum cut speed was determined from cut quality. This was decided on the basis of minimum kerf width and minimum HAZ, and minimum cut surface roughness, all easily measured. The optimum cut speed for each surface treatment is given below:

SEM (Scanning Electron Microscope) observation showed that at the same non optimised low cut speeds, the surface roughness was noticeably increased and the surfaces which were produced from the sheets with the thicker anodised layers. Surface roughness measurements confirmed these observations (Fig. 1).

Cut surface roughness v laser cutting speed

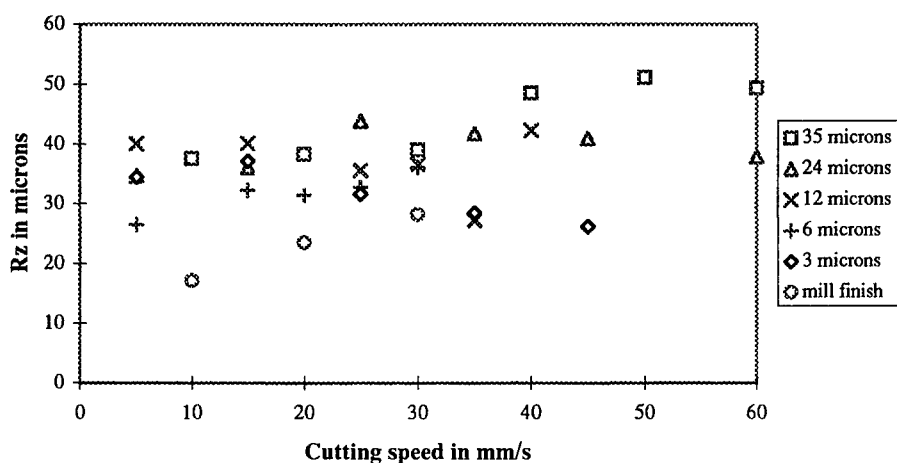


Figure 1. Effect of oxide thickness on cut surface roughness

7. DISCUSSION

Firstly, there is a reduction in cut speed caused by removal of the natural oxide coating. Secondly, it is clear that a thin anodised layer of 3 μm is enough to increase cut speed dramatically. This may well be significant for many of the newer surface treatments for aluminium alloys. Results for the thicker anodised layers also show a significant increase in cut speed associated with the increase in the oxide layer thickness. Aside from a number of possible second order effects, such as the effect of temperature on the diffusivity of the oxide layer itself, these results support the conclusions in ⁹ that there is significant absorptivity increase produced by the increase in thickness of the anodized layer and that this increase in absorptivity leads to significant increases in laser cutting speeds. As most commercial anodized layers are typically in excess of a few microns thick, these increases might be expected for most anodized aluminium surfaces. There is no firm evidence here to explain the continuing significant increase in cut speed with increase in anodised layer thickness.

At identical, but slow cut speeds, the higher absorptivity associated with the thicker anodised layer does not improve cut surface quality, in fact the reverse occurs, as corroborated by optical and Scanning Electron Microscope observations. These results therefore tend to support the proposition that Al_2O_3 is being incorporated in the cut zone hence increasing cut surface roughness. It is hoped that further work using various assist gases might help to understand this effect better.

8. CONCLUSIONS

In the case of inert gas CO_2 laser cutting of aluminium, enhancing the thickness of the oxide layer on the surface of the aluminium produces very significant increases in maximum laser cutting speeds, for a given cut quality. It is safe to assume that the increase in cut speed is associated with enhanced absorption in the surface layer of oxide.

Although the maximum cut speed at which the best cut quality is produced is increased by a thickening of the anodized layer, a thickening of the anodized layer alone does not improve cut quality.

9. REFERENCES

1. J. Powell, K. Frass, K. Sheninger and I.A. Menzies, "CO₂ laser cutting aluminium alloys", *Proc. 5th Int. Conf. Lasers in Manufacturing*, Stuttgart, Germany, pp 15-24, Sept. 1988.
2. M.C. Sharp, "CO₂ laser cutting of high reflectivity materials", *Proc. 6th Int. Conf. on Applications of lasers & electro-optics, ICALEO '87*, Springer-Verlag, pp 149-155.
3. J. Powell, "CO₂ Laser Cutting", Springer-Verlag, London, 1st edition, 1993.
4. R.K. Hart, *Proc. R. Soc. London Sec. A* **236**, 68 (1956)
5. J.A. McKay & J.T. Schriempf, "Transient surface heating of metals by CO₂ laser pulses with air-plasma ignition", *J. App. Phys.* **50**, 3231-3240 (1979).
6. K. Ujihara, "Reflectivity of metals at high temperatures", *J. Appl. Phys.* **43**, 2376-2383, (1972).
7. A.M. Prokhorov, V.I. Konov, I. Ursu & I.N. Mihailescu, "Laser heating of metals", ISBN 0-7503-0040-X, IOP, 1990.
8. Y. Arata & I. Miyamoto, "Some fundamental properties of high power laser beams as a heat source - Report 2, CO₂ laser absorption characteristics of metal", *Trans. Jap. Weld. Soc.* **3**, 152 - 162.
9. Y.S. Touloukian (editor), "Thermophysical properties of Materials", IFI/Plenum Press, 1970.
10. F.M. White, "Heat & mass transfer", Addison-Wesley Publishing, 1991, ISBN 0-201-17099-X.
11. B.S. Yilbas, K. Danisman & Z. Yilbas, "Measurement of temperature dependent reflectivity of Cu & Al in the range 30 - 1000°C", *Meas. Sci. Technol.* **2**, 668-674 (1991).
12. H.O. Ketting, K. Schwendner, G. Bech-Nielsen, I. Chorkendorff & F.O. Olsen, "Advanced surface analysis on high pressure CO₂ laser cut test pieces in pure and alloyed aluminium", *SPIE* **2207**, pp 534-545, 1994.
13. Alusuisse Ltd, Technical data sheet for Anticorodal -120©.

High-Power Iodine Laser Application for Remote D&D Cutting

John Vetrovec, Robert N. Hindy, Ganesan Subbaraman, and Lyle Spiegel

Energy Technology Engineering Center, Rocketdyne Division of Rockwell International Corp.,
6633 Canoga Avenue, Canoga Park, California, 91309, U.S.A.

(818) 586-3101 or -0443, (818) 586-3074 (fax), email: jvetrove@rdyne.rockwell.com or rnhindy@rdyne.rockwell.com

ABSTRACT

This paper discusses the use of high-power lasers to remotely process material for decommissioning and dismantlement of nuclear facilities. Process requirements are established and suitable laser systems are compared. The Chemical Oxygen-Iodine Laser was identified as the leading candidate for long term dismantlement activities because it offers a high-power, high-brightness beam that can be remotely delivered into radiation containment by optical fibers.

Key Words: Iodine laser, COIL, decontamination and decommissioning, D&D, laser cutting, nuclear facilities

1. INTRODUCTION

A large number of nuclear material processing facilities and reactors around the world are scheduled for shutdown, decontamination and decommissioning (D&D) within the next 30 years [1]. Lasers have been previously identified as a potentially suitable tool for D&D processes such as cutting, welding, surface decontamination, and contamination diagnostics. The advantages of using lasers are fast processing speed, reduced secondary waste, and easy integration into robotics systems for remote operation. In the past, the lack of high-power lasers with suitable beam delivery schemes confined the laser assisted D&D only to laboratory experiments. The recent commercial availability of multi-kW fiber-delivered Nd:YAG lasers [2] provides an opportunity for immediate, if limited, deployment in D&D. Emergence of the high-power, high-brightness industrial COIL [3] promises a long term D&D solution by providing sufficient power to cut through very thick components at economically advantageous rates. System studies at Rocketdyne and initial testing performed at the U.S. Air Force Phillips Laboratory indicate that COIL can provide significant benefits to D&D.

2. NEED FOR NEW TECHNOLOGIES FOR REMOTE D&D OF NUCLEAR FACILITIES

The U.S. Department of Energy (DOE) weapons complex encompasses hundreds of aging nuclear material processing facilities and reactors that are now being shut down and which require dismantlement [1]. Commercial nuclear reactors within the U.S. and around the world further extend the need for suitable D&D technologies [4], Figure 1. All of these facilities contain large inventories of complex and massive nuclear material processing equipment, reactors, hot cells, and structures, Figure 2. The D&D task is made difficult by limited access into highly contaminated areas and requires techniques which can be applied remotely.

The criticality of suitable D&D technologies is accentuated by the need for regulatory compliance and economic considerations. For example, the Environmental Protection Agency's "Debris Ruling" of August 1992 [5] requires that components with complex geometries and enclosed volumes be cut open for decontamination and inspection prior to disposal. Also, the volume-dependent cost of radioactive waste disposal dictates that contaminated material be cut-up before burial [6]. Thus, cutting technologies play a key role in the economics and scheduling of the D&D process.

The present technologies for dismantlement of nuclear equipment (e.g., band saws, plasma arc torches, oxy-acetylene torches, grinders, shears, water jets, etc.) are generally labor-intensive, slow, costly, require manual operation/intervention, subject workers to the risk of exposure to chemical, physical, and radiological hazards, and often contaminate the material being dismantled or generate secondary wastes [7]. The nature and magnitude of the facility D&D problems require the development of advanced cutting and other material processing technologies. Specific requirements include capability for remote application, improved economy and safety, and compatibility with standard D&D robots, manipulators and procedures.

3. LASER ASSISTED D&D

Studies, experiments, and demonstrations performed in the U.S. [8,9,10,11], Japan [12], and the European Community [13,14] indicate that lasers offer several distinct benefits, including high speed, low production of secondary waste, capability of increased tool-to-workpiece (stand-off) distance, and capacity to handle complex components, Figure 3. The usefulness of lasers to D&D is not limited to cutting. Lasers are also effective for welding closure of hazardous waste containers, surface decontamination by ablation [15,16], and contamination diagnostics by plasma spectroscopy [17,18]. In each case a high power laser beam has to be delivered into a radiation containment area. There are also strong prospects for combining many of these functions into one system, thereby creating a multiple purpose tool, Figure 4.

Many of D&D operations involve in-situ demolition of contaminated facilities and equipment. Laser power can be generated by a source outside the radiation containment and remotely delivered into the contaminated zone. This process requires an easy-to-reconfigure beam delivery system to allow movement and relocation of the D&D robots. Such requirement renders

hard-optics (mirror train) delivery schemes impractical and the optical fiber remains as the only realistic choice. Suitable fibers are commercially available in lengths of up to 150 meters and are relatively inexpensive [19].

The unique capability of laser cutting for nuclear D&D is best illustrated in recent experiments conducted by the Nuclear Power Engineering Corporation (NUPEC) of Japan [12]. A 20-kW carbon monoxide (CO) laser was used to cut in a single sweep through stainless steel reactor components up to 12" thick in air, Figure 5, and 2" thick under water. The same laser was also used to perform a simple-sweep cut through a 15" thick array of 10 rows of 1" diameter stainless-steel tubes, and a simple-sweep to cut-off a 4" diameter tube [20].

The advantages of using lasers for D&D cutting include easy integration into robotics for remote operation, fast processing speed, prospects for multipurpose tools, capability of cutting complex shapes in simple-sweep motion, low secondary waste, and a non-contact and non-wear cutting head that requires only minimum maintenance. Laser cutting overcomes many of the limitations of plasma torches and mechanical saws. A suitable D&D laser material processing system should have about 20 of kW of laser power for fast processing and thick section cutting, good beam quality for long standoff, higher intensity for ablative material removal, and practical means for beam delivery into radiological containment areas.

4. Nd:YAG AND COIL LASERS FOR D&D

This investigation considered four high-power industrial lasers: CO₂, Nd:YAG, CO and COIL. The table in Figure 6 compares the suitability of each of these lasers for specific D&D tasks. Only the first two lasers listed are commercially available. All but the Nd:YAG have demonstrated power capability over 20 kW, while only Nd:YAG and COIL are compatible with optical fibers for beam delivery. This suggests that 1) the Nd:YAG laser is suitable for immediate but lighter duty deployment and 2) COIL is the leading candidate for future deployment in heavy-duty tasks benefiting from 20 kW of beam power delivered by optical fiber.

Recent study [21] conducted by Rocketdyne for the DOE shows that Nd:YAG lasers can fulfill many D&D needs and economically justify their deployment in small scale operations. Typical laser systems for D&D materials processing consists of a laser source (with its associated power supply and chiller), fiber optics for beam delivery, a beam focusing head, gas assist system, and a conventional remote manipulator or robot. Figure 7 shows a setup planned by Rockwell/ETEC for a laser D&D experiment at the DOE's Hanford nuclear site in Washington State. The laser source is located in a non-hazardous environment where it is protected from radiation and is accessible for maintenance. The fiber optics and the focusing head are relatively inexpensive and robust, and can be remotely replaced with minimum downtime.

Reference [3] shows that COIL is an emerging high-power industrial laser which has an unique capability of simultaneously producing high quality beams at high power (39 kW was demonstrated [22]) that can be delivered through optical fibers (1 kW transmission was demonstrated [23] and over 25 kW is projected [24]). Other advantages of COIL include short wavelength, which is less susceptible to plasma absorption, capability to cut with a small kerf which minimizes secondary waste, and prospects for ablative cutting. In particular, high-intensity (on the order of 10^8 W/cm²) COIL beam can cut components of greater thickness at higher speed and larger stand-off distances.

COIL appears uniquely suited for D&D applications for which there are no attractive alternatives, such as in-situ reduction of difficult-to-access structures and components with large wall thicknesses and complex geometries. For these reasons COIL investigations for D&D applications were conducted at Rocketdyne [21] and Kawasaki [25, 26, 27]. The Rocketdyne study baselined a D&D COIL system along the lines of the 20 kW industrial COIL described in reference [3]. A general configuration of the system is shown in Figure 8. The system is entirely portable and configured on three trailers. The first trailer contains the laser device, another holds the laser fuel regenerator, and the third houses the process control center.

5. LASER CUTTING EXPERIMENTS

The greatest challenge in D&D laser cutting is to maintain reasonable rates while the distance between the head and the workpiece varies. In production cutting, the cutting head is held closely to the workpiece to optimize coupling of the assist gas jet and to produce a quality cut. In D&D cutting maintaining close proximity of the head and the workpiece often impractical (and sometimes impossible). The resulting uneven cut is of little concern since D&D cutting is of the demolition type and the quality of the edges is essentially irrelevant. However, it is desirable to keep the slag at minimum.

The simple-sweep cutting capability of a Nd:YAG laser was evaluated by Rocketdyne with the Hobart 3000 laser, which delivered 3 kW of power through a 20-meters-long optical fiber [28]. The cutting head used a special coaxial assist-gas nozzle integrated with a standard Hobart f/3 optics. Test articles were components representative of the PUREX plutonium processing system at the Hanford nuclear facility and scheduled for D&D. The overall test setup was similar to that in Figure 7. Specific results include single-sweep cuts through 3" ϕ stainless steel tubes, 2" carbon steel angle irons, and a variety of other shapes, Figure 9. COIL capability to cut through thick slabs of steel has been established in separate experiments at the U.S. Air Force Phillips Laboratory [24]. Tests to cut shapes representative of components at nuclear installations were

conducted. Specific results include cutting of 2"Ø tube and array of 0.5"Ø tubes in the simple-sweep manner, and cutting of a 1" thick plate, Figure 10.

6. CONCLUSION

The advantages of using high power lasers for D&D of nuclear installations were discussed and requirements for prospective laser systems established. The importance of beam delivery through optical fibers was emphasized. Trade studies indicated that Nd:YAG laser is suitable for immediate deployment in lighter-duty D&D activities whereas a high-power COIL is suitable for future heavy-duty work. Experimental results show that both lasers can perform simple-sweep cutting of representative materials and complex shapes.

7. REFERENCES

1. U.S. Dept. of Energy, "Estim. the Cold War mortgage-The baseline environ. mgmt....," Summary, DOE/EM-0232 (1995)
2. D. Filgas, "Advances in high-power CW YAG lasers and fiberoptic beam delivery," proc. ICALEO (1992), p. 63
3. J. Vetrovec, "Prospects for an industrial Chemical Oxygen-Iodine Laser," presented at this conference
4. B. Fisher et al, "Handbook of Nuclear Countries 1992/1993," Lexographisches Institut, Berlin, 1992
5. U.S. Environmental Protection Agency, "Land disposal restrict...", Feder. Register, vol 57-160 pp.37,194-37,282 (1992)
6. U.S. Dept. of Energy, "Estim. the Cold War mortgage-The baseline environ. mgmt. report," ch. 4, DOE/EM-0232 (1995)
7. P.T. Spampinato et al, "Workshop on vacuum vessel cutting," TFTR D&D project, Princeton Univ., D&D-41 DDOC
8. B.S. Weil, "A laser cutting system for nuclear fuel disassembly," ICALEO (1985), p. 145
9. R.S.Frazier et al, "Production declading of ..., " Proc. 35th Conf. on Remote Syst. Technol., pp. 82-86 (1987)
10. L.Spiegel, "Applic. of lasers to remote D&D activit.," Rocketdyne rep. to U.S. DOE, contr. TTP: SF3-5-20-03 (1995)
11. T.R. Kugler, "The application of YAG laser technology for repair, decontamination....," proc. ICALEO (1995), p. 789
12. NUPEC, Tokyo, Japan, "Verific. Tests on Decomm. Technol. for Commer. Nucl. Power Facil.," brochure, (1994).
13. J. Perrin, "Adv. cutting technol....," Proc. of Euro. Conf. on Decomm. Nucl. Power Plants, May 1994, Luxembourg
14. S. Beppu et al, "Local drying....," Proc. Laser Adv. Mater. Proc. Conf., LAMP '92, June 1992, Nagaoka, Japan (1992)
15. L. Li et al, "Laser removal of surface and embedded contamin. on/in building structures," Proc. ICALEO '94, (1994)
16. D. Smith et al, "Laser processing of hazardous materials," ICALEO (1993), p. 536
17. I. Schechter et al, "Real time detection of hazardous elements in sand and soils," SPIE vol. 2092, p. 174, (1993)
18. D.A.Cremers, "The analysis of metals at distance," Appl. Spectroscopy. 41 (4), p. 572 (1987)
19. T. Webber, Hobart Laser Products, Livermore, Calif., Communications
20. NUPEC, Tokyo, Japan, "Development of laser cutting for decommissioning," video, 1994.
21. Rocketdyne/ETEC, Canoga Park, Calif., "Remote Laser Proc. of Radioact. Components," TTP: SF3-5-20-03 (1994)
22. K.A. Truesdell, et al, "A history of COIL development in the USA," 10-th GCL Conf., SPIE vol. 2502 (1994)
23. H. Fujii, "COIL develop. in Japan," 25-th AIAA Plasmadynamics & Laser Conf., Colorado Springs, U.S.A. (1994)
24. J. E. Scott et al, "The use of COIL for high speed cutting of thick stainless steel," SPIE vol. 2702, p. 339, (1996)
25. Kawasaki Heavy Industries, Kobe, Japan, "COIL applic. to D&D," presented to U.S. DOE visitors in Nagaoka, (1995)
26. K. Yatsuda et al, "Study on mater. processing of chem. iodine laser," Int'l. Conf. on Nucl. Engr., Kyoto, Japan (1995)
27. S. Takeda, "Industrial and reverse-industrial applications of COIL," SPIE vol. 2702, p. 191, (1996)
28. L. Spiegel, "D&D cutting with 3 kW Nd:YAG laser," Rocketdyne rep. to U.S. DOE, contr. TTP: SF3-5-20-03 (1995)
29. Welding and Metal Fabrication, November 1990, p. 472

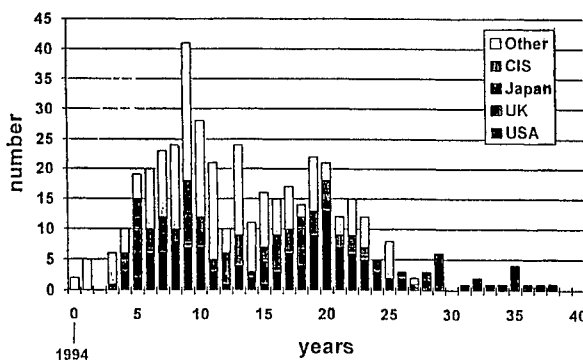


Figure 1: Age distribution of the world's 427 nuclear power reactors [4]

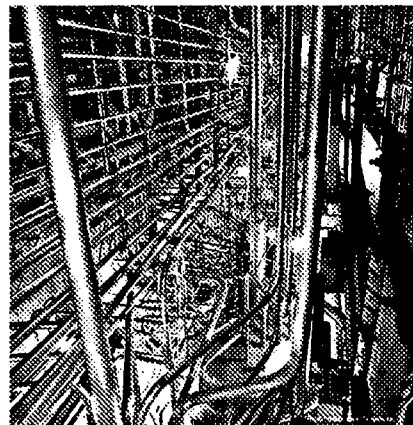


Figure 2: Piping in the THORP nuclear material processing plant, Sellafield, UK [29]

Benefits of laser cutting to D&D	Rationale and Comments
1. Fast cutting speed saves time and reduces cost of operation	Laser light can be focused to produce power densities orders of magnitude higher than standard thermal cutting techniques such as torches
2. Reduced secondary waste	Cutting with a focused laser beam produces smaller kerf than with conventional cutting techniques such as torches
3. Easy integration into remote manipulators and robotics	The end-effector is compact, light-weight, and produces no reaction force during operation. Light robots can be used.
4. Can easily handle complex workpiece contours	Stand-off distance between the end-effector and the workpiece together with a long depth of focus eliminate the need to follow complex surface contours for linear cuts
5. Reduced downtime due to end-effector maintenance	No wear end-effector requires virtually zero maintenance
6. Can be configured into a multi-purpose tool	The same system could be used for demolition cutting, welding, ablative cleaning, and diagnostics
7. Improved operational safety	Multi-purpose system which does not require change of end-effector

Figure 3: Benefits of laser material processing to D&D

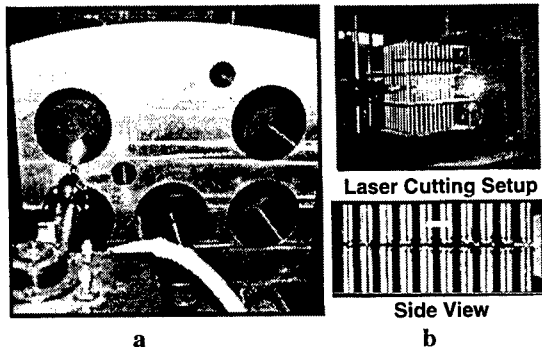


Figure 5: Cutting by NUPEC's 20-kW CO laser; a) 12" thick reactor plate, b) 15" thick tube array, [12]

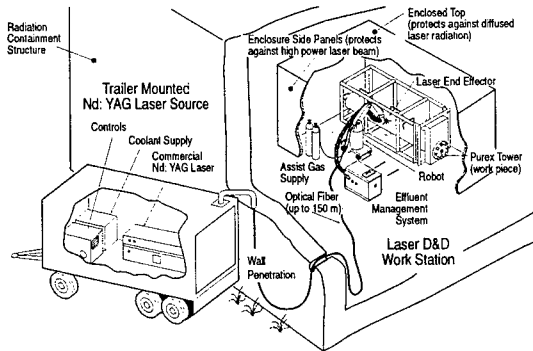


Figure 7: D&D laser cutting setup with a 3 kW Nd:YAG

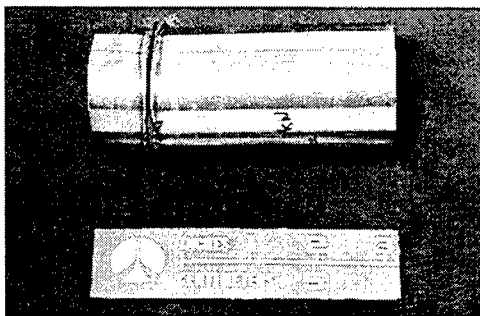


Figure 9: 2"Ø tube cut in a single sweep with a 3 kW Nd:YAG

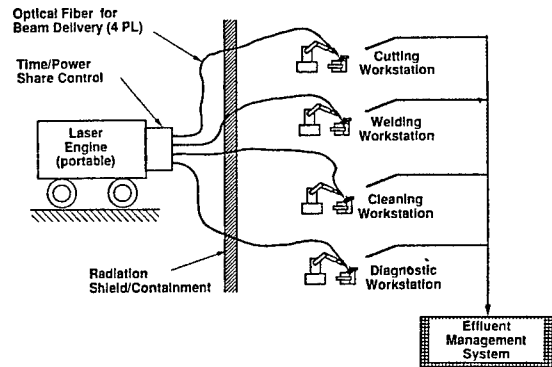


Figure 4: Multi-purpose laser engine for D&D applications

D&D Process	Laser Engine Requirements for a Multi-Purpose D&D System				Laser Engine Candidates							
	Power* (P)	Fiber Compat. (F)	Beam Quality (Q)	Time Format (T)	Nd:YAG		COIL		CO*		CO2*	
Cutting	3-20 kW	Yes	Good	CW	●	○	●	●	●	●	●	●
Welding	3-5 kW	Yes	Good	CW	●	○	●	●	●	●	●	●
Cleaning	3-10 kW	Yes	Not critical	CW or Pulsed	●	○	●	●	●	●	●	●
Diagnost	<1 kW	Yes	Good	Pulsed	●	○	●	●	●	●	●	●

Key: ● = Meets requirements
○ = Approaches requirements
x = Does not meet requirements

Approaches and/or meets requirements: Suitable for near term use
Meets all requirements: Desirable for long term use

*) This assessment ignores the fact that due to reflection and plasma blocking the CO and CO2 lasers may actually need 2-3x more power than equivalent Nd:YAG or COIL

Figure 6: Requirements vs. capabilities of D&D lasers

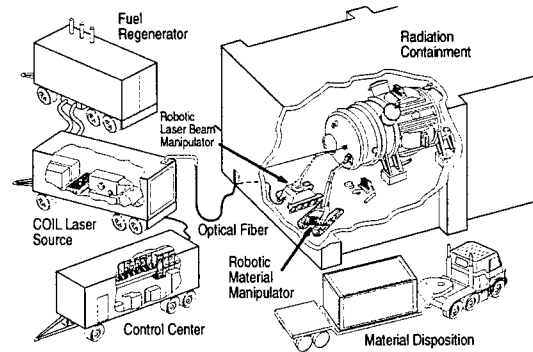


Figure 8: D&D with a high power COIL

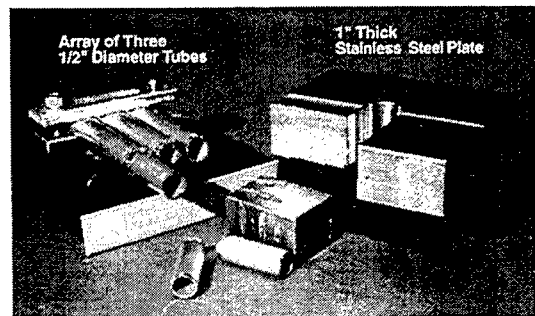


Figure 10: Components cut in a single sweep with a 7 kW COIL (courtesy of the Phillips Laboratory)

Author Index

- Abram, R., 100
 Abramovic, Dov, 273
 Abramski, Krzysztof M., 206, 325
 Adachi, Kyoichi, 269
 Adamenkov, A. A., 265, 581
 Afanas'ev, L., 142, 305
 Alexandrov, B. S., 309, 448, 606
 Althaus, Marion, 610
 Amarande, Stefan, 345
 Anderson, B. T., 76
 Andrzejewski, H., 748
 Asanuma, Hiroshi, 647
 Ashidate, Shu-ichi, 740
 Ashworth, Dominic, 471
 Atanasov, Peter A., 594, 772
 Atsuta, Toshio, 573, 700
 Autric, Michel L., 406, 585, 647, 671
 Azami, Naoki, 573
 Azarov, M. A., 598, 606
 Baeva, Margarita G., 772
 Baik, Sung-Hoon, 538
 Baker, Howard J., 25, 100, 178, 297, 321, 325
 Baranov, Igor M., 444
 Barmashenko, B. D., 682, 690
 Bastiaens, H. M., 374
 Basting, Dirk, 485
 Bastue, Jens, 130
 Beach, Raymond J., 16
 Beairsto, Chris T., 337
 Beck, M., 516, 526
 Beck, Thilo, 174
 Beck, Thomas, 44
 Belavin, V. A., 309
 Bell, A., 426
 Beránek, Jaroslav, 569
 Berger, Peter, 398, 526
 Bergmann, Hans W., 169, 281, 477
 Berkermann, U., 243, 247
 Besaucèle, H., 362
 Betev, Alexei A., 313
 Betterton, J. G., 178
 Bibeau, Camille, 16
 Bielesch, Ulrich, 631
 Biesenbach, Jens, 17
 Blair, P., 100
 Blayvas, I., 690
 Blidegn, M. Sc. K., 615
 Bochum, H., 88
 Bohn, Willy L., 553, 706
 Boiron, O., 200
 Bollanti, Sarah, 357
 Bonnet, Jean C., 161, 370
 Booth, H., 732
 Bor, Zsolt, 462
 Boreisho, Anatoly S., 456
 Bostanjoglo, Georg, 44
 Botha, Lourens R., 138
 Bouesc, J., 585
 Bourgeois, Patrick, 610
 Bournot, Philippe, 200
 Bragin, Igor, 485
 Brown, Daniel J., 68
 Brunet, Henri, 362, 494, 589
 Bryden, B., 776
 Bulkin, Yu. N., 265
 Buyko, S. A., 341
 Buzoverya, V. V., 265
 Callies, Gert, 398
 Campbell, M. J., 33
 Cao, Q., 297
 Carman, R. J., 68
 Carroll, David L., 758
 Cashmore, Julian S., 471
 Cavallaro, Joseph R., 462
 Chatwin, Christopher R., 219
 Chen, Kuntetsu, 561
 Choo, D., 210
 Christiansen, J., 169
 Chudzicki, J., 426
 Chung, Chin-Man, 538
 Colley, Alan D., 100, 325
 Copland, Richard J., 676, 710
 Cresswell, Brian, 655
 Cybulski, Ray, 467
 Dahmen, M., 619
 Danilov, Leonid I., 313
 Danilov, O. B., 349
 Das, Palash P., 467
 Dascalu, Traian, 52
 Dausinger, Friedrich, 516
 Delaporte, Philippe C., 382, 386
 Deryugin, Yu. N., 581
 Desoppere, E., 96
 Di Lazzaro, Paolo, 357
 Dolgoplov, A. V., 341
 Dommaschk, R., 44
 Doussiet, F., 506
 Dragsted, Birgitte, 627
 Drozdov, V. A., 606
 Du, Hao, 647
 Du, Keming, 17
 Ducharme, R., 530
 Dudov, A. M., 341
 Duffet, G., 748
 Duschek, Frank, 686
 Dutems, Cyril, 161
 Dutov, Alexander I., 260
 Dyer, Peter E., 412
 Dymshits, Boris M., 309, 448
 Eichhorn, A., 522
 Eichler, Hans J., 9
 Eisner, Klaus, 169
 Elutin, A. S., 602
 Emanuel, Mark A., 16

- Entress-Fürsteneck, Lutz v., 553, 706
 Erdelyi, Miklos, 462
 Eroshenko, V. A., 341
 Ezaki, Mizunori, 269
 Fakler, K., 247
 Faulstich, A., 25
 Fedenev, A. V., 289
 Flora, Francesco, 357
 Fomenkov, Igor V., 467
 Fontaine, Bernard L., 382, 386
 Forestier, Bernard M., 382, 386
 Foster-Turner, G., 426
 Frerking, S., 676
 Fürst, B., 619
 Fujii, Hiroo, 573, 694, 700
 Fujinaga, Shigeki, 736
 Fujioka, Tomoo, 317, 715
 Funatsu, Masato, 651
 Furlinski, G. I., 594
 Furman, D., 690
 Furuya, Nobuaki, 210
 Gabay, Amnon, 104
 Gagnol, Claude, 362
 Galun, R., 744
 Galushkin, M. G., 134, 252, 333
 Gan, Eric K., 281
 Gastaud, Michel, 585
 Gautier, Bernard, 663
 Geiger, Manfred, 768
 Gerasimenko, Natalia N., 581
 Giesen, Adolf, 190, 227
 Giordano, Gualtiero, 357
 Girard, Genevieve M., 589
 Glassman, J., 76
 Godard, Bruno, 161, 370
 Godfried, Herman P., 29
 Golubev, Vladimir S., 134, 252
 Gordon, Shawn J., 502
 Gorton, E. K., 223, 498
 Gower, Malcolm C., 471
 Grangeon, F., 406
 Greenough, R. D., 643
 Grozdanov, K. A., 594
 Grubert, B., 88, 329
 Gruenewald, Karin, 553, 706
 Haas, C. R., 17
 Haase, Andreas, 9
 Habich, Uwe, 126, 174
 Hager, Gordon D., 76, 544, 676, 710
 Hall, Denis R., 25, 100, 297, 321, 325
 Hall, Thomas, 88, 182, 215, 250
 Hamada, Naoya, 418
 Hand, Duncan P., 534
 Handerek, J., 402
 Handke, Juergen, 553, 706
 Hannemann, R., 243
 Haran, Frank M., 534
 Harris, M. R., 498
 Hartmann, Martin, 281
 Hasatani, Masanobu, 452
 Hashimoto, Katsuki, 561
 Hayes, J. P., 643
 Helms, Charles A., 544, 676, 710
 Henning, Thomas, 126
 Hertzler, Christoph, 174
 Herziger, Gerd, 126
 Hindy, Robert N., 780
 Hintz, Gerd, 169
 Hishida, Manabu, 573
 Hodgson, Elizabeth M., 655
 Hoffmann, D., 481
 Hoffmann, D. H., 169
 Hoffmann, Peter, 768
 Hofmann, Thomas, 165
 Hogan, G. P., 732
 Hollins, Richard C., 82
 Honea, Eric C., 16
 Hoshino, Yuko, 549
 Hotta, Eiki, 366
 Hoult, Anthony P., 776
 Hügel, Helmut, 190, 227, 398, 516, 526
 Hugenschmidt, Manfred, 610, 623, 639
 Hull, Robert J., 186
 Igarashi, Tatsushi, 394
 Ilyin, S. P., 581
 Ioannou, A., 659
 Ionin, Andrei A., 142, 301, 305, 333, 337, 422
 Iskhakov, V. A., 598
 Itaya, Yoshinori, 452
 Ivarson, Anders, 530
 Iyoda, Mitsuhiro, 293
 Jackel, Steven M., 48
 Jakob, G., 243
 Jandeleit, Juergen, 481
 Janke, W., 277
 Jardine, S. E., 33
 Jarosch, Uwe-Klaus, 174
 Jenkins, David S., 502
 Jenner, A. G., 643
 Joecklé, Rene C., 663
 Jones, Julian D., 321, 534
 Jüptner, Werner P., 329
 Jung, M., 114, 231
 Jurewicz, A., 277
 Kaierle, S., 619
 Kakinuma, Tadashi, 715
 Kanazawa, Hirotaka, 38, 436
 Kapadia, P. D., 530
 Kapitan, D., 732
 Kar, Aravinda, 719, 764
 Karpukhin, Vyatcheslav T., 313
 Kasuya, Koichi, 366, 651
 Kato, M., 210
 Kato, S., 366
 Kaufman, Alon, 48
 Kawakita, Y., 366
 Kawamura, Yousuke, 452
 Kawanaka, Junji, 378
 Kearsley, Andrew J., 426
 Kern, M., 526
 Keusch, C., 169
 Kim, Cheol-Jung, 538
 Kim, Min-Suk, 538
 Kirat, P., 748

Kirillov, Gennadi A., 510
 Kleine, Klaus R., 422
 Kleinschmidt, Juergen, 485
 Klimachev, Yu., 142, 301, 305
 Klimck, Daniel E., 56
 Knowles, M., 426
 Kobayashi, Noriyuki, 452
 Kobayashi, S., 92
 Kobsa, Henry, 305, 422
 Koch, Juergen, 281
 Kochemasov, Gennadiy G., 341
 Kochetov, Igor V., 301
 Kodymová, Jarmila, 565, 569
 Kolobyanin, Yu. V., 265
 Konev, Yuri B., 301, 313
 Konkin, D. V., 602
 Koretskiy, J. P., 309
 Korotchenko, A. V., 134
 Kostadinov, I. Z., 277
 Kosyrev, F. K., 635
 Kotkov, A. A., 142, 305, 333, 337
 Koval'chuk, Alexandr V., 289
 Kozlov, B. M., 313
 Králiková, Bozena, 557
 Krása, Josef, 557
 Krasjukov, A. G., 635
 Kreutz, Ernst W., 481, 619
 Krukovsky, I. M., 581
 Kubodera, Shoichi, 378
 Kudriavtsev, E. M., 671
 Kudryashov, E. A., 265, 581
 Kuleshov, Alexei A., 260
 Kulikov, Stanislav M., 341, 602
 Kumagai, Hiroshi, 269
 Kurosawa, Kou, 394
 Laborde, Patrick, 161
 Lacour, Bernard, 362
 Lallouz, Raphael, 48
 Lampa, C., 530
 Lampson, A. I., 76
 Lander, Michael L., 186
 Lang, Adolf, 169, 281, 477
 Lapucci, Antonio, 196
 Láska, L., 557
 Latham, William P., 719, 764
 Lavenant, Annick, 589
 Lavi, Raphael, 48
 Le Palec, G., 200
 Lebert, Rainer, 126
 Legentil, M., 506
 Lemaigren, Pierre, 589
 Leont'ev, V. G., 256
 Letardi, Tommaso, 357
 Leys, C., 96
 Liebenberg, Christo J., 138
 Liffers, A., 243
 Lipukhin, Yurii V., 313
 Little, Chris E., 62, 277, 285
 Little, L., 62, 285
 Liu, Baining, 9
 Livingstone, Ewan S., 277
 Loosen, Peter, 17, 174
 Lücking, C., 243, 247
 Lyubimov, Vladimir V., 349
 Maeda, Keinosuke, 38
 Maeno, Kazuo, 647
 Magnusson, Claes, 530
 Makarov, Maxim K., 370
 Maley, Cynthia A., 467
 Maly, Heiko, 174
 Mandl, Alexander E., 56
 Marine, Wladimir I., 406
 Marsden, P. J., 431
 Marshall, Christopher D., 16
 Mascacchi, Silvano, 196
 Mašek, Karel, 557
 Mashendzhinov, V. I., 598
 Mason, P. D., 223
 Masuda, Wataru, 573
 Matsuno, Hiromotsu, 394
 Matsuoka, Naoya, 235
 Matsuura, Yuji, 120
 Maxwell, Keith J., 186
 Mayerhofer, Roland, 281
 Mayerhofer, Wilhelm, 114, 182, 215
 McDonald, Donald W., 219
 McLean, Marc, 753
 McNaught, W. G., 440
 Mehl, Oliver, 9
 Mentel, Juergen A., 243, 247
 Meyer, Rudolph, 174
 Michel, G., 239
 Miller, Harold C., 76
 Minamida, K., 418
 Mishimi, Akihiro, 38
 Mitin, K. V., 333
 Mitko, S. V., 390
 Miura, Hiroshi, 736
 Miyagi, Mitsunobu, 120
 Mizeraczyk, Jerzy, 277
 Moeglin, J. P., 663
 Mohamed-Seghir, M., 277
 Mordike, Barry L., 744
 Morris, A. V., 498
 Morton, Richard G., 467
 Moshe, I., 48
 Murata, T., 92
 Murra, D., 357
 Murray, G. J., 732
 Naftali, Nir, 273
 Nanri, Kenzo, 317
 Napp, M., 631
 Narikiyo, Toru, 736
 Nassisi, Vincenzo, 402
 Naumov, V. G., 635
 Negendanck, Matthias, 169
 Neubauer, Norbert, 768
 Nikolaev, Valery D., 565
 Notenboom, Gerard J., 2
 Noter, Yoram, 273
 Novgorodov, M. Z., 256
 Novikov, V. N., 341, 602
 Novoselov, N. A., 260
 Nowack, Rolf R., 88, 329

- Obara, Minoru, 21, 269, 740
 Ochkin, V. N., 256, 390
 Offerhaus, H. L., 29
 Ohmori, Akira, 736
 Okino, Keiji, 736
 Olsen, Flemming O., 130, 615, 627
 Orchard, D. A., 82
 Otta, A., 277
 Paetzel, Reiner, 485
 Panchenko, Vladislav Y., 252
 Parthenios, J., 659
 Partlo, Bill, 467
 Pashby, Ian, 776
 Pasquiers, S., 506
 Payne, Stephen A., 16
 Pe'er, Idit, 273
 Pelaez-Millas, D., 25
 Penny, R., 337
 Persephonis, Peter, 659
 Peshev, Zachary Y., 594
 Peters, C., 534
 Peters, Peter J., 374
 Petrucci, C., 357
 Pfeiffer, W., 190, 227
 Philipps, Gerd, 52
 Phipps, Claude R., 728
 Phipps, S. P., 544, 710
 Pigache, Daniel R., 161, 370
 Pinho, George, 398
 Piper, James A., 68
 Plinski, E. F., 206
 Plock, Ina, 577
 Plummer, David N., 676
 Poprawe, Reinhard, 17, 619
 Postel, C., 506
 Powell, J., 530
 Prat, Christophe, 647
 Prigent, Pascale, 589
 Prochasson, Sylvie, 161
 Puech, Vincent, 506
 Queitsch, Robert, 477
 Rafferty, B. D., 76
 Rapp, J., 516
 Reilly, James P., 186, 728
 Renz, Guenther, 114, 215, 231
 Revich, V. E., 598
 Richeboeuf, Laurent, 506
 Riede, Wolfgang, 182, 215, 250
 Riege, H., 402
 Rittenhouse, Tilghman L., 544
 Rizvi, Nadeem H., 471
 Roberts, N. C., 431
 Rodin, A. V., 635
 Rohlena, Karel, 557, 569
 Rosenwaks, Salman, 682, 690
 Rossetti, Francesco, 196
 Rothenflue, James A., 719, 758, 764
 Rozanov, N. N., 349
 Rudolph, Wolfgang G., 710
 Russbueldt, P., 481
 Rutterford, G., 426
 Ryzhov, V. V., 667
 Sabotinov, Nikola V., 72, 277
 Sakai, Tatsuhiko, 418
 Sands, D., 643
 Sandstrom, Richard L., 467
 Sasaki, Takatomo, 394
 Sasaki, Wataru, 378, 394
 Sassoli, H., 406
 Sato, Osamu, 715
 Sato, Shuichi, 293
 Schäfer, Johannes H., 631
 Schall, Wolfgang O., 553, 577, 686, 706
 Schellhorn, Martin, 522
 Schiffner, G., 243, 247
 Schina, Giovanni, 357
 Schindler, Klaus, 239
 Schittenhelm, Henrik, 398
 Schmiedberger, Josef, 694
 Schmitt, Ruediger, 623, 639
 Schmitz, C., 190, 227
 Schock, W., 231
 Scholl, Marcus, 126
 Schröder, Kurt, 353
 Schuöcker, Dieter, 353
 Schutte, Karsten, 169, 281, 477
 Scott, Andrew M., 341
 Scott, Brian F., 219
 Sekiguchi, Tomoyuki, 549
 Seleznev, L., 142, 305, 337
 Sentis, Marc L., 382, 386
 Sentman, Lee H., 502
 Shan, M. Y., 776
 Shannon, G. J., 753
 Shaw, M. J., 154
 Shchurov, V. V., 510
 Shimizu, Tomohiro, 561
 Shirai, Hiroyuki, 651
 Shiratori, Akira, 21
 Shishkanov, E. F., 256
 Shkapa, A. F., 341
 Sidhu, J., 431
 Sinitsyn, D., 142, 305
 Sinitsyn, V., 301
 Sinitzyn, M. V., 510, 602
 Sintov, Yoav, 104
 Skála, Jiri, 557
 Skidmore, Jay A., 16
 Slunecko, Tomas, 281
 Smayling, Michael C., 462
 Snelling, H. V., 643
 Somkuampanit, Suripon, 321
 Spalek, Otomar, 565, 569
 Spiegel, Lyle P., 780
 Squires, Stephen M., 337
 Stamm, Uwe, 485
 Staudigel, J., 169
 Staupendahl, Gisbert, 239
 Steen, William M., 753
 Stehle, Marc X., 161, 370
 Stepanov, V. A., 256
 Straka, Petr, 557
 Su, Daoning, 321
 Subbaraman, Ganesan, 780

- Sukharev, Stanislav A., 341, 602
 Sunako, Katsuhiko, 715
 Sunami, Hiroyasu, 366
 Sutton, Steven B., 16
 Synitsin, M. V., 602
 Szabo, Gabor, 462
 Taghizadeh, Mohammad R., 100
 Takahashi, Sanyo, 694
 Takahashi, Shunsuke, 549
 Takami, Chihomi, 452
 Takenaka, Y., 210
 Takezoe, Noritaka, 394
 Tamagawa, Tohru, 92
 Taniwaki, Manabu, 293
 Tarasenko, Victor F., 148, 289
 Tarras, Ch., 386
 Tassy, I., 382
 Temelkov, Krassimir A., 72
 Terai, K., 92
 Tezuka, Takeo, 561
 Timmermans, J. C., 165
 Tittel, Frank K., 462
 Tkotz, R., 169
 Tokoro, Tomokazu, 235
 Toyoda, Koichi, 269
 Treusch, Hans-Georg, 17, 481
 Trofimovich, Andrew G., 456
 Troshchenko, G. A., 606
 Truesdell, Keith A., 544, 676, 710
 Turchanovsky, I. Y., 667
 Turichin, G., 619
 Uchiyama, Taro, 235, 549, 561
 Uehara, Minoru, 38, 436
 Uhlenbusch, Juergen, 631
 Unnebrink, Lars, 126
 Urbasch, G., 481
 Urlin, Vitali D., 510
 Uteza, O., 357, 382, 386
 van Egmond, C., 96
 van Goor, Frederik A., 165, 390
 Vannes, A. B., 748
 Velikanov, S. D., 510, 602
 Venables, Mark A., 431
 Vetovec, John, 723, 780
 Villarreal, Francisco J., 100
 Vincent, Bernard, 362
 Vlad, G., 200
 Voitik, M., 386
 Vorobjev, A. P., 598
 Voss, Frank, 485
 Vuchkov, Nikolay K., 72
 Vyskubenko, B. A., 581
 Wakasa, Yutaka, 38
 Wakefield, Clare, 655
 Walter, Robert F., 337
 Walther, S., 182, 215
 Wasilewski, Bartosz, 325
 Wasilewski, J., 277
 Watanabe, Syuichi, 736
 Watson, Ian A., 219
 Webb, Colin E., 732
 Weber, Horst, 44, 52
 Wei, Mao-Kuo, 477
 Weingartner, W., 353
 Weisheit, Andreas, 744
 Wessel, K., 88, 231
 Wheatley, David, 109
 Williams, S. W., 431
 Withford, Michael J., 68
 Witkowski, J. S., 206
 Witteman, Wilhelmus J., 165, 374, 390
 Wlodarczyk, George, 440
 Wolf, Norbert, 174
 Wollermann-Windgasse, Reinhard, 174
 Wu, Chunglei, 366
 Xie, J., 764
 Yamane, Shigeki, 210
 Yasuda, Masayuki, 235
 Yatsiv, Shaul, 104
 Yoge, Amnon, 273
 Yokotani, Atsushi, 394
 Yoshida, Kunio, 394
 Yoshihara, R., 418
 Yur'ev, Michail S., 260
 Zabelin, A. M., 134
 Zagidullin, Marsel V., 565, 690
 Zahorski, Dorian, 161
 Zapolsky, A. F., 602
 Zavalov, Yu. N., 252
 Zavalova, V. Y., 252
 Zavriyev, Anton, 56
 Zelensky, D. K., 581
 Zeyfang, E., 114
 Zheng, Cheng-En, 357
 Ziener, C., 239
 Zykov, L. I., 341